Igor L. Shabalin

Ultra-High Temperature Materials I

Carbon (Graphene/Graphite) and Refractory Metals

Springer

Ultra-High Temperature Materials I

Igor L. Shabalin

Ultra-High Temperature Materials I

Carbon (Graphene/Graphite) and Refractory Metals

A Comprehensive Guide and Reference Book

Springer

Igor L. Shabalin
Materials and Physics Research Centre
The University of Salford
Manchester
UK

ISBN 978-94-007-7586-2 ISBN 978-94-007-7587-9 (eBook)
DOI 10.1007/978-94-007-7587-9
Springer Dordrecht Heidelberg New York London

Library of Congress Control Number: 2013948865

Printed on acid-free paper

Springer is part of Springer Science+Business Media (www.springer.com)

This book is dedicated to two noble Russian ladies:

—Countess Valentina G. Getmanoff (1889–1978), one of the best military interpreters in Russia during WWII, my beloved granny

and

—Miss Vera L. Shabalin (born in 2012), my beloved granddaughter

Preface

I am a Materials Designer. During my long-term professional career, from the early 1970s till date, my particular job is to invent, explore and develop novel types and compositions of special materials for technical applications at high and ultra-high temperatures. My customers and consumers are numerous enterprises in the aerospace industry, nuclear engineering, machinery and metallurgy. With my assistance they would like to overcome the troubles, which are directly connected with the deleterious effect of high and ultra-high temperatures on various machines, mechanisms, devices and installations. In this way I have been involved in several materials design projects focused, for example, upon leading edges of anti-ballistic missiles, critical cross-sections of nozzles in rocket and torpedo motors, nuclear fuels for spacecraft power stations, thermo-electrical insulation for Hall thrusters (ion engines), refractory diaphragms for continuing casting of metals and alloys and many other apparatuses affected by the intensive thermo-mechanical and/or thermo-chemical loading, which results in fracture or severe erosion (corrosion) of the main parts. From the beginning of my career I have collected all the information about physical and chemical properties of high and ultra-high temperature substances: elements, chemical compounds, alloys and composites, which are extremely necessary for the selection of known materials as well as for the design of new ones. I believe, now it is the time to share this collection with all the specialists who are just working in the area of the ultra-high temperature applications of carbons, metals, ceramics and composites, or intend to do similar projects in the future. During the last three years I have updated considerably all my previous records on the ultra-high temperature materials and accommodated new experimental and calculated data recently obtained for these types of materials, including some last achievements of nanotechnology in this area. Thus, I would like to offer my readers and users a reference book containing the comprehensive physico-chemical description of all the substances and materials with melting (sublimation or decomposition) points around or above 2500 °C. The first volume of the book contains data on the elemental materials (carbon and refractory metals); the next volumes will include the information on chemical compounds (carbides, nitrides, oxides, borides, silicides) and complex

materials (refractory alloys, carbon and ceramics containing composites). I hope that the book will be of interest to many researchers, engineers, postgraduate and undergraduate students working or studying in the different engineering and technological areas connected with high and ultra-high temperature environments.

Also, I would like to ask everybody, who has any remarks, observations, or possibly corrections and personal opinions, concerning the book and its contents, to send them directly to my e-mail. It will be very useful for the author to take into account all these responses before publishing the next volumes.

Like any author of a scientific book, I am indebted to previous researchers and writers on ultra-high temperature materials from USA, UK, Ukraine, Russia and many other countries. However, first of all I have to acknowledge the encouragement of my colleagues and friends from Manchester and UK, who helped me to adapt to the British Academy conditions since I immigrated to the UK in 2003. I am absolutely sure that this book had no chance to appear without their kind assistance to me in continuing my career here. Since 2005 I have been supported by Prof. Keith Ross, former Director of Institute for Materials Research (University of Salford, Manchester) in all my undertaking activities in the university. Also, I would like to express my sincere gratitude to other Mancunians, my friends and colleagues: Prof. Alan Oates, Dr. Daniel Roach, Dr. Olga Umnova, Ms. Vera Barron, all from the University of Salford; Prof. Frank Sale and Prof. Kostya Novoselov from the University of Manchester; Dr. Vlad Vishnyakov and Prof. John Colligon from the Manchester Metropolitan University, as well as Oxbridge and London representatives: Prof. Richard Brook and Prof. Richard Todd from the University of Oxford; Dr. Kevin Knowles from the University of Cambridge; Prof. Xiao Guo and Prof. Mohan Edirisinghe from the University College of London; Prof. Mike Reece from Queen Mary, University of London, and finally my special thankfulness to Prof. Julie Yeomans from the University of Surrey and all our colleagues from the SCERN project.

During the preparation of the book I obtained invaluable assistance and support from my Russian and Ukrainian colleagues. So, I owe many thanks to Dr. Alexander Savvatimskiy (Joint Institute for High Temperatures, Russian Academy of Sciences, Moscow), Dr. Andrey Basharin (Institute of High Energy Density, IVTAN Scientific Association, Russian Academy of Sciences, Moscow), Prof. Rostislav Andrievski (Institute of Problems of Chemical Physics, Russian Academy of Sciences, Chernogolovka, Moscow Region), Dr. Andrey Enyashin and Dr. Irina Nikolaenko (Institute of Solid State Chemistry, Ural Branch of the Russian Academy of Sciences, Yekaterinburg), Prof. Leonid Yamshchikov and Prof. Ivan Kashcheev (Ural Federal University, Yekaterinburg), Dr. Valeriy Churkin (Samara State Aerospace University, Togliatti Branch, Samara Region), Prof. Vasily Lutsyk (Buryat State University, Ulan-Ude), Prof. George Gnesin, Dr. Anatoliy Bondar, Dr. Miron Luchka and Dr. Dmitry Schur (Institute for Problems of Materials Science, National Academy of Science of Ukraine, Kyiv),

Prof. Mikhail Turchanin (Kramatorsk Industrial Institute, Donetsk Region). I also acknowledge the permanent encouragement of my friends Prof. Yury Gogotsi (Drexel University, Philadelphia, USA), Prof. László Gömze and Dr. Ludmila Gömze (University of Miscolc, Hungary), Dr. Djamila Hourlier (Institut d'Electronique, de Microélectronique et de Nanotechnologie, Villeneuve d'Ascq, France) and Prof. Shiro Shimado (Hokkaido University, Japan).

Manchester, UK, July 2013 Igor L. Shabalin

Contents

About the Author

In his professional career Igor L. Shabalin has over 40 years experience in Ultra-High Temperature Materials Design, Science and Engineering. He was born in Russia, graduated in Technology of Less-Common Metals and received his M.Sc. and Ph.D. from the Ural Polytechnic University (UPI), Yekaterinburg (former—Sverdlovsk), Russia. He has held academic positions at the UPI and was the founder of the Special Research Laboratory for Aerospace Industry (ONIL-123). As head of the laboratory and member of several scientific councils, he established collaboration between universities and industry by running a variety of R&D projects and was involved in the management of some world leading programmes in rocketry and spacecraft development in the USSR Ministry of Aerospace Industry (MOM). In 2003, Prof. Shabalin immigrated to the UK, and joined the University of Salford, Manchester, as a researcher in Materials in 2005. He has published about 250 scientific and technical papers and holds more than 40 patents. His research focuses mainly on high and ultra-high temperature hetero-modulus ceramic composites with graphene-like (carbon and boron nitride) constituents.

Abstract

This work represents a thorough treatment of ultra-high temperature materials with melting points over 2500 °C. In the first volume are included physical (structural, thermal, electro-magnetic, optical, mechanical, nuclear) and chemical (binary, ternary and multi-component systems, solid-state diffusion, wettability, interaction with chemicals, gases and aqueous solutions) properties of elemental materials: carbon (graphene/graphite) C and refractory metals (tungsten W, rhenium Re, osmium Os, tantalum Ta, molybdenum Mo, niobium Nb and iridium Ir). It will be of interest to researchers, engineers, postgraduate, graduate and undergraduate students alike. The reader is provided with the full qualitative and quantitative assessment for the materials, which could be applied in various engineering devices and environmental conditions at ultra-high temperatures, on the basis of the latest updates in the fields of physics, chemistry, materials science, engineering and nanotechnology.

Chapter 1
Introduction

From the dawn of human existence materials have been fundamental to the development of any civilization and determined its level as a whole; that is why specialists in anthropology, archaeology and sociology define the historical epochs by the materials used by the different civilizations such as Stone, Copper, Bronze and Iron ages [1]. However, during all this historical way, the "main stream" in materials development and design has been directly connected with continuing exploration of higher and higher temperatures in the practice of human society [2]. Step-by-step due to the advancement of materials humanity has been moving from primitive aids and appliances for heating food and water up to the first wall of thermonuclear fusion reactor, from the ambient temperatures of 250–300 K to the ultra-high and super-high temperatures, which are being measured by thousands and millions of kelvins. Thus, a physical parameter such as temperature or better to say, the temperature range of materials application and exploitation has become an actual measure of the technical progress of all of human society; that was also a good reason to term high-temperature materials as strategic ones.

Certainly, whilst a "record bar" in the "competition for temperatures" has been rising, the definition of "high-temperature" has changed considerably. On the basis of the currently achieved level in our knowledge and engineering practice, the most appropriate terms for the scaled temperature ranges in materials science and engineering could be arranged as follows:

0–200 K—cryogenic (additionally sectioned) temperatures;
200–300 K—ambient temperatures;
300–700 K—moderate (or middle) temperatures;
700–1500 K—elevated temperatures;
1500–2700 K—high temperatures;
2700–5000 K—ultra-high temperatures;
>5000 K—super-high temperatures.

Thus the purpose of the book you have just opened is to give a comprehensive answer (with analysis) to the question of what materials or constituents of materials we have to use in machines, mechanisms, installations and devices, which are

I. L. Shabalin, *Ultra-High Temperature Materials I*,
DOI: 10.1007/978-94-007-7587-9_1, © Springer Science+Business Media Dordrecht 2014

Table 1.1 Melting points T_m (°C) of chemical elements in the periodic table [3, 4]

1/IA	2/IIA	3/IIIB	4/IVB	5/VB	6/VIB	7/VIIB	8/VIIIa	9/VIIIb	10/VIIIc	11/IB	12/IIB	13/IIIA	14/IVA	15/VA	16/VIA	17/VIIA	18/VIIIA
H																	**He**
–259																	–272
Li	**Be**											**B**	**C**	**N**	**O**	**F**	**Ne**
181	1278											2300	3930	–210	–218	–220	–249
Na	**Mg**											**Al**	**Si**	**P**	**S**	**Cl**	**Ar**
98	650											660	1410	44	112	–101	–189
K	**Ca**	**Sc**	**Ti**	**V**	**Cr**	**Mn**	**Fe**	**Co**	**Ni**	**Cu**	**Zn**	**Ga**	**Ge**	**As**	**Se**	**Br**	**Kr**
64	839	1539	1660	1890	1857	1245	1535	1495	1453	1083	420	30	937	817	217	–7	–157
Rb	**Sr**	**Y**	**Zr**	**Nb**	**Mo**	**Tc**	**Ru**	**Rh**	**Pd**	**Ag**	**Cd**	**In**	**Sn**	**Sb**	**Te**	**I**	**Xe**
39	764	1523	1852	2470	2620	2200	2250	1966	1552	962	321	157	232	630	450	114	–112
Cs	**Ba**	**La***	**Hf**	**Ta**	**W**	**Re**	**Os**	**Ir**	**Pt**	**Au**	**Hg**	**Tl**	**Pb**	**Bi**	**Po**	**At**	**Rn**
29	725	920	2150	3000	3410	3180	3050	2450	1772	1064	–39	304	328	271	254	302	–71
Fr	**Ra**	**Ac****	**Rf**	**Db**	**Sg**	**Bh**	**Hs**	**Mt**	**Ds**	**Rg**	**Cn**	**Uut**	**Fl**	**Uup**	**Lv**	**Uus**	**Uuo**
27	700	1050	2100	?	?	?	?	?	?	?	?	?	?	?	?	?	?

*	**Ce**	**Pr**	**Nd**	**Pm**	**Sm**	**Eu**	**Gd**	**Tb**	**Dy**	**Ho**	**Er**	**Tm**	**Yb**	**Lu**
	795	935	1010	1042	1072	822	1311	1360	1412	1470	1522	1545	824	1656
**	**Th**	**Pa**	**U**	**Np**	**Pu**	**Am**	**Cm**	**Bk**	**Cf**	**Es**	**Fm**	**Md**	**No**	**Lr**
	1750	1600	1132	640	640	994	1340	986	900	860	1527	827	827	?

exploiting in stationary or non-stationary conditions at temperatures of around 2500 °C and higher, up to the edge of the existence area of solid substances.

If you look at the periodic table (Table 1.1), you will find only eight chemical elements with the melting points met the requirements mentioned above; so, only the atoms of carbon (C) and termed as refractory metals tungsten (W), rhenium (Re), osmium (Os), tantalum (Ta), molybdenum (Mo), niobium (Nb) and iridium (Ir) can form the elemental substances and materials, which are solid at the temperature of 2700 K or around 2500 °C.

However, the chemical bonding between heterogeneous atoms can realize the structures, which are "energetically" much stronger than elemental substances. Such chemical compounds as carbides, nitrides, oxides, borides, silicides and phosphides (Table 1.2) have often higher melting points than pure elements that have been proved out by the variety of persuasive examples:

tantalum carbide (TaC_{1-x}) and hafnium carbide (HfC_{1-x}) have higher melting points than that of carbon, these chemical compounds are the actual "champions" in this property among all the solids;
niobium carbide (NbC_{1-x}) and zirconium carbide (ZrC_{1-x}) have higher melting points than those of all the refractory metals including W, Re, Os and others;
hafnium nitride ($HfN_{1\pm x}$), hafnium diboride ($HfB_{2\pm x}$) and some hafnium intermetallides (e.g. $Hf_5Re_{24\pm x}$, $HfRe_{2\pm x}$, $HfW_{2\pm x}$) have considerably higher melting points than that of hafnium metal (Hf);
refractory oxides of thorium, hafnium, uranium, magnesium, cerium, zirconium, beryllium, calcium (ThO_{2-x}, γ-HfO_{2-x}, UO_{2+x}, MgO, CeO_{2-x}, γ-ZrO_{2-x}, BeO, CaO) have considerably higher melting points than those of corresponding metals (elements).

Table 1.2 Ultra-high temperature phases: chemical elements and compounds [4–8]

T_m,°C	Elements	Carbides	Nitrides	Oxides	Borides	Silicides	Sulphides	Phosphides	Intermetallides
↑4000–		TaC_{1-x}							
↑3900–	C	HfC_{1-x}							
↑3800–									
↑3700–									
↑3600–		NbC_{1-x}							
↑3500–		ZrC_{1-x}							
↑3400–	W								
↑3300–		β-$Ta_{2\pm x}C$	$HfN_{1\pm x}$						
↑3200–				ThO_{2-x}	$HfB_{2\pm x}$				
↑3100–	Re				$TaB_{2\pm x}$				$Hf_5Re_{24\pm x}$, $HfRe_{2\pm x}$
↑3000–	Os, Ta	γ$Nb_{2\pm x}C$, TiC_{1-x}	δ-TaN_{1-x}, $ZrN_{1\pm x}$,		$ZrB_{2\pm x}$, $NbB_{2\pm x}$				$W_2Re_{3\pm x}$, $OsW_{3\pm x}$
↑2900–			α-BN, δ-$TiN_{1\pm x}$	γ-HfO_{2-x}	$TiB_{2\pm x}$				
↑2800–		α, β-SiC, VC_{1-x}	UN_{1-x}	UO_{2+x}, MgO					$TaRe_{3\pm x}$, $ZrRe_{2-x}$
↑2700–		γ-$W_{2\pm x}C$, δ-$WC_{1\pm x}$	$ThN_{1\pm x}$	CeO_{2-x}, γ-ZrO_{2-x}					$NbRe_{3\pm x}$, Ta_2Re_{3-x}
↑2600–	Mo	γ-ThC_{2-x}	YN_{1-x}, ScN_{1-x}	CeO	$W_{2\pm x}B$, β-$WB_{1\pm x}$				Ti_5Re_{24}, $Mo_2Re_{3\pm x}$
↑2500–		β-UC_{2-x}	PuN_{1-x}	BeO, CaO	βMo$B_{1\pm x}$ $LaB_{6\pm x}$,	β-Ta_5Si_3, βNb_5Si_{3+x}	ThS	UP, PuP	Nb_2Re_{3-x}, Sc_5Re_{24}
	Nb, Ir	$UC_{1\pm x}$	(RE)N_{1-x}	SrO	ThB_4, $UB_{2\pm x}$	Hf_3Si_2	US, CeS	(RE[a])P	$HfW_{2\pm x}$, YRe_2

[a] RE – rare-earth elements

The distribution of ultra-high and high temperature ($T_m > \sim 2000$ K) phases (chemical elements and compounds) in accordance with their types and melting points is given in Table 1.3 [4].

Knowledge of the general totality of properties in a wide range of temperatures is very important for the preliminary selection and/or subsequent technical application of ultra-high temperature materials in practice. In this reference book for each individual material being considered, a section devoted to its structural features forestalls the description of its physical and chemical properties. The physical properties of all the ultra-high temperature materials (elements, chemical compounds, alloys and composites) are presented in four sections: thermal,

Table 1.3 Distribution of ultra-high and high temperature phases (chemical elements and compounds) in accordance with their types and melting points [4][a]

Melting point, °C	Elements[b]	Carbides	Nitrides	Oxides	Borides, borocarbides	Silicides	Sulphides, oxysulphides	Phosphides	Intermetallides and others	Total
3700–4100	1 (**C**)	2	–	–	–	–	–	–	–	3
3300–3700	1 (**W**)	2	–	–	–	–	–	–	–	3
2900–3300	3 (**Re**, **Os**, **Ta**)	3	5	1	9	–	–	–	5	26
2500–2900	1 (**Mo**)	14	6	14	20	4	1	3	10	73
2100–2500	7 (**Nb, Ir,** B, Ru, Tc, Hf, Rf)	27	21	59	69	12	25	6	34	260
1700–2100	6 (Rh, V, Cr, Zr, Pt, Th)	41	13	50	61	21	74	21	45	332
Total	19	89	45	124	159	37	100	30	94	697

[a] The range of ultra-high temperatures is shaded grey

[b] The elements, which are included for consideration in this reference book, are marked in bold

electro-magnetic and optical, physico-mechanical and nuclear physical properties. The chemical behaviour of the materials is demonstrated in a special section mainly by the analysis of binary, ternary and multicomponent systems with its participation. All these sections on structural features and physical and chemical properties form a chapter or sub-chapter to describe each of individual ultra-high temperature materials comprehensively. Some data on materials are grouped under general table headings in the Addendum where you can also find the summarized data on all the materials included in the book, which are mainly based on the information given in the main chapters. This order allows making all the kinds of comparison, which are extremely necessary for solving materials selection problems.

The full amount of data on the structures and properties of ultra-high temperature materials collected in this reference book is quite large, so it has been decided to divide all the information into three parts (volumes). The first volume is devoted to the elemental materials, which are listed in order of decreasing melting points of elements—from carbon to iridium. The next volumes will include data on ultra-high temperature chemical compounds (carbides, nitrides, oxides, borides, silicides) listed in the same order and complex materials (refractory alloys, carbon and ceramics containing composites).

For better understanding the nature of ultra-high temperature materials, level of our knowledge in this area and perfect systematization of this type of engineering materials some novel approaches to the description of the materials have been applied in the reference book:

the intervals of temperatures and compositions for the melting and invariant equilibria points, homogeneity ranges and thermal stability regions of constituent phases in binary, ternary, quaternary and multicomponent systems containing ultra-high temperature materials are given taking into account the minimal and maximal values (data spread) available in the literature;
all the constituent phases considered in the book in the systems containing ultra-high temperature materials are provided with the chemical formulae, which always (!) contain stoichiometry indices (in spite of the fact that sometimes these indices are only approximate) with some kind of the indication of deviation (plus, or minus, or plus-minus) from the strict stoichiometric ratio, but sometimes these phase significations are also provided with ancient Greek letters earlier applied in materials science for the identification of phase modifications or rarely for the only (unique) identification of the phase (more often the unique phase identification was established for intermetallic phases; however, in this reference book, for example, instead of simple "χ" the formula "χ-WRe_{3-x}" is applied in the text everywhere, and so on in accordance with this approach);
all the data on ultra-high temperature materials, which are not accurate enough, or sometimes doubtful in author's opinion, have been provided with tilde ($\sim$) or question mark (?).

The author hopes that these approaches would be judged by readers and users only positively.

As the requirements to the properties and behaviour of ultra-high temperature materials in practice spread within the whole area from cryogenic to ultra-high temperatures, some systems containing these materials, which are related actually to lower temperature ranges, have been included for the thorough consideration in the reference book too. The reason for this is explained by the fact that knowledge of these systems became often very important for the foundation of efficient technologies in the production and manufacture of ultra-high temperature materials in the industry.

References

1. Ferguson C (2008) Historical introduction to the development of materials science and engineering as a teaching discipline. The Higher Education Academy, UK Centre for Materials Education, Liverpool
2. Gnesin GG (2010) Materials scientists: researchers, engineers, inventors. Logos, Kyiv (in Russian)
3. Bentor Y (2012) Chemical Elements.com. An online interactive periodic table of the elements: melting point. http://www.chemicalelements.com/show/meltingpoint.html. Accessed 20 June 2013
4. Kotelnikov RB, Bashlykov SN, Galiakbarov ZG, Kashtanov AI (1968) Osobo tugoplavkie elementy i soedineniya (Extra refractory elements and compounds). Metallurgiya, Moscow (in Russian)
5. Hague JR, Lynch JF, Rudnick A, Holden FC, Duckworth WH (1964) Refractory ceramics for aerospace: materials selection handbook. Battelle Memorial Institute, American Ceramic Society, Columbus
6. Samsonov GV, Vinitskii IM (1980) Handbook on refractory compounds. IFI/Plenum, New York
7. Andrievskii RA, Spivak II (1989) Prochnost tugoplavkikh soedinenii i materialov na ikh osnove (Strength of refractory compounds and materials based on them). Metallurgiya, Chelyabinsk (in Russian)
8. Kosolapova TYa (ed) (1990) Handbook of high-temperature compounds: properties, production and applications. Hemisphere, New York

Chapter 2
Carbon (Graphene/Graphite)

2.1 Structures

Carbon is the sixth element of the periodic table with the ground state level $^3P_0$ and electron configuration $1s^2 2s^2 2p^2$, which is hybridized to form sp^1, sp^2 and sp^3 chemical bonds between atoms. The general oxidation states (numbers) of carbon in numerous inorganic compounds are (−4) (+4) and (+2); the radii of carbon are:

atomic (metallic, CN = 12)—0.091 nm,
atomic (van der Waals)—0.170 nm,
atomic (covalent)—various, see Table 2.1,
ionic (+4)—0.015 nm (CN = 4) or 0.016 nm (CN = 6);

its electronegativity is 2.55 in Pauling scale, or 2.50 in Allred–Rochow scale. The hybridized sp^n-bonding ($1 \leq n \leq 3$) differs considerably from common *s*- or *p*-bonds inherent to other chemical elements of the basic periods. The values of energy characteristics, in particular, specific bond energies (average bond energy per bond order) of carbon–carbon sp^n-bonds occupy a wide area of intermediate positions between those characteristics of *s*- and *p*-elements, depending substantially on the hybridisation type of bonding: $s > sp^3 > sp^2 > sp^1 > p$ (Table 2.1). The electron hybridization predetermines the ability of carbon atoms to arrange numerous compounds with other elements of the periodic table, but also the various allotropes, such as carbyne/carbyte, graphene/graphite and diamond (Table 2.2), which are structured with linear, planar and tetrahedral symmetry, coordination numbers of 2, 3 and 4 and the bond angles of 180°, 120° and 109.47°, respectively for sp^1-, sp^2- and sp^3-hybridized forms. According to Mendeleev "none of the elements can compete with carbon in ability to form complex structures" [1, 540].

There has been a new wave of interest in carbon materials caused by the recent discoveries in the nanoscience [2, 9–14, 31, 42, 45–53], which has affected all science and engineering fields. Some points of view are developed in literature to classify carbon macro- and nanostructures. In this way, schemes based on hybridization characteristics were suggested by McEnaney [9], Heimann et al. [10],

I. L. Shabalin, *Ultra-High Temperature Materials I*,
DOI: 10.1007/978-94-007-7587-9_2,

Table 2.1 Comparative atomic bonding characteristics of *s*- and *p*-elements of the periodic table [2–9]

Outer electronic configuration	Bond type (examples)	Bond order	Specific bond enthalpy[a], kJ mol^{-1}	Bond length, nm	Covalent atomic radius, nm	Frequency,[b] cm^{-1}	Force constant,[b] N/m
s	H–H	1	435	–	–	–	–
	Hydrogen molecule			0.074	0.030		
sp^3	C–C	1	369	–	–	997	3.5
	Diamond			0.154	–		
	sp^3–sp^3 (6 peripheral atoms in total)			0.153[c]	0.077		
	sp^3–sp^2 (5 peripheral atoms in total)			0.151[c]	–		
	sp^3–sp^1 (4 peripheral atoms in total)			0.149[c]	–		
	sp^2–sp^2 (4 peripheral atoms in total)			0.146[c]	0.073		
	sp^2–sp^1 (3 peripheral atoms in total)			0.143[c]	–		
	sp^1–sp^1 (2 peripheral atoms in total)			0.138[c]	0.069		
sp^2 (aromatic)	C=C	1.5	345	–	–	–	–
	Graphene			0.142	0.071		
	Benzene (4 peripheral atoms in total)			0.140	–		
sp^2	C=C	2	306	–	–	1620	9.3
	sp^2–sp^2 (4 peripheral atoms in total)			0.134[c]	0.067		
	sp^2–sp^1 (3 peripheral atoms in total)			0.132[c]	–		
	sp^1–sp^1 (2 peripheral atoms in total)			0.128[c]	0.064		
sp^1	C≡C	3	279	–	–	2100	15.6
	Carbyne			0.128	–		
	sp^1–sp^1 (2 peripheral atoms in total)			0.121[c]	–		
p	F–F	1	159	–	–	–	–
	Fluorine molecule			0.141	0.071		

[a] Average bond enthalpy per bond order
[b] From infrared absorption and combination scattering spectra data
[c] Average values

Table 2.2 Systematic classification of carbon nano- and macrostructures

Hybridisation types (proposed terms)	Existing (or predicted) structural forms of carbon				References
	Nanostructures			Macrostructures	
	Submolecular	Molecular (mesostructures)	Supramolecular		
σ-$sp^1 + 2\pi$ (carbyne general family)	Short polyyne and polycumulene chains	α- and β-Carbyne[a] (methine[b])	Carbyne nanobundles Carbyne nanorings "Chain armour" structures	Carbyte[c] (carbolite, crystal forms of carbynes and their polytypes)	[9, 10, 15–20]
$(\sigma\text{-}sp^1 + 2\pi) - (\sigma\text{-}sp^2 + \pi)$ or $\sigma\text{-}sp^{1<n<2} + (3–n)\pi$ (graphyne intermediate family)[e]	Nanographynes (?) Graphyne nanoribbons (?)	Graphynes Graphdiynes Graphynes-n Supergraphene	Bilayered graphyne Multi-layered graphynes (?)	α,β,γ-Graphyte[d] (various polytypes) Intermediate graphite (graphene) to carbyte (carbyne) transition phases (?)	[21–29, 53, 179, 187, 694]
$\sigma\text{-}sp^2 + \pi$ (graphene general family)	Nanographenes Graphene nanoribbons	Graphene	Bilayered graphene Multi-layered graphenes Expanded nano-platelets Nanofiber (nanowire, nanorods)	Graphite (H- and R-polymorphs/polytypes) Natural graphite Kish graphite Pyrolitic graphite Expanded (exfoliated) graphite Carbon (graphite) fiber Carbon (graphite) clothes, fabrics and prepregs (woven or non-woven)	[11, 30–44, 74–85, 136–138, 676, 694]
$(\sigma\text{-}sp^2 + \pi) - \sigma\text{-}sp^3$ or $\sigma\text{-}sp^{2<n<3} + (3 - n)\pi$ (fullerene intermediate family)[e]	Nanoclusters of conjugated pentagon and hexagon cycles	Fullerenes (buckminsterfullerene C_{60} and other forms in C_{2n} series with $n = 10, 12, 13, 14, \ldots$, e.g. C_{20}, C_{22}, C_{24}, C_{26}, C_{28}, C_{30}, C_{32}, C_{34}, C_{36}, C_{38}, C_{40}, C_{42}, C_{44}, C_{46}, C_{48}, C_{50}, C_{52}, C_{54},	Fullerene rings Fullerene nanotubes Fullerene nanowhiskers (fullerene nanofibers) Nanobeads ("pearl necklace" structures) Fullerene polymers	Fullerites (polymorph forms of fullerene molecular crystals and fullerene polymers) Nanotubular crystals (nanotube yarn) Nanotube lattices	[21, 42, 45–71, 75, 86–167, 649–652, 669–676, 682–688, 694–699]

(continued)

Table 2.2 (continued)

Hybridisation types (proposed terms)	Existing (or predicted) structural forms of carbon				References
	Nanostructures			Macrostructures	
	Submolecular	Molecular (mesostructures)	Supramolecular		
		C_{56}, C_{58}, C_{70}, C_{72}, C_{76}, C_{78}, C_{82}, C_{84}, C_{90}, C_{94}, C_{120}, C_{240}, C_{540}, C_{960}, etc.)	Hyperfullerenes (multi-walled fullerenes, onion-like fullerenes, "Russian doll" structures)	Haeckelites (pentaheptites, octites)	
		Single-walled nanotubes (zigzag, arm-chair and intermediate chiral configurations)	Fullerene intercalated graphite compounds	Schwarzites	
		Capped (closed) single-walled nanotubes	Astralens	Soot	
		Defective single-walled nanotubes	Double-walled nanotubes	Carbon black (channel black, thermal black, lamp black, acetylene black)	
		Nanotubes (nanoscrolls) with polygonal cross-sections	Multi-walled nanotubes	Defected graphite (armchair prismatic edge dislocations)	
		Nanoscrolls (whiskers, "Swiss roll" structures)	Capped (closed) multi-walled nanotubes	Defected graphite (zig-zag prismatic edge dislocations)	
		Nanobarrels	Defective multi-walled nanotubes	Amorphous carbon	
		Nanocones	Nanohorn particles	Pyrolytic carbon	
		Nanodisks	Megatubes	Coke	
		Nanobreadsticks	Giant nanotubes	Charcoal	
		Toroids (toroidal cages)	Supertubes	Activated carbon	
		Helical nanocoils (coiled cages)	Nanotube bundles (ropes, strands)	Molecular-sieve carbon	
		Squarographenes	Nanofiber (nanowire, nanorods)	Carbon (amorphous) fiber	
		Glitter	Nanotube lattices	Carbon (amorphous) clothes, fabrics, felts, prepregs	
			Nanobuds	Aerogel (cryogels, xerogels)	
			Nanopeapods	Glassy (vitreous) carbon	
			Nanofoams (glitter-like and defected graphene-like networks)	Glassy (vitreous) carbon foam	
				Carbon bead powder (mesocarbon microbeads)	
				Carbide derived carbon	

(continued)

Table 2.2 (continued)

Hybridisation types (proposed terms)	Existing (or predicted) structural forms of carbon				References
	Nanostructures			Macrostructures	
	Submolecular	Molecular (mesostructures)	Supramolecular		
			Ortho-graphite-diamond hybrids Para-graphite-diamond hybrids Hexagonite (based on barrelene fragment molecules) Haeckelones Schwarzones	Diamond-like carbon films n-diamond (or γ-carbon, shock-compressed graphite phase) i-carbon (shock-compressed graphite phase) Intermediate graphite-to-diamond transition phases	
σ-sp^3 (diamond general family)	Diamondoids Ultra-nanocrystalline (ultra-dispersed) particulate diamond	Nanocrystalline particulate diamond Diamond nanorods Diamond nanotubes Diamond nanowhisckers Diamond nanocylinders Diamond nanocones Diamond nanoplatelets	Ultra-nanocrystalline aggregated diamond Nanocrystalline aggregated diamond Aggregated diamond nanorods (hyperdiamond) Diamond nanofiber (filaments) Ultra-nanocrystalline diamond films Polycrystalline diamond nanopowder Carbide derived diamond-structured carbon	Diamond (3C-diamond) single crystal (or polycrystalline) Lonsdaleite (hexagonal diamond, H- and R-polytypes) Hexagonite (cold compressed nanotubes) Diamond D_5 Lonsdaleite L_5 Octacarbon (supercubane, prismane, BC8, ?)	[6, 9, 13, 42, 53, 72, 78, 168–177, 666–668]

[a] Despite many publications on various carbyne types, the existence of this allotrope has not been universally accepted [73]
[b] According to IUPAC recommendation, the term "methine" has to replace "carbyne", as the latter one is used to term an organic radical
[c] The term "carbyte" is suggested for carbyne crystal forms by analogy with "graphene–graphite" and "fullerene–fullerite" correlations
[d] The term "graphyte" is suggested for graphyne crystal forms by analogy with "graphene–graphite" and "fullerene–fullerite" correlations
[e] σ-sp^m and σ-sp^n indicate intermediate carbon forms with a non-integer degree of carbon bond hybridization

Inagaki [11], Belenkov [12], Shenderova et al. [13, 78] and Falcao and Wudl [14]. The systematic classification of all the experimentally confirmed and theoretically predicted carbon structures, which is given in Table 2.2, is based mainly on the relative values of the specific bond energies of sp^n-hybridized carbons as well as carbon phase transformation diagram (see Sect. 2.2). This approach, employing within the overall hierarchy of classified carbon structures from submolecular to macroscopic scales, in accordance to the bonding energy criteria, allows marking out among the variety of carbon structures three general families (with integer degree of hybridisation index n):

carbyne general family ($n = 1$), including sp^1-hybridized (σ-$sp^1 + 2\pi$) carbons from nanostructured carbyne to its macrostructural crystalline form "carbyte" (the existence of carbyne (or carbolite) has not been universally accepted; the proposed term for a macrostructural form is given on the basis of analogy with graphene–graphite and fullerene–fullerite correlations);
graphene general family ($n = 2$), including sp^2-hybridized (σ-$sp^2 + \pi$) carbons from nanostructured graphene to macrostructural crystalline graphite with its polytypic (hexagonal and rhombohedral) forms;
diamond general family ($n = 3$), including sp^3-hybridized (σ-sp^3) carbons from various nanostructured diamonds to macrostructural crystalline diamond with its polytypic (cubic and hexagonal) forms.

and two intermediate (or transitional) families (with non-integer degree of hybridisation index n):

graphyne intermediate family ($1 < n < 2$), including $sp^{1<n<2}$-hybridized (σ-$sp^{1<n<2} + (3 - n)\pi$) carbons from nanostructured graphyne (analogue of graphene modified by triple bonds) to macrostructural "graphyte" with various polytypes, which are characterized by the intermediate between carbyne and graphene hybridisation type (currently, hypothetical structures calculated and predicted only theoretically; the proposed term for a macrostructural form is given on the basis of analogy with graphene–graphite and fullerene–fullerite correlations);
fullerene intermediate family ($2 < n < 3$), including $sp^{2<n<3}$-hybridized (σ-$sp^{2<n<3} + (3 - n)\pi$) carbons from numerous species of nanostructured fullerenes and hyperfullerenes, single-walled and multi-walled nanotubes, nanoscrolls, nanobarrels, nanocones and other nanostructures to macrostructural forms, such as fullerites, nanotubular crystals, hypothetical structures of haeckelites and schwarzites, as well as plenty of carbon/carbonaceous products, such as soot, carbon black, so-called "amorphous" carbon, pyrolitic carbon, coke, charcoal, activated carbon, molecular-sieve carbons, glassy carbon, carbide derived carbons, intermediate graphite-to-diamond transition phases, diamond-like carbon films and others, which are characterized by the intermediate between graphene and diamond hybridisation type (mainly, the fullerene family structures can be considered as distorted graphene related structures, where deviation from planarity is occured because of the partial heptagons and/or pentagons substitution for hexagons in graphene networks; special measures

Table 2.3 Characteristic and structural features of allotropic, polymorphic and polytypic carbon forms

Form	Character	Structure parameters (at ambient conditions)	Density, g cm^{-3}	Thermal stability	References
Carbyne Family[a]					
α-Carbyne (methine)	1D carbon polymer with polyyne bonding $(–C\equiv C–)_n$	Max. length 3.6–4.8 nm, with larger length—degenerate into β-carbyne polycumulene chains (predicted theoretically)	–	Extremely unstable	[9–10, 15–20]
β-Carbyne (methine)	1D carbon polymer with polycumulene bonding $(=C=C=)_n$	Chains length 50–250 nm stabilized by impurities and formation of covalent bonds between chains, C–C bond length—0.128 nm (predicted theoretically)	–	Unstable	[9–10, 15–20]
Carbyne nanobundles	Aggregates of various aligned 1D carbon polymers	–	–	–	[9, 11, 16–17]
Carbyne nanorings	Hypothetical 1D and 2D structures (calculated by molecular mechanics and *ab initio* methods)	Various structures (predicted theoretically)	–	–	[19]
"Chain armour" structures	Hypothetical 3D complex structures of carbyne nanorings (calculated by molecular mechanics and *ab initio* methods)	Various structures (predicted theoretically)	–	–	[19]
Carbyte	Molecular crystal of β-carbyne arranged in hexagonal bundles	Crystal structure—trigonal (rhombohedral), space group—*P3m1*, lattice parameters: $a = b = c = 0.3580$ nm, $\alpha = \beta = \gamma = 118.5°$, $Z^c = 1$ (calculated by molecular mechanics methods)	1.36[b]	Unstable (predicted)	[20]
Carbyte (carbolite)[d]	Molecular crystal of carbyne chains (C–C bond length—0.133 nm) arranged in hexagonal bundles	Crystal structure—hexagonal, lattice parameters: $a = 1.193$ nm, $c = 1.062$ nm; interchain distance—0.344 nm (XRD)	1.46	–	[18]
Graphyne Family					
Graphynes (α-graphynes)	Hypothetical flat monolayers of atoms packed into 2D polyhexagonal lattices (basic blocks predicted for graphyne family materials)	C–C bond length—0.1421 nm, C–C (in phenyl rings) bond length—0.1428 nm, C≡C bond length—0.1202 nm (calculated by modified neglect of differential overlap (MNDO) quantum chemical method)	–	Stable (predicted)	[22, 53, 694]

(continued)

Table 2.3 (continued)

Form	Character	Structure parameters (at ambient conditions)	Density, g cm^{-3}	Thermal stability	References
Graphdiynes (β- and γ-graphynes)	Hypothetical flat monolayers of atoms packed into 2D polyhexagonal lattices, where hexagons are linked through (–C≡C–) units	–	–	–	[53, 694]
Graphynes-n	Hypothetical flat monolayers of atoms packed into 2D polyhexagonal lattices, where hexagons are linked by polyyne bonding $(–C≡C–)_n$	–	–	–	[53, 694]
Supergraphene	Hypothetical flat monolayers of atoms packed into distorted 2D hexagonal lattices, where 2/3 of all bonds are replaced by carbyne-like bonding	–	–	–	[694]
6,6,6-Graphyte (polytype with next-nearest layers eclipsed, like in graphite)	Graphynes AB-stacked into 3D structures	Crystal structure—monoclinic, space group—*Pm*, lattice parameters: $a = b = 0.686$ nm, $c = 0.672$ nm, $\gamma = 120°$, Z = 24 (calculated by MNDO quantum chemical method)	1.75	Stable at high temp. (predicted)	[22]
6,6,6-Graphyte (polytype with next-nearest-neighbour layers related by a centre of symmetry)	Graphynes ABC-stacked into 3D structures	Crystal structure—triclinic, space group—*P(-1)*, lattice parameters: $a = b = 0.686$ nm, $c = 0.760$ nm, $\alpha = 76.5°$, $\beta = 117.9°$, $\gamma = 120°$, Z = 24 (calculated by MNDO quantum chemical method)	1.75	Stable at high temp. (predicted)	[22]
Intermediate graphene-to-carbyne (graphite-to-carbyte) transition phases	?	–	–	At ultra-high temp. and pressures (predicted)	[9, 28, 179, 187]
Graphene Family					
Nanographenes	2D flat hexagonal carbon atoms ring network with open edges	Average diameter <10 nm	–	–	[30]
Graphene nanoribbons	2D thin strips of graphene or unrolled single-walled carbon nanotubes	Width is less than 50 nm and lengths—below 500 nm	–	–	[30, 74]

(continued)

Table 2.3 (continued)

Form	Character	Structure parameters (at ambient conditions)	Density, g cm^{-3}	Thermal stability	References
Graphene	Flat monolayer of atoms tightly packed into a 2D hexagonal lattice (basic block for all graphene family materials)	C–C bond length—0.142 nm	–	At higher temp. unstable with respect to scrolling	[31–38, 75, 694]
2H-Graphite (α-carbon, α-Graphite)	Graphenes AB-stacked into 3D structures (main graphite polytype)	Crystal structure—hexagonal, space group–$P6_3/mmc$, lattice parameters: $a = 0.2464$ nm, $c = 0.6711$ nm, Z = 4, interlayer spacing—0.3356 nm (neutron diffraction, XRD)	2.267	Stable, sublimates at ultra-high temp., binding energy—7.99 eV $atom^{-1}$	[41–43, 76, 676]
1H-Graphite	α-Graphite polytype with A-over-A-stacked graphenes (hypothetical)	–	–	–	[10]
10H-Graphite	α-Graphite polytype	–	–	–	[10]
12H-Graphite	α-Graphite polytype	–	–	–	[10]
3R-Graphite (β-Graphite)	Graphenes ABC-stacked into 3D structures	Crystal structure—trigonal (rhombohedral), space group–*R(-3)m*, lattice parameters: $a = b = c = 0.3635$ nm, $\alpha = \beta = \gamma = 39.49°$, Z = 2 (in hexagonal setting: $a = 0.2456$ nm, $c = 1.0039$ nm, XRD)	2.267	Completely transforms to 2H-graphite (α-graphite) at temp. 1300–2100 °C	[44, 77]
6R-Graphite	β-Graphite polytype	–	–	–	[10]
Natural graphite	Powdered aggregates composed from α- and β-graphites with β-phase content 7.5–15 %	–	2.20–2.25	–	[42–44]
Kish graphite	Graphite quasi-single crystals	–	–	Stable at high temp.	[11]
Pyrolytic graphite	Highly oriented aggregates of graphenes with some covalent bonding between graphene sheets	Composed from crystallites with deviation from perfect parallel order less than 1 % and apparent size perpendicular to the graphene planes L_c—up to 50–500 nm	2.10–2.25	Stable, sublimates at ultra-high temp.	[10, 42, 136]
Expanded nano-platelets	Nanoparticles consist of small stacks of graphene	Thickness—1–25 nm, other linear sizes—ranging from 0.1 to 100 μm, increased spacing between graphene layers	–	–	[79–81]
Expanded (exfoliated) graphite	Aggregates of graphene prepared by decomposition of intercalated graphite compounds	Increased spacing between graphene layers	10^{-3}–10^{-1} (powd.) 0.7–1.3 (packed)	Stable, sublimates at ultra-high temp.	[11, 82–83]

(continued)

Table 2.3 (continued)

Form	Character	Structure parameters (at ambient conditions)	Density, g cm^{-3}	Thermal stability	References
Carbon (graphite) fiber	Bundle of graphitic filaments with prevailing alignment of graphene sheets parallel to the fiber axis, needle-shaped voids between crystallites and sheets essentially parallel to the surface	Diameter of filaments—5–8 μm, apparent crystallite thickness L_c–6 nm and sizes L_a–15–50 nm, 2H-graphite lattice parameters: $a = 0.246$ nm, $c = 0.671$–0.687 nm, length-to-diameter ratio >100	1.5–2.2	Stable, sublimates at ultra-high temp.	[8, 42, 84–85, 127, 136–137]
Carbon (graphite) clothes, fabrics and prepregs (woven or non-woven)	(2, 2.5, 3,…n) D-components made from carbon (graphite) fiber	Variety of structures	–	Stable, sublimates at ultra-high temp.	[8, 84, 136–137]
Fullerene Family					
Fullerene C_{60} (buckminster-fullerene)	Spherical molecule with polyhedral form containing 60 atoms (most abundant)	Truncated icosahedron made of 20 hexagons and 12 pentagons (ratio of pentagon/hexagon rings—0.6) with an atom at the vertices of each polygon and a bond along each polygon edge, each atom is covalently bonded to three others, nucleus-to-nucleus diameter—0.714 nm, C–C bond lengths: between two hexagons—0.1391 nm and between a hexagon and a pentagon—0.1455 nm, pyramidalization angle (obtained from π-orbital axis vector analysis)—11.6°	–	Destruction temp. of molecule (in gas phase) >2700 °C	[42, 52, 68, 78, 86–88]
Fullerene C_{70}	Spherical molecule with polyhedral form containing 70 atoms	Polyhedron made of 25 hexagons and 12 pentagons (ratio of pentagon/hexagon rings—0.48) with an atom at the vertices of each polygon and a bond along each polygon edge, each atom is covalently bonded to three others, molecule sizes: full height (distance between 2 pentagons in mutually opposite polar areas)—0.780 nm and diameter of equator circle via atomic nuclei—0.694 nm, 8 types of C–C bonds with lengths from 0.137 to 0.147 nm, pyramidalization angle—10.7°	–	Destruction temp. of molecules (in gas phase) >2700 °C	[42, 52, 68, 86–88]

(continued)

Table 2.3 (continued)

Form	Character	Structure parameters (at ambient conditions)	Density, g cm^{-3}	Thermal stability	References
Fullerene C_{32}	Spherical molecule with polyhedral form containing 32 atoms	Polyhedron made of hexagons and pentagons (ratio of pentagon/hexagon rings—2)	–	–	[51–52, 68, 78, 86–88]
Fullerene C_{28}	Spherical molecule with polyhedral form containing 28 atoms	Polyhedron made of hexagons and pentagons (ratio of pentagon/hexagon rings—3)	–	–	[51–52, 68, 78, 86–88]
Fullerene C_{20}	Spherical molecule with polyhedral form containing 20 atoms	Polyhedron made of pentagons (ratio of pentagon/hexagon rings—∞)	–	–	[51–52, 68, 78, 86–88]
Fullerenes in C_{2n}-series (buckyballs, carbon cages)	Variety of spherical molecules with polyhedral forms containing $2n$ ($n = 10$, 12, 13, 14, 15…) atoms	Various polyhedral structures with pyramidalization angles in the range of 0° (graphene, sp^2-bonding) to 19.5° (diamond, sp^3-bonding) …	–	–	[42, 51–52, 58, 68, 78, 86–88]
Fullerene rings	Variety of C_{2n}-polymerized 2D ring-based structures	E.g., $(C_{60})_n$-rings with number of members $n = 3$–8	–	Stable (predicted)	[106]
Fullerene nanotubes	Tubular thin fiber composed of C_{2n} molecules or their derivatives	E.g., C_{60}- or C_{70}-, or C_{60}-C_{70}-two-component nanotubes with diameter of ~0.24–1.5 μm and length of ~5–60 μm; crystal structure—hexagonal in solvated forms and cubic (face-centred) after losing the contained solvent molecules	–	Stable, decompose in air at temp. >415 °C	[651–652]
Fullerene nanowhiskers (fullerene nanofibers)	Single crystalline nanofibers composed of C_{2n} molecules with non-tubular morphologies	E.g., C_{60}- or C_{70}-nanowhiskers (needle-like crystals) with diameter from 80 nm up to ~1 μm and length from ~1–10 μm up to ~1–10 mm; crystal structure—hexagonal in solvated forms and cubic (face-centred) after losing the contained solvent molecules	–	Stable, decompose in air at temp. >450 °C	[649–650, 652]
Nanobeads (“pearl necklace” structures)	Quasi-1D-structures based on fullerenes, in particular, small fullerenes C_{2n} ($2n < 60$)	Participation of ordinary, double, ternary, etc. chains of carbon atoms bonding vertices, edges and faces of neighbouring fullerenes	–	–	[53]
Fullerene polymers	Variety of C_{2n}-polymerized structures such as dimmers, trimers,…, 1D chains and 2D lattices	E.g., $(C_{60})_n$ 2D orthorhombic, tetragonal and hexagonal (rhombohedral) lattices are bonded by the combination of parallel double bonds on adjacent molecules with intermolecular spacing reduced	–	Stable, decompose in air at temp. >470 °C	[55, 90, 91, 652]

(continued)

Table 2.3 (continued)

Form	Character	Structure parameters (at ambient conditions)	Density, g cm^{-3}	Thermal stability	References
Fullerites C_{60}	Molecular crystals of C_{60} fullerenes and/or C_{60} fullerene polymers or 3D C_{60} fullerene polymers	Crystal structure—cubic (simple), space group–*Pa(-3)*, lattice parameter: $a = 1.404$ nm, Z = 240 (neutron diffraction)	1.729	Stable at lower temp.	[92]
		Crystal structure—cubic (face-centred), space group—*Fm(-3)m*, lattice parameter: $a = 1.416$ nm, Z = 240 (XRD)	1.686	Stable, melting point >280 °C, sublimates at 530 C^{oe}	[93]
		Crystal structure—cubic (face-centred), space group—*Fm(-3)*, lattice parameter: $a = 1.426$ nm, Z = 240 (electron diffraction)	1.651	Stable, melting point >280 °C, sublimates at 530 C^{oe}	[94]
		Crystal structure—orthorhombic (tetragonal), space group—*Immm*, lattice parameter: $a = 0.909$ nm, $c = 1.495$ nm, Z = 120 (calculated)	1.938	Stable under high pressures	[95]
		Crystal structure—orthorhombic (tetragonal), space group—*Immm*, lattice parameter: $a = 0.9026$ nm, $b = 0.9083$ nm, $c = 1.5077$ nm, Z = 120 (XRD)	1.937	–	[96]
		Crystal structure—trigonal (rhombohedral), space group–*R(-3)m*, lattice parameters: $a = 0.9175$ nm, $c = 2.4568$ nm, Z = 180 (XRD)	2.005	–	[97]
		Crystal structure—tetragonal, space group—$P4_2/mmc$, lattice parameter: $a = 0.9064$ nm, $c = 1.5039$ nm, Z = 120 (XRD)	1.938	–	[98]
Fullerites C_{70}	Molecular crystals of C_{70} fullerenes and/or C_{70} fullerene polymers or 3D C_{60} fullerene polymers	Crystal structure—orthorhombic, space group—*Pnma*, lattice parameter: $a = 1.0016$ nm, $b = 1.7349$ nm, $c = 1.853$ nm, Z = 280 (XRD)	1.734	Stable at lower temp.	[99]
		Crystal structure—orthorhombic, space group—*Cmcm*, lattice parameter: $a = 1.7303$ nm, $b = 0.9990$ nm, $c = 1.7924$ nm, Z = 280 (XRD)	1.802	Stable at lower temp.	[100]

(continued)

Table 2.3 (continued)

Form	Character	Structure parameters (at ambient conditions)	Density, g cm^{-3}	Thermal stability	References
Fullerites C_{28}	Molecular crystals of C_{28} fullerenes and/or C_{28} fullerene polymers or 3D C_{28} fullerene polymers, including lattices similar to diamond and lonsdaleite (so-called hyperdiamonds and hyperlonsdaleites)	–	1.10 (hyperdiamond)	–	[697]
Self-intercalated fullerites C_{28}	Hypothetical 3D C_{28} fullerene network formed on the basis of hyperdiamonds, when two similar lattices inserted into one another	–	2.18	–	[697]
Fullerite C_{20}	Molecular crystals of C_{20} fullerenes and/or C_{20} fullerene polymers or 3D C_{20} fullerene polymers	Crystal structure—cubic (body-centred), space group—*Im(-3)*, lattice parameter: $a = 0.6897$ nm, $Z = 40$ (calculated by density-functional-based tight-binding (DFTB) method)	2.431	–	[101]
Fullerites C_{2n}	Molecular crystals of C_{2n} fullerenes and/or C_{2n} fullerene polymers or 3D C_{2n} fullerene polymers	Variety of different structures	–	–	[50, 91, 101]
Hyperfullerenes (multi-walled fullerenes, onion-like fullerenes, buckyonions or "Russian doll" structures)	Spherical nanoparticles based on multiple atomic layers surrounding an initial fullerene core	E.g., $C_{60}@C_{240}$, $C_{60}@C_{240}@C_{540}$, $C_{60}@C_{240}@C_{540}@C_{1500}$,…, outer diameter—from 10 nm to 1 μm, inner diameter for C_{60}–0.7–1.0 nm, interlayer spacing for $C_{60}@C_{240}$–0.3524 nm (calculated)	–	–	[50, 68, 78]
Astralens	Polyhedral multi-shell fullerene-like nanoparticles consist of large defect-free flat graphitic faces connected by defective edge regions presumably pentagon-like structured	Particles average size ~40 nm and its graphitic faces sizes ~15 nm (stacking of 20–50 graphene sheets with interlayer spacing ~0.340 nm)	2.1–2.3	–	[57]
Fullerene intercalated graphite compounds	Graphene/C_{60} (or C_{70}), $(C_{60})_n$-clusters/graphene systems, where the surface contacts between fullerene "quasi-spheres" and graphene sheets are reduced to "point-like contacts"	For C_{60} intercalated graphite compound—interlayer spacing ~1.3 nm (TEM), for $(C_{60})_{14}$-cluster graphite compound the formation of 2 parallel 7-fullerene monolayers for 2.2–2.7 nm spacing is predicted theoretically	–	–	[698–699]

(continued)

Table 2.3 (continued)

Form	Character	Structure parameters (at ambient conditions)	Density, g cm^{-3}	Thermal stability	References
Single-walled nanotubes (buckytubes, SWCNT)	Cylindrical tube-like molecules with atoms tightly packed into a 2D hexagonal lattice	Molecular diameter—0.43–100 nm (typical—1–10 nm), length: typical—from 50 nm to 1 μm and max.—up to centimetre scale, max. length-to-diameter ratio—up to 1.32×10^8:1	–	Stable at ultra-high temp.	[58–59, 68, 78, 104–106]
SWCNT capped (closed)	Cylindrical tube-like molecules with atoms tightly packed into a 2D hexagonal lattice with the ends capped by hemispheres of the fullerene structures	–	–	–	[58, 105]
Defective SWCNT	Cylindrical tube-like molecules with the defects in 2D hexagonal lattices (bent and toroidal tube-like structures)	Variety of different forms	–	–	[111]
Double-walled nanotubes (DWCNT)	Assemblies of two concentric cylindrical tube-like molecules with atoms tightly packed into a 2D hexagonal lattice	Outer molecule diameter—3–5 nm, interlayer (intertube) spacing—$\sim$0.39 nm	–	–	[58]
Multi-walled nanotubes (MWCNT)	Assemblies of several (up to 50 and even more) concentric cylindrical tube-like molecules with atoms tightly packed into a 2D hexagonal lattices	Outer molecule diameter—from 2.5 to 80 nm (the diameter of thinnest armchair (2,2)-type nanotube inside a multi-walled nanotube—0.3 nm), length (typical)—from 10 nm to 1 μm, interlayer (intertube) spacing—about 0.34 nm	–	Stable at ultra-high temp.	[58, 68, 78, 103–105]
MWCNT capped (closed)	Assemblies of concentric cylindrical tube-like molecules with atoms tightly packed into a 2D hexagonal lattice with the ends capped by hemispheres of the fullerene structures	–	–	–	[58]
Defective MWCNT	Assemblies of concentric cylindrical tube-like molecules with the defects in 2D hexagonal lattices (bent and L-, Y- and T-branched and helical multi-layered tube-like and bamboo-like structures)	Variety of forms, containing either topological (pentagon-heptagon) defects or structural (discontinuous or cone-shaped walls or bamboo structures)	–	–	[111]

(continued)

Table 2.3 (continued)

Form	Character	Structure parameters (at ambient conditions)	Density, g cm^{-3}	Thermal stability	References
Nanotubes (nanoscrolls) with polygonal cross-sections	1D needle-like molecules or assemblies of these molecules (with non-symmetric 2D hexagonal lattice fringes) shaped as twisted polygons	Outermost diameter of 10–50 nm, while the internal channel diameter varies in the range of 2–10 nm	–	–	[105, 145–147]
Nanobarrels	Imperfect cylindrical nanotubes with barrel-like forms	–	–	–	[53, 71]
Nanohorn particles	Spherical aggregates of capped SWCNTs	With average diameter—80–100 nm (each individual tube with diameter—2–3 nm and cap cone angle of 120°)	–	–	[113–114]
Megatubes	Self-assembled structures formed by branched nanotubes	Exceeding 5 μm in diameter	–	Stable	[89]
Giant nanotubes	Self-assembled knitted structures formed by nanotubes	With average sizes 5 μm in diameter and 100 μm in length	–	Stable	[63]
Supertubes	Hypothetical cylindrical structures built of single-walled nanotube fragments with Y-junctions	–	–	–	[53]
Nanotube bundles (ropes, strands)	Tightly packed aggregates of various aligned SWCNTs or MWCNTs	E.g., a typical bundle of SWCNTs with diameter range from 10 to 20 nm and length—between 10 μm and 1 mm (typical—10–100 μm) consist of 10 to 500 nanotubes, bundles (ropes, strands) are far longer than any individual tube in them	1.3–1.4 (in ropes)	Stable at ultra-high temp.	[78, 104–105, 108]
Nanotube lattices	2D ordered aggregates of various aligned single- or multi-walled nanotubes	Gap between the tubes (with average diameter 1.4 nm)—0.315 nm	–	–	[58, 110]
Nanotubular crystals (nanotube yarn)	Polycrystalline aggregates of various spun nanotube bundles	Length—up to 30 cm	–	Stable at ultra-high temp.	[104–105, 109]
Nanocones	Conical molecules with atoms tightly packed into a 2D polygonal (hexagonal and pentagonal) lattice	Dimensions—up to 1 μm, height and base diameter are of the same order of magnitude, the preferred values of apex angles are approximately 19°, 39°, 60°, 84° and 113°	–	–	[115–118]
Nanodisks	Hypothetical non-spherical (discoidal) molecules formed by cross-linking graphene layers, containing from 44 to 296 atoms	Diameters—from 0.675 nm to 1.952 nm and heights—from 0.307 nm to 0.472 nm (calculated by MM+ molecular mechanics and Hückel semiempirical methods)	–	–	[21]

(continued)

Table 2.3 (continued)

Form	Character	Structure parameters (at ambient conditions)	Density, g cm^{-3}	Thermal stability	References
Nanobreadsticks	Hypothetical non-spherical (discoidal-tubular) molecules formed by cross-linking graphene layers, adopting different conformations (similar to those in nanotubes) and containing from 148 to 248 atoms	Widths—from 1.078 nm to 1.156 nm, thicknesses—from 0.347 nm to 0.359 nm and lengths—from 1.536 nm to 2.621 nm (calculated by MM+ molecular mechanics and Hückel semiempirical methods)	–	–	[21]
Toroids (toroidal cages)	Giant ring tubular molecules with atoms tightly packed into a 2D hexagonal lattice or 2D hexagonal lattice with inserted pentagons and heptagons into the structures	E.g., series of molecules from C_{120} to C_{1920} with 10 pentagons and 10 heptagons inserted within the each structure and approximate sizes: outer radii from 0.6 nm to 2.5 nm, inner and transverse radii from 0.25 nm to 1 nm (calculated by molecular dynamics method)	–	Stable	[53, 119–121, 125]
Helical nanocoils (coiled cages)	Giant tubular helical molecules with atoms tightly packed into a 2D hexagonal lattice or 2D hexagonal lattice with inserted pentagons and heptagons into the structures	E.g., derivatives of toroids with similar dimensions (calculated by molecular dynamics method)	–	Stable	[125]
Haeckelones, haeckelites (pentaheptites, octites)	Hypothetical structures of hexagonal lattice distorted by the equal number of inserted pentagons and heptagons in order to compensate negative and positive curvatures, containing sometimes octagons	–	–	–	[53, 126, 694–696]
Schwarzones, schwarzites	Hypothetical negative curvature structures of hexagonal lattice distorted by the inserted heptagons	Various (predicted)	1.0–1.3 (calc.)	Stable (predicted)	[53, 126]
Squarographenes	Hypothetical structures formed by distorted hexagons and regular squares or by undistorted hexagons and rhombuses	–	–	–	[694]

(continued)

Table 2.3 (continued)

Form	Character	Structure parameters (at ambient conditions)	Density, g cm^{-3}	Thermal stability	References
Nanobuds	Combined (0D + 1D) molecules of fullerenes covalently attached to the outer sidewalls of underlying nanotubes	Two types of fullerene-nanotube bonding: sp^2- and sp^3-hybridized	–	–	[61]
Nanopeapods	Combined (0D + 1D) molecules of fullerenes encapsulated inside nanotubes C_{2n}@SWCNT (e.g. C_{60}, C_{70}, C_{80}, C_{84})	Orientation of the fullerenes with strong anisotropy is controllable by changing the nanotube radius (on the basis of density-functional theory (DFT) calculations)	–	Stable to 800 °C, at higher temp. transform to bilayered nanotubes	[53, 62]
Nanoscrolls (whiskers, "Swiss roll" structures)	Cylindrical molecules of graphene sheets rolled into scrolls	Molecular dimensions: outermost diameter—up to 80 nm, innermost diameter—1–4 nm, length—0.5–10 μm	–	Stable at ultra-high temp.	[60, 68, 75, 123–124]
Nanofiber (nanowire, nanorods)	Cylindrical nanostructures with graphene layers arranged as stacked plates, cones and other configurations	Diameter—less than 0.5 μm, length—up to 1 cm	–	Stable at ultra-high temp.	[68, 91, 127–135]
Nanofoam	Low-density (nanoporous) assembly of graphene clusters (nanoplatelets) with negative curvature bonded with each other by sp^3-hybridized atoms and strung together in a loose 3D network	Dimensions of graphene clusters with inclusions of heptagons among the regular hexagonal lattice–about 6 nm (~4000 atoms)	Very low, up to 0.002–0.010	Stable	[53, 64, 122, 676]
Defected graphite (armchair prismatic edge dislocations)	Distorted graphite structure characterized by formation of wrinkled unbonded graphene layers (well-defined cavities and expansion of interlayer spacing due to the bends of layers)	Structure built from sp^2-hybridized atoms with max. separation between the flat and curled graphene layers—~0.68 nm and min. separation—~0.32 nm; the bent layers perform as spacers in the AA-stacked graphite with spacing of ~1 nm	1.62	Very stable with binding energy—7.94 eV $atom^{-1}$	[676]
Defected graphite (zig-zag prismatic edge dislocations)	Distorted graphite structure characterized by the local interconnection of neighboring graphene layers by sp^3-hybridized atoms (reorientation of graphene layers and formation of connected double layers with cavities and loops)	Structure formed by the graphitic stripes connected by sp^3-hybridized atoms with sp^3–sp^2 bond length—0.1491 nm; the cavities have a max. height of 0.67 nm, each double layer is repeated with ~1 nm distance and min. distance between two graphitic fragments—0.33 nm	1.62	Very stable with binding energy—7.88 eV $atom^{-1}$	[676]

(continued)

Table 2.3 (continued)

Form	Character	Structure parameters (at ambient conditions)	Density, g cm^{-3}	Thermal stability	References
Glitter	Hypothetical 3D structure (3,4-connected atomic net) forming 3D network of interconnected channels constructed from a structural basis constituted by a 1,4-cyclohexadienoid motif (viewed as a plausible model of n-diamond, ?)	Crystal structure—tetragonal, space group—$P4_2/mmc$, lattice parameters: $a = b = 0.2560–0.2564$ nm, $c = 0.5925–0.6064$ nm, Z = 6 (trigonal sp^2-hybridized atoms to tetrahedral sp^3-hybridized atoms ratio—2:1, C–C bond length—0.1510–0.1534 nm, C=C bond length—0.1348–0.1350 nm, DFT and DFTB calculated)	3.00–3.12	Stability is similar to that of diamond (binding energy–7.52 eV $atom^{-1}$)	[673, 676]
Soot	Randomly formed spherical particulates with loose grape-like aggregates (various in origin and contamination), having dominant turbostratic order with graphenes stacked in the manner of roof tiles	Particles with common sizes 10–500 nm consist of small domains—up to 3 nm along the graphene sheets and 2 nm perpendicular to them, interlayer spacing—about 0.344 nm	1.85–2.18	Stable at ultra-high temp.	[42, 58, 136, 138]
Carbon black (channel black, thermal black, lamp black, acetylene black)	Partly crystallized or amorphous spherical particulates (colloids with various origin and contaminations)	Particles with common sizes—10–500 nm, high specific surface area (10–150 m^2/g) and low apparent density (0.01–0.1 g/cm^3)	2.04–2.18	Stable at ultra-high temp.	[42, 136, 138]
Amorphous carbon	Structures (including films, porous and contaminated materials) without long-range crystalline order, or having polycrystalline (nanocrystalline) areas distributed by various ways within an amorphous matrix	Deviation of interatomic distances (or interbonding angles) from the perfect graphite crystal is greater than 5 % in both a graphene plane and between graphene planes	1.8–2.1	Stable in some ranges of temp., transforms to crystalline materials	[42, 69, 78, 136, 138]
Pyrolytic carbon	Aggregates of graphenes with covalent bonding between graphene sheets	E.g., material deposited at low temp. composed from crystallites with average dimensions $L_a = 4$ nm, $L_c = 2$ nm and interlayer spacing—more than 0.344 nm	1.1–2.1	Stable, at ultra-high temp. transforms to highly ordered materials	[8, 43, 136]
Coke	Graphene containing products of hydrocarbons pyrolysis (partly contaminated)	Composed from crystallites with L_c—about 5 nm and interlayer spacing—more than 0.344 nm	1.7–2.2	Stable, at ultra-high temp. commonly transforms to highly ordered materials	[42–43, 136, 138–139]

(continued)

Table 2.3 (continued)

Form	Character	Structure parameters (at ambient conditions)	Density, g cm^{-3}	Thermal stability	References
Charcoal	Graphene containing biomorphous products of pyrolysis (porous, contaminated)	Similar to coke	1.5–2.0	Stable, at ultra-high temp. commonly transforms to highly ordered materials	[42, 136, 138]
Activated carbon	Nanoporous assemblies of defective graphene layers	Ratio of pentagons-to-hexagons in the atomic network (estimated by HRTEM for high temp. heat-treated material)—approximately 1:50, average pore diameter—1–5 nm and specific surface area—in the range of 300–2600 $m^2\ g^{-1}$	1.4–1.7	Stable	[42, 58, 69, 136, 138, 140]
Molecular-sieve carbon	Nanoporous assemblies of roughly parallel graphene sheets with no 3D crystalline order	Disorientation angles of graphene sheets—up to several degrees, formed from packing imperfection pore structures, consist of relatively wide openings of 0.6–2.0 nm with small ultramicropores of 0.3–0.6 nm (bimodal pore distribution)	1.3–1.8	Stable	[69, 141–144]
Carbon (amorphous) fiber	Bundle of filaments without long-range crystalline order, or having polycrystalline (nanocrystalline) areas distributed by various ways within an amorphous matrix	Various structures	1.4–1.8	Stable at high temp.	[8, 42, 84, 136–137]
Carbon (amorphous) clothes, fabrics, felts and prepregs	(2, 2.5, 3,…n)D-components made from carbon (amorphous) fiber	Various structures	–	Stable at high temp.	[8, 84, 136–137]
Aerogels (cryogels, xerogels)	Assemblies of nanoporous (microporous) spherical nanoparticles formed by defective graphene layers	Particles with diameter of 6–40 nm composed from crystallites with sizes: L_c of 0.6–0.9 nm and L_a of 2.5–4.5 nm, interparticulate mesopores with dimensions of 3–15 nm and interior micropores—0.7–1.5 nm, specific surface area—400–1400 $m^2\ g^{-1}$	–	Stable at high temp.	[69, 70, 148–150]
Glassy (vitreous) carbon	3D random tough network of 2D hexagonal lattice ribbons tangled and joined with each other	Graphitic ribbon crystallites with dimensions—L_c of 1.5–3 nm and interlayer spacing—0.360–349 nm, total porosity—~30 % with pore diameters of 1 to 3.5 nm (most of the pore entrances—0.4–0.5 nm)	1.4–1.6	Stable at ultra-high temp.	[42, 151–153]

(continued)

Table 2.3 (continued)

Form	Character	Structure parameters (at ambient conditions)	Density, g cm^{-3}	Thermal stability	References
Glassy (vitreous) carbon foam	Cellular (highly porous) structures of 2D hexagonal lattice ribbons networks	Total porosity—97 %, specific surface area—1–2 m^2 g^{-1}	~0.05 (bulk), ~1.5 (strut)	Stable at high temp.	[42]
Carbon bead powder (mesocarbon micro-beads)	Spherical particles (contaminated by hydrogen) consist of quasi-graphene (planar aromatic compounds) sheets (lamellae) stacked in parallel array	Particle diameters of 1–80 μm, the sheets are arranged perpendicularly along one diameter of a sphere, but curved and normal to the surface with interlayer (interlamellar) spacing—0.346–0.348 nm	1.3–2.2	Stable	[154–156]
Carbide derived carbon	Tunable nanoporous carbons formed by chemically removing metallic or non-metallic elements from carbides and leaving a systematic array of pores	Variety of nanostructures with different parameters	–	–	[71, 157–165]
Diamond-like carbon	Amorphous or semi-crystalline films (partly contaminated by hydrogen) with no lattice long-range order	Broad range of structures (film thickness of 0.1–5 μm) composed of very small crystallites having either tetrahedral or planar threefold local atomic configuration	1.8–2.8	Metastable, convert to graphite at 250–400 °C	[13, 42]
Hexagonite (based on barrelene generating fragment molecules)[f]	Hypothetical 3D structure (3-, 4-connected network) with a large number of derivatives formed by the insertion of 1,4-dimethylene-2,5-cyclohexa-dieneoid organic spacers	Crystal structure—hexagonal, space group—*P6/mmm*, lattice parameters: $a = 0.4772$ nm, $c = 0.4129$ nm, $Z = 10$ (C–C bond length—0.1521 nm, C=C bond length—0.1326 nm, C–C–C trigonal angles—130°, C=C–C trigonal angles—~115°, tetrahedral angles within the cage of barrelene substructures—103°, tetrahedral angles outside the cage of barrelene substructures—115°, calculated and optimized by a DFT algorithm)	2.449	–	[669–671]
Ortho-graphite-diamond hybrids	Hypothetical 3D structure (3-, 4-connected network) with graphene fragments connected with each other in perpendicular directions by sp^3-bonding	–	–	–	[672]

(continued)

Table 2.3 (continued)

Form	Character	Structure parameters (at ambient conditions)	Density, g cm^{-3}	Thermal stability	References
Para-graphite-diamond hybrids	Hypothetical 3D structure (3-, 4-connected network) with graphene fragments connected with each other in parallel directions by sp^3-bonding	–	–	–	[672]
Intermediate graphite-to-diamond transition phases	Hypothetical 3D structures as progressive intermediates in graphite-to-diamond phase transition	Crystal structure—orthorhombic, space group—*Cmmm*, lattice parameters: $a = 0.4525$ nm, $b = 0.5334$ nm, $c = 0.5925$ nm, Z = 16 (calculated by molecular mechanics methods)	2.222	Metastable	[166]
		Crystal structure—orthorhombic, space group—*Cmme*, lattice parameters: $a = 0.4575$ nm, $b = 0.5304$ nm, $c = 0.5635$ nm, Z = 16 (calculated by molecular mechanics methods)	2.334	Metastable	[166]
		Crystal structure—orthorhombic, space group—*Pban*, lattice parameters: $a = 0.4048$ nm, $b = 0.4885$ nm, $c = 0.6495$ nm, Z = 16 (calculated by molecular mechanics methods)	2.484	Metastable	[166]
		Crystal structure—orthorhombic, space group—*Pcca*, lattice parameters: $a = 0.4700$ nm, $b = 0.5978$ nm, $c = 0.4448$ nm, Z = 16 (calculated by molecular mechanics methods)	2.554	Metastable	[166]
		Crystal structure—orthorhombic, space group—*Cmmm*, lattice parameters: $a = 0.4870$ nm, $b = 0.5565$ nm, $c = 0.4406$ nm, Z = 16 (calculated by molecular mechanics methods)	2.673	Metastable	[166]
		Crystal structure—orthorhombic, space group—*Cmme*, lattice parameters: $a = 0.4964$ nm, $b = 0.5163$ nm, $c = 0.4387$ nm, Z = 16 (calculated by molecular mechanics methods)	2.839	Metastable	[166]
		Crystal structure—orthorhombic, space group—*Pban*, lattice parameters: $a = 0.4127$ nm, $b = 0.4937$ nm, $c = 0.4819$ nm, Z = 16 (calculated by molecular mechanics methods)	3.250	Metastable	[166]
		Crystal structure—cubic, space group—*Ia(-3)*, lattice parameters: $a = 0.4591$ nm, Z = 16 (calculated by molecular mechanics methods)	3.297	Metastable	[166]

(continued)

Table 2.3 (continued)

Form	Character	Structure parameters (at ambient conditions)	Density, g cm^{-3}	Thermal stability	References
i-carbon (shock-compressed graphite phase)	Nanocrystals in intermediate states between graphite and diamond (or glitter modification, ?)	Thin films or spherical particles with diameter of ~25 nm (crystal structure of glitter, ?)	–	–	[675, 682–685]
n-diamond (or γ-carbon, shock-compressed graphite phase)	Nanocrystals in intermediate states between graphite and diamond (or glitter modification, ?)	Crystal structure—cubic, space group—*Fm(-3)m*, or crystal structure of glitter, ?	–	–	[170, 674, 682, 684, 686–688]
n-diamond	Hypothetical 3D structure as an intermediate state between rhombohedral graphite and diamond	Crystal structure—trigonal (rhombohedral), space group—*R3*, lattice parameters: $a = b = c = 0.35809$ nm, Z = 8 (calculated)	3.474	–	[167]
Diamond Family					
Diamondoids	Hydrogen-terminated molecules	Various shapes with sizes of 1–2 nm	–	–	[72, 677]
Ultra-nanocrystalline (ultra-dispersed) particulate diamond	3D tetrahedral atomic structure in substantially monocrystalline particles (often with multiple twins)	Range of primary particles sizes—2–20 nm, average (or typical) size—4–5 nm, minimal size—1.8 nm, specific surface area—300–400 m^2/g, crystal structure—cubic with lattice parameter: $a = 0.3573 \pm 0.0005$ nm	3.1–3.4	Stable in some ranges of temp., initial vacuum graphitization temp.—1100–1200 °C	[72, 78]
Ultra-nanocrystalline aggregated diamond	Agglomerates of 3D tetrahedral structured particles	Dimensions of agglomerates—from 40–50 nm to 0.1–1 mm	–	–	[72]
Nanocrystalline particulate diamond	3D tetrahedral atomic structure in monocrystalline particles	Range of smallest fraction sizes—0–50 nm with average size—ca. 25 nm, other fractions—0–100 nm (average size—~50 nm), 0–150 nm and up	–	More stable than graphite nanoparticles being in clusters with less than 10^4 carbon atoms	[72, 78]
Nanocrystalline aggregated diamond	Polycrystalline agglomerates of 3D tetrahedral structured particles	Average grain size—~20 nm	–	–	[72]
Diamond nanorods	1D form of 3D tetrahedral atomic structure	Diameter of 5–200 nm, length—up to 1–10 μm	–	–	[72, 78]
Aggregated diamond nanorods (hyperdiamond)	Assembly of interconnected diamond nanorods	Nanorods with diameters of 5–20 nm and lengths of ~1 μm	3.526	–	[168–169]
Diamond nanotubes	1D form of 3D tetrahedral atomic structure	Diameter of 50–160 nm	–	–	[72]

(continued)

Table 2.3 (continued)

Form	Character	Structure parameters (at ambient conditions)	Density, g cm^{-3}	Thermal stability	References
Diamond nanowhisckers	1D form of 3D tetrahedral atomic structure	Diameter of 10–60 nm, length—~300 nm	–	–	[72]
Diamond nanocylinders	1D forms of nanodiamond with circular, triangular or squared cross-sections	Diameter—up to 600 nm, length—~5 mm	–	–	[72]
Diamond nanocones	1D form of 3D tetrahedral atomic structure	Diameters at base—0.1–1 μm	–	–	[72]
Diamond nanofiber (filaments)	1D form of polycrystalline ultra-dispersed diamond	Diameter of 0.1–1μm, length of 2–3 μm, average grain size <10 nm	–	–	[72, 78]
Diamond nanoplatelets	2D form of 3D tetrahedral atomic structure with triangular and parallelogram shapes	Thickness ranges from 20 to 70 nm and length—0.1–10 μm	–	–	[72]
Ultra-nanocrystalline diamond films	3D form of polycrystalline ultra-dispersed diamond with grain boundaries formed by sp^2-hybridized atoms	Average grain size—2–5 nm, grain boundaries width—0.2–0.4 nm	–	–	[72]
Polycrystalline diamond nanopowder	3D form of polycrystalline ultra-dispersed diamond	Grain sizes with bimodal distribution—1–4 nm and 10–160 nm	–	–	[72]
Carbide derived diamond-structured carbon	Wide variety of nanoporous diamond polytype structures formed by chemically removing non-metallic elements from carbides	Grain sizes—5–10 nm	–	–	[71–72, 78, 170–171]
Diamond (3C-diamond, β-carbon) single crystal (or polycrystalline)	Giant molecule with atoms tightly packed into a 3D tetrahedral lattice (or assemblies of grains with similar structure)	Crystal structure—cubic, space group—*Fd(-3)m*, lattice parameter: $a = 0.35667$ nm, Z = 8 (C–C bond length—0.1545 nm, XRD)	3.516	Thermodynamically unstable with respect to graphite with a negative free-energy change of 2.88 kJ mol^{-1} at standard conditions	[9, 42, 58, 172]
Lonsdaleite (2H-diamond, γ-carbon)	Diamond polytype	Crystal structure—hexagonal, space group—*P6₃/mmc*, lattice parameters: $a = 0.25221$ nm, $c = 0.41186$ nm, Z = 4 (XRD)	3.521	–	[42, 166, 172]
Lonsdaleite (4H-diamond)	Diamond polytype	Crystal structure—hexagonal, space group—*P6₃/mmc*, lattice parameters: $a = 0.25221$ nm, $c = 0.82371$ nm, Z = 8 (XRD)	3.521	–	[42, 166, 172]

(continued)

Table 2.3 (continued)

Form	Character	Structure parameters (at ambient conditions)	Density, g cm^{-3}	Thermal stability	References
Lonsdaleite (6H-diamond)	Diamond polytype	Crystal structure—hexagonal, space group—*P6₃/mmc*, lattice parameters: $a = 0.25221$ nm, $c = 1.23557$ nm, Z = 12 (XRD)	3.521	–	[42, 172]
Lonsdaleite (8H-diamond)	Diamond polytype	Crystal structure—hexagonal, space group—*P6₃/mmc*, lattice parameters: $a = 0.25221$ nm, $c = 1.64743$ nm, Z = 16 (XRD)	3.521	–	[10, 42, 172]
Lonsdaleite (10H-diamond)	Diamond polytype	–	–	–	[42]
Lonsdaleite (12H-diamond)	Diamond polytype	–	–	–	[10]
Lonsdaleite (16H-diamond)	Diamond polytype	–	–	–	[10]
Lonsdaleite (20H-diamond)	Diamond polytype	–	–	–	[10]
Lonsdaleite (15R-diamond)	Diamond polytype	Crystal structure—trigonal (rhombohedral), space group—*R(-3)m*, lattice parameters: $a = 0.25221$ nm, $c = 3.08893$ nm, Z = 30 (XRD)	3.521	–	[172]
Lonsdaleite (21R-diamond)	Diamond polytype	Crystal structure—trigonal (rhombohedral), space group—*R(-3)m*, lattice parameters: $a = 0.25221$ nm, $c = 4.3245$ nm, Z = 42 (XRD)	3.521	–	[172]
Hexagonite (cold compressed nanotubes)[f]	Super-hard phase	Crystal structure—hexagonal, space group—*P(-6)2c*, lattice parameters: $a = 0.2496$ nm, $c = 0.4123$ nm, Z = 4 (interlayer spacing—0.21 nm, C–C bond length—0.143 nm, electron diffraction, XRD)	3.65 (or 3.6 ± 0.2)[g]	Quenched from ~75 GPa, preserved at room conditions	[668]
Diamond D_5	Hypothetical diamond-like networks consisting mostly of pentagon rings	The ratio of pentagon/hexagon rings is going up to 9	–	More stable than C_{60} (calculated)	[666–667]

(continued)

Table 2.3 (continued)

Form	Character	Structure parameters (at ambient conditions)	Density, g cm^{-3}	Thermal stability	References
Lonsdaleite L_5	Hypothetical lonsdaleite -like networks consisting mostly of pentagon rings	The ratio of pentagon/hexagon rings is going up to 9	–	More stable than C_{60} (calculated)	[666–667]
Octacarbon (supercubane, prismane, BC8)	High-temp. modification of diamond (?)	Crystal structure—cubic (body-centred), space group—*Im(-3)*, lattice parameter: $a = 0.428$ nm, $Z = 16$ (electron diffraction and calculated by molecular mechanics methods)	4.1	Stable at ulra-high temp. and pressures	[166, 176–177, 187, 189]
		Crystal structure—cubic (body-centred), space group—*Ia(-3)*, lattice parameter: $a = 0.4293$ nm, $Z = 16$ (calculated by molecular mechanics methods)	4.03	–	[166, 173–175, 187, 189]

[a] Concerning the carbyne family, see notes *a-c* to Table 2.2
[b] Calculated on the basis of data [20]
[c] Number of formula units per lattice
[d] Some other forms have been reported in literature [9]
[e] Data available in literature are controversial [112]
[f] Not to be confused with the inorganic mineral structure and some trademark names
[g] Average (reduced) density due to possibly amorphous carbon on the grain boundaries

termed pyramidalization angle and/or curvature are used for evaluation of nonplanarity (deviation from graphene plane geometry) in fullerene family structures),

which differ in the sp^n-hybridisation ($1 \leq n \leq 3$) types of carbon structures.

The main structural characteristics, including crystal lattice parameters and densities, and relative thermal stabilities of the various carbon allotropic, polymorphic and polytypic forms, grouped under family headings within the overall hierarchy from submolecular to macrostructural scales, are summarized in Table 2.3.

2.2 Thermal Properties

2H-graphite (or α-graphite) is the most stable thermodynamically form of carbon under standard conditions, so its standard enthalpy of formation (at 298.15 K) $\Delta H^{\circ}_{f,298}$ is zero, similar to those characteristics for all other chemical elements. The generalized phase and transition diagram of carbon based on several main sources [28, 176–190, 535–538] is given in Fig. 2.1. In the region of moderate pressures, this variant of carbon phase diagram assumes the sequence of transformations with temperature (energy) increase from sp^3 (diamond) through sp^2 (graphite/graphene) to sp^1 (carbyte/carbyne), which is corresponding to the specific bond energy approach established for the carbon structures classification previously (see Sect. 2.1). The general thermodynamic properties of carbon (graphite) are summarized in Table 2.4.

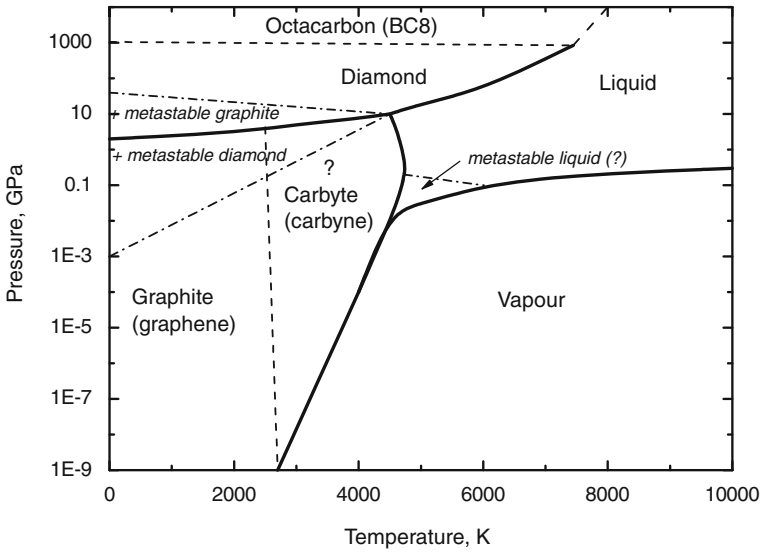

Fig. 2.1 The generalized phase and transformation diagram of carbon according to the several main sources [28, 176–190, 535–538]

Table 2.4 General thermodynamic properties of graphite

Characteristics	Symbol	Unit	Value	References
Standard molar entropy (at 298.15 K and 100 kPa)	$S°_{298}$	J mol^{-1} K^{-1}	5.74	[4]
			5.697–5.743	[42]
Molar enthalpy difference	$H_{298} - H_0$	kJ mol^{-1}	1.054	[540]
Standard molar heat capacity (at 298.15 K and 100 kPa)	$c°_{p,298}$	J mol^{-1} K^{-1}	8.517	[4]
			8.544	[227]
			8.033–8.635	[42]
Specific heat capacity (at 298.15 K)	c	J kg^{-1} K^{-1}	690–719	[42]
			651	[138]
Molar enthalpy (heat) of melting	ΔH_m	kJ mol^{-1}	117 (for triple point)	[3–4]
			146	[138]
Specific enthalpy (heat) of melting		MJ kg^{-1}	12.2	[138]
			10 (for melt. point)	[180]
Molar enthalpy (heat) of vaporization	ΔH_v	MJ mol^{-1}	0.717 (for 298 K)	[6]
			0.71	[138]
Specific enthalpy (heat) of vaporization		MJ kg^{-1}	59.1	[138]
Sublimation point (at 0.1013 MPa)	T_{sub}	K (°C)	4000 (3730)[a]	[42]
			4100 (3825)	[3]
Melting point (at 10 MPa)[b]	T_m	K (°C)	4020 (3750)	[6, 138]
			4200 (3930)	[42]
Melting point (at 12 MPa)[b]			4160 ± 50 (3890 ± 50)	[186]
Melting point (at 10–100 MPa)[b]			4800 ± 100 (4530 ± 100)	[180]
Melting point (at 300 MPa)[b]			4750 (4480)	[138]
Boiling point	T_b	K (°C)	4200 (3930)	[6]
			4560 (4290)[a]	[42]
Triple point (graphite-liquid-vapour)[b]	T_{tr}, p	K (°C), MPa	3800 (3530), 0.02	[28]
			4000 (3730), 0.1	[179]
			4200 (3930), 10	[42]
			4500 (4230), 10	[178]
			4760 (4490), 10,3	[3]
Triple point (graphite-diamond-liquid)[b]		K (°C), GPa	4100 (3830), 12.5	[6]
			4250 (3980), 16.4[c]	[190]
			4300 (4030), 9.4[d]	[188]
			4500 (4230), 10	[178]

(continued)

Table 2.4 (continued)

Characteristics	Symbol	Unit	Value	References
Triple point (diamond—octacarbon (BC8)—liquid)[e]		K (°C), GPa	7400 (7130), 850[f]	[189]
Critical point[g]		K (°C), GPa	6810 (6540), 0.22	[911]

[a] Estimated values (for practical application approximate values are recommended: total pressure of carbon over graphite surface at 3790 K (3520 °C) −0.1 MPa, mass vaporization rate of graphite at 3300 K (3030 °C)−10^{-2} kg m^{-2} s^{-1}, linear vaporization rate of graphite at 3100 K (2830 °C)—$\sim 10^{-6}$ m s^{-1} [138])

[b] The main divergences in the experimental results available in literature [178–186] are in the values of the true melting temperature and triple point of graphite in the range of 4000 or 5000 K

[c] Determined using a semi-empirical long-range carbon bond-order potential partly based on *ab initio* data

[d] Calculated within the framework of the statistical model

[e] Melting point of carbon (diamond) at 12.4 GPa–4710 K (4440 °C)

[f] Predicted from first-principles calculations based on density functional theory

[g] Critical density—0.64 g cm^{-3} [911]

For the molar heat capacity $c_p = f(T, \text{K})$, J mol^{-1} K^{-1}, the following relationship for the range of temperatures from 298 to 2500 K is recommended [227]:

$$c_p = 17.17 + \left(4.27 \times 10^{-3}\right)T - \left(8.79 \times 10^{5}\right)T^{-2}. \tag{2.1}$$

The heat capacity of carbon (graphite) materials increases rapidly with temperature up to 1000 °C, where it levels off at approximately 2 kJ kg^{-1} K^{-1} with the subsequent increase beginning at 2800−3000 °C (Fig. 2.2). The important remark, which should be made in regard to the thermal behaviour of carbon at ultra-high temperatures, is connected with its vaporization (especially, in vacuum). At moderate pressures carbon (graphite) does not melt but sublimates very intensively with vaporization rate exceeding 0.01 kg m^{-2} s^{-1} when temperature reaches more than 3000 °C. The values of standard molar entropy $S°_{298}$, molar c_p and specific c heat capacities, enthalpies (heats) of melting and vaporization, molar and specific enthalpy differences $H_T - H_{298}$, vapour pressures and mass/linear vaporization rates are given in Addendum in comparison with other ultra-high temperature elements (refractory metals) in the wide ranges of temperatures.

All vector-defined thermal properties of carbon (graphite) reflect extremely high anisotropy inherent to graphite crystals. The properties can vary considerably depending on geometrical directions in carbon (graphite) structures. The main anisotropy coefficient

$$\zeta = a_{\text{para}}/a_{\text{perp}}, \tag{2.2}$$

where a_{para}, a_{perp} are, respectively, the values of a physical property in parallel and perpendicular directions to the graphene basal plane (or axis of symmetry), for thermal conductivity of quasi-single crystalline graphite material, such as highly oriented pyrolytic graphite, reaches up to 200.

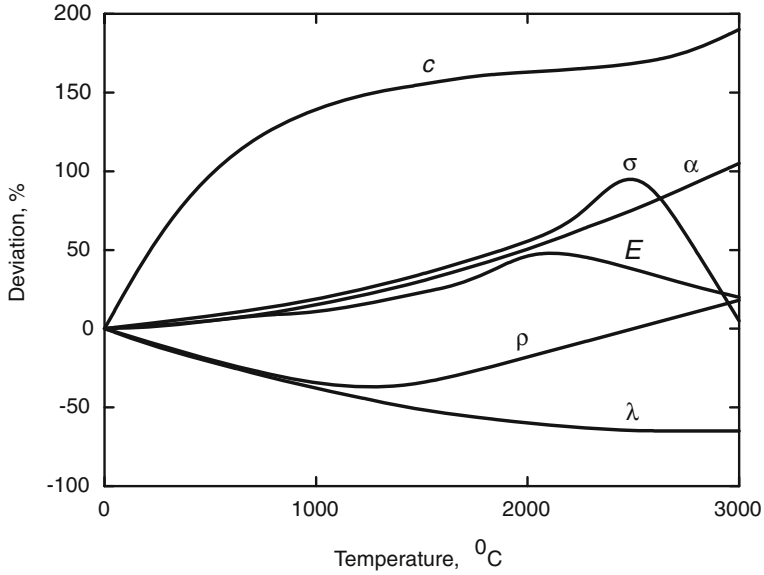

Fig. 2.2 Relative variations of some physical properties of common industrial graphite materials with temperature: c—heat capacity, α—thermal expansion, σ—mechanical strength, E—Young's modulus, ρ—electrical resistivity and λ—thermal conductivity (based on several sources [41–43, 136, 138, 194, 209, 223–224])

Around the hierarchy of graphene/graphite structures from nano- to macro-scales all the materials are characterized by highly anisotropic properties; e.g., carbon nanotubes are very good thermal conductors along the tube, but good insulators laterally to the tube axis (Table 2.5). Some kind of similar particularities are also common for the variety of carbon (graphite) products, including the graphite containing bulk materials, which are very different in structure and composition. The variation of thermal conductivity in the different directions of graphite crystals with temperature is shown in Fig. 2.3.

For bulk carbon (graphite) materials produced in industry, thermal conductivity depends strongly on the various defects of their structures. The values of thermal heat capacity and thermal conductivity of various carbon products: industrial graphitized carbon materials, pyrolitic (pyrographite) and vitreous (glass-like) carbons, thermally expanded (exfoliated) graphite materials and carbon (graphite) filaments in commercial carbon fibres are given in Tables 2.6, 2.7, 2.8, 2.9, 2.10.

Table 2.5 Some physical properties of graphitic nanostructured carbons and quasi-single crystalline graphite at room temperature

Nanostructure	Thermal conductivity, W m^{-1} K^{-1}	Electrical resistivity, Ω m	Young's modulus, TPa	Tensile strength, GPa	References
Graphene	4800–5300	$\sim 1 \times 10^{-8}$	0.67–0.91[a]	130[a]	[191, 197–200]
Single-walled nanotubes	3500 (axial direction), 1.5 (radial direction)	$\sim 3 \times 10^{-10}$ (for metal-like nanotubes, axial direction)	~1 (axial direction)	13–53[b], 94.5–126.2[a] (axial direction)	[91, 195, 196, 201–204]
Multi-walled nanotubes (in axial direction)	~1500	$\sim 1 \times 10^{-9}$	0.27–0.95[a]	11–150[a]	[91, 205–206]
Nanoscrolls (whiskers, in axial direction)	~1300	–	0.7–0.8	3–20	[91, 208, 221]
Nanofiber (nanowire, in axial direction)	20–1300	$(0.6–1.4) \times 10^{-6}$	0.01–0.7	up to 4.5[b]	[91, 130]
Quasi-single crystalline graphite (highly oriented pyrolytic graphite)[b,c]	~1500 (in basal plane) ~7.5 (perpendicular to basal plane)	3.85×10^{-7} (in basal plane) 5.2×10^{-5} (perpendicular to basal plane)	~1 (in basal plane)	~100 (in basal plane)	[91, 136, 209]

[a] Theoretical prediction
[b] Experimental observation
[c] Linear coefficient of thermal expansion (20–200 °C): $(-1.1) \times 10^{-6}$ and $(25–27) \times 10^{-6}$ K^{-1} (in basal plane and perpendicular to basal plane, respectively) [138, 209, 214]

The thermal expansion–contraction behaviour of carbon (graphite) is very complicated (Fig. 2.4). To take into account this aspect is a question of vital importance in the materials design for ultra-high temperature applications. The magnitudes of linear thermal expansion coefficients for various industrial carbon (graphite) products are also presented in Tables 2.6–2.10.

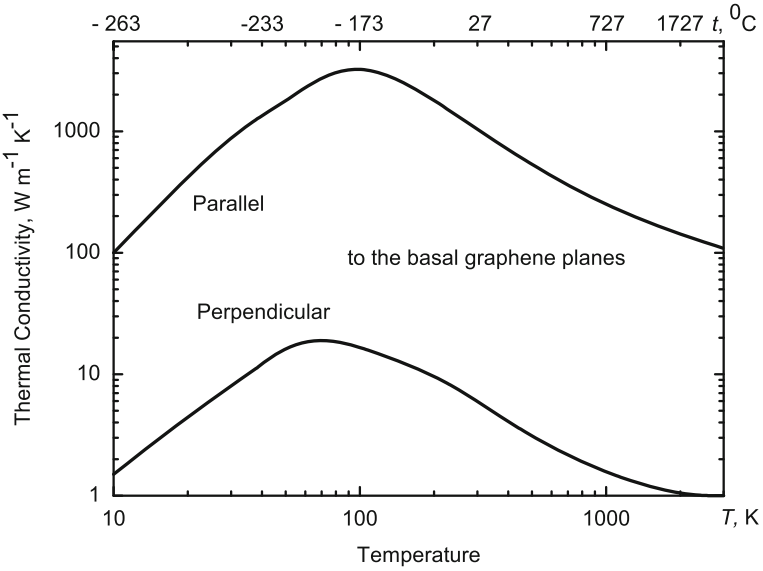

Fig. 2.3 Variation of the thermal conductivity in the different directions of graphite crystals with temperature [41–43, 138, 209]

For averaged highly oriented graphite and quasi-isotropic carbon (graphite), compared with other ultra-high temperature elements (refractory metals), the values of thermal conductivity and thermal expansion in the wide range of temperatures are summarized in Addendum.

2.3 Electro-Magnetic and Optical Properties

Together with thermal properties, electrical resistivity of carbon (graphite) materials and its property-temperature relationship are also extremely anisotropic and sensitive to the order/disorder of carbon atoms in graphitic materials structures. For well-ordered crystals (highly oriented pyrolytic graphite), the variations of specific electrical resistance in the general crystallographic directions and in the wide range of temperatures are presented in Fig. 2.5.

Indeed, the character of these plots differs essentially from the electrical resistivity—temperature relationships observed for the common graphite materials (see Fig. 2.2), which are far from the ideal structure. The values of electrical resistance of graphitic nanostructured carbons, various industrial graphitized carbon materials, pyrolitic (pyrographite) and vitreous (glass-like) carbons, thermally expanded (exfoliated) graphite materials and carbon (graphite) filaments in commercial carbon fibres are given in Tables 2.5–2.10.

Carbon (graphite) is highly diamagnetic with molar magnetic susceptibility χ_{mol} (SI) $= -75.4 \times 10^{-6}$ cm^3 mol^{-1} in parallel direction to the basal graphene planes

Table 2.6 Physical properties[a] of industrial graphitized carbon materials [11, 42, 136, 138, 192–194, 209–211, 215, 222–225, 228, 230, 237, 539]

Trade mark or grade[b]	d, g cm^{-3}	P, %	c, kJ kg^{-1} K^{-1}	λ, W m^{-1} K^{-1}	α, 10^{-6} K^{-1}	ρ, μΩ m	E^c, GPa	σ_t, MPa	σ_f, MPa	σ_c, MPa	K_{IC}, MPa m$^{1/2}$
Structural and electrode graphite materials (Union Carbide)											
AGSR	1.53–1.58	23–28	–	130–180/–	1–2/–	7–10/–	10/6	10–14/–	15–20/–	22–30/22–30	–
	1.53–1.65	26–32	–	130–200/90–140	0.5–1.5/1.0–2.5	6.5–10/9–14	10/6	3–5/2–5	4–6/3–5	7–13/7–13	–
	1.58–1.64	26–32	–	130–180/90–130	1–2/1.5–3	7–10/10–14	10/6	3–5/2–5	5–8/4–7	9–15/7–15	–
	1.60–1.67	23–28	–	130–180/–	1–2.5/2.5–4	7–10/–	10/6	7–12/4–9	7–14/6–12	16–23/16–23	–
	1.60–1.70	23–28	–	130–180/–	1–2/–	7–10/–	10/6	9–13/–	12–18/–	25–33/25–33	–
CS	1.60–1.75	15–20	–	140–170/ 110–140	1.5–3/2.7–4.5	7.5–9/9–12	14/8	–	15–20/–	45–55/–	–
	1.70–1.80	14–19	–	150–200/ 110–150	1.5–3/2.7–4.5	6.5–8.5/ 8.5–12	14/8	8–20/5–15	15–30/10–20	35–65/30–40	–
AJL	–	9	–	100/–	3.4/–	14/–	8.5/–	25/–	25/–	70/–	–
ATJ	1.69–1.76	9–13	–	120/100	2.3/3.4	11/14	7.7–8.4/ 11.3–11.8[d]	21/26–27	30/25	63–68/70–79	–
RVA	1.84–1.87	–	–	–	–	–	9.0–9.2/ 13.1–13.9	16.5/ 21.9–23.3	–	71.5/70.7	–
RVC	1.84–1.85	–	–	–	–	–	9.2–9.9/ 12.1–12.6	10.3/ 16.4–16.5	–	72.2/75.8	–
RVD	1.88–1.93	–	–	–	–	–	8.0–9.4/ 14.6–16.1	19.6/ 27.0–27.9	–	86.0/88.9	–
CFW	1.89–1.91	–	–	–	–	–	10.3–10.5/ 11.0–11.4	11.9/ 13.2–13.4	–	62.0/60.9	–
CFZ	1.92–1.93	–	–	–	–	–	9.9–10.6/ 13.0–14.2	16.2/ 24.2–24.6	–	80.0/83.8	–
CHQ	1.58–1.61	–	–	–	–	–	6.6/8.6–9.4	–/19.0–19.7	–	68.9/102.4	–
ZTA	1.94–1.96	–	–	–	–	–	4.6–4.9/ 17.7–23.0	11.2/ 30.0–30.3	–	101.3/57.9	–

(continued)

Table 2.6 (continued)

Trade mark or grade[b]	d, g cm^{-3}	P, %	c, kJ kg^{-1} K^{-1}	λ, W m^{-1} K^{-1}	α, 10^{-6} K^{-1}	ρ, μΩ m	E^c, GPa	σ_t, MPa	σ_f, MPa	σ_c, MPa	K_{IC}, MPa m$^{1/2}$
Carbonix® structural graphite materials (Groupe Carbone Lorraine)											
6250	1.67	–	–	–	3.8/2.3 (100–600 °C)	12/7	–	–	12/20	27/45	–
2191	1.74–1.75	12	–	116	4.2 (20–1000 °C)	10.7–10.9	–	–	44	97	–
2020	1.77	9	–	81–85	4.3–4.5 (20–1000 °C)	15.5–18	–	–	33–45	66–99	–
2910	1.74	17	–	77	4.1 (20–1000 °C)	16	–	–	30	–	–
2114	1.80–1.81	10	–	104–116	5.0–5.3 (20–1000 °C)	12.4–12.95	–	–	52	114	–
2120	1.84	7	–	106	6.0 (20–1000 °C)	12.2	–	–	65	–	–
2123	1.84	8	–	112	5.5 (20–1000 °C)	11.4	–	–	58	–	–
2124	1.83	8	–	112	5.4–5.7 (20–1000 °C)	11.25	–	–	52	114	–
2318	1.86	6	–	81	5.7 (20–1000 °C)	16	–	–	76	–	–
2320	1.82	10	–	122	5.0 (20–1000 °C)	10.6	–	–	50	–	–
2333	1.86	6	–	81	6.0 (20–1000 °C)	16	–	–	76	167	–
2340	1.88	13	–	102	7.2 (20–1000 °C)	12.7	–	–	90	–	–
2450	1.86	8	–	85	4.3 (20–1000 °C)	15.5	–	–	45	–	–
2715	1.82	10	–	56	5.1–6.5 (20–1000 °C)	23	–	–	55	121	–
2720	1.80	10	–	60	5.0 (20–1000 °C)	21.6	–	–	53	117	–

(continued)

Table 2.6 (continued)

Trade mark or grade[b]	d, g cm^{-3}	P, %	c, kJ kg^{-1} K^{-1}	λ, W m^{-1} K^{-1}	α, 10^{-6} K^{-1}	ρ, μΩ m	E[c], GPa	σ_t, MPa	σ_f, MPa	σ_c, MPa	K_{IC}, MPa m$^{1/2}$
Structural and electrode graphite materials (SGL Carbon Group)											
MKS	1.73	16	–	–	–	10	10	–	18	45	–
MSY	1.78	13	–	190/120	2.5/3.5	7/11	12/7	12/7	24/14	45/40	–
	1.83	11	–	160/100	2/3.5	8/13	15/8	16/9	30/17	55/50	–
HLM	1.70–1.78	17–23	–	105–180	1.4–3.6 (20–200 °C)	9.4–12.4	7.4–10.2	–	15–18	37–44	–
MNC	1.80	14	–	130	1.5 (20–200 °C)	10	16	–	40	55–60	–
MNT	1.75	16	–	130	1.0 (20–200 °C)	10	15	–	20	28–30	–
R4340	1.72	15	–	90	2.9 (20–200 °C)	12	10.5	–	45	90	–
R4500	1.77	13	–	80	3.9 (20–200 °C)	14	10.5	–	50	120	–
R4550	1.83	10	–	100	4.0 (20–200 °C)	13	11.5	–	60	125	–
R4810	1.83	10	–	135	4.1 (20–200 °C)	10.5	10	–	50	105	–
R4820	1.82	10	–	125	4.2 (20–200 °C)	11.5	11	–	45	105	–
R6300	1.73	15	–	65	3.8 (20–200 °C)	17	10	–	40	90	–
R6340	1.72	15	–	90	4.0 (20–200 °C)	12	10.5	–	45	90	–
R6500	1.77	13	–	80	5.0 (20–200 °C)	14	10.5	–	50	120	–
R6510	1.83	10	–	90	5.1 (20–200 °C)	13	11.5	–	60	125	–
R6650	1.84	10	–	90	5.0 (20–200 °C)	14	12.5	–	65	150	–
R6710	1.88	10	–	100	5.8 (20–200 °C)	13	13.5	–	85	170	–
R6810	1.80	11	–	130	5.2 (20–200 °C)	10	10	–	45	100	–
R6830	1.82	9.5	–	130	5.0 (20–200 °C)	10	10	–	50	100	–
R8710	1.88	10	–	100	4.7 (20–200 °C)	13	13.5	–	85	170	–
Structural and electrode graphite materials (Conradty)											
CCF/XN	1.70–1.74	16–18	–	100–120	1.8–2.5	–	–	–	18–20	27–32	–
	1.72–1.76	14–16	–	100–120	1.8–2.5	–	–	–	20–25	30–40	–
	1.75–1.78	15	–	110–130	1.8–2.5	–	–	–	20–25	30–40	–
	1.76–1.80	15	–	120–130	2.2–2.6	–	–	–	40	60	–
B497XN	1.75	13	–	120	2.3	11	11.4	30	30	68	–
B650XN	1.82	14	–	80	4.5	13	–	–	60	105	–

(continued)

Table 2.6 (continued)

Trade mark or grade[b]	d, g cm^{-3}	P, %	c, kJ kg^{-1} K^{-1}	λ, W m^{-1} K^{-1}	α, 10^{-6} K^{-1}	ρ, μΩ m	E^c, GPa	σ_t, MPa	σ_f, MPa	σ_c, MPa	K_{IC}, MPa m$^{1/2}$
Structural and electrode graphite materials (The Carbon/Graphite Group)											
AI1RL	1.72	–	–	–	3.2 (100–600 °C)	16	–	–	28	–	–
AI4RL	1.82	–	–	–	5.7 (100–600 °C)	18	–	–	42	–	–
AI5RL	1.90	–	–	–	7 (100–600 °C)	20	–	–	77	–	–
Structural and electrode graphite materials (Toshiba Ceramics)											
IP40	1.7	–	–	–	3.8	12	–	–	30	–	–
NP60	1.8	–	–	–	4.5	14	–	–	45	–	–
Structural and electrode graphite materials (Nihon Carbon)											
EGM-63	1.78	–	–	–	4.8	15	–	–	38	–	–
EGM-74	1.82	–	–	–	4.8	14.5	–	–	40	–	–
Structural and electrode graphite materials (Tokai Carbon)											
G345	1.76	–	–	–	3.7	11	–	–	42	–	–
G548	1.85	–	–	–	4.5	12	–	–	70	–	–
Electrode graphite materials (HTU Industrial)											
Electrode RP	1.52–1.58	–	–	–	≤2.9/– (20–100 °C)	≤8.5/–	≤9.3/–	–	7.0–9.8	–	–
Electrode HD	≥1.60	–	–	–	≤2.7/– (20–100 °C)	7.0–7.5/–	≤10.0/–	–	≥10.0	–	–
Electrode HP	≥1.63	–	–	–	≤2.4/– (20–100 °C)	≤6.5/–	≤12.0/–	–	≥10.5	–	–
Electrode SHP	≥1.65	–	–	–	≤1.8/– (20–100 °C)	≤6.0/–	≤14.0/–	–	≥12.0	–	–
Electrode UHP	≥1.68	–	–	–	≤1.5/– (20–100 °C)	≤5.8/–	≤14.0/–	–	≥14.0	–	–
Nipple RP	1.63–1.72	–	–	–	2.7–2.8/– (20–100 °C)	7.5–8.2/–	13.7–14.0/–	–	13.0–15.0	–	–
Nipple HD	≥1.73	–	–	–	≤2.5/– (20–100 °C)	≤6.5/–	≤14.0/–	–	≥15.0	–	–

(continued)

Table 2.6 (continued)

Trade mark or grade[b]	d, g cm^{-3}	P, %	c, kJ kg^{-1} K^{-1}	λ, W m^{-1} K^{-1}	α, 10^{-6} K^{-1}	ρ, μΩ m	E^c, GPa	σ_b, MPa	σ_f, MPa	σ_c, MPa	K_{IC}, MPa m$^{1/2}$
Nipple HP	≥1.73	–	–	–	≤2.2/– (20–100 °C)	≤5.5/–	≤16.0/–	–	≥18.0	–	–
Nipple SHP	≥1.74	–	–	–	≤1.6/– (20–100 °C)	≤5.0/–	≤18.0/–	–	≥19.0	–	–
Nipple UHP	≥1.77	–	–	–	1.4 (20–100 °C)	≤4.5/–	≤18.0/–	–	≥20.0	–	–
Structural and electrode graphite materials ("Soyuzuglerod"/"Uglerodprom")											
PG-50	0.90–1.05	48–52	1.16 (0–1000 °C) 1.45 (0–1500 °C) 1.6 (0–2000 °C) 1.69 (0–2500 °C) 1.72 (0–2800 °C)	45/– (20 °C) 33/– (200 °C) 30/– (300 °C) 27/– (400 °C) 26/– (500 °C) 24/– (600 °C) 23/– (700 °C) 20/– (1000 °C) 16/– (1200 °C) 12/– (1700 °C) 11/– (2200 °C)	3.8/3.5 (20–100 °C) 4.3/4.0 (20–500 °C) 5.2/4.8 (20–1000 °C) 5.7/5.2 (20–1500 °C) 6.0/5.5 (20–2000 °C) 6.3/5.9 (20–2500 °C)	37.2/– (20 °C) 32.2/– (200 °C) 30.5/– (300 °C) 29.2/– (400 °C) 28.4/– (500 °C) 27.8/– (600 °C) 27.4/– (700 °C) 28.9/– (1200 °C) 33.2/– (1700 °C) 37.6/– (2200 °C)	1.66	3.4–4.4 /4.6–6.0 (20 °C) 5.6–7.5 /9.0–10.5 (2000 °C) 8.0–11.5 /12.0–17.0 (2500 °C) 6.7–9.9 /9.5–10.5 (2800 °C)	6.5–8.0 /7.0–9.5 (20 °C)	11.0–12.0 /10.8–12.0 (20 °C) 13.0–15.5 /13.5–15.0 (2000 °C) 13.5–20.0 /14.0–19.0 (2500 °C)	–
GÈ	1.52	24	–	–	–	7.6 (1000 °C)	–	–	–	24.5	–

(continued)

Table 2.6 (continued)

Trade mark or grade[b]	d, g cm^{-3}	P, %	c, kJ kg^{-1} K^{-1}	λ, W m^{-1} K^{-1}	α, 10^{-6} K^{-1}	ρ, μΩ m	E[c], GPa	σ_t, MPa	σ_f, MPa	σ_c, MPa	K_{IC}, MPa m$^{1/2}$
MG	1.49–1.60	28	–	65/75 (20 °C) 49/60 (200 °C) 45/55 (300 °C) 42/51 (400 °C) 38/48 (500 °C) 36/44 (600 °C) 34/41 (700 °C) 27/30 (1200 °C) 22/24 (1700 °C) 20/21 (2200 °C)	4.5/3.3 (20–100 °C) 5.3/4.1 (20–500 °C) 5.8/4.6 (20–1000 °C) 6.3/5.1 (20–1500 °C) 6.7/5.4 (20–2000 °C) 7.2/5.9 (20–2500 °C) 6.7 (1000–2500 °C)	22.6/19.0 (20 °C) 14.5/16.5 (200 °C) 13.6/15.5 (300 °C) 13.1/14.7 (400 °C) 12.8/14.4 (500 °C) 12.7/14.4 (700 °C) 14.2/16.1 (1200 °C) 16.0/18.0 (1700 °C) 17.7/20.0 (2200 °C)	2.7–5.0	–/5–8 (20 °C) –/8–10 (1000 °C) –/8–11 (1500 °C)	13 (20 °C)	–/24.0–26.5 (20 °C) –/26 (1000 °C) –/29 (1500 °C) –/38 (2000 °C)	–
MG–1	1.60–1.68	25	–	86/97 (20 °C) 71/84 (200 °C) 66/78 (300 °C) 60/73 (400 °C) 58/69 (500 °C) 54/64 (600 °C) 51/61 (700 °C) 42/48 (1200 °C) 36/41 (1700 °C) 32/36 (2200 °C)	4.5/3.3 (20–100 °C) 5.3/4.1 (20–500 °C) 5.8/4.6 (20–1000 °C) 6.3/5.1 (20–1500 °C) 6.7/5.4 (20–2000 °C) 7.2/5.9 (20–2500 °C) 6.7 (1000–2500 °C)	14.8/12.3 (20 °C) 12.7/10.5 (200 °C) 12.1/10.1 (300 °C) 11.8/9.8 (400 °C) 11.6/9.7 (500 °C) 11.4/9.5 (600 °C) 12.3/10.5 (1200 °C) 13.9/12.0 (1700 °C) 15.6/13.5 (2200 °C)	–	11.0–12.0 (20 °C) 11.5–12.5 (500 °C) 12.0–13.5 (1000 °C) 13.5–15.5 (1500 °C) 15–20 (2000 °C) 28 (2500 °C) 19.5 (2800 °C)	–	34–47 (20 °C) 40.5 (500 °C) 41.5–48.5 (1000 °C) 50.5–53.0 (1500 °C) 51.5–61.5 (2000 °C)	–

(continued)

Table 2.6 (continued)

Trade mark or grade[b]	d, g cm^{-3}	P, %	c, kJ kg^{-1} K^{-1}	λ, W m^{-1} K^{-1}	α, 10^{-6} K^{-1}	ρ, μΩ m	E^c, GPa	σ_t, MPa	σ_f, MPa	σ_c, MPa	K_{IC}, MPa m$^{1/2}$
PROG	1.60–1.70	24	1.63 (0–2500 °C)	120/– (20 °C) 75/47 (200 °C) 67/44 (300 °C) 61/41 (400 °C) 56/37 (500 °C) 51/34 (600 °C) 47/32 (700 °C) 37/23 (1200 °C) 32/21 (1700 °C) 28/20 (2200 °C)	3.5/4.7 (20–100 °C) 4.2/5.3 (20–500 °C) 4.8/5.9 (20–1000 °C) 5.2/6.4 (20–1500 °C) 5.6/6.6 (20–2000 °C) 5.9/6.9 (20–2500 °C)	10.5/– (20 °C) 8.3/13.0 (200 °C) 7.9/12.6 (300 °C) 7.7/12.2 (500 °C) 7.8/12.2 (600 °C) 7.9/12.4 (700 °C) 9.1/13.6 (1200 °C) 10.4/14.8 (1700 °C) 11.7/16.0 (2200 °C)	6.5–8.6 /5.5–6.0 (20 °C)	8.0–10.7 /4.5–7.2 (20 °C) 13.5–18.5 /6.0–13.5 (2000 °C) 17.0–28.5 /12.0–25.0 (2500 °C) 16.0–25.0 /8.0–12.1 (2800 °C)	10–19/10–15 (20 °C)	31–49/28–46 (20 °C) 40–68/35–61 (2000 °C) 62–71/60–69 (2500 °C)	–
ÈÈG	1.55–1.80	–	1.38 (0–1000 °C) 1.92 (0–2500 °C)	–/102 (20 °C) 59/79 (200 °C) 56/73 (300 °C) 52/68 (400 °C) 50/64 (500 °C) 47/60 (600 °C) 44/56 (700 °C) 32/42 (1200 °C) 23/30 (1700 °C) 20/17 (2200 °C)	5.0/4.5 (20–100 °C) 5.6/5.2 (20–500 °C) 6.3/5.8 (20–1000 °C) 7.0/6.3 (20–1500 °C) 7.4/6.8 (20–2000 °C) 7.6/7.2 (20–2500 °C) –/6.5 (500–2500 °C)	–/14.1 (20 °C) 15.1/11.7 (200 °C) 14.2/11.0 (300 °C) 13.6/10.5 (400 °C) 13.2/10.3 (500 °C) 13.0/10.2 (700 °C) 13.5/10.6 (1200 °C) 15.0/12.8 (1700 °C) 16.6/13.3 (2200 °C)	–	21.6–23.0 /34.0–41.5 (20 °C) 35.5–37.2 /47.5–59.0 (2000 °C) 30.3–45.3 /41.5–58.7 (2500 °C) 41.0–57.6 /47.7–76.7 (2800 °C) 8.8–13.4 /19.4–22.2 (3200 °C)	–	76–93/64–75 (20 °C) 103.0–129.5 /95.0–103.0 (2000 °C)	–

(continued)

Table 2.6 (continued)

Trade mark or grade[b]	d, g cm^{-3}	P, %	c, kJ kg^{-1} K^{-1}	λ, W m^{-1} K^{-1}	α, 10^{-6} K^{-1}	ρ, μΩ m	E^c, GPa	σ_t, MPa	σ_f, MPa	σ_c, MPa	K_{IC}, MPa m$^{1/2}$
GMZ	1.60–1.70	24	1.45 (0–1000 °C) 1.61 (0–2500 °C)	120/103 (20 °C) 92/72 (200 °C) 83/64 (300 °C) 75/58 (400 °C) 68/52 (500 °C) 62/48 (600 °C) 58/44 (700 °C) 39/32 (1200 °C) 33/28 (1700 °C) 31–42/24–32 (2200–2500 °C)	3.7/4.1 (20–100 °C) 4.5/4.8 (20–500 °C) 5.1/5.4 (20–1000 °C) 5.5/6.1 (20–1500 °C) 33/28 (1700 °C) (20–2000 °C) 5.1/5.8 (1000–2000 °C) 6.1/6.7 (20–2500 °C)	9.6/11.3 (20 °C) 7.8/9.7 (200 °C) 7.5/9.2 (500 °C) 7.8/9.5 (700 °C) 9.2/11.0 (1200 °C) 10.7/12.5 (1700 °C) 12.3–16.7 /14.0–19.2 (2200 °C) 17.7/19.9 (2600 °C) –/20.0 (2800 °C)	6.4–6.6/4.8 (20 °C) 7.6/5.4 (1000 °C)	8.8–9.0/ 6.8–7.0 (20 °C) 10/7.5 (1000 °C) 10/22 (2000 °C) –/23.5 (2700 °C)	12.6/10.8	34–33/ 33–32	–
Nuclear graphite materials[b]											
RBMK (*RU*)	1.68	–	–	103/89	3.8/4.2 (250–500 °C)	10/13	6.5/5.0	7.6/6.0	19/14	34/33	0.37/0.33
ÈGP–6 (*RU*)	1.69	–	–	80/75	3.7/4.9 (250–500 °C)	5.9/10.4	11.2/5.2	–	11.7/5.5	28/25	–
PPG (*RU*)	1.76	20	–	120	4.5 (250–500 °C)	8	–	–	21.2	45	–

(continued)

Table 2.6 (continued)

Trade mark or grade[b]	d, g cm^{-3}	P, %	c, kJ kg^{-1} K^{-1}	λ, W m^{-1} K^{-1}	α, 10^{-6} K^{-1}	ρ, μΩ m	E^c, GPa	σ_t, MPa	σ_f, MPa	σ_c, MPa	K_{IC}, MPa m$^{1/2}$
VPG (*RU*)	1.84	–	–	160–192/115 (20 °C) 134/– (200 °C) 114/– (300 °C) 99/– (400 °C) 88/– (500 °C) 80/– (600 °C) 74/– (700 °C) 56/– (1200 °C) 45/– (1700 °C) 41/– (2300 °C)	3.7/4.1 (20–100 °C) 4.5/4.8 (20–500 °C) 5.1/5.4 (20–1000 °C) 5.5/6.1 (20–1500 °C) 5.8/6.3 (20–2000 °C) 6.1/6.7 (20–2500 °C)	7/8/10 (20 °C) 5.4/– (200 °C) 5.15/– (300 °C) 5.10/– (400 °C) 5.15/– (500 °C) 5.20/– (600 °C) 5.30/– (700 °C) 6.20/– (1200 °C) 7.20/– (1700 °C) 8.20/– (2200 °C)	12/9	16/8	35/20	60/58	1.2

(continued)

Table 2.6 (continued)

Trade mark or grade[b]	d, g cm^{-3}	P, %	c, kJ kg^{-1} K^{-1}	λ, W m^{-1} K^{-1}	α, 10^{-6} K^{-1}	ρ, μΩ m	E^c, GPa	σ_t, MPa	σ_f, MPa	σ_c, MPa	K_{IC}, MPa m$^{1/2}$
VPP (*RU*)	1.75–2.05	–	–	130/198 (20 °C) 106/143 (200 °C) 96/123 (300 °C) 87/110 (400 °C) 80/100 (500 °C) 72/90 (600 °C) 68/84 (700 °C) –/63 (1000 °C) 50/58 (1200 °C) 45/48 (1700 °C) 43/45 (2200 °C)	4.1/3.9 (20–100 °C) 4.8/4.6 (20–500 °C) 5.4/5.2 (20–1000 °C) 5.9/5.5 (20–1500 °C) 6.2/5.9 (20–2000 °C) 6.65/6.3 (20–2500 °C)	7.8/5.4 (20 °C) 7.0/4.5 (200 °C) 6.7/4.8 (500 °C) 7.8/6.3 (1200 °C) 9.0/7.4 (1700 °C) 10.0/8.3 (2200 °C)	8.6–8.8/9.1 (20 °C) 9.6/10.3 (1000 °C) 12.3/12.8 (1500 °C) 14.2/16.0 (2000 °C) 14.5/16.3 (2200 °C) 12.9/14.2 (2500 °C)	14.5–15.0 /8.5–13.5 (20 °C) 14.5/12.0 (500 °C) 18/15 (1000 °C) 20–22/15 (1500 °C) 21–28/18 (2000 °C) 25/22 (2500 °C) 25.5–32.5/– (2800 °C) 22.5/– (3000 °C)	24–25/– (20 °C)	60–69/41–65 (20 °C) 60/48 (500 °C) 63.5–73.5 /50.5 (1000 °C) 61–77/48 (1500 °C) 71.5–93.5 /58.5 (2000 °C)	–
MIG–1 (*RU*)	1.73	–	–	120	4.8 (250–500 °C)	11	7.9	16	24	55	–
MIG–2 (*RU*)	1.67	–	–	90	5.1 (250–500 °C)	13	–	35	70	75	–
ARV (*RU*)	1.60–1.76	17	–	87	4.5/3.3 (20–100 °C) 5.8/4.6 (20–1000 °C) 6.7/5.4 (20–2000 °C) 7.2/5.9 (20–2500 °C)	11	5.9–7.9	11/12	15–17	44–46	–

(continued)

Table 2.6 (continued)

Trade mark or grade[b]	d, g cm^{-3}	P, %	c, kJ kg^{-1} K^{-1}	λ, W m^{-1} K^{-1}	α, 10^{-6} K^{-1}	ρ, μΩ m	E^c, GPa	σ_t, MPa	σ_f, MPa	σ_c, MPa	K_{IC}, MPa m$^{1/2}$
ARVu (*RU*)	1.67–1.80	–	–	51/61	5.3/4.1 (250–500 °C)	16/13	6.8/7.8 (20 °C) 6.9/7.9 (500 °C) 7.5/8.9 (1000 °C) 9.2/10.7 (1500 °C) 10.7/12.1 (2000 °C) 10.6/12.0 (2200 °C) 9.7/11.2 (2500 °C) 8.8/10.7 (2700 °C)	14.5–15 (20 °C) 16 (1000 °C) 16.5 (1500 °C) 20 (2000 °C) 36 (2500 °C) 25.5 (2800 °C)	26–46	62 (20 °C) 60 (1000 °C) 63 (1500 °C) 84.5 (2000 °C)	–
GR–1 (*RU*)	1.73	–	–	86/90	5.2/5.4 (250–500 °C)	15/14	8-10	15/18	30/25	70/84	0.8
GR–280 (*RU*)	1.72	–	–	103/89	3.2/4.9 (250–500 °C)	–	6.5/5	7.6/6	–	34/24	–
GR2–125 (*RU*)	1.85	–	–		3.9/5.2 (250–500 °C)	–	12/8.5	15/8	–	59/59	–
AG–1500 (*RU*)	1.73–1.85	14–15	–	80/90	4.0/4.3 (25–500 °C)	9–12/13	8/10–13	–	41	73–60	–
KPG (*RU*)	1.80	–	–	140/140	6.8/6.8 (250–500 °C)	9/12/2013	9.0/11	14	30/27	64	1.2/–
MPG (*RU*)	1.80	–	–	95/95	7.3/6.6 (250–500 °C)	11.7/10.7	11	32	55	100	1.1

(continued)

Table 2.6 (continued)

Trade mark or grade[b]	d, g cm^{-3}	P, %	c, kJ kg^{-1} K^{-1}	λ, W m^{-1} K^{-1}	α, 10^{-6} K^{-1}	ρ, μΩ m	E^c, GPa	σ_t, MPa	σ_f, MPa	σ_c, MPa	K_{IC}, MPa m$^{1/2}$
MPG–6 (*RU*)	1.72–1.85	–	–	95/– (20 °C) 75/– (200 °C) 70/– (300 °C) 66/– (400 °C) 62/– (500 °C) 58/– (600 °C) 55/– (700 °C) 48/– (1000 °C) 43/– (1200 °C) 37/– (1700 °C) 33/– (2200 °C)	6.6/6.0 (20–100 °C) 7.3/6.6 (20–500 °C) 7.9/7.2 (20–1000 °C) 8.5/7.7 (20–1500 °C) 8.8/8.1 (20–2000 °C) 9.15/8.8 (20–2500 °C)	14.2/– (20 °C) 11.2/– (200 °C) 10.4/– (300 °C) 9.9/– (400 °C) 9.7/– (500 °C) 9.5/– (600 °C) 9.4/– (700 °C) 9.5/– (1200 °C) 10.2/– (1700 °C) 11.2/– (2200 °C)	10.3–10.5 /10.3–10.5 (20 °C) 10.7/– (500 °C) 11.3/11.3 (1000 °C) 11.5/– (1500 °C) 10.9/– (2000 °C) 10.7/– (2200 °C) 9.9/– (2500 °C)	31.0–32.0 /33.5 (20 °C) 33.5/36.5 (1000 °C) 43.5/42.0 (2000 °C) 46.5/53.5 (2500 °C) 34.0/41.5 (2800 °C) 25.5/23.0 (3000 °C)	54/52–53 (20 °C)	96–100 /96–100 (20 °C) 109/106 (1000 °C) 119/124 (2000 °C)	–

(continued)

Table 2.6 (continued)

Trade mark or grade[b]	d, g cm^{-3}	P, %	c, kJ kg^{-1} K^{-1}	λ, W m^{-1} K^{-1}	α, 10^{-6} K^{-1}	ρ, μΩ m	E^c, GPa	σ_t, MPa	σ_f, MPa	σ_c, MPa	K_{IC}, MPa m$^{1/2}$
MPG–8 (*RU*)	1.75–1.85	–	–	87/122 (20 °C) 70/90 (200 °C) 64/83 (300 °C) 60/76 (400 °C) 55/70 (500 °C) 51/65 (600 °C) 47/61 (700 °C) 35/48 (1000 °C) 33/44 (1200 °C) 27/35 (1700 °C) 25/31 (2200 °C)	6.9/5.9 (20–100 °C) 7.6/6.6 (20–500 °C) 8.3/7.25 (20–1000 °C) 8.7/7.8 (20–1500 °C) 9.05/8.0 (20–2000 °C) 9.30/8.35 (20–2500 °C)	10.8/8.7 (100 °C) 9.8/8.2 (200 °C) 9.3/7.7 (300 °C) 9.1/7.5 (400 °C) 9.0/7.3 (500 °C) 9.1/7.4 (700 °C) 10.5/8.8 (1200 °C) 12.1/10.3 (1700 °C) 13.7/11.8 (2200 °C)	9.8/11.5 (20 °C) 10.2/11.9 (500 °C) 10.6/13.3 (1000 °C) 11.5/15.4 (1500 °C) 12.0/14.9 (2000 °C) 11.3/14.2 (2200 °C) 9.6/12.7 (2500 °C)	28.0/27.5 (20 °C) 28.5/31.5 (1000 °C) 32.5/36.0 (1500 °C) 37.5/41.5 (2000 °C) 45.0/60.5 (2500 °C) 48.0/48.5 (2800 °C) 30.0/26.5 (3000 °C) 18.5/24.0 (3200 °C)	35–60 (20 °C)	88.5/96.0 (20 °C) 92.0/98.5 (1000 °C) 88.5/93.5 (1500 °C) 97.0/102.5 (2000 °C)	–
SPP (*RU*)	1.56	–	–	80	5.8 (250–500 °C)	13.5	8.3	–	17	49	0.8
ER (*RU*)	1.60	–	–	50/170	5.9/1.2 (250–500 °C)	25/5.5	7.5/17.5	–	20/8	28/25	0.1/–
GSP–50 (*RU*)	1.72	–	–	86	5.8 (250–500 °C)	21	17	33	70	205	–
GSP–90 (*RU*)	1.79	–	–	90	5.5 (250–500 °C)	32	21	–	95	352	–
ChKG–3 (*RU*)	1.79–1.82	15–17	–	105–116	4.2–4.5 (250–500 °C)	10.3–12.0	8.9–10.0	–	21–30	53–62	–
ChKG–4 (*RU*)	1.82–1.83	15	–	118–137	4.1–4.3 (250–500 °C)	9.4–11.5	11.3	–	20–26	59–71	–

(continued)

Table 2.6 (continued)

Trade mark or grade[b]	d, g cm^{-3}	P, %	c, kJ kg^{-1} K^{-1}	λ, W m^{-1} K^{-1}	α, 10^{-6} K^{-1}	ρ, μΩ m	E^c, GPa	σ_t, MPa	σ_f, MPa	σ_c, MPa	K_{IC}, MPa m$^{1/2}$
GRCh (*RU*)	1.77–1.89	9–19	–	113–217	3.6–5.0 (250–500 °C)	6–10	7.7–12.9	–	14.9–32.6	33–83	–
GRCh–G (*RU*)	1.82–1.89	13–16	–	133–165	4.1–4.5 (250–500 °C)	8.0	11.0	–	17.0–23.7	52–65	–
AGOT (*US*)	1.7	–	–	227/138	2.2/3.8 (250–500 °C)	–	10/8	10/9	16/13	41/41	–
TSGBF (*US*)	1.65	–	–	–	2.7/3.9 (250–500 °C)	14/20	16/8.6	–	–	–	–
TSX (*US*)	1.71	–	–	–	1.1/4.1 (250–500 °C)	6.0/12.6	11.4–14/ 3.8–6.3	–	25/7	38/37	–
CSF (*US*)	1.68	–	–	255/132	1.8/3.8 (250–500 °C)	4.5/7.7	11/5	–	17/14	52/46	–
H–327 (*US*)	1.78	–	–	150/140	1.3/3.1 (250–500 °C)	5.6/11	–/4.5	13/8	21/15	32/28	0.64/–
H–451 (*US*)	1.76	–	–	135–150/ 125–135	3.6/4.6 (250–500 °C)	–	11–9/9.6–8	16–15/14–13	20–16/28–24	60–56/60–54	1.45/–
IG–11 (*JP*)	1.77	–	–	–	4.6 (250–500 °C)	11	–	–	40	–	–
IG–110 (*JP*)	1.75–1.78	–	–	124/128–138	4.0–4.2/3.6–4.2 (250–500 °C)	11.5–10/–	9.4–10/10	25	39–34	80–71	0.78/–
ISO–88 (*JP*)	1.90	–	–	–	6.5 (250–500 °C)	15	–	–	95	–	–
PGA (*UK*)	1.68–1.74	–	–	140–200/109	1.3/3.3 (250–500 °C)	6	12/5.6	17–10/11–6	19–15/12–11	34–27/35–27	–
SM2–24 (*UK*)	1.7	–	–	–	–	–	8/8.5	12	19	47	–
IM1–24 (*UK*)	1.81	–	–	131	4.3 (250–500 °C)	–	11	27.5	23	70	–
Pitch–coke (*UK/FR*)	1.8	–	–	130/135	4.0/3.8 (250–500 °C)	–	13/10	25/17	32/26	70/63	–

(continued)

Table 2.6 (continued)

Trade mark or grade[b]	d, g cm^{-3}	P, %	c, kJ kg^{-1} K^{-1}	λ, W m^{-1} K^{-1}	α, 10^{-6} K^{-1}	ρ, μΩ m	E^c, GPa	σ_t, MPa	σ_f, MPa	σ_c, MPa	K_{IC}, MPa m$^{1/2}$
PPEA (*FR*)	1.85	–	–	140/130	5.0/5.3 (250–500 °C)	9/10	12/11	22/19	34/28	82/–	–
SLWXX (*FR*)	1.83	–	–	165/146	4.6/5.1 (250–500 °C)	7/9	11/10	20/16	24/21	64	1.3/–
DM332PU (*FR*)	1.81	–	–	117	4.6 (250–500 °C)	11	12	34	43	91	1.0
P3AN (*FR*)	1.68	–	–	–	2.5/3.9 (250–500 °C)	–	11/7.5	14/9.2	–	42/38	–
P3JHA2N (*FR*)	1.78	–	–	126	2.9/4.1 (250–500 °C)	10/16	11	16	–	–	–
ASR–1RS (*GE*)	1.78	–	–	125	4.7/4.9 (250–500 °C)	–	9.9/9.2	15/14	26/23	67/63	–
ATR–2E (*GE*)	1.8	–	–	179/163	4.4/4.9 (250–500 °C)	–	9.6/8.4	12.5	23/9	57/57	–

[a] Physical properties: d—bulk density, P—porosity, c—specific heat capacity (averaged for the range of temperatures), λ—thermal conductivity, α—coefficient of thermal expansion, ρ—specific electrical resistivity, E—Young's modulus, σ_t—Tensile, σ_f—flexural (bending) and σ_c—compressive strengths, K_{IC}—Fracture toughness (critical stress intensity factor); anisotropic properties a_i/a_j are given in parallel and perpendicular directions to the transversely isotropic symmetry axis of materials, respectively, so for quasi-isotropic materials average values $a_m = (a_i + 2a_j)/3$; values of properties given for the various temperatures or ranges of temperatures (different from the room temperature) are accompanied with special notations in brackets

[b] Country of origin for trade marks or grades is given in brackets: *RU*—Russia, *US*—United States of America, *JP*—Japan, *UK*—United Kingdom, *FR*—France, *GE*—Germany

[c] Indicated values of ranges include the results of measurements made by different methods

[d] For tension loading: in parallel direction to the transversely isotropic symmetry axis initial static modulus and sonic modulus are 8.1 and 7.7 GPa, respectively, and in perpendicular directions to the axis initial static modulus and sonic modulus are 11.3–11.5 and 11.3–11.4 GPa, respectively (Poisson's ratio values: $\nu_{12} = 0.10$, $\nu_{13} = 0.11$ and $\nu_{23} = 0.16$); for compression loading: in parallel and perpendicular directions to the transversely isotropic symmetry axis initial static moduli are 8.4 and 11.8 GPa, respectively

Table 2.7 General physical properties of pyrolytic carbon (graphite) materials[a]

Property	Unit	T, °C	Direction to deposition plane		References
			perpendicular	parallel	
Density	g cm^{-3}	20	1.4–2.24		[138, 194, 208–209]
Specific heat capacity	kJ kg^{-1} K^{-1}	20	0.962–1.00		[138, 194]
		250	1.25		
		500	1.55		
		750	1.8		
		1000	2.0		
		1500	2.05		
		2000	2.08		
		2500	2.1		
Thermal conductivity	W m^{-1} K^{-1}	20	1–6.5	190–1100	[42, 136, 138, 194, 209, 539]
		200	1.5–5.4	290–500	
		700	1.2–4.6	150–310	
		1200	0.96–3.9	120–210	
		1700	0.7–3.8	97–170	
		2200	0.5–2.0	70–140	
			15–25		
Coefficient of linear thermal expansion[b]	10^{-6} K^{-1}	20–100	15–25	(–1.3)–(+1.0)	[42, 136, 138, 194, 209, 539]
		20–500	20–24	(–0.4)–(+2.1)	
		20–800	–	0.5–2.6	
		20–1000	22–25.5	0.7–1.1	
		20–1500	22–26.5	1.2–1.6	
		20–2000	24–26.5	1.2–1.9	
		20–2500	24–27	2	
Electrical resistivity	μΩ m	20	(0.25–10) × 10^3	0.5–10	[42, 136, 138, 194, 208–209, 539]
		500	3.4 × 10^3	2.6	
		700	(2.8–3.5) × 10^3	2.5–2.7	
		1700	1.25 × 10^3	3.5	
		2200	0.7 × 10^3	4.0	
Young's modulus	GPa	20	3–11	7.5–41	[42, 138, 194, 207–208]
		600	–	10.3–28	
		1650	–	23.3–24.0	
		2200	–	18.5–20.6	
		2700	–	9.6–17.8	
Coulomb's (shear) modulus	GPa	20	–	14.5–15.5	[209]

(continued)

Table 2.7 (continued)

Property	Unit	T, °C	Direction to deposition plane		References
			perpendicular	parallel	
Tensile strength	MPa	20	4.8	21–170	[42, 138, 194, 207–209]
		1650	–	116–125	
		2200	–	152–188	
		2500	–	180–240	
		2800	–	316–415	
Flexural (bending) strength	MPa	20	80–250	10–20	[42, 136, 138, 194, 207–209]
		1000	180–206	–	
		2200	100–213	–	
Compressive strength		20	56–100	282–480	[208–209]
Hardness, Mohs HM		20	4.5	1.0	[194]

[a] For isotropic pyrolytic carbon: density—2.1 g cm^{-3}, Young's modulus—28 GPa and flexural (bending) strength—350 MPa (at 25 °C) [42, 136]; for isotropic "pyroceramic" carbon: density—1.8–2.1 g cm^{-3}, specific electrical resistivity—12–18 μΩ m, Young's modulus—16–21 GPa, tensile strength—87–123 MPa, flexural (bending) strength—45–250 MPa, compressive strength—380–550 MPa (at 20 °C), coefficient of thermal expansion (20–500 °C)—(2.6–6.0) × 10^{-6} K^{-1}, thermal conductivity (1000–2000 °C)—14–17 W m^{-1} K^{-1} [207, 209]

[b] Coefficient of volumetric thermal expansion, 10^{-6} K^{-1}—19–25 (20–100 °C), 21–26.5 (20–500 °C), 24–27 (20–1000 °C), 26–27.5 (20–1500 °C) and 28–29 (20–2000 °C) [539]

at room temperature [3, 539–540], the χ_{mol} versus temperature relationships for both main directions in the graphite crystals are shown in Fig. 2.6.

The general optical properties of carbon (graphite) for wavelength $\lambda = 0.620$ μm are following: index of refraction (single crystal)—2.6, index of absorptance (single crystal)—1.4, reflective index under normal incidence—0.24 (polished graphite) and 0.35 (cleaned single crystal surface) [6]. In visible-light spectrum the monochromatic emittance (spectral emissivity) ε_λ of graphite is near to that of a grey body and varies for $\lambda = 0.65$ μm from 0.77 (well-polished surfaces) to 0.95 (roughened surfaces). The integral emittance ε_T of graphite ranges from 0.6 to 0.9. The temperature variations for the both coefficients of emittance are linear:

$$\varepsilon = \varepsilon_0 \pm aT, \tag{2.3}$$

with the positive values of a for integral emittance ε_T and negative value—for spectral emittance ε_λ ($\lambda = 0.665$) [138]. The recommended values of electrical resistivity, magnetic susceptibility, integral and spectral emittances and thermoionic emission characteristics for carbon (graphite) materials are given in comparison with other ultra-high temperature elements (refractory metals) in Addendum.

2.4 Physico-Mechanical Properties

Hardness of carbon (graphite) materials ranges widely depending on their macro- and microstructures and bulk densities. To compare this property for the various graphitic products or with other ultra-high temperature materials is often

Table 2.8 General physical properties[a] of common vitreous (glass-like) carbon materials [11, 42, 136, 207, 209, 539]

Trade mark or grade[b]	d, g cm^{-3}	P_o, %	T_t, °C	T_s, °C	Π, cm^2 s^{-1}	λ, W m^{-1} K^{-1}	α, 10^{-6} K^{-1}	ρ, μΩ m	E, GPa	σ_f, MPa	σ_c, MPa	H
S-100 (*JP*)	1.45	–	1200	–	–	3.3–3.8	3.5 (20–200 °C)	45	20	98	–	120[c]
GC-10 (*JP*)	1.47–1.51	0.2–0.4	1300	–	10^{-12}–10^{-11}	3.5–4.7	2.2–3.2 (20–200 °C)	45–65	27–32	88–100	–	100–120[c]
GC-20 (*JP*)	1.46–1.50	1–3	2000	–	10^{-12}–10^{-11}	8.1–9.3	2.0–2.2 (20–1500 °C)	40–45	25–32	70–118	–	100–110[c]
GC-30 (*JP*)	1.43–1.47	3–5	3000	–	10^{-9}–10^{-7}	15.0–17.6	2.0–2.2 (20–1500 °C)	30–40	15–25	40–59	–	70–80[c]
SU-1200 (*RU*)	1.45–1.55	0.2–1.3	1200	1000	–	–	3.5–4.0 (20–1500 °C)	45–50	28–31	70–100	–	–
SU-1300 (*RU*)	1.49–1.52	0.2–1.0	1300	1300	10^{-12}–10^{-11}	3.7–4.1	4.4–5.1 (20–1500 °C)	45–50	25–30	107–127	–	30–33[d]
SU-2000 (*RU*)	1.38–1.54	0.7–2.0	2000	2000	10^{-11}–10^{-10}	5.1–6.1 (20 °C)	2.3–2.4 (20–100 °C)	40–44 (20 °C)	27–30	130–160	–	20–23[d]
						8.3 (500 °C)	2.7–2.9 (20–500 °C)	38 (300 °C)				
						9.0 (700 °C)	3.5–4.05 (20–1500 °C)	35 (500 °C)				
						10 (1200 °C)		27 (1200 °C)				
						11.5 (2200 °C)	5.0 (20–2500 °C)	20 (2200 °C)				
SU-2500 (*RU*)	1.44–1.50	1.5–2.5	2500	2500	10^{-10}–10^{-9}	6.4–7.8 (20 °C)	2.3–2.4 (20–100 °C)	38–44 (20 °C)	25–30	70–100 (20 °C)	260 (20 °C)	18–20[d]
						8.3 (500 °C)	2.7–2.9 (20–500 °C)	38 (300 °C)		80 (1000 °C)	135 (1000 °C)	
						9.0 (700 °C)	3.5–4.05 (20–1500 °C)	35 (500 °C)		110 (2000 °C)	280 (1500 °C)	
						10 (1200 °C)		27 (1200 °C)				
						11.5 (2200 °C)	5.0 (20–2500 °C)	20 (2200 °C)				

(continued)

Table 2.8 (continued)

Trade mark or grade[b]	d, g cm^{-3}	P_o, %	T_t, °C	T_s, °C	Π, cm^2 s^{-1}	λ, W m^{-1} K^{-1}	α, 10^{-6} K^{-1}	ρ, μΩ m	E, GPa	σ_f, MPa	σ_c, MPa	H
SU-3000 (*RU*)	1.06–1.27	1.8–2.2	3000	–	–	7.5	3.5–4.0 (20–1500 °C)	40–45	15–17	70–100	–	–
V10 (*FR*)	1.50–1.55	~0	–	–	–	–	3.2 (20–1500 °C)	55	28.5	100	–	–
V25 (*FR*)	1.50–1.55	~0	–	–	–	–	3.2 (20–1500 °C)	45	22	60–80	–	–
Sigradur (*GE*)	1.42	~0	2200	3000	10^{-9}	6.3	2.6 (20–200 °C)	–	35	260	480	230[e]
	1.54	~0	1100	1100	10^{-11}	4.6 (20 °C) 11 (1000 °C)	3.5 (20–200 °C) 4 (20–1000 °C)	45 (20 °C) 30 (1000 °C)	35	210	580	340[e]

[a] Physical properties: d—bulk density, P_o—open porosity, T_t—final temperature of heat treatment, T_s—maximal service temperature, Π—gas permeability, λ—thermal conductivity, α—coefficient of thermal expansion, ρ—specific electrical resistivity, E—Young's modulus, σ_f—flexural (bending) and σ_c—compressive strengths, H—hardness; values of properties given for the various temperatures or ranges of temperatures (different from the room temperature) are accompanied with special notations in brackets

[b] For trade marks or grades country of origin is given in brackets: *JP*—Japan, *RU*—Russia, *FR*—France, *GE*—Germany

[c] Shore hardness

[d] Microhardness, MPa

[e] Vickers hardness HV_1

Table 2.9 General physical properties[a] of common thermally expanded (exfoliated) graphite materials [212–213, 216]

Trade mark or grade[b]	d, g cm^{-3}	c, kJ kg^{-1} K^{-1}	Π, cm^2 s^{-1}	λ, W m^{-1} K^{-1}	α, 10^{-6} K^{-1}	ρ, μΩ m	σ_t, MPa	β, 10^{-3} MPa^{-1}	β', %
Sigraflex Foil[c] (*GE*)	0.7–1.3	0.7	$<5 \times 10^{-5}$/–	4.8/155	~30/~1 (20–1000 °C)	≥650/~9	–/≥ 4[d]	–	–
Grafoil (*US*)	1.1	–	–	5/140	–	–	–/4.4–6.9	11/–	20/–
Grafleks (*RU*)	0.6–1.1	–	–	3–5/130–200	–	–	–/3.5–7.0	10–11/–	10–20/–
Termografenit (*UA*)	0.6–1.5	–	–	–/130–200	–	–	–/5.0–6.0[e]	6–13[f]/–	12–30[f]/–

[a] Physical properties: d—bulk density, c—specific heat capacity, Π—gas permeability, λ—thermal conductivity, α—coefficient of thermal expansion, ρ—specific electrical resistivity, σ_t—tensile strength, β—compressibility (for loading pressure $P = 35$ MPa), β'—recoverability (for loading pressure $P = 35$ MPa); anisotropic properties a_i/a_j are given in parallel and perpendicular directions to the transversely isotropic symmetry axis of materials, respectively; values of properties given for the various temperatures or ranges of temperatures (different from the room temperature) are accompanied with special notations in brackets

[b] For trade marks or grades country of origin is given in brackets: *GE*—Germany, *US*—United States of America, *RU*—Russia, *UA*—Ukraine

[c] Physical properties are given for materials with bulk density $d = 1.0$ g cm^{-3} and ash content ≤0.15 %

[d] Elongation at break ≥1 %

[e] For materials with bulk density $d = 1.0$ g cm^{-3}

[f] For materials with bulk density $d = 1.2$–1.5 g cm^{-3}

Table 2.10 General physical properties[a] of carbon (graphite) filaments in commercial carbon fibres [84, 136, 207, 217–221]

Trade mark and grade[b]	D, μm	d, g cm^{-3}	E, GPa	σ_t, GPa	δ, %	λ, W m^{-1} K^{-1}	α, 10^{-6} K^{-1}	ρ, μΩ m
High-modulus (low strain to failure) PAN-based carbon fibres								
BASF GY70 (*GE*)	8.0	1.96	520	1.9	0.3	175	–	6.5
Celion GY70 (*US*)	–	–	430–520	1.80–1.86	0.4	–	–	–
Kulon (*RU*)	–	1.90	400–600	2.0	0.4	–	–	–
Besfight HM45 (*JP*)	6.4	1.90	441	3.10	0.48	–	–	–
Modmor I (*UK*)	7.5–7.8	2.00	380–450	1.77–2.26	0.5	–	–	–
Torayca M50 (*JP*)	7.0	1.90–1.91	500	2.35–2.5	0.5	100	–0.7	9.5
Torayca M40A (*JP*)	6.0–7.0	1.78–1.84	340–450	2.0–2.5	0.5–0.6	–	–1.2	8–10
Grafil HMS (*UK*)	7.6	1.88	320–400	2.0–2.1	0.5–0.7	–	–	–
Hexcel HM-S (Magnamite, *US*)	–	–	345	2.21	0.6	–	–	–
Besfight UM40 (*JP*)	6.6	1.83	392	2.55	0.65	–	–	–
Tenax HMA (*GE*)	6.75	1.77	358	3.00	0.7	–	–	–
Grafil HM (*UK*)	–	–	370	2.75	0.7	–	–	–
Torayca M40[c] (*JP*)	6.5–7.0	1.81	392–400	2.40–2.74	0.6–0.75	45	–0.75	11
Torayca M60J[c] (*JP*)	4.7	1.94	585–588	3.80–3.82	0.7	–	–	–
Acif HM (*UK*)	6.6	1.86	335	2.20	0.75	–	–	–
Hexcel HMS4 (*US*)	8.0	1.80	360	2.3	0.8	–	–	–
Hexcel UHM (*US*)	–	1.87	441	3.45	0.8	–	–	–
Besfight HM35 (*JP*)	6.7	1.79	343	2.74	0.8	–	–	–
Torayca M50J[c] (*JP*)	5.0	1.88	475	4.12	0.8	–	–	–
Torayca M55J[c] (*JP*)	5.0	1.91	540	4.02	0.8	–	–	–
Torayca M46J[c] (*JP*)	5.0	1.84	436–450	4.20–4.21	1.0	–	–	–
Pyrofil HS40 (*JP*)	5.0	1.85	450	4.41	1.0	–	–	–
Pyrofil HR40 (*JP*)	6.0	1.82	390	4.41	1.1	–	–	–
Tenax UMS 2526 (*GE*)	4.8	1.78	395	4.56	1.1	–	–	–
Tenax UMS 3536 (*GE*)	4.7	1.81	435	4.50	1.1	–	–	–
Torayca M40J[c] (*JP*)	5.0	1.77	377–390	4.30–4.41	1.2	–	–	–
Pyrofil MS40 (*JP*)	6.0	1.77	345	4.61	1.3	–	–	–
Torayca M35J[c] (*JP*)	6.0	1.75	343	4.70	1.4	–	–	–
	4.7–7.8	1.75–2.00	320–600	1.45–4.7	0.4–1.4	–	–	–

(continued)

Table 2.10 (continued)

Trade mark and grade[b]	D, μm	d, g cm^{-3}	E, GPa	σ_t, GPa	δ, %	λ, W m^{-1} K^{-1}	α, 10^{-6} K^{-1}	ρ, μΩ m
Intermediate-modulus (intermediate strain to failure) PAN-based carbon fibres								
Avcarb HCB (*US*)	–	–	260	1.90	0.7	–	–	–
Elur (*RU*)	–	–	150	2.00	–	–	–	–
LU-2 (*RU*)	–	–	230	2.0–2.5	–	–	–	–
LU-3 (*RU*)	–	–	250	2.5–3.0	–	–	–	–
LU-4 (*RU*)	–	1.70	230	3.0–3.5	–	–	–	–
UKN-5000 (*RU*)	7.0–8.0	1.75	180–230	3.0–3.5	0.9	–	–	–
Grafil A (*UK*)	–	1.76	192	2.55	–	–	–	–
Grafil HTS (*UK*)	8.0	1.77	240	2.5–2.9	–	–	–	–
Avcarb HC (*US*)	–	–	207	2.07	–	–	–	–
SGL Technic C10 (*UK*)	–	–	180–240	≥2.00	–	–	–	–
SGL Technic C25 (*UK*)	–	–	215–240	≥2.50	1.05–1.40	–	–	–
Indcarf 25 (*IN*)	–	–	215–240	≥2.50	1.05–1.40	–	–	–
Torayca T300 (*JP*)	7.0	1.76	230–250	3.0–3.5	1.2–1.5	10	–0.6	18
Indcarf 30 (*IN*)	6.8	1.78	220–240	≥3.00	1.25–1.60	–	–	–
SGL Technic C30 (*UK*)	7.0	1.78	220–240	≥3.00	1.25–1.60	–	–	–
Apollo IM 43-600 (*UK*)	–	–	300	4.00	1.3	–	–	–
Acif IS (*UK*)	6.8	1.78	230	2.50	1.3	–	–	–
Kosca GP250 (*KR*)	6.8	1.80	220	2.80	1.3	–	–	–
Thornel T300 (*US*)	6.4–7.0	1.76	230–235	3.1–3.75	1.3–1.4	–	–	–
Acif HT (*UK*)	6.8	1.78	230	2.90	1.4	–	–	–
Kosca HS300 (*KR*)	6.8	1.80	230	3.30	1.4	–	–	–
Tenax IMS 3131 (*GE*)	6.4	1.76	295	4.12	1.4	–	–	–
Celion 1000 (*US*)	7.0–8.0	–	234	3.24	1.4	–	–0.7	15–16
Granit 40 (*RU*)	~7	1.76	~230	≤3.65	1.4	–	–	–
Hexcel IM6 (*US*)	5.0–5.2	1.76	276–280	4.4–5.6	1.4–2.0	–	–	–
Pyrofil MR35E (*JP*)	7.0	1.75	295	4.41	1.5	–	–	–
Pyrofil MR40 (*JP*)	6.0	1.76	295	4.41	1.5	–	–	–
Tenax HTA (*GE*)	7.0	1.77	238	3.95	1.5	–	–	–
Tenax HTS (*GE*)	7.0	1.77	238	4.30	1.5	–	–	–
Tenax STS (*GE*)	7.0	1.79	240	4.00	1.5	–	–	–

(continued)

Table 2.10 (continued)

Trade mark and grade[b]	D, μm	d, g cm^{-3}	E, GPa	σ_b, GPa	δ, %	λ, W m^{-1} K^{-1}	α, 10^{-6} K^{-1}	ρ, μΩ m
Besfight IM400 (*JP*)	6.4	1.75	295	4.31	1.5	–	–	–
Besfight HM30 (*JP*)	6.4	1.75	295	4.30	1.5	–	–	–
Acif XHT (*UK*)	6.8	1.78	230	3.30	1.55	–	–	–
Fortafil 506…509 (*US*)	7.0	1.80	217	3.45	1.59	–	–	–
Besfight HTA (*JP*)	7.0	1.77	235	3.92	1.6	–	–	–
Besfight STA (*JP*)	–	–	240	3.73	1.6	–	–	–
Panex 33 (*US*)	7.2	1.81	228	3.80	1.6	–	–	–
Fortafil 502…505, 510…513 (*US*)	6.0	1.80	231	3.80	1.64	–	–	–
Fortafil 555…556 (*US*)	6.2	1.80	231	3.80	1.65	–	–	–
	5.2–8.0	1.71–1.81	150–300	1.45–5.6	0.7–1.65	–	–	–
High strain to failure PAN-based carbon fibres								
Besfight ST1 (*JP*)	–	–	240	3.6	1.5	–	–	–
Hexcel AS4 (*US*)	7.0–8.0	1.78–1.81	227–235[f]	3.6–4.3	1.5–1.9	7.2–16.0[g]	–(1.2–1.7)[h]	15.3
BASF G40 (*GE*)	7.0	1.77	300	5.0	1.6	–	–	13
Besfight ST2 (*JP*)	–	–	240	4.08	1.7	–	–	–
Besfight IM500 (*JP*)	5.0	1.76	300	5.0	1.7	–	–	–
Thornel T650/35 (*US*)	6.8	1.77	255	4.28	1.7	–	–	–
Hexcel AS6 (*US*)	–	–	241	4.14	1.7	–	–	–
Torayca T400 (*JP*)	5.6–6.8		250–310	4.5–5.1	1.7–1.8	–	–	–
Hexcel IM4 (*US*)	6.7	1.78	276	4.80	1.74	–	–	–
Hexcel IM6 (*US*)	–	–	280	5.0	1.8	–	–	–
Besfight ST3 (*JP*)	–	–	240	4.32	1.8	–	–	–
Celion ST (*US*)	–	–	235	4.34	1.8	–	–	–
Torayca T300J[c] (*JP*)	7.0	1.78	230	4.21	1.8	–	–	–
Torayca T400H[c] (*JP*)	7.0	1.80	250	4.41	1.8	–	–	–
Grafil 34–600…34-600WD (*UK*)	7.0	1.80	234	4.15	1.8	–	–	–
Pyrofil MR50 (*JP*)	6.0	1.80	290	5.40	1.8	–	–	–
Hexcel IM8 (*US*)	5.1	1.79–1.80	303–304	5.45–5.59	1.84	–	–	–
Hi-Carbolon (*JP*)	7.0	1.78	230	4.31	1.87	–	–	–
Hexcel IM7 (5000 Spec, *US*)	5.2	1.78–1.80	276–292	5.18–5.76	1.87–2.01	–	–	–
Hexcel AS4C (*US*)	6.9	1.78	231	4.35	1.88	–	–	–

(continued)

Table 2.10 (continued)

Trade mark and grade[b]	D, μm	d, g cm^{-3}	E, GPa	σ_t, GPa	δ, %	λ, W m^{-1} K^{-1}	α, 10^{-6} K^{-1}	ρ, μΩ m
Grafil 34-700 (*UK*)	7.0	1.80	234	4.50	1.9	–	–	–
Torayca M30S[c] (*JP*)	6.5	1.73	294	5.49	1.9	–	–	–
Torayca T600S[c] (*JP*)	–	1.79	230	4.31	1.9	–	–	–
Torayca T800 (*JP*)	5.1–7.0	1.81	250–300	5.0–5.7	1.9–2.0	15	–0.75	14
Torayca T800H[c] (*JP*)	5.0	1.81	290–294	5.49–5.60	1.9	–	–	–
Apollo HS 38-750 (*UK*)	–	–	260	5.00	1.9	–	–	–
Tenax IMS 5131 (*GE*)	5.0	1.80	290	5.60	1.9	–	–	–
Besfight ST3 (*JP*)	7.0	1.77	235	4.41	1.9	–	–	–
Pyrofil TR30S (*JP*)	7.0	1.79	235	4.41	1.9	–	–	–
Pyrofil TRH50 (*JP*)	7.0	1.80	255	4.90	1.9	–	–	–
Hexcel IMC (*US*)	5.4	1.80	290	5.52	1.90	–	–	–
Hexcel PV36/700 (*US*)	–	–	248	4.69	1.90	–	–	–
Hexcel PV42/800 (*US*)	5.4	1.80	290	5.52	1.90	–	–	–
Hexcel IMC (*US*)	–	1.80	290	5.52	1.90	–	–	–
Hexcel IM7C (*US*)	5.4	1.80	290	5.52	1.90	–	–	–
Hexcel AS4D (*US*)	6.7	1.79	245	4.69	1.92	–	–	–
Hexcel PV42/850 (*US*)	4.4	–	292	5.76	1.97	–	–	–
Hexcel IM7 (6000 Spec, *US*)	5.1	1.79	290	5.76	1.99	–	–	–
Pyrofil TR40 (*JP*)	7.0	1.80	235	4.70	2.0	–	–	–
Pyrofil TR50S (*JP*)	7.0	1.82	240	4.90	2.0	–	–	–
Tenax UTS (*GE*)	7.0	1.80	240	4.70	2.0	–	–	–
Hexcel IM9 (*US*)	4.4	1.80	290	6.07–6.14	2.10	–	–	–
Torayca T700S[c] (*JP*)	7.0	1.80	230	4.90	2.1	–	–	–
Torayca T700G[c] (*JP*)	–	1.80	240	4.90	2.1	–	–	–
Torayca T1000G[c] (*JP*)	5.0	1.80–1.82	294	6.37–7.06	2.2	–	–	–
Torayca T1000 (*JP*)	5.7	1.80–1.82	255–300	6.4–7.2	2.2–2.4	–	–	–
	4.4–7.0	1.73–1.82	230–310	3.6–7.2	1.5–2.4	–	–	–
Coal tar and petroleum pitches based carbon fibres								
Thornel P75 (*US*)	9.6–10.0	2.00	500–520	2.0–2.1	0.25–0.40	150	–1.4	7
Thornel P100S (*US*)	10	2.16	758	2.07	0.27	–	–	–
Thornel P120S (*US*)	10	2.17	827	2.24	0.29	–	–	–

(continued)

Table 2.10 (continued)

Trade mark and grade[b]	D, μm	d, g cm^{-3}	E, GPa	σ_t, GPa	δ, %	λ, W m^{-1} K^{-1}	α, 10^{-6} K^{-1}	ρ, μΩ m
Thornel P120 (*US*)	9.6–10.6	2.10–2.17	820–827	2.20–2.41	0.29–0.30	640	–1.6	–
Thornel K1100X, K1000X (*US*)	10	2.20	965	3.10	0.30	1100	–1.6	–
Thornel P100 (*US*)	8.8–10.0	2.16–2.20	690–760	2.2–2.4	0.30–0.35	300–520	–(1.4–1.6)	2.5–3.0
Dialead K139 (*JP*)	10	2.14	735	2.75	0.37	–	–	–
Granoc XN85A[d] (*JP*)	8.5	2.17	830	3.63	0.4	–	–	–
Granoc YS90A[e] (*JP*)	7	2.19	880	3.63	0.4	–	–	–
Dialead K137 (*JP*)	–	2.12	637	2.65	0.42	–	–	–
Carbonic HM70 (*JP*)	10	2.18	686	2.94	0.43	–	–	–
Dialead K135 (*JP*)	–	2.10	539	2.55	0.47	–	–	–
Thornel P55S (*US*)	10	2.00	379	1.90	0.50	–	–	–
Thornel P55 (*US*)	8.7–10.0	2.00	380	1.90–2.10	0.50–0.55	100	–1.3	7.5–8.5
Thornel P100HTS (*US*)	10	2.17	724	3.62	0.50	–	–	–
Granoc XN70A[d] (*JP*)	10	2.16	720	3.63	0.5	–	–	–
Granoc XN80A[d] (*JP*)	10	2.17	785	3.63	0.5	–	–	–
Granoc YS70A[e] (*JP*)	7	2.16	720	3.63	0.5	–	–	–
Granoc YS70[e] (*JP*)	7	2.14	690	3.53	0.5	–	–	–
Granoc YS80[e] (*JP*)	7	2.15	785	3.53	0.5	–	–	–
Carbonic HM60 (*JP*)	10	2.17	588	2.94	0.50	–	–	–
Forca FT700 (*JP*)	10	2.16	700	3.30	0.5	–	–	–
Dialead K133 (*JP*)	–	2.08	441	2.35	0.53	–	–	–
Carbonic HM50 (*JP*)	10	2.16	490	2.75	0.56	–	–	–
Forca FT500 (*JP*)	10	2.14	500	3.00	0.6	–	–	–
Granoc YS60[e] (*JP*)	7	2.12	590	3.53	0.6	–	–	–
Donacarbo (*JP*)	9	2.10	500	3.00	0.6	–	–	–
Granoc XN50A[d] (*JP*)	10	2.14	520	3.83	0.7	–	–	–
Granoc YS50A[e] (*JP*)	7	2.14	520	3.83	0.7	–	–	–
Granoc YT50-10S (*JP*)	6		490	4.1	0.8	–	–	–
Granoc YS50[e] (*JP*)	7	2.09	490	3.73	0.8	–	–	–
Thornel P25 (*US*)	8.6–11.0	1.90	125–159	1.40	0.9–1.0	–	–	–
Dialead K321 (*JP*)	–	1.90	176	1.96	1.08	–	–	–

(continued)

Table 2.10 (continued)

Trade mark and grade[b]	D, μm	d, g cm^{-3}	E, GPa	σ_t, GPa	δ, %	λ, W m^{-1} K^{-1}	α, 10^{-6} K^{-1}	ρ, μΩ m
Dialead K223 (*JP*)	–	2.00	225	2.84	1.2	–	–	–
	6.0–11.0	1.90–2.20	125–965	1.4–4.1	0.25–1.2	120–1100	–	2–13
Viscose rayon (cellulose) based carbon fibres								
Thornel 25 (*US*)	–	–	170	1.25	–	–	–	–
Thornel 40 (*US*)	6.9	1.55	276	1.72	0.8	–	–	–
Thornel 50 (*US*)	6.6	1.63	340–350	1.97–2.00	0.8	–	–	–
Thornel 50S (*US*)	–	1.67	392	1.96	–	–	–	–
Thornel 60 (*US*)	6.1	1.69–1.70	400–420	2.20–2.27	–	–	–	–
Thornel 70 (*US*)	–	1.86	520	2.60	–	–	–	–
Thornel 75 (*US*)	–	1.86	517–525	2.45–2.59	–	–	–	–
Thornel 75S (*US*)	–	1.82	540	2.35	–	–	–	–
Thornel 100 (*US*)	9.4	1.95–2.00	690	3.45–3.95	–	–	–	–
Thornel 300 (*US*)	–	1.70	225	2.06	0.8	–	–	–
VMN-3 (*RU*)	7.0		250	1.45	–	–	–	–
VMN-4 (*RU*)	6.0	1.71–1.75	250–300	2.0–2.5	0.8	–	–	–
VMN-5 (*RU*)	–	1.75	330–500	2.5–3.0	–	–	–	–
Ural 24 (*RU*)	–	1.70–1.80	150–200	1.7–2.0	–	–	–	–
Modmor II (*UK*)	8.1	1.74–1.80	245–275	2.45–3.15	0.8–1.0	–	–	–
Thornel 400 (*US*)	–	1.78	206	2.75	1.0	–	–	–
Hitex 46H (*US*)	5.0	1.80	322	5.6	1.7	–	–	–
	5.0–9.4	1.55–2.00	170–690	1.25–5.6	0.8–1.7	–	–	–

[a] Physical properties: D—mean single filament diameter, d—bulk density, E—Young's modulus, σ_t—tensile strength, δ—strain to failure (elongation), λ—thermal conductivity, α—coefficient of thermal expansion, ρ—specific electrical resistivity; properties are given in the longitudinal (axial) direction to the axis of fibre filament at room temperature

[b] For trade marks or grades country of origin is given in brackets: *US*—United States of America, *RU*—Russia, *JP*—Japan, *UK*—United Kingdom, *GE*—Germany, *IN*—India, *KR*—Korea

[c] Young's modulus and tensile strength values are based on the tow test

[d] Based on petroleum pitch

[e] Based on coal tar pitch

[f] Transverse tensile modulus—15 GPa, axial shear modulus—20 GPa, torsional shear modulus—5 GPa, Poisson's ratios: transverse contraction with axial extension—0.25, transverse contraction with transverse extension—0.40, axial contraction with transverse extension—0.013

[g] Thermal conductivity across the fiber—3 W m^{-1} K^{-1}, specific heat—0.75 (23 °C), 0.99 (143 °C), 1.42 (380 °C) kJ kg^{-1} K^{-1}

[h] Transversal coefficient of thermal expansion—12 × 10^{-6} K^{-1}

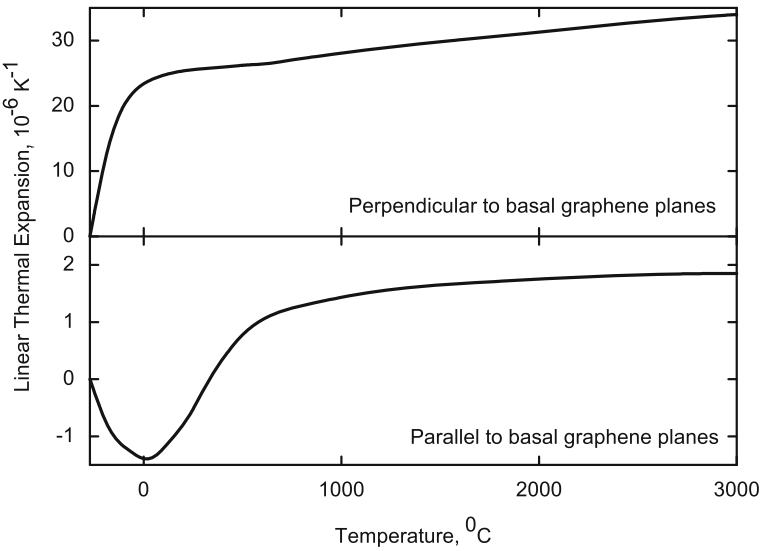

Fig. 2.4 Variations of linear thermal expansion coefficients in the different directions of graphite crystals with temperature [41–42, 209]

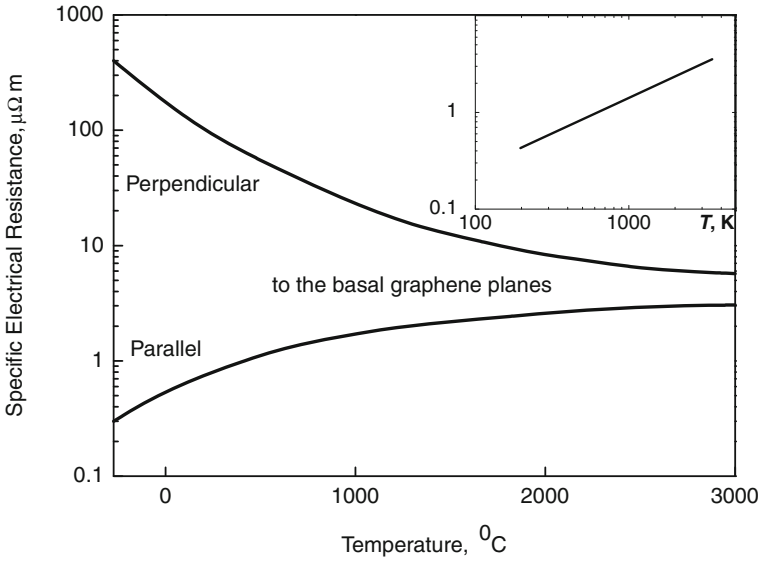

Fig. 2.5 Variations of specific electrical resistance in the different directions of graphite crystals with temperature (*Inset*–for the parallel direction to the basal planes in temperature (T, K) logarithm scale) [41, 209]

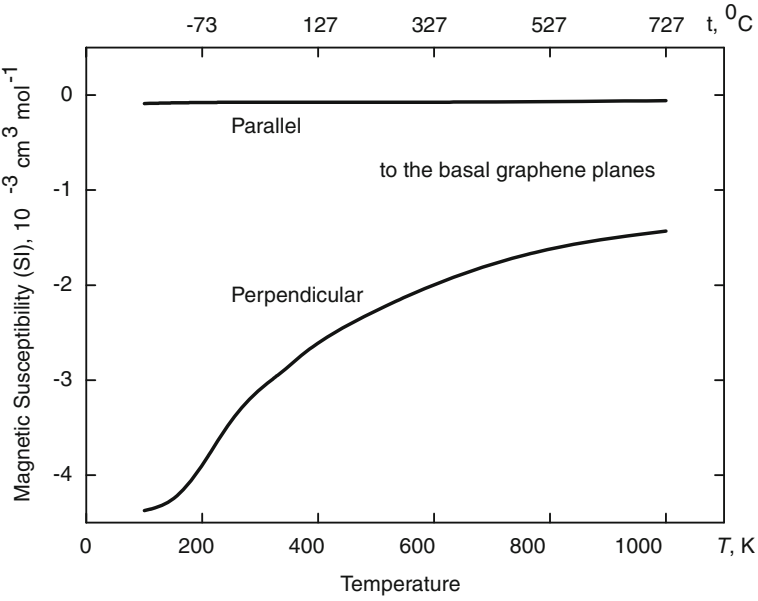

Fig. 2.6 Variations of molar magnetic susceptibility in the different directions of graphite crystals with temperature [539]

connected with certain difficulties because the hardness measurements have been made in practice by differing methods (Shore HS, Vickers HV, Rockwell HR, Brinell HB, Knoop HK, Mohs HM scales [192]). For the main types of carbon (graphite) materials approximate hardness values are following:

industrial structural and electrode graphitized (molded) products—HV 30−100 kgf mm^{-2} (0.3–1 GPa) [42], HM 1, HR 70−110 or HS 50−80 hardness numbers [192];
vitreous carbon (graphite)—HV 150–340 kgf mm^{-2} (1.5–3.4 GPa);
pyrolytic carbon (graphite)—HV 140–370 kgf mm^{-2} (1.4–3.7 GPa) [42, 136, 192].

At ambient temperatures, because of pores, flaws and microstructural defects concentrating the applied mechanical stresses, carbon (graphite) polycrystalline materials fails at much lower level than the theoretical strength of the graphite crystal, and mechanical failure occurs by absolutely brittle fracture. The flaws and defects are gradually annealed, stresses are relieved and plastic deformation becomes more probable with increasing temperature [42]. This evolution results in the general increase of the mechanical properties of graphite, so at the temperature range of about 2500 °C the strength of graphitized carbon materials is almost twice the value corresponding to room temperature. Theoretical predictions and experimental observations of tensile strength of graphitic nanostructured carbons are shown in Table 2.5. The values of strength characteristics of structural,

electrode and nuclear graphite materials for the different types of mechanical loading (tension, flexure and compression) are given in Table 2.6. Commonly, the physico-mechanical properties of graphitized materials, because of the preferential orientation of graphite grains (microcrystallites), vary with parallel and perpendicular directions to the axis of processing (extrusion, molding, pressing etc.). However, in spite of the fact that the individual crystals of graphite always perform super-high grade of anisotropy, special technological routes are elaborated for the industrial production of quasi-isotropic graphite materials [11]. The ratios between tensile σ_t, flexural (bending) σ_f and compressive σ_c strength characteristics for structural graphite materials

$$\sigma_f/\sigma_t \approx 2 \tag{2.4}$$

ranges from 1.5 to 2.1, and

$$\sigma_c/\sigma_f \approx 2 \tag{2.5}$$

ranges from 1.6 to 2.9 [194]. The various strength properties of pyrolytic carbon (graphite) materials are presented in Table 2.7. The flexural (bending) and compressive strengths of vitreous (glass-like) carbon materials are given in Table 2.8 and tensile strength of thermally expanded (exfoliated) graphite materials is included in Table 2.9. The tensile strength and strain to failure (elongation) of carbon (graphite) fibres are given in Table 2.10. Data on the fracture toughness (critical stress intensity factor) of some nuclear graphites are included in Table 2.6.

Although the strength of graphite rises with temperature increase, at the same time creep resistance of graphitized materials falls. Commonly, the creep characteristics of carbon (graphite) materials are higher in parallel direction to the preferential orientation of the normals to the basal planes of graphite grains (or in parallel direction to molding axis) than analogous characteristics in perpendicular directions. The strain rate of graphitized materials during steady-state stage of creep is defined by general relationship

$$\dot{\varepsilon} = C\left(\frac{\sigma}{\sigma_b}\right)^n \exp\left(-\frac{Q}{RT}\right) \tag{2.6}$$

where $\dot{\varepsilon} = \partial\varepsilon/\partial t = \partial l/l\partial t$ is the creep rate in s^{-1}, $C \approx 40$ is the constant independent of applied stress σ and temperature T in K, σ_b ultimate strength, $n \approx 4$ is the creep exponent constant, $Q \approx 210$ kJ mol^{-1} is the activation energy of creep and R is the gas constant [194, 908]. At the same temperature the creep rate of graphitized materials is higher in vacuum and reduces with inert gas pressure increase.

Quasi-single crystalline graphite (e.g. highly oriented pyrolytic graphite) is a typical transversely isotropic material, and most graphitic and graphite containing materials applied in practice possess the infinite order axis of symmetry as well. In the expression for the elastic constants of graphite crystals

$$\Sigma_i = c_{ij}\Xi_j (i, j = 1, 2, \ldots, 6), \tag{2.7}$$

linking the stresses Σ_i and the strains Ξ_j in the low strain limit, only 12 parameters (stiffness coefficients or modules) c_{ij} are non-zero: $c_{11} = c_{22}$, $c_{12} = c_{21}$, $c_{13} = c_{31} = c_{23} = c_{32}$, c_{33}, $c_{44} = c_{55}$ and $c_{66} = (c_{11}–c_{12})/2$.

Thus, the elasticity tensor for single crystal graphite material is symmetrical, and the stress–strain relationship (representation of Hooke's law) expressed by the matrix notations is read [217, 229, 231]:

$$\begin{Bmatrix} \sigma_{xx} \\ \sigma_{yy} \\ \sigma_{zz} \\ \sigma_{yz} \\ \sigma_{xz} \\ \sigma_{xy} \end{Bmatrix} = \begin{pmatrix} c_{11} & c_{12} & c_{13} & 0 & 0 & 0 \\ c_{12} & c_{11} & c_{13} & 0 & 0 & 0 \\ c_{13} & c_{13} & c_{33} & 0 & 0 & 0 \\ 0 & 0 & 0 & c_{44} & 0 & 0 \\ 0 & 0 & 0 & 0 & c_{44} & 0 \\ 0 & 0 & 0 & 0 & 0 & \frac{1}{2}(c_{11} - c_{12}) \end{pmatrix} \begin{Bmatrix} \varepsilon_{xx} \\ \varepsilon_{yy} \\ \varepsilon_{zz} \\ \varepsilon_{yz} \\ \varepsilon_{xz} \\ \varepsilon_{xy} \end{Bmatrix} \tag{2.8}$$

or in the inverse form with compliances s_{ij}:

$$\begin{Bmatrix} \varepsilon_{xx} \\ \varepsilon_{yy} \\ \varepsilon_{zz} \\ \varepsilon_{yz} \\ \varepsilon_{xz} \\ \varepsilon_{xy} \end{Bmatrix} = \begin{pmatrix} s_{11} & s_{12} & s_{13} & 0 & 0 & 0 \\ s_{12} & s_{11} & s_{13} & 0 & 0 & 0 \\ s_{13} & s_{13} & s_{33} & 0 & 0 & 0 \\ 0 & 0 & 0 & s_{44} & 0 & 0 \\ 0 & 0 & 0 & 0 & s_{44} & 0 \\ 0 & 0 & 0 & 0 & 0 & 2(s_{11} - s_{12}) \end{pmatrix} \begin{Bmatrix} \sigma_{xx} \\ \sigma_{yy} \\ \sigma_{zz} \\ \sigma_{yz} \\ \sigma_{xz} \\ \sigma_{xy} \end{Bmatrix}. \tag{2.9}$$

The compliance coefficients are readily expressed in terms of the stiffness coefficients:

$$2s_{11} = \frac{c_{33}}{c^2} + \frac{1}{c_{11} - c_{12}}, \tag{2.10}$$

$$2s_{12} = \frac{c_{33}}{c^2} - \frac{1}{c_{11} - c_{12}}, \tag{2.11}$$

$$s_{13} = -\frac{c_{13}}{c^2}, \tag{2.12}$$

$$s_{33} = \frac{c_{11} + c_{12}}{c^2}, \tag{2.13}$$

$$s_{44} = \frac{1}{c_{44}}, \tag{2.14}$$

$$c^2 \equiv c_{33}(c_{11} + c_{12}) - 2c_{13}^2 = \frac{1}{s^2} > 0, \tag{2.15}$$

$$s^2 \equiv s_{33}(s_{11} + s_{12}) - 2s_{13}^2. \tag{2.16}$$

The reciprocal expressions of stiffness coefficients in terms of compliance coefficients have the same form if c^2 is replaced with s^2.

In particular, there are seven elastic characteristics of graphitic materials, which can be defined and measured (various designations of them applied in the literature are given in brackets) [217, 226, 229, 231]:

E_1 (E, E_x, E_a or E_{11})—in-plane Young's modulus (for directions within the isotropic (isometric) plane, or in the parallel directions to the basal graphene planes; for carbon (graphite) high-modulus fiber filament—longitudinal modulus, commonly);
E_2 (E', E_z, E_c or E_{33})—out-of-plane Young's modulus (for the direction perpendicular to the isotropic (isometric) plane, or in the perpendicular direction to the basal graphene planes; for carbon (graphite) high-modulus fiber filament—transversal modulus, commonly);
G_{12} (G or G_{xy})—Coulomb's (shear) modulus for the isotropic (isometric) plane, or in the parallel planes to the basal graphene planes;
G_{13} (G' or $G_{yz} = G_{zx}$,)—Coulomb's (shear) modulus for planes normal to the isotropic (isometric) plane, or in the perpendicular planes to the basal graphene planes;
ν_{12} (ν or ν_{xy})—Poisson's ratio (major), which characterizes the contraction within the isotropic (isometric) plane due to forces applied within this plane;
ν_{13} (ν' or ν_{xz})—Poisson's ratio, which characterizes the contraction within the isotropic (isometric) plane due to forces applied in the direction perpendicular to it;
ν_{23} (ν'' or ν_{zx})—Poisson's ratio, which characterizes the contraction in the direction perpendicular to the isotropic (isometric) plane due to forces applied within this plane.

However, only five from seven characteristics mentioned above are independent. The equality $E_1\nu_{13} = E_2\nu_{23}$ exists because of the symmetry of the elasticity tensor.

Young's and Coulomb's (shear) moduli and Poisson's ratios are associated with the stiffness coefficients c_{ij} in the following forms:

$$\begin{pmatrix} 1/E_1 & -\nu_{12}/E_1 & -\nu_{13}/E_2 & 0 & 0 & 0 \\ -\nu_{12}/E_1 & 1/E_1 & -\nu_{13}/E_2 & 0 & 0 & 0 \\ -\nu_{13}/E_2 & -\nu_{13}/E_2 & 1/E_2 & 0 & 0 & 0 \\ 0 & 0 & 0 & 1/G_{13} & 0 & 0 \\ 0 & 0 & 0 & 0 & 1/G_{13} & 0 \\ 0 & 0 & 0 & 0 & 0 & 1/G_{12} \end{pmatrix} = \begin{pmatrix} c_{11} & c_{12} & c_{13} & 0 & 0 & 0 \\ c_{12} & c_{11} & c_{13} & 0 & 0 & 0 \\ c_{13} & c_{13} & c_{33} & 0 & 0 & 0 \\ 0 & 0 & 0 & c_{44} & 0 & 0 \\ 0 & 0 & 0 & 0 & c_{44} & 0 \\ 0 & 0 & 0 & 0 & 0 & \frac{1}{2}(c_{11} - c_{12}) \end{pmatrix}^{-1} \tag{2.17}$$

Table 2.11 Elastic properties of graphite crystals at room temperature

Property	Methods of determination			
	Ultrasonic, sonic resonance and static testing[a] [232]	Inelastic x-ray scattering [233]	Theoretical estimation [229, 235]	
			2H-graphite[b]	3R-graphite
c_{11} (E_x), GPa	1060 ± 20	1109 ± 16	1020	1020
c_{12}, GPa	180 ± 20	139 ± 36	–	–
c_{13}, GPa	15 ± 5	~0	–	–
c_{33} (E_z), GPa	36.5 ± 1.0	38.7 ± 0.7	36.1	36.4
c_{44}, (G_{zx}), GPa	0.18–0.35[c]	5.0 ± 0.3	–	–
c_{66}[d] (G_{xy}), GPa	440 ± 20	485 ± 10	–	–
v_{12} (v_{xy})	0.16	0.12	0.16	0.16
v_{13} (v_{xz})	0.012	~0	0.012	0.0065
v_{23} (v_{zx})	0.34	~0	0.34	0.18

[a] Compliance coefficients $s_{ij} = \Xi_j/\Sigma_i$: $1/s_{11} = 1.02 \pm 0.03$ TPa, $s_{12} = 0.16 \pm 0.06$ TPa^{-1}, $s_{13} = 0.33 \pm 0.08$ TPa^{-1}, $1/s_{33} = 36.5 \pm 1.0$ GPa, $s_{66} = 2.3 \pm 0.2$ TPa^{-1} [232]

[b] *Ab initio* calculations: $c_{11} + c_{12} = 1280$ GPa, $c_{13} = -0.5$ GPa, $c_{33} = 40.8$ GPa [236]

[c] The spread in the value for c_{44} is due to the presence of dislocations and the value is ≥4.0 GPa for dislocation-free graphite [136, 234]

[d] $c_{66} = (c_{11}-c_{12})/2$

The experimental estimates of the elastic properties of 2H-graphite crystals were based on rather indirect data on the ensembles of small pyrolytic graphite crystals with close orientations along the hexagonal axis of symmetry (axis c) and with a wide orientation scatter in perpendicular directions [232, 234]; later more direct experimental data on 2H-graphite single crystals were extracted using the method of inelastic x-ray scattering [233]. These experimental data together with some theoretical estimates for 2H- and 3R-graphites are shown in Table 2.11.

The condition for the isotropic character of media is

$$2c_{44}/(c_{11} - c_{12}) = 1, \tag{2.18}$$

so substituting the values for these elastic constants of graphite, this ratio becomes 0.0004 [136], which means that the Young's modulus varies appreciably with orientation and graphite materials are extremely anisotropic. The Young's modulus of graphite crystals as a function of angle θ with c axis (perpendicular to the basal graphene planes) is symmetric for 2H-graphite (or near-symmetric for 3R-graphite) reaching in both cases the highest values ($E > 1$ TPa) with sharp maximum at $\theta = \pi/2$ and the lowest values ($E < 5$ GPa) with low-grade minimum at $\theta \approx 0.2\pi$. For the analogous angular dependence of Poisson's ratio v_{xy}, the asymmetry about $\theta = \pi/2$ for 3R-graphite is somewhat larger; v_{xy} is limited by the value 0.16 reached in the neighborhood of $\theta = \pi/2$ and is rapidly reduced for both graphite polytypes. In the range of angles $\theta = (0.13-0.38)\pi$ Poisson's ratio v_{xy} becomes negligible (less than 0.01) and even negative. In the transverse direction, orthogonal to the previous one, the behaviour of Poisson's ratio v_{zx} is quite different, since its value can be higher than the upper limit of Poisson's ratio for a

elastic isotropic medium (its thermodynamic limits are $-1 < v < 0.5$) [229]. The values of Young's modules for graphitic nanostructured carbon forms are summarized in Table 2.5. For large stresses in reality, the stress-strain relationship for polycrystalline graphite materials is non-linear and approximated by the equation of Jenkins [237]

$$\varepsilon = A\sigma + B\sigma^2, \tag{2.19}$$

where A is equal to s_{33} for specimens cut off in parallel direction to the preferential orientation of the normals to the basal planes of graphite flake-like grains (against-grain specimens) or s_{11} for specimens cut off in perpendicular direction to the preferential orientation of the same normals (with-grain specimens), and in accordance to Jenkins' model

$$B = 2\varepsilon_0/\sigma_m^2, \tag{2.20}$$

where ε_0 is the longitudinal residual strain after the graphite has been subjected to a maximum stress σ_m. For various industrial graphitized carbon products (for specimens cut off in different directions), the values of A range from 0.044 to 0.207 GPa^{-1} and B range from 0.232 to 3.262 GPa^{-2} [237]. The elasticity of commercially available graphitic products is considerably different from those values of the ideal crystals since they are controlled by the preferential crystallite orientation, porosity and structural defects. The elastic properties of various industrial graphitized carbon materials, pyrolitic (pyrographite) and vitreous (glass-like) carbons and carbon (graphite) fibres are given in Tables 2.6–2.8 and 2.10. The temperature variation of Young's modulus and strength characteristics of averaged industrial graphitized materials is presented in Fig. 2.2.

For averaged highly oriented graphite and quasi-isotropic carbon (graphite), compared with other ultra-high temperature elements (refractory metals), the values of physico-mechanical (strength, elasticity) properties in the wide range of temperatures are summarized in Addendum.

2.5 Nuclear Physical Properties

The isotopes of carbon (standard atomic mass—12.0107 u) from ^{8}C to ^{22}C and their general characteristics are summarized in Table 2.12; the naturally occurring isotopes are listed in order of decreasing abundance, and unstable radioactive isotopes—in order of decreasing half-life period of decay.

Nuclear physical properties of carbon (isotopic mass range, total number of isotopes, thermal neutron macroscopic cross sections, moderating ability and capture resonance integral), compared with other ultra-high temperature elements (refractory metals), are given in Addendum.

Table 2.12 General characteristics of the isotopes of carbon [3, 6, 576–578]

Isotope	Mass, u	Abundance, %	Half-life period	Decay mode, excitation (radiation) energy, MeV
^{12}C	12.000000	98.93[a]	–	–
^{13}C	13.003355	1.07[b]	–	–
^{14}C	14.003242	$<10^{-10}$	5.70×10^3 y	β^-, 0.155
^{11}C	11.011434	–	20.33 min	β^+, 0.99
^{10}C	10.016853	–	19.29 s	β^+, 2.2; γ, 0.72, 1.05
^{15}C	15.010599	–	2.45 s	β^-, 4.3 (80 %), 9.8 (20 %)
^{16}C	16.014701	–	0.75 s	β^-, n (97.9 %), β^- (2.1 %)
^{17}C	17.022586	–	0.19 s	β^- (71.59 %), β^-, n (28.41 %)
^{9}C	9.0310367	–	0.127 s	β^+ (60 %); β^+, p (23 %); β^+, α (17 %)
^{18}C	18.02676	–	92 ms	β^- (68.5 %), β^-, n (31.5 %)
^{19}C	19.03481	–	46.2 ms	β^-, n (47.0 %), β^- (46.0 %), β^-, 2n (7.0 %)
^{20}C	20.04032	–	16 ms	β^-, n (72.0 %), β^- (28.0 %)
^{22}C	22.05720 (?)	–	6.2 ms	β^-
^{21}C	21.04934 (?)	–	<30 ns	n
^{8}C	8.037675	–	2.0×10^{-21} s	2p, 0.230

[a] Range of natural variation—98.853–99.037 at.%
[b] Range of natural variation—0.963–1.147 at.%

2.6 Chemical Properties

The specific electron configuration of carbon atoms has been proved in the numberless variety of carbon containing compounds formed by the chemical interaction between carbon and other elements of the periodic table. Organic chemistry as a special discipline is devoted directly to the carbon compounds with hydrogen, oxygen and nitrogen and their multi-component derivatives, which are termed organic compounds and, correspondingly, differed from inorganic compounds. The various inorganic compounds of carbon are classified in the following types:

simple molecular compounds (with *p*-elements of groups 15–17: halogens (F, Cl, Br, I), chalcogens (O, S, Se) and pnictogens (N, P)), covalent bonded;
salt-like carbides (or acetylenides, compounds with *s*-elements of groups 1–2: alkali metals (Li, Na, K, Rb, Cs) and alkaline earth metals (Be, Mg, Ca, Sr, Ba) and *d*-elements of groups 11–12: Cu, Ag, Au, Zn, Cd, Hg), mainly ionic or covalent-ionic (e.g. Be and Mg carbides) bonded;
interstitial carbides (or metal-like carbides, compounds with *d*-elements of groups 4–6: Ti, Zr, Hf, V, Nb, Ta, Cr, Mo, W), mainly metallic bonded;
intermediate carbides (compounds with *d*- and *f*-elements of group 3: Sc, Y, lanthanoides (La, Ce, Pr, Nd, Sm, Eu, Gd, Tb, Dy, Ho, Er, Tm, Yb, Lu) and actinoids (Th, Pa, U, Np, Pu, Am) and light *d*-elements of groups 7–10: Mn, Fe, Co, Ni), ionic-metallic or covalent-metallic bonding;
covalent carbides (compounds with *p*-elements of groups 13–14: B, Al, Si), mainly covalent or covalent-ionic (e.g. Al carbides) bonded;

graphitic/graphene and fullerene compounds (or intercalation (lamellar) compounds, with some elements, ions and molecules), mainly molecular bonded; carbon containing complex compounds (ternary, quaternary and higher order compounds) with the combination of the different types of chemical bonding.

The comprehensive information on the chemical interaction of carbon with all the elements of the periodic table is given in Table 2.13. The carbon containing systems and corresponding binary compounds are considered there in accordance to the groups of elements from 1 to 17.

Table 2.13 Chemical interaction of carbon (graphite) with elements of the periodic table (binary systems in accordance to the groups of elements)[a]

System	Type of phase diagram (constituent phases, temperatures and compositions of transformations)	Character of chemical interaction	References
Group 1			
C–H	H, variety of hydrocarbon compounds (e.g. CH_4, C_2H_2 etc.), C	No interaction with H_2 at normal conditions. At temp. ≤600–800 °C and $p \approx 0.1$ MPa, the interaction is extremely slow. Practically graphite is highly resistant to H_2 at 800–2200 °C. With catalyst (Ni) at 900–1000 °C CH_4 is formed, at temp. >1730 °C C_2H_2 and other hydrocarbons are produced. The corrosion rate of commercial graphite in H_2 gas flow (56 kg m^{-2} s^{-1}) at 1400 °C–0.13, 1580 °C–0.3 2230 °C–3.3 and 2730 °C–33 kg m^{-2} s^{-1}.	[5, 138, 238]
C–Li	α-Li, β-Li, γ-Li, α-Li_2C_2 (<∼410–800 °C, invariable compos.), β-Li_2C_2 (∼410–440 °C, ?), γ-Li_2C_2 (∼440–560 °C, ?), δ-Li_2C_2 (at least at 560 °C, ?), layered compounds ($LiC_{6\pm x}$, $LiC_{12\pm x}$, $LiC_{18\pm x}$, $LiC_{24\pm x}$, $LiC_{36\pm x}$, $LiC_{72\pm x}$), C Eutectic γ-Li–α-Li_2C_2 (175 °C, <1 at.% C)	The solubility of C in liquid Li: at 200 °C–∼2 × 10^{-4} at.% and at 735 °C–∼0.4 at.%. The presence of ∼0.26 wt.% N_2 does not affect the solubility of C in Li at temp. >∼350 °C, but at lower temp. it increases the solubility of C considerably. At 600 °C the corrosion resistance of graphite in liquid Li is low. The mixture of Li and C reacts at 800 °C with the formation of carbide (acetylenide) Li_2C_2. A number of C-rich lamellar or intercalate compounds are formed by the reaction of Li vapour with graphite. The wetting angle of molten pure Li: 115° (Ar, 200 °C), 110° (Ar, 400 °C).	[138, 238–241, 530, 905, 1004]

(continued)

Table 2.13 (continued)

System	Type of phase diagram (constituent phases, temperatures and compositions of transformations)	Character of chemical interaction	References
C–Na	α-Na, β-Na, NaC (?), α-Na_2C_2, β-Na_2C_2, layered compounds ($NaC_{8\pm x}$, $NaC_{16\pm x}$, $NaC_{56\pm x}$, $NaC_{64\pm x}$), intercalated fullerenes ($Na_2(C_{60})$, $Na_3(C_{60})$, $Na_4(C_{60})$, $Na_6(C_{60})$, $Na_{9.7}(C_{60})$ and other), C No diagram plot	The solubility of C in liquid Na: with O = 0.004 wt.%, at 300 °C–0.90, 500 °C–1.22, 700 °C–1.44, and with O = 0.026 wt.%, at 300 °C–2.70, 500 °C–3.22, 700 °C–3.56, 10^{-2} at.%. At 300 °C the corrosion resistance of graphite in liquid Na is low. Na_2C_2 is synthesized by the interaction of Na with C_2H_2 at 300–400 °C.	[138, 238, 241, 290, 916–918, 920, 1003]
C–K	K, KC (?), K_2C_2, layered compounds ($KC_{8\pm x}$, $KC_{16\pm x}$, $KC_{24\pm x}$, $KC_{36\pm x}$, $KC_{40\pm x}$, $KC_{48\pm x}$, $KC_{60\pm x}$, $KC_{72\pm x}$ and some other), intercalated fullerenes (α-$K(C_{60})$, β-$K(C_{60})$, γ-$K(C_{60})$, δ-$K(C_{60})$, $K_3(C_{60})$, α-$K_4(C_{60})$, β-$K_4(C_{60})$, $K_6(C_{60})$, $K(C_{70})$, $K_4(C_{70})$, $K_9(C_{70})$, $K(C_{72})$ and other), C No diagram plot	Binary compounds are synthesized by the interaction of K melt or vapour with graphite or C_2H_2 at 300–400 °C.	[138, 238, 241, 290, 919–921, 923]
C–Rb	Rb, RbC (?), Rb_2C_2 (?), layered compounds ($RbC_{8\pm x}$, $RbC_{16\pm x}$, α-$RbC_{24\pm x}$, β-$RbC_{24\pm x}$, $RbC_{36\pm x}$, $RbC_{48\pm x}$, $RbC_{60\pm x}$ and some other), intercalated fullerenes (α-$Rb(C_{60})$, β-$Rb(C_{60})$, γ-$Rb(C_{60})$, $Rb_3(C_{60})$, $Rb_4(C_{60})$, $Rb_6(C_{60})$, $Rb_{8.8}(C_{84})$ and other), C Order–disorder or structural transformations α-RbC_n → β-RbC_n (?) No diagram plot	Binary compounds are synthesized by the interaction of Rb melt or vapour with graphite or C_2H_2 at 300–450 °C.	[138, 238, 241, 922–923, 925]
C–Cs	Cs, CsC (?), Cs_2C_2 (?), layered compounds ($CsC_{8\pm x}$, $CsC_{10\pm x}$, $CsC_{16\pm x}$, α-$CsC_{24\pm x}$, β-$CsC_{24\pm x}$, $CsC_{36\pm x}$, $CsC_{48\pm x}$, $CsC_{60\pm x}$, $CsC_{84\pm x}$ and some other), intercalated fullerenes (α-$Cs(C_{60})$, β-$Cs(C_{60})$, $Cs_3(C_{60})$, α-$Cs_4(C_{60})$, β-$Cs_4(C_{60})$, $Cs_6(C_{60})$ and other), C Order–disorder or structural transformations α-CsC_n → β-CsC_n (?) No diagram plot	Binary compounds are synthesized by the interaction of Cs melt or vapour with graphite or C_2H_2 at 300–400 °C.	[138, 238, 241, 922, 924]
C–Fr	No data	–	–

(continued)

Table 2.13 (continued)

System	Type of phase diagram (constituent phases, temperatures and compositions of transformations)	Character of chemical interaction	References
Group 2			
C–Be	α-Be, β-Be, Be_2C (<~2100–2200 °C), BeC_2, C No diagram plot	Be_2C is formed directly from the elements, BeC_2—by the interaction of Be with dry C_2H_2. The max. solid solubility of C in Be is <0.1 at.% (?). For diffusion rate in the system at various temp. see Addendum.	[138, 238, 241–242]
C–Mg	Mg, MgC (<2625 °C, invariable compos., ?), Mg_2C_3 (<~600–760 °C), MgC_2 (<at least ~2200 °C, invariable compos., ?), C	Carbides are formed by the interaction of Mg with hydrocarbons at elevated temp. For diffusion rate in the system at various temp. see Addendum.	[138, 238, 241, 700, 926]
C–Ca	α-Ca, β-Ca, α-CaC_2 (<~25 °C, ?), β-CaC_2 (~25–450 °C), γ-CaC_2 (~350–435 °C), δ-CaC_2 (from ~435–500 °C to ~2160–2980 °C, invariable compos.), layered compounds ($CaC_{6\pm x}$ and other), intercalated fullerenes ($Ca_{3+x}(C_{60})$, $Ca_5(C_{60})$, $Ca_7(C_{60})$ and other), C Eutectic δ-CaC_2–Ca (820 °C, 2 at.% C) Eutectic δ-CaC_2–C (2100 °C, 75 at.% C)	CaC_2 is formed directly from the elements at 1250 °C in Ar atmosphere. For diffusion rate in the system at various temp. see Addendum.	[138, 238, 241–243, 701, 927–928]
C–Sr	α-Sr, β-Sr, α-SrC_2 (<–30 °C, ?), β-SrC_2 (from –30 °C to ~370 °C), γ-SrC_2 (~370–1800 °C, invariable compos., ?), layered compounds ($SrC_{6\pm x}$, $SrC_{12\pm x}$, $SrC_{18\pm x}$, $SrC_{24\pm x}$ $SrC_{30\pm x}$, $SrC_{36\pm x}$), intercalated fullerenes ($Sr_{2.08}(C_{60})$, $Sr_3(C_{60})$, $Sr_6(C_{60})$ and other), C Eutectic γ-SrC_2–C (?)	SrC_2 is formed directly from the elements at 1250 °C in Ar atmosphere.	[138, 238, 241–243, 702, 929, 930]

(continued)

Table 2.13 (continued)

System	Type of phase diagram (constituent phases, temperatures and compositions of transformations)	Character of chemical interaction	References
C–Ba	Ba, α-BaC_2 (<∼25 °C), β-BaC_2 (∼25–2000 °C, invariable compos., ?), layered compounds ($BaC_{6\pm x}$, $BaC_{8\pm x}$, $BaC_{12\pm x}$, $BaC_{18\pm x}$, $BaC_{24\pm x}$, $BaC_{30\pm x}$, $BaC_{36\pm x}$), intercalated fullerenes ($Ba_6(C_{60})$, $Ba_3(C_{70})$ and other), C Eutectic β-BaC_2–Ba (?)	Carbides are synthesized directly from the elements at 575–700 °C in vacuum (∼10^{-3} Pa).	[138, 238, 241–243, 703, 930, 937]
C–Ra	No data	–	–
Group 3			
C–Sc	α-Sc, β-Sc, ScC_{1-x} (or $Sc_{2\pm x}C$, <∼2255–2285 °C, congruent melt. point corresp. to ∼$ScC_{0.46}$, homog. range—21.5–38.5 at.% C at 1860–1865 °C and 23.5–34.5 at.% C at 20–30 °C), Sc_3C (?), α-Sc_4C_3 (from ∼950 °C to ∼1500–1510 °C, invariable compos.), β-Sc_4C_{3+x} (or $Sc_{13}C_{10\pm x}$, from ∼1500–1510 °C to ∼1860–1865 °C, incongruent melt. point, homog. range—42.8–48.5 at.% C), Sc_3C_{4-x} (or $Sc_{15}C_{19\pm x}$, <∼1790–1800 °C, incongruent melt. point, homog. range—54.1–55.9 at.% C), intercalated fullerenes ($Sc_2(C_{84})$ and other), C Eutectic Sc_3C_{4-x}–C (∼1720–1725 °C, 62 at.% C)	The presence of C increases the melt. point of Sc from 1541 °C to 1579 °C and temp. of polymorphic transformation α-Sc → β-Sc from 1337 °C to 1543 °C. The max. solubility of C in α-Sc is ∼4.5 at.% (at 1540–1545 °C) and in β-Sc is ∼2.5 at.% (at 1575–1580 °C). The elemental Sc and C interact at 1800–2000 °C in vacuum (or reductive conditions) with the formation of ScC_{1-x} and Sc_4C_{3-x}. For diffusion rate in the system at various temp. see Addendum.	[138, 238, 241–245, 602, 931]

(continued)

Table 2.13 (continued)

System	Type of phase diagram (constituent phases, temperatures and compositions of transformations)	Character of chemical interaction	References
C–Y	α-Y, β-Y, Y_3C (or $YC_{0.25 \div 0.40}$, ?), $Y_{2\pm x}C$ (<∼905–990 °C, homog. range—28.5–36.0 at.% C at 900 °C, ?), $YC_{1\pm x}$ (or $YC_{0.33}$, γ-phase, continuous solid solution with β-$YC_{2\pm x}$, from ∼905–1325 °C (?) to ∼1805–2360 °C, with congruent melt. points corresp. to ∼$YC_{0.38 \div 0.43}$, at ∼2000–2020 °C and ∼$YC_{1.94 \div 2.17}$ at ∼2360–2415 °C and with min. melt. point corresp. to ∼$YC_{0.90 \div 1.17}$ at ∼1805–1810 °C, homog. range—from ∼61.5 to ∼69–72 at.% C at 2020 °C, ∼18.0–67.5 at.% C at 1660 °C, ∼17–49.5 at.% C and ∼63–67.5 at.% C at 1560 °C, ∼17–42 at.% C at 1300 °C and ∼18–37 at.% C at 1000 °C), α-Y_4C_5 (<∼1305 °C, invariable compos.), β-Y_4C_5 (∼1305–1530 °C, invariable compos.), α-Y_3C_{4-x} (or α-$Y_{15}C_{19\pm x}$, <∼1185–1325 °C, homog. range—∼54–59 at.% C, ?), β-Y_3C_{4-x} (or β-$Y_{15}C_{19\pm x}$, from ∼1185–1325 °C to ∼1525–1655 °C, homog. range—∼54–59 at.% C, ?), α-Y_2C_{3-x} (<∼1185 °C, homog. range—∼58–60 at.% C, ?), β-Y_2C_{3-x} (<∼1185–1645 °C, homog. range—∼56–60 at.% C, ?), α-YC_2 (<∼1320–1325 °C, invariable compos.), β-$YC_{2\pm x}$ (or γ-phase, continuous solid solution with $YC_{1\pm x}$, see $YC_{1\pm x}$ above), intercalated fullerenes ($Y(C_{82})$ and other), C	The presence of C increases the melt. point of Y from 1522 °C to 1560 °C and temp. of polymorphic transformation α-Y → β-Y from 1478 °C to 1520 °C. The max. solubility of C in α-Y is 8.8 at.% (at 1520 °C) and in β-Y is ∼7.0 at.% (at 1560 °C). Y carbides are formed directly from the elements at 1560–1600 °C in vacuum (or reductive conditions). For diffusion rate in the system at various temp. see Addendum.	[238, 241–242, 244, 246, 932–934]

(continued)

Table 2.13 (continued)

System	Type of phase diagram (constituent phases, temperatures and compositions of transformations)	Character of chemical interaction	References
	Continuous solid solution YC_{1-x}–β-YC_{2+x} (or γ phase, see $YC_{1\pm x}$ above, miscibility gap: critical point—~57–58 at.% C at ~1645–1655 °C, from ~40–42 to ~66–67 at.% C at 1325 °C) Eutectic β-$YC_{2\pm x}$–C (2290 °C, 74 at.% C)		
Lanthanides			
C–La	α-La, β-La, γ-La, La_2C_{3-x} (<1415 °C, incongruent melt. point, homog. range—~54–60 at.% C at 800 °C), α-LaC_2 (<~1060–1080 °C, invariable compos. at low temp. and restricted homog. range (~1 at.% C) at 1060 °C), β-$LaC_{2\pm x}$ (from ~1060–1080 °C to ~2440–2360 °C, congruent melt. point corresp. to ~$LaC_{2.0}$, homog. range—~65.5–68 at.% C at 2250 °C and ~63–67 at.% C at 1415 °C), ε-LaC_2 (?), intercalated fullerenes ($La(C_{82})$ and other), C Eutectic β-La–La_2C_{3-x} (~800–805 °C, ~20.6–20.8 at.% C) Eutectic β-$LaC_{2\pm x}$–C (~2235–2270 °C, ~69.5–71.5 at.% C)	At 800–875 °C the solubility of C in β-La is ~3.4–4.3 at.%. La carbides are formed directly from the elements at 920–1000 °C in vacuum (or reductive conditions). For diffusion rate in the system at various temp. see Addendum.	[138, 241–242, 244, 247, 935]

(continued)

Table 2.13 (continued)

System	Type of phase diagram (constituent phases, temperatures and compositions of transformations)	Character of chemical interaction	References
C–Ce	α-Ce, β-Ce, γ-Ce, δ-Ce, Ce_2C (?), CeC (?), Ce_2C_3 (<~1535–1900 °C, incongruent melt. point, invariable compos.), α-CeC_2 (<~1050–1110 °C with invariable compos. at low temp. and restricted homog. range (~1.5 at.% C) at 1050–1110 °C), β-$CeC_{2\pm x}$ (from ~1050–1110 °C to ~2250–2340 °C, congruent melt. point corresp. to ~$CeC_{2.0}$, homog. range width—~1.5–2 at.% C), CeC_3 (?), intercalated fullerenes ($Ce(C_{82})$ and other), C Eutectic δ-Ce–Ce_2C_3 (~660–700 °C, ~19.5–20 at.% C) Eutectic β-$CeC_{2\pm x}$–C (~2220–2250 °C, ~69.0–69.5 at.% C)	The presence of C decreases the melt. point of Ce from 798 °C to ~700–705 °C and temp. of polymorphic γ-Ce → δ-Ce transformation from 726 °C to 630 °C (corresp. to content ~6 at.% C). At elevated temp. the substantial solubility of C in δ-Ce and γ-Ce is observed. The max. solubility is ~10 at.% C at 650–700 °C. Ce carbides are formed directly from the elements at 800–900 °C in vacuum (or reductive conditions).	[138, 241–242, 244, 391, 936]
C–Pr	α-Pr, β-Pr, Pr_2C_{3-x} (<~1540–1555 °C, incongruent melt. point, homog. range ~55–60 at.% C at 800 °C), α-PrC_2 (<~1130–1150 °C, invariable compos. at low temp. and restricted homog. range (~1 at.% C) at 1130–1150 °C), β-$PrC_{2\pm x}$ (from ~1130–1150 °C to 2320 °C, congruent melt. point, homog. range width–~1.5–2 at.% C), C Eutectic β-Pr–Pr_2C_{3-x} (~795–805 °C, ~15 at.% C) Eutectic β-$PrC_{2\pm x}$–C (~2250–2260 °C, 71.5 at.% C)	The presence of C decreases the melt. point of Pr from 931 °C to ~795–805 °C and temp. of polymorphic α-Pr → β-Pr transformation from 795 °C to ~670–680 °C. At elevated temp. the substantial solubility of C in β-Pr and α-Pr is observed. The max. solubility achieves ~8 at.% in β-Pr and ~5 at.% in α-Pr. Pr carbides are formed directly from the elements at 900–1000 °C in vacuum (or reductive conditions).	[238, 241–242, 244]

(continued)

Table 2.13 (continued)

System	Type of phase diagram (constituent phases, temperatures and compositions of transformations)	Character of chemical interaction	References
C–Nd	α-Nd, β-Nd, Nd_2C_{3-x} (<~1570–1670 °C, melt. point, homog. range—~54–60 at.% C), α-NdC_2 (<~1130–1170 °C), β-NdC_2 (from ~1130–1170 °C to ~2180–2340 °C, melt. point, ?), C Eutectic β-NdC_2–C (~2255–2295 °C) No diagram plot	No solubility of C in Nd at room temp. Nd carbides are formed directly from the elements at 1000–1100 °C in vacuum (or reductive conditions).	[238, 241–242]
C–Pm	No data	–	–
C–Sm	α-Sm, β-Sm, γ-Sm, $Sm_{3-x}C$ (or SmC_{1-x}, homog. range—~25–33 at.% C), Sm_2C_{3-x} (<at least 1325 °C, melt. point, homog. range—~54–60 at.% C), α-SmC_2 (<~1150–1190 °C, invariable compos.), β-SmC_2 (<~2200–2300 °C, melt. point), layered compounds ($SmC_{6\pm x}$, $SmC_{12\pm x}$, $SmC_{18\pm x}$, $SmC_{24\pm x}$, $SmC_{30\pm x}$, $SmC_{36\pm x}$ and other), intercalated fullerenes ($Sm_3(C_{60})$, $Sm_6(C_{60})$, $Sm_3(C_{70})$ and other), C Eutectic β-SmC_2–C (~2210–2270 °C) No diagram plot	Sm carbides are formed directly from the elements at 1075–1150 °C in vacuum (or reductive conditions). For diffusion rate in the system at various temp. see Addendum.	[238, 241–242, 929, 937]
C–Eu	Eu, $Eu_{3-x}C$ (or EuC_{1-x}, homog. range—~25–33 at.% C), Eu_2C_3, α-EuC_2 (<~345–375 °C, invariable compos.), β-EuC_2 (from ~345–375 °C to at least 1700 °C, melt. point), layered compounds ($EuC_{6\pm x}$, $EuC_{12\pm x}$, $EuC_{18\pm x}$, $EuC_{24\pm x}$, $EuC_{30\pm x}$, $EuC_{36\pm x}$ and other), intercalated fullerenes ($Eu_{2.82}(C_{60})$, $Eu_6(C_{60})$, $Eu_3(C_{70})$, $Eu_9(C_{70})$ and other), C No diagram plot	Eu carbides are formed directly from the elements at 800–900 °C in vacuum (or reductive conditions).	[238, 241, 938–939]

(continued)

Table 2.13 (continued)

System	Type of phase diagram (constituent phases, temperatures and compositions of transformations)	Character of chemical interaction	References
C–Gd	α-Gd, β-Gd, β-$Gd_{3-x}C$ (or GdC_{1-x}, homog. range—~25–33 at.% C), α-Gd_2C, Gd_4C_5 (?), Gd_2C_{3-x} (homog. range—~54–60 at.% C), α-GdC_2 (<~1220–1290 °C, invariable compos.), β-GdC_2 (from ~1220–1290 °C to ~2340–2400 °C, melt. point), $GdC_{6\pm x}$ (layered compound, ?), C Eutectic β-GdC_2–C (~2280–2345 °C) No diagram plot	Gd carbides are formed directly from the elements at 1300–1400 °C in vacuum (or reductive conditions).	[238, 241, 616]
C–Tb	α′-Tb, α-Tb, β-Tb, $Tb_{3-x}C$ (or TbC_{1-x}, homog. range—~25–33 at.% C), α-Tb_2C (?), β-Tb_2C (?), Tb_4C_5 (?), $Tb_{15}C_{19}$ (?), Tb_2C_{3-x} (homog. range—~54–60 at.% C), α-TbC_2 (<~1100–1305 °C), β-TbC_2 (from ~1100–1305 °C to ~2040–2280 °C, melt. point, ?), C Eutectic β-TbC_2–C (~2255–2295 °C) No diagram plot	Tb carbides are formed directly from the elements at 1350–1400 °C in vacuum (or reductive conditions).	[238, 241]
C–Dy	α′-Dy, α-Dy, β-Dy, $Dy_{3-x}C$ (or DyC_{1-x}, homog. range—~25–33 at.% C), α-Dy_2C, β-Dy_2C (?), Dy_4C_5 (?), $Dy_{15}C_{19}$ (?), Dy_2C_{3-x} (homog. range—~54–60 at.% C), α-DyC_2 (<~1275–1315 °C), α′-DyC_2 (?), β-DyC_2 (from ~1275–1315 °C to at least 2250 °C, melt. point, ?), C Eutectic β-DyC_2–C (~2265–2315 °C) No diagram plot	Dy carbides are formed directly from the elements at 1400–1500 °C in vacuum (or reductive conditions).	[238, 241]

(continued)

Table 2.13 (continued)

System	Type of phase diagram (constituent phases, temperatures and compositions of transformations)	Character of chemical interaction	References
C–Ho	α-Ho, β-Ho, $Ho_{3-x}C$ (or HoC_{1-x}, homog. range—~25–33 at.% C), α-Ho_2C, β-Ho_2C (?), Ho_4C_5 (?), $Ho_{15}C_{19}$ (or Ho_5C_6, ?), Ho_3C_4 (?), Ho_4C_7 (?), Ho_2C_{3-x} (homog. range—~54–60 at.% C), α-HoC_2 (<~1280–1330 °C), α′-HoC_2 (at least 1145–1165 °C, ?), β-HoC_2 (from ~1280–1330 °C to at least 2250–2290 °C, melt. point), C Eutectic β-HoC_2–C (~2250–2290 °C) No diagram plot	The solubility of C in Ho at ~1300 °C is negligible. Ho carbides are formed directly from the elements at 1480–1550 °C in vacuum (or reductive conditions). For diffusion rate in the system at various temp. see Addendum.	[238, 241]
C–Er	α-Er, β-Er, $Er_{3-x}C$ (or ErC_{1-x}, homog. range—~25–33 at.% C), $Er_{15}C_{19}$, Er_3C_4 (?), Er_4C_7 (?), Er_2C_3 (metastable, ?), α-ErC_2 (<1330 °C), α′-ErC_2 (at least at 1145–1165 °C, ?), β-ErC_2 (from 1330 °C to at least 2230–2280 °C, melt. point), C Eutectic β-ErC_2–C (~2220–2290 °C) No diagram plot	Er carbides are formed directly from the elements at 1500–1600 °C in vacuum (or reductive conditions). For diffusion rate in the system at various temp. see Addendum.	[238, 241]
C–Tm	α-Tm, β-Tm, $Tm_{3-x}C$ (or TmC_{1-x}, homog. range—~25–33 at.% C), $Tm_{15}C_{19}$, Tm_3C_4 (?), Tm_4C_7 (?), Tm_2C_3 (metastable, ?), α-TmC_2 (<~1120–1370 °C), α′-TmC_2 (?), β-TmC_2 (from ~1120–1370 °C to ~2130–2230 °C, melt. point, ?), TmC_3, intercalated fullerenes ($Tm(C_{82})$ and other), C Eutectic β-TmC_2–C (~2225–2265 °C) No diagram plot	Tm carbides are formed directly from the elements at 1550–1600 °C in vacuum (or reductive conditions).	[238, 241, 940]

(continued)

Table 2.13 (continued)

System	Type of phase diagram (constituent phases, temperatures and compositions of transformations)	Character of chemical interaction	References
C–Yb	α-Yb, β-Yb, γ-Yb, $Yb_{3-x}C$ (YbC_{1-x}, homog. range—~25–39 at.% C, at least <1500 °C, ?), $YbC_{0.95}$ (?), α-YbC_{1-x} (at least <1500 °C, ?), $YbC_{1.25+y}$ (homog. range—~56.9–58.8 at.% C, ?), $Yb_{15}C_{19}$, $Yb_3C_{4\pm x}$ (at least <1500 °C), Yb_2C_3 (metastable, ?), α-YbC_2 (at least <1500 °C), β-YbC_2 (?), layered compounds ($YbC_{6\pm x}$, $YbC_{12\pm x}$ and other), intercalated fullerenes ($Yb_{2.75}(C_{60})$ and other), C Eutectic β-YbC_2–C (~2175–2255 °C)	Yb carbides are formed directly from the elements at 800–900 °C in vacuum (or reductive conditions).	[238, 241, 938, 941–942]
C–Lu	α-Lu, β-Lu, $Lu_{3-x}C$ (or LuC_{1-x}, ?), $Lu_{15}C_{19}$, Lu_3C_4 (?), Lu_4C_7 (?), Lu_2C_3 (metastable, ?), α-LuC_2 (<~1390–1520 °C), β-LuC_2 (from ~1390–1520 °C to melt. point, ?), C Eutectic β-LuC_2–C (~2210–2250 °C) No diagram plot	Lu carbides are formed directly from the elements at 1650–1750 °C in vacuum (or reductive conditions).	[238, 241]
Actinides			
C–Ac	No data	–	–

(continued)

Table 2.13 (continued)

System	Type of phase diagram (constituent phases, temperatures and compositions of transformations)	Character of chemical interaction	References
C–Th	α-Th, β-Th, $ThC_{1\pm x}$ (α-Th–$ThC_{1\pm x}$ and $ThC_{1\pm x}$–γ-ThC_{2-x} continuous solid solutions (with miscibility gaps), <2500–2625 °C, congruent melt. point corresp. to ~$ThC_{1.0}$, homog. ranges—~0–7 at.% C and ~40–50 at.% C at 720–920 °C, ~22–66 at.% C at 2000 °C), Th_2C_3 (metastable, ?), α-ThC_{2-x} (<1255–1440 °C, homog. range—~64–66 at.% C), β-ThC_{2-x} (from 1255–1440 °C up to 1470–1495 °C, homog. range—~62.5–66.0 at.% C at 1440–1450 °C), γ–ThC_{2-x} (from 1470–1495 °C up to ~2550–2670 °C, congruent melt. point corresp. to ~$ThC_{1.9}$), C Continuous solid solution α-Th–$ThC_{1\pm x}$ (homog. range—from ~8 at.% C up to ~51 at.% C at 1570 °C; miscibility gap in the solid state: critical point—~1140–1570 °C at ~30 at.% C, ranges from ~6 at.% C to ~40 at.% C at 900 °C) Continuous solid solution $ThC_{1\pm x}$–γ-ThC_{2-x} (min. melt point 2430 °C corresp. to ~$ThC_{1.2}$, homog. range—from ~15 at.% C up to ~66 at.% C at 1800 °C, miscibility gap in the solid state: critical point—1850 °C at ~55 at.% C, ranges from ~50 at.% C to ~62 at.% C at 1470 °C) $ThC_{1\pm x}$ + β-ThC_{2-x} miscibility gap in the solid state (1255–1470 °C, ranges from ~50 at.% C to ~63 at.% C at 1255 °C) $ThC_{1\pm x}$ + α-ThC_{2-x} miscibility gap in the solid state (<1255 °C, ranges from ~50 at.% C to ~67 at.% C at 1000 °C) Eutectic γ-ThC_{2-x}–C (~2445–2500 °C, ~70 at.% C)	Max. solid solubilities of C in Th are ~66.0 at.% (α-Th) at 1500–2400 °C and ~9.2 at.% (β-Th) at 1710 °C. Th carbides are formed directly from the elements at 1700–1900 °C in vacuum (or reductive conditions). For diffusion rate in the system at various temp. see Addendum.	[138, 238, 241–244, 248, 492]

(continued)

Table 2.13 (continued)

System	Type of phase diagram (constituent phases, temperatures and compositions of transformations)	Character of chemical interaction	References
C–Pa	α-Pa, β-Pa, PaC, PaC_2, C No diagram plot	–	[241]
C–U	α-U, β-U, γ-U, $UC_{1\pm x}$ (or δ-phase, <∼2490–2590 °C, congruent melt. point corresp. to ∼$UC_{0.99}$, invariable compos.—∼50 at.% C at temp. <∼1000 °C, homog. range—∼47–56.5 at.% C at 2050 °C), ζ-U_2C_3 (from ∼860 °C (?) to ∼1730–1825 °C, invariable compos.), α-UC_{2-x} (from ∼1475–1515 °C to ∼1760–1795 °C, homog. range—63.9–65.0 at.% C at 1755–1775 °C, max. C content corresp. to $UC_{1.94}$), β-UC_{2-x} (or δ-phase, <∼2435–2585 °C, congruent melt. point corresp. to ∼$UC_{1.94\div1.96}$, represents the $UC_{1\pm x}$ phase in equilibrium with graphite), C Continuous solid solution $UC_{1\pm x}$–β-UC_{2-x} (min. melt point ∼2405 °C corresp. to ∼$UC_{1.5}$, homog. range—from ∼47 at.% C to 66.7 at.% C at 2200 °C; miscibility gap in the solid state: critical point—∼2050–2105 °C at ∼56.5 at.% C, ranges—from 52.8 at.% C to 62.3 at.% C at 1820 °C) Eutectic γ-U–$UC_{1\pm x}$ (∼1115–1120 °C, ∼1 at.% C) Eutectic β-UC_{2-x}–C (∼2400–2555 °C, ∼67 at.% C)	The solubility of C in α-U at 660 °C is <0.006 at.%, in β-U at 770 °C–0.02 at.% and in γ-U at 1115–1120 °C–0.22–0.37 at.% C. The solubility of C in molten U is obeyed the rule: lg$x$ (in at.% C) = 2.87–4000/T (in K). $UC_{1\pm x}$ and UC_{2-x} are formed directly from the elements at 1700–1900 °C in vacuum (or reductive conditions). The $UC_{1\pm x}$–β-UC_{2-x} continuous solid solution alloys cannot be fixed by tempering, in the contrast to the U–$UC_{1\pm x}$ solid solution alloys. At the temp. range of 1300–1600 °C molten U wets $UC_{1\pm x}$ perfectly, the wetting contact angles in the U–$UC_{1\pm x}$ are close to 40–60°. For diffusion rate in the system at various temp. see Addendum.	[138, 238, 241–244, 248, 492, 910]

(continued)

Table 2.13 (continued)

System	Type of phase diagram (constituent phases, temperatures and compositions of transformations)	Character of chemical interaction	References
C–Np	α-Np, β-Np, γ-Np, NpC_{1-x} (homog. range—~45–49 at.% C at 950 °C), Np_2C_3, NpC_2, C No diagram plot	Np carbides are formed directly from the elements at 1700–1900 °C in vacuum (or reductive conditions).	[238, 241]
C–Pu	α-Pu, β-Pu, γ-Pu, δ-Pu, δ′-Pu, ε-Pu, Pu_3C_2 (<575 °C, incongruent melt. point, invariable compos.), PuC_{1-x} (<~1655 °C, incongruent melt. point corresp. to $PuC_{0.89}$, homog. range—~44.5–47.5 at.% C at 400–600 °C and—~38–47.5 at.% C at 630–640 °C), Pu_2C_{3-x} (<2020–2050 °C, incongruent melt. point, homog. range—58.5–60 at.% C at 610 °C and ~57–61 at.% C at 1660 °C), α-PuC_2 (<~1660 °C, invariable compos., metastable, ?), β-PuC_2 (from ~1660 °C to ~2200–2250 °C, incongruent melt. point, invariable compos.), C Eutectic (degenerative) ε-Pu–PuC_{1-x} (~634 °C, ?)	The presence of C decreases the melt. point of Pu from 640 °C to 634 °C, but slightly affects the temp. of polymorphic transitions. At 700–900 °C the solubility of C in molten Pu is obeyed the rule: lg$x$ (in at.% C) = 2.5–2300/T (in K). Pu carbides are formed directly from the elements at 1500–1700 °C in vacuum (or reductive conditions).	[138, 238, 241–242, 244, 248, 492, 998]
C–Am	α-Am, β-Am, γ-Am, Am_2C_3, AmC_2, C No diagram plot	–	[241]
C–Cm	No data	–	–

(continued)

Table 2.13 (continued)

System	Type of phase diagram (constituent phases, temperatures and compositions of transformations)	Character of chemical interaction	References
Group 4			
C–Ti	α-Ti, β-Ti, $Ti_{2\pm x}C$ (< ~ 1900 °C, ?), $Ti_3C_{2\pm x}$ (?), $Ti_6C_{5\pm x}$ (?), TiC_{1-x} (< ~ 3065–3080 °C, congruent melt. point corresp. to ~ $TiC_{0.77 \div 0.80}$, homog. range— ~ 38–50 at.% C at 2780 °C, ~ 28.5–49.0 at.% C at 1650 °C and ~ 34.0–48.5 at.% C at 920 °C), C Order–disorder transformations (~ 590–785 °C (?), in TiC_{1-x} homog. range ~ 31.5–39.0 at.% C (?); $Ti_{2\pm x}C$, $Ti_3C_{2\pm x}$ and $Ti_6C_{5\pm x}$–the ordered phases of TiC_{1-x}, ?) Eutectic β-Ti–TiC_{1-x} (~ 1640–1655 °C, ~ 1.5–4.4 at.% C) Eutectic TiC_{1-x}–C (~ 2775–2785 °C, ~ 63 at.% C)	The presence of C decreases the melt. point of Ti from 1670 °C to ~ 1640–1655 °C and increases the temp. of α-Ti → β-Ti transition from 882 –920 °C. At the β-Ti–TiC_{1-x} eutectic temp. the solubility of C in β-Ti is 0.55 at.% C. At 920 °C the solubility of C in β-Ti is 0.5 at.% C and in α-Ti–2 at.% C. In the wide ranges of temp. the solubility of C is obeyed the rules: lg$x$ (in at.% C) = 1.74–1800/T (in K) for α-Ti (600–900 °C) and lg$x$ (in at.% C) = 1.40–2100/T (in K) for β-Ti (920–1645 °C). TiC_{1-x} is formed directly from the elements at 1700–2100 °C in vacuum (or reductive conditions). The reaction between C and Ti (in powdered mixtures) relates to the gasless combustion or solid flame phenomena, which are termed the self-propagating high temp. synthesis (SHS). The reaction is passing in the narrow layer called the combustion zone, which travels through the initial mixture by a wave spreading mechanism due to the great exothermic heat effect of the reaction and heat transfer of reagents. The reaction converts C and Ti to the carbide phase (products) after the only local initial ignition of the reaction.	[138, 238, 241–244, 248–252, 411, 530, 579, 594, 600, 606, 904, 1018]

(continued)

Table 2.13 (continued)

System	Type of phase diagram (constituent phases, temperatures and compositions of transformations)	Character of chemical interaction	References
		During the SHS extremely high temp. of heating are reached, so the necessary condition for its realisation is the high thermal stability of products. 2D-nano-sheets Ti_xC_y (graphene-like nanocrystals) is synthesized by the exfoliation of Ti_3AlC_2 in hydrofluoric acid. The wetting angle of molten pure Ti: 0° (vacuum, 1725 °C); for Ti containing alloys, see Table 2.16. For diffusion rate in the system at various temp. see Addendum.	
C–Zr	α-Zr, β-Zr, $Zr_{2\pm x}C$ (?), $Zr_3C_{2\pm x}$ (?), $Zr_6C_{5\pm x}$ (?), ZrC_{1-x} (< ~3420–3540 °C, congruent melt. point corresp. to $\sim ZrC_{0.80\div0.86}$, homog. range— ~38.5–49.0 at.% C at 2910 °C, ~36–50 at.% C at 1820 °C and ~37–50 at.% C at 870 °C), C Order–disorder transformations (max. temp. ~900–945 °C, in ZrC_{1-x} homog. range ~26–49 at.% C (?), $Zr_{2\pm x}C$, $Zr_3C_{2\pm x}$, $Zr_6C_{5\pm x}$–the ordered phases of ZrC_{1-x}, ?) Eutectic β-Zr–ZrC_{1-x} (~1805–1835 °C, ~1.4–3.0 at.% C) Eutectic ZrC_{1-x}–C (~2850–2930 °C, ~64.5–65.0 at.% C)	The presence of C decreases the melt. point of Zr from 1855 °C to ~1805–1835 °C and increases the temp. of α-Zr → β-Zr transition from 863 °C to ~870–885 °C. At this temp. the solubility of C in α-Zr is ~3 at.%. At the β-Zr–ZrC_{1-x} eutectic temp. the solubility of C in β-Zr is ~1 at.% C. At lower temp. the solubility of C in β-Zr decreases to ~0.8 at.% at 1400 °C, ~0.5 at.% at 1330 °C and ~0.3 at.% at 1175 °C. At 1000–1800 °C the solubility of C in β-Zr is obeyed the rule: $\lg x$ (in at.% C) = 2.2–3800/T (in K) ZrC_{1-x} is formed directly from the elements at 1800–2200 °C in vacuum (or reductive conditions). The reaction between C and Zr (in powdered mixtures) relates to the SHS type (see special notes for the C–Ti system). The wetting angle of molten pure Zr: 0° (vacuum, 1900 °C). For diffusion rate in the system at various temp. see Addendum.	[138, 238, 241–244, 248–256, 530, 579, 1017]

(continued)

Table 2.13 (continued)

System	Type of phase diagram (constituent phases, temperatures and compositions of transformations)	Character of chemical interaction	References
C–Hf	α-Hf, β-Hf, $Hf_3C_{2\pm x}$ (?), $Hf_6C_{5\pm x}$ (?), HfC_{1-x} (<∼3930–3960 °C, congruent melt. point corresp. to ∼$HfC_{0.89\div0.94}$, homog. range—∼37.0–49.5 at.% C at 3180 °C, ∼34.0–49.5 at.% C at 2360 °C and ∼38.0–49.5 at.% C at 1200 °C), C Order–disorder transformations (max. temp. ∼505–535 °C, in HfC_{1-x} homog. range ∼38–49 at.% C (?), $Hf_3C_{2\pm x}$, $Hf_6C_{5\pm x}$—the ordered phases of HfC_{1-x}, ?) Eutectic α-Hf–β-Hf (∼2180–2220 °C, ∼1.5 at.% C) Peritectic α-Hf (∼2240–2360 °C, ∼14–15 at.% C) Eutectic HfC_{1-x}–C (∼3150–3185 °C, ∼65–68 at.% C)	The presence of C decreases the melt. point of Hf from 2231 °C to ∼2180–2220 °C. C stabilizes α-Hf and increases the temp. of α-Hf → β-Hf transition from 1743 °C to ∼2240–2360 °C. In α-(Hf,C)–β-(Hf,C) eutectic alloy the solubility of C in β-Hf is ∼0.6–1.0 at.% and in α-Hf–∼2–3 at.%. The max. solid solubility of C in α-Hf is ∼14–15 at.% (at 2240–2360 °C). HfC_{1-x} is formed directly from the elements at 1900–2300 °C in vacuum (or reductive conditions). The reaction between C and Hf (in powdered mixtures) relates to the SHS type (see special notes for the C–Ti system). For diffusion rate in the system at various temp. see Addendum.	[138, 238, 241–244, 248–252, 254, 257, 579, 1006]
Group 5			
C–V	V, $V_{64}C$ (?), V_5C (?), α-$V_{2+x}C$ (<∼800–850 °C, homog. range—∼31–33 at.% C), β-$V_{2\pm x}C$ (from ∼800–850 °C to ∼2185–2190 °C, incongruent melt. point, homog. range—∼26.5–36.5 at.% C at 1650 °C), β′-$V_{2+x}C$ (<∼1500–1610 °C, homog. range—27.5–32.0 at.% C), ζ-V_4C_{3-x} (or V_3C_2, or ξ-phase, <∼1320–1700 °C, ∼37.7–42.8 at.% C), $V_6C_{5\pm x}$ (<∼1180–1260 °C, homog. range—∼43–45.5 at.% C), $V_8C_{7\pm x}$ (<∼1080–1160 °C, homog. range—∼46.3–48.1 at.% C), VC_{1-x} (<∼2625–2800 °C, congruent melt. point corresp. to ∼$VC_{0.75\div0.86}$, homog. range—∼42.5–46.0 at.% C at 2650–2670 °C, ∼37–47 at.% C at 2185 °C and ∼40.5–48.0 at.% C at 1320 °C, max. C content corresp. to ∼$VC_{0.88\div0.89}$), C	The solubility of C in V: 0.13 at.% at 700 °C, 0.5 at.% at 1100 °C and 2.3–2.6 at.% at 1600 °C. At 1500–1600 °C the solubility of C in V is obeyed the rule: lg$x$ (in at.% C) = 7.4–12,800/T (in K) The max. solubility of C in V is ∼4.3–5.5 at.% (at V–β-$V_{2\pm x}C$ eutectic temp.). V carbides are formed directly from the elements at 1100–1200 °C in vacuum (or reductive conditions). The reaction between C and V (in powdered mixtures) relates to the SHS type (see special notes for the C–Ti system). For diffusion rate in the system at various temp. see Addendum.	[241–244, 248–251, 258–260, 579, 720, 723, 1000, 1020]

(continued)

Table 2.13 (continued)

System	Type of phase diagram (constituent phases, temperatures and compositions of transformations)	Character of chemical interaction	References
	Eutectic V–β-$V_{2\pm x}C$ (1650 °C, 15 at.% C) Eutectic VC_{1-x}–C (~2625–2670 °C, ~49.5–53.5 at.% C)		
C–Nb	Nb, α-Nb_2C (<~1200–1230 °C, invariable compos.), β-$Nb_{2+x}C$ (from ~1200–1230 °C to ~2450–2575 °C, homog. range—~28–33 at.% C at 2350 °C), γ-$Nb_{2\pm x}C$ (from ~2450–2575 °C to ~3035–3090 °C, incongruent melt. point, homog. range—~27–35 at.% C), ζ-Nb_4C_{3-x} (or Nb_3C_{2+x}, <~1575–1750 °C, homog. range—~40.0–41.5 at.% C), $Nb_6C_{5\pm x}$ (ordered, <~1050–1320 °C, homog. range—~42–49 at.% C), NbC_{1-x} (<~3600–3615 °C, congruent melt. point corresp. to ~$NbC_{0.79\div0.84}$, homog. range—~38–49 at.% C at 3300 °C, 29.2–49.6 at.% C at 2600 °C, 37.6–49.8 at.% C at 2350 °C and ~41–50 at.% C at 1200 °C, max. C content corresp. to ~$NbC_{0.99}$), C Eutectic Nb–β-$Nb_{2+x}C$ (~2335–2355 °C, ~10.5–10.7 at.% C) Eutectic NbC_{1-x}–C (~3250–3305 °C, ~58–60 at.% C)	The solubility of C in Nb: 0.1 at.% at 1200 °C, 0.26 at.% at 1500 °C and ~5.5–7.2 at.% at 2230–2350 °C. At 1500–2200 °C the solid solubility of C in Nb is obeyed the rule: lg$x$ (in at.% C) = 3.65–7600/T (in K) The solubility of Nb in graphite is ≤0.001 at.% C. Nb carbides are formed directly from the elements at 1300–1400 °C in vacuum (or reductive conditions). The reaction between C and Nb (in powdered mixtures) relates to the SHS type (see special notes for the C–Ti system). The limiting wetting angle of molten pure Nb: 60° (vacuum, 2700 °C); for Nb containing alloys, see Table 2.16. For diffusion rate in the system at various temp. see Addendum.	[138, 241–244, 248–251, 254, 258, 260–262, 530, 579, 719–720]

(continued)

Table 2.13 (continued)

System	Type of phase diagram (constituent phases, temperatures and compositions of transformations)	Character of chemical interaction	References
C–Ta	Ta, $Ta_{64}C$ (?), α-$Ta_{2+x}C$ (<~1930–2270 °C, homog. range—~31.0–32.5 at.% C at 1930 °C), β-$Ta_{2\pm x}C$ (from ~1930–2270 °C to ~3330–3400 °C, incongruent melt. point, homog. range—~26–35 at.% C at 2830–2850 °C), ε-$Ta_3C_{2\pm x}$ (~2000 °C, invariable compos., ?), ζ-Ta_4C_{3-x} ($0.44 \leq x \leq 0.53$, or ζ-TaC_{1-x}, <~2170–2800 °C, homog. range—~38.0–42.8 at.% C), $Ta_6C_{5\pm x}$ (ordered, <1160 °C), TaC_{1-x} (<3985–4000 °C, congruent melt. point corresp. to ~$TaC_{0.88\div0.89}$, homog. range—37.9–49.9 at.% C at 3450 °C, 36.5–49.9 at.% C at 3340 °C, 39.6–49.9 at.% C at 2850 °C and 41.5–49.9 at.% C at 1930 °C, max. C content corresp. to ~$TaC_{0.99}$), C Eutectic Ta–β-$Ta_{2\pm x}C$ (~2800–2860 °C, ~12.0–12.3 at.% C) Eutectic TaC_{1-x}–C (~3400–3450 °C, ~61 at.% C)	The max. solubility of C in Ta is ~7.0–7.5 at.% (at Ta–β-$Ta_{2\pm x}C$ eutectic temp.). The solid solubility of C in Ta is obeyed the rules: $\ln x$ (in at.% C) = 8.23–16,700/T (in K) at 1500–1950 °C and $\ln x$ (in at.% C) = 5.18–9900/T (in K) at 1950–2640 °C. Ta carbides are formed directly from the elements at 1300–1500 °C in vacuum (or reductive conditions). The reaction between C and Ta (in powdered mixtures) relates to the SHS type (see special notes for the C–Ti system). For diffusion rate in the system at various temp. see Addendum.	[138, 241–244, 248–251, 254, 260, 579, 720, 722–723]
Group 6			
C–Cr	Cr, $Cr_{23}C_{6\pm x}$ (<~1575–1610 °C, incongruent melt. point corresp. to $CrC_{0.27}$, homog. range—~20–21 at.% C at 1530 °C, ~20–22 at.% C at 1200 °C), Cr_3C (metastable, ?), $Cr_7C_{3\pm x}$ (<~1765–1790 °C, congruent melt. point corresp. to $CrC_{0.43}$, homog. range—~29.5–31.5 at.% C at 1730 °C and ~28.5–31 at.% C at 1575 °C), Cr_2C (?), Cr_3C_{2-x} (<1810–1830 °C, incongruent melt. point corresp. to $CrC_{0.67}$,	The max. solid solubility of C in Cr is ~0.3–1.9 at.% C (?) at 1530–1580 °C. Cr carbides are formed directly from the elements at 1400–1800 °C in vacuum (or reductive conditions). For diffusion rate in the system at various temp. see Addendum.	[138, 241–242, 244, 248–250, 394, 417, 579, 841]

(continued)

Table 2.13 (continued)

System	Type of phase diagram (constituent phases, temperatures and compositions of transformations)	Character of chemical interaction	References
	homog. range—~39.7–40.0 at.% C at 1730 °C and ~39.8–40.0 at.% C at 1400 °C), CrC (metastable, ?), C Eutectic Cr–$Cr_{23}C_{6\pm x}$ (~1530–1580 °C, ~14–14.5 at.% C) Eutectic $Cr_7C_{3\pm x}$–Cr_3C_{2-x} (~1725–1740 °C, 32.6 at.% C)	The max. solid solubility of C in Cr is ~0.3–1.9 at.% C (?) at 1530–1580 °C. Cr carbides are formed directly from the elements at 1400–1800 °C in vacuum (or reductive conditions). For diffusion rate in the system at various temp. see Addendum.	
C–Mo	Mo, α-$Mo_{2+x}C$ (or β′-$Mo_{2+x}C$, <1430–1440 °C, homog. range—~31.3–33.3 at.% C at 1230 °C), α′-$Mo_{2+x}C$ (or ε-$Mo_{2+x}C$, ordered), β-$Mo_{2\pm x}C$ (from ~1200–1650 °C to ~2520–2540 °C, congruent melt. point corresp. to $MoC_{0.52}$, homog. range—26.0–35.7 at.% C at 2205 °C, ~30.0–35.5 at.% C at 1655 °C and ~31–34 at.% C at 1430 °C), η-MoC_{1-x} (or Mo_3C_{2-x}, from ~1650–1655 °C to ~2530–2560 °C, congruent melt. point corresp. to $MoC_{0.61}$, homog. range—36.5–39.2 at.% C at 2510 °C and ~38.5–39.5 at.% C at 1960 °C, invariable compos. ~39 at.% C at temp. <1800 °C), α-MoC_{1-x} (from ~1950–1960 °C to ~2530–2650 °C, congruent melt. point corresp. to $MoC_{0.72}$, homog. range—~41.0–43.1 at.% C at 2585 °C, ~39.6–43.0 at.% C at 2545 °C and ~39.8–42.2 at.% C at 2200 °C), γ-MoC (<1200–1220 °C, invariable compos. ~50 at.% C), C Eutectic Mo–β-$Mo_{2\pm x}C$ (~2200–2205 °C, ~16.7–18.0 at.% C) Eutectic β-$Mo_{2\pm x}C$–η-MoC_{1-x} (~2510 °C, ~36 at.% C, ?) Eutectic α-MoC_{1-x}–C (~2584–2589 °C, 45 at.% C)	The max. solubility of C in Mo is ~1.1–1.3 at.% C at 2200–2205 °C. At 1330–2205 °C the solubility of C in Mo is obeyed the rule: ln$x$ (in at.% C) = 3.97–21,000/T (in K) Mo carbides are formed directly from the elements at 1200–1400 °C in vacuum (or reductive conditions). Under specific pressure 5 MPa the diffusion welded joint between β-$Mo_{2\pm x}C$ and Mo is produced at 1600 °C (5–15 min exposure). For diffusion rate in the system at various temp. see Addendum.	[138, 241–244, 248–250, 260, 579, 723]

(continued)

Table 2.13 (continued)

System	Type of phase diagram (constituent phases, temperatures and compositions of transformations)	Character of chemical interaction	References
C–W	W, α-$W_{2+x}C$ (or β''-$W_{2+x}C$, from 1250 °C to ~2100–2140 °C, homog. range—~30–33 at.% C), β-$W_{2+x}C$ (or β'-$W_{2+x}C$, from ~2100–2140 °C to ~2320–2490 °C, homog. range—~29.6–33.4 at.% C), γ-$W_{2\pm x}C$ (or β-$W_{2\pm x}C$, from ~2320–2490 °C to ~2775–2795 °C, congruent melt. point corresp. to $WC_{0.43\div0.45}$, homog. range—~27.5–35.5 at.% C at 2735 °C, ~26–35 at.% C at 2710 °C and ~28–34 at.% C at 2530 °C), γ-WC_{1-x} (or α-WC_{1-x}, β-WC_{1-x}, from ~2530–2535 °C to ~2745–2785 °C, congruent melt. point corresp. to $WC_{0.64}$, homog. range—~37.4–40.0 at.% C at 2720 °C), δ-$WC_{1\pm x}$ (or α-$WC_{1\pm x}$, <~2745–2785 °C, incongruent melt. point corresp. to $WC_{1.00\div1.01}$, homog. range—~49.6–50.6 at.% C at 2720 °C, ~49.9–50.6 at.% C at 2530 °C and ~50.1–50.6 at.% C at 2000 °C, invariable compos. at temp. <2000 °C), C Eutectic W–γ-$W_{2\pm x}C$ (~2710–2715 °C, ~22–25 at.% C) Eutectic γ-$W_{2\pm x}C$–γ-WC_{1-x} (~2735–2760 °C, ~36.0–36.5 at.% C) Eutectic γ-WC_{1-x}–δ-$WC_{1\pm x}$ (~2720–2760 °C, ~36–41 at.% C) Phase diagram data available in literature are controversial	The max. solubility of C in W is <1 at.% C (at 2710–2715 °C). At 1400–2600 °C the solubility of C in W is obeyed the rule: ln$x$ (in at.% C) = 4.67–15,000/T (in K) W carbides are formed directly from the elements at 1400–1600 °C in vacuum (or reductive conditions). For diffusion rate in the system at various temp. see Addendum.	[138, 241–242, 244, 248–250, 263, 419, 579, 603, 721, 1001, 1005]

(continued)

Table 2.13 (continued)

System	Type of phase diagram (constituent phases, temperatures and compositions of transformations)	Character of chemical interaction	References
Group 7			
C–Mn	α-Mn, β-Mn, γ-Mn, δ-Mn, ε-$Mn_{4\pm x}C$ (from ~990 °C to ~1305–1310 °C, incongruent melt. point corresp. to $MnC_{0.32\div0.39}$, homog. range—~13–28 at.% C), $Mn_{23}C_6$ (<~1020–1035 °C, invariable compos.), $Mn_{15}C_4$ (or $Mn_{11}C_3$ (?), from ~850 °C to 1020 °C, invariable compos. ~21.1–21.5 at.% C, ?), Mn_3C (from ~970 °C to ~1050–1060 °C, invariable compos.), Mn_5C_2 (from ~425 °C (?) to ~1090–1170 °C, invariable compos. ~28.5–28.6 at.% C), Mn_7C_3 (<~1330–1340 °C, incongruent melt. point corresp. to $MnC_{0.43}$, invariable compos. ≤30 at.% C), C	The max. solid solubility of C in Mn modifications: α-Mn–~6.5–7.0 at.% (at ~770–900 °C), β-Mn–~1.0–2.5 at.% (at ~820–900 °C), γ-Mn–~13–16 at.% (at ~990–1240 °C), and δ-Mn–~1–2 at.% (at ~1220–1240 °C). Mn carbides are formed directly from the elements at 1200–1300 °C in non-oxidative conditions.	[138, 238, 241, 244, 264]
C–Tc	Tc, TcC_{1-x} (or $Tc_{3\pm x}C$, ?), C Eutectic TcC_{1-x}–C (~1650–1885 °C, ~25–33 at.% C, ?) Eutectic Tc–C (1660 °C, ~30 at.% C, ?) Phase diagram data available in literature are controversial	At 910 °C the solubility of C in Tc is ~1 at.% C.	[241, 391, 840, 943]
C–Re	Re, metastable carbides (?), C Eutectic Re–C (~2480–2505 °C, ~16.5–23 at.% C)	The max. solubility of C in Re is ~11–17 at.% C at the Re–C eutectic temp. The solubility decreases with temp. decline and amounts ~4.2 at.% C at 1800 °C. Metastable Re carbides are synthesized at ultra-high pressures (6–18 GPa).	[138, 241, 265–266]

(continued)

Table 2.13 (continued)

System	Type of phase diagram (constituent phases, temperatures and compositions of transformations)	Character of chemical interaction	References
Group 8			
C–Fe	α-Fe, γ-Fe, δ-Fe, metastable compounds Fe_4C, θ-Fe_3C (<~1207–1252 °C), χ-Fe_5C_2, α-Fe_7C_3, β-Fe_7C_3, η-Fe_2C, ε-Fe_2C and α-Fe_2C, C (see refs. for details) Eutectic γ-Fe–C (1153 °C, 17.1 at.% C) Metastable eutectic γ-Fe–Fe_3C (1147 °C, 17.3 at.% C)	The max. solid solubility of C in Fe modifications: α-Fe– ~0.090–0.096 at.% (at 727–740 °C), γ-Fe–~8.9–9.1 at.% (at 1147–1153 °C) and δ-Fe– ~0.4–0.5 at.% (at 1493–1499 °C). The presence of various contaminations decreases the γ-Fe–C eutectic temp. (see refs. for details). Molten Fe dissolves considerable amounts of C; the solubility of C increases with increasing temp. linearly and reaches >24 at.% C at 2000 °C. Fe carbides are not formed directly from the elements. The limiting wetting angle of molten pure Fe is 60° (vacuum, 1425–1540 °C), 0° (vacuum, ≥1550 °C), 37° (H_2, 1550 °C); for Fe–4.3 at.% C alloy: 90° (vacuum, 1540 °C); for Fe–5 at.% C alloy: 130° (vacuum, 1540 °C). For diffusion rate in the system at various temp. see Addendum.	[138, 238, 241, 244, 267–268, 530, 907]
C–Ru	Ru, metastable carbides (?), C Eutectic Ru–C (~1940–1965 °C, ~18 at.% C)	The max. solubility of C in solid Ru is ~3–4 at.% C (at eutectic temp.). At 1000 °C the solubility amounts ~0.4 at.% C. At 800–1200 °C the solubility of C in Ru is obeyed the rule: $\lg x$ (in at.% C) = 3.02–4438/T (in K) The solubility of C in liquid Ru at boil. point (4150 °C) is ~30 at.% C.	[238, 241, 244, 945]
C–Os	Os, metastable carbides (?), C Eutectic Os–C (~2730 °C, ~10–17 at.% C)	The max. solubility of C in solid Os is ~2 at.% C (~2730 °C); in liquid Os at boil. point (5010 °C) it is 39.1–39.7 at.% C.	[138, 238, 241, 244]

(continued)

Table 2.13 (continued)

System	Type of phase diagram (constituent phases, temperatures and compositions of transformations)	Character of chemical interaction	References
Group 9			
C–Co	ε-Co, α-Co, metastable compounds Co_3C and Co_2C, C Eutectic α-Co–C (~1310–1320 °C, ~11.2–12.5 at.% C) Metastable eutectic α-Co–Co_3C (~1190 °C, ~17.4–21.0 at.% C) Gas-eutectic Co–C (gas–liquid-graphite non-variant equilibrium, ~2415 °C, ~38–39 at.% C)	The presence of C decreases the ε-Co → α-Co transition temp. up to ~400–420 °C and magnetic (paramagnetic-ferromagnetic) phase transition up to 1035 °C. The max. solubility of C is ~4.1–4.3 at.% (in α-Co at the α-Co–C eutectic temp.) At room temp. the solubility of C in ε-Co–0.49 at.% C. Molten Co dissolves considerable amounts of C (from ~12 at.% at 1320 °C to ~28 at.% C at 2400–2415 °C). Practically, no solubility of Co in graphite. Co carbides are not formed directly from the elements. The limiting wetting angle of molten pure Co is 82° (vacuum, 1425 °C); for Co–2.7 at.% C alloy: 130° (vacuum, 1495 °C). For diffusion rate in the system at various temp. see Addendum.	[138, 238, 241, 244, 269, 530, 1021]
C–Rh	Rh, metastable carbides (?), C Eutectic Rh–C (~1670–1700 °C, ~15 at.% C)	The max. solubility of C in solid Rh is ~1.5–4.0 at.% C (at eutectic temp.). At 1000 °C the solubility amounts ~0.2 at.% C. At 800–1250 °C the solubility of C in Rh is obeyed the rule: $\lg x$ (in at.% C) = 3.05–4013/T (in K). The solubility of C in liquid Rh at boil. point (3700 °C) is ~16 at.% C.	[238, 241, 244, 945]
C–Ir	Ir, metastable carbides (?), C Eutectic Ir–C (~2280–2310 °C, ~21–29 at.% C)	The solubility of C in solid Ir is ~3 at.% at the eutectic temp. and ~0.01 at.% C at 1000 °C. At 800–1250 °C the solubility of C in Ir is obeyed the rule: $\lg x$ (in at.% C) = 1.45–3244/T (in K). The solubility of C in liquid Ir at boil. point (4400 °C) is ~31.5 at.% C.	[138, 238, 241, 244]

(continued)

Table 2.13 (continued)

System	Type of phase diagram (constituent phases, temperatures and compositions of transformations)	Character of chemical interaction	References
Group 10			
C–Ni	Ni, Ni_3C (metastable), C Eutectic Ni–C (~1317–1327 °C, ~8.5–10 at.% C) Metastable eutectic Ni–Ni_3C (~1050–1120 °C, ~20–23 at.% C) Gas-eutectic Ni–C (gas–liquid-graphite non-variant equilibrium, ~2490 °C, ~33–34 at.% C)	The solubility of C in solid Ni–2.5–2.7 at.% at the eutectic temp. and 0.2–0.4 at.% C at 700 °C. It is obeyed the rule: lg$x$ (in at.% C) = 0.2–2600/T (in K) at the range of temp. from 500 °C to 1300 °C. The max. C content in Ni metastable solid solution reaches ~7.4 at.% C. Molten Ni dissolves considerable amounts of C (from 10.9 at.% at 1450 °C to 25 at.% C at 2490 °C). The solubility of C in liquid Ni is obeyed the rule: lg$x$ (in at.% C) = 1.55–896/T (in K) at the range of temp. from 1400 °C to 1700 °C. Practically, no solubility of Ni in graphite. Ni carbide is not formed directly from the elements. The wetting angle of molten pure Ni: 50° (vacuum, 1455 °C), 68° (H_2, 1500 °C); Ni–2.3 at.% C alloy: 145° (vacuum, 1455 °C); for other Ni containing alloys, see Table 2.16. For diffusion rate in the system at various temp. see Addendum.	[138, 238, 241, 244, 269–271, 530, 848]
C–Pd	Pd, no binary compounds, C Eutectic Pd–C (~1505–1515 °C, ~8–19 at.% C, ?)	The max. solubility of C in solid Pd is ~7–9 at.% C (at eutectic temp.). At 900 °C the solubility amounts ~3 at.% C. At 900–1500 °C the solubility of C in Pd is obeyed the rule: lg$x$ (in at.% C) = 3.58–1262/T (in K). The solubility of C in liquid Pd at boil. point (2965 °C) is ~16–18 at.% C.	[138, 238, 241, 244, 944, 1022]

(continued)

Table 2.13 (continued)

System	Type of phase diagram (constituent phases, temperatures and compositions of transformations)	Character of chemical interaction	References
C–Pt	Pt, metastable compounds Pt_7C (?) and Pt_2C, C Eutectic Pt–C (~1705–1740 °C, 16.8 at.% C)	The solubility of C in solid Pt is ~2.5–4.0 at.% at the eutectic temp., ~1.7 at.% C at 1245 °C and ~0.8 at.% C at 875 °C. At 870–1250 °C the solubility of C in Pt is obeyed the rule: $\lg x$ (in at.% C) = 1.4–1800/T (in K) The solubility of C in liquid Pt at boil. point (3800 °C) is ~19 at.% C.	[138, 238, 241, 244]
Group 11			
C–Cu	Cu, unstable compounds (e.g. Cu_2C_2 and CuC_2), C Peritectic Cu (~1100 °C, ~0.04 at.% C)	No interaction. At melt. point (1084.87 °C) the solubility of C in solid Cu is ~100 times higher than the similar value in liquid Cu: ~0.03 and ~0.0003 at.% C, respectively. The solubility of C in liquid Cu is very low (~0.0027 at.% at 1500 °C and ~0.016 at.% C at 1700 °C). Chemical compounds, e.g. Cu_2C_2 and CuC_2, are unstable and formed only indirectly. The wetting angle of molten pure Cu: 120–150° (high vacuum, 1090–1100 °C), 139–145° (on vitreous carbon, high vacuum, 1090–1100 °C), 157° (vacuum, 1100 °C), 150° (H_2, 1100 °C), 170° (vacuum, 1200 °C); for Cu containing alloys, see Table 2.16.	[138, 238, 241, 244, 530, 910]

(continued)

Table 2.13 (continued)

System	Type of phase diagram (constituent phases, temperatures and compositions of transformations)	Character of chemical interaction	References
C–Ag	Ag, unstable compounds, C Peritectic Ag (962.23 °C, 0.036 at.% C)	No interaction. At melt. point (961.93 °C) the solubility of C in solid Ag is $>10^5$ times higher than the similar value in liquid Ag (>0.035 and $<\sim 10^{-7}$ at.% C, respectively). The solubility of C in liquid Ag is very low (~0.01 at.% at 1660 °C and ~0.02 at.% C at 1940 °C). Chemical compounds, e.g. Ag_2C_2, are unstable and formed only indirectly. The wetting angle of molten pure Ag: 135–150° (high vacuum, 970–1100 °C), 167° (vacuum, 1000 °C); for Ag containing alloys, see Table 2.16.	[138, 238, 241, 530, 910]
C–Au	Au, unstable compounds (e.g. Au_2C_2), C Eutectic Au–C (~1040–1050 °C, ~4.7 at.% C, ?)	The max. solubility of C in solid Au is ~0.080–0.082 at.% C (at eutectic temp.). The solubility of C in liquid Au at boil. Point (2860 °C) is ~4.9 at.% C. Chemical compounds, e.g. Au_2C_2, are unstable and formed only indirectly. The wetting angle of molten pure Au on graphite single crystal–119° (vacuum, 1100 °C) and vitreous carbon—135–138° (high vacuum, 1100 °C).	[138, 238, 241, 910]
Group 12			
C–Zn	Zn, unstable compounds (e.g. ZnC_2), C No diagram plot	No interaction. The solubility of C in liquid Zn at boil. point is negligible (traces). Zn carbide ZnC_2 is unstable and formed only indirectly. At 600–700 °C the corrosion resistance of graphite in liquid Zn is very high. For diffusion rate in the system at various temp. see Addendum.	[138, 238, 241]

(continued)

Table 2.13 (continued)

System	Type of phase diagram (constituent phases, temperatures and compositions of transformations)	Character of chemical interaction	References
C–Cd	Cd, unstable compounds, C No diagram plot	No interaction. The solubility of C in liquid Cd at boil. point is negligible (traces). For the range of temp. from melt. point (321.1 °C) to boil. point (767 °C), theoretical estimation gives the values of C solubility in molten Cd from 3×10^{-14} to 2×10^{-7} at.% C, respectively. Carbide CdC_2 is unstable and formed only indirectly	[138, 238, 241]
C–Hg	Hg, unstable (e.g. Hg_2C_2, HgC_2,) and lamellar (e.g. HgC_{16}, at least at 25–105 °C, ?) compounds, C No diagram plot	No interaction. The solubility of C in liquid Hg at boil. point is negligible (traces). C is the least soluble element in Hg. For the range of temp. from melt. point (–38.8 °C) to boil. point (356.6 °C), theoretical estimation gives the values of the C solubility in molten Hg from $\sim 10^{-40}$ to 2×10^{-15} at.% C, respectively. Carbides HgC_2 and Hg_2C_2 are metastable and formed only indirectly. At 300–600 °C the corrosion resistance of graphite in liquid Hg is very high (30 days exposure with circulating Hg). The contact wetting angle of molten pure Hg: 154° (air, 20 °C).	[138, 238, 241, 530, 913–914]

(continued)

Table 2.13 (continued)

System	Type of phase diagram (constituent phases, temperatures and compositions of transformations)	Character of chemical interaction	References
Group 13			
C–B	β-B, $B_{51}C$ (or $B_{50}C$, <1280 °C, metastable, ?), $B_{56}C_2$ (?), $B_{50}C_2$ (or $B_{25}C$, $C_2B_2B_{48}$, <1100–1245 °C, metastable, ?), $B_{49}C_3$ (?), $B_{24}C$ (?), B_8C (?), $B_{13}C_{2\pm x}$ (<2450 °C, congruent melt. point corresp. to ~$B_{5.25}C$, homog. range—~11.5–20.0 at.% C at 2350 °C, ~9.5–19.7 at.% C at 1980 °C and ~12.0–13.4 at.% C at 1400 °C, ?), $B_{13}C_{3-x}$ (1200–1980 °C, homog. range—18.0–18.5 at.% C at 1850 °C, ?), $B_{4\pm x}C$ (<~2450 °C, congruent melt. point corresp. to ~$B_{3.95–4.45}C$, homog. range—~10.0–24.3 at.% C at 2375–2245 °C, ~9.3–22.3 at.% C at 2080 °C and ~9.2–21.6 at.% C at 1800 °C, ?), $B_{11}C_4$ (?), ~BC_2 (?), ~BC_3 (or B_nC_m, ?), C Peritectic β-B (~2080–2105 °C, ~1.0–1.4 at.% C, ?) Eutectic β-B–$B_{4\pm x}C$ (~2075–2080 °C, <1 at.% C, ?) Eutectic $B_{4\pm x}C$–C (~2245–2390 °C, ~28.5–30.0 at.% C) Phase diagram data available in literature are controversial	The solubility of C in B is negligible. The max. solubility of B in graphite is 2.3 at.% at 2390 °C. It decreases with temp. decreasing and amounts ~1 at.% C at 1700 °C. B carbides are formed directly from the elements at elevated temp. For diffusion rate in the system at various temp. see Addendum.	[138, 238, 241, 244, 252, 272–279, 321, 359, 724, 1019]

(continued)

Table 2.13 (continued)

System	Type of phase diagram (constituent phases, temperatures and compositions of transformations)	Character of chemical interaction	References
C–Al	Al, Al_3C_2 (<1730 °C, ?), Al_4C_3 (<~1970–2250 °C (?), incongruent melt. point, invariable compos.), C Data on phase diagram available in literature are controversial.	Practically, no solubility of C in solid Al. The solubility of C in liquid Al is extremely low: 0.7 at.% at 1200 °C, 0.31 at.% at 1000 °C and 0.22 at.% at 800 °C. Al carbide is formed directly from the elements in H_2 at 1200–1300 °C. The wetting angle of molten pure Al in vacuum is 123° at 830 °C (initially, before reaction), ~145–160° at 875–1000 °C, ~140° at 1100 °C, ~85° at 1200 °C (5 min exposure), ~50–70° at 1200 °C (long-term exposure), 139° at 830 °C (on vitreous carbon, before reaction); pure Al wets sintered Al_4C_3 with a contact angle of 55° at 1100 °C; for Al containing alloys, see Table 2.16.	[138, 238, 241, 244, 277, 278–280, 307, 530, 661, 910, 946–947, 1016]
C–Ga	Ga, no binary compounds, C No diagram plot	No interaction. Ternary compounds are formed by the interaction of transition metal carbides with Ga. At 600 °C the corrosion resistance of graphite in liquid Ga is very high. The wetting angle of molten pure Ga on vitreous carbon: 138° (high vacuum, 30 °C), 125° (high vacuum, 900 °C).	[138, 238, 278, 681, 910]
C–In	In, no binary compounds, C	No interaction. Ternary compounds are formed by the interaction of transition metal carbides with In. The wetting angle of molten pure In on graphite or vitreous carbon: 135–150° (high vacuum, 200–800 °C).	[238, 278, 681, 704, 910]
C–Tl	α-Tl, β-Tl, TlC_x (metastable, ?), C No diagram plot	No solubility of C in liquid Tl. Ternary carbides are formed by the interaction of transition metal carbides with Tl. For the range of temp. from melt. point (304 °C) to boil. point (1473 °C), theoretical estimation gives the values of C solubility in molten Tl from 4×10^{-17} to 1×10^{-4} at.% C, respectively.	[238, 241, 278, 681]

(continued)

Table 2.13 (continued)

System	Type of phase diagram (constituent phases, temperatures and compositions of transformations)	Character of chemical interaction	References
Group 14			
C–Si	Si, Si_5C_3 (?), α-SiC (variety of polytypes), β-SiC (<~2500–2830 °C, incongruent melt. point, invariable compos.), SiC_2 (?), C Eutectic Si–SiC (~1400–1410 °C, ~0.03–1.25 at.% C, ?) Data available in literature on α-SiC ↔ β-SiC transformation are controversial.	The solubility of C at eutectic temp.: in liquid Si–5×10^{-3} at.%. and in solid Si–$(7 \div 9) \times 10^{-4}$ at.% (?). At 1150–1350 °C the solubility of C in Si is obeyed the rule: lg$x$ (in at.% C) = 3.2–10,400/T (in K) Si carbides are formed directly from the elements at elevated temp. At temp. >2000 °C in vacuum, SiC decomposes with the formation of graphite. Data available in literature on the solubility of C in Si are controversial. SiC is perfectly wetted by molten Si, the contact angle of Si on α-SiC is 30–40°. The wetting kinetics of Si on C is fast, the contact angle of 40–50° is reached in less than 40–60 s; on polycrystalline graphite the final contact angle is 10–30°. For diffusion rate in the system at various temp. see Addendum.	[138, 238, 241–244, 252, 278–282, 359, 705–708, 1015]
C–Ge	Ge, no binary compounds, C Eutectic (degenerative) Ge–C (~938 °C, ?)	No interaction. Ge ternary carbides are formed by the interaction of transition metal carbides with Ge. Practically, no solubility of C in solid Ge. Near the melt. point (938 °C) the solubility of C in liquid Ge is 0.23 at.%, but it increases near the boil. point (2834 °C) considerably. The wetting angle of molten pure Ge on graphite or vitreous carbon: 135–150° (high vacuum, 950–1100 °C).	[238, 241, 244, 681, 709, 910]

(continued)

Table 2.13 (continued)

System	Type of phase diagram (constituent phases, temperatures and compositions of transformations)	Character of chemical interaction	References
C–Sn	α-Sn, β-Sn, intercalated fullerenes ($Sn(C_{60})$, $Sn_x(C_{60})$ and other), C No diagram plot	For the range of temp. from melt. point (232 °C) to boil. point (2270 °C), theoretical estimation, in accordance to $\lg x$ (in at.% C) = –1.685–13,800/T (in K), gives the values of C solubility in molten Sn from 1×10^{-25} to 8×10^{-4} at.% C, respectively. Sn ternary carbides are formed by the interaction of transition metal carbides with Sn. The corrosion resistance of graphite in liquid Sn is very high. The wetting angle of molten pure Sn on graphite or vitreous carbon: ~135–150° (high vacuum, 250–800 °C).	[138, 238, 241, 681, 910, 948]
C–Pb	Pb, PbC_2 (metastable, ?), C	Practically, no solubility of C in solid Pb. The solubility of C in liquid Pb is: 0.41 at.% at 1170 °C, 0.79 at.% at 1415 °C and 1.6 at.% C at 1555 °C. Pb ternary carbides are formed by the interaction of transition metal carbides with Pb. Data on C solubility available in literature are controversial. At 300 °C the corrosion resistance of graphite in liquid Pb is very high. The wetting angle of molten pure Pb on vitreous carbon: 142° (high vacuum, ~330 °C).	[138, 238, 241, 681, 710, 910]
Group 15			
C–N	N, variety of compounds (e.g. C_2N_2, some polymorphs of C_3N_4, azafullerenes $(C_{59}N)_2$, $C_{58}N_2$, $C_{57}N_3$, $C_{48}N_{11}$, cyanofullerenes $(C_{60}(CN)_{2n}$, $n = 1 \div 9$), percyanoalkynes (-alkenes, -alkanes), perazidoalkynes (-alkenes, -alkanes), percyanoheterocycles, dicyanopolyynes, aromatic cyanocarbons etc.), C	No direct interaction at high temp. without any special activation (e.g. microwave radiation, electrical discharge etc.), so N_2 is recommended for graphite as a protective atmosphere at temp. ≤2500–3000 °C. At higher temp. gas cyanogen (dicyan) C_2N_2 is formed. Several polymorphs of C nitride (C_3N_4) and related structures are prepared in the form of films by employing special technological routes.	[5, 138, 238, 283–284, 359, 531, 711–717]

(continued)

Table 2.13 (continued)

System	Type of phase diagram (constituent phases, temperatures and compositions of transformations)	Character of chemical interaction	References
C–P	P, some unstable compounds (e.g. C_6P_6), intercalated fullerenes ($P_8(C_{60})$ and other), C	No direct interaction. C_6P_6 is formed by special reaction pathways. Ternary carbides are formed by the interaction of transition metal carbides with P.	[238, 681, 718, 949, 1024]
C–As	As, AsC_3 (?), C No diagram plot	The solubility of C in As near the boil. point is extremely low. As carbide has been prepared indirect methods; ternary carbides are formed by the interaction of transition metal carbides with As.	[138, 238, 241, 681]
C–Sb	Sb, no binary compounds, C No diagram plot	At 1300 °C the solubility of C in liquid Sb is ~1 at.%. At 600 °C the corrosion resistance of graphite in liquid Sb is very high.	[138, 238, 241]
C–Bi	Bi, no binary compounds, C No diagram plot	No interaction. The solubility of C in Bi near the boil. point (1565 °C) is very low. At 600 °C the corrosion resistance of graphite in liquid Bi is very high. The wetting angle of molten pure Bi on vitreous carbon: 142° (high vacuum, ~300 °C).	[138, 238, 241, 910]
Group 16			
C–O	O, CO_2, CO, C_3O_2 (metastable), fullerene containing compounds $(O_3)_x(C_{60})$, $(O_3)_x(C_{70})$ and other, C	Graphite is in equilibrium with CO_2 (<400 °C), or CO + CO_2 (~400–1000 °C), or CO (~1000–3200 °C). In common conditions the oxidation of carbon in air initiates from 450–500 °C. The oxidation process is controlled by the mechanisms of the chemical reaction of gasification at 600–800 °C (Q = 170–200 kJ mol^{-1}), or gas diffusion at 800–1000 °C (Q = 20–45 kJ mol^{-1}). At temp. <600 °C the main product of oxidation is CO_2, at higher temp.—CO. The average oxidation rate of pyrolytic carbon is ~0.12 (<900 °C) and ~1.2 (>2000 °C) kg m^{-2} s^{-1}. The oxidation rate of graphitized materials in air flow (150 cm^3 s^{-1}): at 350 °C–0.1, 400 °C–0.6, 500 °C–80 and 600 °C–800 kg m^{-2} s^{-1}.	[5, 136, 238, 285–289, 531, 664, 996, 1025]

(continued)

Table 2.13 (continued)

System	Type of phase diagram (constituent phases, temperatures and compositions of transformations)	Character of chemical interaction	References
C–S	α-S, β-S, $S_{12}CS_2$ (?), C_3S_8 (?), CS_2, α-C_2S_3 (?), β-C_2S_3 (?), C_3S_4 (?), CS, C_3S_2, C_2S (?), fullerene containing compounds ($S_8CS_2(C_{60})$, $(S_8)_2(C_{60})$, $S_{48}(C_{70})$, $S_{48}(C_{76})$ and other), C No complete diagram plot	C sulfides are formed directly from the elements at elevated temp. S ternary carbides are formed by the interaction of transition metal carbides with S.	[5, 238, 681, 950, 997]
C–Se	Se, CSe_2, C No diagram plot	No direct interaction. CSe_2 is synthesized by special reaction pathways.	[5, 238, 241]
C–Te	Te, no binary compounds, C No diagram plot	No interaction	[238, 850]
C–Po	α-Po, β-Po, no binary compounds, C No diagram plot	No interaction with Po vapours at temp. ≤700 °C.	[241]
Group 17			
C–F	F, variety of compounds, including fullerene containing (e.g. $(C_{60})F_{18}$ and other), C	The intensive interaction of C with F_2 begins at 500–600 °C CF_4, C_2F_6 and other fluoro-carbons are formed directly from the elements. At 450 °C CF_n ($n \leq 1$, variable compos. from CF to C_4F) intercalation (lamellar) compounds are synthesized.	[5, 238, 290, 953]
C–Cl	Cl, variety of compounds, including fullerene containing (e.g. $(C_{60})Cl_5$ and other), C	No direct interaction with Cl_2 at temp. <2300 °C. C_8Cl and other lamellar (intercalate) compounds are synthesized by special reaction pathways.	[138, 238, 290, 952, 999]
C–Br	Br, CBr_4, C_8Br, (or $C_{16}Br_2$, or $C_{56}Br{\cdot}3Br_2$, lamellar compound), fullerene containing compounds ($(C_{60})Br$, α-$(C_{60})Br_{24}{\cdot}Br_2$, β-$(C_{60})Br_{24}{\cdot}Br_2$, $(C_{70})Br_{14}$ and some other), C No diagram plot	Intercalation (lamellar) and fullerene containing compounds are synthesized.	[5, 238, 290, 951]
C–I	I, CI_4, C_2I_4 (?), C_2I_2 (?), fullerene containing compounds ($(C_{60})(I_2)$, $(C_{60})(I_2)_2$ and some other), C No diagram plot	–	[238, 954]
C–At	No data	–	–

[a] The intervals of temperatures and compositions for the melting and invariant equilibria points, homogeneity ranges and thermal stability regions of constituent phases are given taking into account the minimal and maximal values (data spread) available in literature

The data on the selected ternary, quaternary, quasi-binary, quasi-ternary and multi-component carbon containing systems, which are the most important for the design, manufacture and application of ultra-high temperature materials, are summarized in Table 2.14. The composition and temperature stability regions for the main binary and ternary carbon containing high temperature phases are given in Tables 2.13, 2.14 taking into account the spread of numerical magnitudes available in literature currently.

Table 2.14 Chemical interaction of carbon (graphite) with elements and compounds at elevated, high and ultra-high temperatures (selected ternary, quaternary, quasi-binary, quasi-ternary and multi-component systems in alphabetical order)[a]

System	Type of phase diagram (temperature and composition sections, constituent phases or phase fields) and/or character of interphase interaction and materials compatibility	References
C–Al–B	Plotted at 900, 1000 and 1400 °C: $Al_{2+x}B_{51}C_8$ ($x = 0.1$), $AlB_{40}C_4$ (eventually high-temp. phase of $Al_{2+x}B_{51}C_8$, ?), α-$Al_3B_{48}C_2$ (<650 °C), β-$Al_3B_{48}C_2$ (or $Al_3B_{44}C_2$, >650 °C), Al_3BC_3 (or $Al_8B_4C_7$, $2Al_4C_3{\cdot}B_4C$, <1835 °C), Al_3BC (<1100 °C), Al_2B_3 (≤ ~ 955 °C, ?), AlB_2 (≤ ~ 955–980 °C), AlB_{10} (1660–1850 °C), α-AlB_{12} (≤ ~ 1450–1550 °C), β-AlB_{12} (~ 1450–2150 °C, ?), γ-AlB_{12} (~ 1550–2150 °C, ?), $B_{4\pm x}C$, Al_4C_3, Al, β-B, C	[241–242, 244, 277, 291, 313]
C–Al–B–N	No diagram plot $Al_{1-x}B_{24}C_4N_{1+y}$ (or $Al_{0.185}B_6CN_{0.256}$) No interaction between $B_{4\pm x}C$ and AlN in powder mixtures at 1500–1850 °C (hot pressing in graphite dies without protective environment).	[892, 955]
C–Al–B–Si	Al_4C_3–B_4C–SiC is plotted at 1800 °C: $Al_8B_4C_7$ (or $2Al_4C_3{\cdot}B_4C$), Al_4SiC_4 (or $Al_4C_3{\cdot}SiC$), $Al_4Si_2C_5$ (or $Al_4C_3{\cdot}2SiC$), Al_4C_3, $B_{4\pm x}C$, SiC	[292]
C–Al–Be–Si	Al_4C_3–Be_2C–SiC is plotted at 1860 °C: $Al_{16}Be_2SiC_{14}$ (or $4Al_4C_3{\cdot}Be_2C{\cdot}SiC$), $Al_{24}Be_2Si_4C_{23}$ (or $6Al_4C_3{\cdot}Be_2C{\cdot}4SiC$, ?), $Al_{16}Be_4SiC_{15}$ (or $4Al_4C_3{\cdot}2Be_2C{\cdot}SiC$), $Al_8Be_2SiC_8$ (or $2Al_4C_3{\cdot}Be_2C{\cdot}SiC$), Al_6BeC_5 (or $3Al_4C_3{\cdot}Be_2C$), Al_2BeC_2 (or $Al_4C_3{\cdot}Be_2C$), $Al_2Be_3C_3$ (or $Al_4C_3{\cdot}3Be_2C$), Al_4SiC_4 (or $Al_4C_3{\cdot}SiC$), Al_4C_3, Be_2C, SiC	[295–297]
C–Al–Cr–Ti	No diagram plot $(Ti,Cr)_2AlC$ ($M_{n+1}AX_n$-phase solid solution)	[680–681, 860]
C–Al–Cr–V	No diagram plot $(V,Cr)_2AlC$, $(V,Cr)_3AlC_2$ ($M_{n+1}AX_n$-phase solid solutions), $(V,Cr)_5Al_2C_3$ ($M_{n+1}AX_n$-phase solid solution, intergrown structure, ?)	[680–681, 744–745, 860]
C–Al–Hf	Plotted at 700 °C: $Hf_2Al_3C_4$, $Hf_3Al_3C_5$ (or $HfAlC_{1.67}$), Hf_5Al_3C, $HfAl_3$ (<1590 °C), $HfAl_2$ (<1650 °C), Hf_2Al_3 (<1640 °C), HfAl (<1800 °C), Hf_4Al_3 (< ~ 1420 °C), Hf_3Al_2 (< ~ 1595 °C), Hf_2Al (< ~ 1145 °C), Al_4C_3. HfC_{1-x}, α-Hf, β-Hf, C Depending on compos., graphite is in equilibrium with $Hf_2Al_3C_4$ + HfC_{1-x}, or $Hf_2Al_3C_4$ + Al_4C_3. The interaction between HfC_{1-x} and Al at temp. >1250 °C leads to the formation of solid solutions (?).	[242, 896, 956, 965]

(continued)

Table 2.14 (continued)

System	Type of phase diagram (temperature and composition sections, constituent phases or phase fields) and/or character of interphase interaction and materials compatibility	References
C–Al–Ir	Plotted partially at 1100 °C: no ternary compounds (at least in the Ir rich part of the system), $IrAl_{1\pm x}$ (<2120 °C), $Ir_2Al_{5\pm x}$ (<~1615 °C), $IrAl_3$ (<1450 °C), Ir_4Al_{13} (<1015 °C), Ir_2Al_9 (<900 °C), Al_4C_3, Al, Ir, C In the wide compos. range graphite is in equilibrium with metal Ir based solid solution and $IrAl_{1\pm x}$.	[241, 244, 593, 995]
C–Al–Mn–Si	$Mn_5Si_3C_x$–Mn_3AlC_x–$Mn_{15}Si_3C_2$–C and $Mn_5Si_3C_x$–Mn_3AlC_x–Al_4C_3–C are plotted schematically.	[298–299]
C–Al–Mo	Plotted at 1000 and 1450 °C: $Mo_{3-x}Al_{2+x}C$ ($-0.12 \le x \le 0.24$, or $Mo_{0.46\div0.52}Al_{0.31\div0.37}C_{0.17}$), $(Al,Mo)_4C_3$ (solid solution based on Al_4C_3; ≤ 5 at.% Mo), $MoAl_{12}$ (<~690 °C), $MoAl_5$ (<735 °C), $MoAl_4$ (or Mo_4Al_{17}, <1130 °C), $Mo_3Al_{8\pm x}$ (<~1550 °C), $MoAl_{2-x}$ ($x = 0.3$, ~1490–1570 °C), $MoAl_{1\pm x}$ (~1470–1720 °C), $Mo_{3\pm x}Al$ (<2150 °C), α-$Mo_{2+x}C$, α′-$Mo_{2+x}C$, β-$Mo_{2\pm x}C$, η-MoC_{1-x}, α-MoC_{1-x}, γ-MoC, Al, Mo, C The interaction between β-$Mo_{2\pm x}C$ and Al at temp. >1250 °C leads to the formation of solid solutions (?).	[242, 896, 957]
C–Al–Mo–Ni	Plotted schematically and partially General consideration of the system.	[851]
C–Al–N–Si	Al_4C_3–AlN–SiC is plotted at 1860 °C: $Al_{9+x}Si_{1-x}N_{1+x}C_{7-x}$ ($-0.04 \le x \le 0.04$), Al_5SiNC_4 (or $Al_4C_3{\cdot}AlN{\cdot}SiC$), Al_8SiC_7 (or $2Al_4C_3{\cdot}SiC$), Al_4SiC_4 (or $Al_4C_3{\cdot}SiC$), $Al_4Si_2C_5$ (or $Al_4C_3{\cdot}2SiC$, ?), Al_5NC_3 (or $Al_4C_3{\cdot}AlN$), Al_3NC (?), AlN (<2400–2450 °C), Al_4C_3, SiC Si_3N_4–AlN–SiC and Al_4C_3–AlN–SiC are plotted at 1760 and 1860 °C, respectively: $Al_{5-x}Si_xN_{1-x}C_{3+x}$ ($0 < x \le 0.4$), $Al_{5-x}Si_xN_{1-x}C_{3+x}$ ($x \approx 0.5$), $Al_{5-x}Si_xN_{1-x}C_{3+x}$ ($0.85 \le x < 1$), Al_5SiNC_4 (or $Al_4C_3{\cdot}AlN{\cdot}SiC$), Al_5NC_3 (or $Al_4C_3{\cdot}AlN$), Al_4SiC_4 (or $Al_4C_3{\cdot}SiC$), AlN (<2400–2450 °C), β-Si_3N_4 (<~1800–1900 °C), Al_4C_3, SiC	[280, 297, 300–302]
C–Al–N–Ti	No diagram plot $Ti_2AlC_{x-y}N_y$ ($x = \sim0.8$, $0 \le y \le \sim0.8$), $Ti_3Al(C,N)_2$ ($M_{n+1}AX_n$-phase solid solutions)	[680–681, 744–745, 860]
C–Al–Nb	Plotted at 700 and 800 °C: Nb_2AlC ($M_{n+1}AX_n$-phase), α-Nb_4AlC_3, β-Nb_4AlC_3 ($M_{n+1}AX_n$-phases, ?), $NbAl_{3-x}$ (<1680 °C), $Nb_{2\pm x}Al$ (<1940 °C), $Nb_{3+x}Al$ (<2060 °C), Al_4C_3, α-Nb_2C, β-$Nb_{2+x}C$, γ-$Nb_{2\pm x}C$, ζ-Nb_4C_{3-x}, $Nb_6C_{5\pm x}$, NbC_{1-x}, Al, Nb, C No solid solutions based on ternary and binary compounds.	[680–681, 744–745, 860, 896, 898, 958–959, 965]
C–Al–Nb–Ti	No diagram plot $(Ti,Nb)_2AlC$ ($M_{n+1}AX_n$-phase solid solution)	[680–681, 860]
C–Al–Nb–V	No diagram plot $(V,Nb)_2AlC$ ($M_{n+1}AX_n$-phase solid solution)	[680–681, 860]

(continued)

Table 2.14 (continued)

System	Type of phase diagram (temperature and composition sections, constituent phases or phase fields) and/or character of interphase interaction and materials compatibility	References
C–Al–Nb–Zr	No diagram plot $(Nb,Zr)_2AlC$ ($M_{n+1}AX_n$-phase solid solution)	[680–681, 860]
C–Al–O	Plotted at 1000–2400 °C: Al_2OC, Al_4O_4C, AlC_9O_{10} (at least at 2000–2050 °C), AlC_2O_2 (at least at 2100 °C), $Al_4C_7O_9$ (at least at 2100 °C), AlCO (at least at 2400 °C), Al_2O (?), γ-Al_2O_{3-x}, α-Al_2O_3 (<~2030–2055 °C), Al_4C_3, Al, O, C Al_2O_3–Al_4C_3 is plotted: Al_2OC (1650–2000 °C), Al_4O_4C (<1890 °C), α-Al_2O_3, Al_4C_3 In vacuum, the interaction between C and α-Al_2O_3 initiates in powdered mixtures from ~1350 °C, on bulk materials contacts—from ~1800 °C, and is ruled by diffusion stage (parabolic law) with formation of Al_4C_3.	[138, 194, 303–304, 382, 960]
C–Al–O–Si	No diagram plot At 2000 °C in powdered mixtures, the interaction between SiC and Al_2O_3 in air leads to the formation of elemental Al, Si and phases close to nonstoichiometric mullite $xAl_2O_3{\cdot}ySiO_2$ (?).	[891]
C–Al–O–Ti	No diagram plot $Ti_2Al(C,O)$ ($M_{n+1}AX_n$-phase oxycarbide solid solution)	[744–745]
C–Al–O–U	No diagram plot At 1900 °C the interaction between β-UC_{2-x} and Al_2O_3 is weak.	[242]
C–Al–Si	Plotted at <580, 2000 and 2150 °C: Al_8SiC_7 (or $2Al_4C_3{\cdot}SiC$), Al_4SiC_4 (or $Al_4C_3{\cdot}SiC$), Al_4C_3, SiC, Al, Si, C Al_4C_3–SiC is plotted: Al_8SiC_7 (<2085 °C, incongruent melt. point), α-Al_4SiC_4, β-Al_4SiC_4 (<2080 °C, congruent melt. point), $Al_4Si_2C_5$ (or $Al_4C_3{\cdot}2SiC$, ?), $Al_4Si_3C_6$ (or $Al_4C_3{\cdot}3SiC$, ?), $Al_4Si_4C_7$ (or $Al_4C_3{\cdot}4SiC$, ?), Al_4C_3, SiC The presence of Si in Al alloys results in the predominant formation of SiC and suppresses the formation of Al_4C_3 during the contact interaction of the Al–Si alloys with graphite.	[242, 292–294, 661, 1002]
C–Al–Ta	Plotted at 700 and 1000 °C: Ta_2AlC, Ta_3AlC_2, $Ta_5Al_3C_{1-x}$, α-Ta_4AlC_3 (<~1600 °C), β-Ta_4AlC_3 ($M_{n+1}AX_n$-phases), Ta_3Al_2C (?), $TaAl_3$ (<1550–1630 °C, ?), $TaAl_2$ (<~1595 °C, ?), α-Ta_2Al_3 (<1225 °C, ?), β-Ta_2Al_3 (~1225–1550 °C, ?), TaAl (<1770 °C, ?), δ-$Ta_{2\pm x}Al$ (<~2000–2100 °C), Ta_3Al (?), Al_4C_3, α-$Ta_{2+x}C$, β-$Ta_{2\pm x}C$, ζ-Ta_4C_{3-x}, $Ta_6C_{5\pm x}$, TaC_{1-x}, Al, Ta, C The interaction between TaC_{1-x} and Al at temp. ≥1250 °C leads to the formation of solid solutions (?).	[242, 680–681, 744–745, 860, 881, 896, 965]
C–Al–Ta–Ti	Plotted at 1100 °C (for 9.1 and 25 at.% C): $(Ti,Ta)_2AlC$ ($M_{n+1}AX_n$-phase solid solution), $(Ta,Ti)C_{1-x}$ (TaC_{1-x}–TiC_{1-x} monocarbide continuous solid solution with the critical point of the miscibility gap calculated to be below 0 °C)	[680–681, 860, 881]

(continued)

Table 2.14 (continued)

System	Type of phase diagram (temperature and composition sections, constituent phases or phase fields) and/or character of interphase interaction and materials compatibility	References
C–Al–Ta–V	No diagram plot $(V,Ta)_2AlC$ ($M_{n+1}AX_n$-phase solid solution)	[680–681, 860]
C–Al–Ti	Plotted at 750–1300 °C: Ti_3AlC_{1-x} ($x = 0.5$, <1570–1590 °C), Ti_2AlC_{1-x} ($x = 0.2$, <1615–1635 °C, $M_{n+1}AX_n$-phase), Ti_3AlC_{2-x} (at least at ~1300 °C, $M_{n+1}AX_n$-phase), β-(Ti,Al) (ordered, ~1105–1425 °C), α_2-$Ti_{3\pm x}Al$ (<~1180–1195 °C), α-$Ti_{2\pm x}Al$ (<~1500 °C, ?), γ-$TiAl_{1\pm x}$ (<~1455–1480 °C), $Ti_{1-x}Al_{1+x}$ (disordered, 1170–1480 °C), Ti_3Al_5 (<700–810 °C, ?), α-$TiAl_{2\pm x}$ (<~1225–1240 °C), β-$TiAl_{2\pm x}$ (?), ξ-Ti_5Al_{11} (from 990–995 °C to ~1415 °C, ?), ζ-$Ti_2Al_{5\pm x}$ (or δ-$Ti_2Al_{5\pm x}$, or Ti_9Al_{23}, from ~975–1150 °C to ~1385–1430 °C), α-$TiAl_3$ (<~600–930 °C), β-$TiAl_3$ (from ~600–930 to 1355–1395 °C), Al_4C_3 (no solubility for Ti), TiC_{1-x}, α-Ti, β-Ti, Al, C TiC_{1-x}–γ-$TiAl_{1\pm x}$ is partially plotted: Ti_2AlC_{1-x}, TiC_{1-x}, γ-$TiAl_{1\pm x}$; the max. solubility of TiC_{1-x} in γ-$TiAl_{1\pm x}$ at 1530 °C is 0.9 mol.% and it decreases to <0.7 mol.% as the temp. decreases to 600–1200 °C. Non-stoichiometric TiC_{1-x} ($0.09 < x < 0.18$) is resistant to corrosion in molten Al at temp. <1000–1100 °C; the interaction of near-stoichiometric TiC_{1-x} ($x < 0.09$) with Al leads to the formation of Al_4C_3, whereas highly non-stoichiometric TiC_{1-x} ($x > 0.18$) interacts with the formation of β-$TiAl_3$. At 1250–1400 °C weak interaction between TiC_{1-x} and Al with the formation of Al_4C_3 is observed. At 1700 °C Al vapour penetrates into the porous structure of TiC_{1-x} without chemical interaction. The $M_{n+1}AX_n$-phase of Ti_3AlC_2 exfoliated in hydrofluoric acid are employed for the fabrication of Ti_xC_y 2D-nanosheets (graphene-like nanocrystals).	[241–242, 244, 305–312, 605–606, 624, 680–681, 744–745, 830, 859–860, 881, 896, 903–904, 962]
C–Al–Ti–V	No diagram plot $(Ti,V)_2AlC$ ($M_{n+1}AX_n$-phase solid solution)	[680–681, 860]
C–Al–U	Plotted at 600 °C: UAl_5C_4, α-UAl_3C_3 (?), β-UAl_3C_3, $U_2Al_3C_4$ (?), α-UAl_{4+x} (<~645 °C), β-UAl_{4+x} (~645–730 °C), UAl_3 (<1350 °C), UAl_2 (<1620 °C), Al_4C_3, $UC_{1\pm x}$, ζ-U_2C_3, α-UC_{2-x}, β-UC_{2-x}, α-U, β-U, γ-U, Al, C $UC_{1\pm x}$–UAl_2 is plotted: eutectic—1540 °C, ~10 mol.% $UC_{1\pm x}$ (~3.5 at.% C) No solid solutions based on ternary and binary compounds. The interactions between $UC_{1\pm x}$ and Al at temp. ≥500 °C, and between α-UC_{2-x} and Al at temp. ≥600 °C are active; and lead to the formation of C, UAl_3 and UAl_{4+x}.	[242, 961]

(continued)

Table 2.14 (continued)

System	Type of phase diagram (temperature and composition sections, constituent phases or phase fields) and/or character of interphase interaction and materials compatibility	References
C–Al–V	Plotted at 800 and 1000 °C: V_2AlC, V_3AlC_2 ($M_{n+1}AX_n$-phases), V_4AlC_{3-x} ($x = 1/3$, $M_{n+1}AX_n$-phase, ?), V_2Al_{21} (<~665 °C), V_7Al_{45} (<~690 °C), V_4Al_{23} (<~735 °C), VAl_3 (<1360 °C), V_5Al_8 (<1670 °C), Al_4C_3, α-$V_{2+x}C$, β-$V_{2\pm x}C$, β′-$V_{2+x}C$, ζ-V_4C_{3-x}, $V_6C_{5\pm x}$, $V_8C_{7\pm x}$, VC_{1-x}, V, Al, C No solid solutions based on ternary and binary compounds.	[680–681, 744–745, 748, 860, 896, 898, 962]
C–Al–W	Plotted at 900 °C: $WAlC_{2-x}$ ($x = 0 \div 1.0$, or $(W_{0.5}Al_{0.5})C_{1-y}$ with $y = 0 \div 0.5$, ?), $W_xAl_yC_z$ (ordered phase W_2AlC, ?), γ-WAl_{12} (<697 °C), δ-WAl_{5-x} (<870–871 °C), ε-$WAl_{4\pm x}$ (<~1325 °C), ζ-$WAl_{3\pm x}$ (~1300–1345 °C), η-$W_3Al_{7\pm x}$ (~1325–1420 °C), θ-$WAl_{2\pm x}$ (~1335–1650 °C), Al_4C_3, α-$W_{2+x}C$, β-$W_{2+x}C$, γ-$W_{2\pm x}C$, γ-WC_{1-x}, δ-$WC_{1\pm x}$, W, Al, C The interaction between δ-$WC_{1\pm x}$ and Al at temp. ≥1250 °C leads to the formation of solid solutions (?).	[242, 541, 644, 896, 963]
C–Al–Zr	Plotted at 600, 700 and 1000 °C: $Zr_3Al_3C_5$, $Zr_2Al_3C_5$, Zr_5Al_3C, $Zr_2Al_3C_4$ (?), $ZrAlC_{2-x}$ (?), $ZrAl_3$ (<1580 °C), $ZrAl_2$ (<1645 °C), Zr_2Al_3 (<1595 °C), ZrAl (<1275 °C), Zr_5Al_4 (~1000–1530 °C), Zr_4Al_3 (<~1035 °C), Zr_3Al_2 (<~1480 °C), Zr_5Al_3 (~1000–1400 °C), Zr_2Al (<1250 °C), Zr_3Al (<~990 °C), Al_4C_3, ZrC_{1-x}, α-Zr, β-Zr, Al, C The interaction between ZrC_{1-x} and Al at temp. ≥1250 °C leads to the formation of solid solutions (?).	[242, 744–745, 882–883, 896, 964–965]
C–As–Nb	No diagram plot Nb_2AsC ($M_{n+1}AX_n$-phase)	[680–681, 744–745, 860]
C–As–V	Plotted at 1100 °C: V_2AsC ($M_{n+1}AX_n$-phase), V_3AsC (wide homog. range), $V_5As_3C_{1-x}$ ($x \approx 0.3$), VAs_2, VAs, α-V_4As_3, β-V_4As_3, V_3As_2, α-V_5As_3, β-V_5As_3, γ-V_5As_3,V_2As, V_3As, α-$V_{2+x}C$, β-$V_{2\pm x}C$, β′-$V_{2+x}C$, ζ-V_4C_{3-x}, $V_6C_{5\pm x}$, $V_8C_{7\pm x}$, VC_{1-x}, V, As, C	[680–681, 744–745, 860, 956–967]
C–Au–Th	No diagram plot At 850 °C, in vacuum the interaction between $ThC_{1\pm x}$ and Au leads to the formation of C and $Th_{14}Au_{51}$ (or $ThAu_3$).	[242]
C–Au–U	No diagram plot At 950–1100 °C, in vacuum the interaction between $UC_{1\pm x}$ and Au leads to the formation of C and $U_{14}Au_{51}$ (or UAu_3).	[242]
C–B–Be	No diagram plot BeB_2C (?), $BeB_{12}C$ (?) The interactions of C with Be_4B (or Be_5B) and BeB_2 at temp. ≥900 °C, with Be_2B at temp. ≥1000 °C and with BeB_4 at temp. ≥1200 °C lead to the formation of Be_2C.	[242]

(continued)

Table 2.14 (continued)

System	Type of phase diagram (temperature and composition sections, constituent phases or phase fields) and/or character of interphase interaction and materials compatibility	References
C–B–Ce	Plotted at 1730 °C: $Ce_5B_3C_{12}$, $Ce_5B_2C_{6+x}$ ($0 \le x \le 0.2$, ?), $Ce_5B_4C_5$ (?), α-CeB_2C_2 (?), β-CeB_2C_2 (?), CeB_2C_4 (?), CeB_2C (?), $Ce_{10}B_9C_{12}$ (?), CeBC (?), CeB_4 (<~2380–2390 °C), $CeB_{6\pm x}$ (<~2290–2550 °C), Ce_2C_3, α-CeC_2, β-$CeC_{2\pm x}$, $B_{4\pm x}C$, α-Ce, β-Ce, γ-Ce, β-B, C	[241, 244, 391, 690, 958]
C–B–Co	No equilibrium phase diagram plot $Co_{22}B_4C_2$ The interaction between $B_{4\pm x}C$ and Co leads to the formation of eutectic alloy and solid solutions.	[242, 727]
C–B–Cr	Plotted at 1100 and 1450 °C: $Cr_3(B,C)C_{1-x}$ (or $Cr_3B_xC_{1-x}$, ~1550–1710 °C), $Cr_3(B_xC_{1-x})_2$ (or $Cr_3(C,B)_{2-x}$, Cr_3BC, <1810–1830 °C), $Cr_7(B_xC_{1-x})_{3\pm x}$ (or $Cr_7(C,B)_{3\pm x}$, Cr_7BC_4, <1765–1780 °C), $Cr_{23}(B_xC_{1-x})_{6\pm x}$ (or $Cr_{23}(C,B)_{6\pm x}$, <1575–1615 °C), $Cr_{2\pm x}B$ (<~1870 °C), $Cr_5B_{3\pm x}$ (<~1900 °C), α-$CrB_{1\pm x}$ (≤1000 °C, ?), β-$CrB_{1\pm x}$ (~1000–2150 °C, ?), $Cr_3B_{4\pm x}$ (<2070–2075 °C), Cr_2B_3 (at least at ~1000–1500 °C), $CrB_{2\pm x}$ (<~2150–2250 °C), CrB_4 (<~1450–1500 °C), $B_{4\pm x}C$, Cr, β-B, C CrB_2–$B_{4\pm x}C$ is plotted: eutectic—2150 °C, ~40 mol.% $B_{4\pm x}C$ (~7–8 at.% C) CrB_2–C is plotted: eutectic—~1875–1980 °C	[241–242, 244, 276, 314–317, 320, 322–323, 394, 690, 725–726]
C–B–Cr–N	No diagram plot At 1650 °C the interaction between α-BN and Cr_3C_{2-x} leads to the formation of Cr and $Cr_{2+x}N$.	[242]
C–B–Cr–Si	SiC–CrB_2 is plotted: eutectic—2030 °C, ~25 mol.% SiC (12.5 at.% C); the max. solid solubility of CrB_2 in SiC is ~2 mol.% and that of SiC in CrB_2 is ~2.5 mol.% (at the eutectic temp.)	[318, 566–567]
C–B–Dy	No diagram plot DyBC, DyB_2C, DyB_2C_2, $Dy_5B_2C_5$, Dy_2B_4C, $Dy_5B_2C_6$, ?	[391, 690]
C–B–Eu	Plotted at 1500 °C: EuB_2C_2, EuB_xC_y (or $Eu_2(C,B)_3$), $EuB_{6-x}C_x$, ($0 \le x \le 0.25$, or $Eu(C,B)_6$), $EuB_{6\pm x}$ (<~2580–2710 °C), $Eu_{3-x}C$, Eu_2C_3, α-EuC_2, β-EuC_2, EuC_6, $B_{4\pm x}C$, Eu, β-B, C	[241, 319, 690]
C–B–Er	No diagram plot ErB_2C, ErB_2C_2, $Er_5B_2C_5$, Er_2B_4C, $Er_5B_2C_6$, $ErB_{28.5}C_4$, ?	[391, 690]
C–B–Gd	Plotted at 2000–3000 °C: GdBC, GdB_2C_2, GdB_2C_4, Gd_2B_2C, $Gd_2B_3C_2$, $Gd_3B_2C_3$, $Gd_3B_4C_2$, $Gd_3B_4C_3$ (or $Gd_{0.3}B_{0.4}C_{0.3}$), $Gd_3B_5C_2$, $Gd_4B_3C_3$, $Gd_4B_3C_4$, $Gd_5B_2C_5$, $Gd_5B_2C_6$, $Gd_5B_8C_4$, $Gd_6B_9C_4$, $Gd_7B_4C_9$ (or $Gd_{0.35}B_{0.19}C_{0.46}$, ?), $Gd_7B_5C_4$ (or $Gd_{0.35}B_{0.45}C_{0.2}$, ?), $Gd_8B_7C_5$ (or $Gd_{0.4}B_{0.35}C_{0.25}$, ?), $Gd_8B_8C_9$, $Gd_8B_9C_7$, $Gd_9B_8C_5$ (or $Gd_{10}B_9C_5$), $Gd_9B_8C_7$, $Gd_9B_{10}C_6$, $Gd_{10}B_9C_6$, $Gd_{15}B_4C_{16}$, GdB_2 (~1280–2050 °C), ~Gd_2B_5 (<2100 °C), GdB_4 (<~2650 °C), $GdB_{6\pm x}$ (<2510 °C), GdB_{66} (or GdB_{100}, <2150 °C), $Gd_{3+x}C$, Gd_2C, GdC_{1-x}, Gd_2C_{3-x}, α-GdC_2, β-GdC_2, GdC_6, $B_{4\pm x}C$, Gd, β-B, C No solid solutions based on binary and ternary compounds.	[241, 391, 616–618, 690]

(continued)

Table 2.14 (continued)

System	Type of phase diagram (temperature and composition sections, constituent phases or phase fields) and/or character of interphase interaction and materials compatibility	References
C–B–Fe	Plotted at 700–1080 °C: $Fe_3(B_xC_{1-x})$ (or $Fe_3(C,B)$, $<\sim$1190–1250 °C, $0.05 \le x \le 0.90$ at 1050 °C), $Fe_{23}(B_xC_{1-x})_6$ (or $Fe_{23}(C,B)_6$, $Fe_{23}C_3B_3$, <800–965 °C), Fe_2B ($<\sim$1405 °C), FeB ($<\sim$1590 °C), Fe_3C, $B_{4\pm x}C$, α-Fe, γ-Fe, δ-Fe, β-B, C	[241–242, 244, 324–327, 391]
C–B–Fe–Ti	TiC_{1-x}–$TiB_{2\pm x}$–Fe is plotted: eutectic—1170 °C, 1 mol.% TiC_{1-x}, 7.5 mol.% $TiB_{2\pm x}$ (0.8 at.% C)	[834]
C–B–Hf	Plotted at 1400–3200 °C: $HfB_{1\pm x}$ (<2100 °C), $HfB_{2\pm x}$ ($<\sim$3250–3410 °C), HfC_{1-x}, $B_{4\pm x}C$, α-Hf, β-Hf, β-B, C Eutectic $HfB_{1\pm x}$–α-Hf–β-Hf (1850 °C) Eutectic $HfB_{2\pm x}$–$B_{4\pm x}C$–β-B (1950 °C) Eutectic $HfB_{2\pm x}$–$B_{4\pm x}C$–C ($\sim$2260–2320 °C, $\sim$6.5–9.0 at.% Hf, $\sim$25.0–28.5 at.% C) Eutectic $HfB_{2\pm x}$–HfC_{1-x}–C ($\sim$2480–2515 °C, $\sim$21–24 at.% Hf, $\sim$38.0–39.7 at.% C) $HfB_{2\pm x}$–$B_{4\pm x}C$ is plotted: eutectic—$\sim$2330–2410 °C, $\sim$68–78 mol.% $B_{4\pm x}C$ ($\sim$15.0–15.8 at.% C); the max. solid solubility of $HfB_{2\pm x}$ in $B_{4\pm x}C$ is <1 mol.% and that of $B_{4\pm x}C$ in $HfB_{2\pm x}$ is <2 mol.% (at the eutectic temp.) $HfB_{2\pm x}$–HfC_{1-x} is plotted: eutectic—$\sim$3110–3140 °C, $\sim$35 mol.% HfC_{1-x} ($\sim$16.0–16.3 at.% C); the max. solid solubility of $HfB_{2\pm x}$ in HfC_{1-x} is $\sim$10 mol.% and that of HfC_{1-x} in $HfB_{2\pm x}$ is <2 mol.% (at the eutectic temp.) $HfB_{2\pm x}$–C is plotted: eutectic—$\sim$2340–2515 °C, $\sim$24–38 mol.% $HfB_{2\pm x}$ ($\sim$35–40 at.% C); the max. solubility of C in $HfB_{2\pm x}$ is <3 at.% (at the eutectic temp.)	[138, 241–242, 244, 328–333, 573]
C–B–Hf–Si	No diagram plot The general consideration of $HfB_{2\pm x}$–SiC phase relations.	[566–567, 653]
C–B–Hf–W	No diagram plot The general consideration of $HfB_{2\pm x}$–α-WC phase relations.	[653]
C–B–Ho	Plotted at 1500 °C: HoBC, HoB_2C, HoB_2C_2, $Ho_2B_2C_3$, $Ho_3B_2C_3$, $Ho_5B_2C_6$, $Ho_5B_2C_5$, $Ho_{15}B_2C_{17}$, HoB_2 (<2200 °C), HoB_4 (<2500 °C), $HoB_{6\pm x}$ (<2180 °C), HoB_{12} (<2100 °C), HoB_{66} (<2025 °C), Ho_2C, Ho_5C_6, Ho_2C_3, HoC_2, $B_{4\pm x}C$, α-Ho, β-Ho, β-B, C No solid solutions based on binary and ternary compounds.	[241, 334, 690]
C–B–Ir–Th	No diagram plot $ThIr_2B_2C$, ?	[976]

(continued)

Table 2.14 (continued)

System	Type of phase diagram (temperature and composition sections, constituent phases or phase fields) and/or character of interphase interaction and materials compatibility	References
C–B–La	No complete diagram plot LaBC, LaB_2C_2, LaB_2C_4, $La_5B_2C_6$, (?), $La_{10}B_9C_{12}$, (?), $La_{15}B_{14}C_{19}$, (?), $La_{10}B_{5-y}C_{11-x}$, (or $La_5B_{2.1\div2.5}C_{5.1\div5.5}$, ?), $La_5B_4C_{5-x}$, ($x \approx 0.15$, ?), LaB_4 (<1800 °C), $LaB_{6\pm x}$ (<~2500–2715 °C), La_2C_{3-x}, α-LaC_2, β-$LaC_{2\pm x}$, $B_{4\pm x}C$, α-La, β-La, γ-La, β-B, C $LaB_{6\pm x}$–$B_{4\pm x}C$ is plotted: eutectic—~2220–2260 °C, ~70 mol.% $B_{4\pm x}C$ (~12.5 at.% C); mutual solubilities of the components are very low	[241–242, 244, 370, 391, 690]
C–B–La–Mo	No diagram plot $LaB_{6\pm x}$ and β-$Mo_{2\pm x}C$ are stable and compatible with each other at 1800–2100 °C	[242]
C–B–La–Si	$LaB_{6\pm x}$–SiC is plotted: eutectic—~2090–2130 °C, ~75 mol.% SiC	[568]
C–B–La–Si–W	α-W_2B_{5-x}–$LaB_{6\pm x}$–SiC is plotted: triple eutectic—~1860–1900 °C, ~45 mol.% SiC, ~10 mol.% $LaB_{6\pm x}$; virtually no mutual solubilities between the components	[570]
C–B–Lu	No diagram plot LuB_2C_2, Lu_3BC_3, LuB_2C, ?	[690]
C–B–Mn	Plotted at 800, 850 and 1000 °C: Mn_7BC_2 (?), $Mn_{23}B_3C_3$ (?), $Mn_{23}(C,B)_6$ (extended solid solution based on $Mn_{23}C_6$), $Mn_7(C,B)_3$ (extended solid solution based on Mn_7C_3), $Mn_5(C,B)_2$ (extended solid solution based on Mn_5C_2), MnB_4 (<~1380 °C), MnB_2 (~1100–1830 °C), Mn_3B_4 (<~1825 °C), MnB (<~1890 °C), Mn_2B (<~1580 °C), Mn_4B (<~1120 °C), ε-$Mn_{4\pm x}C$, $Mn_{15}C_4$, Mn_3C, $B_{4\pm x}C$, α-Mn, β-Mn, γ-Mn, δ-Mn, β-B, C	[242, 391, 969–970]
C–B–Mo	Plotted at 1300 and 1800 °C: Mo_2BC_{1-x} (<2100–2300 °C), $Mo_{2\pm x}B$ (<2280 °C), Mo_3B_2 (1920–2070 °C), α-MoB_{1-x} (<2180 °C), β-$MoB_{1\pm x}$ (~1800–2610 °C), MoB_{2-x} (~1515–2375 °C), Mo_2B_{5-x} (<2140 °C), MoB_{4-x} (or MoB_{3+x}, <~1805 °C), α-$Mo_{2+x}C$, α′-$Mo_{2+x}C$, β-$Mo_{2\pm x}C$, η-MoC_{1-x}, α-MoC_{1-x}, γ-MoC, $B_{4\pm x}C$, Mo, β-B, C Eutectic MoB_{2-x}–$B_{4\pm x}C$–C (~2250–2280 °C, ~22 at.% Mo, ~17 at.% C) Eutectic Mo_2BC_{1-x}–β-$MoB_{1\pm x}$–C (~2170–2215 °C, ~43 at.% Mo, ~30 at.% C) Eutectic Mo_2BC_{1-x}–α-MoC_{1-x}–C (~2115–2165 °C, ~48 at.% Mo, ~41 at.% C) Eutectic β-$MoB_{1\pm x}$–β-$Mo_{2\pm x}C$–Mo_2BC_{1-x} (~2260–2270 °C, ~56 at.% Mo, ~18 at.% C) Eutectic $Mo_{2\pm x}B$–β-$Mo_{2\pm x}C$–Mo (~2100–2155 °C, ~76 at.% Mo, ~10 at.% C) β-$MoB_{1\pm x}$–C is plotted: eutectic—~2300 °C, ~45 mol.% β-$MoB_{1\pm x}$ (~36 at.% C)	[138, 241–242, 244, 320, 335–337, 394, 690, 853, 877]

(continued)

Table 2.14 (continued)

System	Type of phase diagram (temperature and composition sections, constituent phases or phase fields) and/or character of interphase interaction and materials compatibility	References
	MoB_{2-x}–C is plotted: eutectic—2180 °C (?) Mo_2BC_{1-x}–C is plotted: eutectic—1825 °C (?) Mo_2B_{5-x}–C is plotted: eutectic—2175–2200 °C (?) MoB_{2-x}–$B_{4\pm x}C$ is plotted: eutectic—~30–40 mol.% $B_{4\pm x}C$ (?)	
C–B–Mo–N	No diagram plot In vacuum the interaction between metal Mo and composition of α-BN + 23 mol.% $B_{4\pm x}C$ begins from 1600 °C (in powder mixtures–from 1500 °C) and leads to the formation of $Mo_{2\pm x}B$, α-MoB_{1-x} (frontal layers) and β-$Mo_{2\pm x}C$ (inclusions); at temp. >1700 °C dense specimens weld together.	[829]
C–B–Mo–Ni	No diagram plot The intensive interaction between $B_{4\pm x}C$ and Ni–Mo alloy is observed.	[242]
C–B–Mo–Si	No diagram plot The general consideration of MoB_{2-x}–SiC phase relations.	[566–567]
C–B–N	Plotted at 1530–4030 °C: B_3CN_3 (or $B(CN)_3$, <450 °C), α-BC_xN_y ($0 \le x \le \sim 2$, BN–C substitutional solid solution, graphene/graphite-like), β-BC_xN_y ($0 \le x \le \sim 1$, BN–C substitutional solid solution, diamond-like), variety of metastable phases–B_2CN_2, BCN, BC_2N, BC_3N, $(BN)_xC_{1-x}$, $B_{1-x}C_xN$, $BC_{4-x}N$, $B_{50}(C_{1-x}N_x)_2$ and others, α-BN (or h-BN, graphene/graphite-like, <2770–3170 °C), α′-BN (or r-BN, β-graphite-like), β-BN (or c-BN, diamond-like), γ-BN (lonsdaleite-like), $B_{4\pm x}C$, β-B, N, C α-BN–C is plotted: gas-eutectic $B_{4\pm x}C$–C (2385 °C, ~30 at.% C) The interaction between graphite materials and α-BN initiates from 1900 °C and leads to the formation of $B_{4\pm x}C$ and some complex phases. The solubility limit of carbon in the α-BN is ~15 at.%. The chemical composition of nanotubular structures varies widely within the C–B–N system. The stacking of C-rich or BN-rich tubular shells in multiwalled structures can be varied as well.	[241–242, 244, 338–346, 359, 571–572, 635–638, 735, 862, 867, 878–879, 886]
C–B–N–Nb	No diagram plot In vacuum the interaction between metal Nb and composition of α-BN + 23 mol.% $B_{4\pm x}C$ begins from 1600 °C and leads to the formation of $NbB_{1\pm x}$ and $NbB_{2\pm x}$; at 1900 °C dense specimens weld together.	[829]
C–B–N–Si	Plotted at 1400 and 2000 °C: $Si_3B_{20}C_2$ (?), α-BN (or h-BN, graphene/graphite-like, <2770–3170 °C), $SiB_{3\pm x}$ (<~1270 °C), SiB_6 (<1850 °C), SiB_n (<~2020–2035 °C), α-Si_3N_4 (metastable, ?), β-Si_3N_4 (<~1800–1900 °C), $B_{4\pm x}C$, α-SiC, β-SiC, Si, β-B, N, C	[241, 244, 359, 571–572, 762]

(continued)

Table 2.14 (continued)

System	Type of phase diagram (temperature and composition sections, constituent phases or phase fields) and/or character of interphase interaction and materials compatibility	References
C–B–N–Ta	No diagram plot In vacuum the interaction between metal Ta and composition of α-BN + 23 mol.% $B_{4\pm x}C$ begins from 1600 °C and leads to the formation of $Ta_3B_{4\pm x}$ (traces of λ-$TaB_{1\pm x}$, $TaB_{2\pm x}$ and γ-$Ta_{2\pm x}N$).	[829]
C–B–N–Ti	Plotted schematically General consideration of the system.	[571]
C–B–N–W	No diagram plot In vacuum the interaction between metal W and composition of α-BN + 23 mol.% $B_{4\pm x}C$ begins from 1900 °C (in powder mixtures—from 1800 °C) and leads to the formation of $W_{2\pm x}B$ and α-$WB_{1\pm x}$ (at temp. >2100 °C).	[829]
C–B–Nb	Plotted at 1750 °C: Nb_3B_3C (<2970 °C), $Nb_4B_3C_2$ (?), $Nb_7B_6C_3$ (?), $Nb_7B_4C_4$ (?), Nb_3B_2 (<~1800–2230 °C), $NbB_{1\pm x}$ (<~2270–2915 °C), Nb_5B_6 (<~2295–2870 °C, ?), Nb_3B_4 (<~2700–2935 °C), $NbB_{2\pm x}$ (<~3000–3035 °C), α-Nb_2C, β-$Nb_{2+x}C$, γ-$Nb_{2\pm x}C$, ζ-Nb_4C_{3-x}, $Nb_6C_{5\pm x}$, NbC_{1-x}, $B_{4\pm x}C$, Nb, β-B, C Eutectic $NbB_{2\pm x}$–Nb_3B_4–Nb_3B_3C (2900 °C, ~43 at.% Nb, ~12.5 at.% C) Eutectic $NbB_{2\pm x}$–NbC_{1-x}–Nb_3B_3C (2700 °C, ~41.5 at.% Nb, ~15.5 at.% C) Eutectic $NbB_{1\pm x}$–Nb_5B_6–NbC_{1-x} (2730 °C, ~49.5 at.% Nb, ~8 at.% C) Eutectic Nb_3B_4–NbC_{1-x}–Nb_3B_3C (2340 °C, ~44.5 at.% Nb, ~12.5 at.% C) Eutectic Nb–$NbB_{1\pm x}$–β-$Nb_{2+x}C$ (2060 °C, ~75 at.% Nb, ~7 at.% C) Eutectic $NbB_{2\pm x}$–NbC_{1-x}–C (2570 °C, 28.5 at.% Nb, 31.5 at.% C) Eutectic $NbB_{2\pm x}$–$B_{4\pm x}C$–C (2245 °C, ~15 at.% Nb, ~22.5 at.% C) Nb_3B_4–Nb_3B_3C is plotted: eutectic—2940 °C, ~12–13 mol.% Nb_3B_4 (~12.5 at.% C) $NbB_{2\pm x}$–Nb_3B_3C is plotted: eutectic—2910 °C, ~16–17 mol.% $NbB_{2\pm x}$ (~13 at.% C) Nb_3B_3C–NbC_{1-x} is plotted: eutectic—2790 °C, ~3–5 mol.% NbC_{1-x} (~14.5 at.% C) $NbB_{1\pm x}$–NbC_{1-x} is plotted: eutectic—~2800 °C, ~20 mol.% NbC_{1-x} (~8.5 at.% C) Nb_3B_4–NbC_{1-x} is plotted: eutectic—2830 °C, ~50 mol.% NbC_{1-x} (~10 at.% C) $NbB_{2\pm x}$–NbC_{1-x} is plotted: eutectic—~2600–2900 °C (?), ~43–47 mol.% NbC_{1-x} (~16–18 at.% C) $NbB_{2\pm x}$–$B_{4\pm x}C$ is plotted: eutectic—~2220–2280 °C, ~60–65 mol.% $B_{4\pm x}C$ (~12–13 at.% C, ?); the max. solid solubility of $NbB_{2\pm x}$ in $B_{4\pm x}C$ is ~3 mol.% and that of	[138, 241–244, 336, 347–351, 394, 832, 877]

(continued)

Table 2.14 (continued)

System	Type of phase diagram (temperature and composition sections, constituent phases or phase fields) and/or character of interphase interaction and materials compatibility	References
	$B_{4\pm x}C$ in $NbB_{2\pm x}$ is ~2 mol.% (at the eutectic temp.) $NbB_{2\pm x}$–C is plotted: eutectic—~2360–2710 °C, ~32–40 mol.% $NbB_{2\pm x}$ (~29 at.% C) At 2200 °C in vacuum the interaction of graphite with $NbB_{1\pm x}$ results in the formation of $NbB_{2\pm x}$ and NbC_{1-x}. Some data on the system available in literature are controversial.	
C–B–Nb–Si	No diagram plot The general consideration of $NbB_{2\pm x}$–SiC phase relations.	[566–567]
C–B–Nd	No diagram plot NdB_2C_2, $Nd_5B_2C_5$, Nd_2BC, $Nd_{10}B_9C_{12}$, $Nd_5B_2C_{7+x}$ ($x \approx 0.1$), NdBC, ?	[391, 690]
C–B–Ni	Plotted at 900–1300 °C: $Ni_xB_yC_z$ (or $Ni_2B_{1-x}C_x$, $Ni_{6.6}B_{2.7}C_{0.6}$, ?), Ni_3B (<~1155 °C), Ni_2B (<1125 °C), Ni_4B_{3-x} (or *o*-Ni_4B_3, $x \approx 0.2$, <1025 °C), Ni_4B_{3+x} (or *m*-Ni_4B_3, $x \approx 0.1$, <~1030 °C), NiB (<1035 °C), $B_{4\pm x}C$, Ni, β-B, C The contact interaction between $B_{4\pm x}C$ and Ni results in the formation of multi-phase transition zone, including Ni_4B_3 phase.	[241–242, 244, 727–729]
C–B–Ni–Si	No diagram plot The intensive interaction between $B_{4\pm x}C$ and Ni-Si alloy is observed at 1450–1480 °C.	[242]
C–B–Ni–Y	Plotted at 1300 °C: $YNi_2B_{2-y}C_x$ ($x = 1$, $0 \le y \le 1$), $YNiB_{4-x}C_x$, YNiBC, $Ni_xB_yC_z$ (or $Ni_2B_{1-x}C_x$, $Ni_{6.6}B_{2.7}C_{0.6}$, ?), YNi_4B, $YNi_{12}B_6$, $YNiB_4$, $Y_2Ni_3B_6$, YNi_8B_3, Y_4NiB_{13}, $Y_3Ni_7B_2$, YNi_2C_2, $Y_5Ni_{29}C_3$, $YNiC_2$, YBC, YB_2C_2, YB_2C, Y_2BC_2, YB_2 (<~2100–2320 °C), YB_4 (<~2610–2800 °C), $YB_{6\pm x}$ (<~2600–2780 °C), YB_{12} (<2200 °C), YB_{66} (<2100 °C), Ni_3B (<~1155 °C), Ni_2B (<1125 °C), Ni_4B_{3-x} ($x \approx 0.2$, or *o*-Ni_4B_3, <1025 °C), Ni_4B_{3+x} ($x \approx 0.1$, or *m*-Ni_4B_3, <~1030 °C), NiB (<1035 °C), $Y_{2\pm x}C$, $YC_{1\pm x}$, α-Y_3C_{4-x}, β-Y_3C_{4-x}, α-Y_2C_{3-x}, β-Y_2C_{3-x}, α-YC_2, β-$YC_{2\pm x}$, $B_{4\pm x}C$, α-Y, β-Y, Ni, β-B, C At 1300 °C the complex compounds $YNiB_{4-x}C_x$ and YB_2C_2 are stable in the presence of graphite.	[241–242, 244, 728, 730]
C–B–Os–Th	No diagram plot $ThOs_2B_2C$?	[976]
C–B–Pd	No diagram plot Pd_5BC_x ($x \approx 0.2$, ?) At 1480–1500 °C the interaction between $B_{4\pm x}C$ and Pd results in the formation of Pd borides.	[242]
C–B–Pr	No diagram plot PrB_2C_2, $Pr_{10}B_9C_{12}$, Pr_2BC, $Pr_5B_2C_5$, PrBC, $Pr_{10}B_4C_{13-x}$ ($0 \le x \le 0.5$, or $Pr_5B_2C_{6.25\div6.50}$), ?	[391, 690]

(continued)

Table 2.14 (continued)

System	Type of phase diagram (temperature and composition sections, constituent phases or phase fields) and/or character of interphase interaction and materials compatibility	References
C–B–Pt	No diagram plot At 1480–1500 °C the interaction between $B_{4\pm x}C$ and Pt results in the formation of Pt borides.	[242]
C–B–Pt–Th	No diagram plot $ThPt_2B_2C$, ?	[983]
C–B–Sc	Plotted at 25 and 1700 °C: ScB_2C_2, Sc_2BC_2, Sc_4BC_4 (or $Sc_3B_{0.75}C_3$), ~Sc_2BC_3 (or $Sc_{98}B_{54}C_{157}$, $Sc_2B_{1.1}C_{3.2}$), ~$Sc_2B_{30}C_3$ (or $ScB_{15}C_{1.60}$, ?), ~$Sc_4B_{68}C$ (or $ScB_{17}C_{0.25}$, ?), ScB_2C (?), $ScB_{13}C$ (?), ScB_2 (<2250 °C), ScB_{12} (<2040 °C), ScC_{1-x}, α-Sc_4C_3, β-Sc_4C_{3+x}, Sc_3C_{4-x}, $B_{4\pm x}C$, α-Sc, β-Sc, β-B, C No solid solutions based on binary and ternary compounds.	[391, 690, 971–972]
C–B–Si	Plotted at 1130–2480 °C: SiB_nC_x ($n \approx 30$, $x = 0.35$), ~SiB_6C_9 (?), $SiB_{3\pm x}$ (<~1270 °C), SiB_6 (<1850 °C), SiB_n (<~2020–2035 °C), $B_{4\pm x}C$, SiC, Si, β-B, C Eutectic SiC–$B_{4\pm x}C$–C (~2245–2300 °C, ~62–70 mol.% $B_{4\pm x}C$, ~30 mol.% SiC, ?) Transition reaction: liquid + C (graphite) ↔ SiC + $B_{4\pm x}C$ (2295 °C, ?) SiC–$B_{4\pm x}C$ is plotted: eutectic—~2240–2300 °C (?)	[241–242, 244, 352–359, 571–572, 889–890]
C–B–Si–Ta	No diagram plot The general consideration of TaB $_{2\pm x}$–SiC phase relations.	[566–567]
C–B–Si–Ti	Plotted schematically: $Ti_5Si_3(B,C)_{1-x}$ (Nowotny phase), $Ti_5Si_{3\pm y}C_x$ ($0 \le x \le 0.99$, solid solution based on $Ti_5Si_{3\pm x}$, <~2130–2335 °C), Ti_3SiC_2 (<2375 °C, narrow homog. range at lower temp., $M_{n+1}AX_n$-phase), SiB_nC_x ($n \approx 30$, $x = 0.35$), ~SiB_6C_9 (?), $SiB_{3\pm x}$ (<~1270 °C), SiB_6 (<1850 °C), SiB_n (<~2020–2035 °C), Ti_3Si (<1170 °C), Ti_5Si_4 (<1920 °C), TiSi (<1570 °C), $TiSi_2$ (<1490–1500 °C), TiB_{1-x} (<~2180–2200 °C), Ti_3B_4 (<~2200–2205 °C), $TiB_{2\pm x}$ (<3200–3250 °C), TiC_{1-x}, $B_{4\pm x}C$, SiC, α-Ti, β-Ti, Si, β-B, C TiC_{1-x}–SiC–$TiB_{2\pm x}$ is plotted: eutectic—~2110–2190 °C, ~16–34 mol.% TiC_{1-x}, ~44–56 mol.% SiC (~32–35 at.% C) SiC–$B_{4\pm x}C$–$TiB_{2\pm x}$ is plotted: eutectic—~2200–2250 °C, ~51 mol.% $B_{4\pm x}C$, ~41 mol.% SiC (~25 at.% C) SiC–$TiB_{2\pm x}$ is plotted: eutectic—~2150–2250 °C, ~64–68 mol.% SiC (~27 at.% C)	[241–242, 244, 419, 463, 487, 503, 506–509, 566–567, 571, 640–642, 654–659, 680–681, 691, 731–734, 860, 889]
C–B–Si–V	No diagram plot The general consideration of VB_2–SiC phase relations	[566–567]

(continued)

Table 2.14 (continued)

System	Type of phase diagram (temperature and composition sections, constituent phases or phase fields) and/or character of interphase interaction and materials compatibility	References
C–B–Si–W	SiC–β-W_2B_{5-x} is plotted: eutectic—~2030–2090 °C, ~40 mol.% SiC	[566–567, 569]
C–B–Si–Zr	SiC–$ZrB_{2\pm x}$ is plotted: eutectic—2270 °C, 23 mol.% $ZrB_{2\pm x}$; the max. solid solubility of $ZrB_{2\pm x}$ in SiC is ~2.7 mol.% and that of SiC in $ZrB_{2\pm x}$ is ~3 mol.% (at the eutectic temp.) At 2000 °C SiC, $ZrB_{2\pm x}$ and $B_{4\pm x}C$ within the mol. ratios ~(20–45) : (30–70) : (10–25) are compatible with each other.	[360, 566–567, 590, 654]
C–B–Sm	No diagram plot α-SmB_2C_2, β-SmB_2C_2, $Sm_5B_2C_5$, $Sm_5B_2C_6$, SmBC, ?	[391, 690]
C–B–Ta	Plotted at 1750 °C: $Ta_{2+x}B$ (~1900–2420 °C), $Ta_3B_{2\pm x}$ (<2180 °C), λ-$TaB_{1\pm x}$ (<3090 °C), $Ta_3B_{4\pm x}$ (<3030 °C), $TaB_{2\pm x}$ (<~3040 °C), α-$Ta_{2+x}C$, β-$Ta_{2\pm x}C$, ζ-Ta_4C_{3-x}, $Ta_6C_{5\pm x}$, TaC_{1-x}, $B_{4\pm x}C$, Ta, β-B, C Eutectic $TaB_{2\pm x}$–$B_{4\pm x}C$–β-B (~2000 °C, ?) Eutectic $TaB_{2\pm x}$–$B_{4\pm x}C$–C (~2150 °C) Eutectic $TaB_{2\pm x}$–TaC_{1-x}–C (2550 °C) $TaB_{2\pm x}$–$B_{4\pm x}C$ is plotted: eutectic—~2340–2400 °C, ~67–69 mol.% $B_{4\pm x}C$ (~14.5 at.% C); the max. solid solubility of $TaB_{2\pm x}$ in $B_{4\pm x}C$ is <1 mol.% and that of $B_{4\pm x}C$ in $TaB_{2\pm x}$ is ~1 mol.% (at the eutectic temp.) $TaB_{2\pm x}$–TaC_{1-x} is plotted: eutectic—~2690–2770 °C, ~34–35 mol.% TaC_{1-x} (~12 at.% C); the max. solid solubility of $TaB_{2\pm x}$ in TaC_{1-x} is ~7 mol.% (at the eutectic temp.), the components are virtually insoluble in each other at temp. ≤2100 °C $TaB_{2\pm x}$–C is plotted: eutectic—~2390–2650 °C, ~32 mol.% $TaB_{2\pm x}$ (~40 at.% C)	[138, 241–242, 244, 349, 351, 361–365, 723, 832]
C–B–Tb	No diagram plot TbB_2C, TbB_2C_2, Tb_2B_4C, $Tb_5B_2C_5$, $Tb_5B_2C_6$, ?	[391, 690]
C–B–Th	Plotted at 900, 1300 and 1400 °C: ThB_2C, $ThBC_2$, Th_2BC_2, ThBC, Th_3BC_3, ThB_4 (<2475 °C), ThB_{6+x} (<2450 °C), ~$ThB_{66\div77}$ (<~2150 °C), $ThC_{1\pm x}$, α-ThC_{2-x}, β-ThC_{2-x}, γ-ThC_{2-x}, $B_{4\pm x}C$, α-Th, β-Th, β-B, C No mutual solid solubility between Th carbides and borides.	[138, 238, 241, 244, 391]

(continued)

Table 2.14 (continued)

System	Type of phase diagram (temperature and composition sections, constituent phases or phase fields) and/or character of interphase interaction and materials compatibility	References
C–B–Ti	Plotted at 1500–2900 °C: TiB_xC_y (?), TiB_{1-x} (<~2180–2200 °C), Ti_3B_4 (<~2200–2205 °C), $TiB_{2\pm x}$ (<3200–3250 °C), $B_{4\pm x}C$, TiC_{1-x}, α-Ti, β-Ti, β-B, C Eutectic TiB_{1-x}–TiC_{1-x} ($x \approx 0.5$)–β-Ti (~1450–1535 °C, ~91–93 at.% Ti, ~2–3 at.% C) Eutectic $TiB_{2\pm x}$–$B_{4\pm x}C$ ($x \approx 4 \div 7$, ~$B_{8 \div 11}C$)–β-B (~1990–2060 °C, ~1.5–1.9 at.% Ti, ~0.2–1.5 at.% C) Eutectic $TiB_{2\pm x}$–$B_{4\pm x}C$ ($x \approx 0$)–C (~2110–2245 °C, ~7–10 at.% Ti, ~23–28 at.% C) Eutectic $TiB_{2\pm x}$–TiC_{1-x} ($x \approx 0$)–C (~2380–2400 °C, ~26–29 at.% Ti, 37.4–38.0 at.% C) $TiB_{2\pm x}$–$B_{4\pm x}C$ ($x \approx 0$) is plotted: eutectic—~1900–2240 °C, ~58–60 mol.% $B_{4\pm x}C$ (~14 at.% C); the max. solid solubility of $TiB_{2\pm x}$ in $B_{4\pm x}C$ is ~2 mol.% and that of $B_{4\pm x}C$ in $TiB_{2\pm x}$ is ~0.5 mol.% (at the eutectic temp.) $TiB_{2\pm x}$–$B_{4\pm x}C$ ($x \approx 0.5 \div 2.0$, ~$B_{4.5 \div 6.0}C$) is plotted: eutectic—~2160–2380 °C, ~70–75 mol.% $B_{4\pm x}C$ (~11–16 at.% C); the max. solid solubility of $TiB_{2\pm x}$ in $B_{4\pm x}C$ is ~2.4–4.0 mol.% and that of $B_{4\pm x}C$ in $TiB_{2\pm x}$ is ~1.0–1.5 mol.% (at the eutectic temp.) $TiB_{2\pm x}$ ($x \approx 0$)–TiC_{1-x} ($x = 0.05$) is plotted: eutectic—~2480–2700 °C, ~54–70 mol.% TiC_{1-x} (~21–29 at.% C); the max. solid solubility of $TiB_{2\pm x}$ in TiC_{1-x} is ~2–3.5 mol.% and that of TiC_{1-x} in $TiB_{2\pm x}$ is <2 mol.% (at the eutectic temp.) $TiB_{2\pm x}$ ($x \approx 0$)–TiC_{1-x} ($x = 0.08$) is plotted: eutectic—~2600–2685 °C, ~67–70 mol.% TiC_{1-x} (~27–29 at.% C); the max. solid solubility of $TiB_{2\pm x}$ in TiC_{1-x} is ~2–5 mol.% and that of TiC_{1-x} in $TiB_{2\pm x}$ is ~2–3 mol.% (at the eutectic temp.) $TiB_{2\pm x}$ ($x \approx 0$)–TiC_{1-x} ($x = 0.20$) is plotted: eutectic—~2450–2690 °C, ~62–71 mol.% TiC_{1-x} (~22–26.5 at.% C); the max. solid solubility of $TiB_{2\pm x}$ in TiC_{1-x} is ~3–5 mol.% and that of TiC_{1-x} in $TiB_{2\pm x}$ is ~1–5 mol.% (at the eutectic temp.) $TiB_{2\pm x}$ ($x \approx 0$)–TiC_{1-x} ($x = 0.32$) is plotted: eutectic—~2380–2675 °C, ~76 mol.% TiC_{1-x} (~28–29 at.% C); the max. solid solubility of $TiB_{2\pm x}$ in TiC_{1-x} is ~5–7 mol.% and that of TiC_{1-x} in $TiB_{2\pm x}$ is ~5 mol.% (at the eutectic temp.) $TiB_{2\pm x}$–C is plotted: eutectic—~2490–2555 °C, ~39–42 mol.% $TiB_{2\pm x}$ (~32–34.5 at.% C); the max. solid solubility of C in $TiB_{2\pm x}$ is ~2–5 mol.% (at the eutectic temp.)	[138, 241–242, 244, 252, 330, 364–366, 391, 567, 571, 573, 596–599, 627, 691, 838, 889, 985]

(continued)

Table 2.14 (continued)

System	Type of phase diagram (temperature and composition sections, constituent phases or phase fields) and/or character of interphase interaction and materials compatibility	References
	At 1600 °C TiB_{1-x} is in equilibrium with TiC_{1-x} ($TiC_{0.4 \div 0.65}$), $TiB_{2\pm x}$—with TiC_{1-x} ($TiC_{0.65 \div 1.0}$) and Ti_3B_4—with $TiC_{0.65}$. In the $TiB_{2\pm x}$–TiC_{1-x} system, with increasing C content in TiC_{1-x} from $TiC_{0.6}$ to $TiC_{0.8}$, the eutectic temp. increases; and further increase in C content from $TiC_{0.8}$ to $TiC_{1.0}$ leads to the decrease of the eutectic temp. With increasing C content in TiC_{1-x}, the solubility of $TiB_{2\pm x}$ in TiC_{1-x} declines. In the wide temp. ranges, depend. on compos., graphite is in equilibrium with $TiB_{2\pm x}$ + TiC_{1-x} or $TiB_{2\pm x}$ + $B_{4\pm x}C$.	
C–B–Tm	No diagram plot TmB_2C_2, TmB_2C, $Tm_5B_2C_6$, $Tm_5B_2C_5$, $Tm_2B_{57}C_8$, ?	[690]
C–B–U	Plotted at 1300–1600 °C: $UB_{1-x}C_{1+x}$ (<2145 °C), UB_2C (<2280 °C), ~$U_5B_2C_7$, $UB_{2\pm x}$ (<2385 °C), UB_4 (<2495 °C), UB_{12} (<~2145–2235 °C), $UC_{1\pm x}$, ζ-U_2C_3, α-UC_2, β-UC_{2-x}, $B_{4\pm x}C$, U, β-B, C	[138, 241, 244, 367–368, 391, 690]
C–B–V	Plotted at 1450, 1600 and 2000 °C: $V_{1-x}B_{24}C$ ($V_{1-x}B_{25}$–$B_{25}C$ solid solution, metastable, ?), V_3B_2 (or $V_3(B_{1-x}C_x)_2$, <~1900–1915 °C), VB (<~2550–2570 °C), V_5B_6 (<~1725–2560 °C), V_3B_4 (<~2600–2615 °C), V_2B_3 (<~2610–2665 °C), $VB_{2\pm x}$ (<2700–2750 °C), α-$V_{2+x}C$, β-$V_{2\pm x}C$, β′-$V_{2+x}C$, ζ-V_4C_{3-x}, $V_6C_{5\pm x}$, $V_8C_{7\pm x}$, VC_{1-x}, $B_{4\pm x}C$, V, β-B, C $VB_{2\pm x}$–$B_{4\pm x}C$ is plotted: eutectic—~2140–2200 °C, ~52–55 mol.% $B_{4\pm x}C$ (~13 at.% C); the max. solid solubility of $VB_{2\pm x}$ in $B_{4\pm x}C$ is <1.5 mol.% and that of $B_{4\pm x}C$ in $VB_{2\pm x}$ is ~2 mol.% (at the eutectic temp.) $VB_{2\pm x}$–VC_{1-x} ($x = 0.12$) is plotted: eutectic—~2100–2140 °C, ~54 mol.% VC_{1-x} (~20 at.% C); the max. solid solubility of $VB_{2\pm x}$ in VC_{1-x} is ~8.5–10.0 mol.% and that of VC_{1-x} in $VB_{2\pm x}$ is <2 mol.% (at the eutectic temp.) $VB_{2\pm x}$–C is plotted: eutectic—2450 °C, ~30–32 mol.% $VB_{2\pm x}$ (~44 at.% C); the solubility of C in $VB_{2\pm x}$ is low Some data on the system available in literature are controversial.	[138, 241–242, 244, 349, 362, 364–365, 369, 371, 832]

(continued)

Table 2.14 (continued)

System	Type of phase diagram (temperature and composition sections, constituent phases or phase fields) and/or character of interphase interaction and materials compatibility	References
C–B–W	Plotted at 1500–2800 °C: $W_{2\pm x}B$ (<2670 °C), α-$WB_{1\pm x}$ (<2110–2170 °C), β-$WB_{1\pm x}$ (from 2110–2170 °C to 2665 °C), β-W_2B_{5-x} (~900–2365 °C), WB_{4+x} (<2020 °C), α-$W_{2+x}C$, β-$W_{2+x}C$, γ-$W_{2\pm x}C$, β-WC_{1-x}, δ-$WC_{1\pm x}$ $B_{4\pm x}C$, W, β-B, C Eutectic WB_{4+x}–$B_{4\pm x}C$–β-B (1950 °C) Eutectic $W_{2\pm x}B$–γ-$W_{2\pm x}C$–W (~2355–2385 °C, ~70.7–71.0 at.% W, ~11–12 at.% C) Eutectic $W_{2\pm x}B$–β-$WB_{1\pm x}$–γ-$W_{2\pm x}C$ (~2305–2325 °C, ~60–62 at.% W, ~14 at.% C) Eutectic β-$WB_{1\pm x}$–γ-$W_{2\pm x}C$–δ-$WC_{1\pm x}$ (~2300–2325 °C, ~55–58 at.% W, ~16–19 at.% C) Eutectic β-$WB_{1\pm x}$–α-W_2B_{5-x}–C (~2240–2260 °C, ~32–35 at.% W, ~7.4–7.9 at.% C) Eutectic α-W_2B_{5-x}–$B_{4\pm x}C$–C (2180 °C, ~18–20 at.% W, ~8–11 at.% C) $W_{2\pm x}B$–γ-$W_{2\pm x}C$ is plotted: eutectic—~2370–2390 °C, ~41 mol.% γ-$W_{2\pm x}C$ (~12.0–12.5 at.% C); the max. solid solubility of $W_{2\pm x}B$ in γ-$W_{2\pm x}C$ is ~7 mol.% and that of γ-$W_{2\pm x}C$ in $W_{2\pm x}B$ is ~3 mol.% (at the eutectic temp.) $W_{2\pm x}B$–δ-$WC_{1\pm x}$ is plotted: eutectic—2290 °C β-$WB_{1\pm x}$–γ-$W_{2\pm x}C$ is plotted: eutectic—~2325–2330 °C, ~38 mol.% γ-$W_{2\pm x}C$ (~15 at.% C); the max. solid solubility of β-$WB_{1\pm x}$ in γ-$W_{2\pm x}C$ is ~5 mol.% and that of γ-$W_{2\pm x}C$ in β-$WB_{1\pm x}$ is ~5.5 mol.% (at the eutectic temp.) α-W_2B_{5-x}–$B_{4\pm x}C$ is plotted: eutectic—~2130–2220 °C, ~76 mol.% W_2B_{5-x} (~6.0–7.2 at.% C); the max. solid solubility of α-W_2B_{5-x} in $B_{4\pm x}C$ is ~1.5 mol.% and that of $B_{4\pm x}C$ in α-W_2B_{5-x} is ~3 mol.% (at the eutectic temp.) β-$WB_{1\pm x}$–C is plotted: eutectic—~2270–2400 °C, ~77 mol.% β-$WB_{1\pm x}$ (~13–14 at.% C); the max. solubility of C in β-$WB_{1\pm x}$ is 2–3 at.% (at the eutectic temp.) α-W_2B_{5-x}–C is plotted: eutectic—~2190–2285 °C, ~63–65 mol.% α-W_2B_{5-x} (~7.0–7.6 at.% C); the max. solubility of C in α-W_2B_{5-x} is 2.0–2.5 at.% (at the eutectic temp.) At 2000 °C the interaction of graphite with $W_{2\pm x}B$ results in the formation of α-$WB_{1\pm x}$ and δ-$WC_{1\pm x}$. At 1100–1600 °C $B_{4\pm x}C$ reacts with metal W with the formation of $W_{2\pm x}B$ and α-$WB_{1\pm x}$.	[138, 241–242, 244, 320, 372–377, 394, 564–565, 912]

(continued)

Table 2.14 (continued)

System	Type of phase diagram (temperature and composition sections, constituent phases or phase fields) and/or character of interphase interaction and materials compatibility	References
C–B–Y	Plotted schematically: YBC, YB_2C_2, YB_2C, Y_2BC_2, YB_2 (<~2100–2320 °C), YB_4 (<~2610–2800 °C), $YB_{6\pm x}$ (<~2600–2780 °C), YB_{12} (<2200 °C), YB_{66} (<2100 °C), $Y_{2\pm x}C$, $YC_{1\pm x}$, α-Y_3C_{4-x}, β-Y_3C_{4-x}, α-Y_2C_{3-x}, β-Y_2C_{3-x}, α-YC_2, β-$YC_{2\pm x}$, $B_{4\pm x}C$, α-Y, β-Y, β-B, C	[241, 244, 391, 690, 728]
C–B–Yb	No diagram plot YbB_2C, YbB_2C_2, ?	[391, 690]
C–B–Zr	Plotted at 1400–3000 °C: $ZrB_{2\pm x}$ (<3220–3265 °C), ZrB_{12-x} (~1695–2290 °C), ZrC_{1-x}, $B_{4\pm x}C$, α-Zr, β-Zr, β-B, C Eutectic $ZrB_{2\pm x}$–ZrC_{1-x}–β-Zr (~1615–1650 °C, ~86–88 at.% Zr, ~1.4–2.0 at.% C) Eutectic ZrB_{12-x}–$B_{4\pm x}C$–β-B (~1990 °C) Eutectic $ZrB_{2\pm x}$–$B_{4\pm x}C$–C (~2165–2190 °C, ~11 at.% Zr, ~23–25 at.% C) Eutectic $ZrB_{2\pm x}$–ZrC_{1-x}–C (2360 °C) $ZrB_{2\pm x}$–$B_{4\pm x}C$ is plotted: eutectic—~2200–2300 °C, ~65–75 mol.% $B_{4\pm x}C$ (~13–16 at.% C); the max. solid solubility of $ZrB_{2\pm x}$ in $B_{4\pm x}C$ is ~1 mol.% and $B_{4\pm x}C$ in $ZrB_{2\pm x}$ is ~1.5 mol.% (at the eutectic temp.) $ZrB_{2\pm x}$ ($x \approx 0$)–ZrC_{1-x} ($x = 0.03 \div 0.12$) is plotted: eutectic—~2620–2850 °C, ~42–43 mol.% ZrC_{1-x} (~19–20 at.% C); the max. solid solubility of $ZrB_{2\pm x}$ in ZrC_{1-x} is ~1–5 mol.% and that of ZrC_{1-x} in $ZrB_{2\pm x}$ is <2 mol.% (at the eutectic temp.); some data on this quasibinary system available in literature are controversial $ZrB_{2\pm x}$–C is plotted: eutectic—~2230–2390 °C, ~40 mol.% $ZrB_{2\pm x}$ (~33 at.% C); the max. solubility of C in $ZrB_{2\pm x}$ is ≤2 at.% C (at the eutectic temp.)	[138, 241–242, 244, 252, 330, 364–365, 378–381, 391, 394, 567, 573–574]
C–Be–O	No diagram plot In vacuum (~10^{-2}–10^{-4} Pa), the interaction in powdered mixtures between C and BeO with the formation of Be_2C initiates from 1300–1315 °C and that on bulk materials contacts—from 2000–2300 °C. In air, heating the powdered mixture BeO + C at 1800–1900 °C results in the reduction of BeO with the subsequent secondary oxidation of Be_2C and Be vapour.	[138, 194, 382]
C–Be–O–Th	No diagram plot At temp. ≥1100 °C BeO and $ThC_{1\pm x}$ interact with the formation of ThO_{2-x}.	[242]
C–Be–O–Ti	No diagram plot At 1500–2200 °C BeO and TiC_{1-x} interact with the formation of Be_2C.	[242]
C–Be–O–U	No diagram plot At 1600–2000 °C BeO and $UC_{1\pm x}$ interact with the formation of Be_2C and intermetallic compounds.	[592]

(continued)

Table 2.14 (continued)

System	Type of phase diagram (temperature and composition sections, constituent phases or phase fields) and/or character of interphase interaction and materials compatibility	References
C–Be–Si	Plotted schematically at 1000 °C: Be_2C, α-SiC, Be, Si, C Graphite is in equilibrium with Be_2C + SiC. In vacuum at 1000–1150 °C SiC interacts with Be negligibly; at higher temp. the interaction leads to the formation of Be_2C and Si.	[242, 814]
C–Be–Ta	No diagram plot $Be_xTaC_{0.76}$, ? At 1400–2800 °C the addition of Be (1 %) does not affect the densification process of TaC_{1-x} powder by hot pressing.	[138]
C–Be–Th	Plotted at 1000 °C: no ternary compounds, $ThBe_{13}$ (<~1930 °C), $ThC_{1\pm x}$, α-ThC_{2-x}, β-ThC_{2-x}, γ-ThC_{2-x}, Be_2C, BeC_2, α-Th, β-Th, α-Be, β-Be, C No solid solutions based on binary compounds.	[244, 973]
C–Be–U	Plotted at 1000 °C: no ternary compounds, UBe_{13} (<~1980 °C), $UC_{1\pm x}$, ζ-U_2C_3, α-UC_{2-x}, β-UC_{2-x}, Be_2C, BeC_2, α-U, β-U, γ-U, α-Be, β-Be, C No solid solutions based on binary compounds. α-UC_{2-x}–$UC_{1\pm x}$–Be_2C is plotted at 1700 °C: $UC_{1\pm x}$ (solid solution), ζ-U_2C_3, α-UC_{2-x} (solid solution), Be_2C	[242, 244, 383, 973]
C–Bi–Pb	No diagram plot The corrosion resistance of graphite in liquid eutectic alloy Bi–Pb in the wide range of temp. is very high: no corrosion/erosion in dynamic conditions (4 m/s) testing at 1095 °C for 24 h.	[138]
C–Ca–O	Plotted at 25 °C: $CaCO_3$, CaO (<2565–2585 °C), α-CaC_2, β-CaC_2, γ-CaC_2, δ-CaC_2, $CaC_{6\pm x}$, α-Ca, β-Ca, O, C The interaction between C and CaO in powdered mixtures initiates in vacuum from 1300 °C and under atmospheric pressure—from 2130 °C.	[194, 382, 974]
C–Ca–O–U	No diagram plot At 1900 °C the interaction between β-UC_{2-x} and CaO is weak.	[242]
C–Cd–Ti	No diagram plot Ti_2CdC ($M_{n+1}AX_n$-phase)	[680–681, 744–745, 860]
C–Ce–Ir	Plotted partially at 1100–1400 °C: Ce_4Ir (<710 °C), Ce_3Ir (<~880–950 °C), Ce_7Ir_3 (<950 °C), Ce_2Ir (or Ce_3Ir_2 (?), <1100 °C), Ce_5Ir_3 (<1100 °C), Ce_5Ir_4 (or $Ce_{15}Ir_{13}$ (?), <1180 °C), $CeIr_{2\pm x}$ (<2250 °C), $CeIr_3$ (<2105–2120 °C), Ce_2Ir_7 (<2000 °C), $CeIr_5$ (<1955–1960 °C), Ce_2C_3, α-CeC_2, β-$CeC_{2\pm x}$, α-Ce, β-Ce, γ-Ce, δ-Ce, Ir, C Depend. on compos., graphite is in equilibrium with $CeIr_5$ + Ir, or $CeIr_5$ + $CeIr_{2\pm x}$, or $CeIr_{2\pm x}$ + β-$CeC_{2\pm x}$.	[990]
C–Ce–Mo	Plotted at 1600 °C: Ce_2C_3, β-$CeC_{2\pm x}$, β-$Mo_{2\pm x}C$, α-Ce, β-Ce, γ-Ce, δ-Ce, Mo, C No solubility between Ce and Mo carbides	[391]

(continued)

Table 2.14 (continued)

System	Type of phase diagram (temperature and composition sections, constituent phases or phase fields) and/or character of interphase interaction and materials compatibility	References
C–Ce–N–Th	No diagram plot $ThC_{1\pm x}$–$CeN_{1\pm x}$ carbonitride continuous solid solution	[391]
C–Ce–N–U	No diagram plot $UC_{1\pm x}$–$CeN_{1\pm x}$ carbonitride continuous solid solution	[391]
C–Ce–Si	Plotted at 400 °C: Ce_3SiC, $Ce_3Si_2C_2$ (?), $(Ce_3Si_2)C_x$ (interstitial solid solution based on Ce_3Si_2—up to ~12–14.5 at.% C, <~1390 °C), $CeSi_{2-x}$ (<1620 °C), Ce_3Si_5 (<~1560 °C), CeSi (<1470 °C), Ce_5Si_4 (<~1440 °C), Ce_5Si_3 (<~1400 °C), CeC, Ce_2C_3, α-CeC_2, β-$CeC_{2\pm x}$, β-SiC, α-Ce, β-Ce, γ-Ce, δ-Ce, Si, C No solid solutions based on binary and ternary compounds apart from Ce_3Si_2.	[628]
C–Ce–Th	Plotted at 1600 °C: $(Th,Ce)C_{1-x}$ (monocarbide solid solution based on ThC_{1-x}—up to 40 mol.% 'CeC'), $(Ce,Th)_2C_3$ (solid solution based on Ce_2C_3), $(Th,Ce)C_{2\pm x}$ (γ-ThC_{2-x}–β-$CeC_{2\pm x}$ dicarbide continuous solid solution), α-Ce, β-Ce, γ-Ce, δ-Ce, α-Th, β-Th, C	[391]
C–Ce–U	Plotted at 1600 °C: $(U,Ce)C_{1\pm x}$ (monocarbide solid solution based on $UC_{1\pm x}$—up to 15 mol.% 'CeC'), ζ-U_2C_3, Ce_2C_3, $(U,Ce)C_{2\pm x}$ (α-UC_{2-x}–β-$CeC_{2\pm x}$ dicarbide continuous solid solution), α-Ce, β-Ce, γ-Ce, δ-Ce, α-U, β-U, γ-U, C	[391]
C–Ce–U–Zr	No diagram plot The solubility of 'CeC' in $(U,Zr,Ce)C_{1-x}$ decreases sharply with increasing concentration of Zr	[391]
C–Ce–Zr	Plotted at 1600 °C: ZrC_{1-x}, Ce_2C_3, α-CeC_2, β-$CeC_{2\pm x}$, α-Ce, β-Ce, γ-Ce, δ-Ce, α-Zr, β-Zr, C No solubility between Ce and Zr carbides.	[391]
C–Co–Fe–Ni–W	Plotted partially General consideration of the system	[757]
C–Co–Hf	Plotted at 1100 °C: $Hf_{2+x}Co$ (<1315 °C), $HfCo_{1\pm x}$ (<1640 °C), $HfCo_{2\pm x}$ (<1670 °C), Hf_2Co_7 (or $HfCo_4$, <1350 °C), Hf_6Co_{23} (~950–1280 °C), $HfCo_7$ (~1050–1250 °C), HfC_{1-x}, α-Hf, β-Hf, α-Co, C HfC_{1-x}–Co is plotted: eutectic—1370 °C, ~3 mol.% HfC_{1-x} HfC_{1-x} is in equilibrium with Co and series of Co-Hf intermetallides.	[242, 244, 391, 417]
C–Co–Hf–Nb	HfC_{1-x} ($x = 0.06$)–NbC_{1-x} ($x = 0.18$)–Co is plotted The eutectic equilibrium between two solid solutions based on HfC_{1-x}–NbC_{1-x} monocarbide continuous solid solution and metal Co at 1360–1435 °C.	[621]
C–Co–Hf–Ta	HfC_{1-x} ($x = 0.06$)–TaC_{1-x} ($x = 0.08$)–Co is plotted The eutectic equilibrium between two solid solutions based on HfC_{1-x}–TaC_{1-x} monocarbide continuous solid solution and metal Co at 1420–1445 °C.	[621]

(continued)

Table 2.14 (continued)

System	Type of phase diagram (temperature and composition sections, constituent phases or phase fields) and/or character of interphase interaction and materials compatibility	References
C–Co–Hf–Ti	HfC_{1-x} ($x = 0.06$)–TiC_{1-x} ($x = 0.20$)–Co is plotted There are three binary and one ternary (1370 °C, 3.5 mol.% HfC_{1-x}, 5.5 mol.% TiC_{1-x}) eutectics in the system.	[622]
C–Co–Hf–V	HfC_{1-x} ($x = 0.06$)–VC_{1-x} ($x = 0.17$)–Co is plotted There are three binary and one ternary (1320 °C, 3.5 mol.% HfC_{1-x}, 10.0 mol.% VC_{1-x}) eutectics in the system.	[622]
C–Co–Hf–Zr	HfC_{1-x} ($x = 0.06$)–ZrC_{1-x} ($x = 0.19$)–Co is plotted The eutectic equilibrium between two solid solutions based on HfC_{1-x}–ZrC_{1-x} monocarbide continuous solid solution and metal Co at 1380–1435 °C.	[621]
C–Co–Mo	Plotted at 1000 °C: ~$Mo_{3\div4}Co_{2\div3}C$ (or η_2, η_1-Mo_3Co_3C), η_1-Mo_6Co_6C, σ-Mo_3Co_{2-x} (~1000–1620 °C), μ-$Mo_6Co_{7\pm x}$ (or μ-$MoCo_{1+x}$, ε-$MoCo_{1+x}$, <~1510 °C), κ-$MoCo_{3\pm x}$ (<1025 °C), θ-Mo_2Co_{9-x} (~1015–1200 °C), α-$Mo_{2+x}C$, Mo, α-Co, C	[242, 244, 391, 417]
C–Co–Nb	Plotted at 1100 °C: η-Co_2Nb_4C, Co_3Nb_3C (?), μ-$CoNb_{1\pm x}$ (or μ-$Co_7Nb_{6\pm x}$, <~1400–1480 °C), λ_1-Co_5Nb_{3-x} (1200–1420 °C), $\lambda_2(\beta)$-$Co_{2\pm x}Nb$ (<~1480–1520 °C), λ_3-Co_3Nb (from 1030 °C to 1240–1250 °C), χ-$Co_7Nb_{2\pm x}$ (<1050 °C), α-Nb_2C, β-$Nb_{2+x}C$, NbC_{1-x}, Nb, α-Co, ε-Co, C NbC_{1-x}–Co is plotted: eutectic—~1360–1380 °C, ~5 mol.% NbC_{1-x}; the max. solubility of NbC_{1-x} in Co is ~1.5 mol.% and that of Co in NbC_{1-x} is 8 mol.% (at the eutectic temp.)	[242, 244, 384–385, 391, 417]
C–Co–Nb–Ta	NbC_{1-x} ($x = 0.18$)–TaC_{1-x} ($x = 0.18$)–Co is plotted The eutectic equilibrium between two solid solutions based on NbC_{1-x}–TaC_{1-x} monocarbide continuous solid solution and metal Co at 1410–1445 °C.	[621]
C–Co–Nb–Ta–Ti–W	General consideration of the system.	[1023]
C–Co–Nb–Ti	NbC_{1-x} ($x = 0.10$)–TiC_{1-x} ($x = 0.14$)–Co is plotted The eutectic equilibrium between two solid solutions based on NbC_{1-x}–TiC_{1-x} monocarbide continuous solid solution and metal Co at 1390–1410 °C.	[621]
C–Co–Nb–V	NbC_{1-x}–VC_{1-x}–Co is plotted schematically and partially at 1100 °C: $(Nb,V)C_{1-x}$ (monocarbide solid solution based on NbC_{1-x}), $(V,Nb)C_{1-x}$ (monocarbide solid solution based on VC_{1-x}), Co Eutectic $(Nb,V)C_{1-x}$–$(V,Nb)C_{1-x}$–Co (~1310–1350 °C, 2 mol.% NbC_{1-x}, 11 mol.% VC_{1-x}) NbC_{1-x} ($x = 0.18$)–VC_{1-x} ($x = 0.12$)–Co is plotted: eutectic—1330 °C, 3.0 mol.% NbC_{1-x}, 10.5 mol.% VC_{1-x} In total, there are three binary and one ternary eutectics in the system.	[385–386, 622]

(continued)

Table 2.14 (continued)

System	Type of phase diagram (temperature and composition sections, constituent phases or phase fields) and/or character of interphase interaction and materials compatibility	References
C–Co–Nb–W	General consideration of the system.	[1023]
C–Co–Nb–Zr	NbC_{1-x} ($x = 0.18$)–ZrC_{1-x} ($x = 0.19$)–Co is plotted The eutectic equilibrium between two solid solutions based on NbC_{1-x}–ZrC_{1-x} monocarbide continuous solid solution and metal Co at 1380–1410 °C.	[621]
C–Co–Ni–W	No diagram plot Some phase fields are considered.	[755, 848]
C–Co–Os–W	No diagram plot Os promotes α-Co → ε-Co transformation in the WC–Co system.	[856]
C–Co–Re–W	No diagram plot Re promotes α-Co → ε-Co transformation in the WC–Co system.	[856]
C–Co–Ru–W	No diagram plot Ru promotes α-Co → ε-Co transformation in the WC–Co system.	[856]
C–Co–Si	Plotted at 1000, 1100 and 1500 °C: Co_3Si (~1170–1215 °C), α-$Co_{2\pm x}Si$ (<1320 °C), β-$Co_{2-x}Si$ (~1240–1335 °C), $CoSi_{1\pm x}$ (<1460 °C), $CoSi_2$ (<~1325 °C), SiC, ε-Co, α-Co, Si, C In vacuum, the contact melting between SiC and Co is observed at 1150–1160 °C. At 1500 °C $CoSi_2$ reacts with C to form $CoSi_{1\pm x}$ and SiC. $CoSi_{1\pm x}$ and β-$Co_{2-x}Si$ are more stable in equilibrium with C.	[242, 244, 417, 503, 645]
C–Co–Ta	Plotted at 1100 °C: η-Ta_4Co_2C, λ_3-$Co_{3-x}Ta$ (or $Co_{2.7}Ta$, $Co_{2.2}Ta_{0.8}$, <1450 °C), λ_2-$Co_{2\pm x}Ta$ (<1595–1650 °C), λ_1-Co_3Ta_{2-x} (from 1110–1150 °C to 1540 °C), μ-$CoTa_{1\pm x}$ (or μ-$Co_7Ta_{6\pm x}$, <1700 °C), $CoTa_2$ (<1800 °C), α-$Ta_{2+x}C$, β-$Ta_{2\pm x}C$, ζ-Ta_4C_{3-x}, $Ta_6C_{5\pm x}$, TaC_{1-x}, Ta, α-Co, C TaC_{1-x}–Co is plotted: eutectic—~1340–1370 °C, ~3 mol.% TaC_{1-x} TaC_{1-x} is in equilibrium with Co and λ_2-$Co_{2\pm x}Ta$.	[242, 244, 391, 417]
C–Co–Ta–Ti	TaC_{1-x} ($x = 0.18$)–TiC_{1-x} ($x = 0.20$)–Co is plotted The eutectic equilibrium between two solid solutions based on TaC_{1-x}–TiC_{1-x} monocarbide continuous solid solution and metal Co at 1390–1445 °C.	[621]
C–Co–Ta–V	TaC_{1-x} ($x = 0.18$)–VC_{1-x} ($x = 0.17$)–Co is plotted There are three binary and one ternary (1320 °C, 4.0 mol.% TaC_{1-x}, 7.0 mol.% VC_{1-x}) eutectics in the system.	[622]
C–Co–Ta–W	General consideration of the system.	[1023]

(continued)

Table 2.14 (continued)

System	Type of phase diagram (temperature and composition sections, constituent phases or phase fields) and/or character of interphase interaction and materials compatibility	References
C–Co–Ta–Zr	TaC_{1-x} ($x = 0.18$)–ZrC_{1-x} ($x = 0.19$)–Co is plotted There are three binary and one ternary (1250 °C, 3.0 mol.% TaC_{1-x}, 5.0 mol.% ZrC_{1-x}) eutectics in the system.	[622]
C–Co–Ti	Plotted at 1000 and 1100 °C: $Ti_{2\pm x}Co$ (<~1060 °C), $TiCo_{1\pm x}$ (<1325 °C), α-$TiCo_{2\pm x}$ (or *c*-$TiCo_{2\pm x}$, <1235 °C), *β*-$TiCo_{2+x}$ (or *h*-$TiCo_{2+x}$, <~1210–1220 °C), $TiCo_{3\pm x}$ (<1190 °C), TiC_{1-x}, *β*-Ti, α-Co, C TiC_{1-x}–Co is plotted: eutectic—~1360–1400 °C, ~6 mol.% TiC_{1-x} At 1230–1360 °C the solubility of TiC_{1-x} in Co is ~1 mol.%; TiC_{1-x} is in equilibrium with Co, $TiCo_{1\pm x}$, α-$TiCo_{2\pm x}$ and Ti-Co melt.	[242, 244, 391, 417, 609, 1009]
C–Co–Ti–V	TiC_{1-x} ($x = 0.20$)–VC_{1-x} ($x = 0.17$)–Co is plotted The eutectic equilibrium between two solid solutions based on TiC_{1-x}–VC_{1-x} monocarbide continuous solid solution and metal Co at 1330–1390 °C.	[621]
C–Co–Ti–W	No diagram plot Some phase fields are considered.	[848, 1023]
C–Co–Ti–Zr	TiC_{1-x} ($x = 0.20$)–ZrC_{1-x} ($x = 0.19$)–Co is plotted There are three binary and one ternary (1320 °C, 5.0 mol.% TiC_{1-x}, 5.0 mol.% ZrC_{1-x}) eutectics in the system.	[622]
C–Co–U	No diagram plot $UCoC_2$, ?	[391]
C–Co–V	Plotted at 1100 °C: *η*-V_4Co_2C, V_3Co (<~1025 °C), *σ*-$VCo_{1\pm x}$ (<~1420 °C), $VCo_{3\pm x}$ (<~1070 °C), α-$V_{2+x}C$, *β*-$V_{2\pm x}C$, *β′*-$V_{2+x}C$, *ζ*-V_4C_{3-x}, $V_6C_{5\pm x}$, $V_8C_{7\pm x}$, VC_{1-x}, α-(Co,V), (V,Co), C VC_{1-x}–Co is plotted: eutectic—~1320–1360 °C, ~14–16 mol.% VC_{1-x}; the max. solubility of VC_{1-x} in Co is ~5–11 mol.% and that of Co in VC_{1-x} is 3 mol.% (at the eutectic temp.) VC_{1-x} is in equilibrium with α-(Co,V) and *σ*-$VCo_{1\pm x}$.	[242, 244, 385–386, 391, 417]
C–Co–V–Zr	ZrC_{1-x} ($x = 0.19$)–VC_{1-x} ($x = 0.17$)–Co is plotted There are three binary and one ternary (1300 °C, 4.0 mol.% ZrC_{1-x}, 9.0 mol.% VC_{1-x}) eutectics in the system.	[622]

(continued)

Table 2.14 (continued)

System	Type of phase diagram (temperature and composition sections, constituent phases or phase fields) and/or character of interphase interaction and materials compatibility	References
C–Co–W	Plotted at 1000–1500 °C: η_1-$(Co,W)_{12}C$, (or $Co_{6-x}W_{6+x}C$, $x \approx 0 \div 0.1$, $<\sim$1730 °C), η_2-$(Co,W)_6C$ (or $Co_{2+x}W_{4-x}C$, $Co_{3+x}W_{3-x}C$, $x \approx 0 \div 0.2$, $<\sim$1965 °C), κ-$(Co,W)_4C$ (or CoW_3C, or $Co_3W_9C_4$, metastable), κ-$Co_{3\pm x}W$ ($<\sim$1090–1100 °C), μ-$Co_7W_{6\pm x}$ ($<\sim$1690 °C), α-$W_{2+x}C$, β-$W_{2+x}C$, γ-$W_{2\pm x}C$, γ-WC_{1-x}, δ-$WC_{1\pm x}$, α-Co, W, C Eutectic δ-$WC_{1\pm x}$–α-Co–C ($\sim$1300 °C, 4.6 at.% W, 11.5 at.% C) Eutectic δ-$WC_{1\pm x}$–α-Co–$Co_{2+x}W_{4-x}C$ (1325 °C) δ-$WC_{1\pm x}$–Co is plotted: eutectic—$\sim$1290–1340 °C, $\sim$19.5 mol.% δ-$WC_{1\pm x}$; the max. solid solubility of δ-$WC_{1\pm x}$ in Co is 7–10 mol.% (at the eutectic temp.); the solubility of Co in δ-$WC_{1\pm x}$ is very low.	[242, 244, 387–391, 417, 513, 755, 786, 796–800]
C–Co–Zr	Plotted at 800, 1200 and 1400 °C: $Zr_{3\pm x}Co$ ($<\sim$980 °C), η-Zr_2Co ($<\sim$1090–1100 °C), ζ-ZrCo ($<\sim$1370–1400 °C), ε-$ZrCo_{2\pm x}$ (or λ_2-$ZrCo_{2\pm x}$, $<\sim$1560–1590 °C), δ-$ZrCo_4$ (or Zr_6Co_{23}, $<\sim$1350–1450 °C), γ-Zr_2Co_{11} (or Zr_5Co_{28}, ($<\sim$1270 °C), ZrC_{1-x}, β-Zr, α-Co, C ZrC_{1-x}–Co is plotted: eutectic—1360 °C, $\sim$4–5 mol.% ZrC_{1-x} The mutual solubilities between the components of the system are low; ZrC_{1-x} is in equilibrium with Co and series of Co–Zr intermetallides.	[138, 242, 244, 391, 417, 547]
C–Cr–Fe–Mo	Plotted partially at 1000 °C	[842]
C–Cr–Fe–Ti	No diagram plot TiC interacts with Fe–Cr alloy intensively.	[242]
C–Cr–Fe–V	Plotted partially at 700–1150 °C	[841, 843]
C–Cr–Fe–W	Plotted partially at 700, 1000 and 1150 °C	[841]
C–Cr–Hf	Plotted at 1350 °C: λ_2-$HfCr_{2\pm x}$ ($<\sim$1335–1420 °C), λ_1-$HfCr_{2\pm x}$ (from $\sim$1335–1420 °C to 1825 °C), $Cr_{23}C_{6\pm x}$, $Cr_7C_{3\pm x}$, Cr_3C_{2-x}, HfC_{1-x}, α-Hf, β-Hf, Cr, C HfC_{1-x}–Cr is plotted: eutectic—1810 °C, $\sim$13 mol.% HfC_{1-x} The max. solubility of Cr in HfC_{1-x} is corresp. to compos. $(Hf_{0.91}Cr_{0.09})C_{1-x}$. The mutual solubilities of other constituent binary phases in the system are low too.	[242, 244, 391, 417, 583, 603]
C–Cr–Ir	No diagram plot $\sim Cr_2Ir_2C$ (at least at $\sim$1500 °C)	[391, 583]

(continued)

Table 2.14 (continued)

System	Type of phase diagram (temperature and composition sections, constituent phases or phase fields) and/or character of interphase interaction and materials compatibility	References
C–Cr–Mo	Plotted at 1000–1800 °C: ζ-$(Mo_yCr_z)_4C_{3-x}$ ($y/z \approx 3$, at least at 1650–2290 °C, ?), β-$(Mo,Cr)_{2\pm x}C$ (semicarbide extended solid solution based on β-$Mo_{2\pm x}C$ with max. solubility of "imaginary" phase '$Cr_{2\pm x}C$'—up to ~60–90 mol.%.), $(Cr,Mo)_{23}C_{6\pm x}$ (extended solid solution based on $Cr_{23}C_{6\pm x}$ with max. solubility of "imaginary" phase '$Mo_{23}C_{6\pm x}$'—up to ~20 mol.%), α-$(Mo,Cr)C_{1-x}$ (extended solid solution based on α-MoC_{1-x}—up to ~$(Mo_{0.3}Cr_{0.7})C_{1-x}$) at higher temp.), η-$(Mo,Cr)C_{1-x}$ (extended solid solution based on η-MoC_{1-x} with max. solubility of Cr—up to 30 at.% at 2005–2035 °C), $Cr_7C_{3\pm x}$ (max. solubility of Mo–5.0 at.% at 1350 °C and 6.3 at.% at 1515 °C), Cr_3C_{2-x} (no solubility of Mo at 1350 °C and max. solubility of Mo–10.4 at.% at 1810 °C), (Mo,Cr), C Eutectic β-$(Mo,Cr)_{2\pm x}C$–$Cr_7C_{3\pm x}$ (~1740 °C, 62 at.% Cr, 31 at.% C) Eutectic β-$(Mo,Cr)_{2\pm x}C$–$Cr_7C_{3\pm x}$–Cr_3C_{2-x} (~1685–1710 °C, 63 at.% Cr, 32.5 at.% C) Eutectic β-$(Mo,Cr)_{2\pm x}C$–(Mo,Cr)–$(Cr,Mo)_{23}C_{6\pm x}$ (~1500–1515 °C, 55.5 at.% Cr, 19 at.% C) Eutectic β-$(Mo,Cr)_{2\pm x}C$–α-$(Mo,Cr)C_{1-x}$–η-$(Mo,Cr)C_{1-x}$ (~2020 °C) Eutectic β-$(Mo,Cr)_{2\pm x}C$–α-$(Mo,Cr)C_{1-x}$–Cr_3C_{2-x} (~1800 °C) Eutectic β-$(Mo,Cr)_{2\pm x}C$–$(Cr,Mo)_{23}C_{6\pm x}$–$Cr_7C_{3\pm x}$ (~1540 °C) Eutectic α-$(Mo,Cr)C_{1-x}$–Cr_3C_{2-x}–C (~1840 °C) Depend. on compos., graphite is in equilibrium: at 1300 °C—with β-$(Mo,Cr)_{2\pm x}C$, β-$(Mo,Cr)_{2\pm x}C$ + Cr_3C_{2-x} and Cr_3C_{2-x}; at 1800 °C—with η-$(Mo,Cr)C_{1-x}$, η-$(Mo,Cr)C_{1-x}$ + α-$(Mo,Cr)C_{1-x}$, α-$(Mo,Cr)C_{1-x}$, α-$(Mo,Cr)C_{1-x}$ + ζ-$(Mo_yCr_z)_4C_{3-x}$ and Cr_3C_{2-x}. Practically, at 1800–2000 °C Mo is compatible with $Cr_7C_{3\pm x}$.	[138, 242, 244, 391, 402–403, 417, 580–583, 603, 794–795, 837, 842]
C–Cr–Mo–Re–Ti	No diagram plot General consideration of the system	[852]
C–Cr–Mo–Ti	Plotted partially Eutectic (Mo,Cr)–TiC_{1-x} (~1630 °C, ~4–8 at.% Mo)	[852]

(continued)

Table 2.14 (continued)

System	Type of phase diagram (temperature and composition sections, constituent phases or phase fields) and/or character of interphase interaction and materials compatibility	References
C–Cr–Nb	Plotted at 1050–1750 °C: $(Nb,Cr)C_{1-x}$ (monocarbide extended solid solution based on NbC_{1-x}—up to $(Nb_{0.72\div0.74}Cr_{0.26\div0.28})C_{1-x}$), λ_2-$NbCr_{2\pm x}$ (<1585–1625 °C), λ_1-$NbCr_{2\pm x}$ (from 1585–1625 °C to ~1670–1820 °C), $Cr_{23}C_{6\pm x}$, $Cr_7C_{3\pm x}$, Cr_3C_{2-x}, α-Nb_2C, β-$Nb_{2+x}C$ (solubility of C at 1050 °C is 6 at.% Cr), γ-$Nb_{2\pm x}C$, ζ-Nb_4C_{3-x}, $Nb_6C_{5\pm x}$, Nb, Cr, C Eutectic β-$Nb_{2+x}C$–λ_1-$NbCr_{2\pm x}$–Nb (~1660–1665 °C) Eutectic $(Nb,Cr)C_{1-x}$–β-$Nb_{2+x}C$–λ_1-$NbCr_{2\pm x}$ (~1670–1690 °C) Eutectic $(Nb,Cr)C_{1-x}$–λ_1-$NbCr_{2\pm x}$–Cr (~1610–1630 °C) Eutectic $(Nb,Cr)C_{1-x}$–$Cr_{23}C_{6\pm x}$–Cr (~1540–1560 °C) Eutectic $(Nb,Cr)C_{1-x}$–$Cr_7C_{3\pm x}$–$Cr_{23}C_{6\pm x}$ (~1565–1595 °C) Eutectic $(Nb,Cr)C_{1-x}$–Cr_3C_{2-x}–$Cr_7C_{3\pm x}$ (~1650–1680 °C) Eutectic $(Nb,Cr)C_{1-x}$–Cr_3C_{2-x}–C (~1740 °C) NbC_{1-x}–Cr is plotted: eutectic—1640 °C; the solubility of Cr in NbC_{1-x} is ~3–9 mol.% and that of NbC_{1-x} in Cr is ~2 mol.% NbC_{1-x}–(Cr_yNb_z) is plotted ($x \approx 0.1\div0.2$, $y \approx 0.98$, $z \approx 0.02$): eutectic—≥ 1640 °C, ~12 mol.% NbC_{1-x} (12.2 at.% Nb, 8.3 at.% C) NbC_{1-x}–λ_1-$NbCr_{2\pm x}$ is plotted: eutectic—~1690–1695 °C; the max. solubility of λ_1-$NbCr_{2\pm x}$ in NbC_{1-x} is corresp. to compos. $(Nb_{0.98}Cr_{0.02})C_{1-x}$ and that of NbC_{1-x} in λ_1-$NbCr_{2\pm x}$ is corresp. to ~0.8 at.% C NbC_{1-x}–$Cr_7C_{3\pm x}$ is plotted: eutectic—~1685 °C; the max. solubility of $Cr_7C_{3\pm x}$ in NbC_{1-x} is corresp. to compos. $(Nb_{0.90}Cr_{0.10})C_{1-x}$ and that of NbC_{1-x} in $Cr_7C_{3\pm x}$—to compos. $(Cr_{0.99}Nb_{0.01})_7C_{3\pm x}$ The solubility of Nb in Cr carbides is low. Depend. on compos., graphite is in equilibrium with one $(Nb,Cr)C_{1-x}$, or two carbide $(Nb,Cr)C_{1-x}$ + Cr_3C_{2-x} phases. Some data on the mutual solubilities of the compounds available in literature are controversial.	[242, 244, 391, 417, 581–583, 603, 663, 784, 837, 858]
C–Cr–O–W	No diagram plot. At 1300 °C, in vacuum δ-$WC_{1\pm x}$ interacts with Cr_2O_3 in powder mixtures intensively; W–Cr alloy is formed (100 % reduction time–30 min.).	[242, 808]
C–Cr–O–Zr	No diagram plot At 1300–1800 °C, in vacuum the interaction between Cr_3C_{2-x} and ZrO_{2-x} led to the formation of $Cr_7C_{3\pm x}$ and ZrC_xO_y.	[242]

(continued)

Table 2.14 (continued)

System	Type of phase diagram (temperature and composition sections, constituent phases or phase fields) and/or character of interphase interaction and materials compatibility	References
C–Cr–Re	Plotted at 1300–1800 °C: $(Re,Cr)_{2\pm x}C$ (extended solid solution based on Re; at 1700 °C the combined max. solid solubilities of Cr and C in Re are 53 and 36 at.%, respectively, and corresp. to compos. ~$(Cr_{0.8}Re_{0.2})_{2\pm x}C$), σ-$Cr_2Re_{3\pm x}$, $Cr_{23}C_{6\pm x}$, $Cr_7C_{3\pm x}$, Cr_3C_{2-x}, Re, Cr, C Eutectic $(Re,Cr)_{2\pm x}C$–$Cr_{23}C_{6\pm x}$–Cr (~1650–1665 °C) Eutectic $(Re,Cr)_{2\pm x}C$–$Cr_{23}C_{6\pm x}$–σ-$Cr_2Re_{3\pm x}$ (~1665–1680 °C) Eutectic $(Re,Cr)_{2\pm x}C$–$Cr_7C_{3\pm x}$–Cr_3C_{2-x} (~1705–1730 °C) Eutectic $(Re,Cr)_{2\pm x}C$–$Cr_7C_{3\pm x}$–$Cr_{23}C_{6\pm x}$ (~1625–1640 °C) Eutectic $(Re,Cr)_{2\pm x}C$–Cr_3C_{2-x}–C (~1750–1780 °C) $(Re,Cr)_{2\pm x}C$–$Cr_{23}C_{6\pm x}$ is plotted: eutectic—~1675 °C; the max. solubility of $Cr_{23}C_{6\pm x}$ in $(Re,Cr)_{2\pm x}C$ is corresp. to compos. $(Re_{0.4}Cr_{0.6})_{2\pm x}C$ and that of $(Re,Cr)_{2\pm x}C$ in $Cr_{23}C_{6\pm x}$—to compos. $(Cr_{0.76}Re_{0.24})_{23}C_{6\pm x}$ At 1665 °C the max. solubility of Re in $Cr_{23}C_{6\pm x}$ is corresp. to compos. $(Cr_{0.80}Re_{0.20})_{23}C_{6\pm x}$ and in $Cr_7C_{3\pm x}$—to compos. $(Cr_{0.92}Re_{0.08})_7C_{3\pm x}$; at 1300 °C the max. solubility of Re in $Cr_{23}C_{6\pm x}$ (~10 at.%) is also higher than in $Cr_7C_{3\pm x}$ and Cr_3C_{2-x}. Depend. on compos., graphite is in equilibrium with $(Re,Cr)_{2\pm x}C$, or $(Re,Cr)_{2\pm x}C$ + Cr_3C_{2-x}, or Cr_3C_{2-x}.	[244, 391, 417, 580, 583, 603, 837]
C–Cr–Re–Ti	No diagram plot General consideration of the system	[852]
C–Cr–Si	Plotted at 1000, 1400 and 1600 °C: $Cr_5Si_3C_x$ ($x \approx 0.8 \div 1.0$, or $Cr_{5-x}Si_{3-z}C_{x+z}$ ($0.25 \le x + z \le 1.05$), or $Cr_5Si_{3-x}C_x$, at least <1400 °C), $Cr_{3\pm x}Si$ (<1770 °C), α-$Cr_5Si_{3\pm x}$ (<1505 °C), β-$Cr_5Si_{3\pm x}$ (1505–1680 °C), CrSi (<~1415 °C), $CrSi_2$ (<1490 °C), $Cr_{23}C_{6\pm x}$, $Cr_7C_{3\pm x}$, Cr_3C_{2-x}, SiC, Si, Cr, C The max. solubility of C in $Cr_5Si_3C_x$, $Cr_{3\pm x}Si$, CrSi and $CrSi_2$ is about 11, <4, 1 and 0.06 mol.% C, respectively; no Si solubility—in $Cr_7C_{3\pm x}$ and Cr_3C_{2-x}. Graphite is in equilibrium with SiC + Cr_3C_{2-x}, SiC—with Cr_3C_{2-x}, $Cr_5Si_3C_x$, CrSi and $CrSi_2$, and $Cr_{3\pm x}Si$—with $Cr_{23}C_{6\pm x}$, $Cr_7C_{3\pm x}$, and $Cr_5Si_3C_x$. At 1000–1200 °C the sequence of reaction layers observed in the diffusion couples is following: $Cr/Cr_{23}C_{6\pm x}/Cr_7C_{3\pm x}/Cr_7C_{3\pm x}$ + $Cr_{3\pm x}Si/Cr_{3\pm x}Si/Cr_5Si_3C_x/SiC$. In inert gas or H_2 atmosphere the interaction in powder Cr-SiC mixtures initiates at temp. ≥1000–1100 °C; at 1450–1650 °C, depend. on compos., the formation of solid solution of C and Si in Cr, $Cr_{23}C_{6\pm x}$, $Cr_7C_{3\pm x}$, Cr_3C_{2-x}, $Cr_{3\pm x}Si$ and $Cr_5Si_3C_x$ is observed.	[242, 244, 267, 392–394, 417, 503, 623, 792–793, 854]

(continued)

Table 2.14 (continued)

System	Type of phase diagram (temperature and composition sections, constituent phases or phase fields) and/or character of interphase interaction and materials compatibility	References
C–Cr–Ta	Plotted at 1000–2000 °C: (Ta,Cr)C_{1-x} (monocarbide extended solid solution based on TaC_{1-x}—up to ~$(Ta_{0.64\div0.73}Cr_{0.27\div0.36})C_{1-x}$), λ_2-$TaCr_{2\pm x}$ (<1660–1695 °C), λ_1-$TaCr_{2\pm x}$ (from 1660–1695 °C to ~2010–2040 °C), $Cr_{23}C_{6\pm x}$, $Cr_7C_{3\pm x}$, Cr_3C_{2-x}, α-$Ta_{2+x}C$ (solubility of Cr is <2 at.%), β-$Ta_{2\pm x}C$, ζ-Ta_4C_{3-x}, $Ta_6C_{5\pm x}$, Ta, Cr, C Eutectic β-$Ta_{2\pm x}C$–λ_1-$TaCr_{2\pm x}$–Ta (~1935–1950 °C) Eutectic (Ta,Cr)C_{1-x}–β-$Ta_{2\pm x}C$–λ_1-$TaCr_{2\pm x}$ (~1945–1960 °C) Eutectic (Ta,Cr)C_{1-x}–λ_1-$TaCr_{2\pm x}$–Cr (~1665–1685 °C) Eutectic (Ta,Cr)C_{1-x}–$Cr_{23}C_{6\pm x}$–Cr (~1540–1545 °C) Eutectic (Ta,Cr)C_{1-x}–$Cr_7C_{3\pm x}$–$Cr_{23}C_{6\pm x}$ (~1560–1590 °C) Eutectic (Ta,Cr)C_{1-x}–Cr_3C_{2-x}–$Cr_7C_{3\pm x}$ (~1700–1710 °C) Eutectic (Ta,Cr)C_{1-x}–Cr_3C_{2-x}–C (~1745–1755 °C) (Ta,Cr)C_{1-x} ($x = 0.21$)–(Cr_yTa_z) ($y = 0.991$, $z = 0.009$) is plotted: eutectic—~1695 °C, ~10–11 mol.% (Ta,Cr)C_{1-x} TaC_{1-x}–Cr is plotted: eutectic—~1675–1695 °C; the max. solubility of Cr in TaC_{1-x} is ~3.4 mol.% and that of TaC_{1-x} in Cr is ~2 mol.% TaC_{1-x}–λ_1-$TaCr_{2\pm x}$ is plotted: eutectic—~1990 °C; the max. solubility of λ_1-$TaCr_{2\pm x}$ in TaC_{1-x} is corresp. to compos. $(Ta_{0.98}Cr_{0.02})C_{1-x}$ and that of TaC_{1-x} in λ_1-$TaCr_{2\pm x}$ is 1 at.% C TaC_{1-x}–$Cr_7C_{3\pm x}$ is plotted: eutectic—~1720 °C; the max. solubility of $Cr_7C_{3\pm x}$ in TaC_{1-x} is corresp. to compos. ~$(Ta_{0.9}Cr_{0.1})C_{1-x}$ and that of TaC_{1-x} in $Cr_7C_{3\pm x}$—to compos. ~$(Cr_{0.99}Ta_{0.01})_7C_{3\pm x}$ β-$Ta_{2\pm x}C$–λ_1-$TaCr_{2\pm x}$ is plotted: eutectic—~1960 °C Depend. on compos., graphite is in equilibrium with one (Ta,Cr)C_{1-x}, or two (Ta,Cr)C_{1-x} + Cr_3C_{2-x} carbide phases.	[242, 244, 391, 417, 581–583, 603, 784, 837, 865, 876]
C–Cr–Tc	Plotted schematically	[583, 840]
C–Cr–Ti	Plotted at 800–2800 °C: (Ti,Cr)C_{1-x} (monocarbide extended solid solution based on $TiC_{1—x}$—up to $(Ti_{0.32}Cr_{0.68})C_{1-x}$), λ_2-$TiCr_{2-x}$ (<1220 °C), λ_1'-$TiCr_{2-x}$ (800–1270 °C), λ_1''-$TiCr_{2-x}$ (1270–1370 °C), $Cr_{23}C_{6\pm x}$, $Cr_7C_{3\pm x}$, Cr_3C_{2-x}, (β-Ti,Cr), C Eutectic (Ti,Cr)C_{1-x}–Cr_3C_{2-x}–$Cr_7C_{3\pm x}$ (1695 °C) Eutectic (Ti,Cr)C_{1-x}–$Cr_{23}C_{6\pm x}$–Cr (1540 °C) (Ti,Cr)C_{1-x}–$Cr_7C_{3\pm x}$ ($TiC_{0.98}$–$CrC_{0.40}$) is plotted: eutectic—1725 °C, ~65 mol.% $Cr_7C_{3\pm x}$ (~5 at.% Ti, ~31 at.% C) (Ti,Cr)C_{1-x}–Cr_3C_{2-x} is plotted: eutectic—~1700 °C, ~90 mol.% Cr_3C_{2-x}; the max. solubility of Cr_3C_{2-x} in (Ti,Cr)C_{1-x} is ~25 mol.% (Ti,Cr)C_{1-x} ($x = 0.04$)–(Cr_yTi_z) ($y \approx 1.0$, $z \approx 0$) is plotted: eutectic—~1100–1130 °C, ~10 mol.%	[242, 244, 391, 395–396, 417, 581–583, 603, 788–791, 837]

(continued)

Table 2.14 (continued)

System	Type of phase diagram (temperature and composition sections, constituent phases or phase fields) and/or character of interphase interaction and materials compatibility	References
	$(Ti,Cr)C_{1-x}$ ($\sim$9 at.% Ti, $\sim$8.5 at.% C); at 1100 °C the max. solubility of $TiC_{0.96}$ in Cr is $\sim$3 mol.% and that of Cr in $TiC_{0.96}$ is $\sim$4 mol.% $(Ti,Cr)C_{1-x}$–(Cr_yTi_z) is plotted ($x = 0.20$, $y = 0.95$, $z = 0.05$): eutectic—1685 °C, $\sim$15 mol.% $(Ti,Cr)C_{1-x}$ ($\sim$14 at.% Ti, $\sim$8 at.% C) $(Ti,Cr)C_{1-x}$–(Cr_yTi_z) is plotted ($x = 0.33$, $y = 0.40$, $z = 0.60$): eutectic—1360 °C, $\sim$5 mol.% $(Ti,Cr)C_{1-x}$ ($\sim$60 at.% Ti, $\sim$2 at.% C)	
C–Cr–U	Plotted at 1200 °C: $UCrC_2$, $U_2Cr_9C_9$, UCr_2C_{3+x}, $U_xCr_4C_2$, $UC_{1\pm x}$, ζ-U_2C_3, $Cr_{23}C_{6\pm x}$, $Cr_7C_{3\pm x}$, Cr_3C_{2-x}, U, Cr, C $UC_{1\pm x}$–Cr is plotted: eutectic—$\sim$1430 °C, $\sim$28 mol.% $UC_{1\pm x}$ $UC_{1\pm x}$ is in equilibrium with Cr and Cr carbides. The max. solubility of "imaginary" phase 'CrC' in hypostoichiometric $(U,Cr)C_{1-x}$ is $\sim$20 mol.%.	[242, 244, 391, 417, 612]
C–Cr–V	Plotted at 1000 and 1350 °C: VCr_2C_{2-x} (ordered phase $(V,Cr)_3C_{2-x}$, $x \approx 0.5$, or $V_{20\div25}Cr_{38\div43}C_{37}$, $\leq$1750 °C), $(V,Cr)C_{1-x}$ (extended monocarbide solid solution based on VC_{1-x}—up to $\sim(V_{0.43\div0.58}Cr_{0.42\div0.57})C_{1-x}$ at 1000–1350 °C, ?), β-$(V,Cr)_{2\pm x}C$ (extended semicarbide solid solution based on β-$V_{2\pm x}C$—up to $\sim(V_{0.5}Cr_{0.5})_{2\pm x}C$ at 1000 °C and $\sim(V_{0.4}Cr_{0.6})_{2\pm x}C$ at 1350 °C), $(Cr,V)_{23}C_{6\pm x}$ (solid solution based on $Cr_{23}C_{6\pm x}$—up to $\sim(Cr_{0.91}V_{0.09})_{23}C_{6\pm x}$ at 1000 °C and $\sim(Cr_{0.82}V_{0.18})_{23}C_{6\pm x}$ at 1350 °C), $(Cr,V)_7C_{3\pm x}$ (solid solution based on $Cr_7C_{3\pm x}$— up to $\sim(Cr_{0.9}V_{0.1})_7C_{3\pm x}$ at 1000 °C and $\sim(Cr_{0.8}V_{0.2})_{23}C_{6\pm x}$ at 1350 °C), Cr_3C_{2-x}, α-$V_{2+x}C$, β'-$V_{2+x}C$, ζ-V_4C_{3-x}, $V_6C_{5\pm x}$, $V_8C_{7\pm x}$, (V,Cr), C Eutectic β-$(V,Cr)_{2\pm x}C$–$(Cr,V)_{23}C_{6\pm x}$–(V,Cr) ($\sim$1490 °C) Eutectic β-$(V,Cr)_{2\pm x}C$–$(Cr,V)_{23}C_{6\pm x}$–$(Cr,V)_7C_{3\pm x}$ ($\sim$1520 °C) In general, V carbides dissolve a large amount of Cr, in comparison with it the solubility of V in Cr carbides is low.	[242, 391, 417, 583, 603, 782–787, 837, 843]
C–Cr–W	Plotted at 1300–1600 °C: WCr_6C_3, $W_3Cr_2C_4$, WCr_5C_3 (?), α-$(W,Cr)_{2+x}C$ (extended semicarbide solid solution based on α-$W_{2+x}C$—up to compos. $(W_{0.1}Cr_{0.9})_{2+x}C$), γ-$(W,Cr)C_{1-x}$ (extended monocarbide solid solution based on γ-WC_{1-x}—up to $\sim(W_{0.3}Cr_{0.7})C_{1-x}$ at higher temp.), $(Cr,W)_{23}C_{6\pm x}$ (extended solid solution based on $Cr_{23}C_{6\pm x}$—up to compos. $\sim(Cr_{0.8}W_{0.2})_{23}C_{6\pm x}$), $(Cr,W)_3C_{2-x}$ (extended solid solution based on Cr_3C_{2-x}—up to $\sim(Cr_{0.85}W_{0.15})_3C_{2-x}$ at 1350 °C), $(Cr,W)_7C_{3\pm x}$ (solid solution based on $Cr_7C_{3\pm x}$—up to $\sim(Cr_{0.95}W_{0.05})_7C_{3\pm x}$ at 1350 °C), δ-$WC_{1\pm x}$, (W,Cr), (Cr,W), C The max. solubility of "imaginary" phase '$W_{23}C_{6\pm x}$' in $(Cr,W)_{23}C_{6\pm x}$ is $\sim$20 mol.% at 1300 °C, $\sim$13 mol.% at 1350 °C and $\sim$10 mol.% at 1400 °C.	[242, 244, 391, 397–399, 404, 417, 580–583, 603, 780, 781, 837]

(continued)

Table 2.14 (continued)

System	Type of phase diagram (temperature and composition sections, constituent phases or phase fields) and/or character of interphase interaction and materials compatibility	References
C–Cr–Zr	Plotted at 1300–1800 °C: λ_2-$ZrCr_{2-x}$ (<~1530–1590 °C), λ_1'-$ZrCr_{2-x}$ (from ~1530–1590 °C to 1620 °C), λ_1''-$ZrCr_{2-x}$ (1620–1675 °C), $Cr_{23}C_{6\pm x}$, $Cr_7C_{3\pm x}$, Cr_3C_{2-x}, ZrC_{1-x}, β-Zr, Cr, C Eutectic ZrC_{1-x}–Cr_3C_{2-x}–$Cr_7C_{3\pm x}$ (1730 °C) Eutectic ZrC_{1-x}–$Cr_{23}C_{6\pm x}$–Cr (1575 °C) Eutectic ZrC_{1-x}–λ_1'-$ZrCr_{2-x}$–Cr (1595 °C) Eutectic ZrC_{1-x}–λ_2-$ZrCr_{2-x}$–Zr (1330 °C) ZrC_{1-x}–$Cr_7C_{3\pm x}$ is plotted: eutectic—1750 °C ZrC_{1-x}–λ_1''-$ZrCr_{2-x}$ is plotted: eutectic—1630 °C ZrC_{1-x}–Cr_yZr_z ($x = 0.28$, $y = 0.998$, $z = 0.002$) is plotted: eutectic—~1760–1775 °C, ~5.0–5.6 mol.% ZrC_{1-x} (~91 at.% Cr, ~3.7 at.% C) ZrC_{1-x}–Cr ($x = 0.095$) is plotted: eutectic—~1730–1805 °C (?), ~4–5 mol.% ZrC_{1-x} (~91 at.% Cr, ~4.3 at.% C); max. solubility of ZrC_{1-x} in Cr is 1.3 mol.% (at eutectic temp.) ZrC_{1-x}–Cr ($x = 0.03$) is plotted: eutectic—1120–1140 °C (?), ~3.5–6.4 mol.% ZrC_{1-x} (~93.5 at.% Cr, ~3.2 at.% C); max. Cr solubility in ZrC_{1-x} is ~2.3–8.5 mol.% (?) and that of ZrC_{1-x} in Cr is ≤0.1 mol.% The max. solubility of Cr in ZrC_{1-x} is ~1.5–3.0 mol.% and corresp. to compos. ~$(Zr_{0.97}Cr_{0.03})C_{1-x}$; the solubility of Zr in Cr carbides is very low. Data on the system available in literature are very controversial.	[242, 244, 391, 395, 400, 417, 581–583, 603, 775–779, 837]
C–Cs–Zr	No diagram plot The solubility of Cs in ZrC_{1-x} decreases with increasing temp. from 1.5×10^{-2} mol.% at 1210 °C to 0.4×10^{-4} mol.% at 1210 °C.	[833]
C–Cu–Si	No diagram plot At 1100–1600 °C, in the reducing atmosphere the interaction between SiC and Cu results in the formation of C and Cu silicides, which dissociate at higher temp., forming secondary SiC.	[242]
C–Cu–Zr	No diagram plot $Zr_xCu_yC_z$ (?)	[902]
C–Dy–U	No diagram plot $UC_{1\pm x}$–DyC_{1-x} monocarbide continuous solid solution or extended solid solution based on $UC_{1\pm x}$ (?).	[391]
C–Er–Ir	Plotted partially at 1100–1400 °C: Er_3Ir, Er_5Ir_2, α-$Er_5Ir_{3\pm x}$ (?), β-$Er_5Ir_{3\pm x}$, Er_3Ir_2, ErIr, $ErIr_{2\pm x}$, $Er_{3-x}C$, $Er_{15}C_{19}$, α-ErC_2, β-ErC_2, α-Er, β-Er, Ir, C Depend. on compos., graphite is in equilibrium with $ErIr_{2\pm x}$ + Ir, or $ErIr_{2\pm x}$ + α-ErC_2.	[990]
C–Er–N–Th	No diagram plot $ThC_{1\pm x}$–$ErN_{1\pm x}$ continuous solid solution	[391]

(continued)

Table 2.14 (continued)

System	Type of phase diagram (temperature and composition sections, constituent phases or phase fields) and/or character of interphase interaction and materials compatibility	References
C–Er–U	No diagram plot $UC_{1\pm x}$–ErC_{1-x} monocarbide continuous solid solution or extended solid solution based on $UC_{1\pm x}$.	[391]
C–Eu–U	No diagram plot $UC_{1\pm x}$–EuC_{1-x} monocarbide continuous solid solution or extended solid solution based on $UC_{1\pm x}$.	[391]
C–Fe–Hf	Plotted at 1100 °C: $Hf_{2\pm x}Fe$ (<1260 °C), α-$HfFe_{2\pm x}$ (<~1200 °C), β-$HfFe_{2\pm x}$ (~1200–1640 °C), λ-$Hf_3Fe_{7\pm x}$ (<~1820 °C), Fe_3C, HfC_{1-x}, α-Fe, γ-Fe, δ-Fe, α-Hf, β-Hf, C HfC_{1-x}–Fe is plotted: eutectic—~1410–1490 °C, ~2–4 mol.% HfC_{1-x}; at the eutectic temp. the solubility of HfC_{1-x} in Fe is ≤0.3 mol.% HfC_{1-x} is in equilibrium with Fe and Fe–Hf intermetallides.	[242, 244, 391, 417]
C–Fe–Mo	Plotted at 550–1800 °C: η_1-$(Mo_{1-x}Fe_x)_6C$ (or Mo_3Fe_3C, Mo_2Fe_4C, <2065 °C), ξ-$(Fe_{1-x}Mo_x)_3C$ (or $MoFe_2C$, $Mo_{12}Fe_{22}C_{10}$, 655–1085 °C), $(Fe,Mo)_{23}C_6$ (or $Mo_2Fe_{21}C_6$, metastable, ?) and other metastable ternary phases, λ-Fe_2Mo (<~900–1000 °C), ρ-Fe_3Mo_{2-x} (or $Fe_{62}Mo_{38}$, R-phase, from ~1190–1210 °C to ~1490 °C), μ-Fe_7Mo_{6-x} (<1370 °C), σ-$FeMo_{1\pm x}$ (from ~1540–1610 °C to 1215–1255 °C), Fe_3C, α-$Mo_{2+x}C$, α′-$Mo_{2+x}C$, β-$Mo_{2\pm x}C$, η-MoC_{1-x}, α-MoC_{1-x}, γ-MoC, α-Fe, γ-Fe, δ-Fe, Mo, C Eutectic ξ-$(Fe_{1-x}Mo_x)_3C$–$(Fe_{1-x}Mo_x)_3C$–γ-Fe (1065 °C, 7.7 at.% Mo, 18 at.% C) At 1000 °C β-$Mo_{2\pm x}C$ is in equilibrium with steel phase containing 2 at.% Mo and 4 at.% C.	[138, 242, 244, 391, 417, 542–545, 610, 846, 900]
C–Fe–N–Nb	No diagram plot General consideration of the system	[869]
C–Fe–N–Nb–Ti	NbC_{1-x}–TiC_{1-x}–$TiN_{1\pm x}$–Fe and NbC_{1-x}–δ-NbN_{1-x}–$TiN_{1\pm x}$–Fe are plotted schematically at 1200 °C	[870–871]
C–Fe–N–Nb–Ti–V	NbC_{1-x}–VC_{1-x}–δ-NbN_{1-x}–$TiN_{1\pm x}$–δ-VN_{1-x}–Fe is plotted schematically at 1000 °C	[871]
C–Fe–N–Ti	No diagram plot General consideration of the system	[872]
C–Fe–Nb	Plotted at 800–2000 °C: ε-$Fe_{2\pm x}Nb$ (or λ-$Fe_{2\pm x}Nb$ <~1625–1665 °C), μ-$FeNb_{1\pm x}$ (or μ-Fe_7Nb_{6+x}, or $Fe_{21}Nb_{19\pm x}$, <~1600–1700 °C), Fe_3C, α-Nb_2C, β-$Nb_{2+x}C$, γ-$Nb_{2\pm x}C$, ζ-Nb_4C_{3-x}, $Nb_6C_{5\pm x}$, NbC_{1-x}, α-Fe, γ-Fe, δ-Fe, Nb, C Eutectic μ-$FeNb_{1\pm x}$–ε-$Fe_{2\pm x}Nb$–β-$Nb_{2+x}C$ (1595 °C) Eutectic μ-$FeNb_{1\pm x}$–β-$Nb_{2+x}C$–Nb (~1400 °C) Eutectic ε-$Fe_{2\pm x}Nb$–NbC_{1-x}–δ-Fe (~1370 °C) Eutectic NbC_{1-x}–γ-Fe–C (~1150 °C) NbC_{1-x}–Fe is plotted: eutectic—1420 °C, ~3–5 mol.% NbC_{1-x}; at 1250 °C the max. solubility of NbC_{1-x} in Fe is ~2 mol.% The solubility of C in ε-$Fe_{2\pm x}Nb$ and μ-$FeNb_{1\pm x}$ is negligible. NbC_{1-x} is in equilibrium with Fe and ε-$Fe_{2\pm x}Nb$.	[138, 242, 244, 391, 417, 546–548, 868]

(continued)

Table 2.14 (continued)

System	Type of phase diagram (temperature and composition sections, constituent phases or phase fields) and/or character of interphase interaction and materials compatibility	References
C–Fe–Nb–V	NbC_{1-x}–VC_{1-x}–Fe is plotted schematically at 1000 °C	[871]
C–Fe–Ni–Ti	No diagram plot At 1500 °C TiC_{1-x} interacts with Fe–Ni alloy intensively.	[242]
C–Fe–Ni–W	No diagram plot Some phase fields are considered.	[755, 848]
C–Fe–Si	Plotted at 800–1450 °C: Fe_6SiC, Fe_5SiC (?), Fe_8Si_2C (?), Fe_9SiC_2 (?), α_2-$Fe_{3+x}Si$ (<~1300 °C), α_1-$Fe_{3\pm x}Si$ (<~1155 °C), α_1'-$Fe_{3\pm x}Si$ (or $Fe_5Si_{2\pm x}$, 965–1250 °C), β-$Fe_{2\pm x}Si$ (1040–1210 °C), η-Fe_5Si_3 (~825–1100 °C), ε-$FeSi_{1\pm x}$ (<1410 °C), ζ_1-$FeSi_2$ (~935–1220 °C), ζ_2-$FeSi_2$ (<980 °C), $Fe_3Si_{7\pm x}$ (or $FeSi_{2+x}$, $x \approx 0.3$, 935–1220 °C), Fe_3C, SiC, α-Fe, γ-Fe, δ-Fe, Si, C Eutectic Fe_6SiC–γ-Fe–Fe_3C (1030 °C, 8.8 at.% Si, 15.2 at.% C) Eutectic α,δ-Fe–γ-Fe–C (1156 °C, 15.0 at.% Si, 7.6 at.% C) Eutectic α,δ-Fe–ε-$FeSi_{1\pm x}$–C (1182 °C, 31.9 at.% Si, 0.6 at.% C) At 1100 °C in H_2 the interaction between SiC and Fe results in the formation of η-Fe_5Si_3; in vacuum the contact melting is observed at 1165 °C.	[242, 244, 267, 393, 401, 417, 503, 505, 549–550]
C–Fe–Si–Ti	No diagram plot At 1500 °C TiC_{1-x} interacts with Fe–Si alloy intensively.	[242]
C–Fe–Si–V	Plotted partially and schematically. Eutectic VC_{1-x}–Fe_3C–γ-Fe–C (1150 °C)	[608]
C–Fe–Ta	Plotted at 1100 °C: ε-$Fe_{2\pm x}Ta$ (<~1775 °C), μ-$FeTa_{1\pm x}$ (or μ-Fe_7Ta_{6+x}, <~1800–1900 °C), Fe_3C, α-$Ta_{2+x}C$, β-$Ta_{2\pm x}C$, ζ-Ta_4C_{3-x}, $Ta_6C_{5\pm x}$, TaC_{1-x}, α-Fe, γ-Fe, δ-Fe, Ta, C TaC_{1-x}–Fe is plotted: eutectic—1440 °C, ~2–3 mol.% TaC_{1-x} α-$Ta_{2+x}C$ is in equilibrium with ε-$Fe_{2\pm x}Ta$ and μ-$FeTa_{1\pm x}$, TaC_{1-x} ($x > 0.15$)—with ε-$Fe_{2\pm x}Ta$ and TaC_{1-x} ($0.01 \le x \le 0.15$)—with Fe.	[242, 244, 391, 417]
C–Fe–Ti	Plotted at 25–1600 °C: $TiFe_{1\pm x}$ (<~1315 °C), $TiFe_{2\pm x}$ (<~1425 °C), Fe_3C, TiC_{1-x}, α-Fe, γ-Fe, δ-Fe, β-Ti, α-Ti, C Eutectic $TiFe_{2\pm x}$–TiC_{1-x} (~1425 °C, 33.4 at.% Ti, 0.5 at.% C) Eutectic $TiFe_{1\pm x}$–TiC_{1-x}–β-Ti (~1070 °C, 71.8 at.% Ti, 0.1 at.% C) Eutectic $TiFe_{2\pm x}$–TiC_{1-x}–δ-Fe (~1290 °C, 16.4 at.% Ti, 0.2 at.% C) Eutectic TiC_{1-x}–γ-Fe–C (1150 °C, 0.9 at.% Ti, 17.6 at.% C) TiC_{1-x}–Fe is plotted: eutectic—~1380–1475 °C, ~6–10 mol.% TiC_{1-x} At 1250–1260 °C the solubility of TiC_{1-x} in γ-Fe is $\le 0.6 \div 0.7$ mol.%; depend. on temp., TiC_{1-x} is in equilibrium with γ-Fe or α-Fe and Fe–Ti intermetallides.	[242, 244, 391, 405–406, 417, 551–556, 611]

(continued)

Table 2.14 (continued)

System	Type of phase diagram (temperature and composition sections, constituent phases or phase fields) and/or character of interphase interaction and materials compatibility	References
C–Fe–U	Plotted at 1000–1400 °C: $UFeC_2$ (<1615 °C), ~$U_3Fe_2C_5$ (<1500 °C), ~U_3FeC_6 (at least ≥ 1150–1400 °C), $U_{11}Fe_{12}C_{18}$ (<1200 °C), U_6Fe (<795–805 °C), UFe_{2-x} (<1230 °C), Fe_3C, $UC_{1\pm x}$, ζ-U_2C_3, α-UC_{2-x}, β-UC_{2-x}, δ-Fe, γ-Fe, α-Fe, γ-U, β-U, α-U, C Eutectic $UC_{1\pm x}$–UFe_{2-x}–γ-Fe (1040 °C); no mutual solid solubilities between the components Eutectic $UC_{1\pm x}$–UFe_{2-x}–U_6Fe (720 °C); no mutual solid solubilities between the components $UC_{1\pm x}$–UFe_{2-x} is plotted: eutectic—~1040–1200 °C, ~11 mol.% $UC_{1\pm x}$ (~3.8 at.% C); no mutual solid solubilities between the components $UC_{1\pm x}$–γ-Fe is plotted: eutectic—~1120–1205 °C, ~17 mol.% $UC_{1\pm x}$ (~15 at.% C); no mutual solid solubilities between the components $UFeC_2$–γ-Fe is plotted: eutectic—1160 °C, ~14 mol.% $UFeC_2$ (~20 at.% C); no mutual solid solubilities between the components	[242, 244, 391, 452]
C–Fe–V	Plotted at 500–1150 °C: η-V_3Fe_3C (?), σ-$VFe_{1\pm x}$ (from ~100–650 to ~1200–1250 °C), Fe_3C, α-$V_{2+x}C$, β-$V_{2\pm x}C$, β′-$V_{2+x}C$, ζ-V_4C_{3-x}, $V_6C_{5\pm x}$, $V_8C_{7\pm x}$, VC_{1-x}, δ-Fe, γ-Fe, α-Fe, V, C Eutectic Fe_3C–ζ-V_4C_{3-x} (~1150 °C, 10.2 at.% V, 27.7 at.% C) Eutectic β-$V_{2\pm x}C$–VC_{1-x}–α-Fe (~1390 °C, ~36 at.% V, ~4.5 at.% C) Eutectic Fe_3C–VC_{1-x}–γ-Fe (~1120 °C, 2.75 at.% V, 17.1 at.% C) VC_{1-x}–Fe is plotted: eutectic—~1390–1415 °C, ~7–8 mol.% VC_{1-x} VC_{1-x} is in equilibrium with α-(Fe,V) and γ-Fe, β-$V_{2\pm x}C$—with α-(Fe,V), σ-$VFe_{1\pm x}$ and (V,Fe)	[242, 244, 391, 417, 557–558, 843, 845, 873]
C–Fe–W	Plotted at 600–1500 °C: κ-W_3FeC (≤~1600 °C), η_1-W_3Fe_3C (<~1670 °C), η_1-W_6Fe_6C (≤~1400 °C), $W_2Fe_{21}C_6$ (metastable), WFeC (metastable, ?), λ-Fe_2W (≤~1060 °C), μ-Fe_7W_{6-x} (or Fe_3W_2, ~1190–1635 °C), δ-$FeW_{1\pm x}$ (~400–1215 °C), Fe_3C, α-$W_{2+x}C$, β-$W_{2+x}C$, γ-$W_{2\pm x}C$, γ-WC_{1-x}, δ-$WC_{1\pm x}$, δ-Fe, γ-Fe, α-Fe, W, C Eutectic δ-$WC_{1\pm x}$–γ-Fe–C (~1145 °C, 1.3 at.% W, 17.5 at.% C)	[242, 244, 391, 417, 559–562, 604, 662, 755–847]
C–Fe–Zr	Plotted at 1100 °C: Zr_3Fe_3C (?), $Zr_{3\pm x}Fe$ (<~885 °C), $Zr_{2+x}Fe$ (~775–975 °C), $ZrFe_{2+x}$ (<~1675 °C), $ZrFe_3$ (<~1480 °C), Fe_3C, ZrC_{1-x}, γ-Fe, β-Zr, C ZrC_{1-x}–Fe is plotted: eutectic—~1400–1475 °C, ~3–4 mol.% ZrC_{1-x} The solubility of ZrC_{1-x} in γ-Fe is ≤0.5 mol.%; ZrC_{1-x} is in equilibrium with Fe and Fe-Zr intermetallides.	[241–242, 244, 391, 417]

(continued)

Table 2.14 (continued)

System	Type of phase diagram (temperature and composition sections, constituent phases or phase fields) and/or character of interphase interaction and materials compatibility	References
C–Ga–Mo	No diagram plot Mo_2GaC ($M_{n+1}AX_n$-phase)	[680–681, 744–745, 860]
C–Ga–Nb	Plotted partially at 800 °C: Nb_2GaC ($M_{n+1}AX_n$-phase), $NbGa_{3-x}$ (<1235 °C), Nb_4Ga_5 (<1300 °C), Nb_5Ga_4 (<1540 °C), $Nb_5Ga_{3\pm x}$ (<1950 °C), $Nb_{3-x}Ga$ (<1860 °C), α-Nb_2C, β-$Nb_{2+x}C$, γ-$Nb_{2\pm x}C$, ζ-Nb_4C_{3-x}, $Nb_6C_{5\pm x}$, NbC_{1-x}, Nb, Ga, C	[244, 680–681, 744–745, 860, 975]
C–Ga–Ta	No diagram plot Ta_2GaC ($M_{n+1}AX_n$-phase)	[680–681, 744–745, 860]
C–Ga–Ti	No diagram plot Ti_2GaC, Ti_4GaC_3 ($M_{n+1}AX_n$-phases)	[680–681, 744–745, 859–860]
C–Ga–V	Plotted partially at 800 °C: V_2GaC ($M_{n+1}AX_n$-phase), V_8Ga_{41} (<495 °C), V_2Ga_5 (<1050 °C), $V_6Ga_{7\pm x}$ (~995–1155 °C), $V_6Ga_{5\pm x}$ (<1095 °C), $V_{3\pm x}Ga$ (<1300 °C), α-$V_{2+x}C$, β-$V_{2\pm x}C$, β′-$V_{2+x}C$, ζ-V_4C_{3-x}, $V_6C_{5\pm x}$, $V_8C_{7\pm x}$, VC_{1-x}, V, Ga, C	[244, 680–681, 744–745, 860, 975]
C–Gd–U	Plotted at 1000–1500 °C: $(U,Gd)C_{1\pm x}$ ($UC_{1\pm x}$–β-GdC_{1-x} (or β-$Gd_{3-x}C$) monocarbide continuous solid solution), α-Gd_2C, $(Gd,U)_2C_{3-x}$ (solid solution based on Gd_2C_{3-x}), ζ-$(U,Gd)_2C_3$ (solid solution based on ζ-U_2C_3), β-$(Gd,U)C_{2-x}$ (solid solution based on β-GdC_2), γ-U, β-U, α-U, α-Gd, β-Gd, C α-UC_{2-x}–α-GdC_2 and β-UC_{2-x}–β-GdC_2 series of dicarbide continuous solid solutions are also formed. At temp. <1000 °C $UC_{1\pm x}$–β-GdC_{1-x} (or β-$Gd_{3-x}C$) monocarbide continuous solid solution has a miscibility gap.	[241, 391]
C–Gd–N–Th	No diagram plot $ThC_{1\pm x}$–GdN_{1-x} continuous solid solution	[391]
C–Ge–Si–Ti	No diagram plot $Ti_3Si_xGe_{1-x}C_2$ ($0 \le x \le 1$, $M_{n+1}AX_n$-phase solid solution)	[680–681, 860]
C–Ge–Ti	Plotted at 1200 °C: Ti_2GeC, Ti_3GeC_2 ($M_{n+1}AX_n$-phases), Ti_4GeC_3 ($M_{n+1}AX_n$-phase, metastable, ?), Ti_5Ge_3 (<1980 °C), Ti_6Ge_5 (<1650 °C), $TiGe_2$ (<1075 °C), TiC_{1-x}, α-Ti, β-Ti, Ge, C	[244, 633, 680–681, 744–745, 860]
C–Ge–V	Plotted partially at 800 °C: V_2GeC ($M_{n+1}AX_n$-phase), V_3GeC (?), $V_{17}Ge_{31}$ (<955–965 °C), $V_{11}Ge_8$ (<1565–1585 °C), V_5Ge_{3-x} (~1930 °C), $V_{3\pm x}Ge$ (<1690 °C), α-$V_{2+x}C$, β-$V_{2\pm x}C$, β′-$V_{2+x}C$, ζ-V_4C_{3-x}, $V_6C_{5\pm x}$, $V_8C_{7\pm x}$, VC_{1-x}, V, Ge, C	[680–681, 744–745, 748, 860]

(continued)

Table 2.14 (continued)

System	Type of phase diagram (temperature and composition sections, constituent phases or phase fields) and/or character of interphase interaction and materials compatibility	References
C–H–Hf	No diagram plot HfC_xH_y ($x = 0.55 \div 0.58$, $y = 0.42 \div 0.43$, or $Hf_2C_{1+x}H_{1-y}$ ($HfC_{1+x}{\cdot}HfH_{1-y}$), $x = 0.1$, $y = 0.14$)	[825]
C–H–La	No diagram plot LaC_xH_y (or La_2CH_z, $LaC{\cdot}LaH_z$)	[825]
C–H–Nb	No diagram plot NbC_xH_y ($0.71 \leq x \leq 0.81$, $0 \leq y \leq 0.30$, ?)	[825, 888]
C–H–O–Zr	No diagram plot $ZrO_{0.6}C_{0.2}H_x$	[825]
C–H–Th	No diagram plot Th_2CH_2 (or $ThC{\cdot}ThH_2$), Th_3CH_4 (or $ThC{\cdot}2ThH_2$)	[825]
C–H–Ti	No diagram plot TiC_xH_y ($x = 0.460 \div 0.675$, $y = 0.158 \div 0.625$, or Ti_2CH_x ($TiC{\cdot}TiH_x$), $x = 0.46 \div 0.60$), TiC_xH_z ($x = 0.4$, $z = 1.2$)	[825]
C–H–V	No diagram plot VC_xH_y ($x = 0.75$, $y = 0.25$), V_2CH_x ($x = 0.3$)	[825]
C–H–Y	No diagram plot YC_xH_y (or Y_2CH_z, $YC{\cdot}YH_z$, $z = 2.55$)	[825]
C–H–Zr	No diagram plot ZrC_xH_y ($x = 0.30 \div 0.65$, $y = 0.30 \div 1.25$, or Zr_2CH_x, $Zr_2C_{1\pm x}H_{1\pm y}$, $ZrC_{1\pm x}{\cdot}ZrH_{1\pm y}$, or Zr_3CH_x, $Zr_3C_{1\pm x}H_{1\pm y}$, $ZrC_{1\pm x}{\cdot}2ZrH_{1\pm y}$)	[825–826, 866]
C–Hf–In	No diagram plot Hf_2InC ($M_{n+1}AX_n$-phase)	[680–681, 744–745, 860]
C–Hf–In–Ti	No diagram plot $(Ti,Hf)_2InC$ ($M_{n+1}AX_n$-phase solid solution)	[680–681, 860]
C–Hf–Ir	Plotted at 1500 °C: $Hf_{2+x}Ir$ (<~1720–1775 °C), Hf_3Ir_2 (or Hf_5Ir_3, <~1930–1970 °C), $HfIr_{1+x}$ (or $Hf_{47}Ir_{53}$, <~2410–2440 °C), $HfIr_{3+x}$ (<~2460–2470 °C), HfC_{1-x}, α-Hf, β-Hf, Ir, C Depend. on compos., graphite is in equilibrium with $HfIr_{3+x}$ + HfC_{1-x} or $HfIr_{3+x}$ + (Ir,Hf).	[244, 391, 417]
C–Hf–Mn	No diagram plot The interaction between HfC_{1-x} and Mn leads to the formation of eutectic alloy and solid solutions.	[242]

(continued)

Table 2.14 (continued)

System	Type of phase diagram (temperature and composition sections, constituent phases or phase fields) and/or character of interphase interaction and materials compatibility	References
C–Hf–Mo	Plotted at 1250–2100 °C: (Hf,Mo)C_{1-x} (HfC_{1-x}–α-MoC_{1-x} monocarbide continuous solid solution at temp. >∼1700–2000 °C, or extended solid solution based on HfC_{1-x} with homog. range from $HfC_{0.56\div0.99}$ to $(Hf_{0.15}Mo_{0.85})C_{0.72\div0.77}$ at 1400 °C, from $HfC_{0.54\div0.99}$ to $(Hf_{0.11}Mo_{0.89})C_{0.72\div0.77}$ at 1700 °C, from $HfC_{0.54\div0.99}$ to $MoC_{0.64\div0.71}$ at 2000 °C; the C content of the mixed monocarbide phase increases as Hf substitutes for Mo), β-$(Mo,Hf)_{2\pm x}C$ (semicarbide solid solution based on β-$Mo_{2\pm x}C$ with homog. range from $MoC_{0.4\div0.55}$ to $(Mo_{0.9}Hf_{0.1})C_{0.475\div0.50}$ at 1400–2000 °C), α-$(Mo,Hf)C_{1-x}$ (extended monocarbide solid solution based on α-MoC_{1-x} with homog. range from $MoC_{0.65\div0.70}$ to $(Mo_{0.93\div0.95}Hf_{0.05\div0.07})C_{0.65\div0.70}$ at 1400–1700 °C; α-MoC_{1-x}–HfC_{1-x} monocarbide continuous solid solution at temp. >∼1700–2000 °C), η-$(Mo,Hf)C_{1-x}$ (solid solution based on η-MoC_{1-x} with max. solubility of Hf—up to 3 at.% at 1700 °C), α-$HfMo_{2\pm x}$ (<∼1770–1875 °C), β-$HfMo_{2-x}$ (from ∼1770–1875 °C to ∼2130–2210 °C), α-Hf, β-(Hf,Mo), Mo, C Eutectic (Hf,Mo)C_{1-x}–Mo–β-$(Mo,Hf)_{2\pm x}C$ (∼2100–2140 °C, 6 at.% Hf, 20 at.% C) Eutectic (Hf,Mo)C_{1-x}–β-(Hf,Mo)–α-Hf (∼1740–1780 °C, 83 at.% Hf, 2.5 at.% C) Eutectic (Hf,Mo)C_{1-x}–β-(Hf,Mo)–β-$HfMo_{2-x}$ (∼1850 °C) Eutectic (Hf,Mo)C_{1-x}–η-$(Mo,Hf)C_{1-x}$–β-$(Mo,Hf)_{2\pm x}C$ (∼2470 °C) HfC_{1-x}–Mo is plotted: eutectic—∼2310–2370 °C, ∼11–15 mol.% HfC_{1-x} (∼11.5 at.% C); at eutectic temp. the max. solid solubility of Mo in HfC_{1-x} is ≥15 mol.% and that of HfC_{1-x} in Mo is ∼1.6 mol.%, the latter one decreases with decreasing temp. up to—0.4 mol.% at 2100 °C and 0.25 mol.% at 1250 °C Additions of Hf affect the solid solubility of C in Mo; at higher Hf content, the solubility of C decreases obviously. The presence of Hf stabilizes α-MoC_{1-x}. The interaction between HfC_{1-x} and Mo initiates from 1500–1800 °C (5 h exposure) and becomes noticeable at 2000–2200 °C (2 h exposure). Some data available on the system in literature are controversial.	[138, 242, 391, 407, 409–410, 579, 614, 772–774, 827–828, 832, 835, 837]
C–Hf–Mo–Ni	HfC_{1-x}–β-$Mo_{2\pm x}C$–Ni is plotted at 1220 °C: eutectic—∼1200–1240 °C, ∼7 mol.% β-$Mo_{2\pm x}C$, ∼4 mol.% HfC_{1-x}; the max. mutual solubilities of the components at eutectic temp. are: in HfC_{1-x}–9 mol.% β-$Mo_{2\pm x}C$ and 15.5 mol.% Ni, in β-$Mo_{2\pm x}C$–3 mol.% HfC_{1-x} and 20 mol.% Ni and in Ni–1 mol.% HfC_{1-x} and 4 mol.% β-$Mo_{2\pm x}C$.	[408]

(continued)

Table 2.14 (continued)

System	Type of phase diagram (temperature and composition sections, constituent phases or phase fields) and/or character of interphase interaction and materials compatibility	References
C–Hf–Mo–Si	No diagram plot. At 1900–1950 °C in Ar atmosphere or low vacuum (~100 Pa) the interaction in HfC_{1-x}–$MoSi_2$ powder mixtures leads to the formation of SiC and $(Mo,Hf)_5Si_{3\pm x}$.	[894, 899]
C–Hf–Mo–Ti	HfC_{1-x} ($x = 0.02$)–TiC_{1-x} ($x = 0.03$)–'MoC' is plotted at 1500–1650 °C: a small miscibility gap forms at temp. <1630 °C at compos. $Hf_{0.45}Mo_{0.55}C_{1.0}$; at lower temp. a large miscibility gap connects the TiC_{1-x}–HfC_{1-x} and HfC_{1-x}–'MoC' boundary systems; addition of 'MoC' to the TiC_{1-x}–HfC_{1-x} solid solution decreases the critical miscibility temp., while addition of TiC_{1-x} to HfC_{1-x}–'MoC' raises the critical temp.; no max. type ternary critical point.	[409]
C–Hf–Mo–V	HfC_{1-x} ($x = 0.02$)–VC_{1-x} ($x = 0.12$)–'MoC' is plotted at 1500–2750 °C: addition of VC_{1-x} to the HfC_{1-x}–'MoC' monocarbide solid solution increases the critical miscibility temp.; phase equilibria are dominated by a large miscibility gap at 1500 °C.	[410]
C–Hf–N	HfC_{1-x}–$HfN_{1\pm x}$–Hf is plotted at 1150 and ~2000 °C: HfC_xN_z ($0.6 \le x + z \le 1$, HfC_{1-x}–$HfN_{1\pm x}$ carbonitride continuous solid solution, homog. range at 1150 °C: ~$HfC_{0.60}$–$HfN_{0.72}$–$HfN_{1.0}$–$HfC_{0.98}$), β-Hf	[138, 242, 391, 411, 454]
C–Hf–N–O	HfC_{1-x}–$HfN_{1\pm x}$–'HfO' is plotted at 1600 and 2000 °C: homog. limits of HfC_{1-x}–$HfN_{1\pm x}$ continuous solid solution ($HfC_xN_yO_z$) are $HfC_{0.75}O_{0.25}$ and $HfN_{0.80}O_{0.20}$ (1600 °C) and $HfC_{0.70}O_{0.30}$ and $HfN_{0.75}O_{0.25}$ (2000 °C)	[411–412]
C–Hf–Nb	Plotted at 1200–2050 °C: $(Hf,Nb)C_{1-x}$ (HfC_{1-x}–NbC_{1-x} monocarbide continuous solid solution), β-$Nb_{2+x}C$ (max. solubility of Hf is ~5 at.%), γ-$Nb_{2\pm x}C$, ζ-Nb_4C_{3-x}, $Nb_6C_{5\pm x}$, β-(Hf,Nb), C Graphite is in equilibrium with $(Hf,Nb)C_{1-x}$.	[138, 242, 391, 413, 813, 824, 837, 844]
C–Hf–Nb–U	HfC_{1-x}–NbC_{1-x}–$UC_{1\pm x}$ is plotted at 2050 °C: (Hf,Nb,U)C (based on HfC_{1-x}–NbC_{1-x} and NbC_{1-x}–$UC_{1\pm x}$ monocarbide continuous solid solutions with homog. range depend. on temp.), 2 monocarbide solid solutions region (or miscibility gap, limited by compos. ~$(Hf_{0.4}U_{0.6})C_{1-x}$–~$(Hf_{0.75}U_{0.25})C_{1-x}$–~$(Hf_{0.5}Nb_{0.2}U_{0.3})C_{1-x}$)	[391]
C–Hf–Nb–V	HfC_{1-x}–NbC_{1-x}–VC_{1-x} is plotted at 2050 °C: $(Hf,Nb,V)C_{1-x}$ (based on HfC_{1-x}–NbC_{1-x} and VC_{1-x}–NbC_{1-x} monocarbide continuous solid solutions, with homog. range depend. on temp.), 2 monocarbide solid solutions region (or miscibility gap, limited by compos. ~$(Hf_{0.98}V_{0.02})C_{1-x}$–~$(Hf_{0.03}V_{0.97})C_{1-x}$–~$(Hf_{0.2\div0.3}Nb_{0.51\div0.52}V_{0.2\div0.3})C_{1-x}$)	[413]

(continued)

Table 2.14 (continued)

System	Type of phase diagram (temperature and composition sections, constituent phases or phase fields) and/or character of interphase interaction and materials compatibility	References
C–Hf–Ni	Plotted at 1100 °C: Hf_2Ni (<~1195–1200 °C), α-HfNi (<1170 °C), β-HfNi (1170–1530 °C), Hf_9Ni_{11} (<1335–1340 °C), Hf_7Ni_{10} (or Hf_2Ni_3, <1290–1295 °C), Hf_3Ni_7 (or Hf_2Ni_5, from ~1015–1020 °C to 1250 °C), Hf_8Ni_{21} (from ~1175–1180 °C to 1300 °C), α-$HfNi_3$ (<1200 °C), β-$HfNi_3$ (from 1200 °C to ~1300–1340 °C), Hf_2Ni_7 (<1480 °C), $HfNi_5$ (<1240 °C), HfC_{1-x}, Ni, α-Hf, β-Hf, C HfC_{1-x}–Ni is plotted: eutectic—~1320–1330 °C, ~3–5.6 mol.% HfC_{1-x}; at the eutectic temp. the solubility of HfC_{1-x} in Ni is $\leq 0.7 \div 1.0$ mol.% and that of Ni in HfC_{1-x}–~7.5 mol.% HfC_{1-x} is in equilibrium with Ni and Ni-Hf intermetallides	[242, 244, 391, 414–415, 417, 839]
C–Hf–Ni–Ti	HfC_{1-x}–TiC_{1-x}–Ni is plotted at 1225 °C: eutectic—~1205–1235 °C, ~1.0–1.2 mol.% HfC_{1-x}, ~5–6 mol.% TiC_{1-x}	[414]
C–Hf–Ni–W	HfC_{1-x}–δ-$WC_{1\pm x}$–Ni is plotted at 1000 °C: eutectic—15 mol.% HfC_{1-x}, 15 mol.% δ-$WC_{1\pm x}$; regions of solid solutions based on the individual components are not large (6–7 mol.%)	[415]
C–Hf–Ni–Zr	HfC_{1-x} ($x = 0.02$)–ZrC_{1-x} ($x = 0.17$)–Ni is plotted partially: HfC_{1-x}–ZrC_{1-x} monocarbide continuous solid solution forms in the presence of Ni; minimum on the line of eutectic solidification (Hf,Zr)C_{1-x}–Ni is lower by 100–150 °C than eutectic temp. in the HfC_{1-x}–Ni and ZrC_{1-x}–Ni systems and corresp. to compos. 4 mol.% HfC_{1-x}, 4 mol.% ZrC_{1-x} and 92 mol.% Ni	[839]
C–Hf–O	C–Hf–β-HfO_{2-x} is partially plotted at 1900 °C: homog. limits of HfC_xO_y (HfC_{1-x}–'HfO' oxycarbide solid solution) are ~$HfC_{0.75}O_{0.25}$–$HfC_{0.55}$–$HfC_{0.99}$ The equilibrium pressure of CO over graphite in the mixture with α-HfO_{2-x} and HfC_{1-x} is ~0.1 MPa at 1640 °C, ~0.05 MPa at 1600 °C, ~0.02 MPa at 1500 °C and ~0.01 MPa at 1400 °C.	[411, 416]
C–Hf–O–Ti	No diagram plot. At 1500–2200 °C the interaction between TiC_{1-x} and HfO_{2-x} leads to the formation of TiC_xO_y.	[242]
C–Hf–Os	Plotted at 1500 °C: θ-$Hf_{3+x}Os$ (<1640–1680 °C), ε-$Hf_{2+x}Os$ (<1860–1900 °C), η-$Hf_{2\pm x}Os$ (<2040–2080 °C), δ-$HfOs_{1\pm x}$ (<2500–2540 °C), λ-$HfOs_{2\pm x}$ (<~2700 °C), HfC_{1-x}, α-Hf, β-Hf, Os, C Graphite is in equilibrium with (Os,Hf) + HfC_{1-x}. The solubility of Hf in Os (with the presence of C) and solubility of Os in HfC_{1-x} are low.	[391, 417]
C–Hf–Pb	No diagram plot Hf_2PbC ($M_{n+1}AX_n$-phase)	[680–681, 744–745, 860]

(continued)

Table 2.14 (continued)

System	Type of phase diagram (temperature and composition sections, constituent phases or phase fields) and/or character of interphase interaction and materials compatibility	References
C–Hf–Pd	Plotted at 1300 °C: Hf_2Pd (<1405–1425 °C), HfPd (<1600–1620 °C), Hf_3Pd_4 (<1550–1570 °C), $HfPd_2$ (from 1350–1390 °C to 2075 °C), $HfPd_3$ (<1955–1975 °C), HfC_{1-x}, α-Hf, β-Hf, Pd, C Depend. on compos., graphite is in equilibrium with (Pd,Hf) alloy, or $HfPd_3$, or $HfPd_3 + HfC_{1-x}$.	[244, 391, 417]
C–Hf–Pt	Plotted at 1500 °C: Hf_2Pt (<1620 °C), HfPt (<2100 °C), Hf_9Pt_{11} (<1550 °C), Hf_2Pt_3 (1400–1670 °C), $HfPt_2$ (1630–1960 °C), $HfPt_{3\pm x}$ (<2150 °C), HfC_{1-x}, α-Hf, β-Hf, Pt, C Depend. on compos., graphite is in equilibrium with (Pt,Hf) alloy + $HfPt_{3\pm x}$ or $HfPt_{3\pm x} + HfC_{1-x}$.	[391, 417]
C–Hf–Re	Plotted at 1500 °C: $HfRe_{1\pm x}$ (or $Hf_{11}Re_9$, or Hf_3Re_2, <~2280–2445 °C), λ-$HfRe_{2\pm x}$ (<~2850–3160 °C), χ-$Hf_5Re_{24\pm x}$ (or $HfRe_7$, <~2800–3100 °C), HfC_{1-x}, α-Hf, β-Hf, Re, C HfC_{1-x}–Re is plotted: eutectic—2720 °C, ~20–30 mol.% HfC_{1-x}; the mutual solubilities of the components are low Graphite is in equilibrium with Re + HfC_{1-x}.	[242, 244, 391, 417, 835, 837]
C–Hf–Rh	Plotted at 1500 °C: $HfRh_3C_x$ ($x \approx 0.4$), γ-$Hf_{2\pm x}Rh$ (<~1450–1520 °C), δ-$HfRh_{1\pm x}$ (<~2180–2290 °C), $Hf_3Rh_{5\pm x}$ (or Hf_2Rh_{3+x}, <2040 °C), $HfRh_{3\pm x}$ (<2130 °C), HfC_{1-x}, α-Hf, β-Hf, Rh, C The solubility of C in $HfRh_{3\pm x}$ is ~5–10 at.%; no solubility of Rh in HfC_{1-x}. Depend. on compos., graphite is in equilibrium with Rh + $HfRh_3C_x$ or $HfRh_3C_x + HfC_{1-x}$	[244, 391, 417]
C–Hf–Ru	Plotted at 1500 °C: $HfRu_3C_{1-x}$ ($x \approx 0.3$), $HfRu_{1\pm x}$ (<~2350–2400 °C), $HfRu_2$ (<~1900–1950 °C), HfC_{1-x}, α-Hf, β-Hf, Ru, C HfC_{1-x}–Ru is plotted: eutectic—~2000 °C Graphite is in equilibrium with Ru + HfC_{1-x}	[391, 417]
C–Hf–S	No diagram plot Hf_2SC ($M_{n+1}AX_n$-phase)	[680–681, 744–745, 860]
C–Hf–Si	Plotted at 1300 °C: $Hf_5Si_3C_{1+x}$ ($x = 0.09$), Hf_2Si (<~2070–2095 °C), Hf_3Si_2 (<2460–2500 °C), Hf_5Si_4 (or Hf_5Si_3, <2305–2335 °C), HfSi (<~2125–2155 °C), $HfSi_2$ (<~1535–1550 °C), HfC_{1-x}, SiC, α-Hf, Si, C Graphite is in equilibrium with SiC + HfC_{1-x}.	[242, 417–419, 503, 771]
C–Hf–Sn	No diagram plot Hf_2SnC ($M_{n+1}AX_n$-phase)	[680–681, 744–745, 860]

(continued)

Table 2.14 (continued)

System	Type of phase diagram (temperature and composition sections, constituent phases or phase fields) and/or character of interphase interaction and materials compatibility	References
C–Hf–Ta	Plotted at 1000–3950 °C: (Hf,Ta)C_{1-x} (HfC_{1-x}–TaC_{1-x} monocarbide continuous solid solution), α-(Ta,Hf)$_{2+x}$C (extended semicarbide solid solution based on α-$Ta_{2+x}C$, ~1000–2230 °C, max. solubility of Hf, depend. on temp.—~1.5–10.7 at.%), β-(Ta,Hf)$_{2\pm x}$C (extended semicarbide solid solution based on β-$Ta_{2\pm x}C$, ~2000–3200 °C, max. solubility of Hf, depend. on temp.—~1.5–18.5 at.%), ζ-Ta_4C_{3-x}, $Ta_6C_{5\pm x}$, α-Hf, β-Hf, Ta, C HfC_{1-x}–TaC_{1-x} is plotted: miscibility gap in the solid state (critical point—890 °C, at compos. ~$Hf_{0.5\div0.6}Ta_{0.4\div0.5}C_{1-x}$) The data on the higher melting points of (Hf,Ta)C_{1-x} in comparison with individual HfC_{1-x} and TaC_{1-x} are not confirmed. Graphite is in equilibrium with (Hf,Ta)C_{1-x}.	[138, 242, 391, 419–423, 723, 813, 837, 885]
C–Hf–Ta–U	HfC_{1-x}–TaC_{1-x}–$UC_{1\pm x}$ is plotted at 2050 °C: (Hf,Ta,U)$C_{1\pm x}$ (based on HfC_{1-x}–TaC_{1-x} and TaC_{1-x}–$UC_{1\pm x}$ monocarbide continuous solid solutions with homog. range depend. on temp.), 2 monocarbide solid solutions region (or miscibility gap, limited by compos. ~$(Hf_{0.4}U_{0.6})C_{1-x}$–~$(Hf_{0.75}U_{0.25})C_{1-x}$–~$(Hf_{0.55}Ta_{0.15}\ U_{0.3})C_{1-x}$)	[391]
C–Hf–Tc	Plotted schematically	[840]
C–Hf–Th	No diagram plot HfC_{1-x}–$ThC_{1\pm x}$ extended monocarbide solid solutions (terminal solubility).	[138]
C–Hf–Ti	Plotted at 800, 1500 and 2000 °C: (Hf,Ti)C_{1-x} (HfC_{1-x}–TiC_{1-x} monocarbide continuous solid solution at higher temp. with miscibility gap at lower temp.), two monocarbide extended solid solutions region (Hf,Ti)C_{1-x} (based on HfC_{1-x}) + (Ti,Hf)C_{1-x} (based on TiC_{1-x}), α-Hf, β-Hf, α-Ti, β-Ti, C HfC_{1-x}–TiC_{1-x} is plotted: miscibility gap in the solid state (critical point—~1765–2050 °C (?), at ~$Hf_{0.40\div0.45}Ti_{0.55\div0.60}C_{1-x}$, gap width at 1500 °C—from ~$Hf_{0.1\div0.2}Ti_{0.8\div0.9}C_{1-x}$ to ~$Hf_{0.50\div0.75}Ti_{0.25\div0.50}C_{1-x}$) Graphite is in equilibrium with (Hf,Ti)C_{1-x} or (Hf,Ti)C_{1-x} + (Ti,Hf)C_{1-x}.	[138, 242, 391, 414, 424–426, 625, 813, 816]
C–Hf–Ti–V	HfC_{1-x}–TiC_{1-x}–VC_{1-x} is plotted at 2050 °C: (Hf,Ti,V)C_{1-x} (based on HfC_{1-x}–TiC_{1-x} and VC_{1-x}–TiC_{1-x} monocarbide continuous solid solutions with homog. range depend. on temp.), 2 monocarbide solid solutions region (or miscibility gap, limited by compos. ~$(Hf_{0.98}V_{0.02})C_{1-x}$–~$(Hf_{0.03}V_{0.97})C_{1-x}$–~$(Hf_{0.14\div0.17}Ti_{0.73\div0.74}V_{0.09\div0.12})C_{1-x}$)	[413]

(continued)

Table 2.14 (continued)

System	Type of phase diagram (temperature and composition sections, constituent phases or phase fields) and/or character of interphase interaction and materials compatibility	References
C–Hf–Ti–W	HfC_{1-x}–TiC_{1-x}–δ-$WC_{1\pm x}$ is plotted at 1500–3100 °C: $(Hf,Ti,W)C_{1-x}$ (monocarbide solid solution based on HfC_{1-x}), $(Ti,Hf,W)C_{1-x}$ (monocarbide solid solution based on TiC_{1-x}), $(Hf,Ti,W)C_{1-x}$ + $(Ti,Hf,W)C_{1-x}$, $(Hf,Ti,W)C_{1-x}$ (monocarbide solid solution based on $(Hf,Ti)C_{1-x}$) + δ-$(W,Hf,Ti)C_{1\pm x}$ (monocarbide solid solution based on δ-$WC_{1\pm x}$) $(Hf,W)C_{1-x}$–$(Ti,W)C_{1-x}$ miscibility gap in the solid state: limited by compos. $Hf_{0.64}Ti_{0.36}C_{1-x}$–$Hf_{0.22}Ti_{0.78}C_{1-x}$–$Hf_{0.41}Ti_{0.27}W_{0.32}C_{1\pm x}$ (at 1540 °C)	[426]
C–Hf–Tl	No diagram plot Hf_2TlC ($M_{n+1}AX_n$-phase)	[680–681, 744–745, 860]
C–Hf–U	Plotted at 1800 and 2000 °C: $(Hf,U)C_{1-x}$ (HfC_{1-x}–$UC_{1\pm x}$ monocarbide continuous solid solution, or extended monocarbide solid solutions based on HfC_{1-x} and $UC_{1\pm x}$ at lower temp.), α-UC_{2-x}, α-Hf, β-Hf, U, C HfC_{1-x}–$UC_{1\pm x}$ is plotted: miscibility gap in the solid state (critical point—~1730 °C, ?) At higher temp., depend. on compos., graphite is in equilibrium with $(Hf,U)C_{1-x}$ or $(Hf,U)C_{1-x}$ + UC_{2-x}; the compos. of $(Hf,U)C_{1-x}$ in equilibrium with C + UC_{2-x} is corresp. to ~$(Hf_{0.9}U_{0.1})C_{1-x}$ (at 2200 °C) and shifts to lower U concentrations with temp. increase.	[138, 391]
C–Hf–U–Zr	HfC_{1-x}–ZrC_{1-x}–$UC_{1\pm x}$ is plotted at 2050 °C: $(Hf,Zr,U)C_{1\pm x}$ (based on HfC_{1-x}–ZrC_{1-x} and ZrC_{1-x}–$UC_{1\pm x}$ monocarbide continuous solid solutions with homog. range depend. on temp.), 2 monocarbide solid solutions region (or miscibility gap, limited by compos. ~$(Hf_{0.4}U_{0.6})C_{1\pm x}$–~$(Hf_{0.75}U_{0.25})C_{1\pm x}$–~$(Hf_{0.45}Zr_{0.10}U_{0.45})C_{1\pm x}$)	[391]
C–Hf–V	Plotted at 1000 °C: $HfV_{2\pm x}$ (<1550 °C), α-$V_{2+x}C$, β-$V_{2\pm x}C$, β'-$V_{2+x}C$, ζ-V_4C_{3-x}, $V_6C_{5\pm x}$, $V_8C_{7\pm x}$, VC_{1-x}, HfC_{1-x}, α-Hf, V, C HfC_{1-x}–VC_{1-x} is plotted: eutectic—~2580–2650 °C, ~70–75 mol.% VC_{1-x}; the mutual solubilities of HfC_{1-x} and VC_{1-x} in each other are ~15 vol.% (at eutectic temp.) The mutual solubilities of other components are lower.	[391, 427, 813, 837]
C–Hf–V–W	HfC_{1-x}–VC_{1-x}–δ-$WC_{1\pm x}$ is plotted at 1750–2970 °C: $(Hf,V,W)C_{1-x}$ (monocarbide solid solution based on $(Hf,V)C_{1-x}$), $(Hf,V,W)C_{1-x}$ (monocarbide solid solution based on HfC_{1-x}), $(V,Hf,W)C_{1-x}$ (monocarbide solid solution based on VC_{1-x}) $(Hf,W)C_{1-x}$–$(V,W)C_{1-x}$ miscibility gap in the solid state: limited by compos. ~$(Hf_{0.9}V_{0.1})C_{1-x}$–~$(Hf_{0.1}V_{0.9})C_{1-x}$–~$(Hf_{0.40\div0.45}V_{0.40\div0.45}W_{0.15})C_{1\pm x}$ (at 2580 °C) Addition of δ-$WC_{1\pm x}$ decreases the critical temp. of miscibility gap.	[427]

(continued)

Table 2.14 (continued)

System	Type of phase diagram (temperature and composition sections, constituent phases or phase fields) and/or character of interphase interaction and materials compatibility	References
C–Hf–W	Plotted at 1500–2660 °C: (Hf,W)C_{1-x} (HfC_{1-x}–γ-WC_{1-x} monocarbide continuous solid solution at higher temp.), $HfW_{2\pm x}$ (<~2495–2530 °C), α-$W_{2+x}C$, β-$W_{2+x}C$, γ-$W_{2\pm x}C$, γ-WC_{1-x}, δ-$WC_{1\pm x}$, α-Hf, β-Hf, W, C Eutectic (Hf,W)C_{1-x}–γ-$W_{2\pm x}C$–W (2660 °C, 8 at.% Hf, 22 at.% C); at the eutectic temp. the monocarbide solid solution compos. is $(Hf_{0.83}W_{0.17})C_{0.89}$ and semicarbide solid solution compos. is $(W_{0.94}Hf_{0.06})_2C_{0.99}$ (with max. solubility of Hf in γ-$W_{2\pm x}C$); the max. solid solubilities of C and Hf in metal W are ~1 at.% HfC_{1-x}–W is plotted: eutectic—~2790–2930 °C, ~20–25 mol.% HfC_{1-x} (~20 at.% C); the solubility of W in HfC_{1-x} is 6 mol.% (at eutectic temp.) The presence of Hf stabilizes γ-WC_{1-x}	[242, 244, 391, 415, 417, 428–430, 773, 827, 835, 837]
C–Hf–Zr	Plotted at 1600–3900 °C: (Hf,Zr)C_{1-x} (HfC_{1-x}–ZrC_{1-x} monocarbide continuous solid solution), α-(Hf,Zr), β-(Hf,Zr), C Eutectic (Hf,Zr)C_{1-x}–β-(Zr,Hf)–α-(Hf,Zr) (2030 °C) HfC_{1-x}–ZrC_{1-x} is plotted: continuous solid solution Graphite is in equilibrium with (Hf,Zr)C_{1-x}.	[138, 391, 424–425, 634, 813, 1006]
C–Ho–U	No diagram plot $UC_{1\pm x}$–HoC_{1-x} monocarbide continuous solid solution or extended solid solution based on $UC_{1\pm x}$.	[391]
C–In–Nb	No diagram plot Nb_2InC ($M_{n+1}AX_n$-phase)	[680–681, 744–745, 860]
C–In–Ti	Plotted partially at 1300 °C: Ti_2InC ($M_{n+1}AX_n$-phase), Ti_3InC, Ti_3In_4 (<~795 °C), TiC_{1-x} (solubility of In ≤ 5 at.%), α-Ti, β-Ti, In, C The extension of homog. range for both ternary compounds in the system is ~2–4 at.%.	[587, 680–681, 744–745, 859–860]
C–In–Zr	No diagram plot Zr_2InC ($M_{n+1}AX_n$-phase)	[680–681, 744–745, 860]
C–Ir–Mo	Plotted at 1500 °C: ~Mo_2Ir_2C (stable at least at temp. <1500 °C, ?), $Ir_{3-x}Mo$ (<2300 °C), ε-$IrMo_{1\pm x}$ (from 1400–1620 °C to 2270 °C), $IrMo_{1\pm x}$ (<1600–1620 °C), σ-Ir_3Mo_{7+x} (from ~1970–1980 °C to ~2080–2110 °C), $IrMo_{3+x}$ (<2100–2120 °C), β-$Mo_{2\pm x}C$, Mo, Ir, C	[244, 391, 431]
C–Ir–Nb	Plotted at 1500 °C: $Ir_{3\pm x}Nb$ (<2435–2440 °C), α_2-$IrNb_{1-x}$ (<~1985 °C), α_1-$IrNb_{1-x}$ (<~1900 °C), σ-$IrNb_{2-x}$ (<~2060 °C), $IrNb_{3\pm x}$ (<2125–2130 °C), β-$Nb_{2+x}C$, ζ-Nb_4C_{3-x}, NbC_{1-x}, Nb, Ir, C Depend. on compos., graphite is in equilibrium with $Ir_{3\pm x}Nb$ + NbC_{1-x} or $Ir_{3\pm x}Nb$ + (Ir,Nb).	[244, 391, 431]
C–Ir–Rh	No diagram plot Eutectic (50 % Ir + 50 % Rh)–C (1930 °C)	[138]

(continued)

Table 2.14 (continued)

System	Type of phase diagram (temperature and composition sections, constituent phases or phase fields) and/or character of interphase interaction and materials compatibility	References
C–Ir–Sc	No digram plot $ScIr_3C$, α-Sc_3IrC_4, β-Sc_3IrC_4	[986–988]
C–Ir–Si	Plotted at 1340 °C: $IrSi_3$ (at least at ~1400–1500 °C), $IrSi_2$ (at least at ~1400–1500 °C), Ir_2Si_3 (or $IrSi_{\sim 1.5}$, at least at ~1250–1400 °C), IrSi (at least at ~1500 °C), Ir_3Si_2 (or $Ir_{1.5}Si$, at least from ~500–700 °C to ~1500 °C), Ir_2Si (at least at ~1500 °C), Ir_3Si (at least at ~1500 °C), SiC, Si, Ir, C	[431, 503–504]
C–Ir–Ta	Plotted at 1500 °C: β-$Ir_{3\pm x}Ta$ (<2450–2455 °C), γ-Ir_3Ta_{2+x} (or α_2-Ir_3Ta_{2+x}, <1860–1865 °C), δ-$IrTa_{1-x}$ (or α_1-$IrTa_{1-x}$, <~2120–2125 °C), σ-$IrTa_{3\pm x}$ (<2475–2480 °C), α-$Ta_{2+x}C$, β-$Ta_{2\pm x}C$, ζ-Ta_4C_{3-x}, $Ta_6C_{5\pm x}$, TaC_{1-x},Ta, Ir, C Depend. on compos., graphite is in equilibrium with β-$Ir_{3\pm x}Ta$ + TaC_{1-x} or β-$Ir_{3\pm x}Ta$ + (Ir,Ta).	[244, 391, 431]
C–Ir–Th	No diagram plot $Th_xIr_yC_z$ (?)	[391]
C–Ir–Ti	Plotted at 1500 °C: $Ti_{3-x}Ir$ (<1515 °C), α-$TiIr_{1\pm x}$ (<~1745 °C), β-$TiIr_{1\pm x}$ (<~2130 °C), $TiIr_{3\pm x}$ (<~2115–2125 °C), TiC_{1-x}, β-Ti, Ir, C Depend. on compos., graphite is in equilibrium with $TiIr_{3\pm x}$ + TiC_{1-x} or $TiIr_{3\pm x}$ + (Ir,Ti).	[244, 391, 431]
C–Ir–U	Plotted at 1300 °C: U_2IrC_2, U_3Ir (~750–945 °C), U_2Ir (<~775 °C), α-U_3Ir_2 (<~900 °C), β-U_3Ir_2 (~900–1120 °C), UIr (<1470 °C), UIr_2 (<~1850–1875 °C), UIr_3 (<~2000–2005 °C), $UC_{1\pm x}$, ζ-U_2C_3, U, Ir, C	[242, 244, 391, 431, 693]
C–Ir–V	Plotted at 1500 °C: $V_{3\pm x}Ir$ (<~1900–1960 °C), VIr_{1+x} (≤~at least 1880 °C), $V_{1-x}Ir_{1+x}$ (or $(V_{1-x}Ir_x)Ir$, $0.04 < x < 0.19$, ≤at least 1900 °C), $VIr_{3\pm x}$ (≤at least 2000 °C), β-$V_{2\pm x}C$, β'-$V_{2+x}C$, ζ-V_4C_{3-x}, $V_6C_{5\pm x}$, $V_8C_{7\pm x}$,VC_{1-x}, V, Ir, C Depend. on compos., graphite is in equilibrium with $VIr_{3\pm x}$ + VC_{1-x} or $VIr_{3\pm x}$ + (Ir,V).	[391, 431]
C–Ir–W	Plotted at 2000 °C: ~W_2Ir_2C (?), δ-$Ir_{3-x}W$ (?), β-$Ir_3W_{2\pm x}$ (<~2500 °C), ε-$IrW_{1\pm x}$ (?), σ-$IrW_{3\pm x}$ (from 1795–1850 °C to 2520–2570 °C), α-$W_{2+x}C$, β-$W_{2+x}C$, γ-$W_{2\pm x}C$, γ-WC_{1-x}, δ-$WC_{1\pm x}$, W, Ir, C	[244, 391, 431]
C–Ir–Y	Plotted partially at 1100–1500 °C: Y_3Ir (<1425 °C), Y_5Ir_2 (<1525 °C), $Y_{64}Ir_{37}$ (?), α'-$Y_5Ir_{3\pm x}$ (?), α-$Y_5Ir_{3\pm x}$ (?), β-$Y_5Ir_{3\pm x}$ (<1600 °C), Y_3Ir_2 (<1725 °C), YIr (<2150 °C), $YIr_{2\pm x}$ (<2400 °C), YIr_3 (<2100 °C), $Y_{2\pm x}C$, $YC_{1\pm x}$, α-Y_4C_5, β-Y_4C_5, α-Y_3C_{4-x}, β-Y_3C_{4-x}, α-Y_2C_{3-x}, β-Y_2C_{3-x}, α-YC_2, β-$YC_{2\pm x}$, α-Y, β-Y, Ir, C Depend. on compos., graphite is in equilibrium with $YIr_{2\pm x}$ + Ir, or $YIr_{2\pm x}$ + α-YC_2.	[990]

(continued)

Table 2.14 (continued)

System	Type of phase diagram (temperature and composition sections, constituent phases or phase fields) and/or character of interphase interaction and materials compatibility	References
C–Ir–Zr	Plotted at 1500 °C: Zr_3Ir (<1305 °C), Zr_2Ir (<1340 °C), Zr_5Ir_3 (<1730 °C), α-$ZrIr_{1-x}$ (<900–950 °C), β-$ZrIr_{1\pm x}$ (from 900–950 °C to 2050 °C), $ZrIr_2$ (<2085 °C), $ZrIr_{3\pm x}$ (<2280 °C), ZrC_{1-x}, α-Zr, β-Zr, Ir, C Depend. on compos., graphite is in equilibrium with $ZrIr_{3\pm x}$ + ZrC_{1-x}, or $ZrIr_{3\pm x}$ + (Ir,Zr).	[244, 391, 431]
C–La–N–Th	No diagram plot $ThC_{1\pm x}$–$LaN_{1\pm x}$ carbonitride continuous solid solution	[391]
C–La–U	Plotted at 1500 °C: β-$(La,U)C_{2\pm x}$ (extended dicarbide solid solution based on β-$LaC_{2\pm x}$), $UC_{1\pm x}$, ζ-U_2C_3, La_2C_{3-x}, U, La, C The solubilities of 'LaC' in $UC_{1\pm x}$ and La_2C_{3-x} in ζ-U_2C_3 are <1 mol.%.	[244, 391]
C–Lu–U	No diagram plot $UC_{1\pm x}$–LuC_{1-x} (or $Lu_{3-x}C$) monocarbide continuous solid solution or extended solid solution based on $UC_{1\pm x}$.	[391]
C–Mg–Mo–O	No diagram plot At 1800–2300 °C the interaction between MgO and β-$Mo_{2\pm x}C$ is weak.	[242]
C–Mg–Nb–O	No diagram plot At 1800–2300 °C, in vacuum MgO and NbC_{1-x} interact with the formation of Nb and NbC_xO_y	[242]
C–Mg–O	No diagram plot $MgCO_3$, MgC_2O_4 In vacuum (0.01–0.05 Pa), the interaction between C and MgO is ruled by chemical boundary reaction stage (linear law) and initiates in powdered mixtures from ~1350 °C and on bulk materials contacts—from ~1800 °C.	[138, 194]
C–Mg–O–Si	No diagram plot At 1600 °C MgO and SiC interact intensively.	[242]
C–Mg–O–Ta	No diagram plot In vacuum, the interaction between MgO and TaC_{1-x} initiates at temp. >2200–2300 °C.	[138, 242]
C–Mg–O–Ti	No diagram plot At 1600–1900 °C, in He MgO and TiC_{1-x} interact with the formation of Mg_2TiO_4, $TiO_{1\pm x}$ and CO; at 1800–2300 °C, in vacuum—with the formation of C, Mg and TiC_xO_y.	[242]
C–Mg–O–W	No diagram plot At 1800–2300 °C the interaction between MgO and δ-$WC_{1\pm x}$ is weak.	[242]
C–Mg–O–Zr	No diagram plot At 2000–2300 °C in vacuum MgO and ZrC_{1-x} interact with the formation of C, Mg and ZrC_xO_y.	[242]

(continued)

Table 2.14 (continued)

System	Type of phase diagram (temperature and composition sections, constituent phases or phase fields) and/or character of interphase interaction and materials compatibility	References
C–Mn–Nb	No diagram plot At 1350 °C the interaction between NbC_{1-x} and Mn leads to the formation of eutectic alloy and solid solutions.	[242]
C–Mn–Mo	Plotted at 800 °C: η-Mo_3Mn_3C, Mo_2Mn_4C, α-$(Mo,Mn)_{2+x}C$ (extended solid solution based on α-$Mo_{2+x}C$), σ-Mn_5Mo_{3-x} (from 1075–1105 °C to 1300–1500 °C), μ-$Mn_5Mo_{4\pm x}$ (<1400–1600 °C), ε-$Mn_{4\pm x}C$, $Mn_{23}C_6$, $Mn_{15}C_4$, Mn_3C, Mn_5C_2, Mn_7C_3, α'-$Mo_{2+x}C$, γ-MoC, α-Mn, β-Mn, γ-Mn, Mo, C Depend. on compos., graphite is in equilibrium with α-$(Mo,Mn)_{2+x}C$, or α-$(Mo,Mn)_{2+x}C$ + Mn_7C_3, or Mn_7C_3.	[391]
C–Mn–Si	Plotted at 1000 and 1130 °C: Mn_5SiC (Nowotny phase), Mn_8Si_2C, $Mn_5Si_3C_x$ (<1285–1300 °C, solid solution based on Mn_5Si_3), $Mn_{6\pm x}Si$ (<880 °C), ν-$Mn_9Si_{2\pm x}$ (<1060 °C), α-$Mn_{3-x}Si$ (<~675 °C), β-$Mn_{3\pm x}Si$ (from ~675 °C to 1070–1075 °C), Mn_5Si_2 (<850 °C), $MnSi_{1-x}$ (<1270–1275 °C), $Mn_{11}Si_{19\pm x}$ (or $MnSi_{1.75-x}$, <1150–1155 °C), θ-$MnSi_2$ (or θ-$Mn_{15}Si_{26}$, ?), ε-$Mn_{4\pm x}C$, $Mn_{23}C_6$, $Mn_{15}C_4$, Mn_3C, Mn_5C_2, Mn_7C_3, SiC, β-Mn, γ-Mn, δ-Mn, Si, C The solubility of Mn in SiC is very low (~2×10^{-4} at.% at 1850 °C and ~2×10^{-2} at.% at 1950 °C).	[244, 299, 393, 431, 503, 769–770]
C–Mn–U	No diagram plot $UMnC_2$	[391]
C–Mn–W	Plotted at 800 °C: η-W_3Mn_3C, κ-W_3MnC_{1-x}, $(Mn,W)_2C$ (or ~$Mn_7W_{0.5\div1}C_{2\div2.5}$), ε-$Mn_{4\pm x}C$, $Mn_{23}C_6$, $Mn_{15}C_4$, Mn_3C, Mn_5C_2, Mn_7C_3, δ-$WC_{1\pm x}$, α-Mn, β-Mn, W, C Depend. on compos., graphite is in equilibrium with δ-$WC_{1\pm x}$ + Mn_7C_3 or Mn_7C_3.	[391]
C–Mn–Zr	No diagram plot At 1300 °C the interaction between ZrC_{1-x} and Mn leads to the formation of eutectic alloy and solid solutions.	[242]
C–Mo–N	Plotted at 1100 °C: δ-$Mo(C,N)_{1\pm x}$ (extended solid solution based on δ-MoN or δ-MoN–'MoC' carbonitride continuous solid solution at higher temp.), α-$Mo_{2+x}(C,N)$ (extended solid solution based on α-$Mo_{2+x}C$ with max. solubility of γ-$Mo_{2\pm x}N$–65 mol.%), γ-$Mo_{2\pm x}N$, Mo, N, C	[391, 431, 476, 853]
C–Mo–N–Ti	TiC_{1-x}–$TiN_{1\pm x}$–α-MoC_{1-x}–δ-MoN is plotted at 1450 °C ($p_{N2} \leq 0.2$ MPa) and 1600–1650 °C ($p_{N2} \leq 0.3$ MPa): $(Ti,Mo)(C,N)_{1\pm x}$ (extended solid solution based on TiC_{1-x}–$TiN_{1\pm x}$ carbonitride continuous solid solution) TiC_{1-x}–$TiN_{1\pm x}$–α-MoC_{1-x} is partially plotted at 1600 °C: $(Ti,Mo)(C,N)_{1-x}$ (extended solid solution based on TiC_{1-x}) (Ti,Mo)(C,N) phase separates into two phases, of which one is richer in Ti and N than another; the two-phase field becomes smaller at higher temp.	[432, 584, 588]

(continued)

Table 2.14 (continued)

System	Type of phase diagram (temperature and composition sections, constituent phases or phase fields) and/or character of interphase interaction and materials compatibility	References
C–Mo–Nb	Plotted at 1400–3000 °C: (Nb,Mo)C_{1-x} (extended solid solution based on NbC_{1-x}, or NbC_{1-x}–α-MoC_{1-x} monocarbide continuous solid solution at 2000–2600 °C), β-$(Mo,Nb)_{2\pm x}C$ (extended solid solution based on β-$Mo_{2\pm x}C$ with max. Nb solubility corresp. to ~$(Mo_{0.6}Nb_{0.4})_2C$), β-$(Nb,Mo)_{2+x}C$ (solid solution based on β-$Nb_{2+x}C$ with max. Mo solubility—~3 at.%), η-MoC_{1-x}, (Nb,Mo), C The interaction between NbC_{1-x} and Mo initiates from 1700–1800 °C (5 h exposure) and becomes noticeable at 2000–2200 °C (2 h exposure). Under specific pressure 5 MPa the diffusion welded joint between NbC_{1-x} and Mo is produced at 1600 °C (5–15 min exposure).	[138, 242, 391, 433–434, 773, 827, 837, 853]
C–Mo–Nb–Ta	β-$Mo_{2\pm x}C$–β-$Nb_{2+x}C$–α-$Ta_{2+x}C$ is plotted at 1650 and 2000 °C: $(Ta,Nb,Mo)_{2\pm x}C$ (based on β-$Nb_{2+x}C$–α-$Ta_{2+x}C$ semicarbide continuous solid solution), β-$(Mo,Ta,Nb)_{2\pm x}C$ (solid solution based on β-$Mo_{2\pm x}C$), $(Ta,Nb,Mo)_{2\pm x}C$ + (Ta,Nb,Mo)C_{1-x} + (Mo,Nb,Ta), (Ta,Nb,Mo)C_{1-x} + (Mo,Nb,Ta), β-$(Mo,Ta,Nb)_{2\pm x}C$ + (Ta,Nb,Mo)C_{1-x} + (Mo,Nb,Ta)	[435]
C–Mo–Nb–U	α-MoC_{1-x}–NbC_{1-x}–$UC_{1\pm x}$ is plotted at 2000 °C: (U,Nb,Mo)C_{1-x} (based on NbC_{1-x}–$UC_{1\pm x}$ monocarbide continuous solid solution), $UMoC_2$, α-(Mo,Nb,U)C_{1-x} (based on α-MoC_{1-x})	[436]
C–Mo–Nb–Zr	α-MoC_{1-x}–NbC_{1-x}–ZrC_{1-x} is plotted at 2000 °C: (Zr,Nb,Mo)C_{1-x} (based on NbC_{1-x}–ZrC_{1-x} continuous solid solution), α-(Mo,Zr,Nb)C_{1-x} (based on α-MoC_{1-x})	[436]
C–Mo–Ni	Plotted at 1000 °C: η_1-Mo_6Ni_6C, $\eta_{1,2}$-$Mo_{3\div4}Ni_{2\div3}C$, β-$Ni_{4+x}Mo$ (<865–875 °C), γ-$Ni_{3+x}Mo$ (<905–915 °C), δ-$NiMo_{1\pm x}$ (or μ-$MoNi_{1\pm x}$, <~1360–1365 °C), α-$Mo_{2+x}C$, α′-$Mo_{2+x}C$, Mo, Ni, C β-$Mo_{2\pm x}C$–Ni is plotted: eutectic—1265 °C, ~9 mol.% β-$Mo_{2\pm x}C$; the solubility of β-$Mo_{2\pm x}C$ in Ni is ~2.5 mol.% (at eutectic temp.) and ~1.5 mol.% (at 950 °C), and that of Ni in β-$Mo_{2\pm x}C$ is ~21 mol.% (at eutectic temp.) and ~10–11 mol.% (at 950 °C)	[242, 244, 391, 408]
C–Mo–O	Plotted partially at 930 and 1530 °C: β-$MoO_{2\pm x}$ (<2125–2325 °C), α-$Mo_{2+x}C$, α′-$Mo_{2+x}C$, β-$Mo_{2\pm x}C$, Mo, O, C	[431, 575, 853]
C–Mo–O–Zr	No diagram plot At 1500–2000 °C the interaction between β-$Mo_{2\pm x}C$ and ZrO_{2-x} results in the formation of ZrC_xO_y and Mo.	[242]
C–Mo–Os	Plotted at 1500 °C: ~$Mo_3Os_3C_2$ (<1500–1530 °C), β-$Mo_{3\pm x}Os$ (<2210 °C), σ-$Mo_{2\pm x}Os$ (<2420–2440 °C), β-$Mo_{2\pm x}C$, Mo, Os, C The mutual solubilities of all the constituent binary phases are low. Depend. on compos., graphite is in equilibrium with (Os,Mo) or (Os,Mo) + β-$Mo_{2\pm x}C$.	[244, 391, 431]

(continued)

Table 2.14 (continued)

System	Type of phase diagram (temperature and composition sections, constituent phases or phase fields) and/or character of interphase interaction and materials compatibility	References
C–Mo–Pt	Plotted at 1100 and 1500 °C: $\sim Mo_{5\text{-}6}Pt_{4\text{-}5}C_{1\text{-}1.1}$ (at least $>$ 1230–1260 °C), η-$Pt_{2\pm x}Mo$ ($<\sim$ 1780–1820 °C), δ-$PtMo_{1\pm x}$ ($<$1280–1320 °C), ε'-$PtMo_{3-x}$ ($<\sim$ 1455–1910 °C), ε-$PtMo_{3-x}$ (from 1455–1495 °C to $\sim$2155–2195 °C), β-$PtMo_{6-x}$ (from 1270–1290 °C to 1760–1800 °C), α-$Mo_{2\pm x}C$, α'-$Mo_{2+x}C$, β-$Mo_{2\pm x}C$, Mo, Pt, C	[244, 391, 431]
C–Mo–Pu	Plotted at 20, 900 and 1000 °C: α-$PuMoC_2$ ($<$1680 °C), β-$PuMoC_2$ (from 1680 °C to 2130–2170 °C, congruent melt. point), η-$Pu_4Mo_3C_3$ (or Pu_2MoC_2, $<\sim$ 1900 °C, congruent melt. point, ?), PuC_{1-x}, Pu_2C_{3-x}, α-$Mo_{2+x}C$, α'-$Mo_{2+x}C$, β-$Mo_{2\pm x}C$, η-MoC_{1-x}, α-Pu, β-Pu, γ-Pu, δ-Pu, δ'-Pu, ε-Pu, Mo, C Eutectic η-$Pu_4Mo_3C_3$–PuC_{1-x}–ε-Pu ($\sim$610–630 °C) Depending on compos., graphite is in equilibrium with $PuMoC_2 + Pu_2C_{3-x}$ or $PuMoC_2 + \alpha$-$Mo_{2+x}C$.	[242, 391, 906]
C–Mo–Pu–U	No diagram plot (U,Pu)MoC_2 ($PuMoC_2$–$UmoC_2$ dicarbide continuous solid solution), (U,Pu)MoC_{2-x} (or (U,Pu)$MoC_{1.7}$, solid solution based on $UMoC_{2-x}$, or $UMoC_{1.7}$)	[391]
C–Mo–Re	Plotted at 1400 and 1500 °C: π-Mo_3Re_2C (at least at 1400 °C, ?), $\sim MoReC_{1-x}$ ($x \approx 0.2$ at least at $\sim$1400–1500 °C, ?), β-$(Mo,Re)_{2\pm x}C$ (β-$Mo_{2\pm x}C$–Re continuous solid solution), α-$(Mo,Re)C_{1-x}$ (extended solid solution based on α-MoC_{1-x} with the max. solubility of Re corresp. to compos. $\sim(Mo_{0.2}Re_{0.8})C_{1-x}$), σ-$Mo_2Re_{3\pm x}$ (from 1100–1150 to 2620–2670 °C), χ-$MoRe_{3+x}$ ($<$1970–2030 °C), Mo, Re, C The presence of Re stabilizes α-MoC_{1-x}.	[138, 244, 391, 431, 581–583, 603, 811]
C–Mo–Rh	Plotted at 1100 and 1500 °C: $\sim Mo_2Rh_2C$ (at least $>\sim$ 1360 °C), $Rh_{3\pm x}Mo$ ($<$1180–1220 °C), ε-$Rh_{2\pm x}Mo$ (from $\sim$1000–1200 to 2065–2085 °C), ε'-$RhMo_{1\pm x}$ ($<$975–1125 °C), β-$Mo_{2\pm x}C$, Mo, Rh, C	[244, 391, 431]
C–Mo–Ru	Plotted at 1100 and 1500 °C: $\sim Mo_3Ru_3C_2$ (at least $>\sim$ 1300 °C), σ-$Ru_3Mo_{5\pm x}$ (from $\sim$1145 °C to 1915–1920 °C), α-$Mo_{2+x}C$, α'-$Mo_{2+x}C$, β-$Mo_{2\pm x}C$, Mo, Ru, C	[244, 391, 431, 853]
C–Mo–Sc	Partially plotted at 1200 °C: $(Sc,Mo)C_{1-x}$ (α-MoC_{1-x}–ScC_{1-x} monocarbide continuous solid solution), α-Sc_4C_3, β-Sc_4C_{3+x}, Sc_3C_{4-x} (or $Sc_{15}C_{19\pm x}$), α-$Mo_{2+x}C$, α'-$Mo_{2+x}C$, β-$Mo_{2\pm x}C$, η-MoC_{1-x}, γ-MoC, Mo, α-Sc, β-Sc, C	[244–245, 431]

(continued)

Table 2.14 (continued)

System	Type of phase diagram (temperature and composition sections, constituent phases or phase fields) and/or character of interphase interaction and materials compatibility	References
C–Mo–Si	Plotted at 1100–1730 °C: $Mo_{5-y}Si_3C_x$ ($x \approx 0.6 \div 1.0$, $y \approx 0.2 \div 1.0$, or $Mo_3(Si_xMo_{1-x})_2(C_ySi_{1-x})_3$, $x = 0.10 \div 0.55$, $y = 0.15 \div 0.40$, or $Mo_9Si_7C_4$, Mo_8Si_5C, Mo_4Si_3C, at least at 1200–1700 °C, Nowotny phase), α-$MoSi_2$ (<1900 °C), β-$MoSi_2$ (from 1850–1900 °C to 2020 °C), $Mo_5Si_{3\pm x}$ (<2170–2180 °C), Mo_3Si (<2025–2065 °C), α-$Mo_{2+x}C$, α′-$Mo_{2+x}C$, β-$Mo_{2\pm x}C$, η-MoC_{1-x}, α-MoC_{1-x}, γ-MoC, SiC, Mo, Si, C SiC–Mo is plotted: $Mo_{5-y}Si_3C_x$, Mo_3Si, $Mo_5Si_{3\pm x}$ β-$Mo_{2\pm x}C$, α-MoC_{1-x}, SiC, Mo At 1600 °C, depend. On compos., graphite is in equilibrium with $Mo_{5-y}Si_3C_x$, $Mo_{5-y}Si_3C_x$ + SiC, or $Mo_{5-y}Si_3C_x$ + β-$Mo_{2\pm x}C$. In vacuum, the reaction between graphite and α-$MoSi_2$ begins at ~1500 °C (2 h contact exposure) and leads to the formation of $Mo_{5-y}Si_3C_x$ and SiC.	[138, 242, 244, 431, 437, 503, 630–632, 665, 736–738, 819]
C–Mo–Si–Ta	No diagram plot. At 1900–1950 °C in Ar atmosphere or low vacuum (~100 Pa) the interaction in TaC_{1-x}–$MoSi_2$ powder mixtures leads to the formation of SiC and $(Mo,Ta)_5Si_{3\pm x}$.	[894, 899]
C–Mo–Si–Zr	No diagram plot. At 1950 °C in Ar atmosphere the interaction in ZrC_{1-x}–$MoSi_2$ powder mixtures leads to the formation of SiC and $(Mo,Zr)_5Si_{3\pm x}$.	[894]
C–Mo–Ta	Plotted at 1400–3500 °C: $(Ta,Mo)C_{1-x}$ (extended solid solution based on TaC_{1-x}, or TaC_{1-x}–α-MoC_{1-x} monocarbide continuous solid solution at 2000–2600 °C), β-$(Mo,Ta)_2C$ (extended solid solution based on β-$Mo_{2\pm x}C$ or β-$Mo_{2\pm x}C$–β-$Ta_{2\pm x}C$ semicarbide continuous solid solution at 2300–2500 °C), α-$Ta_{2+x}C$, ζ-Ta_4C_{3-x}, (stabilized by Mo), $Ta_6C_{5\pm x}$, η-MoC_{1-x}, (Mo,Ta), C At higher temp. graphite is in equilibrium with single solid phase $(Ta,Mo)C_{1-x}$. In vacuum the interaction between TaC_{1-x} and Mo initiates from 2000 °C (5 h exposure). Under specific pressure 5 MPa the diffusion welded joint between TaC_{1-x} and Mo is produced at 1400 °C (5–15 min exposure).	[138, 242, 391, 419, 438–439, 723, 773, 827, 837]
C–Mo–Ta–V	β-$Mo_{2\pm x}C$–β-$V_{2\pm x}C$–α-$Ta_{2+x}C$ is plotted at 1650 and 2000 °C: $(Ta,V,Mo)_{2\pm x}C$ (based on β-$V_{2\pm x}C$–α-$Ta_{2+x}C$ and β-$V_{2\pm x}C$–β-$Mo_{2\pm x}C$ semicarbide continuous solid solutions), $(Ta,V,Mo)_{2\pm x}C$ + $(Ta,V,Mo)C_{1-x}$ + (Ta,V,Mo), $(Ta,V,Mo)C_{1-x}$ + (Ta,V,Mo)	[435]
C–Mo–Tc	Plotted schematically	[840]
C–Mo–Th	Plotted at 1500 °C: $Th_xMo_yC_z$ (?), η-$(Mo,Th)C_{1-x}$, β-$Mo_{2\pm x}C$, $ThC_{1\pm x}$ (γ-ThC_{2-x}), β-Th, Mo, C	[138, 391]

(continued)

Table 2.14 (continued)

System	Type of phase diagram (temperature and composition sections, constituent phases or phase fields) and/or character of interphase interaction and materials compatibility	References
C–Mo–Ti	Plotted at 1200–2750 °C: (Ti,Mo)C_{1-x} (TiC_{1-x}–α-MoC_{1-x} monocarbide continuous solid solution at 1900–2600 °C, or extended solid solution based on TiC_{1-x} with the max. solubility of Mo corresp. to compos. ~$Ti_{0.1}Mo_{0.9}C_{0.8}$ at 1500 °C and ~$Ti_{0.05}Mo_{0.95}C_{0.8}$ at 1750 °C), β-$Mo_{2\pm x}C$, η-MoC_{1-x}, β-Ti, Mo, C Eutectic (Ti,Mo)C_{1-x}–β-$Mo_{2\pm x}C$–(β-Ti,Mo) (2160 °C) Eutectic (Ti,Mo)C_{1-x}–(β-Ti,Mo) (2240 °C) TiC_{1-x}–Mo is plotted: eutectic—~2160–2310 °C, ~20 mol.% TiC_{1-x}; the solubility of Mo in TiC_{1-x} is ~35 mol.% and that of TiC_{1-x} in Mo is ~4–6 mol.% (at eutectic temp.) At higher temp. graphite is in equilibrium with single solid phase (Ti,Mo)C_{1-x}. In vacuum the interaction between TiC_{1-x} and Mo initiates at temp. >2000 °C (5 h exposure). Under specific pressure 5 MPa the diffusion welded joint between TiC_{1-x} and Mo is produced at 1600 °C (5–15 min exposure).	[138, 242, 391, 419, 440, 579, 767–768, 773, 821, 823, 827, 837, 1013]
C–Mo–U	Plotted at 550–2000 °C: $UMoC_{2-x}$ ($x \approx 0.3$, a low C form of $UMoC_2$), $UMoC_2$ (<2230–2350 °C (?), congruent melt. point), ω-UMo_2C_2 (metastable, ?), χ-UMoC (metastable, ?), UMo_2C (?), $MoU_{2\pm x}$ (<595–630 °C), $UC_{1\pm x}$, ζ-U_2C_3, α-UC_{2-x}, β-UC_{2-x}, α-$Mo_{2+x}C$, α′-$Mo_{2+x}C$, β-$Mo_{2\pm x}C$, η-MoC_{1-x}, α-MoC_{1-x}, γ-MoC, α-U, β-U, γ-U, Mo, C $UC_{1\pm x}$–Mo is plotted: eutectic—~1700–1800 °C $UMoC_{2-x}$–$UC_{1\pm x}$ is plotted: eutectic—2160 °C $UMoC_{2-x}$–β-$Mo_{2\pm x}C$ is plotted: eutectic—2270 °C $UMoC_{2-x}$–Mo is plotted: eutectic—~2000 °C $UMoC_{2-x}$–C is plotted: eutectic—2200 °C $UC_{1\pm x}$ and Mo are compatible with each other at temp. ≤1000–1100 °C; at 1000 °C (500 h exposure) the dimension of reaction zone between them reaches 10 μm. At 1200 °C the reaction results in the formation of β-$Mo_{2\pm x}C$ and metal U. At 1000–1200 °C the performance of UC_{2-x} in the contact with Mo is very similar.	[138, 242, 244, 391, 431, 441, 453, 612, 620, 812]
C–Mo–U–Zr	α-MoC_{1-x}–ZrC_{1-x}–$UC_{1\pm x}$ is plotted at 2000 °C: (U,Zr,Mo)$C_{1\pm x}$ (based on ZrC_{1-x}–$UC_{1\pm x}$ monocarbide continuous solid solution), $UMoC_2$, α-(Mo,Zr,U)C_{1-x} (solid solution based on α-MoC_{1-x}) At ~2000 °C ($U_{0.5}Zr_{0.5}$)$C_{1\pm x}$ reacts vigorously with metal Mo.	[436, 812]
C–Mo–V	Plotted at 1500–2000 °C: (V,Mo)C_{1-x} (extended solid solution based on VC_{1-x} or VC_{1-x}–α-MoC_{1-x} monocarbide continuous solid solution at higher temp.), β-$(V,Mo)_{2\pm x}C$ (β-$V_{2\pm x}C$–β-$Mo_{2\pm x}C$ semicarbide continuous solid solution), η-MoC_{1-x}, α-MoC_{1-x}, (V,Mo), C	[242, 391, 442, 773, 827, 837]

(continued)

Table 2.14 (continued)

System	Type of phase diagram (temperature and composition sections, constituent phases or phase fields) and/or character of interphase interaction and materials compatibility	References
C–Mo–W	Plotted at 1000–2500 °C: (W,Mo)C (γ-MoC–δ-$WC_{1\pm x}$ monocarbide continuous solid solution at temp. <1100–1200 °C, or extended solid solution based on δ-$WC_{1\pm x}$ at higher temp.), α-$(Mo,W)C_{1-x}$ (α-MoC_{1-x}–γ-WC_{1-x} continuous solid solution at ~2550–2650 °C, or extended high temp. solid solution based on α-MoC_{1-x} with the max. solubility of W corresp. to compos. ~$(Mo_{0.75}W_{0.25})C_{0.65}$ at 2000 °C, ~$(Mo_{0.67}W_{0.33})C_{0.65}$ at 2100 °C, ~$(Mo_{0.33}W_{0.67})C_{0.65}$ at 2230 °C and ~$(Mo_{0.03}W_{0.97})C_{0.62}$ at 2500 °C), η-$(Mo,W)C_{1-x}$ (extended solid solution based on η-MoC_{1-x} with max. solubility of W corresp. to compos. ~$(Mo_{0.75}W_{0.25})C_{0.64}$ at 1850–2000 °C, ~$(Mo_{0.67}W_{0.33})C_{0.64}$ at 2100 °C and ~$(Mo_{0.5}W_{0.5})C_{0.64}$ at 2200–2500 °C), β-$(Mo,W)_{2\pm x}C$ (β-$Mo_{2\pm x}C$–α/β-$W_{2+x}C$ semicarbide continuous solid solution or extended solid solution based on β-$Mo_{2\pm x}C$ at lower temp.), (W,Mo), C At 1800–2000 °C Mo is compatible with δ-$WC_{1\pm x}$. Under specific pressure 5 MPa the diffusion welded joint between δ-$WC_{1\pm x}$ and Mo is produced at 1600 °C (5–15 min exposure).	[138, 241–242, 244, 391, 443, 764–766, 827, 837, 853]
C–Mo–W–Zr	ZrC_{1-x}–Mo–W is plotted partially at 1200, 1600 and 2000 °C: solubility of ZrC_{1-x} in the Mo-W solid solution decreases with fall in temp.; homog. range of the solid solution steadily decreases with rise in W content	[831]
C–Mo–Zr	Plotted at 1400–2100 °C: $(Zr,Mo)C_{1-x}$ (extended solid solution based on ZrC_{1-x}, or ZrC_{1-x}–α-MoC_{1-x} monocarbide continuous solid solution at higher temp.), β-$Mo_{2\pm x}C$, η-MoC_{1-x}, α-MoC_{1-x}, σ-$ZrMo_{2\pm x}$ (<~1880–2000 °C), Zr, Mo, C ZrC_{1-x}–Mo is plotted: eutectic—~2240–2280 °C, ~20–30 mol.% ZrC_{1-x}; the solubility of Mo in ZrC_{1-x} is >10 mol.% and that of ZrC_{1-x} in Mo is <20 mol.% (at eutectic temp.) At higher temp. graphite is in equilibrium with single solid phase $(Zr,Mo)C_{1-x}$. At 2000–2200 °C Mo is compatible with ZrC_{1-x} (2–5 h exposure). In vacuum the interaction between ZrC_{1-x} and Mo initiates from 1900 °C (5 h exposure). Under specific pressure 5 MPa the diffusion welded joint between ZrC_{1-x} and Mo is produced at 1300 °C (5–15 min exposure).	[138, 242, 244, 391, 431, 579, 773, 827, 835, 837]
C–N–Nb	NbC_{1-x}–δ-NbN_{1-x}–Nb is plotted at 1250–1450 °C: $Nb(C,N)_{1-x}$ (or NbC_yN_z, NbC_{1-x}–δ-NbN_{1-x} monocarbonitride continuous solid solution), β-$Nb_{2\pm x}(C,N)$ (or $Nb_2C_yN_z$, β-$Nb_{2+x}C$–β-$Nb_{2\pm x}N$ semicarbonitride continuous solid solution), Nb	[242, 391, 444, 662, 863]
C–N–Nb–W	General consideration of the system	[915, 1023]

(continued)

Table 2.14 (continued)

System	Type of phase diagram (temperature and composition sections, constituent phases or phase fields) and/or character of interphase interaction and materials compatibility	References
C–N–Nd–Th	No diagram plot $ThC_{1\pm x}$–$NdN_{1\pm x}$ carbonitride continuous solid solution	[391]
C–N–O–Pu–U	See C–N–Pu–U in this table.	
C–N–O–Si	Plotted schematically at 1430–1840 °C: Si_2ON_2 (<∼1860 °C), SiO_2 (<∼1700 °C), β-Si_3N_4 (<∼1800–1900 °C), SiC, Si, O, N, C Si_3N_4–SiO_2–C is plotted at 1480–1850 °C: Si_2ON_2, SiO_2, β-Si_3N_4, SiC, C Si_3N_4–SiC–SiO_2 is plotted at 1810–1850 °C: Si_2ON_2, SiO_2, β-Si_3N_4, SiC, Si Si_2ON_2–SiC is plotted: gas eutectic—∼1840 °C, ∼25 mol.% SiC Si_2ON_2–C is plotted: graphite is in equilibrium with SiC + Si_2ON_2 at ∼1490 °C and ∼37 mol.% C	[244, 445–446]
C–N–O–Ti	No diagram plot $Ti(C,N,O)_{1\pm x}$ (or $TiC_xN_yO_z$, oxycarbonitride phase, TiC_{1-x}–$TiO_{1\pm x}$ oxycarbide, TiC_{1-x}–δ-$TiN_{1\pm x}$ carbonitride and δ-$TiN_{1\pm x}$–$TiO_{1\pm x}$ oxynitride continuous solid solutions)	[411]
C–N–O–Zr	ZrC_{1-x}–$ZrN_{1\pm x}$–'ZrO' is plotted at 1600 and 2000 °C: homog. range limits of ZrC_{1-x}–$ZrN_{1\pm x}$ carbonitride continuous solid solution ($ZrC_xN_yO_z$, oxycarbonitride phase) are ∼$ZrC_{0.45}O_{0.55}$ and ∼$ZrN_{0.65}O_{0.35}$ (1600 °C) and ∼$ZrC_{0.25}O_{0.75}$ and ∼$ZrN_{0.45}O_{0.55}$ (2000 °C)	[411–412]
C–N–Pr–Th	No diagram plot $ThC_{1\pm x}$–$PrN_{1\pm x}$ carbonitride continuous solid solution	[391]
C–N–Pu–U	(U,Pu)–C–N is plotted at 1480 °C (taking into account the presence of O): $(U_{1-x}Pu_x)C_{1-y-z}N_yO_z$ ($(U_{1-x}Pu_x)C_{1\pm u}$–$(U_{1-x}Pu_x)N_{1-u}$ carbonitride continuous solid solution contaminated with O, $z = 0 \div 0.15$), $(U_{1-x}Pu_x)_2C_{3-x}$, α-$(U_{1-x}Pu_x)C_2$, α-U_2N_{3+x} (<∼1130 °C), β-U_2N_{3-x} (from ∼940–1100 °C to ∼1350 °C), (U,Pu), N, C $(U,Pu)_{0.49}N_{0.49}C_{0.02}$–$(U,Pu)_{0.49}N_{0.51}$–$(U,Pu)_{0.51}N_{0.49}$ is plotted at 730 °C and 1230 °C (O concentration—500 and 2000 ppm): $(U_{1-x}Pu_x)C_{1-y-z}N_yO_z$, $(U,Pu)O_{2\pm x}$ (<∼2370–2860 °C), α-U_2N_{3+x}, β-U_2N_{3-x}, (U,Pu), N, C Graphite is in equilibrium with $(U_{1-x}Pu_x)C_{1-y-z}N_yO_z$, or α-U_2N_{3+x} (β-U_2N_{3-x}) and $(U_{1-x}Pu_x)C_{1-y-z}N_yO_z$.	[447–448, 595]

(continued)

Table 2.14 (continued)

System	Type of phase diagram (temperature and composition sections, constituent phases or phase fields) and/or character of interphase interaction and materials compatibility	References
C–N–Si	Plotted at 1415–2700 °C (total pressure—0.1 MPa): α-SiC_2N_4 (?), β-SiC_2N_4 (<900 °C), α-Si_2CN_4 (?), β-Si_2CN_4 (<1000 °C), SiC_xN_y (?), α-Si_3N_4 (metastable, ?), β-Si_3N_4 (<~1800–1900 °C), SiC, Si, N, C Si_3N_4–SiC is plotted: Si_3N_4, SiC, Si At 1780 °C the solubility limit of SiC in β-Si_3N_4 is ~2 mol.%. At temp. <1500 °C the nitridation of C–Si mixtutres leads to the formation of β-Si_3N_4 and β-SiC. The polytype stability and the structural failures in SiC are affected by N_2 pressure.	[138, 359, 445, 571–572, 760–763, 887]
C–N–Si–Ti	Plotted at 1650 °C: TiC_xN_z (TiC_{1-x}–δ-$TiN_{1\pm x}$ carbonitride continuous solid solution), β-Si_3N_4 (<~1800–1900 °C), SiC, Ti, Si, N, C Graphite is in equilibrium with $TiC_{1-x}N_x$ ($0 < x < 0.66$) and $TiC_{0.34}N_{0.66}$ + SiC, SiC—with $TiC_{1-x}N_x$ ($0.66 < x < 0.87$) and $TiC_{0.13}N_{0.87}$ + β-Si_3N_4 and β-Si_3N_4 + Si, β-Si_3N_4—with $TiC_{1-x}N_x$ ($0.87 < x < 1.0$) and δ-$TiN_{1\pm x}$ + N_2. Thin film $Ti_3Si(C,N)_2$ ($M_{n+1}AX_n$-phase carbonitride solid solution) were synthesized.	[571, 642, 744–745]
C–N–Sm–Th	No diagram plot $ThC_{1\pm x}$–$SmN_{1\pm x}$ carbonitride continuous solid solution	[391]
C–N–Ta	TaC_{1-x}–δ-TaN_{1-x}–Ta is plotted at 1250, 1450 and 1900 °C: $Ta(C,N)_{1-x}$ (or TaC_yN_z, TaC_{1-x}–δ-TaN_{1-x} monocarbonitride continuous solid solution), $Ta_{2\pm x}(C,N)$ (or $Ta_2C_yN_z$, α-$Ta_{2+x}C$–γ-$Ta_{2\pm x}N$ semicarbonitride continuous solid solution at higher temp., or extended solid solutions based on α-$Ta_{2+x}C$ and γ-$Ta_{2\pm x}N$ at lower temp.), ε-TaN, ζ-Ta_4C_{3-x}, Ta At 1150–2370 °C the interaction between C and δ-TaN_{1-x} converts the nitride phase into carbonitride or carbide phases.	[138, 242, 244, 391, 431, 662]
C–N–Ta–U	No diagram plot At 1400 °C (66 h exposure) small reaction zone was found on the contact surface between metal Ta with $UC_{0.7}N_{0.3}$ and $UC_{0.4}N_{0.6}$, at 1800 °C (3 h exposure)—the interaction is noticeable.	[822]
C–N–Ta–W	General consideration of the system	[803, 1023]
C–N–Th	Plotted at 1500–2200 °C: ThCN, $Th(C,N)_{1-x}$ (or ThC_yN_z, $ThC_{1\pm x}$–$ThN_{1\pm x}$ and $ThC_{1\pm x}$–α-Th continuous solid solutions with miscibility gaps), $Th_3N_{4\pm x}$, γ-ThC_{2-x}, α-Th, β-Th, N, C	[391, 449]

(continued)

Table 2.14 (continued)

System	Type of phase diagram (temperature and composition sections, constituent phases or phase fields) and/or character of interphase interaction and materials compatibility	References
C–N–Ti	TiC_{1-x}–δ-$TiN_{1\pm x}$–Ti is plotted at 500–2000 °C: $Ti(C,N)_{1-x}$ (or TiC_xN_z, $0.33 \le x + z \le 1.04$, TiC_{1-x}–δ-$TiN_{1\pm x}$ carbonitride continuous solid solution with homog. range: $TiC_{0.48}$–$TiC_{0.95}$–$TiN_{0.43}$–$TiN_{1.0}$ at 1650 °C and $TiC_{0.75}$–$TiC_{1.0}$–$TiN_{0.69}$–$TiN_{1.0}$ at 500 °C), ζ-Ti_4N_{3-x} (at least at ~1000–1200 °C, ?), η-Ti_3N_{2-x} (at least at ~1000 °C, ?), δ'-$Ti_5N_{3\pm x}$ (<800 °C), ε-$Ti_{2\pm x}N$ (<~1100 °C), α-Ti, β-Ti TiC_{1-x} ($x = 0.05$)–δ-$TiN_{1\pm x}$ ($TiN_{1.0}$) is plotted at pressure N_2 0.1 MPa	[138, 242, 391, 411, 454, 571, 584, 643, 977–979, 1010]
C–N–Ti–V	No diagram plot TiC_{1-x}–δ-VN_{1-x} carbonitride continuous solid solution	[241, 244, 391, 431]
C–N–Ti–W	TiC_{1-x}–δ-$WC_{1\pm x}$–δ-$TiN_{1\pm x}$–δ-WN_{1-x} is plotted at 1425 °C: $(Ti,W)(C,N)_{1\pm x}$ (extended solid solution based on TiC_{1-x}–δ-$TiN_{1\pm x}$ carbonitride continuous solid solution), δ-$W(C,N)_{1\pm x}$, C Upon increasing C concentration, graphite and δ-$W(C,N)_{1\pm x}$ are formed together with two (Ti,W)(C,N) phases, of which one is richer in Ti and N than another. The addition of N to $(Ti,W)C_{1-x}$ at 1750 °C also results in partitioning of the mixed carbonitride phase in a W-rich carbide with low N content $(W,Ti)(C,N)_{1\pm x}$ and W-poor Ti carbonitride $(Ti,W)(C,N)_{1\pm x}$.	[563, 584–586, 880, 1013]
C–N–U	Plotted at 800–2100 °C: $U_5C_8N_2$ (?), $U_6C_{13}N$ (?), $U(C,N)_{1\pm x}$ (or UC_xN_z, $UC_{1\pm x}$–UN_{1-x} monocarbonitride continuous solid solution with wider homog. range ($x + z \ne 1$) in the $UC_{1\pm x}$-rich area; in UC_xN_z + C equilibrium index z in compos. is affected by the pressure of N_2 and structural form of C), α-U_2N_{3+x} (<~1130 °C), β-U_2N_{3-x} (from ~940–1100 °C to ~1350–1550 °C at N_2 pressure 0.1 MPa), ζ-U_2C_3, α-UC_{2-x}, β-UC_{2-x}, U, N, C $UC_{1\pm x}$–UN_{1-x} is plotted: continuous solid solution, max. melt. point 2910 °C is corresp. to ~$UC_{0.3}N_{0.7}$ Essentially no solid solubility of N in ζ-U_2C_3, α-UC_{2-x}, β-UC_{2-x} or that of C in β-U_2N_{3-x}. At N_2 pressure 0.1 MPa, the U nitrides are more stable than the U carbides up to 1800 °C, but at 2000 °C, the U carbides β-UC_{2-x} and $U(C,N)_{1\pm x}$ become more stable. In vacuum or Ar graphite is in equilibrium with $U(C,N)_{1\pm x}$ + β-UC_{2-x}. For diffusion rate in the system at various temp. see Addendum.	[138, 244, 391, 450–451, 740–743, 759]
C–N–U–V	No diagram plot At 1000 °C (66 h exposure) the carburization or nitridation of metal V is occurred on the contact surface with $UC_{0.7}N_{0.3}$ and $UC_{0.4}N_{0.6}$, at 1400 °C (66 h exposure)—the interaction is significant.	[822]

(continued)

Table 2.14 (continued)

System	Type of phase diagram (temperature and composition sections, constituent phases or phase fields) and/or character of interphase interaction and materials compatibility	References
C–N–U–Zr	No diagram plot. At 1000 °C (66 h exposure) no appreciable reaction was occurred on the contact surface of metal Zr with $UC_{0.7}N_{0.3}$ and $UC_{0.4}N_{0.6}$, at 1400 °C (66 h exposure)—small reaction zone was found.	[822]
C–N–V	VC_{1-x}–δ-VN_{1-x}–V is plotted at 1400 °C: $V(C,N)_{1-x}$ (or VC_yN_z, VC_{1-x}–δ-VN_{1-x} continuous solid solution, ordering at low temp.), $V_{2\pm x}(C,N)$ (or $V_2C_yN_z$, β-$V_{2\pm x}C$–β-$V_{2+x}N$ continuous solid solution), V The ordering of VC_yN_z leads to the formation of a $V_6C_{5\pm x}$- or $V_8C_{7\pm x}$-type superstructure, depend. on compos.	[138, 391, 411, 643, 884]
C–N–W	No diagram plot. $WC_{1\pm x}N_y$ (extended solid solution based on δ-$WC_{1\pm x}$, ?)	[391, 541]
C–N–Zr	ZrC_{1-x}–$ZrN_{1\pm x}$–Zr is plotted at 1120–2000 °C: $Zr(C,N)_{1\pm x}$ (or ZrC_xN_z, $0.54 \le x + z \le 1.04$, ZrC_{1-x}–$ZrN_{1\pm x}$ continuous solid solution with homog. range: $ZrC_{0.59}$–$ZrC_{0.95}$–$ZrN_{0.56}$–$ZrN_{1.0}$ at 1150 °C), α-Zr, β-Zr ZrC_{1-x} ($x = 0.07$)–$ZrN_{1\pm x}$ ($ZrN_{0.81}$) is plotted	[138, 242, 244, 391, 411, 454, 584, 980]
C–Nb–Ni	Plotted at 1100 °C: η-Nb_4Ni_2C, Nb_3Ni_3C (?), Nb_6Ni_6C (?), Ni_8Nb (<535 °C), $Ni_{3\pm x}Nb$ (<~1400 °C), μ-Ni_6Nb_{7-x} (or μ-$NiNb_{1+x}$, <1290 °C), α-Nb_2C, β-$Nb_{2+x}C$, NbC_{1-x}, Ni, Nb, C NbC_{1-x}–Ni is plotted: eutectic—~1320–1345 °C, ~5–6 mol.% NbC_{1-x}; at the eutectic temp. the solubility of NbC_{1-x} in Ni is ~2–3 mol.% and that of Ni in NbC_{1-x}–~9 mol.%	[242, 244, 391, 431, 455–458]
C–Nb–Ni–Ta	NbC_{1-x} ($x = 0.2$)–TaC_{1-x} ($x = 0.1$)–Ni is plotted schematically: eutectic—from 1330 °C (NbC_{1-x}–Ni) to 1350 °C (TaC_{1-x}–Ni), ~5–6 mol.% $(Nb,Ta)C_{1-x}$ (NbC_{1-x}–TaC_{1-x} monocarbide continuous solid solution); at the eutectic temp. the solubility of $(Nb,Ta)C_{1-x}$ in Ni is ~3.0–3.5 mol.%	[459]
C–Nb–Ni–V	NbC_{1-x} ($x = 0.1$)–VC_{1-x} ($x \approx 0.1$)–Ni is plotted: eutectic—~1285–1315 °C, 3 mol.% $(Nb,V)C_{1-x}$, 6 mol.% $(V,Nb)C_{1-x}$; at the eutectic temp. the max. solubility of NbC_{1-x} in VC_{1-x} is ~15 mol.%, in Ni is ~3 mol.% and that of VC_{1-x} in NbC_{1-x} is ~20 mol.%, in Ni is ~3 mol.% and that of Ni in NbC_{1-x} is ~9 mol.%, in VC_{1-x} is ~4 mol.%	[458]
C–Nb–Ni–Zr	NbC_{1-x}–ZrC_{1-x}–Ni is plotted: eutectic—from 1290 °C (ZrC_{1-x}–Ni) to 1330 °C (NbC_{1-x}–Ni), ~5–6 mol.% $(Nb,Zr)C_{1-x}$ (NbC_{1-x}–ZrC_{1-x} monocarbide continuous solid solution); at the eutectic temp. the solubility of $(Nb,Zr)C_{1-x}$ in Ni is 2–3 mol.% and that of Ni in $(Nb,Zr)C_{1-x}$ is ~6 mol.%	[460]

(continued)

Table 2.14 (continued)

System	Type of phase diagram (temperature and composition sections, constituent phases or phase fields) and/or character of interphase interaction and materials compatibility	References
C–Nb–O	Plotted at 1300–2000 °C: $Nb(C,O)_{1-x}$ (or NbC_xO_y, extended solid solution based on NbC_{1-x} with homog. limits: $NbC_{0.7}$–$Nb(C_{0.5}O_{0.15})$–$Nb(C_{0.35}O_{0.45})$–$Nb(C_{0.35}O_{0.65})$–$NbC_{0.99}$), β-$Nb_{2\pm x}(C,O)$ (or $Nb_2C_xO_y$, extended solid solution based on β-$Nb_{2+x}C$ with homogeneity limits: $Nb_2C_{0.8}$–$Nb_2(C_{0.3}O_{0.3})$–$Nb_2(C_{0.15}O_{0.7})$–$Nb_2(C_{0.35}O_{0.8})$–$Nb_2C_{1.0}$), NbO (<1945 °C), γ-$NbO_{2\pm x}$ (from ~900 °C to ~1910–1920 °C), β-Nb_2O_5 (<1495–1510 °C), Nb, O, C	[242, 244, 411, 431, 461]
C–Nb–O–Si	No diagram plot At 1100 °C (4 h exposure, C and O contamination from the vacuum system during annealing) in the reaction zone formed between SiC and Nb the following layer sequence is observed: SiC → Nb_5Si_4C (or NbC_{1-x}) → α-Nb_5Si_{3+x} → β-$Nb_{2+x}C$ → NbO → Nb.	[607]
C–Nb–O–W	No diagram plot At 1300–1400 °C, in vacuum the interaction between δ-$WC_{1\pm x}$ and β-Nb_2O_5 in powder mixtures results in the formation of W-Nb alloy.	[242, 808]
C–Nb–O–Zr	No diagram plot At 1300–2400 °C the interaction between NbC_{1-x} and ZrO_{2-x} results in the formation of mixed (complex) oxides and carbides.	[242]
C–Nb–Os	Plotted at 1500 °C: β-$Nb_{3-x}Os$ (<1975 °C), σ-$Nb_3Os_{2\pm x}$ (<2200 °C), χ-$Nb_2Os_{3\pm x}$ (<2270 °C), β-$Nb_{2+x}C$, NbC_{1-x}, Nb, Os, C Graphite is in equilibrium with (Os,Nb) + NbC_{1-x}. The solubility of Nb in Os (with the presence of C) and that of Os in NbC_{1-x} are low.	[244, 391, 431]
C–Nb–P	No diagram plot Nb_2PC ($M_{n+1}AX_n$-phase)	[680–681, 744–745, 860]
C–Nb–Pd	Plotted at 1300 °C: β-$Pd_{3\pm x}Nb$ (<~1610 °C), $Pd_{2\pm x}Nb$ (<~1610 °C), α-$Pd_{1\pm x}Nb$ (1255–1565 °C), β-$Nb_{2+x}C$, NbC_{1-x}, Nb, Pd, C Depend. on compos., graphite is in equilibrium with (Pd_xNb_{1-x}) alloy or ($Pd_{0.85}Nb_{0.15}$) alloy + NbC_{1-x}.	[242, 244, 391, 431]
C–Nb–Pt	Plotted at 1500 °C: α-$Pt_{3\pm x}Nb$ (<2040 °C), β-$Pt_{3\pm x}Nb$ (?), $Pt_{2\pm x}Nb$ (<1990 °C), α'-$PtNb_{1-x}$ (or α'-Pt, 1670–1780 °C), $Pt_{1+x}Nb_{1-x}$ (<1750 °C), σ-$PtNb_{2\pm x}$ (<1800 °C), $PtNb_{3\pm x}$ (<2040 °C), β-$Nb_{2+x}C$, NbC_{1-x}, Nb, Pt, C Depend. on compos., graphite is in equilibrium with (Pt,Nb) alloy + α-$Pt_{3\pm x}Nb$ or α-$Pt_{3\pm x}Nb$ + NbC_{1-x}.	[242, 244, 391, 431]
C–Nb–Pu	Plotted at 1600 °C: $(Nb,Pu)C_{1-x}$ (NbC_{1-x}–PuC_{1-x} monocarbide continuous solid solution, ?), Pu_2C_{3-x}, α-PuC_2, β-PuC_2, β-$Nb_{2+x}C$, Nb, Pu, C	[138, 242, 244, 391]

(continued)

Table 2.14 (continued)

System	Type of phase diagram (temperature and composition sections, constituent phases or phase fields) and/or character of interphase interaction and materials compatibility	References
C–Nb–Re	Plotted at 1800 and 2000 °C: σ-Nb_2Re_{3-x} (from 2160–2300 °C to 2400–2565 °C), χ-$NbRe_{3\pm x}$ (<2520–2745 °C), β-$Nb_{2+x}C$, NbC_{1-x}, Nb, Re, C NbC_{1-x}–Re is plotted: eutectic—2225 °C, ~30 mol.% NbC_{1-x}; the mutual solid solubilities of the components are low Graphite is in equilibrium with Re + NbC_{1-x}.	[244, 391, 431, 818]
C–Nb–Rh	Plotted at 1500 °C: $Rh_{3\pm x}Nb$ (<1950 °C), η-$Rh_{2\pm x}Nb$ (<~1900 °C), ζ-$Rh_{3\pm x}Nb_2$ (<~1625 °C), ε-$RhNb_{1-x}$ (from ~1335–1420 °C to ~1580–1600 °C), β-$RhNb_{1\pm x}$ (from ~1335–1420 to ~1550–1580 °C), δ-$RhNb_{1-x}$ (<~1420 °C), γ-$RhNb_{1-x}$ (<~1350 °C), σ-$RhNb_{2\pm x}$ (<1660 °C), $RhNb_{3\pm x}$ (<1220 °C), β-$Nb_{2+x}C$, NbC_{1-x}, Nb, Rh, C The solubility of C in $Rh_{3\pm x}Nb$ is low.	[391, 431]
C–Nb–Ru	Plotted at 1600 °C: $NbRu_3C_{1-x}$ ($x \approx 0.6$, stable in the limited range of temp.), $Ru_{3\pm x}Nb$ (<1540 °C), β-$Nb_{2+x}C$, NbC_{1-x}, Nb, C Graphite is in equilibrium with Ru + NbC_{1-x}.	[391, 431, 897]
C–Nb–S	No diagram plot Nb_2SC_{1-x} ($x = 0.6$, $M_{n+1}AX_n$-phase), α-Nb_2CS_2, β-Nb_2CS_2, ?	[680–681, 744–745, 860]
C–Nb–Si	Plotted at 800, 1300 and 1730 °C: α-$Nb_5Si_3C_x$ ($x = 0.04$), β-$Nb_5Si_3C_x$ ($0.04 < x < 0.33$), γ-$Nb_5Si_3C_x$ ($0.33 \le x \le 0.50$, ?), $Nb_3(Si_{1-x}C_x)$ ($x = 0.1$), Nb_2SiC, Nb_3SiC_2, α-Nb_4SiC_3, β-Nb_4SiC_3 ($M_{n+1}AX_n$-phases, ?), Nb_5Si_4C, $NbSi_3C$ (?), $Nb_{12}Si_7C$ (?), $Nb_{15}Si_4C$ (?), $NbSi_2$ (<~1920–1960 °C), α-Nb_5Si_{3+x} (<~1635–1960 °C), β-Nb_5Si_{3+x} (from ~1635 to 1960 °C to ~2490–2545 °C), Nb_3Si (~1655–2000 °C), α-Nb_2C, β-$Nb_{2+x}C$, NbC_{1-x}, SiC, Si, Nb, C NbC_{1-x}–$NbSi_2$ is plotted: eutectic (degenerated)—~1880–1920 °C, ~1 mol.% NbC_{1-x}; no mutual solubility Graphite is in equilibrium with SiC + NbC_{1-x}. In vacuum the reaction between graphite and $NbSi_2$ begins at ~1500 °C (2 h contact exposure) and leads to the formation of SiC and NbC_{1-x}.	[138, 242, 419, 431, 462–463, 503, 739, 744–745, 819, 836, 898, 901]
C–Nb–Sn	Plotted at 1300 °C: $Nb_{2\pm x}Sn_{1\pm y}C_{1-z}$ (from $Nb_{2.20}Sn_{0.80}C_{0.93}$ to $Nb_{1.92}Sn_{1.08}C_{0.91}$, $M_{n+1}AX_n$-phase), $Nb_{3\pm x}SnC_y$ (extended solid solution based on $Nb_{3\pm x}Sn$ with C content—up to 5 at.%, 775–2130 °C), β-$Nb_{2+x}C$, NbC_{1-x}, Sn, Nb, C The solubility of Sn in β-$Nb_{2+x}C$ and NbC_{1-x} is extremely low. Graphite is in equilibrium with NbC_{1-x} + Sn	[678–681, 744–745, 860]

(continued)

Table 2.14 (continued)

System	Type of phase diagram (temperature and composition sections, constituent phases or phase fields) and/or character of interphase interaction and materials compatibility	References
C–Nb–Ta	Plotted at 1500–3800 °C: (Nb,Ta)C_{1-x} (NbC_{1-x}–TaC_{1-x} monocarbide continuous solid solution), (Nb,Ta)$_{2\pm x}$C (β-$Nb_{2+x}C$–α-$Ta_{2+x}C$, β-$Nb_{2+x}C$–β-$Ta_{2\pm x}C$ and γ-$Nb_{2\pm x}C$–β-$Ta_{2\pm x}C$ (?) semicarbide continuous solid solutions with probable miscibility gaps (extended solid solutions) at 2200–2600 °C), (Nb,Ta), C Graphite is in equilibrium with (Nb,Ta)C_{1-x}.	[138, 242, 391, 419, 464, 813]
C–Nb–Ta–Ti	No diagram plot (Nb,Ta,Ti)C_{1-x} (NbC_{1-x}–TaC_{1-x}–TiC_{1-x} monocarbide continuous solid solution)	[138]
C–Nb–Ta–W	β-$Nb_{2+x}C$–α-$Ta_{2+x}C$–γ-$W_{2\pm x}C$ is plotted at 1650 and 2000 °C: (Nb,Ta,W)$_{2\pm x}$C (based on β-$Nb_{2+x}C$–α-$Ta_{2+x}C$ semicarbide continuous solid solution), (W,Nb,Ta)$_{2\pm x}$C (based on γ-$W_{2\pm x}C$), (Nb,Ta,W)$_{2\pm x}$C + (Nb,Ta,W)C_{1-x} + (Nb,Ta,W), (Nb,Ta,W)C_{1-x} + (Nb,Ta,W), (W,Nb,Ta)$_{2\pm x}$C + (Nb,Ta,W)C_{1-x} + (Nb,Ta,W) At 1650–2000 °C the max. solubilities of γ-$W_{2\pm x}C$ in (Nb,Ta,W)$_{2\pm x}$C (based on β-$Nb_{2+x}C$–α-$Ta_{2+x}C$ semicarbide continuous solid solution) reach ~3.5–14.0 mol.% (depend. on (Nb,Ta)$_{2+x}$C compos.). At 1450 °C the max. solubility of δ-$WC_{1\pm x}$ in (Nb,Ta,W)C_{1-x} (based on NbC_{1-x}–TaC_{1-x} monocarbide continuous solid solution) is ~9 mol.%.	[419, 435, 465–466]
C–Nb–Tc	Plotted schematically	[840]
C–Nb–Th	Plotted at 1500 °C: β-$Nb_{2+x}C$, NbC_{1-x}, $ThC_{1\pm x}$, (γ-ThC_{2-x}), β-Th, Nb, C The mutual solid solubilities of the components are low.	[391]
C–Nb–Ti	Plotted at 1500–3100 °C: (Nb,Ti)C_{1-x} (NbC_{1-x}–TiC_{1-x} monocarbide continuous solid solution), β-(Nb,Ti)$_{2+x}$C (semicarbide extended solid solution based on β-$Nb_{2+x}C$ at temp. ≤2280 °C, the max. solubility of Ti varies from ~5 to ~9 at.%), γ-$Nb_{2\pm x}C$ (at 2600 °C the max. solubility of Ti is ~1 at.%, ?), (β-Ti,Nb), C The (Nb,Ti)C_{1-x} monocarbide continuous solid solution miscibility gap (critical point—~50 °C at ~$Nb_{0.4}Ti_{0.6}C_{1-x}$, at 0 °C ranges from ~$Nb_{0.15}Ti_{0.85}C_{1-x}$ to ~$Nb_{0.7}Ti_{0.3}C_{1-x}$, calculated). Graphite is in equilibrium with (Nb,Ti)C_{1-x}. For diffusion rate in the system at various temp. see Addendum.	[138, 242, 391, 419, 440, 467–468, 813, 837, 1007]
C–Nb–Ti–U	NbC_{1-x}–TiC_{1-x}–$UC_{1\pm x}$ is plotted at 2000–2050 °C: (Nb,Ti,U)C_{1-x} (extended solid solution based on NbC_{1-x}–TiC_{1-x} and NbC_{1-x}–$UC_{1\pm x}$ monocarbide continuous solid solutions with great miscibility gap because of low mutual solubilities in the pair TiC_{1-x}–$UC_{1\pm x}$)	[391]

(continued)

Table 2.14 (continued)

System	Type of phase diagram (temperature and composition sections, constituent phases or phase fields) and/or character of interphase interaction and materials compatibility	References
C–Nb–Ti–V	NbC_{1-x}–TiC_{1-x}–VC_{1-x} is plotted schematically at 1000 °C	[871]
C–Nb–Ti–W	NbC_{1-x}–TiC_{1-x}–δ-$WC_{1\pm x}$ is plotted at 1450 °C: $(Nb,Ti,W)C_{1-x}$ (extended solid solution based on NbC_{1-x}–TiC_{1-x} monocarbide continuous solid solution) The max. solubilities of δ-$WC_{1\pm x}$ in NbC_{1-x} and TiC_{1-x} are ~10 and ~35 mol.%, respectively; the solubilities of NbC_{1-x} and TiC_{1-x} in δ-$WC_{1\pm x}$ are low.	[419, 465]
C–Nb–U	Plotted at 1200 and 1700 °C: $(Nb,U)C_{1-x}$ (NbC_{1-x}–$UC_{1\pm x}$ monocarbide continuous solid solution), β-$Nb_{2+x}C$, ζ-U_2C_3, α-UC_{2-x}, β-UC_{2-x} U, Nb, C At higher temp., depend. on compos. graphite is in equilibrium with $(Nb,U)C_{1-x}$ or $(Nb,U)C_{1-x}$ + UC_{2-x}; the compos. of $(Nb,U)C_{1-x}$ in equilibrium with C + UC_{2-x} is corresp. to $(Nb_{0.75\div0.77}U_{0.23\div0.25})C_{1-x}$ (at 2200 °C) and shifts to lower U concentrations with temp. increase.	[138, 242, 391, 436, 812]
C–Nb–U–V	NbC_{1-x}–VC_{1-x}–$UC_{1\pm x}$ is plotted at 2000–2050 °C: $(Nb,V,U)C_{1-x}$ (extended solid solution based on NbC_{1-x}–VC_{1-x} and NbC_{1-x}–$UC_{1\pm x}$ monocarbide continuous solid solutions with great miscibility gap because of low mutual solubilities in the pair VC_{1-x}–$UC_{1\pm x}$)	[391]
C–Nb–U–Zr	NbC_{1-x}–ZrC_{1-x}–$UC_{1\pm x}$ is plotted at 2050 °C: $(Nb,Zr,U)C_{1-x}$ (NbC_{1-x}–ZrC_{1-x}–$UC_{1\pm x}$ monocarbide continuous solid solution) At ~2000 °C $(U_{0.5}Zr_{0.5})C_{1\pm x}$ reacts vigorously with metal Nb.	[391, 436, 812]
C–Nb–V	Plotted at 1400–3310 °C: $(Nb,V)C_{1-x}$ (NbC_{1-x}–VC_{1-x} monocarbide continuous solid solution), $(Nb,V)_{2\pm x}C$ (β-$Nb_{2+x}C$–β-$V_{2\pm x}C$ semicarbide continuous solid solution at temp. <2200 °C, extended solid solution based on β-$Nb_{2+x}C$ at temp. 2200–2445 °C and extended solid solution based on γ-$Nb_{2\pm x}C$ at temp. 1780–2650 °C with miscibility gaps (two solid solution phases regions) at temp. 1780–2445 °C), β-$(V,Nb)_{2\pm x}C$ (extended solid solution based on β-$V_{2\pm x}C$), (Nb,V), C NbC_{1-x}–VC_{1-x} is plotted: miscibility gap (critical point—~1400–1480 °C at compos. ~$Nb_{0.4\div0.5}V_{0.5\div0.6}C_{1-x}$, at 1300 °C ranges from ~$Nb_{0.8}V_{0.2}C_{1-x}$ to ~$Nb_{0.15}V_{0.85}C_{1-x}$). Graphite is in equilibrium with $(Nb,V)C_{1-x}$.	[138, 242, 391, 419, 458, 469, 813, 871]

(continued)

Table 2.14 (continued)

System	Type of phase diagram (temperature and composition sections, constituent phases or phase fields) and/or character of interphase interaction and materials compatibility	References
C–Nb–W	Plotted at 1700–2860 °C: $(Nb,W)C_{1-x}$ (monocarbide extended solid solution based on NbC_{1-x} at temp. $\leq\sim$2500 °C and $\geq\sim$2700–2850 °C, or NbC_{1-x}–β-WC_{1-x} monocarbide continuous solid solution at temp. $\sim$2500–2850 °C), β-$(Nb,W)_{2+x}C$ (semicarbide extended solid solution based on β-$Nb_{2+x}C$ at temp. $<\sim$2500 °C with the max. solubility of W—up to $\sim$8 at.% at 2000 °C), γ-$(Nb,W)_{2\pm x}C$ (semicarbide solid solution based on γ-$Nb_{2\pm x}C$ at temp. $\sim$2500–3000 °C with the max. solubility of W—up to $\sim$8 at.% at 2500 °C and $\sim$2 at.% at 2690 °C), α-$(W,Nb)_{2+x}C$ (semicarbide extended solid solution based on α-$W_{2+x}C$ at temp. $<\sim$2000 °C with the max. solubility of Nb–up to $\sim$20 at.% at 1700 °C and $\sim$12 at.% at 2000 °C), γ-$(W,Nb)_{2\pm x}C$ (semicarbide extended solid solution based on γ-$W_{2\pm x}C$ at temp. $\sim$2500–2800 °C with the max. solubility of Nb—up to $\sim$15 at.% at 2500 °C and $\sim$25 at.% at 2690 °C), δ-$WC_{1\pm x}$, (Nb,W), C In the wide range of temp. the solid solubility of Nb in δ-$WC_{1\pm x}$ is low. Depend. on compos., graphite is in equilibrium with δ-$WC_{1\pm x}$ + $(Nb,W)C_{1-x}$ or $(Nb,W)C_{1-x}$.	[138, 242, 391, 419, 470, 758, 773, 827, 837]
C–Nb–Zr	Plotted at 1500 and 1800 °C: $(Nb,Zr)C_{1-x}$ (NbC_{1-x}–ZrC_{1-x} monocarbide continuous solid solution), β-$Nb_{2+x}C$, (β-Zr,Nb), C NbC_{1-x}–ZrC_{1-x} is plotted: miscibility gap (critical point–$\sim$410 °C at $\sim Nb_{0.55\div0.65}Zr_{0.35\div0.45}C_{1-x}$, at 300 °C ranges from $\sim Nb_{0.3}Zr_{0.7}C_{1-x}$ to $\sim Nb_{0.9}Zr_{0.1}C_{1-x}$). The solid solubility of Zr in β-$Nb_{2+x}C$ is low. Graphite is in equilibrium with $(Nb,Zr)C_{1-x}$. For diffusion rate in the system at various temp. see Addendum.	[138, 242, 391, 419, 421, 436, 468, 813, 837, 844, 864, 874–875]
C–Nd–U	Plotted at 1500 °C: $(Nd,U)C_2$ (dicarbide solid solution based on β-NdC_2), Nd_2C_{3-x}, $UC_{1\pm x}$, ζ-U_2C_3, U, Nd, C The max. solubility of "imaginary" phase 'NdC' in $UC_{1\pm x}$ varies from $\sim$4 mol.% ($\sim$1300 °C) to $\sim$6 mol.% ($\sim$1500 °C) and that of Nd_2C_{3-x} in ζ-U_2C_3 is $\sim$2.5 mol.%	[241, 391]
C–Ni–Si	Plotted at 850 and 1150 °C: β_1-$Ni_{3+x}Si$ (<1035 °C), β_2-$Ni_{3\pm x}Si$ (990–1115 °C), β_3-$Ni_{3\pm x}Si$ (1115–1170 °C), γ-Ni_5Si_{2-x} (or $Ni_{31}Si_{12}$, $<\sim$1240 °C), δ-Ni_2Si (<1255 °C), θ-Ni_3Si_{2-x} ($\sim$825–1305 °C), ε-$Ni_3Si_{2\pm x}$ (<830 °C), ε'-$Ni_3Si_{2\pm x}$ (800–845 °C), NiSi ($<\sim$990 °C), α-$NiSi_2$ ($<\sim$980 °C), β-$NiSi_2$ ($\sim$980–995 °C), SiC, Ni, Si, C In vacuum, the contact melting between SiC and Ni is observed at 1130–1140 °C.	[242, 244, 431, 503]

(continued)

Table 2.14 (continued)

System	Type of phase diagram (temperature and composition sections, constituent phases or phase fields) and/or character of interphase interaction and materials compatibility	References
C–Ni–Ta	Plotted at 1100 °C: η-Ta_4Ni_2C, ζ-$Ni_{8\pm x}Ta$ (<1330 °C), κ-$Ni_{3\pm x}Ta$ (<1550 °C), $Ni_{2\pm x}Ta$ (<1405 °C), μ-$NiTa_{1+x}$ (or μ-Ni_7Ta_{6+x} <1570 °C), $NiTa_{2+x}$ (<~1790 °C), α-$Ta_{2+x}C$, β-$Ta_{2\pm x}C$, ζ-Ta_4C_{3-x}, $Ta_6C_{5\pm x}$, TaC_{1-x}, Ta, Ni, C TaC_{1-x}–Ni is plotted: eutectic—~1340–1370 °C, ~3–7 mol.% TaC_{1-x}; at the eutectic temp. the max. solubility of TaC_{1-x} in Ni is ~2–4 mol.% TaC_{1-x} is in equilibrium with Ni and Ni-Ta intermetallides.	[242, 244, 391, 431, 459, 613]
C–Ni–Th	Plotted at 1000 °C: $Th_2Ni_3C_2$, $Th_2Ni_3C_5$, $Th_xNi_yC_z$ (?), Th_7Ni_3 (<~1040–1110 °C), ThNi (<~1185–1190 °C), Th_4Ni_7 (<1075 °C), $ThNi_{2-x}$ (<~1050–1060 °C), α-$Th_2Ni_{7\div 8}$ (or α-$ThNi_4$, <~1195 °C), β-$Th_2Ni_{7\div 8}$ (or β-$ThNi_4$, from 1195 °C to ~1210–1245 °C), $ThNi_{5\div 6}$ (<~1510–1530 °C), $Th_2Ni_{17\div 19}$ (<~1310–1355 °C), $ThC_{1\pm x}$, α-ThC_{2-x}, α-Th, Ni, C	[244, 391, 431]
C–Ni–Ti	Plotted at 870, 1100 and 1600 °C: $Ti_{2\pm x}Ni$ (<~985 °C), $TiNi_{1\pm x}$ (<1310 °C), $TiNi_3$ (<1380 °C), TiC_{1-x}, α-Ti, β-Ti, Ni, C Eutectic TiC_{1-x}–TiNi–$TiNi_3$ (1120 °C) Eutectic TiC_{1-x}–Ni–$TiNi_3$ (1295 °C) Eutectic TiC_{1-x}–Ni–C (1270 °C) TiC_{1-x}–Ni is plotted: eutectic—~1280–1310 °C, ~9–10 mol.% TiC_{1-x} (~83 at.% Ni, ~4 at.% C); at the eutectic temp. the max. solubility of TiC_{1-x} in Ni is ~5–6 mol.% (~5 mol.% at 1260 °C) and that of Ni in TiC_{1-x} is ~2.5 mol.%	[242, 244, 391, 406, 414, 431, 471, 1011]
C–Ni–U	Plotted at 1000 °C: $UNiC_2$ (<1400 °C), $UNiC_3$ (<1800 °C), U_6Ni (<790 °C), U_7Ni_9 (<785 °C), $U_5Ni_{7\pm x}$ (<820 °C), $UNi_{2\pm x}$ (<985 °C), δ-UNi_{3+x} (<1260 °C), ε-UNi_{4-x} (<1290 °C), $UNi_{5\pm x}$ (<1305 °C), $UC_{1\pm x}$, ζ-U_2C_3, γ-U, Ni, C	[242, 391, 431]
C–Ni–V	Plotted at 1100 °C: η_2-V_4Ni_2C, $Ni_{8\pm x}V$ (<405 °C), $Ni_{3\pm x}V$ (<1045 °C), $Ni_{2\pm x}V$ (<~920 °C), σ-$NiV_{2\pm x}$ (<~655–790 °C), σ'-$NiV_{2\pm x}$ (from ~655–790 °C to 1280 °C), NiV_{3+x} (<900 °C), β-$V_{2\pm x}C$, β'-$V_{2+x}C$, ζ-V_4C_{3-x}, $V_6C_{5\pm x}$, $V_8C_{7\pm x}$, VC_{1-x}, V, C VC_{1-x}–Ni is plotted: eutectic—1310 °C, ~9–10 mol.% VC_{1-x}; at the eutectic temp. the max. solubilities of VC_{1-x} in Ni and that of Ni in VC_{1-x} equal ~3 mol.%	[242, 244, 391, 431, 458]
C–Ni–W	Plotted at 700–1500 °C: κ-$(Ni,W)_4C$ (or NiW_3C, $Ni_3W_{16}C_6$), η_1-$(Ni,W)_{12}C$ (or η_{66}-Ni_6W_6C, Ni_5W_6C), η_2-$(Ni,W)_6C$ (or η_{24}-Ni_2W_4C), $W_{16}Ni_3C_6$ (?), β-$Ni_{4+x}W$ (<970 °C), δ-NiW_{1-x} (<~1060 °C), γ-NiW_2 (<~1025 °C), α-$W_{2+x}C$, δ-$WC_{1\pm x}$, Ni, W, C δ-$WC_{1\pm x}$–Ni is plotted: eutectic—1300 °C, ~12 mol.% δ-$WC_{1\pm x}$; at 1000 °C the max. solubilities of δ-$WC_{1\pm x}$ in Ni and that of Ni in δ-$WC_{1\pm x}$ equal to ~7 mol.%	[242, 244, 270, 391, 415, 431, 662, 754–756]

(continued)

Table 2.14 (continued)

System	Type of phase diagram (temperature and composition sections, constituent phases or phase fields) and/or character of interphase interaction and materials compatibility	References
C–Ni–W–Zr	ZrC_{1-x}–δ-$WC_{1\pm x}$–Ni is plotted at 1000 °C: eutectic—15 mol.% ZrC_{1-x}, 15 mol.% δ-$WC_{1\pm x}$; regions of solid solutions based on the individual components are not large (∼6–8 mol.%)	[415]
C–Ni–Zr	Plotted at 1100 °C: Zr_2Ni (<1120 °C), ZrNi (<1260 °C), Zr_9Ni_{11} (∼980–1170 °C), $Zr_7Ni_{10\pm x}$ (<∼1165 °C), Zr_2Ni_5 (or Zr_8Ni_{21}, <1180 °C), $ZrNi_{3\pm x}$ (<920 °C), Zr_2Ni_7 (<1440 °C), $ZrNi_{5\pm x}$ (<1300 °C), ZrC_{1-x}, β-Zr, Ni, C ZrC_{1-x}–Ni is plotted: eutectic—∼1230–1290 °C, ∼5–6 mol.% ZrC_{1-x} (?); at the eutectic temp. the max. solid solubility of ZrC_{1-x} in Ni is ∼3.5 mol.% (∼1 mol.% at 1100 °C) and that of Ni in ZrC_{1-x} is ∼5 mol.%	[242, 244, 391, 415, 431, 460]
C–Np–Th	No diagram plot $ThC_{1\pm x}$–NpC_{1-x} monocarbide continuous solid solution	[391]
C–O–Pu–U	Plotted partially The interaction between C and UO_{2+x}–$Pu_2O_{3\pm x}$ solid solution at 1527 °C with formation of $(U,Pu)_2C_{3-x}$ is analyzed in relationship with CO pressure.	[472]
C–O–Si	Plotted at 1525–1825 °C: SiO_2 (<∼1700 °C), SiC, Si, O, C SiO_2–SiC is plotted SiO_2–C is plotted In vacuum (0.01–0.05 Pa), the interaction between C and SiO_2 initiates in powdered mixtures from ∼1250 °C. In CO-N_2 atmosphere (0.1 MPa), at 1800–1900 °C the reaction rate in SiO_2–SiC powder mixtures is limited by C diffusion from the bulk SiC to the interface SiC/SiO_2.	[194, 242, 445, 473–475, 857, 1012]
C–O–Si–Sr	No diagram plot At 1000 °C the interaction between SiC and SrO leads to the formation of $SrO{\cdot}SiO_2$ and CO_2 (in air), or $2SrO{\cdot}SiO_2$, SrC_2 and Sr (in vacuum or Ar).	[242]
C–O–Si–Ti	No diagram plot $Ti_3Si(C,O)_2$ ($M_{n+1}AX_n$-phase oxycarbide solid solution)	[744–745, 895]
C–O–Si–Zr	No diagram plot At 1600 °C the interaction between SiC and ZrO_{2-x} leads to the formation of ZrC_xO_y oxycarbide phase.	[242]
C–O–Ta	Plotted partly at 1300–1700 °C: $Ta(C,O)_{1-x}$ (or TaC_xO_y, extended solid solution based on TaC_{1-x} with homogeneity limits: $TaC_{0.7}$–$Ta(C_{0.7}O_{<0.05})$–$Ta(C_{0.95}O_{<0.05})$–$TaC_{0.99}$), $Ta_{2+x}(C,O)$ (or $Ta_2C_xO_y$, extended solid solution based on α-$Ta_{2+x}C$ with homogeneity limits: $Ta_2C_{0.8}$–$Ta_2(C_{0.6}O_{0.2})$–$Ta_2(C_{0.4}O_{0.3})$–$Ta_2(C_{0.5}O_{0.4})$–$Ta_2C_{1.0}$), β-Ta_2O_5 (<∼1200–1360 °C), α-Ta_2O_5 (from ∼1200–1360 °C to ∼1620–1900 °C), Ta, O, C	[242, 411, 579, 629, 639]

(continued)

Table 2.14 (continued)

System	Type of phase diagram (temperature and composition sections, constituent phases or phase fields) and/or character of interphase interaction and materials compatibility	References
C–O–Ta–U	No diagram plot At 1400 °C (66 h exposure) small reaction zone was found on the contact surface between metal Ta and $UC_{0.89}O_{0.06}$, at 1800 °C (3 h exposure)—the interaction was noticeable.	[822]
C–O–Ta–W	No diagram plot At 1300–1400 °C, in vacuum the interaction between δ-$WC_{1\pm x}$ and Ta_2O_5 in powder mixtures results in the formation of W–Ta alloy.	[242, 808]
C–O–Ta–Zr	No diagram plot At 2000–2300 °C the interaction between TaC_{1-x} and ZrO_{2-x} results in the formation of new phases.	[242]
C–O–Th	No diagram plot In vacuum (0.01–0.05 Pa), the interaction between C and ThO_{2-x} is ruled by diffusion stage (parabolic law) and initiates in powdered mixtures from $\sim$1400 °C and on bulk materials contacts—from $\sim$2000 °C.	[138, 194, 382]
C–O–Th–Ti	No diagram plot At 1500–2000 °C the interaction between TiC_{1-x} and ThO_{2-x} leads to the formation of metal oxycarbides.	[242]
C–O–Ti	Plotted partly at 800–1500 °C: $Ti(C,O)_{1-x}$ (or TiC_xO_y, TiC_{1-x}–$TiO_{1\pm x}$ oxycarbide continuous solid solution with homog. limits: $TiC_{0.4}$–$TiC_{0.99}$–$TiO_{1.2}$–$TiO_{0.8}$), Ti_3O_2 (<920 °C), β-Ti_2O_3 (<$\sim$1840 °C), Ti_nO_{2n-1} ($4 \le n \le 10$, <$\sim$1600 °C, Magneli phases), TiO_2 (<1870 °C), α-(Ti,C,O), β-(Ti,C,O), O, C C-doped titania nanotubes of the $TiO_{2-x}C_x$ type were synthesized.	[242, 244, 411, 431, 477, 482, 893]
C–O–Ti–W	No diagram plot. At 1300–1400 °C in powder mixtures δ-$WC_{1\pm x}$ interacts with TiO_2 with the formation of W–Ti alloy very intensively.	[242, 808]
C–O–Ti–Zr	No diagram plot. At 1400–2400 °C, in vacuum the interaction between TiC_{1-x} and ZrO_{2-x} leads to the formation of CO and TiC_xO_y oxycarbide phase.	[242]

(continued)

Table 2.14 (continued)

System	Type of phase diagram (temperature and composition sections, constituent phases or phase fields) and/or character of interphase interaction and materials compatibility	References
C–O–U	Plotted at 1000–2000 °C: $U(C,O)_{1\pm x}$ (or $UC_{1-x}O_x$, extended solid solution based on $UC_{1\pm x}$ with max. O solubility corresp. to $UC_{0.12}O_{0.88}$ at <1100 °C and $UC_{0.63\div0.68}O_{0.32\div0.37}$ at ~1300–1800 °C), α-$U(C,O)_{2-x}$ (or α-$UC_{2-x}O_x$, extended solid solution based on α-UC_{2-x}), ζ-U_2C_3, UO_{2+x} (<~2780–2860 °C), U_4O_{9-x} (<~1140 °C), α-U_3O_{8-x} (~350–770 °C), β-U_3O_{8-x} (~770–940 °C), γ-U_3O_{8-x} (~940–1700 °C), α-UO_3 (?), β-UO_3 (<~1900 °C), α-U, β-U, γ-U, O, C UO_{2+x} ($x \approx 0$)–$UC_{1\pm x}$ ($x \approx 0$) is plotted: eutectic—~2250 °C, ~33 mol.% $UC_{1\pm x}$ Depend. on temp. and compos., graphite is in equilibrium: at <1100 °C—with UO_{2+x}, or UO_{2+x} + $UC_{0.2}O_{0.8}$ (?), or $UC_{1-x}O_x$ ($0.1 \le x \le 0.8$, ?), or α-$UC_{2-x}O_x$ + $UC_{0.9}O_{0.1}$ (?), or α-$UC_{2-x}O_x$; at 1300 °C—with UO_{2+x}, or UO_{2+x} + α-$UC_{2-x}O_x$ ($x = 0.08$), or α-$UC_{2-x}O_x$ ($x \le 0.08$, ?); at ~1400–1500 °C—with U_3O_{8-x}, or U_3O_{8-x} + UO_{2+x}, or UO_{2+x}, or UO_{2+x} + α-$UC_{2-x}O_x$, or α-$UC_{2-x}O_x$; at 1700 °C—with UO_{2+x}, or UO_{2+x} + α-$UC_{2-x}O_x$, or α-$UC_{2-x}O_x$. The interaction between C and UO_{2+x} in vacuum leads to the elimination of excess oxygen (at 1000 °C) and then to the formation of carbides (at 1200–1530 °C).	[138, 242, 244, 431, 472, 478–481, 751–753]
C–O–U–V	No diagram plot. At 1000 °C (66 h exposure) the carburization of metal V was occurred on the contact surface with $UC_{0.89}O_{0.06}$, at 1400 °C (66 h exposure)—the interaction was significant.	[822]
C–O–U–Zr	No diagram plot. At 1900 °C the interaction between U carbides and ZrO_{2-x} is weak. At 1000 °C (66 h exposure) no appreciable reaction was occurred on the contact surface between metal Zr and $UC_{0.89}O_{0.06}$, at 1400 °C (66 h exposure)—small reaction zone was found.	[242, 822]
C–O–V	Plotted partly at 1000–1700 °C: $V(C,O)_{1-x}$ (or VC_xO_y, VC_{1-x}–δ-$VO_{1\pm x}$ continuous solid solution with homog. limits: $VC_{0.67}$–$VC_{0.88}$–$VO_{1.25}$–$VO_{0.85}$, <~1185–2800 °C), $V_{2\pm x}(C,O)$ (or $V_2C_xO_y$, extended solid solution based on β-$V_{2\pm x}C$), α′-$V_{8\pm x}O$ (<~520 °C), β-$V_{4\pm x}O$ (from ~320 to 520 °C to 1665 °C), β′-$V_{4\pm x}O$ (or $V_{16}O_{3\pm x}$, <400 °C), γ-$V_{2\pm x}O$ (or $V_{14}O_{6\pm x}$, <1185 °C), δ′-VO_{1+x} (or $V_{52}O_{64\pm x}$, <810 °C), α-V_2O_{3+x} (?), β-V_2O_{3+x} (<~1955 °C), α-V_3O_5 (?), β-V_3O_5 (<~1600 °C), V_4O_7 (<~1600 °C), V_5O_9 (<~1600 °C), V_6O_{11} (<~1600 °C), V_7O_{13} (<~1600 °C), V_8O_{15} (<~1600 °C), α-VO_2 (?), β-VO_2 (<~1540 °C), α-V_6O_{13} (?), β-V_6O_{13} (<700 °C), V_3O_7 (<~670 °C), V_2O_5 (<~680 °C), β′-$V_{2+x}C$, ζ-V_4C_{3-x}, $V_6C_{5\pm x}$, $V_8C_{7\pm x}$, V, O, C	[242, 411, 431, 483]

(continued)

Table 2.14 (continued)

System	Type of phase diagram (temperature and composition sections, constituent phases or phase fields) and/or character of interphase interaction and materials compatibility	References
C–O–V–W	No diagram plot. δ-$WC_{1\pm x}$ interacts in powder mixtures with β-V_2O_{3+x} (at 1300–1400 °C) and V_2O_5 (at 900–1400 °C) intensively with the formation of W–V alloy.	[242, 808]
C–O–V–Zr	No diagram plot At 1500–2000 °C the interaction between VC_{1-x} and ZrO_{2-x} leads to the formation of ZrC_xO_y oxycarbide phase and β-$V_{2\pm x}C$ (at 1600–1700 °C) or metal V (at 1700–2000 °C).	[242]
C–O–W	No diagram plot δ-$WC_{1-x}O_x$ (solid solution based on δ-$WC_{1\pm x}$, ?), $WO_{3-x}C_x$ (solid solution based on WO_{3-x}, ?)	[541, 660, 981]
C–O–W–Zr	No diagram plot At 1400–2000 °C the interaction between δ-$WC_{1\pm x}$ and ZrO_{2-x} results in the formation ZrC_xO_y oxycarbide phase, α-$W_{2+x}C$ and W-Zr alloy.	[242, 808]
C–O–Zr	Plotted partially at 1555, 1600 and 1700 °C: $Zr(C,O)_{1-x}$ (or ZrC_xO_y, extended solid solution based on ZrC_{1-x} with the homog. limits: $ZrC_{0.6}$–$ZrC_{0.5}O_{0.2}$–$ZrC_{0.4\div0.6}O_{0.3\div0.55}$–$ZrC_{0.8}O_{0.2}$–$ZrC_{0.99}$), α-ZrO_{2-x} (<1205 °C), β-ZrO_{2-x} ($\sim$1205–2375 °C), γ-ZrO_{2-x} ($x \leq 0.44$, $\sim$1525–2710 °C), γ-$ZrO_{2-x}C_z$ ($z \approx 0.06$, metastable, ?), α-(Zr,C,O) (metal solid solution with the solubility limits: $ZrC_{0.02\div0.03}$ and $ZrO_{0.41\div0.54}$), β-(Zr,C,O), O, C In vacuum (0.01–0.05 Pa), the interaction between C and ZrO_{2-x} initiates in powdered mixtures from $\sim$1300 °C and on bulk materials contacts—from $\sim$1600 to 1900 °C.	[138, 194, 241–242, 382, 411–412, 431, 484, 861]
C–Os–Sc	No diagram plot Sc_3OsC_4	[988–989]
C–Os–Si	Plotted at 1350 °C: $OsSi_2$ (or $OsSi_{1.8}$, <1620–1660 °C), Os_2Si_3 (<1820–1860 °C), $OsSi_{1\pm x}$ (<1720–1740 °C), SiC, Si, Os, C	[244, 431, 503–504]
C–Os–Ta	Plotted at 1500 °C: σ-$Ta_3Os_{2\pm x}$ (<$\sim$2500 °C), γ-$Ta_2Os_{3\pm x}$ (<$\sim$2420 °C), α-$Ta_{2+x}C$, TaC_{1-x}, Ta, Os, C Graphite is in equilibrium with (Os,Ta) + TaC_{1-x}. The solubility of Ta in Os (with the presence of C) and that of Os in TaC_{1-x} are low.	[391, 431]
C–Os–Th	No diagram plot $Th_xOs_yC_z$ (?)	[391]
C–Os–Ti	Plotted at 1500 °C: δ-$TiOs_{1\pm x}$ (<2160–2180 °C), TiC_{1-x}, α-Ti, β-Ti, Os, C Graphite is in equilibrium with (Os, Ti) + TiC_{1-x}. The solubility of Ti in Os (with the presence of C) and that of Os in TiC_{1-x} are low.	[244, 391, 431]

(continued)

Table 2.14 (continued)

System	Type of phase diagram (temperature and composition sections, constituent phases or phase fields) and/or character of interphase interaction and materials compatibility	References
C–Os–U	Plotted at 1500 °C: U_2OsC_2, U_3Os (<1030 °C), U_2Os (<920 °C), U_5Os_4 (<1280 °C), $UOs_{2\pm x}$ (<2280 °C), $UC_{1\pm x}$, ζ-U_2C_3, α-UC_{2-x}, β-UC_{2-x}, α-U, β-U, γ-U, Os, C The mutual solubilities of all constituent phases in the system are low.	[244, 391, 431]
C–Os–V	Plotted at 1500 °C: $V_3Os_{2\pm x}$ (<2140 °C), VOs_{1-x} (?), α-$V_{2+x}C$, β-$V_{2\pm x}C$, β'-$V_{2+x}C$, ζ-V_4C_{3-x}, $V_6C_{5\pm x}$, $V_8C_{7\pm x}$, VC_{1-x}, V, Os, C Graphite is in equilibrium with (Os,V) + VC_{1-x}. The solubility of V in Os (with the presence of C) and that of Os in VC_{1-x} are low.	[244, 391, 431]
C–Os–W	Plotted at 2000 °C: ~$W_3Os_3C_2$ (<2000–2030 °C), σ-$OsW_{3\pm x}$ (<2945 °C), α-$W_{2+x}C$, δ-$WC_{1\pm x}$, W, Os, C The mutual solubilities of all constituent binary phases are low. Depend. on compos., graphite is in equilibrium with (Os,W) or (Os,W) + δ-$WC_{1\pm x}$.	[244, 391, 431]
C–Os–Y	No diagram plot Y_2OsC_2, $Y_{12}Os_5C_{15}$	[991–992]
C–Os–Zr	Plotted at 1500 °C: $Zr_{11}Os_4$ (<1350 °C), ZrOs (<2040 °C), λ_1-$ZrOs_{2\pm x}$ (<2660 °C), ZrC_{1-x}, α-Zr, β-Zr, Os, C The solubility of Zr in Os (with the presence of C) and that of Os in ZrC_{1-x} are low. Graphite is in equilibrium with (Os,Zr) + ZrC_{1-x}.	[244, 391, 431]
C–P–V	Plotted partially at 1000 °C: V_2PC ($M_{n+1}AX_n$-phase), V_3PC, V_4P_2C, $V_{11}P_5C$ (or $V_{32}P_{15}C_3$), $V_{20}P_{11}C_2$ (or $V_5P_{2.83}C_{0.5}$), VP_4, VP_2, VP, V_4P_3, $V_{12}P_7$, V_2P, V_3P, α-$V_{2+x}C$, β-$V_{2\pm x}C$, β'-$V_{2+x}C$, ζ-V_4C_{3-x}, $V_6C_{5\pm x}$, $V_8C_{7\pm x}$, VC_{1-x}, V, P, C The homog. range extension of non-stoichiometric V_3PC and $V_{20}P_{11}C_2$ is ~3–5 at.%.	[680–681, 744–745, 860, 982]
C–Pb–Ti	No diagram plot Ti_2PbC ($M_{n+1}AX_n$-phase)	[680–681, 744–745, 860]
C–Pb–Zr	No diagram plot Zr_2PbC ($M_{n+1}AX_n$-phase)	[680–681, 744–745, 860]
C–Pd–Si	Plotted at 825 and 1600 °C: Pd_5Si (from ~725 °C to ~815–835 °C), Pd_4Si (or Pd_9Si_2, ~725–830 °C), Pd_3Si (<1070 °C), $Pd_{2\pm x}Si$ (<1395 °C), PdSi (~825–900 °C), SiC, Si, Pd, C	[244, 431, 503–504]
C–Pd–Ta	Plotted at 1300 °C: $Pd_{3\pm x}Ta$ (<1770–1945 °C, ?) $Pd_{2\pm x}Ta$ (<1670–1800 °C, ?), PdTa (<~1720–2000 °C, ?), α-$Pd_{1\pm x}Ta$ (<1410 °C, ?), β-$Pd_{1\pm x}Ta$ (1550–1720 °C, ?), σ-$PdTa_{3\pm x}$ (<2550 °C or 1575–2350 °C, ?), α-$Ta_{2+x}C$, TaC_{1-x}, Ta, Pd, C Depend. on compos., graphite is in equilibrium with (Pd,Ta) alloy or ($Pd_{0.84}Ta_{0.16}$) alloy + TaC_{1-x}.	[242, 244, 391, 431]

(continued)

Table 2.14 (continued)

System	Type of phase diagram (temperature and composition sections, constituent phases or phase fields) and/or character of interphase interaction and materials compatibility	References
C–Pd–Th	Plotted at 1100 °C: δ-$Th_3Pd_{13\pm x}$ (<1215 °C), ε-$ThPd_{4-x}$ (<1340 °C), $ThPd_{3+x}$ (<~1560–1575 °C), Th_3Pd_5 (<~1385 °C), Th_3Pd_4 (<1325 °C), ThPd (<~1410 °C), Th_2Pd (<~1160 °C), $ThC_{1\pm x}$, α-ThC_{2-x}, β-ThC_{2-x}, γ-ThC_{2-x} α-Th, β-Th, Pd, C	[244, 391, 431, 485]
C–Pd–Ti	Plotted at 1300 °C: Ti_4Pd (<~580 °C), Ti_2Pd (<960 °C), α-$TiPd_{1\pm x}$ (<~440–510 °C), β-$TiPd_{1\pm x}$ (~440–1400 °C), Ti_2Pd_3 (<1330 °C), Ti_3Pd_5 (?), α-$TiPd_{2-x}$ (<1280 °C), β-$TiPd_{2-x}$ (~1280–1400 °C), $TiPd_3$ (<1530 °C), γ-$TiPd_{4\pm x}$ (<~1485 °C, ?), TiC_{1-x}, α-Ti, β-Ti, Pd, C Depend. on compos., graphite is in equilibrium with (Pd,Ti) alloy, or $TiPd_3$, or $TiPd_3$ + TiC_{1-x}.	[244, 391, 431]
C–Pd–U	Plotted at 1300 °C: UPd_{1+x} (970–1050 °C), U_5Pd_{6+x} (980–1110 °C), UPd_{3-x} (<1640 °C), $UPd_{4\pm x}$ (<1525–1585 °C), $UPd_{5\pm x}$ (<1445 °C, ?), U_2Pd_{11} (<1015 °C), UPd_8 (or U_2Pd_{17}, <800 °C, ?), $UC_{1\pm x}$, ζ-U_2C_3, α-UC_{2-x}, β-UC_{2-x}, U, Pd, C	[244, 391, 431, 486]
C–Pd–V	Plotted at 1300 °C: $V_{3\pm x}Pd$ (<840 °C), $VPd_{2\pm x}$ (<905 °C), $VPd_{3\pm x}$ (<815 °C), β-$V_{2\pm x}C$, β'-$V_{2+x}C$, ζ-V_4C_{3-x}, $V_6C_{5\pm x}$, $V_8C_{7\pm x}$, VC_{1-x}, V, Pd, C Depend. on compos., graphite is in equilibrium with (Pd,V) alloy or ($Pd_{0.8}V_{0.2}$) alloy + VC_{1-x}.	[244, 391, 431]
C–Pd–W	No diagram plot At 1200–1500 °C δ-$WC_{1\pm x}$ interacts with Pd intensively (W-Pd solid solution is formed, ?).	[242]
C–Pd–Zr	Plotted at 1300 °C: Zr_2Pd (<1085 °C), ZrPd (<~1600 °C), $ZrPd_2$ (<1600 °C), $ZrPd_3$ (<1780 °C), ZrC_{1-x}, α-Zr, β-Zr, Pd, C Depend. on compos., graphite is in equilibrium with (Pd,Zr) alloy, or $ZrPd_3$, or $ZrPd_3$ + ZrC_{1-x}.	[244, 391, 431]
C–Pt–Si	Plotted at 800 and 1600 °C: α-Pt_3Si (<360 °C), β-Pt_3Si (from 360 °C to ~775–880 °C), γ-Pt_3Si (~775–870 °C, ?), α-Pt_7Si_3 (or α-$Pt_{12}Si_5$, <280 °C), β-Pt_7Si_3 (or β-$Pt_{12}Si_5$, ~280–985 °C), α-Pt_2Si (<695 °C), β-Pt_2Si (695–1100 °C), Pt_6Si_5 (<975 °C), PtSi (<~1230 °C), SiC, Si, Pt, C	[244, 487, 503–504]
C–Pt–Ta	Plotted at 1500 °C: $Pt_{3\pm x}Ta$ (<2065–2085 °C), $Pt_{2\pm x}Ta$ (<2245 °C), $Pt_{1\pm x}Ta$ (1635–1795 °C), σ-$PtTa_{2+x}$ (<2470 °C), $PtTa_{3+x}$ (<1725 °C), α-$Ta_{2+x}C$, TaC_{1-x}, Ta, Pt, C Depend. on compos., graphite is in equilibrium with (Pt,Ta) alloy + $Pt_{3\pm x}Ta$ or $Pt_{3\pm x}Ta$ + TaC_{1-x}.	[242, 391, 487]
C–Pt–Th	No diagram plot $Th_xPt_yC_z$, ?	[391]

(continued)

Table 2.14 (continued)

System	Type of phase diagram (temperature and composition sections, constituent phases or phase fields) and/or character of interphase interaction and materials compatibility	References
C–Pt–Ti	Plotted at 1500 °C: $Ti_{3\pm x}Pt$ (<1370 °C), α-$TiPt_{1\pm x}$ (<~960–1025 °C), β-$TiPt_{1\pm x}$ (from ~960–1025 °C to 1830 °C), Ti_3Pt_5 (from ~1000 °C to ~1880–1900 °C), $TiPt_{3-x}$ (<~1900 °C), γ-$TiPt_{3\pm x}$ (<1950 °C), $TiPt_8$ (<1080 °C), TiC_{1-x}, α-Ti, β-Ti, Pt, C Depend. on compos., graphite is in equilibrium with (Pt,Hf) alloy + γ-$TiPt_{3\pm x}$ or γ-$TiPt_{3\pm x}$ + TiC_{1-x}.	[244, 391, 487]
C–Pt–U	Plotted at 1300 °C: U_2PtC_2 (<~1700 °C), UPt (<~960 °C), UPt_2 (<1370 °C), UPt_3 (<1700 °C), UPt_5 (<1460 °C), $UC_{1\pm x}$, ζ-U_2C_3, α-UC_{2-x}, β-UC_{2-x}, U, Pt, C The mutual solubilities of all the constituent binary phases are low.	[244, 391, 487]
C–Pt–V	Plotted at 1500 °C: $VPt_{3\pm x}$ (<~1015 °C), $VPt_{2\pm x}$ (<~1100 °C), $VPt_{1\pm x}$ (<~1500 °C), $V_{3\pm x}Pt$ (<~1800 °C), β-$V_{2\pm x}C$, β′-$V_{2+x}C$, ζ-V_4C_{3-x}, $V_6C_{5\pm x}$, $V_8C_{7\pm x}$, VC_{1-x}, V, Pt, C Depend. on compos., graphite is in equilibrium with (Pt,V) alloy + $VPt_{3\pm x}$ or $VPt_{3\pm x}$ + VC_{1-x}.	[244, 391, 487]
C–Pt–W	Plotted at 2000 °C: $W_5Pt_5C_x$ ($x \approx 1$ at 2000 °C), γ-Pt_2W (~1400 °C, ?), ε-PtW (~1400 °C, ?), α-$W_{2+x}C$, β-$W_{2+x}C$, γ-$W_{2\pm x}C$, γ-WC_{1-x}, δ-$WC_{1\pm x}$ W, Pt, C	[242, 391, 487]
C–Pt–Zr	Plotted at 1500 °C: $Zr_{5+x}Pt_3$ (<~1725 °C), ZrPt (<~2100–2105 °C), Zr_9Pt_{11} (?), Zr_7Pt_{10} (?), $ZrPt_{3\pm x}$ (<~2120–2155 °C, ?), ZrC_{1-x}, α-Zr, β-Zr, Pt, C Depend. on compos., graphite is in equilibrium with (Pt,Zr) alloy + $ZrPt_{3\pm x}$ or $ZrPt_{3\pm x}$ + ZrC_{1-x}.	[244, 391, 487]
C–Pu–Si	Plotted at 20–1000 °C: Pu_5Si_3 (<~1375 °C), Pu_3Si_2 (<~1440 °C), PuSi (<~1575 °C), $Pu_3Si_{5\pm x}$ (<~1645 °C), $PuSi_{2\pm x}$ (<~1640 °C), Pu_3C_2, PuC_{1-x}, Pu_2C_{3-x}, β-PuC_2, SiC, α-Pu, β-Pu, γ-Pu, δ-Pu, δ′-Pu, ε-Pu, Si, C The solubilities of Pu silicides in Pu carbides is very low (<1 mol.%). At temp. <~1600–1750 °C graphite is in equilibrium with Pu_2C_{3-x} and SiC.	[906]
C–Pu–Ta	No diagram plot At temp. ≥1050 °C the interaction between PuC_{1-x} and Ta leads to the formation of α-$(Ta,Pu)_{2+x}C$.	[242]
C–Pu–Th	Plotted at 1050–1600 °C: $(Th,Pu)C_{1\pm x}$ (or $Th_yPu_{1-y}C_{1-x}$, α-Th–$ThC_{1\pm x}$–PuC_{1-x} monocarbide continuous solid solution; at 1050 °C: for $x = 0$, $0.68 \le y \le 1.0$ and for $x = 0.18$, $0 \le y \le 1$), $(Pu,Th)_2C_{3-x}$ (or $(Pu_yTh_{1-y})_2C_{3-x}$, sesquicarbide extended solid solution based on Pu_2C_{3-x}; $0.7 \le y \le 1$ at ~1200 °C), $(Th,Pu)C_{2-x}$ (or $Th_yPu_{1-y}C_{2-x}$, dicarbide continuous or extended solid solutions based on α-ThC_{2-x}, β-ThC_{2-x} and γ-ThC_{2-x}; at ~1100 °C—for α-$Th_yPu_{1-y}C_{2-x}$, $0.45 \le y \le 1$; at ~1200 °C—for γ-$Th_yPu_{1-y}C_{2-x}$, $0 \le y \le 1$; at ~1150–1410 °C β-$Th_yPu_{1-y}C_{2-x}$ exists only as a ternary solution), α-Th, β-(Th,Pu), Pu, C	[138, 391, 906]

(continued)

Table 2.14 (continued)

System	Type of phase diagram (temperature and composition sections, constituent phases or phase fields) and/or character of interphase interaction and materials compatibility	References
C–Pu–Ti	Plotted at 1600 °C: PuC_{1-x}, Pu_2C_{3-x}, TiC_{1-x}, β-Ti, Pu, C The mutual solid solubilities of all the constituent binary phases are low. Graphite is in equilibrium with Pu_2C_{3-x} + TiC_{1-x}.	[391]
C–Pu–U	Plotted at 400–2000 °C: $(U,Pu)C_{1-x}$ (or $U_{1-y}Pu_yC_{1-x}$, $UC_{1\pm x}$–PuC_{1-x} monocarbide continuous solid solution, or extended solid solutions based on $UC_{1\pm x}$ (at temp. >melt. point of PuC_{1-x}); stoichiometric compos. ($x = 0$) are observed at $0 \leq y \leq 0.7$, so for Pu-rich solutions the miscibility occurs only in hypostoichiometric regions), ζ-$(U,Pu)_2C_{3-x}$ (or ζ-$(U_{1-y}Pu_y)_2C_{3-x}$, sesquicarbide continuous solid solution; at higher temp. ζ-U_2C_3 is stabilized by Pu), α-$(U,Pu)C_{2-x}$ (or α-$U_{1-y}Pu_yC_{2-x}$, dicarbide continuous solid solution, or extended solid solutions based on α-UC_{2-x}, metastable at higher Pu concentrations, ?), β-$(U,Pu)C_{2-x}$ (or β-$U_{1-y}Pu_yC_{2-x}$, dicarbide continuous solid solution (at 1800–2200 °C, ?), or extended solid solutions based on β-UC_{2-x}), Pu_3C_{2-x}, η-$(Pu_{1-x}U_x)$ (from ~280 to 700–705 °C), ζ-PuU_{1-x} (<~590–630 °C), α-U, β-U, (ε-Pu,γ-U), γ-Pu, δ-Pu, δ'-Pu, C	[238, 244, 391, 488–493]
C–Pu–U–W	$(U_{0.8}Pu_{0.2})$–W–C is plotted at 1700 °C: $(U_{0.8}Pu_{0.2})WC_2$, $(U_{0.8}Pu_{0.2})_4W_4C_7$, $(U_{0.8}Pu_{0.2})C_{1\pm x}$ (terminal solubility of W is low), ζ-$(U_{0.8}Pu_{0.2})_2C_{3-x}$, β-$W_{2+x}C$, γ-$W_{2\pm x}C$, γ-WC_{1-x}, δ-$WC_{1\pm x}$ ($U_{0.8}Pu_{0.2}$), W, C	[489]
C–Pu–U–Zr	No diagram plot $(U_{1-z-y}Pu_zZr_y)C_{1-x}$ ($UC_{1\pm x}$–PuC_{1-x}–ZrC_{1-x} monocarbide continuous solid solution in the regions with low values of z)	[391]
C–Pu–W	Plotted at 1400 °C: $PuWC_2$, $Pu_4W_4C_7$, PuC_{1-x}, Pu_2C_{3-x}, α-$W_{2+x}C$, δ-$WC_{1\pm x}$, Pu, W, C The mutual solid solubilities of all the constituent binary phases are low. Depend. on compos., graphite is in equilibrium with Pu_2C_{3-x} + $PuWC_2$, or δ-$WC_{1\pm x}$ + $PuWC_2$. At temp. ≥1050 °C the interaction between PuC_{1-x} and W leads to the formation of α-$(W,Pu)_{2+x}C$.	[242, 391]
C–Pu–Zr	Plotted at 1250–1600 °C: $(Pu,Zr)C_{1-x}$ (monocarbide extended solid solution based on PuC_{1-x} with max. terminal solubility of ZrC_{1-x}–~25 mol.%), Pu_2C_{3-x} (terminal solubility of Zr is low), $(Zr,Pu)C_{1-x}$ (monocarbide extended solid solution based on ZrC_{1-x} with max. terminal solubility of PuC_{1-x}–~25 mol.%), Pu, β-Zr, C Graphite is in equilibrium with Pu_2C_{3-x} + $(Zr,Pu)C_{1-x}$.	[391, 494–495]

(continued)

Table 2.14 (continued)

System	Type of phase diagram (temperature and composition sections, constituent phases or phase fields) and/or character of interphase interaction and materials compatibility	References
C–Re–Si	Plotted at 1000 and 1600 °C: $ReSi_2$ (or $ReSi_{1.8}$, <~1930–1980 °C), ReSi (from 1650 °C to ~1820–1880 °C, ?), Re_5Si_3 (<1020 °C, ?), Re_2Si (or $Re_{17}Si_9$, <~1810–1960 °C), SiC, Re, Si, C	[244, 487, 503–504]
C–Re–Ta	Plotted at 1800 and 2100 °C: σ-Ta_2Re_{3-x} (from 2200–2460 °C to 2680–2740 °C), χ-$TaRe_{3\pm x}$ (<2790–2830 °C), α-$Ta_{2+x}C$, TaC_{1-x}, Ta, Re, C TaC_{1-x}–Re is plotted: eutectic—2420 °C, ~30 mol.% TaC_{1-x}; the mutual solid solubilities of the components are low Graphite is in equilibrium with Re + TaC_{1-x}.	[242, 391, 487, 818]
C–Re–Tc	Plotted schematically	[840]
C–Re–Th	No diagram plot $Th_xRe_yC_z$	[391]
C–Re–Ti	TiC_{1-x}–Re is plotted: eutectic—2540 °C, ~44–50 mol.% TiC_{1-x}; the mutual solid solubilities of the components are low Graphite is in equilibrium with Re + TiC_{1-x}.	[242, 391, 581–583, 835]
C–Re–U	Plotted at 1500 and 2110 °C: $UReC_2$ (<~2000 °C), $\sim U_4Re_4C_{7-x}$ (<~2000 °C), $U_5Re_3C_{8-x}$ (?), α-URe_2 (<180 °C), β-URe_2 (180–2200 °C), $UC_{1\pm x}$, ζ-U_2C_3, α-UC_{2-x}, β-UC_{2-x}, U, Re, C $UC_{1\pm x}$–Re is plotted: eutectic—1860 °C, ~40 mol.% $UC_{1\pm x}$	[138, 242, 244, 391, 487, 612, 812]
C–Re–U–Zr	No diagram plot At ~2100 °C $(U_{0.5}Zr_{0.5})C_{1\pm x}$ is compatible for periods of up to 35 min. with metal Re.	[812]
C–Re–V	Plotted at 1950 °C: β-$(V,Re)_{2\pm x}C$ (β-$V_{2\pm x}C$–Re semicarbide continuous solid solution or extended solid solution based on β-$V_{2\pm x}C$, ?), $(V,Re)C_{1-x}$ (monocarbide extended solid solution based on VC_{1-x} with max. terminal solubility of Re–~65 at.%, ?), δ-VRe_{2+x} (from 1470 °C to 1950–2310 °C), σ-VRe_{3+x} (from 1950–1990 °C to 2440–2630 °C), V, Re, C VC_{1-x}–Re is plotted: eutectic—2050 °C, ~60 mol.% Re; the mutual solid solubilities of the components are low (?) Data available on the system in literature are very controversial.	[244, 391, 487, 496, 581–583, 603, 837]
C–Re–W	Plotted at 1500 and 2000 °C: π-W_3Re_2C, $(W,Re)C_{1-x}$ (metastable, ?), β-$(W,Re)_{2+x}C$ (β-$W_{2+x}C$–Re(W,C) continuous solid solution), σ-$W_2Re_{3\pm x}$ (<~2890–3005 °C), χ-WRe_{3-x} (<2125–2130 °C), δ-$WC_{1\pm x}$, W, Re, C Graphite is in equilibrium with δ-$WC_{1\pm x}$, β-$(W,Re)_{2+x}C$ + δ-$WC_{1\pm x}$ and β-$(W,Re)_{2+x}C$	[138, 242, 244, 391, 487, 581–582, 591, 809, 837]

(continued)

Table 2.14 (continued)

System	Type of phase diagram (temperature and composition sections, constituent phases or phase fields) and/or character of interphase interaction and materials compatibility	References
C–Re–Y	No diagram plot Y_2ReC_2, $Y_{12}Re_5C_{15}$	[993–994]
C–Re–Zr	Plotted at 1900 and 2000 °C: σ-Zr_2Re (<~1640–1900 °C, ?), $Zr_{21}Re_{25}$ (?), λ-$ZrRe_{2-x}$ (<2450–2750 °C, ?), χ-Zr_5Re_{24+x} (<2500 °C), ZrC_{1-x}, Zr, Re, C ZrC_{1-x}–Re is plotted: eutectic—~2540–2670 °C, ~20–35 mol.% ZrC_{1-x} (?); at 1900 °C the solubility of Re in ZrC_{1-x} is ~3 mol.% and that of ZrC_{1-x} in Re is <0.5 mol.%; data available in literature on this quasibinary system are controversial Graphite is in equilibrium with Re + ZrC_{1-x}.	[242, 244, 391, 487, 820, 835, 837]
C–Rh–Si	Plotted at 1170 °C: Rh_2Si (<1650 °C), Rh_5Si_3 (<1470 °C), Rh_3Si_2 (<820 °C), $Rh_{20}Si_{13}$ (or $RhSi_{0.7}$, 1050–1225 °C), α-$RhSi_{1\pm x}$ (<1030–1080 °C), β-$RhSi_{1+x}$ (from 1030–1080 °C to 1450 °C), Rh_4Si_5 (<1030 °C), Rh_3Si_4 (<1040 °C), SiC, Si, Rh, C	[244, 487, 503–504]
C–Rh–Ta	Plotted at 1500 °C: $Rh_{3\pm x}Ta$ (<~2125 °C), α-$Rh_{2\pm x}Ta$ (or α_2-$Rh_{2\pm x}Ta$, <~1890 °C), α_1-$Rh_{3\pm x}Ta_2$ (<~1860 °C), α_3-$RhTa_{1-x}$ (from 1355–1395 °C to ~1840 °C), σ-$RhTa_{2\pm x}$ (<~2080–2140 °C), α-$Ta_{2+x}C$, TaC_{1-x}, Ta, Rh, C The solubility of C in $Rh_{3\pm x}Ta$ is low.	[244, 391, 487]
C–Rh–Th	Plotted at 1200 °C: ~$ThRh_3C_x$ ($x \approx 0.3$, ?), Th_7Rh_3 (<1350–1375 °C), ThRh (<at least ~1500 °C), Th_3Rh_4 (<~1475–1500 °C), Th_3Rh_5 (<~1440–1460 °C), α-$ThRh_2$ (<~1250 °C), β-$ThRh_2$ (at least from ~1250 °C to 1500 °C), $ThRh_3$ (<at least ~1500 °C), $ThRh_5$ (<at least ~1500 °C), $ThC_{1\pm x}$, α-ThC_{2-x}, β-ThC_{2-x}, α-Th, β-Th, Rh, C	[391, 487, 497]
C–Rh–Ti	Plotted at 1500 °C: $TiRh_3C_x$ ($x \approx 0.25$, ?), $Ti_{2\pm x}Rh$ (<790 °C), α-$TiRh_{1\pm x}$ (?), β-$TiRh_{1\pm x}$ (<1940 °C), Ti_3Rh_5 (<~1765 °C, ?), $TiRh_{3\pm x}$ (<1750 °C), $TiRh_5$ (<1100 °C, ?), TiC_{1-x}, α-Ti, β-Ti, Rh, C The solubility of C in $TiRh_{3\pm x}$ is ~5 at.%; no solubility of Rh in TiC_{1-x}. Depend. on compos., graphite is in equilibrium with Rh + $TiRh_3C_x$ or $TiRh_3C_x$ + TiC_{1-x}.	[244, 391, 487]
C–Rh–U	Plotted at 700 and 1300 °C: U_2RhC_2 (≤1715 °C), URh_3C (?), α-U_4Rh_3 (<720 °C), β-U_4Rh_3 (720–1155 °C), U_3Rh_4 (<1450 °C), U_3Rh_5 (<1550 °C), URh_3 (<1700 °C), $UC_{1\pm x}$, ζ-U_2C_3, α-U, β-U, γ-U, Rh, C	[242, 244, 391, 487, 498]
C–Rh–V	Plotted at 1500 °C: β-$V_{2\pm x}Rh$ (or $V_{3\pm x}Rh$, <1730 °C), α_1-VRh_{1-x} (~1320–1535 °C, ?), α_2-VRh_{1+x} (<1560 °C), α_3-$VRh_{1\pm x}$ (<~1400–1405 °C), ε-V_2Rh_{3+x} (or $V_3Rh_{5\pm x}$ <1615 °C), γ-$VRh_{3\pm x}$ (<1740 °C), β-$V_{2\pm x}C$, β'-$V_{2+x}C$, ζ-V_4C_{3-x}, $V_6C_{5\pm x}$, $V_8C_{7\pm x}$, VC_{1-x}, V, Rh, C The solubility of C in γ-$VRh_{3\pm x}$ is very low.	[244, 391, 487]

(continued)

Table 2.14 (continued)

System	Type of phase diagram (temperature and composition sections, constituent phases or phase fields) and/or character of interphase interaction and materials compatibility	References
C–Rh–W	Plotted at 1500 and 2000 °C: $(W,Rh)_4C_{1-x}$ ($0 < x < 0.2$, ~1700–2000 °C), Rh_3W (from ~1200 °C to ?), ε-$Rh_{2\pm x}W$ (<~2250–2255 °C), α-$W_{2+x}C$, β-$W_{2+x}C$, δ-$WC_{1\pm x}$, W, Rh, C	[244, 391, 487]
C–Rh–Zr	Plotted at 1500 °C: $ZrRh_3C_x$ ($x \approx 0.5$, ?), Zr_2Rh (<1170–1180 °C), α-$ZrRh_{1+x}$ (<~200–670 °C), β-$ZrRh_{1+x}$ (from ~200–670 °C to 1935 °C), $Zr_3Rh_{4\pm x}$ (<1660 °C), $Zr_3Rh_{5\pm x}$ (<1790 °C), $ZrRh_{3\pm x}$ (<1920 °C), ZrC_{1-x}, β-Zr, Rh, C The solubility of C in $ZrRh_{3\pm x}$ is ~10 at.%; no solubility of Rh in ZrC_{1-x}. Depend. on compos., graphite is in equilibrium with Rh + $ZrRh_3C_x$ or $ZrRh_3C_x$ + ZrC_{1-x}.	[391, 487]
C–Ru–Si	Plotted at 1340 °C: Ru_2Si (<~1225–1545 °C), Ru_5Si_3 (~1330–1550 °C), Ru_4Si_3 (or $RuSi_{0.9}$, <1695 °C), RuSi (<~1800 °C), Ru_2Si_3 (or $RuSi_{1.8}$, <~1710 °C), SiC, Si, Ru, C	[487, 503–504]
C–Ru–Ta	Plotted at 1600 °C: $TaRu_3C_{1-x}$ ($x \approx 0.6$, stable in the limited range of temp.), γ-Ru_3Ta_{2-x} (<~1665 °C), μ-$RuTa_{1\pm x}$ (<~2080 °C), μ'-$RuTa_{1\pm x}$ (<~1400 °C), μ''-$RuTa_{1\pm x}$ (<~800 °C), α-$Ta_{2+x}C$, TaC_{1-x}, Ta, C Graphite is in equilibrium with Ru + TaC_{1-x}.	[391, 487, 897]
C–Ru–Th	Plotted at 900 and 1200 °C: ~$Th_{11}Ru_{12}C_{18}$ (or $Th_{3+x}Ru_{4-x}C_5$, $x \approx 0.3$, ?), ~$Th_2Ru_6C_5$ (or $ThRu_3C_{1.5}$, ?), ~$ThRu_3C_{1-x}$ ($0 < x < 0.1$, ?), Th_7Ru_3 (<~1410 °C), Th_3Ru_2 (<1425 °C), ThRu (<~1460 °C), $ThRu_2$ (<at least 1550 °C), $ThC_{1\pm x}$, α-ThC_{2-x}, β-ThC_{2-x}, α-Th, β-Th, Ru, C	[391, 487, 499–500]
C–Ru–Ti	Plotted at 1500 °C: $TiRu_3C_{1-x}$ (?), $TiRu_{1\pm x}$ (or $TiRu_{1+x}$ <~2130–2150 °C), TiC_{1-x}, β-Ti, Ru, C TiC_{1-x}–Ru is plotted: eutectic—~1700–1840 °C Graphite is in equilibrium with Ru + TiC_{1-x}.	[244, 391, 487]
C–Ru–U	Plotted at 1000 and 1300 °C: U_2RuC_2 (<~1700 °C), URu_3C_x ($0 \le x \le 0.7$ at 1300 °C, extended solid solution based on URu_3, <1850 °C), U_2Ru (<~935 °C), α-URu (<795 °C), β-URu (~795–1160 °C), U_3Ru_4 (<~1165 °C), U_3Ru_5 (<~1180 °C), $UC_{1\pm x}$, ζ-U_2C_3, γ-U, β-U, α-U, Ru, C	[244, 391, 487, 495, 501–502, 619]
C–Ru–V	Plotted at 1600 °C: VRu_3C_{1-x} ($x \approx 0.6$, stable in the limited range of temp.), V_3Ru (at least <1500 °C, ?), $VRu_{1\pm x}$ (<1925–1975 °C), β-$V_{2\pm x}C$, β'-$V_{2+x}C$, ζ-V_4C_{3-x}, $V_6C_{5\pm x}$, $V_8C_{7\pm x}$, VC_{1-x}, V, Ru, C Graphite is in equilibrium with Ru + VC_{1-x}.	[244, 391, 487, 897]
C–Ru–W	Plotted at 1500 and 2000 °C: $(W,Ru)_3C_{1-x}$ (~2000 °C), σ-$Ru_2W_{3\pm x}$ (from ~1665–1670 °C to 2300 °C), α-$W_{2+x}C$, β-$W_{2+x}C$, δ-$WC_{1\pm x}$, W, Ru, C	[244, 391, 487]

(continued)

Table 2.14 (continued)

System	Type of phase diagram (temperature and composition sections, constituent phases or phase fields) and/or character of interphase interaction and materials compatibility	References
C–Ru–Zr	Plotted at 1500 °C: $ZrRu_3C_{1-x}$ ($x \approx 0.3$), δ-$ZrRu_{1\pm x}$ (<2130 °C), λ_1-$ZrRu_2$ (1285–1825 °C), ZrC_{1-x}, β-Zr, Ru, C ZrC_{1-x}–Ru is plotted: eutectic—~1800 °C Graphite is in equilibrium with Ru + ZrC_{1-x}.	[244, 391, 487]
C–S–Ta	No diagram plot Ta_2S_2C (2 polytypes; C in carbosulfides is related to graphene sheets on (111) surfaces of TaC_{1-x})	[855]
C–S–Ti	No diagram plot Ti_2SC ($M_{n+1}AX_n$-phase)	[680–681, 744–745, 860]
C–S–Ti–V	No diagram plot $(Ti,V)_2SC$ ($M_{n+1}AX_n$-phase solid solution)	[680–681, 860]
C–S–Zr	No diagram plot Zr_2SC ($M_{n+1}AX_n$-phase)	[680–681, 744–745, 860]
C–Sc–Tc	Plotted schematically	[840]
C–Sc–Ti	Plotted at 1300–1800 °C: $(Sc,Ti)C_{1-x}$ (ScC_{1-x}–TiC_{1-x} monocarbide continuous solid solution), α-Sc_4C_3, β-Sc_4C_{3+x}, Sc_3C_{4-x} (or $Sc_{15}C_{19\pm x}$), α-Sc, α-Ti, β-(Sc,Ti), C Graphite is in equilibrium with $(Sc,Ti)C_{1-x}$ + Sc_3C_{4-x} (or $Sc_{15}C_{19\pm x}$).	[138, 244, 391, 601]
C–Sc–Zr	Plotted at 1500–1900 °C: $(Sc,Zr)C_{1-x}$ (ScC_{1-x}–ZrC_{1-x} monocarbide continuous solid solution), α-Sc_4C_3, β-Sc_4C_{3+x}, Sc_3C_{4-x} (or $Sc_{15}C_{19\pm x}$), α-(Sc,Zr), β-(Sc,Zr), C Graphite is in equilibrium with $(Sc,Zr)C_{1-x}$ + Sc_3C_{4-x} (or $Sc_{15}C_{19\pm x}$).	[244, 602]
C–Si–Ta	Plotted at 800–1820 °C: $Ta_5Si_3C_{1-x}$ (at least at ~1000–1820 °C), α-Ta_4SiC_3, β-Ta_4SiC_3 ($M_{n+1}AX_n$-phases, ?), Ta_3Si (or $Ta_{4.5}Si$, <~2340–2520 °C), Ta_2Si (<2440–2460 °C), α-Ta_5Si_3 (<~1700–2160 °C), β-Ta_5Si_3 (from ~1700–2160 °C to 2500–2550 °C), $TaSi_2$ (<~2040–2300 °C), α-$Ta_{2+x}C$, TaC_{1-x}, SiC, Ta, Si, C Graphite is in equilibrium with SiC + TaC_{1-x}.	[138, 242, 244, 487, 503, 639, 898]
C–Si–Ti	Plotted at 1100–2875 °C: α-Ti_3SiC_2, β-Ti_3SiC_2 (<2375 °C, small homog. range at lower temp., $M_{n+1}AX_n$-phases), Ti_2SiC ($M_{n+1}AX_n$-phase, ?), Ti_4SiC_3, Ti_5SiC_4 ($M_{n+1}AX_n$-phases, metastable, ?), $Ti_5Si_2C_3$, $Ti_7Si_2C_5$ (intergrown structures, $M_{n+1}AX_n$-phases, ?), $Ti_5Si_{3\pm y}C_x$ ($0 \le x \le 0.99$, solid solution based on $Ti_5Si_{3\pm x}$, <~2130–2335 °C), Ti_3Si (<1170 °C), Ti_5Si_4 (<1920 °C), TiSi (<1570 °C), $TiSi_2$ (<1490–1500 °C), TiC_{1-x}, SiC, β-Ti, Si, C Carbon stabilizes the structure of $Ti_5Si_{3\pm x}$. Graphite is in equilibrium with SiC + TiC_{1-x}. In vacuum, the interaction between graphite and $TiSi_2$ begins at ~1300 °C (2 h contact exposure) and leads to the formation of SiC and $Ti_5Si_{3\pm y}C_x$. At 900–1300 °C, in vacuum the interaction between SiC and Ti results in the formation of $Ti_5Si_{3\pm y}C_x$ and TiC_{1-x}.	[242, 244, 419, 463, 487, 503, 506–509, 640–642, 680–681, 744–746, 819, 860]

(continued)

Table 2.14 (continued)

System	Type of phase diagram (temperature and composition sections, constituent phases or phase fields) and/or character of interphase interaction and materials compatibility	References
C–Si–U	Plotted at 675–1500 °C: $U_3Si_2C_2$ (or $U_3Si_2C_3$, <1750 °C), $U_3Si_2C_{1-x}$ (?), $U_5Si_4C_{1-x}$ ($x = 0.25$, or $U_{20}Si_{16}C_3$, <1600 °C), U_3SiC_3 (?), USi_3 (<1510 °C), USi_2 (<450 °C, metastable, ?), α-USi_{2-x} (?), β-USi_{2-x} ($x = 0.12$, <1710 °C), α-U_3Si_5 (?), β-U_3Si_5 (?), γ-U_3Si_5 (<1770 °C), USi (<1580 °C), U_3Si_2 (<1665 °C), α-U_3Si(<∼−150 °C), β-U_3Si (∼−150–760 °C), γ-U_3Si (∼760–930 °C), $UC_{1\pm x}$, ζ-U_2C_3, α-UC_{2-x}, β-UC_{2-x}, SiC, γ-U, β-U, α-U, Si, C Eutectic $UC_{1\pm x}$–U_3Si_2–γ-U (∼950–980 °C) Eutectic α-UC_{2-x}–β-USi_{2-x}–$U_3Si_2C_2$ (∼1600 °C, ?) $UC_{1\pm x}$–U_3Si_2 is plotted: eutectic—∼1660 °C Mutual solid solubilities between $UC_{1\pm x}$ and SiC are negligible. At 1000 °C the interaction between $UC_{1\pm x}$ and Si leads to the formation of USi_{2-x}.	[138, 242, 244, 533–534, 692, 849]
C–Si–V	Plotted at 800 and 1000 °C: V_2SiC, V_2SiC_2 (predicted $M_{n+1}AX_n$-phases, ?), $V_5Si_3C_{1-x}$ (extended solid solution based on V_5Si_3, <2010 °C, ?), $V_{3+x}Si$ (<1925 °C), V_6Si_5 (1160–1670 °C), VSi_2 (<∼1675 °C), α-$V_{2+x}C$, β-$V_{2\pm x}C$, β'-$V_{2+x}C$, ζ-V_4C_{3-x}, $V_6C_{5\pm x}$, $V_8C_{7\pm x}$, VC_{1-x}, SiC, Si, V, C SiC–VC_{1-x} ($x = 0.17$) is plotted: eutectic—∼2220 °C, ∼38 mol.% SiC; no mutual solubilities between the components At 800 °C the solubility of C in $V_{3+x}Si$ and that of Si in α-$V_{2+x}C$ are ∼2 at.%. Graphite is in equilibrium with SiC + VC_{1-x}.	[244, 267, 393–394, 503, 744–745, 748–750]
C–Si–W	Plotted at 1800 °C:$W_xSi_yC_z$ (or $W_{5-x}Si_{3-y}C_{x+y}$, ?), W_5Si_{3+x} (<2095–2320 °C), WSi_2 (<2020–2160 °C), β-$W_{2+x}C$, δ-$WC_{1\pm x}$, SiC, W, Si, C Graphite is in equilibrium with SiC + δ-$WC_{1\pm x}$. In vacuum the interaction between graphite and WSi_2 begins at ∼1500 °C (2 h contact exposure) and results in the formation of SiC and $W_xSi_yC_z$. At 1100–1900 °C the interaction between SiC and metal W results in the formation of δ-$WC_{1\pm x}$, W_5Si_{3+x} and WSi_2.	[138, 242, 419, 463, 487, 503, 819, 912]
C–Si–Zr	Plotted at 1000–1700 °C: $Zr_5Si_3C_x$ ($0 < x \leq \sim 0.4$ (1200 °C) and $0 < x \leq \sim 0.7$ (1700 °C), solid solution based on Zr_5Si_3, at least at 1745–2180 °C, ?), Zr_3Si (<1650 °C), Zr_2Si (<1925 °C), Zr_3Si_2 (<2215–2220 °C), α-Zr_5Si_4 (<1860 °C), β-Zr_5Si_4 (1860–2250 °C), α-ZrSi (<1460 °C), β-ZrSi (1460–2210 °C), $ZrSi_2$ (<1620 °C), ZrC_{1-x}, SiC, α-Zr, β-Zr, Si, C C stabilizes the structure of Zr_5Si_3 at low temp.; the solubility of C in other Zr silicides is low. Graphite is in equilibrium with SiC + ZrC_{1-x}.	[242, 244, 418–419, 487, 503, 510–512, 689]

(continued)

Table 2.14 (continued)

System	Type of phase diagram (temperature and composition sections, constituent phases or phase fields) and/or character of interphase interaction and materials compatibility	References
C–Sm–U	No diagram plot $UC_{1\pm x}$–SmC_{1-x} monocarbide continuous solid solution or extended solid solution based on $UC_{1\pm x}$.	[391]
C–Sn–Ti	Plotted partially at 1600 °C: Ti_2SnC, Ti_3SnC_2 ($M_{n+1}AX_n$-phases), α-Ti_6Sn_5 (<790 °C), β-Ti_6Sn_5 (790–1490 °C), Ti_5Sn_3 (<1505 °C), $Ti_{2-x}Sn$ (<1550 °C), $Ti_{3+x}Sn$ (<1670 °C), TiC_{1-x}, α-Ti, β-Ti, α-Sn, β-Sn, C	[680–681, 744–745, 860, 984]
C–Sn–Zr	No diagram plot Zr_2SnC ($M_{n+1}AX_n$-phase), Zr_5Sn_3C, ?	[680–681, 744–745, 860]
C–Ta–Tc	Plotted schematically	[840]
C–Ta–Th	Plotted at 1500 °C: $ThC_{1\pm x}$, γ-ThC_{2-x}, α-$Ta_{2+x}C$, TaC_{1-x}, α-Th, β-Th, Ta, C The mutual solid solubilities in the pairs of metals and their carbides are very low. Graphite is in equilibrium with γ-ThC_{2-x} + TaC_{1-x}.	[244, 391]
C–Ta–Ti	Plotted at 1500–3200 °C: (Ta,Ti)C_{1-x} (TaC_{1-x}–TiC_{1-x} monocarbide continuous solid solution with the critical point of the miscibility gap calculated to be <0 °C), α-$(Ta,Ti)_{2+x}C$ (low temp. semicarbide extended solid solution based on α-$Ta_{2+x}C$, the solubility of Ti varies: from ~6 to ~28 at.% at 1500–1800 °C and ~2–30 at.% at 2000 °C), β-$(Ta,Ti)_{2\pm x}C$ (high temp. semicarbide extended solid solution based on β-$Ta_{2\pm x}C$, the solubility of Ti varies: ~0–30 at.% at 2400–2600 °C, ~0–20 at.% at 3000 °C and ~0–10 at.% at 3200 °C), (β-Ti, Ta), C Graphite is in equilibrium with (Ta,Ti)C_{1-x}.	[138, 242, 391, 419, 440, 468, 513, 662, 747, 813, 837, 881]
C–Ta–Ti–U	TaC_{1-x}–TiC_{1-x}–$UC_{1\pm x}$ is plotted at 2000–2050 °C: (Ta,Ti,U)C_{1-x} (TaC_{1-x}–TiC_{1-x}–$UC_{1\pm x}$ extended solid solution based on TaC_{1-x}–TiC_{1-x} and TaC_{1-x}–$UC_{1\pm x}$ monocarbide continuous solid solutions with great miscibility gap because of low mutual solubilities in the TiC_{1-x}–$UC_{1\pm x}$ system)	[391]
C–Ta–Ti–W	TaC_{1-x}–TiC_{1-x}–δ-$WC_{1\pm x}$ is plotted at 1450, 2200 and 2500 °C: (Ta,Ti,W)C_{1-x} (TaC_{1-x}–TiC_{1-x}–δ-$WC_{1\pm x}$ extended solid solution based on TaC_{1-x}–TiC_{1-x} monocarbide continuous solid solution) The solubilities of δ-$WC_{1\pm x}$ in TaC_{1-x} and TiC_{1-x} are ~10 and ~35 mol.%, respectively; the solubilities of TaC_{1-x} and TiC_{1-x} in δ-$WC_{1\pm x}$ are low.	[250, 419, 465, 589]

(continued)

Table 2.14 (continued)

System	Type of phase diagram (temperature and composition sections, constituent phases or phase fields) and/or character of interphase interaction and materials compatibility	References
C–Ta–U	Plotted at 1200 and 1700 °C: (Ta,U)C_{1-x} (TaC_{1-x}–$UC_{1\pm x}$ monocarbide continuous solid solution), α-$Ta_{2+x}C$, ζ-U_2C_3, α-UC_{2-x}, β-UC_{2-x}, U, Ta, C Depend. on compos., graphite is in equilibrium with (Ta,U)C_{1-x} or (Ta,U)C_{1-x} + UC_{2-x}; the compos. of (Ta,U)C_{1-x} in equilibrium with C + UC_{2-x} is corresp. to $(Ta_{0.78}U_{0.22})C_{0.99}$ (at 1700 °C) and $(Ta_{0.85}U_{0.15})C_{1-x}$ (at 2200 °C), and shifts to lower U concentrations with temp. increase. At 1400 °C (66 h exposure) no appreciable reaction is occurred on the contact surface between metal Ta and $UC_{1.06}$, at 1800 °C (3 h exposure)—the interaction is noticeable.	[138, 242, 391, 812, 822]
C–Ta–U–V	TaC_{1-x}–VC_{1-x}–$UC_{1\pm x}$ is plotted at 2000–2050 °C: (Ta,V,U)C_{1-x} (TaC_{1-x}–VC_{1-x}–$UC_{1\pm x}$ extended solid solution based on TaC_{1-x}–VC_{1-x} and TaC_{1-x}–$UC_{1\pm x}$ monocarbide continuous solid solutions with great miscibility gap because of low mutual solubilities in the pair VC_{1-x}–$UC_{1\pm x}$)	[391]
C–Ta–U–Zr	TaC_{1-x}–ZrC_{1-x}–$UC_{1\pm x}$ is plotted at 2050 °C: (Ta,Zr,U)C_{1-x} (TaC_{1-x}–ZrC_{1-x}–$UC_{1\pm x}$ monocarbide continuous solid solution) At ~2100 °C $(U_{0.5}Zr_{0.5})C_{1\pm x}$ is compatible for periods of up to 35 min. with metal Ta.	[391, 812]
C–Ta–V	Plotted at 1400 °C: $Ta_{2\pm y}VC_{2-x}$ ($Ta_{1.80\div2.04}V_{1.0\div0.96}C_{1.74\div1.80}$ at 1650 °C), (Ta,V)C_{1-x} (TaC_{1-x}–VC_{1-x} monocarbide continuous solid solution), (Ta,V)$_{2\pm x}$C (α-$Ta_{2+x}C$–β-$V_{2\pm x}C$ semicarbide continuous solid solution), (Ta,V), C TaC_{1-x}–VC_{1-x} is plotted: miscibility gap (critical point—~1300 °C at ~$Ta_{0.4}V_{0.6}C_{1-x}$, at 1000 °C ranges from ~$Ta_{0.85}V_{0.15}C_{1-x}$ to ~$Ta_{0.05}V_{0.95}C_{1-x}$). Graphite is in equilibrium with (Ta,V)C_{1-x}.	[391, 723, 813, 837]
C–Ta–V–W	α-$Ta_{2+x}C$–β-$V_{2\pm x}C$–α-$W_{2+x}C$ is plotted at 1650 and 2000 °C: (Ta,V,W)$_{2\pm x}$C (extended solid solution based on α-$Ta_{2+x}C$–β-$V_{2\pm x}C$ and β-$V_{2\pm x}C$–α-$W_{2+x}C$ semicarbide continuous solid solutions), (Ta,V,W)$_{2\pm x}$C + (Ta,V,W)C_{1-x} + (Ta,V,W), (Ta,V,W)C_{1-x} + (Ta,V,W)	[435]

(continued)

Table 2.14 (continued)

System	Type of phase diagram (temperature and composition sections, constituent phases or phase fields) and/or character of interphase interaction and materials compatibility	References
C–Ta–W	Plotted at 1500–3500 °C: (Ta,W)C_{1-x} (TaC_{1-x}–γ-WC_{1-x} monocarbide continuous solid solution at temp. ~2500–2750 °C, or monocarbide extended solid solution based on TaC_{1-x} at temp. ≤ ~2500 °C and ≥ ~2750 °C with the max solubility of W corresp. to compos.: ~$(Ta_{0.9}W_{0.1})C_{1-x}$ at 1500 °C, ~$(Ta_{0.8}W_{0.2})C_{1-x}$ at 1800 °C and ~$(Ta_{0.7}W_{0.3})C_{1-x}$ at 2000 °C), $(Ta,W)_{2\pm x}C$ (β-$Ta_{2\pm x}C$–γ-$W_{2\pm x}C$ semicarbide continuous solid solution in the limited range of temp. ~2460–2790 °C), α-$(Ta,W)_{2+x}C$ (semicarbide extended solid solution based on α-$Ta_{2+x}C$ at temp. ≤ ~1950–2200 °C), β-$(Ta,W)_{2\pm x}C$ (semicarbide extended solid solution based on β-$Ta_{2\pm x}C$ at ~1950–2450 °C and ~2750–3400 °C), α-$(W,Ta)_{2+x}C$ (semicarbide extended solid solution based on α-$W_{2+x}C$ at temp. ~1250–2100 °C), β-$(W,Ta)_{2+x}C$ (semicarbide extended solid solution based on β-$W_{2+x}C$ at temp. ~2100–2450 °C), γ-$(W,Ta)_{2\pm x}C$ (semicarbide extended solid solution based on γ-$W_{2\pm x}C$ at temp. ~2300–2450 °C), δ-$WC_{1\pm x}$ (max. solubility of Ta is ~4 at.% at 2760 °C), ζ-Ta_4C_{3-x}, $Ta_6C_{5\pm x}$, (Ta,W), C Eutectic β-$(Ta,W)_{2\pm x}C$–(Ta,W) (2860 °C, ~25 at.% W, ~11 at.% C) Depend. on compos., graphite is in equilibrium with δ-$WC_{1\pm x}$ + (Ta,W)C_{1-x} or (Ta,W)C_{1-x}.	[138, 242, 391, 419, 514, 591, 723, 773, 801–804, 827, 837]
C–Ta–Zr	Plotted at 1000–3900 °C: (Ta,Zr)C_{1-x} (TaC_{1-x}–ZrC_{1-x} monocarbide continuous solid solution at temp. ~940–3400 °C), α-$(Ta,Zr)_{2+x}C$ (semicarbide extended solid solution based on α-$Ta_{2+x}C$ at temp. ≤ ~2100 °C with the solid solubility of Zr—up to ~12 at.% at temp. 1775–1820 °C), β-$(Ta,Zr)_{2\pm x}C$ (semicarbide extended solid solution based on β-$Ta_{2\pm x}C$ at 1930–3300 °C with the solid solubility of Zr—up to ~14 at.% at 2500 °C), (Ta,β-Zr), C Eutectic (Ta,Zr)C_{1-x}–(Ta,β-Zr) (~1800 °C) TaC_{1-x}–ZrC_{1-x} is plotted: miscibility gap (critical point—~940 °C at ~$Ta_{0.65\div0.70}Zr_{0.30\div0.35}C_{1-x}$, at 600 °C ranges from ~$Ta_{0.2}Zr_{0.8}C_{1-x}$ to ~$Ta_{0.95}Zr_{0.05}C_{1-x}$). Graphite is in equilibrium with (Ta,Zr)C_{1-x}.	[138, 242, 391, 419, 421, 423, 468, 515, 622, 805–807, 813, 837]
C–Tb–U	No diagram plot $UC_{1\pm x}$–TbC_{1-x} monocarbide continuous solid solution, or extended solid solution based on $UC_{1\pm x}$ (?).	[391]
C–Tc–Ti	Plotted schematically	[840]
C–Tc–U	Plotted at 1500 °C: $UTcC_2$ (<1800 °C), UTc_3C_{1-x} ($0.55 \le x \le 0.65$, ?), UTc_3C_{1+x} (?), UTc_2, TcC_{1-x} (or $Tc_{3\pm x}C$, ?), $UC_{1\pm x}$, ζ-U_2C_3, α-UC_{2-x}, β-UC_{2-x}, α-U, β-U, γ-U, Tc, C	[391]

(continued)

Table 2.14 (continued)

System	Type of phase diagram (temperature and composition sections, constituent phases or phase fields) and/or character of interphase interaction and materials compatibility	References
C–Tc–V	Plotted schematically	[840]
C–Tc–W	Plotted schematically	[840]
C–Tc–Zr	Plotted schematically	[840]
C–Th–Ti	Plotted at 1500 °C: $ThC_{1\pm x}$, α-ThC_{2-x}, β-ThC_{2-x}, γ-ThC_{2-x}, TiC_{1-x}, α-Ti, β-Ti, α-Th, β-Th, C The solid solubilities of metal Th and Th carbides in TiC_{1-x} and those of TiC_{1-x} in metal Th and Th carbides are low.	[391]
C–Th–U	Plotted at 1000–1800 °C: $(U,Th)C_{1\pm x}$ ($UC_{1\pm x}$–$ThC_{1\pm x}$ monocarbide continuous solid solution based on $UC_{1\pm x}$–β-UC_{2-x}, α-Th–$ThC_{1\pm x}$ and $ThC_{1\pm x}$–γ-ThC_{2-x} continuous solid solutions with specific miscibility gaps, homog. range (limits) at 1800 °C: ~$UC_{0.9}$–$UC_{1.9}$–$ThC_{1.9}$–$ThC_{0.2}$ with two miscibility gaps (two-phase regions) $UC_{1.1}$–$(U_{0.9}Th_{0.1})C_{1.4}$–$UC_{1.7}$ and $ThC_{1.1}$–$(U_{0.15}Th_{0.85})C_{1.2}$–$ThC_{1.3}$), at temp. <1700 °C—separated regions based on $UC_{1\pm x}$, γ-ThC_{2-x}, $ThC_{1\pm x}$ and α-Th solid solutions), α-$(U,Th)C_{2-x}$ (dicarbide extended solid solution based on α-UC_{2-x}), β-$(Th,U)C_{2-x}$ (dicarbide extended solid solution based on β-ThC_{2-x}), α-$(Th,U)C_{2-x}$ (dicarbide extended solid solution based on α-ThC_{2-x}), ζ-U_2C_3, α-Th, β-Th, γ-U, C $UC_{1\pm x}$ ($x = 0$)–$ThC_{1\pm x}$ ($x = 0$) is plotted: no mutual solubilities at 500 °C, the critical point of the miscibility gap—~1600 °C, $(U_{0.5}Th_{0.5})C_{1.0}$ (the compos. corresp. to the min. melt. point of the $(U,Th)C_{1\pm x}$ phase ($x = 0$)–2200 °C).	[138, 242, 391, 516–517]
C–Th–U–Zr	$UC_{1\pm x}$–$ThC_{1\pm x}$–ZrC_{1-x} is plotted at 2000 °C: $(U,Th,Zr)C_{1\pm x}$ ($UC_{1\pm x}$–$ThC_{1\pm x}$–ZrC_{1-x} extended solid solution based on $UC_{1\pm x}$–$ThC_{1\pm x}$ and $UC_{1\pm x}$–ZrC_{1-x} continuous solid solutions with great miscibility gap because of very low mutual solubilities in the pair $ThC_{1\pm x}$–ZrC_{1-x})	[391]
C–Th–W	Plotted at 1500 °C: $ThC_{1\pm x}$, γ-ThC_{2-x}, α-$W_{2+x}C$, δ-$WC_{1\pm x}$, β-Th, W, C The solubilities of Th carbides in W carbides and those of W carbides in Th carbides are low.	[138, 391]
C–Th–Y	Plotted at 1600 °C: $(Th,Y)C_{1-x}$ ($ThC_{1\pm x}$–$YC_{1\pm x}$ monocarbide continuous solid solution), $(Th,Y)C_{2\pm x}$ (γ-ThC_{2-x}–β-$YC_{2\pm x}$ dicarbide continuous solid solution), β-Y_2C_{3-x}, β-Th, β-Y, C Graphite is in equilibrium with $(Th,Y)C_{2\pm x}$.	[391]
C–Th–Zr	Plotted at 1100 and 1500 °C: $ThC_{1\pm x}$, α-ThC_{2-x}, β-ThC_{2-x}, γ-ThC_{2-x}, ZrC_{1-x}, α-Th, β-Th, α-Zr, β-Zr, C The solid solubilities of metal Th and Th carbides in ZrC_{1-x} and those of ZrC_{1-x} in metal Th and Th carbides are low. Graphite is in equilibrium with γ-ThC_{2-x} + ZrC_{1-x}.	[391, 518–520]

(continued)

Table 2.14 (continued)

System	Type of phase diagram (temperature and composition sections, constituent phases or phase fields) and/or character of interphase interaction and materials compatibility	References
C–Ti–Tl	No diagram plot Ti_2TlC ($M_{n+1}AX_n$-phase), Ti_3TlC, ?	[680–681, 744–745, 860]
C–Ti–U	Plotted at 1500 °C: $UC_{1\pm x}$, ζ-U_2C_3, α-UC_{2-x}, β-UC_{2-x}, TiC_{1-x}, α-Ti, β-Ti, α-U, β-U, γ-U, C The max. solid solubilities of U carbides in TiC_{1-x} and those of TiC_{1-x} in U carbides are low. Graphite is in equilibrium with ζ-U_2C_3 + TiC_{1-x}.	[242, 391]
C–Ti–U–Zr	$UC_{1\pm x}$–TiC_{1-x}–ZrC_{1-x} is plotted at 2000–2050 °C: $(U,Ti,Zr)C_{1\pm x}$ ($UC_{1\pm x}$–TiC_{1-x}–ZrC_{1-x} extended solid solution based on TiC_{1-x}–ZrC_{1-x} and $UC_{1\pm x}$–ZrC_{1-x} monocarbide continuous solid solutions with great miscibility gap because of low mutual solubilities in the pair $UC_{1\pm x}$–TiC_{1-x})	[391]
C–Ti–V	Plotted at 1000–2700 °C: $(V,Ti)C_{1-x}$ (VC_{1-x}–TiC_{1-x} monocarbide continuous solid solution at temp. ≤2625 °C; the compos. of the phase at the min. melt point—$\sim(V_{0.9}Ti_{0.1})C_{0.8}$), β-$(V,Ti)_{2\pm x}C$ (semicarbide extended solid solution based on β-$V_{2\pm x}C$ at temp. ≤2000 °C; the max. solubility of Ti corresp. to compos. $(V_{0.82\div0.93}Ti_{0.07\div0.18})_{2\pm x}C$), β'-$V_{2+x}C$, ζ-V_4C_{3-x}, $V_6C_{5\pm x}$, $V_8C_{7\pm x}$, (β-Ti, V), C VC_{1-x} ($x = 0.12$)–TiC_{1-x} ($x \approx 0$) is plotted: completely soluble in each other Graphite is in equilibrium with $(V,Ti)C_{1-x}$.	[138, 242, 391, 419, 425, 521, 615, 810, 813, 815, 837, 1008]
C–Ti–W	Plotted at 1500–3100 °C: $Ti_2W_4C_{3-x}$ ($0 < x < 1$, at least at 1100 °C, ?), $(Ti,W)C_{1-x}$ (extended solid solution based on TiC_{1-x} at temp. <2530 °C with the max. solubility of W corresp. to compos. $(Ti_{0.7}W_{0.3})C_{1-x}$ at 1500 °C, $(Ti_{0.45}W_{0.55})C_{1-x}$ at 2000 °C and $(Ti_{0.3}W_{0.7})C_{1-x}$ at 2400 °C, or TiC_{1-x}–γ-WC_{1-x} monocarbide continuous solid solution at temp. ~2530–2780 °C with max. melt. point 3130 °C corresp. to $(Ti_{0.55}W_{0.45})C_{0.75}$), α-$W_{2+x}C$, β-$W_{2+x}C$, γ-$W_{2\pm x}C$, δ-$WC_{1\pm x}$, (β-Ti,W), C Eutectic $(Ti,W)C_{1-x}$–γ-$W_{2\pm x}C$–W (2680 °C, 13 at.% Ti, 23 at.% C) TiC_{1-x}–W is plotted: eutectic—~2650–2700 °C, ~24–28 mol.% TiC_{1-x} (~19–22 at.% C) $(Ti_{0.5}W_{0.5})C_{1-x}$–C is plotted: eutectic—3030 °C, ~56 at.% C	[138, 242, 391, 522, 662, 773, 827, 835, 837, 848, 1014]

(continued)

Table 2.14 (continued)

System	Type of phase diagram (temperature and composition sections, constituent phases or phase fields) and/or character of interphase interaction and materials compatibility	References
C–Ti–Zr	Plotted at 600, 1500 and 2100 °C: $(Ti,Zr)C_{1-x}$ (TiC_{1-x}–ZrC_{1-x} monocarbide continuous solid solution at higher temp., or monocarbide extended solid solutions based on TiC_{1-x} and ZrC_{1-x} at lower temp.), (β-Ti,β-Zr), C ZrC_{1-x}–TiC_{1-x} is plotted: miscibility gap in the solid state (critical point—$\sim$2000 °C, at $\sim Zr_{0.2\div0.4}Ti_{0.6\div0.8}C_{1-x}$, gap width at 1500 °C—from $Zr_{0.1\div0.2}Ti_{0.8\div0.9}C_{1-x}$ to $Zr_{0.8}Ti_{0.2}C_{1-x}$) Depend. on temp., graphite is in equilibrium with $(Zr,Ti)C_{1-x}$ or $(Zr,Ti)C_{1-x}$ + $(Ti,Zr)C_{1-x}$.	[138, 242, 391, 424–425, 626, 813, 816, 817]
C–Tl–Zr	No diagram plot Zr_2TlC ($M_{n+1}AX_n$-phase)	[680–681, 744–745, 860]
C–Tm–U	No diagram plot $UC_{1\pm x}$–TmC_{1-x} monocarbide continuous solid solution or extended solid solution based on $UC_{1\pm x}$	[391]
C–U–V	Plotted at 1600 °C: UVC_2 (<1800 °C), α-$V_{2+x}C$, β-$V_{2\pm x}C$, β'-$V_{2+x}C$, ζ-V_4C_{3-x}, $V_6C_{5\pm x}$, $V_8C_{7\pm x}$, VC_{1-x}, $UC_{1\pm x}$, ζ-U_2C_3, α-UC_{2-x}, β-UC_{2-x}, α-U, β-U, γ-U, V, C The solubilities of U carbides in V carbides and those of V carbides in U carbides are low. Graphite is in equilibrium with α-UC_{2-x} + VC_{1-x}. At 1000 °C (66 h exposure) the carburization of metal V is occurred on the contact surface with $UC_{1.06}$, at 1400 °C (66 h exposure)—the interaction is significant.	[242, 391, 822]
C–U–W	Plotted at 1700 and 2200 °C: η-UWC_{2-x} ($x \approx 0.3$, from 2150 °C to $\sim$2570–2580 °C, a low C form of UWC_2), UWC_2 (<2570–2580 °C, ?), $U_4W_4C_7$ (or $UWC_{1.75}$, $\leq\sim$2300 °C), α-$W_{2+x}C$, δ-$WC_{1\pm x}$, $UC_{1\pm x}$, ζ-U_2C_3, α-UC_{2-x}, β-UC_{2-x}, U, W, C The homog. ranges of ternary phases are very small. The solubilities of U carbides in W carbides and those of W carbides in U carbides are low. Depend. on compos., graphite is in equilibrium with α-UC_{2-x} + UWC_{2-x}, or δ-$WC_{1\pm x}$ + UWC_{2-x}.	[138, 242, 391, 612, 620, 812]
C–U–W–Zr	No diagram plot At $\sim$2100 °C $(U_{0.5}Zr_{0.5})C_{1\pm x}$ is compatible for periods of up to 35 min. with metal W.	[812]
C–U–Y	Plotted at 1600 °C: $(U,Y)C_{1\pm x}$ ($UC_{1\pm x}$–$YC_{1\pm x}$ monocarbide continuous solid solution), β-$(Y,U)C_{2\pm x}$ (dicarbide extended solid solutions based on β-UC_{2-x} and β-$YC_{2\pm x}$ at temp. <$\sim$1800 °C, or β-UC_{2-x}–β-$YC_{2\pm x}$ continuous solid solution at higher temp.), ζ-U_2C_3, β-Y_2C_{3-x}, α-U, β-U, γ-U, α-Y, β-Y, C	[138, 391]

(continued)

Table 2.14 (continued)

System	Type of phase diagram (temperature and composition sections, constituent phases or phase fields) and/or character of interphase interaction and materials compatibility	References
C–U–Yb	No diagram plot $UC_{1\pm x}$–YbC_{1-x} monocarbide continuous solid solution or extended solid solution based on $UC_{1\pm x}$.	[391]
C–U–Zr	Plotted at 1700–3420 °C: (U,Zr)C_{1-x} ($UC_{1\pm x}$–ZrC_{1-x} monocarbide continuous solid solution), ζ-U_2C_3, α-UC_{2-x}, β-UC_{2-x}, α-U, β-U, γ-U, α-Zr, β–Zr, C $UC_{1\pm x}$ ($x = 0$)–ZrC_{1-x} ($x = 0.19$) is plotted: completely soluble in each other α-UC_{2-x} (β-UC_{2-x})–ZrC_{1-x} ($x \approx 0$) is plotted: quasi-eutectic—2410 °C, ~80 mol.% β-UC_{2-x}, (~12 at.% Zr, ~63 at.% C); at β-(U,Zr)C_{2-x}–(Zr,U)C_{1-x}–(γC) quasi-eutectic temp., max. solubility of Zr in β-(U,Zr)C_{2-x}–~2–4 at.% (corresp. to ~$(U_{0.94}Zr_{0.06})C_{1.94}$ compos.) and in (Zr,U)C_{1-x}–~40 at.% (corresp. to ~80–90 mol.% $(Zr_{0.8\div0.9}U_{0.1\div0.2})C_{1.0}$ + ~10–20 mol.% C) At 1700–2200 °C graphite is in equilibrium with (Zr,U)C_{1-x} or (Zr,U)C_{1-x} + UC_{2-x}. At higher temp.the compos. of (Zr,U)C_{1-x}, which is in equilibrium with C + UC_{2-x}, shifts to lower U concentrations from ~$(Zr_{0.6\div0.65}U_{0.35\div0.4})C_{1-x}$ (at 1700 °C) to ~$(Zr_{0.7\div0.8}U_{0.2\div0.3})C_{1-x}$ (at 2000–2200 °C). At 1000 °C (66 h exposure) no appreciable reaction was occurred on the contact surface of metal Zr with $UC_{1.06}$, at 1400 °C (66 h exposure)—small reaction zone was found.	[138, 242, 391, 436, 520, 523–527, 822]
C–V–W	Plotted at 1500–2600 °C: (V,W)C_{1-x} (monocarbide extended solid solution based on VC_{1-x} at temp. <~2600 °C, VC_{1-x}–γ-WC_{1-x} monocarbide continuous solid solution at temp. ~2600–2700 °C), β-$(V,W)_{2\pm x}C$ (β-$V_{2\pm x}C$–β-$W_{2+x}C$ semicarbide continuous solid solution), δ-$WC_{1\pm x}$, (V,W), C Depend. on compos., graphite is in equilibrium with δ-$WC_{1\pm x}$ + (V,W)C_{1-x}, or (V,W)C_{1-x}.	[138, 242, 391, 528, 773, 827, 837]
C–V–Zr	Plotted at 1000 °C: ZrV_{2-x} (<1280–1300 °C), ZrC_{1-x}, α-$V_{2+x}C$, β-$V_{2\pm x}C$, β′-$V_{2+x}C$, ζ-V_4C_{3-x}, $V_6C_{5\pm x}$, $V_8C_{7\pm x}$, VC_{1-x}, α-Zr, β-Zr, V, C VC_{1-x} ($x = 0.12$)–ZrC_{1-x} ($x \approx 0$) is plotted: eutectic—~2460–2530 °C, ~23–34 mol.% ZrC_{1-x}; at the eutectic temp. the solubility of ZrC_{1-x} in VC_{1-x} is ~2.5–5.0 mol.% and that of VC_{1-x} in ZrC_{1-x} is ~8.0–8.5 mol.%.	[244, 391, 425, 487, 813]

(continued)

Table 2.14 (continued)

System	Type of phase diagram (temperature and composition sections, constituent phases or phase fields) and/or character of interphase interaction and materials compatibility	References
C–W–Zr	Plotted at 1100–2600 °C: (Zr,W)C_{1-x} (ZrC_{1-x}–γ-WC_{1-x} monocarbide continuous solid solution at temp. >2500 °C, or extended solid solution based on ZrC_{1-x}), ZrW_2 (<~2160–2210 °C), α-$W_{2+x}C$, β-$W_{2+x}C$, γ-$W_{2\pm x}C$, δ-$WC_{1\pm x}$, α-Zr, β-Zr, W, C Eutectic (Zr,W)C_{1-x}–γ-$W_{2\pm x}C$–W (2620 °C, 65 at.% W, 26.4 at.% C) Eutectic (Zr,W)C_{1-x}–ZrW_2–β-Zr (≤1740 °C, 7 at.% W, 3.5 at.% C) ZrC_{1-x}–W is plotted: eutectic—2800 °C, ~30 mol.% ZrC_{1-x}; the solubility of W in ZrC_{1-x} is ~7 mol.% The solubility of Zr in γ-$W_{2+x}C$ is 3.5 mol.%. At higher temp. graphite is in equilibrium with single solid phase (Zr,W)C_{1-x}.	[242, 391, 429–430, 529, 591, 647–648, 773, 827, 837]

[a] See notes to Table 2.13

The results obtained by Wang et al. [646] indicate that at room temperature surface energy of graphene, graphene oxide and natural graphite flakes are 47, 62 and 55 mJ m^{-2}, respectively. Before, a 150 mJ m^{-2} value for the surface energy of the basal plane of graphite was measured at room temperature by wetting experiments [910]. The formation of a surface-orientated perpendicular to the basal plane needs the rupture of C–C chemical bonds. The surface energy for this orientation has not been determined experimentally, but is expected to be an order of magnitude higher than that of the basal plane. In the case of vitreous carbon, the value was measured and found to be 32 mJ m^{-2} [910]. This is five times lower than that of the graphite basal plane and may be explained by the low density of vitreous carbon. The average static contact angles of graphene/graphite with some liquids, which were measured by the droplet on the film surface at room temperature, are listed in Table 2.15 [646, 909]. The quantitative characteristics of the

Table 2.15 Average static contact angles (in degrees) of graphite, graphene oxide and graphene with some liquids measured by the droplet on the film surface at room temperature [646][a]

Materials	Water	Formamide	Diiodometane	Ethylene glycol	Glycerol
Graphite	98	45	22	56	67
Graphene oxide	67	19	39	22	50
Graphene	127	80	43	76	111

[a] For water, formamide and glycerol the contact angles on de-ashed natural graphite (in degrees) were 71.5–86.6, 46.5–60.7 and 61.3–77.8, respectively, with measured surface tensions at 20.0 ± 0.5 °C: water—72.6, formamide—58.7, ethylene glycol—47.6 and glycerol—63.7, 10^{-3} N m^{-1} [909]

Table 2.16 Wettability of graphite materials by some non-ferrous metal alloys (melts) in vacuum [530, 661, 910]

Alloy composition	Wetting contact angle, degree	Temperature, °C
Ag–0.1 at.% Ti	85	1000
Ag–1.0 at.% Ti	7	1000
Al–1.7–2.0 at.% Ti	142–145	1000
	140	1100
	75	1200
Al–12 at.% Si	145–150	1000
	140–142	1150
	97	1200
	30	1300
Cu–0.01 at.% Cr	140	1150
Cu–0.1 at.% Cr	90	1150
Cu–0.6 at.% Cr	84	1150
Cu–1.0 at.% Cr	45[b]	1130
	20–30[c]	1500
Cu–6.1 at.% Cr	40	1150
Cu–12.0 at.% Cr	23	1150
Cu–1.25 at.% V	118	1150
	110	1200
	75	1250
Cu–3.75 at.% V	90	1150
	75	1200
Cu–6.2 at.% V	130	1150
	60	1200
	40	1250
Cu–2.9 at.% Sn–2.7 at.% Ti	28	1150
Cu–2.9 at.% Sn–4 at.% Ti	21	1150
Cu–5.6 at.% Sn	135	1150
Cu–5.6 at.% Sn–1.4 at.% Ti	48	1150
Cu–5.6 at.% Sn–3.95 at.% Ti	21	1150
Cu–5.6 at.% Sn–4.1 at.% Ti	10	1150
Cu–11.5 at.% Sn	135	1150
Cu–11.5 at.% Sn–0.75 at.% Ti	70	1150
Cu–11.5 at.% Sn–1.45 at.% Ti	22	1150
Cu–11.5 at.% Sn–2.9 at.% Ti	14	1150
Cu–20 at.% Sn	160	1150
Cu–50 at.% Sn	147	1150
Cu–5.0 at.% Ni	140	1300
Cu–9.3 at.% Ni	140	1300
Cu–9.3 at.% Ni–0.7 at.% Nb	150	1200
	140	1250
	120	1300
Cu–9.3 at.% Ni–1.4 at.% Nb	150	1200
	95	1250
	50	1300

(continued)

Table 2.16 (continued)

Alloy composition	Wetting contact angle, degree	Temperature, °C
Cu–9.3 at.% Ni–2.05 at.% Nb	5	1300
Cu–9.3 at.% Ni–3.45 at.% Nb	35	1250
Cu–9.3 at.% Ni–7.05 at.% Nb	40	1200
Cu–9.3 at.% Ni–1.25 at.% V	110	1150
	67	1200
	55	1250
Cu–9.3 at.% Ni–3.75 at.% V	115	1150
Cu–9.3 at.% Ni–6.2 at.% V	70	1150
	30	1200
Cu–21.0 at.% Ni	134	1500
Cu–25.0 at.% Ni	128	1500
Cu–25.0 at.% Ni–8.0 at.% Sn–6.0 at.% W	115	1300
Cu–28.0 at.% Ni–4.0 at.% Sn–6.0 at.% W	90	1300
Cu–30.0 at.% Ni	120	1500
Cu–35.0 at.% Ni	115	1500
Cu–35.0 at.% Ni–3.0 at.% Sn–9.0 at.% W	85	1300
Cu–36.0 at.% Ni–7.0 at.% Sn–9.0 at.% W	61	1420
Cu–5.0 at.% Co	138	1300
Cu–10.2 at.% Ti	0	1150
Cu–24.0 at.% Mn	70	1200
Ni–45.4 at.% Pd	137	1240
Sn–0.9 at.% Ti	76	1150
Sn–7.1 at.% Ti	5	1150
Sn–25.0 at.% Ni	143	1500

[a] For the same alloy on vitreous carbon in high vacuum, contact angle values (in degrees) are 37–45 at 1100 °C and ~40 at 1150 °C [910]
[b] In Ar atmosphere
[c] In Ar–5 % H_2 gas medium

Table 2.17 Wetting contact angles (in degrees) of pure molten halides MeX (Me = Li, Na, K, Rb; X = F, Cl, Br) on graphite in dry inert gas atmosphere at 1000 °C [910]

Halides	LiX	NaX	KX	RbX
Fluoride	143	139	81	–
Chloride	134	127	73	46
Bromide	–	120	73	–

wettability of graphite materials by some non-ferrous metal alloys (melts) at elevated and high temperatures are shown in Table 2.16 [530, 661, 910], and wetting characteristics in alkali metal halide–graphite systems are given in Table 2.17 [910].

The character of chemical interaction and general reactions of carbon (graphite) with common chemicals (solids, aqueous solutions) and complex gases are summarized in Table 2.18.

Table 2.18 The interaction of carbon (graphite) with some chemicals and complex gases [5, 82, 238, 531–532]

Reagent, formula	Character of chemical interaction, general reactions
Air, $N_2 + O_2$	In air the oxidation of C initiates from 450 to 500 °C and leads to the formation of gaseous oxides: $2C + O_2 \leftrightarrow 2CO$ $C + O_2 \leftrightarrow CO_2$
Water, H_2O	At ambient temp. C adsorbs water vapour from atmosphere intensively. The interaction between C and water vapour initiates from 650 to 800 °C: $C + H_2O \leftrightarrow CO + H_2$
Phosphine, PH_3	The interaction with PH_3 is initiated by electrical discharge between C electrodes: $C + PH_3 \rightarrow HCP + H_2$
Potassium hydroxide, KOH	No interaction
Potassium carbonate, K_2CO_3	During heating in ammonia containing media, the interaction results in the formation of potassium cyanide: $C + K_2CO_3 + 2NH_3 \rightarrow 2KCN + 3H_2O$
Calcium cyanamide with soda, $CaCN_2 + Na_2CO_3$	The interaction between C and calcium cyanamide—soda melt results in the formation of sodium cyanide: $C + CaCN_2 + Na_2CO_3 \rightarrow CaCO_3 + 2NaCN$
Nitric acid, HNO_3	The interaction with hot concentrated nitric acid results in the oxidation of C and formation of mellitic (also called graphitic or benzenehexacarboxylic) acid: $33C + 18HNO_3 \rightarrow 2C_6(COOH)_6 + 9CO_2 + 9N_2O + 3H_2O$
Sulphuric acid, H_2SO_4	No interaction
Hydrochloric acid, HCl	No interaction
Hydrofluoric acid, HF	No interaction
Chromic acid, $H_2CrO_4 + H_2SO_4$, or $K_2Cr_2O_7 + H_2SO_4$	The interaction results in the oxidation of C: $3C + 4H_2CrO_4 + 6H_2SO_4 \rightarrow 2Cr_2(SO_4)_3 + 3CO_2 + 10H_2O$, $3C + 2K_2Cr_2O_7 + 8H_2SO_4 \rightarrow 2Cr_2(SO_4)_3 + 2K_2SO_4 + 3CO_2 + 8H_2O$
Potassium chlorate with nitric acid, $KClO_3 + HNO_3$	The interaction results in the oxidation of C and formation of mellitic (also called graphitic or benzenehexacarboxylic) acid: $15C + 6KClO_3 + 6HNO_3 \rightarrow C_6(COOH)_6 + 3CO_2 + 3Cl_2 + 6KNO_3$
Sulphuric acid with nitric acid, $H_2SO_4 + HNO_3$	During heating, the interaction results in the formation of graphite bisulphate: $192C + 24H_2SO_4 + 2HNO_3 \rightarrow 8C_{24}HSO_4{\cdot}2H_2SO_4 + N_2O + 5H_2O$[a]
Sulphuric acid with chromium trioxide, $H_2SO_4 + CrO_3$	During heating, the interaction results in the formation of graphite bisulphate: $144C + 21H_2SO_4 + 2CrO_3 \rightarrow 6C_{24}HSO_4{\cdot}2H_2SO_4 + Cr_2(SO_4)_3 + 6H_2O$[a]
Sulphuric acid with potassium permanganate,	During heating, the interaction results in the formation of graphite bisulphate:

(continued)

Table 2.18 (continued)

Reagent, formula	Character of chemical interaction, general reactions
$H_2SO_4 + KMnO_4$	$240C + 33H_2SO_4 + 2KMnO_4 \rightarrow 10[C_{24}HSO_4{\cdot}2H_2SO_4] + 2MnSO_4 + K_2SO_4 + 8H_2O$[a]
Aluminium chloride, $AlCl_3$	During heating, the interaction results in the formation of intercalation compound: $9C + AlCl_3 \rightarrow C_9{\cdot}AlCl_3$
Iron (III) chloride, $FeCl_3$	During heating, the interaction results in the formation of intercalation compounds: $nC + FeCl_3 \rightarrow C_n{\cdot}FeCl_3$
Sodium amide, $NaNH_2$	During heating to 500–600 °C, the interaction results in the formation of sodium cyanide and molecular hydrogen: $C + NaNH_2 \leftrightarrow NaCN + H_2$
Lithium amide, $LiNH_2$	The interaction results in the formation of lithium cyanamide and molecular hydrogen: $C + 2LiNH_2 \leftrightarrow Li_2NCN + 2H_2$
Nitrogen–hydrogen gas mixture, $N_2 + H_2$	At higher temp. the interaction results in the formation of hydrogen cyanide: $2C + N_2 + H_2 \rightarrow 2HCN$
Fluorine–fluorine hydride mixture, $F_2 + HF$	The interaction results in the formation of carbon fluorides C_4F and CF: $2C + F_2 \rightarrow 2CF$, $8C + F_2 \rightarrow 2C_4F$

[a] Similar reactions are realized by electrolysis on a graphite anode:
$C_m + 3H_2SO_4 \rightarrow C_mH_2SO_4{\cdot}2H_2SO_4 + H^+ + e^-$

The self-diffusion characteristics of carbon atoms, diffusion characteristics in the carbon—element and carbon—chemical compound systems in the wide range of temperatures, and summarized data on the physico-chemical interaction of carbon with the elements of periodic table are given in Addendum.

References

1. Mendeleev DI (1947) Osnovy khimii (Foundations of chemistry), Vol. 1. Goskhimizdat, Moscow, Leningrad (in Russian)
2. Rao CNR (2010) Understanding chemistry. World Scientific, New Jersey, London
3. Lide DR, ed (2010) CRC handbook of chemistry and physics, 90th ed. CRC Press, Boca Raton, New York
4. Speight JG, ed (2005) Lange's handbook of chemistry, 16th ed. McGraw-Hill, New York
5. Nekrasov BV (1973) Osnovy obschei khimii (Foundations of general chemistry), 3rd ed., Vol. 1. Khimiya, Moscow (in Russian)
6. Samsonov GV, ed (1976) Svoistva elementov (Properties of elements), 2nd ed., Vol. 1. Metallurgiya, Moscow (in Russian)
7. Rabinovich VA, Khavin ZYa (1978) Kratkii khimicheskii spravochnik (Concise handbook of chemistry), 2nd ed. Khimiya, Leningrad (in Russian)

8. Bushuev YuG, Persin MI, Sokolov VA (1994) Uglerod-uglerodnye kompozitsionnye materialy (Carbon-carbon composite materials). Metallurgiya, Moscow (in Russian)
9. McEnaney B (1999) Structure and bonding in carbon materials. In: Burchell TD (ed) Carbon materials for advanced technologies, pp. 1–33. Pergamon, Elsevier, Amsterdam
10. Heimann RB, Evsyukov SE, Koga Y (1997) Carbon allotropes: a suggested classification scheme based on valence orbital hybridization. Carbon 35:1654–1658
11. Inagaki M (2000) New carbons. Elsevier, Amsterdam
12. Belenkov EA (2003) Classification of carbon structures. In: Veziroglu TN, Zaginaichenko SYu, Schur DV et al (eds) Proc. 8th Int. conf. on hydrogen materials science and chemistry of carbon nanomaterials (ICHMS-2003), Sudak, Ukraine, 14–20 Sep 2003, pp. 730–733. IHSE, Kyiv
13. Shenderova OA, Barnard AS, Gruen DM (2006) Carbon family at the nanoscale. In: Shenderova OA, Gruen DM (eds) Ultrananocrystalline diamond, pp. 3–22. William Andrew, Norwich, New York
14. Falcao EHL, Wudl F (2007) Carbon allotropes: beyond graphite and diamond. J Chem Technol Biotechnol 82:524–531
15. Korshak VV, Kasatochkin VI, Sladkov AM, Kudryavtsev YuP, Usenbayev K (1961) O sinteze i svoistvakh poliatsetilena (On synthesis and properties of polyacetylene). Doklady AN SSSR 136(6):1342–1344 (in Russian)
16. Sladkov AM (2003) Karbin – tretya allotropnaya forma ugleroda (Carbyne – the third allotropic form of carbon). Nauka, Moscow (in Russian)
17. Chalifoux WA, Tykwinski RR (2010) Synthesis of polyynes to model the *sp*-carbon allotrope carbine. Nature Chem 2:967–971
18. Tanuma S, Palnichenko A (1995) Synthesis of low density carbon crystal "carbolite" by quenching of carbon gas. J Mater Res 10(5):1120–1125
19. Belenkov EA, Shabiev FK (2007) Structure of new carbon phases from carbyne nanorings. Crystallogr Rep 52(2):343–348
20. Belenkov EA, Mavrinsky VV (2008) Crystal structure of a perfect carbyne. Crystallogr Rep 53(1):83–87
21. Belenkov EA, Ivanovskii AL, Ul'yanov SN, Shabiev FK (2005) New framework nanostructures of carbon atoms in sp^2 and sp^3 hybridized states. J Struct Chem 46(6):961–967
22. Baughman RH, Eckhardt H, Kertesz M (1987) Structure-property predictions for new planar forms of carbon: layered phases containing sp^2 and *sp* atoms. J Chem Phys 87(11):6687–6699
23. Haley MM, Brand SC, Pak JJ (1997) Carbon networks based on dehydrobenzoannulenes: synthesis of graphdiyne substructures. Angew Chem 36:835–838
24. Narita N, Nagai S, Suzuki S, Nakao K (1998) Optimized geometries and electronic structures of graphyne and its family. Phys Rev B 58(16):11009–11014
25. Enyashin AN, Sofronov AA, Makurin YN, Ivanovskii AL (2004) Structural and electronic properties of new α-graphyne-based carbon fullerenes. J Molec Struct 684(1):29–33
26. Zhao X, Ando Y, Liu Y, Jinno M, Suzuki T (2003) Carbon nanowire made of a long linear carbon chain inserted inside a multiwalled carbon nanotube. Phys Rev Lett 90(18):187401
27. Coluci VR, Braga SF, Legoas SB, Galvao DS, Baughman RH (2004) New families of carbon nanotubes based on graphyne motifs. Nanotechnol 15:S142-S149
28. Whittaker AG (1978) Carbon: a new view of its high-temperature behaviour. Science 200:763–764
29. Whittaker AG, Kintner PL (1985) Carbon: analysis of spherules and splats formed from the liquid state and of the forms produced by quenching gas and solid. Carbon 23(3):255–262
30. Pisula W, Feng X, Mullen K (2010) Self-organization of nanographenes. In: Guldi DM, Martin N (eds) Carbon nanotubes and related structures, pp. 405–453. Wiley-VCH, Weinheim

31. Novoselov KS, Geim AK, Morozov SV, Jiang D, Zhang Y, Dubonos SV, Grigorieva IV, Firsov AA (2004) Electric field effect in atomically thin carbon films. Science 306:666–669
32. Novoselov KS, Jiang D, Schedin F, Booth TJ, Khotkevich VV, Morozov SV, Geim AK (2005) Two-dimensional atomic crystals. Proc Nat Acad Sci USA 102(30):10451–10453
33. Neto AC, Guinea F, Peres NM (2006) Drawing conclusions from graphene. Phys World 11:1–5
34. Ishigami M, Chen JH, Cullen WG, Fuhrer MS, Williams ED (2007) Atomic structure of graphene on SiO_2. Nano Lett 7(6):1643–1648
35. Geim AK, MacDonald AH (2007) Graphene: exploring carbon flatland. Phys Today 8:35–41
36. Geim AK, Novoselov KS (2007) The rise of graphene. Nature Mater 6(3):183–191
37. Meyer JC, Geim AK, Katsnelson MI, Novoselov KS, Booth TJ, Roth S (2007) The structure of suspended graphene sheets. Nature 446(3):60–63
38. Geim AK (2009) Graphene: status and prospects. Science 324:1530–1534
39. Liu Z, Suenaga K, Harris PJF, Iijima S (2009) Open and closed edges of graphene layers. Phys Rev Lett 102(1):015501
40. Biswas S, Drzal LT (2010) Multilayered nano-architecture of variable sized graphene nanosheets for enhanced supercapacitor electrode performance. ACS Appl Mater Interfaces 2(8):2293–2300
41. Kelly BT (1981) Physics of graphite. Applied Science, London
42. Pierson HO (1993) Handbook of carbon, graphite, diamond and fullerenes. Noyes, New Jersey
43. Shulepov SV (1990) Fizika uglegrafitovykh materialov (Physics of carbon materials). Metallurgiya, Chelyabinsk (in Russian)
44. Shmakova ES, Lebedev YuN, Nagornyi VG (1979) Temperaturnaya ustoichivost' romboedricheskoi fazy grafita (Temperature stability of the rhombohedral graphite phase). Izv AN SSSR Neorg Mater 15(12):2134–2137 (in Russian)
45. Kroto HW, Heath JR, O'Brien SC, Curl RF, Smalley RE (1985) C_{60}: buckminsterfullerene. Nature 318:162–163
46. Radushkevich LV, Luk'yanovich VM (1952) O structure ugleroda, obrazuyuschegosya pri termicheskom razlozhenii okisi ugleroda na zheleznom kontakte (On carbon structure formed during the thermal decomposition of carbon oxide on iron contact). Zh Fiz Khim 26:88–95 (in Russian)
47. Osawa E (1970) Chohokozoku (Superaromaticity). Kagaku 25:854–863 (in Japanese)
48. Fowler PW (1993) Systematics of fullerenes and related clusters. In: Kroto HW, Walton DRM (eds) The fullerenes, pp. 39–51. Cambridge University Press
49. Iijima S (1991) Helical microtubules of graphitic carbon. Nature 354:56–58
50. Dresselhaus MS, Dresselhaus G, Eklund PC (1996) Science of fullerenes and carbon nanotubes. Academic Press, Elsevier, San Diego
51. Lu X, Chen Z (2005) Curved pi-conjugation, aromaticity, and the related chemistry of small fullerenes ($<C_{60}$) and single-walled carbon nanotubes. Chem Rev 105:3643–3696
52. Trefilov VI, Schur DV, Tarasov BP, Shulga YuM, Chernogorenko AV, Pishuk VK, Zaginaichenko SYu (2001) Fullereny – osnova materialov buduschego (Fullerenes as the basis of future materials). ADEF-Ukraina, Kyiv (in Russian)
53. Pokropivny VV, Ivanovskii AL (2008) New nanoforms of carbon and boron nitride. Russ Chem Rev 77(10):837–873
54. Yudasaka M, Iijima S (2010) Carbon nanohorn. In: Guldi DM, Martin N (eds) Carbon nanotubes and related structures, pp. 385–404. Wiley-VCH, Weinheim
55. Giacalone F, Martin N, Wudl F (2009) Fullerene-containing polymers: an overview. In: Martin N, Giacalone F (eds) Fullerene polymers, pp. 1–14. Wiley-VCH, Weinheim
56. Rettenbacher AS, Elliot B, Hudson JS, Amirkhanian A, Echegoyen L (2006) Preparation and functionalization of multilayer fullerenes (carbon nano-onions). Chem Eur J 12:376–387

57. Shames AI, Katz EA, Panich AM, Mogilyansky D, Mogilko E, Grinblat J, Belousov VP, Belousova IM, Ponomarev AN (2009) Structural and magnetic resonance study of astralen nanoparticles. Diamond Relat Mater 18:505–510
58. Krueger A (2010) Carbon materials and nanotechnology. Wiley-VCH, Weinheim
59. Wang X, Li Q, Xie J, Jin Z, Wang J, Li Y, Jiang K, Fan S (2009) Fabrication of ultralong and electrically uniform single-walled carbon nanotubes on clean substrates. Nano Lett 9(9):3137–3141
60. Savoskin MV, Mochalin VN, Yaroshenko AP, Lazareva NI, Konstantinova TE, Barsukov IV, Prokofiev IG (2007) Carbon nanoscrolls produced from acceptor-type graphite intercalation compounds. Carbon 45:2797–2800
61. Nasibulin AG, Anisimov AS, Pikhitsa PV, Jiang H, Brown P, Choi M, Kauppinen EI (2007) Investigations of nanobud formation. Chem Phys Lett 446:109–114
62. Okada S, Otani M, Oshiyama A (2003) Energetics and electronic structure of C_{70}-peapods and one-dimensional chains of C_{70}. New J Phys 5:122.1–122.11
63. Imaizumi Y, Kushida M, Arakawa Y, Arai F, Fukuda T (2006) TEM observation of the giant carbon nanotube construction using Langmuir-Blodgett films. In: Proc. 6th IEEE conf. on nanotechnology (IEEE-NANO 2006), Cincinnati, 17–20 June 2006, Vol. 2, pp. 628–631
64. Blinc R, Arcon D, Umek P, Apih T, Milia F, Rode AV (2007) Carbon nanofoam as a potential hydrogen storage material. Phys Stat Sol B 244(11):4308–4310
65. Mileeva ZhA, Shabalin IL, Ross DK, Bogolepov VA, Zaginaichenko SYu, Schur DV, Begenev VA, Matysina ZA (2011) Carbon nano/microstructures for hybrid hydrogen storage based on specially treated carbon fibers. In: Zaginaichenko SYu, Schur DV, Skorokhod VV, Veziroglu A, Ibrahimoglu B (eds) Carbon nanomaterials in clean-energy hydrogen systems – II, pp. 107–114. Springer, Dordrecht
66. Zhang S, Koziol KKK, Kinloch IA, Windle AH (2008) Macroscopic fibers of well-aligned carbon nanotubes by wet spinning. Small 4(8):1217–1222
67. Herranz MA, Martin N (2009) Polymers based on carbon nanotubes. In: Martin N, Giacalone F (eds) Fullerene polymers, pp. 271–303. Wiley-VCH, Weinheim
68. Schur DV, Shul'ga YuM, Zaginaichenko SYu (2008) Nanostrukturnye modifikatsii ugleroda (Nanostructured carbon modifications). In: Gnesin GG, Skorokhod VV (eds) Neorganicheskoe materialovedenie (Inorganic materials science), Vol. 1. Naukova Dumka, Kyiv, pp. 437–458 (in Russian)
69. Marsh H, Rodriguez-Reinoso F (2006) Activated carbon. Elsevier, Amsterdam
70. Al-Muhtaseb SA, Ritter JA (2003) Preparation and properties of resorcinol-formaldehyde organic and carbon gels. Adv Mater 15(2):101–114
71. Yushin G, Nikitin A, Gogotsi Y (2006) Carbide-derived carbon. In: Gogotsi Y (ed) Carbon nanomaterials, pp. 211–254. CRC Press, Taylor & Francis, Boca Raton, London
72. Shenderova OA, McGuire G (2006) Types of nanocrystalline diamond. In: Shenderova OA, Gruen DM (eds) Ultrananocrystalline diamond, pp. 79–114. William Andrew, Norwich, New York
73. Kroto H (2010) Carbyne and other myths about carbon. RSC Chemistry World. http://www.rsc.org/chemistryworld/Issues/2010/November/CarbyneOtherMythsAboutCarbon.asp. Accessed 20 January 2011.
74. Nakada K, Fujita M, Dresselhaus G, Dresselhaus MS (1996) Edge state in graphene ribbons: nanometer size effect and edge shape dependence. Phys Rev B 54(24):17954–17961
75. Braga S, Coluci VR, Legoas SB, Giro R, Galvao DS, Baughman RH (2004) Structure and dynamics of carbon nanoscrolls. Nano Lett 4(5):881–884
76. Trucano P, Chen R (1975) Structure of graphite by neutron diffraction. Nature 258:136–137
77. Lipson H, Stokes AR (1942) The structure of graphite. Proc Royal Soc London A 181:101–105

78. Shenderova OA, Zhirnov VV, Brenner DW (2002) Carbon nanostructures. Crit Rev Solid State Mater Sci 27(3/4):227–356
79. Lueking AD, Pan L, Narayanan DL, Clifford EB (2005) Effect of expanded graphite lattice in exfoliated graphite nanofiber on hydrogen storage. J Phys Chem B 109:12710–12717
80. Schniepp HC, Li J-L, McAllister MJ, Sai H, Herrera-Alonso M, Adamson DH, Prud'homme RK, Car R, Saville DA, Aksay IA (2006) Functionalized single graphene sheets derived from splitting graphite oxide. J Phys Chem B 110(17):8535–8539
81. Kim H, Macosko CW (2008) Morphology and properties of polyester / exfoliated graphite nanocomposites. Macromol 41:3317–3327
82. Ubbelohde AR, Lewis FA (1960) Graphite and its crystal compounds. Oxford University Press, London
83. Fialkov AS (1997) Uglerod, mezhsloevye soedineniya i kompozity na ego osnove (Carbon, intercalation compounds and composites on its basis). Aspekt-Press, Moscow (in Russian)
84. Chung DDL (1994) Carbon fibre composites. Butterworth-Heinemann, Boston
85. Edie DD, Stoner EG (1993) Effect of microstructure and shape on carbon fiber properties. In: Buckley JD, Edie DD (eds) Carbon-carbon materials and composites. Noyes, New Jersey
86. Eletskii AV, Smirnov BM (1993) Fullereny (Fullerenes). Usp Fiz Nauk 163(2):33–60 (in Russian)
87. Haddon RC (1993) The fullerenes: powerful carbon-based electron acceptors. In: Kroto HW, Walton DRM (eds) The fullerenes, pp. 53–61. Cambridge University Press
88. Rao CNR, Seshadri R, Govindaraj A, Sen R (1995) Fullerenes, nanotubes, onions and related carbon structures. Mater Sci Eng R 15(95):209–262
89. Mitchell DR, Brown RM Jr, Spires TL, Romanovicz DK, Lagow RJ (2001) The synthesis of megatubes: new dimensions in carbon materials. Inorg Chem 40:2751–2755
90. Rahmani A, Chadli H (2011) Structure and vibrations in C_{60} carbon peapods. In: Sattler KD (ed) Handbook of nanophysics – 2. Clusters and fullerenes, pp. 46–1–46–29. CRC Press, Taylor & Francis, Boca Raton, London
91. Schur DV, Shulga YuM, Zaginaichenko SYu (2008) Uglerodnye nanostrukturnye materialy (Carbon nanostructured materials). In: Gnesin GG, Skorokhod VV (eds) Neorganicheskoe materialovedenie (Inorganic materials science), Vol. 2, Part 2, Naukova Dumka, Kyiv, pp. 530–553 (in Russian)
92. David WIF, Ibberson RM, Mathewman JC, Prassides K, Dennis TJS, Hare JP, Kroto HW, Taylor R, Walton DRM (1991) Crystal structure and bonding of ordered C_{60}. Nature 353:147–149
93. Buergi HB, Restori R, Schwarzenbach D (1993) Structure of C_{60}: partial orientational order in the room-temperature modification of C_{60}. Acta Crystallogr B 49:832–838
94. Dorset DL, McCourt MP (1994) Disorder and the molecular packing of C_{60} buckminsterfullerene: a direct electron-crystallographic analysis. Acta Crystallogr A 50:344–351
95. Okada S, Saito S (1999) Electronic structure and energetics of pressure-induced two-dimensional C_{60} polymers. Phys Rev B 59:1930–1936
96. Chen X, Yamanaka S (2002) Single-crystal X-ray structural refinement of the "tetragonal" C_{60} polymer. Chem Phys Lett 360:501–508
97. Chen X, Yamanaka S, Sako K, Inoue Y, Yasukawa M (2002) First single-crystal X-ray structural refinement of the rhombohedral C_{60} polymer. Chem Phys Lett 356:291–297
98. Narymbetov BZh, Agafonov V, Davydov VA, Kashevarova LS, Rakhmanina AV, Dzyabchenko AV, Kulakov VI, Ceolin R (2003) The crystal structure of the 2D polymerized tetragonal phase of C_{60}. Chem Phys Lett 367:157–162
99. Van Smaalen S, Petricek V, De Boer JL, Dusek M, Verheijen MA, Meijer G (1994) Low-temperature structure of solid C_{70}. Chem Phys Lett 223:323–328

100. Soldatov AV, Roth G, Dzyabchenko A, Johnels D, Lebedkin S, Meingast C, Sundqvist B, Haluska M, Kuzmany H (2001) Topochemical polymerization of C_{70} controlled by monomer crystal packing. Science 293:680–683
101. Seifert G, Enyashin AN, Heine T (2011) Solid-state structures of small fullerenes. In: Sattler KD (ed) Handbook of nanophysics – 2. Clusters and fullerenes, pp. 30–1–30–13. CRC Press, Taylor & Francis, Boca Raton, London
102. Nakamura M (2011) Clusters of fullerenes. In: Sattler KD (ed) Handbook of nanophysics – 2. Clusters and fullerenes, pp. 37–1–30–15. CRC Press, Taylor & Francis, Boca Raton, London
103. Zhao X, Liu Y, Inoue S, Suzuki T, Jones RO, Ando Y (2004) Smallest carbon nanotube is 3 angstroms in diameter. Phys Rev Lett 92:125502
104. Harris PJF (1999) Carbon nanotube and related structures. Cambridge University Press
105. Harris PJF (2009) Carbon nanotube science. Cambridge University Press
106. Li Y, Huang Y, Du S, Liu R (2001) Structures and stabilities of C_{60}-rings. Chem Phys Lett 335:524–532
107. Hayashi T, Kim YA, Matoba T, Esaka M, Nishimura K, Tsukada T, Endo M, Dresselhaus MS (2003) Smallest freestanding single-walled carbon nanotube. Nano Lett 3:887–889
108. Hornbostel B, Haluska M, Cech J, Dettlaff U, Roth S (2006) Arc discharge and laser ablation synthesis of single-walled carbon nanotubes. In: Popov VN, Lambin P (eds) Carbon nanotubes, pp. 1–18. Springer, Dordrecht
109. Salvetat J-P, Desarmot G, Gauthier C, Poulin P (2006) Mechanical properties of individual nanotubes and composites. In: Loiseau A, Launois P, Petit P, Roche S, Salvetat J-P (eds) Understanding carbon nanotubes, pp. 439–493. Springer, Berlin, Heidelberg
110. Fischer JE (2006) Carbon nanotubes: structure and properties. In: Gogotsi Y (ed) Nanotubes and nanofibers, pp. 1–35. CRC Press, Taylor & Francis, Boca Raton, London
111. Han J (2005) Structures and properties of carbon nanotubes. In: Meyyappan M (ed) Carbon nanotubes, pp. 2–24. CRC Press, Taylor & Francis, Boca Raton, London
112. Rich RL (2003) Fullerenes, endohedral fullerenes and the prediction of high boiling points. Phys Chem Chem Phys 5:2053–55
113. Iijima S, Yudasaka M, Yamada R, Bandow S, Suenaga K, Kokai F, Takahashi K (1999) Nano-aggregates of single-walled graphitic carbon nanohorns. Chem Phys Lett 309:165–170
114. Singh P, Da Ros T, Kostarelos K, Prato M, Bianco A (2010) Carbon-based nanomaterial applications in biomedicine. In: Guldi DM, Martin N (eds) Carbon nanotubes and related structures, pp. 199–232. Wiley-VCH, Weinheim
115. Ge M, Sattler K (1994) Observation of fullerene cones. Chem Phys Lett 220(3–5):192–196
116. Balaban A, Klein D, Liu X (1994) Graphitic cones. Carbon 32:357–359
117. Krishnan A, Dujardin E, Treacy MMJ, Hugdahl J, Lynum S, Ebbesen TW (1997) Graphitic cones and the nucleation of curved carbon surfaces. Nature 388:451–454
118. Naess SN, Elgsaeter A, Helgesen G, Knudsen KD (2009) Carbon nanocones: wall structure and morphology. Sci Technol Adv Mater 10:065002
119. Ihara S Itoh S, Kitakami J (1993) Toroidal forms of graphitic carbon. Phys Rev B 47(19):12908–12911
120. Itoh S, Ihara S (1993) Toroidal forms of graphitic carbon. II. Elongated tori. Phys Rev B 48(11):8323–8328
121. Martel R, Shea HR, Avouris P (1999) Rings of single-walled carbon nanotubes. Nature 398:299
122. Rode AV, Hyde ST, Gamaly EG, Elliman RG, McKenzie DR, Bulcock S (1999) Structural analysis of a carbon foam formed by high pulse-rate laser ablation. Appl Phys A Mater Sci Process 69(7): S755-S758
123. Bacon R (1960) Growth, structure and properties of graphite whiskers. J Appl Phys 31:283–290
124. Lavin JG, Subramoney S, Ruoff RS, Berber S, Tomanek D (2002) Scrolls and nested tubes in multiwall carbon nanotubes. Carbon 40:1123–1130

125. Ihara S Itoh S, Kitakami J (1993) Helically coiled cage forms of graphitic carbon. Phys Rev B 48(8):5643–5647
126. Terrones H, Terrones M (2003) Curved nanostructured materials. New J Phys 5:126.1–126.37
127. Dresselhaus MS, Dresselhaus G, Sugihara K, Spain IL, Goldberg HA (1988) Graphite fibers and filaments. Springer, New York
128. Chang Y-H, Chiu H-T, Wang L-S, Wan C-Y, Peng C-W, Lee C-Y (2003) Synthesis of sp^2 carbon nano- and microrods with novel structure and morphology. J Mater Chem 13:981–982
129. Ozkan T, Naraghi M, Chasiotis I (2010) Mechanical properties of vapour grown carbon nanofibers. Carbon 48:239–244
130. Arshad SN, Naraghi M, Chasiotis I (2011) Strong nanofibers from electrospun polyacrylonitrile. Carbon 49:1710–1719
131. Melechko AV, Merkulov VI, McKnight TE, Guillorn MA, Klein KL, Lowndes DH, Simpson ML (2005) Vertically aligned carbon nanofibers and related structures: controlled synthesis and directly assembly. J Appl Phys 97:041301
132. Retterer ST, Melechko A, Hensley DK, Simpson ML, Doktycz MJ (2008) Positional control of catalyst nanoparticles for the synthesis of high density carbon nanofiber arrays. Carbon 46:1378–1383
133. Yoon S-H, Lim S, Hong S, Mochida I, An B, Yokogawa K (2004) Carbon nano-rod as a structural unit of carbon nanofibers. Carbon 42:3087–3095
134. Zheng G-B, Sano H, Uchiyama Y (2003) New structure of carbon nanofiber after high-temperature heat-treatment. Carbon 41:853–856
135. Li J, Vergne MJ, Mowles ED, Zhong W-H, Hercules DM, Lukehart CM (2005) Surface functionalization and characterization of graphitic carbon nanofibers (GCNFs). Carbon 43:2883–2893
136. Morgan P (2005) Carbon fiber and their composites. CRC Press, Taylor & Francis, Boca Raton, London
137. Simamura S, Sindo A, Kotsuka K, Tsutiyama N, Sato T, Ito Y, Ikegami K, Yamada K, Sakamoto A, Vatanabe Y, Takeda H, Isikawa T, Sasaki V, Abe Y (1984) Carbon fibre. Omsya, Tokyo (in Japanese)
138. Kotelnikov RB, Bashlykov SN, Galiakbarov ZG, Kashtanov AI (1968) Osobo tugoplavkie elementy i soedineniya (Extra refractory elements and compounds). Metallurgiya, Moscow (in Russian)
139. Albers PW, Rotgerink HL, Bosing S, Ross DK, Parker SF (2002) Inelastic neutron scattering study on the influence of after-treatments on different technical cokes of varying impurity level and their sp^2/sp^3 character. Carbon 40(9):1549–1558
140. Harris PJF, Liu Z, Suenaga K (2008) Imaging the atomic structure of activated carbon. J Phys Condens Matter 20:362201
141. Kiyono M, Williams PJ, Koros WJ (2010) Effect of pyrolysis atmosphere on separation performance of carbon molecular sieve membranes. J Membr Sci:359:2–10
142. Tin PS, Xiao Y, Chung T-S (2006) Polyimide-carbonized membranes for gas separation: structural, composition and morphological control of precursors. Separation & Purification Rev 35:285–318
143. Koresh JE, Soffer A (1980) Study of molecular sieve carbons. I – Pore structure, gradual pore opening and mechanism of molecular sieving. J Chem Soc Faraday Trans I 76:2457–2471
144. Jenkins GM, Kawamura K (1976) Polymeric carbons – carbon fiber, glass and char. Cambridge University Press, London
145. Liu M, Cowley JM (1994) Structures of the helical carbon nanotubes. Carbon 32:393–403
146. Charlier J-C, Lambin P, Ebbesen TW (1997) Electronic properties of carbon nanotubes with polygonal cross sections. Phys Rev B 54(12):8377–8380
147. Chuvilin AL, Kuznetsov VL, Obraztsov AN (2009) Chiral carbon nanoscrolls with polygonal cross-section. Carbon 47:3099–3105

148. Gavalda S, Kaneko K, Thomson KT, Gubbins KE (2001) Molecular modeling of carbon aerogels. Colloid Surf A 187–188:531–538
149. Gavalda S, Gubbins KE, Hanzawa Y, Kaneko K, Thompson KT (2002) Nitrogen adsorption in carbon aerogels: a molecular simulation study. Langmuir 18(6):2141–2151
150. Job N, Pirard R, Marien J, Pirad J-P (2004) Porous carbon xerogels with textures tailored by pH control during sol-sol process. Carbon 42(3):619–628.
151. Fitzer E, Schafer W (1970) The effect of crosslinking on the formation of glasslike carbons from thermosetting resins. Carbon 8:353–364
152. Mildner DFR, Carpenter JM (1982) On the short range atomic structure of non-crystalline carbon. J Non-Crystalline Solids 47:391–402
153. Pesin LA, Baitinger EM (2002) A new structural model of glass-like carbon. Carbon 40:295–306
154. Brooks JD, Taylor GH (1965) The formation of graphitizing carbons from the liquid phase. Carbon 3:185–193
155. Yamada Y, Imamura T, Kakiyama H, Honda H, Oi S, Fukuda K (1974) Characteristics of meso-carbon microbeads separated from pitch. Carbon 12:307–319
156. Auguie D, Oberlin M, Oberlin A, Hyvernat P (1980) Microtexture of mesophase spheres as studied by high resolution conventional transmission electron microscopy (CTEM). Carbon 18: 337–346
157. Fedorov NF, Ivakhnyuk GK, Tetenov VV, Matyukhin GV (1981) Carbon adsorbents based on silicon carbide. J Appl Chem USSR 54:1239–1242
158. Fedorov NF, Ivakhnyuk GK, Samonin VV (1981) Mesoporous carbon adsorbents from calcium carbide. J Appl Chem USSR 54:2253–2255
159. Fedorov NF, Ivakhnyuk GK, Gavrilov DN (1982) Poristaya struktura uglerodnykh adsorbentov iz karbida titana (Porous structure of carbon adsorbents from titanium carbide). Zh Prikladnoi Khimii 55:46–50 (in Russian)
160. Kusunoki M, Rokkaku M, Suzuki T (1997) Epitaxial carbon nanotube film self-organized by decomposition of silicon carbide. Appl Phys Lett 71:2620–2622
161. Gogotsi Y, Nikitin A, Ye H, Zhou W, Fischer JE, Yi B, Foley HC, Barsoum MW (2003) Nanoporous carbide-derived carbon with tunable pore size. Nature Mater 2:591–594
162. Dash RK, Yushin G, Gogotsi Y (2005) Synthesis, structure and porosity analysis of microporous and mesoporous carbon derived from zirconium carbide. Microporous Mesoporous Mater 86:50–57
163. Yushin G, Hoffman E, Nikitin A, Ye H, Barsoum MW, Gogotsi Y (2005) Synthesis of nanoporous carbide-derived carbon by chlorination of titanium silicon carbide. Carbon 43:2075–2082
164. Dash RK, Nikitin A, Gogotsi Y (2004) Nanoporous carbon derived from boron carbide. Microporous Mesoporous Mater 72:203–208
165. Seredych M, Portet C, Gogotsi Y, Bandosz TJ (2009) Nitrogen modified carbide-derived carbons as adsorbents of hydrogen sulphide. J Colloid Interface Sci 330:60–66
166. Fayos J (1999) Possible 3D carbon structures as progressive intermediates in graphite to diamond phase transition. J Solid State Chem 148:278–285
167. Wen B, Zhao J, Li T, Dong C (2006) n-diamond: an intermediate state between rhombohedral graphite and diamond. New J Phys 8:1–10
168. Irifune T, Kurio A, Sakamoto S, Inoue T, Sumiya H (2003) Materials: ultrahard polycrystalline diamond from graphite. Nature 421:599–600
169. Dubrovinskaia N, Dubrovinsky L, Crichton W, Langenhorst F, Richter A (2005) Aggregated diamond nanorods, the densest and least compressible form of carbon. Appl Phys Lett 87:083106
170. Gogotsi Y, Weltz S, Ersoy DA, McNallan MJ (2001) Conversion of silicon carbide to crystalline diamond-structured carbon at ambient pressure. Nature 411:283–287
171. Gogotsi YG, Kofstad P, Yoshimura M, Nickel KG (1996) Formation of sp^3-bonded carbon upon hydrothermal treatment of SiC. Diamond Relat Mater 5:151–162

172. Ownby PD, Yang X, Liu J (1992) Calculated x-ray diffraction for diamond polytypes. J Am Ceram Soc 75:1876–1883
173. Johnston RL, Hoffmann R (1989) Superdense carbon C_8: supercubane or analogue of gamma-Si. J Am Chem Soc 111:810–815
174. Liu P, Cui H, Yang GW (2008) Synthesis of body-centred cubic carbon nanocrystals. Crystal Growth Design 8:581–586
175. Liu P, Cao YI, Wang CX, Chen XY, Yang GW (2008). Micro- and nanocubes of carbon with C8-like and blue luminescence. Nano Lett 8(8):2570–2575
176. Natyushenko NN, Strelnitsky VE, Gusev VA (1981) An electron-diffraction investigation of the structure of the crystalline phase of carbon C_8. Sov Phys Crystallography 26:274–276
177. Openov LA, Elesin VF (1998) Prismane C8: A new form of carbon. JETP Lett 68:726–731
178. Zazula JM (1997) On graphite transformations at high temperature and pressure induced by absorption of the LHC beam. LHC Project Note 78/97, CERN-SL/BT(TA)
179. Asinovskii EI, Kirillin AV, Kostanovskii AV (2002) Experimental investigation of the thermal properties of carbon at high temperatures and moderate pressures. Phys Usp 45(8):869–882
180. Savvatimskiy AI (2005) Measurements of the melting point of graphite and the properties of liquid carbon (a review for 1963–2003). Carbon 43:1115–1142
181. Savvatimskii AI (2003) Melting point of graphite and liquid carbon. Phys Usp 173(12):1295–303
182. Asinovskii EI, Kirillin AV, Kostanovskii AV (2003) Esche raz ob eksperimentalnom issledovanii termicheskikh svoistv ugleroda (Once more on experimental investigation of the thermal properties of carbon). Usp Fiz Nauk 173(12):1380–1381 (in Russian)
183. Asinovskii EI, Kirillin AV, Kostanovskii AV (1997) The phase diagram of carbon in the vicinity of the solid–liquid–vapour triple point. High Temp 35(5):704–709
184. Sheindlin MA (1998) About the paper by EI Asinovskii, AV Kirillin, and AV.Kostanovskii on ''The phase diagram of carbon in the vicinity of the solid–liquid–vapour triple point''. High Temp 36(4):663–664
185. Asinovskii EI, Kirillin AV, Kostanovskii AV (1998) Melting parameters of carbon. High Temp 36(5):716–721
186. Basharin AY, Dozhdikov VS, Kirilin AV, Turchaninov MA, Fokin LR (2010) Phase diagram with a region of liquid carbon – diamond metastable states. Tech Phys Lett 36(6):559–562
187. Basharin AY, Dozhdikov VS, Dubinchuk VT, Kirilin AV, Lysenko IYu, Turchaninov MA, (2010) Phases formed during rapid quenching of liquid carbon. Tech Phys Lett 35(5):428–431
188. Son LD, Rusakov GM, Katkov NN (2006) The phase diagram of carbon in the vicinity of graphite-diamond transition. Dokl Phys 51(2):56–59
189. Correa AA, Bonev SA, Galli G (2006) Carbon under extreme conditions: phase boundaries and electronic properties from first-principles theory. Proc Nat Acad Sci USA 103(5):1204–1208
190. Ghiringhelli LM, Los JH, Meijer EJ, Fasolino A, Frenkel D (2005) Modeling the phase diagram of carbon. Phys Rev Lett 94:145701
191. Balandin AA, Ghosh S, Bao W, Calizo I, Teweldebrhan D, Miao F, Lau CN (2008) Superior thermal conductivity of single-layer graphene. Nano Lett 8(3):902–907
192. Cardarelli F (2008) Materials handbook, 2nd ed. Springer, London
193. Virgilev YuS, Seleznev AN, Sviridov AA, Kalyagina IP (2006) Reaktornyi grafit: razrabotka, proizvodstvo i svoistva (Nuclear graphite: development, production and properties). Ros Khim Zh 50(1):4–12 (in Russian)
194. Marmer ÉN, Gurvich OS, Maltseva LF (1967) Vysokotemperaturnye materialy (High-temperature materials). Metallurgiya, Moscow (in Russian)
195. Pop E, Mann D, Wang Q, Goodson K, Dai HJ (2006) Thermal conductance of an individual single-wall carbon nanotube above room temperature. Nano Lett 6(1):96–100

196. Sinha S, Barjami S, Iannacchione G, Schwab A, Muench G (2005) Off-axis thermal properties of carbon nanotube films. J Nanoparticle Res 7(6):651–657
197. Lee C, Wei X, Kysar JW, Hone J (2008) Measurement of the elastic properties and intrinsic strength of monolayer graphene. Science 321:385–388
198. Tsai J-L, Tu J-F (2010) Characterizing mechanical properties of graphite using molecular dynamics simulation. Mater Design 31:194–199
199. Chen J-H, Jang C, Xiao S, Ishigami M, Fuhrer MS (2008) Intrinsic and extrinsic performance limits of graphene devices on SiO_2. Nature Nanotechnol 3(4):206–209
200. Akturk A, Goldsman N (2008) Electron transport and full-band electron-phonon interactions in graphene. J Appl Phys 103:053702
201. Belluci S (2005) Carbon nanotubes: physics and applications. Phys Status Solid C 2(1):34–47
202. Chae HG, Kumar S (2006) Rigid rod polymeric fibers. J Appl Polym Sci 100(1):791–802
203. Meo M, Rossi M (2006) Prediction of Young's modulus of single wall carbon nanotubes by molecular-mechanics-based finite element modelling. Compos Sci Technol 66(11–12):1597–1605
204. Sinnott SB, Andrews R (2001) Carbon nanotubes: synthesis, properties and applications. Crit Rev Solid State Mater Sci 26(3):145–249
205. Yu M-F, Lourie O, Dyer MJ, Moloni K, Kelly TF, Ruoff RS (2000) Strength and breaking mechanism of multiwalled carbon nanotubes under tensile load. Science 287:637–640
206. Demczyk BG, Wang YM, Cumings J, Hetman M, Han W, Zettl A., Ritchie RO (2002) Direct mechanical measurement of the tensile strength and elastic modulus of multiwalled carbon nanotubes. Mater Sci Eng A 334(1–2):173–178
207. Schurik AG (2006) Iskusstvennye uglerodnye materialy (Artificial carbon materials). Ural Scientific Research Institute of Composite Materials, Perm (in Russian)
208. Meleshko AI, Polovnikov SP (2007) Uglerod, uglerodnye volokna, uglerodnye kompozity (Carbon, carbon fibre, carbon composites). Science-Press, Moscow (in Russian)
209. Ostrovskii VS, Virgilev YuS, Kostikov VI, Shipkov NN (1986) Iskusstvennyi grafit (Artificial graphite). Metallurgiya, Moscow (in Russian)
210. Burchell TD (1999) Fission reactor applications of carbon. In: Burchell TD (ed) Carbon materials for advanced technologies, pp. 429–484. Pergamon, Elsevier, Amsterdam
211. Nonishneva NT, Bukharova AA, Zheleznyak AYu, Podkopaev SA, Sviridov AA, Seleznev AN, Gnedin YuF (2006) Application of new dual-purpose graphite. Refract Indust Ceram 47(6):348–350
212. Sementsov YuI, Pyatkovskii ML (2008) Termorasshirennyi grafit (Thermal expanded graphite). In: Gnesin GG, Skorokhod VV (eds) Neorganicheskoe materialovedenie (Inorganic materials science), Vol. 2, Part 2, Naukova Dumka, Kyiv, pp. 410–425 (in Russian)
213. Celzard A, Mareche JF, Furdin G (2005) Modelling of exfoliated graphite. Prog Mater Sci 50:93–179
214. Kostikov VI, Samoilov VM, Beilina NYu, Ostronov BG (2004) Novye vysokoprochnye uglerodnye materialy dlya traditsionnykh tekhnologii (New high-strength carbon materials for conventional technologies). Ros Khim Zh 48(5):64–75 (in Russian)
215. Zheleznyak AYu, Seleznev AN, Bukharova AA, Sviridov AA, Gnedin YuF, Podkopaev SA, Nonishneva NP (2004) Promyshlennoe osvoenie tekhnologii proizvodstva perspektivnykh marok grafitov s povyshennoi plotnost'yu (Industrial developing production technologies of high-density advanced graphite grades). Ros Khim Zh 48(5):76–81 (in Russian)
216. SGL Carbon Group (2003) ®Sigraflex foil – flexible graphite foil manufactured from expanded graphite (Technical information brochure). Expanded Graphite SGL Technologies GmbH, Meitingen, Germany
217. Vishnyakov LR, Grudina TV, Kadyrov VKh, Karpinos DM, Oleynik VI, Sapozhnikova AB, Tuchinskii LI (1985) Kompozitsionnye materialy (Composite materials). Naukova Dumka, Kyiv (in Russian)

218. Kostikov VI, Varenkov AN (2003) Sverkhvysokotemperaturnye kompozitsionnye materialy (Ultra-high temperature composite materials). Intermet Engineering, Moscow (in Russian)
219. Fitzer E, Manocha LM (1998) Carbon reinforcements and carbon/carbon composites. Springer, Berlin
220. Thomas CR (1993) Overview – what are carbon-carbon composites and what do they offer. In: Thomas CR (ed) Essentials of carbon-carbon composites, p. 1–36, Royal Society of Chemistry, Cambridge
221. Walker EJ (1993) The importance of fibre type and fibre surface in controlling composite properties. In: Thomas CR (ed) Essentials of carbon-carbon composites, p. 37–66, Royal Society of Chemistry, Cambridge
222. Kostikov VI, Varenkov AN (2008) Uglerodnye i uglegrafitovye materialy (Carbon and graphite materials). In: Gnesin GG, Skorokhod VV (eds) Neorganicheskoe materialovedenie (Inorganic materials science), Vol. 2, Part 2, Naukova Dumka, Kyiv, pp. 553–559 (in Russian)
223. Groupe Carbone Lorraine (2010) Sintering – specialty graphite material for advanced ceramics (Technical information brochure). Carbone Lorraine Composants, Gennevilliers, France
224. Groupe Carbone Lorraine (2010) Purified graphite, silicon carbide, graphite enhancement – innovative solutions for the semiconductor industry (Technical information brochure). Carbone Lorraine Composants, Gennevilliers, France
225. Groupe Carbone Lorraine (2010) Graphite grade 2333 (Technical information brochure). Carbone Lorraine Composants, Gennevilliers, France
226. Ambartsumyan SA (1970) Theory of anisotropic plates. Technomic, Stamford
227. Zefirov AP (ed), Veryatin UD, Mashirev VP, Ryabtsev NG, Tarasov VI, Rogozkin BD, Korobov IV (1965) Termodinamicheskie svoistva neorganicheskikh veschestv (Thermodynamic properties of inorganic substances). Atomizdat, Moscow (in Russian)
228. SGL Group, The Carbon Company (2007) ®Ringsdorff – specialty graphite grades for continuous casting (Technical information brochure). Graphite Specialties, SGL Carbon GmbH, Germany
229. Goldstein RV, Gorodtsov VA, Lisovenko DS (2009) Mesomechanics of multiwall carbon nanotubes and nanowhiskers. Phys Mesomechanics 12(1–2):38–53
230. Nakhodchi S, Flewitt PEJ, Smith DJ (2011) A method of measuring through-thickness internal strains and stresses in graphite. Strain 47:37–48
231. Wang LF, Zheng QS (2007) Extreme anisotropy of graphite and single-walled carbon nanotube bundles. Appl Phys Lett 90:153113
232. Blakslee OL, Proctor DG, Seldin EJ, Spence GB, Weng T (1970) Elastic constants of compression-annealed pyrolytic graphite. J Appl Phys 41(8):3373–3382
233. Bosak A, Krisch M, Mohr M, Maultzsch J, Thomsen C (2007) Elasticity of single-crystalline graphite: inelastic x-ray scattering study. Phys Rev B 75:153408
234. Seldin EJ, Nezbeda CW (1970) Elastic constants and electron-microscope observation of neutron-irradiated compression-annealed pyrolytic and single-crystal graphite. J Appl Phys 41(8):3389–3400
235. Cousins CSG (2003) Elasticity of carbon allotropes. IV. Rhombohedral graphite: zone-center optic modes and phase transformation using transferred Keating parameters. Phys Rev B 67:024110
236. Boettger JC (1997) All-electron full-potential calculation of the electronic band structure, elastic constants and equation of state for graphite. Phys Rev B 55:11202–11211
237. Seldin EJ (1966) Stress-strain properties of polycrystalline graphites in tension and compression at room temperature. Carbon 4:177–191
238. Samsonov GV, ed (1976) Svoistva elementov (Properties of elements), 2nd ed., Vol. 2. Metallurgiya, Moscow (in Russian)
239. DiVincenzo DP, Koch TC (1984) Theoretical phase diagram for Li-intercalated graphite. Phys Rev B 30(12):7092–7096

240. Okamoto H (1989) The C-Li (carbon-lithium) system. Bull Alloy Phase Diagrams 10(1):69–72
241. Lyakishev NP, ed (1996) Diagrammy sostoyaniya dvoinykh metallicheskikh sistem (Phase diagrams of binary metallic systems), Vol. 1. Mashinostroenie, Moscow (in Russian)
242. Kosolapova TYa, ed (1990) Handbook of high-temperature compounds: properties, production and applications. Hemisphere, New York
243. Andrievskii RA, Spivak II (1989) Prochnost tugoplavkikh soedinenii i materialov na ikh osnove (Strength of refractory compounds and materials based on them). Metallurgiya, Chelyabinsk (in Russian)
244. Massalski TB, Subramanian PR, Okamoto H, Kacprzak L, eds (1990) Binary alloy phase diagrams, 2nd ed. ASM International, Metals Park, Ohio
245. Velikanova TYa, Eremenko VN, Artyukh LV, Bondar AA, Gordiichuk OV (1989) Phase diagrams of Sc-M(IV-VII)-C systems. Powder Metall Met Ceram 28(9):711–718
246. Gschneidner KA, Jr, Calderwood FW (1986) The C-Y (carbon-yttrium) system. Bull Alloy Phase Diagrams 7(6):564–568
247. Gschneidner KA, Jr, Calderwood FW (1986) The C-La (carbon-lanthanum) system. Bull Alloy Phase Diagrams 7(5):446–449
248. Storms EK (1967) The refractory carbides. Academic Press, New York and London
249. Toth LE (1971) Transition metal carbides and nitrides. Academic Press, New York, London
250. Kieffer R, Schwarzkopf P (1953) Hartstoffe und Hartmetalle (Refractory hard metals). Springer, Vienna (in German)
251. Merzhanov AG (2004) The chemistry of self-propagating high-temperature synthesis. J Mater Chem 14:1779–1786
252. Shabalin IL, Luchka MV, Shabalin LI (2007) Vacuum SHS in systems with group IV transition metals for production of ceramic compositions. Phys Chem Solid State 8(1):159–175
253. Fernandez Guillermet A (1995) Analysis of thermochemical properties and phase stability in the zirconium-carbon system. J Alloys Compd 217(1):69–89
254. Gusev AI, Rempel AA (1994) Calculation of phase diagrams of interstitial compounds. J Phys Chem Solids 55(3):299–304
255. Gusev AI, Rempel AA (1997) Phase diagrams of metal-carbon and metal-nitrogen systems and ordering in strongly nonstoichiometric carbides and nitrides. Phys Stat Sol A 163:273–304
256. Gusev AI, Rempel AA (1999) Atomic ordering and phase equilibria in strongly nonstoichiometric carbides and nitrides. In: Gogotsi YG, Andrievskii RA (eds) Materials science of carbides, nitrides and borides, pp. 47–64. Kluwer Academic, Dordrecht
257. Okamoto H (1990) The C-Hf (carbon-hafnium) system. Assessed diagram. Bull Alloy Phase Diagrams 11(4):396–403
258. Rudy E, Windisch S, Brukl CE (1968) Revision of the vanadium-carbon and niobium-carbon systems. Planseeber Pulvermet 16(1):3–33
259. Carlson ON, Ghaneya AH, Smith JF (1985) The C-V (carbon-vanadium) system. J Phase Equilib 6(2):115–124
260. Storms EK (1989) Special report to the phase equilibria program. American Ceramic Society, Westerville, Ohio
261. Rudy E, Brukl CE (1967) Lower-temperature modifications of Nb_2C and V_2C. J Am Ceram Soc 50(5):265–268
262. Smith JF, Carlson ON, De Avillez RR (1987) The niobium-carbon system. J Nucl Mater 148(1):1–16
263. Rudy E, Hoffman JR (1967) Phasengleichgewichte im Bereich der kubischen Karbidphase im System Wolfram-Kohlenstoff (Phase equilibria in the cubic carbide phase in the system tungsten-carbon). Planseeber Pulvermet 15(3):174–178 (in German)
264. Benz R, Elliot JF, Chipman J (1973) Solid phases of the Mn-C system. Metall Trans 4(6):1449–1452

265. Kharkova AM, Velikanova TYa (1987) Structure of alloys of the system rhenium-carbon in the region rich with rhenium. Powder Metall Met Ceram 26(12):994–997
266. Popova SV, Boiko LG (1971) A new rhenium carbide formed by high-pressure treatment. High Temp High Press 3(2):237–238
267. Goldschmidt HJ (1967) Interstitial alloys. Butterworths, London, New York
268. Kubashewski O (1982) Iron binary phase diagrams. Springer, Berlin
269. Gabriel A, Chatillon C, Ansara I (1988) Thermochemical and phase diagram analysis of the Ni-C, Co-C and Co-Ni-C systems. High Temp Sci 25(1):17–54
270. Gustafson P, Gabriel A, Ansara I (1987) Thermodynamic evaluation of the C-Ni-W system. Z Metallkd 78(2):151–156
271. Singleton MF, Nash P (1989) The C-Ni (carbon-nickel) system. Bull Alloy Phase Diagrams 10(2):121–126
272. Beauvy M (1983) Stoichiometric limits of carbon-rich boron carbide phases. J Less-Common Met 90(2):169–175
273. Jansson U, Carlsson J-O (1985) Chemical vapour deposition of boron carbides in the temperature range 1300–1500 K and at a reduced pressure. Thin Solid Films 124(2):101–107
274. Lartigue S, Male G (1988) Contribution to the study of tetragonal compounds in the boron carbon system. J Mater Sci Lett 7(2):153–156
275. Ekbom LB, Amundin CO (1981) Microstructural evaluation of sintered boron carbides with different compositions. Sci Ceram 11:237–243
276. Rogl P (2009) Boron – carbon – chromium system. In: Effenberg G, Ilyenko S (eds) Ternary alloy systems. Subvol. E, Part 1, pp. 261–281. Springer, Berlin, Heidelberg
277. Grytsiv A, Rogl P (2009) Aluminium – boron – carbon system. In: Effenberg G, Ilyenko S (eds) Ternary alloy systems. Subvol. E, Part 1, pp. 1–23. Springer, Berlin, Heidelberg
278. Kosolapova TYa (1968) Karbidy (Carbides). Metallurgiya, Moscow (in Russian)
279. Kosolapova TYa, Andreeva TV, Bartnitskaya TB, Gnesin GG, Makarenko GN, Osipova II, Prilutskii ÉV (1985) Nemetallicheskie tugoplavkie soedineniya (Non-metallic refractory compounds). Metallurgiya, Moscow (in Russian)
280. Oden LL, McCune RA (1987) Phase equilibria in the Al-Si-C system. Metall Trans A 18(12):2005–2014
281. Olesinski RW, Abbaschian GJ (1984) The C-Si (carbon-silicon) system. Bull Alloy Phase Diagrams 5(5):486–489
282. Gnesin GG (1977) Karbidokremnievye materialy (Silicon carbide materials). Metallurgiya, Moscow (in Russian)
283. Wang EG (1997) Research on carbon nitrides. Prog Mater Sci 41:241–298
284. Wang EG (2002) Carbon nitride – related nanomaterials from chemical vapor deposition: structure and properties. J Am Ceram Soc 85(1):105–108
285. Cascarini de Torre LE, Llanos LE, Bottani EJ (1991) Graphite oxidation in air at different temperatures. Carbon 29(7):1051–1052
286. Gozzi D, Guzzardi G, Salleo A (1996) High temperature reactivity of different forms of carbon at low oxygen fugacity. Solid State Ionics 83(3–4):177–189
287. Luo X, Robin J-C, Yu S (2004) Effect of temperature on graphite oxidation behaviour. Nucl Eng Des 227(3):273–280
288. Thomas JM (1965) Microscopic study of graphite oxidation. In: Walker PL, Jr (ed) Chemistry and physics of carbon, Vol. 1, pp. 135–168. Marcel Dekker, New York
289. Shabalin IL, Roach DL, Shabalin LI (2008) Oxidation of titanium carbide – graphite hetero-modulus ceramics with low carbon content. II. Physico-chemical interpretation of the ridge effect. J Eur Ceram Soc 28:3177–3188
290. Ubbelohde AR, Lewis FA (1960) Graphite and its crystal compounds, Oxford University Press
291. Inoue Z, Tanaka H, Inomata Y (1980) Synthesis and x-ray crystallography of aluminium boron carbide. J Mater Sci 15:3036–3040

292. Inomata Y, Tanaka H, Inoue Z, Kawabata H (1980) Phase relation in SiC-Al4C3-B4C system at 1800°C. Yogyo-Kyokaishi-Shi 88(6):353–355
293. Oscroft RJ, Korgul P, Thompson DP (1989) Crystal structure and microstructure of some new silicon aluminum carbonitrides. Br Ceram Proc 42:33–47
294. Kidwell BL, Oden LL, McCune RA (1984) $2Al_4C_3{\cdot}SiC$: a new intermediate phase in the Al – Si – C system. J Appl Crystallogr 17(6):481–482
295. Schneider G, Gauckler LJ, Petzow G, Zangvil A (1979) Phase equilibria in the system $A1_4C_3$ – Be_2C – SiC. J Am Ceram Soc 62(11–12):574–576
296. Zangvil A, Gauckler LJ, Schneider G, Ruehle M (1979) TEM studies on $Al_4C_3{\cdot}3Be_2C$. J Mater Sci 14(11):2741–2746
297. Schneider G, Gauckler LJ, Petzow G (1979) Phase equilibria in the Si, Al, Be / C, N system. Ceramurgia Int 5(3):101–104
298. Gasik MI, Myachin VG, Polyakov OI, Kurasov AN (1990) Fazovyi sostav kompleksnykh splavov na osnove silikomargantsa, soderzhashchikh alyuminii i titan (The phase composition of complex alloys on the base of silicon manganese containing aluminium and titanium). Izv Vyssh Uchebn Zaved Chern Metall (9):63–67 (in Russian)
299. Gasik MI, Lysenko BF (1977) Metallofizicheskie issledovaniya fazovogo sostava sinteticheskikh i promyshlennykh splavov sistemy Mn-Fe-Si-C (Metal physics studies of the phase composition of synthetic and industrial alloys of the Mn-Fe-Si-C system). In: Gasik MI, Rostovtsev ST (eds) Vosstanovitelnye protsessy v proizvodstve ferrosplavov (Reduction processes in ferroalloy production). Nauka, Moscow, pp. 12–15 (in Russian)
300. Oden LL, McCune RA (1990) Contribution to the phase diagramm Al_4C_3 – AlN – SiC. J Am Ceram Soc 73(6):1529–1533
301. Oscroft RJ, Thompson DP (1991) Comment on "Contribution to the phase diagram Al_4C_3 – AlN – SiC". J Am Ceram Soc 74(9):2327–2328
302. Oden LL (1991) Reply to "Comment on "Contribution to the phase diagram Al_4C_3 – AlN – SiC". J Am Ceram Soc 74(9):2329
303. Larrere Y, Willer B, Lihrmann JM, Daire M (1984) Diagrammes d'équilibre stable et métastable dans le système Al_2O_3 - Al_4C_3 (Stable and metastable phase equilibrium diagrams in the Al_2O_3-Al_4C_3 binary system). Rev Int Hautes Temp Refract 21(1):3–18 (in French)
304. Foster LM, Long G, Hunter MS (1956) Reactions between aluminum oxide and carbon. The Al_2O_3 – Al_4C_3 phase diagram. J Am Ceram Soc 39(1):1–11
305. Cornish L, Cacciamani G, Cupid DM, De Keyzer J (2009) Aluminium – carbon – titanium system. In: Effenberg G, Ilyenko S (eds) Ternary alloy systems. Subvol. E, Part 1, pp. 41–71. Springer, Berlin, Heidelberg
306. Ge Z, Chen K, Guo J, Zhou H, Ferreira JMF (2003) Combustion synthesis of ternary carbide Ti_3AlC_2 in Ti-Al-C system. J Eur Ceram Soc 23(3):567–574
307. Pietzka MA, Schuster JC (1994) Summary of constitutional data on the aluminium-carbon-titanium system. J Phase Equilib 15(4):392–400
308. Zhang MX, Chang YA (1994) Phase diagrams of Ti-Al-C, Ti-Y-O, Nb-Y-O and Nb-Al-O at 1100 °C. J Phase Equilib 15(5):470–472
309. Bandyopadhyay D, Sharma RC, Chakraborti N (2000) The Ti-Al-C (titanium-aluminium-carbon) system. J Phase Equilib 21(2):195–198
310. Cam G, Flower HM, West DRF (1991) Constitution of Ti-Al-C alloys in the temperature range 1250–750 °C. Mater Sci Technol 7:505–511
311. Riaz S, Flower HM, West DRF (2000) Phase relationships involving TiC and Ti_3AlC (P phase) in Ti-Al-C system. Mater Sci Technol 16:984–992
312. Viala JC, Vincent C, Vincent H, Bouix J (1990) Approche thermodynamique de l'interaction chimique entre l'aluminium et le carbure de titane (Thermodynamic approach of the chemical interaction between aluminium and titanium carbide). Mater Res Bull 25:457–464 (in French)
313. Viala JC, Bouix J, Gonzalez G, Esnouf C (1997) Chemical reactivity of aluminium with boron carbide. J Mater Sci 32:4559–4573

314. Pradelli G (1974) La ricerca sulle on Cr borocarbides (Research on Cr borocarbides). Metall Ital 66(10):551–556 (in Italian)
315. Pradelli G (1978) La ricerca sulle on Cr borocarbides (Research on Cr borocarbides). Metall Ital 70(5):223–226 (in Italian)
316. Papesch G, Nowotny H, Benesovsky F (1973) Untersuchung in den Systemen Cr-B-C, Mn-B-C and Mn-Ge-C (Studies in the systems Cr-B-C, Mn-B-C and Mn-Ge-C). Monatsh Chem 104:933–942 (in German)
317. Lange D, Holleck H (1985) Verschleissfeste Werkstoffe auf Borcarbidbasis (Wear resistant materials based on boron carbide). In: Bildstein H (ed) Proc. 11th Int. Plansee seminar, Vol. 2, pp. 747–759. Plansee GmbH, Reutte (in German)
318. Ordanyan SS, Dmitriev AI, Kapitonova IM (1991) Vzaimodeistvie SiC s CrB_2 (The interaction of SiC with CrB_2). Izv AN SSSR Neorg Mater 27(1):157–159 (in Russian)
319. Schwetz KA, Hoerle M, Bauer J (1979) Contribution to the system europium-boron-carbon. Ceramurgia Int 5:105–109
320. Levinskii YuV, Salibekov SE, Levinskaya MKh (1965) Reaction of chromium, molybdenum and tungsten borides with carbon. Powder Metall Met Ceram 4(12):1004–1009
321. Lowell CE (1967) Solid solution of boron in graphite. J Am Ceram Soc 50:142–144
322. Markovskii LY, Vekshina NV, Bezruk ET (1969) Vzaimodeistvie boridov s uglerodom i karbidami (Reaction of borides with carbon and carbides). In: Samsonov GV (ed) Khimicheskie svoistva i metody analiza tugoplavkikh soedinenii (The chemical properties and analysis methods of refractory compounds). Ukrainian SSR Academy of Sciences, Institute for Problems of Materials Science, Kyiv, pp. 143–148 (in Russian)
323. Ordanyan SS, Dmitriev AI (1989) Reaction in the B_4C-CrB_2 system. Inorg Mater 25(4):593–595
324. Borlera ML, Pradelli G (1967) Solid equilibri dello stato nel sistema Fe-B-C (Solid state equilibria in the system Fe-B-C). Metall Ital 59:907–912 (in Italian)
325. Schürmann E, Li S-X (1985) Untersuchung der Schmelzgleichgewichte im der ternären System Eisen-Kohlenstoff-Bor (Investigation of the liquid equilibria in the ternary system iron-boron-carbon). Giessereiforschung 37(4):121–129 (in German)
326. Fomichev OI, Katkov VF, Kushnereva AK Brekharya GP (1976) Study of the ternary phase in the system Fe-B-C. Inorg Mater 12(1):111–112
327. Rogl P (2008) Boron – carbon – iron system. In: Effenberg G, Ilyenko S (eds) Ternary alloy systems. Subvol. D, Part 1, pp. 279–301. Springer, Berlin, Heidelberg
328. Rogl P (2009) Boron – carbon – hafnium system. In: Effenberg G, Ilyenko S (eds) Ternary alloy systems. Subvol. E, Part 1, pp. 282–305. Springer, Berlin, Heidelberg
329. Levinskii YuV, Salibekov SE (1965) Interaction of titanium, zirconium and hafnium diborides with carbon. Russ J Inorg Chem 10(3):319–320
330. Rudy E, Windisch S (1966) Phase diagrams of the systems Ti-B-C, Zr-B-C and Hf-B-C. In: Ternary phase equilibria in transition metal - boron - carbon - silicon systems. Report AFML-TR-65–2, Contract USAF 33(615)-1249, Part 2, Vol. 13, pp. 1–212. Air Force Materials Laboratory, Wright Patterson Air Force Base, Ohio
331. Ordanyan SS, Unrod VI, Lutsenko AE (1977) Reaction in the system HfC-HfB_2. Inorg Mater 13:451–453
332. Ordanyan SS, Dmitriev AI (1989) Interaction in the B_4C-HfB_2 system. Powder Metall Met Ceram 28(5):424–426
333. Bittermann H, Rogl P (1998) The system boron – carbon – hafnium. In: Effenberg G (ed) Phase diagrams of ternary metal-boron-carbon systems, pp. 102–141. ASM International, Materials Park, Ohio
334. Bauer J, Vennegues P, Vergneau JL (1985) The ternary system holmium-boron-carbon; isothermal section at 1500 °C. J Less-Common Met 110:295–298
335. Rogl P, Korniyenko K, Velikanova T (2009) Boron – carbon – molybdenum system. In: Effenberg G, Ilyenko S (eds) Ternary alloy systems. Subvol. E, Part 1, pp. 306–322. Springer, Berlin, Heidelberg

336. Paderno V, Paderno Yu, Filippov V, Liashchenko A (2004) Directional crystallization of B_4C-NbB_2 and B_4C-MoB_2 eutectic compositions. J Solid State Chem 117:523–528
337. Salibekov SE, Levinskii YuV, Lobankov VU (1970) Synthesis and properties of molybdenum borocarbide. Inorg Mater 6(9):1430–1432
338. Tomashik V (2009) Boron – carbon – nitrogen system. In: Effenberg G, Ilyenko S (eds) Ternary alloy systems. Subvol. E, Part 1, pp. 323–346. Springer, Berlin, Heidelberg
339. Ruh R, Kearns M, Zangvil A, Xu Y (1992) Phase and property studies of boron carbide – boron nitride composites. J Am Ceram Soc 75(4):864–872
340. Lundström T, Andreev YG (1996) Superhard boron-rich borides and studies of the B-C-N system. Mater Sci Eng A 209(1–2):16–22
341. Grigoriev ON, Lyashenko VI, Timofeeva II, Rogozinskaya AA, Tomila TV, Dubovik TV, Panashenko VM (2005) Study of the synthesis of the ternary compound B-N-C. Powder Metall Met Ceram 44(9–10):415–419
342. Pan Z, Sun H, Chen C (2006) Ab initio structural identification of high density cubic BC_2N. Phys Rev B 73(21):214111
343. Nicolich JP, Hofer F, Brey G, Riedel R (2001) Synthesis and structure of three-dimensionally ordered graphite like BC_2N ternary crystals. J Am Ceram Soc 84(2):279–282
344. Gago R, Jimenez I, Agullo-Rueda F, Albella JM, Czigany ZS, Hultman L (2002) Transition from amorphous boron carbide to hexagonal boron carbon nitride thin films induced by nitrogen ion assistance. J Appl Phys 92(9):5177–5182
345. Williams D, Pleune B, Kouvetakis J, Williams MD, Andersen RA (2000) Synthesis of $LiBC_4N_4$, BC_3N_3 and related C-N compounds of boron: new precursors to light element ceramics. J Am Chem Soc 122:7735–7741
346. Huang J, Zhu YT, Mori H (2001) Structure and phase characteristics of amorphous boron-carbon-nitrogen under high pressure and high temperature. J Mater Res 16(4):1178–1184
347. Rogl P, Korniyenko K, Velikanova T (2009) Boron – carbon – niobium system. In: Effenberg G, Ilyenko S (eds) Ternary alloy systems. Subvol. E, Part 1, pp. 347–366. Springer, Berlin, Heidelberg
348. Ordanyan SS, Stepanenko EK, Unrod VI (1977) Reactions in the system NbC-NbB_2. Inorg Mater 13(2):312–314
349. Ordanyan SS, Dmitriev AI, Bizhev KT, Stepanenko EK (1987) Interaction in B_4C – Me^VB_2 systems. Powder Metall Met Ceram 26(10):834–836
350. Rogl P (1998) The system boron – carbon – niobium. In: Effenberg G (ed) Phase diagrams of ternary metal-boron-carbon systems, pp. 197–213. ASM International, Materials Park, Ohio
351. Levinskii YuV, Salibekov SE, Levinskaya MKh (1965) The reaction of vanadium, niobium and tantalum diborides of with carbon. Powder Metall Met Ceram 4(11):923–926
352. Korniyenko K (2009) Boron – carbon – silicon system. In: Effenberg G, Ilyenko S (eds) Ternary alloy systems. Subvol. E, Part 1, pp. 367–394. Springer, Berlin, Heidelberg
353. Lihua Z, Lijun W, Qizhong H, Qiaoqin Y, Shaoli L (1996) Structure of C-B_4C-SiC composites with silicon additive. J Mater Sci Lett 15(4):353–356
354. Lijun W, Qizhong H, Qiaoqin Y, Lihua Z, Zhongyu X (1996) Effect of sintering temperature on structure of C-B_4C-SiC composites with silicon additive. Scr Mater 35(1): 123–127
355. Roger J, Babizhetskyy V, Halet J-F, Guerin R (2004) Boron-silicon solid solution: synthesis and crystal structure of a carbon-doped boron-rich SiB_n ($n \sim 30$) compound. J Solid State Chem 177(11):4167–4174
356. Secrist DR (1964) Phase equilibria in the system boron carbide – silicon carbide. J Am Ceram Soc 47(3):127–130
357. Shaffer PTB (1969) The SiC phase in the system SiC-B_4C-C. Mater Res Bull 4(3):213–220
358. Kieffer R, Gugel E, Leimer G, Ettmayer P (1971) Untersuchungen im System B-C-Si (Investigations in the system B-C-Si). Berich Deut Keram Gesel 49(2):41–72 (in German)

359. Seifert HJ, Aldinger F (2002) Phase equilibria in the Si-B-C-N system. In: Jansen M (ed) High performance non-oxide ceramics. Vol. 1, pp. 1–58. Springer, Berlin, Heidelberg
360. Ordanyan SS, Dmitriev AI, Moroshkina FS (1989) Reaction of SiC with ZrB_2. Inorg Mater 28(10):1487–1489
361. Rogl P (2009) Boron – carbon – tantalum system. In: Effenberg G, Ilyenko S (eds) Ternary alloy systems. Subvol. E, Part 1, pp. 395–407. Springer, Berlin, Heidelberg
362. Rudy E, Benesovsky F, Toth LE (1963) Untersuchungen der ternären Systeme der Gruppe Va und VIa Metalle mit Bor und Kohlenstoff (Studies of the ternary systems of the group Va and VIa metals with boron and carbon). Z Metallkd 54(6):345–353 (in German)
363. Ordanyan SS, Unrod VI, Polishchuk VS, Storonkina NM (1976) Reactions in the system TaC-TaB_2. Powder Metall Met Ceram 15(9):692–695
364. Ordanyan SS (1980) Laws of interaction in the systems $M^{IV,V}C$ – $M^{IV,V}B_2$. Inorg Mater 16(8):961–965
365. Ordanyan SS (1993) O zakonomernostyakh vzaimodeistviya v sistemakh B_4C – Me^{IV}-$Me^{VI}B_2$ (On regularities of interaction in the systems B_4C – Me^{IV}-$Me^{VI}B_2$). Ogneupory, (1):15–17 (in Russian)
366. Ordanyan SS, Unrod VI, Avgustinik AI (1975) Reactions in the system TiC_x – TiB_2. Powder Metall Met Ceram 14(9):729–731
367. Toth LE, Benesovsky F, Nowotny H, Rudy E (1961) Der Dreistoff: Thorium-Bor-Kohlenstoff (The ternary system thorium-boron-carbon). Monatsh Chem 92(5):956–960 (in German)
368. Rogl P, Bauer J, Debuigne J (1989) The ternary system uranium-boron-carbon. J Nucl Mater 165(1):74–82
369. Rogl P (2009) Boron – carbon – vanadium system. In: Effenberg G, Ilyenko S (eds) Ternary alloy systems. Subvol. E, Part 1, pp. 408–426. Springer, Berlin, Heidelberg
370. Ordanyan SS, Yurchenko OV, Vikhman SV (2005) Polythermic section B_4C-LaB_6 in the ternary system La-B-C. Rus J Appl Chem 78(2):333–335
371. Ordanyan SS, Topchii LA, Khoroshilova IK, Chupov VD (1982) Reactions in the $VC_{0.88}$ – VB_2 system. Powder Metall Met Ceram 21(2):122–124
372. Rogl P (2009) Boron – carbon – tungsten system. In: Effenberg G, Ilyenko S (eds) Ternary alloy systems. Subvol. E, Part 1, pp. 427–449. Springer, Berlin, Heidelberg
373. Rudy E (1970) The phase diagram W-B-C. In: Experimental phase equilibria of selected binary, ternary and higher order systems. Report AFML-TR-69–117, Contract USAF 33(615)-67-C-1513, Part 5, pp. 1–51. Air Force Materials Laboratory, Wright-Patterson Air Force Base, Ohio
374. Kiparisov SS, Nikiforov OA, Borisova NV (1968) Psevdobinarnyi razrez sistemy volfram – bor – uglerod (Pseudobinary section of the tungsten – boron – carbon ternary system). Sb Mosk Inst Stali Splavov 45:128–131 (in Russian)
375. Paderno Y, Paderno V, Liashchenko A, Filipov V, Evdokimova A, Martynenko A (2006) The directional crystallization of W-B-C d-transition metal alloys. J Solid State Chem 179:2939–2943
376. Rogl P, Bittermann H (1999) Ternary metal boron carbides – constitution, thermodynamics, compound formation and structural chemistry. In: Gogotsi YG, Andrievskii RA (eds) Materials science of carbides, nitrides and borides, pp. 29–46. Kluwer Academic, Dordrecht
377. Epicier T, Dubois J, Esnouf C, Fantozzi G, Convert P (1988) Neutron powder diffraction studies of transition metal hemicarbides M_2C_{1-x}. II. In situ high temperature study on W_2C_{1-x} and Mo_2C_{1-x}. Acta Metall 36:1903–1921
378. Rogl P (2009) Boron – carbon – zirconium system. In: Effenberg G, Ilyenko S (eds) Ternary alloy systems. Subvol. E, Part 1, pp. 450–475. Springer, Berlin, Heidelberg
379. Ordanyan SS, Unrod VI (1975) Reactions in the system ZrC-ZrB_2. Powder Metall Met Ceram 14(5):393–395
380. Ordanyan SS, Dmitriev AI, Bizhev KT, Stepanenko EK (1988) Interaction in the system B_4C-ZrB_2. Powder Metall Met Ceram 27(1):38–40

381. Kovalev AV, Dubnik EM, Grigoriev ON, Shaposhnikova TI, Martsynyuk IS (2000) Directionally solidified eutectic of the B_4C-ZrB_2 system. Powder Metall Met Ceram 39(1–2):63–66
382. Samsonov GV, ed (1978) Fiziko-khimicheskie svoistva okislov (Physico-chemical properties of oxides), 2nd ed. Metallurgiya, Moscow (in Russian)
383. Burdick MD, Parker HS, Roth RS, McGandy EL (1955) An x-ray study of the system uranium monocarbide – uranium dicarbide – beryllium carbide. J Res Natl Bur Stand 54(4):217–229
384. Lemkey FD, Thompson ER (1971) Nickel and cobalt eutectic alloys reinforced by refractory metal carbides. Metall Trans 2(6):1537–1544
385. Dmitrieva GP, Krasnokutskaya ZB, Belyavina NN, Shurin AK (1989) Phase diagram of the Co-VC-NbC system. Powder Metall Met Ceram 28(3):233–238
386. Samsonov GV, Upadhyaya GS, Neshpor VS (1974) Fizicheskoe materialovedenie karbidov (Physical materials science of carbides). Naukova Dumka, Kyiv (in Russian)
387. Panov VS, Chuvilin AM (2001) Tekhnologiya i svoistva spechennykh tverdykh splavov i izdeliy iz nikh (Technology and properties of sintered hard alloys and their components). MISIS, Moscow (in Russian)
388. Pollock CB, Stadelmaier HH (1970) The η carbides in the Fe-W-C and Co-W-C systems. Metall Trans 1(4):767–770
389. Johansson T, Uhrenius B (1978) Phase equilibria, isothermal reactions and a thermodynamic study in the Co-W-C system at 1150°C. Met Sci 12(2):83–94
390. Fernandez Guillermet A. (1989) Thermodynamic properties of the Co-W-C system. Metall Trans A 20(5):935–956
391. Holleck H (1984) Binäre und ternäre Carbid- und Nitridsysteme der Ubergangsmetalle (Binary and ternary carbide and nitride systems of the transition metals). Gebrüder Borntträeger, Berlin, Stuttgart (in German)
392. Pellegrini PW, Giessen BC, Feldman JM (1972) A survey of the Cr-rich area of the Cr-Si-C phase diagram. J Electrochem Soc 119(4):535–537
393. Gasik MI, Em PA (1978) O vzaimodeistvii komponentov v sistemakh 3d-M – kremnii – uglerod (On the interaction of components in the systems 3d-Me-silicon-carbon). In: Ageev NV (ed) Struktura faz i protsessy vosstanovleniya elementov v tverdykh i zhidkikh sistemakh (Phase structures and reduction processes of elements in solid and liquid systems), pp. 54–58. USSR Academy of Sciences, Institute of Metallurgy, Moscow (in Russian)
394. Dergunova VS, Levinskii YuV, Shurshakov AN, Kravetskii GA (1974) Vzaimodeistvie ugleroda s tugoplavkimi metallami (Interaction of carbon with refractory metals). Metallurgiya, Moscow (in Russian)
395. Guha JP, Kolar D (1973) The systems TiC-Cr and ZrC-Cr. J Less-Common Met 31(3):337–343
396. Eremenko VN, Velikanova TYa, Sleptsov SV, Bondar AA (1990) Fazovye ravnovesiya pri kristallizatsii splavov sistemy Cr – Ti – C (Phase equilibria in the crystallization of the Cr – Ti – C system alloys). Dopov Akad Nauk Ukr RSR Ser A Fiz Mat Tekh Nauki 52(4):75–77 (in Russian)
397. Stecher P, Benesovsky F, Nowotny H (1964) Investigations of the chromium-tungsten-carbon system. Planseeber Pulvermet 12(2):89–95
398. Gladyshevskii EI, Telegus VS, Fedorov TF, Kuzma YuB (1967) Troinaya sistema W-Cr-C (The W-Cr-C ternary system). Izv AN SSSR Metally (1):190–193 (in Russian)
399. Gustafson P (1988) A thermodynamic evaluation of the C – Cr – Fe – W system. Metall Trans A 19(10):2547–2554
400. Eremenko VN, Velikanova TYa, Sleptsov SV, Bondar AA (1990) Diagramma plavkosti sistemy Cr – Zr – C (The meltability diagram of the Cr – Zr – C system). Dopov Akad Nauk Ukr RSR Ser A Fiz Mat Tekh Nauki 52(1):70–72 (in Russian)
401. Bunin KP, Malinochka YaN, Taran YuN (1969) Osnovy metallovedeniya chuguna (Principles of metallography of cast iron). Metallurgiya, Moscow (in Russian)

402. Kuzma YuB, Fedorov TF (1965) Phase equilibria in the system molybdenum-chromium-carbon. Powder Metall Met Ceram 4(11):920–922
403. Eremenko VN, Velikanova TYa, Bondar AA (1987) The phase diagram of the Cr-Mo-C system. II. Phase equilibria in the partial system Mo_2C-Cr_7C_3-C. Powder Metall Met Ceram 26(6):506–511
404. Eremenko VN, Velikanova TYa, Bondar AA (1986) Diagramma sostoyaniya sistemy Cr-W-C pri vysokikh temperaturakh (The constitution diagram of the Cr-W-C system at high temperatures). Dopov Akad Nauk Ukr RSR Ser A Fiz Mat Tekh Nauki 48(11):74–78 (in Russian)
405. Andrievskii RA, Umanskii YaS (1977) Fazy vnedreniya (Interstitial phases). Nauka, Moscow (in Russian)
406. Frage NR, Gurevich YuG, Sokolova EV, Chumanov VI (1989) Stability of titanium carbide in molten iron and nickel. Russ Metall (3):30–34
407. Eremenko VN, Shabanova SV, Velikanova TYa, Petrenko LA (1975) Structure of alloys and the phase equilibrium diagram of the system Hf-Mo-C. II. Powder Metall Met Ceram 14(8):643–648
408. Dmitrieva GP, Razumova NA, Shurin AK (1984) Phase equilibria in alloys of the Ni-HfC-Mo_2C system. Powder Metall Met Ceram 23(9):714–718
409. Rogl P, Naik SK, Rudy E (1977) A constitutional diagram of the system TiC-HfC-MoC. Monatsh Chem 108(6):1325–1337
410. Rogl P, Naik SK, Rudy E (1977) A constitutional diagram of the system $VC_{0.88}$-$HfC_{0.98}$-(MoC). Monatsh Chem 108(6):1339–1352
411. Alyamovskii SI, Zainulin YuG, Shveikin GP (1981) Oksikarbidy i oksinitridy metallov IVA i VA podgrupp (Oxycarbides and oxynitrides of IVA and VA subgroups metals). Nauka, Moscow
412. Constant K, Kieffer R, Ettmayer P. (1975) Über das pseudoternäre System "ZrO"−ZrN−ZrC (On pseudoternary system "ZrO"-ZrN-ZrC). Monatsh Chem 106(4):823–832 (in German)
413. Rudy E, Nowotny H, Benesovsky F, Kieffer R, Neckel A (1960) Über Hafniumkarbid enthaltende Karbidsyteme (On hafnium carbide containing carbide system). Monatsh Chem 91(1):176–187 (in German)
414. Dmitrieva GP, Razumova NA, Shurin AK (1984) Phase equilibrium diagram of the Ni-TiC-HfC system. Powder Metall Met Ceram 23(2):159–162
415. Raevskaya MV, Tatarkina AL, Kulova LK (1981) Fazovye ravnovesiya v kvazi-troinykh sistemakh nikel – karbid volframa (WC) – karbid tsirkoniya (ZrC) i nikel – karbid volframa (WC) – karbid gafniya (HfC) (Phase equilibriums in the nickel – tungsten carbide (WC) – zirconium carbide (ZrC) and nickel – tungsten carbide (WC) – hafnium carbide (HfC) quasiternary systems). In: Drits ME (ed) Fazovye ravnovesiya v metallicheskikh splavakh (Phase equilibriums in metallic alloys), pp. 273–276. Nauka, Moscow (in Russian)
416. Achour M, Pialoux A, Dode M (1975) Etude de la carboreduction progressive du dioxyde de hafnium. 2. Determination de la pression de l'equilibre monovariant: α-HfO_2 + 3C ↔ HfC + 2CO, entre 1300 °C et 1650 °C. Isothermes de carboreduction de l' α-HfO_2 en presence d'un exces de carbone (Study of progressive reduction of hafnium dioxide by carbon. 2. Determination of the monovariant equlibrium pressure: α-HfO_2 + 3C ↔ HfC + 2CO between 1300 °C and 1650 °C. Isotherms of α-HfO_2 reduction by carbon in the presence of carbon excess). Rev Int Hautes Temp Refract 12(3):281–287 (in French)
417. Lyakishev NP, ed (1997) Diagrammy sostoyaniya dvoinykh metallicheskikh sistem (Phase diagrams of binary metallic systems), Vol. 2. Mashinostroenie, Moscow (in Russian)
418. Brukl CE (1966) The Zr-Si-C, Hf-Si-C, Zr-Si-B, and Hf-Si-B systems. In: Ternary phase equilibria in transition metal-boron-carbon-silicon systems. Report AFML-TR-65–2, Contract USAF 33(615)-1249, Part 2, Vol. 10, pp. 1–95. Air Force Materials Laboratory, Wright-Patterson Air Force Base, Ohio

419. Rudy E (1969) Compendium of phase diagram data. In: Ternary phase equilibria in transition metal-boron-carbon-silicon systems. Report AFML-TR-65–2, Contracts USAF 33(615)-1249 and USAF 33(615)-67-C-1513, Part 5, pp. 1–689. Air Force Materials Laboratory, Wright-Patterson Air Force Base, Ohio
420. Rudy E (1965) Ta-Hf-C system. In: Ternary phase equilibria in transition metal-boron-carbon-silicon systems. Report AFML-TR-65–2, Contract USAF 33(615)-1249, Part 2, Vol. 1, pp. 1–84. Air Force Materials Laboratory, Wright-Patterson Air Force Base, Ohio
421. Gusev AI (1985) Prognoz i raschety fazovykh diagramm psevdobinarnykh system na osnove tugoplavkikh soedinenii perekhodnykh metallov. (The prediction and calculation of phase diagrams of pseudobinary systems based on high-melting transition metal compounds). In: Ageev NV (ed) Raschety i eksperimentalnye metody postroeniya diagramm sostoyaniya (Calculation and experimental methods of plotting phase diagrams). Nauka, Moscow, pp. 42–47 (in Russian)
422. Fischer JJ (1964) Hot-pressing mixed carbides of Ta, Hf and Zr. Am Ceram Soc Bull 43(3):183–185
423. Andrievskii RA, Strelnikova NS, Poltaratskii NI, Kharkhardin ED, Smirnov VS (1967) Melting point in systems ZrC – HfC, TaC – ZrC, TaC – HfC. Powder Metall Met Ceram 6(1):65–67
424. Brukl CE, Harmon DP (1966) The Ti-Zr-C, Ti-Hf-C and Zr-Hf-C systems. In: Ternary phase equilibria in transition metal-boron-carbon-silicon systems. Report AFML-TR-65–2, Contract USAF 33(615)-1249, Part 2, Vol. 4, pp. 1–78. Air Force Materials Laboratory, Wright-Patterson Air Force Base, Ohio
425. Gusev AI (1984) Raschet diagram sostoyaniya psevdobinarnykh system na osnove tugoplavkikh karbidov titana, tsirkoniya, gafniya i vanadiya (The calculation of the constitution diagrams of pseudo-binary systems based on titanium, zirconium, hafnium and vanadium carbides). Izv AN SSSR Neorg Mater 20(7):1132–1137 (in Russian)
426. Rogl P, Naik SK, Rudy E (1977) A constitutional diagram of the system TiC−HfC−WC. Monatsh Chem 108(5):1189–1211
427. Rogl P, Naik SK, Rudy E (1977) A constitutional diagram of the system $VC_{0.88}$−$HfC_{0.98}$−WC. Monatsh Chem 108(5):1213–1234
428. Eremenko VN, Velikanova TYa, Artyukh LV, Vishnevskii AS (1975) Phase diagram of ternary system hafnium-tungsten-carbon. Solidus surface projection. Rev Int Hautes Temp Refract 12(3):209–213
429. Eremenko VN, Velikanova TYa, Artyukh LV, Akselrod GM, Vishnevskii AS (1976) Issledovanie splavov troinykh sistem W-HfC-C i W-ZrC-C pri subsolidusnykh temperaturakh (A study of ternary systems W-HfC-C and W-ZrC-C alloys at subsolidus temperatures). Dopov Akad Nauk Ukr RSR Ser A Fiz Mat Tekh Nauki 38(1):83–89 (in Russian)
430. Zakharov AM, Naumkin OP, Kurganov GV (1974) Troinye sistemy W-Zr-C i W-Hf-C v oblastyakh, bogatykh volframom (The W-Zr-C and W-Hf-C ternary systems in the tungsten-rich areas). Izv AN SSSR Metally (1):224–228 (in Russian)
431. Lyakishev NP, ed (2001) Diagrammy sostoyaniya dvoinykh metallicheskikh sistem (Phase diagrams of binary metallic systems), Vol. 3, Part 1. Mashinostroenie, Moscow (in Russian)
432. Rudy E (1973) Boundary phase stability and critical phenomena in higher order solid solution systems. J Less-Common Met 33(1):43–70
433. Rudy E, Benesovsky F, Sedlatschek K (1961) Untersuchungen im System Niob-Molybdän-Kohlenstoff (Investigations in the system niobium-molybdenum-carbon). Monatsh Chem 92(4):841–855 (in German)
434. Rudy E, Brukl CE, Windisch S (1967) Constitution of niobium (columbium) – molybdenum – carbon alloys. Trans Metall Soc AIME 239(11):1796–1808
435. Brukl CE, (1972) Der Einfluß von Vanadin und Niob auf feste Subcarbidlösungen in den Systemen Tantal-Wolfram-Kohlenstoff und Tantal-Molybdän-Kohlenstoff (The influence

of vanadium and niobium in solid subcarbide solutions in the systems tantalum-tungsten-carbon and tantalum-molybdenum-carbon). Monatsh Chem 103(3):820–830 (in German)
436. Funke VF, Pshenichnyi IV, Pliner LA, Loktionov YuD (1983) Phase fields and initial melting diagrams of the pseudoquaternary system UC-MoC_{1-x}-ZrC-NbC. Powder Metall Met Ceram 22(2):110–116
437. Samsonov GV, Portnoy KI (1961) Splavy na osnove tugoplavkikh soedineniy (Alloys based on refractory compounds). Oborongiz, Moscow (in Russian)
438. Rudy E, Brukl CE, Windisch S (1968) Constitution of ternary Ta-Mo-C alloys. J Am Ceram Soc 51(5):239–250
439. Rudy E, Windisch S, Brukl CE (1967) Constitution of ternary Ta-Mo-C alloys. In: Ternary phase equilibria in transition metal-boron-carbide-silicon systems. Report AFML-TR-65–2, Contract USAF 33(615)-1249, Part 2, Vol. 17, pp. 1–71. Air Force Materials Laboratory, Wright-Patterson Air Force Base, Ohio
440. Rudy E (1970) The phase diagram of the systems Ti-Nb-C, Ti-Ta-C and Ti-Mo-C. In: Phase equilibria investigations of binary, ternary and higher order systems. Report AFML-TR-69–117, Contract USAF 33(615)-67-C-1513, Part 1, pp. 1–132. Air Force Materials Laboratory, Wright-Patterson Air Force Base, Ohio
441. Alekseeva ZM (1984) Phase equilibria in the solid state in the U-Mo-UC concentration range of the U-Mo-C system. J Less-Common Met 96:63–68
442. Rudy E, Benesovsky F (1962) Study of the system vanadium-molybdenum-carbon. Stabilization of cubic molybdenum carbides. Planseeber Pulvermet 10:42–64
443. Throop GJ, Rogl P, Rudy E (1978) Calculation of phase equilibria in ternary alloy systems: line compounds. High Temp High Press 10(5):553–559
444. Sudarikov MV, Zhikharev VM (1988) Issledovanie *p–T–x*-diagrammy karbid – nitrid niobiya (A study of niobium carbide – nitride *p–T–x*-diagram). Izv AN SSSR Neorg Mater 24(2):239–242 (in Russian)
445. Weiss J, Lukas HL, Lorenz J, Petzow G, Krieg H (1981) Calculation of heterogeneous phase equilibria in oxide-nitride systems : I. The Quaternary System C – Si – N – O. Calphad 5(2):125–140
446. Ekelund M, Forslund B, Eriksson G, Johansson T (1988) Si-C-O-N high pressure equilibria and ΔG_f° for Si_2ON_2. J Am Ceram Soc 71(11):956–960
447. Srivastava D, Garg SP, Goswami GL (1989) Thermodynamic analysis of mixed carbide, carbonitride and nitride fuels for fast breeder reactors. J Nucl Mater 161(1):44–56
448. Potter PE (1976) Some phase relationships and equilibria for the uranium-plutonium monocarbonitrides including the effects of oxygen on some equilibria. In: Blank H, Lindner R (eds) Plutonium and other actinides, pp. 211–232. Elsevier, New York / North-Holland, Amsterdam
449. Benz R, Troxel JE (1971) Phase diagram carbon-nitrogen-thorium at 1400 to 2200 °C. High Temp Sci 3(5):422–432
450. Potter PE, Spear KE (1980) Advanced fuels for fast breeder reactors. A critical assessment of some phase equilibria. In: Thermodynamics of nuclear materials, Vol. 2, pp. 195–227. IAEA, Vienna
451. Udovskij AL, Ivanov OS (1980) Thermodynamic calculation of the phase diagram of the UC-UN system. In: Thermodynamics of nuclear materials, Vol. 2, pp. 229–246. IAEA, Vienna
452. Kuznetsov V (2007) Carbon – iron – uranium system. In: Effenberg G, Ilyenko S (eds) Ternary alloy systems. Subvol. C, Part 4, pp. 80–89. Springer, Berlin, Heidelberg
453. Korniyenko K (2007) Carbon – molybdenum – uranium system. In: Effenberg G, Ilyenko S (eds) Ternary alloy systems. Subvol. C, Part 4, pp. 90–114. Springer, Berlin, Heidelberg
454. Binder S, Lengauer W, Ettmayer P, Bauer J, Debuigne J, Bohn M (1995) Phase equilibria in the systems Ti – C – N, Zr – C – N and Hf – C – N. J Alloys Compd 217(1):128–136
455. Stadelmaier HH, Fiedler ML (1975) The ternary system nickel-niobium-carbon. Z Metallkd 66(4):224–225

456. Gridnev VN, Barabash OM, Legkaya TN (1985) Termodinamicheskii rascheti eksperimentalnoe issledovanie poverkhnostei likvidusa i solidusa v troinoi sisteme nikel-niobii-uglerod (Thermodynamic calculation and experimental study of liquidus and solidus surfaces in the nickel-niobium-carbon ternary system). In: Ageev NV (ed) Raschety i eksperimentalnye metody postroeniya diagramm sostoyaniya (Calculation and experimental methods of plotting phase diagrams), pp. 130–133. Nauka, Moscow (in Russian)
457. Gridnev VN, Barabash OM, Legkaya TN (1985) Phase equilibria and structure of directionally crystallized alloys of the Ni-Nb-C system. Russ Metall (6):199–204
458. Shurin AK, Dmitrieva GP, Razumova NA, Khandros EL (1987) The phase diagram of the Ni-VC-NbC system. Powder Metall Met Ceram 26(8):658–660
459. Shurin AK, Razumova NA, Dmitrieva GP, Khandros EL (1987) Diagramma sostoyaniya sistemy Ni – $NbC_{0.8}$ – $TaC_{0.9}$ (The constitution diagram of the Ni – $NbC_{0.8}$ – $TaC_{0.9}$ system). Dopov Akad Nauk Ukr RSR Ser A Fiz Mat Tekh Nauki 49(6):81–83 (in Ukrainian)
460. Shurin AK, Dmitrieva GP, Razumova NA, Khandros E L (1987) State diagram of Ni-ZrC-NbC. Russ Metall (6):205–207
461. Ueda Y, Ono K, Moriyama J (1980) Thermodynamic study of the Nb-C-O solid solutions at 2073–2273 K. Nippon Kinzoku Gakkaishi 44(9):1069–1075 (in Japanese)
462. Savitskii EM, Efimov YuV, Bodak OI, Kharchenko OI, Myasnikova EA (1981) The niobium-silicon-carbon system. Inorg Mater 17(12):1649–1652
463. Brukl CE (1965) The Ti-Si-C, Nb-Si-C, and W-Si-C systems. In: Ternary phase equilibria in transition metal-boron-carbon-silicon systems. Report AFML-TR-65–2, Contract USAF 33(615)-1249, Part 2, Vol. 7, pp. 1–57. Air Force Materials Laboratory, Wright-Patterson Air Force Base, Ohio
464. Booker PH, Rudy E (1970) Phase equilibria studies in the Nb-Ta-C system. In: Phase equilibria investigations of binary, ternary and higher order systems. Report AFML-TR-69–117, Contract USAF 33(615)-67-C-1513, Part 3, pp. 1–56. Air Force Materials Laboratory, Wright-Patterson Air Force Base, Ohio
465. Chatfield C (1986) The γ-WC solubility boundary in the quaternary TiC-NbC-TaC-WC system at 1723 K. J Mater Sci 21(2):577–582
466. Brukl CE (1969) The effect of molybdenum and tungsten on the subcarbide solutions in the vanadium-tantalum-carbon and niobium-tantalum-carbon systems. In: Phase equilibria investigation of binary, ternary and higher order systems. Report AFML-TR-69–117, Contract USAF 33(615)-67-C-1513, Part 4, pp. 1–44. Air Force Materials Laboratory, Wright-Patterson Air Force Base, Ohio
467. Ono K, Moriyama J (1981) The phase relationships in the Nb-Ti-C system. J Less-Common Met 79(2):255–260
468. Gusev AI (1985) Phase diagrams of the pseudo-binary TiC – NbC, TiC – TaC, ZrC – NbC, ZrC – TaC and HfC – TaC carbide systems. Russ J Phys Chem 59(3):336–340
469. Chang YA (1967) V-Nb-C system. In: Ternary phase equilibria in transition metal-boron-carbon-silicon systems. Report AFML-TR-65–2, Contract USAF 33(615)-1249, Part 2, Vol. 16, pp. 1–54. Air Force Materials Laboratory, Wright-Patterson Air Force Base, Ohio
470. Rudy E (1966) Constitution of niobium-tungsten-carbon alloys. In: Ternary phase equilibria in transition metal-boron-carbon-silicon systems. Report AFML-TR-65–2, Contract USAF 33(615)-1249, Part 2, Vol. 18, pp. 1–61. Air Force Materials Laboratory, Wright-Patterson Air Force Base, Ohio
471. Stover ER, Wulff J (1959) The nickel-titanium-carbon system. Trans Metall Soc AIME 215:127–136
472. Potter PE (1972) The uranium-plutonium-carbon-oxygen systems: The ternary systems uranium-carbon-oxygen and plutonium-carbon-oxygen and the quaternary system uranium-plutonium-carbon-oxygen. J Nucl Mater 42(1):1–22

473. Goldshleger UI, Merzhanov AG (1983) Termodinamicheskii analiz vosstanovleniya okislov kremniya uglerodom (Thermodynamic analysis of reduction of silicon oxides by carbon). Doklady AN SSSR 269(5):1107–1111 (in Russian)
474. Yakushevich NF, Berdnikov VI (1984) Diagramma fazovo-khimicheskikh ravnovesiy sistemy Si-O-C (The diagram of the phase chemical equilibria of the Si-O-C system). Izv Vyssh Uchebn Zaved Chern Metall (10):4–7 (in Russian)
475. Berdnikov VI, Mizin VG, Karteleva MI (1982) Fazovoe ravnovesie sistemy Si-O-C (The phase equilibrium of the Si-O-C system). Izv Vyssh Uchebn Zaved Chern Metall (12):31–34 (in Russian)
476. Arkharov VI, Konev VN, Timofeeva NF (1960) Issledovanie reaktsionnoy diffuzii v sistemakh metal – slozhnyi gaz. IV. Sistema molibden – azot – uglerod (Study of reaction diffusion in the metal – complex gas systems. IV. Molybdenum – nitrogen – carbon system). Fiz Met Metalloved 9(5):695–700 (in Russian)
477. Stone L, Margolin H (1953) Titanium-rich portion of the Ti-C-N, Ti-C-O and Ti-N-O phase diagrams. J Met 5(11):1498–1502
478. Steele BCH, Javed NA, Alcock CB (1970) Measurement of the equilibrium oxygen, carbon and uranium activities associated with the uranium oxycarbide phase. J Nucl Mater 35(1):1–13
479. Javed NA (1970) Phase relations in the uranium-carbon-oxygen system at 1573 K. J Nucl Mater 37(3):353–354
480. Larin AA, Vlasov VG (1974) Effect of oxygen content on the structural characteristics of uranium oxycarbides. Powder Metall Met Ceram 13(9):761–763
481. Khromov YuF, Lyutikov RA (1980) Thermodynamic analysis of the interaction of $UO_{2\pm x}$ with carbon. At Energ 49(1):28–30
482. Shabalin IL, Vishnyakov VM, Bull DJ, Keens SG, Yamshchikov LF, Shabalin LI (2009) Initial stages of oxidation of near-stoichiometric titanium carbide at low oxygen pressures. J Alloys Compd 472:373–377
483. Koyama K, Hashimoto Y, Hata H (1979) Phase relationship in the V-C-O ternary system. Trans Jpn Inst Met 20(7):371–376
484. Ouensanga AH, Dode M (1976) Etude thermodynamique et structurale a haute temperature du systeme Zr-C-O. Diagramme de phases a 1555 °C. (Thermodynamic and structural study of the system Zr-C-O at high temperatures. The phase diagram at 1555 °C.) J Nucl Mater 59(1):49–60 (in French)
485. Watson A, Cornish L (2007) Carbon – palladium – thorium system. In: Effenberg G, Ilyenko S (eds) Ternary alloy systems. Subvol. C, Part 4, pp. 120–122. Springer, Berlin, Heidelberg
486. Ivanchenko V, Pryadko T (2007) Carbon – palladium – uranium system. In: Effenberg G, Ilyenko S (eds) Ternary alloy systems. Subvol. C, Part 4, pp. 123–127. Springer, Berlin, Heidelberg
487. Lyakishev NP, ed (2000) Diagrammy sostoyaniya dvoinykh metallicheskikh sistem (Phase diagrams of binary metallic systems), Vol. 3, Part 2. Mashinostroenie, Moscow (in Russian)
488. Rosen S, Nevitt MV, Barker JJ (1963) The U-Pu-C ternary phase diagram below 50 atomic percent carbon. J Nucl Mater 9(2):128–136
489. Rosen S, Nevitt MV, Mitchell AW (1963) The uranium monocarbide – plutonium monocarbide system. J Nucl Mater 9(2):137–142
490. Reavis JG, Shupe MW, Bjorklund CW, Leary JA (1967) Phase relations in the high-carbon portion of the U-Pu-C system", Trans Amer Nucl Soc 10:111–112
491. Ugajin M, Abe J, Suzuki Y, Takahashi I, Kurihara M (1976) Phase equilibria in system U-Pu-W-C. J Nucl Sci Technol 13(1):36–39
492. Kotelnikov RB, Bashlykov SN, Kashtanov AI, Menshikova TS (1978) Vysokotemperaturnoe yadernoe toplivo (High-temperature nuclear fuel). Atomizdat, Moscow (in Russian)

493. Korniyenko K, Lebrun N (2007) Carbon – plutonium – uranium system. In: Effenberg G, Ilyenko S (eds) Ternary alloy systems. Subvol. C, Part 4, pp. 138–159. Springer, Berlin, Heidelberg
494. Korniyenko K (2007) Carbon – plutonium – zirconium system. In: Effenberg G, Ilyenko S (eds) Ternary alloy systems. Subvol. C, Part 4, pp. 160–167. Springer, Berlin, Heidelberg
495. Haines HR, Potter PE (1970) Constitutional studies in uranium and plutonium carbide – fission product systems. I. Uranium and plutonium-transition metal-carbon systems. UK Atomic Energy Authority, Report AERE-R 6512, pp. 1–15. Harwell Laboratory, Oxfordshire
496. Eremenko VN, Kharkova AM, Velikanova TYa (1984) Isotermicheskoe sechenie sistemy vanadii – renii – uglerod pri 1950 °C (The isothermal section of the vanadium – rhenium – carbon system at 1950 °C). Dopov Akad Nauk Ukr RSR Ser A Fiz Mat Tekh Nauki 46(5):84–86 (in Russian)
497. Korniyenko K (2007) Carbon – rhodium – thorium system. In: Effenberg G, Ilyenko S (eds) Ternary alloy systems. Subvol. C, Part 4, pp. 168–173. Springer, Berlin, Heidelberg
498. Korniyenko K (2007) Carbon – rhodium – uranium system. In: Effenberg G, Ilyenko S (eds) Ternary alloy systems. Subvol. C, Part 4, pp. 174–183. Springer, Berlin, Heidelberg
499. Korniyenko K (2007) Carbon – ruthenium – thorium system. In: Effenberg G, Ilyenko S (eds) Ternary alloy systems. Subvol. C, Part 4, pp. 184–190. Springer, Berlin, Heidelberg
500. Wachtmann KH, Moss MA, Hoffmann R-D, Jeitschko W (1995) Crystal structures of several ternary lanthanoid and actinoid ruthenium carbides. J Alloys Compd 219:279–284
501. Korniyenko K (2007) Carbon – ruthenium – uranium system. In: Effenberg G, Ilyenko S (eds) Ternary alloy systems. Subvol. C, Part 4, pp. 191–202. Springer, Berlin, Heidelberg
502. Alekseeva ZM (1991) Phase equilibria in the U-Ru-C system. Russ Metall (1):219–224
503. Schuster JC (1993–1994) Silicon carbide and transition metals: a critical evaluation of existing phase diagram data supplemented by new experimental results. Int J Refract Met Hard Mater 12(4):173–177
504. Searcy AW, Finnie LN (1962) Stability of solid phases in the ternary systems of silicon and carbon with rhenium and the six platinum metals. J Amer Ceram Soc 45(6):268–273
505. Schiepers RCJ, Van Loo FJJ, De With G (1988) Reactions between α-silicon carbide ceramic and nickel or iron. J Amer Ceram Soc 71(6):C284-C287
506. Sambasivan S, Petuskey WT (1992) Phase relationship in the Ti-Si-C system at high pressures. J Mater Res 7(6):1473–1479
507. Wakelkamp WJJ, Van Loo FJJ, Metselaar R (1991) Phase relations in the Ti-Si-C system. J Eur Ceram Soc 8(3):135–139
508. Goto T, Hirai T (1987) Chemically vapour deposited Ti_3SiC_2. Mater Res Bull 22(9):1195–1201
509. Du Y, Schuster JC, Seifert HJ, Aldinger F (2000) Experimental investigation and thermodynamic calculations of the titanium-silicon-carbon system. J Am Ceram Soc 83(1):197–203
510. Brewer L, Krikorian OH (1956) Reactions of refractory silicides with carbon and nitrogen. J Electrochem Soc 103:38–51
511. Rother M, Holleck H (1993) The constitution of multicomponent high-tech ceramic systems. J Chim Phys Phys-Chim Biol 90(2):333–339
512. Wang YZ, Carim AH (1995) Ternary phase equlibria in the Zr-Si-C system. J Am Ceram Soc 78(3):662–666
513. Brukl CE, Harmon DP (1965) Ti-Ta-C system. In: Ternary phase equilibria in transition metal-boron-carbon-silicon systems. Report AFML-TR-65–2, Contract USAF 33(615)-1249, Part 2, Vol. 2, pp. 1–67. Air Force Materials Laboratory, Wright-Patterson Air Force Base, Ohio
514. Rudy E (1965) Ta-W-C system. In: Ternary phase equilibria in transition metal-boron-carbon-silicon systems. Report AFML-TR-65–2, Contract USAF 33(615)-1249, Part 2, Vol. 8, pp. 1–141. Air Force Materials Laboratory, Wright-Patterson Air Force Base, Ohio

515. Harmon DP, Brukl CE (1965) Zr-Ta-C system. In: Ternary phase equilibria in transition metal-boron-carbon-silicon systems. Report AFML-TR-65–2, Contract USAF 33(615)-1249, Part 2, Vol. 3, pp. 1–72. Air Force Materials Laboratory, Wright-Patterson Air Force Base, Ohio
516. Henney J, Jones JWS (1966) High-temperature phase equilibria in the Th-U-C system in the presence of free carbon. Trans Brit Ceram Soc 65:613–626
517. Korniyenko K, Lebrun N (2007) Carbon – thorium – uranium system. In: Effenberg G, Ilyenko S (eds) Ternary alloy systems. Subvol. C, Part 4, pp. 203–215. Springer, Berlin, Heidelberg
518. Perrot P (2007) Carbon – thorium – zirconium system. In: Effenberg G, Ilyenko S (eds) Ternary alloy systems. Subvol. C, Part 4, pp. 216–219. Springer, Berlin, Heidelberg
519. Rudy E, Benesovsky F (1962) Untersuchungen im System Th-Zr-C (Investigations of the system Th-Zr-C). Monatsh Chem 93:1279–1283 (in German)
520. Alekseeva ZM (1968) Fazovyi sostav splavov UC-Zr i Zr-ThC i otnositelnoe srodstvo C k Zr, Th i U (The phase composition of UC-Zr and Zr-ThC alloys and the relative affinity of C for Zr, Th and U). In Ivanov OS (ed) Fiziko-khimiya splavov i tugoplavkikh soedineniy (Physico-chemistry of alloys and refractory compounds). Nauka, Moscow, pp. 136–145 (in Russian)
521. Rudy E (1970) The phase diagram Ti-V-C. In: Experimental phase equilibria of selected binary, ternary and higher order systems. Report AFML-TR-69–117, Contract USAF 33(615)-67-C-1513, Part 7, pp. 1–64. Air Force Materials Laboratory, Wright-Patterson Air Force Base, Ohio
522. Rudy E (1973) Constitution of ternary titanium-tungsten-carbon alloys. J Less-Common Met 33(2):245–273
523. Benesovsky F, Rudy E (1961) Auf der Systeme U – Zr (Hf, Nb, Ta) – C (On the systems U – Zr (Hf, Nb, Ta) – C). Planseeber Pulvermet 9:65–76 (in German)
524. Nickel H, Inanc Oe, Lücke K (1968) Auf das Wissen der U-Zr-C System (On the knowledge of the U-Zr-C system). J Nucl Mater 28:79–92 (in German)
525. Storms EK, Griffin J (1973) Thermodynamics and phase relationships of the zirconium-uranium-carbon system. High Temp Sci 5:423–437
526. Butt DP, Wallace TC (1993) The U-Zr-C ternary phase diagram above 2473 K. J Am Ceram Soc 76(6):1409–1419
527. Perrot P (2007) Carbon – uranium – zirconium system. In: Effenberg G, Ilyenko S (eds) Ternary alloy systems. Subvol. C, Part 4, pp. 220–229. Springer, Berlin, Heidelberg
528. Rudy E, Benesovsky F, Rudy El (1962) Untersuchungen im System Vanadin-Wolfram-Kohlenstoff (Investigations of vanadium-tungsten-carbon system). Monatsh Chem 93(3):693–707 (in German)
529. Kuzma YuB, Fedorov TF, Shvets EA (1965) Phase equilibria in the system Zr-W-C. Powder Metall Met Ceram 4(2):106–109
530. Naidich YuV, Kolesnichenko GA (1967) Vzaimodeistvie metallicheskikh rasplavov s poverkhnostyu almaza i grafita (The interaction of metallic melts with the surface of diamond and graphite). Naukova Dumka, Kyiv (in Russian)
531. Cotton FA, Wilkinson G (1965) Advanced inorganic chemistry. Wiley, New York, London
532. Alapati SV, Johnson JK, Sholl DS (2008) Large-scale screening of metal hydride mixtures for high-capacity hydrogen storage from first principles calculations. J Phys Chem C 112(14):5258–5262
533. Rogl P, Noël H (1995) The C-Si-U system (carbon – silicon – uranium). J Phase Equilib 16(1):66–72
534. Pottgen R, Kaczorowski D, Jeitschko W (1993) Crystal structure, magnetic susceptibility and electrical conductivity of the uranium silicide carbides $U_3Si_2C_2$ and $U_{20}Si_{16}C_3$. J Mater Chem 3:253–258
535. Whittaker AG (1978) The controversial carbon solid-liquid-vapour triple point. Nature 276:695–696

536. Gustafson P (1986) An evaluation of the thermodynamic properties and the (p, T) phase diagram of carbon. Carbon 24:169–176
537. Bundy FP (1989) Pressure-temperature phase diagram of elemental carbons. Physica A 156:169–178
538. Bundy FP, Bassett WA, Weathers MS, Hemley RJ, Mao HK, Goncharov AF (1996) The pressure-temperature phase and transformation diagram for carbon; updated through 1994. Carbon 34(2):141–153
539. Nagornyi VG, Kotosonov AS, Ostrovskii VS, Dymov BK, Lutkov AI, Anufriev YuP, Barabanov VN, Belogorskii VD, Kuteynikov AF, Virgilev YuS, Sokker GA (1975) Svoistva konstruktsionnykh materialov na osnove ugleroda (Properties of structural materials based on carbon). Metallurgiya, Moscow (in Russian)
540. Martienssen W (2005) The elements. In: Martienssen W, Warlimont H (eds) Springer handbook of condensed matter and materials data, pp. 45–158. Springer, Berlin, Heidelberg
541. Suetin DV, Shein IR, Ivanovskii AL (2010) Tungsten carbides and nitrides and ternary systems based on them: the electronic structure, chemical bonding and properties. Russ Chem Rev 79(7):611–634
542. Velikanova T, Turchanin M, Dobatkina T, Velikanova T (2008) Carbon – iron - molybdenum system. In: Effenberg G, Ilyenko S (eds) Ternary alloy systems. Subvol. D, Part 2, pp. 124–172. Springer, Berlin, Heidelberg
543. Savitskii EM, Zakharov AM, Burkhanov GS, Kataev RS (1970) Troinaya sistema molibden – zhelezo – uglerod (The ternary system molybdenum – iron – carbon). Izv Vyssh Uchebn Zaved Tsvetn Metall 13(6):113–115 (in Russian)
544. Anderson J-O (1988) A thermodynamic evaluation of the Fe-Mo-C system. Calphad 12(1):9–23
545. Giron G, Durand-Charre M (1995) High temperature phase equilibria in the system Fe-Mo-C. Z Metallkd 86(1):15–21
546. Cornish L, Watson A (2008) Carbon – iron – niobium system. In: Effenberg G, Ilyenko S (eds) Ternary alloy systems. Subvol. D, Part 2, pp. 184–199. Springer, Berlin, Heidelberg
547. Fedorov TF, Kuzma YuB, Skolozdra RV, Popova NM (1965) Phase equilibria in the ternary systems Zr-Co-C and Nb-Fe-C. Powder Metall Met Ceram 4(12):1010–1014
548. Das RC, Jha R, Mukherjee T (1986) Tne carbon – iron – niobium system. J Alloy Phase Diagrams 2(2):131–140
549. Lebrun N (2008) Carbon – iron – silicon system. In: Effenberg G, Ilyenko S (eds) Ternary alloy systems. Subvol. D, Part 2, pp. 240–286. Springer, Berlin, Heidelberg
550. Raghavan V (1992) Phase diagrams of ternary iron alloys. Part 6A, Indian Institute of Metals, Calcutta
551. Lebrun N, Perrot P (2008) Carbon – iron – titanium system. In: Effenberg G, Ilyenko S (eds) Ternary alloy systems. Subvol. D, Part 2, pp. 287–316. Springer, Berlin, Heidelberg
552. Sare IR (1980) Splat-cooled iron-titanium-carbon alloys. Met Sci 14:177–183
553. Ramaekers PPJ, Van Loo FJJ, Bastin GF (1985) Phase relations, diffusion paths and kinetics in the system C-Fe-Ti at 1273 K. Z Metallkd 76(4):245–248 (Erratum – Z Metallkd (1985) 76(9):639)
554. Frage N (1999) Interaction between nonstoichiometric titanium carbide and Fe-C alloys. Metall Mater Trans B 30:857–663
555. Liu C-S, Huang J-H, Sheng Y (2002) Thermodynamic analysis of C-Fe-Ti system. J Inorg Mat 17(2):288–292 (in Chinese)
556. Raghavan V (2003) The C-Fe-Ti (carbon-iron-titanium) system. J Phase Equilib 24(1):62–66
557. Ivanchenko V, Pryadko T (2008) Carbon – iron – vanadium system. In: Effenberg G, Ilyenko S (eds) Ternary alloy systems. Subvol. D, Part 2, pp. 327–356. Springer, Berlin, Heidelberg
558. Huang W (1991) Thermodynamic evaluation of the C-Fe-V system. Z Metallkd 82(5):391–401

559. Korniyenko K (2008) Carbon – iron – tungsten system. In: Effenberg G, Ilyenko S (eds) Ternary alloy systems. Subvol. D, Part 2, pp. 327–356. Springer, Berlin, Heidelberg
560. Bergstroem M (1977) The η-carbides in the ternary system Fe-W-C at 1250 °C. Mater Sci Eng 27:257–269
561. Uhrenius B (1980) Calculation of phase equilibria in the Fe-W-C system. Calphad 4(3):173–191
562. Gustafson P (1987) A thermodynamic evaluation of the C-Fe-W system. Metall Trans A 18(2):175–188
563. Rynemark M (1991) Investigation of equilibria in the Ti-W-C-N system at 1750 °C. Refract Met Hard Mater 10:185–193
564. Ordanyan SS, Boldin AA, Prilutskii EV (2000) Interaction in the B_4C-W_2B_5. Rus J Appl Chem 73(12):2128–2130
565. Ordanyan SS, Vikhman SV, Kuznetsov MN (2004) *T – x* fazovaya diagramma linii B_4C-W_2B_5 v sisteme B-C-Si-W (*T – x* phase diagram of the B_4C-W_2B_5 join in the B-C-Si-W system). Ogneupory Tekh Keram (12)2–4 (in Russian)
566. Ordanyan SS (1993) Obschie aspekty fazovykh otnosheniy v sistemakh SiC – $Me^{IV-VI}B_2$ (Common aspects of phase relations in SiC – $Me^{IV-VI}B_2$ systems). Zh Prikl Khim 66(11):2439–2444 (in Russian)
567. Ordanyan SS, Unrod VI (2005) Eutectics and their models, sintered composites in the systems of refractory materials. Refract Industrial Ceram 46(4):276–281
568. Ordanyan SS, Yurchenko OV, Vikhman SV (2004) Phase relations in the SiC – LaB_6 system. Inorg Mater 40(6):693–696
569. Ordanyan SS, Vikhman SV, Kuznetsov MN (2004) Stroenie politermicheskogo razreza SiC – W_2B_5 sistemy B-C-Si-W (Structure of the polythermal SiC – W_2B_5 section of the B-C-Si-W system). Ogneupory Tekh Keram (12):2–4 (in Russian)
570. Ordanyan SS, Nesmelov DD, Vikhman SV (2009) The system SiC – W_2B_5 – LaB_6. Refract Industrial Ceram 50(5):391–393
571. Seifert HJ (2004) Refractory and hard materials in the Ti-Si-B-C-N system – phase equilibria, phase reactions and thermal stabilities. Technical Report, pp. 1–8. University of Florida, Gainesville
572. Seifert HJ, Peng J, Golczewski J, Aldinger F (2001) Phase equilibria of precursor-derived Si-(B-)C-N ceramics. Appl Organomet Chem 15(10):794–808
573. Johnson WB, Nagelberg AS (1995) Application of phase diagrams to the production of advanced composites. In: Alper AM (ed) Phase diagrams in advanced ceramics, pp. 85–126, Academic Press, San Diego, New York
574. Duschanek H, Rogl P (1998) The system boron – carbon – zirconium. In: Effenberg G (ed) Phase diagrams of ternary metal-boron-carbon systems. ASM International, Materials Park, Ohio, pp. 445–485
575. Young WS (1973) Molybdenum sintering and the molybdenum-oxygen-carbon system. J Less-Common Met 32:321–330
576. Audi G, Wapstra AH, Thibault C, Blachot J, Bersillon O (2003) The NUBASE evaluation of nuclear and decay properties. Nucl Phys A 729:3–128
577. De Laeter JR, Bohlke JK, De Bievre P, Hidaka H, Peiser HS, Rosman KJR, Taylor PDP (2003) Atomic weights of the elements. Review 2000 (IUPAC Technical report). Pure Appl Chem 75(6):683–800
578. Wieser ME (2006) Atomic weights of the elements 2005. (IUPAC Technical report). Pure Appl Chem 78(11):2051–2066
579. Savitskii EM, Burkhanov GS (1971) Metallovedenie splavov tugoplavkikh i redkih metallov (Metallography of refractory and less-common metal alloys), 2nd ed. Nauka, Moscow (in Russian)
580. Grytsiv AV, Bondar AA, Velikanova TYa (1997) Rhenium solid solution in the Cr – Re – C ternary system at solidus temperature. J Alloys Compd 262–263:402–405

581. Eremenko VN, ed (1981) Diagrammy sostoyaniya system soderzhaschikh karbidy i nitridy (Alloy phase diagrams of systems containing carbides and nitrides). Naukova Dumka, Kyiv (in Russian)
582. Eremenko VN, ed (1988) Fizicheskaya khimiya neorganicheskikh materialov (Physical chemistry of inorganic materials), Vol. 1. Naukova Dumka, Kyiv (in Russian)
583. Bondar AA, Velikanova TYa (1996) Aspects of construction diagrams of ternary systems formed by chromium with carbon and *d*-transition metals. Powder Metall Met Ceram 35(7–8):484–496
584. Lengauer W (2000) Transition metal carbides, nitrides and carbonitrides. In: Riedel R (ed) Handbook of ceramic hard materials, pp. 202–252. Wiley-VCH, Weinheim
585. Jonsson S (1996) Assessment of the Ti-W-C system and calculations in the Ti-W-C-N system. Z Metallkd 87(10):788–795
586. Doi A, Nomura T, Tobioka M-A, Takahashi K, Hara A (1986) Thermodynamic evaluation of equilibrium nitrogen pressure and WC separation in Ti-W-C-N system carbonitride. High Temp High Press 18(4):443–452
587. Ganguly A, Barsoum MW, Schuster J (2005) The 1300 °C isothermal section in the Ti-In-C ternary phase diagram. J Am Ceram Soc 88:1290–1296
588. Chung H-J, Shim J-H, Lee DN (1999) Thermodynamic evaluation and calculation of phase equilibria of the Ti-Mo-C-N quaternary system. J Alloys Compd 282(1–2):142–148
589. Chatfield Ch (1983) Redetermination of the γ-α solubility line in the TiC-TaC-WC system at 1723 K. Powder Metall Int 15(1):18–19
590. Fahrenholtz WG, Neuman EW, Brown-Shaklee HJ, Hilmas E (2010) Superhard boride – carbide particulate composites. J Am Ceram Soc 93(11):3580–3583
591. Savitsky EM, Povarova KB, Makarov PV (1982) Physikalisch-chemische Grundlagen des Legierens von warmfesten Wolframlegierungen (Physical and chemical principles underlying alloying of heat-resistant tungsten alloys). Z Metallkd 73(2):92–97 (in German)
592. Shabalin IL (1973) Razrabotka tekhnologii polucheniya teplovydelyayushchikh elementov na osnove kompozitsii karbid urana – okis berilliya dlya yadernykh reaktorov aerokosmicheskoi tekhniki (Development of manufacturing technology of nuclear fuel ceramic elements based on uranium carbide – beryllium oxide composites for aerospace application). MSc Thesis, Ural Polytechnic Institute, Sverdlovsk (in Russian)
593. Kimura Y, Iida K, Wei F-G, Mishima Y (2006) Phase equilibria in the T – Al – C (T: Co, Ni, Rh, Ir) and T – Al – B (T: Rh, Ir) systems for the design of $E2_1$-Co_3AlC based heat resistant alloys. Intermetallics 14:508–514
594. Frisk K (2003) A revised thermodynamic description of the Ti-C system. Calphad 27:367–373
595. Sood DD, Agarwal R, Venugopal V (1997) Phase diagram calculations of U-Pu-N system with carbon and oxygen impurities. J Nucl Mater 247:293–300
596. Telle R, Brook RJ, Petzow G (1991) Phase relations in ceramic systems. J Hard Mater 2:79–114
597. Duschanek H, Rogl P, Lukas HL (1995) A critical assessment and thermodynamic calculation of the boron-carbon-titanium (B-C-Ti) ternary system. J Phase Equilib 16(1):46–60
598. Gusev AI (1997) Phase equilibria in the ternary system titanium – boron – carbon: the sections TiC_y – TiB_2 and B_4C_y – TiB_2. J Solid State Chem 133:205–210
599. Brodkin D, Barsoum MW (1996) Isothermal section of Ti-B-C phase diagram at 1600 °C. J Am Ceram Soc 79(3):785–787
600. Dumitrescu L, Hillert M, Sundman B (1999) Reassessment of Ti-C-N based on a critical review of available assessments of Ti-N and Ti-C. Z Metallkd 90(7):534–541
601. Artyukh LV, Ilyenko SM, Velikanova TYa (1996) The scandium – titanium – carbon phase diagram. J Phase Equilib 17(5):403–413
602. Artyukh LV, Velikanova TYa, Ilyenko SM (1998) Phase equilibria in the Sc-Zr-C system. J Alloys Compd 269:193–200

603. Velikanova TYa, Bondar AA, Grytsiv AV, Dovbenko OI (2001) Metallochemistry of chromium with *d*-metals and carbon. J Alloys Compd 320:341–352
604. Rivlin VG (1985) Critical review of constitution of carbon – iron – tungsten system. Int Met Rev 30(6):259–274
605. Zakharov AM, Lashkova LA, Semeryakova SG (1987) Polythermal section γ-TiAl – TiC of the Ti-Al-C system. Russ Metall (4):197–198
606. Naguib M, Kurtoglu M, Presser V, Lu J, Niu J, Heon M, Hultman L, Gogotsi Y, Barsoum MW (2011) Two-dimensional nanocrystals produced by exfoliation of Ti_3AlC_2. Adv Mater 23(37):4207–4212
607. Yaney DL, Joshi A (1990) Reaction between niobium and silicon carbide at 1373 K. J Mater Res 5(10):2197–2208
608. Silman GO (1995) Diagramma sostoyaniya sistemy Fe-C-V-Si i splavy na ee osnove. 1. Postroenie i analiz chastei diagrammy. (State diagram of Fe-C-V-Si system and alloys on its base. 1. Construction and analysis of diagram sections.) Metallovedenie Termicheskaya Obrabotka Metallov (11):11–13 (in Russian)
609. Ramaekers PPJ, Bastin GF, Van Loo FJJ (1984) Phase relations and diffusion paths in the system Co-Ti-C at 1273 K. Z Metallkd 75(8):639–642
610. Rivlin VG (1985) Phase equilibria in iron alloys. 17. Critical review of constitution of carbon – iron – molybdenum system. Int Met Rev 30(3):109–124
611. Ramaekers PPJ, Van Loo FJJ, Bastin GF (1985) Phase relations, diffusion paths and kinetics in the system Fe-Ti-C at 1273 K. Z Metallkd 76(4):245–248
612. Alekseeva ZM, Ivanov OS (1974) Some new data from the experimental investigation of the phase structure of alloys and the phase diagrams of the U-C-Mo, -W, -Cr, -Re systems. Thermodynamics of nuclear materials. Proc Symp Pap Discuss STI/PUB/380, International Atomic Energy Agency, Vienna
613. Jackson MR (1977) Composites of γ + TaC in the Ni-Ta-C ternary system. Metall Trans A 8(6):905–913
614. Eremenko VN, Shabanova SV, Velikanova TYa (1977) Structure of alloys and the phase equilibrium diagram of the system Hf-Mo-C. VI. Isothermal section of the Hf-Mo-C system at 1400 °C. Powder Metall Met Ceram 16(10):772–777
615. Enomoto M (1996) The C-Ti-V system (carbon-titanium-vanadium). J Phase Equilib 17(3):237–247
616. Wiitkar P, Halet J-F, Saillard J-Y, Rogl P, Bauer J (1994) Crystal and electronic structure of the novel layered rare earth metal boride carbide $Gd_2B_3C_2$. Inorg Chem 33(7):1297–1305
617. Bidaud E, Hiebl K, Hoffman R-D, Pöttgen R, Jardin C, Bauer J, Gautier R, Gougeon P, Saillard J-Y, Halet J-F (2000) Structural, electronic and magnetic properties of ternary rare-earth metal borocarbides $R_5B_2C_5$ (R = Y, Ce-Tm) containing BC_2 "molecules". J Solid State Chem 154(1):286–295
618. Ruiz D, Garland MT, Saillard J-Y, Halet J-F, Bohn M, Bauer J (2002) Electron probe microanalysis in the ternary Gd-B-C system. Solid State Sci 4:1173–1178
619. Holleck H, Kleykamp H (1970) Zur Konstitution und Thermodynamik im System Uran – Ruthenium – Kohlenstoff (Towards the constitution and thermodynamics in the system uranium – ruthenium – carbon). J Nucl Mater 35:158–166 (in German)
620. Ugajin M, Takahashi I (1970) The phase reaction in the UC-W system. J Nucl Mater 35:303–313
621. Shurin AK, Dmitrieva GP, Cherepova TS (1996) Phase equilibria in Co – Me′C – Me″C alloys. 1. Systems with three-phase eutectic equilibria. Powder Metall Met Ceram 35(11–12):615–620
622. Shurin AK, Dmitrieva GP, Cherepova TS (1997) Phase equilibria in Co – Me′C – Me″C alloys. 2. Systems with four-phase eutectic equilibrium. Powder Metall Met Ceram 36(3–4):193–196
623. Bhanumurthy K, Schmid-Fetzer R (1996) Solid state phase equilibria and reactive diffusion in the Cr-Si-C system. Z Metallkd 87(1):61–71

624. Frage N, Frumin N, Levin L, Polak M, Dariel MP (1998) High-temperature phase equilibria in the Al-rich corner of the Al-Ti-C. Metall Mater Trans A 29(4):1341–1345
625. Bandyopadhyay D, Sharma RC, Chakraborti N (2000) The C-Hf-Ti (carbon-hafnium-titanium) system. J Phase Equilib 21(6):535–538
626. Bandyopadhyay D, Sharma RC, Chakraborti N (2001) The C-Ti-Zr (carbon-titanium-zirconium) system. J Phase Equilib 22(1):61–64
627. Halverson DC, Munir ZA (1986) Boron carbide reactive metal cermets: I, Thermodynamic considerations in boron carbide titanium cermets. Ceram Eng Sci Proc 7(7/8):1000–1010
628. Stetskiv AO, Pavlyuk VV (2002) Issledovanie troinykh sistem Ce-Ge-C i Ce-Si-C pri 670 K (Investigation of Ce-Ge-C and Ce-Si-C ternary systems at 670 K). Ukr Khim Zh 68(7–8):80–82 (in Russian)
629. Laurila T, Zeng K, Molarius J, Riekkinen T, Suni I, Kivilahti JK (2002) Effect of oxygen on the reactions in Si/Ta/Cu and Si/TaC/Cu systems. Microelect Eng 64:279–287
630. Van Loo FJJ, Smet FM, Rieck GD, Verspui G (1982) Phase relations and diffusion paths in the Mo-Si-C system at 1200 °C. High Temp High Press 14(1):25–31
631. Costa Silva A, Kaufman MJ (1994) Phase relations in the Mo-Si-C system relevant to the processing of $MoSi_2$-SiC composites. Metall Mater Trans A 25(1):5–15
632. Gan G, Sun J, Chen J, Chen Y, Yan J (2002) Stabilized chemical potential diagrams for Mo-Si-C ternary system. Kuei Suan Jen Hsueh Pao (J Chin Ceram Soc) 30(2):193–197 (in Chinese)
633. Kephart JS, Carim AH (1998) Ternary compounds and phase equilibria in Ti-Ge-C and Ti-Ge-B. J Electrochem Soc 145(9):3253–3258
634. Bittermann H, Rogl P (2002) Critical assessment and thermodynamic calculation of ternary system C-Hf-Zr (carbon-hafnium-zirconium). J Phase Equilib 23(3):218–235
635. Golberg D, Bando Y, Dorozhkin P, Dong Z-C (2004) Synthesis, analysis and electrical property measurements of compound nanotubes in the B-C-N ceramic system. MRS Bull 29(1):38–42
636. Lee CH, Kayastha VK, Wang J, Yap YK (2009) Introduction to B-C-N materials. In: Yap YK (ed) B-C-N nanotubes and related nanostructures, pp. 1–22. Springer, Dordrecht, Heidelberg
637. Arenal R, Loiseau A (2009) Heteroatomic single-wall nanotubes made of boron, carbon and nitrogen. In: Yap YK (ed) B-C-N nanotubes and related nanostructures, pp. 45–82. Springer, Dordrecht, Heidelberg
638. Yu J, Wang EG (2009) Carbon nitride and boron carbon nitride nanostructures. In: Yap YK (ed) B-C-N nanotubes and related nanostructures, pp. 195–222. Springer, Dordrecht, Heidelberg
639. Laurila T, Molarius J, Kivilahti JK (2004) Interfacial reactions in the Si/TaC/Cu systems. Microelect Eng 71:301–309
640. Bandyopadhyay D (2004) The Ti-Si-C (titanium-silicon-carbon) system. J Phase Equilib Diffus 25(5):415–420
641. Choi SK, Chandrasekaran M, Brabers MJ (1990) Interaction between titanium and SiC. J Mater Sci 25(4):1957–1964
642. Seifert HJ (1993) Thermodynamic and phase optimization in the system Ti-Si-C-N. PhD Thesis, Max Plank Institut für Metallforschung, Institut für Metallkunde der Universitiät Stuttgart
643. Ohtani H, Hillert M (1993) Calculation of V-C-N and Ti-C-N phase diagrams. Calphad 17(1):93–99
644. Yan J, Ma X, Zhao W, Tang H, Zhu C, Cai S (2005) Crystal structure and carbon vacancy hardening of $(W_{0.5}Al_{0.5})C_{1-x}$ prepared by a solid-state reaction. Chem Phys Chem 6:2099–2103
645. Guo Y, Yuan W, Song B, Xu Y (2008) Chemical reaction in the Co-Si-C system. Powd Diffraction 23(4):329–333
646. Wang S, Zhang Y, Abidi N, Cabrales L (2009) Wettability and surface free energy of graphene films. Langmuir 25(18):11078–11081

647. Xiong W, Du Y, Zhang W, Xu H (2010) Carbon – tungsten – zirconium system. In: Effenberg G, Ilyenko S (eds) Ternary alloy systems. Subvol. E, Part 3, pp. 31–47. Springer, Berlin, Heidelberg
648. Savitsky EM, Povarova KB, Makarov PV, Zavarzina YaK (1977) Phase-Zusammensetzung, Struktur und Eigenschaften von vakuumgeschmolzenem W-C-(Zr, Hf, Nb, Ta, Re) Legierung (Phase composition, structure and properties of vacuum-melted W-C-(Zr, Hf, Nb, Ta, Re) alloys). Planseeber Pulvermet 25(3):168–185 (in German)
649. Miyazawa K, Obayashi A, Kuwabara M (2001) C_{60} nanowhiskers in a mixture of lead zirconate titanate sol – C_{60} toluene solution. J Am Ceram Soc 84(12):3037–3039
650. Miyazawa K (2002) C_{70} nanowhiskers fabricated by forming liquid/liquid interfaces in the systems of toluene solution of C_{70} and isopropyl alcohol. J Am Ceram Soc 85(5):1297–1299
651. Liu H, Li Y, Jiang L, Luo H, Xiao S, Fang H, Li H, Zhu D, Yu D, Xu J, Xiang B (2002) Imaging as-grown [60]-fullerene nanotubes by template technique. J Am Chem Soc 124:13370–13371
652. Miyazawa K (2010) Synthesis and functions of fullerene nanotubes. In: Kijima T (ed) Inorganic and metallic nanotubular materials, pp. 201–214. Springer, Berlin, Heidelberg
653. Carney CM, Parthasarathy TA, Cinibulk MK (2011) Oxidation resistance of hafnium diboride ceramics with additions of silicon carbide and tungsten boride or tungsten carbide. J Am Ceram Soc 94(8):2600–2607
654. Grigoriev ON, Gogotsi GA, Gogotsi YG, Subbotin VI, Brodnikovskii NP (2000) Synthesis and properties of ceramics in the SiC-B_4C-MeB_2 system. Powder Metall Met Ceram 39(5–6):239–250
655. Ordanyan SS, Dmitriev AI, Stepanenko EK, Aulova NYu, Semenov NE (1987) SiC-TiB_2 system – a base of high-hardness wear-resitant materials. Powder Metall Met Ceram 26(5):375–377
656. Udalov YP, Valova EE, Ordanyan SS (1995) Preparation and abrasive properties of eutectic compositions in the system B_4C-SiC-TiB_2. Refractories 36(7–8):233–234
657. Ordanyan SS, Vikhman SV (1997) Some properties of composite materials in the system SiC-TiB_2. Refract Indust Ceram 38(7–8):251–252
658. Ordanyan SS, Vikhman SV, Prilutskii EV (2002) Investigation of the structure and properties of materials in the SiC-TiB_2 system. Powder Metall Met Ceram 41(1–2):42–46
659. Danilovich DP, Rumyantsev VI, Ordanyan SS (2009) Sistema SiC-TiC-TiB_2 kak osnova keramomatrichnykh kompozitsionnykh materialov (The SiC-TiC-TiB_2 system as a base of ceramic matrix composite materials). Voprosy Materialovedeniya (4):42–47 (in Russian)
660. Suetin DV, Shein IR, Ivanovskii AL (2011) Structural, electronic and magnetic properties of tungsten oxycarbides $WC_{1-x}O_x$ and $WO_{3-x}C_x$ from first principles calculations. Phys Status Solidi B 248(12):2884–2892
661. Pastukhov EA, Chentsov VP, Kiselev AV, Bodrova LE, Dolmatov AV, Popova EA, Petrova SA, Zakharov RG (2006) Wetting of graphite surface by the aluminium alloys melts. In: Proc. 4th Int. Conf. "Mathematical modeling and computer simulation in materials technologies", Vol. 1, pp. 1–178 – 1–181. Ariel, Israel
662. English JJ (1961) Binary and ternary phase diagrams of columbium, molybdenum, tantalum and tungsten. Report DMIC-152, Contract AF-33(616)-7747, pp. 1–226. Defence Metals Information Center, Battelle Memorial Institute, Columbus, Ohio
663. Velikanova TYa, Bondar AA, Dovbenko OI (2002) Melting diagram for the Cr – Nb – C system in the (Cr) – (Nb) – (NbC) region. Powder Metall Met Ceram 41(11–12):620–626
664. FactSage (2011) Data from Tdnucl – Thermodata nuclear database. Collection of phase diagrams. http://www.crct.polymtl.ca/fact/phase_diagram.php?file=C-O.jpg&dir=TDnucl. Accessed 18 May 2011
665. Boettinger WJ, Peperezko JH, Frankwicz PS (1992) Application of ternary phase diagrams to the development of $MoSi_2$-based materials. Mater Sci Eng A 155(1):33–44
666. Diudea MV (2010) Diamond D_5, a novel allotrope of carbon. Studia Universitatis Babes-Bolyai Chemia (4):11–17

667. Diudea MV, Nagy CL, Ilic A (2011) Diamond D_5, a novel class of carbon allotropes. In: Putz MV (ed) Carbon bonding and structures: advances in physics and chemistry, pp. 273–289. Springer, Dordrecht, Heidelberg
668. Wang Z, Zhao Y, Tait K, Liao X, Schiferl D, Zha C, Downs RT, Qian J, Zhu Y, Shen T (2004) A quenchable superhard carbon phase synthesized by cold compression of carbon nanotubes. Proc Nat Acad Sci USA 101(38):13699–13702
669. Karfunkel HR, Dressler T (1992) New hypothetical carbon allotropes of remarkable stability estimated by modified neglect of diatomic overlap solid-state self-consistent field computations. J Am Chem Soc 114(7):2285–2288
670. Bucknum MJ, Castro EA (2006) Hexagonite: a hypothetical organic zeolite. J Math Chem 39(3–4):611–628
671. Bucknum MJ, Castro EA (2011) High pressure synthesis of the carbon allotrope hexagonite with carbon nanotubes in a diamond anvil cell. In: Putz MV (ed) Carbon bonding and structures: advances in physics and chemistry, pp. 79–93. Springer, Dordrecht, Heidelberg
672. Balaban AT, Klein DJ, Folden CA (1994) Diamond-graphite hybrids. Chem Phys Lett 217(3):266–270
673. Bucknum MJ, Hoffmann R (1994) A hypothetical dense 3,4-connected carbon net and related B_2C and CN_2 nets built from 1,4-cyclohexadienoid units. J Am Chem Soc 116(25):11456–11464
674. Bucknum MJ, Stamatin I, Castro EA (2005) A chemically intuitive proposal for the structure of n-diamond. Mol Phys 103(20)2707–2715
675. Bucknum MJ, Pickard CJ, Stamatin I, Castro EA (2006) On the structure of i-carbon. J Theoret Comput Chem 5(2):175–185
676. Seifert G, Kuc A, Heine T (2010) Hexagon preserving carbon nanofoams. In: Colombo L, Fasolino A (eds) Computer-based modeling of novel carbon systems and their properties, pp. 57–77. Springer, Dordrecht, Heidelberg
677. Dahl JE, Liu SG, Carlson RMK (2003) Isolation and structure of higher diamondoids, nanometer-sized diamond molecules. Science 299:96–99
678. Jeitschko W, Nowotny H, Benesovsky F (1964) Die H-phasen Ti_2TlC, Ti_2PbC, Nb_2InC, Nb_2SnC und Ta_2GaC (The H-phases Ti_2TlC, Ti_2PbC, Nb_2InC, Nb_2SnC and Ta_2GaC). Monatsh Chem 95(2):431–435 (in German)
679. Barsoum MW, Ganguly A, Seifert HJ, Aldinger F (2002) The 1300 °C isothermal section in the Nb-Sn-C ternary phase diagram. J Alloys Compd 337:202–207
680. Barsoum MW (2000) The $M_{N+1}AX_N$ phases: a new class of solids. Prog Solid St Chem 28:201–281
681. Barsoum MW (2010) The $M_{n+1}AX_n$ phases and their properties. In: Riedel R, Chen I-W (eds) Ceramics science and technology, Vol. 2 – Properties, pp. 299–347. Wiley-VCH, Weinheim
682. Yamada K, Sawaoka AB (1994) Very small spherical crystals of distorted diamond found in a detonation product of explosive/graphite mixtures and their formation mechanism. Carbon 32(4):665–673
683. Vora H, Moraec TJ (1981) Structural investigation of thin films of diamondlike carbon. J Appl Phys 52(10):6151–6157
684. Bursill LA, Fullerton AL, Bourgeois LN (2001) Size and surface structure of diamond nano-crystals. Int J Modern Phys B 15(31):4087–4102
685. Holland L, Ojha SM (1979) The growth of carbon films with random atomic structure from ion impact damage in a hydrocarbon plasma. Thin Solid Films 58(1):107–116
686. Konyashin I, Zern A, Mayer J, Aldinger F, Babaev V, Khvostov V, Guseva M (2001) A new carbon modification: 'n-diamond' or face-centred cubic carbon. Diamond Relat Mater 10(1):99–102
687. Palatnik LS, Guseva MB, Babaev VG, Savchenko NF, Falko II (1984) γ carbon. Sov Phys JETP 60:520–522

688. Hirai H, Kondo K-I (1991) Modified phases of diamond formed under shock compression and rapid quenching. Science 253:772–774
689. Farr JD (1968) Phase diagrams of selected refractory compounds. In: Hausner HH, Bowman MG (eds) Fundamentals of refractory compounds, pp. 33–48. Plenum Press, New York
690. Nowotny H, Rogl P (1977) Ternary metal borides. In: Matkovich VI (ed) Boron and refractory borides, pp. 413–438. Springer, Berlin, Heidelberg, New York
691. Ma X, Li C, Du Z, Zhang W (2004) Thermodynamic assessment of the Ti-B system. J Alloys Compd 370:149–158
692. Remschnig K, Le Bihan T, Noel H, Rogl P (1992) Structural chemistry and magnetic behaviour of binary uranium silicides. J Solid State Chem 97:391–399
693. Bowman AL, Arnold GP, Krikorian NH, Zachariasen WH (1971) The crystal structure of U_2IrC_2. Acta Crystallogr B 27:1067–1068
694. Enyashin AN, Ivanovskii AL (2011) Graphene allotropes. Phys Status Solidi B 248(8):1879–1883
695. Appelhans DJ, Lin Z, Lusk MT (2010) Two-dimensional carbon semiconductor: density functional theory calculations. Phys Rev B 82(7):073410
696. Appelhans DJ, Carr LD, Lusk MT (2010) Embedded ribbons of graphene allotropes: an extended defect perspective. New J Phys 12:1250006
697. Enyashin AN, Ivanovskii AL (2007) New self-intercalated C_{28}, Ti@C_{28} and Zn@C_{28} hyperdiamonds: crystal structure and elastic and electronic properties. JETP Letters 86(8):537–542
698. Miura K, Tsuda D, Itamura N, Sasaki N (2007) Superlubricity of fullerene intercalated graphite composite. Japan J Appl Phys 46(8A):5269–5274
699. Skrzypek M, Gburski Z (2002) Fullerene cluster between graphite walls – computer simulation. Europhys Lett 59(2):305–310
700. FactSage (2012) Data from Tdnucl – Thermodata nuclear database. Collection of phase diagrams. http://www.crct.polymtl.ca/fact/phase_diagram.php?file=C-Mg.jpg&dir=TDnucl. Accessed 28 August 2012
701. FactSage (2012) Data from Tdnucl – Thermodata nuclear database. Collection of phase diagrams. http://www.crct.polymtl.ca/fact/phase_diagram.php?file=C-Ca.jpg&dir=TDnucl . Accessed 28 August 2012
702. FactSage (2012) Data from Tdnucl – Thermodata nuclear database. Collection of phase diagrams. http://www.crct.polymtl.ca/fact/phase_diagram.php?file=C-Sr.jpg&dir=TDnucl. Accessed 28 August 2012
703. FactSage (2012) Data from Tdnucl – Thermodata nuclear database. Collection of phase diagrams. http://www.crct.polymtl.ca/fact/phase_diagram.php?file=Ba-C.jpg&dir=TDnucl . Accessed 28 August 2012
704. FactSage (2012) Data from Tdnucl – Thermodata nuclear database. Collection of phase diagrams. http://www.crct.polymtl.ca/fact/phase_diagram.php?file=C-In.jpg&dir=TDnucl. Accessed 9 November 2012
705. Khaenko BV, Prilutskii EV, Mikhalik AA, Karpets MV (1995) Formation of a new phase upon heating of the products of interaction of SiC with SiO_2. Powder Metall Met Ceram 34(9–10):513–514
706. Guo LB, Wang YL, Song F, He F, Huang Y, Yan LH, Wan YZ (2007) Formation and characterization of Si_5C_3 type silicon carbide by carbon ion implantation with a MEVVA ion source. Mater Lett 61(19–20):4083–4085
707. Bucknum MJ, Ienco A, Castro EA (2005) Electronic structure and bulk modulus of silicon dicarbide: a glitter phase. J Molec Struct 716:73–78
708. Andrew RC, Braun M, Chetty N (2012) A theoretical investigation of the stability of crystalline silicon dicarbide. Comput Mater Sci 55:186–191
709. Olesinski RW, Abbaschian GJ (1984) The C-Ge (carbon-germanium) system. Bull Alloy Phase Diagrams 5(5):484–486

710. Fromm E, Gebhardt, E (1976) Gase und Kohlenstoff in Metallen (Gases and carbon in metals). Springer, Berlin (in German)
711. FactSage (2007) Data from SGTE 2007 alloy database. Collection of phase diagrams. http://www.crct.polymtl.ca/fact/phase_diagram.php?file=C-N.jpg&dir=SGTE2007. Accessed 24 November 2012
712. Thomas A, Fischer A, Goettmann F, Antonietti M, Muller J-O, Schlogl R, Carlsson JM (2008) Graphitic carbon nitride materials: variation of structure and morphology and their use as metal-free catalysts. J Mater Chem 18(41):4893–4908
713. Dante RC, Martin-Ramos P, Correa-Guimaraes A, Martin-Gil J (2011) Synthesis of graphitic carbon nitride by reaction of melamine and uric acid. Mater Chem Phys 130(3):1094–1102
714. Niu C, Lu YZ, Lieber CM (1993) Experimental realization of the covalent solid carbon nitride. Science 261(5119):334–337
715. Yin LW, Li MS, Liu YX, Sui JL, Wang JM (2003) Synthesis of beta carbon nitride nanosized crystal through mechanochemical reaction. J Phys Condens Matter 15(2):309–314
716. Yin LW, Bando Y, Li MS, Liu YX, Qi YX (2003) Unique single-crystalline beta carbon nitride nanorods. Adv Mater 15(21):1840–1844
717. Hummelen JC, Knight B, Pavlovich J, Gonzales R, Wudl F (1995) Isolation of the heterofullerene $C_{59}N$ as its dimer $(C_{59}N)_2$. Science 269(5230):1554–1556
718. FactSage (2007) Data from SGTE 2007 alloy database. Collection of phase diagrams. http://www.crct.polymtl.ca/fact/phase_diagram.php?file=C-P.jpg&dir=SGTE2007. Accessed 24 November 2012
719. De Avillez RR, Grujicic M, Furtado HS (1989) A computer calculation of the niobium-carbon phase diagram. Calphad 13(1):45–51
720. Wiesenberger H, Lengauer W, Ettmayer P (1998) Reactive diffusion and phase equilibria in the V-C, Nb-C, Ta-C and Ta-N systems. Acta Mater 46(2):651–666
721. Kublii VZ, Velikanova TYa (2004) Ordering in the carbide W_2C and phase equilibria in the tungsten-carbon system in the region of its existence. Powder Metall Met Ceram 43(11–12):630–644
722. Morris RA, Wang B, Matson LE, Thompson GB (2012) Microstructural formations and phase transformation pathways in hot isostatically pressed tantalum carbides. Acta Mater 60:139–148
723. Demyashev GM (2010) Review: transition metal-based nanolamellar phases. Prog Mater Sci 55:629–674
724. Andrievski RA (2012) Micro- and nanosized boron carbide: synthesis, structure and properties. Russ Chem Rev 81(6):549–559
725. Samsonov GV, Serebryakova TI, Neronov VA (1975) Boridy (Borides). Atomizdat, Moscow (in Russian)
726. Rogl P, Schuster JC (1992) Phase diagrams of ternary boron nitride and silicon nitride systems. ASM International, Materials Park, Ohio
727. Markovskii LYa, Bezruk NT, Berkova GE (1971) Ob ustoichivosti boridov nikelya i kobalta po otnosheniyu k uglerodu (On the stability of nickel and cobalt borides with respect to carbon). Izv AN SSSR Neorg Mater 7(1):56–58 (in Russian)
728. Szillat H, Majewski P, Aldinger F (1997) Phase equilibria in the system Y-Ni-B-C. J Alloys Compd 261(1–2):242–249
729. Kudin VG, Makara VA (2004) On the thermodynamic properties of melts and phase equilibria in the Ni-B-C system. Russ Metall (5):436–439
730. Mazumdar C, Nagarajan R (2005) Quaternary borocarbides – a new class of superconductors and materials. Current Sci 88(1):83–95
731. Li W-J, Tu R, Goto T (2005) Preparation of TiB_2-SiC eutectic composite by an arc-melted method and its characterization. Mater Trans 46(11):2504–2508
732. Li W-J, Tu R, Goto T (2005) Preparation of B_4C-TiB_2-SiC ternary eutectic composites by a floating zone method and their properties. Mater Trans 46(9):2067–2072

733. Li W-J, Tu R, Goto T (2006) Preparation of TiC-TiB_2-SiC ternary eutectic composites by an arc-melting and their characterizations. Mater Trans 47(4):1193–1197
734. Zakaryan DA, Kartuzov VV, Khachatryan (2009) Pseudopotential method for calculating the eutectic temperature and concentration of the components of the B_4C-TiB_2, TiB_2-SiC and B_4C-SiC systems. Powder Metall Met Ceram 48(9–10):588–594
735. Saikia N, Deka RC (2012) First principles study on the boron-nitrogen domains segregated within (5,5) and (8,0) single-wall carbon nanotubes: formation energy, electronic structure and reactivity. Comput Theoret Chem 996:11–20
736. Parthe E, Jeitschko W, Sadagopan V (1965) A neutron diffraction study of the Nowotny phase $Mo_{4.8}Si_3C_{0.6}$. Acta Crystallogr 19:1031–1037
737. Guiot JM (1966) Contribution a l'étude des cermets a base de SiC. Etude du système Mo-SiC. (Contribution to the study of SiC cermets. Study of SiC-Mo system.) Silic Ind 31:363–367 (in French)
738. Rokhlin L, Lysova E (2010) Carbon – molybdenum – silicon system. In: Effenberg G, Ilyenko S (eds) Ternary alloy systems. Subvol. E, Part 2, pp. 444–462. Springer, Berlin, Heidelberg
739. Cacciamani G, Riani P (2010) Carbon – niobium – silicon system. In: Effenberg G, Ilyenko S (eds) Ternary alloy systems. Subvol. E, Part 2, pp. 560–566. Springer, Berlin, Heidelberg
740. Katsura M, Sano T (1966) The uranium-carbon-nitrogen system. J Nucl Sci Technol 3(5):194–199
741. Cordfunke EHP, Ouweltjes W (1979) Investigations on uranium carbonitrides. II. Phase relationships. J Nucl Mater 79(2):271–276
742. Perrot P (2010) Carbon – nitrogen – uranium system. In: Effenberg G, Ilyenko S (eds) Ternary alloy systems. Subvol. E, Part 2, pp. 551–559. Springer, Berlin, Heidelberg
743. Besmann TM, Shin D, Lindemer TB (2012) Uranium nitride as LWR TRISO fuel: thermodynamic modelling of U-C-N. J Nucl Mater 427:162–168
744. Eklund P, Beckers M, Jansson U, Hogberg H, Hultman L (2010) The $M_{n+1}AX_n$ phases: materials science and thin-film processing. Thin Solid Films 518:1851–1878
745. Sun ZM (2011) Progress in research and development on MAX phases: a family of layered ternary compounds. Int Mater Rev 56(3):143–166
746. Lin ZJ, Li MS, Zhou YC (2008) High-temperature corrosion mechanism of layered ternary ceramics. In: Gao W, Li Z (eds) Developments in high-temperature corrosion and protection of materials. pp. 255–289, Woodhead, CRC Press, Boca Raton, Boston
747. Lukas HL (2010) Carbon – tantalum – titanium system. In: Effenberg G, Ilyenko S (eds) Ternary alloy systems. Subvol. E, Part 2, pp. 619–631. Springer, Berlin, Heidelberg
748. Savitsky EM, Efimov YV, Mikhailov BP, Moroz EA (1979) Vzaimodeistvie silitsidov, germanidov i drugikh faz struktury A15 s uglerodom (Reaction of silicides, germanides and other phases of the A15 structure type with carbon). Izv AN SSSR Neorg Mater 15(4):658–662 (in Russian)
749. Ordanyan SS, Vikhman SV, Unrod VI (2000) On the interaction in SiC-M′(IV-V)C systems. Russ J Appl Chem 73(12):2009–2012
750. Rokhlin LL, Dobatkina TV (2010) Carbon – silicon – vanadium system. In: Effenberg G, Ilyenko S (eds) Ternary alloy systems. Subvol. E, Part 2, pp. 606–618. Springer, Berlin, Heidelberg
751. Besson J, Blum PL, Morlevat JP (1965) Le diagramme ternaire U-UO_2-UOC (The ternary diagram U-UO_2-UOC). Compt Rend Acad Sci Paris 260:3390–3392 (in French)
752. Blum PL, Morlevat JP (1966) Le diagramme ternaire U-C-O (The ternary diagram U-C-O). Rev Hautes Temp Refract 3:253–254 (in French)
753. Perrot P (2010) Carbon – oxygen – uranium system. In: Effenberg G, Ilyenko S (eds) Ternary alloy systems. Subvol. E, Part 2, pp. 595–605. Springer, Berlin, Heidelberg
754. Fiedler M-L, Stadelmaier HH (1975) The ternary system Ni-W-C. Z Metallkd 66(9):402–404

755. Gabriel A, Pastor H, Deo DM, Basu S, Allibert CH (1986) New experimental data in the C-Fe-W, C-Co-W, C-Ni-W, C-Fe-Ni-W and C-Co-Ni-W cemented carbides systems and their application to sintering conditions. Int J Refract Met Hard Mater 5(4):215–221
756. Bochvar N, Rokhlin L (2010) Carbon – nickel – tungsten system. In: Effenberg G, Ilyenko S (eds) Ternary alloy systems. Subvol. E, Part 2, pp. 579–594. Springer, Berlin, Heidelberg
757. Raghavan V (2007) The C-Co-Fe-Ni-W (carbon-cobalt-iron-nickel-tungsten) system. J Phase Equilib Diffus 28(3):284–285
758. Perrot P, Lebrun N (2010) Carbon – niobium – tungsten system. In: Effenberg G, Ilyenko S (eds) Ternary alloy systems. Subvol. E, Part 2, pp. 567–578. Springer, Berlin, Heidelberg
759. Austin AE, Gerds AF (1958) The uranium-nitrogen-carbon system. Report BMI-1272-UC-25 (TIDD-4500), Contract No. W-7405-eng-92, pp. 1–18. Battelle Memorial Institute, Columbus, Ohio
760. Kandori T, Kamiya N, Kamigato O (1975) Solid solubility of SiC in β-Si_3N_4. Jpn J Appl Phys 14(1):137–138
761. Seifert HJ, Peng J, Lukas HL, Aldinger F (2001) Phase equilibria and thermal analysis of Si-C-N ceramics. J Alloys Compd 320(2):251–261
762. Seifert HJ, Aldinger F (2002) Phase equilibria in the Si-B-C-N System. Struct Bonding 101:1–58
763. Tomashik V (2010) Carbon – nitrogen – silicon system. In: Effenberg G, Ilyenko S (eds) Ternary alloy systems. Subvol. E, Part 2, pp. 531–550. Springer, Berlin, Heidelberg
764. Gorshkova LV, Telegus VS, Shamrai FI, Kuzma YB (1973) System molybdenum-tungsten-carbon. Powder Metall Met Ceram 12(3):237–239
765. Gustafson P (1988) Thermodynamic evaluation of the C-Mo-W system. Z Metallkd 79(7):397–402
766. Rokhlin L, Dobatkina T (2010) Carbon – molybdenum – tungsten system. In: Effenberg G, Ilyenko S (eds) Ternary alloy systems. Subvol. E, Part 2, pp. 516–530. Springer, Berlin, Heidelberg
767. Zakharov AM, Novikov II, Parshikov VG (1970) Troinaya sistema Mo-Ti-C (The Mo-Ti-C ternary system). Izv Vyssh Uchebn Zaved Tsvetn Metall 13(6):106–112 (in Russian)
768. Kroupa A, Watson A (2010) Carbon – molybdenum – titanium system. In: Effenberg G, Ilyenko S (eds) Ternary alloy systems. Subvol. E, Part 2, pp. 463–490. Springer, Berlin, Heidelberg
769. Lyakishev NP, Gasik MI, Polyakov OI (1991) Thermodynamic investigation of the interparticle interactions in the Me(Ti,V,Cr,Mn,Fe,Co,Ni)-Si-C systems as theoretical prerequisites for improving the technology of smelting bulk silicon ferroalloys. Russ Metall (1):1–9
770. Lebrun N, Perrot P (2010) Carbon – manganese – silicon system. In: Effenberg G, Ilyenko S (eds) Ternary alloy systems. Subvol. E, Part 2, pp. 433–443. Springer, Berlin, Heidelberg
771. Cacciamani G, Riani P (2010) Carbon – hafnium – silicon system. In: Effenberg G, Ilyenko S (eds) Ternary alloy systems. Subvol. E, Part 2, pp. 429–432. Springer, Berlin, Heidelberg
772. Ordanyan SS, Kraskovskaya AA, Avgustinnik AI (1966) Fazovaya diagramma sistemy HfC-Mo (Phase diagram of the HfC-Mo). Izv AN SSSR Neorg Mater 2 (2):299–302 (in Russian)
773. Eremenko VN, Velikanova TY, Shabanova SV, Artyukh LV (1973) Continuous series of solid solutions of carbides with NaCl structure in the ternary systems Mo(W)-$Me^{IV,V}$-C. Powder Metall Met Ceram 12(11):909–912
774. Rokhlin L, Kolchugina N, Dobatkina T, Semenova E (2010) Carbon – hafnium – molybdenum system. In: Effenberg G, Ilyenko S (eds) Ternary alloy systems. Subvol. E, Part 2, pp. 409–428. Springer, Berlin, Heidelberg

775. Fedorov TF, Kuzma YuB (1965) Phase equilibria in the system zirconium-chromium-carbon. Powder Metall Met Ceram 4(3):234–237
776. Eremenko VN, Velikanova TYa, Sleptsov SV, Bondar AA (1992) Fazovye ravnovesiya pri subsolidusnykh temperaturakh i skhema kristallizatsii splavov sistemy Cr-Zr-C (Phase equilibria at subsolidus temperatures and solidification behaviour of Cr-Zr-C alloys). Izv AN SSSR Metally (5):144–150 (in Russian)
777. Ivanchenko VG, Pogorelaya VV (2001) Structure formation in eutectic alloys of chromium with carbide $Cr_{23}C_6$ and with carbides of IVa-group metals. Met Phys Adv Techn 19(3):869–874
778. Ivanchenko VG (2001) Phase equilibria and formation of structure and properties in the chromium alloys with interstitial phases. Met Phys Adv Techn 19(3):669–710
779. Ivanchenko V, Pryadko T (2010) Carbon – chromium – zirconium system. In: Effenberg G, Ilyenko S (eds) Ternary alloy systems. Subvol. E, Part 2, pp. 397–408. Springer, Berlin, Heidelberg
780. Velikanova TYa, Eremenko VN (1988) Relationships governing phase equilibria in refractory carbide-bearing systems of transition metals. Powder Metall Met Ceram 27(2):145–149
781. Watson A, Kroupa A (2010) Carbon – chromium – tungsten system. In: Effenberg G, Ilyenko S (eds) Ternary alloy systems. Subvol. E, Part 2, pp. 379–396. Springer, Berlin, Heidelberg
782. Rassaerts H, Kieffer R, Nowotny H (1965) Die V-Cr-C Dreistoffsystem (The V-Cr-C ternary system). Monatsh Chem 96:1536–1542 (in German)
783. Kieffer R, Rassaerts H (1966) Am System V-Cr-C und Verwendung von Vanadium und Chromcarbide in Hartmetallen. I (On system V-Cr-C and use of vanadium and chromium carbides in hard metals. I) Metall 20(7):691–695 (in German)
784. Fedorov TF, Popova NM, Gorshkova LV, Skolozdra RV, Kuzma YuB (1968) Phase equilibria in the systems V-Cr-C, Nb-Cr-C and Ta-Cr-C. Powder Metall Met Ceram 7(3):193–197
785. Steurer W, Rogl P, Boller H (1980) A neutron powder diffraction study of $(V,Cr)_3C_{2-x}$. J Less-Common Met 76:145–151
786. Nowotny H, Rogl P, Schuster JC (1982) Structural chemistry of complex carbides and related compounds. J Solid State Chem 44:126–133
787. Velikanova T, Turchanin M, Pavlyuchkov D, Tomashuk V (2010) Carbon – chromium – vanadium system. In: Effenberg G, Ilyenko S (eds) Ternary alloy systems. Subvol. E, Part 2, pp. 369–378. Springer, Berlin, Heidelberg
788. Booker PH, Kunrath AO, Hepworth MT (1997) Experimental determination of the ternary diagram of the Ti-Cr-C system. Acta Mater 45(4):1625–1632
789. Bandyopadhyay D, Sharma RC, Chakraborti N (1999) The Ti-Cr-C (titanium-chromium-carbon) system. J Phase Equilib 20(3):325–331
790. Schuster JC, Du Y (1999) Thermodynamic description of the system Ti-Cr-C. Calphad 23(3–4):393–408
791. Ivanchenko V, Pryadko T (2010) Carbon – chromium – titanium system. In: Effenberg G, Ilyenko S (eds) Ternary alloy systems. Subvol. E, Part 2, pp. 348–368. Springer, Berlin, Heidelberg
792. Borisova AL, Borisov YuS, Shvedova LK, Kocherzhinskii YuA, Nechiporenko VI, Vasilev MA, Kostyuchenko VG (1979) Reactions in the Cr-SiC system under conditions of ordinary and plasma heating. Powder Metall Met Ceram 18(10):722–728
793. Lebrun N, Perrot P, Serbruyns A, Tedenac J-C (2010) Carbon – chromium – silicon system. In: Effenberg G, Ilyenko S (eds) Ternary alloy systems. Subvol. E, Part 2, pp. 330–347. Springer, Berlin, Heidelberg
794. Eremenko VN, Velikanova TYa, Bondar AA (1990) Zakonomernosti fazovykh ravnovesii v troinyh sistemakh metallov VI gruppy s uglerodom (Regularities of phase equilibria in the ternary systems of the VI group metals with carbon) In: Eremenko VN (ed) Fazovye

ravnovesiya, struktura i svoistva splavov (The phase equilibria, structure and properties of alloys). Naukova Dumka, Kyiv pp. 4–17 (in Russian)
795. Bondar A, Dovbenko O, Ivanchenko V, Kozlov A (2010) Carbon – chromium – molybdenum system. In: Effenberg G, Ilyenko S (eds) Ternary alloy systems. Subvol. E, Part 2, pp. 290–307. Springer, Berlin, Heidelberg
796. Uhrenius B, Carlsson B, Franzen T (1976) A study of the Co-W-C system at liquidus temperatures. Scand J Met 5(2):49–56
797. Uhrenius B (1991) Contribution to the knowledge of phase equilibria in tungsten-carbon based system. Scand J Met 20(1):93–98
798. Kruse O, Jansson B, Frisk K (2001) Experimental study of invariant equilibria in the Co-W-C and Co-W-C-Me (Me = Ti, Ta, Nb) systems. J Phase Equilib 22:552–555
799. Markstrom A, Sundman B, Frisk K (2005) A revised thermodynamic description of the Co-W-C system. J Phase Equilib Diffus 26(2):152–160
800. Bondar A, Bochvar N, Dobatkina T, Krendelsberger N (2010) Carbon – cobalt – tungsten system. In: Effenberg G, Ilyenko S (eds) Ternary alloy systems. Subvol. E, Part 2, pp. 249–289. Springer, Berlin, Heidelberg
801. Hachisuka T (1968) Preparation of TaC-WC solid solutions and their properties. J Jpn Soc Powder Metall 15:110–117 (in Japanese)
802. Eremenko VN, Velikanova TYa (1973) Stroenie diagramm sostoyaniya troinykh sistem (Mo, W) – (Ti, Zr, Hf, V, Nb, Ta) – C (Structure of phase diagrams of the (Mo, W) – (Ti, Zr, Hf, V, Nb, Ta) – C ternary systems). In: Ageev VN (ed) Obshchie zakonomernosti stroeniya diagramm sostoyaniya metallicheskikh sistem (The general regularities of the phase diagrams structures of metal systems). Nauka, Moscow, pp. 49–52 (in Russian)
803. Frisk K (1999) A thermodynamic analysis of the Ta-W-C and the Ta-W-C-N systems. Z Metallkd 90(9):704–711
804. Bochvar N, Rokhlin L, Lysova E (2010) Carbon – tantalum – tungsten system. In: Effenberg G, Ilyenko S (eds) Ternary alloy systems. Subvol. E, Part 3, pp. 1–17. Springer, Berlin, Heidelberg
805. Ogorodnikov VV, Ogorodnikova AA (1982) Calculation of the phase diagrams for pseudo-binary systems of cubic transition metal monocarbides. Russ J Phys Chem 56(11):1749–1751
806. Gusev AI (2000) Order-disorder transformations and phase equilibria in strongly nonstoichiometric compounds. Phys Uspekhi 43(1):1–37
807. Dobatkina T, Bochvar N (2010) Carbon – tantalum – zirconium system. In: Effenberg G, Ilyenko S (eds) Ternary alloy systems. Subvol. E, Part 3, pp. 18–30. Springer, Berlin, Heidelberg
808. Shveikin GP (1962) Reaction of tungsten carbide with oxides of refractory metals in a vacuum. Powder Metall Met Ceram 1(6):454–457
809. Kuzma YuB, Lakh VI, Markiv Vya, Stadnyk BI, Gladyshevskii EI (1963) X-ray diffraction study of the system tugsten-rhenium-carbon. Powder Metall Met Ceram 2(4):286–272
810. Eremenko VN, Tretyachenko LA (1964) The isothermal section of the system Ti-V-C. Powder Metall Met Ceram 3(6):464–469
811. Borusevich LK, Gladyshevskii EI (1964) X-ray diffraction study of alloys in the system Mo-Re-C. Powder Metall Met Ceram 3(6):460–463
812. Allinson JD, Riviere JC (1965) High temperature short-term compatibility of some refractory metals with the thermoionic fuel UC-ZrC. J Nucl Mater 17:97–110
813. Fedorov TF, Gladyshevskii EI (1965) Phase equilibria in ternary systems of transition metals of groups IV and V and carbon. Powder Metall Met Ceram 4(1):27–29
814. Matyushenko NN, Rozen AA, Pugachev NS (1966) Triangulation of the system C-Si-Be. Powder Metall Met Ceram 5(4):310–312
815. Tretyachenko LA, Eremenko VN (1966) Structure and certain properties of alloys of sections TiC-$VC_{0.90}$, TiC-V_2C, TiC-V and in the region TiC-$VC_{0.90}$-C of the ternary system Ti-V-C. Powder Metall Met Ceram 5(7):581–584

816. Voroshilov YuV, Gorshkova LV, Popova AM, Fedorov TF (1967) Ternary systems Ti-Zr-C and Ti-Hf-C. Powder Metall Met Ceram 6(5):403–405
817. Voroshilov YuV (1968) Concerning ternary systems of titanium-zirconium-carbon and titanium-hafnium-carbon. Powder Metall Met Ceram 7(8):669
818. Gorshkova LV, Fedorov TF, Kuzma YuB (1967) Ternary systems niobium-rhenium-carbon and tantalum-rhenium-carbon. Powder Metall Met Ceram 6(4):287–290
819. Evtushok TM, Burykina AL (1969) Interaction of graphite and pyrographite with titanium, niobium, molybdenum and tungsten disilicides. Powder Metall Met Ceram 8(7):581–586
820. Gorshkova LV, Voroshilov YuV, Fedorov TF (1969) Study of the ternary system zirconium-rhenium-carbon. Powder Metall Met Ceram 8(2):146–148
821. Eremenko VN, Velikanova TYa (1969) Phase equilibria in the Mo – TiC – Ti region of the ternary system Mo – Ti – C. Character of solidification of alloys and projection of the solidus surface. Part I. Powder Metall Met Ceram 8(11):931–936
822. Kuroda Y, Tanaka K, Suzuki M, Akimoto Y (1970) Compatibility of U(N,C) with potential cladding materials. J Nucl Mater 34:174–181
823. Eremenko VN, Velikanova TYa (1970) Phase equilibria in the Mo – TiC – Ti region of the ternary system Mo – Ti – C. Part II. Powder Metall Met Ceram 9(9):744–747
824. Williams AJ, Briggs DC (1970) Ageing in niobium-rich niobium-hafnium-carbon alloys. J Less-Common Met 21:255–273
825. Samsonov GV, Antonova MM, Morozov VV (1970) Ternary systems Me-C-H and Me-N-H. Powder Metall Met Ceram 9(4):318–327
826. Khodosov EF, Andrievskii RA (1967) Studying nuclear magnetic resonance spectra of zirconium and yttrium hydrides. Powder Metall Met Ceram 6(8):649–653
827. Velikanova TYa, Eremenko VN (1974) Phase equilibria in the ternary systems formed by molybdenum and tungsten with the groups IV and V transition metals and carbon. Powder Metall Met Ceram 13(4):293–297
828. Eremenko VN, Shabanova SV, Velikanova TYa, Petrenko LA (1975) Structure of alloys and phase equilibria of the system Hf-Mo-C. I. Projection of the solidus surface of the partial system Mo-HfC-Hf. Powder Metall Met Ceram 14(7):555–561
829. Borisova AL, Martsenyuk IS (1975) Reactions of boron and aluminum nitrides and materials based on them with refractory metals. Powder Metall Met Ceram 14(10):822–826
830. Ivchenko VI, Lesnaya MI, Nemchenko VF, Kosolapova TYa (1976) Some physical properties of ternary compounds in the system Ti – Al – C. Powder Metall Met Ceram 15(5):367–369
831. Gorshkova LV (1976) Joint solubility of carbon and zirconium in molybdenum-tungsten solid solutions. Powder Metall Met Ceram 15(3):215–216
832. Eremenko VN, Shabanova SV, Velikanova TYa (1977) Structure of alloys and the phase equilibrium diagram of the system Hf-Mo-C. V. Isothermal section of the system Hf-Mo-C at 1700 °C. Powder Metall Met Ceram 16(9):712–717
833. Stark WA, Jr (1978) Cesium solubility, diffusion and permeation in zirconium carbide. J Nucl Mater 73:169–179
834. Shurin AK, Razumova NA (1979) Quasiternary system Fe-TiC-TiB_2. Powder Metall Met Ceram 18(12):903–905
835. Kosterova NV, Ordanyan SS, Neshpor VS, Ostrovskii EK (1980) Thermoionic properties of cermets of eutectic compositions in Me(IV) – (C,B) – (Mo,Re,W) systems. Powder Metall Met Ceram 19(1):61–66
836. Stepanenko EK, Dogadaeva IM, Ordanyan SS (1982) Reactions in the NbC-$NbSi_2$ and NbB_2-$NbSi_2$ systems. Powder Metall Met Ceram 21(7):568–570
837. Eremenko VN, Velikanova TYa (1983) Use of the phase diagrams of ternary transition metal systems containing carbides in the development of heat-resisting hard alloys. Powder Metall Met Ceram 22(12):1010–1021
838. Ordanyan SS, Stepanenko EK, Dmitriev AI, Shchemeleva MV (1986) Interaction in the B_4C-TiB_2 system. Sov J Superhard Mater 8(5):34–37

839. Shurin AK, Dmitrieva GP, Razumova NA, Khandros EL (1987) Phase diagram of the Ni-ZrC-HfC. Powder Metall Met Ceram 26(9):754–757
840. Eremenko VN, Velikanova TYa, Bondar AA (1989) Phase equilibria at the solidus surface of the equilibrium diagram of ternary systems of technetium with carbon and d-transition metals of groups III-VII. Powder Metall Met Ceram 28(11):868–873
841. Lee B-J (1992) On the stability of Cr carbides. Calphad 16(2):121–149
842. Hillert M, Qiu C (1992) A reassessment of the Fe-Cr-Mo-C system. J Phase Equilib 13(5):512–521
843. Lee B-J, Lee DN (1992) A thermodynamic evaluation of the Fe-Cr-V-C system. J Phase Equilib 13(4):349–364
844. Sheftel EN, Bannykh OA (1993–1994) Niobium-base alloys. Int J Refract Met Hard Mater 12:303–314
845. Raghavan V (1993) The C-Fe-V (carbon-iron-vanadium) system. J Phase Equilib 14(5):622–623
846. Raghavan V (1994) The C-Fe-Mo (carbon-iron-molybdenum) system. J Phase Equilib 15(4):425–427
847. Raghavan V (1994) The C-Fe-W (carbon-iron-tungsten) system. J Phase Equilib 15(4):429–430
848. Uhrenius B, Forsen K, Haglund B-O, Andersson I (1995) Phase equilibria and phase diagrams in carbide systems. J Phase Equilib 16(5):430–440
849. Alekseeva ZM (1992) Phase equilibria in the U-Si-C system. J Nucl Mater 186:294–298
850. Itkin VP (1996) The C-Te (carbon-tellurium) system. J Phase Equilib 17(2):131
851. Barabash OM, Legkaya TN, Petrushin NV, Cherkasova EV (1997) Effect of aluminum on the parameters of eutectic transformation L $\leftrightarrow \gamma$ + Mo_2C in the Ni-Mo-Al-C quaternary system. Powder Metall Met Ceram 36(11–12):664–667
852. Artyukh LV, Belous OA, Bondar AA, Burka MP, Velikanova TYa, Tsyganenko NI (1997) Structure and properties of multicomponent eutectic alloys based on chromium and titanium carbide. Powder Metall Met Ceram 36(1–2):15–23
853. Hugosson HW, Nordstrom L, Jansson U, Johansson B, Eriksson O (1999) Theoretical studies of substitutional impurities in molybdenum carbide. Phys Rev B 60(22):15123–15130
854. Shvedova LK (1999) Contact reaction, structure and phase formation in the chromium – silicon carbide system. Powder Metall Met Ceram 38(9–10):477–481
855. Walter J, Boonchuduang W, Hara S (2000) XPS study on pristine and intercalated tantalum carbosulfide. J Alloys Compd 305:259–263
856. Lisovskii AF (2000) Cemented carbides alloyed with ruthenium, osmium and rhenium. Powder Metall Met Ceram 39(9–10):428–433
857. Khrushchev MS (2000) Kinetics and mechanism of reaction between silicon carbide and silica. Inorg Mater 36(5):462–464
858. Dovbenko OI, Bondar AA, Velikanova TYa, Sleptsov SV (2000) The (Cr) + (NbC) quasibinary eutectic in the Cr-Nb-C system. Powder Metall Met Ceram 39(5–6):256–261
859. Ivanovskii AL, Sabiryanov RF, Skazkin AN, Zhukovskii VM, Shveikin GP (2000) Electronic structure and bonding configuration of the *H*-phases Ti_2MC and Ti_2MN (M = Al,Ga,In). Inorg Mater 36(1):28–31
860. Ivanovskii AL, Gusev AI, Shveikin GP (1996) Kvantovaya khimiya v materialovedenii: troinye karbidy i nitridy perekhodnykh metallov i elementov IIIb, IVb podgrupp (Quantum chemistry in materials science: ternary carbides and nitrides of transition metals and subgroup IIIa, IVa elements). Uralskoe Otdelenie Rossiiskoi Akademii Nauk, Yekaterinburg (in Russian)
861. Ivanovskii AL, Okatov SV, Shveikin GP (2000) Electronic structure of high-temperature ZrO_2C_z. Inorg Mater 36(11):1121–1124
862. Kurdyumov AV, Solozhenko VL, Gubachek M, Borimchuk NI, Zelyavskii VB, Ostrovskaya NF, Yarosh VV (2000) Shock synthesis of ternary diamond-like phases in the B-C-N system. Powder Metall Met Ceram 39(9–10):467–473

863. Sudarikov MV, Zhikharev VM, Lykasov AA (2001) Gibbs energy of formation of cubic NbC_xN_y. Inorg Mater 37(3):243–247
864. Rempel SV, Gusev AI (2001) ZrC segregation to the surface of dilute solid solutions of zirconium carbide in niobium carbide. Inorg Mater 37(10):1024–1029
865. Velikanova TYa, Bondar AA, Dovbenko OI (2002) The Cr-Ta-C melting diagram in the (Cr)-(Ta)-(TaC) region. Powder Metall Met Ceram 41(7–8):400–406
866. leksanyan AG, Aghajanyan NN, Dolukhanyan SK, Mnatsakanyan NL, Harutyunyan KhS, Hayrapetyan VS (2002) Thermal-radiation synthesis of zirconium hydridonitrides and carbohydrides. J Alloys Compd 330–332:559–563
867. Golubenko AN, Kosinova ML, Titov AA, Kuznetsov FA (2003) Thermodynamic modelling of BC_xN_y chemical vapour deposition in the B-C-N-H system. Inorg Mater 39(4):362–365
868. Raghavan V (2003) The C-Fe-Nb (carbon-iron-niobium) system. J Phase Equilib 24(1):57–61
869. Raghavan V (2003) The C-Fe-N-Nb (carbon-iron-nitrogen-niobium) system. J Phase Equilib 24(1):73–74
870. Raghavan V (2003) The C-Fe-N-Nb-Ti (carbon-iron-nitrogen-niobium-titanium) system. J Phase Equilib 24(1):77–78
871. Raghavan V (2003) The C-Fe-N-Nb-Ti-V (carbon-iron-nitrogen-niobium-titanium-vanadium) system. J Phase Equilib 24(1):79–81
872. Raghavan V (2003) The C-Fe-N-Ti (carbon-iron-nitrogen-titanium) system. J Phase Equilib 24(1):75–76
873. Raghavan V (2003) The C-Fe-V (carbon-iron-vanadium) system. J Phase Equilib 24(1):67
874. Tan Y, Ma CL, Kasama A, Tanaka R, Mishima Y, Hanada S, Yang J-M (2003) Effect of alloy composition on microstructure and high temperature properties of Nb-Zr-C ternary alloys. Mater Sci Eng A 341:282–288
875. Gusev AI, Rempel SV (2003) X-ray diffraction study of the nanostructure resulting from decomposition of $(ZrC)_{1-x}(NbC)_x$ solid solutions. Inorg Mater 39(1):43–46
876. Dovbenko OI, Bondar AA, Velikanova TYa, Bilous OO, Burka MP, Martseniuk PS, Shapoval TO, Tsyganenko NI (2003) Quasi-binary metal-carbide eutectic of Cr-Ta-C system. Mater Lett 57:2866–2871
877. Paderno V, Paderno Y, Filippov V, Liashchenko A (2004) Directional crystallization of B_4C-NbB_2 and B_4C-MoB_2 eutectic compositions. J Solid State Chem 177:523–528
878. Grigorev ON, Bega ND, Lyashenko VI, Dubovik TV, Panashenko VM, Shcherbina OD (2005) Dependence of the structure of sintered boron carbonitride on the defect level in the starting BN powder. Powder Metall Met Ceram 44(5–6):287–293
879. Enyashin AN, Seifert G, Ivanovskii AL (2005) Calculation of the electronic and thermal properties of C/BN nanotubular heterostructures. Inorg Mater 41(6):595–603
880. Panteleev IB, Vladimirova MA, Ordanyan SS (2005) Synthesis of complex carbonitrides $Ti_{1-x}W_xC_{1-x}N_y$. Powder Metall Met Ceram 44(11–12):573–577
881. Raghavan V (2006) The Al-C-Ta-Ti (aluminum-carbon-tantalum-titanium) system. J Phase Equilib 27(2):169–170
882. Lin ZJ, Zhuo MJ, He LF, Zhou YC, Li MS, Wang JY (2006) Atomic-scale microstructures of $Zr_2Al_3C_4$ and $Zr_3Al_3C_5$. Acta Mater 54:3843–3851
883. Leela-Adisorn U, Choi SM, Matsunaga T, Hashimoto S, Honda S, Hayakawa K, Awaji H, Yamaguchi A (2006) $AlZrC_2$ synthesis. Ceram Int 32:431–439
884. Lipatnikov VN, Gusev AI (2007) Crystal structure and microstructure of disordered and ordered vanadium carbonitrides. Inorg Mater 43(8):827–833
885. Li J, Han J, Meng S, Zhang X, Liang J (2008) Valence bond structure and properties of 4TaC+HfC solid solutions. Xiyou Jinshu Cailiao Yu Gongcheng 37(5):840–843 (in Chinese)
886. Filonenko VP, Khabashesku VN, Davydov VA, Zibrov IP, Agafonov VN (2008) Synthesis of a new cubic phase in the B-C-N system. Inorg Mater 44(4):395–400

887. Du HJ, Li DC, He JL, Yu DL, Xu B, Liu ZY, Wang H-T, Tian YJ (2009) Hardness of α- and β-$Si_{3-n}C_nN_4$ (n = 0, 1, 2, 3) crystals. Diamond Relat Mater 18:72–75
888. Skripov AV, Wu H, Udovic TJ, Huang Q, Hempelmann R, Soloninin AV, Rempel AA, Gusev AI (2009) Hydrogen in nonstoichiometric cubic niobium carbides: neutron vibrational spectroscopy and neutron diffraction studies. J Alloys Compd 478:68–74
889. Zakaryan DA, Kartuzov VV, Khachatryan AV (2009) Pseudopotential method for calculating the eutectic temperature and concentration of the components of the B_4C-TiB_2, TiB_2-SiC and B_4C-SiC systems. Powder Metall Met Ceram 48(9–10):588–594
890. Hong JD, Spear KE, Stubican VS (1979) Directional solidification of SiC-B_4C eutectic: growth and some properties. Mater Res Bull 14(6):775–783
891. Gadzyra NF, Davidchuk NK, Gnesin GG (2009) Structurization of composite ceramics based on stoichiometric silicon carbide during free sintering and hot pressing. Powder Metall Met Ceram 48(5–6):311–315
892. Grigorev ON, Kotenko VA, Shcherbina OD, Bega ND, Dubovik TV, Subbotin VI, Mosina TV, Lychko VV, Berezhinskii IL (2010) Production and properties of impact-resitant composites based on boron carbide and aluminium nitride. Powder Metall Met Ceram 49(3–4):193–200
893. Kar P (2010) Effect of anodization voltage on the formation of phase pure anatase nanotubes with doped carbon. Inorg Mater 46(4):377–382
894. Silvestroni L, Sciti D (2010) Sintering behaviour, microstructure and mechanical properties: a comparison among pressureless sintered ultra-refractory carbides. Adv Mater Sci Eng ID835018:1–11 (doi:10.1155/2010/835018)
895. Medvedeva NI, Novikov DL, Ivanovsky AL, Kuznetsov MV, Freeman AJ (1998) Electronic properties of Ti_3SiC_2-based solid solutions. Phys Rev B 58(24):16042–16050
896. He X, Bai Y, Zhu C, Sun Y, Li M, Barsoum MW (2010) General trends in the structural, electronic and elastic properties of the M_3AlC_2 phases (M = transition metal): a first-principle study. Comput Mater Sci 49:691–698
897. Haddadi K, Bouhemadou A, Louail L, Maamache M (2011) Density functional study of the structural, electronic, elastic and thermodynamic properties of $ACRu_3$ (A = V, Nb and Ta) compounds. Intermetallics 19:476–485
898. Islam MS, Islam AKMA (2011) Structural, elastic, electronic and optical properties of a new layered-ternary Ta_4SiC_3 compound. Phys B 406:275–279
899. Silvestroni L, Bellosi A, Melandri C, Sciti D, Liu JX, Zhang GJ (2011) Microstructure and properties of HfC and TaC-based ceramics obtained by ultrafine powder. J Eur Ceram Soc 31:619–627
900. Velikanova TA, Karpets MV, Agraval PG, Turchanin MA (2011) Phase states of Fe-Mo-C spinning alloys at high temperatures. Powder Metall Met Ceram 49(9–10):606–615
901. Ghebouli MA, Ghebouli B, Bouhemadou A, Fatmi M (2011) Theoretical study of the structural, elastic, electronic and thermal properties of the MAX phase Nb_2SiC. Solid State Comm 151:382–387
902. Zhao Y-W, Wang Y-J, Zhou Y, Peng H-X, Song G-M (2011) Ternary phase $Zr_xCu_yC_z$ in reactively infiltrated ZrC/W composite. J Am Ceram Soc 94(10):3178–3180
903. Shein IR, Ivanovskii AL (2012) Planar nano-block structures $Ti_{n+1}Al_{0.5}C_n$ and $Ti_{n+1}C_n$ (n = 1 and 2) from MAX phases: structural, electronic properties and relative stability from first principles calculations. Superlattices and microstructures 52:147–157
904. Shein IR, Ivanovskii AL (2012) Graphene-like titanium carbides and nitrides $Ti_{n+1}C_n$, $Ti_{n+1}N_n$ (n = 1, 2 and 3) from de-interclated MAX phases: first-principles probing of their structural, electronic properties and relative stability. Comput Mater Sci 65:104–114
905. Yonco RM, Homa MI (1986) The solubility of carbon in low-nitrogen liquid lithium. J Nucl Mater 138:117–122
906. Dalton JT, Potter PE, Shaw JL (1967) Constitutional studies on the ternary system plutonium-molybdenum-carbon, plutonium-silicon-carbon and plutonium-thorium-carbon. In: Kay AE, Waldron HB (eds) Plutonium 1965. Proc. 3rd Int. Conf. on plutonium, London, 1965, pp. 775–805. Institute of Metals, Chapman & Hall, London

907. Okamoto H (1992) The C-Fe (carbon-iron) system. J Phase Equilib 13(5):543–565
908. Shabalin IL, Tomkinson DM, Shabalin LI (2007) High-temperature hot-pressing of titanium carbide – graphite hetero-modulus ceramics. J Eur Ceram Soc 27(5):2171–2181
909. Eissler RL, Van Holde KE (1962) Wettability of coal, graphite and naphthalene as measured by contact angles. Circular 333. Illinois State Geological Survey, Urbana
910. Eustathopoulos N, Nicholas MG, Drevet B (1999) Wettability at high temperatures. Elsevier Science, Oxford
911. Leider HR, Krikorian OH, Young DA (1973) Thermodynamic properties of carbon up to the critical point. Carbon 11:555–563
912. Lassner E, Schubert W-D (1999) Tungsten. Kluwer Academic / Plenum Publishers, New York
913. Guminski C (1993) The C-Hg (carbon-mercury) system. J Phase Equilib 14(2):219–220
914. Guminski C (1989) Selected properties of simple amalgams. J Mater Sci 24:2661–2676
915. Huang W (1997) Thermodynamic properties of the Nb-W-C-N system. Z Metallkd 84:63–68
916. Rosseinsky MJ, Murphy DW, Fleming RM, Tycko R, Ramirez AP, Siegrist T, Dabbagh G, Barrett SE (1992) Structural and electronic properties of sodium-intercalated C_{60}. Nature (London) 356:416–418
917. Ylldirim T, Zhou O, Fischer JE, Bykovetz N, Strongin RA, Cichy MA, Smith AB, Lin CL, Jelinek R (1992) Intercalation of sodium hetero-clusters into the C_{60} lattice. Nature (London) 360:568–571
918. Klöss KH, Hinz Hübner D, Ruschewitz U (2002) On a new modification of Na_2C_2. Z Anorg Allg Chem 628:2701–2704
919. Fleming RM, Rosseinsky MJ, Ramirez AP, Murphy DW, Tully JC, Haddon RC, Siegrist T, Tycko R, Glarum SH, Marsh P, Dabbagh G, Zahurak SM, Makhija AV, Hampton C (1991) Preparation and structure of the alkali-metal fulleride A_4C_{60}. Nature (London) 352:701–703
920. Hemmersbach S, Zibrowius B, Ruschewitz U (1999) Na_2C_2 and K_2C_2: synthesis, crystal structure and spectroscopic properties", Z Anorg Allg Chem 625:1440–1446
921. Kobayashi M, Akahama Y, Kawamura H, Shinohara H, Sato H, Saito Y (1993) Structure sequence and possible superconductivity in potassium-doped fullerene $C_{70}K_x$. Phys Rev B 48:16877–16880
922. Ruschewitz U, Müller P, Kockelmann W (2001) On the crystal Structure of Rb_2C_2 and Cs_2C_2. Z Anorg Allg Chem 627:513–522
923. Stephens PW, Bortel G, Falgel G, Tegze M, Janossy A, Pekker S, Oszlanyi G, Forro L (1994) Polymeric fullerene chains in RbC_{60} and KC_{60}. Nature (London) 370:636–639
924. Zhou O, Fischer JE, Coustel N, Kycia S, Zhu Q, McGhie AR, Romanow WJ, McCauley JP Jr, Smith AB, Cox DE (1991) Structure and bonding in alkali-metal-doped C_{60}. Nature (London) 351:462–464
925. Rikiishi Y, Kashino Y, Kusai H, Takabayashi Y, Kuwahara E, Kubozono Y, Kambe T, Takenobu T, Iwasa Y, Mizorogi N, Nagase S, Okada S (2005) Metallic phase in the metal-intercalated higher fullerene $Rb_{8.8(7)}C_{84}$. Phys Rev B 71:224118(1–6)
926. Ignateva IY, Barabash OM, Legkaya TN (1990) Evolution of the phase diagram for the magnesium-carbon system as a function of pressure on the basis of thermodynamic calculations. Sverkhtverd Mater 12:1–5
927. Schürmann E, Jacke H (1987) Schmelzgleichgewichte im System Fe-C-Ca (Melting equilibria in the system Fe-C-Ca). Steel Res 58:399–405
928. Claridge JB, Kubozono Y, Rosseinsky MJ (2003) A complex fulleride superstructure – decoupling cation vacancy and anion orientational ordering in $Ca_{3+x}C_{60}$ with maximum entropy data analysis. Chem Mater 15:1830–1839
929. Guérard D, Hérold A (1975) Chimie Macromoléculaire. Synthèse directe de composés d'insertion du strontium dans le graphite (Macromolecular Chemistry. Direct synthesis of strontium intercalation in graphite compounds). C R Seances Acad Sci Ser C 280:729–730 (in French)

930. Saito S, Oshiyama A (1993) Sr_6C_{60} and Ba_6C_{60}: Semimetallic fullerides. Phys Rev Lett 71:121–124
931. Beyers R, Klang C, Johnson RD, Salem JR, De Vrles MS, Yannoni CS, Bethune DS, Dorn HC, Burbank P, Harich K, Stevenson S (1994) Preparation and structure of crystals of the metallofullerene $Sc_2@C_{84}$. Nature (London) 370:196–199
932. Okamoto H (1996) The C-Y (carbon-yttrium) system. J Phase Equilib 17:548
933. Gröbner J, Lukas HL, Aldinger F (1995) Thermodynamic calculations in the Y-Al-C system. J Alloys Compd 220:8–14
934. Takata M, Umeda B, Nishibori E, Sakata M, Saito Y, Ohno M, Shinohara H (1995) Confirmation by x-ray diffraction of the endohedral nature of the metallofullerene $Y@C_{82}$. Nature (London) 377:46–49
935. Kessler B, Bringer A, Cramm S, Schlebusch C, Eberhardt W, Suzuki S, Achiba Y, Esch F, Barnaba M, Cocco D (1997) Evidence for incomplete charge transfer and La-derived states in the valence bands of endohedrally doped $La@C_{82}$. Phys Rev Lett 79:2289–2292
936. Rikiishi Y, Kubozono Y, Hosokawa T, Shibata K, Haruyama Y, Takabayashi A, Fujiwara A, Kobayashi S, Mori S, Iwasa Y (2004) Structural and electronic characterizations of two isomers of $Ce@C_{82}$. J Phys Chem B 108:7580–7585
937. Chen XH, Chi DH, Sun Z, Takenobu T, Liu ZS, Iwasa Y (2000) Synthesis, structure, and transport properties of novel fullerides A_3C_{70} (A = Ba and Sm). J Am Chem Soc 122:5729–5732
938. Molodtsov SL, Laubschat C, Richter M, Gantz T, Shikin AM (1996) Electronic structure of Eu and Yb graphite intercalation compounds. Phys Rev B 53:16621–16630
939. Takenobu T, Chi DH, Margadonna S, Prassides K, Kubozono Y, Fitch AN, Kato KI, Iwasa Y (2003) Synthesis, structure, and magnetic properties of the fullerene-based ferromagnets Eu_3C_{70} and Eu_9C_{70}. J Am Chem Soc 125:1897–1904
940. Pichler T, Golden MS, Knupfer M, Fink J, Kirbach U, Kuran P, Dunsch L (1997) Monometallofullerene $Tm@C_{82}$: proof of an encapsulated divalent Tm ion by high-energy spectroscopy. Phys Rev Lett 79:3026–3029
941. Haschke JM, Eick HA (1970) A phase investigation of the ytterbium-carbon system. J Am Chem Soc 92:1526–1530
942. Margadonna S, Arvanitidis J, Papagelis K, Prassides K (2005) Negative thermal expansion in the mixed valence ytterbium fulleride $Yb_{2.75}C_{60}$. Chem Mater 17:4474–4478
943. Burylev BP (1985) Phase diagram and activity of the components in the Tc-C system. Russ Metall (3):219–221
944. Du Z, Guo C, Yang X, Liu T (2006) A thermodynamic description of the Pd-Si-C system. Intermetallics 14:560–569
945. Savitskii EM, Polyakova VP (1975) Physico-chemical research in noble metals. J Less-Common Met 43:169–177
946. Ohtani H, Yamano M, Hasebe M (2004) Thermodynamic analysis of the Co-Al-C and Ni-Al-C systems by incorporating ab initio energetic calculations into the CALPHAD approach. Calphad 28:177–190
947. Okamoto H (1992) The Al-C (aluminum-carbon) system. J Phase Equilib 13:97–98
948. Baran LV (2006) Spontaneous growth of single crystals of various shapes in tin-fullerite films. Crystallogr Rep 51:690–695
949. Locke IW, Darwish AD, Kroto HW, Prassides K, Taylor R, Walton DRM (1994) Phosphorus/buckminsterfullerene intercalation compound $C_{60}(P_4)_2$. Chem Phys Lett 225:186–190
950. Roth G, Adelmann P, Knitter R (1993) Preparation and crystal structure of $C_{60}S_8CS_2$, a new fullerene-containing heteromolecular solid. Mater Lett 16:357–363
951. Tebbe FN, Harlow RL, Chase DB, Thorn DL, Campbell GC Jr, Calabrese JC, Herron N, Young RJ Jr, Wasserman E (1992) Synthesis and single-crystal x-ray structure of a highly symmetrical C_{60} derivative, $C_{60}Br_{24}$ Science (Washington DC) 256:822–825
952. Troyanov SI, Kemnitz E (2007) Singly-bonded fullerene dimers: neutral $(C_{60}Cl_5)_2$ and cationic $(C_{70})^{2+}$. Chem Commun (Cambridge) 2707–2709

953. Goldt IV, Boltalina OV, Sidorov LN, Kemnitz E, Troyanov SI (2002) Preparation and crystal structure of solvent free $C_{60}F_{18}$. Solid State Sci 4:1395–1401
954. Zhu Q, Cox DE, Fischer JE, Kniaz K, McGhie AR, Zhou O (1992) Intercalation of solid C_{60} with iodine. Nature (London) 355:712–714
955. Rizzoli C, Salamakha PS, Sologub OL, Bocelli G (2002) X-ray investigation of the Al-B-N ternary system: isothermal section at 1500 °C: crystal structure of the $Al_{0.185}B_6CN_{0.256}$ compound. J Alloys Compd 343:135–141
956. Kubaschewski O (1990) The Al-C-Hf (aluminium-carbon-hafnium) system. Ternary Alloys VCH 3:494–496
957. Velikanova TY (1990) The Al-C-Mo (aluminium-carbon-molybdenum) system. Ternary Alloys VCH 3:507–513
958. Monteiro WA (1990) The Al-C-Nb (aluminium-carbon-niobium) system. Ternary Alloys VCH 3:515–517
959. Savitskii EM, Efimov YV, Myasnikova EA, Bodak OI, Ryabtsev LA (1981) The niobium-aluminium-carbon system and the critical temperatures of the alloys (summary). Sov Non-Ferrous Met Res 9:342–343
960. Aponchuk AV, Karpov IK, Katkov OM (1987) On the dependence of triangulation of composition paragenesis diagram for the system Al-O-C on the temperature. Dokl Akad Nauk SSSR 294:1200–1202
961. Alexeeva ZM (1990) The Al-C-U (aluminium-carbon-uranium) system. Ternary Alloys VCH 3:568–574
962. Schuster JC, Nowotny H, Vaccaro C (1980) The ternary systems: Cr-Al-C, V-Al-C, and Ti-Al-C and the behavior of H-Phases (M_2AlC). J Solid State Chem 32:213–219
963. Schuster JC (1990) The Al-C-W (aluminium-carbon-tungsten) system Ternary Alloys VCH 3:575–577
964. Schuster JC (1990) The Al-C-Zr (aluminium-carbon-zirconium) system Ternary Alloys VCH 3:582–586
965. Schuster JC, Nowotny H (1980) Investigations of the ternary systems (Zr,Hf,Nb,Ta)-Al-C and studies on complex carbides. Z Metallkd 71:341–346
966. Schuster JC (1994) The As-C-V (arcenic-carbon-vanadium) system Ternary Alloys VCH 9:277–278
967. Boller H, Nowotny H (1967) Zum Dreistoff: Vanadin-Arsen-Kohlenstoff (On ternary system: vanadium-arsenic-carbon). Monatsh Chem 98:2127–2132
968. Brewer L, Haraldsen H (1955) The thermodynamic stability of refractory borides. J Electrochem Soc 102:399–406
969. Stadelmaier HH, Ballance JB (1967) Das Mischungsverhalten der τ-Boride (The mixing behavior of the τ-borides). Z Metallkd 58:449–451 (in German)
970. Lucco-Borlera M, Pradelli G (1971) Equilibri allo stato solido nel sistema manganese-carbonio-boro (Equilibria in the carbon-manganese-boron system in the solid state). Atti Accad Naz Lincei Mem Cl Sci Fis Mat Nat Ser 2a 10:69–89 (in Italian)
971. Shi Y, Leithe-Jasper A, Tanaka T (1999) New ternary compounds $Sc_3B_{0.75}C_3$, $Sc_2B_{1.1}C_{3.2}$, $ScB_{15}C_{1.60}$ and subsolidus phase relations in the Sc-B-C System at 1700 °C. J Solid State Chem 148:250–259
972. Tanaka T (1998) A new scandium borocarbide: $ScB_{17}C_{0.25}$. J Alloys Compd 270:132–135
973. Brisi C, Abbattista F (1961) Equilibri allo stato solido nei sistemi uranio-berillio-carbinio e torio-berillio-carbinio (Equilibria of uranium-beryllium-carbon and thorium-beryllium-carbon solid-state systems). Ann Chim (Rome) 51:1404–1408 (in Italian)
974. Zimin SS, Zalishchak BL (1986) A new model of the formation of carbonatites and ores associated with them. Dokl Akad Nauk SSSR 289:700–702
975. Savitskii EM, Efimov YV, Myasnikova EA, Bodak OI, Kharchenko OI (1984) Phase equilibria in Nb(V)-Ga-C systems. Inorg Mater 20:350–352
976. Gupta LC, Nagarajan R, Godart C, Dhar SK, Mazumdar C, Hossain Z, Lévy-Clement C, Padalia BD, Vijayaraghavan PR (1994) The new class of superconducting quaternary R-T-B-C systems (R= rare earth, T = Ni, Pd)", Physica C 235–240:150–153

977. Frisk K, Zackrisson J, Jansson B, Makrström A (2004) Experimental investigation of the equilibrium composition of titanium carbonitride and analysis using thermodynamic modelling. Z Metallkd 95:987–992
978. Teyssandier F, Ducarroir M, Bernard C (1984) Thermodynamic study of the titanium-carbon-nitrogen phase diagram at high temperature. Calphad 8:233–242
979. Arbuzov MP, Golub SY, Khaenko BV (1978) Phases of the system Ti-TiC-TiN. Inorg Mater 14:1126–1128
980. Danisina IN, Vilk YN, Avarbé RG, Omelchenko YA, Ryzhkova TP (1968) Phase diagram of the system zirconium – zirconium nitride – zirconium carbide. J Appl Chem USSR 41:478–485
981. Babad-Zakhryapin AA, Gert LM, Valyavko LR (1968) Possibility of forming tungsten oxycarbide with a fcc lattice. Inorg Mater 4:1200–1201
982. Boller H (1973) Röntgenographische Untersuchungen im Dreistoff V-P-C (X-ray studies in the V-P-C ternary system). Monatsh Chem 104:48–56 (in German)
983. Jeng FS, You YB, Ku HC, Ho JC (1996) Superconducting and calorimetric properties of $ThPt_2B_2C$ and the anomalous T_c variation for non-magnetic RPt_2B_2C systems (R= Y, Th, La). Phys Rev B 53:3492–3496
984. Kerans RJ, Mazdiyasni KS, Ruh R, Lipsitt HA (1984) Solubility of metals in substoichiometric TiC_{1-x}. J Am Ceram Soc 67:34–38
985. Pakholkov VV, Brettser-Portnov IV, Grigorov IG, Alyamovskii SI, Zainulin YG (1991) Phase formation in the TiB-TiC system. Russ J Inorg Chem 36:912–915
986. Vogt C, Hoffmann RD, Pöttgen R (2005) The superstructure of Sc_3RhC_4 and Sc_3IrC_4. Solid State Sci 7:1003–1009
987. Holleck H (1977) Carbon- and boron-stabilized ordered phases of scandium. J Less-Common Met 52:167–172
988. Hoffmann RD, Pöttgen R, Jeitschko W (1992) Scandium transition metal carbides Sc_3TC_4 with T = Fe, Co, Ni, Ru, Rh, Os, Ir. J Solid State Chem 99:134–139
989. Vogt C, Hoffmann RD, Rodewald UC, Pöttgen R, Bohrmoser B, Scherer W, Zhang L, Eckert H (2006) Überstruktur, experimentelle Elektronendichte und spektroskopische Eigenschaften der Carbide Sc_3TC_4 (T = Fe, Co, Ni, Ru, Rh, Os, Ir) (On the structure, experimental electron density and spectroscopic properties of the carbides Sc_3TC_4 (T = Fe, Co, Ni, Ru, Rh, Os, Ir)). Z Anorg Allg Chem 632(12–13):2116 (in German)
990. Krikorian NH (1971) The reaction of selected lanthanide carbides with platinum and iridium. J Less-Common Met 23(3):271–279
991. Gerdes MH, Jeitschko W, Wachtmann KH, Danebrock ME (1997) Gd_2OsC_2, a soft ferromagnet with a surprisingly high Curie temperature and other rare-earth osmium and rhenium carbides with Pr_2ReC_2 type structure. J Mater Chem 7(12):2427–2431
992. Hüfken T, Wachtmann KH, Jeitschko W (1998) Preparation and crystal structure of the ternary carbides $R_{12}Os_5C_{15}$ with R = Y, Pr, Nd, Sm, Gd-Tm. J Alloys Compd 281(2):233–236
993. Jeitschko W, Block G, Kahnert GE, Behrens RK (1990) Pr_2ReC_2 and other ternary rare earth metal rhenium carbides with filled $PbCl_2$ (Co_2Si) structure. J Solid State Chem 89(1):191–201
994. Pöttgen R, Block G, Jeitschko W, Behrens RK (1994) Preparation and crystal structure of the carbides $Ln_{15}Re_5C_{15}$ (Ln = Y, La-Nd, Gd-Er). Z Naturforsch B 49:1081–1088
995. Raghavan V (2008) The Al-C-Ir (aluminum-carbon-iridium) system. J Phase Equilib Diffus 29(1):51
996. Okamoto H (2012) The C-O (carbon-oxygen) system. J Phase Equilib Diffus 33(3):244
997. Okamoto H (2012) The C-S (carbon-sulfur) system. J Phase Equilib Diffus 33(3):245
998. Okamoto H (2011) The C-Pu (carbon-plutonium) system. J Phase Equilib Diffus 32(4):389–390
999. Okamoto H (2010) The C-Cl (carbon-chlorine) system. J Phase Equilib Diffus 31(5):496
1000. Okamoto H (2010) The C-V (carbon-vanadium) system. J Phase Equilib Diffus 31(1):91–92

1001. Okamoto H (2008) The C-W (carbon-tungsten) system. J Phase Equilib Diffus 29(6):543–544
1002. Raghavan V (2008) The Al-C-Si (aluminium-carbon-silicon) system. J Phase Equilib Diffus 29(4):365–366
1003. Sangster J (2007) The C-Na (carbon-sodium) system. J Phase Equilib Diffus 28(6):571–579
1004. Sangster J (2007) The C-Li (carbon-lithium) system. J Phase Equilib Diffus 28(6):561–570
1005. Demetriou MD, Ghoniem NM, Lavine AS (2002) Computation of metastable phases in tungsten-carbon system. J Phase Equilib 23(4):305–309
1006. Bittermann H, Rogl P (1997) Critical assessment and thermodynamic calculation of the binary system hafnium-carbon (Hf-C). J Phase Equilib 18(4):344–356
1007. Bandyopadhyay D, Sharma RC, Chakraborti N (2000) The C-Nb-Ti (carbon-niobium-titanium) system. J Phase Equilib 21(1):102–104
1008. Bandyopadhyay D, Sharma RC, Chakraborti N (2000) The Ti-V-C (titanium-vanadium-carbon) system. J Phase Equilib 21(1):199–202
1009. Bandyopadhyay D, Sharma RC, Chakraborti N (2000) The Ti-Co-C (titanium-cobalt-carbon) system. J Phase Equilib 21(2):179–185
1010. Bandyopadhyay D, Sharma RC, Chakraborti N (2000) The Ti-N-C (titanium-nitrogen-carbon) system. J Phase Equilib 21(2):192–194
1011. Bandyopadhyay D, Sharma RC, Chakraborti N (2000) The Ti-Ni-C (titanium-nickel-carbon) system. J Phase Equilib 21(2):186–189
1012. Durand F, Duby JC (2000) Solid-liquid equilibria in the silicon-rich corner of the Si-O-C system. J Phase Equilib 21(2):130–135
1013. Bandyopadhyay D, Haldar B, Sharma RC, Chakraborti N (1999) The Ti-Mo-C (titanium-molybdenum-carbon) system. J Phase Equilib 20(3):332–336
1014. Haldar B, Bandyopadhyay D, Sharma RC, Chakraborti N (1999) The Ti-W-C (titanium-tungsten-carbon) system. J Phase Equilib 20(3):337–343
1015. Durand F, Duby JC (1999) Carbon solubility in solid and liquid silicon – a review with reference to eutectic equilibrium. J Phase Equilib 20(1):61–63
1016. Goksen NA, Oden LL (1998) Phase equilibria in aluminium-carbon system at high temperatures. J Phase Equilib 19(5):409–411
1017. Okamoto H (1996) The C-Zr (carbon-zirconium) system. J Phase Equilib 17(2):162
1018. Okamoto H (1995) Comment on C-Ti (carbon-titanium) system. J Phase Equilib 16(6):532–533
1019. Okamoto H (1992) The B-C (boron-carbon) system. J Phase Equilib 13(4):436
1020. Okamoto H (1991) The C-V (carbon-vanadium) system. J Phase Equilib 12(6):699
1021. Ishida K, Nishizawa T (1991) The C-Co (carbon-cobalt) system. J Phase Equilib 12(4):417–424
1022. Okamoto H (2007) The C-Pd (carbon-palladium) system. J Phase Equilib Diffus 28(3):313
1023. Frisk K, Dumitrescu L, Ekroth M, Jansson B, Kruse O, Sundman B (2001) Development of a database for cemented carbides: thermodynamic modelling and experiments. Phase Equilib 22(6):645–655
1024. Claeyssens F, Fuge GM, Allan NL, May PW, Ashfold MNR (2004) Phosphorus carbides: theory and experiment. Dalton Trans (19):3085–3092
1025. Cataldo F (2002) Polymeric fullerene oxide (fullerene ozopolymers) produced by prolonged ozonation of C_{60} and C_{70} fullerenes. Carbon 40(9):1457–1467
1026. Tkachenko YuG, Ordanyan SS, Yulyugin VK, Yurchenko DZ, Unrod VI, Evdokimova NI (1977) High-temperature friction and wear of eutectic carboboride alloys of group V metals. Powder Metall Met Ceram 16(10):781–784

Chapter 3
Tungsten

3.1 Structures

Tungsten (or wolfram) is the element No. 74 of the periodic table (period—6, group—6 (or VIB), relates to transition metals) with the ground state level $^5D_0$ and electron configuration $1s^2 2s^2 2p^6 3s^2 3p^6 3d^{10} 4s^2 4p^6 4d^{10} 4f^{14} 5s^2 5p^6 5d^4 6s^2$. The general oxidation states (numbers) of tungsten in various chemical compounds are (–2), (–1), 0, (+1), (+2), (+3), (+4), (+5) and (+6); the oxidation states (+6) and (+4) are the most common; the radii of tungsten are:

atomic (metallic, CN = 8)—0.137 nm,
atomic (metallic, CN = 12)—0.141 nm,
atomic (covalent, VI, single bond)—0.125 nm,
atomic (covalent, VI, double bond)—0.121 nm,
ionic (−1)—0.2265 nm,
ionic (+1)—0.136 nm,
ionic (+2)—0.117 nm,
ionic (+3)—0.101 nm,
ionic (+4)—0.066 nm (CN = 6),
ionic (+5)—0.062 nm (CN = 6),
ionic (+6)—0.060 nm (CN = 6),
ionic (+6)—0.051 nm (CN = 5),
ionic (+6)—0.042 nm (CN = 4);

its electronegativity is 1.7 in Pauling scale, or 1.40 in Allred—Rochow scale [1–3, 10–11, 87]. The only stable modification of elemental tungsten (or α-W) has body-centred cubic (bcc) metal crystal structure (space group—*Im(−3)m*) with lattice parameter $a = 0.31652$ nm ($Z = 2$) at 25 °C (minimum interatomic distance—0.27412 nm, CN = 8) [4], slip planes are (110) or (122) and slip direction <111> [87, 322].

So-called β-W phase occurs only in the presence of oxygen and has probably the composition, which is close to $\sim W_3O$ (stable at temperatures <630–650 °C, crystal structure—cubic, space group—*Pm(−3)n* and lattice parameter $a = 0.5046$ nm at 25 °C); and so-called γ-W phase (face-centred cubic (fcc) structure,

I. L. Shabalin, *Ultra-High Temperature Materials I*,
DOI: 10.1007/978-94-007-7587-9_3,

$a = 0.413$ nm) was only found in thin sputtered layers and amorphous specimens at very beginning of sputtering [87]. Neither β-W nor γ-W are stable when heated up to temperatures $\geq \sim 700$ °C and both of them transform to α-W.

At room temperature, the XRD density of tungsten is 19.246 g cm^{-3} and recommended value for the bulk density of common metal parts—19.20–19.25 g cm^{-3} (molar volume—9.53 cm^3); at the melting temperature density is 16.7 ± 0.6 g cm^{-3}. The densities of metastable β-W and γ-W are 18.9–19.1 and 15.8 g cm^{-3}, respectively [5, 87].

3.2 Thermal Properties

Tungsten has the highest melting point of all the pure metals and the second highest all over the periodic table after carbon. The general thermodynamic properties of tungsten are summarized in Table 3.1. For the molar heat capacity $c_p = f(T, K)$, J mol^{-1} K^{-1}, the following relationships are recommended:

in the range of temperatures from 298 to 2500 K [6]

$$c_p = 24.03 + \left(3.182 \times 10^{-3}\right)T, \tag{3.1}$$

in the range of temperatures from 388 to 3100 K [5]

$$c_p = 23.25 + \left(4.13 \times 10^{-3}\right)T + \left(1.87 \times 10^{-7}\right)T^2. \tag{3.2}$$

For the specific heat capacity $c = f(T, K)$, J kg^{-1} K^{-1}, in the range of temperatures from 273 to 3300 K the equation is given [7] as

$$c_p = 135.76 + \left(9.1159 \times 10^{-3}\right)T + \left(2.3134 \times 10^{-9}\right)T^3 - \left(6.5233 \times 10^5\right)T^{-2}. \tag{3.3}$$

Tungsten has the lowest vapour pressure of all metals. The equilibrium vapour pressure of tungsten P, Pa, is obeyed the rules:

in the range of temperatures from 298 to 2350 K [10]

$$\lg P = -44094/T + 1.3677 \lg T + 7.951, \tag{3.4}$$

in the range of temperatures from 2200 to 2500 K [10]

$$\lg P = -57687/T - 12.2231 \lg T + 59.533, \tag{3.5}$$

in the range of temperatures from 2600 to 3100 K [12]

$$\lg P = -45385/T + 12.865, \tag{3.6}$$

in the range of temperatures from 3560 to 5645 K [6]

$$\lg P = -43794/T + 1.4927 \lg T + \left(0,0888 \times 10^{-3}\right)T + 7.6203, \tag{3.7}$$

Table 3.1 General thermodynamic properties of tungsten

Characteristics	Symbol	Unit	Value	References
Standard molar entropy (at 298.15 K and 100 kPa)	$S°_{298}$	J $mol^{-1}K^{-1}$	32.76 ± 0.4	[5]
			33.5	[6]
			32.618	[11]
Molar enthalpy difference	$H_{298}–H_0$	kJ mol^{-1}	4.970	[11]
Standard molar heat capacity (at 298.15 K and 100 kPa)	$c°_{p,298}$	J $mol^{-1}K^{-1}$	24.3	[5, 8, 11]
			24.98	[6]
Specific heat capacity (at 298.15 K)	c	J $kg^{-1}K^{-1}$	132.0	[5, 10]
			131.2	[7]
Molar enthalpy (heat) of melting (at the melting point)	ΔH_m	kJ mol^{-1}	52.3	[8, 11]
			46	[87]
			35	[392]
Specific enthalpy (heat) of melting (at the melting point)		kJ kg^{-1}	220 ± 36	[9]
			284.5	[10]
Molar enthalpy (heat) of vaporization (at the boiling point)	ΔH_v	kJ mol^{-1}	797	[5]
			806.7	[8, 11]
Specific enthalpy (heat) of vaporization (at the boiling point)		kJ kg^{-1}	4330	[5]
			4680 ± 25	[12]
Melting point	T_m	K (°C)	3680 ± 20 (3410 ± 20)	[5, 13]
			3693 (3420)	[11]
			3687 (3414)	[10, 23]
			3660 (3390)	[14]
			3650 (3380)	[19]
Boiling point	T_b	K (°C)	6000 ± 200 (5700 ± 200)	[9, 87]
			6200 (5900)	[8]
			5930 (5660)	[23]
			5828 (5555)	[10–11]
			5640 (5370)	[14]
Critical point[a]		K (°C), GPa	13400 ± 1400 (13100 ± 1400), 0.337 ± 0.085	[337]

[a] Critical density—4.31 g cm^{-3}

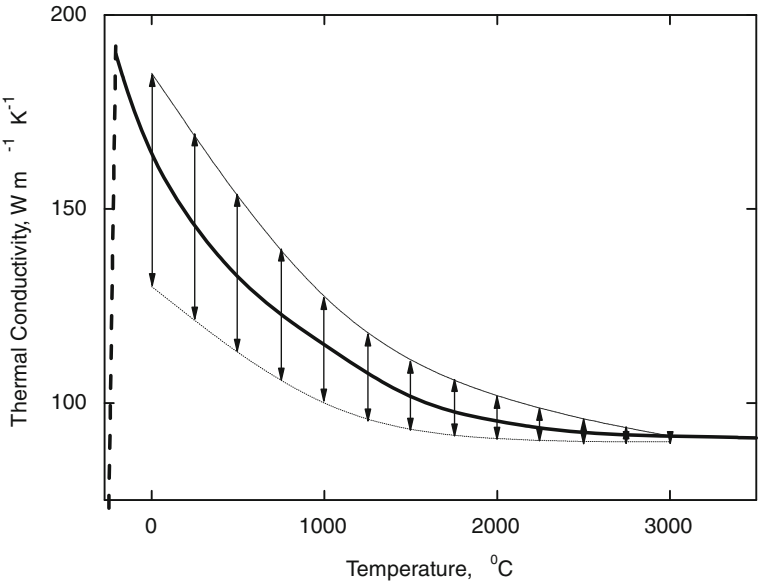

Fig. 3.1 Variation of the thermal conductivity of tungsten with temperature (*curve*—recommended values, *arrows*—data spread available in the literature) [15–19]

where T is temperature, K. At 2000 °C, the vapour pressure is 8.15×10^{-8} Pa and at 3000 °C it is ~0.1 Pa [87]. In high vacuum, the rate of tungsten vaporization at the temperatures of 1880, 2150, and 2500 °C approximately amounts to 0.1, 10 μm, 1 mm per year, respectively [5]. The values of standard molar entropy $S°_{298}$, molar c_p and specific c heat capacities, enthalpies (heats) of melting and vaporization, molar and specific mass enthalpy differences H_T–H_{298}, vapour pressures and mass/linear vaporization rates for tungsten are given in Addendum in comparison with carbon (graphite) and other ultra-high temperature materials (refractory metals) in the wide ranges of temperatures. At room temperature, the thermal conductivity of tungsten is about 175 W m^{-1} K^{-1}. In the range of temperatures 1200–2800 K, the coefficient of thermal conductivity λ, W m^{-1} K^{-1}, obeys the following equation:

$$\lambda = 108.34 - 1.052 \times 10^{-2} T + 23419.9/T, \tag{3.8}$$

where T is temperature, K. At the melting point, the value of λ drops from 89.5 to 70.5 W m^{-1} K^{-1} [87]. The variation of the thermal conductivity of tungsten with temperature is shown on the basis of several studies [15–19] in Fig. 3.1.

At room temperature, the coefficient of linear thermal expansion of pure tungsten $\alpha = (4.3 \div 4.7) \times 10^{-6}$ K^{-1} [11, 87], while for the interval from 20 to 1700 °C the recommended value is 5.0×10^{-6} K^{-1} [5]. For tungsten treated variously, the average value of α increases almost linearly with temperature growth and differs from $(4 \div 6) \times 10^{-6}$ K^{-1} (at 0 °C) to $(7 \div 11) \times 10^{-6}$ K^{-1}

(at 3000 °C) [5, 11, 19]. The relative thermal expansion $\Delta l/l_0$ can be calculated more accurately according to the following equations [87]:

in the range of temperatures from 293 to 1395 K

$$\Delta l/l_0 = 4.266 \times 10^{-6}(T - 293) + 8.479 \times 10^{-10}(T - 293)^2 - 1.974 \times 10^{-13}(T - 293)^3, \quad (3.9)$$

in the range of temperatures from 1395 to 2495 K

$$\Delta l/l_0 = 5.48 \times 10^{-3} + 5.416 \times 10^{-6}(T - 1395) + 1.952 \times 10^{-10}(T - 1395)^2 + 4.422 \times 10^{-13}(T - 1395)^3, \quad (3.10)$$

in the range of temperatures from 2495 to 3600 K

$$\Delta l/l_0 = 12.26 \times 10^{-3} + 7.451 \times 10^{-6}(T - 2495) + 1.654 \times 10^{-9}(T - 2495)^2 + 7.568 \times 10^{-14}(T - 2495)^3, \quad (3.11)$$

where T is temperature, K. The thermal expansion of tungsten components in the range of temperatures from 25 to 2500 °C is expressed by the equation as follows [20–21]:

$$(L_t - L_{25\,^\circ\mathrm{C}})/L_{25\,^\circ\mathrm{C}} = A_0 + A_1 t + A_2 t^2, \quad (3.12)$$

where $L_{25°C}$ and L_t are linear dimensions at 25 °C and higher temperature, respectively; t denotes the value of temperature, °C; A_0, A_1 and A_2 are the coefficients, which mainly depend on manufacturing methods and geometric forms:

for powder metallurgy produced rods $A_0 = -8.69 \times 10^{-5}$, $A_1 = 3.83 \times 10^{-6}$, $A_2 = 7.92 \times 10^{-10}$;
for powder metallurgy produced sheets $A_0 = -4.58 \times 10^{-5}$, $A_1 = 3.65 \times 10^{-6}$, $A_2 = 9.81 \times 10^{-10}$;
for arc cast sheet $A_0 = -6.76 \times 10^{-5}$, $A_1 = 3.91 \times 10^{-6}$, $A_2 = 8.98 \times 10^{-10}$.

At the melting temperature, the surface tension of liquid tungsten is about 2.32–2.55 N m^{-1} (its temperature coefficient is -0.29×10^{-3} N m^{-1} K^{-1}); the molar volume increases by 8 % on melting [11, 87]. In comparison with other ultra-high temperature materials (graphite and refractory metals), the values of thermal conductivity and thermal expansion of tungsten in the wide range of temperatures are summarized in Addendum.

3.3 Electro-Magnetic and Optical Properties

At room temperature, the specific electrical resistance (resistivity) of pure tungsten $\rho = 54.0$–56.5 nΩ m. At higher temperatures the resistivity is almost obeyed the classic metal model (with small negative deviation from linearity) and slightly exceeds 1 μΩ m at 3000 °C [5, 11]. The variation of resistivity at the melting point

of tungsten is $\rho_{liq}/\rho_{sol} = 1.08$ [14]. In the interval from 20 to 1730 °C the temperature coefficient of resistivity of tungsten is $\sim 5.5 \times 10^{-3}$ K^{-1} (the pressure coefficient is -1.33×10^{-5} MPa^{-1}) [5, 11, 23]. The following relationships for resistivity ρ, nΩ m, are recommended [18, 87]:

in the range of temperatures from 300 to 1240 K

$$\rho = -16.4011 + 0.219691T + \left(4.33471 \times 10^{-5}\right)T^2, \tag{3.13}$$

in the range of temperatures from 1240 to 2570 K

$$\rho = -194.101 + 0.467093T + \left(4.06012 \times 10^{-5}\right)T^2, \tag{3.14}$$

where T is temperature, K. Tungsten is a type I superconductor with a transition temperature of 0.0154 ± 0.0005 K. The critical magnetic field strength H_c ($T \to 0$) is 91.5 A m^{-1} [87]. At 20 °C the Hall coefficient of tungsten is $R = 0.856 \times 10^{-10}$ m^3 A^{-1} s^{-1} ($B = 0.5$–2.0 T), Seebeck coefficient (absolute thermoelectric power) is +1.5 μV K^{-1} [11, 23]. Tungsten is a paramagnetic metal with molar magnetic susceptibility χ_m (SI) $= 6.66 \times 10^{-4}$ cm^3 mol^{-1} (at 22 °C) slightly increasing with temperature growth [11, 22].

The variations of main optical properties of tungsten with wavelength λ are following [14]:

index of refraction (single crystal or polycrystalline materials)—from 2.49 ($\lambda = 0.3$ μm) to 3.44 ($\lambda = 0.6$ μm), or to 17.5 ($\lambda = 20.0$ μm);
index of absorptance (single crystals)—from 2.58 ($\lambda = 0.3$ μm) to 2.92 ($\lambda = 0.6$ μm), or to 66.0 ($\lambda = 20.0$ μm);
reflective index under normal incidence (polished materials)—from 0.50 ($\lambda = 0.3$ μm) to 0.51 ($\lambda = 0.6$ μm), or to 0.95 ($\lambda = 9.0$ μm).

The monochromatic emittance (spectral emissivity) ε_λ of tungsten as a function of wavelength has a maximum in the range of 0.3–0.4 μm; the cross-point, where all the emittance wavelength isoterms (from 1600 to 2800 °K) cross, corresponds to $\lambda = 1.27$ μm ($\varepsilon_\lambda = 0.33$). In the range of temperatures 0–3000 °C ε_λ ($\lambda = 0.65$ μm) of non-oxidized tungsten varies from 0.43–0.46 to 0.38 decreasing almost linearly with temperature growth, while the integral emittance ε_T increases with temperature increase and amounts to 0.32–0.34 at ultra-high temperatures [5, 14, 251]; in the wide range of temperatures (400–3600 K) ε_T can be well represented by the following empirical equation [338]:

$$\varepsilon_T = -2.6875 \times 10^{-2} + \left(1.819696 \times 10^{-4}\right)T - \left(2.1946163 \times 10^{-8}\right)T^2, \tag{3.15}$$

where T is temperature, K. The thermoionic emission characteristics (electron work function and Richardson constants) of variously oriented tungsten single crystals [5] are given in Table 3.2.

The recommended values of electrical resistivity, magnetic susceptibility, integral and spectral emittances and thermoionic emission characteristics (electron

Table 3.2 Thermoionic characteristics of single crystal and polycrystalline tungsten [5, 10, 14, 262–263]

(*hkl*)-index	Richardson constant, 10^4 A m^{-2} K^{-2}	Electron work function, eV
(116)	53	4.20–4.39
(111)	36–122	4.20–4.45
(012)	–	4.34
(122)	–	4.35
(113)	–	4.46–4.50
(010)	–	4.47
(112)	125	4.5–5.3
(123)	–	4.52
(001)	156	4.52–4.59
(100)	156	4.56–4.63
(110)	–	5.35
Polycrystalline	–	4.54–4.55

work function and Richardson constant) for tungsten are given in comparison with other ultra-high temperature elements (carbon and refractory metals) in Addendum.

3.4 Physico-Mechanical Properties

Most of the physico-mechanical properties of tungsten are extremely sensitive to the microstructure character, which is strongly dependent on metal working (treatment), as well as to the relatively minute amounts of contaminations by the interstitial atomic species, such as oxygen, nitrogen, carbon and hydrogen. Certainly, hardness of tungsten ranges widely, e.g. in HV_{30} numbers—from 300 (recrystallized) up to 650 (worked/deformed) [11, 23, 87]. For various microstructure states, the hardness (HB) comes to the following values [5]:

cast and cold worked (hardened, purity 99.95 %)—415 kgf mm^{-2} (4.1 GPa);
cast and annealed (recrystallized, purity 99.95 %)—320 kgf mm^{-2} (3.1 GPa);
sintered from powder (density 17.5–18.0 g cm^{-3})—140–150 kgf mm^{-2} (1.4–1.5 GPa).

The hardness of polycrystalline tungsten increases considerably as the grain size is reduced. It was shown that hardness and average grain size follow a Hall—Petch relationship:

$$H = H_0 + K_H L^{-1/2}, \tag{3.16}$$

where $H_0 = 350$ kgf mm^{-2}, $K_H = 10$ kgf $mm^{-3/2}$ and L is the average grain size. Hardness values of up to 1200 kgf mm^{-2} (2 kgf load) were obtained on submicrongrained materials [87]. The temperature behaviour of hardness is complicated because of the presence of two flexion points (approximately, at the temperatures of (0.15–0.25) T_m and (0.3–0.5)T_m) on the hardness-temperature curve, which are connected with changing the mechanism of deformation (Fig. 3.2a) [24].

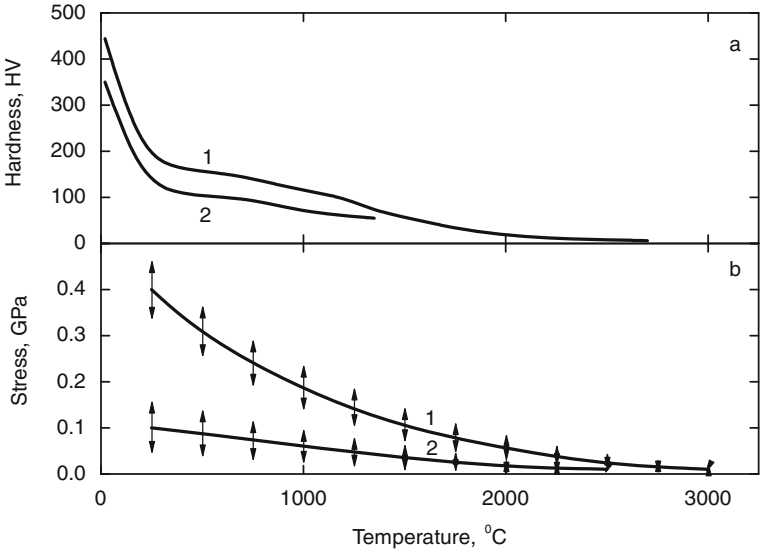

Fig. 3.2 Variation of the hardness (*a*, *1*—work hardened metal, *2*—annealed metal, [24]) and tensile strength (*b*, metal specimens annealed at 1370–2845 °C, *1*—ultimate tensile strength, *2*—0.2 % offset yield strength, *arrows*—data spread, [25–28]) of pure tungsten with temperature

The value of ultimate tensile strength of hardened pure tungsten at room temperature amounts to 1.5–1.9 GPa, while for annealed tungsten it ranges from 0.3 to 0.6 GPa (0.2 % offset yield strength—0.55 GPa, elongation—2 %) [23]. For the various components made from unalloyed tungsten these characteristics comes to the following values [5]:

tungsten wire (diameter 15–20 μm)—4.17–4.60 GPa;
cast and cold worked (hardened, diameter 5 mm, length 25 mm, purity 99.95 %)—~0.9 GPa;
cast and annealed (recrystallized, purity 99.95 %)—~0.5 GPa);
sintered from powder (density 17.5–18.0 g cm^{-3})—0.78–0.88 GPa;
plasma sprayed (density 16–17 g cm^{-3})—0.035–0.046 GPa.

A typical example of the variation of ultimate tensile strength of pure tungsten with temperature is shown in Fig. 3.2b for the specimens (rods, diameter 2.36–4.06 mm) produced by various methods, such as powder metallurgy, arc casting, electron beam melting, and chemical vapour deposition, with subsequent annealing at the various temperatures from 1370 to 2845 °C [25–28]. In general, the following rules exist for tungsten [87]:

a wrought (as-worked) structure, consisting of deformation direction elongated crystals, is stronger than an annealed or recrystallized one (in particular, this is valid for the strength in deformation direction, so-called “texture strengthening”);

the lower the working temperature and the more energy is stored during deformation, the higher is the strength (so-called "work hardening");
the smaller the grain size, the higher is the strength (so-called "fine-grain strengthening");
different fabrication processes (extrusion, swaging, rolling and drawing) yield different properties, and even after final working, there remain origin-related differences in the properties of arc-melted and produced by powder metallurgy methods tungsten.

At room temperature, the fracture toughness of single crystal tungsten varies depending on crystallographic direction from 8 to 31 MPa $m^{1/2}$. With temperature increase the value of this factor rises and for polycrystalline tungsten in the state as-worked it amounts to $\sim$40 MPa $m^{1/2}$ at 800 °C [276]. At room temperature, the apparent work of fracture (impact testing) of tungsten produced by powder metallurgy method (50–60 % wrought additionally) is 245–294 kJ m^{-2} [14]. The fatigue-related properties of tungsten in the various test conditions and frequencies are summarized in [33].

The ductile-to-brittle transition temperature of tungsten is very sensitive to contamination (the higher purity of metal is corresponding to lower transition temperatures) as well as strongly dependent on annealing temperature. The rod (diameter 5 mm, length 25 cm) made from high purity single crystal tungsten has demonstrated plasticity behaviour at cryogenic temperatures $t = -170$ °C [19]. For tungsten produced by powder metallurgy, arc casting or electron beam melting, the ductile-to-brittle transition temperature increases from 100 to 150 °C (for the metal in the state as-worked) up to 300–450 °C (for the metal annealed at 1300–2300 °C) [27]. At the temperatures more than 400 °C the elongation of tungsten amounts to 40–60 %, the reduction in area—more than 60 % (for arc cast rods the reduction in area exceeds 98 %) [19, 25, 28].

The values of prolonged strength are of great importance for the evaluation of operational time of high-temperature components and structures in the engineering practice. Highly strong unalloyed tungsten loses its rupture strength catastrophically with increasing temperature, e.g. 1-h rupture strength of 0.13 mm diameter wire falls below its level at 250 °C five times with temperature increasing to 1400 °C [29]. Some creep properties of tungsten at 2250–2800 °C are given in Table 3.3 [19], the creep rupture data (rupture stress vs. time-to-rupture) for pure tungsten wire (diameters 0.127 and 0.183 mm) in the state as-drawn at the testing temperatures from 649 up to 2527 °C are shown in Fig. 3.3 [29–30]. For polycrystalline tungsten, the creep rate can be expressed by following equation [87, 339]:

$$\dot{\varepsilon} = B\sigma^n \exp\left(-\frac{Q}{RT}\right), \tag{3.17}$$

where $\dot{\varepsilon} = \partial\varepsilon/\partial t = \partial l/l\partial t$ is the steady-state creep rate in s^{-1}, B and n are creep pre-exponential and exponent constants, respectively, σ is the applied stress, Q is the activation energy of creep, R is the gas constant and T is temperature in K. The values for B, n and Q vary considerably, depending on the respective material and testing conditions. They are characteristic for the dominating creep mechanism.

Table 3.3 High-temperature creep rate of tungsten (testing time—4 h)

Temperature, °C	Stress, MPa	Creep rate, s^{-1}
2250	18.6	10^{-6}
	27.4	10^{-5}
	41.2	10^{-4}
	55	10^{-3}
2500	5.4	10^{-6}
	15.2	10^{-5}
	23.5	10^{-4}
2700	13.7	10^{-5}
	18.6	10^{-4}
	23.5	10^{-3}
2800	10.3	5×10^{-6}
	11.7	10^{-5}
	14.2	10^{-4}
	18.6	4×10^{-4}

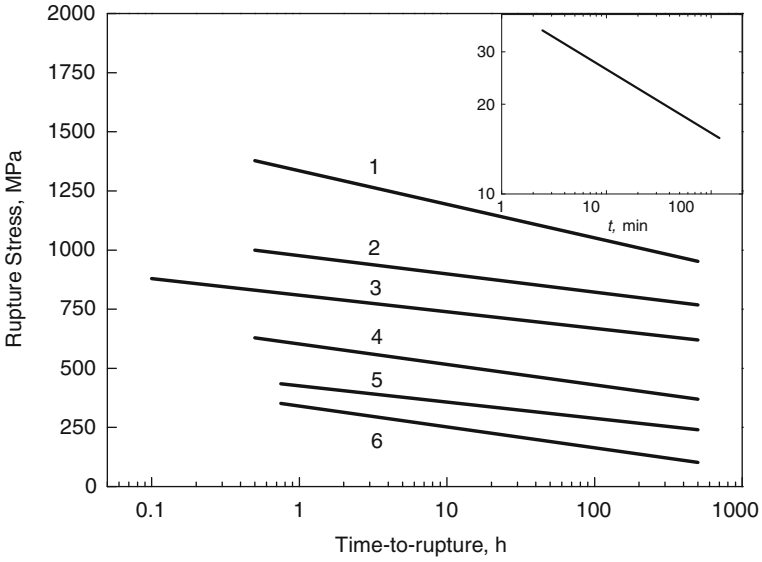

Fig. 3.3 Creep rupture (rupture stress vs. logarithm time-to-rupture) data for pure tungsten wire (diameter 0.127 mm) in the state as-drawn at the temperatures: *1*—649 °C, *2*—816 °C, *3*—982 °C, *4*—1093 °C, *5*—1260 °C and *6*—1371 °C [29] (*Inset*—logarithm rupture stress vs. logarithm time-to-rupture for pure tungsten wire (diameter 0.183 mm) at 2527 °C (heating rate $-\sim$2000 °C s^{-1}), in vacuum higher than 7×10^{-5} Pa [30])

For large samples of unalloyed tungsten at temperatures higher than 2200 °C ($\sim 0.65\ T_m$), $n = 5$ and $Q = 585$ kJ mol^{-2}. This value of the activation energy is close to that of self-diffusion for tungsten atoms in polycrystalline metal tungsten (see Table A.9 in Addendum). It was therefore assumed that under these conditions the deformation of the grains by dislocation climb or glide processes is the

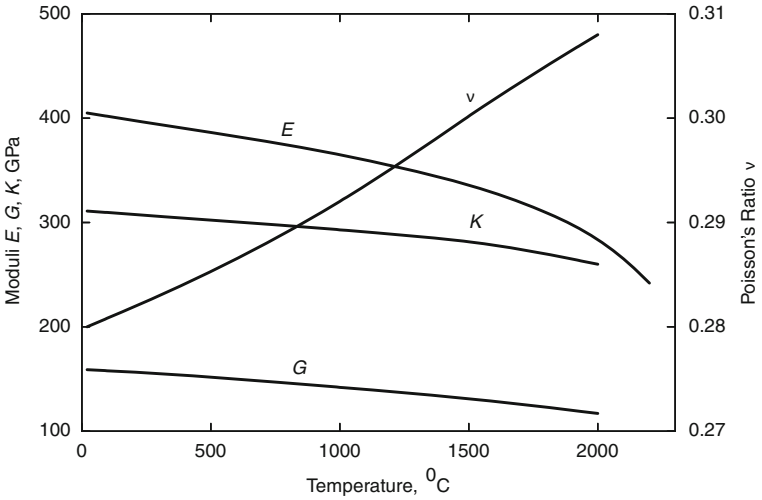

Fig. 3.4 Variations of Young's (E), Coulomb's (shear) (G) and bulk (compression) (K) moduli and Poisson's ratio (v) of pure polycrystalline tungsten with temperature on the basis of several sources [5, 11, 19, 34–35]

rate-controlling stage of the creep. For thin wires, having a grain size comparable to the creep specimen diameter, $n = 2$ and $Q = 276$ kJ mol^{-2} were obtained, as characteristic for grain boundary diffusion. In this case, the creep deformation occurred almost entirely by grain boundary diffusion sliding (offsetting) without extensive grain deformation [87]. In the high stress regime (>60 MPa) and in the range of temperatures 2500–3000 °C, the creep exponent constants n for tungsten were found to be in the interval from 8 up to 25 [30–32].

At room temperature, the main elastic properties of pure tungsten have the following numerical values [11, 19, 23, 87]:

Young's modulus E, GPa		390–415
Coulomb's (shear) modulus G, GPa		152–177
Poisson's ratio v		0.28–0.30
Bulk (compression) modulus K, GPa		305–311
Volume compressibility κ, MPa^{-1}		0.3×10^{-5}
Longitudinal velocity of sound V_S, m s^{-1}		5174–5180
Transversal velocity of sound V_T, m s^{-1}		2840–2870
Elastic compliance	s_{11}, TPa^{-1}	2.45
	s_{44}, TPa^{-1}	6.24
	s_{12}, TPa^{-1}	−0.69
Elastic stiffness	c_{11}, GPa	523
	c_{44}, GPa	160
	c_{12}, GPa	203

The variations of Young's and Coulomb's (shear) moduli and Poisson's ratio of tungsten with temperature are shown in Fig. 3.4 [34–35]. In the range of temperatures from 20 to 1730 °C, the following equation for the magnitude of Young's modulus E_T at temperature T, K was recommended for single crystal tungsten [5]:

$$E_T = E_{293}\left(\frac{T_m - T}{T_m}\right)^n, \tag{3.18}$$

where $n = 0.263$, E_{293} is the magnitude of Young's modulus at 20 °C and T_m is melting temperature, K.

The magnitudes of physico-mechanical (strength, elasticity) properties of unalloyed tungsten in the wide range of temperatures are summarized in Addendum in comparison with other ultra-high temperature materials (graphite and refractory metals).

3.5 Nuclear Physical Properties

The isotopes of tungsten (standard atomic mass—183.84 u) from ^{158}W to ^{192}W, including metastable states (^{158m}W, $^{179m1-3}$W, $^{180m1-2}$W, ^{183m}W, ^{185m}W, $^{186m1-2}$W and ^{190m}W), and their general characteristics are summarized in Table 3.4; the naturally occurring isotopes are listed in order of decreasing abundance, and unstable artificial (radioactive) isotopes—in order of decreasing half-life period of decay.

Table 3.4 General characteristics of the isotopes of tungsten [10, 14, 270–272]

Isotope	Mass, u	Abundance, %	Half-life period	Decay mode, excitation (radiation) energy, MeV
^{184}W[a]	183.950931	30.64	–	–
^{186}W[b]	185.954364	28.43	–	–
^{182}W[c]	181.948204	26.50	–	–
^{183}W[d]	182.950223	14.31	–	–
^{180}W[e]	179.946704	0.12	1.8×10^{18} y	α
^{181}W	180.948197	–	121 d	K-capture; γ, 0.03, 0.6, 0.8
^{185}W	184.953419	–	75.1 d	β^-, 0.426 (90 %), 0.37 (10 %); γ, 0.056, 0.57, 0.77
^{188}W	187.958489	–	69.8 d	β^-
^{178}W	177.945876	–	21.6 d	K-capture; γ, ~0.3
^{187}W	186.957160	–	23.7 h	β^-, 1.33 (30 %), 0.63 (70 %); γ, 0.072, 0.134, 0.48, 0.686, 0.78
^{176}W	175.94563	–	2.5 h	K-capture (99 %); β^+ (0.5 %); γ, ~1.3

(continued)

Table 3.4 (continued)

Isotope	Mass, u	Abundance, %	Half-life period	Decay mode, excitation (radiation) energy, MeV
^{177}W	176.94664	–	132 min	β^+; γ, 0.5, 1.2
^{179}W	178.947070	–	37.05 min	β^+
^{175}W	174.94672	–	35.2 min	β^+
^{174}W	173.94608	–	33.2 min	β^+
^{190}W	189.96318	–	30.0 min	β^-
^{189}W	188.96191	–	11.6 min	β^-
^{173}W	172.94769	–	7.6 min	β^+
^{172}W	171.94729	–	6.6 min	β^+
^{179m1}W	–	–	6.4 min	Isomer, γ (99.72 %); β^+ (0.28 %)
^{170}W	169.949228	–	2.42 min	β^+ (99 %), α (1 %)
^{171}W	170.94945	–	2.38 min	β^+
^{185m}W	–	–	1.60 min	Isomer, γ, 0.197
^{169}W	168.951779	–	1.27 min	β^+
^{168}W	167.951808	–	51 s	β^+ (99.99 %), α (0.032 %)
^{191}W	190.96660 (?)	–	20 s (?)	?
^{167}W	166.954816	–	19.9 s	β^+ (>99.9 %), α (<0.1 %)
^{166}W	165.955027	–	19.2 s	β^+ (99.96 %), α (0.035 %)
^{192}W	191.96817 (?)	–	10 s (?)	?
^{164}W	163.958954	–	6.3 s	β^+ (97.4 %), α (2.6 %)
^{183m}W	–	–	5.2 s	Isomer, γ, 0.309
^{165}W	164.958280	–	5.1 s	β^+ (99.8 %), α (0.2 %)
^{163}W	162.96252	–	2.8 s	β^+ (59 %), α (41 %)
^{162}W	161.963497	–	1.36 s	β^+ (53 %), α (47 %)
^{161}W	160.96736 (?)	–	0.41 s	α (73 %), β^+ (23 %)
^{160}W	159.96848	–	90 ms	α (87 %), β^+ (14 %)
^{159}W	158.97292 (?)	–	8.2 ms	α (82 %), β^+ (18 %)
^{180m1}W	–	–	5.47 ms	Isomer, γ, 1.529
^{190m}W	–	–	<3.1 ms	Isomer, γ, 2.381, (?)
^{186m2}W	–	–	>3 ms	Isomer, γ, 3.542 (?)
^{158}W	157.97456 (?)	–	1.37 ms	α
^{158m}W	–	–	0.14 ms	Isomer, γ, 1.889, (?)
^{186m1}W	–	–	18 μs	Isomer, γ, 1.517, (?)
^{180m2}W	–	–	2.33 μs	Isomer, γ, 3.264, (?)
^{179m3}W	–	–	0.75 μs	Isomer, γ, 3.348, (?)
^{179m2}W	–	–	0.39 μs	Isomer, γ, 1.631, (?)

[a] Believed to undergo α decay with a half-life period $>1.8 \times 10^{20}$ y (?)
[b] Believed to undergo α decay with a half-life period $>4.1 \times 10^{18}$ y (?)
[c] Believed to undergo α decay with a half-life period $>1.7 \times 10^{20}$ y (?)
[d] Believed to undergo α decay with a half-life period $>8 \times 10^{19}$ y (?)
[e] Primordial radionuclide

The nuclear magnetic resonance (NMR) characteristics for ^{183}W are:

Relative sensitivity ($^{1}H = 1$)	7.20×10^{-4}
Recepticity ($^{13}C = 1$)	0.0589
Gyromagnetic ratio, rad T^{-1} s^{-1}	1.1145×10^{7}
Frequency ($^{1}H = 100$ MHz; 2.3488 T), MHz	4.161
Reference	WF_6 [87]

Nuclear physical properties of tungsten (isotopic mass range, total number of isotopes, thermal neutron macroscopic cross sections, moderating ability and capture resonance integral), compared with other ultra-high temperature elements (carbon and refractory metals), are given in Addendum.

3.6 Chemical Properties

The comprehensive information on the chemical properties and interaction of tungsten with all the elements of the periodic table is given in Table 3.5. The tungsten containing systems and corresponding binary compounds is described and considered there in accordance with the groups of elements from 1 to 17.

Table 3.5 Chemical interaction of tungsten with elements of the periodic table (binary systems in accordance with the groups of elements)[a]

System	Type of phase diagram (constituent phases, temperatures and compositions of transformations)	Character of interaction	References
Group 1			
W–H	H, WH_x (?), W No diagram plot	No chemical interaction at high and ultra-high temp. (up to melt. point) under standard pressure. At cryogenic temp. and low pressures, a distinct amount of H is adsorbed. The adsorption declines with temp. growth; at higher temp. the solubility of H in W is very low. Increasing H content in W results in a loss of mechanical strength. The isobaric solubility of H (x, at.%) is obeyed the following rules at 900–1750 °C, 0.1–10 MPa: $\lg x = 0.5\lg p - 1.49 - 5250/T$, at 1600–2430 °C, 0.1–10 MPa: $\lg x = 0.5\lg p - 3.62 - 1090/T$, at 2430–3400 °C, 0.1–10 MPa: $\lg x = 0.5\lg p - 2.40 - 4380/T$, where p is pressure H_2, Pa, and T is temp., K. Metastable WH is synthesized at ultra-high pressures (>15 GPa).	[19, 36–39, 265, 323]

(continued)

Table 3.5 (continued)

System	Type of phase diagram (constituent phases, temperatures and compositions of transformations)	Character of interaction	References
W–Li	α-Li, β-Li, γ-Li, no binary compounds, W No diagram plot	No chemical interaction. At 715 °C the solubility of W in liquid Li was found at $\sim 4 \times 10^{-3}$ at.%; for 650–1150 °C the calculated values of this solubility are in the interval from 10^{-6} to 10^{-11} at.%. The solubility of Li in W is very low too. W is resistant to liquid Li, satisfactory results were gained in the static conditions during 100 and 1000 h exposure testing at 1210–1490 °C.	[5, 40–41, 87]
W–Na	α-Na, β-Na, no binary compounds, W No diagram plot	No chemical interaction. The solubility of W in liquid Na is estimated at $\sim 10^{-11}$ at.%. The solubility of Na in W is very low too. W is highly resistant to corrosion in liquid Na at temp. ≤700 °C.	[5, 40, 42, 87]
W–K	K, no binary compounds, W No diagram plot	No chemical interaction. The solubility of W in molten K is very low.	[87]
W–Rb	Rb, no binary compounds, W No diagram plot	No chemical interaction. The solubility of W in molten Rb is very low.	[46, 87]
W–Cs	Cs, no binary compounds, W No diagram plot	No chemical interaction. W is highly resistant to Cs melt and vapour (with low O contamination), good performance during 4000 h at 35 °C, and 500 h at 980 and 1370 °C. Excellent stability against Cs vapour at elevated temp. up to 1900 °C.	[5, 87]
W–Fr	No data	–	–
Group 2			
W–Be	α-Be, β-Be, WBe_{22} (or WBe_{20}, WBe_{24}, incongruent melting, ?), WBe_{12} (< ~ 1750 °C, incongruent melt. point, invariable compos.), $WBe_{2\pm x}$ (< ~ 2250–2520 °C, congruent melt. point, homog. range — 28–36 at.% W), WBe (metastable, ?), W Eutectic $WBe_{2\pm x}$–W (2100 °C, ~ 60 at.% W)	The solubility of W in β-Be is 0.05 at.% and that of Be in W is ~ 3 at.% at 1000–1300 °C and ~ 5 at.% at 2100 °C. The reaction between mixed W and Be powders initiates from 750 to 880 °C, all the binary compounds are formed by diffusion interaction after heat treatment in vacuum or inert gas atmosphere for 4 h exposure at 1100 °C.	[5, 36, 43–46, 87, 264]

(continued)

Table 3.5 (continued)

System	Type of phase diagram (constituent phases, temperatures and compositions of transformations)	Character of interaction	References
W–Mg	Mg, no binary compounds, W No diagram plot	No chemical interaction, at least at temp. <1000 °C. The solubility of W in solid and molten Mg is very low.	[5, 40, 87]
W–Ca	α-Ca, β-Ca, no binary compounds, W No diagram plot	No chemical interaction. The solubility of W in molten Ca is very low.	[5, 43, 87, 194]
W–Sr	α-Sr, β-Sr, no binary compounds, W No diagram plot	No chemical interaction. The solubility of W in molten Sr is very low.	[87, 194]
W–Ba	Ba, no binary compounds, W No diagram plot	No chemical interaction. The solubility of W in molten Ba is very low. In vacuum at 1300 °C, Ba wets W.	[87, 194, 342]
W–Ra	Ra, no binary compounds, W No diagram plot	No interaction.	[194]
Group 3			
W–Sc	α-Sc, β-Sc, no binary compounds, W Eutectic β-Sc–W (1510 °C, ~1.3–2.7 at.% W)	The solubility of W in liquid Sc is 2.1 at.% (1695 °C), 4.5 at.% (1930 °C) and 7.9 at.% (2045 °C), and that of Sc in solid W is ≤0.0165 at.% (at 1625 °C). For diffusion rate in the system at various temp. see Addendum.	[47–48, 87, 398]
W–Y	α-Y, β-Y, no binary compounds, W Eutectic β-Y–W (~1520 °C, ~0.07–0.5 at.% W)	The solubility of W in liquid Y is 0.5 at.% (2100 °C), and that of Y in solid W is <1 at.% (1625 °C). For diffusion rate in the system at various temp. see Addendum.	[46–48, 397]
Lanthanides			
W–La	α-La, β-La, γ-La, no binary compounds, W Eutectic (degenerated) γ-La–W (~920 °C, <0.01 at.% W, ?) Miscibility gap in the liquid state (~1–99 at.% W at ~3390 °C)	The solubility of W in liquid La is 8×10^{-7} at.% at the melt. point of La (920 °C) and 0.025 at.% at 1940 °C.	[40, 46, 48, 87, 350]
W–Ce	α-Ce, β-Ce, γ-Ce, δ-Ce, CeW (?), CeW_2 (?), W Eutectic (degenerated) δ-Ce–W (~795 °C, <0.01 at.% W, ?) Miscibility gap in the liquid state (~3–97 at.% W at 3340 °C)	The solubility of W in liquid Ce is 2.3×10^{-4} at.% at the melt. point of Ce (795 °C) and 0.09 at.% at 1940 °C. At temp. <1200 °C W is highly resistant to corrosion in liquid Ce. For diffusion rate in the system at various temp. see Addendum.	[5, 43, 48–50, 351]

(continued)

Table 3.5 (continued)

System	Type of phase diagram (constituent phases, temperatures and compositions of transformations)	Character of interaction	References
W–Pr	α-Pr, β-Pr, no binary compounds, W Eutectic (degenerated) β-Pr–W (~935 °C, <0.01 at.% W, ?) Miscibility gap in the liquid state (2–98 at.% W at 3355 °C)	The solubility of W in liquid Pr is 1.3×10^{-4} at.% at the melt. point of Pr (935 °C) and 0.09 at.% at 2035 °C.	[46–49, 348]
W–Nd	α-Nd, β-Nd, no binary compounds, W Eutectic (degenerated) β-Nd–W (~1010 °C, $\sim 6 \times 10^{-4}$ at.%, ?)	The solubility of W in liquid Nd is 5.9×10^{-4} at.% at the melt. point of Nd (1010 °C) and 0.25 at.% at 2140 °C.	[40, 46, 48–49]
W–Pm	No data	–	–
W–Sm	α-Sm, β-Sm, γ-Sm, no binary compounds, W Eutectic (degenerated) γ-Sm–W (~1070 °C, <~0.002 at.% W, ?)	The solubility of W in liquid Sm is 1.8×10^{-3} at.% at the melt. point of Sm (1072 °C) and 0.015 at.% at 1765 °C.	[46–47, 49]
W–Eu	Eu, no binary compounds, W Eutectic (degenerated) Eu–W (~820 °C, $<\sim 5 \times 10^{-4}$ at.% W, ?)	The solubility of W in liquid Eu is $<10^{-3}$ at.% at the melt. point of Eu (822 °C) and 9×10^{-4} at.% at 1820 °C (?).	[37, 46, 48–49, 51]
W–Gd	α-Gd, β-Gd, no binary compounds, W Eutectic (degenerated) β-Gd–W (~1310 °C, <~0.02 at.% W, ?)	The solubility of W in liquid Gd is 1.3×10^{-2} at.% at the melt. point of Gd (1311 °C) and 0.225 at.% at 2020 °C.	[37, 46, 48–49]
W–Tb	α′-Tb, α-Tb, β-Tb, no binary compounds, W Eutectic (degenerated) β-Tb–W (~1355 °C, <~0.03 at.% W, ?)	The solubility of W in liquid Tb is 3.2×10^{-2} at.% at the melt. point of Tb (1360 °C) and 0.47 at.% at 2020 °C.	[46–47, 49, 352]
W–Dy	α′-Dy, α-Dy, β-Dy, no binary compounds, W Eutectic (degenerated) β-Dy–W (~1410 °C, <~0.05 at.% W, ?)	The solubility of W in liquid Dy is 6.5×10^{-2} at.% at the melt. point of Dy (1412 °C) and 0.71 at.% at 2075 °C.	[37, 46, 49]
W–Ho	α-Ho, β-Ho, no binary compounds, W Eutectic (degenerated) β-Ho–W (~1470 °C, <~0.1 at.% W, ?)	The solubility of W in liquid Ho is 7.5×10^{-2} at.% at the melt. point of Ho (1470 °C) and 2.22 at.% at 2070 °C.	[37, 46, 49]
W–Er	α-Er, β-Er, no binary compounds, W Eutectic (degenerated) β-Er–W (~1520 °C, <~0.1 at.% W, ?)	The solubility of W in Er is 8.2×10^{-2} at.% at the melt. point of Er (1522 °C) and 1.1 at.% at 2030 °C.	[37, 46, 49]

(continued)

Table 3.5 (continued)

System	Type of phase diagram (constituent phases, temperatures and compositions of transformations)	Character of interaction	References
W–Tm	α-Tm, β-Tm, no binary compounds, W Eutectic (degenerated) β-Tm–W (~1545 °C, <~0.3 at.% W, ?)	The solubility of W in liquid Tm is 0.322 at.% at the melt. point of Tm (1545 °C) and 1.78 at.% at 2095 °C.	[46–49]
W–Yb	α-Yb, β-Yb, γ-Yb, no binary compounds, W Eutectic (degenerated) γ-Yb–W (~820 °C, ?) No diagram plot	The solubility of W in Yb is $<1.9 \times 10^{-4}$ at.% (820–1685 °C) and 7×10^{-4} at.% at 1710 °C.	[46–49]
W–Lu	α-Lu, β-Lu, no binary compounds, W Eutectic (degenerated) β-Lu–W (~1650 °C, <~0.4 at.% W, ?) Miscibility gap in the liquid state (~17–83 at.% W at ~3080 °C)	The solubility of W in liquid Lu is 0.461 at.% at the melt. point of Lu (1656 °C) and 2.24 at.% at 2100 °C.	[40, 46, 48–49, 349]
Actinides			
W–Ac	No data	–	–
W–Th	α-Th, β-Th, no binary compounds, W Eutectic (degenerated, ?) β-Th–W (~1385–1700 °C, ~0.01–8 at.% W, ?) Data on the system available in literature are controversial.	The solid solubility of Th in W is 0.09 at.% at 1250 °C and 0.24 at.% at 2000 °C. In vacuum, molten Th wets W. For diffusion rate in the system at various temp. see Addendum.	[5, 46–47, 342, 353–356]
W–Pa	No data	–	–
W–U	α-U, β-U, γ-U, no binary compounds, W Peritectic (?) γ-U (~1135-1140 °C, ~0.5–1.5 at.% W, ?) Eutectic (degenerated, ?) γ-U–W (~1135 °C, ?) Data on the system available in literature are controversial	The solid solubility of W in α-U and β-U is negligible and does not affect the temp. of the polymorphic transitions of U. At 1000 °C the solid solubility of U in W is ~0.1 at.% and that of W in γ-U is ~0.2–0.9 at.%. The melt. point of U is raised a little by addition of W (?). The solubility of W in liquid U is 11.9 at.% (2210 °C) and 33.2 at.% (2660 °C). The kinetics of W dissolution in liquid U is very slow. At 1250 °C liquid U impregnates W porous preforms perfectly. For diffusion rate in the system at various temp. see Addendum.	[5, 46–47, 52–53, 193, 357]
W–Np	No data	–	–

(continued)

Table 3.5 (continued)

System	Type of phase diagram (constituent phases, temperatures and compositions of transformations)	Character of interaction	References
W–Pu	α-Pu, β-Pu, γ-Pu, δ-Pu, δ′-Pu, ε-Pu, no binary compounds, W Eutectic (degenerated) ε-Pu–W (~640 °C, ?) Peritectic (?) ε-Pu (?) Data on the system available in literature are controversial	The mutual solid solubilities of Pu in W and W in the modifications of Pu are negligible. W does not affect the temp. of Pu polymorphic transformations. The solubility of W in liquid Pu is 3.8×10^{-3} at.% (700 °C) and 3.8×10^{-2} at.% (950 °C).	[46–47, 54, 358–359]
W–Am	No data	–	–
Group 4			
W–Ti	α-Ti, α′-Ti (metastable martensite, ~0–2 at.% W), α″-Ti (metastable, ~2–5.5 at.% W), ω-(Ti,W) (metastable, intermediate between β-Ti and α-Ti structure, ~6–10 at.% W), β-Ti, TiW_4 (?), W Continuous solid solution β-Ti–W (up to melt. points, miscibility gap: critical point —~1230–1290 °C, 33–35 at.% W; 9.75–72 at.% W at 740 °C)	For the alloys containing 10–50 at.% W, the melt. point increases to 1800–1900 °C. In the presence of W temp. of α-Ti–β-Ti polymorphic transformation decreases to 740 °C (9.75 at.% W). The max. solubility of W in α-Ti is ≤0.2 at.% (740 °C), it corresponds to the ~25 at.% solubility of Ti in W at the same temp. The corrosion resistance of W to liquid Ti is low. For diffusion rate in the system at various temp. see Addendum.	[5, 46–47, 55–56, 87, 211, 292]
W–Zr	α-Zr, β-Zr, ZrW_2 (<~2160–2210 °C, incongruent melt. point, invariable compos.), W Eutectic ZrW_2–β-Zr (~1735–1795 °C, ~9–10 at.% W)	The solid solubility of W in β-Zr is ~4 at.% at ~1735–1795 °C) and ~0.25 at.% at 863 °C, the max. solubility in α-Zr is 0.5 at.%. The solubility of Zr in W is ~3.5–10.0 at.% (~2160–2210 °C), ~1.5 at.% (~1735–1795 °C) and ~0.9 at.% (1500 °C). For diffusion rate in the system at various temp. see Addendum.	[5, 46–47, 57–59, 87]
W–Hf	α-Hf, β-Hf, $HfW_{2\pm x}$ (<~2495–2530 °C, incongruent melt. point, Laves phase, homog. range—66–67 at.% W), W Eutectic $HfW_{2\pm x}$–β-Hf (~1930–1980 °C, ~18–22 at.% W)	The solid solubility of W in β-Hf is ~13.5 at.% (~1930–1980 °C) and ~8 at.% (~1460–1560 °C), and solubility in α-Hf is ~0.7–0.9 at.% (~1460–1560 °C). The solubility of Hf in W is ~9 at.% (~2495–2530 °C), ~1.7–4.0 at.% (2000 °C) and ~1.1–3.0 at.% (1500 °C). For diffusion rate in the system at various temp. see Addendum.	[5, 37, 46, 57, 60–61, 87]

(continued)

Table 3.5 (continued)

System	Type of phase diagram (constituent phases, temperatures and compositions of transformations)	Character of interaction	References
Group 5			
W–V	V, no binary compounds, W Continuous solid solution V–W	For diffusion rate in the system at various temp. see Addendum.	[5, 46–47, 62, 394]
W–Nb	Nb, no binary compounds, W Continuous solid solution Nb–W	For diffusion rate in the system at various temp. see Addendum.	[5, 40, 46, 63–64]
W–Ta	Ta, no binary compounds, W Continuous solid solution Ta–W	For diffusion rate in the system at various temp. see Addendum.	[5, 46–47, 65]
Group 6			
W–Cr	Cr, CrW_3 (?), W Continuous solid solution Cr–W (up to melt. points, miscibility gap: critical point—1677 °C, 50 at.% W; from ~4.5–5 to ~95–95.5 at.% W at 500 °C)	W is resistant to the vapour of Cr at high temp. in vacuum. For diffusion rate in the system at various temp. see Addendum.	[5, 37, 46, 66–68, 87]
W–Mo	Mo, no binary compounds, W Continuous solid solution Mo–W	For diffusion rate in the system at various temp. see Addendum.	[40, 46, 63, 69–71]
Group 7			
W–Mn	α-Mn, β-Mn, γ-Mn, δ-Mn, no binary compounds, W No diagram plot	α-Mn possesses a large solid solubility in W at 800 °C (?). No solubility of W in liquid Mn (?). For diffusion rate in the system at various temp. see Addendum.	[5, 40, 72, 319]
W–Tc	Tc, σ-$Tc_{3\pm x}W$ (<~1900 °C, homog. range—~24.5–26.5 at.% W at 1800 °C, ~22.5–33.0 at.% W at 1200 °C and ~22–35 at.% W at 1000 °C), W Eutectic σ-$Tc_{3\pm x}W$–W (~1800 °C, ~37 at.% W)	The solid solubility of W in Tc is ~14 at.% at 1900 °C and ~7 at.% at 1200 °C, and that of Tc in W is ~55 at.% at 1800 °C and ~33 at.% at 1200 °C.	[46–47, 73, 360]

(continued)

Table 3.5 (continued)

System	Type of phase diagram (constituent phases, temperatures and compositions of transformations)	Character of interaction	References
W–Re	Re, χ-WRe_{3-x} (<2125–2130 °C, homog. range—~25–28 at.% W at 1100 °C and ~26–28 at.% W at 1500 °C), σ-$W_2Re_{3\pm x}$ (<~2890–3005 °C, incongruent melt. point, homog. range—from ~28.5–35 to ~45–56.5 at.% W at 2000 °C and from ~34 to ~60 at.% W at 1100 °C), W Extended solid solution based on Re (up to ~15–20 at.% W at ~2815–2830 °C) Extended solid solution based on W (up to ~37–45 at.% Re at ~2890–3005 °C) Eutectic σ-$W_2Re_{3\pm x}$–Re (~2815–2830 °C, ~25–26 at.% W)	The solid solubility of W in Re is ~15–20 at.% (~2800–2830 °C), ~9–11 at.% (~1600–2100 °C) and ~4.5 at.% (1100 °C). The solid solubility of Re in W is ~37–45 at.% (~2800–3000 °C) and ~28–32 at.% (~1100–1600 °C). For diffusion rate in the system at various temp. see Addendum.	[46–47, 57, 74–77]
Group 8			
W–Fe	α-Fe (δ-Fe), γ-Fe, λ-Fe_2W (≤~1060 °C, Laves phase, metastable), μ-Fe_7W_{6-x} (or Fe_3W_2, ~1190–1635 °C, incongruent melt. point, homog. range—from 39 to ~40.5–44.5 at.% W, metastable, ?), δ-$FeW_{1\pm x}$ (~400–1215 °C, homog. range—~48.5–52.5 at.% W, ?), W	W stabilizes α-Fe modification, increasing the temp. of α-Fe–γ-Fe transformation and decreasing the temp. of γ-Fe–δ-Fe transformation (γ-Fe region is locked by α-Fe region). The max. solid solubility of W in γ-Fe is 1.46 at.% (1140 °C). The max. solubility of W in α-Fe is 14.3 at.% (1548 °C), it declines with temp. decrease to 4.6 at % (1190 °C). The max. solid solubility of Fe in W is ~2.6 at.% (1635 °C). For diffusion rate in the system at various temp. see Addendum.	[5, 37, 46, 78–79, 87, 199]

(continued)

Table 3.5 (continued)

System	Type of phase diagram (constituent phases, temperatures and compositions of transformations)	Character of interaction	References
W–Ru	Ru, σ-$Ru_2W_{3\pm x}$ ($\sim$1670–2300 °C, incongruent melting, homog. range—$\sim$59–63 at.% W at 1700 °C, $\sim$58.5–68.5 at.% W at 1920 °C and $\sim$59–67 at.% W at 2100 °C), W Extended solid solution based on Ru (up to $\sim$48 at.% W at 2205 °C) Extended solid solution based on W (up to $\sim$23 at.% Ru at $\sim$2300 °C) Eutectic σ-$Ru_2W_{3\pm x}$–Ru (2205 °C, $\sim$55 at.% W)	The solid solubility of W in Ru declines from $\sim$48 at.% (2205 °C) to $\sim$42 at.% ($\sim$1670 °C), and that of Ru in W declines from $\sim$23 at.% ($\sim$2300 °C) to $\sim$13 at.% ($\sim$1670 °C).	[5, 46–47]
W–Os	Os, σ-$OsW_{3\pm x}$ (<2945 °C, incongruent melt. point, homog. range—$\sim$64–79 at.% W at 2725 °C and $\sim$65–80 at.% W at 1000 °C), W Extended solid solution based on Os (up to $\sim$55 at.% W at $\sim$2725 °C) Extended solid solution based on W (up to $\sim$18.5 at.% Os at $\sim$2945 °C) Eutectic σ-$OsW_{3\pm x}$–Os ($\sim$2725 °C, $\sim$58 at.% W)	The solid solubility of W in Os declines from $\sim$55 at.% ($\sim$2725 °C) to $\sim$32 at.% (1200 °C), and that of Os in W declines from $\sim$18.5 at.% ($\sim$2945 °C) to $\sim$6 at.% (1200 °C). For diffusion rate in the system at various temp. see Addendum.	[40, 46, 80–82, 87]
Group 9			
W–Co	ε-Co, α-Co, κ-$Co_{3\pm x}W$ (<$\sim$1090–1100 °C, homog. range—22.9–25.3 at.% W), μ-$Co_7W_{6\pm x}$ (<$\sim$1690 °C, incongruent melt. point, homog. range—43.3–48.5 at.% W), Co_2W_3 (?), W Eutectic μ-$Co_7W_{6\pm x}$–α-Co (1470 °C, $\sim$21 at.% W)	The presence of W results in decrease in the temp. of Co magnetic transformation, but does not affect the temp. of α-Co–ε-Co transformation. In the alloys with W content <8 at.% the α-Co–ε'-Co martensite transformation is observed. The solubility of W in α-Co is $\sim$17.5 at.% (1470 °C), 13.0 at.% (1093 °C), 4.0 at.% (865 °C), and solubility in ε-Co is $\sim$1 at.% (350 °C). The max. solubility of Co in W is 0.9 at.% (1690 °C). For diffusion rate in the system at various temp. see Addendum.	[5, 37, 46, 83–85, 396]

(continued)

Table 3.5 (continued)

System	Type of phase diagram (constituent phases, temperatures and compositions of transformations)	Character of interaction	References
W–Rh	Rh, Rh_3W (from ~1200 °C to ?, ordered phase, ?), ε-$Rh_{2\pm x}W$ (<~2250–2255 °C, congruent melt. point corresp. to $RhW_{1.0}$, homog. range—43–58 at.% W at 2240 °C, 19–53 at.% W at 2000 °C and 20.5–42.5 at.% W at 1200 °C), W Peritectic Rh (~2075–2125 °C, ~19 at.% W) Extended solid solution based on Rh (up to ~19 at.% W at ~2100 °C) Extended solid solution based on W (up to ~6 at.% Rh at ~2240 °C) Eutectic ε-$Rh_{2\pm x}W$–W (~2240 °C, ~67 at.% W)	The presence of W results in increase in the melt. temp. of Rh. The max. melt. point (~2100 °C) and max. solid solubility of W in Rh (~19 at.%) are corresponding to the peritectic alloy.	[5, 46–47, 86–87]
W–Ir	Ir, δ-$Ir_{3-x}W$ (?), β-$Ir_3W_{2\pm x}$ (<~2500 °C, congruent melt. point corresp. to $IrW_{1.4}$, homog. range—~22–66 at.% W at 2300–2400 °C, ~22–57 at.% W at ~1815 °C and ~19–53 at.% W at ~1200 °C), ε-$IrW_{1\pm x}$ (?), σ-$IrW_{3\pm x}$ (from 1795–1850 °C to 2520–2570 °C, incongruent melt. point, homog. range—~75–77 at.% W at 2200–2300 °C), W Extended solid solution based on Ir (up to ~19 at.% W at ~2310 °C) Extended solid solution based on W (up to ~10 at.% Ir at ~2545 °C) Eutectic β-$Ir_3W_{2\pm x}$–Ir (~2285–2335 °C, 21 at.% W) Eutectic β-$Ir_3W_{2\pm x}$–σ-$IrW_{3\pm x}$ (~2440–2490 °C, ~70 at.% W)	The presence of W results in decrease in the melt. temp. of Ir alloys. The solubility of W in Ir declines with temp. decreasing: 13.7 at.% (1300 °C), 12.6 at.% (1100 °C) and 11.5 at.% (900 °C). The solid solubility of Ir in W is ~6 at.% (2800 °C), ~10 at.% (max. solubility corresp. to ~2545 °C, peritectic temp. of σ-phase), ~4–5 at.% (~1815 °C), ~2 at.% (1400 °C) and ~1 at.% (1000 °C). For diffusion rate in the system at various temp. see Addendum.	[5, 40, 46, 88]

(continued)

Table 3.5 (continued)

System	Type of phase diagram (constituent phases, temperatures and compositions of transformations)	Character of interaction	References
Group 10			
W–Ni	Ni, Ni_6W (?), β-$Ni_{4+x}W$ (<970 °C, homog. range—18–19.4 at.% W at 200–600 °C), δ-NiW_{1-x} (<~1060 °C, homog. range—49–50 at.% W at 200–900 °C), γ-NiW_2 (<~1025 °C, limited homog. range near 66 at.% W), W Eutectic Ni–W (~1490–1510 °C, 20.7 at.% W)	The direct interaction between W and Ni results in the formation of β-phase. The solid solubility of W in Ni declines with temp. decreasing: 17.5 at.% (~1490–1510 °C), 16.3 at.% (970 °C), 13.1 at.% (800 °C), 12.0 at.% (600 °C) and 11.8 at.% (500 °C). The solubility of Ni in W is 0.6 at.% (1925 °C), 0.5 at.% (1640 °C), and 0.2–0.3 at.% (1500 °C). For diffusion rate in the system at various temp. see Addendum.	[5, 40, 46, 88–90, 399]
W–Pd	Pd, no binary compounds, W Peritectic Pd (~1805–1825 °C, ~20–22 at.% W)	The presence of W results in increase in the melt. temp. of Pd. The max. melt. point (~1815 °C) and max. solid solubility of W in Pd (~20–22 at.%) are corresponding to the peritectic alloy. The solubility of W in Pd declines slightly with temp. decreasing; at 1100 °C it amounts to ~16.0–21.5 at.%. The solubility of Pd in W is ~3.6–5.0 at.% at 1805–1825 °C) and ~2.7 at.% at 1500 °C. In vacuum, molten Pd wets W.	[5, 40, 46, 91, 342]
W–Pt	Pt, γ-Pt_2W (~1400 °C, ?), ε-PtW (~1400 °C, ?), W Peritectic Pt (~2460–2465 °C, ~60–64 at.% W)	The presence of W results in increase in the melt. temp. of Pt. The max. melt. point (~2460–2465 °C) and max. solid solubility of W in Pt (~60–64 at.%) are corresp. to the peritectic alloy. At 2460–2465 °C, the solubility of Pt in W is ≤~3.5–5.0 at.%.	[5, 46–47, 92]

(continued)

Table 3.5 (continued)

System	Type of phase diagram (constituent phases, temperatures and compositions of transformations)	Character of interaction	References
Group 11			
W–Cu	Cu, no binary compounds, W Eutectic (degenerated, ?) Cu–W (~1084 °C, ?) Miscibility gap in the liquid state (from ~3–4 to ~91–93 at.% W at ~3240–3250 °C)	The mutual solid solubilities of W and Cu are extremely low. The solubility of W in molten Cu is negligible; no wetting in standard conditions at temp. >1100 °C. In ultra-high vacuum, the wetting angle of molten pure Cu on W: 40.0° (with special cleaning surface) and 53.5° (without cleaning). For diffusion rate in the system at various temp. see Addendum.	[5, 37, 87, 109–114, 342–343]
W–Ag	Ag, no binary compounds, W Miscibility gap in the liquid state (~1–99 at.% W at ~3400 °C)	The mutual solid solubilities of W and Ag are negligible. No solubility of W in molten Ag; no wetting in standard conditions. In ultra-high vacuum the wetting angle of molten pure Ag on W: 24.7° (with special cleaning surface) and 58.6° (without cleaning).	[5, 43, 87, 93, 342–343]
W–Au	Au, no binary compounds, W Eutectic (degenerated) Au–W (~1063 °C, ~0.14 at.% W, ?)	The mutual solid solubilities of W and Au are negligible. No solubility of W in molten Au. In ultra-high vacuum the wetting angle of molten pure Au on W: 21.8° (with special cleaning surface) and 25.3° (without cleaning).	[43, 46, 87, 343, 361]
Group 12			
W–Zn	Zn, no binary compounds, W No diagram plot	No interaction at least at temp. <1350 °C. W is not dissolved and wetted by molten Zn. W is highly resistant to corrosion and erosion in liquid Zn (after 50 h exposure at 700 °C weight loss of W amounts to 0.04 %).	[5, 46–47, 87, 94]
W–Cd	Cd, no binary compounds, W No diagram plot	No interaction.	[87]
W–Hg	Hg, no binary compounds, W No diagram plot	Practically, no interaction between W and molten (or vaporized) Hg in the wide range of temp. up to 1000 °C. At room temp. the solubility of W in Hg is $<10^{-5}$ at.%. W is highly resistant to corrosion and erosion in Hg.	[5, 37, 87, 95]

(continued)

Table 3.5 (continued)

System	Type of phase diagram (constituent phases, temperatures and compositions of transformations)	Character of interaction	References
Group 13			
W–B	β-B, $WB_{\sim 12}$ (<2440 °C, congruent melt. point, ?), WB_{4+x} (or $W_{1-x}B_3$, $W_{2-x}B_9$, <~1990–2050 °C, incongruent melt. point, homog. range—~18–20 at.% W), α-W_2B_{5-x} (<~900–1500 °C, metastable,?), β-W_2B_{5-x} (or WB_{2-x}, ε-phase, from ~900–1500 °C to ~2300–2380 °C, congruent melt. point corresp. to ~$WB_{2.1}$, homog. range—~32.5–33.5 at.% W at ~2340 °C, ~32–33.5 at.% W at 2170 °C and ~31.5–33.5 at.% W at 1800 °C), α-$WB_{1\pm x}$ (<1960–2400 °C, the temp. of polymorphic transformation increases with the growth of B content, homog. range—~48–51.5 at.% W at 2110–2170 °C and ~50–51 at.% W at 1800 °C), β-$WB_{1\pm x}$ (from 1960–2170 °C to ~2650–2860 °C, congruent melt. point corresp. to ~$WB_{0.9}$, homog. range—~48–52.5 at.% W at ~2340 °C and ~49–52.5 at.% W at 2110–2170 °C), $W_{2\pm x}B$ (<~2650–2770 °C, congruent melt. point corresp. to ~$WB_{0.5}$, homog. range—~66–68 at.% W at 2580–2600 °C, ~67–67.5 at.% W at 2110 °C and ~66.5–67.5 at.% W at 1800 °C), W Eutectic $WB_{\sim 12}$–β-B (~2100 °C, ?) Eutectic WB_{4+x}–β-B (~1900–1990 °C, ~4–9 at.% W) Eutectic $WB_{\sim 12}$–β-W_2B_{5-x} (~2270–2290 °C, ?)	The max. solid solubility of B in W is 0.1–0.2 at.% at 2600 °C and that of W in B is ≤1 at.%. Direct interaction between W and B at 500–1200 °C in vacuum, H_2 or inert gas atmosphere results in the formation of the borides. For diffusion rate in the system at various temp. see Addendum.	[5, 36, 43, 46, 87, 96–98, 102, 160–161, 210, 305, 319, 329]

(continued)

Table 3.5 (continued)

System	Type of phase diagram (constituent phases, temperatures and compositions of transformations)	Character of interaction	References
	Eutectic β-$WB_{1\pm x}$–β-W_2B_{5-x} ($\sim$2330–2345 °C, $\sim$36–38 at.% W) Eutectic $W_{2\pm x}B$–β-$WB_{1\pm x}$ ($\sim$2570–2590 °C, $\sim$56–59 at.% W) Eutectic $W_{2\pm x}B$–W ($\sim$2590–2650 °C, $\sim$72–75 at.% W)		
W–Al	Al, γ-WAl_{12} (<697 °C, incongruent melt. point, invariable compos.), β-WAl_{12} (metastable, ?), β'-WAl_{12} (metastable, ?), δ-WAl_{5-x} (<870–871 °C, incongruent melt. point corresp. to $\sim WAl_{4.6}$, homog. range—17–18 at.% W), ε-$WAl_{4\pm x}$ (<$\sim$1325 °C, incongruent melt. point corresp. to $\sim WAl_{3.7}$, homog. range—19–22.5 at.% W), ζ-$WAl_{3\pm x}$ ($\sim$1300–1345 °C, incongruent melt. point corresp. to $\sim WAl_{3.0}$, homog. range—24–25.5 at.% W), η-$W_3Al_{7\pm x}$ ($\sim$1325–1420 °C, incongruent melt. point corresp. to $\sim WAl_{2.3}$, homog. range—29–30.5 at.% W), θ-$WAl_{2\pm x}$ ($\sim$1335-1650 °C, incongruent melt. point corresp. to $\sim WAl_{1.7}$, homog. range—31–37 at.% W), W Peritectic Al (660.5 °C, 0.0235 at.% W)	The solid solubility of W in Al is $\sim$0.02–0.25 at.% (550–650 °C), and that of Al in W is $\sim$15 at.% (1100–1400 °C). At higher temp. the solid solubility of Al in W declines considerably. The reaction between W and Al initiates at temp. >650–680 °C. In vacuum W is wetted by molten Al poorly and reacts mildly; however, at higher temp. the corrosion resistance of W is low, as W dissolves in molten Al.	[5, 36, 43, 46, 87, 99, 333, 342]
W–Ga	Ga, no binary compounds, W Eutectic (degenerated) Ga–W ($\sim$29 °C, ?)	No interaction in solid state at common conditions. The solubility of W in liquid Ga is $(0.4 \div 3.0) \times 10^{-3}$ at.% (815 °C). W is highly resistant to corrosion in Ga. The metastable binary compounds were synthesized under high pressures (7.7 GPa).	[5, 37, 100, 362]

(continued)

Table 3.5 (continued)

System	Type of phase diagram (constituent phases, temperatures and compositions of transformations)	Character of interaction	References
W–In	In, no binary compounds, W No diagram plot	Practically, no interaction. At 600 °C the solubility of W in molten In is $\sim 10^{-6}$ at.%.	[46, 87, 297]
W–Tl	α-Tl, β-Tl, no binary compounds, W No diagram plot	No interaction. The solubility of W in Tl melt is negligible.	[46, 87]
Group 14			
W–C	See C–W in Table 2.13.		
W–Si	Si, WSi_2 ($<\sim$2020–2180 °C, congruent melt. point, invariable compos.), W_2Si_3 (?), W_5Si_{3+x} (or W_3Si_{2-x}, $<\sim$2095–2370 °C, congruent melt. point corresp. to $\sim WSi_{0.6}$, homog. range—60–62.5 at.% W), W_5Si_2 (?), W_5Si (?), W Eutectic WSi_2–Si ($\sim$1390–1400 °C, $\sim$0.8–2.6 at.% W) Eutectic WSi_2–W_5Si_{3+x} ($\sim$1940–2010 °C, $\sim$41–47 at.% W) Eutectic W_5Si_{3+x}–W ($\sim$2085–2210 °C, $\sim$68–80 at.% W)	The solid solubility of W in Si is very low. The max. solid solubility of Si in W amounts to $\sim$5.5 at.% at 2085–2210 °C; at higher and lower temp. the solubility of Si declines considerably. W silicides are synthesized directly from the elements in vacuum or inert gas atmosphere at 1100–1500 °C. In vacuum, at 1400–1600 °C the contact interaction between W and WSi_2 compact bodies is intensive. For diffusion rate in the system at various temp. see Addendum.	[5, 36, 46–47, 87, 101–102, 327]
W–Ge	Ge, WGe_2 (?), W_2Ge_3 ($<\sim$750 °C, invariable compos., ?), W_5Ge_3 (?), W Eutectic (degenerated) Ge–W ($\sim$935 °C, ?)	The solid solubility of W in Ge is very low. The solubility of W in liquid Ge at 1700 °C is $\sim$3–6 at.%. The max. solubility of Ge in W is $\sim$3 at.% at 935 °C. In vacuum, molten Ge wets W, which is highly resistant to corrosion in Ge.	[5, 36–37, 46, 87, 342, 363]
W–Sn	α-Sn, β-Sn, no binary compounds, W No diagram plot	No interaction in solid and liquid states at temp. <1680 °C. At 2000 °C the solubility of W in molten Sn is $\sim 10^{-3}$ at.%. In H_2 at temp. $\geq$1000 °C, Sn wets W well (contact angle <90°).	[5, 46–47, 87, 342]

(continued)

Table 3.5 (continued)

System	Type of phase diagram (constituent phases, temperatures and compositions of transformations)	Character of interaction	References
W–Pb	Pb, no binary compounds, W Eutectic (degenerated, ?) Pb–W (~328 °C, ?)	The solubility of W in Pb is $\leq 6 \times 10^{-3}$ at.% (1200 °C). In H_2 at temp. ≥1000 °C, molten Pb wets W well (contact angle <90°). The data available in literature on the stability of W in molten Pb are controversial.	[5, 40, 46, 87, 241, 284, 342]
Group 15			
W–N	N, δ_R^V–WN_2 (or WN_2, invariable compos.), δ_H^{IV}-WN_{1+x} (or $WN_{1.67}$, metastable, invariable compos.), δ_H^{III}-WN_{1+x} (or $WN_{1.56}$, metastable, invariable compos.), W_2N_3 (or $WN_{1.5}$, metastable, invariable compos.), γ'-WN_{1+x} (or γ-W_3N_4, $WN_{1.33}$, metastable, invariable compos.), γ-WN (or δ-WN, $WN_{1.0}$, <~985–1020 °C, invariable compos.), δ-WN_{1-x} (or $WN_{\leq 1.0}$, <600 °C), β-$W_{2\pm x}N$ (or γ-WN_x, $WN_{0.67-1.0}$, from ~285–290 °C to ~1880–1875 °C, homog. range—~50–70 at.% W, ?), δ_H^{IV}-WN_{1-x} (or $WN_{0.91}$, metastable, invariable compos.), δ_R^{VI}-WN_{1-x} (or $WN_{0.85}$, metastable, invariable compos.), δ_H^{I}*-WN_{1-x} (or $WN_{0.74}$, superlattice, metastable, invariable compos.), δ_H^{I}-WN_{1-x} (or $WN_{0.74\text{-}0.87}$, metastable, homog. range—53–57 at.% W), δ_H^{II}-W_2N (or $WN_{0.5}$, metastable, invariable compos.), W	The solubility of N in W ($0.001 < x$, at.% <0.01) in the range of temp. 2400–3050 °C is obeyed the rule: $\lg x = 0.5\lg p - 0.036 - 10200/T$, where p is pressure N_2, MPa, and T is temp., K. However, in general, the data available in the literature on the solubility of N in W are controversial. The W nitrides are synthesized mainly by the interaction of W with NH_3. Only WN_2 is formed directly by the reaction with N_2 at temp. >2000 °C. For the most part, the W nitrides are not stable at higher temp., decomposing rapidly, in vacuum and under lower pressures especially.	[5, 36, 40, 103–108, 265, 364–365]

(continued)

Table 3.5 (continued)

System	Type of phase diagram (constituent phases, temperatures and compositions of transformations)	Character of interaction	References
W–P	P, α-WP_2, β-WP_2, WP, W_2P (?), W_3P (?), W No diagram plot	W phosphides are synthesized from the elements at 700–950 °C. The compounds decompose in vacuum at higher temp. For diffusion rate in the system at various temp. see Addendum.	[5, 36, 40, 87]
W–As	As, WAs_2 (<800 °C), W_2As_3, W_4As_5, W_2As (?), W No diagram plot	No solubility of As in W. Only WAs_2 and W_2As_3 could be synthesized from the elements (at 600–620 °C). W arsenides exhibit no homog. range.	[36, 43, 87, 115]
W–Sb	Sb, WSb (?), W	In vacuum at temp. >1200 °C, molten Sb wets W. Data on the interaction between W and Sb available in literature are controversial.	[46–47, 115, 342, 366]
W–Bi	Bi, no binary compounds, W No diagram plot	At temp. <800 °C, no solubility of W in liquid Bi. At 1000 °C W is highly resistant to corrosion in Bi. In H_2 at temp. ≥1000 °C, molten Bi wets W very slowly (contact angle decreases during the wetting process).	[5, 43, 87, 115, 342]
Group 16			
W–O	O, μ-WO_3 (or WO_3(M), <−143°C, ?), λ-WO_3 (or WO_3(L), <−143 °C, ?), κ-WO_3 (or WO_3(K), <−143 °C, ?), θ-WO_3 (or WO_3(H), <−143 °C, ?), η-WO_3 (or WO_3(G), (−143) to (−40) °C), ζ-WO_3 (or WO_3(F), (−40) to (+17) °C), ε-WO_{3-x} (or WO_3(E), 17–330 °C), δ-WO_{3-x} (or WO_3(D), 330–740 °C), γ-WO_{3-x} (or WO_3(C), 740–900 °C, homog. range—26.9–27.2 at.% W), β-WO_{3-x} (or WO_3(B), 900–1230 °C, homog. range—25.6–26 at.% W), α-WO_{3-x} (or WO_3(A), from 1230 to ~1474–2130 °C (?), congruent melt. point, homog. range—25.0–25.2 at.% W), $W_{40}O_{118}$ (?), W_nO_{3n-1}	The solubility of O in W is absolutely negligible. The reaction between W and O starts at ~400 °C. In terms of rate equations the initial oxidation of W at the temp. ≤500 °C is parabolic and results in the formation of dense protective oxide scales. Subsequently with temp. growth the oxidation process shifts to the linear law and formation of outer porous layer of WO_3 without protective properties. At the temp. <1000 °C the formation of solid double-layered (dense and porous) oxide scales is observed. At the higher temp. the vaporization of oxide scales takes on greater importance,	[5, 36, 40, 46, 87, 116–125, 147, 241, 265, 275, 284, 367]

(continued)

Table 3.5 (continued)

System	Type of phase diagram (constituent phases, temperatures and compositions of transformations)	Character of interaction	References
	~600–1400 °C, ?), W_nO_{3n-2} homologous series of oxides (or Magneli's phases, e.g., $W_{25}O_{73}$, $W_{24}O_{70}$, $W_{20}O_{58}$, from ~500 to ~1600 °C, congruent melt. point corresp. to ~$WO_{2.91}$), $W_{24}O_{68}$ (from ~600–800 °C to ~1300–1500 °C, invariable compos.), $W_{18}O_{49}$ (or $WO_{2.72}$ from 585 to ~1600–1900 °C, melt. point, invariable compos., ?), $WO_{2\pm x}$ (<~1230–1570 °C (?), incongruent melt. point, homog. range—~29–48 at.% W, ?), W_3O (?), W Eutectic α-WO_{3-x}–W_nO_{3n-2} (~1460 °C, ~25.2 at.% W) Eutectic $W_{18}O_{49}$–W_nO_{3n-2} (~1590 °C, ~25.9 at.% W)	vaporization equalize with each other. In air at atmospheric pressure the highly intensive oxidation of W begins from 800 to 1000 °C. For diffusion rate in the system at various temp. see Addendum.	
W–S	α-S, β-S, WS_3 (<~300–400 °C, invariable compos.), α-WS_2 (?), β-WS_{2-x} (<~2400 °C, congruent melt. point at the high equilibrium pressure of S vapour, or ~1800 °C, at the low pressure of S vapour; homog. range—33.3–33.9 at.% W), $W_{21}S_8$ (?), $W_{14}S_5$ (?), W Eutectic WS_{2-x}–W (~1800–2000 °C, or 1480 °C at the low pressure of S vapour, ~40–60 at.% W) Miscibility gap in the liquid state (critical point—~2800 °C, ~65–75 at.% W; from ~55–58 to ~85–88 at.% W at ~2100–2400 °C) Miscibility gap in the liquid state (critical point—?; from ~24–26 to ~2–4 at.% W at ~1150 °C)	Practically, no mutual solid solubilities between the elements. Molten and vapour S attacks W slowly. β-WS_{2-x} is synthesized by the interaction of W powder with S vapour at ~700–900 °C. Powder mixtures start reacting at ~400 °C. Nanotubes constructed from β-WS_{2-x} have been prepared. For diffusion rate in the system at various temp. see Addendum.	[5, 36, 46–47, 87, 126, 279–281, 368]

(continued)

Table 3.5 (continued)

System	Type of phase diagram (constituent phases, temperatures and compositions of transformations)	Character of interaction	References
W–Se	Se, WSe_3 (invariable compos.), WSe_{2-x} (homog. range—33.4–33.9 at.% W), WSe, W No diagram plot	Practically, no mutual solid solubilities. WSe and WSe_{2-x} are synthesized directly from the elements; W–Se mixtures start reacting at 300–400 °C. WSe_{2-x} decomposes at temp. >850 °C. Nanotubes constructed from WSe_{2-x} have been prepared.	[5, 36, 47, 87, 298]
W–Te	Te, WTe_2 (<1005–1035 °C, incongruent melt. point, invariable compos., ?), W Peritectic Te (~451 °C, ?)	Practically, no mutual solid solubilities. WTe_2 is synthesized from the elements; W–Te mixtures react slowly at 600–700 °C.	[36, 46–47, 87]
W–Po	α-Po, β-Po, no binary compounds, W Eutectic (degenerated, ?) Po–W (~255 °C, ?) No diagram plot	Practically, no mutual solid solubilities of the components. No interaction with Po vapours at temp. ≤700 °C.	[46–47]
Group 17			
W–F	F, α-WF_6 (<−8 °C), β-WF_6 (from −8 to +2 °C, melt. point, invariable compos.; boil. point +17 °C), WF_5 (?), WF_4 (invariable compos.), W No diagram plot	At room temp. the direct interaction between W and F_2 results in the formation of WF_6. WF_4 is synthesized by indirect chemical reaction pathways.	[2–3, 36, 87, 369–372]
W–Cl	Cl, α-WCl_6 (<150 °C), β-WCl_6 (from 150 to ~275–285 °C, melt. point, invariable compos.), WCl_5 (or W_xCl_{5x}, <248 °C, melt. point, invariable compos.), WCl_4 (invariable compos.), WCl_3 (or W_6Cl_{18}, ?), WCl_2 (or W_6Cl_{12}, high melt. point, invariable compos.), W No diagram plot	At 250–300 °C the direct interaction between W and Cl_2 results in the formation of WCl_6. WCl_2 is a dominant product at temp. >1600–1700 °C. Other W chlorides are synthesized by special chemical reaction pathways.	[2–3, 36, 87, 373, 393]
W–Br	Br, WBr_6 (<309 °C, melt. point, invariable compos.), WBr_5 (<295 °C, melt. point, invariable compos.), WBr_4 (invariable compos.), WBr_3 (invariable compos.), W_3Br_8 (or W_6Br_{16}, ?), W_3Br_7 (or W_6Br_{14}, ?), WBr_2 (or W_6Br_{12}, invariable compos.), W No diagram plot	The direct interaction between W and Br_2 starts at 450–500 °C and mainly results in the formation of WBr_6 at 450–600 °C, or WBr_5 at 600–800 °C. Other W bromides are synthesized indirectly.	[2–3, 36, 87, 374–376]

(continued)

Table 3.5 (continued)

System	Type of phase diagram (constituent phases, temperatures and compositions of transformations)	Character of interaction	References
W–I	I, WI_4(invariable compos.), WI_3(invariable compos.), WI_2 (or W_6I_{12}, invariable compos.), WI (?), W No diagram plot	The direct interaction between W and I_2 vapour starts at 550–700 °C and results in the formation of WI_2 (or W_6I_{12}). Other W iodides are synthesized indirectly.	[2–3, 36, 87]
W–At	No data	–	–

[a] The intervals of temperatures and compositions for the melting and invariant equilibria points, homogeneity ranges and thermal stability regions of constituent phases are given taking into account the minimal and maximal values (data spread) available in literature

The data on the selected ternary, quaternary, quasi-binary and quasi-ternary tungsten containing systems, which are the most important for the design, manufacture and application of ultra-high temperature materials, are summarized in Table 3.6. The composition and temperature stability regions for the main binary and ternary tungsten containing high-temperature phases are given in Tables 3.5, and 3.6 taking into account the spread of numerical magnitudes available in literature currently.

Table 3.6 Chemical interaction of tungsten with elements and compounds at high temperatures (selected ternary, quaternary, quasi-binary and quasi-ternary systems in alphabetical order)[a]

System	Type of phase diagram (temperature and composition sections, constituent phases or phase fields) and/or character of interphase interaction and materials compatibility	References
W–Al–B–N	No diagram plot In vacuum the interaction between metal W and α-BN–AlN equimolar compos. starts from 1600 °C (in powder mixtures—from 1500 °C) and leads to the formation of $W_{2\pm x}B$ and α-$WB_{1\pm x}$.	[146]
W–Al–C	See C–Al–W in Table 2.14.	
W–Al–Mo–Ni	General consideration	[395]
W–Al–O	WO_3–Al_2O_3 is plotted: $Al_2W_nO_{3(n+1)}$ (or $Al_2O_3{\cdot}nWO_3$, $n \approx 2.5 \div 3$, <1254 °C), WO_3, Al_2O_3; $Al_2W_nO_{3(n+1)}$–Al_2O_3 eutectic—~1230 °C, ~60–70 mol.% WO_3; $Al_2W_nO_{3(n+1)}$–WO_3 eutectic—1190 °C, ~70–80 mol.% WO_3 In vacuum the interaction between bulk W and Al_2O_3 initiates from 1900 °C; it is characterized by the increase of porosity in the metal-oxide contact zone because of the vaporization of the volatile products of reaction (metal Al and W oxides), but the rate of this process is very low. W dissolves in molten Al_2O_3 bringing about a marked change in the surface tension of the melt in contact with solid W. Mainly molten Al_2O_3 reacts with W at its grain boundaries (intergranular attack).	[87, 147, 159, 306–307, 326]

(continued)

Table 3.6 (continued)

System	Type of phase diagram (temperature and composition sections, constituent phases or phase fields) and/or character of interphase interaction and materials compatibility	References
W–B–Bi	No diagram plot No interaction between β-W_2B_{5-x} and Bi in Ar at temp. $\leq$320 °C.	[102]
W–B–C	See C–B–W in Table 2.14.	
W–B–C–Hf	See C–B–Hf–W in Table 2.14.	
W–B–C–La–Si	See C–B–La–Si–W in Table 2.14.	
W–B–C–N	See C–B–N–W in Table 2.14.	
W–B–C–Si	See C–B–Si–W in Table 2.14.	
W–B–Ce	Plotted at 600 and 800 °C: $CeB_{6\pm x}$ (<2550 °C), CeB_4 (<2380 °C), $W_{2\pm x}B$, α-$WB_{1\pm x}$, β-$WB_{1\pm x}$, β-W_2B_{5-x}, WB_{4+x}, β-B, α-Ce, β-Ce, γ-Ce, δ-Ce, W No ternary compounds and solid solutions based on binary compounds. At 1800 °C the interaction between $CeB_{6\pm x}$ and W results in the formation of α-$WB_{1\pm x}$, β-$WB_{1\pm x}$ and W solid solution in $CeB_{6\pm x}$.	[102, 127, 309–330]
W–B–Co	Plotted at 800 (partially) and 1000 °C: $W_2Co_{21}B_6$, WCoB, W_2CoB_2, W_3CoB_3, Co_3B (<1125 °C), Co_2B (<1280 °C), CoB (<1460 °C), $W_{2\pm x}B$, α-$WB_{1\pm x}$ (up to 5 at.% Co at 1000 °C), β-$WB_{1\pm x}$, β-W_2B_{5-x}, WB_{4+x}, κ-$Co_3W_{1\pm x}$, μ-$Co_7W_{6\pm x}$, β-B, ε-Co, α-Co, W At 1575 °C the interaction between α-$WB_{1\pm x}$ and Co in H_2 results in the formation of a new phase.	[102, 130, 317–318, 377]
W–B–Co–Ti	No diagram plot Co borides enhance the decomposition of the extended solid solution based on $TiB_{2\pm x}$ into the phases $(Ti,W)B_{2\pm x}$ and β-$(W,Ti)_2B_{5-x}$.	[171, 176]
W–B–Cr	Plotted at 800, 1000 and 1500 °C: W_2CrB_2 (or $W_{3.2}Cr_{1.8}B_3$, or $(W,Cr)_3B_2$), $(W,Cr)B_{4+x}$ (extended solid solution based on WB_{4+x}, <5 at.% Cr), β-$(W,Cr)_2B_{5-x}$ (extended solid solution based on β-W_2B_{5-x}—up to $(W_{0.79}Cr_{0.21})_2B_{5-x}$), α-$(W,Cr)B_{1\pm x}$ (extended solid solution based on α-$WB_{1\pm x}$—up to $(W_{0.86}Cr_{0.14})B_{1\pm x}$), β-$(W,Cr)B_{1\pm x}$ (solid solution based on β-$WB_{1\pm x}$, ?), $(W, Cr)_{2\pm x}B$ (highly extended solid solution based on $W_{2\pm x}B$—up to $(W_{0.08}Cr_{0.92})_{2\pm x}B$), $(Cr,W)B_4$ (or $(Cr,W)B_6$ (?), solid solution based on CrB_4 or CrB_6 (?), < ~1450–1500 °C, <5 at.% W), $(Cr,W)B_{2\pm x}$ (solid solution based on $CrB_{2\pm x}$, <2200 °C, <2 at.% W), $(Cr,W)_3B_{4\pm x}$ (solid solution based on $Cr_3B_{4\pm x}$, <2070–2075 °C, <5 at.% W), α-$(Cr,W)B_{1-x}$ (solid solution based on α-CrB_{1-x}, $\leq$1000 °C, ?), β-$(Cr,W)B_{1-x}$ (highly extended solid solution based on β-CrB_{1-x}—up to $(Cr_{0.2}W_{0.8})B_{1-x}$ (at 1500 °C), or β-CrB_{1-x}–β-$WB_{1\pm x}$ continuous solid solution (?), <2095–2100 °C), $(Cr, W)_5B_{3-x}$ (solid solution based on Cr_5B_{3-x}, <~1900 °C, <5 at.% W), $(Cr,W)_{2\pm x}B$ (solid solution based on $Cr_{2\pm x}B$, <1850–1870 °C, $\leq$3 at.% W), β-B, Cr, W	

(continued)

Table 3.6 (continued)

System	Type of phase diagram (temperature and composition sections, constituent phases or phase fields) and/or character of interphase interaction and materials compatibility	References
	At lower temp. the extent of the solid solutions based on the binary borides with higher boron contents slightly decreases.	[37, 46, 102, 160, 187]
W–B–Cr–Ti	$(Ti,Cr)B_{2\pm x}$–$(W,Cr)_2B_{5-x}$ (with 10 mol.% CrB_2) is plotted: eutectic—~2000 °C, ~80 mol.% β-$(W,Cr)_2B_{5-x}$; the solubility of $(W,Cr)_2B_{5-x}$ in $(Ti,W,Cr)B_{2\pm x}$, extended solid solution based on $TiB_{2\pm x}$, increases with temp. growth considerably and amounts to ≥60 mol.% at the eutectic temp.; at 1000–2000 °C the homog. range of $(Ti,W,Cr)B_{2\pm x}$ is much broader than that of $(Ti,W)B_{2\pm x}$; the solubility limits of $(Ti,Cr)B_{2\pm x}$ in β-$(W,Ti,Cr)_2B_{5-x}$, extended solid solution based on β-W_2B_{5-x}, is much higher than that of $TiB_{2\pm x}$ in β-$(W,Ti)_2B_{5-x}$	[188, 212]
W–B–Dy	Plotted at 1000 °C: $DyWB_4$, Dy_3WB_7, DyB_2 (<2100 °C), DyB_4 (<2500 °C), $DyB_{6\pm x}$ (<2200 °C), DyB_{12} (<2100 °C), DyB_{66} (<2025 °C), $W_{2\pm x}B$, α-$WB_{1\pm x}$, β-$WB_{1\pm x}$, β-W_2B_{5-x}, WB_{4+x}, β-B, α-Dy, β-Dy, W No solid solutions based on binary and ternary compounds.	[314, 317, 330]
W–B–Er	Plotted at 1000 °C: $ErWB_4$, Er_3WB_7, $(Er,W)B_2$ (extended solid solution based on ErB_2—up to ~$(Er_{0.85}W_{0.15})B_2$ compos., <~2185 °C), ErB_4 (<~2500 °C), ErB_{12} (<2080 °C), ErB_{66} (<~2070 °C), $W_{2\pm x}B$, α-$WB_{1\pm x}$, β-$WB_{1\pm x}$, β-W_2B_{5-x}, WB_{4+x}, β-B, Er, W No marked solubility of a third component in binary compounds.	[98, 128, 317, 330]
W–B–Fe	Plotted at 1000 and 1050 °C: WFeB, α-W_2FeB_2 (<1300 °C), β-W_2FeB_2 (or $W_{1.75}Fe_{1.25}B_2$, or $(W_xFe_{1-x})_3B_2$, >1300 °C, ?), W_4FeB_6 (or $W_{0.7}Fe_{0.1\div0.15}B$, ?), W_2FeB_4 (?), $W_{14}Fe_3B_{20}$ (?), $(W_xFe_{1-x})_3B$ (or W_2FeB, ?), Fe_2B (<1407 °C), FeB (<1588 °C), δ-FeW, μ-Fe_7W_{6-x}, λ-Fe_2W, $W_{2\pm x}B$, α-$WB_{1\pm x}$, β-$WB_{1\pm x}$ (stabilized by Fe at lower temp. with $W_{7.5\div14}Fe_{1.5\div3}B_{11\div20}$ compos.), β-W_2B_{5-x}, WB_{4+x}, β-B, α-Fe, γ-Fe, δ-Fe, W In vacuum, at 1550 °C the interaction between β-W_2B_{5-x} and Fe leads to the formation complex borides (ternary compounds).	[102, 129–132, 317–318, 331]
W–B–Gd	Plotted at 1000 °C: $GdWB_4$, Gd_3WB_7, GdB_{66} (<2150 °C), $GdB_{6\pm x}$ (<2510 °C), GdB_4 (<~2650 °C), Gd_2B_5 (<2100 °C), GdB_2 (<~2050 °C), $W_{2\pm x}B$, α-$WB_{1\pm x}$, β-$WB_{1\pm x}$, β-W_2B_{5-x}, WB_{4+x}, β-B, α-Gd, β-Gd, W No solid solutions based on ternary and binary compounds. Gd inhibits α-$WB_{1\pm x}$–β-$WB_{1\pm x}$ solid state phase transformation.	[43, 313, 317, 330]

(continued)

Table 3.6 (continued)

System	Type of phase diagram (temperature and composition sections, constituent phases or phase fields) and/or character of interphase interaction and materials compatibility	References
W–B–Hf	Plotted at 1400 and 1500 °C: Hf_9W_4B (<~1930, °C, incongruent melt. point), HfW_4B_5, $(Hf,W)_{12}B_{2-x}$, $(Hf,W)B_2$ (extended solid solution based on $HfB_{2\pm x}$—up to ~$(Hf_{0.77}W_{0.23})B_{2\pm x}$ compos., <3250–3410 °C), β-$(W,Hf)B_{1\pm x}$ (extended solid solution based on β-$WB_{1\pm x}$—up to ~$(W_{0.8}Hf_{0.2})B_{1\pm x}$ compos.; Hf stabilizes β-$WB_{1\pm x}$,), $HfB_{1\pm x}$ (<2100 °C), HfW_{2-x} (<~2510 °C), $W_{2\pm x}B$, α-$WB_{1\pm x}$, β-W_2B_{5-x}, WB_{4+x}, β-B, α-Hf, β-Hf, W $HfB_{2\pm x}$–W_2B_{5-x} is plotted: eutectic—~2290–2330 °C, ~94 mol.% W_2B_{5-x}; at the eutectic temp. the max. solid solubility of W in $HfB_{2\pm x}$ corresp. to ~$(Hf_{0.77}W_{0.23})B_{2\pm x}$ compos. and that of Hf in β-W_2B_{5-x}—to ~$(W_{>0.97}Hf_{<0.03})_2B_{5-x}$ $HfB_{2\pm x}$–W is plotted: eutectic—~2250–2310 °C, ~15 mol.% $HfB_{2\pm x}$; at the eutectic temp. the max. solid solubility of W in $HfB_{2\pm x}$ corresp. to ~$(Hf_{0.9}W_{0.1})B_{2\pm x}$ compos. and those of Hf and B in W are <1 at.% and <0.5 at.%, respectively	[5, 63, 133–139, 219, 274, 282–283, 317]
W–B–Ho	No diagram plot $HoWB_4$, Ho_3WB_7	[317, 330]
W–B–In	No diagram plot No interaction between β-W_2B_{5-x} and In in Ar at temp. ≤500 °C.	[102]
W–B–Ir	Plotted at 1200 °C: $W_2Ir_3B_5$, (or $(W,Ir)_5B_6$), $W_8Ir_6B_{31}$ (or $(W,Ir)B_2$, $W_{0.52}Ir_{0.38}B_2$), $Ir_2B_{3\pm x}$ (<1300–1330 °C), Ir_3B_{4+x} (<~1600 °C), α-IrB_{1+x}, β-IrB_{1+x}, α-IrB_{1-x} (≤1100 °C, ?), β-IrB_{1-x} (~1100–1340 °C), $Ir_3B_{2\pm x}$ (<1260–1300 °C), $W_{2\pm x}B$, α-$WB_{1\pm x}$, β-$WB_{1\pm x}$, β-W_2B_{5-x}, WB_{4+x}, β-$Ir_3W_{2\pm x}$, ε-$IrW_{1\pm x}$, σ-$IrW_{3\pm x}$ β-B, Ir, W	[317, 320]
W–B–La	Plotted at 600 and 800 °C: $LaB_{6\pm x}$ (<~2500–2715 °C), LaB_4 (<1800 °C), $W_{2\pm x}B$, α-$WB_{1\pm x}$, β-$WB_{1\pm x}$, β-W_2B_{5-x}, WB_{4+x}, β-B, α-La, β-La, γ-La, W W_2B_{5-x}–$LaB_{6\pm x}$ is plotted: eutectic—~2190–2250 °C, ~70 mol.% β-W_2B_{5-x}; virtually no mutual solubility between the components No ternary compounds and solid solutions based on binary compounds. At 1400–1600 °C W and $LaB_{6\pm x}$ are compatible with each other without any contact interaction. At 1600–1800 °C weak interphase interaction is observed. At 1800–2100 °C the interaction between W and $LaB_{6\pm x}$ results in the formation of solid solution of W in $LaB_{6\pm x}$, $W_{2\pm x}B$, α-$WB_{1\pm x}$ and β-$WB_{1\pm x}$.	[5, 102, 127, 140–141, 309–311, 330]

(continued)

Table 3.6 (continued)

System	Type of phase diagram (temperature and composition sections, constituent phases or phase fields) and/or character of interphase interaction and materials compatibility	References
W–B–Lu	Plotted at 800 °C: Lu_3WB_7 (or Lu_2WB_6, ?), $(Lu,W)B_2$ (solid solution based on LuB_2—up to compos. $(Lu_{0.85}W_{0.15})B_2$, <∼2250 °C), LuB_{66} (<∼2100 °C), LuB_{12} (<∼2170 °C), LuB_4 (<∼2550 °C), $W_{2\pm x}B$, α-$WB_{1\pm x}$, β-W_2B_{5-x}, WB_{4+x}, β-B, Lu, W No solid solutions based on binary compounds apart from a solubility of W in LuB_2.	[302, 330]
W–B–Mn	Plotted at 800 °C: $(W,Mn)_3B_2$ (?), $(Mn,W)_3B_4$ (or $(Mn_{1-x}W_x)_3B_4$, at least $0 \le x \le 0.33$, extended solid solution based on Mn_3B_4 <∼1750–1830 °C), MnB_4 (<∼1380–2160 °C, ?), MnB_2 (∼1100–1990 °C), MnB (<1890 °C), Mn_2B (<1580 °C), Mn_4B (<1120–1285 °C), WB_{4+x}, α-W_2B_{5-x}, β-W_2B_{5-x}, α-$WB_{1\pm x}$, β-$WB_{1\pm x}$, $W_{2\pm x}B$, β-B, α-Mn, β-Mn, γ-Mn, δ-Mn, W	[46, 319, 324–325]
W–B–Mo	Plotted at 1100 and 1500 °C: $(W,Mo)B_{\sim 12}$ ($WB_{\sim 12}$−$MoB_{\sim 12}$ continuous solid solution), $(W,Mo)B_{4+x}$ (WB_{4+x}–MoB_{4-x} continuous solid solution, <1755–2050 °C, ?), β-$(W, Mo)_2B_{5-x}$ (solid solution based on β-W_2B_{5-x}, <4 at.% Mo), $(Mo,W)_2B_{5-x}$ (solid solution based on Mo_2B_{5-x}, <1600–2200 °C, < 4 at.% W), α-$(W,Mo)B_{1\pm x}$ (α-$WB_{1\pm x}$−α-$MoB_{1\pm x}$ continuous solid solution at ∼1750–2180 °C, or extended solid solutions based on α-$WB_{1\pm x}$ and α-$MoB_{1\pm x}$ at temp. <∼1750 °C, ?), β-$(W,Mo)B_{1\pm x}$ (β-$WB_{1\pm x}$−β-$MoB_{1\pm x}$ continuous solid solution, ∼1800–2680 °C, ?), $(W,Mo)_{2\pm x}B$ ($W_{2\pm x}B$–$Mo_{2\pm x}B$ continuous solid solution, <2140–2770 °C), $(Mo,W)B_{2\pm x}$ (extended solid solution based on $MoB_{2\pm x}$, 1515–2375 °C), β-B, (W,Mo) At 1600–2200 °C the contact interaction between β-W_2B_{5-x} and compact Mo leads to the formation of $Mo_{2\pm x}B$. The contact interaction between Mo_2B_{5-x} and compact W initiates from 1300 °C and results in the formation of solid solutions and $W_{2\pm x}B$.	[43, 46, 102, 142, 160–163]
W–B–N	Plotted at 1200, 1400 and 1600 °C: (pressure Ar or N_2 − 0.1 MPa): α-BN (<3000 °C), $W_{2\pm x}B$, α-$WB_{1\pm x}$, β-W_2B_{5-x}, WB_{4+x}, β-B, N, W At 1200–1600 °C under gas pressure (0.1 MPa) W and α-BN reacts to form $W_{2\pm x}B + N_2$, at 1600 °C $W_{2\pm x}B$ becomes incompatible with α-BN and decomposes to form α-$WB_{1\pm x}$ and N_2. At temp. >1300 °C in vacuum (10^{-4} Pa) W + α-BN starting compositions decompose into ($W_{2\pm x}B$, α-$WB_{1\pm x}$, α-$WB_{1\pm x}$) + α-BN with N_2 released. At temp. >1600 °C in vacuum (0.1–0.001 Pa) bulk dense W is not compatible in the contact with α-BN, and the reaction takes place also through vapour phase; at 2450 °C the interaction between W and α-BN leads to the formation of β-W_2B_{5-x}.	[5, 87, 102, 143–146]

(continued)

Table 3.6 (continued)

System	Type of phase diagram (temperature and composition sections, constituent phases or phase fields) and/or character of interphase interaction and materials compatibility	References
W–B–N–O	No diagram plot At 1400 °C WO_3 is reduced by α-BN to metal W.	[102, 147]
W–B–Nb	Plotted at 1500 °C: (Nb,W)B (extended solid solution based on $NbB_{1\pm x}$—up to compos. $(Nb_{0.2}W_{0.8})B$, or $NbB_{1\pm x}$–β-$WB_{1\pm x}$ continuous solid solution at higher temp. (?), <2270–2665 °C), $(Nb,W)_3B_2$ (extended solid solution based on Nb_3B_2—up to compos. $(Nb_{0.42}W_{0.58})_3B_2$), <1860–2230 °C), $(W,Nb)_{2\pm x}B$ (extended solid solution based on $W_{2\pm x}B$—up to compos. $(W_{0.78}Nb_{0.22})_{2\pm x}B$), Nb_3B_4 (<2700 °C), Nb_5B_6 (<2295 °C), $NbB_{2\pm x}$ (<3000 °C), α-$WB_{1\pm x}$, β-W_2B_{5-x}, WB_{4+x}, β-B, (W,Nb) The solubilities of W in Nb_3B_4 and $NbB_{2\pm x}$ and that of Nb in α-$WB_{1\pm x}$ and β-W_2B_{5-x} are slight (<5 at.%). In vacuum, at temp. 1400–2200 °C the interaction between β-W_2B_{5-x} and compact Nb leads to the formation of $NbB_{2\pm x}$.	[102, 305]
W–B–Nb–Si	WSi_2–$NbB_{2\pm x}$ is plotted: eutectic—~1960–2000 °C, ~80 mol.% WSi_2; virtually no mutual solubility between the components	[148]
W–B–Ni	Plotted at 800 and 950 °C: ω-W_2NiB_2, W_3NiB_3 (or $(W, Ni)_4B_3$), $WNi_{20}B_{17}$, $W_{7-x}Ni_2B_{7+y}$ ($x \approx 0.2$, $y \approx 0.2$, Y-phase), WNi_4B_{15}, W_3NiB_2 (?), $W_{4/3}Ni_{2/3}B_{\sim 9}$ (or $W_4Ni_2B_{27}$, ?), Ni_3B (<1156 °C), Ni_2B (<1125 °C), α-Ni_4B_{3-x} (or *o*-Ni_4B_3, <1025 °C), β-Ni_4B_{3+x} (or *m*-Ni_4B_3, <1031 °C), NiB (<1035 °C), β-$Ni_{4+x}W$, δ-NiW_{1-x}, γ-NiW_2, $W_{2\pm x}B$, α-$WB_{1\pm x}$, β-W_2B_{5-x}, WB_{4+x}, β-B, Ni, W The mutual solubilities between ternary and binary phases are low. At 1200 °C $W_{2\pm x}B$, α-$WB_{1\pm x}$ and β-W_2B_{5-x} interact with Ni intensively.	[102, 303, 130, 317–318, 379]
W–B–Ni–Ti	No diagram plot Ni borides enhance the decomposition of the extended solid solution based on $TiB_{2\pm x}$ into the phases $(Ti,W)B_{2\pm x}$ and β-$(W,Ti)_2B_{5-x}$.	[171, 175]
W–B–O–Zr	No diagram plot In vacuum, at temp. >1300 °C the interaction between β-W_2B_{5-x} and ZrO_{2-x} results in the formation of $W_{2\pm x}B$, α-$WB_{1\pm x}$ and $ZrB_{2\pm x}$.	[102]
W–B–Os	No diagram plot $W_{2-x}Os_{1+x}B_2$ ($x = 0.15$), WOs_2B_6 (or $W_{0.3}Os_{0.7}B$, $(W,Os)B_2$)	[317, 380–381]

(continued)

Table 3.6 (continued)

System	Type of phase diagram (temperature and composition sections, constituent phases or phase fields) and/or character of interphase interaction and materials compatibility	References
W–B–P	Plotted at 800 °C (in the range of 0–66 at.% P): α-PB (<825 °C), β-PB, P_2B_{13-x}, WP, α-WP_2, β-WP_2, $W_{2\pm x}B$, α-$WB_{1\pm x}$, β-W_2B_{5-x}, WB_{4+x}, P, β-B, W No ternary compounds or solid solutions based on binary compounds. WP, α-$WB_{1\pm x}$ and α-PB are in equilibria with each other. W is in equilibria with $W_{2\pm x}B$ and WP.	[301]
W–B–Pd	No diagram plot $W_4Pd_2B_{15}$ (or $W_{4/3}Pd_{2/3}B_5$, $W_{1.37}Pd_{0.63}B_{15}$), $WPdB_9$ (or $W_{1.5}Pd_{1.5}B_{15}$), $W_4Pd_5B_{11}$ (or $W_{19}Pd_{26}B_{55}$, $W_{1.33}Pd_{1.82}B_{3.65}$)	[317, 382]
W–B–Pr	Plotted at 600–800 °C: no ternary compounds, Pr_2B_5 (or PrB_x, $x \approx 2.5$–2.6, <~2000 °C), PrB_4 (<~2350 °C), $PrB_{6\pm x}$ (<2610 °C), $W_{2\pm x}B$, α-$WB_{1\pm x}$, β-$WB_{1\pm x}$, β-W_2B_{5-x}, WB_{4+x}, β-B, α-Pr, β-Pr, W	[314, 383]
W–B–Re	Plotted at 1500 °C: $W_6Re_{12}B$ (or $W_{6.7}Re_{13.3}B_{1.1}$, ?), WReB (?), $(W,Re)_{2\pm x}B$ (extended solid solution based on $W_{2\pm x}B$—up to ~$(W_{0.4}Re_{0.6})_{2\pm x}B$), α-$(W,Re)B_{1\pm x}$ (extended solid solution based on α-$WB_{1\pm x}$—up to ~$(W_{0.5}Re_{0.5})B_{1\pm x}$, ?), β-$(W,Re)B_{1\pm x}$ (?), $(Re,W)B_{2\pm x}$ (extended solid solution based on $ReB_{2\pm x}$—up to ~$(Re_{0.4}W_{0.6})B_{2\pm x}$, <~2400 °C), $(Re,W)_7B_{3+x}$ (extended solid solution based on Re_7B_{3+x}—up to ~$(Re_{0.7}W_{0.3})_7B_{3+x}$, <~2000 °C), $(Re,W)_{3\pm x}B$ (extended solid solution based on $Re_{3\pm x}B$—up to ~$(Re_{0.6}W_{0.4})_{3\pm x}B$, <~2150 °C), β-$(W,Re)_2B_{5-x}$ (solid solution based on β-W_2B_{5-x}), WB_{4+x}, χ-WRe_{3-x}, σ-$W_2Re_{3\pm x}$, β-B, Re, W	[317, 346–347]
W–B–Ru	No diagram plot $W_{2-x}Ru_{1+x}B_2$ (or $W_{1.75}Ru_{1.25}B_2$, W_2RuB_2, $(W,Ru)_3B_2$), $W_{1-x}Ru_{1+x}B_2$ (or $(W_{0.5}Ru_{0.5})B$, (W,Ru)B), $W_{1-x}Ru_xB_2$ (or $(W_{0.3}Ru_{0.7})B_2$, (W,Ru)B_2)	[317, 320, 378, 380, 384]
W–B–Sc	Plotted at 1000 °C: (Sc,W)B_2 (extended solid solution based on ScB_2—up to compos. ~$(Sc_{0.7}W_{0.3})B_2$, <2250 °C), ScB_{12} (<2040 °C), $W_{2\pm x}B$, α-$WB_{1\pm x}$, β-W_2B_{5-x}, WB_{4+x}, β-B, α-Sc, β-Sc, W No ternary compounds and solid solutions based on binary compounds apart from (Sc, W)B_2.	[43, 46, 286, 330]
W–B–Si	Plotted at 1800 °C: $W_{3-x}SiB$, $W_5Si_{3-x}B_y$ (or $W_{10}Si_3B_3$, $W_5(Si_{0.5}B_{0.5})_3$, $W_5(Si,B)_3$, ~1800–2500 °C, ?), $SiB_{3\pm x}$ (<1270 °C), SiB_6 (<1850 °C), SiB_n (<~2025 °C), WSi_2, $W_{2\pm x}B$, α-$WB_{1\pm x}$, β-$WB_{1\pm x}$, β-W_2B_{5-x}, WB_{4+x}, β-B, Si, W	[5, 46, 149, 284, 385]

(continued)

Table 3.6 (continued)

System	Type of phase diagram (temperature and composition sections, constituent phases or phase fields) and/or character of interphase interaction and materials compatibility	References
W–B–Si–Ta	WSi_2–$TaB_{2\pm x}$ is plotted: eutectic—~1990–2050 °C, ~85 mol.% WSi_2; virtually no mutual solubility between the components	[148]
W–B–Si–Ti	No diagram plot At 2000–2050 °C the weak interaction between W silicides (W_5Si_{3+x}, WSi_2) and $TiB_{2\pm x}$ is observed.	[102, 150]
W–B–Si–V	WSi_2–$VB_{2\pm x}$ is plotted: eutectic—~1920–1960 °C, ~65 mol.% WSi_2; virtually no mutual solubility between the components	[148]
W–B–Si–Zr	No diagram plot At 2000–2050 °C the weak interaction between W silicides (W_5Si_{3+x}, WSi_2) and $ZrB_{2\pm x}$ is observed.	[102, 150]
W–B–Sn	No diagram plot No interaction between β-W_2B_{5-x} and Sn in Ar at temp. ≤800 °C.	[102]
W–B–Ta	Plotted at 1400 °C: λ-(Ta,W)$B_{1\pm x}$ (extended solid solution based on λ-$TaB_{1\pm x}$—up to ~$(Ta_{0.2}W_{0.8})B_{1\pm x}$, <3090 °C), $(Ta,W)_3B_{2\pm x}$ (extended solid solution based on $Ta_3B_{2\pm x}$—up to ~$(Ta_{0.5}W_{0.5})_3B_{2\pm x}$, <2180 °C), $(W,Ta)_{2\pm x}B$ (extended solid solution based on $W_{2\pm x}B$—up to ~$(W_{0.6}Ta_{0.4})_{2\pm x}B$), $Ta_{2+x}B$ (~1900–2420 °C), $Ta_3B_{4\pm x}$ (<3030 °C), $TaB_{2\pm x}$ (<~3040 °C), α-$WB_{1\pm x}$, β-$WB_{1\pm x}$, β-W_2B_{5-x}, WB_{4+x}, β-B, Ta, W In vacuum, at 1500–2000 °C the interaction of the compact W with $TaB_{2\pm x}$ leads to the formation of α-$WB_{1\pm x}$; at higher temp. this interaction is very intensive, and the product on the contact is β-W_2B_{5-x}. The contact interaction between β-W_2B_{5-x} and compact Ta (at temp. >1600 °C, in vacuum) results in the formation of $Ta_3B_{4\pm x}$; at 1980 °C the interaction between $W_{2\pm x}B$ and Ta leads to the formation of W, $Ta_{2+x}B$ and λ-$TaB_{1\pm x}$.	[5, 102, 165]
W–B–Tb	Plotted at 1000 °C: $TbWB_4$, Tb_3WB_7, TbB_2 (<~2100 °C), TbB_4 (<~2600 °C), $TbB_{6\pm x}$ (<2340 °C), TbB_{12} (<2200 °C), TbB_{66} (<~2100 °C), $W_{2\pm x}B$, α-$WB_{1\pm x}$, β-$WB_{1\pm x}$, β-W_2B_{5-x}, WB_{4+x}, β-B, α-Tb, β-Tb, W No solid solutions based on binary compounds.	[314, 317, 330]
W–B–Th	Plotted at 1800 °C: $ThWB_4$, ThB_4 (<2475 °C), ThB_{6+x} (<2450 °C), ~$ThB_{66\div77}$ (<~2150 °C), $W_{2\pm x}B$, α-$WB_{1\pm x}$, β-$WB_{1\pm x}$, β-W_2B_{5-x}, WB_{4+x}, α-Th, β-Th, β-B, W	[5, 317, 386]

(continued)

Table 3.6 (continued)

System	Type of phase diagram (temperature and composition sections, constituent phases or phase fields) and/or character of interphase interaction and materials compatibility	References
W–B–Ti	Plotted at 25, 1000 and 1400 °C: $Ti_2W_3B_5$ (or $Ti_{1\div3}W_{2\div4}B_5$, ?), $TiWB_2$ (?), $(Ti,W)B_{1-x}$ (extended solid solution based on TiB_{1-x}—up to $(Ti_{0.7}W_{0.3})B_{1-x}$, <~2200 °C), α-$(W,Ti)B_{1\pm x}$ (solid solution based on α-$WB_{1\pm x}$, the solubility of Ti < 5 at.%), β-$(W, Ti)B_{1\pm x}$ (solid solution based on β-$WB_{1\pm x}$), $(Ti,W)B_{2\pm x}$ (solid solution based on $TiB_{2\pm x}$, <3225 °C), $(W,Ti)_{2\pm x}B$ (solid solution based on $W_{2\pm x}B$), α-$(W,Ti)_2B_{5-x}$ (solid solution based on α-W_2B_{5-x}), β-$(W,Ti)_2B_{5-x}$ (solid solution based on β-W_2B_{5-x}), WB_{4+x}, β-B, α-Ti, β-Ti, W $TiB_{2\pm x}$—W_2B_{5-x} is plotted: eutectic—~2160–2230 °C, ~80–90 mol.% β-W_2B_{5-x}; the solubility of W_2B_{5-x} in $(Ti, W)B_{2\pm x}$ increases with temp. growth considerably and amounts to ≥63 mol.% at the eutectic temp. (or >85 mol.% in metastable state) and solubility of $TiB_{2\pm x}$ in β-W_2B_{5-x} reaches ~3 mol.% at the same temp. $TiB_{2\pm x}$–W is plotted: $TiWB_2$ (<~2680 °C, congruent melt. point, invariable compos., ?); $TiB_{2\pm x}$–$TiWB_2$ eutectic—~2350–2560 °C (?), ~12 mol.% W; $TiWB_2$–W eutectic—~2180–2390 °C (?), ~88 mol.% W; the solubility of $TiB_{2\pm x}$ in W is ~1 mol.% and that of W in $TiB_{2\pm x}$ is ~5 mol.%. $TiB_{2\pm x}$–W is plotted: eutectic—~2200–2350 °C (?) The solubility of W in $TiB_{2\pm x}$ and that of Ti in WB_{4+x}, β-W_2B_{5-x}, α-$WB_{1\pm x}$ and $W_{2\pm x}B$ are low. Data on the system available in literature are controversial. The interaction of the bulk dense W with TiB_{2+x} at 1800 °C leads to the contact formation of $TiWB_2$ (?), TiB_{1-x}, $W_{2\pm x}B$ and α-$WB_{1\pm x}$ and at temp. ≥2000 °C—$TiWB_2$ (?), TiB_{1-x}, and β-$WB_{1\pm x}$.	[5, 43, 46, 102, 151–154, 164–177, 187–188, 211]
W–B–Tm	Plotted at 800 °C: $TmWB_4$, Tm_3WB_7, TmB_{66} (<2100 °C), TmB_{12} (<2180 °C), TmB_4 (<2550 °C), TmB_2 (<2250 °C), $W_{2\pm x}B$, α-$WB_{1\pm x}$, β-$WB_{1\pm x}$, β-W_2B_{5-x}, WB_{4+x}, β-B, Tm, W No solid solutions based on binary and ternary compounds apart from a low solubility of W in TmB_2.	[302, 330]
W–B–U	Plotted at 1000 °C: UWB_4, U_2WB_6, UB_{12} (<2145 °C), UB_4 (<2495 °C), UB_2 (<2385 °C), $W_{2\pm x}B$, α-$WB_{1\pm x}$, β-$WB_{1\pm x}$, β-W_2B_{5-x}, WB_{4+x}, β-B, α-U, β-U, γ-U, W No solid solutions based on binary and ternary compounds.	[312, 317, 321]
W–B–Y	Plotted at 1000 °C: YWB_4, Y_3WB_7, YB_{66} (<2100 °C), YB_{12} (<2200 °C), $YB_{6\pm x}$ (<2600 °C), YB_4 (<2800 °C), YB_2 (<2100 °C), $W_{2\pm x}B$, α-$WB_{1\pm x}$, β-$WB_{1\pm x}$, β-W_2B_{5-x}, WB_{4+x}, β-B, α-Y, β-Y, W No solid solutions based on binary and ternary compounds apart from a low solubility of Y in β-W_2B_{5-x}. Y inhibits α-$WB_{1\pm x}$–β-$WB_{1\pm x}$ solid state phase transformation.	[309–310, 315, 317, 330]

(continued)

Table 3.6 (continued)

System	Type of phase diagram (temperature and composition sections, constituent phases or phase fields) and/or character of interphase interaction and materials compatibility	References
W–B–Yb	No diagram plot Yb_3WB_7	[330]
W–B–Zr	Plotted at 1400 and 1500 °C: $Zr_xW_yB_z$ (or ZrWB, ?), Zr_9W_4B (or $(Zr,W)_{13}B$, metastable, ?), $ZrB_{2\pm x}$ (<3225–3265 °C), ZrB_{12} (~1695–2290 °C), $W_{2\pm x}B$, α-$WB_{1\pm x}$, β-W_2B_{5-x}, WB_{4+x}, ZrW_2, β-B, α-Zr, β-Zr, W $ZrB_{2\pm x}$–W_2B_{5-x} is plotted: eutectic—~2150–2250 °C, ~80–95 mol.% β-W_2B_{5-x}; the solid solubility of W_2B_{5-x} in $ZrB_{2\pm x}$ is ~5–15 mol.% (?) $ZrB_{2\pm x}$–$WB_{1\pm x}$ is plotted: eutectic—2530 °C, ~70 mol.% β-$WB_{1\pm x}$ $ZrB_{2\pm x}$–$W_{2\pm x}B$ is plotted: eutectic—2480 °C, ~60 mol.% $W_{2\pm x}B$ $ZrB_{2\pm x}$–W is plotted: eutectic—~2210–2290 °C, ~60–70 mol.% W The mutual solubilities of binary compounds in the system are very low. All tie lines are connected to the dominating phase $ZrB_{2\pm x}$. The interaction of the compact W with $ZrB_{2\pm x}$ at 1200–2100 °C is weak and leads to the formation of $W_{2\pm x}B$, α-$WB_{1\pm x}$ and β-W_2B_{5-x}; at temp. ≥2100 °C—β-$WB_{1\pm x}$ and β-W_2B_{5-x}. At 2200 °C, during 3 h sintering procedure the interphase interaction in $ZrB_{2\pm x}$–W powdered mixture results in the formation of $(Zr,W)B_{2\pm x}$ and β-$(W,Zr)B_{1\pm x}$.	[5, 43, 46, 63, 102, 150, 155–157, 166, 178–186, 274, 308, 316–317, 334]
W–Be–O	BeO–WO_3 is plotted: eutectic—1185 °C, ~60–70 mol.% WO_3 In vacuum (0.01–0.05 Pa) the interaction between W and BeO initiates from 1800 to 2000 °C (0.5–1.0 h exposure). It is characterized with the abrupt increase of porosity in the metal-oxide contact zone because of the vaporization of the volatile products of reaction (W oxides and beryllides).	[5, 19, 147, 87, 158]
W–Bi–Pb	No diagram plot At 1095 °C in the dynamic conditions, the Bi–Pb eutectic alloy (55 at.% Bi) penetrates into sintered W intensively.	[5]
W–C–Co	See C–Co–W in Table 2.14.	
W–C–Co–Fe–Ni	See C–Co–Fe–Ni–W in Table 2.14.	
W–C–Co–Ni	See C–Co–Ni–W in Table 2.14.	
W–C–Co–Os	See C–Co–Os–W in Table 2.14.	
W–C–Co–Re	See C–Co–Re–W in Table 2.14.	
W–C–Co–Ru	See C–Co–Ru–W in Table 2.14.	
W–C–Co–Ti	See C–Co–Ti–W in Table 2.14.	
W–C–Cr	See C–Cr–W in Table 2.14.	
W–C–Cr–Fe	See C–Cr–Fe–W in Table 2.14.	
W–C–Cr–O	See C–Cr–O–W in Table 2.14.	
W–C–Fe	See C–Fe–W in Table 2.14.	

(continued)

Table 3.6 (continued)

System	Type of phase diagram (temperature and composition sections, constituent phases or phase fields) and/or character of interphase interaction and materials compatibility	References
W–C–Fe–Ni	See C–Fe–Ni–W in Table 2.14.	
W–C–Hf	See C–Hf–W in Table 2.14.	
W–C–Hf–Ni	See C–Hf–Ni–W in Table 2.14.	
W–C–Hf–Ti	See C–Hf–Ti–W in Table 2.14.	
W–C–Hf–V	See C–Hf–V–W in Table 2.14.	
W–C–Ir	See C–Ir–W in Table 2.14.	
W–C–Mg–O	See C–Mg–O–W in Table 2.14.	
W–C–Mn	See C–Mn–W in Table 2.14.	
W–C–Mo	See C–Mo–W in Table 2.14.	
W–C–Mo–Zr	See C–Mo–W–Zr in Table 2.14.	
W–C–N	See C–N–W in Table 2.14.	
W–C–N–Nb	See C–N–Nb–W in Table 2.14.	
W–C–N–Ti	See C–N–Ti–W in Table 2.14.	
W–C–Nb	See C–Nb–W in Table 2.14.	
W–C–Nb–O	See C–Nb–O–W in Table 2.14.	
W–C–Nb–Ta	See C–Nb–Ta–W in Table 2.14.	
W–C–Nb–Ti	See C–Nb–Ti–W in Table 2.14.	
W–C–Ni	See C–Ni–W in Table 2.14.	
W–C–Ni–Zr	See C–Ni–W–Zr in Table 2.14.	
W–C–O	See C–O–W in Table 2.14.	
W–C–O–Ta	See C–O–Ta–W in Table 2.14.	
W–C–O–Ti	See C–O–Ti–W in Table 2.14.	
W–C–O–V	See C–O–V–W in Table 2.14.	
W–C–O–Zr	See C–O–W–Zr in Table 2.14.	
W–C–Os	See C–Os–W in Table 2.14.	
W–C–Pd	See C–Pd–W in Table 2.14.	
W–C–Pt	See C–Pt–W in Table 2.14.	
W–C–Pu	See C–Pu–W in Table 2.14.	
W–C–Pu–U	See C–Pu–U–W in Table 2.14.	
W–C–Re	See C–Re–W in Table 2.14.	
W–C–Rh	See C–Rh–W in Table 2.14.	
W–C–Ru	See C–Ru–W in Table 2.14.	
W–C–Si	See C–Si–W in Table 2.14.	
W–C–Ta	See C–Ta–W in Table 2.14.	
W–C–Ta–Ti	See C–Ta–Ti–W in Table 2.14.	
W–C–Ta–V	See C–Ta–V–W in Table 2.14	
W–C–Tc	See C–Tc–W in Table 2.14.	
W–C–Th	See C–Th–W in Table 2.14.	
W–C–Ti	See C–Ti–W in Table 2.14.	
W–C–U	See C–U–W in Table 2.14.	
W–C–U–Zr	See C–U–W–Zr in Table 2.14.	
W–C–V	See C–V–W in Table 2.14.	
W–C–Zr	See C–W–Zr in Table 2.14.	

(continued)

Table 3.6 (continued)

System	Type of phase diagram (temperature and composition sections, constituent phases or phase fields) and/or character of interphase interaction and materials compatibility	References
W–Ca–O	Plotted at 1400 and 1700 °C: $CaWO_4$ (<1575–1585 °C), Ca_3WO_6 (<2230–2270 °C), $CaWO_3$, CaO (<2575 °C), WO_2, $W_{18}O_{49}$, $W_{20}O_{58}$, α-WO_{3-x}, β-WO_{3-x}, O, Ca, W WO_3–CaO is plotted: CaO, Ca_3WO_6 (<2230–2270 °C), $CaWO_4$ (<1575–1585 °C), WO_3; $CaWO_4$–α-WO_{3-x} eutectic—~1130–1140 °C, 75 mol.% WO_3; Ca_3WO_6–$CaWO_4$ eutectic—~1485–1540 °C, ~45 mol.% WO_3 The interaction between W and CaO initiates from 1900 to 2000 °C; it is characterized by the reduction of CaO to Ca and formation of $CaWO_3$, $CaWO_4$, Ca_3WO_6, WO_2 and α-WO_{3-x}.	[87, 158, 345]
W–Cd–Bi–Pb–Sn	No diagram plot At 600 °C W is highly resistant to Wood's metal (Bi-26.7Pb-13.3Sn-10Cd).	[5]
W–Ce–O	WO_3–CeO_{2-x}–Ce_2O_3 is plotted at 700–1000 °C: $3Ce_2O_3{\cdot}WO_3$ (or Ce_6WO_{12}), $3Ce_2O_3{\cdot}2WO_3$ (or $Ce_6W_2O_{15}$), β-$Ce_2O_3{\cdot}WO_3$ (or β-Ce_2WO_6, <1360 °C), γ-$Ce_2O_3{\cdot}WO_3$ (or γ-Ce_2WO_6, >1360 °C), α-$Ce_2O_3{\cdot}2WO_3$ (or α-$Ce_2W_2O_9$, <1105 °C), β-$Ce_2O_3{\cdot}2WO_3$ (or β-$Ce_2W_2O_9$, >1105 °C), α-$Ce_2O_3{\cdot}3WO_3$ (or α-$Ce_2W_3O_{12}$), β-$Ce_2O_3{\cdot}3WO_3$ (or β-$Ce_2W_3O_{12}$), $2Ce_2O_3{\cdot}9WO_3$ (or $Ce_4W_9O_{33}$, <1026 °C), CeO_{2-x}, Ce_2O_3, WO_3 In vacuum, at 1700 °C W interacts with CeO_{2-x} intensively.	[5, 147, 240]
W–Co–Mo	Plotted at 1000 °C: κ-$Co_3(W,Mo)_{1\pm x}$, (κ-$Co_3W_{1\pm x}$ –κ-$Co_3Mo_{1\pm x}$ continuous solid solution, <~1025–1095 °C), μ-$Co_7(W,Mo)_{6-x}$ (μ-Co_7W_{6-x}–μ-Co_7Mo_{6-x} continuous solid solution, <~1510–1690 °C), θ-Mo_2Co_{9-x} (~1020–1200 °C), σ-Mo_3Co_{2-x} (~900–1620 °C), ε-Co, α-Co, (W, Mo)	[37, 46, 199–200, 390, 387]
W–Co–Nb	Plotted at 900 °C: χ-$Co_7(Nb,W)_{2\pm x}$ (extended solid solution based on χ-$Co_7Nb_{2\pm x}$, <1050 °C), λ_3-$Co_3(Nb,W)$ (extended solid solution based on λ_3-Co_3Nb, ~1000–1240 °C), $\lambda_2(\alpha)$-$Co_{2\pm x}$ (Nb, W) (<~1200 °C, extended solid solution based on $\lambda_2(\alpha)$-$Co_{2\pm x}$Nb, ?), $\lambda_2(\beta)$-$Co_{2\pm x}$(Nb,W) (solid solution based on $\lambda_2(\beta)$-$Co_{2\pm x}$Nb, from 1200 to ~1480–1520 °C,), λ_1-Co_5Nb_{3-x} (~1200–1420 °C), μ-$Co(Nb,W)_{1\pm x}$ (extended solid solution based on μ-$CoNb_{1\pm x}$, <1480 °C,), κ-$Co_3(W,Nb)_{1\pm x}$ (extended solid solution based on κ-$Co_3W_{1\pm x}$), μ-$Co_7(W,Nb)_{6-x}$ (extended solid solution based on μ-Co_7W_{6-x}), ε-Co, α-Co, (W,Nb)	[37, 46, 199–200, 332]

(continued)

Table 3.6 (continued)

System	Type of phase diagram (temperature and composition sections, constituent phases or phase fields) and/or character of interphase interaction and materials compatibility	References
W–Co–Ta	Plotted at 900 and 1000 °C: $Co_3(Ta,W)$ (extended solid solution based on Co_3Ta with max. W content—up to 5 at.% at 1000 °C, ~950–1000 °C), λ_3-$Co_{3-x}(Ta,W)$ (extended solid solution based on λ_3-$Co_{3-x}Ta$ with max. W content—up to 5 at.% at 1000 °C, <1450 °C), λ_2-$Co_{2\pm x}(Ta,W)$ (extended solid solution based on λ_2-$Co_{2\pm x}Ta$ with max. W content—up to 13 at.%, <~1595–1650 °C), μ-$Co(Ta,W)_{1\pm x}$ (extended solid solution based on μ-$CoTa_{1\pm x}$ with max. W content—up to 9 at.%, <1700 °C), $Co(Ta,W)_2$ (extended solid solution based on $CoTa_2$ with max. W content—up to 9 at.%, <1800 °C), κ-$Co_3(W,Ta)_{1\pm x}$ (extended solid solution based on κ-$Co_3W_{1\pm x}$ with max. Ta content—up to 8 at.%), μ-$Co_7(W,Ta)_{6-x}$ (extended solid solution based on μ-Co_7W_{6-x} with max. Ta content—up to 18 at.%), κ-Co_7Ta_2 (<950 °C), λ_1-Co_5Ta_3 (1130–1540 °C), ε-Co, α-Co, (W,Ta) The solubility of Co in (W,Ta) is $\leq$ 1 at.%	[37, 199–200, 291]
W–Cr–Mo	Plotted at 1000–2400 °C: (W,Cr,Mo) continuous solid solution based on W–Mo and Mo–Cr continuous solid solutions at higher temp. and W–Mo continuous solid solution at lower temp. (miscibility gaps are adjoined to W–Cr side at temp. ~1450–1675 °C, or to W–Cr and Mo–Cr sides at temp. <1450 °C, variable with temp.), (W,Cr,Mo)	[37, 46, 189–190, 265, 284]
W–Cr–Mo–Si	WSi_2–$MoSi_2$–$CrSi_2$ is plotted at 1400 °C: $(W,Mo,Cr)Si_2$ (extended solid solution based on WSi_2–α-$MoSi_2$ continuous solid solution—up to compos. ~$(W_{0.3}Cr_{0.7})Si_2$ and ~$(Mo_{0.5}Cr_{0.5})Si_2$), $(Cr,W,Mo)Si_2$ (extended solid solution based on $CrSi_2$ up to compos. ~$(Cr_{0.8}W_{0.2})Si_2$ and ~$(Cr_{0.6}Mo_{0.4})Si_2$) $(W_{0.5}Mo_{0.5})Si_2$–$CrSi_2$ is plotted: at 1400 °C the solubility of $(W_{0.5}Mo_{0.5})Si_2$ in $CrSi_2$ is 18 mol.% and that of $CrSi_2$ in $(W_{0.5}Mo_{0.5})Si_2$ is 50 mol.%	[227]
W–Cr–N	Plotted at 1100 °C (pressure $N_2 \leq$ 30 MPa): $Cr_{2+x}N$ (<1740–1800 °C), CrN_{1-x} (<~1050 °C), CrN_2 (<~700 °C), N, Cr, W W is in equilibrium with Cr nitrides; the mutual solubilities of metal W and Cr nitrides are low	[37, 46, 143]
W–Cr–Nb	Plotted at 700–1500 °C: (W,Nb,Cr) continuous solid solution based on W–Nb continuous solid solution (wide miscibility gap is adjoined to Nb–Cr side) at higher temp., (Cr,W,Nb) extended solid solution based on Cr at lower temp., λ_2-$(Nb,W)Cr_{2\pm x}$ (<1585–1625 °C, max. solubility of W at 1100–1400 °C—~8 at.%; the addition of W reduces the stability of the phase, depend. on compos. W substitutes whether for Nb or Cr sites), λ_1-$(Nb, W)Cr_{2\pm x}$ (from 1585 to 1625 °C to ~1670–1820 °C), Cr, (W,Nb)	[37, 40, 46, 241, 284, 288, 290]

(continued)

Table 3.6 (continued)

System	Type of phase diagram (temperature and composition sections, constituent phases or phase fields) and/or character of interphase interaction and materials compatibility	References
W–Cr–Os	Plotted at 1000 °C: (W,Cr,Os) extended solid solution based on W–Cr continuous solid solution with miscibility gap adjoined to W–Cr side from ~6.5–10.5 to ~84–88 at.% W and max. solubility of Os—~30-45 at.% (?), or (W,Cr,Os) extended solid solution based on Cr with max. solubility of W—~6.5–10.5 at.% and Os—~30–45 at.% (?), $Cr_{3\pm x}Os$ (<1540 °C), σ-$Cr_{2\pm x}Os$ (975–1675 °C), σ-$OsW_{3\pm x}$, Cr, Os, W	[37, 40, 284]
W–Cr–Re	Plotted at 1000 and 1500 °C: (W,Cr,Re) extended solid solution based on W–Cr continuous solid solution with miscibility gap adjoined to W–Cr side from ~6.5–10.5 to ~84–88 at.% W and max. solubility of Re—~35–40 at.% (?), or (W,Cr,Os) extended solid solution based on Cr with max. solubility of W—~6.5–11 at.% and Re—~35–40 at.% (?), σ-$W_2Re_{3\pm x}$, χ-WRe_{3-x}, σ-Cr_2Re_{3-x} (<2355 °C), Cr, Re, W	[37, 46–47, 284]
W–Cr–Si–Ti	WSi_2–$CrSi_2$–$TiSi_2$ is plotted at 1300 °C: $(Cr,Ti,W)Si_2$ (or $(Cr_{1-x}W_x)Si_2$ ($0 < x < \sim 0.2$)–$(Ti_{1-x}W_x)Si_2$ ($\sim 0.05 < x < \sim 0.4$) continuous solid solution), $(W,Cr,Ti)Si_2$ (extended solid solution based on WSi_2; solubility of Ti is low)	[229]
W–Cr–Ta	Plotted at 1000 and 1500 °C: (W,Ta,Cr) continuous solid solution based on W–Ta continuous solid solution (wide miscibility gaps are adjoined to W–Cr and Ta–Cr sides) at higher temp., extended solid solution based on Cr at lower temp., α-$Cr_{2\pm x}Ta$ (<1660–1695 °C), β-$Cr_{2\pm x}Ta$ (from 1660 to 1695 °C to ~2015–2040 °C), Cr, (W,Ta)	[37, 46–47, 284]
W–Fe–Mo	Plotted at 900–1400 °C: λ-$Fe_2(W,Mo)$ (λ-Fe_2W–λ-Fe_2Mo Laves phase continuous solid solution, ≤~925–1060 °C), μ-$Fe_7(W,Mo)_{6-x}$ (μ-Fe_7W_{6-x}–μ-Fe_7Mo_{6-x} continuous solid solution, ~900–1370 °C, or extended solid solution based on μ-Fe_7W_{6-x}, ~1370–1635 °C, or extended solid solution based on μ-Fe_7Mo_{6-x}, <~900–1200 °C), ρ-$Fe_3(Mo,W)_{2-x}$ (extended solid solution based on ρ-Fe_3Mo_{2-x} (or $Fe_{62}Mo_{38}$, R-phase), 1200–1490 °C, the max. solubility of W is ~15 at.%), σ-$Fe(Mo,W)_{1\pm x}$ (extended solid solution based on σ-$FeMo_{1\pm x}$, from 1235 °C to 1540–1610 °C, the max. solubility of W is ~15 at.%), δ-$FeW_{1\pm x}$, α-Fe, γ-Fe, (W,Mo)	[37, 46, 195–204, 291]
W–Fe–Nb	Plotted at 900 °C: $Fe_2(W,Nb)$ (λ-Fe_2W–ε-$Fe_2Nb_{1\pm x}$ Laves phase continuous solid solution, <~1060–1665 °C), μ-$Fe_7(Nb,W)_{6+x}$ (extended solid solution based on μ-Fe_7Nb_{6+x}, <~1620–1690 °C), μ-$Fe_7(W,Nb)_{6-x}$ (extended solid solution based on μ-Fe_7W_{6-x}), δ-$FeW_{1\pm x}$, α-Fe, γ-Fe, (W,Nb)	[37, 46, 199–200, 291]

(continued)

Table 3.6 (continued)

System	Type of phase diagram (temperature and composition sections, constituent phases or phase fields) and/or character of interphase interaction and materials compatibility	References
W–Fe–Ta	Plotted at 900 °C: $Fe_2(W,Ta)$ (λ-Fe_2W–ε-$Fe_{2\pm x}Ta$ Laves phase continuous solid solution, <~1060–1775 °C), μ-$Fe_7(W,Ta)_{6-x}$ (extended solid solution based on μ-Fe_7W_{6-x} with max. Ta content—up to 6 at.%), μ-$Fe(Ta,W)_{1\pm x}$ (extended solid solution based on μ-$FeTa_{1\pm x}$ with max. W content—up to 8 at.%, <~1800–2000 °C), α-Fe, γ-Fe, (W,Ta) The solubility of Fe in (W,Ta) is ≤1 at.%.	[37, 46, 199–200, 291]
W–Hf–N	$HfN_{1\pm x}$ ($HfN_{0.96}$)–W is plotted (pressure N_2 − 1 MPa): eutectic—~2740–2860 °C, ~51–56 mol.% W; at the eutectic temp. the solid solubility of W in $HfN_{1\pm x}$ is ~2–2.5 mol.% and that of $HfN_{1\pm x}$ in W is <2 mol.% At 2500–2600 °C, in vacuum or inert gas atmosphere W interacts with $HfN_{1\pm x}$ weakly (exposure—1–3 h).	[102, 191]
W–Hf–O	WO_2–WO_3–HfO_{2-x} is plotted at 1200 °C: $(W_{1-x}Hf_x)O_{2.9-0.9x}$ ($0.05 \le x \le 0.08$), HfW_2O_8 (or $HfO_2{\cdot}2WO_3$), $W_{18}O_{49}$, $W_{20}O_{58}$, WO_2, WO_3, HfO_{2-x} WO_2–HfO_{2-x} is plotted: solid solution based on α-HfO_{2-x} (<13 mol.% WO_3), $W_{18}O_{49}$ (>1530 °C), WO_2 (<1530 °C), W; WO_2–HfO_{2-x} quasi-eutectic (Liquid + W ↔ WO_2 + HfO_{2-x})—1430 °C, ~76 mol.% WO_2 WO_3–HfO_{2-x} is plotted: HfW_2O_8 (or $HfO_2{\cdot}2WO_3$, ~1105–1275 °C), WO_3, HfO_{2-x}; HfW_2O_8–WO_3 eutectic—~1230 °C, ~77 mol.% WO_3; the max. solid solubility of WO_3 in HfO_{2-x} is ~6 mol.% and that of HfO_2 in WO_3 is negligible The chemical interaction in solid state between W and HfO_{2-x} is more intensive in vacuum or H_2 than in N_2 or Ar; in vacuum it initiates from 2350 to 2400 °C.	[5, 147, 174, 192]
W–Hf–Os	No diagram plot χ-$Os_{29}W_{19}Hf_{10}$	[389]
W–Hf–Ta	Plotted at 2000 °C and higher temp.: (W,Hf,Ta) continuous solid solution based on W–Ta and β-Hf–Ta continuous solid solutions (wide miscibility gap is adjoined to W–Hf side with Ta content ≤~50–52 at.%), HfW_2, α-Hf, β-Hf, (W,Ta)	[37, 46, 258, 284]
W–K–Na	No diagram plot At 700–1000 °C W is highly resistant to corrosion and erosion in K–Na (31.9 at.% Na) eutectic alloy.	[5]

(continued)

Table 3.6 (continued)

System	Type of phase diagram (temperature and composition sections, constituent phases or phase fields) and/or character of interphase interaction and materials compatibility	References
W–La–O	WO_3–La_2O_3 is plotted: γ-La_2O_3 (<2040 °C), β-La_2O_3 (2040–2110 °C), α-La_2O_3 (~2110–2300 °C), solid solution based on La_6WO_{12} (or $3La_2O_3{\cdot}WO_3$, from ~1740–1820 to ~1960–2150 °C, ?), solid solution based on $La_{10}W_2O_{21}$ (or $5La_2O_3{\cdot}2WO_3$, <1740–1820 °C), solid solution based on γ-$La_6W_2O_{15}$ (or $3La_2O_3{\cdot}2WO_3$, <630 °C), solid solution based on β-$La_6W_2O_{15}$ (or $3La_2O_3{\cdot}2WO_3$, from 630 to ~930–950 °C), solid solution based on α-$La_6W_2O_{15}$ (or $3La_2O_3{\cdot}2WO_3$, from ~930–950 to ~1790–1900 °C), solid solution based on α-La_2WO_6 (or $La_2O_3{\cdot}WO_3$, <1410–1470 °C), solid solution based on β-La_2WO_6 (or $La_2O_3{\cdot}WO_3$, from ~1410–1470 to ~1690–1760 °C), $La_{14}W_8O_{45}$ (or $7La_2O_3{\cdot}8WO_3$, <1700 °C), β-$La_2W_2O_9$ (or $La_2O_3{\cdot}2WO_3$, <~1055–1085 °C), α-$La_2W_2O_9$ (or $La_2O_3{\cdot}2WO_3$, from ~1055–1085 to ~1550–1600 °C), β-$La_2(WO_4)_3$ (or $La_2O_3{\cdot}3WO_3$, <1025 °C), α-$La_2(WO_4)_3$ (or $La_2O_3{\cdot}3WO_3$, from 1025 to 1060–1090 °C), $La_{10}W_{22}O_{81}$ (or $5La_2O_3{\cdot}22WO_3$, <1030 °C, ?), $La_4W_9O_{33}$ (or $2La_2O_3{\cdot}9WO_3$, <1020–1040 °C, ?), γ-WO_3, β-WO_3, α-WO_3; β-$La_2(WO_4)_3$ (?)–α-WO_3 eutectic—1020 °C, ~80 mol.% WO_3 In vacuum, at 1100 °C the interaction of W with γ-La_2O_3 results in the formation of $xLa_2O_3{\cdot}yWO_3$, $3 < x < 5$, $1 < y < 2$.	[5, 147, 213–218]
W–Mg–O	Plotted at 1700 °C: α-$MgWO_4$ (<1165 °C), β-$MgWO_4$ (~1165–1360 °C), MgO (<2825 °C), WO_2, $W_{18}O_{49}$, α-WO_{3-x}, β-WO_{3-x}, O, Mg, W WO_3–MgO is plotted: MgO, α-$MgWO_4$ (<1165 °C), β-$MgWO_4$ (~1165–1360 °C), α-WO_{3-x}, β-WO_{3-x}; α-$MgWO_4$–α-WO_{3-x} eutectic—1120 °C, ~70 mol.% WO_3; β-$MgWO_4$–MgO eutectic—~1320 °C, ~40–50 mol.% WO_3 In vacuum the interaction between W and MgO initiates from 2000 to 2100 °C; it is characterized by the reduction of MgO to Mg and formation of $MgWO_3$, $MgWO_4$, WO_2 and α-WO_{3-x}.	[5, 19, 87, 147, 158]
W–Mo–N	Plotted at 1100 °C (pressure $N_2 \leq 30$ MPa): γ-$(Mo,W)_2N_{1\pm x}$ (extended solid solution based on γ-$Mo_{2\pm x}N$—up to compos. $(Mo_{0.65}W_{0.35})_{2\pm x}N$), N, (W,Mo)	[143, 388]
W–Mo–Nb	Plotted at 2400–3300 °C: W–Mo–Nb continuous solid solution (W,Mo,Nb)	[5, 40, 46, 265, 284]

(continued)

Table 3.6 (continued)

System	Type of phase diagram (temperature and composition sections, constituent phases or phase fields) and/or character of interphase interaction and materials compatibility	References
W–Mo–Nb–Si	WSi_2–$MoSi_2$–$NbSi_2$ is plotted at 1400 °C: (W,Mo,Nb)Si_2 (extended solid solution based on WSi_2–α-$MoSi_2$ continuous solid solution—up to compos. ~$(W_{0.75}Nb_{0.15})Si_2$ and ~$(Mo_{0.75}Nb_{0.15})Si_2$), (Nb,W,Mo)Si_2 (extended solid solution based on $NbSi_2$ up to compos. ~$(Nb_{0.7}W_{0.3})Si_2$ and ~$(Nb_{0.4}Mo_{0.6})Si_2$) $(W_{0.5}Mo_{0.5})Si_2$–$NbSi_2$ is plotted: at 1400 °C the solubility of $(W_{0.5}Mo_{0.5})Si_2$ in $NbSi_2$ is 35 mol.% and that of $NbSi_2$ in $(W_{0.5}Mo_{0.5})Si_2$ is 15 mol.%	[227]
W–Mo–Nb–Zr	(W,Mo,Nb,Zr) extended solid solution based on W–Nb, Mo–Nb and β-Zr–Nb continuous solid solutions, Zr(W, Mo)$_2$ (ZrW_2–$ZrMo_2$ continuous solid solution), α-Zr, β-Zr, (W, Mo, Nb)	[40, 46–47, 265, 269]
W–Mo–Ni	Plotted at 700–1730 °C: β-Ni_4(W, Mo)$_{1-x}$ (β-Ni_4W_{1-x}–β-Ni_4Mo_{1-x} continuous solid solution, <870–970 °C), γ-Ni_3(Mo,W)$_{1-x}$ (extended solid solution based on γ-Ni_3Mo_{1-x}, <910 °C, the max. solubility of W is ~5 at.%), δ-Ni(Mo,W)$_{1\pm x}$ (extended solid solution based on δ-$NiMo_{1\pm x}$, <1360–1365 °C, the max. solubility of W is ~10 at.%), δ-NiW_{1-x}, γ-NiW_2, Ni, (W,Mo)	[40, 46, 189, 199–200, 205–209, 291, 335]
W–Mo–O	Plotted partially at 770 °C: (W,Mo)$O_{2\pm x}$ ($WO_{2\pm x}$–$MoO_{2\pm x}$ continuous solid solution, <1530–2325 °C), $(Mo,W)_nO_{3n-1}$ ($n = 9 \div 12$, 14) or $(Mo,W)_nO_{3n-m}$ ($n = 4, 5, 8 \div 16$, $m = 1$ and $n = 17 \div 22$, $m = 2$) homologous series of oxides (e.g., $(Mo,W)_5O_{14}$, $(Mo,W)_8O_{23}$ (<775–780 °C), $(Mo,W)_9O_{26}$ (<775–785 °C), $(Mo,W)_{10}O_{29}$, $(Mo,W)_{12}O_{35}$, $(Mo,W)_{14}O_{41}$, $(Mo,W)_{17}O_{49}$, $(Mo,W)_{18}O_{52}$), $(Mo,W)_{m+2}O_{3m+4}$ ($m = 6 \div 8$) homologous series of oxides (e.g., α-$(Mo,W)_4O_{11}$ (<550–650 °C), $(Mo,W)_9O_{25}$, $(Mo,W)_5O_{14}$), β-Mo_4O_{11} (from 550–650 °C to 810–825 °C), W_nO_{3n-2} homologous series of oxides, $W_{18}O_{49}$, $W_{24}O_{68}$, (Mo,W)O_{3-x} (<775–805 °C), (W,Mo)O_{3-x} WO_3–MoO_3 is plotted: (Mo,W)O_{3-x} (solid solution based on MoO_{3-x} with compos.—up to $(Mo_{0.97}W_{0.03})O_{3-x}$), α-$(W_{0.35 \div 0.85}Mo_{0.15 \div 0.65})O_{3-x}$ solid solution (<750–870 °C), β-$(W_{0.35 \div 0.85}Mo_{0.15 \div 0.65})O_{3-x}$ solid solution (from 750–870 °C to ?), (W,Mo)O_{3-x} (solid solution based on WO_{3-x} with compos.—up to $(W_{0.97}Mo_{0.03})O_{3-x}$) Data on the system available in literature are contradictory.	[221–223, 294–296, 300]
W–Mo–Os	Plotted at 1000–2375 °C: σ-Os(W,Mo)$_{3\pm x}$ (or σ-phase, σ-$OsW_{3\pm x}$–σ-$OsMo_{2\pm x}$ continuous solid solution, <2430–2945 °C,), β-Os(Mo,W)$_{3\pm x}$ (<~2210 °C, extended solid solution based on β-$OsMo_{3\pm x}$, ≤~25 at.% W), Os, (W,Mo)	[40, 46, 69, 284]

(continued)

Table 3.6 (continued)

System	Type of phase diagram (temperature and composition sections, constituent phases or phase fields) and/or character of interphase interaction and materials compatibility	References
W–Mo–Re	Plotted at 1000, 1500 and 1700 °C: (W,Mo,Re) extended solid solution based on W–Mo continuous solid solution, σ-$(W,Mo)_2Re_{3\pm x}$ (σ-$W_2Re_{3\pm x}$–σ-$Mo_2Re_{3\pm x}$ continuous solid solution), χ-$(W,Mo)Re_{3\pm x}$ (χ-WRe_{3-x}–χ-$MoRe_{3+x}$ continuous solid solution), Re, (W,Mo)	[5, 40, 46–47, 265, 284]
W–Mo–Re–Si	WSi_2–$MoSi_2$–$ReSi_2$ is plotted at 1400 °C: $(W,Mo,Re)Si_2$ (WSi_2–α-$MoSi_2$–$ReSi_2$ continuous solid solution)	[227]
W–Mo–S	Plotted at 500 and 800 °C: $(W,Mo)S_2$ (<~1750–2400 °C, WS_2–MoS_2 continuous solid solution), Mo_2S_3 (from ~600–700 to ~1780–1800 °C), WS_3, S, (W,Mo)	[40, 46, 224]
W–Mo–Si	Plotted at 1000, 1300 and 1900 °C: α-$(W,Mo)Si_2$ (WSi_2–α-$MoSi_2$ continuous solid solution, <1900–2160 °C), β-$(Mo,W)Si_2$ (extended solid solution based on β-$MoSi_2$—up to compos. β-$(Mo_{0.85}W_{0.15})Si_2$, 1900–2020 °C), $(W,Mo)_5Si_{3\pm x}$ (W_5Si_{3+x}–$Mo_5Si_{3\pm x}$ continuous solid solution, <2180–2320 °C), Mo_3Si (<2025 °C, no solubility of W), Si, (W,Mo) At 1300–1700 °C the interaction in the α-$MoSi_2$–W diffusion couple leads to the formation of (W, $Mo)_5Si_{3\pm x}$ and W_5Si_{3+x} layers.	[40, 46, 102, 225–237, 299, 336]
W–Mo–Si–Ta	WSi_2–$MoSi_2$–$TaSi_2$ is plotted at 1400 °C: $(W,Mo,Ta)Si_2$ (extended solid solution based on WSi_2–α-$MoSi_2$ continuous solid solution—up to compos. ~$(W_{0.75}Ta_{0.25})Si_2$ and ~$(Mo_{0.85}Ta_{0.15})Si_2$), $(Ta,W,Mo)Si_2$ (extended solid solution based on $TaSi_2$ up to compos. ~$(Ta_{0.7}W_{0.3})Si_2$ and ~$(Ta_{0.5}Mo_{0.5})Si_2$) $(W_{0.5}Mo_{0.5})Si_2$–$TaSi_2$ is plotted: at 1400 °C the solubility of $(W_{0.5}Mo_{0.5})Si_2$ in $TaSi_2$ is 30 mol.% and that of $TaSi_2$ in $(W_{0.5}Mo_{0.5})Si_2$ is 20 mol.%	[227]
W–Mo–Si–Ti	WSi_2–$MoSi_2$–$TiSi_2$ is plotted at 1300 °C: α-$(W,Mo)Si_2$ (WSi_2–α-$MoSi_2$ continuous solid solution; the solubility of $TiSi_2$ is <5 mol.%), β-$(W,Mo,Ti)Si_2$ (or $(Ti_{1-x}W_x)Si_2$ (~0.05 < x <~0.4) – $(Ti_{1-x}Mo_x)Si_2$ (~0.1 < x <~0.6) continuous solid solution) WSi_2–$MoSi_2$–$TiSi_2$ is plotted at 1400 °C: α-$(W,Mo,Ti)Si_2$ (solid solution based on WSi_2–α-$MoSi_2$ continuous solid solution—up to compos. ~$(W_{0.95}Ti_{0.05})Si_2$ and ~$(Mo_{0.95}Ti_{0.05})Si_2$), $(Ti,W,Mo)Si_2$ (extended solid solution based on $TiSi_2$ up to compos. ~$(Ti_{0.6}W_{0.4})Si_2$ and ~$(Ti_{0.5}Mo_{0.5})Si_2$) $(W_{0.5}Mo_{0.5})Si_2$–$TiSi_2$ is plotted: at 1400 °C the solubility of $(W_{0.5}Mo_{0.5})Si_2$ in $TiSi_2$ is 50 mol.% and that of $TiSi_2$ in $(W_{0.5}Mo_{0.5})Si_2$ is 5 mol.% Data on the system available in literature are controversial.	[227, 229]

(continued)

Table 3.6 (continued)

System	Type of phase diagram (temperature and composition sections, constituent phases or phase fields) and/or character of interphase interaction and materials compatibility	References
W–Mo–Si–V	WSi_2–$MoSi_2$–VSi_2 is plotted at 1400 °C: $(W,Mo,V)Si_2$ (extended solid solution based on WSi_2–α-$MoSi_2$ continuous solid solution—up to compos. $(W_{0.75}V_{0.15})Si_2$ and $(Mo_{0.9}V_{0.1})Si_2$), $(V,W,Mo)Si_2$ (extended solid solution based on VSi_2 up to compos. $\sim(V_{0.7}W_{0.3})Si_2$ and $\sim(V_{0.4}Mo_{0.6})Si_2$) $(W_{0.5}Mo_{0.5})Si_2$–VSi_2 is plotted: at 1400 °C the solubility of $(W_{0.5}Mo_{0.5})Si_2$ in VSi_2 is 31 mol.% and that of VSi_2 in $(W_{0.5}Mo_{0.5})Si_2$ is 15 mol.%	[227]
W–Mo–Ta	Plotted in the wide range of temp. up to 2700–3100 °C: W–Mo–Ta continuous solid solution (W,Mo,Ta)	[40, 46–47, 265, 284, 287]
W–Mo–Ti	Plotted at 1000 and 2230 °C: W–Mo–β-Ti continuous solid solution (at lower temp., small miscibility gap is adjoined to W–Ti side with Mo content ≤12–25 at.%), or W–Mo continuous solid solution (at higher temp.), α-Ti, β-Ti, (W,Mo)	[40, 46–47, 189, 265, 268]
W–Mo–V	Plotted at lower temp.: W–Mo–V continuous solid solution, (W,Mo,V)	[40, 46–47, 265]
W–Mo–Zr	Plotted at 1000 °C: $Zr(W,Mo)_2$ (ZrW_2–$ZrMo_2$ continuous solid solution), α-Zr, β-Zr, (W,Mo)	[40, 46–47, 265, 267–268]
W–N–Nb	Plotted partially at 1500–2200 °C: β-$Nb_{2\pm x}N$, (W,Nb) The active interaction between metal W and Nb nitrides is improbable.	[143, 390]
W–N–Si	Plotted at 1000 and 1400 °C (under Ar pressure): WSi_2, W_5Si_{3+x}, Si_3N_4 (<~1900 °C), N, Si, W At 1000 °C W, WSi_2 and W_5Si_{3+x} are in equilibrium with Si_3N_4, and at 1400 °C WSi_2 and W_5Si_{3+x} are in equilibrium with Si_3N_4. In vacuum at 1300 °C, the interaction between W and Si_3N_4 results in the formation of W silicides.	[87, 144, 289]
W–N–Ti	Plotted at <550 °C: metastable solid solution $(Ti,W)N_{1\pm x}$ based on $TiN_{1\pm x}$ with homog. range $\sim TiN_{0.4}$–$TiN_{1.1}$–$WN_{0.4}$–$WN_{1.5}$ (?), metastable solid solution (W,Ti,N) based on W with homog. range $\sim W$–$W_{0.15}Ti_{0.85}$–$W_{0.4}Ti_{0.4}N_{0.2}$–$W_{0.85}N_{0.15}$ (?), metastable solid solution α-(Ti,N,W) based on α-Ti (?), N In N_2 the interaction between compact W and $TiN_{1\pm x}$ initiates at temp. >2000–2200 °C and results to the formation of N containing solid solution based on W; the interaction in the W–$TiN_{1\pm x}$ powdered mixtures at 2100–2200 °C leads to the formation of complex phases.	[5, 102, 220, 304]
W–N–U	Plotted at 1200 °C: α-U_2N_{3+x} (<1132 °C), β-U_2N_{3-x} (from 940–1100 °C to 1352 °C), UN_{1-x} (<2810–2885 °C), N, α-U, β-U, γ-U, W UN_{1-x}–W is plotted: eutectic—~2700 °C; the mutual solid solubilities of the components are low W is in equilibrium with U nitrides (UN_{1-x}, β-U_2N_{3-x}) in the wide range of temp. Practically, molten UN_{1-x} (~2850 °C, pressure N_2 − 0.25 MPa) does not interact with W; only the weak penetration of UN_{1-x} along the grain boundaries of W and slight dissolution of W into the melt were observed.	[5, 46, 102, 43, 219]

(continued)

Table 3.6 (continued)

System	Type of phase diagram (temperature and composition sections, constituent phases or phase fields) and/or character of interphase interaction and materials compatibility	References
W–N–Zr	No diagram plot Under N_2 pressure (1 MPa), at ultra-high temp. there is no interaction between W and $ZrN_{1\pm x}$ in the solid state.	[5, 102, 143]
W–Nb–Ni	Plotted at 900–1900 °C: κ-$Ni_{3\pm x}$(Nb,W) (extended solid solution based on κ-$Ni_{3\pm x}$Nb (or ρ-$Ni_{3\pm x}$Nb), < ~1400 °C), μ-$Ni_6(Nb,W)_{7-x}$ (extended solid solution based on μ-Ni_6Nb_{7-x}, <1290 °C), β-$Ni_4(W,Nb)_{1-x}$ (extended solid solution based on β-Ni_4W_{1-x}), ζ-$Ni_{8\pm x}$Nb (<535 °C), δ-NiW_{1-x}, γ-NiW_2, Ni, (W,Nb)	[40, 46, 199–200, 291, 328]
W–Nb–O	Plotted partially at 1500 °C: (Nb,W,O), NbO (<1945 °C), NbO_2 (<1915 °C), O, W WO_3–WO_2–Nb_2O_5 is plotted partially: $3Nb_2O_5{\cdot}8WO_3$ (or $Nb_6W_8O_{39}$), $4Nb_2O_5{\cdot}9WO_3$ (or $Nb_8W_9O_{47}$), WO_3, $W_{20}O_{58}$, $W_{18}O_{49}$ WO_3–Nb_2O_5 is plotted: α-Nb_2O_5 (or extended solid solution based on α-Nb_2O_5 (?), <1510 °C), $34Nb_2O_5{\cdot}WO_3$ (or $Nb_{68}WO_{173}$), $30Nb_2O_5{\cdot}WO_3$ (or $Nb_{60}WO_{153}$, <1470 °C, metastable), $20Nb_2O_5{\cdot}WO_3$ (or $Nb_{40}WO_{103}$), $13Nb_2O_5{\cdot}WO_3$ (or $Nb_{26}WO_{68}$), $6Nb_2O_5{\cdot}WO_3$ (or $Nb_{12}WO_{33}$, <1476 °C), $13Nb_2O_5{\cdot}4WO_3$ (or $Nb_{26}W_4O_{77}$, <1435 °C), $7Nb_2O_5{\cdot}3WO_3$ (or $Nb_{14}W_3O_{44}$, <1440 °C), $8Nb_2O_5{\cdot}5WO_3$ (or $Nb_{16}W_5O_{55}$, ~1090–1385 °C), $3Nb_2O_5{\cdot}2WO_3$ (or ξ-$Nb_6W_2O_{21}$, ~ 1170-1400 °C, ?), $9Nb_2O_5{\cdot}8WO_3$ (or $Nb_{18}W_8O_{69}$, ~1265–1375 °C), $Nb_2O_5{\cdot}WO_3$ (or δ-Nb_2WO_8, <1100–1115 °C, ?), $9Nb_2O_5{\cdot}16WO_3$ (or $Nb_{18}W_{16}O_{88}$, ~1250–1380 °C, metastable), $9Nb_2O_5{\cdot}17WO_3$ (or $Nb_{18}W_{17}O_{91}$, ~1210–1375 °C, metastable), $6Nb_2O_5{\cdot}11WO_3$ (or $Nb_{12}W_{11}O_{63}$), $4Nb_2O_5{\cdot}9WO_3$ (or $Nb_8W_9O_{47}$, ~1120–1380 °C), solid solution based on $3Nb_2O_5{\cdot}8WO_3$ (or $Nb_6W_8O_{39}$, <~1290 °C), solid solution based on $Nb_2O_5{\cdot}3WO_3$ (or $Nb_2W_3O_{14}$, <~1400 °C, ?), $2Nb_2O_5{\cdot}7WO_3$ (or $Nb_4W_7O_{31}$, ~1245–1357 °C), $Nb_2O_5{\cdot}11WO_3$ (or $Nb_2W_{11}O_{38}$, ~1275–1356 °C), $Nb_2O_5{\cdot}15WO_3$ (or $Nb_2W_{15}O_{50}$, ~1270–1358 °C), γ-WO_3, β-WO_3, α-WO_3; $Nb_{60}WO_{153}$–$Nb_{12}WO_{33}$ eutectic—1464 °C, ~9.5 mol.% WO_3; ξ-$Nb_6W_2O_{21}$–$Nb_2W_3O_{14}$ eutectic— ~1340 °C, ~61 mol.% WO_3 (?); $Nb_{18}W_8O_{69}$–$Nb_{18}W_{16}O_{88}$ eutectic—1364 °C, ~63 mol.% WO_3; $Nb_{18}W_{17}O_{91}$–$Nb_8W_9O_{47}$ eutectic—1365 °C, ~67 mol.% WO_3; $Nb_8W_9O_{47}$–$Nb_4W_7O_{31}$ eutectic—1335 °C, ~77 mol.% WO_3; $Nb_4W_7O_{31}$–$Nb_2W_{11}O_{38}$ eutectic—1340 °C, ~83 mol.% WO_3; $Nb_2W_3O_{14}$–α-WO_3 eutectic— ~1300 °C, ~89 mol.% WO_3 (?)	[40, 46, 238–239, 254, 275]
W–Nb–Os	Plotted at 1000 and 1500 °C: σ-$Os(W, Nb)_{3\pm x}$ solid solution (?), χ-$Os_3Nb_{2\pm x}$ (<~2270 °C), σ-$OsNb_{2\pm x}$ (<~2200 °C), β-$OsNb_{3-x}$ (<~1975 °C), Os, (W,Nb)	[40, 46, 284]

(continued)

Table 3.6 (continued)

System	Type of phase diagram (temperature and composition sections, constituent phases or phase fields) and/or character of interphase interaction and materials compatibility	References
W–Nb–Re	Plotted at 1000 and 1500 °C: (W, Nb, Re) extended solid solution based on W–Nb continuous solid solution (up to 45.5–46.5 at.% Re at temp. >1500 °C), σ-Nb_2Re_{3-x} (from ~2160–2300 °C to ~2400–2565 °C), χ-$NbRe_{3\pm x}$ (<~2520–2745 °C), σ-$W_2Re_{3\pm x}$, χ-WRe_{3-x}, Re, (W,Nb)	[40, 46, 284]
W–Nb–Si	Plotted at 25–1700 °C: $(W,Nb)Si_2$ (extended solid solution based on WSi_2—up to compos. $(W_{0.85}Nb_{0.15})Si_2$), $(Nb,W)Si_2$ (extended solid solution based on $NbSi_2$—up to compos. $(Nb_{0.6}W_{0.4})Si_2$, <1940 °C), $(W,Nb)_5Si_{3-x}$ (W_5Si_{3+x}–β-Nb_5Si_{3-x} continuous solid solution, ~1940–2320 °C; extended solid solution based on W_5Si_{3+x}, ~1650–1940 °C; W_5Si_{3+x}–α-Nb_5Si_{3-x} continuous solid solution, from ? to 1650 °C), α-$(Nb,W)_5Si_{3-x}$ (extended solid solution based on α-Nb_5Si_{3-x}, ~1650–1940 °C), Nb_3Si (1770–1980 °C), Si, (W,Nb) WSi_2–$NbSi_2$ is plotted: eutectic—1850 °C, ~60 mol.% WSi_2; at the eutectic temp. the solubility of WSi_2 in $NbSi_2$ is ~40 mol.% and that of $NbSi_2$ in WSi_2 is ~15 mol.% The solid solubility of Si in the W–Nb continuous solid solution increases with W content growth considerably.	[102, 227, 242–248]
W–Nb–Ta	Plotted at lower temp.: W–Nb–Ta continuous solid solution, (W,Nb,Ta)	[40, 46, 284]
W–Nb–Ti	Plotted at 600 and 1000 °C: W–Nb–β-Ti continuous solid solution (at higher temp., the miscibility gap is adjoined to W–Ti side) or W–Nb continuous solid solution (at lower temp.), α-Ti, (W,Mo)	[189, 249]
W–Nb–V	Plotted at lower temp.: W–Nb–V continuous solid solution, (W,Nb,V)	[40, 46, 284]
W–Nb–Zr	Plotted at 1100, 1600 and 2000 °C: (W,Nb,Zr) extended solid solution based on W–Nb and β-Zr–Nb continuous solid solutions, ZrW_2, α-Zr, β-Zr, Nb, W The joined solid solubility of W and Zr in Nb is ~5–7 at.% at 1100 °C and ~10–15 at.% at 2000 °C.	[40, 46–47, 265–266]
W–Nd–O	W–WO_3–Nd_2O_3 is plotted at 900–1300 °C: Nd_2O_3, $3Nd_2O_3{\cdot}WO_3$ (or Nd_6WO_{12}), $2Nd_2O_3{\cdot}WO_3$ (or Nd_4WO_9), $Nd_2O_3{\cdot}WO_3$ (or Nd_2WO_6), $Nd_2O_3{\cdot}2WO_3$ (or $Nd_2W_2O_9$), $Nd_2O_3{\cdot}3WO_3$ (or $Nd_2(WO_4)_3$), $xNd_2O_3{\cdot}yWO_2{\cdot}zWO_3$ ($0.03 \le x \le 0.08$, $0.39 \le y \le 0.45$, $0.55 \le z \le 0.61$, or $Nd_{0.06-0.15}WO_{2.64-2.85}$, "tungsten bronze"), WO_3, $W_{20}O_{49}$, WO_2, W WO_3–Nd_2O_3 is plotted: WO_3, $Nd_2O_3{\cdot}4.4WO_3$ (or $Nd_2W_{4.4}O_{16.2}$, <1064 °C), $Nd_2O_3{\cdot}3WO_3$ (or $Nd_2(WO_4)_3$, <1140–1150 °C), α-$Nd_2O_3{\cdot}2WO_3$ (or α-$Nd_2W_2O_9$, <438 °C), β-$Nd_2O_3{\cdot}2WO_3$ (or β-$Nd_2W_2O_9$, 438–1248 °C), γ-$Nd_2O_3{\cdot}2WO_3$ (or γ-$Nd_2W_2O_9$, 1248–1354 °C), $Nd_2O_3{\cdot}WO_3$ (or Nd_2WO_6, <1675 °C), $2Nd_2O_3 \cdot WO_3$ (or Nd_4WO_9), $3Nd_2O_3{\cdot}WO_3$ (or Nd_6WO_{12}), Nd_2O_3;	[5, 214, 250, 252–253]

(continued)

Table 3.6 (continued)

System	Type of phase diagram (temperature and composition sections, constituent phases or phase fields) and/or character of interphase interaction and materials compatibility	References
	$Nd_2(WO_4)_3$–$Nd_2W_{4.4}O_{16.2}$ eutectic—1055 °C, 80.5 mol.% WO_3; $Nd_2W_{4.4}O_{16.2}$–α-WO_3 eutectic—1037–1053 °C, 82.5–83 mol.% WO_3	
W–Ni–Ta	Plotted at 900 °C: no ternary compounds, ζ-$Ni_{8\pm x}Ta$ (< 1330 °C), κ-$Ni_{3\pm x}Ta$ (<1550 °C), $Ni_{2\pm x}Ta$ (<1405 °C), μ-$Ni_{1-x}Ta$ (<1570 °C), $NiTa_{2+x}$ (<∼1790 °C), β-Ni_4W_{1-x}, δ-NiW_{1-x}, γ-NiW_2, Ni, (W,Ta) The solubility of W in κ-$Ni_{3\pm x}Ta$, $Ni_{2\pm x}Ta$, μ-$Ni_{1-x}Ta$ and $NiTa_{2+x}$ and that of Ta in β-Ni_4W_{1-x} are ≤5 at.%. All these binary compounds have a small homog. range (≤∼4 at.% Ni). The solubility of Ni in (W,Ta) is ≤1 at.%.	[40, 46, 199–200, 291]
W–O–Si	Plotted at 700–1000 °C: SiO_2 (<∼1700 °C), WSi_2, W_5Si_{3+x}, WO_2, $W_{18}O_{49}$, $W_{20}O_{58}$, WO_3, O, Si, W At temp. up to 2500 °C, metal W is very stable against liquid SiO_2, if the protecting atmosphere is free of oxidizing species.	[87, 345]
W–O–Sr	Plotted at 1700 °C: α-Sr_3WO_6 (from 1095 to ∼2100 °C, ?), β-Sr_3WO_6 (<1095 °C), Sr_2WO_5 (<1590 °C), $SrWO_4$ (<1540 °C), SrO (<2420–2570 °C), WO_2, $W_{18}O_{49}$, α-WO_{3-x}, β-WO_{3-x}, O, Sr, W WO_3–SrO is plotted: SrO, α-Sr_3WO_6 (from 1095 to ∼2100 °C, ?), β-Sr_3WO_6 (<1095 °C), Sr_2WO_5 (<1590 °C), $SrWO_4$ (<1540 °C), WO_3; $SrWO_4$–α-WO_{3-x} eutectic—1090 °C, ∼75 mol.% WO_3; Sr_2WO_5–$SrWO_4$ eutectic—1470 °C, ∼45 mol.% WO_3 The interaction between W and SrO initiates from 850 to 900 °C; it is characterized by the reduction of SrO to Sr and formation of Sr_3WO_6, Sr_2WO_5, $SrWO_4$, WO_2 and α-WO_{3-x}.	[87, 158]
W–O–Ta	WO_3–WO_2–Ta_2O_5 is plotted partially at 1100 °C: $2Ta_2O_5{\cdot}7WO_3$ (or $Ta_4W_7O_{31}$), WO_3–$W_{24}O_{68}$ solid solution, $W_{18}O_{49}$, WO_3 WO_3–Ta_2O_5 is plotted partially: α-Ta_2O_5, β-Ta_2O_5, $81Ta_2O_5{\cdot}2WO_3$ (or $Ta_{162}W_2O_{411}$, <∼1470 °C), $59Ta_2O_5{\cdot}2WO_3$ (or $Ta_{118}W_2O_{301}$, < ∼1500 °C), $37Ta_2O_5{\cdot}2WO_3$ (or $Ta_{74}W_2O_{191}$, <∼1620 °C), $13Ta_2O_5{\cdot}WO_3$ (or $Ta_{26}WO_{68}$, <∼1640 °C), $67Ta_2O_5{\cdot}6WO_3$ (or $Ta_{134}W_6O_{353}$, <∼1720 °C), $41Ta_2O_5{\cdot}4WO_3$ (or $Ta_{82}W_4O_{217}$, <∼1760 °C), $15Ta_2O_5{\cdot}2WO_3$ (or $Ta_{30}W_2O_{81}$, <1815 °C), $41Ta_2O_5{\cdot}8WO_3$ (or $Ta_{82}W_8O_{229}$, <1750 °C), $67Ta_2O_5{\cdot}14WO_3$ (or $Ta_{134}W_{14}O_{377}$, <∼1605–1700 °C), $13Ta_2O_5{\cdot}3WO_3$ (or $Ta_{26}W_3O_{74}$, <∼1605–1700 °C), $37Ta_2O_5{\cdot}10WO_3$ (or $Ta_{74}W_{10}O_{215}$, <∼1605–1700 °C), $59Ta_2O_5{\cdot}18WO_3$ (or $Ta_{118}W_{18}O_{349}$, <∼1605–1700 °C), $81Ta_2O_5{\cdot}26WO_3$ (or $Ta_{162}W_{26}O_{483}$, <1605 °C), $11Ta_2O_5{\cdot}4WO_3$ (or $Ta_{22}W_4O_{67}$, <1580 °C), $Ta_2O_5{\cdot}WO_3$ (or Ta_2WO_8), WO_3; α-Ta_2O_5–$Ta_{82}W_4O_{217}$ eutectic—∼1750 °C, ∼7–7.5 mol.% WO_3	[254, 277–278]

(continued)

Table 3.6 (continued)

System	Type of phase diagram (temperature and composition sections, constituent phases or phase fields) and/or character of interphase interaction and materials compatibility	References
W–O–Th	No diagram plot $Th(WO_4)_2$ In vacuum or protective atmosphere, the interaction between W and ThO_{2-x} initiates from 2200 to 2300 °C; at temp. >2320 °C the oxide is reduced to the metallic Th.	[5, 19, 87, 147, 391]
W–O–U	WO_{3-x}–UO_3 (in air) is plotted partially: U_3O_8, $UO_3{\cdot}WO_3$ (or UWO_6, <~1100 °C), WO_{3-x}; UWO_6–WO_{3-x} eutectic—1060 °C, ~57 mol.% WO_3 WO_{3-x}–UO_3 (pressure O_2 − 0.1 MPa) is plotted: α-U_3O_8, β-U_3O_8, $UO_3{\cdot}WO_3$ (or UWO_6, <~1100 °C), $UO_3{\cdot}3WO_3$ (or UW_3O_{12}, <1050 °C), α-WO_{3-x}, β-WO_{3-x}; UWO_6–UW_3O_{12} eutectic—1025–1045 °C, ~57 mol.% WO_3; at 1050 °C WO_{3-x} dissolves ~2 mol.% UO_3 In vacuum or inert gas atmosphere, at temp. ≤2760 °C (melt. point of UO_{2+x}), there is no interaction in the solid state between W and UO_{2+x}; in H_2 or inert gas atmosphere, at 3000 °C (exposure—168 h) the interaction between W and liquid UO_{2+x} is weak.	[5, 46, 87, 147, 255–256]
W–O–Y	WO_3–Y_2O_{3-x} is plotted partially: solid solution based on α-Y_2O_{3-x} (<2325–2350 °C, <2 mol.% WO_3), solid solution based on β-Y_2O_{3-x} (from ~2310–2325 to ~2410–2460 °C, <3 mol.% WO_3), $xY_2O_3{\cdot}WO_3$ solid solution ($2 \le x \le 4.4$, or $Y_{4.0\div8.8}WO_{9.0\div16.2}$, 1730–2380 °C), $3Y_2O_3{\cdot}WO_3$ (or Y_6WO_{12}, <1765 °C), $5Y_2O_3{\cdot}2WO_3$ (or $Y_{10}W_2O_{21}$, <1740 °C), $7Y_2O_3{\cdot}4WO_3$ (or $Y_{14}W_4O_{33}$, <~2105 °C), α′-$Y_2O_3{\cdot}WO_3$ (or α′-Y_2WO_6, <~1470 °C), δ-$Y_2O_3{\cdot}WO_3$ (or δ-Y_2WO_6, ~1470–1640 °C), β-$Y_2O_3{\cdot}WO_3$ (or β-Y_2WO_6, ~1640–1705 °C), WO_3; solid solution based on β-Y_2O_{3-x}–$xY_2O_3{\cdot}WO_3$ solid solution eutectic—~2335 °C, 10 mol.% WO_3 In vacuum, at 1100 °C the interaction between W and α-Y_2O_{3-x} results in the formation of $3Y_2O_3{\cdot}WO_3$.	[5, 46, 147, 257]
W–O–Y–Zr	No diagram plot In inert gas atmosphere, the chemical interaction between W and ZrO_{2-x} +9 % Y_2O_{3-x} initiates from 2500 °C.	[147]

(continued)

Table 3.6 (continued)

System	Type of phase diagram (temperature and composition sections, constituent phases or phase fields) and/or character of interphase interaction and materials compatibility	References
W–O–Zr	Plotted partially at 1500 °C: α-ZrO_{2-x}, β-ZrO_{2-x}, γ-ZrO_{2-x}, WO_2, $W_{18}O_{49}$, $W_{20}O_{58}$, WO_{3-x}, O, Zr, W WO_{3-x}–WO_2–ZrO_{2-x} is plotted at 1200–1500 °C: solid solution with compos. From $Zr_xW_{1-x}O_{2+0.9(1-x)}$ to $Zr_xW_{1-x}O_{3(1-x)}$ ($0.05 < x < 0.08$, <~1450 °C), $ZrO_2{\cdot}2WO_3$ (or ZrW_2O_8), α-ZrO_{2-x}, β-ZrO_{2-x}, WO_2, $W_{18}O_{49}$, $W_{20}O_{58}$, WO_{3-x} WO_2–ZrO_{2-x} is plotted: solid solution based on β-ZrO_{2-x} (≤13 mol.% WO_3), $W_{18}O_{49}$ (>1530 °C), WO_2 (<1530 °C), W; WO_2–β-ZrO_{2-x} quasi-eutectic (Liquid + W ↔ WO_2 + β-ZrO_{2-x})—1430 °C, ~75–77 mol.% WO_2 WO_{3-x}–ZrO_{2-x} is plotted: ZrW_2O_8 (or $ZrO_2{\cdot}2WO_3$, ~1105–1255 °C), solid solution based on α-ZrO_{2-x} (<~1160–1180 °C, <5 mol.% WO_3), solid solution based on β-ZrO_{2-x} (<5 mol.% WO_3), WO_{3-x}; ZrW_2O_8–WO_{3-x} eutectic—~1230 °C, ~74–75 mol.% WO_3 In vacuum (0.01–0.05 Pa), the chemical interaction between W and ZrO_{2-x} initiates from 1600 to 1900 °C (exposure—0.5–5 h); at 1900–2300 °C it is characterized with the increase of porosity in the metal-oxide contact zone because of the vaporization of W oxides. In protective atmosphere the starting temp. of the interaction is lower. Its indications in the literature are quite different due to differences in ZrO_{2-x} stabilization.	[5, 19, 87, 147, 192]
W–Os–Re	Plotted partly at 1000–1500 °C: σ-$W_{2\pm x}$(Re,Os) (σ-$W_2Re_{3\pm x}$–σ-$OsW_{3\pm x}$ continuous solid solution, <2890–3005 °C), χ-WRe_{3-x}, (Os,Re), W	[5, 40, 46–47, 273]
W–Os–Ta	Plotted partly at 1000–1500 °C: σ-$Os(W,Ta)_{3\pm x}$ (σ-$OsW_{3\pm x}$–σ-$Ta_3Os_{2\pm x}$ continuous solid solution, <~2500–2945 °C), Os, (W,Ta)	[40, 46–47, 284]
W–Os–V	Plotted partly at 1000–1500 °C: (W,V,Os) extended solid solution based on W–V continuous solid solution with max. solubility of Os—~30–45 at.%, $V_3Os_{2\pm x}$ (<2140 °C), VOs_{1-x} (?), σ-$OsW_{3\pm x}$, Os, (W,V)	[40, 46–47, 284]
W–Re–Si	Plotted at 800 °C: κ-$W_{3\pm y}Re_{1\pm y}Si_4$, $(W,Re)Si_2$ (WSi_2–$ReSi_2$ continuous solid solution, at least at 1400 °C), (Re, W)Si (extended solid solution based on ReSi with max. solubility of W—32 at.%, <~1820–1880 °C, ?), $(W, Re)_5Si_{3+x}$ (extended solid solution based on W_5Si_{3+x} with max. solubility of Re—21 at.%), Re_5Si_3 (<1020 °C, solubility of W—up to 5 at.%, ?), Re_2Si (<~1810–1960 °C), σ-$W_2Re_{3\pm x}$ (solubility of Si—up to 10 at.%), χ-WRe_{3-x} (solubility of Si—up to 5 at.%), Si, Re, W	[102, 227–228, 285]

(continued)

Table 3.6 (continued)

System	Type of phase diagram (temperature and composition sections, constituent phases or phase fields) and/or character of interphase interaction and materials compatibility	References
W–Re–Ta	Plotted at 1200–2680 °C: σ-$(W,Ta)_2Re_{3\pm x}$ (σ-$W_2Re_{3\pm x}$ –σ-Ta_2Re_{3-x} continuous solid solution at temp. ≥2460 °C or extended solid solution based on σ-$W_2Re_{3\pm x}$ at temp. ≤2460 °C), χ-$(W,Ta)Re_{3\pm x}$ (χ-WRe_{3-x}–χ-$TaRe_{3\pm x}$ continuous solid solution at temp. ≤2125 °C or extended solid solution based on χ-$TaRe_{3\pm x}$ at temp. ≥2125 °C), Re, (W,Ta)	[5, 37, 46, 258, 284]
W–Re–V	Plotted at 1000–1500 °C: (W,Re,V) extended solid solution based on W–V continuous solid solution, σ-$(W,V)_yRe_{3\pm x}$ (σ-$W_2Re_{3\pm x}$–σ-VRe_{3+x} continuous solid solution, <~2440–3000 °C), δ-$V_3Re_{7\pm x}$, χ-WRe_{3-x}, Re, (W, V)	[5, 46–47, 273, 284]
W–Si–Ta	WSi_2–$TaSi_2$ is plotted: $(Ta,W)Si_2$ (WSi_2–$TaSi_2$ continuous solid solution, <550 °C, or extended solid solution based on $TaSi_2$ at higher temp.), $(W,Ta)Si_2$ (extended solid solution based on WSi_2 at higher temp.); at 1300 °C: $(Ta,W)Si_2$ (extended solid solution based on $TaSi_2$ with compos.—up to ~$(Ta_{0.7\div0.8}W_{0.2\div0.3})Si_2$), $(W,Ta)Si_2$ (extended solid solution based on WSi_2 with compos.—up to ~$(W_{0.75}Ta_{0.25})Si_2$)	[102, 228–229, 259–260, 299]
W–Si–Ta–Ti	WSi_2–$TaSi_2$–$TiSi_2$ is plotted at 1300 °C: $(Ta,W,Ti)Si_2$ (or $(Ta_{1-x}W_x)Si_2$ ($0 < x <$ ~0.3) − $(Ti_{1-x}W_x)Si_2$ (~$0.05 < x <$ ~0.4) continuous solid solution), $(W,Ta,Ti)Si_2$ (extended solid solution based on WSi_2; solubility of Ti is very low)	[229]
W–Ta–Ti	Plotted at 600–3080 °C: (Ta,Ti,W) continuous solid solution based on Ta–W, Ta–β-Ti and W–β-Ti continuous solid solutions (miscibility gap is adjoined to W–Ti side at temp. <~1290 °C or higher (?), or isolated at temp. ~1230–1290 °C), α-Ti, β-Ti, (Ta,W)	[292–293]
W–Ta–V	Plotted at 1000 °C: (W,Ta,V) continuous solid solution based on W–Ta and W–V continuous solid solutions (wide miscibility gap is adjoined to Ta–V side from ~10 to ~60 at.% Ta), $V_{2\pm x}Ta$ (<~1310–1420 °C, the solubility of W is low)	[46–47, 284]
W–Ta–Zr	Plotted at 800–1600 °C: $Zr(W,Ta)_2$ (extended solid solution based on ZrW_2—up to compos. $Zr(W_{0.83}Ta_{0.17})_2$ at 1600 °C), α-Zr, β-Zr, (W,Ta)	[261]

[a] See notes to Table 3.5

Table 3.7 Wettability of tungsten by some non-ferrous metal alloys (melts of bulk metallic glasses) in vacuum [340–341]

Alloy composition	Wetting contact angle, degree	Temperature, °C
Ti—30.2 at.% Zr—22.5 at.% Be—9 at.% Cu—5.3 at.% Ni[a]	53	700
	50	800
	40	900
	27	1000
	23	1050
Zr—36.45 at.% Cu—9 at.% Al—4.05 at.% Ni[b]	26	900
	16	950

[a] The contact angles at the initial stage of wetting in the range of temperatures 700–1050 °C are 130–140°; the variation of final equilibrium contact angle θ with temperature can be expressed by relationship $\theta = 142.13 - 0.083(T + 91.58)$, where T is temperature, K

[b] The contact angles at the initial stage of wetting in the range of temperatures 900–950 °C are 21–58°, depending on temperature and decreasing remarkably with its growth

The wettabilities of tungsten by some alloys are given in Table 3.7, and character of chemical interaction and general reactions of tungsten with common chemicals (solids, liquids, aqueous solutions) and complex gases are summarized in Table 3.8.

Table 3.8 The interaction of tungsten with some chemicals and complex gases [5, 19, 36, 87, 116–117, 265, 276][a]

Reagent, formula	Character of chemical interaction, examples of general reactions
Air, $N_2 + O_2$	W is stable at room temp. in air, the oxidation initiates from 300 to 500 °C and leads to the formation of W_4O_{11}: $8W + 11O_2 \rightarrow 2W_4O_{11}$, at higher temp. WO_3 is formed: $2W + 3O_2 \rightarrow 2WO_3$. The intensive oxidation of W at air begins from 850 to 900 °C and leads to a marked loss of material by the vaporization of oxides.
Water, H_2O	No interaction at the ambient temp., at temp. >400–600 °C WO_3 is formed: $W + 3H_2O \rightarrow WO_3 + 3H_2$ At temp. >500 °C the oxidation of W in the presence of water vapour is severe and accompanied with the more intensive vaporization of WO_3, which interacts with the formation of the volatile products: $WO_3 + H_2O \leftrightarrow WO_2(OH)_2$ (or H_2WO_4)
Hydrogen peroxide, H_2O_2	The interaction results in the oxidation and dissolution of W: $W + 2H_2O_2 \rightarrow WO_2 + 2H_2O$, $WO_2 + H_2O_2 \rightarrow H_2WO_4$, $2WO_2 + 6H_2O_2 \rightarrow H_2W_2O_{11} + 5H_2O$, $3H_2W_2O_{11} \rightarrow 2H_2W_3O_{12} + H_2O$, $3H_2WO_4 + 2H_2O_2 \rightarrow H_2W_3O_{12} + 4H_2O$; increased temp. enhances the dissolution rate up to 60 °C, higher temp. slow down the reaction because of H_2O_2 decomposition.

(continued)

Table 3.8 (continued)

Reagent, formula	Character of chemical interaction, examples of general reactions
Nitrogen oxides, N_2O, NO, NO_2	At elevated and high temp. the interaction results in the oxidation of W: $W + 3N_2O \rightarrow WO_3 + 3N_2$, $2W + 6NO \rightarrow 2WO_3 + 3N_2$, $4W + 6NO_2 \rightarrow 4WO_3 + 3N_2$.
Sulphur dioxide, SO_2	At temp. ≥700–900 °C the interaction between W and SO_2 leads to the formation of W oxides and S released: $2W + 3SO_2 \rightarrow 2WO_3 + 3S$, $W + 2SO_2 \rightarrow WO_3 + ½O_2 + 3S_2$.
Sulphur hexafluoride, SF_6	At 500–700 °C the ternary compound WSF_4 is formed: $3W + 2SF_6 \rightarrow 2WSF_4 + WF_4$.
Disulphur dichloride, S_2Cl_2	In the presence of air $WOCl_4$ is formed: $W + 2S_2Cl_2 + ½O_2 \rightarrow WOCl_4 + 2S_2$ and, under exclusion—WCl_6: $W + 3S_2Cl_2 \rightarrow WCl_6 + 3S_2$
Boron trichloride, BCl_3	At 900–1000 °C the interaction leads to the formation of W borides.
Carbon monoxide, CO	At 80–200 °C the interaction leads to the formation of W hexacarbonyl: $W + 6CO \rightarrow W(CO)_6$, at temp. >900–1000 °C, bulk W is carburized and carbides are formed: $(2 + x)W + 2CO \rightarrow W_{2+x}C + CO_2$, $W + 2(1 \pm x)CO \rightarrow WC_{1\pm x} + (1\pm x)CO_2$ Nanocrystalline W powders start to carburize from ~550 °C.
Carbon dioxide, CO_2	The interaction initiates at temp. > 600 °C and leads to the formation of lower or higher W oxides: $W + nCO_2 \rightarrow WO_n + nCO$
Hydrogen sulphide, H_2S	At temp. >600–800 °C the interaction between W and H_2S leads to the formation of W sulfides: $W + (2 - x)H_2S \rightarrow WS_{2-x} + (2 - x)H_2$
Hydrogen selenide, H_2Se	The interaction between W and H_2Se at 300–400 °C leads to the formation of W selenide: $W + H_2Se \rightarrow WSe + H_2$, and at 500–800 °C—W diselenide (decomposes at temp. >850 °C): $W + (2 - x)H_2Se \rightarrow WSe_{2-x} + (2 - x)H_2$
Hydrocarbons, C_mH_n	The interaction between W and hydrocarbons initiates from 1000–1200 °C and leads to the formation of W carbides, at 1400–1600 °C the interaction is very intensive. W reacts with CH_4 forming $W_{2+x}C$ and $WC_{1\pm x}$: $W + (1 \pm x)CH_4 \rightarrow WC_{1\pm x} + 2(1 \pm x)H_2$, $(2 + x)W + CH_4 \rightarrow W_{2+x}C + 2H_2$
Hydrogen cyanide, HCN	At 700–2200 °C the interaction leads to the formation of W monocarbide: $W + (1 \pm x)HCN \rightarrow WC_{1\pm x} + ½(1 \pm x)H_2 + ½(1 \pm x)N_2$, at 2200–2600 °C—W semicarbide: $(2 + x)W + HCN \rightarrow W_{2+x}C + ½H_2 + ½N_2$, and at temp. ≥2600 °C, in addition graphite is formed: $(2 + x)W + 2HCN \rightarrow W_{2+x}C + C + H_2 + N_2$

(continued)

Table 3.8 (continued)

Reagent, formula	Character of chemical interaction, examples of general reactions
Carbon tetrafluoride, CF_4	At elevated temp. the interaction results in the formation of WF_6.
Carbon tetrachloride, CCl_4	At temp. ≥600 °C the interaction results in the formation of WCl_6 and WCl_4.
Carbon disulphide, CS_2	At elevated temp. the interaction results in the formation of WS_{2-x}.
Silicon tetrachloride, $SiCl_4$	At 1000–1200 °C in H_2 atmosphere, the interaction leads to the formation of W disilicide: $W + 2SiCl_4 + 4H_2 \rightarrow Wsi_2 + 8HCl$
Silicon tetrabromide, $SiBr_4$	In H_2 atmosphere, the interaction leads to the formation of W disilicide: $W + 2SiBr_4 + 4H_2 \rightarrow Wsi_2 + 8HBr$
Phosphine, PH_3	At temp. ≥850 °C the interaction leads to the formation of WP.
Ammonia (gas), NH_3	At 150–800 °C the interaction between W and NH_3 is accompanied with embrittlement because of the formation of various nitrides; at temp. ≥800 °C the interaction becomes intensive.
Ammonia (aqueous solution), NH_4OH	No interaction (it initiates only in the presence of H_2O_2).
Sodium oxide, Na_2O	At temp. >500 °C Na_2O reacts with W: $W + 4Na_2O \rightarrow Na_2WO_4 + 6Na$
Sodium sulphide, Na_2S	No interaction at temp. <1500 °C.
Sodium hydroxide, NaOH	No interaction with NaOH in aqueous solution (without oxidizing agents including O_2 and air); the slow interaction, which leads to the formation of tungstates (wolframates), is observed between molten NaOH and W in the presence of O_2; the intensive interaction occurs in the presence of oxidizers (KNO_2, KNO_3, $KClO_3$, PbO_2 and others). For the reactions, see the next section on potassium hydroxide, KOH.
Sodium hydroxide with sodium nitrate, $NaOH + NaNO_2$	The dissolution of W occurs due to the following reactions: $W + 6NaNO_2 \rightarrow Na_2WO_4 + 2Na_2O + 6NO$
Sodium hydroxide with sodium nitrite, $NaOH + NaNO_3$	The dissolution of W occurs due to the following reactions: $W + 6NaNO_3 \rightarrow Na_2WO_4 + 2Na_2O + 6NO_2$
Sodium nitrate with soda, $NaNO_3 + Na_2CO_3$	At elevated temp. the interaction results in the formation of tungstates (wolframates) soluble in aqueous solutions: $W + 3NaNO_3 + Na_2CO_3 \rightarrow Na_2WO_4 + 3NaNO_2 + CO_2$.
Sodium sulphate, Na_2SO_4	At temp. >320 °C Na_2SO_4 reacts with W: $(3 - x)W + (2 - x)Na_2SO_4 \rightarrow (2 - x)Na_2WO_4 + WS_{2-x}$
Sodium carbonate, Na_2CO_3	At temp. >950 °C Na_2CO_3 slowly reacts with W: $W + 3Na_2CO_3 \rightarrow Na_2WO_4 + 2Na_2O + 3CO$
Sodium chloride, NaCl	Weak interaction in aqueous solution.
Ammonium chloride, NH_4Cl	Weak interaction in aqueous solution.

(continued)

Table 3.8 (continued)

Reagent, formula	Character of chemical interaction, examples of general reactions
Sodium hypochlorite, NaClO	The interaction results in the dissolution of W: $W + 3NaClO + H_2O \rightarrow Na_2WO_4 + NaCl + 2HCl$
Iron (III) chloride, $FeCl_3$	The intensive interaction results in the dissolution of W: $W + 6FeCl_3 + 4H_2O \rightarrow H_2WO_4 + 6FeCl_2 + 6HCl$
Barium carbonate, $BaCO_3$	At temp. 600–800 °C $BaCO_3$ reacts with W: $W + 3BaCO_3 \rightarrow Ba_3WO_6 + 3CO$
Potassium hydroxide, KOH	No interaction with KOH in aqueous solution (without oxidizing agents including O_2 and air); the slow interaction, which leads to the formation of tungstates (wolframates), is observed between molten KOH and W in the presence of O_2: $2W + 4(n + 1)KOH + 3O_2 \rightarrow 2K_{2(n+1)}WO_{n+4} + 2(n + 1)H_2O$; the intensive interaction occurs in the presence of oxidizers (KNO_2, KNO_3, $KClO_3$, PbO_2 and others): $W + 2nKOH + 2KNO_2 \rightarrow K_{2(n+1)}WO_{n+4} + N_2 + nH_2O$, $W + 2(n + 1)KOH + 3KNO_3 \rightarrow K_{2(n+1)}WO_{n+4} + 3KNO_2 + (n + 1)H_2O$, $W + 2(n + 1)KOH + KClO_3 \rightarrow K_{2(n+1)}WO_{n+4} + KCl + (n + 1)H_2O$.
Potassium hydroxide with potassium hexacyanoferrate (III), $KOH + K_3[Fe(CN)_6]$	The interaction results in the dissolution of W: $W + 6K_3[Fe(CN)_6] + 8KOH \rightarrow K_2WO_4 + 6K_4[Fe(CN)_6] + 4H_2O$
Potassium dichromate, $K_2Cr_2O_7$	Binary powder mixtures of W and $K_2Cr_2O_7$ are easy to ignite (650–660 °C) and burn over a wide range of compos.; there is only little change in weight (gasless pyrotechnical system): $W + K_2Cr_2O_7 \rightarrow K_2WO_4 + Cr_2O_3$.
Nitric acid, HNO_3	Slight interaction at room temp.; at 100–110 °C the interaction leads to the slow oxidation of W.
Sulphuric acid, H_2SO_4	No interaction at room temp.; slight interaction at 100–110 °C (increased attack occurs by fuming H_2SO_4).
Hydrochloric acid, HCl	No interaction at room temp.; slight interaction at 100–110 °C.
Hydrobromic acid, HBr	Weak interaction.
Hydroiodic acid, HI	Weak interaction in concentrated solutions.
Periodic acid, HIO_4	No interaction.
Hydrogen chloride, HCl	At temp. ≥500–700 °C the interaction is very intensive and leads to the formation of various W chlorides.
Hydrofluoric acid, HF	Practically, no interaction at 20–110 °C; any addition of oxydizing agents increases the dissolution rate considerably.
Phosphoric acid, H_3PO_4	No interaction at room temp., and slight interaction at 100–110 °C with diluted H_3PO_4 as long as air is excluded. Concentrated acid easily dissolves W. At temp. ≥250 °C the interaction results in the formation of complex compounds on the surface of W.
Hydrochloric acid with nitric acid (aqua regia), $HCl + HNO_3$	The interaction is slow at room temp. and intensifies on heating. For the reactions, see the next section on hydrofluoric-nitric acid mixtures $HNO_3 + HF$.

(continued)

Table 3.8 (continued)

Reagent, formula	Character of chemical interaction, examples of general reactions
Hydrofluoric-nitric acid mixtures, $HF + HNO_3$	The interaction is intensive and leads to the dissolution of W: $W + 6HNO_3 + 2HF \rightarrow WO_2F_2 + 6NO_2 + 4H_2O$, $5W + 6HNO_3 + 10HF \rightarrow 5WO_2F_2 + 3N_2 + 8H_2O$, $5W + (16 - n)HNO_3 + nHF \rightarrow (5 - n/2)WO_2(NO_3)_2 + n/2WO_2F_2 + 3N_2 + 8H_2O$.
Hydrofluoric-sulphuric-nitric acid mixtures, $HF + H_2SO_4 + HNO_3$	W is dissolved quickly at all concentrations.

[a] Etching agents for tungsten: boiling 3 % H_2O_2 aqueous solution (for grain boundaries and subboundaries), 25 % $CuSO_4 \cdot 5H_2O + NH_4OH$ mixture (ratio 2:1) at 40 °C (for single crystals), 10 % NaOH + 30 % $K_3[Fe(CN)_6]$ aqueous solution (chemical etching), 2–10 % NaOH aqueous solution (electrochemical etching, 1–2 V, 0.017 A cm^{-2})

The self-diffusion characteristics of tungsten atoms, diffusion characteristics in tungsten—element and tungsten—chemical compound systems in the wide range of temperatures, and summarized data on the physico-chemical interaction of tungsten with elements of the periodic table are given in Addendum.

References

1. Steurer W (1996) Crystal structure of the metallic elements. In: Cahn RW, Haasen P (eds) Physical metallurgy, 4th ed., Vol. 1, pp. 1–46. Elsevier Science BV, Amsterdam
2. Cotton FA, Wilkinson G (1965) Advanced inorganic chemistry. Wiley, New York, London
3. Akhmetov NS (2001) Obschaya i neorganicheskaya khimiya (General and inorganic chemistry), 4th ed. Vysshaya Shkola, Moscow (in Russian)
4. Waseda Y, Hirata K, Ohtani M (1975) High-temperature thermal expansion of platinum, tantalum, molybdenum and tungsten measured by X-ray diffraction. High Temp High Pressures 7:221–226
5. Kotelnikov RB, Bashlykov SN, Galiakbarov ZG, Kashtanov AI (1968) Osobo tugoplavkie elementy i soedineniya (Extra refractory elements and compounds). Metallurgiya, Moscow (in Russian)
6. Zefirov AP (ed), Veryatin UD, Mashirev VP, Ryabtsev NG, Tarasov VI, Rogozkin BD, Korobov IV (1965) Termodinamicheskie svoistva neorganicheskikh veschestv (Thermodynamic properties of inorganic substances). Atomizdat, Moscow (in Russian)
7. Hoch M (1969) Thermal properties of tungsten at high temperatures. High Temp High Pressures 1:531–542
8. Speight JG, ed (2005) Lange's handbook of chemistry, 16th ed. McGraw-Hill, New York
9. Rieck GD (1967) Tungsten and its compounds. Pergamon Press, Oxford, New York
10. Lide DR, ed (2010) CRC handbook of chemistry and physics, 90th ed. CRC Press, Boca Raton, New York
11. Martienssen W (2005) The elements. In: Martienssen W, Warlimont H (eds) Springer handbook of condensed matter and materials data, pp. 45–158. Springer, Berlin, Heidelberg
12. Plante ER, Sessoms AB (1973) Vapor pressure and heat of sublimation of tungsten. J Res Nat Bur Stand Sect A Phys Chem 77(2):237–242

13. Cezairliyan A (1972) Measurement of melting point and electrical resistivity (above 3600 K) of tungsten by a pulse heating method. High Temp Sci 4(3):248–252
14. Samsonov GV, ed (1976) Svoistva elementov (Properties of elements), 2nd ed., Vol. 1. Metallurgiya, Moscow (in Russian)
15. Backlund NG (1967) Measurement and analysis of the thermal conductivity of tungsten and molybdenum at 100–400 K. J Phys Chem Solids 28(11):2219–2223
16. Neimark BE, Voronin IK (1968) Teploprovodnost, udelnoe elektrosoprotivlenie i integralnaya stepen chernoty tugoplavkikh metallov pri vysokikh temperaturakh (Thermal conductivity, specific electrical resistance and integral emissivity of refractory metals at high temperatures). Teplofiz Vys Temp 6(6):1044–1056 (in Russian)
17. Taylor RE, Davis FE, Powell RW (1969) Direct heating methods for measuring thermal conductivity of solids at high temperatures. High Temp High Pressures 1(6):663–673
18. Vertogradskii VA, Chekhovskoi VYa (1970) Izmerenie teploprovodnosti volframa pri vysokikh temperaturakh dvukh-mostovym metodom (Measurement of the heat conductivity of tungsten at high temperatures using the 'two bridge' method). Teplofiz Vys Temp 8(4):784–788 (in Russian)
19. Marmer ÉN, Gurvich OS, Maltseva LF (1967) Vysokotemperaturnye materialy (High-temperature materials). Metallurgiya, Moscow (in Russian)
20. Conway JB, Losekamp AC (1966) Thermal expansion characteristics of several refractory metals to 2500 °C. Trans TMS-AIME 236:702–709
21. Conway JB (1984) Mechanical and physical properties of refractory metals and alloys. In: Cooper RH, Jr, Hoffman EE (eds) Refractory alloy technology for space nuclear power applications, pp. 227–251. Technical Information Center, Office of Scientific and Technical Information, US Department of Energy, Oak Ridge
22. Kittel C (1971) Introduction to solid state physics, 3rd ed. Wiley, New York
23. Cardarelli F (2008) Materials handbook, 2nd ed. Springer, London
24. Pisarenko GS, Borisenko VA, Kashtalyan (1962) The effect of temperature on the hardness and modulus of elasticity of tungsten and molybdenum (20–2700 °C). Powder Metall Met Ceram 1(5):371–374
25. Sell HG, Morcom WR, King GW (1966) Development of dispersion strengthened tungsten base alloys. Report AFML-TR-65–407, Part 2. Westinghouse Lamp Division, Bloomfield, New Jersey
26. Klopp WD, Raffo PL (1964) Effect of purity and structure on recrystallization, grain growth, ductility, tensile and creep properties of arc-melted tungsten. Report NASA-TND-2503. NASA Lewis Research Center, Cleveland, Ohio
27. Klopp WD, Witzke WR (1966) Mechanical properties and recrystallization behaviour of electron-beam-melted tungsten compared with arc-melted tungsten. Report NASA-TND-3232. NASA Lewis Research Center, Cleveland, Ohio
28. Taylor JL, Boone DH (1964) Tensile properties of pyrolytic tungsten from 1370 to 2980 °C in vacuum. J Less-Common Met 6:157–164
29. McDanels DL, Signorelli RA (1966) Stress-rupture properties of tungsten wire from 1200 to 2500 °F. Report NASA-TN-D-3467, Glenn Research Center, Cleveland, Ohio
30. Wright PK (1978) The high temperature creep behavior of doped tungsten wire. Metall Trans A 9(7):955–963
31. Moon DM, Stickler R (1971) Creep behaviour of fine wires of P/M pure, doped and thoriated tungsten. High Temp High Pressures 3:503–518
32. Pugh JW (1973) On the short time creep rupture properties of lamp wire. Metall Trans 4:533–538
33. Plansee Aktiengesellschaft (2000) Materials data base. Reutte, Austria
34. Lowrie R, Gonas AM (1965) Dynamic elastic properties of polycrystalline tungsten, 24–1800 °C. J Appl Phys 36:2189–2192
35. Lowrie R, Gonas AM (1967) Single-crystal elastic properties of tungsten from 24 to 1800 °C. J Appl Phys 38:4505–4509

36. Samsonov GV, ed (1976) Svoistva elementov (Properties of elements), 2nd ed., Vol. 2. Metallurgiya, Moscow (in Russian)
37. Lyakishev NP, ed (1997) Diagrammy sostoyaniya dvoinykh metallicheskikh sistem (Phase diagrams of binary metal systems), Vol. 2. Mashinostroenie, Moscow (in Russian)
38. Frauenfelder R (1969) Solution and diffusion of hydrogen in tungsten. J Vac Sci Technol 6(3):388–397
39. Mazaev AA, Avarbe RG, Vilk YuN (1968) O rastvorimosti vodoroda v volframe pri vysokikh temperaturakh i davleniyakh (On the solubility of hydrogen in tungsten at high temperatures and pressures). Izv AN SSSR Metally (6):223–226 (in Russian)
40. Lyakishev NP, ed (2001) Diagrammy sostoyaniya dvoinykh metallicheskikh sistem (Phase diagrams of binary metal systems), Vol. 3, Part 1. Mashinostroenie, Moscow (in Russian)
41. Sangster J, Pelton AD (1991) The Li-W (lithium-tungsten) system. J Phase Equilibria 12(2):203
42. Sangster J, Pelton AD (1991) The Na-W (sodium-tungsten) system. J Phase Equilibria 12(2):204
43. Lyakishev NP, ed (1996) Diagrammy sostoyaniya dvoinykh metallicheskikh sistem (Phase diagrams of binary metal systems), Vol. 1. Mashinostroenie, Moscow (in Russian)
44. Goldschmidt HJ, Ham WM (1966) The tungsten-rich end of the tungsten-beryllium system. J Less-Common Met 10(1):57–65
45. Okamoto H, Tanner LE (1986) The Be-W (beryllium-tungsten) system. Bull Alloy Phase Diagrams 7(4):356–358
46. Massalski TB, Subramanian PR, Okamoto H, Kacprzak L, eds (1990) Binary alloy phase diagrams, 2nd ed. ASM International, Metals Park, Ohio
47. Lyakishev NP, ed (2000) Diagrammy sostoyaniya dvoinykh metallicheskikh sistem (Phase diagrams of binary metal systems), Vol. 3, Part 2. Mashinostroenie, Moscow (in Russian)
48. Pandian S, Naidu SVN, Rao PR (1988) The rare earth – tungsten systems. J Alloy Phase Diagrams 4(2):73–116
49. Dennison DH, Tschetter MJ, Gschneidner KA, Jr (1966) The solubility of tantalum and tungsten in liquid rare-earth metals. J Less-Common Met 11(6):423–435
50. De Boer FR, Dijkman WH, Mattens WCM, Miedema AR (1979) On the valence state of Yb and Ce in transition metal intermetallic compounds. J Less-Common Met 64(2):241–253
51. Miedema AR (1976) On the valence state of europium in alloys. J Less-Common Met 46(1):167–183
52. Chandrasekharaiah MS, Dharwadkar SR, Das D (1986) High-temperature phase diagrams of Re-U, Ta-U and W-U. Z Metallkd 77(8):509–514
53. Pandian S, Naidu SVN, Rao PR (1988) The W-U (tungsten-uranium) system. J Alloy Phase Diagrams 4(3):148–153
54. Pandian S, Naidu SVN, Rao PR (1988) The Pu-W (plutonium-tungsten) system. J Alloy Phase Diagrams 4(3):154–159
55. Murray JL (1981) The Ti-W (titanium-tungsten) system. Bull Alloy Phase Diagrams 2(2):192–196
56. Lee SK, Lee DN (1986) Calculation of phase diagram using partial phase diagram data. Calphad 10(1):61–76
57. Savitskii EM, Povarova KB, Makarov PV (1978) Metallovedenie volframa (Metallography of tungsten). Metallurgiya, Moscow (in Russian)
58. Chang YA (1969) Phase investigations in the system zirconium-tungsten. J Less-Common Met 17(3):325–328
59. Naidu SVN, Rao PR (1987) The W-Zr (tungsten-zirconium) system. J Alloy Phase Diagrams 3(1):47–56
60. Naidu SVN, Rao PR (1987) The Hf-W (hafnium-tungsten) system. J Alloy Phase Diagrams 3(1):38–46
61. Yeremenko VN, Velikanova TYa, Artyukh LV, Vishnevsky AS (1975) Phase diagram of ternary system hafnium-tungsten-carbon. Solidus surface projection. Rev Int Hautes Temp Refract 12(3):209–213

62. Naidu SVN, Sriramamurthy AM, Vijayakumar M, Rao PR (1988) The W-V (tungsten-vanadium) system. J Alloy Phase Diagrams 4(3):191–198
63. Rudy E (1969) Compendium of phase diagram data. In: Ternary phase equilibria in transition metal-boron-carbon-silicon systems. Report AFML-TR-65–2, Contracts USAF 33(615)-1249 and USAF 33(615)-67-C-1513, Part 5, pp. 1–689. Air Force Materials Laboratory, Wright-Patterson Air Force Base, Ohio
64. Naidu SVN, Sriramamurthy AM, Rao PR (1988) The Nb-W (niobium-tungsten) system. J Alloy Phase Diagrams 4(3):184–190
65. Krishnan R, Garg SP, Krishnamurthy N (1987) Tantalum-tungsten system. J Alloy Phase Diagrams 3(1):1–3
66. Den Broeder FJA (1972) Interface reaction and a special form of grain boundary diffusion in the Cr-W system. Acta Metall 20(3):319–332
67. Margaria T, Allbert CH, Ansara Y, Driole J (1976) Study of the W-Ni-Cr system at high temperature. High Temp High Pressures 8(4):451–459
68. Naidu SVN, Sriramamurthy AM, Rao PR (1984) The Cr-W (chromium-tungsten) system. Bull Alloy Phase Diagrams 5(3):289–292
69. Taylor A, Doyle NJ (1965) The constitution diagram of the tungsten-molybdenum-osmium system. J Less-Common Met 9(3):190–205
70. Naidu SVN, Sriramamurthy AM, Rao PR (1984) The Mo-W (molybdenum-tungsten) system. Bull Alloy Phase Diagrams 5(2):177–180
71. Gustafson P (1988) Experimental study and a thermodynamic evaluation of the Fe-Mo-W system. Z Metallkd 79(6):388–396
72. Naidu SVN, Rao PR (1986) The Mn-W (manganese-tungsten) system. J Alloy Phase Diagrams 2(1):38–40
73. Darby JB, Jr, Norton LJ, Downey JW (1964) Technetium compounds with the $MgZn_2$ structure. J Less-Common Met 6(2):165–167
74. Savitskii EM, Tylkina MA, Levin AM (1980) Splavy reniya v elektronike (Rhenium alloys in electronics). Energiya, Moscow (in Russian)
75. Savitskii EM, Tylkina MA, Shishkina LL (1959) Diagramma sostoyaniya sistemy volfram-renii (The constitution diagram of the tungsten-rhenium system). Izv AN SSSR OTN Metallurgiya Toplivo (3):99–107 (in Russian)
76. Savitskii EM, Tylkina MA, Khamidov OKh (1969) Issledovanie rastvorimosti perekhodnykh metallov v renii i nekotorye svoistva splavov (A study of the solubility of transition metals in rhenium and some properties of the alloys). Izv AN SSSR Metally (4):200–208 (in Russian)
77. Khusainov MA, Lakhotkin YuV, Umidov DM, Krasovskii AI (1981) Struktura i fazovyi sostav splavov W-Re, poluchennykh gazofaznym osazhdeniem (The structure and phase composition of the W-Re alloys obtained by gas phase deposition). Izv AN SSSR Metally (4):191–196 (in Russian)
78. Swartzendruber LJ (1982) The Fe-W (iron-tungsten) system. Bull Alloy Phase Diagrams 3(2):161–165
79. Naidu SVN, Sriramamurthy AM, Rao PR (1986) The Fe-W (iron-tungsten) system. J Alloy Phase Diagrams 2(3):176–188
80. Taylor A, Kagle BJ, Doyle NJ (1961) The constitution diagram of the tungsten-osmium binary system. J Less-Common Met 3(4):333–347
81. King HW (1981) Crystal structures of the elements at 25 °C. Bull Alloy Phase Diagrams 2(3):401–402
82. Naidu SVN, Rao PR (1986) The Os-W (osmium-tungsten) system. J Alloy Phase Diagrams 2(2):93–96
83. Gabriel A, Lukas HL, Allbert CH, Ansara I (1985) Experimental and calculated phase diagrams of the Ni-W, Co-W and Co-Ni-W systems. Z Metallkd 76(9):589–595
84. Naidu SVN, Sriramamurthy AM, Rao PR (1986) The Co-W (cobalt-tungsten) system. J Alloy Phase Diagrams 2(1):43–52

85. Fernandez-Guillermet A (1988) Thermodynamic calculation of the Fe-Co-W phase diagram. Z Metallkd 79(10):638–642
86. Giessen BC, Jaehnigen U, Grant NJ (1966) Ordered AB and AB_3 phases in T_6-T_9 alloy systems and a modified Mo-Ir phase diagram. J Less-Common Met 10(2):147–150
87. Lassner E, Schubert W-D (1999) Tungsten. Kluwer Academic / Plenum Publishers, New York
88. Tylkina MA, Polyakova VP, Shekhtman VSh (1963) Sistema iridii-volfram (The iridium-tungsten system). Zh Neorg Khim 8(11):2549–2555 (in Russian)
89. Muster WJ, Yoon DN, Hoppmann WJ (1979) Solubility and volume diffusion of nickel in tungsten at 1640 °C. J Less-Common Met 65(2):211–216
90. Naidu SVN, Sriramamurthy AM, Rao PR (1986) The Ni-W (nickel-tungsten) system. J Alloy Phase Diagrams 2(1):1–11
91. Savitskii EM, Polyakova VP, Gorina NB, Roshan NR (1975) Metallovedenie platinovykh metallov (Metallography of platinum metals). Metallurgiya, Moscow (in Russian)
92. Knapton AG (1980) Alloys of platinum and tungsten. Platinum Met Rev 24(2):64–69
93. FactSage (2007) Data from SGTE alloy database. Collection of phase diagrams. http://www.crct.polymtl.ca/fact/phase_diagram.php?file=Ag-W.jpg&dir=SGTE Accessed 4 July 2011.
94. Naidu SVN, Rao PR (1986) The W-Zn (tungsten-zinc) system. J Alloy Phase Diagrams 2(1):66–67
95. Fleitman AH, Romano AJ, Klamut CJ (1966) Boiling mercury corrosion of certain refractory metals and stainless steels from 593 to 703 °C. Corrosion 22(5):137–142
96. Rudy E, Benesovski F, Toth L (1963) Untersuchungen der Dreistoffsysteme der Va- und VIa-Metalle mit Bor und Kohlenstoff (Studies of the ternary systems of the group Va and VIa metals with boron and carbon). Z Metallkd 54(6):345–353 (in German)
97. Portnoi KI, Romashov VM, Levinskii YuV, Romanovich IV (1967) Phase diagram of the system tungsten-boron. Powder Metall Met Ceram 6(5):398–402
98. Kuzma YuB (1983) Kristallokhimiya boridov (The crystal chemistry of borides). Vyshcha Shkola, Lviv (in Russian)
99. Suryanarayana C (1973) Constitution of liquisol-quenched Al-W alloys. J Mater Sci 8(5):760–761
100. Popova SV, Fomitcheva LN (1981) Crystallization of tungsten-gallium alloys at high pressure. J Less-Common Met 77(1):137–140
101. Kocherzhinskii YuA, Kulik OG, Shishkin EA, Yupko LM (1973) Diagramma sostoyaniya sistemy volfram-kremnii (The constitution diagram of the tungsten-silicon system). Doklady AN SSSR 212(3):642–643 (in Russian)
102. Kosolapova TYa, ed (1990) Handbook of high-temperature compounds: properties, production and applications. Hemisphere, New York
103. Toth LE (1971) Transition metal carbides and nitrides. Academic Press, New York, London
104. Khitrova VI, Pinsker ZG (1961) Nekotorye voprosy kristallokhimii nitridov volframa i ryada drugikh faz vnedreniya (Some problems of the crystal chemistry of tungsten nitrides and series of other interstitial phases). Kristallografiya 6(6):882–891 (in Russian)
105. Wriedt HA (1989) The N-W (nitrogen-tungsten) system. Bull Alloy Phase Diagrams 10(4):358–367
106. Fromm E, Jehn H (1971) Gleichwichte und Ausgasung Kinetik in den Systemen Mo-N, W-N und Re-N (Equilibria and outgassing kinetics in the systems Mo-N, W-N and Re-N). High Temp High Pressures 3:553–564 (in German)
107. Fromm E, Jehn H (1971) Stickstoffloeslichkeit in Wolfram bei hohen Temperaturen (Nitrogen solubility in tungsten at high temperatures). Z Metallkd 62(5):378–381 (in German)
108. Fromm E, Jehn H (1969) Zur Hochtemperaturlöslichkeit von Stickstoff in Wolfram (On the high-temperature solubility of nitrogen in tungsten). J Less-Common Met 17(1):124–126 (in German)
109. Prevarskii AP, Kuzma YuB (1983) Fazovye ravnovesiya i kristallicheskie struktury soedinenii v sisteme W-Cu-Al (The phase equilibria and crystal structures of compounds in the W-Cu-Al system). Izv AN SSSR Metally (5):225–226 (in Russian)

110. Efimov YV, Frolova TM, Bodak OI, Kharchenko OI (1984) Sistema W-WS_2-Cu (The W-WS_2-Cu system). Izv AN SSSR Neorg Mater 20(9):1593–1595 (in Russian)
111. Niessen AK, De Boer FR, Boom R, De Chatel PF, Mattens WCM, Miedema AR (1983) The enthalpy of solution for solid binary alloys of two 4d-transition metals. Calphad 7(1):51–70
112. Vijayakumar M, Sriramamurthy AM, Naidu SVN (1987) Calculated phase diagrams of Cu-W, Ag-W and Au-W binary systems. Calphad 11(4):369–374
113. Vijayakumar M, Sriramamurthy AM, Naidu SVN (1988) Calculated phase diagrams of Cu-W, Ag-W and Au-W. Calphad 12(2):177–184
114. Qui C-A, Jin Z-P, Huang P-Y (1988) Phase equilibria in the W-Ni-Cu system: Part 2. Thermodynamic calculation. Z Metallkd 79(12):767–769
115. Jensen P, Kjekshus A, Skansen T (1966) The systems molybdenum-arsenic, tungsten-arsenic, molybdenum-antimony, tungsten-antimony, niobium-bismuth, tantalum-bismuth, molubdenum-bismuth and tungsten-bismuth. Acta Chem Scand 20(2):403–416
116. Kofstad P (1966) High-temperature oxidation of metals. Wiley, New York, London
117. Kofstad P (1988) High-temperature corrosion. Elsevier Applied Science, London, New York
118. Magneli A (1953) Structures of the ReO_3-type with recurrent dislocations of atoms: 'homologous series' of molybdenum and tungsten oxides. Acta Crystallogr 6:495–500
119. Sundberg M (1976) The crystal and defect structures of $W_{25}O_{73}$, a member of the homologous series W_nO_{3n-2}. Acta Crystallogr B 32(7):2144–2149
120. Salye E (1977) The orthorhombic phase of WO_3. Acta Crystallogr B 33(2):574–577
121. Sundberg M (1980) Structure and "oxidation behaviour" of $W_{24}O_{70}$, a new member of the {103} *CS* series of tungsten oxides. J Solid State Chem 35(1):120–127
122. Booth J, Ekstrom T, Iguchi E, Tilley RJD (1982) Notes on phases occurring in the binary tungsten-oxygen system. J Solid State Chem 41(3):293–307
123. Altstetter CJ (1984) Metal-oxygen systems. Bull Alloy Phase Diagrams 5(6):543–553
124. Wriedt HA (1989) The O-W (oxygen-tungsten) system. Bull Alloy Phase Diagrams 10(4):368–384
125. Ackerman RJ, Rauh EG (1963) A thermodynamic study of the tungsten-oxygen system at high temperatures. J Phys Chem 67(12):2596–2601
126. Raghavan V (1988) The Fe-S-W (iron-sulphur-tungsten) system. J Alloy Phase Diagrams 4(3):175–183
127. Bondarenko VP, Morozov VV, Chernyak LV (1971) Reaction of lanthanum and cerium hexaborides with refractory metals. Powder Metall Met Ceram 10(1):57–61
128. Chaban NF, Kuzma YuB (1990) Isothermal section of the system erbium-tungsten-boron at 1270 K. Powder Metall Met Ceram 29(10):845–847
129. Rogl P (2008) Boron–iron–tungsten system. In: Effenberg G, Ilyenko S (eds) Ternary alloy systems, Subvol. D, Part 1, pp. 455–463, Springer, Berlin, Heidelberg
130. Haschke H, Nowotny H, Benesovsky F (1966) Untersuchungen im der ternären Systeme (Mo,W)-(Fe,Co,Ni)-B (Investigations in the systems (Mo,W)-(Fe,Co,Ni)-B). Monatsh Chem 97:1459–1468 (in German)
131. Hasegawa M, Okamoto M (1966) A study on the ternary alloys of iron and boron. Nippon Kinzoku Gakkai-Si 30(6):533–540 (in Japanese)
132. Leithe-Jasper A, Klesnar H, Rogl P, Komai M, Takagi K-I (2000) Reinvestigation of isothermal section in M(M = Mo,W)-Fe-B ternary systems at 1323 K. J Jpn Inst Met 64(2)154–162 (in Japanese)
133. Rogl P (2009) Boron–hafnium–tungsten system. In: Effenberg G, Ilyenko S (eds) Ternary alloy systems, Subvol. E, Part 1, pp. 523–535. Springer, Berlin, Heidelberg
134. Harmon DP (1966) Hf-Mo-B and Hf-W-B systems. In: Ternary phase equilibria in transition metal-boron-carbon-silicon systems. Report AFML-TR-65–2, Contract USAF 33(615)-1249, Part 2, Vol. 11, pp. 1–41. Air Force Materials Laboratory, Wright-Patterson Air Force Base, Ohio

135. Kuzma YuB, Lakh VI, Stadnyk BI, Kovalyk DA (1970) Systems hafnium-tungsten-boron, hafnium-rhenium-boron and niobium-rhenium-boron. Powder Metall Met Ceram 9(12):1003–1006
136. Rogl P, Nowotny H, Benesovsky F (1971) Complex Boride in den Systemen Hf-Mo-B und Hf-W-B (Complex borides in the systems Hf-Mo-B and Hf-W-B). Monatsh Chem 104:182–193 (in German)
137. Rogl P, Nowotny H, Benesovsky F (1973) Novel κ-Boride und verwandte Phasen (Novel κ-borides and related phases). Monatsh Chem 104:182–193 (in German)
138. Ordanyan SS, Kosterova NV, Maksimova NM (1980) Interaction in the HfB_2-W system. Inorg Mater 16(5):839–841
139. Povarova KB, Zavarzina EK (1994) Tungsten corner of W-Hf-B system. Russ Metall (2):126–130
140. Ordanyan SS (1988) O zakonomernostyakh vzaimodeistviya v sistemakh LaB_6–$M^{IV\text{-}VI}B_2$ (Common aspects of phase relations in LaB_6–$M^{IV\text{-}VI}B_2$ systems). Izv AN SSSR Neorg Mater 24(2):235–238 (in Russian)
141. Ordanyan SS, Nesmelov DD, Vikhman SV (2009) Phase relations in the LaB_6–W_2B_5 system. Inorg Mater 45(7):754–757
142. Bulanova M, Heulens J (2010) Boron–molybdenum–tungsten system. In: Effenberg G, Ilyenko S (eds) Ternary alloy systems, Subvol. E, Part 2, pp. 61–71. Springer, Berlin, Heidelberg
143. Holleck H (1984) Binäre und ternäre Carbid- und Nitridsysteme der Ubergangsmetalle (Binary and ternary carbide and nitride systems of the transition metals). Gebrüder Borntträeger, Berlin, Stuttgart (in German)
144. Rogl P, Schuster JC (1992) Phase diagrams of ternary boron nitride and silicon nitride systems. ASM International, Materials Park, Ohio
145. Artamonov AYa, Lapskov YuK, Kozachenko MV, Yurchenko DZ, Dudnik EM (1967) Physical and technical properties of alloys of the system W–BN. Powder Metall Met Ceram 6(9):727–731
146. Borisova AL, Martsenyuk IS (1975) Reactions of boron and aluminum nitrides and materials based on them with refractory metals. Powder Metall Met Ceram 14(10):822–826
147. Samsonov GV, ed (1978) Fiziko-khimicheskie svoistva okislov (Physico-chemical properties of oxides), 2nd ed. Metallurgiya, Moscow (in Russian)
148. Ordanyan SS, Vikhman SV, Nagaeva YuS (2009) Composite WSi_2–Me^VB_2 in W-Si-Me^V-B systems. Refract Industrial Ceram 50(2):127–130
149. Kieffer R, Schwarzkopf P (1953) Hartstoffe und Hartmetalle (Refractory hard metals). Springer, Vienna (in German)
150. Samsonov GV, Vinitskii IM (1980) Handbook on refractory compounds. IFI/Plenum, New York
151. Perrot P (2010) Boron–titanium–tungsten system. In: Effenberg G, Ilyenko S (eds) Ternary alloy systems, Subvol. E, Part 2, pp. 194–201. Springer, Berlin, Heidelberg
152. Telle R, Sigl LS, Takagi K (2000) Boride-based hard materials. In: Riedel R (ed) Handbook of ceramic hard materials, pp. 802–945. Wiley-VCH, Weinheim
153. Kosterova NV, Ordanyan SS (1977) The system Ti-B-W at 1400 °C. Inorg Mater 13(8):1140–1143
154. Ordanyan SS, Boldin AA, Vikhman SV, Prilutskii EV (2000) Interaction in the W_2B_5–TiB_2 system. Russ J Appl Chem 73(12):2131–2132
155. Kumar KCH, Gröbner J, Malfliet A, Moelans N (2010) Boron–tungsten–zirconium system. In: Effenberg G, Ilyenko S (eds) Ternary alloy systems, Subvol. E, Part 2, pp. 223–229. Springer, Berlin, Heidelberg
156. Chang YA (1966) Zr-W-B system and the pseudobinary system TaB_2-HfB_2. In: Ternary phase equilibria in transition metal-boron-carbon-silicon systems. Report AFML-TR-65–2, Contract USAF 33(615)-1249, Part 2, Vol. 9, pp. 1–26. Air Force Materials Laboratory, Wright Patterson Air Force Base, Ohio

157. Ordanyan SS, Boldin AA, Suvorov SS, Smirnov VV (2005) Phase diagram of the W_2B_5–ZrB_2 system. Inorg Mater 41(3):232–234
158. Chang LLY, Scroger MG, Phillips B (1966) Alkaline-earth tungstates: equilibrium and stability in the M-W-O systems. J Am Ceram Soc 49(7):385–390
159. Waring JL (1965) Phase equilibria in the system aluminium oxide–tungsten oxide. J Am Ceram Soc 48(9):493–494
160. Telegus VS, Kuzma YuB (1968) Phase equilibria in the systems tungsten-chromium-boron and tungsten-molybdenum- boron. Powder Metall Met Ceram 7(2):133–138
161. Kharitonov VI, Shamrai FI (1969) Ternary system Mo-W-B. Powder Metall Met Ceram 8(7):567–570
162. Kharitonov VI, Shamrai FI, Fedotov SG, Tkachev LG (1971) Solubility of boron in an Mo-W solid solution and properties of the alloys. Inorg Mater 7(2):201–203
163. Kharitonov VI, Shamrai FI (1971) Fazovaya diagramma Mo-W-B (The Mo-W-B phase diagram). In: Diagrammy sostoyaniya metallicheskikh sistem (The constitution diagrams of the metallic systems), pp. 109–112. Nauka, Moscow (in Russian)
164. Yasinskaya GA, Groisberg MS (1963) Interaction of titanium boride with niobium and tungsten. Powder Metall Met Ceram 2(6):457–458
165. Kuzma YuB, Svarichevskaya SI, Telegus VS (1971) Systems titanium-tungsten-boron, hafnium-tantalum-boron and tantalum-tungsten-boron. Powder Metall Met Ceram 10(6):478–481
166. Gorbacheva TB, Krylov YuI, Mikova NM (1973) Vysokotemperaturnoe vzaimodeistvie tugoplavkikh metallov s boridami (High-temperature interaction of refractory metals with borides). In: Kolchin OP (ed) Tverdye splavy i tugoplavkie metally (Hard alloys and refractory metals), Vol. 14, pp. 239–243. Metallurgia, Moscow (in Russian)
167. Telle R, Fendler E, Pettsov G (1993) The quasiternary TiB_2-W_2B_5-CrB_2 system and its possibilities in evolution of ceramic hard materials. Powder Metall Met Ceram 32(3):240–248
168. Pohl A, Kizler P, Telle R, Aldinger F (1994) EXAFS studies of $(Ti,W)B_2$ compounds. Z Metallkd 85(9):658–663
169. Okada S, Kudom K, Lundström T (1995) Preparation and some Properties of W_2B, δ-WB and WB_2 crystals from high-temperature metal solutions. Jpn J Appl Phys 34:226–231
170. Schmalzried C, Telle R, Freitag B, Mader W (2001) solid state reactions in transition metal diboride-based materials. Z Metallkd 90(11):1197–1202
171. Shibuya M, Yoneda, T, Yamamoto Y, Ohyanagi M, Munir ZA (2003) Effect of Ni and Co additives on phase decomposition in TiB_2-WB_2 solid solutions formed by induction field activated combustion synthesis. J Am Ceram Soc 86(2):354–356
172. Shibuya M, Kawata M, Ohyanagi M, Munir ZA (2003) Titanium diboride–tungsten diboride solid solutions formed by induction-field-activated combustion synthesis. J Am Ceram Soc 86(4):706–710
173. Schmidt H, Fotsing RE, Borchardt G, Schmalzried C, Telle R (2006) Kinetics of precipitate formation in $(Ti_xW_yCr_z)B_2$ solid solutions: influence of Cr concentration and Co impurities. Int J Mater Res 97(6):821–825
174. Sobol OV, Grigoryev ON, Kunitsky YA, Dub SN, Podtelezhnikov AA, Stetsenko AN (2006) Peculiarities of structure state and mechanical characteristics in ion-plasma condensates of quasibinary system borides W_2B_5-TiB_2. Sci Sintering 38(1):63–72
175. Shibuya M, Ohyanagi M (2007) Effect of nickel boride additive on simultaneous densification and phase decomposition of TiB_2-WB_2 solid solutions by pressureless sintering using induction heating. J Eur Ceram Soc 27(1):301–306
176. Shibuya M, Yamamoto Y, Ohyanagi M (2007) Simultaneous densification and phase decomposition of TiB_2-WB_2 solid solutions activated by cobalt boride addition. J Eur Ceram Soc 27(1):307–312
177. Sobol OV (2007) Nanostructural ordering in W-Ti-B condensates. Phys Solid State 49(6):1161–1167
178. Helgorsky J (1961) Les réactions d'état solide dans le système Zr-W-B (Solid state reactions in the system Zr-W-B). Ann Chim 6:1339–1381 (in French)

179. Voroshilov YuV, Lakh VI, Stadnyk BI, Kuzma YuB (1967) The ternary system zirconium-chromium-boron. Inorg Mater 3(9):1390–1392
180. Gladyshevskii EI, Kuzma YuB, Kripyakevich PI, Skolozdra RV, Voroshilov YuV (1968) Fazovye ravnovesiya v nekotorykh troinykh sistemakh, soderzhaschikh perekhodnyi metal Va ili VIa podgrup s Si ili B (Phase equilibria in some ternary systems containing a transition metal of the Va or VIa sub-groups with Si or B). In: Diagrammy sostoyaniya metallicheskikh sistem (The constitution diagrams of the metallic systems), pp. 70–79. Nauka, Moscow (in Russian)
181. Voroshilov YuV, Kuzma YuB (1969) Reaction of zirconium with the transition metals and boron. Powder Metall Met Ceram 8(11):941–944
182. Avgustinik AI, Ordanyan SS, Serbezova RYa (1971) Reaction of ZrB_2 with tungsten. Inorg Mater 7(5):686–687
183. Kisliy PS, Kuzenkova MA, Zaveruha OV (1971) On the sintering process of zirconium diboride with tungsten. Phys Sintering 3(1):29–44
184. Kuzenkova MA, Kislyi PS, Zaverukha OV, Kuzma YuB (1971) Structure and properties of zirconium diboride-tungsten alloys. Powder Metall Met Ceram 10(11):879–883
185. Kosterova NV, Ordanyan SS, Neshpor VS, Ostrovskii EK (1980) Thermionic emission properties of cermets of eutectic compositions in Me^{IV} – (C, B) – (Mo, Re, W) systems. Powder Metall Met Ceram 19(1):61–66
186. McHale AE (1994) III. Boron plus two metals. In: McHale AE (ed) Phase equilibria diagrams, phase diagrams for ceramists, Vol. 10, pp. 174–175. NIST, Gaithersburg, Maryland
187. Telle R, Fendler E, Petzow G (1992) The quasi-binary systems CrB_2-TiB_2, CrB_2-WB_2 and TiB_2-WB_2. J Hard Mater 3:211–224
188. Mitra I, Telle R (1997) Phase formation during anneal of supersaturated TiB_2-CrB_2-WB_2 solid solutions. J Solid State Chem 133:25–30
189. Kaufman L, Nesor H (1975) Calculation of superalloy phase diagrams: IV. Metall Trans A 6:2123–2131
190. McCormack R, De Fontaine D, Wolverton C, Ceder G. (1995) Nonempirical phase equilibria in the W-Mo-Cr system. Phys Rev B 51(22):15808–15822
191. Ordanyan SS, Chupov VD, Kirshina VYu, Fesenko LV (1985) Reactions of hafnium nitride with molybdenum, tungsten and tantalum. Powder Metall Met Ceram 24(9):714–719
192. Chang LLY, Scroger MG, Phillips B (1967) Condensed phase relations in the systems ZrO_2-WO_2-WO_3 and HfO_2-WO_2-WO_3. J Am Ceram Soc 50(4):211–215
193. Okamoto H (2009) The U-W (uranium-tungsten) system. J Phase Equilibria Diffusion 30(4):415
194. Naidu SVN, Rao PR (1987) Alkaline earth metals – tungsten systems. J Alloy Phase Diagrams 4(1):14–15
195. Vrestal J (2010) Iron– molybdenum – tungsten system. In: Effenberg G, Ilyenko S (eds) Ternary alloy systems, Subvol. E, Part 3, pp. 270–277. Springer, Berlin, Heidelberg
196. Kirchner G, Harvig H, Uhrenius B (1973) Experimental and thermodynamic study of the equilibria between ferrite, austenite and intermediate phases in the Fe-Mo, Fe-W, and Fe-Mo-W systems. Metall Trans 4:1059–1067
197. Raynor GV, Rivlin VG (1981) Critical evaluations of constitution of certain ternary alloys containing iron, tungsten and a third metal. Int Met Rev 4:213–249
198. Ischenko TV, Meshkov LL, Leonov AV (1984) Diagramma fazovogo ravnovesiya systemy zhelezo-molibden-volfram pri 900 °C (The phase-equilibrium diagram of the iron-molybdenum-tungsten system at 900 °C). Vestn Mosk Univ Ser 2 Khim 25(5):503–504 (in Russian)
199. Ishchenko TV, Meshkov LL, Sokolovskaya YeM (1984) On the interaction of μ phases in systems formed by transition metals. J Less-Common Met 97:145–150
200. Meshkov LL, Nesterenko SN, Ishchenko TV (1985) Structural features of phase diagrams formed by molybdenum and tungsten with iron group metals. Russ Metall (2):204–207
201. Gustafson P (1988) An experimental study and a thermodynamic evaluation of the Fe-Mo-W system. Z Metallkd 79(7):388–396

202. Raynor GV, Rivlin VG (1988) Fe-Mo-W system. In: Phase equilibria in iron ternary alloys. Part 4, pp. 414–416, The Institute of Metals, London
203. Raghavan V (1994) The Fe-Mo-W (iron-molybdenum-tungsten). J Phase Equilibria 15(6):627–628
204. Barama SE, Harabi A, Cizeron G (1997) Identification of intermetallic compounds formed during sintering of the Fe-Mo-W ternary system. J Mater Sci Lett 16:1240–1244
205. Kozlov A (2010) Molybdenum – nickel – tungsten system. In: Effenberg G, Ilyenko S (eds) Ternary alloy systems, Subvol. E, Part 3, pp. 377–384. Springer, Berlin, Heidelberg
206. Guzei LS, Meshkov LL, Kazakov VA, Sokolovskaya EM (1973) Izotermicheskiy razrez fazovoy diagrammy sistemy Ni-Mo-W pri 1200 i 700 °C (Isothermal sections of the phase diagram of the Ni-Mo-W system at 1200 and 700 °C). In: Obshchie zakonomernosti stroeniya diagram sostoyaniya metallicheskikh sistem (The general structure regularities of the constitution diagrams of metallic systems), pp. 160–162. Nauka, Moscow (in Russian)
207. Potapov LP, Yedneral AF, Kiriyenko VI, Nikandrova EA (1976) Structure transformation in nickel-molybdenum-tungsten alloys. Phys Met Metallogr 42(1):76–83
208. Maslenkov SB, Nikandrova EA (1980) Examination of the Ni-Mo-W phase diagram. Russ Metall (2):184–187
209. Plastun NA, Sidorenko FA (1988) Ordering in ternary alloys based on Ni_4Mo. Phys Met Metallogr 65(5):196–199
210. Otani S, Ohashi H, Ishizawa Y (1995) Lattice constants and nonstoichiometry of WB_{2-x}. J Alloys Compd 221(1–2):L8-L10
211. Ariel E, Barta J, Niedzwiedz S (1970) Tungsten-titanium-boron metastable phase diagram at room temperature. J Less-Common Met 20:199–206
212. Kaga H, Heian EM, Munir ZA, Schmalzried C, Telle R (2001) Synthesis of hard materials by field activation: the synthesis of solid solutions and composites in the TiB_2-WB_2-CrB_2 system. J Am Ceram Soc 84(12):2764–2770
213. Tyushevskaya GI, Afonskii NS, Spitsyn VI (1966) Issledovanie fazovogo sostava sistemy La_2O_3–WO_3 (A study of phase composition in the La_2O_3 – WO_3 system). Doklady AN SSSR 170(4):859–860 (in Russian)
214. Rode EYa, Balagina GM, Ivanova MM, Karpov VN (1968) Sistemy obrazuemye volframatami redkozemelnykh elementov s volframatami natriya i strontsiya (The systems formed by rare earth elements tungstates with sodium and strontium tungstates). Zh Neorg Khim 13(5):1451–1456 (in Russian)
215. Ivanova MM, Balagina GM, Rode EYa, (1970) Diagramma sostoyanoya sistemy La_2O_3 – WO_3 (The constitution diagram of the La_2O_3 –WO_3 system). Izv AN SSSR Neorg Mater 6(5):914–919 (in Russian)
216. Yoshimura M, Rouanet A (1976) High temperature phase relation in the system La_2O_3-WO_3. Mater Res Bull 11(2):151–158
217. Casteels FG, Brabers MJ, DePaus R (1980) Thermodynamic stability and phase equilibriums in the system lanthanum-thorium-tungsten-oxygen. Rev Int Hautes Temp Refract 16(4):424–436
218. Yanovskii VK, Voronkova VI (1983) Utochnenie fazovykh ravnovesii v sisteme La_2O_3-WO_3 vblizi sostava 1:1 (The refinement of phase equilibria in the La_2O_3-WO_3 system near the 1:1 composition). Izv AN SSSR Neorg Mater 19(3):416–421 (in Russian)
219. Andrievskii RA, Spivak II (1989) Prochnost tugoplavkikh soedinenii i materialov na ikh osnove (Strength of refractory compounds and materials based on them). Metallurgiya, Chelyabinsk (in Russian)
220. Raaijmakers IJ, Setalvad T, Bhansali AS, Burrow BJ, Gutai L, Kim KB (1990) Microstructure and barrier properties of reactively sputtered Ti-W nitride. J Electron Mater 19(11):1221–1230
221. Semikina LE, Limonov VE (1968) Rentgenograficheskoe issledovanie sistemy MoO_3–WO_3 (An x-ray study in the MoO_3–WO_3 system). Zh Neorg Khim 13(7):1932–1935 (in Russian)

222. Knox AK (1967) Properties of WO_3 by substitution of Mo and Cr. Trans Brit Ceram Soc 66(2):85–91
223. Gloeikler D, Jeannot F, Gleitzer C (1974) The MoO_3-WO_3 and Li_2O-MoO_3-WO_3 systems. J Less-Common Met 36(1–2):41–45
224. Gardinier CF, Chang LLY (1978) Phase relationships in the systems Mo-Sn-S, W-Sn-S and Mo-W-S. J Less-Common Met 61(2):221–229
225. Rokhlin L (2010) Molybdenum – silicon – tungsten system. In: Effenberg G, Ilyenko S (eds) Ternary alloy systems, Subvol. E, Part 3, pp. 417–427. Springer, Berlin, Heidelberg
226. Kieffer R, Schob O, Nowotny H, Benesovsky F (1962) Investigation on the ternary systems Cr-W-Si and Mo-W-Si. Monats Chem 9(2):517–521
227. Verkhoglyadova TS, Vivchar OI, Gladyshevskii EI (1966) Solubility of the disilicides of the transition metals in $MoSi_2$ and WSi_2. Powder Metall Met Ceram 5(4):316–319
228. Setton M, Van Der Spiegel J (1991) A review of some aspects of ternary metal-metal-Si and metal-B-Si systems. J Appl Phys 69(2):994–999
229. Boettinger WJ, Peperezko JH, Frankwicz PS (1992) Application of ternary phase diagrams to the development of $MoSi_2$-based materials. Mater Sci Eng A 155(1):33–44
230. Schwartz RB, Srinivasan SR, Petrovic JJ, Maggiore CJ (1992) Synthesis of molybdenum disilicide by mechanical alloying. Mater Sci Eng A 155(1)75–83
231. Harada Y, Funato Y, Morinaga M, Ito A, Sugita Y (1994) Solid solubilities of ternary elements and their effects on microstructure of $MoSi_2$. J Jpn Inst Met 58(11):1239–1247 (in Japanese)
232. Subrahmanyam J, Rao RM (1994) Combustion synthesis of $MoSi_2$-WSi_2 alloys. Mater Sci Eng A 183(1–2):205–210
233. Hojo J, Ishizaka Y (1997) Formation of $MoSi_2$-WSi_2 alloy powder by carbothermal reduction method. J Ceram Soc Jpn 105(12):1053–1056
234. Gnesin BA, Gurzhiyants PA, Borisenko EB (2003) $(Mo,W)_5Si_3$-$(Mo,W)Si_2$ eutectics: properties and application in composite materials. Inorg Mater 39(7):701–709
235. Zhang H, Chen P, Yan J, Tang S (2004) Fabrication and wear characteristics of $MoSi_2$ matrix composite reinforced by WSi_2 and La_2O_3. Int J Refract Met Hard Mater 22(6):271–275
236. Hayashi T, Ito K, Takamoto M, Tanaka K (2005) The effect of Nb and W alloying to the thermal expansion anisotropy and elastic properties of Mo_5Si_3. Metall Mater Trans A 36(3):533–538
237. Li KZ, Hou DS, Li HJ, Fu QG, Jiao GS (2007) Si-W-Mo coating for SiC coated carbon/carbon composites against oxidation. Surf Coat Techn 201(24):9598–9602
238. Taylor A, Doyle NJ (1967) The solid solubility of oxygen in Nb and Nb-rich Nb-Hf, Nb-Mo and Nb-W alloys: Part III: The ternary systems Nb-Mo-O and Nb-W-O. J Less-Common Met 13(3):338–351
239. Roth RS, Waring JL (1966) Phase equilibria as related to crystal structure in the system niobium pentoxide–tungsten trioxide. J Res Natl Bur Stand Sect A 70(4):281–303
240. Yoshimura M, Sibieude F, Rouanet A, Foex M (1976) Identification of binary compounds in the system Ce_2O_3-WO_3. J Solid State Chem 16(3–4):219–232
241. English JJ (1961) Binary and ternary phase diagrams of columbium, molybdenum and tungsten. Report AD-TR-257–739, Contract AF 33(616)-7747, pp. 1–241. Defence Metals Information Center, Battelle Memorial Institute, Columbus, Ohio
242. Cornish L, Watson A (2010) Niobium–silicon–tungsten system. In: Effenberg G, Ilyenko S (eds) Ternary alloy systems, Subvol. E, Part 3, pp. 523–532. Springer, Berlin, Heidelberg
243. Dokukina NV, Shamrai FI (1962) Phase equilibrium in the system W-Nb-Si and some properties of alloys. Powder Metall Met Ceram 1(6):427–435
244. Dokukina NV, Gladyshevskii EI, Shamrai FI (1964) The Nb-Si-W System. Russ J Inorg Chem 9:1031–1034
245. Gladyshevskii EI, Lakh VI, Skolozdra RV, Stadnik BI (1964) The mutual solubility of disilicides of the transition metals from group IV, V and VI. Powder Metall Met Ceram 3(4):278–282

246. Ma C, Tan Y, Kasama A, Hanada S (2002) Phase equilibria in Nb-W-rich zone of the Nb-W-Si ternary system. Mater Trans JIM 43(4):688–693
247. Sha J, Hirai H, Tabaru T, Kitahara A, Ueno H, Hanada S (2003) Toughness and strength characteristics of Nb-W-Si ternary alloys prepared by arc melting. Metall Mater Trans A 34(12):2861–2871
248. Ma CL, Li JG, Tan Y, Tanaka R, Hanada S (2004) Microstructure and mechanical properties of Nb/Nb_5Si_3 *in situ* composites in Nb-Mo-Si and Nb-W-Si systems. Mater Sci Eng A 386:375–383
249. Levanov VI, Mikheyev VS, Chernitsyn AI (1977) Investigation of the Ti-Nb-W system (Nb + W up to 50 wt.%). Russ Metall (1):186–191
250. Rode EYa, Karpov VN (1966) Fazovaya diagramma sistemy $Nd_2(WO_4)_3$–Na_2WO_4 (The phase diagram of the $Nd_2(WO_4)_3$–Na_2WO_4 system). Izv AN SSSR Neorg Mater 2(4):688–692 (in Russian)
251. Gordon AR, Muchnik GF (1964) Opredelenie integralnoi stepeni chernoty metallov v zavisimosti ot stepeni sherokhovatosti poverkhnosti (The determination of the integral emittance of metals affected on surface roughness grade). Teplofiz Vys Temp 2(2):292–294 (in Russian)
252. Belyaev IN, Voropanova LA (1976) Sistema Nd_2O_3–WO_3–W (The Nd_2O_3–WO_3–W system). Zh Neorg Khim 21(11):3107–3110 (in Russian)
253. Yoshimura M, Yamaguchi M, Somiya S (1984) Partial phase diagram of the WO_3-rich region of the system Nd_2O_3-WO_3. Yogyo Kyokaishi 92(8)425–430 (in Japanese)
254. Ekstroem T, Tilley RJD (1976) Structural relations in the Nb-W-O and Ta-W-O systems for the phase region near WO_3. J Solid State Chem 18(2):123–131
255. Cordfunke EHP (1969) The phase diagram of the system WO_3-UO_3. J Inorg Nucl Chem 31(5):1542–1543
256. Hauck J (1974) Uranates (VI) and tungstates (VI) within the system Li_2O-UO_3-WO_3. J Inorg Nucl Chem 36(10):2291–2298
257. Kuribayashi K, Yoshimura M, Ohta T, Sata T (1980) High-temperature phase relations in the system Y_2O_3-WO_3. J Am Ceram Soc 63(11–12):644–647
258. Field AL, Jr, Ammon RL, Lewis AI, Richardson LS (1961) Research and development of tantalum- and tungsten-base alloys. Report AD-TR-259–116, Contract NOas 58–852-C, pp. 1–199. Westinghouse Research Laboratories, Pittsburgh, Pennsylvania
259. Goldschmidt HJ (1967) Interstitial alloys. Butterworths, London, New York
260. Gas P, Tardy J, LeGoues FK, D'Heurie FM (1987) Disilicide solid solutions, phase diagram and resistivities. II. $TaSi_2$–WSi_2. J Appl Phys 61(6):2203–2211
261. Pease LF, Brophy JH (1964) The zirconium-tungsten-tantalum system. J Less-Common Met 6:118–131
262. Fomenko VS, Podchernyaeva IA (1975) Emissionnye i adsorbtsionnye svoistva veshchestv i materialov (The thermoionic emission and absorptance properties of substances and materials). Atomizdat, Moscow (in Russian)
263. Fomenko VS (1981) Emissionnye svoistva materialov (The thermoionic emission properties of materials). Naukova Dumka, Kyiv (in Russian)
264. Samsonov GV (1966) Berillidy (Beryllides). Naukova Dumka, Kyiv (in Russian)
265. Savitskii EM, Burkhanov GS (1971) Metallovedenie splavov tugoplavkikh i redkih metallov (Metallography of refractory and less-common metal alloys), 2nd ed. Nauka, Moscow (in Russian)
266. Savitskii EM, Zakharov AM (1962) Diagramma sostoyaniya troinoi sistemy niobii-volfram-tsirkonii (The constitution diagram of the niobium-tungsten-zirconium ternary system). Zh Neorg Khim 7(11):2575–2580 (in Russian)
267. Savitskii EM, Zakharov AM (1964) Splavy razreza W_2Zr-Mo_2Zr (Alloys in the W_2Zr-Mo_2Zr cross section). Zh Neorg Khim 9(9):2261–2263 (in Russian)
268. Zakharov AM, Savitskii EM (1965) Issledovanie troinoi diagrammy sostoyaniya sistemy W-Mo-Zr (A study of the constitution diagram of the W-Mo-Zr ternary system). Izv AN SSSR Metally (1):151–159 (in Russian)

269. Savitskii EM, Zakharov AM (1964) Sistema niobii-volfram-molibden-tsirkonii (The niobium-tungsten-molybdenum-zirconium system). Zh Neorg Khim 9(10):2424–2432 (in Russian)
270. Audi G, Wapstra AH, Thibault C, Blachot J, Bersillon O (2003) The NUBASE evaluation of nuclear and decay properties. Nucl Phys A 729:3–128
271. De Laeter JR, Bohlke JK, De Bievre P, Hidaka H, Peiser HS, Rosman KJR, Taylor PDP (2003) Atomic weights of the elements. Review 2000 (IUPAC Technical report). Pure Appl Chem 75(6):683–800
272. Wieser ME (2006) Atomic weights of the elements 2005. (IUPAC Technical report). Pure Appl Chem 78(11):2051–2066
273. Savitskii EM, Tylkina MA, Povarova KB (1970) Rhenium alloys. IPST Press, Jerasalem
274. Ordanyan SS (1980) Reactions of HfB_2 with Re and Cr. Powder Metall Met Ceram 19(4):273–277
275. Gehlig R, Salje E, Carley AF, Roberts MW (1983) XPS studies on $WO_{2.90}$ and $WO_{2.72}$ and the influence of metallic impurities. J Solid State Chem 49:318–324
276. Goodwin F, Guruswamy S, Kainer KU, Kammer C, Knabl W, Koethe A, Leichtfried G, Schlamp G, Stickler R, Warlimont H (2005) Metals. In: Martienssen W, Warlimont H (eds) Springer handbook of condensed matter and materials data, pp. 161–430. Springer, Berlin, Heidelberg
277. Roth RS, Waring JL, Parker HS (1970) Effect of oxide additions on the polymorphism of tantalum pentoxide. IV. The system Ta_2O_5-Ta_2WO_8. J Solid State Chem 2(3):445–461
278. Roth RS (1980) Thermal stability of long range order in oxides. Prog Solid State Chem 13(2):159–192
279. Tenne R, Margulis L, Genut M, Hodes G (1992) Polyhedral and cylindrical structures of tungsten disulphide. Nature 360:444–446
280. Feldman Y, Wasserman E, Srolovotz DJ, Tenne R (1995) High-rate gas-phase growth of MoS_2 nested inorganic fullerenes and nanotubes. Science 267:222–225
281. Ohtani T (2010) Synthesis and applications of chalcogenide nanotubes. In: Kijima T (ed) Inorganic and metallic nanotubular materials, pp. 191–200. Springer, Berlin, Heidelberg
282. Rundqvist A, Harsta S (1987) The crystal chemistry of κ-phases. J Solid State Chem 70:210–218
283. Carney CM, Parthasarathy TA, Cinibulk MK (2011) Oxidation resistance of hafnium diboride ceramics with additions of silicon carbide and tungsten boride or tungsten carbide. J Am Ceram Soc 94(8):2600–2607
284. English JJ (1961) Binary and ternary phase diagrams of columbium, molybdenum, tantalum and tungsten. Report DMIC-152, Contract AF-33(616)-7747, pp. 1–226. Defence Metals Information Center, Battelle Memorial Institute, Columbus, Ohio
285. Skolozdra RV, Fedorov TF, Popova NM, Gladyshevskii EI (1969) Tungsten–rhenium–silicon system. Powder Metall Met Ceram 8(9):743–745
286. Mikhalenko SI, Zavalii LV, Kuzma YuD, Boiko LI (1991) The phase diagrams of Sc-W-B and Sc-Re-B systems at 1000 °C. Powder Metall Met Ceram 30(8):681–683
287. Turchi PEA, Drchal V, Kudrnovsky J, Colinet C, Kaufman L, Liu Z-K (2005) Application of *ab initio* and CALPHAD thermodynamics to Mo-Ta-W alloys. Phys Rev B 71:094206
288. Ventura J, Portillo B, Varma SK (2009) Oxidation resistant $NbCr_2$ phase in Nb-W-Cr system. J Alloys Compd 476(1–2):257–262
289. Schuster JC (1988) Silicon nitride–metal joints: phase equilibria in the systems Si_3N_4–Cr, Mo, W and Re. J Mater Sci 23(8):2792–2796
290. Yoshida M, Takasugi T (1999) Phase relation and microstructure of the Nb–Cr–W alloy system. Mater Sci Eng A 262:107–114
291. Asrar N, Meshkov LL, Sokolovskaya EM (1988) Phase equilibria in ternary alloys based on iron-group metals and containing refractory metals (Mo, W, Nb, Ta). J Less-Common Met 144:41–52
292. Kaufman L (1991) Calculation of multicomponent tantalum based phase diagrams. Calphad 15(3):261–282

293. Tolmacheva EI, Kornilova VI (1972) Granitsy fazovykh polei v sisteme W-Ta-Ti pri 1600 °C (The boundaries of phase fields in the W-Ta-Ti system at 1600 °C). Izv AN SSSR Metally (3):211–214 (in Russian)
294. Ekström T, Salje E, Tilley RJD (1981) Phase relations in the ternary W-Mo-O system. J Solid State Chem 40:75–84
295. Portemer F, Sundberg M, Kihlborg L, Figlarz M (1993) Homologues of Mo_4O_{11} (mon) in the Mo-W-O system prepared by soft chemistry. J Solid State Chem 103:403–414
296. Kihlborg L, Marinder B-O, Sundberg M, Portemer F, Ringaby O (1994) Ordered and disoredered homologues of orthorhombic Mo_4O_{11} in the Mo-W-O system. J Solid State Chem 111:111–117
297. Yatsenko SP, Dieva EN (1973) Rastvorimost tugoplavkikh metallov v zhidkom indii (The solubility of refractory metals in liquid indium). Zh Fiz Khim 47(11):2948 (in Russian)
298. Hershfinkel M, Gheber LA, Volterra V, Hutchison JL, Margulis L, Tenne R (1994) Nested polyhedra of MX_2 (M = W, Mo; X = S, Se) probed by high-resolution electron microscopy and scanning tunneling microscopy. J Am Chem Soc 116(5):1914–1917
299. Gladyshevskii EI (1962) Crystal structure of compounds and phase equilibria in ternary systems of two transition metals and silicon. Powder Metall Met Ceram 1(4):262–265
300. Salje E, Gehlig R, Viswanathan K (1978) Structural phase transition in mixed crystals $W_xMo_{1-x}O_3$. J Solid State Chem 25:239–250
301. Ilnitskaya ON, Kuzma YuB (1984) Investigation of the ternary systems W-B-P and W-Si-P in the range 0–0.66 P. Powder Metall Met Ceram 23(8):622–623
302. Chaban NF, Mikhalenko SI, Kuzma YuB (2000) X-ray studies on phase equilibria in (Tm, Lu)–W–B ternary systems at 1070 K. Powder Metall Met Ceram 39(5–6):251–255
303. Kuzma YuB, Chepiga MV (1969) An x-ray diffraction investigation of the systems Ti-Ni-B, Mo-Ni-B and W-Ni-B. Powder Metall Met Ceram 8(10):832–835
304. Kazakov VK (1965) The character of reaction of titanium nitride with the iron group metals, molybdenum and tungsten. Powder Metall Met Ceram 4(10):845–848
305. Kuzma YuB, Lakh VI, Stadnyk BI, Voroshilov YuV (1966) X-ray diffraction study of the system niobium–tungsten–boron. Powder Metall Met Ceram 5(6):491–493
306. Musatov MI, Ivanov AO (1970) Vzaimodeistvie rasplava okislov alyuminiya i khroma s molibdenom, volframom, iridiem i niobiem (The interaction of aluminium and chromium oxides with molybdenum, tungsten, iridium and niobium). Izv AN SSSR Neorg Mater 6(12):2166–2170 (in Russian)
307. Storozh BD, Kislyi PS (1974) Sintering of tungsten–alumina cermets in the presence of a liquid phase. Powder Metall Met Ceram 13(9):712–716
308. Ordanyan SS (1975) Reactions of rhenium and other refractory metals with some metal-like compounds. Powder Metall Met Ceram 14(2):125–129
309. Mikhalenko SI, Kuzma YuB (1976) Reactions of molybdenum and tungsten with rare-earth metals and boron. Powder Metall Met Ceram 15(2):128–130
310. Kuzma YuB, Svarichevskaya SI, Sobolev AS (1973) Sistemy ittrii-molibden-bor i ittrii-volfram-bor (The yttrium-molybdenum-boron and yttrium-tungsten-boron systems). Izv AN SSSR Neorg Mater 9(10):1697–1702 (in Russian)
311. Samsonov GV, Lapshov YuK, Podchernyaeva IA, Fomenko VS, Erosov YuI, Dudnik EM (1966) Preparation and physical properties of alloys of the W-LaB_6 system. Powder Metall Met Ceram 5(6):446–451
312. Kuzma YuB, Valovka IP (1981) Uranium–tungsten–boron system. Powder Metall Met Ceram 20(8):574–576
313. Chaban NF (1982) Ternary systems Cr(Mo,W)–Gd–B. Powder Metall Met Ceram 21(1):53–54
314. Chaban NF, Bilonizhko NS (1993) Isothermal sections of phase equilibrium diagrams for the systems (terbium, dysprosium)–tungsten–boron at 1270 K. Powder Metall Met Ceram 32(11–12):928–929
315. Mikhalenko SI, Chaban NF, Kuzma YuB (1992) Novye boridy so strukturoi tipa Er_3CrB_7 i utochnenie ravnovesnoi fazovoi diagramy sistemy Y–W–B (New borides with a structure of

the type Er_3CrB_7 and refinement of the phase equilibrium diagram for the system Y–W–B). Izv Akad Nauk Rossii Neorg Mater 28(5):2092–2095 (in Russian)
316. Farr JD (1968) Phase diagrams of selected refractory compounds. In: Hausner HH, Bowman MG (eds) Fundamentals of refractory compounds, pp. 33–48. Plenum Press, New York
317. Nowotny H, Rogl P (1977) Ternary metal borides. In: Matkovich VI (ed) Boron and refractory borides, pp. 413–438. Springer, Berlin, Heidelberg, New York
318. Rieger W, Nowotny H, Benesovsky F (1966) Die Kristallstruktur von W_2CoB_2 und isotypen Phasen (The crystal structure of W_2CoB_2 and isotypic phases). Monatsh Chem 97(2):378–382 (in German)
319. Telegus VS, Kuzma YuB (1971) Phase equilibrium in the systems vanadium-manganese-boron, molybdenum-manganese-boron and tungsten-manganese-boron. Powder Metall Met Ceram 10(1):52–56
320. Rogl P, Benesovsky F, Nowotny H (1972) Über einige Komplexboride mit Platinmetallen (About complex borides with some platinum metals). Monatsh Chem 103(4):965–989 (in German)
321. Rogl P, Nowotny H (1975) Uran-haltige Komplexboride (Complex borides with uranium). Monatsh Chem 106(2):381–387 (in German)
322. Argon AS (1996) Mechanical properties of single-phase crystalline media: deformation at low temperatures. In: Cahn RW, Haasen P (eds) Physical metallurgy, 4th ed., Vol. 3, pp. 1877–1955. Elsevier Science BV, Amsterdam
323. Zaleski-Ejgierd P, Labet V, Strobel TA, Hoffman R, Ashcroft NW (2012) WH_n under pressure. J Phys Condens Matter 24:155701 (15pp)
324. Timoshchuk VI (1989) Magnetic properties of alloys of the system $(Mn_{1-x}W_x)_3B_4$. Phys Met Metallogr 65(4):102–106
325. Timoshchuk VI (1990) Magnetic phase diagram of $Mn_{2.7}W_{0.3}B_4$. Phys Met Metallogr 69(5):188–191
326. Hasapis AA, Panish MB, Rosen C (1960) The vaporization and physical properties of certain refractories. Technical Report WADD-TR-60–463, Contract AF 33(616)-6840, Part 1, pp 1–67. Wright Air Development Division, Wright-Patterson Air Force Base, Ohio
327. Vahlas C, Chevalier PY, Blanquet E (1989) A thermodynamic evaluation of four Si-M (M = Mo, Ta, Ti, W) binary systems. Calphad 13(3):273–292
328. Gupta KP, Rajendraprasad SB (1992) The Nb-Ni-W system (niobium-nickel-tungsten). J Phase Equilibria 13(1):87–91
329. Duschanek H, Rogl P (1995) Critical assessment and thermodynamic calculation of the binary system boron-tungsten. J Phase Equilibria 16(2):150–161
330. Mikhalenko SI, Chaban NF, Kuzma YuB (1998) Reaction of rare earth metals with VI- and VII-group transition metals and boron. Powder Metall Met Ceram 37(1–2):99–106
331. Raghavan V (2003) The B-Fe-W (boron-iron-tungsten) system. J Phase Equilibria 24(5):457–458
332. Gupta KP (2003) The Co-Nb-W (cobalt-niobium-tungsten) system. J Phase Equilibria 24(1):82–85
333. Raskolenko LG, Gerulskii AYu (2008) Compounds WAl_4, WAl_3, W_3Al_7 and WAl_2 in Al-W-N combustion products. Inorg Mater 44(1):30–39
334. Leitnaker JM, Bowman MG, Gilles PW (1962) Thermodynamic properties of the Ta and W borides. J Electrochem Soc 109(5):441–443
335. Udovskii AL (1990) Computer modelling of phase diagrams, thermodynamic properties and structure of multicomponent systems. Russ Metall (2):132–153
336. Tortorici PC, Dayananda MA (1998) Interdiffusion and diffusion structure development in selected refractory metal silicides. Mater Sci Eng A 261(1–2):64–77
337. Fucke W, Seydel U (1980) Improved experimental determination of critical-point data for tungsten. High Temp High Pressures 12(4):419–432
338. Hiernaut J-P, Beukers R, Hoch M, Matsu T, Ohse RW (1986) Determination of the melting point and of the spectral and total emissivities of tungsten, tantalum and molybdenum in the

solid and liquid states with a six-wavelength pyrometer. High Temp High Pressures 18(6):627–633
339. Shabalin IL, Tomkinson DM, Shabalin LI (2007) High-temperature hot-pressing of titanium carbide–graphite hetero-modulus ceramics. J Eur Ceram Soc 27(5):2171–2181
340. Liu N, Ma GF, Zhang HF, Li H, Ding BZ, Wang AM, Hu ZQ (2008) Wetting behavior of Zr-based bulk metallic glasses on W substrate. Mater Lett 62:3195–3197
341. Ma GF, Li ZK, He CL, Zhu ZW, Fu HM, Wang AM, Li H, Zhang HF, Hu ZQ (2013) Wetting behaviours and interfacial characteristics of TiZr-based bulk metallic glass / W substrate. J Alloys Compd 549:254–259
342. Bondi A (1953) The spreading of liquid metals on solid surfaces: surface chemistry of high-energy substances. Chem Rev 52(2):417–458
343. Toyota H, Ide T, Yagi H, Mori Y, Hirose K (1998) A new measurement and evaluation of wettability between solid and liquid metals in ultra-high vacuum. Seimutsu Kogaku Kaishi (J Japan Soc Precision Eng) 64(5):753–757 (in Japanese)
344. Beyers R (1984) Thermodynamic considerations in refractory metal – silicon – oxygen systems. J Appl Phys 56(1):147–152
345. Phillips B, Chang LLY, Scroger MG (1964) Research on criteria for selection of alloys and surface treatments for inhibition of tungsten oxidation. Report ML-TDR-640230, Contract AF 33(657)-11235, Part I, pp. 1–34. Tem-Pres Research Inc., State College, Pennsylvania
346. Kuzma YuB, Lakh VI, Stadnyk BI, Voroshilov YuV (1968) Phase equilibria in the systems Zr-Re-B and W-Re-B. Powder Metall Met Ceram 7(6):462–466
347. Havinga EE, Damsma H, Kannis JM (1972) Compounds and pseudo-binary alloys with the $CuAl_2$ ($C16$)-type structure. IV. Superconductivity. J Less-Common Met 27(3):281–291
348. Okamoto H (2002) Pr-W (praseodymium-tungsten) J Phase Equilibria 23(1):113
349. Okamoto H (2002) Lu-W (lutetium-tungsten) J Phase Equilibria 23(2):197
350. Okamoto H (2001) La-W (lanthanum-tungsten) J Phase Equilibria 22(6):693
351. Okamoto H (2001) Ce-W (cerium-tungsten) J Phase Equilibria 22(6):690
352. Okamoto H (2002) Tb-W (terbium-tungsten) J Phase Equilibria 23(1):114
353. Bauer AA, Rough FA (1959) Thorium alloy systems. Prog Nucl Energy Ser 5 2:612–619
354. Pandian S, Naidu SVN, Rao PR (1987) The Th-W (thorium-tungsten) system. J Alloy Phase Diagrams 3:152–155
355. Chiotti P, Akhachinskij VV, Ansara I, Rand MH (1982) The Th-W (thorium-tungsten) system. Bull Alloy Phase Diagrams 3:104–105
356. Ackerman RJ, Rauh EG (1972) Determination of liquidus curves for the Th-W, Th-Ta, Zr-W and Hf-W systems: anomalous behaviour of metallic thorium. High Temp Sci 4:272–282
357. Schramm CH, Gordon P, Kaufman AR (1950) The alloy systems uranium-tungsten, uranium-tantalum and tungsten-tantalum. Trans Am Inst Min Metall Pet Eng 188:195–204
358. Schonfeld FW (1961) Plutonium phase diagrams studied at Los Alamos. In: Coffinberry AS, Miner WN (eds) The metal plutonium, pp. 240–265. University of Chicago Press, Chicago
359. Schonfeld FW, Cramer EM, Miner WN, Ellinger FH, Coffinberry AS (1959) Plutonium constitutional diagrams. Prog Nucl Energy Ser 5 2:579–599
360. Autler SH, Hulm JK, Kemper RS (1965) Superconducting technetium-tungsten alloys. Phys Rev 140:A1177-A1180
361. Okamoto H, Massalski TB (1985) The Au-W (gold-tungsten) system. Bull Alloy Phase Diagrams 6(2):136–137
362. Yvon K, Feschotte P (1979) Constitution et structure des alliages du gallium avec les metaux de transition (Constitution and structure of gallium alloys with transition metals) J Less-Common Met 63(1):1–13 (in French)
363. Naidu SVN, Sriramamurthy AM, Rao PR (1989) The Ge-W (germanium-tungsten) system. J Alloy Phase Diagrams 5:159–163
364. Fernandez Guillermet A, Jonsson S (1993) Thermodynamic analysis of stable and metastable W nitrides and calculation of the W-N phase diagram. Z Metallkd 84:106–117
365. Huang W (1997) Thermodynamic properties of the Nb-W-C-N system. Z Metallkd 84:63–68

366. Moffat WG (1978) The handbook of binary phase diagrams. General Electric Company, Schenectady, New York
367. Opperman H, Stover G, Wolf E (1985) On the preparation of tungsten oxides by chemical transport with $TeCl_4$. Cryst Res Technol 20:883–887
368. Nanjundaswamy KS, Gopalakrishnan J (1987) Formation of novel molybdenum and tungsten sulfides by reduction of MoS_2 and WS_2: a new route to Chevrel phases. J Solid State Chem 68:188–191
369. Siegel S, Northrop DA (1966) X-ray diffraction studies of some transition metal hexafluorides. Inorg Chem 5:2187–2188
370. Levy JH, Taylor JC, Wilson PW (1975) The structures of fluorides. XIII. The orthorhombic form of tungsten hexafluoride at 193 K by neutron diffraction. J Solid State Chem 15:360–365
371. Marx R, Seppelt K, Ibberson RM (1996) Time-of-flight neutron powder diffraction study on the third row transition metal hexafluorides WF_6, OsF_6, and PtF_6. J Chem Phys 104:7658–7664
372. Drews T, Supel J, Hagenbach A, Seppelt K (2006) Solid state molecular structures of transitional metal hexafluorides. Inorg Chem 45:3782–3788
373. Taylor JC, Wilson PW (1974) The structure of β-tungsten hexachloride by powder neutron and x-ray diffraction. Acta Crystallogr B 30:1216–1220
374. Siepmann R, Von Schnering HG (1968) Die Kristallstruktur von W_6Br_{16} Eine Verbindung mit Polykationen $[W_6Br_8]^{6+}$ und Polyanionen $[Br_4]^{2-}$ (The crystal structure of a compound with polycations $[W_6Br_8]^{6+}$ and polyanions $[Br_4]^{2-}$). Z Anorg Allg Chem 357:289–298 (in German)
375. Willing W, Müller U (1987) Wolframhexabromid (Tungsten hexabromide). Acta Crystallogr C 43:1425–1426 (in German)
376. Sassmannshausen J, Von Schnering HG (1994) Synthese und Kristallstruktur der molekularen Clusterverbindung W_6Br_{14} (Synthesis and crystal structure of the molecular cluster W_6Br_{14}). Z Anorg Allg Chem 620:1312–1320 (in German)
377. Staelmaier HH, Lowder JT (1967) Die tau-Phase im Dreistoffsystem Kobalt-Wolfram-Bor (The tau-phase in the cobalt-tungsten-boron ternary system) Metall (Heidelberg) 21:1023–1024 (in German)
378. Rogl P, Benesovsky F, Nowotny H (1970) Komplexboride mit ReB_2-Struktur (Complex borides with ReB_2-structure), Monatsh. Chem. 101:27–31 (in German)
379. Omori S, Koyama K, Hashimoto Y, Yamashita M (1984) Phase relationships in Ni-Mo-B and Ni-W-B systems at 1223 K. J Jpn Inst Met 48:682–687 (in Japanese)
380. Rogl P, Nowotny H, Benesovsky F (1970) Ternäre Komplexboride in den Dreistoffen: (Mo,W)-(Ru,Os)-B und W-Ir-B (Ternary complex borides in ternary systems: (Mo,W)-(Ru,Os)-B and W-Ir-B). Monatsh Chem 101:850–854 (in German)
381. Rogl P, Rudy E (1978) New complex borides with ReB_2- and Mo_2IrB_2-type structure. J Solid State Chem 24:175–181
382. Nowotny H, Haschke H, Benesovsky F (1967) Bor-reiche Wolframboride (Boron-rich tungsten borides). Monatsh Chem 98:547–554 (in German)
383. Kuzma YuB, Mikhalenko SI, Chaban NF (1983) Vzaimodeistvie Mo, W i Re s redkozemelnymi metallami i borom (Interaction of Mo, W and Re with rare-earth metals and boron). In: Savitskii EM (ed) Issledovaniya i primenenie splavov tugoplavkikh metallov (Studies and application of refractory metal alloys), pp. 5–11. Nauka, Moscow (in Russian)
384. Van Den Berg JM, Matthias BT, Corenzwit E, Barz H (1975) Superconductivity of some binary and ternary transition-metal borides. Mater Res Bull 10:889–894
385. Nowotny H, Kieffer R, Benesovsky F (1957) Silicoboride der Übergangsmetalle Vanadin, Niob, Tantal, Molybdän und Wolfram (Silicoborides of the transition metals vanadium, niobium, tantalum, molybdenum and tungsten). Planseeber Pulvermetall 5:86–93
386. Pitman DT, Das DK (1960) A study of the thorium-tungsten-boron system. J Electrochem Soc 107:763–766

387. Gupta KP (2002) The Co-Mo-W (cobalt-molybdenum-tungsten) system. J Phase Equilib 23:274–277
388. Banik G, Ettmayer P, Vendl A, Kieffer R (1979) Investigation of the Mo-W-N system. High Temp High Pressures 11:349–352
389. Waterstrat RM, Kuntzler R (1988) Stabilization of α-Mn structures in new ternary χ phases. J Less-Common Met 142:163–168
390. Taylor A, Doyle NJ (1967) The solid solubility of nitrogen in Nb and Nb-rich Nb-Hf, Nb-Mo and Nb-W alloys. Part II: The ternary systems Nb-Hf-N, Nb-Mo-N and Nb-W-N. J Less-Common Met 13:413–430
391. Rozanova ON, Trunov VK, Kovba LM (1966) New binary oxides of uranium and tungsten. Inorg Mater 2:273–274
392. Winter M (2012) WebElements: the periodic table on the WWW. Tungsten: enthalpies and thermodynamic properties. http://www.webelements.com/tungsten/thermochemistry.html Accessed 20 May 2013.
393. Okamoto H (2010) The Cl-W (chlorine-tungsten) system. J Phase Equilib Diffus 31(4):402–403
394. Okamoto H (2010) The V-W (vanadium-tungsten) system. J Phase Equilib Diffus 31(3):324
395. Raghavan V (2009) The Al-Mo-Ni-W (aluminium-molybdenum-nickel-tungsten) system. J Phase Equilib Diffus 30(3):291
396. Okamoto H (2008) The Co-W (cobalt-tungsten) system. J Phase Equilib Diffus 29(1):119
397. Okamoto H (2000) The W-Y (tungsten-yttrium) system. J Phase Equilib 21(6):575
398. Okamoto H (2000) The Sc-W (scandium-tungsten) system. J Phase Equilib 21(6):574
399. Okamoto H (1991) The Ni-W (nickel-tungsten) system. J Phase Equilib 12(6):706

Chapter 4
Rhenium

4.1 Structures

Rhenium is the element No. 75 of the periodic table (period—6, group—7 (or VIIB), relates to transition metals) with the ground state level $^6S_{5/2}$ and electron configuration $1s^2 2s^2 2p^6 3s^2 3p^6 3d^{10} 4s^2 4p^6 4d^{10} 4f^{14} 5s^2 5p^6 5d^5 6s^2$. The general oxidation states (numbers) of rhenium in various chemical compounds are (–1), 0, (+1), (+2), (+3), (+4), (+5), (+6) and (+7); the oxidation states (+7), (+6), (+4) and (+2) are the most common; the radii of rhenium are:

atomatic (metallic, CN = 12)—0.137 nm,
atomatic (covalent)—0.128 nm,
ionic (+4)—0.063 nm (CN = 6),
ionic (+5)—0.058 nm (CN = 6),
ionic (+6)—0.055 nm (CN = 6),
ionic (+7)—0.038 nm (CN = 4);

its electronegativity is 1.9 in Pauling scale, or 1.46 in Allred–Rochow scale [1–3, 7–8]. Elemental rhenium has a hexagonal close-packed (hcp) metal crystal structure (space group—$P6_3/mmc$, Mg type) with lattice parameters: $a = 0.27615$ nm, $c = 0.44566$ nm, $c/a = 1.6138$ (Z = 2), minimum interatomic distance—0.275 nm (CN = 12), slip planes (0001), $(10\bar{1}1)$ and slip direction $< 2\bar{1}\bar{1}0 >$ [30, 148]. At room temperature, the XRD density of rhenium is 21.012 g cm^{-3} and recommended values for the bulk density of common metal parts is—20.9–21.0 g cm^{-3} [4, 8].

4.2 Thermal Properties

Rhenium is a metal with one of the highest melting points of all the elements, exceeded by only tungsten and carbon. The general thermodynamic properties of rhenium are summarized in Table 4.1. For the molar heat capacity $c_p = f(T, \text{K})$,

I. L. Shabalin, *Ultra-High Temperature Materials I*,
DOI: 10.1007/978-94-007-7587-9_4,

Table 4.1 General thermodynamic properties of rhenium

Characteristics	Symbol	Unit	Value	Reference
Standard molar entropy (at 298.15 K and 100 kPa)	$S°_{298}$	J mol^{-1} K^{-1}	36.482	[8]
			37.18	[4]
			37.22	[5]
Enthalpy difference	$H_{298} - H_0$	kJ mol^{-1}	5.333	[8]
Standard molar heat capacity (at 298.15 K and 100 kPa)	$c°_{p,298}$	J mol^{-1} K^{-1}	25.31	[8]
			25.48	[5]
			25.77	[4]
Specific heat capacity (at 298.15 K)	c	J kg^{-1} K^{-1}	136	[10]
			137	[7]
			138.4	[4]
Molar enthalpy (heat) of melting (at the melting point)	ΔH_m	kJ mol^{-1}	33.2	[4]
			34.08	[7–8]
Specific enthalpy (heat) of melting (at the melting point)		kJ kg^{-1}	178	[4]
Molar enthalpy (heat) of vaporization (at the boiling point)	ΔH_v	kJ mol^{-1}	697	[4]
			704	[6]
			714.8	[8]
Specific enthalpy (heat) of vaporization (at the boiling point)		kJ kg^{-1}	3740	[4]
Melting point	T_m	K (°C)	3450 ± 25 (3180 ± 25)	[4, 6, 33]
			3460 (3185)	[7–8, 11, 16–17]
Boiling point	T_b	K (°C)	5865 (5595)	[7]
			5870 (5600)	[8, 33]
			5950 (5680)	[6]

J mol^{-1} K^{-1}, the following relationship is recommended for the range of temperatures from 298 to 2500 K [5]

$$c_p = 24.49 + \left(3.35 \times 10^{-3}\right)T. \tag{4.1}$$

The equilibrium vapour pressure of rhenium P, Pa, obeys the following rules [5]: for solid rhenium in the range of temperatures up to melting point

$$\lg P = -52564/T - 22.213 \lg T + \left(1.6738 \times 10^{-3}\right)T + 88.571, \tag{4.2}$$

and for liquid rhenium in the range of temperatures up to 5915 K

$$\lg P = -34760/T + 5.668 \lg T - \left(0.4227 \times 10^{-3}\right)T - 7.994, \tag{4.3}$$

where T is temperature, K. In high vacuum, the rate of rhenium vaporization at the temperatures of 1820, 2050 and 2300 °C approximately amounts to 0.1 μm, 10 μm and 1 mm per year, respectively [4]. The values of standard molar entropy $S°_{298}$, molar c_p and specific c heat capacities, enthalpies (heats) of melting and vaporization, molar and specific mass enthalpy differences $H_T - H_{298}$ and vapour pressures and mass/linear vaporization rates for rhenium are given in Addendum in comparison with carbon (graphite) and other ultra-high temperature materials (refractory metals) in the wide ranges of temperatures. At room temperature, the thermal conductivity of rhenium is 71.2 W m^{-1} K^{-1} [4, 8, 10]. In the temperature range of 20–1000 °C, the average magnitude of the coefficient of linear thermal expansion of pure rhenium $\alpha = (6.6 \div 6.7) \times 10^{-6}$ K^{-1} [4, 8]; for the directions parallel and perpendicular to the axis c it is 12.45×10^{-6} K^{-1} and 4.67×10^{-6} K^{-1}, respectively [4]. For the interval from 20 to 1700 °C, the recommended value is 7.0×10^{-6} K^{-1} [4]. The surface tension of liquid rhenium (density 18.8 g cm^{-3}) is 2.65 N m^{-1} (its temperature coefficient is -0.34×10^{-3} N m^{-1} K^{-1}) [8]. In comparison with other ultra-high temperature materials (graphite and refractory metals), the values of thermal conductivity and thermal expansion of rhenium in the wide range of temperatures are summarized in Addendum.

4.3 Electro-Magnetic and Optical Properties

At room temperature, the specific electrical resistance (resistivity) of pure rhenium is 172–194 nΩ m. The oxygen and nitrogen contaminations influence the resistivity of rhenium strongly, e.g. the oxygen content growth in the arc-cast metal from 0.008 to 0.022 mas. % is corresponding to the increase of resistivity from 185 to 230 nΩ m [31]. At higher temperatures, the resistivity of rhenium exceeds 1 μΩ m (>2000 °C) [4, 10]. For various intervals, the temperature coefficients of resistivity are 2.42×10^{-3} K^{-1} (20–1730 °C), 2.23×10^{-3} K^{-1} (20–2225 °C) and 1.98×10^{-3} K^{-1} (20–2715 °C) [4]. At room temperature, the magnitude of Hall coefficient of rhenium $R = 3.15 \times 10^{-10}$ m^3 A^{-1} s^{-1} (B = 0.5–5.0 T). Rhenium is a paramagnetic metal and its molar magnetic susceptibility χ_m (SI) $= 8.42 \times 10^{-4}$ cm^3 mol^{-1} [8].

The variations of main optical properties of polycrystalline rhenium with wavelength λ are following [9]:

index of refraction—from 0.4 (λ = 0.05 μm) to 3.7 (λ = 0.6 μm);
index of absorption—from 0.8 (λ = 0.05 μm) to 3.0 (λ = 0.6 μm);
reflective index under normal incidence—from 0.4 (λ = 0.05 μm) to 0.5 (λ = 0.6 μm).

The monochromatic emittance (spectral emissivity) ε_λ of rhenium decreases at 1700–2780 °C with wavelength from 0.42 ($\lambda = 0.4$ μm) to 0.22–0.26 ($\lambda = 2.8$ μm). In the range of temperatures 700–2200 °C, ε_λ ($\lambda = 0.665$ μm)

Table 4.2 Thermoionic characteristics of single crystal and polycrystalline rhenium [4, 8–9, 32]

Material type	Richardson constant, 10^4 A m^{-2} K^{-2}	Electron work function, eV
Single crystal (1121)	–	4.70
Single crystal (1124)	–	4.72
Single crystal (1120)	–	4.80
Single crystal (2111)	–	4.82
Single crystal (2113)	–	4.84
Single crystal (1011)	–	5.04
Single crystal (2110)	–	5.07
Single crystal (1100)	–	5.15
Single crystal (2112)	–	5.27
Polycrystalline, sheet	–	4.60
Polycrystalline, electrolytic, annealed at 1500–1800 °C (exposure – 300 h)	720	4.74
Polycrystalline, electrolytic	700	4.75
Polycrystalline	66	4.85
Polycrystalline, chemical vapour deposition, thickness −50 μm	195	4.89
Polycrystalline	–	5.0
Polycrystalline, chemical vapour deposition	200	5.10

varies from 0.37 to 0.43 decreasing with temperature growth, while the integral emittance ε_T increases with increasing temperature from 0.17–0.18 at 800–900 °C to 0.325–0.33 at 2500–2700 °C [4, 9–10]. The thermoionic emission characteristics (electron work function and Richardson constants) of various rhenium materials [4] are presented in Table 4.2.

The recommended values of electrical resistivity, magnetic susceptibility, integral and spectral emittances and thermoionic emission characteristics (electron work function and Richardson constants) for rhenium are given in comparison with other ultra-high temperature elements (carbon and refractory metals) in Addendum.

4.4 Physico-Mechanical Properties

Physico-mechanical properties of rhenium are extremely sensitive to the microstructure features, which are strongly dependent on metal working (treatment), as well as to the relatively minute amounts of contaminations by the interstitial atomic species, such as oxygen, nitrogen, carbon and hydrogen. Certainly, hardness of cold-worked rhenium rises almost threefold with 40 % strain; cast rhenium with oxygen content ≥0.02 mas. % is about twice harder than that metal with oxygen content about 0.0002 mas. %. For various microstructure states, the hardness of rhenium comes to the following values [4, 10]:

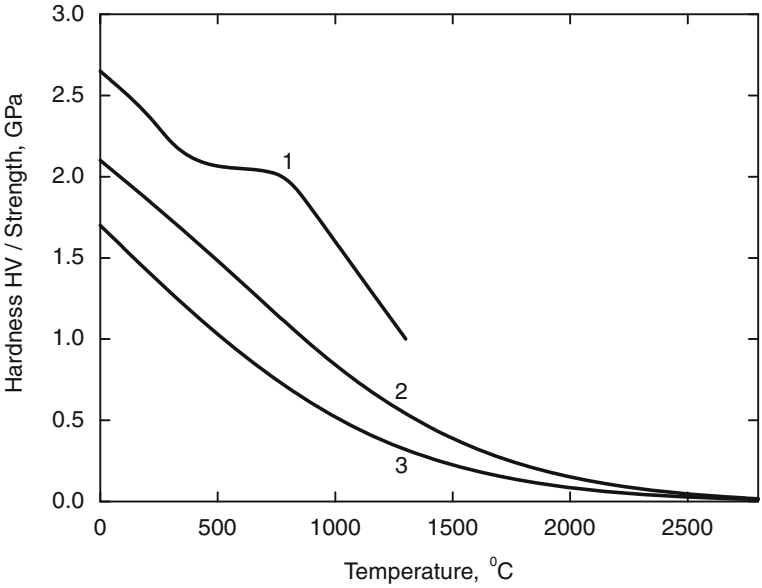

Fig. 4.1 Variation of the hardness *(1)* and ultimate tensile strength *(2–3)* of unalloyed rhenium with temperature (*2*–work hardened and *3*–annealed metal) [8]

as-cast metal—HB = 135 kgf mm^{-2} (1.3 GPa);
electrolytic coating—HB = 250 kgf mm^{-2} (2.5 GPa);
annealed metal—HV = 130–250 kgf mm^{-2} (1.3–2.5 GPa);
compact sintered from powder—HV = 300 kgf mm^{-2} (2.9 GPa);
cold worked (hardened) metal—HV = 500–800 kgf mm^{-2} (4.9–7.8 GPa);

The temperature behaviour of hardness is complicated because of the presence of two flexion points on the hardness-temperature curve, which are connected with changing the deformation mechanism of rhenium (Fig. 4.1) [4].

The value of ultimate tensile strength of work hardened rhenium at room temperature amounts to 2.0–2.1 GPa, while for annealed metal it ranges from 0.5 to 1.0 GPa (elongation—5–20 %). For the various components made from unalloyed rhenium, these characteristics comes to the following values [4]:

sheet cold worked (thickness 0.13 mm, hardened 20 %)—2.00 GPa;
wire produced by powder metallurgy method, annealed—1.13 GPa;
sheet annealed (thickness 0.13 mm)—1.03 GPa;
fused in electron beam furnace—$\sim$0.85 GPa.

The variation of the tensile strength characteristics of rhenium in the wide range of temperatures is shown in Fig. 4.1. The prolonged strength of rhenium (testing exposure—100 h) is 137 MPa at 1000 °C and 5.9 MPa at 2000 °C [10]. Rhenium

Table 4.3 The effect of oxygen content on the mechanical properties of rhenium (hydrogen and nitrogen contents—in the limits of (3 ÷ 8) × 10^{-4} mas.%) [31]

Oxygen content, mas.%	As-cast metal		Hardened (40 %) and annealed metal	
	Hardness HV, GPa		Ultimate tensile strength, MPa	Elongation, %
0.0021	1.45	1.28	522	21.1
0.0081	1.83	1.78	–	–
0.0120	1.87	1.83	645	16.1
0.0180	2.44	2.31	720	11.0
0.0200	2.55	2.50	812	9.2
0.0220	2.67	2.67	845	5.0

has the greatest tensile and creep-rupture strength over a wide range of temperatures among all the refractory metals except osmium [161]. A typical example of profound effect of oxygen contamination on the hardness and ultimate tensile strength of unalloyed rhenium is given in Table 4.3 for as-cast and subsequently hardened (40 %) and annealed metal specimens [4]. The ultimate compression strength of rhenium at room temperature is >1.96 GPa [9]. Purified rhenium is highly ductile; thoroughly annealed, it demonstrates the high grade of elongation (up to ~30 % at room temperature) and does not exhibit ductile-to-brittle transition temperature at the common conditions [10–11]. However, together with that rhenium possesses very high magnitudes of elastic properties at room temperature [4, 8, 10]:

Young's modulus E, GPa		460–520
Coulomb's (shear) modulus G, GPa		180
Poisson's ratio ν		0.26
Volume compressibility κ, MPa^{-1}		0.26×10^{-5}
Longitudinal velocity of sound V_S, ms^{-1}		5360
Transversal velocity of sound V_T, ms^{-1}		2930
Elastic compliance	s_{11}, TPa^{-1}	2.11
	s_{33}, TPa^{-1}	1.70
	s_{44}, TPa^{-1}	6.21
	s_{12}, TPa^{-1}	−0.80
	s_{13}, TPa^{-1}	−0.40
Elastic stiffness	c_{11}, GPa	616
	c_{33}, GPa	683
	c_{44}, GPa	161
	c_{12}, GPa	273
	c_{13}, GPa	206

At elevated temperatures, the value of Young's modulus falls almost linearly with temperature and amounts to 402 GPa at 600 °C and 370 GPa at 880 °C [4, 10].

The magnitudes of physico-mechanical (strength, elasticity) properties of unalloyed rhenium in the wide range of temperatures are summarized in Addendum in comparison with other ultra-high temperature materials (graphite and refractory metals).

4.5 Nuclear Physical Properties

The isotopes of rhenium (standard atomic mass – 186.207 u) from ^{160}Re to ^{194}Re, including metastable states ($^{161m-165m}$Re, $^{167m-169m}$Re, ^{172m}Re, ^{177m}Re, $^{179m1-2}$Re, $^{182m1-3}$Re, $^{183m-186m}$Re, ^{188m}Re and ^{190m}Re), and their general characteristics are summarized in Table 4.4; the naturally occurring isotopes are listed in order of decreasing abundance and unstable artificial (radioactive) isotopes – in order of decreasing half-life period of decay.

Table 4.4 General characteristics of the isotopes of rhenium[a] [7, 9, 86–88]

Isotope	Mass, u	Abundance, %	Half-life period	Decay mode, excitation (radiation) energy, MeV
^{187}Re[b]	186.955753	62.60	41.2×10^9 y[c]	β^- (99.99 %), α (10^{-4} %)
^{185}Re[d]	184.952955	37.40	–	–
^{186m}Re	–	–	2.0×10^5 y	Isomer, β^- (10 %), γ (90 %), 0.149
^{184m}Re	–	–	169 d	Isomer, β^+ (24.6 %), γ (75.4 %), 0.188
^{183}Re	182.950820	–	70.0 d	*K*-capture; γ, 0.081, 0.252
^{184}Re	183.952521	–	38.0 d	β^+; γ, 0.159, 0.206, 0.244, 0.784, 0.89
^{186}Re	185.954986	–	3.72 d	β^- (93.1 %): 1.07 (~76 %), 0.93 (~24 %), 0.3 (0.05 %); *K*-capture (6.9 %); γ, 0.123, 0.237, 0.627, 0.764
^{182}Re	181.95121	–	64.0 h	β^+; γ, 0.11, 0.127, 0.222, 0.250, 0.346
^{189}Re	188.959229	–	24.3 h	β^-, 0.2; γ, 1.0
^{181}Re	180.950068	–	19.9 h	β^+
^{188}Re	187.958114	–	17.0 h	β^-: 1.9 (1 %), 1.961 (20 %), 2.116 (79 %); γ, from 0.15 to 1.95
^{182m1}Re	–	–	12.7 h	Isomer, β^+
^{190m}Re	–	–	3.2 h	Isomer, β^- (54.4 %), γ (45.6 %), 0.210
^{179}Re	178.949988	–	19.5 min	β^+
^{188m}Re	–	–	18.59 min	Isomer, γ, 0.172

(continued)

Table 4.4 (continued)

Isotope	Mass, u	Abundance, %	Half-life period	Decay mode, excitation (radiation) energy, MeV
^{177}Re	176.95033	–	14 min	β^+
^{178}Re	177.95099	–	13.2 min	β^+
^{191}Re	190.963125	–	9.8 min	β^-
^{175}Re	174.95138	–	5.89 min	β^+
^{176}Re	175.95162	–	5.3 min	β^+
^{190}Re	189.96182	–	3.1 min	β^-
^{180}Re	179.950789	–	2.44 min	β^+, 1.1; γ, 0.106, 0.88
^{174}Re	173.95312	–	2.40 min	β^+
^{173}Re	172.95324	–	1.98 min	β^+
^{172m}Re	–	–	55 s	Isomer, β^+
^{193}Re	192.96747 (?)	–	30 s (?)	?
^{192}Re	191.96596 (?)	–	16 s	β^-
^{171}Re	170.95572	–	15.2 s	β^+
^{169m}Re	–	–	15.1 s	Isomer, β^+ (99.8 %), α (0.2 %), 0.145
^{172}Re	171.95542	–	15 s	β^+
^{170}Re	169.958220	–	9.2 s	β^+ (99.99 %), α (0.01 %)
^{169}Re	168.95879	–	8.1 s	β^+ (99.99 %), α (0.005 %)
^{168m}Re	?	–	6.6 s	Isomer, ?
^{167m}Re	–	–	5.9 s	Isomer, β^+ (99.3 %), α (0.7 %), 0.130
^{168}Re	167.96157	–	4.4 s	β^+ (99.99 %), α (0.005 %)
^{167}Re	166.96260	–	3.4 s	α, β^+
^{165m}Re	–	–	2.1 s	Isomer, α (13 %), β^+ (87 %)
^{166}Re	165.96581	–	2 s (?)	α, β^+
^{194}Re	193.97042 (?)	–	2 s (?)	?
^{165}Re	164.967089	–	1 s (?)	α, β^+
^{164}Re	163.97032 (?)	–	0.53 s	α (58 %), β^+ (42 %)
^{164m}Re	–	–	0.53 s	Isomer, 0.120, ?
^{163}Re	162.972081	–	0.39 s	α (32 %), β^+ (68 %)
^{163m}Re	–	–	0.21 s	Isomer, α (66 %), β^+ (34 %), 0.115
^{162}Re	161.97600 (?)	–	0.11 s	α (94 %), β^+ (6 %)
^{162m}Re	–	–	77 ms	Isomer, α (91 %), β^+ (9 %), 0.173
^{161m}Re	–	–	15.6 ms	Isomer, α, 0.123
^{183m}Re	–	–	1.04 ms	Isomer, 1.908
^{160}Re	159.98212 (?)	–	0.82-0.86 ms (?)	p (91 %), α (9 %)
^{161}Re	160.97759	–	0.37 ms (?)	p
^{179m1}Re	–	–	0.095 ms	Isomer, 0.065, ?
^{177m}Re	–	–	0.05 ms	Isomer, 0.084, ?
^{182m3}Re	–	–	0.78 μs	Isomer, 0.461 + X, ?

(continued)

Table 4.4 (continued)

Isotope	Mass, u	Abundance, %	Half-life period	Decay mode, excitation (radiation) energy, MeV
^{182m2}Re	–	–	0.585 μs	Isomer, 0.236 + X, ?
^{179m2}Re	–	–	>0.4 μs	Isomer, 1.685 + Y, ?
^{185m}Re	–	–	0.12 μs	Isomer, 2.124 + X, ?

[a] Naturally occurring rhenium includes stable (or nearly stable, see below note *d*) ^{185}Re (37.4 %) and nearly stable ^{187}Re (62.6 %); the latter has a very long (longer than the age of universe) half-life period

[b] Primordial radionuclide

[c] Fully ionized: 33 y (bound state β^-)

[d] Believed to undergo α decay (?)

Nuclear physical properties of rhenium (isotopic mass range, total number of isotopes, thermal neutron macroscopic cross sections, moderating ability and capture resonance integral), compared with other ultra-high temperature elements (carbon and refractory metals), are given in Addendum.

4.6 Chemical Properties

The comprehensive information on the chemical properties and interaction of rhenium with all the elements of the periodic table is given in Table 4.5. The rhenium containing systems and corresponding binary compounds are described and considered there in accordance to the groups of elements from 1 to 17.

Table 4.5 Chemical interaction of rhenium with elements of the periodic table (binary systems in accordance to the groups of elements)[a]

System	Type of phase diagram (constituent phases, temperatures and compositions of transformations)	Character of interaction	References
Group 1			
Re–H	H, ReH_x (?), Re No diagram plot	No interaction, no solubility at elevated and high temp. The lattice parameters of Re annealed in H_2 (1200 °C) do not change. Fine Re powder adsorbs a distinct amount of H.	[4, 10, 12–13, 34]

(continued)

Table 4.5 (continued)

System	Type of phase diagram (constituent phases, temperatures and compositions of transformations)	Character of interaction	References
Re–Li	α-Li, β-Li, γ-Li, Li_3Re (?), Li_2Re (?), LiRe, $LiRe_2$ (?), Re No diagram plot	In the range of temp. from 1200 to 1600 °C, the solubility of Re in liquid Li rises from 2×10^{-6} to 6.3×10^{-6} at.%. Data on the resistance of Re to Li melt available in the literature are contradictory.	[4, 14, 35–36]
Re–Na	No data	–	–
Re–K	K, K_2Re, KRe (?), KRe_2 (Laves phase, ?), Re No diagram plot	No experimental data.	[35]
Re–Rb	No data	–	–
Re–Cs	No data	–	–
Re–Fr	No data	–	–
Group 2			
Re–Be	α-Be, β-Be, $ReBe_{22}$ (or $ReBe_{20}$, <~1500–1800 °C, invariable compos., ?), $ReBe_{16+x}$ ($x \approx 1.4$, or $Re_{0.23}Be_4$, <~1000 °C, invariable compos., ?), $ReBe_6$ (< ~1000 °C, invariable compos., ?), $ReBe_{2\pm x}$ (<~1550–2000 °C, homog. range—30–40 at.% Re at 400–900 °C), Re Eutectic $ReBe_{22}$–Be (?, ~0.45 at.% Re) No complete diagram plot	The max. solid solubility of Re in Be is 0.5–1 at.% and that of Be in Re is ~10 at.%; the solubility of Re in Be at the $ReBe_{22}$–Be eutectic temp. is 0.048 at.% (?). The addition of Re increases the melt. points of Be–Re alloys (e.g., up to 1840 °C for Be – 5 at.% Re alloy). Re beryllides are formed by the direct interaction of Re and Be powders after heat treatment in Ar at 1200–1650 °C.	[4, 12, 15–16, 37–38]
Re–Mg	Mg, no binary compounds (?), Re Peritectic Mg (650.6 °C, ~0.06 at.% Re, ?) No complete diagram plot	The solubility of Re in liquid Mg is ~0.05 at.% at peritectic temp.	[16, 178]
Re–Ca	No data	–	–
Re–Sr	No data	–	–
Re–Ba	No data	–	–
Re–Ra	No data	–	–
Group 3			
Re–Sc	α-Sc, β-Sc, $ScRe_2$ (<2030 °C, incongruent melt. point, invariable compos., Laves phase), Sc_5Re_{24} (<2570 °C, incongruent melt. point, invariable compos.), Re Eutectic $ScRe_2$–β-Sc (1360 °C, ~0.5–1.0 at.% Re)	The max. solubility of Re in β-Sc is <1 at.% (1360 °C) and that of Sc in Re is ~5 at.% (2570 °C).	[4, 16–17, 39–40]

(continued)

Table 4.5 (continued)

System	Type of phase diagram (constituent phases, temperatures and compositions of transformations)	Character of interaction	References
Re–Y	α-Y, β-Y, YRe_2 (<2520 °C, incongruent melt. point, invariable compos., Laves phase, ?), Re Eutectic YRe_2–α-Y (1450 °C, ~5 at.% Re, ?) Data on the system available in literature are controversial.	The max. solubility of Re in β-Y is <1 at.% and that of Y in Re is ≤1 at.%.	[4, 16–17, 40]
Lanthanides			
Re–La	α-La, β-La, γ-La, no binary compounds (?), Re Miscibility gap in the liquid state (~2–99.5 at.% Re at ~3150 °C)	No interaction. Practically, Re and La are immiscible in the solid and liquid states.	[14, 16]
Re–Ce	α-Ce, β-Ce, γ-Ce, δ-Ce, no binary compounds (?), Re No diagram plot	–	[15, 40]
Re–Pr	α-Pr, β-Pr, α-$PrRe_2$ (Laves phase, ?), β-$PrRe_2$ (Laves phase, ?), Re Eutectic with β-Pr (~925–930 °C, 0.24 at.% Re)	The solubility of Re in liquid Pr is 0.6 at.% at 1140 °C, 2.4 at.% at 1360 °C, 2.6 at.% at 1480 °C and 4.5 at.% at 1765 °C.	[16–17, 40, 42–43, 137]
Re–Nd	α-Nd, β-Nd, $NdRe_2$ (Laves phase, ?), Re No diagram plot	The solubility of Nd in Re is negligible.	[14, 136]
Re–Pm	No data	–	–
Re–Sm	α-Sm, β-Sm, γ-Sm, $SmRe_2$ (Laves phase), Re No diagram plot	The solubility of Sm in Re is negligible.	[17, 40]
Re–Eu	Eu, $EuRe_2$ (Laves phase), Re No diagram plot	–	[13]
Re–Gd	α-Gd, β-Gd, $GdRe_2$ (<2380–2480 °C, incongruent melt. point, invariable compos., Laves phase), Re Eutectic $GdRe_2$–β-Gd (~1280–1300 °C, ~1 at.% Re)	The max. solubility of Re in β-Gd is <1 at.% and that of Gd in Re is ~0.4 at.%.	[13, 16, 44]
Re–Tb	α′-Tb, α-Tb, β-Tb, $TbRe_2$ (<2400–2500 °C, incongruent melt. point, invariable compos., Laves phase), Re Eutectic $TbRe_2$–β-Tb (~1305–1320 °C, <1 at.% Re)	The solubility of Tb in Re is ~0.2 at.%. Re decreases the temp. of melt. point and polymorphic transformation of Tb.	[17, 40, 45]
Re–Dy	α′-Dy, α-Dy, β-Dy, $DyRe_2$ (Laves phase), Re No diagram plot	The solid solubility of Dy in Re is <1 at.%.	[13, 46]

(continued)

Table 4.5 (continued)

System	Type of phase diagram (constituent phases, temperatures and compositions of transformations)	Character of interaction	References
Re–Ho	α-Ho, β-Ho, $HoRe_2$ (Laves phase), Re No diagram plot	The solid solubility of Ho in Re is <1 at.%.	[13, 46]
Re–Er	α-Er, β-Er, $ErRe_2$ (<2450–2550 °C, incongruent melt. point, invariable compos., Laves phase), Re Eutectic $ErRe_2$–β-Er (~1425–1455 °C, ~3 at.% Re)	The max. solubility of Re in Er is ≤1 at.% and that of Er in Re is <0.3 at.%.	[13, 44]
Re–Tm	α-Tm, β-Tm, $TmRe_2$ (Laves phase), Re No diagram plot	–	[17]
Re–Yb	α-Yb, β-Yb, γ-Yb, $YbRe_2$ (Laves phase, ?), Re No diagram plot	–	[17]
Re–Lu	α-Lu, β-Lu, $LuRe_2$ (Laves phase), Re No diagram plot	–	[14, 40]
Actinides			
Re–Ac	No data	–	–
Re–Th	α-Th, β-Th, $ThRe_2$ (<~2500 °C, incongruent melt. point, invariable compos., Laves phase, ?), Re Eutectic $ThRe_2$–β-Th (~1380–1420 °C, 14.9–15.5 at.% Re) Eutectic $ThRe_2$–Re (~2315 °C, 73 at.% Re, ?)	The max. solubility of Re in β-Th is ~1.5 at.% (?). The solubility of Th in Re is negligible.	[4, 16–17, 47]
Re–Pa	No data	–	–
Re–U	α-U, β-U, γ-U, α′-U (metastable, ?), U_2Re (<750 °C, invariable compos.), α-URe_2 (<180 °C), β-URe_2 (180–2200 °C, congruent melt. point, Laves phase), Re Eutectic β-URe_2–γ-U (~1105–1120 °C, ~13 at.% Re) Eutectic β-URe_2–Re (~2105–2160 °C, ~71–72.5 at.% Re)	The solid solubilities of Re in U modifications are following: in α-U – 0.5 at.% at 643 °C, in β-U –2.4 at.% at 680 °C, in γ-U – 7.5 at.% at 680 °C and 8.8 at.% at 1105 °C. The solid solubility of U in Re is ~0.6 at.% at room temp. and ~4 at.% at 2105 °C. Fast cooling of γ-U with Re content >7 at.% results in the formation of α′-U metastable oversaturated solid solutions.	[4, 16–17, 47–49, 189, 198]

(continued)

Table 4.5 (continued)

System	Type of phase diagram (constituent phases, temperatures and compositions of transformations)	Character of interaction	References
Re–Np	α-Np, β-Np, γ-Np, $NpRe_2$ (Laves phase), Re No diagram plot	–	[179]
Re–Pu	α-Pu, β-Pu, γ-Pu, δ-Pu, δ′-Pu, ε-Pu, $PuRe_2$ (<2000 °C, invariable compos., Laves phase), Re Eutectic $PuRe_2$–ε-Pu (625 °C, ~1 at.% Re, ?)	–	[16]
Re–Am	No data	–	–
Group 4			
Re–Ti	α-Ti, β-Ti, ω-Ti (metastable solid solution), χ-Ti_5Re_{24} (<2750 °C, incongruent melt. point, invariable compos.), Re Extended solid solution based on β-Ti (<2025 °C, up to 50 at.% Re)	Re diminishes the temp. of α-Ti–β-Ti polymorphic transformation to 650 °C (for the alloy containing ~7 at.% Re). The solubility of Re in α-Ti is ~8 at.% (600 °C). and that of Ti in Re is 2.3 at.% at 2750 °C, 0.8 at.% at 2100 °C and 0.4 at.% at 1500 °C.	[4, 16–19, 50–51]
Re–Zr	α-Zr, β-Zr, σ-Zr_2Re (<~1640–1900 °C, incongruent melt. point, invariable compos., ?), $Zr_{21}Re_{25}$ (?), λ-$ZrRe_{2-x}$ (<2450–2750 °C, melt. point, homog. range—~65–67 at.% Re at 2500 °C and ~62–67 at.% Re at 1600 °C, Laves phase, ?), χ-Zr_5Re_{24+x} (<2500 °C, incongruent melt. point, homog. range—~83–85 at.% Re), Re Eutectic σ-Zr_2Re–β-Zr (~1590–1600 °C, ~14–23.5 at.% Re) Eutectic χ-Zr_5Re_{24+x}–Re (~2430 °C, ~87 at.% Re, ?)	Re stabilizes β-Zr and diminishes the temp. of α-Zr–β-Zr polymorphic transformation to 550–575 °C (for the alloy containing ~2 at.% Re). The solid solubility of Re in β-Zr is 8 at.% at 1590–1600 °C and 3–4 at.% at 550–575 °C; in α-Zr it is ~0.2 at.% at 700–800 °C and ~1.5 at.% at 400–500 °C. The solubility of Zr in Re is ~0.2 at.% at 2500 °C; it decreases at lower temp. to 0.1 at.% (1500–2100 °C).	[4, 16–17, 19, 52–55]

(continued)

Table 4.5 (continued)

System	Type of phase diagram (constituent phases, temperatures and compositions of transformations)	Character of interaction	References
Re–Hf	α-Hf, β-Hf, $HfRe_{1\pm x}$ (or $Hf_{11}Re_9$, or Hf_3Re_2, <~2280–2445 °C, incongruent melt. point, ?), λ-$HfRe_{2\pm x}$ (<~2850–3160 °C, melt. point, Laves phase, homog. range—~65–67.5 at.% Re at 3085 °C and ~62–67 at.% Re at 2445 °C), χ-$Hf_5Re_{24\pm x}$ (or $HfRe_7$, <2800–3100 °C (?), incongruent melt. point, homog. range—~82.5–89.5 at.% Re at 2930 °C and ~82.5–88 at.% Re at 2500 °C), Re Eutectic $HfRe_{1\pm x}$ (or Hf_3Re_2) –β-Hf (~1840–2100 °C, ~16.4–23.5 at.% Re) Eutectic χ-$Hf_5Re_{24\pm x}$–Re (~2915–2945 °C, ~89.5–91.5 at.% Re, ?) Data on the system available in literature are controversial	Re stabilizes β-Hf and diminishes the temp. of α-Hf–β-Hf polymorphic transformation to 1300 °C (for the alloy containing 12 at.% Re). The solid solubility of Re in β-Hf is 12.5 at.% at ~1840–2100 °C and 12 at.% at 1300 °C; in α-Hf it is ~0.8–3.0 at.% at 1250–1300 °C and ~0.5 at.% at 1000 °C. The max. solid solubility of Hf in Re is ~0.2–3.5 at.% at 2915–2975 °C; at lower temp. it decreases to 0.1–0.05 at.% (1100 °C).	[4, 13, 16, 18, 56–57]
Group 5			
Re–V	V, δ-$V_3Re_{7\pm x}$ (from 1470 °C to 1950–2310 °C, homog. range—68–72 at.% Re at 1970 °C), σ-VRe_{3+x} (from 1950–1990 °C to 2440–2630 °C, melt. point, homog. range—~75–78 at.% Re at 2250–2310 °C, ?), Re Extended solid solution based on V (<2400 °C, up to 66 at.% Re) Eutectic σ-VRe_{3+x}–(V,Re) extended solid solution (~2360–2400 °C, ~70 at.% Re)	The solubility of V in Re is 10–14 at.% at 2460 °C, ~5.5 at.% at 1800 °C and ~5 at.% at 1400 °C.	[4, 16–17, 58–65]

(continued)

Table 4.5 (continued)

System	Type of phase diagram (constituent phases, temperatures and compositions of transformations)	Character of interaction	References
Re–Nb	Nb, σ-Nb_2Re_{3-x} (from 2160–2300 °C to 2400–2565 °C, incongruent melt. point, homog. range—~53–57 at.% Re at 2350–2435 °C), χ-$NbRe_{3\pm x}$ (<2520–2745 °C, melt. point, homog. range—61.5–87 at.% Re at 2160–2220 °C and from 63.5–69 to 87–89 at.% Re at 1000 °C), Re Extended solid solution based on Nb (up to 45.5–46.5 at.% Re at 2350–2435 °C) Eutectic σ-Nb_2Re_{3-x}–(Nb,Re) extended solid solution (~2350–2435 °C, ~48–52 at.% Re) Eutectic χ-$NbRe_{3\pm x}$ – Re (~2715 °C, ~88 at.% Re, ?)	Re diminishes the melt. temp. of Nb slightly. The solubility of Nb in Re is 3.5–4.5 at.% at 2520–2715 °C; at lower temp. it decreases to ~0.4 at.% (1500 °C).	[14, 16, 18, 66–69, 118, 133]
Re–Ta	Ta, σ-Ta_2Re_{3-x} (from 2200–2460 °C to 2680–2740 °C, incongruent melt. point, homog. range—~34–60 at.% (?) Re at 2400–2690 °C), χ-$TaRe_{3\pm x}$ (<2790–2830 °C, melt. point, homog. range—60–84.5 at.% Re at 2460 °C and 64–80 at.% Re at 2000 °C, ?), Re Extended solid solution based on Ta (up to 47 at.% Re at 2460 °C) Eutectic σ-Ta_2Re_{3-x}–(Ta,Re) extended solid solution (~2400–2690 °C, ~49.7–50.3 at.% Re) Eutectic χ-$TaRe_{3\pm x}$–Re (~2760 °C, ~ 84 at.% Re, ?)	Re diminishes the melt. temp. of Ta considerably. The solubility of Ta in Re is ~3–5 at.% at 2755–2830 °C; at lower temp. it decreases to ~0.25 at.% (1100 °C).	[16–18, 70–73, 196]
Group 6			
Re–Cr	Cr, σ-$Cr_2Re_{3\pm x}$ (<2320–2355 °C, incongruent melt. point, homog. range—~50–72 at.% Re), Re Extended solid solution based on Cr (<2135–2285 °C, up to ~43–50 at.% Re) Extended solid solution based on Re (up to ~17–25 at.% Cr at 2320–2355 °C)	The solubility of Re in Cr increases with temperature growth from ~36 at.% at 1500 °C to the max. magnitude ~43–50 at.% at 2135–2285 °C.	[4, 13, 16, 74–76, 133, 135]

(continued)

Table 4.5 (continued)

System	Type of phase diagram (constituent phases, temperatures and compositions of transformations)	Character of interaction	References
Re–Mo	Mo, σ-$Mo_2Re_{3\pm x}$ (from 1100–1150 °C (?) to 2500–2670 °C, incongruent melt. point, homog. range—~55–70.5 at.% Re at 2500 °C and ~52–72 at.% Re at 2000 °C), χ-$MoRe_{3+x}$ (<1970–2030 °C, homog. range—~76–79 at.% Re at 1100 °C), Re Extended solid solution based on Mo (up to ~42–43 at.% Re at ~2440–2525 °C) Eutectic σ-$Mo_2Re_{3\pm x}$–(Mo,Re) extended solid solution (~2440–2525 °C, ~49–50 at.% Re)	Re diminishes the melt. temp. of Mo slightly. The solid solubility of Re in Mo is 42–43 at.% at 2440–2525 °C and ~29–30.5 at.% at 1100–1200 °C. The solid solubility of Mo in Re is ~15–21 at.% at 2645 °C, ~12–18 at.% at 2520–2570 °C, ~8 at.% at 2100 °C and ~2–6 at.% at 1100–1500 °C. For diffusion rate in the system at various temp. see Addendum.	[14, 16, 19, 77–78, 118, 187]
Re–W	See W–Re in Table 3.5.		
Group 7			
Re–Mn	α-Mn, β-Mn, γ-Mn, δ-Mn, σ-$MnRe_{1+x}$ (<~1700–2280 °C (?), incongruent melt. point, homog. range–?), Re	The solubility of Re in α-Mn is 5.5 at.%; the solubilities of Re in other Mn modifications are lower.	[4, 14, 79]
Re–Tc	Tc, no binary compounds, Re Continuous solid solution Tc–Re	–	[17, 80]
Group 8			
Re–Fe	α-Fe, γ-Fe, δ-Fe, η-$Fe_{3\pm x}Re$ (from 1205 °C, homog. range—~7–36 at.% Re), Fe_2Re (<~1400 °C, homog. range—~28–32 at.% Re), σ-Fe_3Re_2 (from ~850 °C, homog. range—~36–47 at.% Re), Fe_2Re_3 (<~1600 °C, homog. range—~60–64 at.% Re), Re	Practically, Re does not affect the melt. temp. of Fe, its presence changes the temp. of α-Fe–γ-Fe and γ-Fe–δ-Fe transformations only slightly. The max. solubilities of Re in Fe polymorphic modifications are following: ~18–19 at.% in α-Fe (895 °C), ~16.0–16.5 at % in γ-Fe (1205 °C) and ~8 at.% in δ-Fe (1375 °C). Molten Fe has a catastrophic effect on Re metal; direct contact is not recommended.	[4, 13, 16, 18, 81, 161]
Re–Ru	Ru, no binary compounds, Re Continuous solid solution Ru–Re	–	[4, 16–17, 82–83]

(continued)

Table 4.5 (continued)

System	Type of phase diagram (constituent phases, temperatures and compositions of transformations)	Character of interaction	References
Re–Os	Os, no binary compounds, Re Continuous solid solution Os–Re	–	[14, 83–84]
Group 9			
Re–Co	ε-Co, α-Co, no binary compounds, Re Continuous solid solution ε-Co–Re Peritectic α-Co (1550 °C, 15 at.% Re)	Re stabilizes ε-Co modification; the min. limit of solid solubility of Re in ε-Co at 1550 °C is 25 at.%.	[4, 13, 16]
Re–Rh	Rh, no binary compounds, Re Peritectic Rh (∼2595–2645 °C, ∼25–26 at.% Re)	The presence of Re results in increase in the melt. temp. of Rh. The max. melt. point (∼2595–2645 °C) and max. solid solubility of Re in Rh (∼25–26 at.%) are corresponding to the peritectic alloy. The solubility of Re in Rh declines slightly with temp. decreasing; at 1000 °C it amounts to ∼12 at.%. The max. solid solubility of Rh in Re is ∼24 at.% (∼2595–2645 °C); at lower temp. the solubility of Rh declines (>20 at.% at 500 °C).	[4, 16–17, 83, 85]
Re–Ir	Ir, no binary compounds, Re Peritectic Ir (∼2775–2825 °C, ∼36–40 at.% Re) Extended solid solution based on Ir (up to ∼36–40 at.% Re at 2800 °C) Extended solid solution based on Re (up to ∼44 at.% Ir at 2800 °C) Some data on the system available in literature are controversial.	The presence of Re results in increase in the melt. temp. of Ir. The max. melt. point (∼2800 °C) and max. solid solubility of Re in Ir (∼36–40 at.%) are corresponding to the peritectic alloy. The solubility of Re in Ir declines slightly with temp. decreasing; at 1000 °C it amounts to ∼28 at.%. The max. solid solubility of Ir in Re is ∼44 at.% (2800 °C); at lower temp. the solubility of Ir declines slightly (∼39 at.% at 1000 °C and <38 at.% at 500 °C).	[4, 14, 16, 85, 160]

(continued)

Table 4.5 (continued)

System	Type of phase diagram (constituent phases, temperatures and compositions of transformations)	Character of interaction	References
Group 10			
Re–Ni	Ni, no binary compounds, Re Peritectic Ni (1595–1645 °C, ~17 at.% Re, ?) Extended solid solution based on Ni (up to ~17 at.% Re at 1620 °C)	The presence of Re results in increase in the melt. temp. of Ni. The max. melt. point (~1595–1645 °C) and max. solid solubility of Re in Ni (~17 at.%) are corresponding to the peritectic alloy. The solubility of Re in Ni declines slightly with temp. decreasing; at 800 °C it amounts to 12 at.%. The max. solid solubility of Ni in Re is ~14–18 at.% (1620 °C); at lower temp. the solubility of Ni declines slightly (~9–10 at.% at 600 °C). Data on solubility in the system are controversial. Molten Ni has a catastrophic effect on Re metal; direct contact is not recommended.	[4, 14, 16, 18, 89–90, 161, 190–191, 199]
Re–Pd	Pd, no binary compounds, Re Peritectic Pd (~1625–1675 °C, ~16 at.% Re) Extended solid solution based on Pd (up to ~16 at.% Re at 1650 °C)	The presence of Re results in increase in the melt. temp. of Pd. The max. melt. point (~1650 °C) and max. solid solubility of Re in Pd ~16 at.%) are corresponding to the peritectic alloy. The solubility of Re in Pd declines slightly with temp. decreasing; at 1000–1500 °C it amounts to ~11 at.%. The max. solid solubility of Pd in Re is >5 at.% (1650 °C); at lower temp. the solubility of Pd declines.	[4, 14, 83, 85]
Re–Pt	Pt, no binary compounds (ordered phases, ?), Re Peritectic Pt (~2450 °C, ~40–42 at.% Re) Extended solid solution based on Pt (up to ~40–42 at.% Re at ~2450 °C) Extended solid solution based on Re (up to ~40–44 at.% Pt at ~2450 °C)	The presence of Re results in increase in the melt. temp. of Pt. The max. melt. point (~2450 °C) and max. solid solubility of Re in Pt (~40–42 at.%) are corresponding to the peritectic alloy. The mutual solid solubilities of Re and Pt in each other are affected by temp. very slightly.	[4, 16–17, 91]

(continued)

Table 4.5 (continued)

System	Type of phase diagram (constituent phases, temperatures and compositions of transformations)	Character of interaction	References
Group 11			
Re–Cu	Cu, no binary compounds, Re Eutectic (degenerated) Cu–Re (~1083 °C, ?) Miscibility gap in the liquid state (~6.5–87 at.% Re at 2900 °C)	Practically, the components are immiscible in the solid and liquid states. The solid solubility of Re in Cu is $<10^{-4}$ at.%. Molten Cu has no effect on Re metal.	[4, 13, 16, 161]
Re–Ag	Ag, no binary compounds, Re Eutectic (degenerated) Ag–Re (~961 °C, ?)	Practically, the components are immiscible in the solid and liquid states. Molten Ag has no effect on Re metal.	[4, 15–16, 83, 161]
Re–Au	Au, no binary compounds, Re No diagram plot	Practically, the components are immiscible in the solid and liquid states. The solid solubility of Re in Au at 1000 °C is ~0.1 at.%.	[4, 15, 92]
Group 12			
Re–Zn	Zn, no binary compounds, Re No diagram plot	No interaction; Re is not dissolved and resistant to corrosion in molten Zn (1 h exposure at 520 °C).	[4, 17]
Re–Cd	No data	–	–
Re–Hg	Hg, no binary compounds, Re	At 500 °C the solubility of Re in liquid Hg is $\sim 10^{-5}$ at.%; the solubility of Hg in solid Re is extremely small. No interaction between Re powder and Hg in reductive gas atmosphere at 300 °C.	[4, 13, 16]
Group 13			
Re–B	β-B, $ReB_{2\pm x}$ (or ReB_3, <~2400 °C, congruent melt. point corresp. to ~$ReB_{3.0}$, homog. range—~22–33.5 at.% Re at ~2050 °C, ~27–35 at.% Re at ~1830 °C and ~30–35 at.% Re at 1600 °C), ReB (?), Re_7B_{3+x} (<~2000 °C, incongruent melt. point corresp. to $ReB_{0.43}$, homog. range—~68.5–70 at.% Re at ~1830 °C and ~69.5–70 at.% Re at 1600 °C), $Re_{3\pm x}B$ (<~2150 °C, incongruent melt. point corresp. to $ReB_{0.33}$,	The max. solid solubility of Re in B is <1 at.% (2030–2050 °C) and that of B in Re is <2.5 at.% (2150 °C). Re borides are formed directly from the elements in vacuum at 1400–1900 °C.	[4, 12, 15–16, 93]

(continued)

Table 4.5 (continued)

System	Type of phase diagram (constituent phases, temperatures and compositions of transformations)	Character of interaction	References
	homog. range—~73.5–75.5 at.% Re at ~2000 °C and ~74.5–75.5 at.% Re at 1600 °C), Re Eutectic $ReB_{2\pm x}$–β-B (~2030–2050 °C, ~8–8.5 at.% Re) Eutectic $ReB_{2\pm x}$–Re_7B_{3+x} (~1830 °C, ~58 at.% Re)		
Re–Al	Al, $ReAl_{12}$ (<~600 °C, incongruent melt. point, invariable compos., 7.7 at.% Re), $ReAl_6$ (<~750 °C, incongruent melt. point, invariable compos.), $ReAl_4$ (<~1100 °C, incongruent melt. point, invariable compos.), $ReAl_2$ (<~1460–1510 °C, incongruent melt. point, invariable compos., 33.3 at. Re), ReAl (<~1565–1615 °C, incongruent melt. point, ?), Re_3Al_2 (<~1975–2025 °C, incongruent melt. point, ?), Re	The solid solubility of Re in Al is ~0.25 at.% at 600 °C and ~0.2 at.% at 500 °C. The solubility of Al in Re is ~2.8 at.% at 1900–2000 °C; it declines with temp. decreasing. Practically, Re is not dissolved in molten Al and reacts with it slightly. Re aluminides are formed from powders in inert gas atmosphere at temp. >800 °C.	[4, 15–16, 94–98, 161, 194–195]
Re–Ga	Ga, no binary compounds at normal conditions, Re	No interaction in solid and liquid states at common conditions. The metastable binary compounds were synthesized only under high pressures (7.7 GPa).	[4, 13, 16, 99]
Re–In	In, no binary compounds, Re No diagram plot	The solubility of Re (x, at.%) in liquid In is obeyed the following rule at 330–970 °C: $\lg x = 1.67 - 5340/T$ where T is temp., K.	[175, 180]
Re–Tl	No data	–	–

(continued)

Table 4.5 (continued)

System	Type of phase diagram (constituent phases, temperatures and compositions of transformations)	Character of interaction	References
Group 14			
Re–C	See C–Re in Table 2.13.		
Re–Si	Si, $ReSi_2$ (or $ReSi_{1.8}$, $<\sim$1930–1980 °C, congruent melt. point, invariable compos.), ReSi (from 1650 °C to $\sim$1820–1880 °C (?), incongruent melt. point corresp. to $\sim ReSi_{1.0}$, invariable compos.), Re_5Si_3 (<1020 °C, ?), Re_2Si (or $Re_{17}Si_9$, $<\sim$1810–1960 °C, congruent melt. point corresp. to $ReSi_{0.5}$, invariable compos., 33.3 at.% Re), Re_3Si (?), Re Eutectic $ReSi_2$–Si ($\sim$1125–1380 °C, $\sim$10 at.% Re) Eutectic Re_2Si–ReSi ($\sim$1770–1820 °C, $\sim$53–61 at.% Re) Eutectic Re_2Si–Re ($\sim$1710–1900 °C, $\sim$67–74 at.% Re)	The solid solubility of Re in Si is low. The data on solid solubility of Si in Re available in the literature are controversial. Re silicides are synthesized directly from the elements in vacuum or inert gas atmosphere at 1400–1500 °C.	[4, 12, 16–17, 100–102, 197]
Re–Ge	Ge, $ReGe_2$ ($<\sim$1130 °C, incongruent melt. point, metastable, ?), Re_3Ge_7 ($<\sim$1130 °C, incongruent melt. point, invariable compos.), Re Eutectic Re_3Ge_7 (or $ReGe_2$, ?)–Ge ($\sim$930 °C, $\sim$3–5 at.% Re, ?)	The max. solid solubility of Re in Ge is $\sim$3 at.% (930 °C).	[4, 12–13, 103–105]
Re–Sn	α-Sn, β-Sn, no binary compounds, Re Eutectic (degenerated) Sn–Re ($\sim$230 °C, ?)	No interaction. Practically, Re is not dissolved in molten Sn and the components are immiscible in the solid and liquid states. Molten Sn has no effect on Re metal.	[4, 16–17, 161, 181]
Re–Pb	No data	–	–

(continued)

Table 4.5 (continued)

System	Type of phase diagram (constituent phases, temperatures and compositions of transformations)	Character of interaction	References
Group 15			
Re–N	N, $ReN_{2\pm x}$ (<280 °C, homog. range—wide, unstable, ?), $Re_{2+x}N$ (or $ReN_{0.43}$, <280 °C), $Re_{3\pm x}N$ (<280 °C, homog. range—wide, unstable, ?), Re No diagram plot	The solubility of N in Re in the range of temp. 2000–2750 °C is $(0.6 \div 1.5) \times 10^{-3}$ at.% at pressure 0.1 MPa. Re does not interact with N_2 at temp. ≤900 °C. The Re nitrides are synthesized by the decomposition of NH_4ReO_4 at 270–450 °C or by interaction with NH_3 at temp. ≥600 °C. For the most part, the Re nitrides are not stable at higher temp., decomposing rapidly, in vacuum and under lower pressures especially.	[4, 12, 14, 106–107]
Re–P	P, ReP_4, ReP_3, Re_2P_5, ReP_2 (or Re_6P_{13}, $Re_{12}P_{26}$, ?), Re_3P_4, ReP, Re_2P, Re No diagram plot	Re phosphides are formed directly from the elements at temp. ≥800 °C.	[12, 14, 108]
Re–As	As, Re_3As_7 (or $ReAs_{2.3}$, invariable compos.), Re No diagram plot	Re interacts with As vapour at elevated temp.	[12, 15, 108–109]
Re–Sb	Sb, no binary compounds, Re	No interaction. No solubility of the components in the solid state.	[16]
Re–Bi	Bi, no binary compounds, Re	No interaction; Re is not dissolved and resistant to corrosion in molten Bi (24 d exposure at 800 °C).	[16, 182]
Group 16			
Re–O	O, ReO_4 (?), Re_2O_7 (<297–303 °C, melt. point), Re_3O_{10} (or $Re_2O_7{\cdot}ReO_3$, ?), ReO_3 (<300 °C), $Re_2O_{5\pm x}$ (or $Re_{1+x}O_3$, $0.14 \le x \le 0.21$, ?), Re_7O_{18} (or $3Re_2O_5{\cdot}ReO_3$), α-ReO_{2+x} (<300 °C), β-ReO_{2+x} (300–1050 °C), Re_2O_3 (?), ReO (?), Re_2O (?), Re Eutectic Re_2O_7–ReO_3 (~300 °C, ~22.2–22.5 at.% Re) No complete diagram plot	The max. solubility of O in Re is ~0.2 at.%. In O_2 the oxidation of Re initiates from the temp. ≥150 °C and leads to the direct formation of Re_2O_7. All other oxides are formed indirectly. ReO_3 is prepared by the reduction of Re_2O_7, ReO_2—by the decomposition of ReO_3, $Re_2O_{5\pm x}$—at high pressures.	[4, 12, 14, 108, 110–114, 126, 176]

(continued)

Table 4.5 (continued)

System	Type of phase diagram (constituent phases, temperatures and compositions of transformations)	Character of interaction	References
Re–S	α-S, β-S, Re_2S_7 (metastable, ?), ReS_3 (<800 °C), Re_2S_5, ReS_2, Re_2S_3, ReS, Re No diagram plot	ReS_2 is formed by the direct interaction of Re powder with S vapour at 700–800 °C.	[4, 12, 17, 108, 115–116]
Re–Se	Se, Re_2Se_7 (<330 °C), $ReSe_2$, Re No diagram plot	$ReSe_2$ is formed by the direct interaction of Re with Se in vacuum at 700 °C.	[4, 12, 17, 108, 121]
Re–Te	Te, Re_2Te_7 (<1000 °C, congruent melt. point, ?), $Re_2Te_{5\pm x}$ (<970 °C, incongruent melt. point, ?), β-$ReTe_{2+x}$ (<935–1200 °C (?), congruent melt. point corresp. to ~$ReTe_{2.4}$, homog. range—~25.5–35 at.% Re at 850–870 °C and ~27–35 at.% Re at 430 °C), α-$ReTe_{1-x}$ (or $Re_5Te_{4\pm x}$, <900 °C, congruent melt. point corresp. to ~$ReTe_{0.8}$, homog. range—~50–56.5 at.% Re at 850 °C and ~53–57 at.% Re at 200 °C), Re_2Te (<~1200 °C, incongruent melt. point, invariable compos.), Re Eutectic β-$ReTe_{2+x}$ (or Re_2Te_7, ?)–Te (~430–448 °C, ~2–7 at.% Re, ?) Eutectic Re_2Te_7–$Re_2Te_{5\pm x}$ (910 °C, 25 at.% Re, ?) Eutectic β-$ReTe_{2+x}$–α-$ReTe_{1-x}$ (~850 °C, 40 at.% Re) Eutectic Re_2Te–α-$ReTe_{1-x}$ (~850 °C, 60 at.% Re) Miscibility gap in liquid state (>870 °C, 3–20 at.% Re) Data on the system available in literature are controversial	Re tellurides are synthesized directly from the elements.	[12, 16–17, 117, 122]
Re–Po	No data	–	–
Group 17			
Re–F	F, ReF_7 (<48 °C, melt. point), α-ReF_6 (?), β-ReF_6 (<19 °C, melt. point), ReF_5 (<48 °C, melt. point), ReF_4 (<125 °C, melt. point), Re No diagram plot	The direct interaction between Re and F_2 results in the formation of ReF_4, ReF_6 and ReF_7. ReF_5 is synthesized by indirect chemical reaction pathways.	[2–4, 12, 108, 115, 183]

(continued)

Table 4.5 (continued)

System	Type of phase diagram (constituent phases, temperatures and compositions of transformations)	Character of interaction	References
Re–Cl	Cl, $ReCl_6$ (<~22 °C, melt. point), $ReCl_5$ (<~260–280 °C, congruent melt. point, invariable compos.), α-$ReCl_4$ (?), β-$ReCl_4$ (<350 °C, incongruent melt. point, invariable compos.), $ReCl_3$ (or Re_xCl_{3x} ($x = 3$), <660–725 °C, congruent melt. point), $ReCl_2$ (?), Re	At 200–600 °C the direct interaction between Re and Cl_2 results in the formation of $ReCl_6$ and $ReCl_5$; at higher temp. $ReCl_5$ decomposes to $ReCl_3$. $ReCl_4$ is synthesized by special chemical reaction pathways.	[2–4, 12–13, 108, 115, 188]
Re–Br	Br, $ReBr_5$, $ReBr_4$, $ReBr_3$ (or Re_xBr_{3x} ($x = 3$), <627 °C, melt. point), Re No diagram plot	The direct interaction between the elements results in the formation of $ReBr_3$ at 450 °C, and $ReBr_4$ and $ReBr_5$ at 650 °C.	[2–4, 12]
Re–I	I, ReI_4, ReI_3 (or Re_xI_{3x}, $x = 3$), ReI_2, ReI, Re No diagram plot	The direct interaction between Re and I_2 results in the formation of ReI_4. Other Re iodides are synthesized indirectly.	[2–4, 12]
Re–At	No data	–	–

[a] The intervals of temperatures and compositions for the melting and invariant equilibria points, homogeneity ranges and thermal stability regions of constituent phases are given taking into account the minimal and maximal values (data spread) available in literature

The data on the selected ternary, quaternary and quasi-binary rhenium containing systems, which are the most important for the design, manufacture and application of ultra-high temperature materials, are summarized in Table 4.6. The composition and temperature stability regions for the main binary and ternary rhenium containing high-temperature phases are given in Tables 4.5 and 4.6 taking into account the spread of numerical magnitudes available in the literature currently.

Table 4.6 Chemical interaction of rhenium with elements and compounds at high temperatures (selected ternary, quaternary and quasi-binary systems in alphabetical order)[a]

System	Type of phase diagram (temperature and composition sections, constituent phases or phase fields) and/or character of interphase interaction and materials compatibility	References
Re–B–Ce	Plotted at 600 and 800 °C: $CeReB_4$, $Ce_2Re_3B_6$, $Ce_8Re_{13-x}B_{12}$, $CeRe_4B_4$, $Ce_5Re_2B_6$, $CeB_{6\pm x}$ (<2550 °C), CeB_4 (<2380 °C), $ReB_{2\pm x}$, Re_7B_{3+x}, $Re_{3\pm x}B$, β-B, α-Ce, β-Ce, γ-Ce, δ-Ce, Re No solid solutions based on binary and ternary compounds. At 1800 °C the interaction between Re and $CeB_{6\pm x}$ leads to the formation of $ReB_{2\pm x}$ and dissolution of Re in $CeB_{6\pm x}$.	[21–22, 136, 140, 153–154, 162]

(continued)

Table 4.6 (continued)

System	Type of phase diagram (temperature and composition sections, constituent phases or phase fields) and/or character of interphase interaction and materials compatibility	References
Re–B–Cr	Plotted at 1400 °C: $CrRe_3B_{4-x}$ (or $Cr_{0.25}Re_{0.75}B_{1-x}$, <1400 °C), $Cr_{3+y}Re_{2-y}B_5$ (at least at 1400 °C), $(Cr,Re)_{2\pm x}B$ (highly extended solid solution based on $Cr_{2\pm x}B$—up to $(Cr_{0.25}Re_{0.75})_{2\pm x}B$, <1850–1870 °C), $(Re,Cr)_{3\pm x}B$ (extended solid solution based on $Re_{3\pm x}B$—up to $(Re_{0.87}Cr_{0.13})_{3\pm x}B$), $(Cr,Re)B_{1-x}$ (solid solution based on CrB_{1-x}, <2095–2100 °C), $(Re,Cr)_7B_{3+x}$ (solid solution based on Re_7B_{3+x}), Cr_5B_{3-x} (<~1900 °C), $Cr_3B_{4\pm x}$ (<2070–2075 °C), $CrB_{2\pm x}$ (<2200 °C), CrB_4 (or CrB_6 (?), <~1450–1500 °C), $ReB_{2\pm x}$, β-B, Cr, Re	[134, 142]
Re–B–Dy	Plotted at 1000 °C: $DyReB_4$, Dy_3ReB_7, Dy_2ReB_6, $DyRe_4B_4$, $DyRe_{11}B$ (?), DyB_2 (<2100 °C), DyB_4 (<2500 °C), $DyB_{6\pm x}$ (<2200 °C), DyB_{12} (<2100 °C), DyB_{66} (<2025 °C), $ReB_{2\pm x}$, Re_7B_{3+x}, $Re_{3\pm x}B$, $DyRe_2$, β-B, α-Dy, β-Dy, Re No solid solutions based on binary and ternary compounds.	[139, 142, 155, 162]
Re–B–Er	No diagram plot $ErReB_4$, Er_3ReB_7, Er_2ReB_6, $ErRe_4B_4$	[139, 142, 162]
Re–B–Fe–Y	No diagram plot $Y_2Fe_{14-x}Re_xB$	[152]
Re–B–Gd	Plotted at 1000 °C: $GdRe_4B_4$, $Gd_2Re_3B_6$, Gd_3ReB_7, $GdReB_4$, Gd_2ReB_6, $Gd_8Re_{13-x}B_{12}$, ~GdReB (?), GdB_{66} (<2150 °C), $GdB_{6\pm x}$ (<2510 °C), GdB_4 (<~2650 °C), Gd_2B_5 (<2100 °C), GdB_2 (<~2050 °C), $GdRe_2$, $ReB_{2\pm x}$, Re_7B_{3+x}, $Re_{3\pm x}B$, β-B, α-Gd, β-Gd, Re No solid solutions based on binary and ternary compounds.	[136–137, 139–140, 142, 162]
Re–B–Hf	Plotted at 1500 °C: Hf_9Re_4B, $HfRe_{14}B_5$ (or $Hf_{0.2}Re_{2.8}B$, ?), $HfRe_{13}B_6$ (or $Hf_{0.5}Re_{6.5}B_3$, ?), $(Re,Hf)_7B_{3+x}$ (solid solution based on Re_7B_{3+x}—up to ~5 at.% Hf), $(Re,Hf)_{3\pm x}B$ (solid solution based on $Re_{3\pm x}B$—up to ~5 at.% Hf), $HfB_{1\pm x}$ (<2100 °C), $HfB_{2\pm x}$ (<~3250–3410 °C), $ReB_{2\pm x}$, $HfRe_{1\pm x}$, λ-$HfRe_{2\pm x}$, χ-$Hf_5Re_{24\pm x}$, α-Hf, β-Hf, β-B, Re $HfB_{2\pm x}$–Re is plotted: eutectic—2110–2170 °C, ~80 mol. % Re; at the eutectic temp. the solubility of Re in $HfB_{2\pm x}$ and that of $HfB_{2\pm x}$ in Re are low At 1500 °C, metal Re and all its binary compounds (borides and intermetallides) are in equilibrium with $HfB_{2\pm x}$.	[23, 124, 142–143]

(continued)

Table 4.6 (continued)

System	Type of phase diagram (temperature and composition sections, constituent phases or phase fields) and/or character of interphase interaction and materials compatibility	References
Re–B–Ho	Plotted at 800 °C: $HoReB_4$, Ho_3ReB_7, Ho_2ReB_6, $HoRe_4B_4$, HoB_2 (<2200 °C), HoB_4 (<2500 °C), $HoB_{6\pm x}$ (<2180 °C), HoB_{12} (<2100 °C), HoB_{66} (<2025 °C), $ReB_{2\pm x}$, Re_7B_{3+x}, $Re_{3\pm x}B$, $HoRe_2$ β-B, Ho, Re No solid solutions based on binary and ternary compounds.	[139, 142, 153, 162]
Re–B–La	Plotted at 600 and 800 °C: $LaRe_4B_4$, $La_3Re_3B_4$, $\sim La_2Re_3B_{6\div 7}$, $LaB_{6\pm x}$ (<~2500–2715 °C), LaB_4 (<1800 °C), $ReB_{2\pm x}$, Re_7B_{3+x}, $Re_{3\pm x}B$, β-B, α-La, β-La, γ-La, Re No solid solutions based on binary and ternary compounds. At 1800 °C the interaction between Re and $LaB_{6\pm x}$ leads to the formation of $ReB_{2\pm x}$ and dissolution of Re in $LaB_{6\pm x}$.	[21–22, 136, 151, 162]
Re–B–Lu	No diagram plot Lu_2ReB_6	[137, 142, 162]
Re–B–Mo	No diagram plot MoReB, $Mo_{\sim 4.5}Re_{\sim 15.5}B_{\sim 2.2}$ (or Mo_2Re_3B, ?)	[128, 142]
Re–B–N	Plotted at 1200 °C (Ar pressure 0.1 MPa): $ReB_{2\pm x}$, Re_7B_{3+x}, $Re_{3\pm x}B$, α-BN, N, β-B, Re The mutual solubilities of the components are negligible. Re is in equilibrium with α-BN.	[25]
Re–B–Nb	Plotted at 1400 °C: $Nb_3Re_3B_4$ (or $Nb_{1.5}Re_{1.5}B_2$), $NbRe_{14}B_5$ (or $Nb_{0.2}Re_{2.8}B$), $NbRe_{13}B_6$ (or $Nb_{0.5}Re_{6.5}B_3$), Nb_8ReB_{12} (or $Nb_{2.65}Re_{0.35}B_4$), Nb_9ReB_{10} (or $Nb_{0.9}Re_{0.1}B$), Nb_3B_2 (<~1800–2230 °C), $NbB_{1\pm x}$ (<~2270–2915 °C), Nb_5B_6 (<~2295–2870 °C, ?), Nb_3B_4 (<~2700–2935 °C), $NbB_{2\pm x}$ (<~3000–3035 °C), $ReB_{2\pm x}$, Re_7B_{3+x}, $Re_{3\pm x}B$, σ-Nb_2Re_{3-x}, χ-$NbRe_{3\pm x}$ β-B, Nb, Re At 2250 °C the contact interaction between compact metal Re and NbB_{2+x} leads to the formation of $(Nb,Re)B_{2+x}$ (1 h exposure).	[21, 23, 142]
Re–B–Nd	Plotted at 600 and 800 °C: $Nd_8Re_{13-x}B_{12}$ ($x \approx 0.1$), $NdRe_4B_4$, $Nd_5Re_2B_6$, $Nd_2Re_3B_6$, Nd_2B_5 (<~2000 °C), NdB_4 (<~2350 °C), $NdB_{6\pm x}$ (<2610 °C), NdB_{66} (<2150 °C), $ReB_{2\pm x}$, Re_7B_{3+x}, $Re_{3\pm x}B$, α-Nd, β-Nd, β-B, Re No solid solutions based on binary and ternary compounds.	[136, 162]

(continued)

Table 4.6 (continued)

System	Type of phase diagram (temperature and composition sections, constituent phases or phase fields) and/or character of interphase interaction and materials compatibility	References
Re–B–Pr	Plotted at 600 and 800 °C: $Pr_2Re_3B_6$, Pr_3ReB_6, $Pr_8Re_{13-x}B_{12}$ ($x \approx 0.38$), $Pr_7(Re_4B_4)_6$, Pr_2B_5 (or PrB_x, $x \approx 2.5$–2.6, <~2000 °C), PrB_4 (<~2350 °C), $PrB_{6\pm x}$ (<2610 °C), $ReB_{2\pm x}$, Re_7B_{3+x}, $Re_{3\pm x}B$, β-B, α-Pr, β-Pr, Re No solid solutions based on binary and ternary compounds.	[136–137, 140–141, 162]
Re–B–Sc	Plotted at 1000 °C: Sc_2ReB_6, $(Sc,Re)B_2$ (extended solid solution based on ScB_2—up to compos. ~$(Sc_{0.8}Re_{0.2})B_2$, <2250 °C), ScB_{12} (<2040 °C), $ScRe_2$, Sc_5Re_{24}, $ReB_{2\pm x}$, Re_7B_{3+x}, $Re_{3\pm x}B$, β-B, α-Sc, β-Sc, Re No solid solutions based on binary compounds apart from $(Sc,Re)B_2$.	[15–16, 129, 162]
Re–B–Sm	Plotted at 1000 °C: $SmRe_4B_4$, $SmReB_4$, $Sm_2Re_3B_6$, $SmReB_2$ (?), $Sm_3Re_5B_2$ (?), Sm_2B_5 (<~2000 °C), SmB_4 (<~2400 °C), $SmB_{6\pm x}$ (<2580 °C), SmB_{66} (<2150 °C), $ReB_{2\pm x}$, Re_7B_{3+x}, $Re_{3\pm x}B$, $SmRe_2$, α-Sm, β-Sm, γ-Sm, β-B, Re No solid solutions based on binary and ternary compounds.	[136–137, 140, 157, 162]
Re–B–Ta	Plotted at 1400 °C: $Ta_3Re_3B_4$ (or $Ta_{1.5}Re_{1.5}B_2$), $TaRe_6B_3$ (or $Ta_{1.2}Re_{5.8}B_3$, ?), $Ta_2Re_{11}B_{26}$ (or $Ta_{0.15}Re_{0.85}B_2$, ?), $TaRe_{14}B_5$ (or $Ta_{0.2}Re_{2.8}B$, ?), $Ta_{2+x}B$ (~1900–2420 °C), $Ta_3B_{2\pm x}$ (<2180 °C), λ-$TaB_{1\pm x}$ (<3090 °C), $Ta_3B_{4\pm x}$ (<3030 °C), $TaB_{2\pm x}$ (<~3040 °C), $ReB_{2\pm x}$, Re_7B_{3+x}, $Re_{3\pm x}B$, σ-Ta_2Re_{3-x}, χ-$TaRe_{3\pm x}$, β-B, Ta, Re At 2350 °C, the contact interaction between bulk dense Re and $TaB_{2\pm x}$ leads to the formation of $(Re,Ta)B_{2\pm x}$ (?) (1 h exposure).	[21, 145]
Re–B–Tb	Plotted at 1000 °C: $TbReB_4$, Tb_3ReB_7, $Tb_{11}Re_{36}B_{36}$, Tb_2ReB_6, $Tb_8Re_{13-x}B_{12}$ ($x = 0.04$), TbB_2 (<~2100 °C), TbB_4 (<~2600 °C), $TbB_{6\pm x}$ (<2340 °C), TbB_{12} (<2200 °C), TbB_{66} (<~2100 °C), $ReB_{2\pm x}$, Re_7B_{3+x}, $Re_{3\pm x}B$, $TbRe_2$, β-B, α-Tb, β-Tb, Re No solid solutions based on binary and ternary compounds.	[137, 139, 142, 157, 162]
Re–B–Th	No diagram plot $ThReB_4$	[142, 146]
Re–B–Ti	Plotted at 1400 °C: Ti_2ReB_2, TiB_{1-x} (<~2180–2200 °C), Ti_3B_4 (<~2200–2205 °C), $TiB_{2\pm x}$ (<3200–3250 °C), $ReB_{2\pm x}$, Re_7B_{3+x}, $Re_{3\pm x}B$, χ-Ti_5Re_{24}, α-Ti, β-Ti, β-B, Re $TiB_{2\pm x}$–Re is plotted: eutectic—2180–2280 °C, ~53–55 mol. % Re At 1900–2200 °C the interaction between Re and $TiB_{2\pm x}$ leads to the formation of Re_7B_{3+x} and TiB_{1-x} (2 h exposure).	[21, 27, 123–124, 142, 144, 149]

(continued)

Table 4.6 (continued)

System	Type of phase diagram (temperature and composition sections, constituent phases or phase fields) and/or character of interphase interaction and materials compatibility	References
Re–B–Tm	No diagram plot $TmReB_4$, Tm_3ReB_7, Tm_2ReB_6, $TmRe_4B_4$	[137, 139, 142, 162]
Re–B–U	Plotted at 800 °C: $UReB_3$, $UReB_4$, U_2ReB_6, UB_{12} (<2145 °C), UB_4 (<2495 °C), UB_2 (<2385 °C), $ReB_{2\pm x}$, Re_7B_{3+x}, $Re_{3\pm x}B$, U_2Re, α-URe_2, β-URe_2, β-B, α-U, β-U, γ-U, Re No solid solutions based on binary and ternary compounds. At 800 °C Re is in equilibrium with UB_2.	[142, 147, 150]
Re–B–W	See W–B–Re in Table 3.6.	
Re–B–Y	Plotted at 1000 °C: $YReB_4$, Y_2ReB_6, Y_3ReB_7, YRe_4B_4, ~$YRe_{11}B$ (?), YB_4 (<~2610–2800 °C), $YB_{6\pm x}$ (<~2600–2780 °C), YB_{12} (<2200 °C), YB_{66} (<2100 °C), $ReB_{2\pm x}$, Re_7B_{3+x}, $Re_{3\pm x}B$, YRe_2, β-B, α-Y, β-Y, Re No solid solutions based on binary and ternary compounds.	[20, 136, 139, 142, 151, 162]
Re–B–Yb	No diagram plot $YbReB_4$	[137, 162]
Re–B–Zr	Plotted at 1500 °C: Zr_9Re_4B (?), $ZrB_{2\pm x}$ (<3220–3265 °C), ZrB_{12-x} (~1695–2290 °C), $ReB_{2\pm x}$, Re_7B_{3+x}, $Re_{3\pm x}B$, σ-Zr_2Re, λ-$ZrRe_{2-x}$, χ-Zr_5Re_{24+x}, α-Zr, β-Zr, β-B, Re $ZrB_{2\pm x}$–Re is plotted: eutectic—2060–2150 °C, ~70–71 mol. % Re; the mutual solubilities of the components are low At 1500 °C metal Re and all its binary compounds (borides and intermetallides) are in equilibrium with $ZrB_{2\pm x}$. At 1950–2200 °C the interaction between Re and $ZrB_{2\pm x}$ leads to the formation of Re_7B_{3+x} (2 h exposure).	[21, 27–28, 125, 138, 142, 158]
Re–C–Co–W	See C–Co–Re–W in Table 2.14.	
Re–C–Cr	See C–Cr–Re in Table 2.14.	
Re–C–Cr–Mo–Ti	See C–Cr–Mo–Re–Ti in Table 2.14.	
Re–C–Cr–Ti	See C–Cr–Re–Ti in Table 2.14.	
Re–C–Hf	See C–Hf–Re in Table 2.14.	
Re–C–Mo	See C–Mo–Re in Table 2.14.	
Re–C–Nb	See C–Nb–Re in Table 2.14.	
Re–C–Si	See C–Re–Si in Table 2.14.	
Re–C–Ta	See C–Re–Ta in Table 2.14.	
Re–C–Tc	See C–Re–Tc in Table 2.14.	
Re–C–Th	See C–Re–Th in Table 2.14.	
Re–C–Ti	See C–Re–Ti in Table 2.14.	
Re–C–U	See C–Re–U in Table 2.14.	
Re–C–U–Zr	See C–Re–U–Zr in Table 2.14.	

(continued)

Table 4.6 (continued)

System	Type of phase diagram (temperature and composition sections, constituent phases or phase fields) and/or character of interphase interaction and materials compatibility	References
Re–C–V	See C–Re–V in Table 2.14.	
Re–C–W	See C–Re–W in Table 2.14.	
Re–C–Y	See C–Re–Y in Table 2.14.	
Re–C–Zr	See C–Re–Zr in Table 2.14.	
Re–Ca–O	No diagram plot $Ca_5Re_2O_{12}$ (or $5CaO{\cdot}Re_2O_7$), $Ca_{11}Re_4O_{24}$ (or $11CaO{\cdot}Re_2O_7{\cdot}2ReO_3$), $Ca_5Re_3O_{15-x}$ ($x = 0.25$, or $Ca_5Re_3O_{14.75}$, $20CaO{\cdot}3Re_2O_7{\cdot}6ReO_3$), Ca_3ReO_6 (or $3CaO{\cdot}ReO_3$)	[163–167]
Re–Ce–O	No diagram plot $Ce_4Re_6O_{19}$ (or $2Ce_2O_3{\cdot}Re_2O_5{\cdot}4ReO_2$)	[173–174]
Re–Co–Os–Ru	(Re,Os,Ru,ε-Co) continuous solid solution, α-Co, (Re,Os,Ru)	[41]
Re–Cr–Nb	No diagram plot λ_2-$Nb(Cr_{1-x}Re_x)_2$ ($0.075 \le x \le 0.5$, ternary Laves phase)	[133]
Re–Cr–W	See W–Cr–Re in Table 3.6.	
Re–Hf–N	No diagram plot At 2500 °C bulk dense Re and $HfN_{1\pm x}$ are compatible with each other (1 h exposure).	[21]
Re–Hf–O	No diagram plot In vacuum, at 2400 °C the interaction between dense metal Re and γ-HfO_{2-x} is weak.	[26]
Re–Hf–Mo–O	No diagram plot In vacuum, at 2400 °C the interaction between Re–Mo alloys and γ-HfO_{2-x} is weak.	[26]
Re–Mo–N	No diagram plot Mo_7ReN (or $Mo_{1.76}Re_{0.24}N$, solid solution based on γ-$Mo_{2\pm x}N$)	[24]
Re–Mo–Nb	Plotted at 1700 °C: σ-$(Mo,Nb)_2Re_{3\pm x}$ (σ-Nb_2Re_{3-x} –σ-$Mo_2Re_{3\pm x}$ continuous solid solution, ?), χ-$(Mo,Nb)Re_{3\pm x}$ (χ-$NbRe_{3\pm x}$–χ-$MoRe_{3+x}$ continuous solid solution, ?), Re, (Mo,Nb)	[14, 16, 130, 177]
Re–Mo–Ni	Plotted at 1150 °C: $\sim(Re_{1-y}Mo_y)_2Ni_{1\pm x}$ (or P-phase, $0.3 \le y \le 0.85$), δ-$(Mo,Re)Ni_{1\pm x}$ (<1365 °C, extended solid solution based on δ-$MoNi_{1\pm x}$—up to compos. δ-$(Mo_{0.4}Re_{0.6})Ni_{1\pm x}$), σ-$(Mo,Ni)_2(Re,Ni)_{3\pm x}$ (extended solid solution based on σ-$Mo_2Re_{3\pm x}$—up to 23 at.% Ni), χ-$Mo(Re,Ni)_{3+x}$ (extended solid solution based on χ-$MoRe_{3+x}$—up to 12 at.% Ni), γ-Ni_3Mo (<905–915 °C), β-Ni_4Mo (<865–875 °C), Ni, Mo, Re Re noticeably stabilizes δ-$MoNi_{1\pm x}$ and increases its homog. range.	[120, 192]

(continued)

Table 4.6 (continued)

System	Type of phase diagram (temperature and composition sections, constituent phases or phase fields) and/or character of interphase interaction and materials compatibility	References
Re–Mo–O	Plotted partly at 700 and 1000 °C: $(Re_{1-y}Mo_y)O_2$ ($0 < y < 0.37$, extended solid solution based on ReO_2), $(Mo_{1-y}Re_y)O_2$ ($0 < y < 0.42$, extended solid solution based on MoO_2, $<\sim$2125–2325 °C), γ-$(Mo_{1-y}Re_y)_4O_{11}$ ($0 < y < \sim 0.11 \div 0.25$, extended solid solution based on γ-Mo_4O_{11}, $<\sim$550–650 °C), η-$(Mo_{1-y}Re_y)_4O_{11}$ ($0 < y < \sim 0.11 \div 0.25$, extended solid solution based on η-Mo_4O_{11}, from $\sim$550–650 to $\sim$810–825 °C), $(Mo,Re)_8O_{23}$($<\sim$780 °C), Mo_9O_{26} (or Mo_9O_{24}, $<\sim$780 °C), MoO_3 ($<\sim$775–790 °C), ReO_3, O, Mo, Re	[14, 16, 127, 132]
Re–Mo–Si	No diagram plot $ReSi_2$–α-$MoSi_2$ continuous solid solution at 1400 °C.	[21, 29]
Re–Mo–Si–W	See W–Mo–Re–Si in Table 3.6.	
Re–Mo–Ta	Plotted at 2300 °C: (Re,Mo,Ta) (extended solid solution based on Mo–Ta continuous solid solution with homog. range $\sim$Mo–$Mo_{0.6}Re_{0.4}$–$Ta_{0.55}Re_{0.45}$–Ta), σ-$Mo_2Re_{3\pm x}Ta_y$ (extended solid solution based on σ-$Mo_2Re_{3\pm x}$—up to $\sim$40 at.% Ta), χ-$TaRe_{3\pm x}Mo_y$ (extended solid solution based on χ-$TaRe_{3\pm x}$—up to $\sim$20 at.% Mo), Re	[185]
Re–Mo–V	Plotted at 1825 °C: σ-$(Mo,V)Re_{3\pm x}$ (σ-$Mo_2Re_{3\pm x}$ –σ-VRe_{3+x} continuous solid solution, ?), χ-$(Mo,V)Re_{3+x}$ (extended solid solution based on χ-$MoRe_{3+x}$), δ-$(V,Mo)_3Re_{7\pm x}$ (solid solution based on δ-$V_3Re_{7\pm x}$), Re, (Mo,V)	[14, 16–17, 130]
Re–Mo–W	See W–Mo–Re in Table 3.6.	
Re–N–Si	Plotted at 1200 and 1400 °C (under Ar pressure): $ReSi_2$, ReSi, Re_2Si, Si_3N_4 ($<\sim$1900 °C), N, Si, Re At 1200 °C Re, $ReSi_2$ and Re_2Si are in equilibrium with Si_3N_4, and at 1400 °C $ReSi_2$ and Re_2Si are in equilibrium with Si_3N_4	[25, 131]
Re–N–Zr	No general diagram plot Zr_4Re_2N $ZrN_{1\pm x}$–Re is plotted: eutectic—$\sim$2460 °C	[24, 138]
Re–Nb–Ni	Plotted at 1150 °C: $\sim$Nb(Ni,Re)$_{1-x}$ (or $Nb_7(Ni,Re)_6$, $<\sim$1290 °C, extended solid solution based on $NbNi_{1-x}$—up to 15 at.% Re), χ-$Nb(Re,Ni)_{4\pm x}$ (extended solid solution based on χ-$NbRe_{3\pm x}$—up to 10 at.% Ni), κ-$Ni_{3\pm x}Nb$ (<1400 °C, solid solution with max. Re content – 2 at.%), ζ-$Ni_{8\pm x}Nb$ (<535 °C), σ-Nb_2Re_{3-x}, Ni, Nb, Re	[120, 193]

(continued)

Table 4.6 (continued)

System	Type of phase diagram (temperature and composition sections, constituent phases or phase fields) and/or character of interphase interaction and materials compatibility	References
Re–Nb–Ta	Plotted at 1700 °C: χ-(Ta,Nb)$Re_{3\pm x}$ (χ-$NbRe_{3\pm x}$ –χ-$TaRe_{3\pm x}$ continuous solid solution), (Ta,Nb,Re) (extended solid solution based on Ta–Nb continuous solid solution with homog. range ~Ta–$Re_{0.45}Ta_{0.55}$–$Re_{0.32}Nb_{0.45}Ta_{0.23}$–$Re_{0.45}Nb_{0.55}$–Nb), Re	[186]
Re–Nb–V	Plotted at 1825 °C: χ-(Nb,V)$Re_{3\pm x}$ (extended solid solution based on χ-$NbRe_{3\pm x}$), δ-$(V,Nb)_3Re_{7\pm x}$ (solid solution based on δ-$V_3Re_{7\pm x}$), σ-VRe_{3+x}, σ-Nb_2Re_{3-x}, Re, (Nb,V)	[14, 16–17, 130]
Re–Nb–W	See W–Nb–Re in Table 3.6.	
Re–Ni–Ta	Plotted at 1150 °C: ~$Ta(Ni,Re)_{1-x}$ (extended solid solution based on μ-$Ni_{1-x}Ta$—up to 15 at.% Re, <1570 °C), ~Ta_{2+x}(Ni,Re) (extended solid solution based on $NiTa_{2+x}$—up to 6 at.% Re, <1790 °C,), χ-$Ta(Re,Ni)_{4\pm x}$ (extended solid solution based on χ-$TaRe_{4\pm x}$—up to 6 at.% Ni), $Ni_{2\pm x}Ta$ (solid solution with max. Re content—1 at.%, <1405 °C), κ-$Ni_{3\pm x}Ta$ (solid solution with max. Re content—3 at.%, <1550 °C), ζ-$Ni_{8\pm x}Ta$ (<535 °C), σ-Ta_2Re_{3-x}, Ni, Ta, Re	[120]
Re–O–Os	Re_2O_7–OsO_4 is plotted: Re_2O_7, OsO_4; eutectic (degenerated) Re_2O_7–OsO_4—41 °C, very close to the OsO_4 end-member	[126]
Re–O–Sr	No diagram plot $Sr_3Re_2O_{10}$ (or $3SrO{\cdot}Re_2O_7$), α-$Sr_5Re_2O_{12}$ (or $5SrO{\cdot}Re_2O_7$), β-$Sr_5Re_2O_{12}$ (or $5SrO{\cdot}Re_2O_7$), $Sr_{11}Re_4O_{24}$ (or $11SrO{\cdot}Re_2O_7{\cdot}2ReO_3$), $SrReO_4$ (or $SrO{\cdot}ReO_3$), $Sr_3Re_2O_9$ (or $3SrO{\cdot}2ReO_3$), $Sr_7Re_4O_{19}$ (or $7SrO{\cdot}4ReO_3$), $Sr_6Re_{15}O_{45}$ (or $Sr_{1.2}Re_3O_9$, $6SrO{\cdot}3ReO_3{\cdot}6Re_2O_5$), $Sr_2Re_3O_9$ (or $2SrO{\cdot}Re_2O_5{\cdot}ReO_2$)	[165–166, 168–172]
Re–Os–Ru	(Re,Os,Ru) continuous solid solution Complete miscibility in the solid and liquid states.	[41, 118–119]
Re–Os–Ta	Plotted partially at 1000–1500 °C (Ta-rich area: (Ta,Re,Os) solid solution based on Ta)	[184]
Re–Os–W	See W–Os–Re in Table 3.6.	
Re–Si–Ta	No diagram plot ReTaSi (?) At 1150–1370 °C bulk dense Re and $TaSi_2$ are compatible with each other.	[21, 159]
Re–Si–W	See W–Re–Si in Table 3.6.	
Re–Ta–W	See W–Re–Ta in Table 3.6.	
Re–V–W	See W–Re–V in Table 3.6.	

[a] See notes to Table 4.5

The character of chemical interaction and general reactions of rhenium with common chemicals (solids, liquids, aqueous solutions) and complex gases are summarized in Table 4.7.

Table 4.7 The interaction of rhenium with some chemicals and complex gases [4, 10, 12]

Reagent, formula	Character of chemical interaction, examples of general reactions
Air, $N_2 + O_2$	No interaction at room temp. At atmospheric pressure the oxidation of Re initiates at 300–400 °C, the intensive oxidation begins from 500–600 °C: $4Re + 7O_2 \rightarrow 2Re_2O_7$ (sublimates at temp. >350 °C); at various temp. the oxidation rate of Re is characterized by the following values: 700 °C—0.03, 900 °C—3.2, 1200 °C—7.4, 1500 °C—14 g m^{-2} s^{-1} (0.25–1 h exposure). In humid air the interaction results in the formation of volatile $HReO_4$: $4Re + 7O_2 + 2H_2O \rightarrow 4HReO_4$
Water, H_2O	No interaction at the ambient temp. in the absence of O_2, at higher temp. water vapour (without O_2) interacts with Re slightly.
Hydrogen peroxide (20–30 % aqueous solution), H_2O_2	Re interacts with H_2O_2 on heating: $2Re + 7H_2O_2 \rightarrow 2HReO_4 + 6H_2O$
Carbon monoxide, CO	No interaction at temp. ≤1100 °C.
Hydrocarbons, C_mH_n	No interaction at temp. ≤800 °C.
Ammonia (aqueous solution), NH_4OH	Weak interaction
Sodium hydroxide, NaOH	No interaction with NaOH in aqueous solution at room temp., the slow interaction of Re with the aqueous solution initiates only on heating; the intensive interaction occurs between Re and molten NaOH and leads to the formation of Na perrhenate: $4Re + 4NaOH + 7O_2 \rightarrow 4NaReO_4 + 2H_2O$
Potassium hydroxide, KOH	No interaction with KOH in aqueous solution at room temp., the slow interaction of Re with the aqueous solution initiates only on heating; the intensive interaction occurs between Re and molten KOH and leads to the formation of K perrhenate: $4Re + 4KOH + 7O_2 \rightarrow 4KReO_4 + 2H_2O$.
Potassium nitrate with calcium oxide, $KNO_3 + CaO$	At 700–800 °C the interaction results in the formation of perrhenates: $2Re + 7KNO_3 + CaO \rightarrow Ca(ReO_4)_2 + 7KNO_2$
Nitric acid, HNO_3	Re interacts with HNO_3 at room temp.; the interaction is more intensive on heating and leads to the formation of $HReO_4$: $3Re + 7HNO_3 \rightarrow 3HReO_4 + 7NO + 2H_2O$ $Re + 7HNO_3 \rightarrow HReO_4 + 7NO_2 + 3H_2O$
Sulphuric acid, H_2SO_4	Slow interaction with the formation of $HReO_4$: $2Re + 7H_2SO_4 \rightarrow 2HReO_4 + 7SO_2 + 6H_2O$
Hydrochloric acid, HCl	No interaction.
Hydrofluoric acid, HF	No interaction.

The self-diffusion characteristics of rhenium atoms, diffusion characteristics in rhenium—element systems in the wide range of temperatures, and summarized data on the physico-chemical interaction of rhenium with elements of the periodic table are given in Addendum.

References

1. Steurer W (1996) Crystal structure of the metallic elements. In: Cahn RW, Haasen P (eds) Physical metallurgy, 4th ed., Vol. 1, pp. 1–46. Elsevier Science BV, Amsterdam
2. Cotton FA, Wilkinson G (1965) Advanced inorganic chemistry. Wiley, New York, London
3. Akhmetov NS (2001) Obschaya i neorganicheskaya khimiya (General and inorganic chemistry), 4th ed. Vysshaya Shkola, Moscow (in Russian)
4. Kotelnikov RB, Bashlykov SN, Galiakbarov ZG, Kashtanov AI (1968) Osobo tugoplavkie elementy i soedineniya (Extra refractory elements and compounds). Metallurgiya, Moscow (in Russian)
5. Zefirov AP (ed), Veryatin UD, Mashirev VP, Ryabtsev NG, Tarasov VI, Rogozkin BD, Korobov IV (1965) Termodinamicheskie svoistva neorganicheskikh veschestv (Thermodynamic properties of inorganic substances). Atomizdat, Moscow (in Russian)
6. Speight JG, ed (2005) Lange's handbook of chemistry, 16th ed. McGraw-Hill, New York
7. Lide DR, ed (2010) CRC handbook of chemistry and physics, 90th ed. CRC Press, Boca Raton, New York
8. Martienssen W (2005) The elements. In: Martienssen W, Warlimont H (eds) Springer handbook of condensed matter and materials data, pp. 45–158. Springer, Berlin, Heidelberg
9. Samsonov GV, ed (1976) Svoistva elementov (Properties of elements), 2nd ed., Vol. 1. Metallurgiya, Moscow (in Russian)
10. Marmer ÉN, Gurvich OS, Maltseva LF (1967) Vysokotemperaturnye materialy (High-temperature materials). Metallurgiya, Moscow (in Russian)
11. Cardarelli F (2008) Materials handbook, 2nd ed. Springer, London
12. Samsonov GV, ed (1976) Svoistva elementov (Properties of elements), 2nd ed., Vol. 2. Metallurgiya, Moscow (in Russian)
13. Lyakishev NP, ed (1997) Diagrammy sostoyaniya dvoinykh metallicheskikh sistem (Phase diagrams of binary metal systems), Vol. 2. Mashinostroenie, Moscow (in Russian)
14. Lyakishev NP, ed (2001) Diagrammy sostoyaniya dvoinykh metallicheskikh sistem (Phase diagrams of binary metal systems), Vol. 3, Part 1. Mashinostroenie, Moscow (in Russian)
15. Lyakishev NP, ed (1996) Diagrammy sostoyaniya dvoinykh metallicheskikh sistem (Phase diagrams of binary metal systems), Vol. 1. Mashinostroenie, Moscow (in Russian)
16. Massalski TB, Subramanian PR, Okamoto H, Kacprzak L, eds (1990) Binary alloy phase diagrams, 2nd ed. ASM International, Metals Park, Ohio
17. Lyakishev NP, ed (2000) Diagrammy sostoyaniya dvoinykh metallicheskikh sistem (Phase diagrams of binary metal systems), Vol. 3, Part 2. Mashinostroenie, Moscow (in Russian)
18. Savitskii EM, Tylkina MA, Levin AM (1980) Splavy reniya v elektronike (Rhenium alloys in electronics). Energiya, Moscow (in Russian)
19. Savitskii EM, Tylkina MA, Khamidov OKh (1969) Issledovanie rastvorimosti perekhodnykh metallov v renii i nekotorye svoistva splavov (A study of the solubility of transition metals in rhenium and some properties of the alloys). Izv AN SSSR Metally (4):200–208 (in Russian)
20. Kuzma YuB (1983) Kristallokhimiya boridov (The crystal chemistry of borides). Vyshcha Shkola, Lviv (in Russian)
21. Kosolapova TYa, ed (1990) Handbook of high-temperature compounds: properties, production and applications. Hemisphere, New York

22. Bondarenko VP, Morozov VV, Chernyak LV (1971) Reaction of lanthanum and cerium hexaborides with refractory metals. Powder Metall Met Ceram 10(1):57–61
23. Kuzma YuB, Lakh VI, Stadnyk BI, Kovalyk DA (1970) Systems hafnium-tungsten-boron, hafnium-rhenium-boron and niobium-rhenium-boron. Powder Metall Met Ceram 9(12):1003–1006
24. Holleck H (1984) Binäre und ternäre Carbid- und Nitridsysteme der Ubergangsmetalle (Binary and ternary carbide and nitride systems of the transition metals). Gebrüder Borntträeger, Berlin (in German)
25. Rogl P, Schuster JC (1992) Phase diagrams of ternary boron nitride and silicon nitride systems. ASM International, Materials Park, Ohio
26. Samsonov GV, ed (1978) Fiziko-khimicheskie svoistva okislov (Physico-chemical properties of oxides), 2nd ed. Metallurgiya, Moscow (in Russian)
27. Samsonov GV, Vinitskii IM (1980) Handbook on refractory compounds. IFI/Plenum, New York
28. Kosterova NV, Ordanyan SS, Neshpor VS, Ostrovskii EK (1980) Thermionic emission properties of cermets of eutectic compositions in Me^{IV}–(C, B)–(Mo, Re, W) systems. Powder Metall Met Ceram 19(1):61–66
29. Verkhoglyadova TS, Vivchar OI, Gladyshevskii EI (1966) Solubility of the disilicides of the transition metals in $MoSi_2$ and WSi_2. Powder Metall Met Ceram 5(4):316–319
30. Finkel VA, Palatnik MI, Kovtun GB (1972) X-ray diffraction study of the thermal expansion of Ru, Os and Re at 77–300 K. Z Metallkd 63:12–16
31. Savitskii EM, Chuprikov GE (1962) Vliyanie kisloroda na mekhanicheskie i elektricheskie svoistva metallicheskogo reniya (The effect of oxygen on the mechanical and electrical properties of metal rhenium). Izv AN SSSR OTN Metallurgiya Toplivo (4):137–142 (in Russian)
32. Fomenko VS, Podchernyaeva IA (1975) Emissionnye i adsorbtsionnye svoistva veschestv i materialov (The thermoionic emission and absorptance properties of substances and materials). Atomizdat, Moscow (in Russian)
33. Habashi F (1997) Handbook of extractive metallurgy. Wiley-VCH, Weinheim, New York
34. Sonchina OA (1955) Redkie metally (Less-common metals). Metallurgizdat, Moscow (in Russian)
35. Savitskii EM, Gribulya VB (1977) Prognozirovanie neorganicheskikh soedinenii s pomoschyu EVM (The prediction of inorganic compounds by means of computing). Nauka, Moscow (in Russian)
36. Sangster J, Pelton AD (1991) The Li-Re (lithium-rhenium) system. J Phase Equilibria 12(6):681
37. Samsonov GV (1966) Berillidy (Beryllides). Naukova Dumka, Kyiv (in Russian)
38. Papirov II (1981) Struktura i svoistva splavov berilliya (Structure and properties of beryllium alloys). Energoizdat, Moscow (in Russian)
39. Savitskii EM, Tylkina MA, Khamidov OKh (1966) Diagramma sostoyaniya sistemy skandii-renii (The constitution diagram of the scandium-rhenium system). Izv AN SSSR Metally (4):116–122 (in Russian)
40. Gladyshevskii EI, Bodak OI (1982) Kristallokhimiya intermetallicheskikh soedinenii redkozemelnykh metallov (The crystal chemistry of intermetallic compounds of rare earth metals). Vyshcha Shkola, Lviv (in Russian)
41. Savitskii EM, Burkhanov GS (1971) Metallovedenie splavov tugoplavkikh i redkih metallov (Metallography of refractory and less-common metal alloys), 2nd ed. Nauka, Moscow (in Russian)
42. Savitskii EM, Khamidov OKh (1965) Kristallicheskaya struktura soedineniya reniya s praseodimom (The crystal structure of rhenium compound with praseodymium). Izv AN SSSR Neorg Mater 1(9):1621–1622 (in Russian)
43. Griffin RB, Gschneidner KA, Jr (1971) Effect of the sixth period elements on the melting and transformation temperatures of praseodymium: Part I. Experimental. Metal Trans 2(9):2517–2524

44. Savitskii EM, Khamidov OKh (1967) Diagrammy sostoyaniya system gadolinii-renii i erbii-renii (The constitution diagrams of the gadolinium-rhenium and erbium-rhenium systems). Izv AN SSSR Neorg Mater 3(4):649–655 (in Russian)
45. Savitskii EM, Khamidov OKh (1968) Diagramma sostoyaniya sistemy Tb-Re (The constitution diagram of the Tb-Re system). Izv AN SSSR Metally (6):158–162 (in Russian)
46. Savitskii EM, Khamidov OKh (1965) Metallicheskie soedineniya v splavakh reniya s redkozemelnymi metallami (Metallic compounds in rhenium alloys with rare earth metals). Izv AN SSSR Neorg Mater 1(11):1873–1877 (in Russian)
47. Garg SP, Ackermann RJ (1977) The high temperature phase diagrams for Th-Mo, Th-Re, U-Mo and U-Re; derived thermodynamic properties of refractory metal solutes in liquid thorium and uranium. J Nucl Mater 64(3):265–274
48. Jackson RJ, Williams DE, Larsen WL (1963) The uranium – rhenium system. J Less-Common Met 5(6):443–461
49. Chandrassekharaian MS, Dharwadkar SR, Das D (1986) High-temperature phase diagrams of Re-U, Ta-U and W-U. Z Metallkd 77(8)509–514
50. Savitskii EM, Tylkina MA, Zotev YuA (1959) Diagramma sostoyaniya sistemy renii-titan (The constitution diagram of the rhenium-titanium system). Zh Neorg Khim 4(3):702–704 (in Russian)
51. Murray JL (1982) The Re-Ti (rhenium-titanium) system. Bull Alloy Phase Diagrams 2(4):462–466
52. Savitskii EM, Tylkina MA, Tsyganova IA (1961) Phase diagram of the zirconium-rhenium system. Sov J Atomic Energy 7(3):724–727
53. Kripyakevich PI, Tylkina MA, Savitskii EM (1960) Novoe soedinenie v sisteme renii-tsirkonii i ego kristallicheskaya struktura (A new compound in the rhenium-zirconium system and its crystal structure). Izv Vyssh Uchebn Zaved Chern Metall (1):12–15 (in Russian)
54. Krikorian NH, Witteman WG, Bowman MG (1960) The preparation, crystal structures and some properties of zirconium and hafnium dirhenide. J Phys Chem 64(10):1517–1519
55. Garg SP, Ackermann RJ (1979) Zr-Re phase diagram between 1866 to 1913 K. Scr Metall 13(7):611–613
56. Savitskii EM, Tylkina MA, Tsyganova IA, Gladyshevskii EI, Mulyava MP (1962) Diagramma sostoyaniya sistemy gafnii-renii (The constitution diagram of the hafnium-rhenium system). Zh Neorg Khim 7(7):1608–1610 (in Russian)
57. Taylor A, Kagle BJ, Doyle NJJ (1963) The constitution diagram of the rhenium-hafnium system. J Less-Common Met 5(1):26–40
58. Tylkina MA, Savitskii EM, Povarova KB (1960) Diagramma sostoyaniya sistemy vanadii-renii (The constitution diagram of the vanadium-rhenium system). Zh Neorg Khim 5(8):1907–1910 (in Russian)
59. Tylkina MA, Povarova KB, Savitskii EM (1960) Sigma-faza v sisteme renii-vanadii (Sigma-phase in the rhenium-vanadium system). Doklady AN SSSR 131(2):332–334 (in Russian)
60. Kuzma YuB, Kovalik DA (1969) Sistema vanadii-renii-bor (The vanadium-rhenium-boron system). Izv AN SSSR Neorg Mater 5(10):1687–1690 (in Russian)
61. Giorgi AL, Matthias BT, Stewart GR (1978) Discovery of a superconducting A-15 phase in the V-Re system. Solid State Commun 27(3):291–294
62. Eremenko VN, Kharkova AM, Velikanova TYa, (1983) Promezhutochnye fazy v sisteme vanadii – renii (Intermediate phases in the vanadium – rhenium system). Dopov Akad Nauk Ukr RSR Ser A Fiz Mat Tekh Nauki 45(1):78–81 (in Russian)
63. Eremenko VN, Kharkova AM, Velikanova TYa, (1983) Diagramma fazovykh ravnovesii sistemy vanadii – renii (Phase equilibrium diagram of the vanadium – rhenium system). Dopov Akad Nauk Ukr RSR Ser A Fiz Mat Tekh Nauki 45(2):75–79 (in Russian)
64. Smolyaninova EA, Stribuk EK (1985) Struktura, temperature perekhoda v sverkhprovodyashchee sostoyanie i magnitnaya vospriimchivost splavov vanadiya s

reniem (The structure, temperature of transition to superconducting state and magnetic susceptibility of vanadium-rhenium alloys). Doklady AN BSSR 29(7):601–603 (in Russian)
65. Jorda JL, Müller J (1986) The vanadium-rhenium system: phase diagram and superconductivity. J Less-Common Met 119(2):337–345
66. Savitskii EM, Tylkina MA, Povarova KB (1961) The phase diagram for the niobium-rhenium system. Sov J Atomic Energy 7(5):937–940
67. Knapton AG (1959) The niobium-rhenium system. J Less-Common Met 1(6):480–486
68. Glessen BC, Nordheim R, Grant NJ (1961) The constitution diagram niobium (columbium) – rhenium. Trans AIME 221:1009–1013
69. Grant NJ, Glessen BC (1961) The structure of niobium (columbium)–rhenium alloys. J Metals 13:87–90
70. Tylkina MA, Tsyganova IA, Savitskii EM (1960) Diagramma sostoyaniya sistemy tantal-renii (The constitution diagram of the tantalum-rhenium system). Zh Neorg Khim 5(8):1905–1907 (in Russian)
71. Brophy JH, Schwarzkopf P, Wullf J (1960) The tantalum-rhenium system. Trans AIME 218(5):910–914
72. Knapton AG (1960) Niobium and tantalum alloys. J Less-Common Met 2(2–4):113–124
73. Tylkina MA, Savitskii EM, Alyushin VE (1973) Diagramma sostoyaniya Ta-Nb-Re (The Ta-Nb-Re constitution diagram). Izv AN SSSR Metally (4):225–229 (in Russian)
74. Savitskii EM, Tylkina MA, Povarova KB (1959) Diagramma sostoyaniya sistemy khrom-renii (The constitution diagram of the chromium-rhenium system). Zh Neorg Khim 4(8):1928–1930 (in Russian)
75. Larikov LN, Baklanova LM, Barabash OM (1977) Diagrama stanu sistemy Cr-Re v oblasti kontsenratsiy do 50% reniyu (za masoy) (The constitution diagram of the Cr-Re system in the range of compositions to 50 mas.% Re). Dopov Akad Nauk Ukr RSR Ser A Fiz Mat Tekh Nauki 39(3):258–260 (in Ukrainian)
76. Venkatraman M, Neumann JP (1987) The Cr-Re (chromium-rhenium) system. J Phase Equilib 8(2):105–107
77. Savitskii EM, Tylkina MA, Povarova KB (1959) Diagramma sostoyaniya sistemy renii-molibden (The constitution diagram of the rhenium-molybdenum system). Zh Neorg Khim 4(2):424–434 (in Russian)
78. Brewer L, Lamoreaux RH (1980) Phase diagrams. In: Brewer L (ed) Molybdenum. Physico-chemical properties of its compounds and alloys. Atomic Energy Review, Special Issue N 7, pp. 195–356. International Atomic Energy Agency, Vienna
79. Savitskii EM, Tylkina MA, Kirilenko RV, Kopetskii ChV (1961) Diagramma sostoyaniya sistemy marganets-renii (The constitution diagram of the manganese-rhenium system). Zh Neorg Khim 6(6):1474–1476 (in Russian)
80. Kotegov KV, Pavlov ON, Shvedov VP (1965) Tekhnetsii (Technetium). Atomizdat, Moscow (in Russian)
81. Kripyakevich PI, Kuzma YuB, Protasov VS (1964) Renii (Rhenium). Nauka, Moscow (in Russian)
82. Savitskii EM, Tylkina MA, Polyakova VP (1962) Diagramma sostoyaniya splavov sistemy rutenii-renii (The constitution diagram of the ruthenium-rhenium alloys system). Zh Neorg Khim 7(2):439–441 (in Russian)
83. Savitskii EM, ed (1984) Blagorodnye metally (Noble metals). Metallurgiya, Moscow (in Russian)
84. Tylkina MA, Polyakova VP, Savitskii EM (1962) Diagramma sostoyaniya sistemy osmii-renii (The constitution diagram of the osmium-rhenium system). Zh Neorg Khim 7(6):1469–1470 (in Russian)
85. Tylkina MA, Tsyganova IA, Savitskii EM (1962) Diagrammy sostoyaniya splavov reniya s metallami platinovoi gruppy (The constitution diagrams of rhenium alloys with platinum group metals). Zh Neorg Khim 7(8):1917–1927 (in Russian)
86. Audi G, Wapstra AH, Thibault C, Blachot J, Bersillon O (2003) The NUBASE evaluation of nuclear and decay properties. Nucl Phys A 729:3–128

87. De Laeter JR, Bohlke JK, De Bievre P, Hidaka H, Peiser HS, Rosman KJR, Taylor PDP (2003) Atomic weights of the elements. Review 2000 (IUPAC Technical report). Pure Appl Chem 75(6):683–800
88. Wieser ME (2006) Atomic weights of the elements 2005. (IUPAC Technical report). Pure Appl Chem 78(11):2051–2066
89. Savitskii EM, Tylkina MA, Arskaya EP (1970) Diagramma sostoyaniya sistemy nikel-renii (The constitution diagram of the nickel-rhenium system). Izv Vyssh Uchebn Zaved Tsvet Metall (4):113–116 (in Russian)
90. Nash A, Nash P (1985) Ni-Re (nickel-rhenium) system. Bull Alloy Phase Diagrams 6(4):348–350
91. Voronova LI, Polyakova VP, Savitskii EM (1984) Study of alloys of the system Pt-Re. Rus Metall (1):185–187
92. Okamoto H, Massalski TB (1984) The Au-Re (gold-rhenium) system. Bull Alloy Phase Diagrams 5(4):383
93. Portnoi KI, Romashov VM (1972) Binary constitution diagrams of systems composed of various elements and boron – a review. Powder Metall Met Ceram 11(5):378–384
94. Savitskii EM, Tylkina MA, Povarova KB (1961) Diagramma sostoyaniya sistemy alyuminii-renii (The constitution diagram of the aluminium-rhenium system). Zh Neorg Khim 6(8):1962–1965 (in Russian)
95. Chaban NF, Kuzma YuB (1972) Rentgenograficheskoe issledovanie troinykh system renii-alyuminii-bor i renii-kremnii-bor (An x-ray study of the rhenium-aluminium-boron and rhenium-silicon-boron systems). Izv AN SSSR Neorg Mater 8(6):1065–1068 (in Russian)
96. Prevarskii AP, Kuzma YuB, Zrada MS (1979) Issledovanie sistemy Re-Cu-Al (A study of the Re-Cu-Al system). Izv AN SSSR Metally (4):199–201 (in Russian)
97. Burnashova VV, Starodub PK, Stroganov GB, Doronin VN (1977) Fiziko-khimicheskoe issledovanie splavov Re-Fe-Al (A physico-chemical study of Re-Fe-Al alloys). Izv AN SSSR Metally (4):211–214 (in Russian)
98. Schuster JC (1984) X-ray investigation of phase relations and crystal structures in the binary system Re-Al. J Less-Common Met 98(2):215–220
99. Popova SV, Fomitcheva LN (1982) Novye fazy v sistemakh Re-Ga i Os-Ga, poluchennye pri vysokom davlenii (The new phases in the Re-Ga and Os-Ga systems obtained at high pressure). Izv AN SSSR Neorg Mater 18(2):251–255 (in Russian)
100. Gladyshevskii EI (1971) Kristallokhimiya silitsidov i germanidov (The crystal chemistry of silicides and germanides). Metallurgiya, Moscow (in Russian)
101. Siegrist T, Hulliger F, Travaglini G (1983) The crystal structure and some properties of $ReSi_2$. J Less-Common Met 92(1):119–121
102. Siegrist T, Greedan JE, Garrett JD, Wenhe G, Stager CV (1991) Crystal structure and superconductivity in Re_2Si. J Less-Common Met 171(2):171–177
103. Samsonov GV, Bondarev VN (1968) Germanidy (Germanides). Metallurgiya, Moscow (in Russian)
104. Siegrist T, Hulliger F, Petter W (1983) The crystal structure of Re_3Ge_7. J Less-Common Met 90(1):143–151
105. Larchev VI, Popova SV (1982) The new chimney-ladder phases Co_2Si_3 and Re_4Ge_7 formed by treatment at high temperatures and pressures. J Less-Common Met 84:87–91
106. Samsonov GV, Verkhoglyadova GS (1964) K voprosu o poluchenii nitrida reniya (To the question of the fabrication of rhenium nitride). Ukr Khim Zh 30(2):143–146 (in Russian)
107. Jehn H, Hohloch KD, Fromm E (1972) Hochtemperatur-Löslichkeit von Stickstoff in Rhenium (High-temperature solubility of nitrogen in rhenium). J Less-Common Met 27(1):98–100 (in German)
108. Borisova LV, Ermakov AN (1974) Analiticheskaya khimiya reniya (The analytical chemistry of rhenium). Nauka, Moscow (in Russian)
109. Klein H, Von Schnering HG (1966) Untersuchungen an Re_3As_7 (Studies on Re_3As_7). J Less-Common Met 11(4):298–299 (in German)
110. Sims CT (1962) Rhenium. Elsevier, Amsterdam, New York

111. Jeitschko W, Sleight AW (1972) The rhenium-oxygen system at high pressure: structure and characterization of a new rhenium oxide. J Solid State Chem 4(2):324–330
112. Shcheglov PA, Drobot DV (2000) *p–T–x*-diagramma sostoyaniya sistemy renii-kislorod (The constitution *p–T–x*-diagram of the rhenium-oxygen system). Izv Vyssh Uchebn Zaved Tsvet Metall (3):23–27 (in Russian)
113. Dyuzheva TI, Bendeliani NA, Glushko AN, Kabalkina SS (1989) Phase diagram of ReO_3 up to 10 GPa. Phys Scr 39(3):341–342
114. Dyuzheva TI, Bendeliani NA, Kabalkina SS (1987) New high-pressure phases of ReO_3. J Less-Common Met 133(2):313–317
115. Lebedev KB (1963) Renii (Rhenium), 2nd ed. Metallurgizdat, Moscow (in Russian)
116. Samsonov GV, Drozdova SV (1972) Sulfidy (Sulfides). Metallurgiya, Moscow (in Russian)
117. Kurbanov TKh, Dovlyatshina RA, Dzhavadova IA, Akhmedov FA (1977) Sistema Re–Te (The Re–Te system). Zh Neorg Khim 22(4):1137–1139 (in Russian)
118. Savitskii EM, Tylkina MA, Povarova KB (1970) Rhenium alloys. IPST Press, Jerasalem
119. Savitskii EM, Tylkina MA, Polyakova VP (1963) Diagramma sostoyaniya sistemy rutenii-renii-osmii (The constitution diagram of the ruthenium-rhenium-osmium system). Zh Neorg Khim 8(1):146–148 (in Russian)
120. Slyusarenko EM, Peristyi AV, Kerimov EYu, Sofin MV, Skorbov DYu (1998) Ternary systems of nickel and rhenium with transition metals. J Alloys Compd 264(1–2):180–189
121. Alcock NW, Kjekshus A (1965) Crystal structure of $ReSe_2$. Acta Chem Scand 19(1):79–94
122. Sorrell CA (1968) Synthesis of rhenium ditelluride. J Am Ceram Soc 51(5):285–286
123. Ordanyan SS, Chupov VD, Plakhuta OV (1982) Reaction of TiB_2 with Re. Powder Metall Met Ceram 21(2):145–147
124. Ordanyan SS (1980) Reactions of HfB_2 with Re and Cr. Powder Metall Met Ceram 19(4):273–277
125. Avgustinik AI, Ordanyan SS, Sarbezova RYa, Fonareva NF (1970) Diagramma sostoyaniya sistemy ZrB_2-Re (The constitution diagram of the ZrB_2-Re system). Izv AN SSSR Neorg Mater 6(8):1414–1416 (in Russian)
126. Niselson AA, Sokolova TD, Orlov AM, Shorikov YuS (1981) Sistemy OsO_4–RuO_4 i Re_2O_7–OsO_4 (The OsO_4–RuO_4 and Re_2O_7–OsO_4 systems). Zh Neorg Khim 26(3):765–767 (in Russian)
127. Doerr M, Feller J, Oppermann H (1996) Coexistent phases and their electrical and structural behaviour in the ternary Re/Mo/O system. Cryst Res Technol 31(2):231–241
128. Havinga EE, Van Maaren MH, Damsma H (1969) Superconductivity of compounds having the Si_2U_3-type structure. Phys Lett A 29(3):109–110
129. Mikhalenko SI, Zavalii LV, Kuzma YuD, Boiko LI (1991) The phase diagrams of Sc-W-B and Sc-Re-B systems at 1000 °C. Powder Metall Met Ceram 30(8):681–683
130. Smolyaninova EA, Stribuk EK, Tyavlovskii VI (1987) Phase equilibrium diagrams of ternary rhenium system with vanadium, niobium and molybdenum. Russ Metall (3):204–206
131. Schuster JC (1988) Silicon nitride—metal joints: phase equilibria in the systems Si_3N_4–Cr, Mo, W and Re. J Mater Sci 23(8):2792–2796
132. Feller J, Oppermann H, Kucharkowski R, Däbritz S (1998) Phase Beziehungen und chemische Transport der Verbindungen in dem ternären System Re/Mo/O (Phase relations and chemical transport of the compounds in the ternary system Re/Mo/O). Z Naturforsch B 53(4):397–404 (in German)
133. Balykova YuV, Knyazev AV, Kerimov EYu, Kalmykov KB, Slyusarenko EM (2009) New Laves phase in the Nb-Cr-Re ternary system. Metal Sci Heat Treatment 51(9–10):411–414
134. Telegus VS, Kuzma YuB, Stefanishina TsK (1969) The ternary chromium–rhenium–boron system. Powder Metall Met Ceram 8(2):133–136
135. Gritsiv AV, Bondar AA, Velikanova TYa, Vereshchak VM (1999) The Cr–Re phase diagram. Powder Metall Met Ceram 38(3–4):166–171
136. Mikhalenko SI, Kuzma YuB (2000) Phase equilibria in the Nd–Re–B system. Powder Metall Met Ceram 39(11–12):563–566

137. Mikhalenko SI, Kuzma YuB (2005) Phase equilibria in the Pr – Re – B system. Powder Metall Met Ceram 44(1–2):35–39
138. Ordanyan SS (1975) Reactions of rhenium and other refractory metals with some metal-like compounds. Powder Metall Met Ceram 14(2):125–129
139. Kuzma YuB, Mykhalenko SI, Akselrud LG (1986) Redetermination of the structure of the compound Y_3ReB_7 and related compounds. J Less-Common Met 117:29–35
140. Chaban NF, Mikhalenko SI, Kuzma YuB (1989) Isothermal section at 1270 K of the equilibrium diagram of the Gd-Re-B system. Powder Metall Met Ceram 28(2):124–128
141. Zavalij PYu, Mykhalenko SI, Kuzma YuB (1994) New incommensurate structures of the borides $Pr_{41}(Mn_4B_4)_{35}$ and $Pr_7(Re_4B_4)_6$. J Alloys Compd 203:55–59
142. Nowotny H, Rogl P (1977) Ternary metal borides. In: Matkovich VI (ed) Boron and refractory borides, pp. 413–438. Springer, Berlin, Heidelberg, New York
143. Rogl P, Nowotny H (1973) Neue κ- (kappa-) Phasen (New κ- (kappa-) phases). Monatsh Chem 104(6):1497–1504 (in German)
144. Kuzma YuB, Sobolev AS, Fedorov TF (1971) Phase equilibria in the ternary systems tantalum-iron-boron and tantalum-nickel-boron. Powder Metall Met Ceram 10(5):410–414
145. Kuzma YuB, Lakh VI, Stadnyk BI, Chaban NF (1971) Sistema tantal-renii-bor (The tantalum-rhenium-boron system). Dopov Akad Nauk Ukr RSR Ser A Fiz Mat Tekh Nauki 33(9):849–851 (in Russian)
146. Rogl P, Nowotny H (1974) Ternäre Komplexboride mit $ThMoB_4$-Typ (Ternary complex borides with $ThMoB_4$-type structure). Monatsh Chem 105(5):1082–1098 (in German)
147. Rogl P, Nowotny H (1975) Uran-haltige Komplexboride (Complex borides with uranium). Monatsh Chem 106(2):381–387 (in German)
148. Argon AS (1996) Mechanical properties of single-phase crystalline media: deformation at low temperatures. In: Cahn RW, Haasen P (eds) Physical metallurgy, 4th ed., Vol. 3, pp. 1877–1955. Elsevier Science BV, Amsterdam
149. Kuzma YuB (1971) Sistemy titan-kobalt-bor i titan-renii-bor (The titanium-cobalt-boron and titanium-rhenium-boron systems). Izv AN SSSR Neorg Mater 7(3):514–517 (in Russian)
150. Valovka IP, Kuzma YuB (1986) Isothermal section of the diagram of the systems U-Mo-B and U-Re-B. Powder Metall Met Ceram 25(12):986–988
151. Mikhalenko SI, Kuzma YuB, Sobolev AS (1977) Yttrium-rhenium-boron and lanthanum-rhenium-boron systems. Powder Metall Met Ceram 16(1):36–38
152. Jurczyk M, Chistyakov OD (1989) Structure and magnetic properties of $Y_2Fe_{14-x}Re_xB$. Phys Status Solidi A Appl Res 114(2):K219-K221
153. Kuzma YuB, Mikhalenko SI, Chaban NF (1983) Vzaimodeistvie Mo, W i Re s redkozemelnymi metallami i borom (Interaction of Mo, W and Re with rare-earth metals and boron). In: Savitskii EM (ed) Issledovaniya i primenenie splavov tugoplavkikh metallov (Studies and application of refractory metal alloys), pp. 5–11. Nauka, Moscow (in Russian)
154. Chaban NF, Mikhalenko SI, Kuzma YuB (1996) New compounds with the $YCrB_4$ structure. Inorg Mater 32(1):36–40
155. Mykhalenko SI (1981) Sistema disprozii-renii-bor (The dysprosium-rhenium-boron system). Visn Lviv Derzh Univ Ser Khim 23:52–54 (in Ukrainian)
156. Mikhalenko SI, Kuzma YuB (1982) Phase equilibria in the Sm-Re-B system. Powder Metall Met Ceram 21(9):725–727
157. Mykhalenko SI, Kuzma YuB (2000) The Tb-Re-B system: phase equilibria and crystal structures. Polish J Chem 74(2):163–171
158. Kuzma YuB, Lakh VI, Stadnyk BI, Voroshilov YuV (1968) Phase equilibria in the systems Zr-Re-B and W-Re-B. Powder Metall Met Ceram 7(6):462–466
159. Yarmolyuk YP, Gladyshevskii EI (1974) Novye troinye soedineniya ekviatomnogo sostava (New ternary compounds of equiatomic compositions). Dopov Akad Nauk Ukr RSR Ser B Heol Khim Biol Nauki 36:1030–1032 (in Russian)
160. Okamoto H (1992) The Ir-Re (iridium-rhenium) system. J Phase Equilib 13(6):649–650
161. Diaz JJ (1996) Pure rhenium metal. IEEE Potentials (2–3):37–39

162. Mikhalenko SI, Chaban NF, Kuzma YuB (1998) Reaction of rare earth metals with VI- and VII-group transition metals and boron. Powder Metall Met Ceram 37(1–2):99–106
163. Jeitschko W, Mons HA, Rodewald UCh, Möller MH (1998) The crystal structure of the potential ferroelectric calcium rhenate (VI, VII) $Ca_{11}Re_4O_{24}$ and its relation to the structure of $Sr_{11}Os_4O_{24}$. Z Naturforsch B 53(1):31–36
164. Jeitschko W, Mons HA, Rodewald UCh (1999) Preparation and crystal structure of the calcium rhenate (VI, VII) $Ca_5Re_3O_{15-x}$. Z Naturforsch B 54(12):1483–1488
165. Mons HA, Schriewer MS, Jeitschko W (1992) The crystal structure of the isotypic perrhenates $Ca_5Re_2O_{12}$ and $Sr_5Re_2O_{12}$. J Solid State Chem 99(1):149–157
166. Baud G, Besse JP, Levasseur G, Chevalier R (1978) Crystalchemical study of the double oxides of rhenium and the alkaline-earth elements. J Inorg Nucl Chem 40(8):1605–1606
167. Abakumov AM, Shpanchenko RV, Antipov EV, Lebedev OI, Van Tendeloo G (1997) The crystal structure of Ca_3ReO_6. J Solid State Chem 131(2):305–309
168. Suzuki H, Ozawa H, Sato H (2007) Anomalous electric conductions in $KSbO_3$-type metallic rhenium oxides. J Phys Soc Japan 76(4):044805
169. Bramnik KG, Miehe G, Ehrenberg H, Fuess H, Abakumov AM, Shpanchenko RV, Pomjakushin VYu, Balagurov AM (2000) Preparation, structure and magnetic studies of a new $Sr_{11}Re_4O_{24}$ double oxide. J Solid State Chem 149(1):49–55
170. Bramnik KG, Ehrenberg H, Fuess H (2001) Preparation, crystal structure and magnetic studies of a new $Sr_7Re_4O_{19}$ double oxide and its relation to the structure of $Ba_7Ir_6O_{19}$. J Solid State Chem 160(1):45–49
171. Chamberland BL, Hubbard FC (1978) The characterization of $Ba_3Re_2O_9$ and $Sr_3Re_2O_9$. J Solid State Chem 26(1):79–82
172. Baud G, Besse JP, Chevalier R, Chamberland BL (1979) Structure d'un oxyde double de rhenium à charpente de type $KSbO_3$ cubique: Sr_xReO_3 ($0.4 \leq x \leq 0.5$) (A double structure of rhenium oxide frame-type cubic $KSbO_3$: Sr_xReO_3 ($0.4 \leq x \leq 0.5$). J Solid State Chem 28(2):157–162 (in French)
173. Jeitschko W, Heumannskämper DH, Schriewer-Pöttgen MS, Rodewald UC (1999) Preparation, crystal structures and properties of rhenates with multiple Re-Re bonds: Ln_2ReO_5 (Ln = Sm, Eu, Gd), $Ln_3Re_2O_9$ (Ln = Pr, Nd, Sm), and $Ln_4Re_6O_{19}$ (Ln = La-Nd). J Solid State Chem 147(1):218–228
174. Bramnik KG, Abakumov AM, Shpanchenko RV, Antipov EV, Van Tendeloo G (1998) Synthesis and structure of $Ln_4Re_{6-x}O_{19}$ (Ln = Ce, Pr, Nd) complex oxides. J Alloys Compd 278(1–2):98–102
175. Okamoto H (1988) The In-Re (indium-rhenium) system. Bull Alloy Phase Diagrams 9(6):702
176. Jeitschko W, Sleight AW (1972) The rhenium-oxygen system at high pressure: structure and characterization of a new rhenium oxide. J Solid State Chem 4(2):324–330
177. ASM International (2013) Alloy phase diagram database. Version 1.0.5.0 http://www1.asminternational.org/asmenterprise/APD/SearchAPD.aspx Accessed 18 April 2013
178. Gulyaev BB (1968) Obobshchenie diagram sostoyaniya metallicheskikh system (Generalization of the phase diagrams of metallic systems). In: Savitskii EM (ed) Diagrammy sostoyaniya metallicheskikh system (Phase diagrams of metallic systems), p.257–267. Nauka, Moscow (in Russian)
179. Lam DJ, Mitchell AW (1972) Laves phases of actinide elements. J Nucl Mater 44(3):279–284
180. Dieva EN (1974) Rastvorimost tugoplavkikh metallov v zhidkom indii (The solubility of refractory metals in liquid indium). In: Bamburov VG (ed) Fiziko-khimicheskie issledovaniya zhidkikh metallov i splavov (Physico-chemical studies of liquid metals and alloys), p. 105–106. Uralskii Nauchnyi Tsentr AN SSSR, Sverdlovsk (in Russian)
181. Tsyganova IA, Tylkina MA, Savitskii EM (1971) Sn-Hf and Sn-Re phase diagrams. Russ Metall (3):129–130
182. Weeks JR (1965) Liquidus curves of nineteen dilute binary alloys of bismuth. ASM Trans Q 58:302–320

183. Drews T, Supel J, Hagenbach A, Seppelt K (2006) Solid state molecular structures of transitional metal hexafluorides. Inorg Chem 45:3782–3788
184. English JJ (1961) Binary and ternary phase diagrams of columbium, molybdenum and tungsten. Report AD-TR-257–739, Contract AF 33(616)-7747, pp. 1–241. Defence Metals Information Center, Battelle Memorial Institute, Columbus, Ohio
185. Tregubov IA, Evseyeva LN, Ivanov OS (1977) Investigation of the Re-Ta-Mo phase diagram. Russ Metall (2):173–176
186. Savitskii EM, Tylkina MA, Alyushin VE, Kuzma YuB, Telegus VS (1974) Ternary σ- and χ-phases in the Ta-Nb-Re system. Russ Metall (1):139–141
187. Okamoto H (2010) The Mo-Re (molybdenum-rhenium) system. J Phase Equilib Diffus 31(6):580–581
188. Okamoto H (2010) The Cl-Re (chlorine-rhenium) system. J Phase Equilib Diffus 31(4):401
189. Okamoto H (2012) The Re-U (rhenium-uranium) system. J Phase Equilib Diffus 33(6):498
190. Saito S, Kurokawa K, Hayashi S, Takashima T, Narita T (2007) Tie-lined compositions of the γ and σ phases in a ternary Re-Cr-Ni system at 1423 K. Nippon Kinzoku Gakkaishi 71(8):608–614 (in Japanese)
191. Okamoto H (2012) The Ni-Re (nickel-rhenium) system. J Phase Equilib Diffus 33(4):346
192. Gupta KP (2010) The Mo-Ni-Re (molybdenum-nickel-rhenium) system. J Phase Equilib Diffus 31(6):564–568
193. Gupta KP (2010) The Nb-Ni-Re (niobium-nickel-rhenium) system. J Phase Equilib Diffus 31(6):569–572
194. Okamoto H (2009) The Al-Re (aluminum-rhenium) system. J Phase Equilib Diffus 30(2):208–209
195. Huang W, Chang YA (1998) A thermodynamic analysis of the Al-Re system. J Phase Equilib 19(4):361–366
196. Okamoto H (2000) The Re-Ta (rhenium-tantalum) system. J Phase Equilib 21(6):573
197. Gokhale AB, Abbaschian R (1996) The Re-Si (rhenium-silicon) system. J Phase Equilib 17(5):451–454
198. Okamoto H (1996) The Re-U (rhenium-uranium) system. J Phase Equilib 17(5):464
199. Okamoto H (1992) The Ni-Re (nickel-rhenium) system. J Phase Equilib Diffus 13(3):335

Chapter 5
Osmium

5.1 Structures

Osmium is the element No. 76 of the periodic table (period—6, group—8 (or VIIIa), relates to transition metals) with the ground state level $^5D_4$ and electron configuration $1s^2 2s^2 2p^6 3s^2 3p^6 3d^{10} 4s^2 4p^6 4d^{10} 4f^{14} 5s^2 5p^6 5d^6 6s^2$. The general oxidation states (numbers) of osmium in various chemical compounds are (–2), (–1), 0, (+1), (+2), (+3), (+4), (+5), (+6), (+7) and (+8); the oxidation states (+8), (+4), (+3) and (+2) are the most common; the radii of osmium are:

atomic (metallic, CN = 12)—0.134 nm,
atomic (covalent)—0.126 nm,
ionic (+4)—0.063 nm (CN = 6),
ionic (+5)—0.058 nm (CN = 6),
ionic (+6)—0.055 nm (CN = 6),
ionic (+8)—0.039 nm (CN = 4),

its electronegativity is 2.2 in Pauling scale, or 1.52 in Allred–Rochow scale [1–3, 7–8]. Elemental osmium has hexagonal close-packed (hcp) metal crystal structure (space group—$P6_3/mmc$, Mg type) with lattice parameters: $a = 0.27338$ nm, $c = 0.43195$ nm, $c/a = 1.5800$ (Z = 2), minimum interatomic distance—0.267 nm (CN = 12), slip planes (0001), $(10\bar{1}1)$, $(10\bar{1}0)$ and slip directions $<2\bar{1}\bar{1}0>$, $<2\bar{1}10>$ [28, 76]. At room temperature the XRD density of osmium is 22.60 g cm^{-3}, and recommended value for the bulk density of osmium metal parts—22.4–22.5 g cm^{-3} [4, 8].

5.2 Thermal Properties

Osmium is a refractory noble metal; it belongs to the platinum family and is the densest natural element. The general thermodynamic properties of osmium are summarized in Table 5.1. For the molar heat capacity $c_p = f(T, \text{K})$, J mol^{-1} K^{-1},

I. L. Shabalin, *Ultra-High Temperature Materials I*,
DOI: 10.1007/978-94-007-7587-9_5, © Springer Science+Business Media Dordrecht 2014

Table 5.1 General thermodynamic properties of osmium

Characteristics	Symbol	Unit	Value	References
Standard molar entropy (at 298.15 K and 100 kPa)	$S°_{298}$	J mol^{-1} K^{-1}	32.635	[4, 6, 8– 9, 29]
			32.7	[5]
Standard molar heat capacity (at 298.15 K and 100 kPa)	$c°_{p,298}$	J mol^{-1} K^{-1}	24.90	[4]
			24.92	[5]
			24.7	[6–8]
Specific heat capacity (at 298.15 K)	c	J kg^{-1} K^{-1}	130.9	[4]
			130	[7]
Molar enthalpy (heat) of melting (at the melting point)	ΔH_m	kJ mol^{-1}	57.86	[6–8]
			31	[111]
Specific enthalpy (heat) of melting (at the melting point)		kJ kg^{-1}	304	[7]
Molar enthalpy (heat) of vaporization (at the boiling point)	ΔH_v	kJ mol^{-1}	731	[4]
			738	[6]
			746	[8]
Specific enthalpy (heat) of vaporization (at the boiling point)		kJ kg^{-1}	3840	[4]
Melting point	T_m	K (°C)	3320 ± 30 (3045 ± 30)	[4, 6, 9]
			3305 (3030)	[7–8, 14]
Boiling point	T_b	K (°C)	5285 (5010)	[7–8]
			5300 (5030)	[9]
			5500 (5225)	[6]

the following relationship is recommended for the range of temperatures from 298 to 2500 K [5]

$$c_p = 23.82 + \left(3.684 \times 10^{-3}\right)T. \tag{5.1}$$

The equilibrium vapour pressure of osmium P, Pa, at temperatures 298–2500 K is obeyed the rule [7]:

$$\lg P = -41198/T - 0.3896 \lg T + 14.425, \tag{5.2}$$

where T is temperature, K. The values of standard molar entropy $S°_{298}$, molar c_p and specific c heat capacities, enthalpies (heats) of melting and vaporization, molar and specific enthalpy differences $H_T - H_{298}$, vapour pressures and mass/linear vaporization rates for osmium are given in Addendum in comparison with carbon (graphite) and other ultra-high temperature materials (refractory metals) in the wide ranges of temperatures. At room temperature the thermal conductivity of polycrystalline osmium is 88 W m^{-1} K^{-1} [8], at higher temperatures it declines noticeably [29]. In the temperature range of 20–550 °C, the average value of the coefficient of linear thermal expansion of unalloyed osmium $\alpha \approx 7 \times 10^{-6}$ K^{-1};

at 50 °C for the directions parallel and perpendicular to the axis c the values are 5.8×10^{-6} and 4.0×10^{-6} K^{-1}, respectively, and those values at 550 °C are 8.3×10^{-6} K^{-1} and 5.8×10^{-6} K^{-1}, respectively [29]. For the ambient temperature the recommended value is $\alpha = 6.1 \times 10^{-6}$ K^{-1} [8]. The surface tension of liquid osmium (density 20.1 g cm^{-3}) is 2.5 N m^{-1} (its temperature coefficient is -0.33×10^{-3} N m^{-1} K^{-1}) [8]. In comparison with other ultra-high temperature materials (graphite and refractory metals), the values of thermal conductivity and thermal expansion of osmium in the wide range of temperatures are summarized in Addendum.

5.3 Electro-Magnetic and Optical Properties

At room temperature the specific electrical resistance (resistivity) of unalloyed osmium is 81–95 nΩ m; at 1530 °C it amounts to 0.86 μΩ m. In the range of temperatures from 0 to 100 °C the thermal coefficient of resistivity is 5.1×10^{-3} K^{-1} [9]. The Hall coefficient of osmium at room temperature is negative [9]. Osmium is a paramagnetic metal with magnitude of molar magnetic susceptibility χ_m (SI) $= 138 \times 10^{-6}$ cm^3 mol^{-1} (22 °C) [8]; the relative magnetic susceptibility $\chi(T)/\chi(293\ K)$ amounts to $\sim$1.4 at 400 °C [30]. At 1730–2230 °C the monochromatic emittance (spectral emissivity) ε_λ of osmium is $\sim$0.4 [4], and electron work function is 4.7–4.8 eV [4, 9]. The recommended values of electrical resistivity, magnetic susceptibility, spectral emittances and thermoionic emission characteristics (electron work function and Richardson constants) for osmium are given in comparison with other ultra-high temperature elements (carbon and refractory metals) in Addendum.

5.4 Physico-Mechanical Properties

Unalloyed metallic osmium is very hard and has the brittle character of fracture (zero elongation) at room temperature, its physico-mechanical properties are anisotropic, e.g. the hardness (HV) of osmium varies in magnitude in the wide ranges depending on crystal orientation [29]:

at 20 °C—from 300 kgf mm^{-2} (2.9 GPa) to 680 kgf mm^{-2} (6.7 GPa);
at 200 °C—from 260 kgf mm^{-2} (2.5 GPa) to 580 kgf mm^{-2} (5.7 GPa);
at 600 °C—from 200 kgf mm^{-2} (2.0 GPa) to 410 kgf mm^{-2} (4.0 GPa);
at 1200 °C—from 130 kgf mm^{-2} (1.3 GPa) to 400 kgf mm^{-2} (3.9 GPa);

also it possesses very high magnitudes of elastic properties at room temperature [4, 8]:

Young's modulus E, GPa	560
Coulomb's (shear) modulus G, GPa	220
Poisson's ratio ν	0.25
Volume compressibility κ, MPa^{-1}	0.26×10^{-5}
Longitudinal velocity of sound V_S, m s^{-1}	5480
Transversal velocity of sound V_T, m s^{-1}	3340

At elevated temperatures, the value of Young's modulus falls with temperature and amounts to ~500 GPa at 700 °C [4]. The magnitudes of physico-mechanical properties (hardness, strength, elasticity) of pure osmium are summarized in Addendum in comparison with other ultra-high temperature materials (graphite and refractory metals).

5.5 Nuclear Physical Properties

The isotopes of osmium (standard atomic mass—190.23 u) from ^{162}Os to ^{197}Os, including metastable states ($^{181m1-181m2}$Os, ^{183m}Os, $^{185m1-185m2}$Os, $^{189m-192m}$Os), and their general characteristics are summarized in Table 5.2; the naturally occurring isotopes are listed in order of decreasing abundance, and unstable artificial (radioactive) isotopes—in order of decreasing half-life period of decay.

Table 5.2 General characteristics of the isotopes of osmium[a] [7, 9, 21–23]

Isotope	Mass, u	Abundance, %	Half-life period	Decay mode, excitation (radiation) energy, MeV
^{192}Os[b]	191.961481	40.78	–	–
^{190}Os[c]	189.958447	26.26	–	–
^{189}Os[d]	188.958148	16.15	–	–
^{188}Os[e]	187.955838	13.24	–	–
^{187}Os[f]	186.955751	1.96	–	–
^{186}Os[g]	185.953838	1.59	2.0×10^{15} y	α
^{184}Os[h]	183.952489	0.02	–	–
^{194}Os	193.965182	–	6.0 y	β^-
^{185}Os	184.954042	–	93.6 d	K-capture; γ, 0.23, 0.65, 0.88
^{191}Os	190.960930	–	15.4 d	β^-, 0.143; γ, 0.129, 0.042
^{193}Os	192.964152	–	30.1 h	β^-, 1.10; γ, 0.065
^{182}Os	181.952110	–	22.1 h	K-capture

(continued)

Table 5.2 (continued)

Isotope	Mass, u	Abundance, %	Half-life period	Decay mode, excitation (radiation) energy, MeV
^{191m}Os	–	–	13.1 h	Isomer; γ, 0.074
^{183}Os	182.95313	–	13.0 h	β^+; γ, 0.3, 1.6
^{183m}Os	–	–	9.9 h	Isomer (15 %); β^+ (85 %); γ, 0.171
^{189m}Os	–	–	5.8 h	Isomer; γ, 0.031
^{181}Os	180.95324	–	105 min	β^+
^{196}Os	195.96964	–	34.9 min	β^-
^{180}Os	179.952379	–	21.5 min	β^+
^{190m}Os	–	–	9.9 min	Isomer; γ, 0.186, 0.356, 0.401, 0.56, 0.62
^{179}Os	178.953816	–	6.5 min	β^+
^{195}Os	194.96813	–	6.5 min	β^-
^{178}Os	177.953251	–	5.0 min	β^+
^{176}Os	175.95481	–	3.6 min	β^+
^{177}Os	176.954965	–	3.0 min	β^+
^{197}Os	–	–	2.8 min	?
^{181m1}Os	–	–	2.7 min	Isomer; β^+; γ, 0.049
^{175}Os	174.956946	–	1.4 min	β^+
^{174}Os	173.957062	–	44 s	β^+ (99.97 %); α (0.024 %)
^{173}Os	172.959808	–	22.4 s	β^+ (99.6 %); α (0.4 %)
^{172}Os	171.960023	–	19.2 s	β^+ (98.9 %); α (1.1 %)
^{171}Os	170.963185	–	8.3 s	β^+ (98.3 %); α (1.7 %)
^{170}Os	169.963577	–	7.5 s	β^+ (91.4 %); α (8.6 %)
^{192m}Os	–	–	5.9 s	Isomer (87 %); β^- (13 %); γ, 2.015
^{169}Os	168.967019	–	3.4 s	β^+ (89 %); α (11 %)
^{168}Os	167.967804	–	2.1 s	β^+ (51 %); α (49 %)
^{167}Os	166.97155	–	0.81 s	α (67 %); β^+ (33 %)
^{166}Os	165.972691	–	0.22 s	α (72 %); β^+ (28 %)
^{165}Os	164.97676 (?)	–	71 ms	α (60 %); β^+ (40 %)
^{164}Os	163.97804	–	21 ms	α (98 %); β^+ (2 %)
^{163}Os	162.98269 (?)	–	5.5 ms	α; β^+, p (rare); β^+ (rare)
^{162}Os	161.98443 (?)	–	1.87 ms	α
^{185m1}Os	–	–	3.0 μs	Isomer; γ, 0.102, ?
^{185m2}Os	–	–	0.78 μs	Isomer; γ, 0.276, ?
^{181m2}Os	–	–	0.32 μs	Isomer; γ, 0.157, ?

[a] Naturally occurring osmium includes six stable (or nearly stable, see below notes *b-f*, *h*) isotopes (^{184}Os, ^{187}Os, ^{188}Os, ^{189}Os, ^{190}Os and most abundant ^{192}Os) and one nearly stable ^{186}Os; the latter has a very long (longer than the age of universe) half-life period

[b] Believed to undergo α decay or β^- β^- decay with a half-life over 9.8×10^{12} years (?)

[c] Believed to undergo α decay (?)

[d] Believed to undergo α decay (?)

[e] Believed to undergo α decay (?)

[f] Believed to undergo α decay (?)

[g] Primordial radionuclide

[h] Believed to undergo α decay or β^- β^- decay with a half-life over 5.6×10^{13} years (?)

Nuclear physical properties of osmium (isotopic mass range, total number of isotopes, thermal neutron macroscopic cross sections, moderating ability and capture resonance integral), compared with other ultra-high temperature elements (carbon and refractory metals), are given in Addendum.

5.6 Chemical Properties

The comprehensive information on the chemical properties and interaction of osmium with all the elements of the periodic table is given in Table 5.3. The osmium containing systems and corresponding binary compounds are described and considered there in accordance to the groups of elements from 1 to 17.

Table 5.3 Chemical interaction of osmium with elements of the periodic table (binary systems in accordance to the groups of elements)[a]

System	Type of phase diagram (constituent phases, temperatures and compositions of transformations)	Character of interaction	References
Group 1			
Os–H	H, no binary compounds, Os No diagram plot	Fine Os powder adsorbs a distinct amount of H_2 with exothermic effect.	[4, 10–11, 31]
Os–Li	α-Li, β-Li, γ-Li, no binary compounds, Os No diagram plot	No interaction between the components, at least at temp. ≤900 °C.	[80]
Os–Na	α-Na, β-Na, no binary compounds, Os No diagram plot	No mutual solubility of the components in the solid and liquid states.	[81]
Os–K	K, KOs (?), KOs_2 (Laves phase, ?), Os No diagram plot	No experimental data.	[12, 17]
Os–Rb	Rb, no binary compounds, Os No diagram plot	The mutual solubilities of the components in the solid and liquid states are very low.	[81]
Os–Cs	Cs, no binary compounds, Os No diagram plot	The mutual solubilities of the components in the solid and liquid states are very low.	[81–82]
Os–Fr	No data	–	–
Group 2			
Os–Be	α-Be, β-Be, $OsBe_{12}$, Os_2Be_{17}, Os_3Be_{17} (?), $OsBe_2$, OsBe (?), Os No diagram plot	Os beryllides are formed by the direct interaction of Os and Be powders after heat treatment at temp. ≥1150 °C.	[4, 13, 32–33]
Os–Mg	Mg, no binary compounds (?), Os Eutectic (degenerated) Mg–Os (~649 °C, ~0.1 at.% Os, ?) No complete diagram plot	The solubility of Os in solid Mg is ~0.06 at.% at eutectic temp.	[12, 83]

(continued)

Table 5.3 (continued)

System	Type of phase diagram (constituent phases, temperatures and compositions of transformations)	Character of interaction	References
Os–Ca	α-Ca, β-Ca, Ca_2Os_3 (?), $CaOs_2$ (Laves phase, ?), $CaOs_5$ (?), Os No diagram plot	No experimental data.	[13, 17]
Os–Sr	No data	–	–
Os–Ba	No data	–	–
Os–Ra	No data	–	–
Group 3			
Os–Sc	α-Sc, β-Sc, $Sc_{44}Os_7$, $Sc_{11}Os_4$, $ScOs_2$ (Laves phase, ?), Os No diagram plot	–	[12, 77, 86]
Os–Y	α-Y, β-Y, Y_3Os (<1290 °C, incongruent melt. point, invariable compos.), YOs_2 (<~2470–2500 °C, congruent melt. point, invariable compos., Laves phase), Os Eutectic Y_3Os–α-Y (1150 °C, ~12 at.% Os) Eutectic YOs_2–Os (2100 °C, ~92–94 at.% Os)	No mutual solubilities between the components in the system.	[12, 14, 84–86]
Lanthanides			
Os–La	α-La, β-La, γ-La, La_3Os, α-$LaOs_2$ (<~1000 °C, Laves phase), β-$LaOs_2$ (?), Os No diagram plot	–	[12, 20, 34, 85–86]
Os–Ce	α-Ce, β-Ce, γ-Ce, δ-Ce, Ce_3Os, α-$CeOs_2$ (Laves phase, ?), β-$CeOs_2$ (<~1000 °C, Laves phase), Os No diagram plot	–	[13, 18, 85–86]
Os–Pr	α-Pr, β-Pr, Pr_3Os (<670 °C, incongruent melt. point, invariable compos.), α-$PrOs_2$ (Laves phase, ?), β-$PrOs_2$ (<2200 °C, incongruent melt. point, invariable compos., Laves phase), Os Eutectic α-Pr–β-$PrOs_2$ (670 °C, 13.8 at.% Os, ?)	The low solid solubility of Os in β-Pr has been found out.	[12, 14, 85–86]
Os–Nd	α-Nd, β-Nd, Nd_3Os, $NdOs_2$ (Laves phase), Os No diagram plot	–	[12, 85–86]

(continued)

Table 5.3 (continued)

System	Type of phase diagram (constituent phases, temperatures and compositions of transformations)	Character of interaction	References
Os–Pm	No data	–	–
Os–Sm	α-Sm, β-Sm, γ-Sm, Sm_3Os, $SmOs_2$ (Laves phase), Os No diagram plot	–	[12, 85–86]
Os–Eu	No data	–	–
Os–Gd	α-Gd, β-Gd, Gd_3Os, $GdOs_2$ (Laves phase), Os No diagram plot	–	[11, 18, 85–86]
Os–Tb	α′-Tb, α-Tb, β-Tb, Tb_3Os, $TbOs_2$ (Laves phase), Os No diagram plot	–	[12, 85–86]
Os–Dy	α′-Dy, α-Dy, β-Dy, Dy_3Os, $DyOs_2$ (Laves phase), Os No diagram plot	–	[85–86]
Os–Ho	α-Ho, β-Ho, Ho_3Os, $HoOs_2$ (Laves phase), Os No diagram plot	–	[11, 85–86]
Os–Er	α-Er, β-Er, Er_3Os, $ErOs_2$ (Laves phase), Os No diagram plot	–	[85–86]
Os–Tm	α-Tm, β-Tm, Tm_3Os, $TmOs_2$ (Laves phase), Os No diagram plot	–	[12, 85–86]
Os–Yb	α-Yb, β-Yb, γ-Yb, $YbOs_2$ (Laves phase, ?), Os No diagram plot	–	[12, 35, 86]
Os–Lu	α-Lu, β-Lu, Lu_3Os, $LuOs_2$ (Laves phase), Os No diagram plot	–	[12, 85–86]
Actinides			
Os–Ac	No data	–	–
Os–Th	α-Th, β-Th, Th_7Os_3 (<at least ~1500–1600 °C, congruent melt. point, invariable compos.), $ThOs_{1-x}$ ($x \approx 0.33$, or Th_3Os_2, <at least ~1500 °C, incongruent melt. point, invariable compos., ?), $ThOs_2$ (<2480 °C, congruent melt. point, invariable compos., Laves phase, ?), Os Eutectic Th_7Os_3–α-Th (~1285 °C, 13 at.% Os) Eutectic Th_7Os_3–$ThOs_{1-x}$ (~1480–1490 °C, 36 at.% Os) Eutectic $ThOs_2$–Os (2200 °C, ~75–85 at.% Os, ?)	–	[12, 14, 20, 78, 82, 87–88, 90]

(continued)

Table 5.3 (continued)

System	Type of phase diagram (constituent phases, temperatures and compositions of transformations)	Character of interaction	References
Os–Pa	No data	–	–
Os–U	α-U, β-U, γ-U, U_3Os (<1030 °C, congruent melt. point), U_2Os (<920 °C, incongruent melt. point, ?), U_5Os_4 (<1280 °C, incongruent melt. point), $UOs_{2\pm x}$ (<2280 °C, congruent melt. point, homog. range—~32.5–33.5 at.% Os, Laves phase, ?), Os Eutectic U_3Os–γ-U (970 °C, 22 at.% Os) Eutectic U_2Os–U_5Os_4 (900 °C, 60 at.% Os) Eutectic $UOs_{2\pm x}$–Os (2170 °C, 28 at.% Os)	The max. solubility of U in Os is <1 at.%. The solubilities of Os in U modifications are following: in α-U—<0.5 at.% at 620 °C, in β-U—4 at.% at 685 °C, in γ-U—18 at.% at 970 °C.	[4, 12, 14, 37, 89–90]
Os–Np	α-Np, β-Np, γ-Np, ?, $NpOs_2$ (Laves phase), Os No diagram plot	–	[90]
Os–Pu	α-Pu, β-Pu, γ-Pu, δ-Pu, δ′-Pu, ε-Pu, η-$Pu_{19\pm x}Os$ (or $Pu_{4.75}Os_{0.25}$, <425 °C, homog. range—~4–8 at.% Os), α-$Pu_{3\pm x}Os$ (<620–625 °C, homog. range—~22–27 at.% Os), β-$Pu_{3+x}Os$ (from 620–625 to 680 °C, incongruent melt. point, homog. range—~25–29 at.% Os), Pu_5Os_3 (<1010 °C, incongruent melt. point, invariable compos.), $PuOs_2$ (<at least 1500 °C, congruent melt. point, invariable compos., Laves phase, ?), Os Eutectic α-$Pu_{3\pm x}Os$–ε-Pu (495 °C, 11 at.% Os)	The solubility of Os in Pu modifications are following: in α-Pu, β-Pu and γ-Pu—<0.3 at.%, in δ-Pu—0.4 at.% at 418 °C, in ε-Pu—6.8 at.% at 495 °C.	[4, 12, 14, 90]
Os–Am	α-Am, β-Am, γ-Am, ?, $AmOs_2$ (Laves phase), Os No diagram plot	–	[90]
Os–Cm	No data		

(continued)

Table 5.3 (continued)

System	Type of phase diagram (constituent phases, temperatures and compositions of transformations)	Character of interaction	References
Group 4			
Os–Ti	α-Ti, β-Ti, δ-$TiOs_{1\pm x}$ (<2160–2180 °C, congruent melt. point, homog. range—~38–51 at.% Os at 1710–2100 °C and ~44.0–50.5 at.% Os at 500–600 °C), Os Eutectic δ-$TiOs_{1\pm x}$–Os (2100 °C, 65 at.% Os)	Os diminishes the temp. of α-Ti–β-Ti polymorphic transformation. The max. solid solubility of Os in β-Ti is ~20–23 at.% at 1710 °C. The solubility of Os in α-Ti at 600 °C is ~1 at.%, and that of Ti in Os is ~21 at.% at 2100 °C, ~13 at.% at 1000 °C and <10 at.% at 500–600 °C.	[4, 12, 14, 38]
Os–Zr	α-Zr, β-Zr, $Zr_{11}Os_4$ (<1350 °C, incongruent melt. point, invariable compos.), ZrOs (<2040 °C, incongruent melt. point, invariable compos.), λ_1-$ZrOs_{2\pm x}$ (<2660 °C, congruent melt. point, homog. range—~61–70 at.% Os at 2040–2440 °C, invariable compos. ($x = 0$) at temp. <1200–1600 °C, Laves phase, ?), Os Eutectic $Zr_{11}Os_4$–β-Zr (~1260–1280 °C, 20 at.% Os) Eutectic λ_1-$ZrOs_{2\pm x}$–Os (~2420–2460 °C, 81 at.% Os)	Os stabilizes β-Zr and diminishes the temp. of α-Zr–β-Zr polymorphic transformation. The solid solubility of Os in β-Zr is ~14 at.% at 1260–1280 °C; it is affected by temp. decrease very slightly. The max. solubility of Os in α-Zr is <1 at.%. The solubility of Zr in Os is ~8 at.% at 2420–2460 °C; it decreases at lower temp.—to 4 at.% at 1100–1200 °C and <3 at.% at 400–500 °C.	[4, 12, 14, 39–43, 77]
Os–Hf	α-Hf, β-Hf, θ-$Hf_{3+x}Os$ (or $Hf_{54}Os_{17}$, <1640–1680 °C, incongruent melt. point, homog. range—~21–23 at.% Os), ε-$Hf_{2+x}Os$ (or $Hf_{71}Os_{29}$, <1860–1900 °C, incongruent melt. point, homog. range—~28–30 at.% Os), η-$Hf_{2\pm x}Os$ (<2040–2080 °C, incongruent melt. point, homog. range—~32–35 at.% Os at 1880 °C and ~33–35 at.% Os at 1000 °C), δ-$HfOs_{1\pm x}$ (<2500–2540 °C, incongruent melt. point, homog. range—~47–52 at.% Os at	Os stabilizes β-Hf and diminishes the temp. of α-Hf–β-Hf polymorphic transformation. The max. solid solubility of Os in β-Hf is ~12 at.% (1580 °C), and in α-Hf it is <2 at.% (1200–1250 °C). The max. solid solubility of Hf in Os is >10 at.% (2600 °C); at lower temp. the solubility decreases to <6 at.% (1000 °C).	[11, 44, 73, 114–115]

Table 5.3 (continued)

System	Type of phase diagram (constituent phases, temperatures and compositions of transformations)	Character of interaction	References
	2060–2520 °C and ~48–50 at.% Os at 1000 °C), λ-$HfOs_{2\pm x}$ (<~2700 °C, congruent melt. point, homog. range—~62–73 at.% Os at 2520–2600 °C and ~64–69 at.% Os at 1000 °C, Laves phase, ?), Os Eutectic θ-$Hf_{3+x}Os$–β-Hf (1580 °C, ~18–20 at.% Os) Eutectic λ-$HfOs_{2\pm x}$–Os (2600 °C, ~80 at.% Os)		
Group 5			
Os–V	V, $V_3Os_{2\pm x}$ (~1570–2140 °C (?), congruent melt. point (?), homog. range—~38–45 at.% Os at 1910 °C and ~38–43 at.% Os at 400–1200 °C, ?), VOs_{1-x} (available data are very controversial), Os Extended solid solution based on V (<1910–2290 °C, up to ~30–46 at.% Os, ?) Extended solid solution based on Os (up to 46–48 at.% V, ?) Eutectic $V_3Os_{2\pm x}$—(Os,V) extended solid solution (1910 °C, ~51–53 at.% Os, ?) Eutectic (V,Os) extended solid solution—(Os,V) extended solid solution (2240 °C, ~41 at.% Os, ?) Peritectic V (~2010 °C, ~31 at.% Os, ?) Phase diagram data available in literature are controversial.	The presence of Os increases the melt. point of V up to 2010–2290 °C. The max. solid solubility of Os in V is ~30–46 at.% at 1570–2010 °C (?) and that of V in Os is 46–48 at.% at 1910–2240 °C. The data on the solubility of Os in V available in literature are very controversial.	[12, 14, 45, 91–92]

(continued)

Table 5.3 (continued)

System	Type of phase diagram (constituent phases, temperatures and compositions of transformations)	Character of interaction	References
Os–Nb	Nb, β-$Nb_{3-x}Os$ (<1975 °C, homog. range—~26–27.5 at.% Os at 1900 °C and ~25–29 at.% Os at 1000 °C), σ-$Nb_3Os_{2\pm x}$ (<2200 °C, congruent melt. point, homog. range—27–46 at.% Os at 1975 °C and ~34.5–44.5 at.% Os at 1000 °C), χ-$Nb_2Os_{3\pm x}$ (<2270 °C, incongruent melt. point, homog. range—~49–63.5 at.% Os at 2120 °C and ~49.5–65 at.% Os at 1000 °C), Os Eutectic σ-$Nb_3Os_{2\pm x}$–Nb (~2175 °C, ~26 at.% Os) Eutectic σ-$Nb_3Os_{2\pm x}$–χ-$Nb_2Os_{3\pm x}$ (~2120 °C, 47 at.% Os)	Os diminishes the melt. temp. of Nb. The max. solid solubility of Nb in Os is 27 at.% at 2270 °C; at lower temp. it decreases to ~20 at.% (1000 °C). The max. solid solubility of Os in Nb is ~19 at.% at 2175 °C; at lower temp. it decreases to ~14–15 at.% (1000 °C).	[12, 14, 46]
Os–Ta	Ta, σ-$Ta_3Os_{2\pm x}$ (<~2500 °C, incongruent melt. point, homog. range—~22–44 at.% Os), γ-$Ta_2Os_{3\pm x}$ (<~2420 °C, incongruent melt. point, homog. range—48–63 at.% Os), Os Extended solid solution based on Ta (up to ~22 at.% Os at 2500 °C) Extended solid solution based on Os (~25 at.% Ta at 1600 °C) Eutectic σ-$Ta_3Os_{2\pm x}$–γ-$Ta_2Os_{3\pm x}$ (~2360–2400 °C, ~47 at.% Os)	Os diminishes the melt. temp. of Ta considerably. The solubility of Ta in Os is ~19 at.% at 2420 °C, ~20 at.% at 2000 °C and ~25 at.% at 1600 °C. The solubility of Os in Ta is ~22 at.% at 2500 °C and ~14 at.% at 2200 °C.	[4, 12, 14]

(continued)

Table 5.3 (continued)

System	Type of phase diagram (constituent phases, temperatures and compositions of transformations)	Character of interaction	References
Group 6			
Os–Cr	Cr, $Cr_{3\pm x}Os$ (<1540 °C, homog. range—~23–29 at.% Os), σ-$Cr_{2\pm x}Os$ (975–1675 °C, homog. range—30–35 at.% Os (?) at 1540 °C), Os Extended solid solution based on Cr (<~1900 °C, up to ~28 at.% Os, ?) Extended solid solution based on Os (up to ~62 at.% Cr, ?) Eutectic (Cr,Os) extended solid solution—(Os,Cr) extended solid solution (~1835–1855 °C, ~33 at.% Os)	The solubility of Os in Cr is ~28 at.% at 1845 °C, ~22 at.% at 1675 °C, ~20 at.% at 1540 °C and ~9.5–18.0 at.% at 1300 °C; practically, at temp. <1300 °C it is not affected by temp. The solubility of Cr in Os is ~62 at.% at 1845 °C, ~55 at.% at 1675 °C and ~50–52 at.% at 1500 °C; practically, at <1500 °C it is not affected by temp. too.	[4, 11, 15, 47–48]
Os–Mo	Mo, β-$Mo_{3\pm x}Os$ (<2210 °C, homog. range—~25–26 at.% Os at 2100 °C and ~24–26 at.% Os at 1000 °C), σ-$Mo_{2\pm x}Os$ (<2420–2440 °C, homog. range—~30–37 at.% Os at 2370–2390 °C and ~30–40 at.% Os at 1000 °C), Os Extended solid solution based on Mo (up to 19.5 at.% Os at 2370–2390 °C) Extended solid solution based on Os (up to 52 at.% Mo at 2420–2440 °C) Eutectic σ-$Mo_{2\pm x}Os$–(Mo, Os) extended solid solution (~2370–2390 °C, ~20.5–21.0 at.% Os)	Os diminishes the melt. temp. of Mo. The solubility of Os in Mo is 19.5 at.% at 2370–2390 °C and <8 at.% at 1000 °C. The solubility of Mo in Os is 52 at.% at 2420–2440 °C and <40 at.% at 1000–1200 °C.	[12, 14, 19, 49–50]
Os–W	See W–Os in Table 3.5.		

(continued)

Table 5.3 (continued)

System	Type of phase diagram (constituent phases, temperatures and compositions of transformations)	Character of interaction	References
Group 7			
Os–Mn	α-Mn, β-Mn, γ-Mn, δ-Mn, no binary compounds (?), Os No complete diagram plot	The presence of Os increases the temp. of α-Mn–β-Mn transition from 727 to 762 °C. At 400–600 °C the solubility of Os in α-Mn is ~17 at.% and in β-Mn >40 at.%.	[93]
Os–Tc	Tc, no binary compounds, Os Continuous solid solution Tc–Os (?) No diagram plot	–	[12–51]
Os–Re	See Re–Os in Table 4.5.		
Group 8			
Os–Fe	α-Fe, γ-Fe, δ-Fe, no binary compounds, Os Extended solid solution based on Os (up to 75–78 at.% Fe at 400–600 °C) Peritectic δ-Fe (~1535–1565 °C, ~1.5–3.0 at.% Os) Peritectic γ-Fe (1720 °C, ~25 at.% Os)	Os raises the melt. temp. of Fe and temp. of δ-Fe–γ-Fe polymorphic transformation. In the presence of Os the γ-Fe phase exists in the wide range of temp. from ~620 °C to 1720 °C. The max. solubilities of Os in Fe polymorphic modifications are following: ~5 at.% in α-Fe (620 °C), ~25 at.% in γ-Fe (1720 °C) and ~1.5–3.0 at.% in δ-Fe (1535–1565 °C).	[4, 11, 14, 52–54]
Os–Ru	Ru, no binary compounds, Os Continuous solid solution Ru–Os	–	[12, 14, 20, 55]
Group 9			
Os–Co	ε-Co, α-Co, no binary compounds, Os Continuous solid solution ε-Co–Os Peritectic α-Co (~1600 °C, ~20–22 at.% Os)	Os stabilizes ε-Co modification; at 1200 °C the limit of solid solubility of Os in ε-Co is ~20 at.%.	[4, 11, 14]

(continued)

Table 5.3 (continued)

System	Type of phase diagram (constituent phases, temperatures and compositions of transformations)	Character of interaction	References
Os–Rh	Rh, no binary compounds, Os Peritectic Rh (~2575–2625 °C, ~55 at.% Os)	The presence of Os results in increase in the melt. temp. of Rh. The max. melt. point (~2575–2625 °C) and max. solid solubility of Os in Rh (~55 at.%) are corresponding to the peritectic alloy. The solubility of Os in Rh declines slightly with temp. decreasing; at 1500 °C it amounts to ~50–51 at.%. The max. solid solubility of Rh in Os is ~30 at.% (~2575–2625 °C); at lower temp. the solubility of Rh declines (≤20 at.% at 1500 °C).	[12, 14]
Os–Ir	Ir, no binary compounds, Os Peritectic Ir (~2625–2695 °C, 44.5 at.% Os) Extended solid solution based on Ir (up to 44.5 at.% Os at ~2625–2695 °C) Extended solid solution based on Os (up to 38 at.% Ir at ~2625–2695 °C)	The presence of Os results in increase in the melt. temp. of Ir. The max. melt. point (~2625–2695 °C) and max. solid solubility of Os in Ir (44.5 at.%) are corresponding to the peritectic alloy. At 2200 °C the solubility of Os in Ir and that of Ir in Os are 42–43 and 36–37 at.%, respectively. At lower temp. the mutual solid solubilities of the components are not affected by temp.	[4, 12, 14, 113]
Group 10			
Os–Ni	Ni, no binary compounds, Os Peritectic Ni (~1465–1500 °C, ~12.0–13.3 at.% Os) Extended solid solution based on Os (up to ~12–64 at.% Ni (?) at 1465–1500 °C)	Practically, the melt. temp. of Ni is affected by the presence of Os only slightly. The max. solid solubility of Os in Ni (~12.0–13.3 at.%) is corresponding to the peritectic alloy. The data on the mutual solubilities of Os and Ni available in literature are controversial.	[4, 12, 14, 112]

(continued)

Table 5.3 (continued)

System	Type of phase diagram (constituent phases, temperatures and compositions of transformations)	Character of interaction	References
Os–Pd	Pd, no binary compounds, Os Peritectic Pd (1615–1665 °C, ~1–3 at.% Os)	The solubility of Os in Pd declines with temp. decreasing considerably. The max. solid solubility of Pd in Os is 5.2 at.% (1615–1665 °C); at lower temp. the solubility of Pd declines.	[12, 14–15, 20, 56]
Os–Pt	Pt, no binary compounds, Os Peritectic Pt (~1940–1970 °C, ~25 at.% Os) Extended solid solution based on Pt (up to 25 at.% Os at ~1940–1970 °C)	The presence of Os results in increase in the melt. temp. of Pt. The max. melt. point (~1940–1970 °C) and max. solid solubility of Os in Pt (~25 at.%) are corresponding to the peritectic alloy. The solid solubility of Os in Pt is affected by temp. slightly. The max. solubility of Pt in Os is ≤9.3 at.%.	[4, 12, 14, 57]
Group 11			
Os–Cu	Cu, no binary compounds, Os Eutectic (degenerated, ?) Cu–Os (~1081 °C, <0.5 at.% Os, ?) Miscibility gap in the liquid state (?) Phase diagram data available in literature are controversial	At 900 °C the solubility of Os in Cu is negligibly small.	[4, 11, 14]
Os–Ag	Ag, no binary compounds, Os Eutectic (degenerated, ?) Ag–Os (~961 °C, ?)	Practically, the components are immiscible in the solid and liquid states.	[13–14, 58]
Os–Au	Au, no binary compounds, Os No diagram plot	At 900–950 °C the solubility of Os in Au is absolutely negligible.	[4, 13, 59]
Group 12			
Os–Zn	Zn, no binary compounds, Os No diagram plot	No interaction.	[4, 12]
Os–Cd	No data	–	–

(continued)

Table 5.3 (continued)

System	Type of phase diagram (constituent phases, temperatures and compositions of transformations)	Character of interaction	References
Os–Hg	Hg, no binary compounds, Os The eutectic depression or peritectic elevation of Hg melt. by Os addition are indistinguishable.	The theoretically estimated solubility of Os in liquid Hg at 25 °C is $\sim 10^{-19} \div 10^{-24}$ at.%. The solubility of Hg in solid Os is <1 at.%. Os is highly resistant to corrosion in liquid Hg (no evidence of interaction after 350 h exposure at 800 °C).	[14, 94–95]
Group 13			
Os–B	β-B, OsB_{12} (?), OsB_3 (?), Os_2B_5 (?), OsB_2, (<~2175–2200 °C, congruent melt. point, invariable compos.), Os_2B_3 (or $OsB_{1.6}$, <at least ~1600 °C, incongruent melt. point, invariable compos.), OsB_{1+x} (or $OsB_{1.2}$, <~1575–1600 °C, congruent melt. point, invariable compos.), Os Eutectic OsB_2–β-B (>~1995–2000 °C, ~20 at.% Os) Eutectic Os_2B_3–OsB_{1+x} (~1500 °C, ~44–45 at.% Os) Eutectic OsB_{1+x}–Os (<~1450–1500 °C, ~55 at.% Os)	No data on mutual solubilities of the components. Os borides are formed directly from the elements in vacuum at 800–1400 °C.	[4, 10, 13, 14, 60–61, 71]
Os–Al	Al, $OsAl_5$ (?), $OsAl_3$ (or Os_4Al_{13}, ?), $OsAl_2$, Os_2Al_3, OsAl, Os No diagram plot	No data on mutual solubilities of the components. Os aluminides are formed directly from the elements.	[10, 13, 62]
Os–Ga	Ga, $OsGa_3$, $OsGa_2$, ?, Os No diagram plot	Other binary compounds were synthesized only under high pressures (6.5–7.7 GPa).	[11, 24]
Os–In	In, In_3Os (?), In_2Os (?), InOs (?), $InOs_2$ (Laves phase, ?), Os Miscibility gap in the liquid state (?) No diagram plot Data on the system available in literature are controversial.	No interaction in the liquid state (?).	[12, 96]
Os–Tl	No data	–	–

(continued)

Table 5.3 (continued)

System	Type of phase diagram (constituent phases, temperatures and compositions of transformations)	Character of interaction	References
Group 14			
Os–C	See C–Os in Table 2.13.		
Os–Si	Si, $OsSi_3$ (?), $OsSi_2$ (or $OsSi_{1.8}$, <1620–1660 °C, incongruent melt. point, invariable compos.), Os_2Si_3 (<1820–1860 °C, congruent melt. point, invariable compos.), $OsSi_{1\pm x}$ (<1720–1740 °C, incongruent melt. point corresp. to ~$OsSi_{1.04}$, homog. range—~49–50 at.% Os at 1700 °C and ~49–51 at.% Os at 1000 °C), Os Eutectic $OsSi_2$–Si (~1340–1370 °C, ~10–13 at.% Os) Eutectic $OsSi_{1\pm x}$–Os (~1710–1730 °C, ~54–58 at.% Os)	No data on mutual solubilities of the components. Os silicides are formed directly from the elements in vacuum or inert gas atmosphere at 1000–1200 °C.	[4, 10, 12, 14, 25, 63–66, 79, 97, 116]
Os–Ge	Ge, $OsGe_2$, Os_2Ge_3, Os No diagram plot	–	[4, 10–11, 25–26]
Os–Sn	α-Sn, β-Sn, no binary compounds at normal pressure, Os No diagram plot	No interaction. At normal pressure the mutual solubilities of the components are extremely low. A binary compound was synthesized only under high pressures (7.7 GPa).	[4, 12, 20, 36]
Os–Pb	No data	–	–
Group 15			
Os–N	N, Os_2N (metastable, ?), Os No diagram plot	No interaction at normal pressures in the wide range of temp.; at high pressures (43 GPa) OsN_2 is synthesized.	[12, 98]
Os–P	P, α-OsP_4 (invariable compos., ?), β-OsP_4 (<~425 °C, invariable compos.), OsP_2 (<1095 °C, invariable compos.), Os	Os diphosphide is formed directly from the elements in sealed ampules at 500–800 °C.	[4, 10, 12, 14, 99–100, 102]
Os–As	As, $OsAs_{2\pm x}$ ($0 \leq x \leq 0.2$, <at least 1600 °C, ?), Os	Os arsenide is formed directly from the elements in sealed ampules.	[10, 13–14, 102]

(continued)

Table 5.3 (continued)

System	Type of phase diagram (constituent phases, temperatures and compositions of transformations)	Character of interaction	References
Os–Sb	Sb, $OsSb_2$, Os No diagram plot	–	[12, 101–102]
Os–Bi	Bi, no binary compounds, Os	At 750–800 °C the solubility of Os in liquid Bi is $<8 \times 10^{-4}$ at.%.	[13–14, 103]
Group 16			
Os–O	O, OsO_4 (<40–42 °C, melt. point), OsO_3 (?), OsO_2 (<650 °C, decomposes), Os_2O_3 (?), Os No diagram plot	In pure O_2 the oxidation of Os in powder form initiates from room temp. and leads to the direct formation of OsO_4, which vaporizes above 130 °C. OsO_2 is formed by indirect reaction pathways. For diffusion rate in the system at various temp. see Addendum.	[2, 4, 10, 12, 20, 70]
Os–S	α-S, β-S, OsS_2 (<at least 2450 °C, invariable compos.), Os Eutectic OsS_2–Os (~2000 °C, ~50 at.% Os)	OsS_2 is formed by the direct interaction between Os and S at temp. ≥950 °C.	[4, 10, 12, 14, 20, 27, 104]
Os–Se	Se, $OsSe_2$ (<at least 700 °C, invariable compos.), Os	$OsSe_2$ is formed by the direct interaction between Os and Se.	[4, 10, 12, 14, 67]
Os–Te	Te, α-$OsTe_2$ (?), β-$OsTe_2$ (<at least 800 °C, invariable compos.), Os	$OsTe_2$ is formed by the direct interaction between Os and Te.	[10, 12, 14, 68, 105]
Os–Po	No data	–	–
Group 17			
Os–F	F, OsF_8 (?), OsF_7 (?), OsF_6 (<33–35 °C, melt. point), OsF_5 (<70 °C, melt. point), OsF_4, Os No diagram plot	The direct interaction between Os and F_2 at 280–300 °C results in the formation of OsF_4 and OsF_6. OsF_5 is synthesized by decomposition of OsF_6.	[2–4, 10, 69, 106]
Os–Cl	Cl, $OsCl_4$, $OsCl_3$ (or Os_xCl_{3x}), $OsCl_2$, Os No diagram plot	The direct interaction between Os and Cl_2 results in the formation of $OsCl_3$ at temp. <500 °C, or $OsCl_4$ at temp. >650 °C. $OsCl_3$ decomposes to $OsCl_2$ in vacuum.	[2–3, 10]

(continued)

Table 5.3 (continued)

System	Type of phase diagram (constituent phases, temperatures and compositions of transformations)	Character of interaction	References
Os–Br	Br, $OsBr_4$, $OsBr_3$, Os No diagram plot	The direct interaction between the elements in sealed ampules at ~500 °C results in the formation of $OsBr_4$. $OsBr_3$ is synthesized by decomposition of $OsBr_4$ in vacuum.	[2–3, 10, 69]
Os–I	I, OsI_4, OsI_3, OsI_2, OsI, Os No diagram plot	Os iodides are synthesized by indirect reaction pathways.	[2–3, 10]
Os–At	No data	–	–

[a] The intervals of temperatures and compositions for the melting and invariant equilibria points, homogeneity ranges and thermal stability regions of constituent phases are given taking into account the minimal and maximal values (data spread) available in literature

The data on the selected ternary, quaternary and quasi-binary osmium containing systems, which are the most important for the design, manufacture and application of ultra-high temperature materials, are summarized in Table 5.4. The composition and temperature stability regions for the main binary and ternary osmium containing high temperature phases are given in Tables 5.3 and 5.4 taking into account the spread of numerical magnitudes available in literature currently.

Table 5.4 Chemical interaction of osmium with elements and compounds at high temperatures (selected ternary, quaternary and quasi-binary systems in alphabetical order)[a]

System	Type of phase diagram (temperature and composition sections, constituent phases or phase fields) and/or character of interphase interaction and materials compatibility	References
Os–B–Hf	No diagram plot Hf_9Os_4B	[74]
Os–B–Mo	No diagram plot Mo_2OsB_2, $(Mo,Os)B_2$	[74–75]
Os–B–C–Th	See C–B–Os–Th in Table 2.14	
Os–B–W	See W–B–Os in Table 3.6	
Os–C–Co–W	See C–Co–Os–W in Table 2.14	
Os–C–Hf	See C–Hf–Os in Table 2.14	
Os–C–Mo	See C–Mo–Os in Table 2.14	
Os–C–Nb	See C–Nb–Os in Table 2.14	
Os–C–Sc	See C–Os–Sc in Table 2.14	
Os–C–Si	See C–Os–Si in Table 2.14	
Os–C–Ta	See C–Os–Ta in Table 2.14	

(continued)

Table 5.4 (continued)

System	Type of phase diagram (temperature and composition sections, constituent phases or phase fields) and/or character of interphase interaction and materials compatibility	References
Os–C–Th	See C–Os–Th in Table 2.14	
Os–C–Ti	See C–Os–Ti in Table 2.14	
Os–C–U	See C–Os–U in Table 2.14	
Os–C–V	See C–Os–V in Table 2.14	
Os–C–W	See C–Os–W in Table 2.14	
Os–C–Y	See C–Os–Y in Table 2.14	
Os–C–Zr	See C–Os–Zr in Table 2.14	
Os–Co–Re–Ru	See Re–Co–Os–Ru in Table 4.6	
Os–Cr–W	See W–Cr–Os in Table 3.6	
Os–Fe–Ir	Plotted at 650 and 900 °C: (Ir,Fe,Os) extended solid solution based on Ir–γ-Fe continuous solid solution at higher temp., or (Ir,Fe,Os) extended solid solution based on Ir at lower temp., (Os,Fe,Ir) extended solid solution based on Os, ε-$IrFe_{2\pm x}$ ($<\sim$625 °C), α-Fe, δ-Fe	[11– 12, 14, 72]
Os–Hf–Ir	Plotted schematically: $Hf(Os,Ir)_{1\pm x}$ (δ-$HfOs_{1\pm x}$–$HfIr_{1\pm x}$ continuous solid solution, <2440–2540 °C), $Hf_{2+x}(Ir,Os)$ (extended solid solution based on $Hf_{2+x}Ir$, $<\sim$1720–1775 °C), $Hf_5(Ir,Os)_3$ (extended solid solution based on Hf_5Ir_3, $<\sim$1930–1970 °C), $Hf(Ir,Os)_{3\pm x}$ (extended solid solution based on $HfIr_{3\pm x}$, <2460–2470 °C), θ-$Hf_{3+x}(Os,Ir)$ (solid solution based on θ-$Hf_{3+x}Os$), ε-$Hf_{2+x}Os$, η-$Hf_{2\pm x}Os$, λ-$Hf(Os,Ir)_{2\pm x}$ (extended solid solution based on λ-$HfOs_{2\pm x}$), α-Hf, β-(Hf,Ir,Os) (extended solid solution based on β-Hf), (Ir,Os,Hf) (extended solid solution based on Ir), (Os,Ir,Hf) (extended solid solution based on Os)	[73]
Os–Ir–Th	No diagram plot $ThOs_2$–$ThIr_{2\pm x}$ continuous solid solution (?)	[108]
Os–Ir–Ti	Plotted schematically: $Ti(Os,Ir)_{1\pm x}$ (δ-$TiOs_{1\pm x}$–α-$TiIr_{1\pm x}$ (<1040 °C), δ-$TiOs_{1\pm x}$–β-$TiIr_{1\pm x}$ (at least from $\sim$1040 to 1750 °C) and δ-$TiOs_{1\pm x}$–γ-$TiIr_{1\pm x}$ (from ? to 2130–2180 °C) continuous solid solutions, ?), $Ti_{3-x}(Ir,Os)$ (solid solution based on $Ti_{3-x}Ir$, <1515 °C), $Ti(Ir,Os)_{3\pm x}$ (extended solid solution based on $TiIr_{3\pm x}$, $<\sim$2115–2125 °C), α-Ti, β-(Ti,Ir,Os) (extended solid solution based on β-Ti), (Ir,Os,Ti) (extended solid solution based on Ir), (Os,Ir,Ti) (extended solid solution based on Os)	[73]

(continued)

Table 5.4 (continued)

System	Type of phase diagram (temperature and composition sections, constituent phases or phase fields) and/or character of interphase interaction and materials compatibility	References
Os–Ir–Zr	Plotted schematically: $Zr(Os,Ir)_{1\pm x}$ (ZrOs–α-$ZrIr_{1-x}$ (<900–950 °C) and ZrOs–β-$ZrIr_{1\pm x}$ (from 900–950 °C to 2040–2050 °C) continuous solid solutions), $Zr_3(Ir,Os)$ (solid solution based on Zr_3Ir, <1305 °C), $Zr_2(Ir,Os)$ (solid solution based on Zr_2Ir, <1340 °C), $Zr_5(Ir,Os)_3$ (solid solution based on Zr_5Ir_3, <1730 °C), $Zr(Ir,Os)_2$ (solid solution based on $ZrIr_2$, <2085 °C), $Zr(Ir,Os)_{3\pm x}$ (extended solid solution based on $ZrIr_{3\pm x}$, <2280 °C), $Zr_{11}(Os,Ir)_4$ (solid solution based on $Zr_{11}Os_4$), λ_1-$Zr(Os,Ir)_{2\pm x}$ (extended solid solution based on λ_1-$ZrOs_{2\pm x}$), α-Zr, β-(Zr,Ir,Os) (extended solid solution based on β-Zr), (Ir,Os,Zr) (extended solid solution based on Ir), (Os,Ir,Zr) (extended solid solution based on Os)	[73, 107]
Os–Hf–W	See W–Hf–Os in Table 3.6	
Os–Mo–Ta	Plotted partially at 1000 °C (Mo,Ta-rich area: (Mo,Ta,Os) solid solution based on (Mo,Ta) continuous solid solutions)	[109]
Os–Mo–W	See W–Mo–Os in Table 3.6	
Os–N–Zr	No diagram plot $Zr_{\sim 4}Os_{\sim 2}N$	[16]
Os–Nb–Rh	No diagram plot β-$Nb_{3-x}Os$–$Nb_{3\pm x}Rh$ continuous solid solution (?)	[110]
Os–Nb–Ta	Plotted partially at 1000 °C (Nb,Ta-rich area: (Nb,Ta,Os) solid solution based on (Nb,Ta) continuous solid solutions)	[109]
Os–Nb–W	See W–Nb–Os in Table 3.6	
Os–O–Re	See Re–O–Os in Table 4.6	
Os–Re–Ru	See Re–Os–Ru in Table 4.6	
Os–Re–Ta	See Re–Os–Ta in Table 4.6	
Os–Re–W	See W–Os–Re in Table 3.6	
Os–Ta–V	Plotted partially at 1000 °C (Ta,V-rich area: (Ta,V,Os) solid solution based on (Ta,V) continuous solid solutions with $\sim V_{0.9}Ta_{0.1}$–$V_{0.6}Ta_{0.225}Os_{0.175}$–$V_{0.5}Ta_{0.5}$ miscibility gap, $V_{2\pm x}Ta$)	[109]
Os–Ta–W	See W–Os–Ta in Table 3.6	
Os–V–W	See W–Os–V in Table 3.6	

[a] See notes to Table 5.3

The character of chemical interaction and general reactions of osmium with common chemicals (solids, liquids, aqueous solutions) and complex gases are summarized in Table 5.5.

Table 5.5 The interaction of osmium with some chemicals and complex gases [4, 10, 70]

Reagent, formula	Character of chemical interaction, examples of general reactions
Air, $N_2 + O_2$	No interaction at room temp. At atmospheric pressure the oxidation of Os in powder form initiates at ~200 °C, the intensive oxidation of Os compact parts begins from 500–600 °C: $Os + 2O_2 \rightarrow OsO_4$ (boil. point—131 °C).
Water, H_2O	No interaction at room temp., at temp. >200 °C water vapour interacts with Os intensively: $Os + 4H_2O \rightarrow OsO_4 + 4H_2$.
Sodium hydroxide, NaOH	No interaction with NaOH in aqueous solution; the weak interaction occurs between Os and molten NaOH.
Potassium hydroxide, KOH	No interaction with KOH in aqueous solution.
Potassium nitrate with potassium hydroxide (melt), $KNO_3 + KOH$	The interaction results in the formation of osmates: $Os + 3KNO_3 + 2(n + 1)KOH \rightarrow K_{2(n+1)}OsO_{n+4} + 3KNO_2 + (n + 1)H_2O$.
Potassium chlorate with potassium hydroxide (melt), $KClO_3 + KOH$	The interaction results in the formation of osmates: $Os + KClO_3 + 2(n + 1)KOH \rightarrow K_{2(n+1)}OsO_{n+4} + KCl + (n+1)H_2O$.
Potassium peroxide with potassium hydroxide (melt), $K_2O_2 + KOH$	The interaction results in the formation of osmates: $Os + 3K_2O_2 + 2nKOH \rightarrow K_{2(n+3)}OsO_{n+6} + nH_2O$.
Potassium nitrate with potassium carbonate (melt), $KNO_3 + K_2CO_3$	The interaction results in the formation of osmates: $Os + 3KNO_3 + (n+1)K_2CO_3 \rightarrow K_{2(n+1)}OsO_{n+4} + 3KNO_2 + (n + 1)CO_2$.
Nitric acid, HNO_3	No interaction in the absence of O_2.
Sulphuric acid, H_2SO_4	No interaction in the absence of O_2.
Hydrofluoric acid, HF	No interaction.
Hydrochloric acid, HCl	No interaction.
Hydrochloric acid with nitric acid (aqua regia), $HCl + HNO_3$	No interaction in the absence of O_2.

The diffusion characteristics in osmium containing systems in the wide range of temperatures, and summarized data on the physico-chemical interaction of osmium with elements of the periodic table are given in Addendum.

References

1. Steurer W (1996) Crystal structure of the metallic elements. In: Cahn RW, Haasen P (eds) Physical metallurgy, 4th ed., Vol. 1, pp. 1-46. Elsevier Science BV, Amsterdam
2. Cotton FA, Wilkinson G (1965) Advanced inorganic chemistry. Wiley, New York, London
3. Akhmetov NS (2001) Obschaya i neorganicheskaya khimiya (General and inorganic chemistry), 4th ed. Vysshaya Shkola, Moscow (in Russian)

4. Kotelnikov RB, Bashlykov SN, Galiakbarov ZG, Kashtanov AI (1968) Osobo tugoplavkie elementy i soedineniya (Extra refractory elements and compounds). Metallurgiya, Moscow (in Russian)
5. Zefirov AP (ed), Veryatin UD, Mashirev VP, Ryabtsev NG, Tarasov VI, Rogozkin BD, Korobov IV (1965) Termodinamicheskie svoistva neorganicheskikh veschestv (Thermodynamic properties of inorganic substances). Atomizdat, Moscow (in Russian)
6. Speight JG, ed (2005) Lange's handbook of chemistry, 16th ed. McGraw-Hill, New York
7. Lide DR, ed (2010) CRC handbook of chemistry and physics, 90th ed. CRC Press, Boca Raton, New York
8. Martienssen W (2005) The elements. In: Martienssen W, Warlimont H (eds) Springer handbook of condensed matter and materials data, pp. 45-158. Springer, Berlin, Heidelberg
9. Samsonov GV, ed (1976) Svoistva elementov (Properties of elements), 2nd ed., Vol. 1. Metallurgiya, Moscow (in Russian)
10. Samsonov GV, ed (1976) Svoistva elementov (Properties of elements), 2nd ed., Vol. 2. Metallurgiya, Moscow (in Russian)
11. Lyakishev NP, ed (1997) Diagrammy sostoyaniya dvoinykh metallicheskikh sistem (Phase diagrams of binary metal systems), Vol. 2. Mashinostroenie, Moscow (in Russian)
12. Lyakishev NP, ed (2001) Diagrammy sostoyaniya dvoinykh metallicheskikh sistem (Phase diagrams of binary metal systems), Vol. 3, Part 1. Mashinostroenie, Moscow (in Russian)
13. Lyakishev NP, ed (1996) Diagrammy sostoyaniya dvoinykh metallicheskikh sistem (Phase diagrams of binary metal systems), Vol. 1. Mashinostroenie, Moscow (in Russian)
14. Massalski TB, Subramanian PR, Okamoto H, Kacprzak L, eds (1990) Binary alloy phase diagrams, 2nd ed. ASM International, Metals Park, Ohio
15. Savitskii EM, Polyakova VP, Gorina NB, Roshan NR (1975) Metallovedenie platinovykh metallov (Metallography of platinum metals). Metallurgiya, Moscow (in Russian)
16. Holleck H (1984) Binäre und ternäre Carbid- und Nitridsysteme der Ubergangsmetalle (Binary and ternary carbide and nitride systems of the transition metals). Gebrüder Borntträeger, Berlin (in German)
17. Savitskii EM, Gribulya VB (1977) Prognozirovanie neorganicheskikh soedinenii s pomoschyu EVM (The prediction of inorganic compounds by means of computing). Nauka, Moscow (in Russian)
18. Gladyshevskii EI, Bodak OI (1982) Kristallokhimiya intermetallicheskikh soedinenii redkozemelnykh metallov (The crystal chemistry of intermetallic compounds of rare earth metals). Vyshcha Shkola, Lviv (in Russian)
19. Brewer L, Lamoreaux RH (1980) Phase diagrams. In: Brewer L (ed) Molybdenum. Physico-chemical properties of its compounds and alloys. Atomic Energy Review, Special Issue N 7, pp. 195-356. International Atomic Energy Agency, Vienna
20. Savitskii EM, ed (1984) Blagorodnye metally (Noble metals). Metallurgiya, Moscow (in Russian)
21. Audi G, Wapstra AH, Thibault C, Blachot J, Bersillon O (2003) The NUBASE evaluation of nuclear and decay properties. Nucl Phys A 729:3-128
22. De Laeter JR, Bohlke JK, De Bievre P, Hidaka H, Peiser HS, Rosman KJR, Taylor PDP (2003) Atomic weights of the elements. Review 2000 (IUPAC Technical report). Pure Appl Chem 75(6):683-800
23. Wieser ME (2006) Atomic weights of the elements 2005. (IUPAC Technical report). Pure Appl Chem 78(11):2051-2066
24. Popova SV, Fomitcheva LN (1982) Novye fazy v sistemakh Re-Ga i Os-Ga, poluchennye pri vysokom davlenii (The new phases in the Re-Ga and Os-Ga systems obtained at high pressure). Izv AN SSSR Neorg Mater 18(2):251-255 (in Russian)
25. Gladyshevskii EI (1971) Kristallokhimiya silitsidov i germanidov (The crystal chemistry of silicides and germanides). Metallurgiya, Moscow (in Russian)
26. Samsonov GV, Bondarev VN (1968) Germanidy (Germanides). Metallurgiya, Moscow (in Russian)
27. Samsonov GV, Drozdova SV (1972) Sulfidy (Sulfides). Metallurgiya, Moscow (in Russian)

28. Schroder RH, Schmitz-Pranghe N, Kohlhaas R (1972) Experimentelle Bestimmung der Gitterparameter der Platinmetalle im Temperaturbereich –190 bis 1709 °C (Experimental determination of the lattice parameters of platinum metals in the temperature range from –190 to 1709 °C). Z Metallkd 63:12-16 (in German)
29. Degussa AG (1995) Edelmetal – Taschenbuch (Precious Metal – Paperback), 2nd ed. Hüthig, Heidelberg (in German)
30. Benner LS, Suzuki T, Meguro K, Tanaka S, eds (1991) Precious metals, science, technology. International Precious Metals Institute, Allentown
31. Antonov VE, Belash IT, Malyshev VYu, Ponyatovsky EG (1984) Solubility of hydrogen in the platinum metals under high pressure. Platinum Met Rev 28(4):158-163
32. Obrowski W (1963) Alloys of ruthenium with boron, beryllium and aluminium. Metall 17(2):108-112
33. Verkhorobin LF, Kovtun GP, Kruglykh AA, Matyushenko NN, Pugachev AS, Tikhinskii GF (1971) Berillidy ruteniya, osmiya, rodiya i iridiya sostava M_2Be_{17} (Ruthenium, osmium, rhodium and iridium beryllides with M_2Be_{17} composition). Izv AN SSSR Metally (6):168-171 (in Russian)
34. Cannon JF, Robertson DL, Tracy HH, Lawson AC (1973) The effect of high pressure on the crystal structure of $LaOs_2$ and $CeOs_2$. J Less-Common Met 31(1):174-176
35. Iandelli A, Palenzona A (1976) Das Verhalten des Ytterbiums mit den Metallen der achten Gruppe des periodischen Systems (The reaction of the ytterbium to the metals of the eighth group of the periodic table). Rev Chim Miner 13(1):55-61 (in German)
36. Kalyaeva NV, Popova SV (1983) Vliyanie vysokogo davleniya na obrazovanie promezhutochnykh faz v sisteme Os-Sn (The effect of high pressure on the formation of intermediate phases in the Os-Sn system). Izv AN SSSR Neorg Mater 19(7):1106-1109 (in Russian)
37. Knapton AG (1963) The uranium-osmium system. J Nucl Mater 9(3):309-319
38. Eremenko VN, Shtepa TD, Semenova OL (1971) Diagramma sostoyaniya Ti-Os (The Ti-Os constitution diagram). Izv AN SSSR Metally (4):210-213 (in Russian)
39. Eremenko VN, Shtepa TD, Semenova OL (1972) Diagrama stanu tsirkonii – osmii v oblasti 50-100 at.% osmiyu (Constitution diagram zirconium – osmium in the area of 50-100 at.% osmium). Dopov Akad Nauk Ukr RSR Ser B 34(1):50-52 (in Ukrainian)
40. Eremenko VN, Semenova OL, Shtepa TD (1976) Diagrama stanu tsirkonii – osmii (Constitution diagram zirconium – osmium). Dopov Akad Nauk Ukr RSR Ser A Fiz Mat Tekh Nauki 38(7):661-664 (in Ukrainian)
41. Eremenko VN, Semenova EA, Shtepa TD (1978) Vliyanie rodiya, iridiya i osmiya na polimorfnoe ($\alpha \leftrightarrow \beta$)-prevrashchenie tsirkoniya (The effects of rhodium, iridium and osmium on the ($\alpha \leftrightarrow \beta$)-transformation of zirconium). Izv AN SSSR Metally (2):200-203 (in Russian)
42. McCarthy SL, Schmidt L (1971) A new compound in the zirconium-osmium alloy system. J Less-Common Met 23(2):241-242
43. Inoue A, Matsuzaki K, Masumoto T, Chen HS (1986) Superconducting and electrical properties of amorphous zirconium – transition metal binary alloys. J Mater Sci 21(4):1258-1268
44. Waterstrat RM (1983) The Hf-Os constitution diagram. J Less-Common Met 95(2):335-339
45. Raub E, Röschel E (1966) Die Vanadium-Osmium-Legierungen (The vanadium-osmium alloys). Z Metallkd 57(6):470-472
46. Waterstrat RM, Manuszewski RC (1977) The niobium-osmium constitution diagram. J Less-Common Met 51(1):55-67
47. Svechnikov VN, Dmitrieva GV, Kobzenko GF, Shurin AK (1964) Diagramma fazovykh ravnovesii sistemy khrom-osmii (Phase equilibrium diagram in the chromium-osmium system). Doklady AN SSSR 158(3):668-670 (in Russian)
48. Venkatraman M, Neumann JP (1990) The Cr-Os (chromium-osmium) system. Bull Alloy Phase Diagrams 11(1):8-11
49. Taylor A, Doyle N, Kagle BJ (1962) The constitution diagram of the system molybdenum-osmium. J Less-Common Met 4(5):436-450

50. Erley W, Wagner H (1973) Interdiffusion in the system molybdenum-osmium. Phys Status Solidi A 19(1):K23-K26
51. Darby JB, Jr, Lam DJ, Norton LJ, Downey JW (1962) Intermediate phases in binary systems of technetium-99 with several transition elements. J Less-Common Met 4(6):558-563
52. Kubaschewski O (1982) Iron binary phase diagrams. Springer, Berlin
53. Swartzendruber LJ, Sundman B (1983) The Fe-Os (iron-osmium) system. Bull Alloy Phase Diagrams 4(4):396-399
54. Bannykh OA, Budberg SP, Alisova SP (1986) Diagrammy sostoyaniya dvoinykh i mnogokomponentnykh system na osnove zheleza (The constitution diagrams of binary and multi-component systems based on iron). Metallurgiya, Moscow (in Russian)
55. Tylkina MA, Polyakova VP, Savitskii EM (1962) Diagramma sostoyaniya splavov sistemy osmii-rutenii (The constitution diagram of the ruthenium-osmium alloys system). Zh Neorg Khim 7(6):1467-1468 (in Russian)
56. Tylkina MA, Polyakova VP, Khamidov OKh (1963) Diagramma sostoyaniya sistemy palladii-osmii (The constitution diagram of the palladium-osmium system). Zh Neorg Khim 8(3):776-779 (in Russian)
57. Voronova LI, Polyakova VP, Savitskii EM (1984) Alloys of the system Pt-Os. Rus Metall (5):201-203
58. Karakaya I, Thompson WT (1986) The Ag-Os (silver-osmium) system. Bull Alloy Phase Diagrams 7(4):360-362
59. Okamoto H, Massalski TB (1984) The Au-Os (gold-osmium) system. Bull Alloy Phase Diagrams 5(4):382
60. Kempter CP, Fries RG (1961) Crystallography of the Ru-B and Os-B systems. J Chem Phys 34(6):1994-1995
61. Roof RB Jr, Kempter CP (1962) New orthorhombic phases in the Ru-B and Os-B systems. J Chem Phys 37(7):1473-1476
62. Esslinger P, Schubert K (1957) Zur Systematik der Strukturfamilie des NiAs. I. Verbeitung der Strukturen der NiAs-Familie (The systematics of the family structure of NiAs. I. Distribution of the structures of NiAs family). Z Metallkd 48(3):126-134 (in German)
63. Berezhnoy AS (1958) Kremnii i ego binarnye sistemy (Silicon and its binary systems). UkrSSR Academy of Sciences, Kyiv (in Russian)
64. Finnie LN (1962) Structures and compositions of the silicides of ruthenium, osmium, rhodium and iridium. J Less-Common Met 4(1):24-34
65. Samsonov GV, Dvorina LA, Rud BM (1979) Silitsidy (Silicides). Metallurgiya, Moscow (in Russian)
66. Schellenberg L, Braun HF, Muller J (1988) The osmium-silicon phase diagram. J Less-Common Met 144(2):341-350
67. Obolonchik VA (1972) Selenidy (Selenides). Metallurgiya, Moscow (in Russian)
68. Chizhikov DM, Schastlivyi VP (1966) Tellur i telluridy (Tellurium and tellurides). Nauka, Moscow (in Russian)
69. Nekrasov BV (1973) Osnovy obschei khimii (Foundations of general chemistry), 3rd ed., Vol. 2. Khimiya, Moscow (in Russian)
70. Goodwin F, Guruswamy S, Kainer KU, Kammer C, Knabl W, Koethe A, Leichtfried G, Schlamp G, Stickler R, Warlimont H (2005) Metals. In: Martienssen W, Warlimont H (eds) Springer handbook of condensed matter and materials data, pp. 161-430. Springer, Berlin, Heidelberg
71. Hebbache M, Stuparevic L, Zivkovic D (2006) A new superhard material: osmium diboride OsB_2. Solid State Commun 139:227-231
72. FactSage (2010) Data from SGnobl – SGTE noble metal alloy database. http://www.crct.polymtl.ca/fact/phase_diagram.php?file=Fe-Ir-Os_650.jpg&dir=SGnobl and http://www.crct.polymtl.ca/fact/phase_diagram.php?file=Fe-Ir-Os_900.jpg&dir=SGnobl Collection of phase diagrams. Accessed 6 September 2011.
73. Khoruzhaya VG (1996) Interaction of transition metals of group IV with high-melting platinum metals in binary and ternary systems. Powder Metall Met Ceram 35(7-8):433-440

74. Nowotny H, Rogl P (1977) Ternary metal borides. In: Matkovich VI (ed) Boron and refractory borides, pp. 413-438. Springer, Berlin, Heidelberg, New York
75. Rogl P, Benesovsky F, Nowotny H (1972) Über einige Komplexboride mit Platinmetallen (About complex boride with some platinum metals). Monatsh Chem 103(4):965-989 (in German)
76. Argon AS (1996) Mechanical properties of single-phase crystalline media: deformation at low temperatures. In: Cahn RW, Haasen P (eds) Physical metallurgy, 4th ed., Vol. 3, pp. 1877-1955. Elsevier Science BV, Amsterdam
77. Chabot B, Cenzual K, Parthe E (1980) $Sc_{11}Ir_4$, $Sc_{11}Os_4$, $Sc_{11}Ru_4$, $Zr_{11}Os_4$ with a new cubic structure type described by means of a cluster concept. Acta Crystallogr B 36:7-11
78. Thompson JR (1964) Alloys of thorium with certain transition metals. II. The systems thorium-osmium, thorium-iridium and thorium-platinum. J Less-Common Met 6(1):3-10
79. Korst WL, Finnie LN, Searcy AW (1957) The crystal structure of the monosilicides of osmium, iridium and ruthenium. J Phys Chem 61(11):1541-1543
80. Sangster J, Pelton AD (1992) The Li-Os (lithium-osmium) system. J Phase Equilib 13(1):62-63
81. Loebich O Jr, Raub ChJ (1981) Reactions beween some alkali metals and platinum group metals. Platinum Met Rev 25(3):113-120
82. Moffatt WG (1986) Binary phase diagrams handbook. General Electric Co., Schenectady, New York
83. Gulyaev BB (1968) Obobshchenie diagram sostoyaniya metallicheskikh system (Generalization of the phase diagrams of metallic systems). In: Savitskii EM (ed) Diagrammy sostoyaniya metallicheskikh system (Phase diagrams of metallic systems), p. 257-267. Nauka, Moscow (in Russian)
84. Savitskii EM, Polyakova VP (1975) Physico-chemical research in noble metals. J Less-Common Met 43(1-2):169-177
85. Palenzona A (1980) The crystal structure of the rare-earth-rich osmium compounds R_3Os and Y_3Os. J Less-Common Met 72(1):P21-P24
86. Dwight AE, Downey JW, Conner RA Jr (1966) Laves phases of the scandium group elements with ruthenium, rhodium, osmium, iridium and platinum. Trans Metall Soc AIME 236:1509-1510
87. Chiotti P, Akhachinksij VV, Ansara I, Rand MH (1982) The Os-Th (osmium-thorium) system. Bull Alloy Phase Diagrams 3:101-102
88. Thomson JR (1964) Alloys of thorium with certain transition metals. II. The systems thorium-osmium, thorium-iridium and thorium-platinum", J Less-Common Met 6:3-10
89. Nishioka T, Kimura K, Matsui H, Kontani M (1994) Magnetic, transport and thermal properties of itinerant magnetic U-T (T = Os, Ru and Rh) systems. J Phys Soc Jpn 63:2722-2730
90. Lam DJ, Mitchell AW (1972) Laves phases of actinide elements. J Nucl Mater 44(3):279-284
91. Susz CP, Flükiger R, Jorda JL, Muller J (1979) Equilibrium phase fields in the vanadium-osmium system. J Less-Common Met 63:P45–P52
92. Smith JF (1988) The Os-V (osmium-vanadium) system. J Alloy Phase Diagrams 4:122-126
93. Yamauchi R, Miyakawa M, Sasao K, Fukamichi K (2000) X-ray diffraction and magnetic properties of β-$Mn_{1-x}Os_x$ alloys. J Alloys Compd 311:124-129
94. Guminski C (1995) The Hg-Os (mercury-osmium) system. J Phase Equilib 16:81-82
95. Guminski C (1989) Selected properties of simple amalgams. J Mater Sci 24:2661-2676
96. Dieva EN (1974) Rastvorimost tugoplavkikh metallov v zhidkom indii (The solubility of refractory metals in liquid indium). In: Bamburov VG (ed) Fiziko-khimicheskie issledovaniya zhidkikh metallov i splavov (Physico-chemical studies of liquid metals and alloys), p. 105-106. Uralskii Nauchnyi Tsentr AN SSSR, Sverdlovsk (in Russian)
97. Liu YQ, Shao G, Homewood KP (2001) Thermodynamic assessment of the Ru-Si and Os-Si systems. J Alloys Compd 320:72-79

98. Yu R, Zhan Q, De Jonghe LC (2007) Crystal structures of and displacive transitions in OsN_2, IrN_2, RuN_2 and RhN_2. Angew Chem Int Ed 46:1136-1140
99. Chernogorenko VB, Solomatina LY (1983) The synthesis and properties of osmium diphosphide and the equilibrium diagram of the Os-P system. Russ J Inorg Chem 28:1100-1102
100. Flörke U, Jeitschko W (1982) Preparation and properties of new modifications of RuP_4 and OsP_4 with CdP_4-type structure. J Less-Common Met 86:247-253
101. Kuzmin RN, Zhuravlev NN, Losievskaya SA (1960) The atomic structure of $RuSb_2$ and $OsSb_2$. Sov Phys Crystallogr 5:202-206
102. Kjekshus A, Rakke T, Andresen AF (1977) Compounds with the marcasite type crystal structure. XII. Structural data for RuP_2, $RuAs_2$, $RuSb_2$, OsP_2, $OsAs_2$, and $OsSb_2$. Acta Chem Scand A 31:253-259
103. Okamoto H (1994) The Bi-Os (bismuth-osmium) system. J Phase Equilib 15:189-190
104. Okamoto H (1994) Comment on Os-S (osmium-sulfur) system. J Phase Equilib 15:455
105. Kjekshus A, Rakke T (1975) Compounds with the marcasite type crystal structure. XI. High temperature studies of chalcogenides. Acta Chem Scand A 29:443-452
106. Drews T, Supel J, Hagenbach A, Seppelt K (2006) Solid state molecular structures of transitional metal hexafluorides. Inorg Chem 45:3782-3788
107. Waterstrat RM, Kuentzler R, Muller J (1990) Structural instabilities and superconductivity in quasi-binary Mn_5Si_3-type compounds. J Less-Common Met 167:169-178
108. Houghton JS, Dewees M, Lawson AC, Smith JL (1982) Superconductivity of $Th(Ir,Os)_2$ and $Th(Ir,Ru)_2$ alloys. J Less-Common Met 83:L47–L49
109. English JJ (1961) Binary and ternary phase diagrams of columbium, molybdenum and tungsten. Report AD-TR-257-739, Contract AF 33(616)-7747, pp. 1-241. Defence Metals Information Center, Battelle Memorial Institute, Columbus, Ohio
110. Zegler ST (1965) Superconductivity in Cr_3Si-type ternary phases with niobium and group VIII metals. Phys Rev 137:A1438–A1440
111. Winter M (2012) WebElements: the periodic table on the WWW. Osmium: enthalpies and thermodynamic properties. http://www.webelements.com/osmium/thermochemistry.html Accessed 20 May 2013.
112. Okamoto H (2009) The Ni-Os (nickel-osmium) system. J Phase Equilib Diffus 30(6):662
113. Okamoto H (1994) The Ir-Os (iridium-osmium) system. J Phase Equilib 15(1):55-57
114. Okamoto H (2007) The Hf-Os (hafnium-osmium) system. J Phase Equilib Diffus 28(6):593
115. Okamoto H (1994) Comment on Hf-Os (hafnium-osmium) system. J Phase Equilib 15(6):653-654
116. Okamoto H (2007) The Os-Si (osmium-silicon) system. J Phase Equilib Diffus 28(4):410

Chapter 6
Tantalum

6.1 Structures

Tantalum is element No. 73 of the periodic table (period—6, group—5 (or VB), relates to transition metals) with the ground state level $^4F_{3/2}$ and electron configuration $1s^2 2s^2 2p^6 3s^2 3p^6 3d^{10} 4s^2 4p^6 4d^{10} 4f^{14} 5s^2 5p^6 5d^3 6s^2$. The general oxidation states (numbers) of tantalum in various chemical compounds are (–1), (+1), (+2), (+3), (+4) and (+5); the oxidation state (+5) is the most common; the radii of tantalum are:

atomic (metallic, CN = 8)—0.143 nm,
atomic (metallic, CN = 12)—0.147 nm,
atomic (covalent)—0.134 nm,
ionic (+3)—0.072 nm (CN = 6),
ionic (+4)—0.068 nm (CN = 6),
ionic (+5)—0.064 nm (CN = 6);

its electronegativity is 1.5 in Pauling scale, or 1.47 in Allred–Rochow scale [1–3, 6–8, 11]. Elemental tantalum has body-centred cubic (bcc) metal crystal structure (space group—*Im(–3)m*, W type) with lattice parameter $a = 0.33026$ nm (Z = 2) at 20 °C (minimum interatomic distance—0.2860 nm, CN = 8), slip (cleavage) plane (110) and slip direction <111> [50, 179].

So-called β-Ta phase usually occurs as thin films, obtained by magnetron sputtering, chemical vapour deposition or electrochemical deposition from molten salts [51]; it is metastable and converts to the common state upon heating to 750–775 °C, its crystal structure—tetragonal, space group—*P(–4)2₁m* and lattice parameters $a = 1.0184$ nm, $c = 0.5306$ nm [52].

At room temperature the XRD density of tantalum is 16.68 g cm^{-3} and recommended value for the bulk density of common metal parts—16.60–16.65 g cm^{-3} [4, 6, 11].

I. L. Shabalin, *Ultra-High Temperature Materials I*,
DOI: 10.1007/978-94-007-7587-9_6,

6.2 Thermal Properties

The melting point of tantalum is one of the highest among the elements of the periodic table; it is exceeded only by tungsten, rhenium and osmium for metals and carbon. The general thermodynamic properties of tantalum are summarized in Table 6.1. For the molar heat capacity $c_p = f(T, \text{K})$, J mol^{-1} K^{-1}, the following relationships are recommended:

in the range of temperatures from 298 to 2500 K [5]:

$$c_p = 24.37 + \left(3.266 \times 10^{-3}\right)T, \tag{6.1}$$

in the range of temperatures from 400 to 2400 K [9]

$$c_p = 24.26 + \left(2.958 \times 10^{-3}\right)T + \left(0.2038 \times 10^{-6}\right)T^2, \tag{6.2}$$

For the specific heat capacity $c_p = f(T, \text{K})$, J kg^{-1} K^{-1} the equation is given [53] as

$$c_p = 139.04 + \left(1.757 \times 10^{-2}\right)T + \left(1.375 \times 10^{-6}\right)T^2. \tag{6.3}$$

The equilibrium vapour pressure of tantalum P, Pa, at temperatures 298–2500 K is obeyed the rule [7]:

$$\lg P = -41346/T + 0.7437/T^3 - 3.2152 \lg T + 21.813, \tag{6.4}$$

where T is temperature, K. In high vacuum, the rate of tantalum vaporization at the temperatures of 1800, 2050 and 2300 °C approximately amounts to 0.1 μm, 10 μm, 1 mm per year, respectively [4]. The values of standard molar entropy $S°_{298}$, molar c_p and specific c heat capacities, enthalpies (heats) of melting and vaporization, molar and specific mass enthalpy differences $H_T - H_{298}$, vapour pressures and mass/linear vaporization rates for tantalum are given in Addendum in comparison with carbon (graphite) and other ultra-high temperature materials (refractory metals) in the wide ranges of temperatures. At ambient temperatures the thermal conductivity of unalloyed tantalum λ = 54–61 W m^{-1} K^{-1} [8, 11, 53]; the character of its variation with temperature [4, 10] is shown in Fig. 6.1.

At room temperature the coefficient of linear thermal expansion of unalloyed tantalum $\alpha = (6.3–6.6) \times 10^{-6}$ K^{-1} [8, 10–11, 53], while for the interval from 20 to 1700 °C the recommended value is 7.7×10^{-6} K^{-1} [4]. The variation of the coefficient of linear thermal expansion α with temperature is expressed by the equation as follows [53]:

$$\alpha = 6.5 + \left(0.34 \times 10^{-3}\right)t + \left(0.12 \times 10^{-6}\right)t^2 \tag{6.5}$$

where t denotes the value of temperature, °C; for the wide range of temperatures the variation of α is also presented in Fig. 5.1. The surface tension of liquid tantalum (density 15.0 g cm^{-3}) is 2.15 N m^{-1} (its temperature coefficient is -0.25×10^{-3} N m^{-1} K^{-1}) [8]. In comparison with other ultra-high temperature

Table 6.1 General thermodynamic properties of tantalum

Characteristics	Symbol	Unit	Value	References
Standard molar entropy (at 298.15 K and 100 kPa)	S°_{298}	J mol^{-1} K^{-1}	41.50 ± 0.17	[4, 7]
			41.47	[6, 8, 11]
			41.4	[5, 9, 53]
Enthalpy difference	H_{298}–H_0	kJ mol^{-1}	5.682	[8]
Standard molar heat capacity (at 298.15 K and 100 kPa)	$c^\circ_{p,298}$	J mol^{-1} K^{-1}	25.40	[6–7, 9]
			25.39	[4]
			25.30	[8]
Specific heat capacity (at 298.15 K)	c	J kg^{-1} K^{-1}	140.3	[4]
			139.8	[11]
			138	[6]
Molar enthalpy (heat) of melting (at the melting point)	ΔH_m	kJ mol^{-1}	36.57	[6–8, 11]
			31.4	[5, 9]
Specific enthalpy (heat) of melting (at the melting point)		kJ kg^{-1}	202	[11]
			155	[4]
			145–174	[53]
Molar enthalpy (heat) of vaporization (at the boiling point)	ΔH_v	kJ mol^{-1}	751	[4]
			743	[8]
			733	[6, 11]
Specific enthalpy (heat) of vaporization (at the boiling point)		kJ kg^{-1}	4150	[4]
			4050	[11]
			4160–4270	[53]
Melting point	T_m	K (°C)	3290 (3020)	[7–8]
			3270 (3000)	[4, 6, 9, 11]
			3265 (2995)	[53]
Boiling point	T_b	K (°C)	5780 (5510)	[8]
			5730 (5460)	[7]
			5700 (5430)	[11, 53]
			5690 (5420)	[6]
			5560 (5290)	[9]

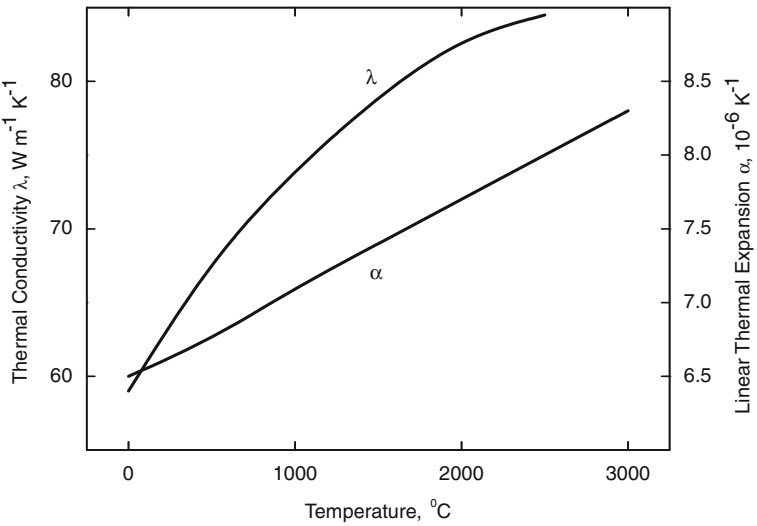

Fig. 6.1 The generalized variations of the thermal conductivity (λ) and linear thermal expansion (α) of unalloyed tantalum with temperature [4, 8, 10, 53]

materials (graphite and refractory metals), the values of thermal conductivity and thermal expansion of tantalum in the wide range of temperatures are summarized in Addendum.

6.3 Electro-Magnetic and Optical Properties

At room temperature the specific electrical resistance (resistivity) of pure tantalum $\rho = 125-140$ nΩ m; in the range of cryogenic temperatures 10–100 K it varies from 6 to 40 nΩ m, and at elevated and ultra-high temperatures the resistivity is almost obeyed the classic metal model (with small deviation from linearity) and slightly exceeds 1 μΩ m at 2400–2600 °C. In the interval 0–100 °C the temperature coefficient of resistivity equals 3.82×10^{-3} K^{-1}, and in the interval 20–1730 °C it is 2.53×10^{-3} K^{-1} (the pressure coefficient is -1.62×10^{-5} MPa^{-1}) [4, 8, 10–11, 53]. Together with the temperature growth, relatively minute amounts of contaminations by the interstitial atomic species, such as oxygen, nitrogen and carbon also increase the electrical resistance of refractory metals; the following relationship for the resistivity of tantalum ρ, nΩ m, was recommended by Gebhardt et al. [54]:

$$\rho = 136 + \left(367.2 \times 10^{-3}\right)t + 59.84c_O \tag{6.6}$$

where t is temperature, °C and c_O is oxygen content in contaminated metal tantalum, mas. %. At 0 °C the Hall coefficient of tantalum equals $R = 1.01 \times 10^{-10}$

$m^3\ A^{-1}\ s^{-1}$ ($B = 0.5$–2.9 T), Seebeck coefficient (absolute thermoelectric power) is -5.0 μV K^{-1} [8, 11]. Tantalum is a paramagnetic metal with molar magnetic susceptibility χ_m (SI) $= 1.935 \times 10^{-3}\ cm^3\ mol^{-1}$ at 22 °C [8].

The variations of main optical properties of tantalum with wavelength λ are following [9, 11]:

index of refraction (single crystal)—from 0.5 ($\lambda = 0.05$ μm) to 2.2 ($\lambda = 0.60$ μm);
index of absorptance (polycrystalline materials)—from 0.2 ($\lambda = 0.05$ μm) to 2.0 ($\lambda = 0.60$ μm);
reflective index under normal incidence (polished polycrystalline materials)—from 0.13 ($\lambda = 0.05$ μm) to 0.46 ($\lambda = 0.65$ μm), or to 0.95 ($\lambda = 12.0$ μm).

In the range of temperatures from 0 to 2900 °C the monochromatic emittance (spectral emissivity) ε_λ ($\lambda = 0.65$ μm) of non-oxidized tantalum varies from 0.51 to 0.37 decreasing linearly with temperature growth, while the integral emittance ε_T increases with temperature growth from 0.03 at 20 °C to 0.27–0.35 at 2000–2700 °C [4, 9–10]. For the surface of oxidized tantalum ε_λ varies from 0.79 at 830 °C to 0.77 at 1230 °C, and ε_T varies from 0.045 at 70 °C to 0.448 at 960 °C [9–10]. The averaged magnitude of electron work function of pure tantalum is 4.12–4.25 eV [4, 8–9]; for the faces of single crystal with various (*hkl*)-indices the magnitudes are: (100)—4.15 eV, (110)—4.80 eV, (111)—4.00 eV, (112)—4.3–4.4 eV, (116)—~3.9 eV, (130)—4.57 eV and (211)—4.35 eV [9]. The approximate Richardson constant (thermoelectronic emission constant) of tantalum is 37 A $m^{-2}\ K^{-1}$ [4]. The recommended values of electrical resistivity, magnetic susceptibility, integral and spectral emittances and thermoionic emission characteristics (electron work function and Richardson constants) for tantalum are given in comparison with other ultra-high temperature elements (carbon and refractory metals) in Addendum.

6.4 Physico-Mechanical Properties

Most of the physico-mechanical characteristics of tantalum are extremely sensitive to the microstructure features, which are strongly dependent on metal working (treatment), as well as to the relatively minute amounts of contaminations by the interstitial atomic species, such as oxygen, nitrogen, carbon and hydrogen. The oxygen content increases the hardness of tantalum from 0.4 GPa (HV) for highly purified tantalum to 2.5 GPa (HV) for tantalum containing about 1 at.% oxygen, or 5.6 GPa (HV) for tantalum with 3 at.% oxygen [4]. For various microstructure states, the hardness (HB) comes to the following values:

arc cast and cold worked (hardened)—230 kgf mm^{-2} (2.25 GPa);
identical metal annealed (recrystallized)—140 kgf mm^{-2} (1.37 GPa);

electron-beam refined (one remelting procedure)—70 kgf mm^{-2} (0.69 GPa);
electron-beam refined (two remelting procedures)—45–55 kgf mm^{-2} (0.44–0.54 GPa).

The temperature behaviour of hardness for tantalum is rather complicated because of the presence of two flexion points on the hardness-temperature curve, which are connected with changing the mechanism of deformation [4].

The retardation of grain growth (recrystallization) process by the interstitial impurities is the main reason why melt-processed tantalum has a lower tensile strength at ambient temperatures compared to the metal produced by powder metallurgy methods. An example of the profound influence of oxygen impurities on the ultimate tensile strength, fracture elongation and reduction in area of tantalum specimens tested at room temperature is given in Fig. 6.2 [49]. The fracture elongation of tantalum is in the inverse relation with its hardness [10]. Contrary to tungsten and molybdenum, pure tantalum is deformed at room temperature easily and characterized by a high ductility and low work-hardening rate. The deformation dependences of yield strength and elongation of pure tantalum are presented in Fig. 6.3 [55]. The ultimate tensile strength of unalloyed tantalum at room temperature in various microstructure states comes to the following values [4]:

arc cast and cold worked (hardened)—0.93–0.96 GPa;
identical metal annealed (recrystallized)—0.44–0.54 GPa;
tantalum wire (diameter 0.3–1.5 mm)—0.88–1.13 GPa;
tantalum wire (diameter 10–100 μm)—1.52–1.76 GPa.

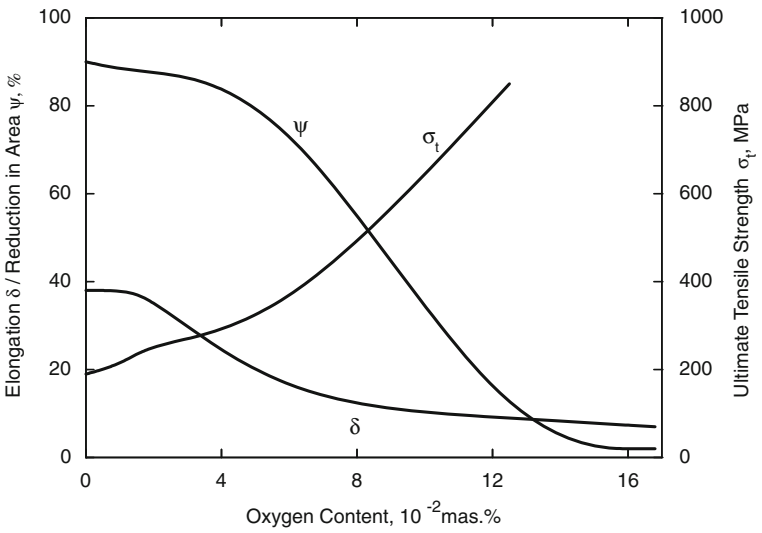

Fig. 6.2 Variations of ultimate tensile strength (σ_t), fracture elongation (δ) and reduction in area (ψ) of tantalum with oxygen content at room temperature [49]

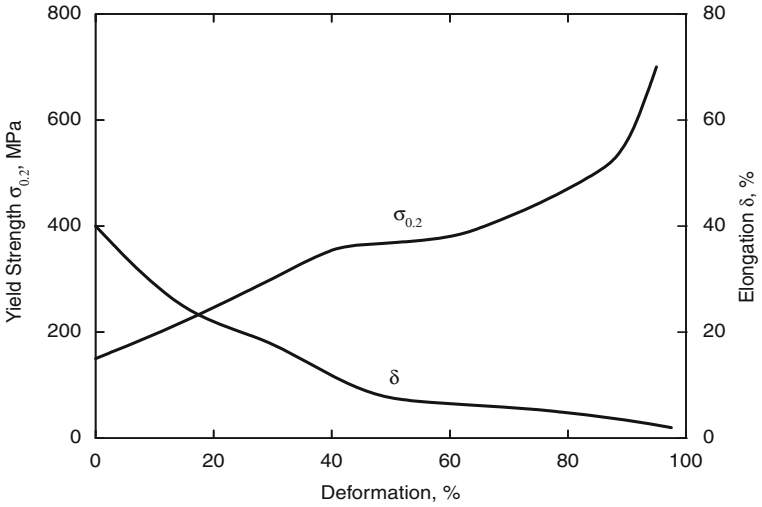

Fig. 6.3 Deformation dependencies of yield strength ($\sigma_{0.2}$) and fracture elongation (δ) of unalloyed tantalum [55]

The generalized variations of ultimate tensile strength of annealed commercially pure tantalum with temperature for high and low strain rates and interstitial contents are shown in Fig. 6.4 [4, 53]. The values of prolonged strength are of great importance for the evaluation of operational time at high-temperatures; examples of the creep behaviour of electron-beam melted tantalum together with general data on 100 h creep rupture for pure tantalum are presented in Fig. 6.5. Some information on the impact and fatigue strength of tantalum is given in [53], and the fatigue properties of tantalum are summarized in [12].

At room temperature the main elastic properties of pure tantalum have the following numerical values [4, 8, 10–11, 53]:

Young's modulus E, GPa		185–186
Coulomb's (shear) modulus G, GPa		65–69
Poisson's ratio ν		0.34–0.35
Bulk (compression) modulus K, GPa		193–207
Volume compressibility κ, MPa^{-1}		0.5×10^{-5}
Longitudinal velocity of sound	V_S, m s^{-1}	3400–4100
Transversal velocity of sound	V_T, m s^{-1}	2030–2900
Elastic compliance	s_{11}, TPa^{-1}	6.89
	s_{44}, TPa^{-1}	12.1
	s_{12}, TPa^{-1}	–2.58
Elastic stiffness	c_{11}, GPa	264
	c_{44}, GPa	82.6
	c_{12}, GPa	158

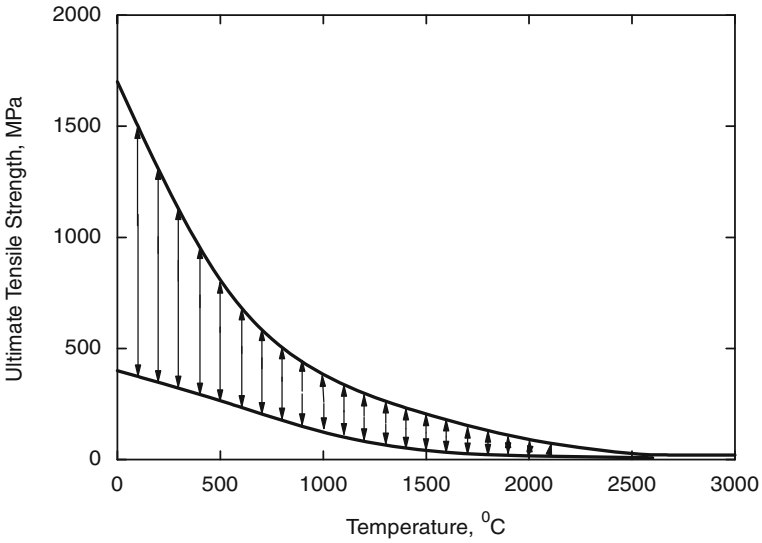

Fig. 6.4 The generalized variation of ultimate tensile strength of annealed commercially pure tantalum with temperature (the upper portion of the marked area is characterized by high strain rates and high interstitial content, whereas the lower portion of the marked area is characterized by low strain rates and low interstitial content) [4, 8, 53]

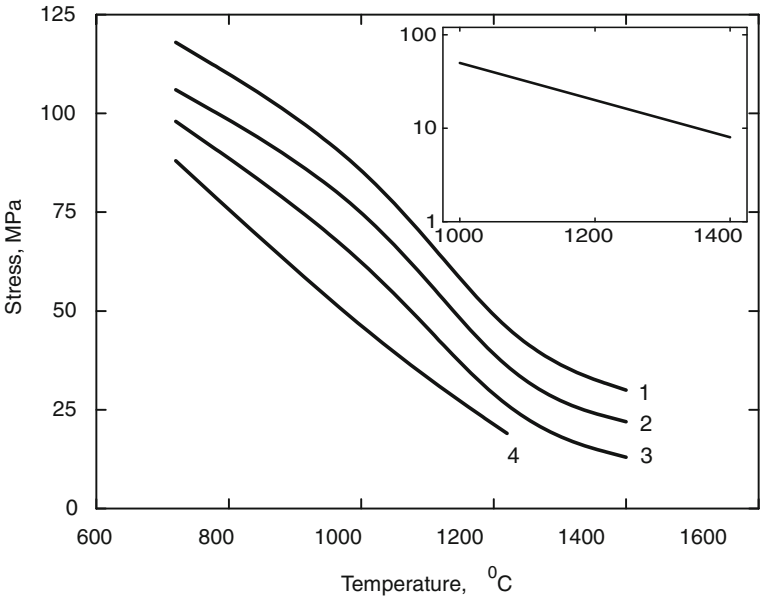

Fig. 6.5 5 % creep characteristics of electron-beam melted tantalum (1 mm sheet, 75 % cold rolled and annealed at 1200 °C for 1 h, impurities: C 0.30, O 0.16, N 0.10 and other <0.4, 10^{-2} mas. %): *1*—0.1 h; *2*—1 h; *3*—10 h; *4*—100 h [53] (*Inset*—100 h rupture stress creep characteristics of unalloyed tantalum [56])

The presence of the interstitial impurities in tantalum affects the value of Young's modulus considerably, e.g. the oxygen content growth to 2 at.% leads to the increase of Young's modulus of tantalum—up to 193 GPa [4].

The magnitudes of physico-mechanical (strength, elasticity) properties of unalloyed tantalum in the wide range of temperatures are summarized in Addendum in comparison with other ultra-high temperature materials (graphite and refractory metals).

6.5 Nuclear Physical Properties

The isotopes of tantalum (standard atomic mass—180.94788 u) from ^{155}Ta to ^{190}Ta, including metastable states (^{156m}Ta, $^{157m1-2}$Ta, $^{158m-161m}$Ta, ^{165m}Ta, $^{176m1-3}$Ta, $^{177m1-4}$Ta, $^{178m1-3}$Ta, $^{179m1-6}$Ta, $^{180m1-4}$Ta, $^{181m1-4}$Ta, $^{182m1-2}$Ta, ^{183m}Ta, ^{185m}Ta and ^{186m}Ta), and their general characteristics are summarized in Table 6.2; the naturally occurring isotopes are listed in order of decreasing abundance, and unstable artificial (radioactive) isotopes—in order of decreasing half-life period of decay.

Table 6.2 General characteristics of the isotopes of tantalum [7, 9, 41–43]

Isotope	Mass, u	Abundance, %	Half-life period	Decay mode, excitation (radiation) energy, MeV
^{181}Ta[a]	180.947996	99.99	–	–
^{180m1}Ta[b]	–	0.01	–	Isomer, γ, 0.077
^{179}Ta	178.945930	–	1.82 y	*K*-capture; γ, 0.7
^{182}Ta	181.950152	–	114 d	β^-; γ, from ~0.06 to 1.60
^{183}Ta	182.951373	–	5.1 d	β^-, 0.675 (>95 %); 1.0 (<5 %); γ, 0.24
^{177}Ta	176.944472	–	2.4 d	β^+; γ, 1.4
^{175}Ta	174.94374	–	10.5 h	β^+
^{184}Ta	183.954008	–	8.7 h	β^-, 1.26 (70 %), 0.15 (30 %); γ, 0.410, 0.86, 1.1 and others
^{180}Ta	179.947465	–	8.15 h	*K*-capture (86 %); β^- (14 %), 0.7 (50 %), 0.61 (50 %); γ, 0.093, 0.102
^{176}Ta	175.94486	–	8.1 h	β^+; γ, ~2
^{173}Ta	172.94375	–	3.1 h	β^+
^{178m1}Ta	–	–	2.4 h	Isomer; β^+, 0.100
^{174}Ta	173.94445	–	1.14 h	β^+
^{185}Ta	184.955559	–	49.4 min	β^-, 1.72 (70 %), 0.15 (30 %); γ, 0.06, 0.125, 0.175, 0.235
^{172}Ta	171.94490	–	36.8 min	β^+

(continued)

Table 6.2 (continued)

Isotope	Mass, u	Abundance, %	Half-life period	Decay mode, excitation (radiation) energy, MeV
^{171}Ta	170.94448	–	23.3 min	β^+
^{182m2}Ta	–	–	15.8 min	Isomer; γ, 0.519
^{178}Ta	177.945778	–	9.3 min	β^+, ~1; γ, ~1.5
^{186}Ta	185.95855	–	10.5 min	β^-, 2.26; γ, from 0.125 to 1.100
^{170}Ta	169.94618	–	6.8 min	β^+
^{169}Ta	168.94601	–	4.9 min	β^+
^{168}Ta	167.94805	–	2.0 min	β^+
^{187}Ta	186.96053 (?)	–	2.0 min (?)	β^-
^{186m}Ta	–	–	1.54 min	Isomer, ?
^{167}Ta	166.94809	–	1.33 min	β^+
^{166}Ta	165.95051	–	34.4 s	β^+
^{165}Ta	164.950773	–	31.0 s	β^+
^{188}Ta	187.96370 (?)	–	20 s (?)	β^-
^{164}Ta	163.95353	–	14.2 s	β^+
^{163}Ta	162.95433	–	10.6 s	β^+ (99.8 %), α (0.2 %)
^{162}Ta	161.95729	–	3.6 s	β^+ (99.92 %), α (0.073 %)
^{161}Ta	160.95842 (?)	–	3 s (?)	β^+ (95 %), α (5 %)
^{189}Ta	188.96583 (?)	–	3 s (?)	–
^{161m}Ta	–	–	2.9 s	Isomer; γ, 0.050
^{160}Ta	159.96149	–	1.7 s	α, β^+
^{160m}Ta	–	–	1.55 s	Isomer; β^+ (66 %), α (34 %), γ, 0.31
^{159}Ta	158.963018	–	1.04 s	β^+ (66 %), α (34 %)
^{159m}Ta	–	–	0.51 s	Isomer; α (56 %), β^+ (44 %), γ, 0.064
^{156m}Ta	–	–	0.36 s	Isomer; p, γ, 0.102
^{190}Ta	189.96923 (?)	–	0.3 s (?)	–
^{178m3}Ta	–	–	0.29 s	Isomer; γ, 3.000
^{182m1}Ta	–	–	0.28 s	Isomer; γ, 0.016
^{156}Ta	155.97230 (?)	–	0.14 s	β^+ (95.8 %), p (4.2 %)
^{178m2}Ta	–	–	59 ms	Isomer; γ, 1.570
^{179m6}Ta	–	–	54 ms	Isomer; γ, 2.639
^{158}Ta	157.96670 (?)	–	49 ms	α (96 %), β^+ (4 %)
^{158m}Ta	–	–	36 ms	Isomer; α (93 %), β^+, γ, 0.141
^{157}Ta	156.96819	–	10.1 ms	α (91 %), β^+ (9 %)
^{179m4}Ta	–	–	9.0 ms	Isomer; γ, 1.317
^{157m1}Ta	–	–	4.3 ms	Isomer; γ, 0.022
^{157m2}Ta	–	–	1.7 ms	Isomer; γ, 1.317
^{176m1}Ta	–	–	1.1 ms	Isomer; α, γ, 1.593
^{185m}Ta	–	–	>1 ms	Isomer; γ, 1.308
^{176m3}Ta	–	–	0.97 ms	Isomer; γ, 2.820
^{181m4}Ta	–	–	0.21 ms	Isomer; γ, 2.230
^{177m4}Ta	–	–	0.13 ms	Isomer; γ, 4.656
^{180m2}Ta	–	–	31 μs	Isomer; γ, 1.452
^{181m3}Ta	–	–	25 μs	Isomer; γ, 1.485
^{181m2}Ta	–	–	18 μs	Isomer; γ, 0.615

(continued)

Table 6.2 (continued)

Isotope	Mass, u	Abundance, %	Half-life period	Decay mode, excitation (radiation) energy, MeV
^{180m4}Ta	–	–	17 μs	Isomer; γ, 4.171 (?)
^{155}Ta	154.97459 (?)	–	13 μs (?)	–
^{181m1}Ta	–	–	6.05 μs	Isomer; γ, 6.238
^{177m3}Ta	–	–	5.3 μs	Isomer; γ, 1.355
^{176m2}Ta	–	–	3.8 μs	Isomer; γ, 1.372 (?)
^{177m2}Ta	–	–	3.6 μs	Isomer; γ, 0.186
^{180m3}Ta	–	–	2.0 μs	Isomer; γ, 3.679
^{179m5}Ta	–	–	1.6 μs	Isomer; γ, 1.326
^{179m1}Ta	–	–	1.4 μs	Isomer; γ, 0.030
^{177m1}Ta	–	–	0.41 μs	Isomer; γ, 0.073
^{179m2}Ta	–	–	0.335 μs	Isomer; γ, 0.520
^{179m3}Ta	–	–	0.32 μs	Isomer; γ, 1.253
^{183m}Ta	–	–	0.11 μs	Isomer; γ, 0.073
^{165m}Ta	–	–	?	Isomer; γ, 0.060

[a] Believed to undergo α decay (?)

[b] Only known observationally stable nuclear isomer, believed to undergo decay by isomeric transition, β^- decay or *K*-capture with a half-life period $>1.2 \times 10^{15}$ y (?); it is the only naturally occurring nuclear isomer, excluding radiogenic and cosmogenic short-living nuclides, and also the rarest primordial nuclide in the Universe observed for any element that has any stable isotopes

Nuclear physical properties of tantalum (isotopic mass range, total number of isotopes, thermal neutron macroscopic cross sections, moderating ability and capture resonance integral), compared with other ultra-high temperature elements (carbon and refractory metals), are given in Addendum.

6.6 Chemical Properties

The comprehensive information on the chemical properties and interaction of tantalum with all the elements of the periodic table is given in Table 6.3. The tantalum containing systems and corresponding binary compounds are described and considered there in accordance to the groups of elements from 1 to 17.

Table 6.3 Chemical interaction of tantalum with elements of the periodic table (binary systems in accordance to the groups of elements)[a]

System	Type of phase diagram (constituent phases, temperatures and compositions of transformations)	Character of interaction	References
Group 1			
Ta–H	H, δ-TaH_{1-x} (or $TaH_{0.7}$, <~70 °C, homog. range—~54–59 at.% (?) Ta), γ-$Ta_{4\div5}H_{3\div4}$ (<−65 °C, invariable compos., ~56 at.% (?) Ta), ζ-Ta_3H_{2+x} (<−38 °C, homog. range—~58–59 at.% Ta), η-Ta_3H_{2-x} (<–165 °C, homog. range—~60–63 at.% Ta), θ-$Ta_{2-x}H$ (–215 to –78 °C, homog. range—~62–66 at.% Ta), β-TaH_x (<46 °C, homog. range—~62–68 at.% Ta), ε-$Ta_{2\pm x}H$ (10–61 °C, homog. range—~63–71 at.% Ta), Ta (δ-, γ-, ζ- and β-phases are ordered interstitial phases, ε-phase is partially ordered) Extended solid solution based on Ta (up to ~42–44 at.% H at 20–70 °C)	The interaction between Ta and H is highly exothermic and initiates at ~300 °C with intensive weight gain. In the range of temp. 460–540 °C the process is accompanied with weight loss; at higher temp. the weight gain continues. The solubility of H in Ta amounts to 43.1 at.% at 20 °C, 37.25 at.% at 260 °C, 27.3 at.% at 430 °C, 3.6 at.% at 830 °C, 1.2 at.% at 1330 °C; in the range of temp. 40–95 °C the solubility of H (x, at.%) is obeyed the following rule $\lg x = 0.5\lg p - 3.56 + 1800/T$, where p is pressure H_2, Pa, and T is temp., K. Ta is considerably affected by brittleness in H_2 atmosphere. For diffusion rate in the system at various temp. see Addendum.	[4, 10, 13–14, 57–62]
Ta–D (^{2}H)	D, γ-TaD_x (<−65 °C, ?), ζ-TaD_x (<–70 °C, ?), β-TaD_x (<60 °C, wide homog. range, ?), ε-$Ta_{2\pm x}D$ (~15–65 °C, homog. range—~49–80 at.% (?) Ta), Ta Extended solid solutions based on Ta	–	[14, 63, 271]
Ta–T (^{3}H)	T, γ-TaT_x (<–65 °C, ?), ζ-TaT_x (<–70 °C, ?), β-TaT_x (<60 °C, wide homog. range, ?), ε-$Ta_{2\pm x}T$ (~15–65 °C, homog. range—~50–75 at.% (?) Ta), Ta Extended solid solutions based on Ta	–	[18, 63, 270]
Ta–Li	α-Li, β-Li, γ-Li, no binary compounds, Ta	No chemical interaction. The solubility of Ta in liquid Li is $\sim 8 \times 10^{-5}$ at.% at 730 °C and $\sim 7 \times 10^{-3}$ at.% at 1005 °C. Ta is resistant to corrosion in liquid Li at 1000 °C.	[4, 15, 64]

(continued)

Table 6.3 (continued)

System	Type of phase diagram (constituent phases, temperatures and compositions of transformations)	Character of interaction	References
Ta–Na	α-Na, β-Na, no binary compounds, Ta	No chemical interaction, no miscibility in the solid and liquid states. The solubility of Ta in liquid Na is $\sim 2 \times 10^{-6}$ at.%. at 325 °C, $\sim 4 \times 10^{-5}$ at.%. at 425 °C and $\sim 3 \times 10^{-4}$ at.%. at 525 °C; the solubility is considerably dependent on the O contamination of liquid Na, e.g. Na contaminated with O up to 0.5 % dissolves Ta 11 times more than highly purified Na. Ta is resistant to corrosion in liquid Na at 1100–1200 °C.	[4, 15, 65–66]
Ta–K	K, no binary compounds, Ta	No chemical interaction, no miscibility in the solid and liquid states. At 400–1330 °C the solubility of Ta in liquid K (with O content <0.002 %) is 1.4×10^{-4}–3×10^{-3} at.%; the solubility increases noticeably in the case of O contamination. Ta is resistant to corrosion in liquid K at 1000 °C.	[4, 15, 67–69]
Ta–Rb	Rb, no binary compounds, Ta	No chemical interaction. Ta is resistant to overheated oxygen-free Rb melt and vapour.	[128, 185]
Ta–Cs	Cs, no binary compounds, Ta	No chemical interaction. Ta is resistant to Cs melt and vapour (with low O contamination); good performance during 4000 h at 35 °C and 500 h at 980–1370 °C.	[4, 186]
Ta–Fr	No data	–	–
Group 2			
Ta–Be	α-Be, β-Be, $TaBe_{12}$ (<1850 C, melt. point), Ta_2Be_{17} (<1980 °C, melt. point), $TaBe_3$ (<at least 1800 °C), $TaBe_2$ (<1800 °C), Ta_3Be_2 (<at least 1300 °C), Ta_2Be (<1300 °C), Ta	The direct interaction between Ta and Be leads to the formation of $TaBe_{12}$.	[4, 16–17, 37, 70–71, 187]
Ta–Mg	Mg, no binary compounds, Ta Peritectic Mg (~652 °C, ~0.2 at.% Ta, ?) No complete diagram plot	Practically, no interaction between Ta and Mg at temp. <600 °C. The solubility of Ta in liquid Mg is ~0.1 at.% at peritectic temp.	[4, 188]
Ta–Ca	No data	–	–

(continued)

Table 6.3 (continued)

System	Type of phase diagram (constituent phases, temperatures and compositions of transformations)	Character of interaction	References
Ta–Sr	No data	–	–
Ta–Ba	No data	–	–
Ta–Ra	No data	–	–
Group 3			
Ta–Sc	α-Sc, β-Sc, no binary compounds, Ta Eutectic β-Sc–Ta (1519 °C, 3.2 at.% Ta)	The solubility of Ta (x, at.%) in liquid Sc is obeyed the following rule $\lg x = -2317/T + 1.7921$, where T is temp., K.	[18, 72]
Ta–Y	α-Y, β-Y, no binary compounds, Ta Eutectic (degenerated) β-Y–Ta (~1502–1513 °C, <0.5 at.% Ta, ?) Miscibility gap in the liquid state (from ~3.5–9 to ~98–99 at.% Ta at ~3000 °C)	The solubility of Ta in liquid Y is 0.52 at.% at 1635 °C, 0.96 at.% at 1905 °C and 1.35 at.% at 2085 °C; and that of Y in Ta is $\leq 2 \times 10^{-4}$ at.% at 1585 °C. For diffusion rate in the system at various temp. see Addendum.	[17–19]
Lanthanides			
Ta–La	α-La, β-La, γ-La, no binary compounds, Ta Eutectic (degenerated) β-La–Ta (~845–855 °C, <~0.015–0.020 at.% Ta) Miscibility gap in the liquid state (from ~0 to ~84–93 at.% Ta at 2915 °C, ?)	The solubility of Ta in liquid La is 0.02 at.% at, 1355 °C, 0.04 at.% at 1810 °C and 0.05 at.% at 2015 °C.	[15, 17, 19, 189]
Ta–Ce	α-Ce, β-Ce, γ-Ce, δ-Ce, no binary compounds, Ta Eutectic (degenerated) δ-Ce–Ta (?) Miscibility gap in the liquid state (from ~1 to ~88 at.% Ta at ~2860 °C)	The solubility of Ta in liquid Ce near the melt. point of Ce (~795 °C) is <0.04 at.%. In the presence of Ta the temp. of β-Ce–γ-Ce polymorphic transformation is reduced.	[16–17, 189]
Ta–Pr	α-Pr, β-Pr, no binary compounds, Ta Eutectic (degenerated) β-Pr–Ta (~930 °C, <0.005 at.% Ta, ?) Miscibility gap in the liquid state (from ~0.5 to ~90 at.% Ta at ~2875 °C)	The solubility of Ta in liquid Pr near the melt. point of Pr (~935 °C) is ~0.006 at.%; in the range of temp. 1200–2000 °C it increases from 0.04 to 0.17 at.%.	[17–19, 189–190]

(continued)

Table 6.3 (continued)

System	Type of phase diagram (constituent phases, temperatures and compositions of transformations)	Character of interaction	References
Ta–Nd	α-Nd, β-Nd, no binary compounds, Ta Eutectic (degenerated) β-Nd–Ta (~1020 °C, <0.01 at.% Ta, ?) Miscibility gap in the liquid state (from ~0.5 to ~90 at.% Ta at ~2875 °C)	No solubilities between the components in the solid state. The solubility of Ta in liquid Nd is very low.	[15, 17, 189]
Ta–Pm	No data	–	–
Ta–Sm	α-Sm, β-Sm, γ-Sm, no binary compounds, Ta Eutectic (degenerated) γ-Sm–Ta (~990–1020 °C, ~0.01–0.02 at.% Ta, ?) Miscibility gap in the liquid state (?)	No solubilities between the components in the solid state.	[17–19, 189]
Ta–Eu	Eu, no binary compounds, Ta Eutectic (degenerated) Eu–Ta (~822 °C, ?) Miscibility gap in the liquid state (from ~2.5–3.0 to ~100 at.% Ta at ~3020 °C, ?)	The solubility of Ta in liquid Eu near the melt. point of Eu (~822 °C) is $\sim 2\times10^{-4}$ at.%; in the range of temp. 1675–1870 °C it increases from 0.03 to 0.05 at.%.	[14, 17, 19, 189]
Ta–Gd	α-Gd, β-Gd, no binary compounds, Ta Eutectic (degenerated) β-Gd–Ta (~1305–1312 °C, ~0.04–0.08 at.% Ta) Miscibility gap in the liquid state (from ~4 to ~81–82 at.% Ta at ~2780 °C, ?)	At 1770 °C the solubility of Ta in liquid Gd is ≤0.4 at.%.	[14, 17, 19, 72, 189]
Ta–Tb	α′-Tb, α-Tb, β-Tb, no binary compounds, Ta Eutectic (degenerated) β-Tb–Ta (~1345–1365 °C, 0.15 at.% Ta) Miscibility gap in the liquid state (from ~4 to ~82 at.% Ta at 2790 °C, ?)	No solubilities between the components in the solid state. In the range of temp. 1430–1745 °C the solubility of Ta in liquid Tb increases from ~0.1 to ~0.6 at.%.	[17–18, 72, 189]
Ta–Dy	α′-Dy, α-Dy, β-Dy, no binary compounds; Ta Eutectic (degenerated) β-Dy–Ta (~1408–1410 °C, ~0.10–0.25 at.% Ta) Miscibility gap in the liquid state (?)	No solubilities between the components in the solid state. At 1730 °C the solubility of Ta in liquid Dy is ~0.4 at.%.	[14, 17, 72, 189]

(continued)

Table 6.3 (continued)

System	Type of phase diagram (constituent phases, temperatures and compositions of transformations)	Character of interaction	References
Ta–Ho	α-Ho, β-Ho, no binary compounds, Ta Eutectic (degenerated) β-Ho–Ta (~1468–1470 °C, ~0.30–0.36 at.% Ta) Miscibility gap in the liquid state (?)	No solubilities between the components in the solid state.	[14, 17, 72, 189]
Ta–Er	α-Er, β-Er, no binary compounds, Ta Eutectic (degenerated) β-Er–Ta (~1470–1522 °C, ~0.35–0.50 at.% Ta) Miscibility gap in the liquid state (from ~15 to ~70–71 at.% Ta at ~2665 °C, ?)	No solubilities between the components in the solid state. The solubility of Ta in liquid Er is 0.51 at.% at 1530 °C, 0.71 at.% at 1605 °C, 0.82 at.% at 1655 °C, 1.13 at.% at 1750 °C and 1.24 at.% at 1775 °C.	[14, 17, 72, 189, 191]
Ta–Tm	α-Tm, β-Tm, no binary compounds, Ta Eutectic (degenerated) β-Tm–Ta (~1534–1545 °C, ~0.55–0.70 at.% Ta, ?) Miscibility gap in the liquid state (?)	No solubilities between the components in the solid state. The solubility of Ta in liquid Tm is ~0.4 at.% at 1500 °C and ~1.6 at.% at 1800 °C	[17–19, 72, 189]
Ta–Yb	α-Yb, β-Yb, γ-Yb, no binary compounds, Ta Eutectic (degenerated) γ-Yb–Ta (~819 °C, ~0.003 at.% Ta, ?) Miscibility gap in the liquid state (from ~2–3 to ~99 at.% Ta at 3120 °C, ?)	No solubilities between the components in the solid state. The solubility of Ta in liquid Yb is 0.017 at.% at 1595 °C and 0.028 at.% at 1750 °C.	[17–19, 189]
Ta–Lu	α-Lu, β-Lu, no binary compounds, Ta Eutectic (degenerated) β-Lu–Ta (~1640–1675 °C, ~1.0–6.5 at.% Ta, ?) Miscibility gap in the liquid state (from ~18 to ~68–70 at.% Ta at ~2645 °C, ?)	No solubilities between the components in the solid state. At 1730 °C the solubility of Ta in liquid Lu is ~1.7 at.%.	[15, 17, 72, 189, 191]
Actinides			
Ta–Ac	No data	–	–
Ta–Th	α-Th, β-Th, $ThTa_2$ (<~1890 °C, incongruent melt. point, Laves phase, ?), Ta Eutectic β-Th–Ta (~1565–1680 °C, ~2–5 at.% Ta)	The max. solid solubility of Ta in Th is 0.5 at.% at eutectic temp., and that of Th in Ta is 0.25 at.% at the same temp.	[4, 17–18, 73–74]

(continued)

Table 6.3 (continued)

System	Type of phase diagram (constituent phases, temperatures and compositions of transformations)	Character of interaction	References
Ta–Pa	No data	–	–
Ta–U	α-U, β-U, γ-U, no binary compounds, Ta Peritectic γ-U (1160 °C, ~3 at.% Ta)	The max. solid solubility of Ta in γ-U is corresponding to the peritectic alloy. The solid solubility of Ta in α-U and β-U is negligible and does not affect the temp. of the polymorphic transitions of U. The max. solid solubility of U in Ta is ~2.5 at.% (1160 °C). At temp. <1200–1250 °C the kinetics of Ta dissolution in liquid U is very slow. Liquid U impregnates Ta porous preforms perfectly. For diffusion rate in the system at various temp. see Addendum.	[4, 17–18, 75– 76]
Ta–Np	No data	–	–
Ta–Pu	α-Pu, β-Pu, γ-Pu, δ-Pu, δ′-Pu, ε-Pu, no binary compounds, Ta Peritectic Pu (~660–680 °C, ~0.8–1.5 at.% Ta, ?) Eutectic (degenerated) ε-Pu–Ta (~625–640 °C, ?) Data on the system available in the literature are controversial.	Data on mutual solid solubilities between the components in the system are extremely contradicting. At 900–1150 °C Ta is not stable in the contact with liquid Pu; the corrosion and fracture of Ta occurs because of the penetration of Pu along the grain boundaries.	[4, 17–18, 149, 192–193]
Ta–Am	No data	–	–
Group 4			
Ta–Ti	α-Ti, β-Ti, no binary compounds, Ta Continuous solid solution β-Ti–Ta (up to melt. points)	Ta stabilizes β-Ti phase; in the presence of Ta the melt. point of Ti increases, and temp. of α-Ti–β-Ti polymorphic transformation decreases considerably. The max. solubility of Ta in α-Ti is ~3 at.% (600 °C). The corrosion resistance of Ta to liquid Ti is very low. For diffusion rate in the system at various temp. see Addendum.	[4, 17–18, 77–78]

(continued)

Table 6.3 (continued)

System	Type of phase diagram (constituent phases, temperatures and compositions of transformations)	Character of interaction	References
Ta–Zr	α-Zr, β-Zr, no binary compounds, Ta Continuous solid solution β-Zr–Ta (up to melt. points, min. melt. point 1875 °C corresp. to ~15 at.% Ta; miscibility gap: critical point—1775–1780 °C, 33 at.% Ta; from ~6.5–9.5 to ~93.5–95.5 at.% Ta at ~775–800 °C)	Ta stabilizes β-Zr phase; in the presence of Ta the temp. of α-Zr–β-Zr polymorphic transformation decreases. The max. solid solubility of Ta in α-Zr is ~1.0–2.5 at.% at ~775–800 °C, and the solubility of Zr in Ta at the same temp. is ~6.5–9.5 at.%; at lower temp. the mutual solid solubilities decrease considerably. For diffusion rate in the system at various temp. see Addendum.	[17–18, 79–80, 262]
Ta–Hf	α-Hf, β-Hf, no binary compounds, Ta Continuous solid solution β-Hf–Ta (up to melt. points, min. melt. point 2130 °C corresp. to 20 at.% Ta; miscibility gap: critical point—~1140 °C (or ~1670 °C, ?), ~58.5–64.0 (or ~35–40, ?) at.% Ta; from ~30–50 (or ~17.5, ?) to ~81–91 at.% Ta at ~1020–1085 °C)	Ta stabilizes β-Hf phase; in the presence of Ta the temp. of α-Hf–β-Hf polymorphic transformation decreases. The max. solubility of Ta in α-Hf is ~7 at.% (~1020–1085 °C); at lower temp. the mutual solid solubilities decrease considerably.	[4, 14, 17, 81, 265]
Group 5			
Ta–V	V, $V_{2\pm x}Ta$ (<~1310–1420 °C, homog. range—from ~30–33 to ~35–43 at.% Ta at 900 °C), Ta Continuous solid solution V–Ta (up to melt. points, min. melt. point 1825 °C corresp. to 15 at.% Ta; miscibility gap: critical point—~1310–1420 °C, ~33–34 at.% Ta, from ~5–9 to ~52–65 at.% Ta at 900 °C)	For diffusion rate in the system at various temp. see Addendum.	[4, 17–18, 82, 260]
Ta–Nb	Nb, no binary compounds, Ta Continuous solid solution Nb–Ta	For diffusion rate in the system at various temp. see Addendum.	[15, 17]

(continued)

Table 6.3 (continued)

System	Type of phase diagram (constituent phases, temperatures and compositions of transformations)	Character of interaction	References
Group 6			
Ta–Cr	Cr, $TaCr_3$ (<1825 °C, incongruent melt. point, ?), λ_2-$TaCr_{2\pm x}$ (<1660–1805 °C, homog. range—33–36 at.% Ta, Laves phase), λ_1-$TaCr_{2\pm x}$ (from 1660–1805 °C to ~2010–2040 °C, congruent melt. point, homog. range—30–38 at.% Ta, Laves phase), Ta Eutectic λ_1-$TaCr_{2\pm x}$–Cr (~1700–1775 °C, ~9.5–13 at.% Ta) Eutectic λ_1-$TaCr_{2\pm x}$–Ta (~1945–1985 °C, ~46–54 at.% Ta)	The max. solid solubility of Ta in Cr is ~3.5–4.0 at.% at 1700–1775 °C, and that of Cr in Ta is ~27.0–27.5 at.% at 1945–1985 °C. At lower temp. the solubility of Ta decreases up to ~2.4 at.% at 1600 °C, ~0.9 at.% at ~1400 °C and ~0.3–0.5 at.% at ~1200 °C, and that of Cr decreases up to ~13 at.% at ~1600 °C, ~9 at.% at ~1400 °C and ~5.5 at.% at ~1200 °C. The direct interaction between Ta and Cr leads to the formation of λ_2-$TaCr_{2\pm x}$.	[4, 14, 17, 20, 83–85, 165, 175, 263]
Ta–Mo	Mo, no binary compounds, Ta Continuous solid solution Mo–Ta	For diffusion rate in the system at various temp. see Addendum.	[15, 17, 20, 39]
Ta–W	See W–Ta in Table 3.5.		
Group 7			
Ta–Mn	α-Mn, β-Mn, γ-Mn, δ-Mn, Mn_2Ta (<~1600–1750 °C, congruent melt. point (?), Laves phase), MnTa (<~1700 °C, incongruent melt. point, ?), Ta Eutectic Mn_2Ta–MnTa (~1600 °C, ~34–35 at.% Ta, ?) Eutectic Mn_2Ta–γ-Mn (~1150–1175 °C, ~2.5–7.0 at.% Ta, ?)	The max. solid solubility of Ta in Mn modifications is ~1 at.% in α-Mn (750 °C), ~0.7 at.% in β-Mn (1060–1070 °C), ~1.5 at.% in γ-Mn (1150–1175 °C) and ~0.5 at.% in δ-Mn (1190–1200 °C); the max. solid solubility of Mn in Ta is ~3–4 at.% (1700 °C).	[15, 17, 86, 194–195]
Ta–Tc	Tc, Tc_5Ta (?), TcTa (?), Ta No diagram plot	–	[18, 46]
Ta–Re	See Re–Ta in Table 4.5.		

(continued)

Table 6.3 (continued)

System	Type of phase diagram (constituent phases, temperatures and compositions of transformations)	Character of interaction	References
Group 8			
Ta–Fe	α-Fe, γ-Fe, δ-Fe, ε-$Fe_{2\pm x}Ta$ (<∼1775 °C, congruent melt. point, homog. range—∼28–36 at.% Ta at 1300 °C, Laves phase), μ-Fe_7Ta_{6+x} (or μ-$FeTa_{1\pm x}$, <∼1800–1900 °C, congruent melt. point, homog. range—∼49–54 at.% Ta at 800–1500 °C), $FeTa_4$ (?), Ta Eutectic ε-$Fe_{2\pm x}Ta$–μ-$FeTa_{1\pm x}$ (∼1570 °C, ∼42 at.% Ta) Eutectic ε-$Fe_{2\pm x}Ta$–δ-Fe (1442 °C, 7.9 at.% Ta) Eutectic μ-Fe_7Ta_{6+x}–Ta (∼1670 °C, ∼84 at.% Ta)	The max. solubility of Ta in Fe modifications is: 2.8 at.% in δ-Fe (1442 °C), 0.85–0.90 at.% in γ-Fe (1215 °C) and 0.7 at.% in α-Fe (965 °C); at lower temp. the solubility of Ta decreases up to 0.34 at.% at 950 °C, 0.28 at.% at 900 °C and 0.185 at.% at 800 °C. The max. solubility of Fe in Ta is ∼7 at.% (∼1670 °C). The corrosion resistance of Ta to Fe melts and molten alloys is very low. For diffusion rate in the system at various temp. see Addendum.	[4, 14, 17, 32, 47–48, 87–90, 255, 266–267
Ta–Ru	Ru, γ-Ru_3Ta_{2-x} (<∼1665 °C, homog. range—∼36–39 at.% Ta at 1200–1300 °C), μ-$RuTa_{1\pm x}$ (<∼2080 °C, incongruent melt. point, homog. range—from ∼38 to ∼49–51 at.% Ta at 1970 °C, from ∼39 to 53–56 at.% Ta at ∼1665 °C, ∼40–60 at.% Ta at 1500 °C, ∼50–65 at.% Ta at 1000 °C and from 55–60 to (?) at.% Ta at 500 °C), μ′-$RuTa_{1\pm x}$ (<∼1400 °C, homog. range—∼45–50 at.% Ta at 1000 °C), μ″-$RuTa_{1\pm x}$ (<∼800 °C, homog. range—∼48–53 at.% Ta at 500 °C), Ta Extended solid solution based on Ru (up to ∼24–28 at.% Ta at 1665 °C) Extended solid solution based on Ta (up to ∼50 at.% Ru at 2080 °C) Eutectic μ-$RuTa_{1\pm x}$–Ru (1970 °C, ∼29 at.% Ta)	The solid solubility of Ta in Ru is ∼21 at.% at 1970 °C and ∼24–28 at.% at 1665 °C, and that of Ru in Ta is ∼50 at.% at ∼2080 °C; at lower temp. the mutual solubilities decline considerably.	[4, 18, 91–94]
Ta–Os	See Os–Ta in Table 5.3.		

(continued)

Table 6.3 (continued)

System	Type of phase diagram (constituent phases, temperatures and compositions of transformations)	Character of interaction	References
Group 9			
Ta–Co	ε-Co, α-Co, κ-Co_7Ta_2 (<930–970 °C, invariable compos., ?), Co_3Ta (~950–1000 °C, metastable, ?), λ_3-$Co_{3-x}Ta$ (or $Co_{2.7}Ta$, or $Co_{2.2}Ta_{0.8}$, <1450 °C, incongruent melt. point, homog. range—26.5–28 at.% Ta at 600–1300 °C), λ_2-$Co_{2\pm x}Ta$ (<1595–1650 °C, congruent melt. point, homog. range—29.5–36 at.% Ta at 1450 °C and 30–36 at.% Ta at 600–1400 °C), λ_1-Co_3Ta_{2-x} (from 1110–1150 °C to 1540 °C, invariable compos.), μ-$Co_7Ta_{6\pm x}$ (or μ-$CoTa_{1\pm x}$, <1700 °C, congruent melt. point, homog. range—from ~44–48 to ~54–56 at.% Ta), $CoTa_2$ (<1800 °C, incongruent melt. point, invariable compos.), Ta Eutectic λ_3-$Co_{3-x}Ta$ (or λ_2-$Co_{2\pm x}Ta$, ?)–α-Co (~1270–1280 °C, ~8–13.5 at.% Ta) Eutectic λ_2-$Co_{2\pm x}Ta$–μ-$Co_7Ta_{6\pm x}$ (1560 °C, ~43 at.% Ta) Eutectic $CoTa_2$–μ-$Co_7Ta_{6\pm x}$ (1670 °C, 58 at.% Ta)	The presence of Ta results in increase in the temp. of α-Co–ε-Co transformation. The max. solid solubility of Ta in Co modifications is: ~4.2–4.4 at.% in α-Co (~1200–1270 °C) and ~4.6–4.7 at.% in ε-Co (1008 °C). The max. solubility of Co in Ta is ~20 at.% (1800 °C); at lower temp. the solubility declines up to ~2 at.% (at 500 °C). The direct interaction between Ta and Co leads to the formation of λ_2-$Co_{2\pm x}Ta$. For diffusion rate in the system at various temp. see Addendum.	[4, 14, 17, 32, 95]

(continued)

Table 6.3 (continued)

System	Type of phase diagram (constituent phases, temperatures and compositions of transformations)	Character of interaction	References
Ta–Rh	Rh, $Rh_{3\pm x}Ta$ (<~2125 °C, congruent melt. point corresp. to ~Rh_3Ta, homog. range—~22–31 at.% Ta at ~1900–2000 °C and ~23–28 at.% Ta at 1000 °C), α_2-$Rh_{2\pm x}Ta$ (or α-$Rh_{2\pm x}Ta$, <~1890 °C, incongruent melt. point, homog. range—~32–34.5 at.% Ta), α_1-$Rh_{3\pm x}Ta_2$ (<~1860 °C, incongruent melt. point, homog. range—~36–46.5 at.% Ta), α_3-$RhTa_{1-x}$ (from 1355–1395 °C to ~1840 °C, incongruent melt. point, homog. range—~38–51 at.% Ta), σ-$RhTa_{2\pm x}$ (<~2080–2140 °C, incongruent melt. point, homog. range—~60.0–80.5 at.% Ta), Ta Peritectic Rh (~1995–2035 °C, ~17.5 at.% Ta) Extended solid solution based on Rh (up to 17.5 at.% Ta at ~1995–2035 °C) Extended solid solution based on Ta (up to ~16 at.% Rh at ~2080–2140 °C) Eutectic α_3-$RhTa_{1-x}$–σ-$RhTa_{2\pm x}$ (1740 °C, 55 at.% Ta)	The presence of Ta results in increase in the melt. temp. of Rh. The max. melt. point (~ 1995–2035 °C) and max. solid solubility of Ta in Rh (17.5 at.%) are corresponding to the peritectic alloy. At lower temp. the mutual solid solubilities of the components decline; at temp. <1000 °C the solubility of Ta in Rh is <10 at.% and that of Rh in Ta is <8 at.%.	[4, 17–18, 96]

(continued)

Table 6.3 (continued)

System	Type of phase diagram (constituent phases, temperatures and compositions of transformations)	Character of interaction	References
Ta–Ir	Ir, β-$Ir_{3\pm x}Ta$ (<2450–2455 °C, congruent melt. point corresp. to ~Ir_3Ta, homog. range—~23.5–26.5 at.% Ta at 2385 °C, ~24.0–33.5 at.% Ta at 2120–2115 °C, ~24.5–31.0 at.% Ta at 1860–1865 °C and ~25–29 at.% Ta at 1600 °C), γ-Ir_3Ta_{2+x} (or α_2-Ir_3Ta_{2+x}, <1860–1865 °C, homog. range—~41–42.5 at.% Ta at 1600 °C), δ-$IrTa_{1-x}$ (or α_1-$IrTa_{1-x}$, <~2120–2125 °C, incongruent melt. point, homog. range—~39.0–49.6 at.% Ta), σ-$IrTa_{3\pm x}$ (<2475–2480 °C, incongruent melt. point, homog. range—~59.0–88.6 at.% Ta), Ta Extended solid solution based on Ir (up to 15.5 at.% Ta at 2380–2385 °C) Peritectic Ir (?, ~15.5–16.0 at.% Ta, ?) Eutectic δ-$IrTa_{1-x}$–σ-$Ta_{3\pm x}Ir$ (~1950–1955 °C, ~55.5 at.% Ta) Eutectic β-$Ir_{3\pm x}Ta$–Ir (~2380–2385 °C, ~16 at.% Ta, ?) Data on the system available in the literature are controversial.	The influence of Ta on the melt. temp. of Ir alloys is uncleared. The solubility of Ta in Ir declines with temp. decreasing: ~13 at.% at 2100 °C and ~12 at.% at 1600–1900 °C. The max. solid solubility of Ir in Ta is 7.2–7.3 at.% (2475–2580 °C) (corresp. to the peritectic temp. of σ-phase); at lower temp. the solubility of Ir declines noticeably.	[15, 17, 97]

(continued)

Table 6.3 (continued)

System	Type of phase diagram (constituent phases, temperatures and compositions of transformations)	Character of interaction	References
Group 10			
Ta–Ni	Ni, ζ-$Ni_{8\pm x}Ta$ (<1330 °C, homog. range—~10.5–12.5 at.% Ta at 800 °C), κ-$Ni_{3\pm x}Ta$ (<1550 °C, congruent melt. point corresp. to ~Ni_3Ta, homog. range—~23–28.5 at.% Ta), $Ni_{2\pm x}Ta$ (<1405 °C, incongruent melt. point, homog. range—~32.5–34.5 at.% Ta at 800 °C), μ-Ni_7Ta_{6+x} (or μ-$Ni_{1-x}Ta$, <1570 °C, incongruent melt. point, homog. range—~50–54 at.% Ta at 800 °C), $NiTa_{2+x}$ (<~1790 °C, incongruent melt. point, homog. range—~66.7–71.0 at.% Ta at 800 °C), Ta Extended solid solution based on Ni (up to 14–15 at.% Ta at 1360 °C) Extended solid solution based on Ta (up to ~20 at.% Ni at ~1790 °C) Eutectic $Ni_{2\pm x}Ta$–μ-Ni_7Ta_{6+x} (1350 °C, 36 at.% Ta) Eutectic κ-$Ni_{3\pm x}Ta$–Ni (1360 °C, 17.2 at.% Ta) Data on the system available in the literature are controversial.	The direct interaction between Ta and Ni results in the formation of κ-$Ni_{3\pm x}Ta$. The mutual solid solubilities of the components decline with temp. decrease considerably: the solubility of Ta in Ni—from 14–15 at.% (1360 °C) to ~3 at.% (800 °C), and that of Ni in Ta—from ~20 at.% (1790 °C) to ~1.5–2.0 at.% (800 °C). For diffusion rate in the system at various temp. see Addendum.	[4, 15, 17, 98–100, 156–158, 261, 264]
Ta–Pd	Pd, $Pd_{17}Ta$ (?), $Pd_{12}Ta$ (?), Pd_6Ta (?), $Pd_{15}Ta_4$ (?), $Pd_{3\pm x}Ta$ (<1770–1945 °C (?), melt. point, homog. range—~23.5–26.0 at.% Ta (?) at 1000 °C), $Pd_{2\pm x}Ta$ (<1670–1800 °C (?), melt. point, homog. range—~33–34.5 at.% Ta (?) at 1000 °C), PdTa (<~1720–2000 °C, melt. point, ?), α-$Pd_{1\pm x}Ta$ (<1410 °C (?), homog. range—~49–51 at.% Ta (?) at 1000 °C), β-$Pd_{1\pm x}Ta$	The presence of Ta results in increase in the melt. temp. of Pd. The max. melt. point (~1730–1860 °C, ?) and max. solid solubility of Ta in Pd (~18–22 at.%) are corresponding to the peritectic alloy. The solubility of Ta in Pd declines with temp. decrease; at 800–900 °C it amounts to ~5 at.%. The solubility of Pd in Ta also declines with temp. decrease: from ~20–25 at.% at 2350–2550 °C (?) to ~8–10 at.% at 1000 °C.	[4, 15, 17, 101–106]

(continued)

Table 6.3 (continued)

System	Type of phase diagram (constituent phases, temperatures and compositions of transformations)	Character of interaction	References
	(1550–1720 °C (?), homog. range—~46–52 at.% Ta (?) at 1700–1720 °C), σ-$PdTa_{3\pm x}$ (<2550 °C or 1575–2350 °C (?), incongruent melt. point, homog. range—~70–77.5 at.% Ta at 1700 °C and ~75.5–78 at.% Ta at 1000 °C, ?), Ta Peritectic Pd (~1730–1860 °C (?), ~18–22 at.% Ta) Extended solid solution based on Pd (up to ~18–22 at.% Ta at ~1730–1860 °C, ?) Extended solid solution based on Ta (up to ~20–25 at.% Pd at 2350–2550 °C, ?) Eutectic $Pd_{3\pm x}Ta$–$Pd_{2\pm x}Ta$ (1720–1730 °C, 28 at.% Ta, ?) Eutectic PdTa (or β-$Pd_{1\pm x}Ta$)–σ-$PdTa_{3\pm x}$ (~1700–1745 °C, ~52–57 at.% Ta) Data on the system available in the literature are controversial.		
Ta–Pt	Pt, Pt_4Ta (?), $Pt_{3\pm x}Ta$ (<2065–2085 °C, congruent melt. point corresp. to ~Pt_3Ta, homog. range—limited near 25 at.% Ta), $Pt_{2\pm x}Ta$ (<2245 °C, congruent melt. point corresp. to ~Pt_2Ta, homog. range—limited near 33 at.% Ta), $Pt_{1\pm x}Ta$ (1635–1795 °C, incongruent melt. point, homog. range—limited near 50 at.% Ta), σ-$PtTa_{2+x}$ (<2470 °C, incongruent melt. point, homog. range—~66–86 at.% Ta), $PtTa_{3+x}$ (<1725 °C, homog. range—~85–88 at.% Ta), Ta Peritectic Pt (1970 °C, 19 at.% Ta)	The presence of Ta results in increase in the melt. temp. of Pt. The max. melt. point (1970 °C) and max. solid solubility of Ta in Pt (19 at.%) are correspond. to the peritectic alloy. The solubility of Pt in Ta is $\leq$ 8 at.% at 2470 °C and $\leq$ 3 at.% at 1000–1500 °C.	[4, 18, 40, 107–108]

(continued)

Table 6.3 (continued)

System	Type of phase diagram (constituent phases, temperatures and compositions of transformations)	Character of interaction	References
	Extended solid solution based on Pt (up to 19 at.% Ta at 1970 °C) Eutectic $Pt_{3\pm x}Ta$–$Pt_{2\pm x}Ta$ (2050 °C, ~26–28 at.% Ta) Eutectic $Pt_{1\pm x}Ta$–σ-$PtTa_{2+x}$ (1760 °C, ~53–55 at.% Ta)		
Group 11			
Ta–Cu	Cu, no binary compounds, Ta Eutectic (degenerated) Cu–Ta (~1083 °C, ?) Miscibility gap in the liquid state (critical point—2325 °C, ~25 at.% Ta; from ~3–4 to ~65 at.% Ta at 2025 °C)	The mutual solid solubilities of Ta and Cu are extremely low. At 1200 °C the solubility of Ta in liquid Cu is 0.009 at.%.	[4, 14, 17, 194]
Ta–Ag	Ag, no binary compounds, Ta Peritectic Ag (~962 °C, ?) Miscibility gap in the liquid state (?)	The mutual solid solubilities of Ta and Ag are negligible.	[4, 16, 196–197]
Ta–Au	Au, Au_2Ta (<~700–800 °C, invariable compos., ?), AuTa (?), α-Au_2Ta_3 (< at least ~1600 °C, invariable compos.), β-Au_2Ta_3 (~1600–1700 °C, incongruent melt. point, invariable compos.), $AuTa_3$ (?), σ-$AuTa_{3\pm x}$ (or $AuTa_{2+x}$, <~2000 °C, incongruent melt. point, homog. range—~67–78 at.% Ta at ~1600–1700 °C and ~74–78 at.% Ta at 400 °C), $AuTa_{5\pm x}$ (or $AuTa_{3+x}$ (?), <~1600–1680 °C, homog. range—~82–84 at.% Ta at 400–1500 °C), Ta Peritectic Au (~1200–1300 °C, ~10–30 at.% Ta, ?) Extended solid solution based on Au (up to ~10–30 at.% Ta at ~1200–1300 °C, ?)	At 1000 °C the solubility of Ta in Au is 10.8–11.3 at.%; it declines with temp. decrease up to 8.5 at.% at 500 °C. The max. solubility of Au in Ta is near ~20 at.% (?); the solubility declines considerably with temp. decrease. In general, data on the solubility in the system available in the literature are controversial.	[16–17, 109–110, 195]

(continued)

Table 6.3 (continued)

System	Type of phase diagram (constituent phases, temperatures and compositions of transformations)	Character of interaction	References
	Extended solid solution based on Ta (up to ~20 at.% Au at 1600 °C, ?) Eutectic α-Au_2Ta_3–Au (~1000 °C, ~20 at.% Ta, ?) Data on the system available in the literature are controversial.		
Group 12			
Ta–Zn	Zn, $TaZn_2$ (Laves phase, ?), Ta_6Zn_7 and some other compounds (?), Ta (most of binary compounds melt incongruently) No diagram plot	At 440 °C Ta is wetted by molten Zn; at 440–800 °C Ta is resistant to liquid Zn in the static conditions, but the resistance in the dynamic conditions is poor.	[4, 18, 198]
Ta–Cd	No data	–	–
Ta–Hg	Hg, no binary compounds, Ta No diagram plot	No interaction in the wide range of temp. At 300–600 °C Ta is highly resistant to corrosion and erosion in Hg.	[4, 14]
Group 13			
Ta–B	β-B, $TaB_{2\pm x}$ (<3035–3200 °C, congruent melt. point corresp. to ~$TaB_{1.9}$, homog. range—~31–38 at.% Ta at 2800 °C, ~28–37 at.% Ta at 2055 °C, ~27.5–36.5 at.% Ta at 1800 °C and ~33–34 at.% Ta at 530 °C), $Ta_3B_{4\pm x}$ (<~2620–3030 °C (?), incongruent melt. point, homog. range—~42–44 at.% Ta at 2800 °C and ~42.5–43.5 at.% Ta at 1800 °C), λ-$TaB_{1\pm x}$ (<2400–3090 °C, congruent melt. point corresp. to ~$TaB_{1.0}$, homog. range—~48–50 at.% Ta at 2800 °C, ~48–51.5 at.% Ta at 2415 °C, ~48.5–50.5 at.% Ta at 2180 °C and ~48.5–50.0 at.% Ta at 1800 °C), $Ta_3B_{2\pm x}$	The mutual solid solubilities of Ta and B are ~2 at.%. Ta bo-rides are formed by the direct interaction between the elements at 1500–1600 °C in vacuum or inert gas atmosphere. The contact interaction between compact metal Ta and $TaB_{2\pm x}$ initiates from 1600 °C and leads to the formation of $Ta_3B_{4\pm x}$, $Ta_3B_{2\pm x}$ and $Ta_{2+x}B$. For diffusion rate in the system at various temp. see Addendum.	[4, 13, 16–17, 21, 33, 44, 111–113, 259, 269]

(continued)

Table 6.3 (continued)

System	Type of phase diagram (constituent phases, temperatures and compositions of transformations)	Character of interaction	References
	(<2180 °C, homog. range—~59–61 at.% Ta at 2040 °C, invariable compos. at temp. <1800 °C), $Ta_{2+x}B$ (<~2040–2415 °C, incongruent melt. point, homog. range—~68.5–72 at.% Ta), Ta Eutectic $TaB_{2\pm x}$–$Ta_3B_{4\pm x}$ (~2400–2990 °C (?), ~39.5 at.% Ta) Eutectic $Ta_{2+x}B$–Ta (~2360–2385 °C, 77 at.% Ta) Eutectic $TaB_{2\pm x}$–β-B (~2055–2070 °C, 2 at.% Ta)		
Ta–Al	Al, $TaAl_3$ (<1550–1630 °C (?), melt. point, invariable compos.), $TaAl_2$ (<~1595 °C, incongruent melt. point, invariable compos., ?), α-Ta_2Al_3 (<1225 °C, invariable compos., ?), β-Ta_2Al_3 (~1225–1550 °C, incongruent melt. point, invariable compos., ?), TaAl (<1770 °C, incongruent melt. point, invariable compos., ?), δ-$Ta_{2\pm x}Al$ (or σ-$Ta_{2\pm x}Al$, <~2000–2100 °C, incongruent melt. point corresp. to ~$Ta_{1.95}Al$, homog. range—~50–73 at.% Ta at ~1550–1770 °C and ~60–80 at.% Ta at 600 °C), Ta_3Al (?), Ta Peritectic Al (~667–668 °C, ~0.25 at.% Ta, ?) Eutectic β-Ta_2Al_3–δ-$Ta_{2\pm x}Al$ (~1550 °C, ~43–45 at.% Ta, ?) Data on the system available in the literature are controversial.	The max. solid solubility of Ta in Al is ≤0.25 at.% (the solubility of Ta declines with temp. decrease, but it is affected by temp. slightly), and that of Al in Ta is ~4–12 at.% (?) at ~2000–2100 °C. At higher and lower temp. the solid solubility of Al in Ta declines considerably. The reaction between Ta and Al with the formation of aluminides initiates on sintering the powder mixtures or impregnating Ta preforms by molten Al. The corrosion resistance of Ta to Al melts is low. Data on the solubility of Al in Ta available in the literature are controversial. For diffusion rate in the system at various temp. see Addendum.	[4, 13, 16–17, 114–115, 151, 256]

(continued)

Table 6.3 (continued)

System	Type of phase diagram (constituent phases, temperatures and compositions of transformations)	Character of interaction	References
Ta–Ga	Ga, $TaGa_3$ (<at least 1300 °C, ?), $TaGa_2$ (?), Ta_4Ga_5 (<~1145–1150 °C, ?), Ta_3Ga_2 (< at least 1300 °C, ?), α-Ta_5Ga_3 (<980 °C), β-Ta_5Ga_3 (from 980 °C to at least 1300 °C), Ta_2Ga (?), Ta	At 450 °C Ta is highly resistant to corrosion in Ga. Some metastable binary compounds were synthesized under high pressures (7.7 GPa).	[4, 14, 17, 116–118, 184]
Ta–In	In, no binary compounds, Ta	Practically, no interaction in solid and liquid states at normal conditions (at least at temp. ≤700 °C). The solubility of Ta in molten In at its melt. point is ~10^{-9} at.%.	[15, 17, 119–120]
Ta–Tl	α-Tl, β-Tl, no binary compounds, Ta	No interaction in solid and liquid states (at least at temp. ≤700 °C and pressures ≤0.7 GPa).	[17–18, 119]
Group 14			
Ta–C	See C–Ta in Table 2.13.		
Ta–Si	Si, $TaSi_2$ (<2040–2300 °C, congruent melt. point, invariable compos.), α-Ta_5Si_3 (<~1700–2160 °C, invariable compos.), β-Ta_5Si_3 (from ~1700–2160 °C to 2490–2550 °C, congruent melt. point, invariable compos.), Ta_2Si (<2440–2460 °C, incongruent melt. point, invariable compos.), $Ta_{3+x}Si$ (or $Ta_{5-x}Si$, or $Ta_{4.5}Si$, <2340–2520 °C (?), melt. point, invariable compos.), Ta Eutectic α-Ta_5Si_3 (or β-Ta_5Si_3, ?)–$TaSi_2$ (~1960–2100 °C, ~38–42 at.% Ta) Eutectic Ta_2Si–$Ta_{3+x}Si$ (~2400 °C, ~70–72 at.% Ta, ?) Eutectic $TaSi_2$–Si (~1385–1400 °C, ~0.75–1.5 at.% Ta)	The max. solid solubility of Si in Ta amounts to ~1.3–6.0 at.% at ~2260–2300 °C; at higher or lower temp. the solubility of Si declines significantly. Solid Si has practically no solubility for Ta. Silicides are synthesized directly from the elements in vacuum or inert gas atmosphere at 1000–1500 °C. In vacuum, at 1150–1370 °C the contact interaction between compact Ta and $TaSi_2$ results in the formation of α-Ta_5Si_3. For diffusion rate in the system at various temp. see Addendum.	[4, 13, 17–18, 21, 160, 233, 257, 268]

(continued)

Table 6.3 (continued)

System	Type of phase diagram (constituent phases, temperatures and compositions of transformations)	Character of interaction	References
	Eutectic $Ta_{3+x}Si$–Ta (~2260–2300 °C, ~83–86 at.% Ta) Data on the system available in the literature are controversial.		
Ta–Ge	Ge, $TaGe_2$ (<1260–1300 °C, incongruent melt. point), α-Ta_5Ge_3 (<1100 °C), β-Ta_5Ge_3 (> 1100 °C), α-Ta_2Ge, β-Ta_2Ge, γ-Ta_2Ge, δ-Ta_2Ge, α-Ta_3Ge (<1550 °C), β-Ta_3Ge (>1550 °C),Ta (melt. points of Ta germanides ≤1300–1600 °C) No diagram plot	The solid solubility of Ta in Ge is 0.045 at.% at 910 °C, 0.147 at.% at 875 °C, 0.079 at.% at 850 °C, 0.043 at.% at 825 °C, 0.016 at.% at 800 °C and 0.008 at.% at 775 °C. The direct interaction between Ta and Ge leads to the formation of Ta germanides.	[4, 17–18, 45, 121, 199]
Ta–Sn	α-Sn, β-Sn, Ta_2Sn_3 (or $Ta_{12}Sn_{18}$, <595 °C, invariable compos.), Ta_3Sn (<~1200–1550 °C, incongruent melt. point, invariable compos.), Ta Peritectic β-Sn (~232 °C, ?)	The direct interaction between Ta and Sn leads to the formation of Ta_3Sn.	[4, 18, 200]
Ta–Pb	Pb, no binary compounds, Ta No diagram plot	Ta is highly resistant to corrosion in molten Pb; at 1000 °C Ta parts are fit for long-term applications in Pb.	[4]
Group 15			
Ta–N	N, TaN_2 (?), Ta_3N_5 (<900 °C, decomposition, homog. range—~37.5–39.1 at.% Ta, ?), Ta_4N_5 (?), ε-TaN_{1-x} ($x \approx 0 \div 0.02$, <~2000–2100 °C, homog. range—~50.0–50.5 at.% Ta, ?), δ-TaN_{1-x} ($x \approx 0.01 \div 0.33$, from 1700 °C to ~2000–3140 °C, congruent melt. point, homog. range—~50–60 at.% Ta, ?), γ-$Ta_{2\pm x}N$ (<~2050–3000 °C (?), congruent melt. point, homog. range—~65–79	At elevated temp. the solubility of N in Ta is 0.45 at.% at 350 °C, 1 at.% at 500 °C 4 at.% at 1000 °C and ~14 at.% (?) at ~2900 °C. In the range of temp. 1600–2380 °C the solubility of N in Ta (x, at.%) is obeyed the rule: $x = p^{2.4} \times 10^{10} exp(-43500/T)$, where p is pressure N_2, Pa, and T is temp., K. The interaction between Ta and N_2 initiates at temp. ≥300 °C. In terms of rate equations the initial nitridation of Ta at 400–700 °C is cubic, at 800–1400 °C the process is obeyed the parabolic law.	[4, 13, 15, 17, 21–22, 30, 33,122, 124–127, 195, 201–202, 258]

(continued)

Table 6.3 (continued)

System	Type of phase diagram (constituent phases, temperatures and compositions of transformations)	Character of interaction	References
	at.% Ta at ~1750–2900 °C and ~67–72 at.% Ta at room temp.), Ta_3N (invariable compos., ?), Ta_9N_2 (<790 °C, homog. range—~81–83 at.% Ta at 450–500 °C, ?), β-TaN_x ($x \approx 0.05$, ~600–750 °C, invariable compos.), $Ta_{27\pm x}N$ (homog. range—~96.0–99.9 at.% Ta, ?), Ta Extended solid solution based on Ta (≥10 at.% N at 2875 °C, ?) Eutectic γ-$Ta_{2\pm x}N$–δ-TaN_{1-x} (~2900 °C, ~64–65 at.% Ta, ?) Eutectic γ-$Ta_{2\pm x}N$–Ta (~2300–2900 °C, ~82–84 at.% Ta, ?) Data on the system available in the literature are controversial.	The average mass gain of Ta samples at 1000 °C in N_2 atmosphere is 2 g m^{-2} s^{-1} (1 h exposure). The main products of the interaction between Ta and N_2 are γ-$Ta_{2\pm x}N$ at 800–1000 °C and δ-TaN_{1-x} at 1200–1400 °C. For diffusion rate in the system at various temp. see Addendum.	
Ta–P	P, TaP_5, TaP_2, α-TaP (?), β-TaP (?), Ta_5P_4, Ta_5P_3, Ta_2P (?), Ta_3P (?), Ta No diagram plot	Ta phosphides are synthesized directly from the elements in vacuum at higher temp.	[4, 13, 15, 203]
Ta–As	As, $TaAs_2$, TaAs, Ta_5As_4, Ta_2As, α-Ta_3As, β-Ta_3As (?), Ta No diagram plot	Ta arsenides are synthesized directly from the elements at 800–1200 °C.	[13, 16, 129–131, 155]
Ta–Sb	Sb, $TaSb_2$, Ta_5Sb_4, Ta_3Sb, Ta No diagram plot	–	[18]
Ta–Bi	Bi, no binary compounds, Ta	No interaction and miscibility between the components. At 900 °C Ta is resistant to corrosion in molten Bi.	[4, 17, 273]

(continued)

Table 6.3 (continued)

System	Type of phase diagram (constituent phases, temperatures and compositions of transformations)	Character of interaction	References
Group 16			
Ta–O	O, β-Ta_2O_5 (<~1200–1360 °C, invariable compos.), α-Ta_2O_5 (from ~1200–1360 °C to ~1620–1900 °C, melt. point, invariable compos.), TaO_2 (?), TaO (?), Ta_2O (?), Ta_4O (?), TaO_x (sub-oxides, ?), Ta Eutectic α-Ta_2O_5–Ta (1520–1580 °C, ~29 at.% Ta) Miscibility gap in the liquid state (critical point–?, 35–57 at.% Ta at 1850–1910 °C)	The max. solubility of O in Ta is ~4–6 at.% in the range of temp. 1500–1900 °C; at higher and lower temp. it declines considerably and amounts to ~2 at.% at 1100 °C, ~1.5 at.% at 900 °C and ~1 at.% at 750 °C. Due to oxidation the surface of Ta parts loses its lustre at pressure O_2 >1,4 Pa and temp. >1000 °C; it is corresp. to O concentration >1.7 at.%. In terms of rate equations the oxidation of Ta varies considerably with temp. growth: logarithmic at 280–350 °C, cubic at 350–450 °C, parabolic at 450–600 °C, paralinear at 600–800 °C, linear at 800–1100 °C, post-parabolic at 1100–1250 °C and accelerated (up to oxidation failure) at the temp. >1250 °C. The mechanism of oxidation is very complicated, e.g. the rate of oxidation at 1000–1050 °C is higher than that is at 1100–1200 °C. At the temp. >1700 °C the vaporization of Ta oxides takes on great importance. The oxide melting at temp. >1800 °C results in the increase of oxidation rate. In air at atmospheric pressure the intensive oxidation of Ta and formation of noticeable oxide scales starts from 500–800 °C. For diffusion rate in the system at various temp. see Addendum.	[4, 10, 13, 15, 23–24, 28, 132–135, 145, 204]

(continued)

Table 6.3 (continued)

System	Type of phase diagram (constituent phases, temperatures and compositions of transformations)	Character of interaction	References
Ta–S	α-S, β-S, α-TaS_3, β-TaS_3, α-TaS_2, β-TaS_2, γ-TaS_2, δ-TaS_2, ε-TaS_2, α-TaS_{2-x} ($x \approx 0.25$, or $Ta_{\sim 1.15}S_2$), β-TaS_{2-x} ($x \approx 0.33$, or $Ta_{\sim 1.2}S_2$), γ-TaS_{2-x} ($x \approx 0.35$–0.5, or $Ta_{1+y}S_2$, $y \approx 1.2 \div 1.35$), TaS, Ta_3S_2, Ta_2S, Ta_6S, Ta (most of binary compounds have variable compos.) No diagram plot	Ta sulphides are synthesized by the direct interaction between the elements in sealed vacuum ampules at 450–600 °C. For diffusion rate in the system at various temp. see Addendum.	[4, 13, 18, 136]
Ta–Se	Se, η-$TaSe_3$ (at least at 500–850 °C, ?), ε-$TaSe_{2-x}$ (at least at 500–1000 °C, invariable compos.), ζ-$TaSe_{2-x}$ (at least at 500–1000 °C, invariable compos.), δ-$TaSe_{1+x}$ (or δ-Ta_2Se_{3+x}, at least from 500 to 800–1000 °C, homog. range—~35–46 at.% Ta), γ-$TaSe_{1+x}$ (or γ-Ta_2Se_{3+x}, at least at 800–1000 °C, homog. range—~38–41 at.% Ta), β-$TaSe_{1+x}$ (at least at 800–1000 °C, homog. range—~48–49 at.% Ta), α-$TaSe_{1+x}$ (at least at 500–800 °C, homog. range —~46–49 at.% Ta), Ta	Ta selenides are synthesized by the direct interaction between the elements at temp. >800 °C.	[4, 13, 18, 137–138]
Ta–Te	Te, $TaTe_4$ (or $TaTe_3$, ?), β-$TaTe_{2-x}$ (<900 °C, homog. range—33–50 at.% Ta, ?), α′-$TaTe_{2-x}$ (<800–840 °C, homog. range—33–54 at.% Ta), α″-$TaTe_{2-x}$ (from 800–840 °C to ?, homog. range—33–37 at.% Ta), $TaTe_{1-x}$ ($x > \sim 0.15$, ?), Ta	At temp. >800 °C the interaction between Te vapour and Ta is intensive and leads to the formation of tellurides having variable compos.	[4, 13, 17–18, 138–141, 272]
Ta–Po	α-Po, β-Po, no binary compounds, Ta No diagram plot	No interaction with Po vapour at temp. ≤700 °C.	[18, 142]

(continued)

Table 6.3 (continued)

System	Type of phase diagram (constituent phases, temperatures and compositions of transformations)	Character of interaction	References
Group 17			
Ta–F	F, TaF_5 (<95–97 °C, melt. point, invariable compos.), TaF_3 (invariable compos.), Ta No diagram plot	The direct interaction between Ta and F_2 initiates at room temp. At temp. ≥250 °C the intensive interaction results in the formation of TaF_5.	[2–4, 13, 143]
Ta–Cl	Cl, $TaCl_5$ (<217–220 °C, melt. point, invariable compos.), $TaCl_4$ (invariable compos.), $TaCl_3$ (or $TaCl_{2.9 \div 3.1}$, variable compos.), Ta_2Cl_5 (or Ta_6Cl_{15}, or $TaCl_{2.5}$, invariable compos.), Ta No diagram plot	Ta is resistant to dry and humid Cl_2 at temp. <150–250 °C. At 250 °C the interaction between Ta and Cl_2 is noticeable and results in the formation of $TaCl_5$; at 450 °C the interaction accompanied with the formation of $TaCl_3$ is intensive, at temp. ≥500 °C it proceeds immediately. $TaCl_4$ and Ta_2Cl_5 are synthesized by special chemical reaction pathways.	[2–4, 13, 143]
Ta–Br	Br, $TaBr_5$ (<~270–280 °C, congruent melt. point, invariable compos.), $TaBr_4$ (<~390 °C, invariable compos.), $TaBr_3$ (or Ta_6Br_{17}, $TaBr_{2.9 \div 3.1}$, <450 °C, variable compos., ?), Ta_2Br_5 (or Ta_6Br_{15}, or $TaBr_{2.5}$, <~675 °C, invariable compos.), Ta_3Br_7 (or Ta_6Br_{14}, or $TaBr_{2.33}$, at least at 200–750 °C, invariable compos.), $TaBr_2$ (?), Ta Eutectic $TaBr_5$–$TaBr_4$ (~265 °C, ~17 at.% Ta)	Ta is resistant to Br at temp. <150–250 °C. At 250–300 °C the interaction between the elements is noticeable; it is intensive at temp. >500 °C and results in the formation of $TaBr_5$. Ta bromides with lower valencies are synthesized by special chemical reaction pathways.	[2–4, 13, 143, 205–206]
Ta–I	I, TaI_5 (<~370–495 °C, congruent melt. point, invariable compos.), TaI_4 (<~380–400 °C, invariable compos.), TaI_3 (invariable compos.), Ta_3I_7 (or Ta_6I_{14}, $TaI_{2.33}$, at least at 300–550 °C, invariable compos.), Ta Eutectic Ta_3I_7–TaI_4 (365 °C, ~18.5 at.% Ta, ?)	Ta is resistant to I at temp. <150–250 °C. At 300 °C the interaction between the elements is noticeable; it is intensive at temp. >500 °C and results in the formation of TaI_5. Ta iodides with lower valencies are synthesized by special chemical reaction pathways.	[2–4, 13, 143, 206–207]
Ta–At	No data	–	–

[a] The intervals of temperatures and compositions for the melting and invariant equilibria points, homogeneity ranges and thermal stability regions of constituent phases are given taking into account the minimal and maximal values (data spread) available in the literature

The data on the selected ternary, quaternary, quasi-binary and quasi-ternary tantalum containing systems, which are the most important for the design, manufacture and application of ultra-high temperature materials, are summarized in Table 6.4. The composition and temperature stability regions for the main binary and ternary tantalum containing high-temperature phases are given in Tables 6.3 and 6.4 taking into account the spread of numerical magnitudes available in the literature currently.

Table 6.4 Chemical interaction of tantalum with elements and compounds at high temperatures (selected ternary, quaternary, quasi-binary and quasi-ternary systems in alphabetical order)[a]

System	Type of phase diagram (temperature and composition sections, constituent phases or phase fields) and/or character of interphase interaction and materials compatibility	References
Ta–Al–B	No diagram plot $Ta_5Al_3B_x$ ($x < 1$), Ta_3AlB_8 (or $Ta_{0.75}Al_{0.25}B_2$, ?)	[177, 208]
Ta–Al–B–N	No diagram plot In vacuum the interaction between metal Ta and α-BN–AlN equimolar compos. starts from 1500 °C and leads to the formation of $Ta_3B_{4\pm x}$ (traces of λ-$TaB_{1\pm x}$ and γ-$Ta_{2\pm x}N$).	[27]
Ta–Al–C	See C–Al–Ta in Table 2.14.	
Ta–Al–C–Ti	See C–Al–Ta–Ti in Table 2.14.	
Ta–Al–C–V	See C–Al–Ta–V in Table 2.14.	
Ta–Al–Ir	Plotted partially at 1650 °C: β-$Ir_{3\pm x}$(Ta,Al) (extended solid solution based on β-$Ir_{3\pm x}Ta$), $IrAl_{1\pm x}$, (<2120 °C), Ir_2Al_{5+x} (<1615 °C), $IrAl_3$ (<1450 °C), Ir_4Al_{13} (<1015 °C), Ir_2Al_9 (<900 °C), γ-Ir_3Ta_{2+x}, δ-$IrTa_{1-x}$, σ-$IrTa_{3\pm x}$, $TaAl_3$, $TaAl_2$, TaAl, δ-$Ta_{2\pm x}Al$, Al, Ir, Ta	[15–17, 163, 252]
Ta–Al–N	Plotted partially at 1250 °C: AlN (<2400–2450 °C), $TaAl_3$, $TaAl_2$, α-Ta_2Al_3, β-Ta_2Al_3, TaAl, δ-$Ta_{2\pm x}Al$, Ta_3N_5, ε-TaN_{1-x}, δ-TaN_{1-x}, γ-$Ta_{2\pm x}N$, Ta_9N_2, β-TaN_x, N, Al, Ta No solid solutions based on binary compounds. In vacuum (or Ar atmosphere), the interaction between bulk dense Ta and AlN initiates from 1600 °C and leads to the formation of δ-TaN_{1-x} and γ-$Ta_{2\pm x}N$	[21, 27, 209–210]
Ta–Al–Nb	Plotted at 630–2300 °C: $(Ta,Nb)Al_{3-x}$ ($TaAl_3$–$NbAl_{3-x}$ continuous solid solution, <~1550–1605 °C), δ-$(Ta,Nb)_{2\pm x}Al$ (δ-$Ta_{2\pm x}Al$–$Nb_{2\pm x}Al$ continuous solid solution at temp. ~930–1700 °C, or extended solid solution based on $Ta_{2\pm x}Al$ at temp. <~930 °C and >~1700 °C), $(Nb,Ta)_{3+x}Al$ (extended solid solution based on $Nb_{3+x}Al$ with compos.—up to ~$(Nb_{0.5}Ta_{0.5})_{3+x}Al$, <2060 °C), $(Nb,Ta)_{2\pm x}Al$ (solid solution based on $Nb_{2\pm x}Al$, <~930 °C), $(Ta,Nb)Al_2$ (solid solution based on $TaAl_2$), (Ta,Nb)Al (solid solution based on TaAl), Al, (Ta,Nb)	[15–17, 151, 154]

(continued)

Table 6.4 (continued)

System	Type of phase diagram (temperature and composition sections, constituent phases or phase fields) and/or character of interphase interaction and materials compatibility	References
Ta–Al–O	Ta_2O_5–Al_2O_3 is plotted partially: α-Ta_2O_5, β-Ta_2O_5, $81Ta_2O_5{\cdot}Al_2O_3$ (or $Al_2Ta_{162}O_{408}$, <~1370 °C), $59Ta_2O_5{\cdot}Al_2O_3$ (or $Al_2Ta_{118}O_{298}$, <~1400 °C), $37Ta_2O_5{\cdot}Al_2O_3$ (or $Al_2Ta_{74}O_{188}$, <~1415 °C), $26Ta_2O_5{\cdot}Al_2O_3$ (or $Al_2Ta_{52}O_{133}$, <~1440 °C), $67Ta_2O_5{\cdot}3Al_2O_3$ (or $Al_6Ta_{134}O_{344}$, <~1465 °C), $41Ta_2O_5{\cdot}2Al_2O_3$ (or $Al_4Ta_{82}O_{211}$, <~1500 °C), $15Ta_2O_5{\cdot}Al_2O_3$ (or $Al_2Ta_{30}O_{78}$, <~1605 °C), $27Ta_2O_5{\cdot}2Al_2O_3$ (or $Al_4Ta_{54}O_{141}$, <~1650 °C), α-$TaAlO_4$, β-$TaAlO_4$ In vacuum the interaction between Ta and Al_2O_3 initiates from 1600–1900 °C and results in the decomposition of oxide.	[4, 10, 28, 144]
Ta–As–Mo	Plotted partially at 1050 and 1400 °C: $Mo_xTa_{1-x}As$ (~0.5 ≤ x ≤ ~0.8), (Ta,Mo)As_2 ($TaAs_2$–$MoAs_2$ continuous solid solution), (Ta,Mo)$_5As_4$ (Ta_5As_4–Mo_5As_4 continuous solid solution), (Ta,Mo)$_3As$ (extended solid solution based on Ta_3As with compos.—up to ~$(Ta_{0.7}Mo_{0.3})_3As$), Ta_2As (solubility of Mo is low), TaAs (solubility of Mo is negligible), Mo_2As_3, MoAs (?), As, (Ta,Mo) The solubility of As in (Ta,Mo) varies from 0.6 to 3.1 at.%	[155]
Ta–B–C	See C–B–Ta in Table 2.14.	
Ta–B–C–N	See C–B–N–Ta in Table 2.14.	
Ta–B–C–Si	See C–B–Si–Ta in Table 2.14.	
Ta–B–Ce	No diagram plot In vacuum, at 1800 °C the interaction between Ta and $CeB_{6\pm x}$ leads to the formation of $TaB_{2\pm x}$ and solid solution of Ta in $CeB_{6\pm x}$.	[21]
Ta–B–Co	Plotted at 800 °C: CoTaB, $CoTaB_2$, Co_5TaB_2, Co_2TaB_3 (or $Co_7Ta_3B_{10}$), $Co_5Ta_3B_2$ (extended homog range, ?), $Co_{21}Ta_2B_6$, Co_3B (<1125 °C), Co_2B (<1280 °C), CoB (<1460 °C), $TaB_{2\pm x}$, $Ta_3B_{4\pm x}$, λ-$TaB_{1\pm x}$, $Ta_3B_{2\pm x}$, $Ta_{2+x}B$, κ-Co_7Ta_2, λ_3-$Co_{3-x}Ta$, λ_2-$Co_{2\pm x}Ta$, λ_1-Co_3Ta_{2-x}, μ-$CoTa_{1\pm x}$, $CoTa_2$, ε-Co, α-Co, β-B, Ta No solid solutions based on binary and ternary compounds.	[177, 211–212]

(continued)

Table 6.4 (continued)

System	Type of phase diagram (temperature and composition sections, constituent phases or phase fields) and/or character of interphase interaction and materials compatibility	References
Ta–B–Cr	Plotted at 1400 °C: $Ta_2Cr_9B_9$, $(Ta,Cr)B_{2\pm x}$ (extended solid solutions based on $TaB_{2\pm x}$ and $CrB_{2\pm x}$, or $TaB_{2\pm x}$–$CrB_{2\pm x}$ continuous solid solution at higher temp., <~2150–3200 °C), $(Ta,Cr)_3B_{2\pm x}$ (extended solid solution based on $Ta_3B_{2\pm x}$—up to ~$(Ta_{0.66}Cr_{0.34})_3B_{2\pm x}$ compos. at 1400 °C), λ-$(Ta,Cr)B_{1\pm x}$, (extended solid solution based on λ-$TaB_{1\pm x}$—up to ~$(Ta_{0.9}Cr_{0.1})B_{1\pm x}$ compos. at 1400 °C), $Cr_{2\pm x}B$ (<~1870 °C), $Cr_5B_{3\pm x}$ (<~1900 °C), α-$CrB_{1\pm x}$ (≤1000 °C, ?), β-$CrB_{1\pm x}$ (~1000–2150 °C, ?), $Cr_3B_{4\pm x}$ (<2070–2075 °C), Cr_2B_3 (at least at ~1000–1500 °C), CrB_4 (<~1450–1500 °C), $Ta_3B_{4\pm x}$, $Ta_{2+x}B$, $TaCr_3$, λ_2-$TaCr_{2\pm x}$, λ_1-$TaCr_{2\pm x}$, Cr, β-B, Ta At 1400 °C the max. solid solubility of Ta in $Cr_3B_{4\pm x}$, β-$CrB_{1\pm x}$, $Cr_5B_{3\pm x}$ and $Cr_{2\pm x}B$ is ~1.5–2.0 at.% and that of Cr in $Ta_3B_{4\pm x}$ is ~2 at.%.	[4, 213]
Ta–B–Fe	Plotted at 950 °C: FeTaB, $FeTa_2B_2$, $FeTaB_3$, $FeTaB_2$ (?), Fe_5TaB_2 (?), $(Ta,Fe)_3B_{2\pm x}$ (extended solid solution based on $Ta_3B_{2\pm x}$—up to ~$(Ta_{0.67}Fe_{0.33})_3B_{2\pm x}$ compos. at 950 °C), Fe_2B (<1407 °C), FeB (<1588 °C), $TaB_{2\pm x}$, $Ta_3B_{4\pm x}$, λ-$TaB_{1\pm x}$, $Ta_{2+x}B$, ε-$Fe_{2\pm x}Ta$, μ-$FeTa_{1\pm x}$, α-Fe, γ-Fe, δ-Fe, β-B, Ta No solid solutions based on binary and ternary compounds apart from $Ta_3B_{2\pm x}$ (at 950 °C).	[177–178]
Ta–B–Ge	Plotted at 700 °C: $Ta_5Ge_3B_{1-x}$, Ta_5Ge_2B, $TaB_{2\pm x}$, $Ta_3B_{4\pm x}$, λ-$TaB_{1\pm x}$, $Ta_3B_{2\pm x}$, $Ta_{2+x}B$, $TaGe_2$, α-Ta_5Ge_3, β-Ta_5Ge_3, α-Ta_2Ge, β-Ta_2Ge, γ-Ta_2Ge, δ-Ta_2Ge, α-Ta_3Ge, β-Ta_3Ge, Ge, β-B, Ta No solid solutions based on binary and ternary compounds.	[177, 214]
Ta–B–Hf	Plotted at 1400 °C: $(Ta,Hf)B_{2\pm x}$ ($TaB_{2\pm x}$–$HfB_{2\pm x}$ continuous solid solution), λ-$(Ta,Hf)B_{1\pm x}$ (extended solid solution based on λ-$TaB_{1\pm x}$—up to ~$(Ta_{0.4}Hf_{0.6})B_{1\pm x}$), $(Ta,Hf)_3B_{4\pm x}$ (extended solid solution based on $Ta_3B_{4\pm x}$—up to ~$(Ta_{0.78}Hf_{0.22})_3B_{4\pm x}$), $(Ta,Hf)_3B_{2\pm x}$ (extended solid solution based on $Ta_3B_{2\pm x}$—up to ~$(Ta_{0.83}Hf_{0.17})_3B_{2\pm x}$), $HfB_{1\pm x}$ (<2100 °C), $Ta_{2+x}B$, α-Hf, β-B, (Ta,β-Hf)	[21, 215]
Ta–B–La	$LaB_{6\pm x}$–$TaB_{2\pm x}$ is plotted: eutectic—~2460 °C, ~40 mol.% $TaB_{2\pm x}$ (~81.5 at.% B); the max. solubility of $LaB_{6\pm x}$ in $TaB_{2\pm x}$ and that of $TaB_{2\pm x}$ in $LaB_{6\pm x}$ are ≤2 mol.% (at eutectic temp.) At 1600–2000 °C (2–5 h exposure) the interaction between Ta and $LaB_{6\pm x}$ leads to the formation of the following phases (in sequence): $Ta_{2+x}B$ → λ-$TaB_{1\pm x}$ → $Ta_3B_{4\pm x}$ → $TaB_{2\pm x}$ and LaB_4; at 2100 °C (2–5 h exposure) the interaction is very intensive.	[4, 21, 216]

(continued)

Table 6.4 (continued)

System	Type of phase diagram (temperature and composition sections, constituent phases or phase fields) and/or character of interphase interaction and materials compatibility	References
Ta–B–Mo	Plotted at 1200 and 1650 °C (schematically): $(Ta,Mo)B_{2\pm x}$ ($TaB_{2\pm x}$–MoB_{2-x} continuous solid solution), λ-$(Ta,Mo)B_{1\pm x}$ (extended solid solution based on λ-$TaB_{1\pm x}$—up to $\sim(Ta_{0.2}Mo_{0.8})B_{1\pm x}$ at 1200 °C), $(Ta,Hf)_3B_{2\pm x}$ (extended solid solution based on $Ta_3B_{2\pm x}$—up to $\sim(Ta_{0.34}Mo_{0.66})_3B_{2\pm x}$ at 1200 °C), $(Mo,Ta)_{2\pm x}B$ (extended solid solution based on $Mo_{2\pm x}B$—up to $\sim(Mo_{0.85}Ta_{0.15})_{2\pm x}B$ at 1200 °C, <2280 °C), α-$(Mo,Ta)B_{1-x}$ (solid solution based on α-MoB_{1-x}—up to $\sim(Mo_{0.95}Ta_{0.05})B_{1-x}$ at 1200 °C, <2180 °C), $Ta_3B_{4\pm x}$ (solubility of Mo ≤1.5 at.% at 1200 °C), $Ta_{2+x}B$ (solubility of Mo <1 at.% at 1200 °C), Mo_3B_2 (1920–2070 °C), β-$MoB_{1\pm x}$ (∼1800–2610 °C), Mo_2B_{5-x} (<2140 °C), MoB_{4-x} (<∼1805 °C), β-B, (Mo,Ta) The contact interaction between Ta and Mo_2B_{5-x} initiates at 1300 °C and leads to the formation of $Ta_3B_{2\pm x}$, $Ta_3B_{4\pm x}$ and $TaB_{2\pm x}$; the contact interaction between $TaB_{2\pm x}$ and Mo initiates from 1400–1800 °C (2–5 h exposure), it is intensive at temp. ≥2000 °C and results in the formation of $Mo_{2\pm x}B$ at 2000 °C and $Mo_{2\pm x}B$ + α-MoB_{1-x} at temp. ≥2100 °C.	[4, 10, 21, 217]
Ta–B–Mo–Si	$TaB_{2\pm x}$–$MoSi_2$ is plotted: eutectic—∼1870–1930 °C, ∼10–15 mol.% $TaB_{2\pm x}$; no mutual solubilities between the components	[274]
Ta–B–N	Plotted at 1200 °C (Ar pressure—0.1 MPa) and 1400 °C (vacuum, pressure—10^{-3} Pa): α-BN (<2400 °C), ε-TaN_{1-x}, δ-TaN_{1-x}, γ-$Ta_{2\pm x}N$, $TaB_{2\pm x}$, $Ta_3B_{4\pm x}$, λ-$TaB_{1\pm x}$, $Ta_3B_{2\pm x}$, N, β-B, Ta Ta is in equilibrium with γ-$Ta_{2\pm x}N$ and $Ta_3B_{2\pm x}$. In vacuum, the contact interaction between metal Ta and α-BN initiates from 1500–1700 °C and leads to the formation of λ-$TaB_{1\pm x}$ and small amounts of $Ta_3B_{4\pm x}$ and γ-$Ta_{2\pm x}N$. In Ar atmosphere, the interaction between powdered Ta and α-BN results to the formation of λ-$TaB_{1\pm x}$, δ-TaN_{1-x} and small amounts of $TaB_{2\pm x}$. At 2400 °C the main product of the interaction between Ta and α-BN is $TaB_{2\pm x}$.	[4, 21, 26–27, 29]
Ta–B–N–O	No diagram plot The interaction between α-Ta_2O_5 and α-BN leads to the formation of λ-$TaB_{1\pm x}$ (at 1600 °C) and $TaB_{2\pm x}$ (at 2000 °C).	[21, 28]

(continued)

Table 6.4 (continued)

System	Type of phase diagram (temperature and composition sections, constituent phases or phase fields) and/or character of interphase interaction and materials compatibility	References
Ta–B–Nb	Plotted at 1400 °C: (Ta,Nb)$B_{2\pm x}$ ($TaB_{2\pm x}$–$NbB_{2\pm x}$ continuous solid solution), (Ta,Nb)$_3B_{4\pm x}$ ($Ta_3B_{4\pm x}$–Nb_3B_4 continuous solid solution), (Ta,Nb)$B_{1\pm x}$ (λ-$TaB_{1\pm x}$–$NbB_{1\pm x}$ continuous solid solution), (Ta,Nb)$_3B_{2\pm x}$ ($Ta_3B_{2\pm x}$–Nb_3B_2 continuous solid solution), Nb_5B_6 (<~2295–2870 °C, ?), $Ta_{2+x}B$, β-B, (Nb,Ta) No interaction between Ta and $NbB_{2\pm x}$ at 1800–2000 °C, the interaction between $TaB_{2\pm x}$ and Nb initiates from 1400–1600 °C and leads to the formation of $NbB_{2\pm x}$ and λ-$TaB_{1\pm x}$.	[4, 21, 177, 232]
Ta–B–Nb–Ni	No diagram plot (Ta,Nb)NiB_2	[177]
Ta–B–Nb–Ru	No diagram plot (Ta,Nb)$_{2\div3}Ru_{20\div21}B_6$ (or (Ta,Nb,Ru)$_{23}B_6$)	[177]
Ta–B–Ni	Plotted at 800 and 950 °C: NiTaB, $NiTaB_2$ (<1500 °C), $Ni_{21}Ta_2B_6$, $Ni_{21}Ta_2B_6$ (or $Ni_{20.7}Ta_{2.3}B_6$, <1180–1220 °C, homog. range—~7.5–8.5 at.% Ta, ~70.0–72.5 at.% Ni at 700 °C), Ni_5TaB_2 (?), Ni_3B (<~1155 °C), Ni_2B (<1125 °C), Ni_4B_{3-x} (or o-Ni_4B_3, $x \approx 0.2$, <1025 °C), Ni_4B_{3+x} (or m-Ni_4B_3, $x \approx 0.1$, <~1030 °C), NiB (<1035 °C), $TaB_{2\pm x}$, $Ta_3B_{4\pm x}$, λ-$TaB_{1\pm x}$, $Ta_3B_{2\pm x}$, $Ta_{2+x}B$, ζ-$Ni_{8\pm x}Ta$, κ-$Ni_{3\pm x}Ta$, $Ni_{2\pm x}Ta$, μ-$Ni_{1-x}Ta$ (or μ-Ni_7Ta_{6+x}), $NiTa_{2+x}$, β-B, Ni, Ta $Ni_{21}Ta_2B_6$–Ni plotted: eutectic—~1070–1090 °C, ~5.5–7.5 at.% Ta, ~77.5–80.0 at.% Ni No solid solutions based on binary and ternary compounds.	[177–178, 218–220]
Ta–B–O	No diagram plot $TaBO_4$ The interaction between $TaB_{2\pm x}$ and Ta_2O_5 results in the formation of $Ta_3B_{4\pm x}$ at 1100 °C, λ-$TaB_{1\pm x}$ at 1200–1700 °C, λ-$TaB_{1\pm x}$ + Ta at 1800 °C and $Ta_{2+x}B$ + Ta at 1900–2000 °C	[21, 221]
Ta–B–Re	See Re–B–Ta in Table 4.6.	
Ta–B–Si	Plotted at 1500 °C: $Ta_xSi_yB_z$ ($x \approx 5.2 \div 5.7$, $y \approx 3.1 \div 3.7$, $z \approx 0.5 \div 1.4$), $Ta_5Si_{3-x}B_x$ ($x \approx 0.2 \div 1.2$), Ta_2(Si,B) (extended solid solution based on Ta_2Si with max. B solubility—up to ~6–7 at.%), SiB_n ($n \approx 23$, <2040 °C), SiB_6 (<1850 °C), $SiB_{3\pm x}$ (<1270 °C), $TaB_{2\pm x}$, $Ta_3B_{4\pm x}$, λ-$TaB_{1\pm x}$, $Ta_3B_{2\pm x}$, $Ta_{2+x}B$, $TaSi_2$, α-Ta_5Si_3, β-Ta_5Si_3, $Ta_{3+x}Si$, β-B, Si, Ta $TaB_{2\pm x}$ is stable in contact with Si.	[4, 29, 34, 224]
Ta–B–Si–Ti	No diagram plot At 2000–2200 °C the interaction between Ta silicides (β-Ta_5Si_3, $TaSi_2$) and $TiB_{2\pm x}$ is weak.	[21]
Ta–B–Si–W	See W–B–Si–Ta in Table 3.6.	

(continued)

Table 6.4 (continued)

System	Type of phase diagram (temperature and composition sections, constituent phases or phase fields) and/or character of interphase interaction and materials compatibility	References
Ta–B–Si–Zr	No diagram plot At 2000–2200 °C the interaction between Ta silicides (β-Ta_5Si_3, $TaSi_2$) and $ZrB_{2\pm x}$ is weak.	[21]
Ta–B–Ti	Plotted at 1650 °C: (Ta,Ti)$B_{2\pm x}$ ($TaB_{2\pm x}$–$TiB_{2\pm x}$ continuous solid solution, <3035–3250 °C), λ-(Ta,Ti)$B_{1\pm x}$ (extended solid solution based on λ-$TaB_{1\pm x}$—up to ~$(Ta_{0.8}Ti_{0.2})B_{1\pm x}$ at 1650 °C), (Ti,Ta)B_{1-x} (extended solid solution based on TiB_{1-x}—up to ~$(Ti_{0.8}Ta_{0.2})B_{1-x}$ at 1650 °C, <~2180–2200 °C), Ti_3B_4 (<~2200–2205 °C), $Ta_3B_{4\pm x}$, $Ta_3B_{2\pm x}$, $Ta_{2+x}B$, β-B, α-Ti, (β-Ti,Ta) At 1650 °C the max. solid solubility of Ti in $Ta_3B_{4\pm x}$, $Ta_3B_{2\pm x}$ and $Ta_{2+x}B$ is ~1.0–2.5 at.%. The interaction between Ta and $TiB_{2\pm x}$ results in the formation of TiB_{1-x}, $Ta_3B_{2\pm x}$ and λ-$TaB_{1\pm x}$ at 1500–1800 °C, TiB_{1-x}, $Ta_3B_{2\pm x}$, λ-$TaB_{1\pm x}$, $Ta_3B_{4\pm x}$ and $TaB_{2\pm x}$ at 1900–2200 °C.	[4, 21, 217]
Ta–B–W	See W–B–Ta in Table 3.6.	
Ta–B–Zr	Plotted at 1500 °C: (Ta,Zr)$B_{2\pm x}$ ($TaB_{2\pm x}$–$ZrB_{2\pm x}$ continuous solid solution), λ-(Ta,Zr)$B_{1\pm x}$ (extended solid solution based on λ-$TaB_{1\pm x}$—up to ~$(Ta_{0.4}Zr_{0.6})$ $B_{1\pm x}$ at 1500 °C), $(Ta,Zr)_3B_{2\pm x}$ (extended solid solution based on $Ta_3B_{2\pm x}$—up to ~$(Ta_{0.9}Zr_{0.1})_3B_{2\pm x}$ at 1500 °C), ZrB_{12-x} (~1695–2290 °C), $Ta_3B_{4\pm x}$, $Ta_{2+x}B$, β-B, α-Zr, (β-Zr,Ta) At 1500 °C the max. solid solubility of Zr in $Ta_3B_{4\pm x}$ and $Ta_{2+x}B$ is ~2.0–2.5 at.%. The interaction between Ta and $ZrB_{2\pm x}$ initiates from 1200–1500 °C and results in the formation of Ta-Zr boride solid solutions.	[4, 21, 222–223]
Ta–Be–C	See C–Be–Ta in Table 2.14.	
Ta–Be–O	No diagram plot In vacuum, the interaction between metal Ta and BeO initiates from 1600 °C and leads to the formation of complex phases.	[10, 28]
Ta–Bi–Pb	No diagram plot At 1095 °C the resistance of Ta to pitting corrosion in Bi–Pb alloy is low.	[4]
Ta–Bi–U	No diagram plot At 1100 °C Ta is resistant to corrosion in Bi–U eutectic alloy for ~1000 h.	[4]
Ta–C–Co	See C–Co–Ta in Table 2.14.	
Ta–C–Co–Hf	See C–Co–Hf–Ta in Table 2.14.	
Ta–C–Co–Nb	See C–Co–Nb–Ta in Table 2.14.	
Ta–C–Co–Ti	See C–Co–Ta–Ti in Table 2.14.	
Ta–C–Co–V	See C–Co–Ta–V in Table 2.14.	

(continued)

Table 6.4 (continued)

System	Type of phase diagram (temperature and composition sections, constituent phases or phase fields) and/or character of interphase interaction and materials compatibility	References
Ta–C–Co–Zr	See C–Co–Ta–Zr in Table 2.14.	
Ta–C–Cr	See C–Cr–Ta in Table 2.14.	
Ta–C–Fe	See C–Fe–Ta in Table 2.14	
Ta–C–Ga	See C–Ga–Ta in Table 2.14.	
Ta–C–Hf	See C–Hf–Ta in Table 2.14.	
Ta–C–Hf–U	See C–Hf–Ta–U in Table 2.14.	
Ta–C–Ir	See C–Ir–Ta in Table 2.14.	
Ta–C–Mg–O	See C–Mg–O–Ta in Table 2.14.	
Ta–C–Mo	See C–Mo–Ta in Table 2.14.	
Ta–C–Mo–Nb	See C–Mo–Nb–Ta in Table 2.14.	
Ta–C–Mo–Si	See C–Mo–Si–Ta in Table 2.14.	
Ta–C–Mo–V	See C–Mo–Ta–V in Table 2.14.	
Ta–C–N	See C–N–Ta in Table 2.14.	
Ta–C–N–U	See C–N–Ta–U in Table 2.14.	
Ta–C–Nb	See C–Nb–Ta in Table 2.14.	
Ta–C–Nb–Ni	See C–Nb–Ni–Ta in Table 2.14.	
Ta–C–Nb–Ti	See C–Nb–Ta–Ti in Table 2.14.	
Ta–C–Nb–W	See C–Nb–Ta–W in Table 2.14.	
Ta–C–Ni	See C–Ni–Ta in Table 2.14.	
Ta–C–O	See C–O–Ta in Table 2.14.	
Ta–C–O–U	See C–O–Ta–U in Table 2.14.	
Ta–C–O–W	See C–O–Ta–W in Table 2.14.	
Ta–C–O–Zr	See C–O–Ta–Zr in Table 2.14.	
Ta–C–Os	See C–Os–Ta in Table 2.14.	
Ta–C–Pd	See C–Pd–Ta in Table 2.14.	
Ta–C–Pt	See C–Pt–Ta in Table 2.14.	
Ta–C–Pu	See C–Pu–Ta in Table 2.14.	
Ta–C–Re	See C–Re–Ta in Table 2.14.	
Ta–C–Rh	See C–Rh–Ta in Table 2.14.	
Ta–C–Ru	See C–Ru–Ta in Table 2.14.	
Ta–C–S	See C–S–Ta in Table 2.14.	
Ta–C–Si	See C–Si–Ta in Table 2.14.	
Ta–C–Tc	See C–Ta–Tc in Table 2.14.	
Ta–C–Th	See C–Ta–Th in Table 2.14.	
Ta–C–Ti	See C–Ta–Ti in Table 2.14.	
Ta–C–Ti–U	See C–Ta–Ti–U in Table 2.14	
Ta–C–Ti–W	See C–Ta–Ti–W in Table 2.14.	
Ta–C–U	See C–Ta–U in Table 2.14.	
Ta–C–U–V	See C–Ta–U–V in Table 2.14.	
Ta–C–U–Zr	See C–Ta–U–Zr in Table 2.14.	
Ta–C–V	See C–Ta–V in Table 2.14.	
Ta–C–V–W	See C–Ta–V–W in Table 2.14.	
Ta–C–W	See C–Ta–W in Table 2.14.	

(continued)

Table 6.4 (continued)

System	Type of phase diagram (temperature and composition sections, constituent phases or phase fields) and/or character of interphase interaction and materials compatibility	References
Ta–C–Zr	See C–Ta–Zr in Table 2.14.	
Ta–Ca–O	Ta_2O_5–CaO is plotted: CaO (<2570 °C), $5CaO{\cdot}Ta_2O_5$ (or $Ca_5Ta_2O_{10}$, 1460–1590 °C), $4CaO{\cdot}Ta_2O_5$ (or $Ca_4Ta_2O_9$, <1990 °C), $2CaO{\cdot}Ta_2O_5$ (or $Ca_2Ta_2O_7$, <1895 °C), β-$CaO{\cdot}Ta_2O_5$ (or β-$CaTa_2O_6$, <~1560 °C), α-$CaO{\cdot}Ta_2O_5$ (or α-$CaTa_2O_6$, ~1560–1960 °C), $CaO{\cdot}2Ta_2O_5$ (or $CaTa_4O_{11}$, <1730 °C), α-Ta_2O_5, β-Ta_2O_5; $Ca_4Ta_2O_9$–$Ca_2Ta_2O_7$ eutectic—1780 °C, 29 mol.% Ta_2O_5; $Ca_2Ta_2O_7$–α-$CaTa_2O_6$ eutectic—1775 °C, 40 mol.% Ta_2O_5; $CaTa_4O_{11}$–α-Ta_2O_5 eutectic—1700 °C, 73 mol.% Ta_2O_5	[166]
Ta–Ce–O	Ta_2O_5–Ce_2O_3–CeO_{2-x} is plotted: $Ce_2O_3{\cdot}Ta_2O_5$ (or $CeTaO_4$), $Ce_2O_3{\cdot}3Ta_2O_5$ (or $CeTa_3O_9$), $Ce_2O_3{\cdot}7Ta_2O_5$ (or $CeTa_7O_{19}$), Ce_2O_3, CeO_{2-x}, α-Ta_2O_5, β-Ta_2O_5 Ta_2O_5–CeO_{2-x} is plotted: $(Ce,Ta)O_{2-x}$ (solid solution based on CeO_{2-x}—up to ~3.5 mol.% Ta_2O_5, <2800 °C), $Ce_2O_3{\cdot}Ta_2O_5$ (or $CeTaO_4$, at least at ~1265–1600 °C), $Ce_2O_3{\cdot}3Ta_2O_5$ (or $CeTa_3O_9$, <at least ~1600 °C), $Ce_2O_3{\cdot}7Ta_2O_5$ (or $CeTa_7O_{19}$, <1525 °C), α-Ta_2O_5, β-Ta_2O_5	[181–182]
Ta–Co–Ir	Plotted at 950 °C: TaCoIr, Ta_6CoIr (or $Ta_3Co_{0.5}Ir_{0.5}$), μ-$CoTa_{1\pm x}Ir_y$ (extended solid solution based on μ-$CoTa_{1\pm x}$—up to ~25 at.% Ir), σ-$IrTa_{3\pm x}Co_y$ (extended solid solution based on σ-$IrTa_{3\pm x}$—up to ~22 at.% Co), δ-$(Ir,Co)Ta_{1-x}$ (extended solid solution based on δ-$IrTa_{1-x}$—up to ~20 at.% Co), γ-$(Ir,Co)_3Ta_{2+x}$ (extended solid solution based on γ-Ir_3Ta_{2+x}—up to ~15 at.% Co), β-$(Ir,Co)_{3\pm x}Ta$ (extended solid solution based on β-$Ir_{3\pm x}Ta$—up to ~20 at.% Co), $(Co,Ir)Ta_2$ (extended solid solution based on $CoTa_2$—up to ~8 at.% Ir), λ_1-$(Co,Ir)_3Ta_{2-x}$ (extended solid solution based on λ_1-Co_3Ta_{2-x}—up to ~7 at.% Ir), λ_2-$(Co,Ir)_{2\pm x}Ta$ (extended solid solution based on λ_2-$Co_{2\pm x}Ta$—up to ~7 at.% Ir), λ_3-$(Co,Ir)_{3-x}Ta$ (extended solid solution based on λ_3-$Co_{3-x}Ta$—up to ~12 at.% Ir), κ-Co_7Ta_2, ε-Co, (α-Co,Ir), Ta	[246]
Ta–Co–Mo	Plotted at 1000 °C: κ-$Co_{3\pm x}(Mo,Ta)$ (extended solid solution based on κ-$Co_{3\pm x}Mo$, <~1040 °C), μ-$Co_7(Mo,Ta)_{6\pm x}$ (extended solid solution based on μ-$Co_7Mo_{6\pm x}$, <~1510 °C), $Co_3(Ta,Mo)$ (extended solid solution based on Co_3Ta), λ_3-$Co_{3-x}(Ta,Mo)$ (extended solid solution based on λ_3-$Co_{3-x}Ta$), λ_2-$Co_{2\pm x}(Ta,Mo)$ (extended solid solution based on λ_2-$Co_{2\pm x}Ta$), μ-$CoTa_{1\pm x}$ (extended solid solution based on μ-$CoTa_{1\pm x}$), $Co(Ta,Mo)_2$ (extended solid solution based on $CoTa_2$), σ-$Co_{2-x}Mo_3$ (from ~900–1100–1620 °C), θ-$Co_9Mo_{2\pm x}$ (~1020–1200 °C), α-Co, (Ta,Mo)	[14–15, 17, 32, 150]

(continued)

Table 6.4 (continued)

System	Type of phase diagram (temperature and composition sections, constituent phases or phase fields) and/or character of interphase interaction and materials compatibility	References
Ta–Co–N	No diagram plot $Ta_4Co_2N_5$ (or $Ta_2CoN_{2.5}$), η-$Ta_4Co_2N_{1-x}$, η-Ta_3Co_3N	[25]
Ta–Co–Nb	Plotted at 1100 °C: λ-Co_{3-x}(Ta,Nb) (λ_2-$Co_{2\pm x}$Ta–λ_3-Co_3Nb continuous solid solution, ~1000–1240 °C), μ-$Co(Ta,Nb)_{1\pm x}$ (μ-$CoTa_{1\pm x}$–μ-$NbCo_{1\pm x}$ continuous solid solution, <1480–1700 °C), $\lambda_2(\alpha)$-Co_{2+x}(Nb,Ta) (extended solid solution based on $\lambda_2(\alpha)$-Co_{2+x}Nb, <~1200 °C), λ_3-Co_{3-x}(Ta,Nb) (extended solid solution based on λ_3-Co_{3-x}Ta), $Co(Ta,Nb)_2$ (extended solid solution based on $CoTa_2$ with compos.—up to ~$Co(Ta_{0.4}Nb_{0.6})_2$), α-Co, ε-Co, (Ta,Nb)	[14–15, 17, 32, 148, 150]
Ta–Co–W	See W–Co–Ta in Table 3.6.	
Ta–Cr–Mo	Plotted at 1000 °C: (Ta,Cr,Mo) (extended solid solution based on Mo–Cr and Mo–Ta continuous solid solutions with miscibility gap adjoined to Cr–Ta side: ~$Ta_{0.015}Cr_{0.985}$–$Ta_{0.275}Cr_{0.34}Mo_{0.385}$–$Ta_{0.88}Cr_{0.12}$), λ_1/λ_2-$TaCr_{2\pm x}$	[195]
Ta–Cr–Mo–Si	$TaSi_2$–$MoSi_2$–$CrSi_2$ is plotted at 1300 °C: $(Ta,Cr,Mo)Si_2$ (or extended solid solution based on $TaSi_2$–$CrSi_2$ continuous solid solution with the max. solubility of Mo corresp. to compos.—~$(Ta_{0.45}Mo_{0.55})Si_2$ and ~$(Cr_{0.7}Mo_{0.3})Si_2$), $(Mo,Cr,Ta)Si_2$ (or extended solid solution based on α-$MoSi_2$; solubility of $CrSi_2$ is ~45 mol.% and that of $TaSi_2$ is ~15 mol.%)	[35]
Ta–Cr–N	No diagram plot Ta_3Cr_3N, $TaCr_3N_4$, ? In Ar atmosphere the interaction between δ-TaN_{1-x} and Cr (exposure—up to 1.5 h) leads to the formation of $Cr_{2\pm x}N$ at 1600 °C and $Cr_{2\pm x}N$ + λ_2-$TaCr_{2\pm x}$ at 1700–1800 °C (the liquid phase appears at the contact boundary at ~1680 °C).	[176, 225–226]
Ta–Cr–Nb	Plotted partially at 1300 °C: λ_2-$(Ta,Nb)Cr_{2\pm x}$ (λ_2-$TaCr_{2\pm x}$–λ_2-$NbCr_{2\pm x}$ continuous solid solution, <1585–1805 °C), λ_1-$(Ta,Nb)Cr_{2\pm x}$ (λ_1-$TaCr_{2\pm x}$–λ_1-$NbCr_{2\pm x}$ continuous solid solution, from 1585–1805 °C to 1720–2020 °C) $TaCr_{2\pm x}$–$NbCr_{2\pm x}$ is plotted: λ_1-$TaCr_{2\pm x}$–λ_1-$NbCr_{2\pm x}$ and λ_2-$TaCr_{2\pm x}$–λ_2-$NbCr_{2\pm x}$ continuous solid solutions	[164–165, 175]
Ta–Cr–Nb–Ti	$TaCr_{2\pm x}$–$NbCr_{2\pm x}$–$TiCr_{2-x}$ is 3D-plotted: α-$(Ta,Nb,Ti)Cr_{2\pm x}$ (λ_2-$TaCr_{2\pm x}$–λ_2-$NbCr_{2\pm x}$–α-$TiCr_{2-x}$ continuous solid solution, <1220–1805 °C), β-$(Ta,Nb,Ti)Cr_{2\pm x}$ (λ_2-$TaCr_{2\pm x}$–λ_2-$NbCr_{2\pm x}$–β-$TiCr_{2-x}$ continuous solid solution, from 1220–1350 °C to 1620–2020 °C), γ-$TiCr_{2-x}$ (?), β-(Ta,Nb,Ti,Cr) (extended solid solution based on β-Ti–Cr continuous solid solution, ~1350–1450 °C (?), <~3 at.% Ta + Nb in total)	[175]

(continued)

Table 6.4 (continued)

System	Type of phase diagram (temperature and composition sections, constituent phases or phase fields) and/or character of interphase interaction and materials compatibility	References
Ta–Cr–Si	No diagram plot Ta_2Cr_3Si, $Ta_2Cr_4Si_5$, $Ta_3Cr_8Si_8$, ? $TaSi_2$–$CrSi_2$ is plotted: max. solubility of $CrSi_2$ in $TaSi_2$ is 40 mol.% and that of $TaSi_2$ in $CrSi_2$ is 12 mol.%	[134, 36, 227–228]
Ta–Cr–Si–Ti	$TaSi_2$–$CrSi_2$–$TiSi_2$ is plotted at 1300 °C: $(Ta,Cr,Ti)Si_2$ (extended solid solution based on $TaSi_2$–$CrSi_2$ continuous solid solution with the max. solubility of Ti corresp. to compos.—$\sim(Ta_{0.5}Ti_{0.5})Si_2$ and $\sim(Cr_{0.15}Ti_{0.85})Si_2$); the solubilities of $TaSi_2$ and $CrSi_2$ in $TiSi_2$ is extremely low	[35]
Ta–Cr–W	See W–Cr–Ta in Table 3.6.	
Ta–Cu–N	No diagram plot $CuTaN_2$, $Cu_6Ta_9N_{25}$, ? No interaction between δ-TaN_{1-x} and liquid Cu.	[21, 229–230]
Ta–Cu–Nb	Plotted at 1700–2800 °C: Ta–Nb continuous solid solution, Cu Practically, no solubility between (Ta,Nb) and Cu.	[151–152]
Ta–Fe–Mo	Plotted at 900–1250 °C: $Fe_{2\pm x}(Ta,Mo)$ (ε-$Fe_{2\pm x}Ta$–λ-Fe_2Mo continuous solid solution), μ-Fe_7Mo_{6-x} (<1370 °C), ρ-$Fe_{3+x}Mo_2$ ($\sim$1200–1490 °C), σ-$FeMo_{1\pm x}$ (1235–1540 °C), μ-$FeTa_{1\pm x}$, α-Fe, γ-Fe, δ-Fe, (Ta,Mo)	[14–15, 17, 32, 238–239]
Ta–Fe–N	Plotted schematically at 1000–1700 °C: $Ta_4Fe_2N_5$ (or $Ta_2FeN_{2.5\div2.6}$), η-$Ta_{3+y}Fe_{3-y}N$ (or η-Ta_4Fe_2N), ?	[25, 231]
Ta–Fe–Nb	Plotted at 1100 °C: μ-$Fe(Ta,Nb)_{1\pm x}$ (μ-$FeTa_{1\pm x}$–μ-Fe_7Nb_{6+x} continuous solid solution, ?), ε-$Fe_{2\pm x}Nb$ (<$\sim$1625–1665 °C), ε-$Fe_{2\pm x}Ta$, α-Fe, γ-Fe, δ-Fe, (Ta,Nb)	[14–15, 17, 32]
Ta–Fe–Pu	No diagram plot At 900–1150 °C Ta is not stable in the contact with Pu—10 at.% Fe alloy; the interaction of Ta occurs because of the penetration of Pu–Fe alloy along the Ta grain boundaries.	[4]
Ta–Fe–W	See W–Fe–Ta in Table 3.6.	
Ta–H–Ir	No diagram plot $(Ta_{1-x}Ir_x)_2H_y$	[240]
Ta–H–Mo	No diagram plot $(Ta_{1-x}Mo_x)_2H_y$	[240]
Ta–H–Nb	No diagram plot $(Ta_{1-x}Nb_x)_2H_{1-y}$, $(Ta_{1-x}Nb_x)H_2$	[244]

(continued)

Table 6.4 (continued)

System	Type of phase diagram (temperature and composition sections, constituent phases or phase fields) and/or character of interphase interaction and materials compatibility	References
Ta–Hf–N	Plotted partially at 1000–3200 °C: (Hf,Ta)$N_{1\pm x}$ (extended solid solution based on $HfN_{1\pm x}$, <3385 °C; at 1600–2200 °C the max. solubility of δ-TaN_{1-x} in $HfN_{1\pm x}$ amounts to ~75 mol.%), ε-$(Hf,Ta)_{2\pm x}N$ (solid solution based on $Hf_{2\pm x}N$ (?) with max. solubility of Ta ≤ 2.5 at.%, ?), γ-$(Ta,Hf)_{2\pm x}N$ (extended solid solution based on γ-$Ta_{2\pm x}N$ with max. solubility of Hf ≤ ~9 at.% at ~2800 °C), (Hf,Ta,N) (extended solid solution based on α-Hf, <1743 °C), (Ta,Hf,N) (extended solid solution based on Ta–β-Hf continuous solid solution with miscibility gap), N, Hf, Ta $HfN_{1\pm x}$ ($HfN_{0.82\div0.83}$)–Ta is plotted (Ar pressure—1 MPa): eutectic—~2630–2730 °C, ~65–70 mol.% Ta; the max. solid solubility of Ta in $HfN_{1\pm x}$ is ~10 mol.% and that of $HfN_{1\pm x}$ in Ta is ~2.4–2.8 mol.% (at the eutectic temp.) Data on the system available in the literature are controversial.	[4, 14, 21–22, 29, 31, 167]
Ta–Hf–O	Ta_2O_5–HfO_2 is plotted partially and schematically at 1200–1500 °C: α-HfO_{2-x} (<~1670–2000 °C), $Ta_2O_5{\cdot}(5\div7)HfO_2$ (or $Hf_{5\div7}Ta_2O_{15\div19}$), α-$(Ta,Hf)_2O_5$ (extended solid solution based on α-Ta_2O_5)	[4, 123]
Ta–Hf–W	See W–Hf–Ta in Table 3.6.	
Ta–Ir–Nb	Plotted partially at 2000 °C: $Ir_{3\pm x}$(Ta,Nb) (β-$Ir_{3\pm x}$Ta–$Ir_{3\pm x}$Nb continuous solid solution)	[253–254]
Ta–Ir–Ni	Plotted at 900 °C: $Ta_5Ir_4Ni_{11}$ (homog. range—~20–30 at.% Ta, ~47–65 at.% Ni, ~10–27 at.% Ir), $Ta_{15}Ir_3Ni_2$ (or $Ta_3Ir_{0.6}Ni_{0.4}$, homog. range—~65–70 at.% Ta, ~7–20 at.% Ni, ~15–20 at.% Ir), $Ta_8Ir_5Ni_7$, $Ta_5Ir_8Ni_7$, σ-$IrTa_{3\pm x}Ni_y$ (extended solid solution based on σ-$IrTa_{3\pm x}$—up to ~30 at.% Ni), δ-$IrTa_{1-x}Ni_y$ (extended solid solution based on δ-$IrTa_{1-x}$—up to ~9 at.% Ni), γ-$Ir_3Ta_{2+x}Ni_y$ (extended solid solution based on γ-Ir_3Ta_{2+x}—up to ~8 at.% Ni), β-$Ir_{3\pm x}TaNi_y$ (extended solid solution based on β-$Ir_{3\pm x}$Ta—up to ~17 at.% Ni), $Ni_{2\pm x}Ta$ (solubility of Ir is ~5 at.%), ζ-$Ni_{8\pm x}Ta$, κ-$Ni_{3\pm x}Ta$, μ-$Ni_{1-x}Ta$, $NiTa_{2+x}$ (Ni,Ir), Ta The solubility of Ir in Ta nickelides is low.	[247]
Ta–Ir–Pt	No diagram plot $(Ir_{1-y}Pt_y)_{3\pm x}Ta$ (β-$Ir_{3\pm x}$Ta–$Pt_{3\pm x}$Ta continuous solid solution, ?)	[248]
Ta–Ir–Si	No diagram plot TaIrSi, ?	[249]
Ta–Ir–Te	No diagram plot $TaIrTe_4$, ?	[250]

(continued)

Table 6.4 (continued)

System	Type of phase diagram (temperature and composition sections, constituent phases or phase fields) and/or character of interphase interaction and materials compatibility	References
Ta–K–Na	No diagram plot At temp. ≥1000 °C Ta is resistant to corrosion in K–Na alloys and recommended for long-term applications.	[4]
Ta–Mg–O	Ta_2O_5–MgO is plotted: MgO (<2825 °C), $4MgO{\cdot}Ta_2O_5$ (or $Mg_4Ta_2O_9$, <~1830 °C), $3MgO{\cdot}Ta_2O_5$ (or $Mg_3Ta_2O_8$, ~1470–1660 °C), $MgO{\cdot}Ta_2O_5$ (or $MgTa_2O_6$, <~1765 °C), α-$(Ta,Mg)_2O_5$ (extended solid solution based on α-Ta_2O_5), β-Ta_2O_5; $MgTa_2O_6$–α-$(Ta,Mg)_2O_5$ eutectic—~1570–1750 °C, ~80 mol.% Ta_2O_5; $Mg_4Ta_2O_9$–$MgTa_2O_6$ eutectic—~1690 °C (?) The interaction between Ta and MgO initiates from 1600 °C and leads to the formation of complex phases.	[4, 10, 28, 168–170]
Ta–Mg–Pu	No diagram plot At 1150 °C Ta is resistant to corrosion in Mg–Pu eutectic alloy.	[4]
Ta–Mg–Th	No diagram plot At 800 °C Ta is resistant to corrosion in Mg–Th eutectic alloy and recommended for long-term applications.	[4]
Ta–Mg–U	No diagram plot At 1150 °C Ta is resistant to corrosion in Mg–U alloys.	[4]
Ta–Mn–N	No diagram plot Ta_3MnN_4, η-$Ta_{\sim 3}Mn_{\sim 3}N$	[25, 225]
Ta–Mo–N	Plotted at 1100 °C (pressure $N_2 \leq 30$ MPa): $TaMoN_{1-x}$ (Z-phase), γ-$(Mo,Ta)_{2\pm x}N$ (extended solid solution based on γ-$Mo_{2\pm x}N$—up to compos. ~$(Mo_{0.6}Ta_{0.4})_{2\pm x}N$, <~1910–2010 °C), δ-$TaN_{1-x}$, γ-$Ta_{2\pm x}N$, N, (Mo,Ta) Ta nitrides dissolve inconsiderable amount of Mo. At higher pressures of N_2 (36 MPa) $(Ta,Mo)_2N_2$ was synthesized.	[25]
Ta–Mo–Nb	Plotted at 2550–2800 °C: Ta–Mo–Nb continuous solid solution (Ta,Mo,Nb)	[162]
Ta–Mo–Ni	Plotted at 900–2500 °C: $Ni_{3\pm x}(Ta,Mo)$ (κ-$Ni_{3\pm x}$Ta–γ-Ni_{3+x}Mo continuous solid solution, <~905–1550 °C), ζ-$Ni_{8\pm x}(Ta,Mo)$ (extended solid solution based on ζ-$Ni_{8\pm x}$Ta), $Ni_{2\pm x}(Ta,Mo)$ (extended solid solution based on $Ni_{2\pm x}$Ta), μ-$Ni_{1-x}(Ta,Mo)$ (extended solid solution based on μ-Ni_{1-x}Ta), $Ni(Ta,Mo)_{2+x}$ (extended solid solution based on $NiTa_{2+x}$), δ-$NiMo_{1\pm x}$ (<~1360–1365 °C), β-Ni_{4+x}Mo (<865–875 °C), Ni, (Ta,Mo).	[15, 17, 32, 150–151, 153, 156, 159]
Ta–Mo–O	Ta_2O_5–MoO_3 is plotted: MoO_3 (<~800 °C), $Ta_2O_5{\cdot}2MoO_3$ (or $Ta_2Mo_2O_{11}$, <950 °C), $6Ta_2O_5{\cdot}MoO_3$ (or $Ta_{12}MoO_{33}$, <~1520 °C), α-$(Ta,Mo)_2O_5$ (solid solution based on α-Ta_2O_5), β-$(Ta,Mo)_2O_5$ (solid solution based on β-Ta_2O_5); $Ta_2Mo_2O_{11}$–MoO_3 eutectic—~780 °C, ~5 mol.% Ta_2O_5	[171]

(continued)

Table 6.4 (continued)

System	Type of phase diagram (temperature and composition sections, constituent phases or phase fields) and/or character of interphase interaction and materials compatibility	References
Ta–Mo–Os	See Os–Mo–Ta in Table 5.4.	
Ta–Mo–Re	See Re–Mo–Ta in Table 4.6.	
Ta–Mo–Ru	Plotted at 1000 and 1500 °C: (Ta,Mo,Ru) (extended solid solution based on Mo–Ta continuous solid solution with homog. range ~Mo–$Mo_{0.85}Ru_{0.15}$–$Mo_{0.27}Ru_{0.20}Ta_{0.53}$–$Ta_{0.42}Ru_{0.58}$–Ta at 1500 °C), (Ru,Mo,Ta) (extended solid solution based on Ru with homog. range ~$Ru_{0.55}Mo_{0.45}$–$Ru_{0.75}Ta_{0.25}$–Ru at 1500 °C), σ-$Ru_3(Mo,Ta)_{5\pm x}$ (extended solid solution based on σ-$Ru_3Mo_{5\pm x}$—up to ~$Ru_3(Mo_{0.65}Ta_{0.35})_{5\pm x}$ at 1500 °C)	[241–242]
Ta–Mo–Si	Plotted partially at 1300–1900 °C: $(Ta,Mo)Si_2$ (extended solid solution based on $TaSi_2$—up to ~$(Ta_{0.15}Mo_{0.85})Si_2$ at 1800 °C), α-$(Ta,Mo)_5Si_3$ (extended solid solution based on α-Ta_5Si_3—up to ~$(Ta_{0.65}Mo_{0.35})_5Si_3$ at 1800 °C), $(Mo,Ta)_5Si_{3\pm x}$ (extended solid solution based on $Mo_5Si_{3\pm x}$—up to ~$(Mo_{0.65}Ta_{0.35})_5Si_{3\pm x}$ at 1800 °C, <2170–2180 °C), α-$(Mo,Ta)Si_2$ (solid solution based on α-$MoSi_2$—up to ~$(Mo_{0.95}Ta_{0.05})Si_2$ at 1800 °C, <1900 °C), β-$MoSi_2$ (from 1850–1900 °C to 2020 °C; solubility of Ta < 0.5 at.%), Mo_3Si (<2025–2065 °C), β-Ta_5Si_3, Ta_2Si, $Ta_{3+x}Si$, Si, (Mo,Ta) Eutectic α-$(Mo,Ta)Si_2$–$(Ta,Mo)Si_2$–Si (~1400 °C, ~2 at.% Mo, ~1 at.% Ta) $TaSi_2$–$MoSi_2$ is plotted: eutectic—~1900–2000 °C (?), ~30 mol.% $TaSi_2$ (at 1300 °C the max. solubility of $TaSi_2$ in $MoSi_2$ is 16 mol.% and that of $MoSi_2$ in $TaSi_2$ is 56 mol.%, ?), or peritectic $(Ta,Mo)Si_2$ (extended solid solution based on $TaSi_2$) —~1900 °C (?), ~90 mol.% $MoSi_2$ with min. melt. point—~1850 °C, corresp. to ~$(Ta_{0.3}Mo_{0.6})Si_2$ compos. (max. solid solubility of $MoSi_2$ in $TaSi_2$ is ~90 mol.% at ~1900 °C and ~65 mol.% at ~1300 °C, and that of $TaSi_2$ in α-$MoSi_2$ at 1200–1900 °C is ≤~2 mol.%, ?) Data on the system available in the literature are very controversial. At 1900–2050 °C the interaction between Ta and β-$MoSi_2$ results to the formation of Mo_3Si and $TaSi_2$.	[21, 34–35, 174, 233]
Ta–Mo–Si–Ti	$TaSi_2$–$MoSi_2$–$TiSi_2$ is plotted at 1300 °C: $(Ta,Mo,Ti)Si_2$ (or $(Ta_{1-x}Mo_x)Si_2$ ($0 < x <$ ~0.55)–$(Ti_{1-x}Mo_x)Si_2$ (~$0.1 < x <$ ~0.6) continuous solid solution), $(Mo,Ta,Ti)Si_2$ (extended solid solution based on α-$MoSi_2$; solubility of $TaSi_2$ is ~15 mol.% and that of $TiSi_2$ is very low)	[35]
Ta–Mo–Si–W	See W–Mo–Si–Ta in Table 3.6.	

(continued)

Table 6.4 (continued)

System	Type of phase diagram (temperature and composition sections, constituent phases or phase fields) and/or character of interphase interaction and materials compatibility	References
Ta–Mo–Ti	Plotted at 600 °C: (Ta,Mo,β-Ti) (extended solid solution based on Ta–Mo–β-Ti continuous solid solution), (α-Ti,Ta,Mo) (solid solution based on α-Ti with homog. range $\sim Ti_{0.005}Mo_{0.995}$–$Ti_{0.03}Ta_{0.97}$–Ti at 600 °C)	[243]
Ta–Mo–W	See W–Mo–Ta in Table 3.6.	
Ta–N–Nb	Plotted at 1400 and 1800 °C: $(Ta,Nb)_{2\pm x}N$ (γ-$Ta_{2\pm x}N$–β-$Nb_{2\pm x}N$ seminitride continuous solid solution), δ-$(Nb,Ta)N_{1-x}$ (δ-TaN_{1-x}–δ-NbN_{1-x} mononitride continuous solid solution at higher temp., or extended solid solution based on δ-NbN_{1-x} at lower temp.), $(Nb_{1-x}Ta_x)_8N_9$ (?), ε-$NbN_{1\pm x}$, γ-Nb_4N_{3+x} Ta_3N_5, ε-TaN_{1-x}, Ta_9N_2, β-TaN_x, N, (Nb,Ta)	[234, 245]
Ta–N–Ni	Plotted at 1200 °C (pressure N_2−1 MPa): η-Ta_4Ni_2N, $Ta_2NiN_{2.45}$ (?), Ni_3N (<480 °C), ζ-$Ni_{8\pm x}Ta$, κ-$Ni_{3\pm x}Ta$, $Ni_{2\pm x}Ta$, μ-$Ni_{1-x}Ta$, $NiTa_{2+x}$, δ-TaN_{1-x}, γ-$Ta_{2\pm x}N$, N, Ni, Ta The interaction between δ-TaN_{1-x} and liquid Ni leads to the formation of solid solutions.	[21, 25]
Ta–N–O–U	No diagram plot In vacuum, at 2760 °C no interaction between δ-TaN_{1-x} and UO_{2+x}.	[21]
Ta–N–Si	Plotted at 1000 °C (vacuum), 1325 °C (N_2 atmosphere) and 1500 °C (Ar atmosphere): $Ta_5Si_3N_{1-x}$ (or $Ta_{5-x}Si_{3-x}N_z$, ~1300–1500 °C, ?), $Ta_5Si_3N_7$ (?), Si_3N_4 (<~1900 °C), δ-TaN_{1-x}, γ-$Ta_{2\pm x}N$, $TaSi_2$, α-Ta_5Si_3, β-Ta_5Si_3, Ta_2Si, $Ta_{3+x}Si$, Si, N, Ta Data on the system available in the literature are controversial. In N_2 atmosphere, at 1400–1900 °C the interaction between Ta and Si_3N_4 results in the formation of α-Ta_5Si_3, $TaSi_2$, $Ta_5Si_3N_7$ (?) and γ-$Ta_{2\pm x}N$; in Ar atmosphere, at 1100–1900 °C the compact Ta interacts with Si_3N_4 forming δ-TaN_{1-x} and $TaSi_2$. The interaction between γ-$Ta_{2\pm x}N$ and Si_3N_4 in N_2 atmosphere at 1840 °C results in the formation of $TaSi_2$ and $Ta_5Si_3N_7$ (?).	[4, 21, 26, 29–30, 147]
Ta–N–Ti	Plotted at 1600 °C: δ-$(Ti,Ta)N_{1\pm x}$ (extended mononitride solid solution based on δ-$TiN_{1\pm x}$—up to ~$(Ti_{0.1}Ta_{0.9})N_{1\pm x}$), γ-$(Ta,Ti)_{2\pm x}N$ (extended solid solution based on γ-$Ta_{2\pm x}N$—up to ~$(Ta_{0.65}Ti_{0.35})_{2\pm x}N$), ε-$(Ti,Ta)_{2\pm x}N$ (extended solid solution based on ε-$Ti_{2\pm x}N$—up to ~$(Ti_{0.75}Ta_{0.25})_{2\pm x}N$), δ'-$Ti_5N_{3\pm x}$ (<800 °C), ε-TaN_{1-x}, δ-TaN_{1-x}, N, α-Ti, (β-Ti,Ta) In vacuum, at 1900–2200 °C the interaction between compact metal Ta and $TiN_{1\pm x}$ leads to the formation of γ-$Ta_{2\pm x}N$ and δ-TaN_{1-x}–$TiN_{1\pm x}$ solid solutions; at temp. ≥2100 °C this interaction is very intensive.	[4, 21, 234]

(continued)

Table 6.4 (continued)

System	Type of phase diagram (temperature and composition sections, constituent phases or phase fields) and/or character of interphase interaction and materials compatibility	References
Ta–N–Zr	No diagram plot In vacuum, at 2100–2200 °C the interaction between compact Ta and $ZrN_{1\pm x}$ (2–5 h exposure) leads to the formation of N containing solid solutions based on Ta.	[4, 21]
Ta–Nb–Ni	Plotted at 900 °C: κ-$Ni_{3\pm x}$(Ta,Nb) (κ-$Ni_{3\pm x}$Ta–κ-$Ni_{3\pm x}$Nb continuous solid solution, $<\sim$1400–1550 °C), μ-Ni_{1-x}(Ta,Nb) (μ-Ni_{1-x}Ta–μ-Ni_{1-x}Nb continuous solid solution, $<\sim$1290–1570 °C), $Ni_{2\pm x}Ta$, $NiTa_{2+x}$, ζ-$Ni_{8\pm x}$Nb (<535 °C), ζ-$Ni_{8\pm x}$Ta, Ni, (Ta,Nb)	[15, 17, 32]
Ta–Nb–O	Ta_2O_5–Nb_2O_5 is plotted: α-$(Nb,Ta)_2O_5$ (extended solid solution based on α-Nb_2O_5 with compos—up to $\sim(Nb_{0.75}Ta_{0.25})_2O_5$, $<\sim$1485–1550 °C), $Nb_{\sim 3.85\div 4.0}Ta_{\sim 2.0\div 2.15}O_{15}$ (or $Ta_2O_5{\cdot}nNb_2O_5$, $n \approx 1.925\div 2.00$, solid solution based on $Ta_2O_5{\cdot}2Nb_2O_5$, or $Nb_4Ta_2O_{15}$, $\sim$1390–1605 °C), β-$(Ta,Nb)_2O_5$ (extended solid solution based on β-Ta_2O_5 with compos.—up to $\sim(Ta_{0.50\div 0.51}Nb_{0.49\div 0.50})_2O_5$, $<\sim$1360–1450 °C), α-$(Ta,Nb)_2O_5$ (extended solid solution based on α-Ta_2O_5 with compos.—up to $\sim(Ta_{0.53\div 0.55}Nb_{0.45\div 0.47})_2O_5$, $\sim$1320–1885 °C)	[15, 170, 172–173, 180 , 251]
Ta–Nb–Os	See Os–Nb–Ta in Table 5.4.	
Ta–Nb–Re	See Re–Nb–Ta in Table 4.6.	
Ta–Nb–Si	No diagram plot $TaSi_2$–$NbSi_2$, α-Ta_5Si_3–α-Nb_5Si_{3+x}, β-Ta_5Si_3–β-Nb_5Si_{3+x} continuous solid solutions (?) In vacuum, at 1150–1370 °C the contact interaction between compact $TaSi_2$ and Nb results in the formation of α-Nb_5Si_{3+x}.	[21, 34, 160]
Ta–Nb–Ti	Plotted at 400–650 °C: (Ta,Nb,β-Ti) (extended solid solution based on Ta–Nb–β-Ti continuous solid solution at temp. $<\sim$880 °C, or continuous solid solution at higher temp.), (α-Ti,Ta,Nb) (extended solid solution based on α-Ti)	[15, 17– 18, 146]
Ta–Nb–V	Plotted in the wide range of temp.: Ta–Nb–V continuous solid solution (Ta,Nb,V)	[38]
Ta–Nb–W	See W–Nb–Ta in Table 3.6.	
Ta–Nb–Zr	Plotted at 1200 °C: (Ta,Nb,β-Zr) (extended solid solution based on Ta–Nb–β-Zr continuous solid solution with miscibility gap), (α-Zr,Ta,Nb) (extended solid solution based on α-Zr)	[161]
Ta–Ni–Re	See Re–Ni–Ta in Table 4.6.	
Ta–Ni–W	See W–Ni–Ta in Table 3.6.	
Ta–O–Pu	No diagram plot In vacuum, the contact interaction between Ta and PuO_{2-x} initiates from 1500 °C and leads to the formation of complex phases; at 1730–2130 °C $Pu_2O_{3\pm x}$ is formed.	[28]

(continued)

Table 6.4 (continued)

System	Type of phase diagram (temperature and composition sections, constituent phases or phase fields) and/or character of interphase interaction and materials compatibility	References
Ta–O–Th	No diagram plot $Ta_2O_5{\cdot}2ThO_2$ (or $Th_2Ta_2O_9$), $2Ta_2O_5{\cdot}ThO_2$ (or $ThTa_4O_{12}$) In vacuum, the contact interaction between Ta and ThO_{2-x} initiates from 1900 °C.	[4, 10, 28, 183]
Ta–O–U	No diagram plot $U_2Ta_6O_{19}$ (or $2UO_2{\cdot}3Ta_2O_5$), $U_4Ta_{18}O_{53}$ (or $4UO_2{\cdot}9Ta_2O_5$), UTa_3O_{10} (or $½UO_2{\cdot}½UO_3{\cdot}1½Ta_2O_5$), UTa_2O_8 (or $UO_3{\cdot}Ta_2O_5$), $U_2Ta_2O_7$ (or $2UO{\cdot}Ta_2O_5$), ? In vacuum and inert gas atmosphere, there is no interaction between Ta and UO_{2+x} (at 1930–2760 °C) during 10 min contact exposures; long-term contact at 2200 °C leads to the formation of volatile sub-oxide phases.	[4, 28, 235]
Ta–O–W	See W–O–Ta in Table 3.6.	
Ta–O–Zr	Ta_2O_5–ZrO_2 is plotted: α-ZrO_2 (<~1205 °C), β-ZrO_2 (~1205–2375 °C), γ-ZrO_{2-x} (~1525–2710 °C), $Ta_2O_5{\cdot}(2 \div 6)ZrO_2$ (or $Zr_{2 \div 6}Ta_2O_{9 \div 17}$, extended solid solution, ?), $ZrTa_6O_{17}$ (or $3Ta_2O_5{\cdot}ZrO_2$, <~1500 °C), $Zr_6Ta_{118}O_{307}$ (or $59Ta_2O_5{\cdot}6ZrO_2$,<~1325 °C), $Zr_2Ta_{54}O_{139}$ (or $27Ta_2O_5{\cdot}2ZrO_2$, <~1330 °C), $ZrTa_{38}O_{97}$ (or $19Ta_2O_5{\cdot}ZrO_2$, <~1335 °C), $Zr_2Ta_{98}O_{249}$ (or $49Ta_2O_5{\cdot}2ZrO_2$, <~1340–1345 °C), β-Ta_2O_5, α-$(Ta,Zr)_2O_5$ (extended solid solution based on α-Ta_2O_5 with compos.—up to ~$(Ta_{0.8}Zr_{0.2})_2O_5$, ~1320–1885 °C) Data on the system available in the literature are controversial. In vacuum, the contact interaction between Ta and ZrO_2 initiates from 1600 °C and leads to the formation of complex phases (at 1800–2100 °C).	[4, 10, 15, 17, 28, 144, 168]
Ta–Os–Re	See Re–Os–Ta in Table 4.6.	
Ta–Os–V	See Os–Ta–V in Table 5.4.	
Ta–Os–W	See W–Os–Ta in Table 3.6.	
Ta–Re–Si	See Re–Si–Ta in Table 4.6.	
Ta–Re–W	See W–Re–Ta in Table 3.6.	
Ta–Si–Ti	$TaSi_2$–$TiSi_2$ is plotted: eutectic—~1490 °C, ~15 mol.% $TaSi_2$; max. solubility of $TiSi_2$ in $TaSi_2$ is 52 mol.% at eutectic temp. and 50 mol.% at 1300 °C, and that of $TaSi_2$ in $TiSi_2$ is negligible at the same temp. At 1150–1370 °C the interaction between $TaSi_2$ and metal Ti leads to the formation of α-Ta_5Si_3.	[21, 228, 245, 236]
Ta–Si–Ti–W	See W–Si–Ta–Ti in Table 3.6.	

(continued)

Table 6.4 (continued)

System	Type of phase diagram (temperature and composition sections, constituent phases or phase fields) and/or character of interphase interaction and materials compatibility	References
Ta–Si–V	Plotted at 1400 °C: $V_4Ta_2Si_5$ (?), (Ta,V)Si_2 ($TaSi_2$–VSi_2 continuous solid solution), β-(Ta,V)$_5Si_3$ (β-Ta_5Si_3–V_5Si_3 continuous solid solution), $(V,Ta)_{3+x}Si$ (extended solid solution based on $V_{3+x}Si$—up to $\sim(V_{0.85}Ta_{0.15})_{3+x}Si$ at 1400 °C, <1925 °C), (Ta,V)$_2$Si (extended solid solution based on Ta_2Si—up to $\sim(Ta_{0.85}V_{0.15})_2Si$ at 1400 °C), $(Ta,V)_{3+x}Si$ (solid solution based on $Ta_{3+x}Si$—up to $\sim(Ta_{0.95}V_{0.05})_{3+x}Si$ at 1400 °C), V_6Si_5 (1160–1670 °C), α-Ta_5Si_3, $V_{2\pm x}Ta$, Si, (V,Ta)	[34, 36, 195, 237]
Ta–Si–W	See W–Si–Ta in Table 3.6.	
Ta–Si–Zr	$TaSi_2$–$ZrSi_2$ is plotted: at 1300 °C max. solubility of $ZrSi_2$ in $TaSi_2$ is 32 mol.% and that of $TaSi_2$ in $ZrSi_2$ is negligible At 1150–1370 °C the interaction between $TaSi_2$ and metal Zr leads to the formation of Zr_5Si_3 (?).	[21, 34, 36, 160]
Ta–Ti–W	See W–Ta–Ti in Table 3.6.	
Ta–V–W	See W–Ta–V in Table 3.6.	
Ta–W–Zr	See W–Ta–Zr in Table 3.6.	

[a] See notes to Table 6.3

The character of chemical interaction and general reactions of tantalum with common chemicals (solids, liquids, aqueous solutions) and complex gases are summarized in Table 6.5.

Table 6.5 The interaction of tantalum with some chemicals and complex gases [4, 10, 13, 38][a]

Reagent, formula	Character of chemical interaction, examples of general reactions
Air, $N_2 + O_2$	In air the oxidation of Ta initiates from 500–800 °C and leads to the formation of β-Ta_2O_5 at temp. $\leq$1200–1300 °C or α-Ta_2O_5 at higher temp.: $4Ta + 5O_2 \rightarrow 2Ta_2O_5$.
Water, H_2O	No interaction at the moderate conditions (e.g. Ta is absolutely resistant to steam at temp. 200 °C and pressure 1.4 MPa), at temp. >900–1100 °C Ta decomposes H_2O with O consumption and H release: $4Ta + 5H_2O \rightarrow 2Ta_2O_5 + 5H_2$. However, at 930 °C this reaction passes very slowly.
Hydrogen peroxide, H_2O_2	No interaction.
Carbon monoxide, CO	The interaction initiates from 900–1000 °C and leads to the formation of carbide TaC_{1-x} or oxycarbide TaC_xO_y; at 950–1500 °C the rate of the reaction is not affected by gas pressure.

(continued)

Table 6.5 (continued)

Reagent, formula	Character of chemical interaction, examples of general reactions
Carbon dioxide, CO_2	The interaction with dry CO_2 initiates from 400–500 °C and leads to the formation of Ta_2O_5; at 500–1500 °C the rate of the reaction is not affected by gas pressure. At temp. 500 °C and pressure CO_2 0.1 MPa the weight gain of Ta amounts to 0.5 kg m^{-2} for 60 days exposure.
Hydrogen sulphide, H_2S	At elevated temp. the interaction between Ta and H_2S leads to the formation of Ta sulphides: $Ta + 2H_2S \rightarrow TaS_2 + 2H_2$.
Hydrocarbons, CH_n	At 1200–1400 °C the interaction between Ta and hydrocarbons leads to the formation of Ta carbides; near-stoichiometric TaC_{1-x} ($x = 0.04$) was prepared by the reaction of Ta with CH_4.
Sodium hydroxide, NaOH	The interaction with molten NaOH results in the formation of Na tantalates.
Potassium hydroxide, KOH	The interaction with molten KOH results in the formation of K tantalates.
Nitric acid, HNO_3	No interaction.
Sulphuric acid, H_2SO_4	No interaction.
Hydrochloric acid, HCl	No interaction.
Hydrofluoric acid, HF	Ta dissolves in HF slowly.
Hydrochloric acid with nitric acid (aqua regia), $HCl + HNO_3$	The interaction is very slow.
Nitric acid with hydrofluoric acid, $HNO_3 + HF$	The interaction is intensive: $3Ta + 5HNO_3 + 21HF \rightarrow 3H_2[TaF_7] + 5NO + 10H_2O$

[a] Etching agents for tantalum: 20 % NH_4OH aqueous solution +30 % HF aqueous solution mixture (ratio 1:1) at 50–60 °C (for dislocations, grain boundaries and sub-boundaries), 2–7 % $HF + 32–38$ % H_2SO_4 aqueous solution (electrochemical polishing, 0.06–0.07 A cm^{-2})

The self-diffusion characteristics of tantalum atoms, diffusion characteristics in tantalum—element systems in the wide range of temperatures, and summarized data on the physico–chemical interaction of tantalum with elements of the periodic table are given in Addendum.

References

1. Steurer W (1996) Crystal structure of the metallic elements. In: Cahn RW, Haasen P (eds) Physical metallurgy, 4th ed., Vol. 1, pp. 1–46. Elsevier Science BV, Amsterdam
2. Cotton FA, Wilkinson G (1965) Advanced inorganic chemistry. Wiley, New York, London
3. Akhmetov NS (2001) Obschaya i neorganicheskaya khimiya (General and inorganic chemistry), 4th ed. Vysshaya Shkola, Moscow (in Russian)
4. Kotelnikov RB, Bashlykov SN, Galiakbarov ZG, Kashtanov AI (1968) Osobo tugoplavkie elementy i soedineniya (Extra refractory elements and compounds). Metallurgiya, Moscow (in Russian)

5. Zefirov AP (ed), Veryatin UD, Mashirev VP, Ryabtsev NG, Tarasov VI, Rogozkin BD, Korobov IV (1965) Termodinamicheskie svoistva neorganicheskikh veschestv (Thermodynamic properties of inorganic substances). Atomizdat, Moscow (in Russian)
6. Speight JG, ed (2005) Lange's handbook of chemistry, 16th ed. McGraw-Hill, New York
7. Lide DR, ed (2010) CRC handbook of chemistry and physics, 90th ed. CRC Press, Boca Raton, New York
8. Martienssen W (2005) The elements. In: Martienssen W, Warlimont H (eds) Springer handbook of condensed matter and materials data, pp. 45–158. Springer, Berlin, Heidelberg
9. Samsonov GV, ed (1976) Svoistva elementov (Properties of elements), 2nd ed., Vol. 1. Metallurgiya, Moscow (in Russian)
10. Marmer ÉN, Gurvich OS, Maltseva LF (1967) Vysokotemperaturnye materialy (High-temperature materials). Metallurgiya, Moscow (in Russian)
11. Cardarelli F (2008) Materials handbook, 2nd ed. Springer, London
12. Plansee Aktiengesellschaft (2000) Materials data base. Reutte, Austria
13. Samsonov GV, ed (1976) Svoistva elementov (Properties of elements), 2nd ed., Vol. 2. Metallurgiya, Moscow (in Russian)
14. Lyakishev NP, ed (1997) Diagrammy sostoyaniya dvoinykh metallicheskikh sistem (Phase diagrams of binary metal systems), Vol. 2. Mashinostroenie, Moscow (in Russian)
15. Lyakishev NP, ed (2001) Diagrammy sostoyaniya dvoinykh metallicheskikh sistem (Phase diagrams of binary metal systems), Vol. 3, Part 1. Mashinostroenie, Moscow (in Russian)
16. Lyakishev NP, ed (1996) Diagrammy sostoyaniya dvoinykh metallicheskikh sistem (Phase diagrams of binary metal systems), Vol. 1. Mashinostroenie, Moscow (in Russian)
17. Massalski TB, Subramanian PR, Okamoto H, Kacprzak L, eds (1990) Binary alloy phase diagrams, 2nd ed. ASM International, Metals Park, Ohio
18. Lyakishev NP, ed (2000) Diagrammy sostoyaniya dvoinykh metallicheskikh sistem (Phase diagrams of binary metal systems), Vol. 3, Part 2. Mashinostroenie, Moscow (in Russian)
19. Dennison DH, Tschetter MJ, Gschneidner KA, Jr (1966) The solubility of tantalum and tungsten in liquid rare-earth metals. J Less-Common Met 11(6):423–435
20. Rudy E (1969) Compendium of phase diagram data. In: Ternary phase equilibria in transition metal-boron-carbon-silicon systems. Report AFML-TR-65–2, Contracts USAF 33(615)-1249 and USAF 33(615)-67-C-1513, Part 5, pp. 1–689. Air Force Materials Laboratory, Wright-Patterson Air Force Base, Ohio
21. Kosolapova TYa, ed (1990) Handbook of high-temperature compounds: properties, production and applications. Hemisphere, New York
22. Toth LE (1971) Transition metal carbides and nitrides. Academic Press, New York, London
23. Kofstad P (1966) High-temperature oxidation of metals. Wiley, New York, London
24. Kofstad P (1988) High-temperature corrosion. Elsevier Applied Science, London, New York
25. Holleck H (1984) Binäre und ternäre Carbid- und Nitridsysteme der Ubergangsmetalle (Binary and ternary carbide and nitride systems of the transition metals). Gebrüder Borntträeger, Berlin, Stuttgart (in German)
26. Rogl P, Schuster JC (1992) Phase diagrams of ternary boron nitride and silicon nitride systems. ASM International, Materials Park, Ohio
27. Borisova AL, Martsenyuk IS (1975) Reactions of boron and aluminum nitrides and materials based on them with refractory metals. Powder Metall Met Ceram 14(10):822–826
28. Samsonov GV, ed (1978) Fiziko-khimicheskie svoistva okislov (Physico-chemical properties of oxides), 2nd ed. Metallurgiya, Moscow (in Russian)
29. Kieffer R, Schwarzkopf P (1953) Hartstoffe und Hartmetalle (Refractory hard metals). Springer, Vienna (in German)
30. Samsonov GV, Vinitskii IM (1980) Handbook on refractory compounds. IFI/Plenum, New York
31. Ordanyan SS, Chupov VD, Kirshina VYu, Fesenko LV (1985) Reactions of hafnium nitride with molybdenum, tungsten and tantalum. Powder Metall Met Ceram 24(9):714–719

32. Ishchenko TV, Meshkov LL, Sokolovskaya YeM (1984) On the interaction of μ phases in systems formed by transition metals. J Less-Common Met 97:145–150
33. Andrievskii RA, Spivak II (1989) Prochnost tugoplavkikh soedinenii i materialov na ikh osnove (Strength of refractory compounds and materials based on them). Metallurgiya, Chelyabinsk (in Russian)
34. Setton M, Van Der Spiegel J (1991) A review of some aspects of ternary metal-metal-Si and metal-B-Si systems. J Appl Phys 69(2):994–999
35. Boettinger WJ, Peperezko JH, Frankwicz PS (1992) Application of ternary phase diagrams to the development of $MoSi_2$-based materials. Mater Sci Eng A 155(1):33–44
36. Gladyshevskii EI, Lakh VI, Skolozdra RV, Stadnik BI (1964) The mutual solubility of disilicides of the transition metals from group IV, V and VI. Powder Metall Met Ceram 3(4):278–282
37. Papirov II (1981) Struktura i svoistva splavov berilliya (Structure and properties of beryllium alloys). Energoizdat, Moscow (in Russian)
38. Savitskii EM, Burkhanov GS (1971) Metallovedenie splavov tugoplavkikh i redkih metallov (Metallography of refractory and less-common metal alloys), 2nd ed. Nauka, Moscow (in Russian)
39. Brewer L, Lamoreaux RH (1980) Phase diagrams. In: Brewer L (ed) Molybdenum. Physico-chemical properties of its compounds and alloys. Atomic Energy Review, Special Issue N 7, pp. 195–356. International Atomic Energy Agency, Vienna
40. Savitskii EM, ed (1984) Blagorodnye metally (Noble metals). Metallurgiya, Moscow (in Russian)
41. Audi G, Wapstra AH, Thibault C, Blachot J, Bersillon O (2003) The NUBASE evaluation of nuclear and decay properties. Nucl Phys A 729:3–128
42. De Laeter JR, Bohlke JK, De Bievre P, Hidaka H, Peiser HS, Rosman KJR, Taylor PDP (2003) Atomic weights of the elements. Review 2000 (IUPAC Technical report). Pure Appl Chem 75(6):683–800
43. Wieser ME (2006) Atomic weights of the elements 2005. (IUPAC Technical report). Pure Appl Chem 78(11):2051–2066
44. Portnoi KI, Romashov VM (1972) Binary constitution diagrams of systems composed of various elements and boron – a review. Powder Metall Met Ceram 11(5):378–384
45. Samsonov GV, Bondarev VN (1968) Germanidy (Germanides). Metallurgiya, Moscow (in Russian)
46. Darby JB, Jr, Lam DJ, Norton LJ, Downey JW (1962) Intermediate phases in binary systems of technetium-99 with several transition elements. J Less-Common Met 4(6):558–563
47. Kubaschewski O (1982) Iron binary phase diagrams. Springer, Berlin
48. Bannykh OA, Budberg SP, Alisova SP (1986) Diagrammy sostoyaniya dvoinykh i mnogokomponentnykh system na osnove zheleza (The constitution diagrams of binary and multi-component systems based on iron). Metallurgiya, Moscow (in Russian)
49. Goodwin F, Guruswamy S, Kainer KU, Kammer C, Knabl W, Koethe A, Leichtfried G, Schlamp G, Stickler R, Warlimont H (2005) Metals. In: Martienssen W, Warlimont H (eds) Springer handbook of condensed matter and materials data, pp. 161–430. Springer, Berlin, Heidelberg
50. Mueller MH (1977) The lattice parameter of tantalum. Scr Metall 11:693
51. Lee SL, Doxbeck M, Mueller J, Cipollo, Cote P (2004) Texture, structure and phase transformation in sputter beta-tantalum coating. Surf Coat Techn 177–178:44–51
52. Shamrai VF, Warhulska AV, Arakcheeva AV, Grinevich VV (2004) Magnetic properties and crystal structure of β-tantalum. Crystallogr Rep 49:930–935
53. Schussler M, Droegkamp RE (1990) Tantalum. In: Metals handbook, Vol. 2 – Properties and selection: nonferrous alloys and special-purpose materials, pp. 3164–3176. ASM International, Metals Park, Ohio
54. Gebhardt E, Seghezzi HD (1957) Gerät zur Untersuchung von Gas-Metall-Systemen und Messergebnisse im System Tantal-Sauerstoff (Device for the investigation of gas-metal

systems for the measurement in tantalum-oxygen system). Z Metallkd 48(8):430–435 (in German)
55. Cardonne SM, Kumar P, Michaluk CA, Schwartz HD (1992) Tantalum and its alloys. Advanced Mater Processes 9:16–20
56. Conway JB, Flagella BN (1971) Creep rupture data for the refractory metals to high temperatures. Gordon Breach, New York
57. Schober T, Carl A (1977) A revision of the Ta-H phase diagram. Scr Met 11(5):397–400
58. Köbler U, Schober T (1978) Susceptibility and phase diagram of the Ta-H system. J Less-Common Met 60(1):101–107
59. Köbler U, Welter J-M (1982) Low temperature susceptibility and phase diagrams of the Nb-H and Ta-H systems. J Less-Common Met 84:225–235
60. Flanagan TB, Schober T, Wenzl H (1983) The solvus behaviour of the tantalum-hydrogen (deuterium) system. Acta Met 31(4):483–487
61. Fromm E, Jehn H (1984) Solubility hydrogen in the elements. Bull Alloy Phase Diagrams 5(3):323–326
62. San-Martin A, Manchester FD (1991) The H-Ta (hydrogen-tantalum) system. J Phase Equilib 12(3):332–343
63. Condon JB, Schober T, Lässer R (1990) On the Ta-D and Ta-T phase diagrams. J Nucl Mater 170(1):24–30
64. Garg SP, Venkatraman M, Krishnamurthy N (1990) Li-Ta (lithium-tantalum) system. J Alloy Phase Diagrams 6(1):8–9
65. Barker MG (1979) Reactions of the liquid alkali metals with the metals Zr, Nb, Ta, Mo and W and their oxides. Rev Int Haut Temp Refract 16(3):237–243
66. Garg SP, Venkatraman M, Krishnamurthy N (1990) Na-Ta (sodium-tantalum) system. J Alloy Phase Diagrams 6(1):10–11
67. Klueh RL (1969) Effect of oxygen on the compatibility of niobium with potassium. Corrosion 25(10):416–422
68. Stecura S (1970) Corrosion by liquid metals. Plenum Press, New York, London
69. Garg SP, Venkatraman M, Krishnamurthy N (1990) K-Ta (potassium-tantalum) system. J Alloy Phase Diagrams 6(1):12–13
70. Havinga EE, Damsma H, Kannis JM (1972) Compounds and pseudo-binary alloys with the $CuAl_2$ ($C16$)-type structure. IV. Superconductivity. J Less-Common Met 27(3):281–291
71. Stuemke M, Petzow G (1975) Kristallstrukturen und Gitterabmessungen von Übergangsmetall -Diberylliden und -Diboriden in ternären Mischkristallbereichen (Crystal structure and lattice constants of transition metal diberyllides and diborides in ternary solid solutions). Z Metallkd 66(5):292–297 (in German)
72. Dennison DH, Tschetter MJ, Gschneidner KA, Jr (1965) The solubility of tantalum in eight liquid rare-earth metals. J Less-Common Met 10(2):108–115
73. McMasters OD, Larsen WL (1961) Phase equilibria in the thorium-tantalum system. J Less-Common Met 3(4):312–320
74. Ackerman RJ, Rauh EG (1972) Determination of liquidus curves for the Th-W, Th-Ta, Zr-W and Hf-W: the anomalous behaviour of metallic thorium. High Temp Sci 4(4):272–282
75. Krishnan R, Garg SP, Krishnammurthy N (1988) Ta-U (tantalum-uranium) system. J Alloy Phase Diagrams 4(3):204–208
76. Chandrasekharian MS, Dharwadkar SR, Das D (1986) High temperature phase diagrams of Re-U, Ta-U and W-U. Z Metallkd 77(8):509–514
77. Budberg PB, Shakhova KI (1967) Diagramma sostoyaniya sistemy titan-tantal (The constitution diagram of the titanium-tantalum system). Izv AN SSSR Neorg Mater 3(4):656–660 (in Russian)
78. Nikitin PN, Mikheev VS (1969) Rastvorimost tantala v alfa-titane (The solubility of tantalum in alpha-titanium). Fiz Metal Metalloved 28(6):1127–1129 (in Russian)
79. Williams DE, Jackson RJ, Larsen WL (1962) The tantalum-zirconium alloy system. Trans AIME 224(4):751–756

80. Pease LF, Brophy JH (1963) Some modifications in the diagram for the tantalum-zirconium system. Trans AIME 227(5):1245–1249
81. Krishnan R, Garg SP, Krishnamurthy N (1989) Hf-Ta (hafnium-tantalum) system. J Alloy Phase Diagrams 5(2):117–124
82. Nefedov AP, Sokolovskaya EM, Grigorev AT, Sokolova IG, Nedumov NA (1964) Fazovye prevrashcheniya v tverdom sostoyanii v splavakh vanadiya s tantalum (Solid state phase transformations in the alloys of vanadium with tantalum). Zh Neorg Khim 9(4):883–889 (in Russian)
83. Auld JH, Ryan NE (1961) The solid solubility of tantalum in chromium. J Less-Common Met 3(3):221–225
84. Gebhardt E, Rexer J (1967) Precipitation phenomena in Ta-Cr solid solution. Z Metallkd 58:611–616
85. Venkatraman M, Neuman JP (1987) The Cr-Ta (chromium-tantalum) system. J Phase Equilib 8(2):112–116
86. Savitskii EM, Kopetskii ChV (1960) Diagramma sostoyaniya sistemy marganets-tantal (The constitution diagram of the manganese-tantalum system). Zh Neorg Khim 5(11):2638–2640 (in Russian)
87. Raman A (1966) On the tantalum-iron system. Trans Indian Inst Met 19:202–205
88. Abrahamson EP, Lopata SL (1966) The lattice parameters and solubility limits of alpha iron as affected by some binary transition-element additions. Trans AIME 236(1):76–87
89. Fischer WA, Lorenz K, Fabritius H, Schiegel D (1970) Untersuchung der α/γ-Umwandlung in hochreinen Zweistofflegierungen des Eisens mit Molybdän, Vanadin, Wolfram, Niob, Tantal, Zirkon und Kobalt (Examination of the α/γ transformation in highly pure binary alloys of iron with molybdenum, vanadium, tungsten, niobium, tantalum, zirconium and cobalt). Arch Eisenhüttenwes 41(5):489–498 (in German)
90. Swartzendruber LJ, Paul E (1986) The Fe-Ta (iron-tantalum) system. Bull Alloy Phase Diagrams 7(3):254–259
91. Raub E, Beeskow H, Fritzsche WZ (1963) Die Struktur der festen Tantal-Ruthenium-Legierungen (The structure of the solid tantalum-ruthenium alloys). Z Metallkd 54(8):451–454 (in German)
92. Rietveld HM (1969) A profile refinement method for nuclear and magnetic structures. J Appl Crystallogr 2:65–71
93. Chen BH, Franzen HF (1990) Phase transitions and heterogeneous equilibria in the TaRu homogeneity range. J Less-Common Met 157(1):37–45
94. Okamoto H (1991) The Ru-Ta (ruthenium-tantalum) system. J Phase Equilib 12(3):395–397
95. Raman A (1967) Röntgenographische Untersuchungen im System Tantal-Kobalt (X-ray examinations in the tantalum-cobalt system). Metall 21(9):900–903
96. Giessen BC, Ibach H, Grant NJ (1964) The constitution diagram tantalum-rhodium. Trans AIME 230(1):113–122
97. Ferguson WH, Giessen BC, Grant NJ (1963) The constitution diagram tantalum-iridium. Trans AIME 227:1401–1406
98. Pimenov VN, Ugaste YuÉ, Akkushkarova KA (1977) Issledovanie vzaimnoi diffuzii i diagrammy sostoyanii v sisteme Ni-Ta (A study of the mutual diffusion and constitution diagram of the Ni-Ta system). Izv AN SSSR Metally (1):184–189 (in Russian)
99. Nash P, West DRF (1983) Ni-Al and Ni-Ta phase diagrams. Met Sci 17(2):99–100
100. Nash A, Nash P (1984) The Ni-Ta (nickel-tantalum) system. Bull Alloy Phase Diagrams 5(3):259–265
101. Darby JB, Jr, Downey JW, Norton LJ (1963) Intermediate phases in the tantalum-palladium system. Trans AIME 227:1028–1029
102. Savitskii EM, Polyakova VP, Tylkina MA, Burkhanov GS (1964) Sistema palladii-tantal (The palladium-tantalum system). Zh Neorg Khim 9(7):1645–1649 (in Russian)
103. Maldonado A, Schubert K (1964) Strukturuntersuchungen in einigen zu T^5-T^{10} homologen und quasihomologen Legierungssystemen (The structural studies of some T^5-T^{10}

homologous and quasi-homologous alloy systems). Z Metallkd 55(10):619–626 (in German)
104. Savitskii EM, Polyakova VP, Tylkina MA (1967) Splavy palladiya (Palladium alloys). Nauka, Moscow (in Russian)
105. Brunsch A, Steeb S (1971) Diffusionsuntersuchung in System Pd-Ta mittels Mikrosond (Diffusion investigation into Pd-Ta system by microsonde). Z Naturforsch (2):274–279 (in German)
106. Waterstrat RM, Gissen RC, Kosh R, Manuzewski RC (1978) The tantalum-palladium constitution diagram. Metal Trans A 9(5):643–648
107. Giessen BC, Kane RH, Grant NJ (1965) On the constitution diagram Ta-Pt between 50–100 at.% Pt. Trans AIME 233(5):855–864
108. Waterstrat RM (1981) Analysis of selected alloys in the systems Cr-Pd, Cr-Ru, V-Pd and Ta-Pt. J Less-Common Met 80(1):P31-P36
109. Raub E, Beeskow H, Menzel D (1961) Tantal-Gold-Legierungen (Tantalum-gold alloys). Z Metallkd 52(3):189–193 (in German)
110. Okamoto H, Massalski TB (1985) The Au-Ta (gold-tantalum) system. Bull Alloy Phase Diagrams 6(4):365–368
111. Nowotny H, Benesovsky F, Kieffer R (1959) Beitrag zum Aufbau der Syteme Niob-Bor und Tantal-Bor (Contribution to building the systems niobium-boron and tantalum-boron). Z Metallkd 50(7):417–423 (in German)
112. Portnoi KI, Romashov VM, Salibekov SE (1971) Constitution diagram of the system tantalum-boron. Powder Metall Met Ceram 10(11):925–927
113. Crespo AJ, Tergenius L-E, Lundström T (1981) The solid solution of 4*d*, 5*d* and some *p* elements in β rhombohedral boron. J Less-Common Met 77(1):147–150
114. Kimura H, Nakano O, Ohkoshi T (1973) On the aluminum-tantalum system. J Japan Inst Light Metals 23(3):106–112 (in Japanese)
115. Schuster JC (1985) Phases and phase relations in the system Ta-Al. Z Metallkd 76(11):724–727
116. Meissner H-G, Schubert K (1965) Zum Aufbau einiger zu T^5-Ga homologer und quasihomologer Systeme. I. Die Systeme Vanadium-Gallium, Niob-Gallium und Tantal-Gallium und die Struktur von Ti_6Sn_5(h) (Structure of some T^5-Ga homologous and quasi-homologous systems. I. The systems vanadium-gallium, niobium-gallium and tantalum-gallium and the structure of Ti_6Sn_5(h)). Z Metallkd 56(7):475–484 (in German)
117. Havinga EE, Van Maaren MH, Damsma H (1969) Superconductivity of compounds having the Si_2U_3-type structure. Phys Lett A 29(3):109–110
118. Brown PW (1977) Phases in the Ta-Ga binary system. J Less-Common Met 52(1):77–80
119. Villars P, Girgis K (1982) Die Zustandbilder Nb-In, Nb-Tl, Ta-In und Ta-Tl (Phase diagrams of Nb-In, Nb-Tl, Ta-In and Ta-Tl alloys). Z Metallkd 73(3):169–171 (in German)
120. 120.Okamoto H (1988) The In-Ta (indium-tantalum) system. Bull Alloy Phase Diagrams 9(1):56–58
121. Sandulova AV, Khe Yu-L (1959) Diffuziya i rastvorimost tantala v germanii (Diffusion and solubility of tantalum in germanium). Doklady AN SSSR 128(2):329–332 (in Russian)
122. Andrievskii RA, Lanin AG, Rymashevskii GA (1974) Prochnost tugoplavkikh soedinenii (Strength of refractory compounds). Metallurgiya, Moscow (in Russian)
123. Spiridonov FM, Mulenkova MN, Tsirelnikov VI, Komissarova LN (1981) Promezhutochnye fazy v sisteme HfO_2 – Ta_2O_5 (The intermediate phases in the HfO_2 – Ta_2O_5 system). Zh Neorg Khim 26(6):1705–1707 (in Russian)
124. Samsonov GV (1969) Nitridy (Nitrides). Naukova Dumka, Kyiv (in Russian)
125. Östhagen K, Kofstad P (1963) The reaction between tantalum and nitrogen at 800–1300 °C. J Less-Common Met 5(1):7–25
126. Bunn P, Wert C (1964) Solubility of nitrogen in tantalum. Trans AIME 230:936–937
127. Geils RH, Potter DJ (1973) Phase equilibria in the metal-rich side of the Ta-N system. Met Trans 4(6):1469–1474

128. Korovin SS, Bukin VI, Fedorov PI, Reznik AM (2003) Redkie i rasseyannye elementy (Less-common and dissipated elements), Vol. 3. MISIS, Moscow (in Russian)
129. Wang Y, Calvert LD, Gabe EJ, Taylor JB (1979) Structures of Ta_3As and $(Nb,Ta)_3As$. Acta Crystallogr B 35:1447–1450
130. Ling RG, Belin C (1980) Affinement de la structure cristalline du diarséniure de tantale (Refinement of the crystal structure of tantalum diarsenide). Compt Rend Acad Sci Paris Ser C 202:891–893 (in French)
131. Saini GS, Calvert LD, Taylor JB (1964) Preparation and characterization of crystals of MX- and MX_2-type arsenides of niobium and tantalum. Canad J Chem 42(3):630–634
132. Dubrovskaya LB, Shveikin GP, Geld PV (1964) Sistema Ta-Ta_2O_5 (The Ta-Ta_2O_5 system). Zh Neorg Khim 9(5):1182–1186 (in Russian)
133. Jehn H, Olzi E (1972) High temperature solid-solubility limit and phase studies in the system tantalum-oxygen. J Less-Common Met 27(3):297–309
134. Stecura S (1974) Observation of oxide particles below the apparent oxygen solubility limit in tantalum. Metal Trans 5(6):1337–1340
135. Fromm E, Kirchheim R (1975) EMK-Messungen in den Sauerstoffsystemen der Va-Metalle mit einem ThO_2-Y_2O_3 Festelektrolyten (EMF-measurements in oxygen – Va metals systems using a ThO_2-Y_2O_3 solid electrolyte). Z Metallkd 66(3):144–150 (in German)
136. Aslanov LA, Simanov YuP, Novoselova AV, Ukrainskii YuM (1963) Triselenid i trisulfid tantala (Tantalum triselenide and trisulfide). Zh Neorg Khim 8(12):2635–2637 (in Russian)
137. Aslanov LA, Simanov YuP, Novoselova AV, Ukrainskii YuM (1964) Fazy peremennogo sostava v sisteme tantal-selen (The variable composition phases in the tantalum-selenium system). Zh Neorg Khim 9(9):2264–2265 (in Russian)
138. Revolinsky E, Brown BE, Beerntsen DJ, Armitage CH (1965) The selenide and telluride systems of niobium and tantalum. J Less-Common Met 8(1):63–75
139. Ukrainskii YuM, Novoselova AV, Simanov YuP (1959) Issledovanie sistemy tantal-tellur (A study in the tantalum-tellurium system). Zh Neorg Khim 4(1):148–152 (in Russian)
140. Ukrainskii YuM, Kovba LM, Simanov YuP, Novoselova AV, (1959) O β-faze sistemy tantal-tellur (On β-phase in the tantalum-tellurium system). Zh Neorg Khim 4(12):2820–2822 (in Russian)
141. Bjerkelund E, Kjekshus A (1964) On the crystal structure of $TaTe_4$. J Less-Common Met 7(3):231–234
142. Witteman WG, Giorgi AL, Vier DT (1960) The preparation and identification of some intermetallic compounds of polonium. J Phys Chem 64(4):434–440
143. Nekrasov BV (1973) Osnovy obschei khimii (Foundations of general chemistry), 3rd ed., Vol. 1. Khimiya, Moscow (in Russian)
144. Roth RS, Waring JL (1970) Effect of oxide additions on the polymorphism of tantalum pentoxide. III. "Stabilization" of the low temperature structure type. J Res Natl Bur Stand Sect A 74(4):485–493
145. Laurila T, Zeng K, Molarius J, Riekkinen T, Suni I, Kivilahti JK (2002) Effect of oxygen on the reactions in Si/Ta/Cu and Si/TaC/Cu systems. Microelect Eng 64:279–287
146. Li N, Warnes WH (2001) Estimation of the Nb-Ti-Ta phase diagram. IEEE Trans Appl Superconductivity 11(1):3800–3803
147. Cao P, Lau SP, Tay BK (2001) Phase formation in Ta-Si-N ternary system using the Gibbs free energy. In: Low power and low voltage integrated systems. Proceedings of 9th International symposium on IC technology, systems and applications, Vol. 9, pp. 315–318. Nanyang Technological University, Singapore
148. Kumar KCH, Van Rompaey T, Wollants P (2002) Thermodynamic calculation of the phase diagram of the Co-Nb-Ta system. Z Metallkd 93(11):1146–1153
149. Garg SP, Venkatraman M, Krishnamurthy N (1990) The Pu-Ta (plutonium-tantalum) system. J Alloy Phase Diagrams 6:111–115
150. Asrar N, Meshkov LL, Sokolovskaya EM (1988) Phase equilibria in ternary alloys based on iron-group metals and containing refractory metals (Mo, W, Nb, Ta). J Less-Common Met 144:41–52

151. Kaufman L (1991) Calculation of multicomponent tantalum based phase diagrams. Calphad 15(3):261–282
152. Frelin C, Desre P, Bonnier E (1968) Contribution a l'etude du diagramme d'equilibre de phases ternaire cuivre-niobium-tantale (Contribution to the study of equilibrium of ternary phase diagram copper-niobium-tantalum). Rev Int Haute Temp Refract (4):261 (in French)
153. Virkir AV, Raman A (1969) Alloy chemistry of sigma U related phases – 2. Z Metallkd 60(7):594–600
154. Hansen RC, Raman A (1970) Alloy chemistry of sigma U related phases – 3. Z Metallkd 61(2):115–120
155. Raffelsletter P, Richter KW (2009) Phase equilibria and chemical vapour transport in the system Mo-Ta-As. J Alloys Compd 480(2):397–402
156. Zhou SH, Wang Y, Chen L-Q, Liu Z-K, Napolitano RE (2009) Solution-based thermodynamic modelling of the Ni-Ta and Ni-Mo-Ta systems using first-principle calculations. Calphad 33:631–641
157. Cui YW, Jin ZP (1999) Experimental study and reassessment of the Ni-Ta binary system. Z Metallkd 90(3):233–241
158. Pan XM, Jin ZP (2002) Experimental determination and re-optimization of Ni-Ta system. Trans Nonferr Met Soc China 12:748–753
159. Cui YW, Lu XG, Jin ZP (1999) Experimental study and thermodynamic assessment of the Ni-Mo-Ta ternary system. Metall Mater Trans A 30(11):2735–2744
160. Zakharov AM, Novikov II, Pshokin VP (1971) Niobievyi ugol troinoi sistemy Nb-Ti-B (The niobium-rich angle of the Nb-Ti-B ternary system). Izv Vyssh Uchebn Zaved Tsvet Metall (4):111–114 (in Russian)
161. Emelianov VS, Godin IuG, Evstiukhin AI (1958) Study of the zirconium apex of the Zr-Ta-Nb phase diagram. Sov J Atom Energy 4(2):211–220
162. Xiong W, Du Y, Liu Y, Huang BY, Xu HH, Chen HL, Pan Z (2004) Thermodynamic assessment of the Mo-Nb-Ta system. Calphad 28:133–140
163. Miura S, Ohkubo K, Terada Y, Kimura Y, Mishima Y, Yamabe-Mitarai Y, Harada H, Mohri T (2005) Phase equilibria in Ir-rich portion of Ir-Al-X (X: V, Nb and Ta) ternary systems. J Alloys Compd 395(1–2):263–271
164. Fujita M, Kaneno Y, Takasugi T (2006) Phase field and room-temperature mechanical properties of C15 Laves phase in Nb-Hf-Cr and Nb-Ta-Cr alloy systems. J Alloys Compd 424(1–2):283–288
165. Velikanova TYa, Bondar AA, Grytsiv AV, Dovbenko OI (2001) Metallochemistry of chromium with *d*-metals and carbon. J Alloys Compd 320(2):341–352
166. Reeve DA (1969) The binary system $CaO\text{-}Ta_2O_5$. J Less-Common Met 17(2):215–222
167. Booker PH, Brukl CE (1970) The phase equilibria in the metal-rich region of the hafnium – tantalum – nitrogen system. In: Phase equilibria investigations of binary, ternary and higher order systems. Report AFML-TR-69–117, Contract USAF 33(615)-67-C-1513, Part 6, pp. 1–73. Air Force Materials Laboratory, Wright-Patterson Air Force Base, Ohio
168. King BW, Schultz J, Durbin EA, Duckworth WH (1956) Properties of tantala systems. Report BMI-1106, pp. 1–40. USAEC
169. Baskin Y, Schell DC (1963) Phase studies in the binary system $MgO\text{-}Ta_2O_5$. J Am Ceram Soc 46(4):174–177
170. Roth RS, Waring JL, Brower WS (1970) Effect of oxide additions on the polymorphism of tantalum pentoxide. II. "Stabilization" of the high temperature structure type. J Res Natl Bur Stand Sect A 74(4):477–484
171. Roth RS, Parker HS, Brower WS, Waring JL (1973) Phase equilibriums, crystal chemistry and crystal growth of alkali oxide – metal oxide systems. In: Van Gool W (ed) Fast ion transport solids, solid state batteries devices, pp. 217–232. North Holland, Amsterdam
172. Mohanty GP, Fiegel LJ, Healy JH (1964) On the system niobium pentoxide – tantalum pentoxide. J Phys Chem 68(1):208–210
173. Holtzberg F, Reisman A (1961) Sub-solidus equilibria in the system $Nb_2O_5\text{-}Ta_2O_5$. J Phys Chem 65(7):1192–1196

174. Gladyshevskii EI (1962) Crystal structure of compounds and phase equilibria in ternary systems of two transition metals and silicon. Powder Metall Met Ceram 1(4):262–265
175. Budberg PB, Alisova SP (1966) The system $TiCr_2$ – $TaCr_2$ – $NbCr_2$. Powder Metall Met Ceram 5(10):814–817
176. Egorov FF, Pshenichnaya OV, Matsera VE, Mamonova AA (1997) Interaction of nitrides of group IV-V transition metals with chromium. Powder Metall Met Ceram 36(3–4):197–202
177. Nowotny H, Rogl P (1977) Ternary metal borides. In: Matkovich VI (ed) Boron and refractory borides, pp. 413–438. Springer, Berlin, Heidelberg, New York
178. Kuzma YuB, Sobolev AS, Fedorov TF (1971) Phase equilibria in the ternary systems tantalum-iron-boron and tantalum-nickel-boron. Powder Metall Met Ceram 10(5):410–414
179. Argon AS (1996) Mechanical properties of single-phase crystalline media: deformation at low temperatures. In: Cahn RW, Haasen P (eds) Physical metallurgy, 4th ed., Vol. 3, pp. 1877–1955. Elsevier Science BV, Amsterdam
180. Gruehn R, Schäfer H (1966) Oxidische Nb- und Ta-Verbindungen mit O/Me = 2.33 – 2.50 (Nb and Ta oxide compounds with O/Me = 2.33 – 2.50). J Less-Common Met 10(2):152–154 (in German)
181. Negas T, Roth RS, McDaniel CL, Parker HS, Olson CD (1977) Oxidation-reduction reactions of $CeMO_{4+x}$ (M = Ta or Nb) phases. Mater Res Bull 12(12):1161–1171
182. Roth RS, Negas T, Parker HS, Minor DB, Jones C (1977) Crystal chemistry of cerium titanates, tantalates and niobates. Mater Res Bull 12(12):1173–1182
183. Keller C (1965) Die reaktion der dioxide der elemente thorium bis americium mit niob- und tantalpentoxid (The reaction of the dioxides of the elements thorium to americium with niobium and tantalum pentoxide). J Inorg Nucl Chem 27(6):1233–1246 (in German)
184. Holleck H, Nowotny H, Benesovsky F (1963) Die Verbindungen Ta_3Ga_2 and IrGa (The connections of Ta_3Ga_2 and IrGa). Monatsh Chem 94(5):841–843 (in German)
185. Garg SP, Venkatraman M, Krishnamurthy N (1990) The Rb-Ta (rubidium-tantalum) system. J Alloy Phase Diagrams 6:145–146
186. Garg SP, Venkatraman M, Krishnamurthy N (1990) The Cs-Ta (cesium-tantalum) system. J Alloy Phase Diagrams 6:116–117
187. Samsonov GV (1966) Berillidy (Beryllides). Naukova Dumka, Kyiv (in Russian)
188. Gulyaev BB (1968) Obobshchenie diagram sostoyaniya metallicheskikh system (Generalization of the phase diagrams of metallic systems). In: Savitskii EM (ed) Diagrammy sostoyaniya metallicheskikh system (Phase diagrams of metallic systems), p.257–267. Nauka, Moscow (in Russian)
189. Garg SP, Venkatraman M, Krishnamurthy N, Vijaykar SR (1998) The RE-Ta (rare earth – tantalum) system. J Phase Equilib 19:385–394
190. Griffin RB, Gschneidner KA Jr (1971) Effect of the sixth period elements on the melting and transformation temperatures of praseodymium. Part I. Experimental. Metall Trans 2:2517–2524
191. Savitskii EM, Efimov YV, Kozlova ND, Zvolinskii OI (1973) The influence of rare-earth metals on superconductivity of vanadium, niobium, and tantalum. Dokl Akad Nauk SSSR 213:826–829
192. Baxi HC, Massalski TB, Rizzo HF (1991) The Pu-Ta (plutonium-tantalum) system. J Phase Equilib 12(5):593–598
193. Schonfeld FW, Cramer EM, Miner WN, Ellinger FH, Coffinberry AS (1959) Plutonium constitutional diagrams. Prog Nucl Energy Ser 5 2:579–599
194. Kaufman L (1991) Coupled thermochemical and phase diagram data for tantalum based binary alloys. Calphad 15:243–259
195. English JJ (1961) Binary and ternary phase diagrams of columbium, molybdenum, tantalum and tungsten. Report DMIC-152, Contract AF-33(616)-7747, pp. 1–226. Defence Metals Information Center, Battelle Memorial Institute, Columbus, Ohio
196. Moffatt WG (1986) Binary phase diagrams handbook. General Electric Co., Schenectady, New York
197. Baren MR (1988) The Ag-Ta (silver-tantalum) system. Bull Alloy Phase Diagrams 9:244

198. Chasanov MG, Schablaske RV, Johnson I (1968) The system Ta-Zn: phase studies. J Electrochem Soc Jpn 36:192–196
199. Garg SP, Krishnamurathy N, Venkatraman M, Raju S (1991) The Ge-Ta (germanium-tamtalum) system. J Phase Equilib 12(6):661–663
200. Okamoto H (1991) The Sn-Ta (tin-tantalum) system. J Phase Equilib 24:484
201. Frisk K (1998) Analysis of the phase diagram and thermochemistry in the Ta-N and the Ta-C-N systems. J Alloys Compd 278:216–226
202. Gatterer J, Dufek G, Ettmayer P, Kieffer R (1975) Das kubische Tantalmononitrid (B1) und seine Mischbarkeit mit den isotypen Übergangsmetall-nitriden und –carbiden (The cubic tantalum mononitride (B1) and its miscibility with the isotypic transition metal nitrides and carbides). Monatsh Chem 106:1137–1147 (in German)
203. Thomas JO, Ersson NO, Anderson Y (1980) An x-ray film powder profile refinement of the crystal structure of Ta_5P_3. J Appl Crystallogr 13:605–607
204. Garg SP, Krishnamurthy N, Awasthi A, Venkatraman M (1996) The O-Ta (oxygen-tantalum) system. J Phase Equilib 17(1):63–77
205. Okamoto H (1999) The Br-Ta (bromine-tantalum) system. J Phase Equilib 20:635
206. McCarley RE, Boatman JC (1965) The equilibrium phase diagrams for the tantalum – tantalum bromide and tantalum – tantalum iodide systems. Inorg Chem 4:1486–1491
207. Okamoto H (2001) The I-Ta (iodine-tantalum) system. J Phase Equilib 22:93
208. Rieger W, Nowotny H, Benesovsky F (1965) Über einige Komplexboride von Übergangsmetallen (Some complex borides of transition metals). Monatsh Chem 96:844–851
209. Schuster JC, Nowotny H (1985) Phase equilibria in the ternary systems Nb-Al-N and Ta-Al-N. Z Metallkd 76:728–729
210. Jehn HA (1993) The Al-N-Ta (aluminium-nitrogen-tantalum) system. Ternary Alloys VCH 7:301–303
211. Kuzma YuB, Chaban NF, Vityk OS (1979) Phase equilibria at 800 °C in the Ta-Co-B and Nb-Co-B systems. Powder Metall Met Ceram 18:672–674
212. Stadelmaier HH, Hofer G (1964) Die kobaltreichen Kobalt-Tantal-Bor-Legierungen um die Phase $Co_{21}Ta_2B_6$ (The cobalt-rich tantalum-cobalt-boron alloys the phase $Co_{21}Ta_2B_6$). Metall 18:460–462 (in German)
213. Kuzma YuB, Telegus VS, Marko MA (1972) Phase equilibria in the systems hafnium-niobium-boron and tantalum-chromium-boron. Powder Metall Met Ceram 11:308–312
214. Marko MA, Kuzma YuB, Gladyshevskii EI (1976) Rentgenograficheskoe issledovanie sistem Nb-Ge-B i Ta-Ge-B (The x-ray study of Nb-Ge-B and Ta-Ge-B systems). Dopov Akad Nauk Ukr RSR Ser A Fiz Mat Tekh Nauki 38:555–558 (in Russian)
215. Kuzma YuB, Svarichevskaya SI, Telegus VS (1971) Systems titanium-tungsten-boron, hafnium-tantalum-boron and tantalum-tungsten-boron. Powder Metall Met Ceram 10:478–481
216. Ordanyan SS, Nikolaeva EE, Kozlovskii LV (1984) Interactions in LaB_6-M^5B_2 systems. Inorg Mater 20:1580–1583
217. Sobolev AS, Kuzma YuB, Soboleva TE, Fedorov TF (1968) Phase equilibria in tantalum-titanium-boron and tantalum-molybdenum-boron systems. Powder Metall Met Ceram 7:48–51
218. Stadelmaier HH, Kotyk M, Hofer G (1964) Die nickelreichen Legierungen im Dreistoffsystem Nickel-Tantal-Bor (The nickel-rich alloys in the ternary system nickel-tantalum-boron). Metall 18:1065–1066 (in German)
219. Lugscheider E, Reimann H, Pankert R (1982) Mit 4a- und 5a-Metallen stabilisierte tau-Boride des Nickel (Tau-borides of nickel stabilized by 4a and 5a metals). Metall 36:247–251 (in German)
220. Lavendel HW (1961) Alloys of tantalum diboride with iron, cobalt, and nickel. Planseeber Pulvermetall 9:80–95
221. Range KJ, Wildenauer M, Andratschke M (1996) Crystal structure of tantalum orthoborate $TaBO_4$. Z Kristallogr 211:815
222. Voroshilov YuV, Kuzma YuB (1969) Reaction of zirconium with the transition metals and boron. Powder Metall Met Ceram 8:941–944

223. Leitnaker JM, Bowman MG, Gilles PW (1962) Thermodynamic properties of the tantalum and tungsten borides. J Electrochem Soc 109:441–443
224. Nowotny H, Lux B, Kudielka H (1956) Das Verhalten metallreicher, hochschmelzender Silizide gegenüber Bor, Kohlenstoff, Stickstoff und Sauerstoff (The reaction of metal-rich refractory silicides with boron, carbon, nitrogen and oxygen). Monatsh Chem 87:447–470 (in German)
225. Holleck H, Thümmler F (1967) Ternäre Komplex-carbide, -nitride und -oxide mit teilweise aufgefüllter Ti_2Ni-Struktur (Ternary complex carbides, nitrides and oxides with partially filled Ti_2Ni structure). Monatsh Chem 98:133–134 (in German)
226. Schönberg N (1954) An x-ray investigation on ternary phases in the Ta-Me-N systems (Me = Ti, Cr, Mn, Fe, Co, Ni). Acta Chem Scand 8:213–220
227. Steinmetz J, Malaman B, Roques B (1978) Trois nouveaux siliciures ternaires ordonnes: $(Cr,Nb,Ta)_{11}Si_8$, $(Mn,Mo)_{11}Si_8$ et les germaniures isotypes $(T,Nb)_{11}Ge_8$, T = V, Cr, Mn (Three new ternary silicides ordered: $(Cr,Nb,Ta)_{11}Si_8$, $(Mn,Mo)_{11}Si_8$ and isotypic germanides $(T,Nb)_{11}Ge_8$, T = V, Cr, Mn). J Less-Common Met 57:133–146 (in French)
228. Blazina Z, Pavkovic SF (1989) On Friauf-Laves phases in the $Ta_{1-x}Al_xT_2$ and $Ta_{1-x}Si_xT_2$ (T = Cr, Mn, Fe, Co, Ni) systems. J Less-Common Met 155:247–253
229. Zachwieja U, Jacobs H (1991) $CuTaN_2$, a copper(I)-tantalum(V)-nitride with delafossite structure. Eur J Solid State Inorg Chem 28:1055–1062
230. Marchand R, Tessier F, DiSalvo FJ (1999) New routes to transition metal nitrides: preparation and characterization of new phases. J Mater Chem 9:297–304
231. Raghavan V (1987) Phase diagrams of ternary iron alloys, Part 1. The Indian Institute of metals, Calcutta
232. Kuzma YuB, Marko MA, Petrovskaya MV (1972) Rentgenograficheskoe issledovanie troinykh sistem V-(Nb,Ta)-B, Nb-Ta-B i V-(Mo,W)-B (X-ray investigation of the ternary systems V-(Nb,Ta)-B, Nb-Ta-B and V-(Mo,W)-B). Visn Lviv Derzh Univ Ser Khim 13:3–8 (in Russian)
233. Rokhlin L (2010) Molybdenum – silicon – tantalum system. In: Effenberg G, Ilyenko S (eds) Ternary alloy systems, Subvol. E, Part 3, pp. 385–397. Springer, Berlin, Heidelberg
234. Frisk K, Dumitrescu L, Ekroth M, Jansson B, Kruse O, Sundman B (2001) Development of a database for cemented carbides: thermodynamic modeling and experiments. J Phase Equilib 22:645–655
235. Gasperin M (1960) Contribution a l'etude de quelques oxydes doubles que forme le tantale avec l'etain, l'uranium et le calcium. Application a la cassiterite et a la betafite (Contribution to the study of some double oxides formed tantalum with tin, uranium and calcium. Application of cassiterite and betafite) Bull Soc Fr Mineral Cristallogr 83:1–21 (in French)
236. Kudielka H, Nowotny H (1956) Disilizidsysteme (The disilicide systems) Monatsh Chem 87:471–482 (in German)
237. Steinmetz J, Roques B (1977) Une famille de siliciures ternaires isotypes de V_6Si_5: $(T,T')_6Si_5$ ou T = V, Cr, Mn et T' = Ti, Nb, Ta (A family of isotypic ternary silicides V_6Si_5: $(T,T')_6Si_5$ or T = V, Cr, Mn and T' = Ti, Nb, Ta). J Less-Common Met 52(2):247–258 (in French)
238. Raghavan V (1992) Phase diagrams of ternary iron alloys, Part 6B. The Indian Institute of metals, Calcutta
239. Kumar KCH, Raghavan V (1989) B.c.c.-f.c.c. equilibrium in ternary iron alloys – II. J Alloy Phase Diagrams 5:77–96
240. Griessen R, Driessen A, De Groot DG (1984) Search for new metal-hydrogen systems for energy storage. J Less-Common Met 103:235–244
241. Kabanov SV, Subbotin IM, Loboda TP (1981) Fiziko-khimicheskoe issledovanie vzaimodeistviya molibdena i ruteniya s tantalom i volframom (Physico-chemical investigation of molybdenum and ruthenium with tantalum and tungsten interaction). In: Phase equilibria in metal alloys (Fazovye ravnovesiya v metallicheskikh splavakh), pp. 266–269. Nauka, Moscow (in Russian)
242. Subbotin IM, Raevskaya MV, Loboda TP, Sokolovskaya EM (1981) (Vzaimodeistvie molybdena i ruteniya s perekhodnymi metallami VI perioda (The reaction of molybdenum

and ruthenium with transition metals of period VI). Moscow Univ Chem Bull 36(5):51–54 (in Russian)
243. Nikitin PN, Mikheyev VS (1971) Examination of the titanium corner of the Ti-Ta-Mo equilibrium diagram. Russ Metall (1):144–147
244. Weymann K, Müller H (1986) Deuterides of Nb-Ta, Nb-V and Ta-V solid solutions. J Less-Common Met 119:127–130
245. Ettmayer P, Vendl A (1980) Vorschlag zur Kristallstruktur des Komplexnitrids $(Nb,Ta)_8N_9$ (Proposition of complex nitride crystal structure of $(Nb,Ta)_8N_9$) J Less-Common Met 72:209–217 (in German)
246. Bernard VB, Burnasheva VV, Kuprina VV (1978) Issledovanie troinoi sistemy iridii-tantal-kobalt (A study of the ternary system iridium-tantalum-cobalt). Moscow Univ Chem Bull 33(1):40–43 (in Russian)
247. Bernard VB, Kuprina VV, Burnasheva VV (1973) Issledovanie troinoi sistemy iridii-tantal-nikel (Investigation of the ternary iridium-tantalum-nickel system). Moscow Univ Chem Bull 28(3):71–73 (in Russian)
248. Seung AC, Giessen BC, Grant NJ (1987) Formation of close-packed-ordered $A(B_{1-x}B'_x)_3$-type intermediate phases in some metallic AB_3-AB'_3 pseudobinary alloy system. Rev Latinoam Metalurgia Materiales 7:27–35
249. Mishra R, Pöttgen R, Kotzyba G (2001) New metal-rich compounds NbIrSi, NbIrGe and TaIrSi – synthesis, structure and magnetic properties Z Naturforsch B 56:463–468
250. Mar A, Ibers JA (1992) Synthesis and physical properties of the new layered ternary tellurides $MIrTe_4$ (M = Nb, Ta) and the structure of $NbIrTe_4$. J Solid State Chem 97:366–376
251. Yamaguchi O, Tomihisa DO, Shirai M, Shimizu K (1988) Formation and transformation of solid solutions in the system Nb_2O_5-Ta_2O_5. J Am Ceram Soc 71:C260-C262
252. Raghavan V (2008) The Al-Ir-Ta (aluminum-iridium-tantalum) system. J Phase Equilib Diffus 29(4):370
253. Huang C, Yamabe-Mitarai Y, Harada H (2007) Morphology evolution of Ir-Nb-X (X = Hf, Ta, or Ti) ternary alloys. J Alloys Compd 428:220–229
254. Huang C, Yamabe-Mitarai Y, Nakazawa S, Nishida K, Harada H (2005) Investigation on phase relationships and creep properties of Ir-Nb-X (X = Hf, Ta, or Ti) ternary alloys. Mater Sci Eng A 412(1–2):191–197
255. Okamoto H (2013) The Fe-Ta (iron-tantalum) system. J Phase Equilib Diffus 34(2):165–166
256. Okamoto H (2013) The Al-Ta (aluminum-tantalum) system. J Phase Equilib Diffus 31(6):578–579
257. Guo Z, Yuan W, Sun Y, Cai Z, Qiao Z (2009) Thermodynamic assessment of the Si-Ta and Si-W systems. J Phase Equilib Diffus 30(5):564–570
258. Okamoto H (2008) The N-Ta (nitrogen-tantalum) system. J Phase Equilib Diffus 29(3):291
259. Chad VM, Ramos ECT, Coelho GC, Nunes CA, Suzuki PA, Ferreira F, Rogl P (2006) Evaluation of the invariant reactions in the Ta-rich region of the Ta-B system. J Phase Equilib Diffus 27(5):452–455
260. Okamoto H (2005) The Ta-V (tantalum-vanadium) system. J Phase Equilib Diffus 26(3):298–299
261. Okamoto H (2000) The Ni-Ta (nickel-tantalum) system. J Phase Equilib 21(5):497
262. Okamoto H (1996) The Ta-Zr (tantalum-zirconium) system. J Phase Equilib 17(6):555
263. Okamoto H (1996) The Cr-Ta (chromium-tantalum) system. J Phase Equilib 17(5):457
264. Okamoto H (1996) The Ni-Ta (nickel-tantalum) system. J Phase Equilib 17(4):371
265. Okamoto H (1996) The Hf-Ta (hafnium-tantalum) system. J Phase Equilib 17(3):270
266. Okamoto H (1996) The Fe-Ta (iron-tantalum) system. J Phase Equilib 17(1):81–82
267. Coelho GC, Neto JGC, Gama S, Ribeiro CA (1995) Experimental study of the iron-tantalum equilibrium diagram. J Phase Equilib 16(2):121–128
268. Schlesinger ME (1994) The Si-Ta (silicon-tantalum) system. J Phase Equilib 15(1):90–95
269. Okamoto H (1993) Comment on B-Ta (boron-tantalum) system. J Phase Equilib 14(3):393–394

270. Okamoto H (1992) The T-Ta (tritium-tantalum) system. J Phase Equilib 13(4):445–446
271. Okamoto H (1992) The D-Ta (deuterium-tantalum) system. J Phase Equilib 13(4):440–441
272. Garg SP, Krishnamurthy N (1992) The Te-Ta (tellurium-tantalum) system. J Phase Equilib 13(3):270–271
273. Garg SP, Krishnamurthy N (1992) The Bi-Ta (bismuth-tantalum) system. J Phase Equilib 13(3):269–270
274. Ordanyan SS, Vikhman SV, Nagaeva YuS (2011) Reaction of $MoSi_2$ with niobium and tantalum diborides. Refract Indust Ceram 52(4):282–285

Chapter 7
Molybdenum

7.1 Structures

Molybdenum is the element No. 42 of the periodic table (period—5, similar to tungsten group—6 (or VIB), relates to transition metals) with the ground state level $^7S_3$ and electron configuration $1s^2 2s^2 2p^6 3s^2 3p^6 3d^{10} 4s^2 4p^6 4d^5 5s^1$. The general oxidation states (numbers) of molybdenum in various chemical compounds are (–2), (–1), 0, (+1), (+2), (+3), (+4), (+5) and (+6); the oxidation states (+6) and (+4) are the most common; the radii of molybdenum are:

atomic (metallic, CN = 8)—0.136 nm,
atomic (metallic, CN = 12)—0.140 nm,
atomic (covalent)—0.130 nm,
ionic (+3)—0.069 nm (CN = 6),
ionic (+4)—0.065 nm (CN = 6),
ionic (+5)—0.061 nm (CN = 6),
ionic (+5)—0.046 nm (CN = 4),
ionic (+6)—0.073 nm (CN = 7),
ionic (+6)—0.059 nm (CN = 6),
ionic (+6)—0.041 nm (CN = 4);

its electronegativity is 2.16 in Pauling scale, or 1.30 in Allred–Rochow scale [2, 8, 9, 12]. Molybdenum has body-centred cubic (bcc) metal crystal structure (space group—*Im(–3)m*, W type) with lattice parameter $a = 0.31470$ nm ($Z = 2$) at 25 °C (minimum interatomic distance—0.2725 nm, CN = 8), slip planes (112) at 20 °C and (110) at 1000 °C [1, 4, 9, 271, 272]. At room temperature the XRD density of molybdenum is 10.220 g cm^{-3} and recommended value for the bulk density of common metal parts—10.20–10.25 g cm^{-3} [5, 8–9, 11–12].

I. L. Shabalin, *Ultra-High Temperature Materials I*,
DOI: 10.1007/978-94-007-7587-9_7,

7.2 Thermal Properties

Molybdenum is a refractory metal; of the naturally occurring elements, only carbon, tungsten, rhenium, osmium and tantalum have higher melting points. The general thermodynamic properties of molybdenum are summarized in Table 7.1. For the molar heat capacity $c_p = f(T, \text{K})$, J mol^{-1} K^{-1}, the following relationships are recommended:

in the range of temperatures from 298 to 2500 K [6]

$$c_p = 22.94 + \left(5.443 \times 10^{-3}\right)T, \tag{7.1}$$

in the range of temperatures from 400 to 2400 K [10]

$$c_p = 24.15 + \left(1.18 \times 10^{-3}\right)T + \left(2.26 \times 10^{-6}\right)T^2. \tag{7.2}$$

For the specific heat capacity $c_p = f(T, K)$, J kg^{-1} K^{-1}, in the range of temperatures from 298 to 2900 K the equation was applied [5] as

$$c_p = 249.8 + \left(59.26 \times 10^{-3}\right) \times (T - 273) + \left(96.7 \times 10^{-7}\right) \times (T - 273)^2. \tag{7.3}$$

The equilibrium vapour pressure of molybdenum P, Pa, is obeyed by the following rules:

in the range of temperatures from 298 to 2500 K [8]

$$\lg P = -34626/T - 1.1331 \lg T + 16.535, \tag{7.4}$$

in the range of temperatures from 300 to 2800 K [6]

$$\lg P = -20738/T + 31.4799 \lg T - (3{,}5228 \times 10^{-3})T - 91.1078, \tag{7.5}$$

in the range of temperatures from 2890 to 5100 K (for liquid molybdenum) [6]

$$\lg P = 1186374/T + 33.61361 \lg T + 0{,}13399T - 913.520, \tag{7.6}$$

where T is temperature, K. In high vacuum the rate of molybdenum vaporization at the temperatures of 1380, 1630 and 1900 °C approximately amounts to 0.1 μm, 10 μm, 1 mm per year, respectively [5]. The values of standard molar entropy $S°_{298}$, molar c_p and specific c heat capacities, enthalpies (heats) of melting and vaporization, molar and specific mass enthalpy differences $H_T - H_{298}$, vapour pressures and vaporization rates for molybdenum are given in Addendum in comparison with other ultra-high temperature materials. The variation of the thermal conductivity of molybdenum with temperature is shown in Fig. 7.1 on the basis of several studies taking into account data spread in literature [5, 11, 53].

At room temperature the coefficient of linear thermal expansion of pure molybdenum $\alpha = (5.35 \div 5.43) \times 10^{-6}$ K^{-1} [9, 12], while for the interval 20–1700 °C the recommended value is 6.7×10^{-6} K^{-1} [5]. The values of the coefficient of thermal expansion are very sensitive to the character of

Table 7.1 General thermodynamic properties of molybdenum

Characteristics	Symbol	Unit	Value	References
Standard molar entropy (at 298.15 K and 100 kPa)	S°_{298}	J mol^{-1} K^{-1}	28.6 ± 2.1	[5]
			28.56	[9, 12]
			28.6	[10]
			28.7	[8]
Enthalpy difference	H_{298}–H_0	kJ mol^{-1}	4.589	[9]
Standard molar heat capacity (at 298.15 K and 100 kPa)	$c^\circ_{p,298}$	J mol^{-1} K^{-1}	23.93	[9]
			23.8	[10]
			24.06	[8]
			24.1	[5]
Specific heat capacity (at 298.15 K)	c	J kg^{-1} K^{-1}	251	[5, 7–8]
			250	[11]
			250.8	[12]
Molar enthalpy (heat) of melting (at the melting point)	ΔH_m	kJ mol^{-1}	37.48	[7–9, 12]
Specific enthalpy (heat) of melting (at the melting point)		kJ kg^{-1}	290	[5]
			210	[11]
			270	[62]
			292	[45]
Molar enthalpy (heat) of vaporization (at the boiling point)	ΔH_v	kJ mol^{-1}	582.2	[9]
			591	[5]
			594.1	[12]
			617	[7]
Specific enthalpy (heat) of vaporization (at the boiling point)		kJ kg^{-1}	6160	[5]
			6192	[12]
			6700	[11]
Melting point	T_m	K (°C)	2890 ± 5 (2620 ± 5)	[5, 10]
			2880 (2610)	[11, 45, 62]
			2890 (2617)	[43]
			2893 (2620)	[9]
			2895 (2622)	[7–8, 12]
Boiling point	T_b	K (°C)	5100 (4830)	[10]
			4912 (4639)	[8]
			4952 (4679)	[9, 12]
			5095 (4825)	[7]
			5830 (5560)	[45, 62]
Critical temperature/pressure[a]	T_c/P_c	K/MPa	11000/540	[9]

[a] Corresponds to the critical density of 2.63 g cm^{-3}

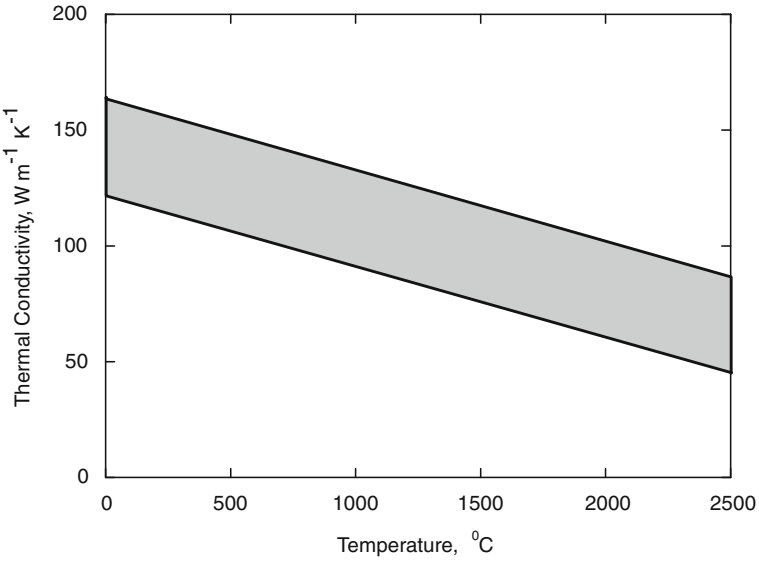

Fig. 7.1 Variation of the thermal conductivity of unalloyed molybdenum with temperature, taking into account data spread available in literature [5, 11, 53]

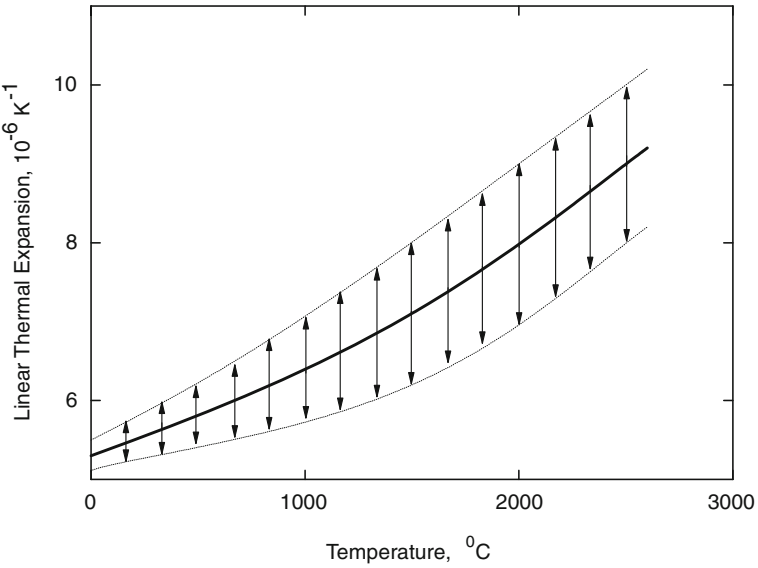

Fig. 7.2 Variation of the linear thermal expansion of pure molybdenum with temperature (*curve*—recommended values, *arrows*—data spread available in literature) [5, 11, 53]

thermomechanical treatment and impurities. For molybdenum treated variously, the average value of α increases with temperature growth and differs from $(5.2 \div 5.5) \times 10^{-6}$ K^{-1} at 0 °C to $(8 \div 10) \times 10^{-6}$ K^{-1} at 2500 °C (Fig. 7.2)

[5, 11, 53]. The surface tension of liquid molubdenum is 2.25 N m^{-1}, its temperature coefficient is –0.3 × 10^{-3} N m^{-1} K^{-1} [9].

In comparison with other ultra-high temperature materials (graphite and refractory metals), the values of thermal conductivity and thermal expansion of molybdenum in the wide range of temperatures are summarized in Addendum.

7.3 Electro-Magnetic and Optical Properties

At room temperature the specific electrical resistance (resistivity) of pure molybdenum $\rho = 50 \div 60$ nΩ m [5, 9, 11–12, 62]. At higher temperatures the resistivity almost obeyed the classic metal model (with small positive deviation from linearity) and exceeds 0.5 μΩ m at 2500 °C [5, 11, 53]. Taking into account the data spread available in literature, the thermal dependence of the specific electrical resistance is shown in Fig. 7.3 [5, 11]. The variation of resistivity at the melting point of molybdenum is $\rho_{liq}/\rho_{sol} = 1.23$ [10]. The recommended values of thermal coefficient of resistivity are 3.6 × 10^{-3} K^{-1} for the interval from 20 to 1730 °C and 4.8 × 10^{-3} K^{-1} for the interval from 20 to 2630 °C (the pressure coefficient is –1.29 × 10^{-5} MPa^{-1}) [5, 9]. At room temperature the Hall coefficient of molybdenum is $R = 1.26 \times 10^{-10}$ m^3 A^{-1} s^{-1} ($B = 0.5$–2.0 T), and Seebeck coefficient (absolute thermoelectric power) is +5.9 μV K^{-1} [9, 12]. Molybdenum is a paramagnetic metal with molar magnetic susceptibility χ_m (SI) = 9.05 × 10^{-4} cm^3 mol^{-1} at 22 °C [9].

The variations of main optical properties of tungsten with wavelength λ are the following [10, 12, 62]:

index of refraction (single crystal or polycrystalline materials)—from 2.21 ($\lambda = 0.3$ μm) to 6.40 ($\lambda = 7$ μm);
index of refraction (0.137 μm thin film)—from 0.615 ($\lambda = 0.25$ μm) to 0.918 ($\lambda = 1.0$ μm);
index of absorptance (single crystals or polycrystalline materials)—from 3.56 ($\lambda = 0.3$ μm) to 78.0 ($\lambda = 20.0$ μm);
index of absorptance (0.137 μm thin film)—from 1.222 ($\lambda = 0.25$ μm) to 2.207 ($\lambda = 1.0$ μm);
reflective index under normal incidence (polished polycrystalline materials, thin films or single crystal)—from 0.10 ($\lambda = 0.124$ μm) to 0.50 ($\lambda = 0.62$ μm), or from 0.46–0.576 ($\lambda = 0.5$–0.65 μm) to 0.93–0.95 ($\lambda = 10.0$–12.0 μm).

In the range of temperatures 700–2700 °C the monochromatic emittance (spectral emissivity) ε_λ ($\lambda = 0.65$ μm) of non-oxidized molybdenum varies from 0.34 to 0.415 decreasing almost linearly with temperature growth, while the integral emittance ε_T increases with temperature increase and amounts to 0.24–0.28 at 2000–2500 °C [5, 10]. The electron work function of polycrystalline molybdenum is ~4.3–4.4 eV [5, 9–10], and for variously oriented molybdenum single crystals

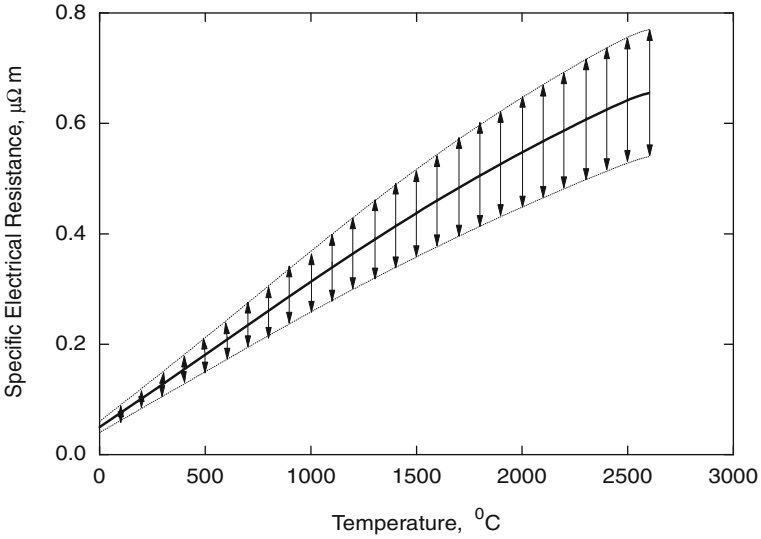

Fig. 7.3 Variation of specific electrical resistance of unalloyed molybdenum with temperature (*curve*—recommended values, *arrows*—data spread available in literature) [5, 9, 11]

these values are ~4.0 (116), 4.1 (111), 4.4 (100), 4.5 (001), 4.55 (112) and 5.0 (110) [10]. The Richardson constant (thermoelectronic emission constant) of molybdenum is $\sim(55 \div 115) \times 10^4$ A m^{-2} K^{-2} [5, 12].

The recommended values of electrical resistivity, magnetic susceptibility, integral and spectral emittances and thermoionic emission characteristics (electron work function and Richardson constant) for molybdenum are given in comparison with other ultra-high temperature elements (carbon and refractory metals) in Addendum.

7.4 Physico-Mechanical Properties

The physico-mechanical properties of molybdenum are strongly dependent on microstructure character (grain size and shape, dislocation network and grain boundary constitution, stress system), which is affected by metal working and heat treatment, as well as by the concentration of interstitial atoms (contaminations). Hardness of molybdenum ranges widely, e.g. for the various microstructure states of metal produced by powder metallurgy method, the hardness (*HB*) comes to the following values [5]:

as-sintered (density—9.8–10.0 g cm^{-3})—100–123 kgf mm^{-2} (0.98–1.20 GPa); sintered and cold worked (density—10.2–10.3 g cm^{-3})—150–180 kgf mm^{-2} (1.17–1.76 GPa).

The temperature behaviour of hardness is complicated because of the presence of two flexion points (approximately, at the temperatures of $(0.15 \div 0.25)T_m$ and $(0.3 \div 0.5)\ T_m$) on the hardness-temperature curve, which are connected with changing the deformation mechanism. The hardness of molybdenum declines with increasing temperature significantly, e.g. from 24.5 kgf mm^{-2} (0.26 GPa) at 1400 °C to 2.3 kgf mm^{-2} (0.02 GPa) at 2500 °C in *HV* scale [5, 11].

The value of ultimate tensile strength of pure molybdenum at room temperature amounts up to 2.0 GPa, for the various components made from it and different states of metal structure these characteristics comes to the following values [5, 66]:

sintered from powder (as-sintered, density—9.8–10.0 g cm^{-3})
—0.235–0.295 GPa;
sintered from powder (wrought 70–90 %, density—10.2–10.3 g cm^{-3})
—0.47–0.59 GPa;
bar, diameter 15–20 mm (as-cast, vacuum arc casting)—0.69 GPa;
bar, diameter 15–20 mm (stress relieved at 985 °C for 1 h, vacuum arc casting)
—0.67 GPa;
bar, diameter 15–20 mm (recrystallized at 1175 °C for 1 h, vacuum arc casting)
—0.46 GPa;
plate, thickness 1.25 mm (arc cast, annealed at 1000 °C)—0.74–0.80 GPa;
plate, thickness 0.33 mm (arc cast, annealed at 985 °C)—0.79–0.80 GPa
wire, diameter 30–50 μm (sintered at 1650–2000 °C for 1–2 h)—0.88–0.97 GPa;
wire, diameter 100 μm (hard drawn)—$\sim$2.06 GPa;
wire, diameter 100 μm (hard drawn and then annealed at 1250 °C)
—$\sim$0.59 GPa;

Typical examples of the variation of ultimate tensile strength of unalloyed molybdenum with temperature are shown in Figs. 7.4, 7.5 [5, 11, 63–66]. The yield strength of recrystallized molybdenum produced by arc casting decreases from 0.44 to 0.45 GPa at 25 °C to 0.06–0.11 GPa at 1100 °C [10]. At the temperatures $\geq$1000 °C for wrought molybdenum the elongation exceeds 20 % and reduction in area—80 % [66]. The correlation between ultimate tensile strength and hardness in *HV* scale at 1100–2000 °C could be expressed as following:

$$\sigma_t = cHV, \tag{7.7}$$

where c is the coefficient, which varies approximately from ¼ to ½ [11]. At room temperature, the fracture toughness of molybdenum differs from 5 to 12 MPa $m^{1/2}$ for the metal produced by powder metallurgy methods to 18–20 MPa $m^{1/2}$ for the metal produced by vacuum arc casting. With temperature increase the magnitude of this factor rises considerably, and for stress relieved and recrystallized molybdenum it amounts to 60–70 MPa $m^{1/2}$ just at 300 °C; increasing degree of recrystallization results in evident decline of the fracture toughness of forged molybdenum from 13 to 5 MPa $m^{1/2}$ [53]. A fatigue limit for molybdenum may be approached for $N > 10^7$ under stress-controlled conditions [65], the reported data

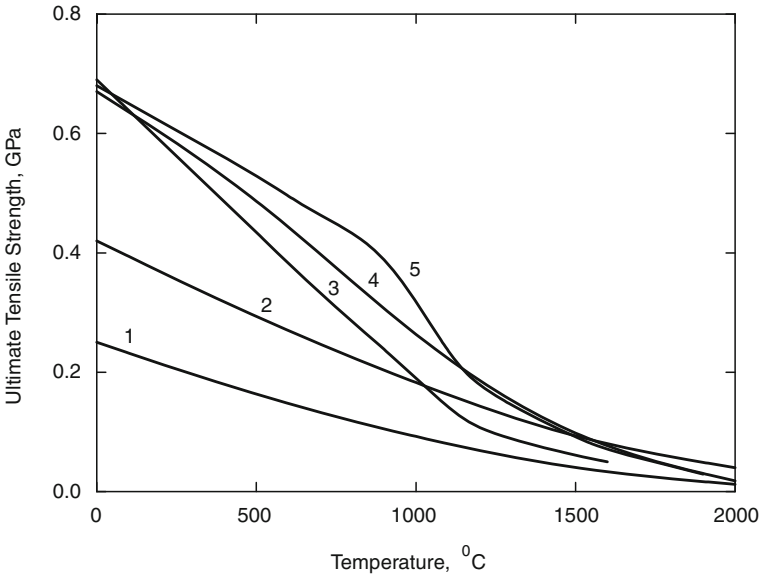

Fig. 7.4 Variation of the ultimate tensile strength of unalloyed molybdenum with temperature: *1*, *2*—recrystallized metal, *3*—metal in its usual delivering condition (hardened, stress relieved), *4*, *5*—hardened (cold worked) metal (based on various summarizing sources *1*, *4*—[5], *2*—[11], *3*—[63], *5*—[64])

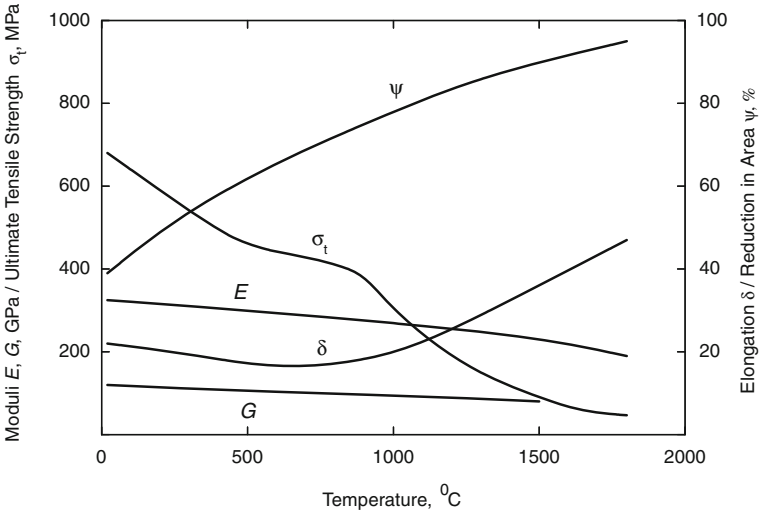

Fig. 7.5 Variations of Young's (E) and Coulomb's (shear) (G) moduli, ultimate tensile strength (σ_t), fracture elongation (δ) and reduction in area (ψ) with temperature of wrought molybdenum produced by arc casting [11, 53, 66]

on fatigue related properties of molybdenum for various test conditions and frequencies are summarized in [13].

The ductile-to-brittle transition temperature of molybdenum is very sensitive to contamination and degree of recrystallization. The transition temperature is also strongly dependent on treatment (annealing temperature) and test methods (character of stressed state). The concentrations of nitrogen $\geq\sim 0.01$ at.%, oxygen $\geq\sim 0.02$ at.% and carbon $\geq\sim 0.05$ at.% make molybdenum brittle at room temperature. The purity is directly correlated with the value of elongation in tensile loading tests at room temperature. For molybdenum wire with ultimate tensile strength 0.9–1 GPa, the elongation amounts to 13–21 %, for hardened metal with strength ~ 0.45 GPa and yield strength ~ 0.35 GPa the elongation is ~ 25 % [11–12]. High purity molybdenum prepared by multiple vacuum zone refining has demonstrated plasticity behaviour at cryogenic temperatures $t = -190$ °C. For molybdenum produced by vacuum arc casting or powder metallurgy methods the ductile-to-brittle transition temperature varies from –50 to +700 °C [66].

The values of long-term strength are of great importance for the evaluation of operational time of high-temperature components and structures. Unalloyed molybdenum loses its long-term rupture strength considerably with increasing temperature, e.g. 100 h rupture strength of molybdenum at 800 °C is only 62.5 % of its value at 20 °C. Some creep properties of molybdenum, produced by different methods and tested in the range of temperatures from 870 to 2500 °C, are given in Table 7.2 [10–11] and Fig. 7.6 [53–54].

At room temperature the main elastic properties of pure molybdenum have the following numerical values [5, 9–12]:

Young's modulus E, GPa		320–330
Coulomb's (shear) modulus G, GPa		120–126
Poisson's ratio ν		0.29–0.31
Bulk (compression) modulus K, GPa		260–295
Volume compressibility κ, MPa^{-1}		0.34×10^{-5}
Longitudinal velocity of sound V_S, m s^{-1}		6250–6370
Transversal velocity of sound V_T, m s^{-1}		3350–3510
Elastic compliance	s_{11}, TPa^{-1}	2.63
	s_{44}, TPa^{-1}	9.20
	s_{12}, TPa^{-1}	–0.68
Elastic stiffness	c_{11}, GPa	460–465
	c_{44}, GPa	109–110
	c_{12}, GPa	163–176

Table 7.2 High-temperature creep rate of molybdenum produced by arc casting and powder metallurgy methods [10–11]

Production method	Temperature, °C	Stress, MPa	Testing time, h	Steady-state creep rate, s^{-1}	
				In vacuum	In hydrogen
Arc casting	870	113	136	–	5.85×10^{-7}
		127	110	1.67×10^{-7}	–
		137	32	–	2.36×10^{-6}
		137	70	1.11×10^{-6}	–
		170	–	5.5×10^{-5}	–
		202	–	2.55×10^{-4}	–
		237	–	7.65×10^{-4}	–
		278	–	6.46×10^{-3}	–
Powder metallurgy	870	92.5	328	2.03×10^{-7}	–
		103	94	5.56×10^{-7}	–
Arc casting	980	68.5	147	–	3.9×10^{-7}
		68.5	482	3.62×10^{-8}	–
		86	58	1.39×10^{-6}	–
		106	–	2.7×10^{-5}	–
		114	–	7.0×10^{-5}	–
		154	–	4.3×10^{-4}	–
		185	–	3.5×10^{-3}	–
		240	–	3.7×10^{-2}	–
Powder metallurgy	980	58.3	724	7.5×10^{-8}	–
		68.5	158	2.78×10^{-7}	–
Arc casting	1100	41.2	259	–	2.36×10^{-7}
		58.3	28	–	2.08×10^{-6}
		58.3	1410	1.86×10^{-8}	–
		68.5	103	3.06×10^{-7}	–
		86	15	2.78×10^{-6}	–
		89.3	–	7.1×10^{-5}	–
		105	–	7.3×10^{-4}	–
		129	–	2.1×10^{-3}	–
		157	–	1.2×10^{-2}	–
Powder metallurgy	1100	32.8	301	1.95×10^{-8}	–
		41.2	85	1.39×10^{-7}	–
Powder metallurgy	1650[a]	36.2	–	2×10^{-5}	–
		55	–	2×10^{-4}	–
	1700[a]	27.5	–	3×10^{-6}	–
	2000[a]	3.43	–	5×10^{-8}	–
		6.17	–	10^{-6}	–
		13.7	–	10^{-4}	–
	2250[a]	4.8	–	10^{-6}	–
		6.86	–	10^{-5}	–
	2500[a]	2.06	–	10^{-6}	–
		6.17	–	2×10^{-4}	–
		10.3	–	2×10^{-3}	–

[a] Data on creep rate are given for helium atmosphere

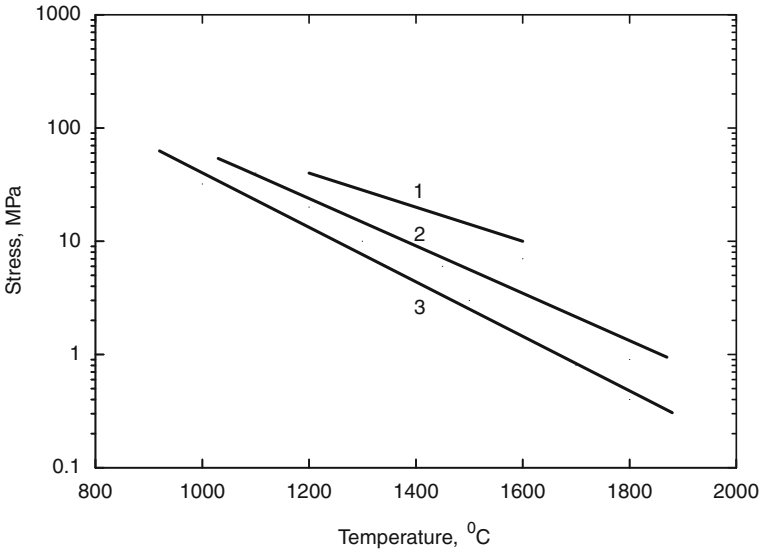

Fig. 7.6 High-temperature creep properties of molybdenum: *1*—100 h rupture stress; *2*—stress for steady-state creep rate of 10^{-4}/h; *3*—stress for 1 % elongation in 10000 h [53–54]

The variations of Young's and Coulomb's (shear) moduli of wrought molybdenum produced by arc casting with temperature are shown in Fig. 7.5 [11, 53, 66].

The magnitudes of physico-mechanical (strength, elasticity) properties of unalloyed molybdenum in the wide range of temperatures are summarized in Addendum in comparison with other ultra-high temperature materials (graphite and refractory metals).

7.5 Nuclear Physical Properties

The isotopes of molybdenum (standard atomic mass—95.96 u) from ^{83}Mo to ^{115}Mo, including metastable states ($^{89m-93m}$Mo, $^{99m1-2}$Mo, ^{107m}Mo), and their general characteristics are summarized in Table 7.3; the naturally occurring isotopes are listed in order of decreasing abundance, and unstable artificial (radioactive) isotopes—in order of decreasing half-life period of decay.

Table 7.3 General characteristics of the isotopes of molybdenum [8, 10, 48–50]

Isotope	Mass, u	Abundance, %	Half-life period	Decay mode, excitation (radiation) energy, MeV
^{98}Mo[a]	97.905408	24.19	–	–
^{96}Mo[b]	95.904680	16.68	–	–
^{95}Mo[c]	94.905842	15.90	–	–
^{92}Mo[d]	91.906811	14.77	–	–
^{100}Mo[e]	99.907477	9.67	8.5×10^{18} y	$\beta^-\beta^-$
^{97}Mo[c]	96.906022	9.56	–	–
^{94}Mo[b]	93.905088	9.23	–	–
^{93}Mo	92.906813	–	4.0 y	*K*-capture
^{99}Mo[f]	98.907712	–	2.75 d	β^-, 1.23 (80 %); 0.45 (20 %); γ from 0.002 to 0.779
^{93m}Mo	–	–	6.85 h	Isomer, γ (99.88 %), 0.262, 0.69, 1.51; β^+ (0.12 %)
^{90}Mo	89.913937	–	5.56 h	β^+, 1.15; γ, 0.120, 0.250, 1.1
^{91}Mo	90.911750	–	15.49 min	β^+, 3.7
^{101}Mo	100.910347	–	14.61 min	β^-, 1.2 (70 %), 2.2 (30 %); γ, 0.192, 0.960
^{102}Mo	101.910297	–	11.3 min	β^-
^{88}Mo	87.921953	–	8.0 min	β^+
^{89}Mo	88.919480	–	2.11 min	β^+
^{103}Mo	102.91321	–	1.125 min	β^-
^{91m}Mo	–	–	1.08 min	Isomer (50.1 %), γ, 0.105, 0.054, 1.210, 1.54; β^+ (49.9 %), 2.6
^{104}Mo	103.91376	–	1 min	β^-
^{105}Mo	104.91697	–	35.6 s	β^-
^{86}Mo	85.93070	–	19.6 s	β^+
^{87}Mo	86.92733	–	14.05 s	β^+ (85 %), β^+, p (15 %)
^{106}Mo	105.918137	–	8.73 s	β^-
^{107}Mo	106.92169	–	3.5 s	β^-
^{85}Mo	84.93655 (?)	–	3.2 s	β^+
^{108}Mo	107.92345 (?)	–	1.09 s	β^-
^{109}Mo	108.92781 (?)	–	0.53 s	β^-
^{110}Mo	109.92973 (?)	–	0.27 s	β^- (>99.9 %), β^-, n (<0.1 %)
^{111}Mo	110.93441 (?)	–	0.2 s (?)	β^-
^{89m}Mo	–	–	0.19 s	Isomer, γ, 0.387
^{112}Mo	111.93684 (?)	–	0.15 s (?)	β^-
^{113}Mo	112.94188 (?)	–	0.1 s (?)	β^-
^{114}Mo	113.94492 (?)	–	80 ms (?)	
^{115}Mo	114.95029 (?)	–	60 ms (?)	
^{83}Mo	82.94874 (?)	–	23 ms	$\beta^+\beta^+$, p
^{84}Mo	83.94009 (?)	–	3.8 ms	β^+
^{99m1}Mo	–	–	15.5 μs	Isomer, γ, 0.098
^{90m}Mo	–	–	1.12 μs	Isomer, γ, 2.874
^{99m2}Mo	–	–	0.76 μs	Isomer, γ, 0.684

(continued)

Table 7.3 (continued)

Isotope	Mass, u	Abundance, %	Half-life period	Decay mode, excitation (radiation) energy, MeV
^{107m}Mo	–	–	0.47 μs	Isomer, γ, 0.066
^{92m}Mo	–	–	0.19 μs	Isomer, γ, 2.760

[a] Believed to undergo $\beta^-\beta^-$ decay with a half-life period $>1.8 \times 10^{14}$ y (?); fission product
[b] Believed to be capable of spontaneous fission (?)
[c] Believed to be capable of spontaneous fission (?); fission product
[d] Believed to undergo $\beta^+\beta^+$ decay with a half-life period $>1.9 \times 10^{20}$ y (?)
[e] Primordial radionuclide; fission product
[f] Fission product

Nuclear physical properties of molybdenum (isotopic mass range, total number of isotopes, thermal neutron macroscopic cross sections, moderating ability and capture resonance integral), compared with other ultra-high temperature elements (carbon and refractory metals), are given in Addendum.

7.6 Chemical Properties

The comprehensive information on the chemical properties and interaction of molybdenum with all the elements of the periodic table are given in Table 7.4. The molybdenum containing systems and corresponding binary compounds are described and considered there in accordance to the groups of elements from 1 to 17.

Table 7.4 Chemical interaction of molybdenum with elements of the periodic table (binary systems in accordance to the groups of elements)[a]

System	Type of phase diagram (constituent phases, temperatures and compositions of transformations)	Character of interaction	References
Group 1			
Mo–H	H, MoH_x (?), Mo	No chemical interaction at high and ultra-high temp. (up to the melt. point). In the range of pressures <10 MPa the solubility of H is obeyed Sieverts's law, i.e. it is proportional to $p^{1/2}$, where p is pressure H_2. At 1600 °C the solubility of H in Mo is ≤0.01 at.%. The data on solid solubility of H in Mo available in literature are controversial, especially in the range of temp. around 800 °C. For diffusion rate in the system at various temp. see Addendum.	[5, 11, 14–15, 18, 47, 55, 67–69, 273]

(continued)

Table 7.4 (continued)

System	Type of phase diagram (constituent phases, temperatures and compositions of transformations)	Character of interaction	References
Mo–Li	α-Li, β-Li, γ-Li, no binary compounds, Mo	The solubility of Mo in liquid Li varies from 3.7×10^{-5} at.% to 1.1×10^{-4} at.% with temp. increase from 675 to 925 °C; however, the data on Mo solubility in Li available in literature differ considerably. The solubility of Li in Mo is very low too. At 600–500 °C Mo is highly resistant to liquid Li. At 1490 °C, in the static conditions during 1000 h exposure testing the concentration of Mo in Li increases up to 3.6×10^{-3} at.%. During 40 h exposure testing the mass loss of Mo in liquid Li is 8.4 g m^{-2} at 600 °C, 20.8 g m^{-2} at 800 °C and 180.2 g m^{-2} at 1000 °C. At 930–1020 °C the rate of dissolution of Mo in liquid Li is less than those of W, Ta or Nb. For diffusion rate in the system at various temp. see Addendum.	[5, 16, 18, 47, 70]
Mo–Na	α-Na, β-Na, no binary compounds, Mo	At 700–1000 °C the solubility of Mo in liquid Na is $<6 \times 10^{-4}$ at.%. At 600–1500 °C Mo is highly resistant to corrosion in liquid and vaporized Na. At 1000 °C, in the static conditions during 400 h exposure testing the mass loss of Mo in liquid Li is 0.52 mg m^{-2}.	[5, 16, 18, 47]
Mo–K	K, no binary compounds, Mo	At 1205 °C the solubility of Mo in liquid K is $<8 \times 10^{-6}$ at.%; however, the data on Mo solubility in K available in literature differ considerably. The solubility of K in solid Mo is negligible and controlled by its crystal lattice defects. At temp. <900–1000 °C Mo is resistant to corrosion in K. In the dynamic conditions (in K flow) the mass loss of Mo is ~ 6 g m^{-2} at 540–620 °C (11 h exposure) and ~ 30 g m^{-2} at 650–1930 °C (4.5 h exposure). For diffusion rate in the system at various temp. see Addendum.	[5, 16, 18, 47]
Mo–Rb	Rb, no binary compounds, Mo	No interaction in the dynamic conditions at 730–960 °C (500 h exposure testing)	[5, 16, 18, 47]

(continued)

Table 7.4 (continued)

System	Type of phase diagram (constituent phases, temperatures and compositions of transformations)	Character of interaction	References
Mo–Cs	Cs, no binary compounds, Mo	The solubility of Mo in Cs is strongly dependent on concentration of impurities (O, N, C) in Cs. The solubility of Cs in solid Mo is negligible and controlled by its crystal lattice defects. No reliable data on mutual solubility. At temp. <300 °C Mo is resistant to Cs during long-term (up to 4000 h) applications. At 250–1000 °C, in the static conditions during 100–200 h exposure testing the mass gain of Mo in Cs is <0.7 g m^{-2}. At 1000 °C the destruction of Mo pipes in a Cs supply system was observed.	[5, 15, 18, 47, 274]
Mo–Fr	Fr, no binary compounds, Mo	No interaction.	[18, 47]
Group 2			
Mo–Be	α-Be, β-Be, $MoBe_{22}$ (or $MoBe_{20}$, $MoBe_{28}$, <1300 °C, incongruent melt. point, invariable compos.), $MoBe_{12}$ (<~1700 °C, congruent melt. point, invariable compos.), $MoBe_2$ (<~1840–2045 °C, congruent melt. point, invariable compos., Laves phase), Mo_3Be (<890–910 °C, invariable compos., ?), Mo Eutectic $MoBe_2$–$MoBe_{12}$ (~1680–1700 °C, ~9–10 at.% Mo) Eutectic $MoBe_2$–Mo (~1775–1875 °C, ~57–57.5 at.% Mo) Eutectic (degenerated) $MoBe_{22}$–Be (~1289 °C)	The solubility of Be in Mo is ≤0.5 at.% at 1970 °C, 0.53 at.% at ~1830 °C, 0.42 at.% at 1740 °C and 0.2 at.% at 1480 °C. The solubility of Mo in solid Be is negligible and controlled by its crystal lattice defects. Mo beryllides are formed by the direct interaction between elements in solid or liquid state in inert gas atmosphere; in mixed powdered compositions the reaction initiates at 800–945 °C.	[5, 14, 17–18, 44, 47, 71]
Mo–Mg	Mg, no binary compounds, Mo	No interaction, at least at temp. <1000 °C. The mutual solubilities of the elements are negligible. At 600 °C Mo is compatible with Mg.	[5, 16, 18]
Mo–Ca	α-Ca, β-Ca, no binary compounds, Mo	No interaction. The estimated solubility of Mo in liquid Ca is ~10^{-4} at.% at 840 °C and 3.5 × 10^{-2} at.% at 1480 °C.	[17–18, 47, 275]

(continued)

Table 7.4 (continued)

System	Type of phase diagram (constituent phases, temperatures and compositions of transformations)	Character of interaction	References
Mo–Sr	α-Sr, β-Sr, no binary compounds, Mo	No interaction.	[18, 47]
Mo–Ba	Ba, no binary compounds, Mo	No interaction. The estimated solubility of Mo in liquid Ba is $\sim 10^{-8}$ at.% at 730 °C and 6×10^{-3} at.% at 1680 °C.	[17–18, 47]
Mo–Ra	Ra, no binary compounds, Mo	No interaction.	[18, 47]
Group 3			
Mo–Sc	α-Sc, β-Sc, no binary compounds, Mo Eutectic β-Sc–Mo (~1340–1420 °C, ~7–13 at.% Mo)	The presence of Mo decreases the temp. of α-Sc–β-Sc polymorphic transformation. The max. solubility of Sc in Mo is 7×10^{-3} at.% at ~2125 °C, it decreases to 2×10^{-3} at.% at ~1370 °C; however the data on solubilities in the system available in literature differ considerably.	[16, 18, 47]
Mo–Y	α-Y, β-Y, no binary compounds, Mo Eutectic α-Y–Mo (~1380–1500 °C (?), ~9–11 at.% Mo) Miscibility gap in the liquid state (around 90 at.% Mo, ?)	The solubility of Mo is ~0.02 at.% in β-Y (1500 °C) and 0.1 at.% in α-Y (1475 °C). The solubility of Y in solid Mo is 0.2 at.% at 2130 °C and ~0.030–0.065 at.% at 1450 °C. For diffusion rate in the system at various temp. see Addendum.	[16, 18, 47, 72, 276]
Lanthanides			
Mo–La	α-La, β-La, γ-La, no binary compounds, Mo Eutectic (degenerated) γ-La–Mo (~918 °C, ~0.1 at.% Mo, ?) Peritectic γ-La (920 °C, ?) Miscibility gap in the liquid state (critical point—3540–3550 °C, 64–65 at.% Mo; from ~3–21 to ~75–96 at.% Mo at ~2545 °C) Data on the system available in literature are controversial.	The solid solubility of Mo in La is <0.01 at.% and that of La in Mo is ~0.2 at.% at 2545 °C and ~0.01 at.% at 625 °C.	[16, 18, 47, 72]

(continued)

Table 7.4 (continued)

System	Type of phase diagram (constituent phases, temperatures and compositions of transformations)	Character of interaction	References
Mo–Ce	α-Ce, β-Ce, γ-Ce, δ-Ce, no binary compounds, Mo Eutectic (degenerated) δ-Ce–Mo or peritectic δ-Ce (∼795 °C, ?) Miscibility gap in the liquid state (critical point—∼3200–3210 °C, ∼72–73 at.% Mo; from ∼24–40 to ∼92.5–94.5 at.% Mo at ∼2515–2535 °C)	The solubility of Mo in liquid Ce is <0.3 at.% at 1300 °C, 0.0175 at.% at 1200 °C and 0.001 at.% at 800 °C. The solid solubility of Ce in Mo is 0.10–0.15 at.%. At temp. >800 °C the dissolution of Mo in liquid Ce is noticeable.	[5, 17–18, 47, 277]
Mo–Pr	α-Pr, β-Pr, no binary compounds, Mo Eutectic (degenerated) β-Pr–Mo (∼931 °C, ∼0.09–0.11 at.% Mo, ?) Miscibility gap in the liquid state (critical point—∼3345–3360 °C, ∼66–67 at.% Mo; from ∼20–36 to ∼94–96 at.% Mo at ∼2535–2555 °C)	The solubility of Pr in Mo is ∼0.02–0.30 at.%.	[16, 18, 47]
Mo–Nd	α-Nd, β-Nd, no binary compounds, Mo Eutectic (degenerated) β-Nd–Mo (∼1010 °C, ∼0.04–0.4 at.% Mo, ?) Miscibility gap in the liquid state (critical point—∼3350 °C, ∼70 at.% Mo; from ∼17–33 to ∼95–97 at.% Mo at ∼2535–2570 °C)	The solubility of Nd in Mo is ∼0.3 at.% at 2570 °C and ∼0.05–0.07 at.% at lower temp.	[16, 18, 47]
Mo–Pm	α-Pm, β-Pm, no binary compounds, Mo Eutectic (degenerated) β-Pm–Mo (∼1042 °C, ?) Miscibility gap in the liquid state (critical point—∼3360 °C, ∼70 at.% Mo; from ∼15–30 to ∼95–97 at.% Mo at ∼2560–2570 °C)	The solubility of Pm in Mo is ∼0.3 at.% at 2560–2570 °C.	[16, 18, 47]

(continued)

Table 7.4 (continued)

System	Type of phase diagram (constituent phases, temperatures and compositions of transformations)	Character of interaction	References
Mo–Sm	α-Sm, β-Sm, γ-Sm, no binary compounds, Mo Eutectic (degenerated) γ-Sm–Mo (~1068 °C, ?)	–	[18, 47]
Mo–Eu	Eu, no binary compounds, Mo Eutectic (degenerated) Eu–Mo (~822 °C, ?)	–	[18, 47, 275]
Mo–Gd	α-Gd, β-Gd, no binary compounds, Mo Eutectic β-Gd–Mo (~1295–1310 °C, ~1.0–2.5 at.% Mo, ?) Miscibility gap in the liquid state (critical point—~2870–2950 °C, ~60–70 at.% Mo; from ~32–36 to ~85–90 at.% Mo at ~2455–2485 °C)	The presence of Mo decreases the temp. of α-Gd–β-Gd polymorphic transformation to ~1215–1230 °C. The solubility of Gd in solid Mo is 0.05 at.% at 2570 °C, 0.93 at.% at 2510 °C, 0.67 at.% at 2400 °C, 0.24 at.% at 2200 °C, 0.18 at.% at 2000 °C, 0.12 at.% at 1800 °C and 0.09 at.% at 1600 °C.	[15, 18, 47, 73, 278]
Mo–Tb	α′-Tb, α-Tb, β-Tb, no binary compounds, Mo Eutectic β-Tb–Mo (~1330 °C, ~2 at.% Mo, ?) Miscibility gap in the liquid state (critical point—~3100 °C, ~65–67 at.% Mo; ~33–93 at.% Mo at ~2510–2530 °C)	–	[18, 47]
Mo–Dy	α′-Dy, α-Dy, β-Dy, no binary compounds, Mo Eutectic β-Dy–Mo (~1375 °C, ~1.5–2.5 at.% Mo, ?)	At least at temp. 825–1115 °C the components are soluble in each other (?).	[15, 18, 47, 275]
Mo–Ho	α-Ho, β-Ho, no binary compounds, Mo Eutectic β-Ho–Mo (~1430 °C, 3 at.% Mo, ?) Miscibility gap in the liquid state (critical point—~2800 °C, ~65–66 at.% Mo; from ~35–36 to 92 at.% Mo at ~2515–2530 °C)	The max. solid solubility of Mo in Ho is 0.6 at.% at ~1430 °C and that of Ho in Mo is ~0.6 at.% at 2515 °C.	[18, 47]

(continued)

Table 7.4 (continued)

System	Type of phase diagram (constituent phases, temperatures and compositions of transformations)	Character of interaction	References
Mo–Er	α-Er, β-Er, no binary compounds, Mo Eutectic β-Er–Mo (~1480 °C, ~3.5–4.0 at.% Mo, ?) Miscibility gap in the liquid state (critical point—~2750–2760 °C, ~75–78 at.% Mo; from ~40–42 to 90–98 at.% Mo at ~2435–2495 °C)	At least at temp. ~725–1125 °C the mutual solubilities of the components are <0.1 at.%.	[15, 18, 47, 275]
Mo–Tm	α-Tm, β-Tm, no binary compounds, Mo Eutectic β-Tm–Mo (~1475–1480 °C, ~5 at.% Mo, ?)	–	[18, 47]
Mo–Yb	α-Yb, β-Yb, γ-Yb, Yb_3Mo (?), Yb_2Mo (Laves phase, ?), YbMo (?), $YbMo_2$ (Laves phase, ?), $YbMo_3$ (?), $YbMo_5$ (?), Mo Eutectic (degenerated) γ-Yb–Mo (~824 °C, $\sim(0.4 \div 2.4) \times 10^{-3}$ at.% Mo, ?) Miscibility gap in the liquid state (critical point—>3500 °C; from ~1.5–2.0 to ~99.0–99.5 at.% Mo at ~2610–2620 °C) Data on the system available in literature are contradicting.	The mutual solubilities between the components are absent (?).	[16, 18, 47, 74–77, 279]
Mo–Lu	α-Lu, β-Lu, no binary compounds, Mo Eutectic β-Lu–Mo (1545 °C, 9 at.% Mo, ?)	The max. solid solubility of Lu in Mo is ~1.5 at.% (1900–2100 °C) and that of Mo in Lu is ~3.5 at.% (1545 °C).	[16, 18, 47]

(continued)

Table 7.4 (continued)

System	Type of phase diagram (constituent phases, temperatures and compositions of transformations)	Character of interaction	References
Actinides			
Mo–Ac	Ac, no binary compounds, Mo Eutectic Ac–Mo (~1000–1050 °C, ~0.3–1.5 at.% Mo, ?) Miscibility gap in the liquid state (critical point—~3400 °C, ~45–46 at.% Mo; from ~9–33 to ~77–99 at.% Mo at ~2040–2520 °C, ?)	The solid solubility of Ac in Mo is ~0.01–8 at.% (?) at ~1500–1515 °C and ~0.15–10 (?) at.% at 2040 °C, that of Mo in Ac is 9×10^{-5} at.% at 925–1050 °C; the data on solubilities in the system available in literature differ considerably.	[17, 18, 47]
Mo–Th	α-Th, β-Th, no binary compounds, Mo Eutectic β-Th–Mo (1370–1390 °C, ~14–16 at.% Mo) Some data on the system available in literature are controversial.	The presence of Mo decreases temp. of Th polymorphic transformation to ~1325–1355 °C. The max. solid solubility of Th in Mo is ~1.5 at.% at 1370–1390 °C. The solubility of Mo is 0.8–2.0 at.% in β-Th at 1370–1390 °C and 0.12 at.% in α-Th at 1335 °C; at lower temp. it declines considerably—up to 0.01 at.% at ~875 °C. For diffusion rate in the system at various temp. see Addendum.	[5, 16, 18, 46–47, 78, 280]
Mo–Pa	α-Pa, β-Pa, $MoPa_2$ (<375 °C, metastable, ?), Mo Eutectic β-Pa–Mo (~1415–1515 °C, ~20–24 at.% Mo)	The max. solid solubility of Pa in Mo is ~3–4 at.% at 1700–2100 °C; it declines at lower temp.—up to <0.01 at.% at 415–515 °C. The max. solid solubility of Mo in β-Pa is ~20 at.% at 1415–1515 °C.	[16, 47]
Mo–U	α-U, α′-U (metastable, ~0–6 at.% Mo), α″-U (martensite, ~6–10 at.% Mo), β-U, γ^0-U (martensite, partly ordered, ~12–14 at.% Mo), γ^v-U (martensite, ~14 at.% Mo), γ-U, $MoU_{2\pm x}$ (<595–640 °C, homog. range—29.5–35 at.% Mo), Mo Peritectic γ-U (~1280–1285 °C, 40–43 at.% Mo)	The solubility of Mo in α-U is <0.1 at.% at 650 °C and 0.2–0.7 at.% at 570 °C; max. solid solubility of Mo in β-U is ~1.2–3.0 at.% (at 635–650 °C) and in γ-U is 40–43 at.% at peritectic temp. The solid solubility of U in Mo is ~0.5 at.% at 510–580 °C, ~2–3 at.% at 1285 °C and ~3.5 at.% at 1500–1900 °C. The kinetics of Mo dissolution in liquid U is fast. At 1250 °C liquid U impregnates Mo porous preforms perfectly. For diffusion rate in the system at various temp. see Addendum.	[5, 16, 18, 46–47, 79–81, 322]

(continued)

Table 7.4 (continued)

System	Type of phase diagram (constituent phases, temperatures and compositions of transformations)	Character of interaction	References
Mo–Np	α-Np, β-Np, γ-Np, $MoNp_2$ (<~225 °C, ?), Mo Eutectic γ-Np–Mo (~415–575 °C, ~7–11 at.% Mo)	The presence of Mo decreases temp. of Np polymorphic transformations. The solubility of Np in Mo is ≤0.01 at.% at ~505 °C and that of Mo in Np is controlled considerably by impurities.	[16, 47]
Mo–Pu	α-Pu, β-Pu, γ-Pu, δ-Pu, δ′-Pu, ε-Pu, no binary compounds, Mo Eutectic (degenerated) ε-Pu–Mo (~590–630 °C, ~1.0–2.5 at.% Mo, ?)	The solubility of Mo in ε-Pu is ~0.2 at.% at eutectic temp. and that of Pu in Mo is ~2 at.% at 2100 °C.	[16, 18, 47, 281–282]
Mo–Am	α-Am, β-Am, γ-Am, no binary compounds, Mo Eutectic (degenerated) γ-Am–Mo (~1175 °C, <4 at.% Mo, ?)	The max. solid solubility of Mo in γ-Am is ~0.4 at.% (~1175 °C) and that of Am in Mo is ~1.25 at.% (~1900 °C).	[18, 47, 275]
Mo–Cm	α-Cm, β-Cm, no binary compounds, Mo Eutectic (degenerated) β-Cm–Mo (~1345 °C, <3 at.% Mo, ?)	The max. solid solubility of Mo in β-Cm is ~0.4 at.% (~1345 °C) and that of Cm in Mo is ~0.3 at.% at 1345 °C and ~2 at.% at ~2000 °C.	[18, 47, 275]
Mo–Bk	α-Bk, β-Bk, no binary compounds, Mo Eutectic (degenerated) β-Bk–Mo (~1050 °C, <~3–5 at.% Mo, ?)	No interaction, the mutual solid solubilities of the components are negligible (?).	[18, 47, 275]
Mo–Cf	α-Cf, β-Cf, no binary compounds, Mo Eutectic (degenerated) β-Cf–Mo (~1075 °C, ?)	No interaction. The estimated solid solubility of Mo in Cf is $\sim 10^{-2}$ at.% at 830 °C.	[15, 18, 47]
Mo–Es	α-Es, β-Es, no binary compounds, Mo Eutectic (degenerated) β-Es–Mo (~925 °C, ?)	No interaction, the mutual solid solubilities of the components are negligible (?).	[18, 47]
Mo–Fm	Fm, no binary compounds, Mo	No interaction, the mutual solid solubilities of the components are negligible (?).	[18, 47]
Mo–Md	Md, no binary compounds, Mo	No interaction, the mutual solid solubilities of the components are negligible (?).	[18, 47]
Mo–No	No, no binary compounds, Mo	No interaction, the mutual solid solubilities of the components are negligible (?).	[18, 47]

(continued)

Table 7.4 (continued)

System	Type of phase diagram (constituent phases, temperatures and compositions of transformations)	Character of interaction	References
Mo–Lr	Lr, no binary compounds, Mo Eutectic Lr–Mo (~1385 °C, ~12 at.% Mo, ?)	The max. solid solubility of Mo in Lr is ~5 at.% (~1385 °C) and that of Lr in Mo is ~3 at.% at 1385 °C and ~5 at.% at 2000–2200 °C.	[16, 18, 47]
Group 4			
Mo–Ti	α-Ti, α′-Ti (metastable martensite, 0–2 at.% Mo), α″-Ti (metastable, from 2.0–4.7 to 4.0–6.9 at.% Mo), ω-(Ti,Mo) (metastable, intermediate between β-Ti and α-Ti structure, from 4.0–6.4 to 6–15 at.% Mo), β-Ti, no binary compounds, Mo (the composition ranges of metastable phases are affected considerably by the minute amounts of O contamination) Continuous solid solution β-Ti–Mo (up to melt. points, miscibility gap: critical point—~795–850 °C, ~20–35 at.% Mo; from ~12–14 to ~45–60 at.% Mo at ~650–695 °C)	The melt. point of Ti increases to 1700–2000 °C for the alloys containing 10–50 at.% Mo. In the presence of Mo temp. of α-Ti–β-Ti polymorphic transformation decreases to 650–695 °C (12–14 at.% Mo). The max. solubility of Mo in α-Ti is ≤0.4 at.% (650–695 °C). For diffusion rate in the system at various temp. see Addendum.	[5, 16, 18, 47, 82–85]
Mo–Zr	α-Zr, β-Zr, σ-$ZrMo_{2\pm x}$ (<~1880–2000 °C, incongruent melt. point, homog. range—~60–70 at.% Mo, ?), Mo Peritectic β-Zr (~1545–1605 °C, ~31–35.5 at.% Mo, ?) Eutectic $ZrMo_{2\pm x}$–β-Zr (~1500–1550 °C, ~37–48.5 at.% Mo, ?) Data on the system available in literature are controversial	The melt. point of Zr decreases to ~1525–1750 °C for the alloys containing ~10–40 at.% Mo. Min. melt. temp. (~1525–1585 °C) corresp. to 27–29 at.% Mo compos. (?). In the presence of Mo temp. of α-Zr–β-Zr polymorphic transformation decreases to ~630–755 °C (~6.5–8.5 at.% Mo). Mo sta-bizes β-Zr modification. The max. solid solubility of Mo in β-Zr is ~31–41 at.% (1500–1600 °C); it declines to ~6.5–8.5 at.% at ~630–755 °C. The solubility of Mo in α-Zr is very low; at temp. <400 °C it is <0.01 at.%. The max. solid solubility of Zr in Mo is ~10–20 at.% (1880–2000 °C); it declines to ~3–7 at.% (?) at ~600–1100 °C. For diffusion rate in the system at various temp. see Addendum.	[5, 16, 18–19, 47, 86–89]

(continued)

Table 7.4 (continued)

System	Type of phase diagram (constituent phases, temperatures and compositions of transformations)	Character of interaction	References
Mo–Hf	α-Hf, β-Hf, α-$HfMo_{2\pm x}$ (<~1770–1875 °C, Laves phase, homog. range—65.5–68.3 at.% Mo), β-$HfMo_{2\pm x}$ (from ~1770–1875 °C to ~2130–2210 °C, incongruent melt. point, Laves phase, homog. range—~65–67at.% Mo), β′-$HfMo_{2\pm x}$ (<~900 °C, ?), Mo Peritectic β-Hf (~1890–1910 °C, ~42–46 at.% Mo, ?) Eutectic β-$HfMo_{2\pm x}$–β-Hf (~1890–1910 °C, ~42–46 at.% Mo, ?) Data on the system available in literature are controversial.	The melt. point of Hf decreases to ~1855–2000 °C for the alloys containing ~10–40 at.% Mo. Min. melt. temp. (~1855–1875 °C) corresp. to ~33–35 at.% Mo compos. (?). In the presence of Mo temp. of α-Hf–β-Hf polymorphic transformation decreases to ~1165–1235 °C (26.5 at.% Mo). Mo stabizes β-Hf modification. The max. solid solubility of Mo in β-Hf is ~42–46 at.% (1890–1910 °C); it declines to 26.5 at.% at 1165–1235 °C. The max. solubility of Mo in α-Hf is 1 at.% at 1165–1235 °C; it declines to ≤0.01 at.% at 480 °C. The max. solid solubility of Hf in Mo is ~26–28 at.% (2130–2210 °C); it declines to ~9.5–17 at.% at ~1000–1800 °C.	[5, 15, 18, 47, 86, 89–90]
Group 5			
Mo–V	V, no binary compounds, Mo Continuous solid solution V–Mo	For diffusion rate in the system at various temp. see Addendum.	[5, 16, 18, 45, 91, 328, 334]
Mo–Nb	Nb, no binary compounds, Mo Continuous solid solution Nb–Mo	For diffusion rate in the system at various temp. see Addendum.	[5, 16, 18, 45, 47, 61, 91–94, 336]
Mo–Ta	See Ta–Mo in Table 6.3.		
Group 6			
Mo–Cr	Cr, no binary compounds, Mo (some metastable phases are formed due to the minute amounts of O contamination) Continuous solid solution Cr–Mo (up to melt. points, miscibility gap: critical point—880 °C, ~39 at.% Mo; from ~5–6 to ~90–91 at.% Mo at 500 °C)	Min. melt. temp. of continuous solid solution (~1790–1860 °C) corresp. to ~12.5 at.% Mo compos. For diffusion rate in the system at various temp. see Addendum.	[5, 15, 18, 95–97]
Mo–W	See W–Mo in Table 3.5.		

(continued)

Table 7.4 (continued)

System	Type of phase diagram (constituent phases, temperatures and compositions of transformations)	Character of interaction	References
Group 7			
Mo–Mn	α-Mn, β-Mn, γ-Mn, δ-Mn, σ-Mn_5Mo_{3-x} (from 1075–1105 °C to 1300–1500 °C, incongruent melt. point, homog. range—~35–37 at.%), μ-$Mn_5Mo_{4\pm x}$ (<1400–1600 °C, incongruent melt. point, homog. range—~40–50 at.%, ?), Mo Extended solid solution based on Mo (up to ~36 at.% Mn at 1500 °C) Extended solid solution based on α-Mn (up to ~20 at.% Mo at ~1050–1150 °C) Extended solid solution based on δ-Mn (up to ~20 at.% Mn at ~1225–1425 °C) Peritectic δ-Mn (~1225–1425 °C, ~20 at.% Mo)	The solubilities of Mo in Mn modifications are: in α-Mn—~14–20 at.% at 1050–1150 °C, in β-Mn–2 at.% at 800 °C and up to 2.6 at.% at 1100–1120 °C, in γ-Mn—≤0.6 at.% at 1100–1120 °C and in δ-Mn—up to ~20 at.% at ~1225–1425 °C. The solubility of Mn in Mo is ~30–32 at.% at 1800 °C, ~36 at.% at 1500 °C and ~16 at.% at 800 °C.	[5, 16, 18, 47, 98]
Mo–Tc	Tc, σ-$Tc_{3-x}Mo$ (<~1975–2175 °C, incongruent melt. point, homog. range—28–32 at.% Mo at 1800 °C, 26–35 at.% Mo at 1200 °C and 27–30 at.% Mo at 1000 °C), β-$TcMo_{1-x}$ (<~1600–1800 °C, homog. range—~45–46 at.% Mo), Mo Extended solid solution based on Tc (up to ~27–30 at.% Mo at ~2080–2090 °C) Extended solid solution based on Mo (up to ~50–52 at.% Tc at ~1925–2125 °C) Eutectic σ-$Tc_{3-x}Mo$–Mo (~1925–2125 °C, ~39–49 at.% Mo)	The solid solubility of Mo in Tc is ~27–30 at.% at ~2080–2090 °C, and that of Tc in Mo is ~50–52 at.% at ~1925–2125 °C, ~45 at.% at ~1600–1800 °C and ~10–15 at.% at ~1000 °C.	[16, 99–100]

(continued)

Table 7.4 (continued)

System	Type of phase diagram (constituent phases, temperatures and compositions of transformations)	Character of interaction	References
Mo–Re	See Re–Mo in Table 4.5.		
Group 8			
Mo–Fe	α-Fe (δ-Fe), γ-Fe, λ-Fe_2Mo (<900–1000 °C, Laves phase, invariable compos.), ρ-Fe_3Mo_{2-x} (or $Fe_{62}Mo_{38}$, R-phase, from 1190–1210 °C to ~1490 °C, incongruent melt. point, homog. range—34–40 at.% Mo), μ-Fe_7Mo_{6-x} (<1370 °C, homog. range—38–45 at.% Mo), σ-$FeMo_{1\pm x}$ (from ~1540–1610 °C to 1215–1255 °C, incongruent melt. point, homog. range—43–58 at.% Mo), Mo Peritectic α-Fe (1449–1450 °C, ~21–25 at.% Mo)	Mo stabilizes α-Fe modification, increasing the temp. of α-Fe–γ-Fe transformation and decreasing the temp. of γ-Fe–δ-Fe transformation (γ-Fe region is locked in α-Fe region). The solubilities of Mo are following: in γ-Fe—1.6–1.7 at.% at ~1140 °C and in α/δ-Fe—21–25 at.% at 1450 °C, 12–14 at.% at 1200 °C and 5–7 at.% at 950 °C. The max. solid solubility of Fe in Mo is ~22–31 at.% at 1540–1610 °C; it declines at lower temp.—up to 6.0–6.2 at.% at 1215–1255 °C. The resistance of Mo to corrosion in Fe and steel melts is low. For diffusion rate in the system at various temp. see Addendum.	[5, 15, 18, 47, 52, 101–104]
Mo–Ru	Ru, σ-$Ru_3Mo_{5\pm x}$ (from ~1145 to 1915–1920 °C, homog. range—~62–64 at.% Mo), Mo Extended solid solution based on Ru (up to 51 at.% Mo at 1945–1955 °C) Extended solid solution based on Mo (up to 30.5–32.0 at.% Ru at 1945–1955 °C) Eutectic Ru–Mo (~1945–1955 °C, ~58.0–58.4 at.% Mo)	The solid solubility of Mo in Ru declines from 51 at.% at eutectic temp. to ~45 at.% at 1500 °C, and that of Ru in Mo declines from 30.5–32.0 at.% at eutectic temp. to ~13–15 at.% at 1500 °C.	[5, 16, 18, 105–106, 326]
Mo–Os	See Os–Mo in Table 5.3.		

(continued)

Table 7.4 (continued)

System	Type of phase diagram (constituent phases, temperatures and compositions of transformations)	Character of interaction	References
Group 9			
Mo–Co	ε-Co, α-Co, θ-Co_9Mo_{2+x} (or Co_4Mo, ~1020–1200 °C, invariable compos.), κ-$Co_{3\pm x}Mo$ (<1025 °C, homog. range—from 22.5–23.5 to 23–25 at.% Mo), μ-$Co_7Mo_{6\pm x}$ (or ε-$CoMo_{1-x}$, <~1510 °C, incongruent melt. point, homog. range—41.5–49.5 at.% Mo at 400–1335 °C), σ-Co_2Mo_{3+x} (or σ-$Co_3Mo_{5\pm x}$, from ~900–1250 to 1620 °C, incongruent melt. point, homog. range—~60–64 at.% Mo), Mo Eutectic μ-$Co_7Mo_{6\pm x}$–α-Co (1335 °C, ~28–29 at.% Mo)	The presence of Mo decreases the melt. temp. of Co (up to 1335 °C) and increases the temp. of α-Co–ε-Co transformation (up to ~550–850 °C). The mutual solubilities of the components are strongly affected by temp. The solubility of Mo in α-Co is 19.5 at.% at 1300 °C, ~17 at.% at 1200 °C, 13.5 at.% at 1100 °C, 11.4 at.% at 1000 °C and 6.8 at.% at 900 °C. The max. solubility of Mo in ε-Co is ≤9 at.% (at 550–850 °C). The max. solid solubility of Co in Mo is ~7.0–11.5 at.% (at 1620 °C); it declines considerably at lower temp.—up to 1.5 at.% at 1300 °C. For diffusion rate in the system at various temp. see Addendum.	[5, 15, 18, 47, 107–109, 329]
Mo–Rh	Rh, $Rh_{3\pm x}Mo$ (<1180–1220 °C, ordered phase, homog. range—~24–26 at.% Mo), ε-$Rh_{2\pm x}Mo$ (from ~1000–1200 to 2065–2085 °C, congruent melt. point corresp. to $RhMo_{0.54}$, homog. range—18.5–57 at.% Mo at 1925–1955 °C, 18–55 at.% Mo at 1300 °C and 44–49 at.% Mo at ~1100 °C), ε′-$RhMo_{1\pm x}$ (<975–1125 °C, homog. range—~49–51 at.% Mo), Mo Extended solid solution based on Rh (up to ~15 at.% Mo at 1990–2010 °C) Extended solid solution based on Mo (up to ~20 at.% Rh at 1925–1955 °C) Peritectic Rh (~1990–2010 °C, ~15 at.% Mo) Eutectic ε-$Rh_{2\pm x}Mo$–Mo (~1925–1955 °C, ~59–61 at.% Mo)	The presence of Mo results in increase in the melt. temp. of Rh. The max. melt. point (~1990–2010 °C) and max. solid solubility of Mo in Rh (~15 at.%) are corresponding to the peritectic alloy. The mutual solubilities of the components, especially the solubility of Rh, decline considerably with temp. decreasing.	[5, 16, 18, 47, 110–111, 333]

(continued)

Table 7.4 (continued)

System	Type of phase diagram (constituent phases, temperatures and compositions of transformations)	Character of interaction	References
Mo–Ir	Ir, $Ir_{3-x}Mo$ (<2300 °C, incongruent melt. point, homog. range—~25–36.5 at.% Mo at 2270 °C and ~25–33 at.% Mo at 1200 °C), ε-$IrMo_{1\pm x}$ (from 1400–1620 to 2270 °C, incongruent melt. point, homog. range—~41.5–63 at.% Mo at 2075–2085 °C, ~43–58 at.% Mo at 1600–1620 °C and two separated areas near ~43 and ~57 at.% Mo at 1400–1450 °C), $IrMo_{1\pm x}$ (<1600–1620 °C, ordered phase, homog. range—~48.5–51 at.% Mo), σ-Ir_3Mo_{7+x} (from ~1970–1980 °C to ~2080–2110 °C, incongruent melt. point, invariable compos.), $IrMo_{3+x}$ (<2100–2120 °C, incongruent melt. point, homog. range—~75–78 at.% Mo), Mo Extended solid solution based on Ir (up to 22–23 at.% Mo at 2300 °C) Extended solid solution based on Mo (up to 16.0–16.5 at.% Ir at 2100–2120 °C) Eutectic ε-$IrMo_{1\pm x}$–σ-Ir_3Mo_{7+x} (2075–2085 °C, 69 at.% Mo)	The presence of Mo results in decrease in the melt. temp. of Ir alloys. Practically, the solid solubility of Mo in Ir is not affected by temp. In opposite, the solid solubility of Ir in Mo is strongly dependent on temp.; at lower temp. it declines to ~7–8 at.% at 1200 °C.	[5, 16, 18, 47, 111–113]

(continued)

Table 7.4 (continued)

System	Type of phase diagram (constituent phases, temperatures and compositions of transformations)	Character of interaction	References
Group 10			
Mo–Ni	Ni, β-$Ni_{4+x}Mo$ (<865–875 °C, homog. range—~19–20 at.% Mo), γ-$Ni_{3+x}Mo$ (<905–915 °C, homog. range—~24–25 at.% Mo), $Ni_{17}Mo_5$ (metastable, ?), Ni_3Mo (metastable, ?), Ni_2Mo (metastable, ?), μ-$NiMo_{1\pm x}$ (or δ-$NiMo_{1\pm x}$, <~1360–1365 °C, incongruent melt. point, homog. range—~47.7–52.5 at.% Mo), Mo Extended solid solution based on Ni (up to 28.5 at.% Mo at ~1315–1320 °C) Eutectic μ-$NiMo_{1\pm x}$–Ni (~1315–1320 °C, ~34.5–36 at.% Mo)	At lower temp. the solid solubility of Mo in Ni declines considerably with temp. decreasing. The max. solid solubility of Ni in Mo is 1.8 at.% (1360–1365 °C); it also declines with temp. decreasing. For diffusion rate in the system at various temp. see Addendum.	[16, 18, 47, 114–116, 335]
Mo–Pd	Pd, $Pd_{2+x}Mo$ (<~900–1100 °C, ordered phase, homog. range—33–34 at.% Mo), ε-$PdMo_{1-x}$ (from 1340–1450 to 1745–1765 °C, incongruent melt. point, homog. range —~46.5–48.5 at.% Mo), Mo Peritectic Pd (~1690–1755 °C, ~32.0–47.5 at.% Mo, ?) Extended solid solution based on Pd (up to ~32.0–47.5 at.% Mo (?) at ~1200–1700 °C) Eutectic ε-$PdMo_{1-x}$–Pd (1670–1730 °C, ~44–48 at.% Mo, ?) Data on the system available in literature are controversial.	The presence of Mo results in increase in the melt. temp. of Pd—up to the max. at 1750–1770 °C corresp. to ~38–39 at.% Mo compos. The max. solid solubility of Mo in Pd is ~32.0–47.5 at.% (?) at ~1200–1700 °C, and that of Pd in Mo is ~5–25 at.% (?) at 1400–1765 °C. The mutual solid solubilities of the components decline slightly with temp. decreasing.	[5, 16, 18, 47, 56, 117–119, 327, 330–332]

(continued)

Table 7.4 (continued)

System	Type of phase diagram (constituent phases, temperatures and compositions of transformations)	Character of interaction	References
Mo–Pt	Pt, η-$Pt_{2\pm x}Mo$ (<~1780–1820 °C, ordered phase, homog. range—from ~26–30 to ~40–44 at.% Mo at 1280–1630 °C and ~32–37.5 at.% Mo at 600 °C), δ-$PtMo_{1\pm x}$ (<1280–1320 °C, homog. range—from ~45–49 to ~55–59 at.% Mo at 800–1000 °C), ε'-$PtMo_{3-x}$ (<~1455–1910 °C, homog. range—from ~53–57 to ~68–70 at.% Mo at 1475–1880 °C and ~61.0–62.5 at.% Mo at 1000 °C), ε-$PtMo_{3-x}$ (from 1455–1495 °C to ~2155–2195 °C, congruent melt. point corresp. to ~$PtMo_{1.04 \div 1.22}$, homog. range—from ~44–48 to ~68–70 at.% Mo at 2020–2080 °C), β-$PtMo_{6-x}$ (from 1270–1290 °C to 1760–1800 °C, homog. range—from ~81–82.5 at.% Mo at 1400–1600 °C), Mo Peritectic Pt (~2000–2040 °C, ~38 at.% Mo) Extended solid solution based on Pt (up to ~54–58 at.% Mo at ~1570–1630 °C) Extended solid solution based on Mo (up to ~14–16 at.% Pt at 2060–2100 °C) Eutectic ε-$PtMo_{3-x}$–Mo (~2060–2100 °C, ~72–75 at.% Mo)	The presence of Mo results in increase in the melt. temp. of Pt; the max. melt. point (~2000–2040 °C) corresp. to the peritectic alloy. The solubility of Pt in Mo declines at lower temp.—up to 12 at.% at 1780–2000 °C and 2 at.% at 1000 °C. The solubility of Mo in Pt is slightly affected by temp.; at lower temp. (≤600 °C) it is ≤20 at.%.	[5, 16, 18, 47,118–123]

(continued)

Table 7.4 (continued)

System	Type of phase diagram (constituent phases, temperatures and compositions of transformations)	Character of interaction	References
Group 11			
Mo–Cu	Cu, no binary compounds, Mo Eutectic (degenerated) Cu–Mo (~1083 °C, 0.067 at.% Mo) Miscibility gap in the liquid state (from 11.8–13.0 to 88.5–89.5 at.% Mo at 2515–2585 °C)	At eutectic temp. the solid solubility of Mo in Cu is 0.061 at.% and that of Cu in Mo is ~0.06 at.%. At 2415–2615 °C the solid solubility of Cu in Mo is 1.6–2.0 at.% and solubility of Mo in liquid Cu is 11.8–13.0 at.%. The max. solubility of Mo in liquid Cu is 13 at.% (at ~2485–2685 °C). The data on mutual solubilities of the components available in literature are controversial	[5, 15, 18, 47, 124–125]
Mo–Ag	Ag, no binary compounds, Mo Eutectic (degenerated) Ag–Mo (~959 °C, 0.33 at.% Mo)	At eutectic temp. the solid solubility of Mo in Ag is 0.15 at.% and that of Ag in Mo is 0.006 at.%. At 1600 °C the solubility of Mo in liquid Ag is 5.6 at.%. At temp. ≤1430 °C Mo is resistant to corrosion in liquid Ag. The data on mutual solubilities of the components available in literature are controversial.	[5, 17–18, 47]
Mo–Au	Au, no binary compounds, Mo Eutectic Au–Mo (1054 °C, 2.1 at.% Mo)	The max. solid solubility of Mo in Au is 1.25 at.% (at eutectic temp.) and that of Au in Mo is 0.4 at.% (at 1260 °C); at eutectic temp. the solubility of Au in Mo is 0.025 at.%. At lower temp. the solid solubility of Mo in Au declines—up to 1.2 at.% at 1000 °C, 1.05–1.10 at.% at 800 °C, 0.90–0.95 at.% at 600 °C and 0.7 at.% at 200 °C.	[5, 17–18, 126]
Group 12			
Mo–Zn	Zn, $MoZn_{22\pm x}$ (<~460–465 °C, incongruent melt. point, homog. range—~3.5–4.5 at.% Mo), $MoZn_{7\pm x}$ (<~570–580 °C, incongruent melt. point, homog. range—~12–13.5 at.% Mo), Mo Peritectic Zn (~419 °C, 1.6×10^{-3} at.% Mo) Data on the system available in literature are controversial.	The solubility of Mo in liquid Zn is 2.5×10^{-3} at.% at its melt. point, 5.2×10^{-3} at.% at 460–465 °C and 1.5×10^{-2} at.% at 550–750 °C. The mutual solid solubilities of the components are extremely low and controlled by crystal lattice defects. At temp. ≤500 °C Mo is resistant to corrosion and erosion in liquid Zn.	[5, 16, 18, 47, 127]

(continued)

Table 7.4 (continued)

System	Type of phase diagram (constituent phases, temperatures and compositions of transformations)	Character of interaction	References
Mo–Cd	Cd, no binary compounds, Mo Eutectic (degenerated) Cd–Mo (~321 °C, ?)	No interaction at least at temp. <1000 °C.	[17, 47, 275]
Mo–Hg	Hg, no binary compounds (at normal conditions), Mo Peritectic Hg (–39 °C, ?)	Some binary compounds are formed at higher pressures. At room temp. the solubility of Mo in Hg is $\sim 10^{-5}$ at.%. At temp. <600 °C Mo is resistant to corrosion and erosion in Hg (no amalgams are formed); at 600–700 °C the resistance is limited.	[5, 15, 283]
Group 13			
Mo–B	β-B, $MoB_{\sim 12}$ (?), MoB_{4-x} (or $Mo_{1-x}B_3$, <~1755–1855 °C, homog. range—~20–22 at.% Mo at 1400 °C), Mo_2B_{5-x} (<1600–2200 °C, incongruent melt. point, homog. range—~30–32 at.% Mo at 1895–1945 °C and ~30–35 at.% Mo at 1500–1530 °C), MoB_{2-x} (from 1500–1600 °C to 2100–2400 °C, incongruent melt. point, homog. range—~34–38 at.% Mo at 2125–2200 °C and ~36–39 at.% Mo at 1720–1880 °C), α-$MoB_{1\pm x}$ (<1720–2210 °C, the temp. of polymorphic transformation decreases with the growth of B content, homog. range—~49–52 at.% Mo at 1400–1880 °C), β-$MoB_{1\pm x}$ (from 1720–2210 °C to ~2350–2610 °C, congruent melt. point corresp. to ~$MoB_{1.0}$, homog. range—~48–51 at.% Mo at 2150–2390 °C), Mo_3B_2 (~1920–2250 °C, invariable compos., ?), $Mo_{2\pm x}B$ (<~2140–2295 °C, incongruent melt. point,	The solid solubility of B in Mo is ~1.0–1.75 at.% at 2000–2200 °C, ~0.5–0.6 at.% at 1400–1600 °C and ~0.04 at.% at 1100–1200 °C. The max. solid solubility of Mo in B is ~1 at.% (at 1895–1945 °C). Direct interaction between Mo and B at 1100–1800 °C in vacuum or inert gas atmosphere results in the formation of the borides with lower B content. The contact interaction between Mo and α-$MoB_{1\pm x}$ leads to the formation of $Mo_{2\pm x}B$ (at 1400–1600 °C), between Mo and Mo_2B_{5-x}—to the formation of $Mo_{2\pm x}B$ (at 1300–1800 °C) and $MoB_{1\pm x}$ (at 1900 °C). For diffusion rate in the system at various temp. see Addendum.	[5, 14, 17–19, 21, 33–34, 47, 128–134, 231, 251]

(continued)

Table 7.4 (continued)

System	Type of phase diagram (constituent phases, temperatures and compositions of transformations)	Character of interaction	References
	homog. range—~65–67 at.% Mo at 2150–2210 °C and 66–67 at.% Mo at 1400–2000 °C), Mo Eutectic Mo_2B_{5-x}–β-B (~1895–1945 °C, ~2–10 at.% Mo) Eutectic $MoB_{\sim 12}$–β-B (~2030–2040 °C, ?) Eutectic $Mo_{2\pm x}B$–Mo (~2165–2215 °C, ~76–78 at.% Mo) Data on the system available in literature are controversial.		
Mo–Al	Al, $MoAl_{12}$ (<680–700 °C, incongruent melt. point, invariable compos.), $MoAl_{6\pm x}$ (<705–735 °C, incongruent melt. point, homog. range—~13.5–14.5 at.% Mo, ?), $MoAl_5$ (from >700 °C (?) to 735–795 °C, incongruent melt. point, invariable compos.), Mo_5Al_{22} (<820–980 °C, incongruent melt. point, invariable compos.), Mo_4Al_{17} (<900–1060 °C, incongruent melt. point, invariable compos.), $MoAl_4$ (from <750 °C (?) to 1110–1150 °C, incongruent melt. point, invariable compos.), $MoAl_{3-x}$ (or $Mo_3Al_{8\pm x}$, <~1545–1605 °C, congruent melt. point corresp. to ~$MoAl_{2.3}$, homog. range—~25–31 at.% Mo), $MoAl_{2-x}$ (or $Mo_{37}Al_{63\pm x}$, from 1480–1500 to 1560–1580 °C, incongruent melt. point, homog. range—~36.5–37.5	The solid solubility of Mo in Al is 0.07 at.% at 660 °C, 0.06 at.% at 640 °C, 0.05 at.% at 550 °C, 0.045 at.% at 500 °C, 0.04 at.% at 450 °C and 0.02 at.% at 400 °C. The max. solid solubility of Al in Mo is ≤19.5 at.% at 2050–2250 °C; at higher and lower temp. the solid solubility of Al in Mo declines considerably. The interaction between Mo and Al initiates from 650 °C; it is characterized by the great exothermic heat effect and relates to the SHS type (see special notes for the C–Ti system). The corrosion resistance of Mo to liquid Al is low.	[5, 14, 17–18, 47, 135–137, 321]

(continued)

Table 7.4 (continued)

System	Type of phase diagram (constituent phases, temperatures and compositions of transformations)	Character of interaction	References
	at.% Mo), Mo_2Al_3 (~1450–1500 °C, ?), $MoAl_{1\pm x}$ (from ~1455–1475 °C to ~1720–1765 °C, congruent (?) melt. point corresp. to ~$MoAl_{1.0}$ (?), homog. range—~48–54 at.% Mo), $Mo_{3\pm x}Al$ (<2050–2250 °C, incongruent melt. point corresp. to ~$Mo_{3.0}Al$, homog. range—~73–78.5 at.% Mo), Mo Extended solid solution based on Mo (up to ~19.5 at.% Al at 2050–2250 °C) Peritectic Al (~660 °C, 0.03 at.% Mo) Eutectic $MoAl_{2-x}$–$MoAl_{3-x}$ (~1510–1545 °C, ~31–38 at.% Mo) Eutectic $Mo_{3\pm x}Al$–$MoAl_{1\pm x}$ (~1720 °C, ~63 at.% Mo, ?) Eutectic $Mo_{3\pm x}Al$–$MoAl_{2-x}$ (~1760 °C, ?) Data on the system available in literature are controversial.		
Mo–Ga	Ga, Mo_8Ga_{41} (<830–840 °C, incongruent melt. point, invariable compos.), Mo_6Ga_{31} (<670–720 °C, invariable compos.), $MoGa_2$ (<~800–830 °C, invariable compos.), MoGa (<~800–830 °C, invariable compos.), $Mo_{3\pm x}Ga$ (<1800–1840 °C, incongruent melt. point, homog. range—~74–76 at.% Mo), Mo	The max. solid solubility of Ga in Mo is ~15 at.% (1800–1840 °C); at lower temp. it declines considerably—up to 10.3 at.% at 1700 °C and 1.75 at.% at 1275 °C. The resistance of Mo to corrosion in liquid Ga is high at temp. <300–400 °C, limited—at 400–450 °C and poor—at temp. >450 °C.	[5, 15, 47, 138]

(continued)

Table 7.4 (continued)

System	Type of phase diagram (constituent phases, temperatures and compositions of transformations)	Character of interaction	References
Mo–In	In, no binary compounds, Mo	The solubility of Mo in liquid In (under gas pressure – 0.1 MPa) is 14.0 at.% at ~2100 °C, 0.036 at.% at 725 °C and $\sim 10^{-7}$ at.% at the melt. point of In (157 °C).	[16, 18, 47, 139, 284]
Mo–Tl	α-Tl, β-Tl, no binary compounds, Mo	No interaction.	[18, 47]
Group 14			
Mo–C	See C–Mo in Table 2.13.		
Mo–Si	Si, α-$MoSi_2$ (<1900 °C, invariable compos.), β-$MoSi_2$ (from 1850–1900 to 2020 °C, congruent melt. point, invariable compos., ?), $Mo_5Si_{3\pm x}$ (or Mo_3Si_{2-x}, <2170–2180 °C, congruent melt. point corresp. to ~$MoSi_{0.6}$, homog. range —60–63 at.% Mo), Mo_3Si (<2025–2065 °C, incongruent melt. point, invariable compos.), Mo Eutectic α-$MoSi_2$–Si (1400–1405 °C, 1.7–2.0 at.% Mo) Eutectic β-$MoSi_2$ (or α-$MoSi_2$, ?)–$Mo_5Si_{3\pm x}$ (1900–1925 °C, 46–55 at.% Mo) Eutectic $Mo_5Si_{3\pm x}$–Mo_3Si (2020–2065 °C, 73.6 at.% Mo) Data on the system available in literature are controversial.	The max. solid solubility of Si in Mo amounts to ~3.5–9.0 at.% (?) at 2025–2070 °C; at lower temp. the solubility of Si declines—up to <3.35 at.% at 1820 °C, ~2.5 at.% at 1425 °C, ~1.1 at.% at 1370 °C and ~0.7 at.% at 1315 °C. The solid solubility of Mo in Si is extremely low. The resistance of Mo to corrosion and erosion in molten Si is poor. Mo silicides are synthesized directly from the elements in vacuum or inert gas atmosphere at 1100–1500 °C. At 1190–1715 °C the contact interaction between Mo and α-$MoSi_2$ compact bodies results in the formation of $Mo_5Si_{3\pm x}$ and Mo_3Si. For diffusion rate in the system at various temp. see Addendum.	[5, 14, 16, 18, 21, 140, 204–207, 323–324]

(continued)

Table 7.4 (continued)

System	Type of phase diagram (constituent phases, temperatures and compositions of transformations)	Character of interaction	References
Mo–Ge	Ge, α-$MoGe_2$ (<~1065–1100 °C, incongruent melt. point, invariable compos.), β-$MoGe_2$ (?), $Mo_{13}Ge_{23\pm x}$ (or Mo_2Ge_{3+x}, <1520 °C, incongruent melt. point, homog. range—36–37 at.% Mo), Mo_3Ge_2 (?), Mo_5Ge_3 (<1730 °C, incongruent melt. point, invariable compos.), Mo_3Ge (<1800 °C, incongruent melt. point, invariable compos.), Mo Eutectic (degenerated) α-$MoGe_2$–Ge (935 °C, ?)	The solid solubility of Mo in Ge is negligible; max. solid solubility of Ge in Mo is ~5.0–5.5 at.% at 1800 °C, and at lower and higher temp. it declines considerably. Mo germanides are synthesized from the powdered compositions of elements in sealed quartz ampules.	[5, 14, 15, 141–143]
Mo–Sn	α-Sn, β-Sn, $MoSn_2$ (<700–900 °C, incongruent melt. point, invariable compos.), $MoSn_{1\pm x}$ (or Mo_2Sn_{3-x}, or Mo_3Sn_{2+x}, <1100–1300 °C, incongruent melt. point, homog. range—48.5–56 at.% Mo), Mo_3Sn (<300 °C, invariable compos.), Mo	At 1450 °C the solubility of Mo in liquid Sn is 5×10^{-3} at.%.	[5, 16, 18, 47, 141, 144]
Mo–Pb	Pb, no binary compounds, Mo Eutectic (degenerated) Pb–Mo (~328 °C, ?)	The solubility of Mo in liquid Pb is $\sim 10^{-4}$ at.% at 880–1010 °C and $\sim 10^{-2}$–10^{-3} at.% at 1200–1750 °C. At 600–1100 °C Mo is highly resistant to corrosion and erosion in molten Pb. No evidence of Mo corrosion was revealed after 500 h exposure testing in Pb at 760–1095 °C. Long-term strength of Mo at 870–980 °C in liquid Pb is higher than in He atmosphere.	[5, 16, 18, 47]

(continued)

Table 7.4 (continued)

System	Type of phase diagram (constituent phases, temperatures and compositions of transformations)	Character of interaction	References
Group 15			
Mo–N	N, MoN_3 (?), $Mo_{1-x}N$ ($x = 0.18$, or $MoN_{1.22}$, invariable compos., ?), δ-MoN (<~600–1150 °C, invariable compos.), δ'-MoN (?), δ''-MoN (?), Mo_3N_2 (<800 °C, ?), γ-$Mo_{2\pm x}N$ (<~1910–2010 °C, incongruent melt. point (?), homog. range—~65–73 at.% Mo), β-$Mo_{2\pm x}N$ (from ~400–600 °C to ~850–1000 °C, homog. range—~65–72 at.% Mo, ?), $Mo_{16}N_7$ (low-temp. ordered phase, ?), Mo Eutectic γ-$Mo_{2\pm x}N$–Mo (~1800–1920 °C, 79–81 at.% Mo)	The max. solid solubility of N in Mo is ~2 at.% (1800–1920 °C). The solubility of N in Mo is obeyed the rules: $\lg x = 3.72 - 7940/T$ (in solid Mo at 900–1800 °C), $\lg x = 0.5\lg p - 0.523 - 4940/T$ (in solid Mo at 1600–2400 °C), $\lg x = 0.5\lg p - 1.46$ (in liquid Mo at 2700 °C and pressures <0.046 MPa), $\lg x = 0.5\lg p - 1.5$ (in liquid Mo at 2650 °C and pressures <0.066 MPa), where x is N content, at.%, p is pressure N_2, MPa, and T is temp., K. In general, the data on solubility of N in Mo available in literature are controversial. Mo nitrides are synthesized by the interaction of Mo with N_2 at 1100–1500 °C or with NH_3 at 400–720 °C. At N_2 pressures ≤1 Pa Mo does not react at temp. ≤2400 °C.	[5, 11, 14, 16, 18, 21–22, 47, 145–148, 285–288]
Mo–P	P, MoP_2 (<~975–1000 °C, dissociation point, invariable compos.), MoP (<~1550–1755 °C (?), dissociation or melt. point (?), invariable compos.), Mo_4P_3 (from 600–800 to 1700 °C, incongruent melt. point, invariable compos.), Mo_8P_5 (or Mo_3P_{2-x}, from 1530–1630 to 1680 °C, incongruent melt. point, invariable compos., ?), $Mo_{2-x}P$ (or $Mo_{1.7}P$, ~1670–1750 °C, ?), Mo_3P (<~1700 °C, incongruent melt. point, invariable compos.), Mo Eutectic Mo_3P (or $Mo_{2-x}P$) –Mo_8P_5 (~1650 °C, ~70 at.% Mo) Eutectic MoP–Mo (~1065–1650 °C, ~70 at.% Mo, ?) Data on the system available in literature are controversial.	The max. solubility of P in Mo is ~14–16 at.% (?). Mo phosphides are synthesized from the powdered compositions of elements in sealed quartz ampules. For diffusion rate in the system at various temp. see Addendum.	[5, 14, 16, 18, 47, 149]

(continued)

Table 7.4 (continued)

System	Type of phase diagram (constituent phases, temperatures and compositions of transformations)	Character of interaction	References
Mo–As	As, $MoAs_5$ (or $Mo_{0.4}As_2$, $<\sim 600$ °C, invariable compos.), $MoAs_2$ (<1015–1115 °C, invariable compos.), Mo_2As_3 (<1200–1300 °C, invariable compos.), Mo_3As_4 (?), Mo_4As_5 (?), $MoAs_{1+x}$ (or $Mo_{49}As_{51}$, at least near ~ 700 °C, ?), MoAs (stabilized by impurities, ?), Mo_5As_4 (<1820–1840 °C, invariable compos.), Mo	Mo arsenides are synthesized from the powdered compositions of elements in sealed quartz ampules at 500–600 °C.	[5, 14, 17, 47, 141, 150–151]
Mo–Sb	Sb, Mo_3Sb_7 (<760–800 °C, incongruent melt. point, invariable compos.), Mo Eutectic (degenerated) Mo_3Sb_7–Sb (~ 630 °C, $\sim 10^{-4}$ at.% Mo)	Sb is soluble in solid Mo.	[16, 47, 141]
Mo–Bi	Bi, no binary compounds, Mo	No interaction. Practically, no mutual solubilities in the solid state. The solubility of Mo in liquid Bi is $\sim$0.005–0.030 at.% (?) at 1010–1030 °C and <0.001–0.003 at.% at 700–800 °C. The data on the solubility of Mo in Bi available in literature are controversial. At 600–1430 °C Mo is resistant to corrosion and erosion in liquid Bi. At 600–1000 °C Mo parts are suitable for long-term applications in Bi melts; at 1000 °C the interaction (damaged) zone is 5–20 μm.	[5, 17, 47, 275]

(continued)

Table 7.4 (continued)

System	Type of phase diagram (constituent phases, temperatures and compositions of transformations)	Character of interaction	References
Group 16			
Mo–O	O, MoO_3 (<775–810 °C, congruent melt. point, invariable compos.), ξ-Mo_9O_{26} (or ξ-Mo_9O_{24} (?), from ~600 to ~725–770 °C, invariable compos.), β-Mo_9O_{26} (or β-Mo_9O_{24} (?), from ~725–770 to ~775–815 °C, congruent melt. point, invariable compos.), Mo_5O_{14} (metastable, ?), $Mo_{17}O_{47}$ (metastable, ?), $Mo_{18}O_{52}$ (metastable, ?), Mo_8O_{23} (<~775–820 °C, incongruent melt. point, invariable compos., ?), η-Mo_4O_{11} (<~550–650 °C, invariable compos.), γ-Mo_4O_{11} (from ~550–650 °C to ~810–860 °C, incongruent melt. point, invariable compos.), Mo_2O_5 (metastable, ?), Mo_nO_{3n-m} homologous series of oxides ($n = 4, 5, 8 \div 14$, $m = 1$ and $n = 18 \div 22$, $m = 2$, in the range of 25.5–26.7 at.% Mo), α-$MoO_{2\pm x}$ (?), β-$MoO_{2\pm x}$ (<2125–2325 °C, incongruent melt. point, homog. range—~33.0–34 at.% Mo), Mo_3O (metastable, ?), Mo Miscibility gap in the liquid state (<33.0–33.3 at.% Mo, ?) Eutectic MoO_3–β-Mo_9O_{26} (~770–780 °C, ~25.3–25.5 at.% Mo) Eutectic β-$MoO_{2\pm x}$–Mo (~2050–2250 °C)	At 1200–1400 °C the solubility of O in Mo is obeyed the rule: $\ln x = 1.67 - 4870/T$, where x is O content, at.% and T is temp., K. At elevated and high temp. the oxidation process of Mo is affected by the vaporization of oxide scales. The rate of Mo oxidation is very sensitive to the velocity of gas flow. In air at atmospheric pressure the intensive oxidation of Mo begins from 300–400 °C. Nanotubes constructed from MoO_3 and $MoO_{2\pm x}$ have been prepared.	[5, 14, 16, 18, 23–24, 47, 152–157, 167, 217, 253]

(continued)

Table 7.4 (continued)

System	Type of phase diagram (constituent phases, temperatures and compositions of transformations)	Character of interaction	References
Mo–S	α-S, β-S, MoS_3 (?), Mo_2S_5 (?), MoS_{2+x} (<1700–1800 °C, incongruent melt. point, homog. range—~31.5–33.3 at.% Mo at 585–715 °C and from ~29.5–30 to 33.3 at.% Mo at 115 °C), Mo_2S_{3-x} (from ~585–715 °C to ~1600–1800 °C, congruent melt. point (?), homog. range—~40–41 at.% Mo), Mo_3S_4 (metastable, ?), Mo Eutectic Mo_2S_{3-x}–MoS_{2+x} (~1580–1680 °C, ~47 at.% Mo) Eutectic Mo_2S_{3-x}–Mo (~1450–1650 °C, ~50–63 at.% Mo)	The max. solubility of S in solid Mo is 3.5 at.% at 1450–1650 °C; it declines considerably at lower temp.—up to 1.5 at.% at 1100 °C and 0.3 at.% at 600 °C. MoS_{2+x} and Mo_2S_{3-x} are synthesized by the interaction of Mo powder with S vapour in sealed quartz ampules at 1000–1200 °C. Nanoparticles with onion-like fullerene type structure and nanotubes constructed from MoS_{2+x} have been prepared. For diffusion rate in the system at various temp. see Addendum.	[5, 14, 16, 18, 47, 57–58, 158–166]
Mo–Se	Se, $MoSe_3$ (?), Mo_2Se_5 (?), $MoSe_{2-x}$ (<1100–1200 °C, homog. range—~33.3–34.5 at.% Mo), $Mo_3Se_{4\pm x}$ (<1300–1500 °C, homog. range—~42–45 at.% Mo), Mo	At higher temp. the solubility of Se in Mo is low (<1–2 at.%); it is negligible and controlled by crystal lattice defects at lower temp. (<530 °C). Mo selenides are synthesized directly from the elements. Nanotubes constructed from $MoSe_{2-x}$ have been prepared.	[14, 16, 47, 58, 161, 168–173]
Mo–Te	Te, α-$MoTe_{2-x}$ (<820–880 °C, max. homog. range—33.3–34.5 at.% Mo at 820 °C), β-$MoTe_{2-x}$ (from 800–820 to 1140–1220 °C, max. homog. range—33.4–34.5 at.% Mo at ~990 °C), α-$Mo_3Te_{4\pm x}$ (?), β-$Mo_3Te_{4\pm x}$ (<1230–1370 °C, homog. range—41.7–44.1 at.% Mo at 1140–1370 °C and 42.6–43.5 at.% Mo at lower temp.), Mo (at higher pressures Te_2 the congruent melt. points of β-$MoTe_{2-x}$ and β-$Mo_3Te_{4\pm x}$ —~1500–1600 °C, ?) Eutectic β-$Mo_3Te_{4\pm x}$–β-$MoTe_{2-x}$ (at higher pressures Te_2, ?) Eutectic β-$Mo_3Te_{4\pm x}$–Mo (at higher pressures Te_2, ?)	The solid solubility of Te in Mo is 0.5–2.0 at.% at 1230–1370 °C. The solubility of Mo in liquid and solid Te is negligible. Mo tellurides are synthesized from the elements at 1000–1100 °C.	[14, 16, 47, 169, 174–177]

(continued)

Table 7.4 (continued)

System	Type of phase diagram (constituent phases, temperatures and compositions of transformations)	Character of interaction	References
Mo–Po	α-Po, β-Po, no binary compounds, Mo No diagram plot	No interaction with Po vapours at temp. ≤700 °C.	[16, 18]
Group 17			
Mo–F	F, α′-MoF_6 (?), α-MoF_6 (<17–18 °C, congruent melt. point, invariable compos.), Mo_4F_{23} (<33 °C, congruent melt. point, invariable compos.), Mo_2F_{11} (or Mo_4F_{22}, <40 °C, congruent melt. point, invariable compos.), α′-MoF_5 (?), α-MoF_5 (or Mo_4F_{20}, <67 °C, congruent melt. point, invariable compos.), Mo_2F_9 (?), MoF_4 (<300 °C, invariable compos.), α-MoF_3 (<1100 °C, invariable compos.), β-MoF_3 (?), Mo Eutectic α′-MoF_5–Mo_2F_{11} (8 °C, 15.7 at.% Mo, ?) Eutectic Mo_4F_{23}–Mo_2F_{11} (1 °C, 15.1 at.% Mo) Eutectic Mo_4F_{23}–α-MoF_6 (8 °C, 14.5 at.% Mo)	At 60 °C the direct interaction between Mo and F_2 results in the formation of MoF_6. Other Mo fluorides are synthesized by special chemical reaction pathways. The data available in literature on the stability of Mo in F_2 are controversial.	[2–3, 5, 14, 18, 47, 275, 289–290]
Mo–Cl	Cl, $MoCl_6$ (<25 °C, invariable compos.), α-$MoCl_5$ (or Mo_2Cl_{10}, <~95–100 °C, invariable compos.), β-$MoCl_5$ (or Mo_2Cl_{10}, from ~95–100 °C to ~195 °C, melt. point, invariable compos.), α-$MoCl_4$ (<~80–240 °C (?), invariable compos.), β-$MoCl_4$ (from ~80–240 °C to ~265–285 °C (?), incongruent melt. point, invariable compos.), β-$MoCl_{3+x}$ (<~280–290 °C, decompos. point, invariable compos.), α-$MoCl_{3-x}$ (<~640–660 °C, decompos. point, invariable compos.), $MoCl_2$	At 250–700 °C the direct interaction between Mo and Cl_2 results in the formation of $MoCl_5$. Other Mo chlorides are synthesized by special chemical reaction pathways. Mo is resistant to corrosion and erosion in Cl_2 at temp. <230 °C.	[2–3, 5, 14–15, 18, 47, 178–183]

(continued)

Table 7.4 (continued)

System	Type of phase diagram (constituent phases, temperatures and compositions of transformations)	Character of interaction	References
	(or Mo_6Cl_{12}, <~940–960 °C, decompos. point, cluster compound, invariable compos.), Mo Eutectic β-$MoCl_5$–α/β(?)-$MoCl_4$ (~180–185 °C, ~18 at.% Mo)		
Mo–Br	Br, $MoBr_4$ (<120–160 °C, decompos. point, invariable compos.), $MoBr_3$ (<680–700 °C, decompos. point, invariable compos.), $MoBr_2$ (or Mo_6Br_{12}, <1050–1110 °C, decompos. point, invariable compos.), Mo	The direct interaction between Mo and Br_2 results in the formation of $MoBr_3$ (at 500 °C), $MoBr_4$ (at 625 °C) and $MoBr_2$ (at 700 °C). Mo is resistant to corrosion in Br_2 vapour at temp. <450 °C.	[2, 3, 5, 14, 17, 47, 178, 184–186]
Mo–I	I, MoI_4 (<~20–100 °C (?), decompos. point, invariable compos.), MoI_3 (<355 °C, invariable compos.), MoI_2 (or Mo_6I_{12}, <~850–1025 °C, decompos. point, invariable compos.), Mo	Mo iodides are synthesized by the direct interaction between the elements at temp. ≥300 °C. Mo is highly resistant to corrosion in I_2 vapour at temp. ≤800 °C.	[2, 3, 5, 14, 18, 47, 178]
Mo–At	At, $MoAt_2$ (<1050 °C, decompos. point, invariable compos.), Mo	–	[18, 47, 275]

[a] The intervals of temperatures and compositions for the melting and invariant equilibria points, homogeneity ranges and thermal stability regions of constituent phases are given taking into account the minimal and maximal values (data spread) available in literature

The data on the selected ternary, quaternary, quasi-binary and quasi-ternary molybdenum containing systems, which are the most important for the design, manufacture and application of ultra-high temperature materials, are summarized in Table 7.5. The composition and temperature stability regions for the main binary and ternary molybdenum containing high-temperature phases are given in Tables 7.4 and 7.5 taking into account the spread of numerical magnitudes available in literature currently.

Table 7.5 Chemical interaction of molybdenum with elements and compounds at high temperatures (selected ternary, quaternary, quasi-binary and quasi-ternary systems in alphabetical order)[a]

System	Type of phase diagram (temperature and composition sections, constituent phases or phase fields) and/or character of interphase interaction and materials compatibility	References
Mo–Al–B	Plotted at 1000 °C: MoAlB (~30–36 at.% Mo, ~31–34.5 at.% B, ≤1000 °C), Mo_9AlB_{10} (43.5–47 at.% Mo, 48–50 at.% B), α-$Mo(B,Al)_{1\pm x}$ (solid solution based on α-$MoB_{1\pm x}$, <5 at.% B), α-AlB_{12} (<1550 °C), β-AlB_{12} (from 1550 to ~2075–2150 °C), AlB_{10} (1660–1850 °C), AlB_2 (from ~213 °C to ~970–980 °C), $MoAl_{12}$, $MoAl_5$, Mo_5Al_{22}, Mo_4Al_{17}, $MoAl_4$, $MoAl_{3-x}$, $MoAl_{2-x}$, Mo_2Al_3, $Mo_{3\pm x}Al$, MoB_{4-x}, Mo_2B_{5-x}, MoB_{2-x}, β-$MoB_{1\pm x}$, Mo_3B_2, $Mo_{2\pm x}B$, β-B, Al, Mo No solid solutions based on binary compounds apart from α-$Mo(B,Al)_{1\pm x}$. Mo is in equilibrium with $Mo_{2\pm x}B$ and $Mo_{3\pm x}Al$.	[17, 18, 245–248]
Mo–Al–B–Hf	No diagram plot $(Hf,Al)_9(Mo,Al)_4B$	[262–263]
Mo–Al–B–N	No diagram plot In vacuum the interaction between metal Mo and α-BN–AlN equimolar compos. starts from 1500 °C (in powder mixtures—from 1200 °C) and leads to the formation of $Mo_{2\pm x}B$ and α-$MoB_{1\pm x}$	[30]
Mo–Al–C	See C–Al–Mo in Table 2.14.	
Mo–Al–C–Ni	See C–Al–Mo–Ni in Table 2.14.	
Mo–Al–Nb	Plotted at 1000 and 1600 °C (partially): $NbMo_3Al_{16}$ (homog. range—~18–23 at.% Mo, ~1–4 at.% Nb, ~75–80 at.% Al at 1000 °C), $(Mo,Nb)_{3\pm x}Al$ ($Mo_{3\pm x}Al$–$Nb_{3+x}Al$ continuous solid solution), $(Nb,Mo)Al_{3-x}$ (extended solid solution based on $NbAl_{3-x}$—up to ~$(Nb_{0.4}Mo_{0.6})Al_{3-x}$ compos. at 1000 °C, <1605–1680 °C), σ-$(Nb,Mo)_{2\pm x}Al$ (extended solid solution based on σ-$Nb_{2\pm x}Al$—up to ~$(Nb_{0.5}Mo_{0.5})_{2\pm x}Al$ compos. at 1000 °C, <~1860–1940 °C), $MoAl_{12}$, $MoAl_{6\pm x}$, Mo_5Al_{22}, Mo_4Al_{17}, $MoAl_4$, $MoAl_{3-x}$, $MoAl_{2-x}$, Mo_2Al_3, $MoAl_{1\pm x}$, $Mo_{3\pm x}Al$, Al, (Mo,Nb)	[16–18, 187, 291, 292]
Mo–Al–Ni–W	See W–Al–Mo–Ni in Table 3.6.	

(continued)

Table 7.5 (continued)

System	Type of phase diagram (temperature and composition sections, constituent phases or phase fields) and/or character of interphase interaction and materials compatibility	References
Mo–Al–O	Plotted at 1400 °C: α-$Al_2(MoO_4)_3$ (or α-$Al_2O_3{\cdot}3MoO_3$), β-$Al_2(MoO_4)_3$ (or β-$Al_2O_3{\cdot}3MoO_3$) γ-$Al_2(MoO_4)_3$ (or γ-$Al_2O_3{\cdot}3MoO_3$), γ-Al_2O_{3-x}, α-Al_2O_3 ($<\sim$2030–2055 °C), $MoAl_{12}$, $MoAl_{6\pm x}$, Mo_5Al_{22}, Mo_4Al_{17}, $MoAl_4$, $MoAl_{3-x}$, $MoAl_{2-x}$, Mo_2Al_3, $MoAl_{1\pm x}$, MoO_3, ξ-Mo_9O_{26}, β-Mo_9O_{26}, Mo_8O_{23}, η-Mo_4O_{11}, γ-Mo_4O_{11}, Mo_nO_{3n-m} homologous series of oxides, β-$MoO_{2\pm x}$, O, Al, Mo In vacuum the interaction between compact metal Mo and Al_2O_3 initiates from 1900 °C; it is characterized with the increase of porosity in the metal-oxide contact zone because of the vaporization of the volatile products of reaction (Mo oxides).	[31, 293–295]
Mo–As–Ta	See Ta–As–Mo in Table 6.4.	
Mo–B–C	See C–B–Mo in Table 2.14.	
Mo–B–C–La	See C–B–La–Mo in Table 2.14.	
Mo–B–C–N	See C–B–Mo–N in Table 2.14.	
Mo–B–C–Ni	See C–B–Mo–Ni in Table 2.14.	
Mo–B–C–Si	See C–B–Mo–Si in Table 2.14.	
Mo–B–Ce	Plotted at 600 and 800 °C: $\sim$$CeMoB_3$, $CeB_{6\pm x}$ (<2550 °C), CeB_4 (<2380 °C), MoB_{4-x}, Mo_2B_{5-x}, MoB_{2-x}, α-$MoB_{1\pm x}$, β-$MoB_{1\pm x}$, Mo_3B_2, $Mo_{2\pm x}B$, β-B, α-Ce, β-Ce, γ-Ce, δ-Ce, Mo No solid solutions based on binary and ternary compounds.	[216, 227, 230]
Mo–B–Co	Plotted at 800 and 1100 °C: Mo_2CoB_2, $MoCo_2B_4$, χ-$MoCo_4B$, τ-$Mo_2Co_{21}B_6$ (or $Mo_{2-x}Co_{21+x}B_6$, $x = 0.7$), MoCoB, Mo_3CoB_3, $(Mo,Co)_{2\pm x}B$ (solid solution based on $Mo_{2\pm x}B$—up to $\sim$$(Mo_{0.9}Co_{0.1})_{2\pm x}B$ compos. at 800 °C), α-$(Mo,Co)B_{1\pm x}$ (solid solution based on α-$MoB_{1\pm x}$—up to $\sim$$(Mo_{0.85}Co_{0.15})B_{1\pm x}$ compos. at 1100 °C), β-$(Mo,Co)B_{1\pm x}$ (solid solution based on β-$MoB_{1\pm x}$, stabilized by Co at lower temp., homog. range—$\sim$7–12 at.% Co at 800 °C, ?), Co_3B (<1125 °C), Co_2B (<1280 °C), CoB (<1460 °C), θ-Co_9Mo_{2+x}, κ-$Co_{3\pm x}Mo$, μ-$Co_7Mo_{6\pm x}$, σ-Co_2Mo_{3+x}, MoB_{4-x}, Mo_2B_{5-x}, MoB_{2-x}, Mo_3B_2, β-B, ε-Co, α-Co, Mo At 1100 °C the interaction between Mo_2B_{5-x} and Co leads to the formation of $MoB_{1\pm x}$ and Co_3B.	[21, 25, 32, 262, 264, 296–297]

(continued)

Table 7.5 (continued)

System	Type of phase diagram (temperature and composition sections, constituent phases or phase fields) and/or character of interphase interaction and materials compatibility	References
Mo–B–Cr	Plotted at 800–1950 °C: Cr_2MoB_4, $(Mo_{1-y}Cr_y)_{2\pm x}B$ ($0.3 \le y \le 0.7$, at least at 1000 °C), $Mo_{0.24\div0.39}Cr_{1.61\div1.76}B$ (or $MoCr_5B_3$, ?), $Mo_{2\div1.5}Cr_{1\div1.5}B_2$ (or $(Mo,Cr)_3B_2$, ?), β-$(Cr,Mo)B_{1\pm x}$ (β-$MoB_{1\pm x}$–β-CrB_{1-x} continuous solid solution at higher temp., or extended (very widely ranged) solid solution based on β-CrB_{1-x} at lower temp. (up to $(Cr_{0.4}Mo_{0.6})B_{1\pm x}$ at 1000 °C), ?), $(Cr,Mo)B_{2\pm x}$ (extended solid solution based on $CrB_{2\pm x}$), $(Cr,Mo)_3B_{4+x}$ (extended solid solution based on Cr_3B_{4+x}), $(Cr,Mo)_5B_{3-x}$ (extended solid solution based on Cr_5B_{3-x}—up to $(Cr_{0.55}Mo_{0.45})_5B_{3-x}$ at 1000 °C), $(Cr,Mo)_{2\pm x}B$ (extended solid solution based on $Cr_{2\pm x}B$—up to $(Cr_{0.7}Mo_{0.3})_{2\pm x}B$ at 1000 °C), $(Mo,Cr)_{2\pm x}B$ (solid solution based on $Mo_{2\pm x}B$), $(Mo,Cr)B_{2-x}$ (solid solution based on MoB_{2-x}, ?), CrB_4 (<1500 °C), MoB_{4-x}, Mo_2B_{5-x}, α-$MoB_{1\pm x}$, Mo_3B_2, β-B, (Mo,Cr) Eutectic Cr_2MoB_4–$CrB_{2\pm x}$ (2120 °C, 6 mol.% Mo) Eutectic Cr_2MoB_4–Mo (1950–1960 °C, 83 mol.% Mo) The solubility of $CrB_{2\pm x}$ in Mo is ~3 mol.%. Mo-based binary borides have low solubilities of Cr, whereas Cr-based binary borides dissolve considerable amounts of Mo.	[5, 21, 188–192, 262]
Mo–B–Dy	Plotted at 1000 °C: $DyMoB_3$, $DyMoB_4$, Dy_3MoB_7, ~$DyMo_4B_8$, $DyMo_3B_7$ (?), $(Mo,Dy)B_{2-x}$ (solid solution based on MoB_{2-x}, ?), DyB_2 (<2100 °C), DyB_4 (<2500 °C), $DyB_{6\pm x}$ (<2200 °C), DyB_{12} (<2100 °C), DyB_{66} (<2025 °C), MoB_{4-x}, Mo_2B_{5-x}, α-$MoB_{1\pm x}$, β-$MoB_{1\pm x}$, Mo_3B_2, $Mo_{2\pm x}B$, β-B, α-Dy, β-Dy, Mo No solid solutions based on binary and ternary compounds apart from $(Mo,Dy)B_{2-x}$ stabilized by Dy.	[216, 230, 262]
Mo–B–Er	Plotted at 1000 °C: $ErMoB_4$, Er_2MoB_6, $Er_3Mo_2B_6$, $ErMo_3B_7$ (?), $ErMoB_3$ (?), $Er_3Mo_3B_4$ (?), ErB_2 (solubility of Mo—up to ~5 at.%, <2185 °C), ErB_4 (<2500 °C), ErB_{12} (<2080 °C), ErB_{66} (<2070 °C), MoB_{4-x}, Mo_2B_{5-x}, MoB_{2-x}, α-$MoB_{1\pm x}$, β-$MoB_{1\pm x}$, Mo_3B_2, $Mo_{2\pm x}B$, β-B, Er, Mo No solid solutions based on binary and ternary compounds apart from ErB_2.	[212, 216, 262, 298]

(continued)

Table 7.5 (continued)

System	Type of phase diagram (temperature and composition sections, constituent phases or phase fields) and/or character of interphase interaction and materials compatibility	References
Mo–B–Fe	Plotted at 1000 and 1050 °C: $Mo_2Fe_{13}B_5$ (<~1000–1100 °C), Mo_2FeB_2, Mo_2FeB_4, Mo_7FeB_{10} (or Mo_4FeB_6, ?), $Mo_{0.4}Fe_{2.6}B$ (or $MoFe_5B_2$, ?), $Mo_{1-x}Fe_xB$ ($0.82 \le x \le 0.87$, ?), $Mo_{1+x}Fe_{2-x}B_4$ ($-0.09 \le x \le 0.75 \div 1.0$, or $(Mo,Fe)_3B_4$, or $MoFe_2B_4$), $(Mo,Fe)_2B_{5-x}$ (solid solution based on Mo_2B_{5-x}, <5 at.% Fe), Fe_2B (<1407 °C), FeB (<1588 °C), λ-Fe_2Mo, μ-Fe_7Mo_{6-x}, MoB_{4-x}, α-$MoB_{1\pm x}$, Mo_3B_2, $Mo_{2\pm x}B$, β-B, α-Fe (δ-Fe), γ-Fe, Mo No solid solutions based on binary compounds apart from $(Mo,Fe)_2B_{5-x}$. At 1100 °C the contact interaction between MoB_{2-x} and Fe results in the formation of liquid phase. The interaction between Mo_2B_{5-x} and Fe at 1120 °C leads to the formation of FeB.	[21, 25–26, 32, 249–250, 262, 266]
Mo–B–Gd	Plotted at 1000 °C: $GdMoB_4$, Gd_3MoB_7, GdB_{66} (<2150 °C), $GdB_{6\pm x}$ (<2510 °C), GdB_4 (<~2650 °C), Gd_2B_5 (<2100 °C), GdB_2 (<~2050 °C), MoB_{4-x}, Mo_2B_{5-x}, α-$MoB_{1\pm x}$, β-$MoB_{1\pm x}$, Mo_3B_2, $Mo_{2\pm x}B$, β-B, α-Gd, β-Gd, Mo No solid solutions based on ternary and binary compounds. Gd inhibits α-$MoB_{1\pm x}$–β-$MoB_{1\pm x}$ solid state phase transformation.	[216, 229, 262]
Mo–B–Hf	Plotted at 1400 °C: Hf_9Mo_4B (or $Hf_9Mo_{\sim 3}B_{2-x}$), $MoHf_{2\div 4}B_{1\div 2.5}$ (?), $(Hf,Mo)B_{2\pm x}$ (extended solid solution based on $HfB_{2\pm x}$—up to compos. ~$(Hf_{0.3}Mo_{0.7})B_{2\pm x}$ at 2380 °C, <3250–3410 °C), $(Mo,Hf)B_{2-x}$ (solid solution based on MoB_{2-x}—up to compos. ~$(Mo_{0.92\div 0.95}Hf_{0.05\div 0.08})B_{2-x}$, from 1500–1600 to 2345–2415 °C), $HfB_{1\pm x}$ (<2100 °C), α-$HfMo_{2\pm x}$, β-$HfMo_{2\pm x}$, MoB_{4-x}, Mo_2B_{5-x}, α-$MoB_{1\pm x}$, β-$MoB_{1\pm x}$, Mo_3B_2, $Mo_{2\pm x}B$, β-B, α-Hf, β-Hf, Mo MoB_{2-x}–$HfB_{2\pm x}$ is plotted: peritectic MoB_{2-x} (2345–2415 °C, 90 mol.% MoB_{2-x}) $HfB_{2\pm x}$–Mo is plotted: eutectic—2045–2095 °C, 84 mol.% Mo; the mutual solubilities of the components are low	[5, 19, 21, 27, 38, 51, 209, 233, 251, 252, 262]
Mo–B–Ho	Plotted at 1000 °C: $HoMoB_3$, $HoMoB_4$, Ho_3MoB_7, ~$HoMo_4B_8$, $HoMo_3B_7$ (?), $(Mo,Ho)B_{2-x}$ (solid solution based on MoB_{2-x}, ?), HoB_2 (<2200 °C), HoB_4 (<2500 °C), $HoB_{6\pm x}$ (<2180 °C), HoB_{12} (<2100 °C), HoB_{66} (<2025 °C), MoB_{4-x}, Mo_2B_{5-x}, α-$MoB_{1\pm x}$, β-$MoB_{1\pm x}$, Mo_3B_2, $Mo_{2\pm x}B$, β-B, α-Ho, β-Ho, Mo No solid solutions based on binary compounds apart from $(Mo,Ho)B_{2-x}$ stabilized by Ho.	[216, 230, 262]

(continued)

Table 7.5 (continued)

System	Type of phase diagram (temperature and composition sections, constituent phases or phase fields) and/or character of interphase interaction and materials compatibility	References
Mo–B–Ir	No diagram plot Mo_2IrB_2, $(Mo,Ir)_5B_6$ (or $\sim Mo_{2.5}Ir_{2.5}B_5$, or $MoIrB_2$), $(Mo,Ir)B_2$ (?).	[262, 268]
Mo–B–La	Plotted at 600 and 800 °C: no ternary compounds, $LaB_{6\pm x}$ (<2715 °C), LaB_4 (<1800 °C), MoB_{4-x}, Mo_2B_{5-x}, MoB_{2-x}, α-$MoB_{1\pm x}$, β-$MoB_{1\pm x}$, Mo_3B_2, $Mo_{2\pm x}B$, β-B, α-La, β-La, γ-La, Mo No solid solutions based on binary compounds. At temp. ≥1000 °C (2–5 h exposure) Mo reacts with $LaB_{6\pm x}$ (at temp. ≥2100 °C the interaction is very intensive); the products of contact interaction are LaB_4 + $Mo_{2\pm x}B$ (1000 °C), La + α-$MoB_{1\pm x}$ (1500 °C) and La + MoB_{2-x} (1800 °C).	[5, 21, 216, 227, 228, 230]
Mo–B–Lu	Plotted at 1000 °C: $Lu_{2-y}Mo_{1+y}B_6$, $(Lu,Mo)B_2$ (extended solid solution based on LuB_2—up to ~10 at.% Mo, <~2250 °C), LuB_{66} (<~2100 °C), LuB_{12} (<~2170 °C), LuB_4 (<~2550 °C), MoB_{4-x}, Mo_2B_{5-x}, MoB_{2-x}, α-$MoB_{1\pm x}$, β-$MoB_{1\pm x}$, $Mo_{2\pm x}B$, β-B, Lu, Mo	[214]
Mo–B–Mn	Plotted at 800 °C: Mo_2MnB_2 (or $(Mo,Mn)_3B_2$, homog. range—~36–42 at.% Mo, ~18–24 at.% Mn), $Mo_2Mn_3B_{10}$ (or $Mo_{0.36\div0.45}Mn_{0.64\div0.55}B_2$), Mo_4MnB_5 (or $Mo_{0.74\div0.84}Mn_{0.12\div0.26}B$), (Mn,Mo)B (extended solid solution based on MnB—up to ~$(Mn_{0.7}Mo_{0.3})B$ compos., <1890 °C), $(Mn,Mo)_3B_4$ (solid solution based on Mn_3B_4—up to ~$(Mn_{0.85}Mo_{0.15})_3B_4$ compos., <~1750–1830 °C), $(Mn,Mo)_2B$ (solid solution based on Mn_2B—up to ~$(Mn_{0.9}Mo_{0.1})_2B$ compos., <1580 °C), $(Mo,Mn)_{2\pm x}B$ (solid solution based on $Mo_{2\pm x}B$—up to ~$(Mo_{0.9}Mn_{0.1})_{2\pm x}B$ compos.), MnB_4 (<~1380–2160 °C, ?), MnB_2 (~1100–1990 °C), Mn_4B (<1120–1285 °C), MoB_{4-x}, Mo_2B_{5-x}, MoB_{2-x}, α-$MoB_{1\pm x}$, β-$MoB_{1\pm x}$, σ-Mn_5Mo_{3-x}, μ-$Mn_5Mo_{4\pm x}$, β-B, α-Mn, β-Mn, γ-Mn, δ-Mn, Mo	[267]

(continued)

Table 7.5 (continued)

System	Type of phase diagram (temperature and composition sections, constituent phases or phase fields) and/or character of interphase interaction and materials compatibility	References
Mo–B–N	Plotted at 1200, 1400 and 1600 °C (pressure Ar—0.1 MPa): no ternary compounds, α-BN (<3000 °C), MoB_{4-x}, Mo_2B_{5-x}, MoB_{2-x}, α-$MoB_{1\pm x}$, β-$MoB_{1\pm x}$, Mo_3B_2, $Mo_{2\pm x}B$, N, β-B, Mo α-BN is in equilibrium with MoB_{4-x}, Mo_2B_{5-x}, α-$MoB_{1\pm x}$ and $Mo_{2\pm x}B$ at 1200 °C; with MoB_{4-x}, Mo_2B_{5-x} and α-$MoB_{1\pm x}$ at 1400 °C; with MoB_{4-x}, Mo_2B_{5-x}, MoB_{2-x} and α-$MoB_{1\pm x}$ at 1600 °C. In vacuum the interaction between Mo and α-BN initiates from 1400–1600 °C, the products of contact interaction are $Mo_{2\pm x}B$, α-$MoB_{1\pm x}$ and slight amounts of Mo_2B_{5-x}; at temp. >1700 °C the reaction takes place also through vapour phase.	[21, 29, 30, 32]
Mo–B–Nb	Plotted at 1400 °C: no ternary compounds, $(Nb,Mo)B_{2\pm x}$ (extended solid solution based on $NbB_{2\pm x}$—up to ~$(Nb_{0.3}Mo_{0.7})B_{2\pm x}$ compos., <3000 °C), $(Nb,Mo)_3B_4$ (extended solid solution based on Nb_3B_4—up to ~$(Nb_{0.3}Mo_{0.7})_3B_4$ compos., <2700 °C), $(Nb,Mo)B_{1\pm x}$ (extended solid solution based on $NbB_{1\pm x}$—up to ~$(Nb_{0.2}Mo_{0.8})B_{1\pm x}$ compos., <~2270–2325 °C), $(Nb,Mo)_3B_2$ (extended solid solution based on Nb_3B_2—up to ~$(Nb_{0.33}Mo_{0.67})_3B_2$ compos., <~1800–2230 °C), $(Mo,Nb)_{2\pm x}B$ (extended solid solution based on $Mo_{2\pm x}B$—up to ~$(Mo_{0.85}Nb_{0.15})_{2\pm x}B$ compos.), α-$(Mo,Nb)B_{1\pm x}$, (solid solution based on α-$MoB_{1\pm x}$—up to ~$(Mo_{0.9}Nb_{0.1})B_{1\pm x}$ compos.), Nb_5B_6 (<at least 2200 °C, ?), MoB_{4-x}, Mo_2B_{5-x}, MoB_{2-x}, β-$MoB_{1\pm x}$, Mo_3B_2, β-B, (Nb,Mo) The solubilities of Mo in Nb borides is higher noticeably than those of Nb in Mo borides. In vacuum the contact interaction between Mo_2B_{5-x} and Nb initiates from 1300 °C and leads to the formation of Nb_3B_2, $NbB_{1\pm x}$ and Nb_3B_4.	[21, 32, 193, 194]
Mo–B–Nb–Si	$MoSi_2$–$NbB_{2\pm x}$ is plotted: eutectic—~1840–1900 °C, ~20 mol.% $NbB_{2\pm x}$; no mutual solubilities between the components	[337]
Mo–B–Nd	Plotted at 800 °C: no ternary compounds, Nd_2B_5 (<~2000 °C), NdB_4 (<~2350 °C), $NdB_{6\pm x}$ (<2610 °C), NdB_{66} (<2150 °C), MoB_{4-x}, Mo_2B_{5-x}, MoB_{2-x}, α-$MoB_{1\pm x}$, β-$MoB_{1\pm x}$, Mo_3B_2, $Mo_{2\pm x}B$, β-B, α-Nd, β-Nd, Mo No solid solutions based on binary compounds.	[230, 298]

(continued)

Table 7.5 (continued)

System	Type of phase diagram (temperature and composition sections, constituent phases or phase fields) and/or character of interphase interaction and materials compatibility	References
Mo–B–Ni	Plotted partially at 800–1200 °C: ω-Mo_2NiB_2 (<1800 °C), $Mo_{7-x}Ni_{2+y}B_{7+z}$ ($0.2 \le x \le 0.6$, $0 \le y \le 0.4$, $z \approx 0.2$, Y-phase), $Mo_3Ni_6B_{11}$, Mo_2NiB_4 (?), Mo_3NiB_6 (?), Ni_3B (<1156 °C), Ni_2B (<1125 °C), α-Ni_4B_{3-x} (or o-Ni_4B_3, <1025 °C), β-Ni_4B_{3+x} (or m-Ni_4B_3, <1031 °C), NiB (<1035 °C), β-$Ni_{4+x}Mo$, γ-$Ni_{3+x}Mo$, δ-$NiMo_{1-x}$, MoB_{4-x}, Mo_2B_{5-x}, MoB_{2-x}, α-$MoB_{1\pm x}$, β-$MoB_{1\pm x}$, $Mo_{2\pm x}B$, β-B, Ni, Mo Eutectic Ni–δ-$NiMo_{1-x}$–ω-Mo_2NiB_2 (~1160–1230 °C, ~56.5–59 at.% Ni, ~30.5–33 at.% Mo) Eutectic Ni–Ni_3B–ω-Mo_2NiB_2 (~1075–1090 °C, ~71.5–72 at.% Ni, ~6–9 at.% Mo) The mutual solubilities between ternary and binary phases are low. α-$MoB_{1\pm x}$ is in equilibrium with α-Ni_4B_{3-x}, β-Ni_4B_{3+x} and Ni_2B. Ni stabilizes β-$MoB_{1\pm x}$. The interaction between Mo_2B_{5-x} and Ni leads to the formation of α-$MoB_{1\pm x}$ and NiB.	[21, 32, 210, 218–222, 262, 265]
Mo–B–O–Zr	No diagram plot In vacuum, at temp. >1100 °C the interaction between Mo_2B_{5-x} and ZrO_2 leads to the formation of Mo borides with lower B content and $ZrB_{2\pm x}$.	[21]
Mo–B–Os	See Os–B–Mo in Table 5.4.	
Mo–B–P	Plotted at 800 °C: Mo_5PB_2, $Mo_3(P,B)$ (extended solid solution based on Mo_3P—up to ~$Mo_3(P_{0.5}B_{0.5})$ compos.), $Mo(B,P)_{2-x}$ (extended solid solution based on MoB_{2-x}—up to ~$Mo(B_{0.85}P_{0.15})_{2-x}$ compos.), α-$Mo(B,P)_{1\pm x}$ (solid solution based on α-$MoB_{1\pm x}$—up to ~$Mo(B_{0.9}P_{0.1})_{1\pm x}$ compos.), $Mo_{2\pm x}(B,P)$ (solid solution based on $Mo_{2\pm x}B$—up to ~$Mo_{2\pm x}(B_{0.9}P_{0.1})$ compos.), PB_{14}, PB_6, α-PB (<825 °C), β-PB (>825 °C), MoB_{4-x}, Mo_2B_{5-x}, β-$MoB_{1\pm x}$, Mo_3B_2, MoP_2, MoP, Mo_4P_3, Mo_8P_5, $Mo_{2-x}P$, P, β-B, Mo The solubilities of Mo in PB_6 and PB, and those of B in MoP_2, MoP and Mo_4P_3 have been discovered to be low.	[211, 299]
Mo–B–Pr	Plotted at 600/800 °C: no ternary compounds, Pr_2B_5 (or PrB_x, $x \approx 2.5$–2.6, <~2000 °C), PrB_4 (<~2350 °C), $PrB_{6\pm x}$ (<2610 °C), MoB_{4-x}, Mo_2B_{5-x}, MoB_{2-x}, α-$MoB_{1\pm x}$, β-$MoB_{1\pm x}$, Mo_3B_2, $Mo_{2\pm x}B$, β-B, α-Pr, β-Pr, Mo No solid solutions based on binary compounds.	[230, 298]

(continued)

Table 7.5 (continued)

System	Type of phase diagram (temperature and composition sections, constituent phases or phase fields) and/or character of interphase interaction and materials compatibility	References
Mo–B–Re	See Re–B–Mo in Table 4.6.	
Mo–B–Rh	No diagram plot. $MoRhB_{\sim 9}$	[262]
Mo–B–Ru	No diagram plot $MoRu_2B_4$, $(Mo,Ru)_3B_2$ (or Mo_2RuB_2, or $Mo_{1.5}Ru_{1.5}B_2$), $(Mo_{0.5}Ru_{0.5})B$ (or $MoRuB_2$), $(Mo,Ru)B_2$	[262, 268]
Mo–B–Si	Plotted at 1600 and 1800 °C: Mo_5SiB_2, $Mo_5Si_{3\pm x}B_z$ (or $Mo_{5+y}Si_{3-y}B_z$, $0 \le z \le \sim 0.16$, $-0.08 \le y \le 0.04$), SiB_n ($n \approx 23$, <2040 °C), SiB_6 (<1850 °C), $SiB_{3\pm x}$ (<1270 °C), α-$MoSi_2$, β-$MoSi_2$, Mo_3Si, MoB_{4-x}, Mo_2B_{5-x}, MoB_{2-x}, α-$MoB_{1\pm x}$, β-$MoB_{1\pm x}$, Mo_3B_2, $Mo_{2\pm x}B$, β-B, Si, Mo	[195–198, 215, 300–301]
Mo–B–Si–Ta	See Ta–B–Mo–Si in Table 6.4.	
Mo–B–Si–Zr	No diagram plot $Mo_5Si_{3\pm x}$ reacts with $ZrB_{2\pm x}$ at temp. ≥2000 °C, and $MoSi_2$—at temp. ≥1800 °C.	[21, 32]
Mo–B–Sm	Plotted at 800 °C: no ternary compounds, Sm_2B_5 (<~2000 °C), SmB_4 (<~2400 °C), $SmB_{6\pm x}$ (<2580 °C), SmB_{66} (<2150 °C), MoB_{4-x}, Mo_2B_{5-x}, MoB_{2-x}, α-$MoB_{1\pm x}$, β-$MoB_{1\pm x}$, Mo_3B_2, $Mo_{2\pm x}B$, α-Sm, β-Sm, γ-Sm, β-B, Mo No solid solutions based on binary compounds.	[230, 298]
Mo–B–Ta	See Ta–B–Mo in Table 6.4.	
Mo–B–Tb	Plotted at 1000 °C: $TbMoB_4$, Tb_3MoB_7, ~$TbMo_4B_8$, $TbMo_3B_7$ (?), $(Mo,Tb)B_{2-x}$ (solid solution based on MoB_{2-x}, ?), TbB_2 (<~2100 °C), TbB_4 (<~2600 °C), $TbB_{6\pm x}$ (<2340 °C), TbB_{12} (<2200 °C), TbB_{66} (<~2100 °C), MoB_{4-x}, Mo_2B_{5-x}, α-$MoB_{1\pm x}$, β-$MoB_{1\pm x}$, Mo_3B_2, $Mo_{2\pm x}B$, β-B, α-Tb, β-Tb, Mo No solid solutions based on binary compounds apart from $(Mo,Tb)B_{2-x}$ stabilized by Tb.	[216, 230, 262]
Mo–B–Th	No diagram plot $ThMoB_4$	[262, 269]

(continued)

Table 7.5 (continued)

System	Type of phase diagram (temperature and composition sections, constituent phases or phase fields) and/or character of interphase interaction and materials compatibility	References
Mo–B–Ti	Plotted at 1200 °C (partially), 1400 and 1950 °C (partially): $MoTi_2B_4$ (?), $MoTiB_4$ (?), Mo_2TiB_2 (?), α-$MoB_{1\pm x}$ (solubility of Ti—up to ~5–6 at.% at 1400 °C), β-$(Mo,Ti)B_{1\pm x}$ (extended solid solution based on β-$MoB_{1\pm x}$, stabilized by Ti at lower temp., homog. range—~15–30 at.% Ti at 1400 °C, ?), $(Ti,Mo)B_{1-x}$ (extended solid solution based on TiB_{1-x}—up to ~10 at.% Mo at 1400 °C, <~2180–2200 °C), $TiB_{2\pm x}$ (solubility of Mo—up to ~3.5 at.% at 1400 °C, <3200–3250 °C), Ti_3B_4 (<~2200–2205 °C), MoB_{4-x}, Mo_2B_{5-x}, MoB_{2-x}, Mo_3B_2, $Mo_{2\pm x}B$, β-B, α-Ti, (β-Ti,Mo) At 1400 °C the solubilities of Ti in Mo borides (apart from $MoB_{1\pm x}$) are low: for $Mo_{2\pm x}B$—≤5 at.%, for Mo_2B_{5-x}—≤4 at.% and for MoB_{4-x}—≤2 at.%. $TiB_{2\pm x}$–Mo is plotted: $MoTi_2B_4$ (or $MoTiB_4$ (?), <3050 °C, congruent melt. point, invariable compos.), Mo_2TiB_2 (<2680 °C, incongruent melt. point, invariable compos., ?); $TiB_{2\pm x}$–$MoTi_2B_4$ eutectic—2800 °C (?), Mo_2TiB_2–Mo eutectic—2000 °C (?), the solubility of $TiB_{2\pm x}$ in Mo is <5 mol.% and that of Mo in $TiB_{2\pm x}$ is inconsiderable. In vacuum the interaction between Mo and $TiB_{2\pm x}$ initiates from 1300 to 1400 °C (5 h exposure); the products of contact interaction are $Mo_{2\pm x}B$ at 1300 °C, TiB_{1-x} + $Mo_{2\pm x}B$ at 1400 °C, TiB_{1-x} + α-$MoB_{1\pm x}$ at 1500–2000 °C and TiB_{1-x} + β-$MoB_{1\pm x}$ at 1950–2050 °C.	[5, 11, 21, 188, 302, 338]
Mo–B–Tm	Plotted at 1000 °C: $TmMoB_3$, $TmMo_3B_7$, Tm_2MoB_6, $(Tm,Mo)B_2$ (solid solution based on TmB_2 up to compos. $(Tm_{0.95}Mo_{0.05})B_2$, <2250 °C), TmB_{66} (<2100 °C), TmB_{12} (<2180 °C), TmB_4 (<2550 °C), MoB_{4-x}, Mo_2B_{5-x}, MoB_{2-x}, α-$MoB_{1\pm x}$, β-$MoB_{1\pm x}$, Mo_3B_2, $Mo_{2\pm x}B$, β-B, Tm, Mo No solid solutions based on binary and ternary compounds apart from a low solubility of Mo in TmB_2.	[20, 213, 216]
Mo–B–U	Plotted at 1000 °C: $UMoB_4$, U_2MoB_6, UMo_2B_6, UMo_4B_4, $U_5Mo_{10}B_{24}$ (?), UB_{12} (<2145 °C), UB_4 (<2495 °C), UB_2 (<2385 °C), MoB_{4-x}, Mo_2B_{5-x}, MoB_{2-x}, α-$MoB_{1\pm x}$, β-$MoB_{1\pm x}$, Mo_3B_2, $Mo_{2\pm x}B$, $MoU_{2\pm x}$, β-B, α-U, β-U, γ-U, Mo No solid solutions based on binary and ternary compounds.	[262, 270, 303–304]

(continued)

Table 7.5 (continued)

System	Type of phase diagram (temperature and composition sections, constituent phases or phase fields) and/or character of interphase interaction and materials compatibility	References
Mo–B–V	Plotted at 1400 °C: no ternary compounds, $(V,Mo)_3B_2$ (extended solid solution based on V_3B_2—up to $\sim(V_{0.25}Mo_{0.75})_3B_2$ compos., $<\sim$1900–1915 °C), (V,Mo)B (extended solid solution based on VB—up to $\sim(V_{0.25}Mo_{0.75})B$ compos., $<\sim$2550–2570 °C), $(V,Mo)_3B_4$ (extended solid solution based on V_3B_4—up to $\sim(V_{0.45}Mo_{0.55})_3B_4$ compos., $<\sim$2600–2615 °C), $(V,Mo)B_{2\pm x}$ (extended solid solution based on $VB_{2\pm x}$—up to $\sim(V_{0.45}Mo_{0.55})B_{2\pm x}$ compos., <2700–2750 °C), α-$(Mo,V)B_{1\pm x}$ (extended solid solution based on α-$MoB_{1\pm x}$—up to $\sim (Mo_{0.85}V_{0.15})B_{1\pm x}$ compos.), $(Mo,V)_{2\pm x}B$ (solid solution based on $Mo_{2\pm x}B$—up to $\sim (Mo_{0.9}V_{0.1})_{2\pm x}B$ compos.), V_5B_6 ($<\sim$1725–2560 °C), V_2B_3 ($<\sim$2610–2665 °C), MoB_{4-x}, Mo_2B_{5-x}, MoB_{2-x}, β-$MoB_{1\pm x}$, Mo_3B_2, β-B, (V,Mo) The solubilities of Mo in V borides are higher noticeably than those of V in Mo borides.	[262, 305]
Mo–B–W	See W–B–Mo in Table 3.6.	
Mo–B–Y	Plotted at 1000 °C: $YMoB_4$, YMo_3B_7 (?), Y_3MoB_7 (?), $(Y,Mo)B_2$ (solid solution based on YB_2, <2100 °C), YB_{66} (<2100 °C), YB_{12} (<2200 °C), $YB_{6\pm x}$ (<2600 °C), YB_4 (<2800 °C), MoB_{4-x}, Mo_2B_{5-x}, MoB_{2-x}, α-$MoB_{1\pm x}$, β-$MoB_{1\pm x}$, Mo_3B_2, $Mo_{2\pm x}B$, β-B, α-Y, β-Y, Mo No solid solutions based on binary and ternary compounds apart from a low solubility of Mo in YB_2; it dissolves up to 5 at.% Mo.	[20, 216, 227–228, 262]
Mo–B–Yb	No diagram plot Yb_2MoB_6	[213]

(continued)

Table 7.5 (continued)

System	Type of phase diagram (temperature and composition sections, constituent phases or phase fields) and/or character of interphase interaction and materials compatibility	References
Mo–B–Zr	Plotted at 1200–1950 °C: Mo_4Zr_9B, $MoZr_2B_4$ (?), Mo_2ZrB_2 (?), ~Mo_7ZrB_{16} (?), $ZrB_{2\pm x}$ (solubility of Mo is ~3 at.% (?) at 1400 °C, <3220–3265 °C), ZrB_{12-x} (~1695–2290 °C), MoB_{4-x}, Mo_2B_{5-x}, MoB_{2-x}, α-$MoB_{1\pm x}$, β-$MoB_{1\pm x}$, Mo_3B_2, $Mo_{2\pm x}B$, $ZrMo_{2\pm x}$, β-B, α-Zr, β-Zr, Mo $ZrB_{2\pm x}$–Mo is plotted: $MoZr_2B_4$ (<3000 °C, congruent melt. point, invariable compos.), Mo_2ZrB_2 (<2850 °C, congruent melt. point, invariable compos.); $ZrB_{2\pm x}$–$MoZr_2B_4$ eutectic—2650 °C, Mo_2ZrB_2–$MoZr_2B_4$ eutectic—~2450 °C, Mo_2ZrB_2–Mo eutectic—1850 °C, (or $ZrB_{2\pm x}$–Mo eutectic—~2050–2060 °C, ~73 mol.% Mo, ?); the solubility of $ZrB_{2\pm x}$ in Mo is <5 mol.% and that of Mo in $ZrB_{2\pm x}$ is inconsiderable. No solid solutions based on binary and ternary compounds. Phase diagram data available in literature are controversial. In vacuum the interaction between $ZrB_{2\pm x}$ and Mo initiates from 1200 °C (5 h exposure) and leads to the formation of boride solid solution in the contact zone.	[5, 11, 21, 35, 51, 188, 208, 226, 262, 306–308]
Mo–Be–O	No diagram plot In vacuum the interaction between Mo and BeO initiates from 1700–1900 °C and leads to the formation of Mo beryllides; at higher temp. it is characterized by the vaporization of the volatile products of reaction.	[5, 11, 31]
Mo–Be–Nb	No diagram plot α/β-(Mo,Nb)Be_2 ($MoBe_2$–$NbBe_2$ continuous solid solution, ?)	[312]
Mo–Bi–Pb	No diagram plot Mo is resistant to corrosion in molten Bi–Pb alloys at temp. ≤800–1000 °C. At 1095 °C in the dynamic conditions, the Bi–Pb eutectic alloy (55 at.% Bi) penetrates into sintered Mo intensively.	[5]
Mo–Bi–Cd–Pb–Sn	No diagram plot Mo is highly resistant to Wood's metal (Bi-26.7Pb-13.3Sn-10Cd) at temp. ≤600 °C.	[5]
Mo–C–Ce	See C–Ce–Mo in Table 2.14.	
Mo–C–Co	See C–Co–Mo in Table 2.14.	
Mo–C–Cr	See C–Cr–Mo in Table 2.14.	

(continued)

Table 7.5 (continued)

System	Type of phase diagram (temperature and composition sections, constituent phases or phase fields) and/or character of interphase interaction and materials compatibility	References
Mo–C–Cr–Fe	See C–Cr–Fe–Mo in Table 2.14.	
Mo–C–Cr–Re–Ti	See C–Cr–Mo–Re–Ti in Table 2.14.	
Mo–C–Cr–Ti	See C–Cr–Mo–Ti in Table 2.14.	
Mo–C–Fe	See C–Fe–Mo in Table 2.14.	
Mo–C–Ga	See C–Ga–Mo in Table 2.14.	
Mo–C–Hf	See C–Hf–Mo in Table 2.14.	
Mo–C–Hf–Ni	See C–Hf–Mo–Ni in Table 2.14.	
Mo–C–Hf–Si	See C–Hf–Mo–Si in Table 2.14.	
Mo–C–Hf–Ti	See C–Hf–Mo–Ti in Table 2.14.	
Mo–C–Hf–V	See C–Hf–Mo–V in Table 2.14.	
Mo–C–Ir	See C–Ir–Mo in Table 2.14.	
Mo–C–Mg–O	See C–Mg–Mo–O in Table 2.14.	
Mo–C–Mn	See C–Mn–Mo in Table 2.14.	
Mo–C–N	See C–Mo–N in Table 2.14.	
Mo–C–N–Ti	See C–Mo–N–Ti in Table 2.14.	
Mo–C–Nb	See C–Mo–Nb in Table 2.14.	
Mo–C–Nb–Ta	See C–Mo–Nb–Ta in Table 2.14.	
Mo–C–Nb–U	See C–Mo–Nb–U in Table 2.14.	
Mo–C–Nb–Zr	See C–Mo–Nb–Zr in Table 2.14.	
Mo–C–Ni	See C–Mo–Ni in Table 2.14.	
Mo–C–O	See C–Mo–O in Table 2.14.	
Mo–C–O–Zr	See C–Mo–O–Zr in Table 2.14.	
Mo–C–Os	See C–Mo–Os in Table 2.14.	
Mo–C–Pt	See C–Mo–Pt in Table 2.14.	
Mo–C–Pu	See C–Mo–Pu in Table 2.14.	
Mo–C–Pu–U	See C–Mo–Pu–U in Table 2.14.	
Mo–C–Re	See C–Mo–Re in Table 2.14.	
Mo–C–Rh	See C–Mo–Rh in Table 2.14.	
Mo–C–Ru	See C–Mo–Ru in Table 2.14.	
Mo–C–Sc	See C–Mo–Sc in Table 2.14.	
Mo–C–Si	See C–Mo–Si in Table 2.14.	
Mo–C–Si–Ta	See C–Mo–Si–Ta in Table 2.14.	
Mo–C–Si–Zr	See C–Mo–Si–Zr in Table 2.14.	
Mo–C–Ta	See C–Mo–Ta in Table 2.14.	
Mo–C–Ta–V	See C–Mo–Ta–V in Table 2.14.	
Mo–C–Tc	See C–Mo–Tc in Table 2.14.	
Mo–C–Th	See C–Mo–Th in Table 2.14.	
Mo–C–Ti	See C–Mo–Ti in Table 2.14.	
Mo–C–U	See C–Mo–U in Table 2.14.	
Mo–C–U–Zr	See C–Mo–U–Zr in Table 2.14.	
Mo–C–V	See C–Mo–V in Table 2.14.	
Mo–C–W	See C–Mo–W in Table 2.14.	
Mo–C–W–Zr	See C–Mo–W–Zr in Table 2.14.	

(continued)

Table 7.5 (continued)

System	Type of phase diagram (temperature and composition sections, constituent phases or phase fields) and/or character of interphase interaction and materials compatibility	References
Mo–C–Zr	See C–Mo–Zr in Table 2.14.	
Mo–Ca–O	Plotted at temp. up to 1100 °C: $CaMo_6O_9$, $Ca_5Mo_{18}O_{29}$, $Ca_8Mo_7O_{20}$, ~$Ca_5Mo_4O_{12}$ (or $Ca_{1.24}Mo_{1.01}O_3$), ~$Ca_4Mo_{13}O_{21}$ (or $CaMo_{3.2}O_{5.3}$), $CaMoO_3$ (or $CaO{\cdot}MoO_2$), $Ca_5Mo_3O_{12}$ (or $5CaO{\cdot}2MoO_2{\cdot}MoO_3$), $CaMoO_4$ (or $CaO{\cdot}MoO_3$), CaO (<2585–2645 °C), β-$MoO_{2\pm x}$, MoO_3, O, Ca, Mo MoO_3–CaO is plotted: MoO_3, $CaMoO_4$ (<1440–1450 °C), Ca_3MoO_6 (or $3CaO{\cdot}MoO_3$, 1270–1370 °C), CaO; MoO_3–$CaMoO_4$ eutectic—~725–730 °C, ~81–88 mol.% MoO_3; Ca_3MoO_6–$CaMoO_4$ eutectic—1320–1330 °C, 40 mol.% MoO_3	[236, 240–243]
Mo–Ce–O	No general diagram plot β-$2CeO_2{\cdot}3MoO_3$ (or β-$Ce_2Mo_3O_{13}$), $¾Ce_2O_3{\cdot}½CeO_2{\cdot}3MoO_3$ (or $Ce_2Mo_3O_{12.25}$) MoO_3–Ce_2O_3 is partially plotted: MoO_3, α-$Ce_2O_3{\cdot}4MoO_3$ (or α-$Ce_2Mo_4O_{15}$, <673 °C), β-$Ce_2O_3{\cdot}4MoO_3$ (or β-$Ce_2Mo_4O_{15}$, 673–802 °C), $Ce_2O_3{\cdot}3MoO_3$ (or $Ce_2(MoO_4)_3$, <1035 °C); MoO_3–β-$Ce_2Mo_4O_{15}$ eutectic—682 °C, 86 mol.% MoO_3	[244]
Mo–Co–N	No diagram plot $Mo_3Co_7N_4$, Mo_3Co_2N, $Mo_8Co_2N_9$ (or $Mo_{0.8}Co_{0.2}N_{0.9}$), Mo_3Co_3N, ?	[28, 309]
Mo–Co–Nb	Plotted at 900 °C: λ_3-Co_3(Nb,Mo) (~1000–1240 °C, extended solid solution based on λ_3-Co_3Nb), $\lambda_2(\alpha)$-Co_2(Nb,Mo)$_{1\pm x}$ (<~1200 °C, extended solid solution based on $\lambda_2(\alpha)$-$Co_2Nb_{1\pm x}$), $\lambda_2(\beta)$-$Co_2Nb_{1\pm x}$ (from 1200 to ~1480–1520 °C), χ-$Co_7Nb_{2\pm x}$ (<1050 °C), λ_1-Co_5Nb_{3-x} (~1200–1420 °C), μ-$CoNb_{1\pm x}$ (<1480 °C), κ-Co_3(Mo,Nb)$_{1\pm x}$ (extended solid solution based on κ-$Co_3Mo_{1\pm x}$), μ-Co_7(Mo,Nb)$_{6\pm x}$ (extended solid solution based on μ-$Co_7Mo_{6\pm x}$), θ-Co_9Mo_{2+x}, σ-Co_2Mo_{3+x}, ε-Co, α-Co, (Mo,Nb)	[15, 18, 37]
Mo–Co–Ta	See Ta–Co–Mo in Table 6.4.	
Mo–Co–W	See W–Co–Mo in Table 3.6.	
Mo–Cr–N	Plotted at 1000 °C (pressure $N_2 \leq 30$ MPa): (Mo,Cr)N_{1-x} (γ-$Mo_{2\pm x}N$–CrN_{1-x} continuous solid solution, <~1050–2010 °C), $(Cr,Mo)_{2+x}N$ (extended solid solution based on $Cr_{2+x}N$—up to compos. ~$(Cr_{0.3}Mo_{0.7})_{2+x}N$, <1740–1800 °C), CrN_2 (<~700 °C), N, (Mo,Cr)	[28]

(continued)

Table 7.5 (continued)

System	Type of phase diagram (temperature and composition sections, constituent phases or phase fields) and/or character of interphase interaction and materials compatibility	References
Mo–Cr–Nb	Plotted at 1350 and 1500 °C: Mo–Nb–Cr continuous solid solution based on Mo–Nb and Mo–Cr continuous solid solutions (miscibility gap is adjoined to Nb–Cr side and located around the intermetallic phase field), λ_2-(Nb,Mo)$Cr_{2\pm x}$ (extended solid solution based on $NbCr_{2\pm x}$ with compos.—up to 15 at.% Mo, <1585–1625 °C), λ_1-(Nb,Mo)$Cr_{2\pm x}$ (from 1585–1625 °C to ~1670–1820 °C), (Mo,Nb,Cr)	[45, 199]
Mo–Cr–Si–Ta	See Ta–Cr–Mo–Si in Table 6.4.	
Mo–Cr–Si–W	See W–Cr–Mo–Si in Table 3.6.	
Mo–Cr–Ta	See Ta–Cr–Mo in Table 6.4.	
Mo–Cr–W	See W–Cr–Mo in Table 3.6.	
Mo–Cu–Nb	Plotted at 1900 and 2100 °C: no ternary compounds, miscibility gap in the liquid state, Cu, (Nb,Mo)	[313]
Mo–Fe–N	Plotted partially at 125–450 °C: $Mo_3Fe_7N_4$, η-Mo_3Fe_3N, $Mo_7Fe_6N_2$, $Mo_{13}Fe_7N_4$ (or $Mo_{3.25}Fe_{1.75}N$), ξ-$Fe_{2\pm x}N$ (<500 °C), ε-(Fe,N), γ'-$Fe_{4+x}N$ (<680 °C), Fe_8N, δ-MoN, Mo_3N_2, γ-$Mo_{2\pm x}N$, β-$Mo_{2\pm x}N$, λ-Fe_2Mo, ρ-Fe_3Mo_{2-x}, μ-Fe_7Mo_{6-x}, σ-$FeMo_{1\pm x}$, N, α-Fe, γ-Fe, Mo	[28, 310]
Mo–Fe–Nb	Plotted at 900 °C: Fe_2(Mo,Nb) (λ-Fe_2Mo–ε-$Fe_{2\pm x}Nb$ Laves phase continuous solid solution, <~900–1665 °C), μ-Fe_7(Nb,Mo)$_{6+x}$ (extended solid solution based on μ-Fe_7Nb_{6+x}, <~1620–1690 °C), μ-Fe_7(Mo,Nb)$_{6-x}$ (extended solid solution based on μ-Fe_7Mo_{6-x}), ρ-Fe_3Mo_{2-x}, σ-$FeMo_{1\pm x}$, α-Fe, γ-Fe, (Mo,Nb)	[15, 18, 37, 60]
Mo–Fe–Ta	See Ta–Fe–Mo in Table 6.4.	
Mo–Fe–W	See W–Fe–Mo in Table 3.6.	
Mo–H–Ta	See Ta–H–Mo in Table 6.4.	
Mo–Hf–N	Plotted at 900–1900 °C: $(Hf,Mo)_yN_z$ (pressure N_2 – 3 MPa, ?), (Hf,Mo)$N_{1\pm x}$ (solid solution based on $HfN_{1\pm x}$, homog. range: ~$(Hf_{0.95}Mo_{0.05})N_{0.95}$ ~$(Hf_{0.95}Mo_{0.05})N_{0.65}$–~$HfN_{0.7}$– ~$HfN_{1.0}$, <~3200 °C), α-$HfMo_{2\pm x}$, β-$HfMo_{2\pm x}$, N, α-Hf, β-Hf, Mo $HfN_{1\pm x}$–Mo is plotted: eutectic—~2360–2470 °C, ~82–97 mol.% Mo; at the eutectic temp. the solid solubility of Mo in $HfN_{1\pm x}$ is ~3–15 mol.% (?) and that of $HfN_{1\pm x}$ in Mo is 0.4 mol.% Some data on the system available in literature are controversial.	[21, 28, 36, 225]

(continued)

Table 7.5 (continued)

System	Type of phase diagram (temperature and composition sections, constituent phases or phase fields) and/or character of interphase interaction and materials compatibility	References
Mo–Hf–Nb	Plotted at 1500 and 1800 °C: no ternary compounds, α-$HfMo_{2\pm x}$, β-$HfMo_{2\pm x}$, (α-Hf,Nb,Mo) (extended solid solution based on α-Hf), (β-Hf,Nb,Mo) (extended solid solution based on Mo–Nb and β-Hf–Nb continuous solid solutions with extended miscibility gap adjoined to Hf–Mo side)	[314]
Mo–Hf–O–Re	See Re–Hf–Mo–O in Table 4.6.	
Mo–K–Na	No diagram plot Mo is highly resistant to corrosion in Na–K alloys at temp. ≤1000 °C.	[5]
Mo–Mg–O	Mo–MoO_3–MgO is schematically plotted at 830–1130 °C: $MgO{\cdot}MoO_3$ (or $MgMoO_4$), $2MgO{\cdot}3MoO_3$ (or $Mg_2Mo_3O_8$), β-$MoO_{2\pm x}$, MgO (<2805–2860 °C), MoO_3, Mo MoO_3–MgO is partially plotted: MoO_3, β-$MgO{\cdot}2MoO_3$ (or β-$MgMo_2O_7$, <840 °C), α-$MgO{\cdot}2MoO_3$ (or α-$MgMo_2O_7$, 840–860 °C), $MgO{\cdot}MoO_3$ (or $MgMoO_4$, <~1300 °C), MgO; MoO_3–β-$MgMo_2O_7$ eutectic—750 °C, 85 mol.% MoO_3 In vacuum the interaction between Mo and MgO initiates from 1600–2000 °C; these components are compatible with each other at temp. ≤2100 °C.	[5, 11, 31, 238–239]
Mo–Mg–Pu	No diagram plot At 1150 °C Mo is resistant to corrosion in molten Mg–Pu alloys.	[5]
Mo–Mg–U	No diagram plot At 1150 °C Mo is resistant to corrosion in molten Mg–U alloys.	[5]
Mo–N–Nb	Plotted at 1100 °C (pressure N_2 ≤ 30 MPa): $NbMoN_{1-x}$ (Z-phase), γ-$(Mo,Nb)_{2\pm x}N$ (extended solid solution based on γ-$Mo_{2\pm x}N$—up to compos. ~$(Mo_{0.7}Nb_{0.3})_{2\pm x}N$), β-$Nb_{2\pm x}N$ (<~2350–2430 °C), Nb_4N_{3+x} (<2200 °C), ε-$NbN_{1\pm x}$ (<~1310–1360 °C), δ-$NbN_{1\pm x}$ (~1310–2200 °C), N, (Mo,Nb) The solubility of Mo in Nb nitrides is low. At 2000 °C (pressure N_2 – 0.1 MPa) γ-$Mo_{2\pm x}N$ dissolves inconsiderable amount of Nb.	[28]
Mo–N–Ni	No diagram plot $Mo_3Ni_7N_4$, Mo_3Ni_2N, ?	[28]
Mo–N–Re	See Re–Mo–N in Table 3.6.	

(continued)

Table 7.5 (continued)

System	Type of phase diagram (temperature and composition sections, constituent phases or phase fields) and/or character of interphase interaction and materials compatibility	References
Mo–N–Si	Plotted at 1000 and 1400 °C (under Ar pressure): α-$MoSi_2$, $Mo_5Si_{3\pm x}$, Mo_3Si, Si_3N_4 (<~1900 °C), N, Si, Mo $Mo_5Si_{3\pm x}$ and α-$MoSi_2$ are in equilibrium with Si_3N_4	[29, 59]
Mo–N–Ta	See Ta–Mo–N in Table 6.4.	
Mo–N–Ti	Plotted at 900–1900 °C: δ-$(Ti,Mo)N_{1\pm x}$ (extended solid solution based on δ-$TiN_{1\pm x}$, homog. range: ~$(Ti_{0.8}Mo_{0.2})N_{0.8}$–~$(Ti_{0.9}Mo_{0.1})N_{0.6}$ – ~$TiN_{0.65}$ –~$TiN_{1.0}$, <3290 °C), ε-$Ti_{2\pm x}N$ (<1100 °C), δ′-TiN_{1-x} (<800 °C), N, α-Ti, (Mo,β-Ti) $TiN_{1\pm x}$–Mo is plotted: eutectic—~2350 °C, ~94–95 mol.% Mo; at the eutectic temp. the solid solubility of Mo in $TiN_{1\pm x}$ is ~3 mol.% and that of $TiN_{1\pm x}$ in Mo is ~1.5 mol.% In vacuum the interaction between $TiN_{1\pm x}$ and bulk metal Mo initiates from 2000 °C (2–5 h exposure); at 2100 °C (5 h exposure) the contact reaction is noticeable, the products of the contact reaction are Mo–N solid solutions.	[5, 11, 21, 32, 224]
Mo–N–U	Plotted at 1200 °C: α-U_2N_{3+x} (<1132 °C), β-U_2N_{3-x} (from 940–1100 to 1352 °C), UN_{1-x} (<2810–2885 °C), N, α-U, β-U, γ-U, Mo UN_{1-x}–Mo is plotted: eutectic—~2400 °C, ~75 mol.% Mo; the mutual solid solubilities of the components are low Mo is in equilibrium with U nitrides (UN_{1-x}, β-U_2N_{3-x}) in the wide range of temp. In vacuum, at 1000 °C the interaction between UN_{1-x} and Mo is weak and the dimension of interaction contact zone amounts to 4 μm (500 h exposure); at 2000 °C— no interaction in N_2 atmosphere, but in vacuum the product of interaction—metal U.	[5, 21, 28, 32, 261]
Mo–N–V	Plotted at 1100 °C (pressure N_2 ≤30 MPa): $(Mo,V)N_{1-x}$ (γ-$Mo_{2\pm x}N$–δ-VN_{1-x} continuous solid solution, <~2010–2340 °C), $(V,Mo)_{2+x}N$ (solid solution based on β-$V_{2+x}N$, <2000 °C), δ′-VN_{1-x} (or δ′-$V_{32}N_{26}$, <520 °C), N, (Mo,V)	[28]
Mo–N–W	See W–Mo–N in Table 3.6.	

(continued)

Table 7.5 (continued)

System	Type of phase diagram (temperature and composition sections, constituent phases or phase fields) and/or character of interphase interaction and materials compatibility	References
Mo–N–Zr	Plotted at 900–1900 °C: $(Zr,Mo)N_{1\pm x}$ (solid solution based on $ZrN_{1\pm x}$, homog. range: ~$(Zr_{0.95}Mo_{0.05})N_{0.95}$–~$(Zr_{0.95}Mo_{0.05})N_{0.65}$–~$ZrN_{0.65}$–~$ZrN_{1.0}$, <2930–3030 °C), $ZrMo_{2\pm x}$, N, α-Zr, β-Zr, Mo $ZrN_{1\pm x}$– Mo is plotted schematically: eutectic—~2400 °C, ~96–97 mol.% Mo; at the eutectic temp. the solid solubility of Mo in $ZrN_{1\pm x}$ is ~3 mol.% and that of $ZrN_{1\pm x}$ in Mo is ~0.7 mol.% In vacuum, the interaction between $ZrN_{1\pm x}$ and compact metal Mo initiates from 2000–2100 °C (5 h exposure) and leads to the formation of N solid solution in Mo.	[5, 11, 21, 32, 223–224]
Mo–Nb–Ni	Plotted at 900 °C: $Ni_{3\pm x}(Nb,Mo)$ (γ-$Ni_{3+x}Mo$–κ-$Ni_{3\pm x}Nb$ continuous solid solution, <~905–1400 °C), μ-$Ni_6(Nb,Mo)_{7-x}$ (extended solid solution based on μ-Ni_6Nb_{7-x}, <1290 °C), ζ-$Ni_{8\pm x}Nb$ (<535 °C), β-$Ni_{4+x}Mo$, δ-$NiMo_{1-x}$, Ni, (Nb,Mo)	[16, 18, 37]
Mo–Nb–O	Plotted partially at 1000–1500 °C: NbO (<1945 °C), NbO_2 (<1915 °C), Nb_2O_5 (<1510 °C), MoO_3, ξ-Mo_9O_{26}, β-Mo_9O_{26}, Mo_8O_{23}, η-Mo_4O_{11}, γ-Mo_4O_{11}, β-$MoO_{2\pm x}$, (Nb,Mo)	[16, 18, 41]
Mo–Nb–P	Plotted partially at 800 °C: no ternary compounds, $(Mo,Nb)_3P$ (extended solid solution based on Mo_3P—up to ~$(Mo_{0.6}Nb_{0.4})_3P$ compos.), $(Nb,Mo)_3P$ (extended solid solution based on Nb_3P—up to ~$(Nb_{0.55}Mo_{0.45})_3P$ compos.), NbP_2 (<~1730 °C), Nb_8P_5, Nb_5P_3, Nb_7P_4, Nb_2P, MoP_2, MoP, Mo_4P_3, Mo_8P_5, $Mo_{2-x}P$, P, (Nb,Mo) No solid solutions based on binary compounds apart from Mo_3P and Nb_3P.	[315]
Mo–Nb–Re	See Re–Mo–Nb in Table 4.6.	

(continued)

Table 7.5 (continued)

System	Type of phase diagram (temperature and composition sections, constituent phases or phase fields) and/or character of interphase interaction and materials compatibility	References
Mo–Nb–Si	Plotted at 800–1800 °C: α-(Mo,Nb)Si_2 (extended solid solution based on α-$MoSi_2$—up to $(Mo_{0.85\div0.95}Nb_{0.05\div0.15})Si_2$), (Nb,Mo)$Si_2$ (extended solid solution based on $NbSi_2$—up to $(Nb_{0.10\div0.34}Mo_{0.66\div0.90})Si_2$), α-(Nb,Mo)$_5Si_{3\pm x}$ ($Mo_5Si_{3\pm x}$—α-Nb_5Si_{3+x} continuous solid solution or extended solid solution based on α-$Nb_5Si_{3\pm x}$), β-(Mo,Nb)$_5Si_{3\pm x}$ ($Mo_5Si_{3\pm x}$–β-$Nb_5Si_{3\pm x}$ continuous solid solution), (Mo,Nb)$_3$Si (extended solid solution based on Mo_3Si—up to $(Mo_{0.69\div0.73}Nb_{0.27\div0.31})_3Si$), Nb_3Si (from 1755–1785 to 1910–2000 °C), Si, (Nb,Mo). Eutectic α-(Mo,Nb)Si_2–(Nb,Mo)Si_2–Si (~1400–1405 °C, 98.1 at.% Si, 1.7 at.% Mo) $MoSi_2$–$NbSi_2$ is plotted: peritectic $NbSi_2$ (~1960–1970 °C, ~85–87 mol.% $MoSi_2$); compos. ~$(Mo_{0.40\div0.65}Nb_{0.35\div0.60})Si_2$ corresp. to congruent melt. point at ~1930–1940 °C At 1500 °C the interaction between $MoSi_2$ and Nb leads to the formation of solid solutions: $MoSi_2$ dissolves ~5 at.% Nb.	[16, 18, 21, 39–40, 42, 200–205]
Mo–Nb–Si–W	See W–Mo–Nb–Si in Table 3.6.	
Mo–Nb–Ta	See Ta–Mo–Nb in Table 6.4.	
Mo–Nb–Ti	Plotted at 600 and 1100 °C: (Mo,Nb,β-Ti) (extended solid solution based on Mo–Nb continuous solid solution at lower temp., or Mo–Nb–β-Ti continuous solid solution at higher temp.), β-Ti, α-Ti, (Mo,Nb)	[16, 18, 232]
Mo–Nb–U	Plotted at 500–1300 °C: no ternary compounds, $MoU_{2\pm x}$, (γ-U,Nb,Mo) (extended solid solution based on Mo–Nb and γ-U–Nb continuous solid solutions with extended miscibility gap adjoined to U–Mo side at higher temp., or extended solid solution based on Mo–Nb continuous solid solution at lower temp.), (β-U,Nb,Mo) (solid solution based on Mo–Nb continuous solid solution), α-U	[316–319, 325]
Mo–Nb–V	Plotted at 1800–2450 °C: Mo–Nb–V continuous solid solution (Mo,Nb,V)	[45]
Mo–Nb–W	See W–Mo–Nb in Table 3.6.	
Mo–Nb–W–Zr	See W–Mo–Nb–Zr in Table 3.6.	
Mo–Nb–Zr	Plotted in the wide range of temp.: no ternary compunds, $ZrMo_{2\pm x}$, (β-Zr,Mo,Nb) (extended solid solution based on Mo–Nb and β-Zr–Nb continuous solid solutions), (α-Zr,Mo,Nb) (extended solid solution based on α-Zr)	[45, 320]

(continued)

Table 7.5 (continued)

System	Type of phase diagram (temperature and composition sections, constituent phases or phase fields) and/or character of interphase interaction and materials compatibility	References
Mo–Ni–Re	See Re–Mo–Ni in Table 4.6.	
Mo–Ni–Ta	See Ta–Mo–Ni in Table 6.4.	
Mo–Ni–W	See W–Mo–Ni in Table 3.6.	
Mo–O–Re	See Re–Mo–O in Table 4.6.	
Mo–O–Si–Zr	No diagram plot At 1700 °C no interaction between α-$MoSi_2$ and ZrO_2.	[32]
Mo–O–Ta	See Ta–Mo–O in Table 6.4.	
Mo–O–Th	No diagram plot α-$Th(MoO_4)_2$, β-$Th(MoO_4)_2$ In vacuum the interaction between Mo and ThO_2 initiates from 1900–2200 °C; these components are compatible with each other at temp. ≤2300 °C.	[5, 11, 31]
Mo–O–U	Plotted at 700–750 °C: $UMoO_5$ (<~1085 °C), $UMoO_6$ (<980 °C), α-UMo_2O_8 (1000–1040 °C), β-UMo_2O_8 (<1000 °C), γ-UMo_2O_8 (?), UMo_7O_{22}, α-$U_3Mo_{20}O_{64}$, β-$U_3Mo_{20}O_{64}$, γ-$U_3Mo_{20}O_{64}$ (or γ-$U_{1.5}Mo_{10}O_{32}$), α-UMo_5O_{16}, β-UMo_5O_{16}, U_2MoO_8, UMo_8O_{26} (or $U_{0.5}Mo_4O_{13}$), $UMo_{10}O_{32}$ (or $U_{0.5}Mo_5O_{16}$, <830 °C), $U_3Mo_{20}O_{64}$ (or $U_{0.75}Mo_5O_{16}$), $U_3Mo_{26}O_{84}$ (or $U_{1.5}Mo_{13}O_{42}$), U_2O_7, α-UO_3, β-UO_3, α-U_3O_8, β-U_3O_8, γ-U_3O_8, U_4O_9 (<1135 °C), UO_{2+x} (<2780–2840 °C), MoO_3, ξ-Mo_9O_{26}, β-Mo_9O_{26}, Mo_8O_{23}, η-Mo_4O_{11}, γ-Mo_4O_{11}, β-$MoO_{2\pm x}$, $MoU_{2\pm x}$, O, α-U, β-U, γ-U, Mo MoO_3–UO_{2+x} is partially plotted: MoO_3, $UMo_{10}O_{32}$, α-UMo_2O_8, β-UMo_2O_8, $UMoO_5$, UO_{2+x}; $UMo_{10}O_{32}$–MoO_3 eutectic—780 °C, ~25 at.% Mo MoO_3–UO_3 is partially plotted: MoO_3, $UMoO_6$, UO_3; $UMoO_6$–MoO_3 eutectic—740 °C, ~88 mol.% MoO_3 In vacuum, no interaction between Mo and UO_{2+x} in solid state (10 min exposure).	[5, 31, 234, 253–260]
Mo–O–W	See W–Mo–O in Table 3.6.	
Mo–O–Y	MoO_3–Y_2O_{3-x} is plotted: MoO_3, $Y_2O_3{\cdot}4MoO_3$ (or $Y_2Mo_4O_{15}$, <830 °C), $Y_2O_3{\cdot}3MoO_3$ (or $Y_2Mo_3O_{12}$, <1310–1325 °C), $Y_2O_3{\cdot}MoO_3$ (or Y_2MoO_6), $2Y_2O_3{\cdot}MoO_3$ (or Y_4MoO_9), α-$3Y_2O_3{\cdot}MoO_3$ (or α-Y_6MoO_{12}), β-$3Y_2O_3{\cdot}MoO_3$ (or β-Y_6MoO_{12}), α-Y_2O_{3-x} (<2325–2350 °C), β-Y_2O_{3-x} (from ~2310–2325 °C to ~2410–2460 °C); MoO_3–$Y_2Mo_4O_{15}$ eutectic—720–740 °C, ~90–93 mol.% MoO_3 Mo and α-Y_2O_{3-x} are compatible with each other at high temp.	[5, 31, 235, 237]

(continued)

Table 7.5 (continued)

System	Type of phase diagram (temperature and composition sections, constituent phases or phase fields) and/or character of interphase interaction and materials compatibility	References
Mo–O–Zr	No diagram plot α'-$Zr(MoO_4)_2$, α-$Zr(MoO_4)_2$, β-$Zr(MoO_4)_2$,? In vacuum the interaction between Mo and ZrO_2 initiates from 1900–2200 °C and leads to the formation of volatile Mo oxides and increase of porosity in the metal-oxide contact zone; these components are compatible with each other at temp. ≤2200 °C. At temp. ≥2300 °C the decomposition of γ-ZrO_{2-x} is observed.	[5, 11, 31, 311]
Mo–Os–Ta	See Os–Mo–Ta in Table 5.4.	
Mo–Os–W	See W–Mo–Os in Table 3.6.	
Mo–Re–Si	See Re–Mo–Si in Table 4.6.	
Mo–Re–Si–W	See W–Mo–Re–Si in Table 3.6.	
Mo–Re–Ta	See Re–Mo–Ta in Table 4.6.	
Mo–Re–V	See Re–Mo–V in Table 4.6.	
Mo–Re–W	See W–Mo–Re in Table 3.6.	
Mo–Ru–Ta	See Ta–Mo–Ru in Table 6.4.	
Mo–S–W	See W–Mo–S in Table 3.6.	
Mo–Si–Ta	See Ta–Mo–Si in Table 6.4.	
Mo–Si–Ta–Ti	See Ta–Mo–Si–Ti in Table 6.4.	
Mo–Si–Ta–W	See W–Mo–Si–Ta in Table 3.6.	
Mo–Si–Ti	$MoSi_2$–$TiSi_2$ is plotted: β-$(Mo_yTi_{1-y})Si_2$ ($0.07 \div 0.45 \leq y \leq 0.6 \div 0.85$ at 1300 °C, extended solid solution based on β-$MoSi_2$, ?), $(Ti,Mo)Si_2$ (solid solution based on $TiSi_2$—up to compos. $(Ti_{0.9 \div 0.95}Mo_{0.05 \div 0.1})Si_2$), α-$MoSi_2$ (the solubility of $TiSi_2$ is inconsiderable); peritectic β-$(Mo_yTi_{1-y})Si_2$ (~1800–1850 °C, ~85 mol.% $MoSi_2$, ?), peritectic $(Ti,Mo)Si_2$ (~1500–1525 °C, ~5–10 mol.% $MoSi_2$) At 900–1300 °C the interaction kinetics between $MoSi_2$ and compact metal Ti is slow. Data on the system available in literature are controversial.	[21, 39–40]
Mo–Si–Ti–W	See W–Mo–Si–Ti in Table 3.6.	
Mo–Si–V–W	See W–Mo–Si–V in Table 3.6.	
Mo–Si–W	See W–Mo–Si in Table 3.6.	
Mo–Ta–Ti	See Ta–Mo–Ti in Table 6.4.	
Mo–Ta–W	See W–Mo–Ta in 3.6.	
Mo–Ti–W	See W–Mo–Ti in Table 3.6.	
Mo–V–W	See W–Mo–V in Table 3.6.	
Mo–W–Zr	See W–Mo–Zr in Table 3.6.	

[a] See notes to Table 7.4

The character of chemical interaction and general reactions of molybdenum with common chemicals (solids, liquids, aqueous solutions) and complex gases are summarized in Table 7.6.

Table 7.6 The interaction of molybdenum with some chemicals and complex gases [5, 11, 14, 23–24, 45, 53][a]

Reagent, formula	Character of chemical interaction, examples of general reactions
Air, $N_2 + O_2$	Mo is stable at room temp. in air, the oxidation initiates from 350–500 °C and leads to the formation of Mo_4O_{11}, Mo_8O_{23} and Mo_9O_{26}: $8Mo + 11O_2 \rightarrow 2Mo_4O_{11}$; $16Mo + 23O_2 \rightarrow 2Mo_8O_{23}$; $18Mo + 26O_2 \rightarrow 2Mo_9O_{26}$; at higher temp. MoO_3 is formed: $2Mo + 3O_2 \rightarrow 2MoO_3$. The intensive oxidation of Mo at air begins from 800–850 °C and leads to a marked loss of material by the vaporization of oxides.
Water, H_2O	At the ambient temp. the interaction is weak, at temp. >400–500 °C MoO_3 is formed: $Mo + 3H_2O \rightarrow MoO_3 + 3H_2$. Mo is resistant to corrosion in water vapour at temp. <700 °C. At 1100–1700 °C the oxidation of Mo in the presence of water vapour is severe and accompanied with the more intensive vaporization of $(MoO_3)_n$, which also interacts with the formation of the volatile products: $MoO_3 + H_2O \leftrightarrow MoO_2(OH)_2$, while the metal is covered by MoO_2 scale.
Nitrogen oxides, NO, NO_2	At 400–500 °C the interaction results in the oxidation of Mo: $2Mo + 6NO \rightarrow 2MoO_3 + 3N_2$, $4Mo + 6NO_2 \rightarrow 4MoO_3 + 3N_2$.
Sulphur dioxide, SO_2	At 700–800 °C the interaction between Mo and SO_2 leads to the formation of Mo oxides and S released: $2Mo + 3SO_2 \rightarrow 2MoO_3 + 3S$.
Carbon monoxide, CO	At 200 °C and CO pressures in the range of 20–25 MPa carbonyl $Mo(CO)_6$ is formed. At lower CO pressures the interaction initiates at 800–1400 °C and leads to the formation of Mo carbides and oxides (some data available in literature are controversial).
Carbon dioxide, CO_2	The interaction initiates at temp. >1100–1200 °C and leads to the formation of Mo oxides.
Hydrogen sulfide, H_2S	At temp. 700–1200 °C the interaction between Mo and H_2S leads to the formation of Mo sulfides: $2Mo + (3 - x)H_2S \rightarrow Mo_2S_{3-x} + (3 - x)H_2$.
Hydrocarbons, CH_n	The interaction between Mo and hydrocarbons initiates from 1100–1200 °C and leads to the formation of Mo carbides, at 1400–1600 °C the interaction is very intensive.

(continued)

Table 7.6 (continued)

Reagent, formula	Character of chemical interaction, examples of general reactions
Ammonia (gas), NH_3	The interaction between Mo and NH_3 leads to the formation of γ-$Mo_{2\pm x}N$ (at 400–1100 °C): $4Mo + 2NH_3 \rightarrow 2Mo_2N + 3H_2$, and/or δ-MoN (at 400–700 °C): $2Mo + 2NH_3 \rightarrow 2MoN + 3H_2$, the latter decomposes at temp. >730–750 °C.
Ammonia (aqueous solution), NH_4OH	No interaction (it initiates only in the presence of H_2O_2).
Sodium hydroxide, NaOH	Weak interaction with NaOH in aqueous solution in the presence of O_2 and intensive interaction in the presence of oxidizers; the slow interaction, which leads to the formation of molybdates, is observed between molten NaOH and Mo in the presence of O_2; the presence of oxidizers (KNO_2, KNO_3, $KClO_3$, PbO_2 and others) intensifies the reactions considerably. For reactions, see the next section on potassium hydroxide, KOH.
Potassium hydroxide, KOH	No interaction with KOH in aqueous solution; the slow interaction, which leads to the formation of molybdates, is observed between molten KOH and Mo in the presence of O_2: $2Mo + 4(n + 1)KOH + 3O_2 \rightarrow 2K_{2(n+1)}MoO_{n+4} + 2(n + 1)H_2O$; and the intensive interaction occurs in the presence of oxidizers (KNO_2, KNO_3, $KClO_3$, PbO_2 and others): $Mo + 2nKOH + 2KNO_2 \rightarrow K_{2(n+1)}MoO_{n+4} + N_2 + nH_2O$; $Mo + 2(n + 1)KOH + 3KNO_3 \rightarrow K_{2(n+1)}MoO_{n+4} + 3KNO_2 + (n + 1)H_2O$; $Mo + 2(n + 1)KOH + KClO_3 \rightarrow K_{2(n+1)}MoO_{n+4} + KCl + (n + 1)H_2O$.
Sodium peroxide, Na_2O_2	The interaction with molten Na_2O_2 is intensive: $Mo + 3Na_2O_2 \rightarrow Na_6MoO_6$.
Potassium nitrate, KNO_3	The interaction with molten KNO_3 is intensive.
Nitric acid, HNO_3	At room temp. the interaction is slow, by heating the dissolution of Mo intensifies considerably.
Sulphuric acid, H_2SO_4	No interaction at room temp., slow dissolution while heating.
Hydrochloric acid, HCl	No interaction at room temp., slow dissolution while heating.
Hydrochloric acid with nitric acid (aqua regia), $HCl + HNO_3$	The interaction is slow at room temp. and intensifies on heating. For reactions, see the next section on nitric acid with hydrofluoric acid $HNO_3 + HF$.
Nitric acid with hydrofluoric acid, $HNO_3 + HF$	The interaction is intensive: $Mo + 6HNO_3 + 2HF \rightarrow MoO_2F_2 + 6NO_2 + 4H_2O$, $5Mo + 6HNO_3 + 10HF \rightarrow 5MoO_2F_2 + 3N_2 + 8H_2O$, $5Mo + (16–n)HNO_3 + nHF \rightarrow (5–n/2)MoO_2(NO_3)_2 + n/2MoO_2F_2 + 3N_2 + 8H_2O$.

[a] Etching agents for molybdenum: boiling 1.5 % H_2O_2 aqueous solution (for grain boundaries and subboundaries), 10 % NaOH + 30 % $K_3[Fe(CN)_6]$ aqueous solution (chemical etching for dislocation structure), 10 % NaOH aqueous solution (electrochemical etching, 0.75 V), 0.5 % aqueous solution of oxalic acid (electrochemical etching, 3 V), Murakami's reagent

The self-diffusion characteristics of molybdenum atoms, diffusion characteristics in molybdenum—element and molybdenum—chemical compound systems in the wide range of temperatures, and summarized data on the physico-chemical interaction of molybdenum with elements of the periodic table are given in Addendum.

References

1. Steurer W (1996) Crystal structure of the metallic elements. In: Cahn RW, Haasen P (eds) Physical metallurgy, 4th ed., Vol. 1, pp. 1–46. Elsevier Science BV, Amsterdam
2. Cotton FA, Wilkinson G (1965) Advanced inorganic chemistry. Wiley, New York, London
3. Akhmetov NS (2001) Obschaya i neorganicheskaya khimiya (General and inorganic chemistry), 4th ed. Vysshaya Shkola, Moscow (in Russian)
4. Waseda Y, Hirata K, Ohtani M (1975) High-temperature thermal expansion of platinum, tantalum, molybdenum and tungsten measured by X-ray diffraction. High Temp High Pressures 7:221–226
5. Kotelnikov RB, Bashlykov SN, Galiakbarov ZG, Kashtanov AI (1968) Osobo tugoplavkie elementy i soedineniya (Extra refractory elements and compounds). Metallurgiya, Moscow (in Russian)
6. Zefirov AP (ed), Veryatin UD, Mashirev VP, Ryabtsev NG, Tarasov VI, Rogozkin BD, Korobov IV (1965) Termodinamicheskie svoistva neorganicheskikh veschestv (Thermodynamic properties of inorganic substances). Atomizdat, Moscow (in Russian)
7. Speight JG, ed (2005) Lange's handbook of chemistry, 16th ed. McGraw-Hill, New York
8. Lide DR, ed (2010) CRC handbook of chemistry and physics, 90th ed. CRC Press, Boca Raton, New York
9. Martienssen W (2005) The elements. In: Martienssen W, Warlimont H (eds) Springer handbook of condensed matter and materials data, pp. 45–158. Springer, Berlin, Heidelberg
10. Samsonov GV, ed (1976) Svoistva elementov (Properties of elements), 2nd ed., Vol. 1. Metallurgiya, Moscow (in Russian)
11. Marmer ÉN, Gurvich OS, Maltseva LF (1967) Vysokotemperaturnye materialy (High-temperature materials). Metallurgiya, Moscow (in Russian)
12. Cardarelli F (2008) Materials handbook, 2nd ed. Springer, London
13. Plansee Aktiengesellschaft (2000) Materials data base. Reutte, Austria
14. Samsonov GV, ed (1976) Svoistva elementov (Properties of elements), 2nd ed., Vol. 2. Metallurgiya, Moscow (in Russian)
15. Lyakishev NP, ed (1997) Diagrammy sostoyaniya dvoinykh metallicheskikh sistem (Phase diagrams of binary metal systems), Vol. 2. Mashinostroenie, Moscow (in Russian)
16. Lyakishev NP, ed (2001) Diagrammy sostoyaniya dvoinykh metallicheskikh sistem (Phase diagrams of binary metal systems), Vol. 3, Part 1. Mashinostroenie, Moscow (in Russian)
17. Lyakishev NP, ed (1996) Diagrammy sostoyaniya dvoinykh metallicheskikh sistem (Phase diagrams of binary metal systems), Vol. 1. Mashinostroenie, Moscow (in Russian)
18. Massalski TB, Subramanian PR, Okamoto H, Kacprzak L, eds (1990) Binary alloy phase diagrams, 2nd ed. ASM International, Metals Park, Ohio
19. Rudy E (1969) Compendium of phase diagram data. In: Ternary phase equilibria in transition metal-boron-carbon-silicon systems. Report AFML-TR-65–2, Contracts USAF 33(615)-1249 and USAF 33(615)-67-C-1513, Part 5, pp. 1–689. Air Force Materials Laboratory, Wright-Patterson Air Force Base, Ohio
20. Kuzma YuB (1983) Kristallokhimiya boridov (The crystal chemistry of borides). Vyshcha Shkola, Lviv (in Russian)

21. Kosolapova TYa, ed (1990) Handbook of high-temperature compounds: properties, production and applications. Hemisphere, New York
22. Toth LE (1971) Transition metal carbides and nitrides. Academic Press, New York, London
23. Kofstad P (1966) High-temperature oxidation of metals. Wiley, New York, London
24. Kofstad P (1988) High-temperature corrosion. Elsevier Applied Science, London, New York
25. Haschke H, Nowotny H, Benesovsky F (1966) Untersuchungen im der ternären Systeme (Mo,W)-(Fe,Co,Ni)-B (Investigations in the systems (Mo,W)-(Fe,Co,Ni)-B). Monatsh Chem 97:1459–1468 (in German)
26. Leithe-Jasper A, Klesnar H, Rogl P, Komai M, Takagi K-I (2000) Reinvestigation of isothermal section in M(M = Mo,W)-Fe-B ternary systems at 1323 K. J Jpn Inst Met 64(2):154–162 (in Japanese)
27. Harmon DP (1966) Hf-Mo-B and Hf-W-B systems. In: Ternary phase equilibria in transition metal-boron-carbon-silicon systems. Report AFML-TR-65–2, Contract USAF 33(615)-1249, Part 2, Vol. 11, pp. 1–41. Air Force Materials Laboratory, Wright-Patterson Air Force Base, Ohio
28. Holleck H (1984) Binäre und ternäre Carbid- und Nitridsysteme der Ubergangsmetalle (Binary and ternary carbide and nitride systems of the transition metals). Gebrüder Borntträeger, Berlin (in German)
29. Rogl P, Schuster JC (1992) Phase diagrams of ternary boron nitride and silicon nitride systems. ASM International, Materials Park, Ohio
30. Borisova AL, Martsenyuk IS (1975) Reactions of boron and aluminum nitrides and materials based on them with refractory metals. Powder Metall Met Ceram 14(10):822–826
31. Samsonov GV, ed (1978) Fiziko-khimicheskie svoistva okislov (Physico-chemical properties of oxides), 2nd ed. Metallurgiya, Moscow (in Russian)
32. Samsonov GV, Vinitskii IM (1980) Handbook on refractory compounds. IFI/Plenum, New York
33. Telegus VS, Kuzma YuB (1968) Phase equilibria in the systems tungsten-chromium-boron and tungsten-molybdenum- boron. Powder Metall Met Ceram 7(2):133–138
34. Kharitonov VI, Shamrai FI (1969) Ternary system Mo-W-B. Powder Metall Met Ceram 8(7):567–570
35. Kosterova NV, Ordanyan SS, Neshpor VS, Ostrovskii EK (1980) Thermionic emission properties of cermets of eutectic compositions in Me^{IV} – (C, B) – (Mo, Re, W) systems. Powder Metall Met Ceram 19(1):61–66
36. Ordanyan SS, Chupov VD, Kirshina VYu, Fesenko LV (1985) Reactions of hafnium nitride with molybdenum, tungsten and tantalum. Powder Metall Met Ceram 24(9):714–719
37. Ishchenko TV, Meshkov LL, Sokolovskaya YeM (1984) On the interaction of μ phases in systems formed by transition metals. J Less-Common Met 97:145–150
38. Andrievskii RA, Spivak II (1989) Prochnost tugoplavkikh soedinenii i materialov na ikh osnove (Strength of refractory compounds and materials based on them). Metallurgiya, Chelyabinsk (in Russian)
39. Setton M, Van Der Spiegel J (1991) A review of some aspects of ternary metal-metal-Si and metal-B-Si systems. J Appl Phys 69(2):994–999
40. Boettinger WJ, Perepezko JH, Frankwicz PS (1992) Application of ternary phase diagrams to the development of $MoSi_2$-based materials. Mater Sci Eng A 155(1):33–44
41. Taylor A, Doyle NJ (1967) The solid solubility of oxygen in Nb and Nb-rich Nb-Hf, Nb-Mo and Nb-W alloys: Part III: The ternary systems Nb-Mo-O and Nb-W-O. J Less-Common Met 13(3):338–351
42. Ma CL, Li JG, Tan Y, Tanaka R, Hanada S (2004) Microstructure and mechanical properties of Nb/Nb_5Si_3 *in situ* composites in Nb-Mo-Si and Nb-W-Si systems. Mater Sci Eng A 386:375–383
43. Habashi F (1997) Handbook of extractive metallurgy. Wiley-VCH, Weinheim, New York
44. Samsonov GV (1966) Berillidy (Beryllides). Naukova Dumka, Kyiv (in Russian)

45. Savitskii EM, Burkhanov GS (1971) Metallovedenie splavov tugoplavkikh i redkih metallov (Metallography of refractory and less-common metal alloys), 2nd ed. Nauka, Moscow (in Russian)
46. Garg SP, Ackermann RJ (1977) The high temperature phase diagrams for Th-Mo, Th-Re, U-Mo and U-Re; derived thermodynamic properties of refractory metal solutes in liquid thorium and uranium. J Nucl Mater 64(3):265–274
47. Brewer L, Lamoreaux RH (1980) Phase diagrams. In: Brewer L (ed) Molybdenum. Physico-chemical properties of its compounds and alloys. Atomic Energy Review, Special Issue N 7, pp. 195–356. International Atomic Energy Agency, Vienna
48. Audi G, Wapstra AH, Thibault C, Blachot J, Bersillon O (2003) The NUBASE evaluation of nuclear and decay properties. Nucl Phys A 729:3–128
49. De Laeter JR, Bohlke JK, De Bievre P, Hidaka H, Peiser HS, Rosman KJR, Taylor PDP (2003) Atomic weights of the elements. Review 2000 (IUPAC Technical report). Pure Appl Chem 75(6):683–800
50. Wieser ME (2006) Atomic weights of the elements 2005. (IUPAC Technical report). Pure Appl Chem 78(11):2051–2066
51. Ordanyan SS (1980) Reactions of HfB_2 with Re and Cr. Powder Metall Met Ceram 19(4):273–277
52. Kubaschewski O (1982) Iron binary phase diagrams. Springer, Berlin
53. Goodwin F, Guruswamy S, Kainer KU, Kammer C, Knabl W, Koethe A, Leichtfried G, Schlamp G, Stickler R, Warlimont H (2005) Metals. In: Martienssen W, Warlimont H (eds) Springer handbook of condensed matter and materials data, pp. 161–430. Springer, Berlin, Heidelberg
54. Conway JB, Flagella BN (1971) Creep rupture data for the refractory metals to high temperatures. Gordon Breach, New York
55. Fromm E, Jehn H (1984) Solubility hydrogen in the elements. Bull Alloy Phase Diagrams 5(3):323–326
56. Maldonado A, Schubert K (1964) Strukturuntersuchungen in einigen zu T^5-T^{10} homologen und quasihomologen Legierungssystemen (The structural studies of some T^5-T^{10} homologous and quasi-homologous alloy systems). Z Metallkd 55(10):619–626 (in German)
57. Feldman Y, Wasserman E, Srolovotz DJ, Tenne R (1995) High-rate gas-phase growth of MoS_2 nested inorganic fullerenes and nanotubes. Science 267:222–225
58. Ohtani T (2010) Synthesis and applications of chalcogenide nanotubes. In: Kijima T (ed) Inorganic and metallic nanotubular materials, pp. 191–200. Springer, Berlin, Heidelberg
59. Schuster JC (1988) Silicon nitride – metal joints: phase equilibria in the systems Si_3N_4 – Cr, Mo, W and Re. J Mater Sci 23(8):2792–2796
60. Asrar N, Meshkov LL, Sokolovskaya EM (1988) Phase equilibria in ternary alloys based on iron-group metals and containing refractory metals (Mo, W, Nb, Ta). J Less-Common Met 144:41–52
61. Xiong W, Du Y, Liu Y, Huang BY, Xu HH, Chen HL, Pan Z (2004) Thermodynamic assessment of the Mo-Nb-Ta system. Calphad 28:133–140
62. Briggs JZ, Linteau J (1992) Properties of pure metals. Molybdenum. In: ASM handbook. Vol. 2 – Properties and selection: nonferrous alloys and special-purpose materials, pp. 3102–3113. ASM International, The Materials Company, Ohio
63. Leichtfried G (2002) Powder metallurgy data. Springer, Berlin, Heidelberg, New York
64. Ovsepyan ES (1964) Molibdenovye splavy (Molybdenum alloys). In: Tumanov AT (ed) Konstruktsionnye materialy (Structural materials). Vol. 2, pp. 218–219. Sovetskaya Entsiklopediya, Moscow (in Russian)
65. Femböck J, Pfaffinger K, Weiss B, Stickler R (1981) Verhalten von Mo-Werkstoffen unter zyklischer Beanspruchung (Behavior of Mo-materials under cyclic loading). In: Proc. 10th Plansee seminar. Vol. 2, pp. 27–35. Plansee AG, Reutte (in German)

66. Ovsepyan ES, Stroev AS (1964) Molibden (Molybdenum). In: Tumanov AT (ed) Konstruktsionnye materialy (Structural materials). Vol. 2, pp. 214–217. Sovetskaya Entsiklopediya, Moscow (in Russian)
67. Mazaev AA, Avarbe RG, Vilk YuN (1969) K rastvorimosti vodoroda v molibdene pri vysokikh temperaturakh i davleniyakh (On the solubility of hydrogen in molybdenum at high temperatures and pressures). Izv AN SSSR Metally (4):255–256 (in Russian)
68. Lange KW, Schenck H (1969) The hydrogen absorption in nickel-molybdenum and nickel-wolfram alloys. Z Metallkd 60(1):62–68
69. Oates WA, McLellan RB (1972) The solubility of hydrogen in molybdenum. Scr Metall 6(5):349–352
70. Leavenworth HW, Cleary RE (1961) The solubility of Ni, Cr, Fe, Ti and Mo in liquid lithium. Acta Metall 9(5):519–520
71. Von Goldbeck O (1973) Phase diagrams. In: Beryllium. Physico-chemical properties of its compounds and alloys. Atomic Energy Review, Special Issue N 4, pp. 45–61. International Atomic Energy Agency, Vienna
72. Gschneidner KA (1961) Rare earth alloys: a critical review of. Van Nostrand Reinhold, New York
73. Chuang Y-C, Li C-W, Chuang H-L, Kao L-M (1966) Phase diagram of the gadolinium-molybdenum system. Acta Metall Sin 9:110–112 (in Chinese)
74. Savitskii EM, Devingtal YuV, Gribulya VB (1968) Prognoz metallicheskikh soedinenii tipa A_3B s pomoshchyu elektronno-vychislitelnoi mashiny (Prognosis of A_3B type metallic compounds by means of computing). Doklady AN SSSR 183(5):1110–1112 (in Russian)
75. Savitskii EM, Devingtal YuV, Gribulya VB (1969) Raspoznavanie tipa reaktsii obrazovaniya i otsenka intervala gomogennosti metallicheskikh faz pri pomoshchi EVM (Identification of formation reaction type and evaluation of homogeneity range of metallic phases by means of computing). Doklady AN SSSR 185(3):561–563 (in Russian)
76. Savitskii EM, Gribulya VB (1970) Opyt prognozirovaniya sostava i svoistv soedinenii s pomoshchyu EVM (Prognosis experience in compound compositions and properties by means of computing). Doklady AN SSSR 190(5):1147–1150 (in Russian)
77. Savitskii EM, Gribulya VB (1972) Prognoz faz Lavesa pri pomoshchi EVM (Prognosis of Laves phases by means of computing). Doklady AN SSSR 206(4):848–851 (in Russian)
78. McMasters OD, Palmer PE, Larsen WL (1962) Thorium-molybdenum phase diagram. J Nucl Mater 7(2):151–156
79. Dwight AE (1960) The uranium-molybdenum equilibrium diagram below 900 °C. J Nucl Mater 2(1):81–87
80. Lehmann J (1964) Phases monocliniques dans les alliages uranium-molybdene (Monoclinic phases in the uranium-molybdenum alloys). J Nucl Mater 4(2):218–225 (in French)
81. Tangri K, Williams GI (1961) Metastable phases in the uranium molybdenum system and their origin. J Nucl Mater 4(2):226–233
82. Ageev NV, Guseva LN, Dolinskaya LK (1975) Metastabilnye fazy v zakalennykh splavakh titana s molibdenom i titana s vanadium i vliyanie na nikh malykh primesei kisloroda (Metastable phases in the hardened alloys of titanium with molybdenum and titanium with vanadium and effect of oxygen minor impurities on them). Izv AN SSSR Metally (4):151–156 (in Russian)
83. Davis R, Flower HM, West DRF (1979) Martensitic transformations in Ti-Mo alloys. J Mater Sci 14(3):712–722
84. Leibovitch C, Gartstein E, Rabinkin AG (1980) Structural stability and superconductivity of Ti-Mo alloys under pressure – 1. Structural stability. Z Metallkd 71(7):438–447
85. Murray JL (1981) The Mo-Ti (molybdenum-titanium) system. Bull Alloy Phase Diagrams 2(2):185–192
86. Rapp Ö (1970) Superconductivity and lattice parameters in the zirconium-molybdenum, zirconium-tungsten, hafnium-molybdenum and hafnium-tungsten alloy systems. J Less-Common Met 21(1):27–44

87. Samsonov GV, Braun SM, Rogozinskaya AA (1972) Nekotorye zakonomernosti vliyaniya legiruyushchikh elementov na temperature polimorfnogo prevrashcheniya tsirkoniya (Some rules of the effect of alloying elements on the polymorphic transformation temperature of zirconium). Izv Vyssh Uchebn Zaved Tsvet Metall (6):118–122 (in Russian)
88. Kubaschewski O, Von Goldbeck O (1976) Phase diagrams. In: Zirconium. Physico-chemical properties of its compounds and alloys. Atomic Energy Review, Special Issue N 6, pp. 67–140. International Atomic Energy Agency, Vienna
89. Garg SP, Ackermann RJ (1977) The high temperature phase diagrams for zirconium-molybdenum and hafnium-molybdenum. Metall Trans A 8(2):239–244
90. Taylor A, Doyle NJ, Kagle BJ (1961) The constitution diagram of the molybdenum-hafnium binary system. J Less-Common Met 3(4):265–348
91. Kocherzhinskii YuA, Vasilenko VI (1985) Diagrammy plavkosti sistem Mo-Nb(V,Cr), V-Nb(Cr) i Mo-V-Nb(Cr) (The meltability diagram of the Mo-Nb(V,Cr), V-Nb(Cr) and Mo-V-Nb(Cr) systems). Izv AN SSSR Metally (2):188–190 (in Russian)
92. Goldschmidt HJ, Brand JA (1961) The constitution of the chromium-niobium-molybdenum system. J Less-Common Met 3(1):44–61
93. Krimer BI (1968) Fazovoe sostoyanie splavov iz tugoplavkikh komponentov (k diagramme Nb-Mo) (Phase constitution of refractory component alloys (towards to Nb-Mo phase diagram)). Izv Vyssh Uchebn Zaved Chern Metall (5):143–145 (in Russian)
94. Okamoto H (1991) Mo-Nb (molybdenum-niobium) system. J Phase Equilibria 12(5):616–617
95. Kaufman L, Nesor H (1973) Theoretical approaches to the determination of phase diagrams. Annual Rev Mater Sci 3:1–30
96. Kocherzhinskii YuA, Vasilenko VI (1979) Diagramma plavkosti Mo-Cr (Mo-Cr meltability diagram). Izv AN SSSR Metally (4):205–207 (in Russian)
97. Venkatraman M, Neumann JP (1987) The Cr-Mo (chromium-molybdenum) system. Bull Alloy Phase Diagrams 8(3):216–220
98. Telegus VS, Kuzma YuB, Marko MA (1971) Phase equilibria in the systems molybdenum-manganese-carbon and tungsten-manganese-carbon. Powder Metall Met Ceram 10(11):898–903
99. Darby JB, Zegler ST (1962) Comments on superconducting phases in the Mo-Tc system. J Phys Chem Solids 23(12):1825–1827
100. Alekseevskii NE, Balakhovskii OA, Kirillov IV (1975) O sverkhprovodimosti tekhnetsiya i nekotorykh ego splavov (On superconductivity of technetium and its some alloys). Fiz Metal Metalloved 40(1):50–54 (in Russian)
101. Higgins J, Wilkes P (1972) Precipitation in the Fe-Mo and Fe-Au systems. Philos Mag 25:599–623
102. Kichner G, Harvig H, Uhrenius B (1973) Experimental and thermodynamic study of the equilibria between ferrite, austenite and intermediate phases in the Fe-W and Fe-Mo-W systems. Metal Trans 4:1059–1067
103. Heijwegen CP, Rieck GD (1974) Determination of the phase diagram of the Mo-Fe system using diffusion couples. J Less-Common Met 37(1):115–121
104. Fernandez-Guillermet A (1982) The Fe-Mo (iron-molybdenum) system. Bull Alloy Phase Diagrams 3(3):359–367
105. Anderson E, Hume-Rothery W (1960) The equilibrium diagram of the system molybdenum-ruthenium. J Less-Common Met 2(6):443–450
106. Moss M, Smith DL, Lefever RA (1964) Metastable phases and sulerconductors produced by plasma-jet spraying. Appl Phys Lett 5(6):120–121
107. Quinn TJ, Hume-Rothery W (1963) The equilibrium diagram of the system molybdenum-cobalt. J Less-Common Met 5(4):314–324
108. Heijwegen CP, Rieck GD (1974) Determination of the phase diagram of the Mo-Co system using diffusion couples. J Less-Common Met 34(2):309–314
109. Takayama T, Wey MY, Nichizawa T (1981) Effect of magnetic transition on the solubility of alloying elements in bcc iron and fcc cobalt. Trans Japan Inst Metals 22(5):315–325

110. Anderson E, Hume-Rothery W (1960) The equilibrium diagram of the system molybdenum-rhodium. J Less-Common Met 2(1):19–28
111. Glessen BC, Jähnigen U, Grant NJ (1966) Ordered AB and AB_3 phases in T_6-T_9 alloy systems and a modified Mo-Ir phase diagram. J Less-Common Met 10(2):147–150
112. Raub E (1959) Metals and alloys of the platinum group. J Less-Common Met 1(1):3–18
113. Raub E, Plate W (1956) Aushärtung und Entmischung der Platin-Iridium-Legierungen (Age hardening and breakdown of solid solution in platinumiridium alloys). Z Metallkd 47(10):688–693 (in German)
114. Casselton REW, Hume-Rothery W (1964) The equilibrium diagram of the system molybdenum-nickel. J Less-Common Met 7(3):212–221
115. Heijwegen CP, Rieck GD (1973) Determination of the phase diagram of the Mo-Ni system using diffusion couples. Z Metallkd 64(6):450–453
116. Van Tendeloo G (1976) Short range order considerations and development of long range order in different Ni-Mo alloys. Mater Sci Eng 26:209–220
117. Raub E (1954) Die Legierungen der Platinmetalle mit Molybdän (The alloys of platinum metals with molybdenum). Z Metallkd 45:23–30 (in German)
118. Anderson E (1964) The equilibrium diagram of the system molybdenum-palladium. J Less-Common Met 6(1):81–84
119. Savitskii EM, Tylkina MA, Khamidov OKh (1964) Sistema palladii-molibden (The palladium-molybdenum system). Zh Neorg Khim 9(12):2738–2742 (in Russian)
120. Rooksby HP, Lewis B (1964) Relations between the structures of phases in the system platinum-molybdenum. J Less-Common Met 6(6):451–460
121. Raub E, Röschel E (1966) Über einige neue A15-Phasen (Several new A15-phases). Naturwissenschaften 53(1):17 (in German)
122. Ocken H, Van Vucht JHN (1968) Phase equilibria and superconductivity in the molybdenum-platinum system. J Less-Common Met 15(2):193–199
123. Flükiger R, Yvon K, Susz Ch, Roggen R, Paoli A, Muller J (1973) Les domaines d'homogénéité des phases supraconductrices dans le système molybdène-platine (The areas of homogeneity of superconducting phases in the system molybdenum-platinum). J Less-Common Met 32(2):207–225 (in French)
124. Driole J, Allibert C, Bonnier E (1979) Elektromagnetische Induktion – ein Mittel zur Untersuchung der Phasengleichgewichte Diagramme (Electromagnetic induction – a means for the investigation of phase equilibrium diagrams). Metall 33(5):471–474 (in German)
125. Subramanian PR, Laughlin DE (1990) The Cu-Mo (copper-molybdenum) system. Bull Alloy Phase Diagrams 11(2):169–172
126. Massalski TB, Okamoto H, Brever L (1986) The Au-Mo (gold-molybdenum). Bull Alloy Phase Diagrams 7(5):449–452
127. Neumann T, Schleicher H, Venker H (1969) Legierungsbildung zwischen niedrig- und höchstschmelzenden Metallen durch Reduktion flüchtiger Metallhalogenide und Klärung des Aufbaus der nach diesem Verfahren erhaltenen Molybdän-Zink-Legierungen (Alloy formation between low- and highest-melting metals by reducing volatile metal halides and clarify the structure of the products obtained by this method molybdenum-zinc alloys). Z Metallkd 60:438–441 (in German)
128. Rudy E, Benesovsky F, Toth L (1963) Untersuchungen der ternären Systeme der Gruppe Va und VIa Metalle mit Bor und Kohlenstoff (Studies of the ternary systems of the group Va and VIa metals with boron and carbon). Z Metallkd 54(6):345–353 (in German)
129. Rudy E, Windisch S (1965) Systems Mo-B and W-B. In: Ternary phase equilibria in transition metal – boron – carbon – silicon systems. Report AFML-TR-65–2, Contract USAF 33(615)-1249, Part 1, Vol. 3, pp. 1–72. Air Force Materials Laboratory, Wright Patterson Air Force Base, Ohio
130. Portnoi KI, Levinskii YuV, Romashov VM, Mordovin OA, Levinskaya MKh (1967) Diagramma sostoyaniya sistemy molibden-bor (The constitution diagram of the molybdenum-boron system). Izv AN SSSR Metally (4):171–176 (in Russian)

131. Zakharov AM, Novikov II, Polkin VS (1971) Sistema Mo-B so storony molibdena (The Mo-B system from the molybdenum side). Izv Vyssh Uchebn Zaved Tsvet Metall (6):126–129 (in Russian)
132. Lundström T, Rosenberg I (1973) The crystal structure of the molybdenum boride $Mo_{1-x}B_3$. J Solid State Chem 6(2):299–305
133. Storms E, Mueller B (1977) Phase relations and thermodynamic properties of transition metal borides. I. The molybdenum-boron system and elemental boron. J Phys Chem 81(4):318–324
134. Spear KE, Liao PK (1988) The B-Mo (boron-molybdenum). Bull Alloy Phase Diagrams 9(4):457–466
135. Vigdorovich VN, Glazov VM, Glagoleva NN (1960) Issledovanie rastvorimosti khroma, molibdena i volframa v alyuminii metodom mikrotverdosti (A study of the solubility of chromium, molybdenum and tungsten in aluminium by microhardness method). Izv Vyssh Uchebn Zaved Tsvet Metall (2):143–146 (in Russian)
136. Pötschke M, Schubert K (1962) Zum Aufbau einiger zu T^4-B^3 homologer und quasi-homologer Systeme. II. Die Systeme Titan-Aluminium, Zirkonium-Aluminium, Hafnium-Aluminium, Molybdän-Aluminium und einige ternäre Systeme (Structure of some homologous to T^4-B^3 and quasi-homologous systems. II. Titanium-aluminum, zirconium-aluminum, hafnium-aluminum, molybdenum-aluminum systems and some of the ternary systems). Z Metallkd 53:548–560 (in German)
137. Rexer J (1971) Die Phasengleichgewichte im System Aluminium-Molybdän bei Temperaturen oberhalb 1400 °C (Phase equilibria in the aluminium-molybdenum system above 1400 °C). Z Metallkd 62(11):844–848 (in German)
138. Bornand JD, Siemens RE, Oden LL (1973) Phase relations in the molybdenum-gallium system. J Less-Common Met 30(2):205–209
139. Yatsenko SP, Dieva EN (1973) Rastvorimost tugoplavkikh metallov v zhidkom indii (The solubility of refractory metals in liquid indium). Zh Fiz Khim 47(11):2948 (in Russian)
140. Gokhale AB, Abbaschian GJ (1991) The Mo-Si (molybdenum-silicon) system. J Phase Equilibria 12(4):493–498
141. Brown A (1965) Structure data for some arsenic- and germanium-rich compounds of molybdenum. Nature 206:502–503
142. Agoshkov VM, Gorbatenkov VD, Popova VS, Fomicheva LN (1981) Crystallization of $MoGe_2$ and WGe_2 at high pressure and some properties of these phases. J Less-Common Met 78(2):235–243
143. Olesinki RW, Abbaschian GJ (1987) The Ge-Mo (germanium-molybdenum) system. Bull Alloy Phase Diagrams 8(1):53–56
144. Killpatrick DH (1964) High-pressure high-temperature synthesis of a new β-wolfram compound Mo_3Sn. J Phys Chem Solids 25(12):1499–1500
145. Kozina LN, Revyakin AV, Samarin AM (1969) Rastvorimost azota v zhidkikh niobii i molibdene (The solubility of nitrogen in liquid niobium and molybdenum). Doklady AN SSSR 184(2):397–399 (in Russian)
146. Fromm E, Jehn H (1971) Gleichgewichtsuntersuchungen im System Molybdän-Stickstoff (Study of equilibria in the molybdenum-nitrogen system). Z Metallkd 62(5):372–377 (in German)
147. Domke H, Frohberg MG (1974) Die Bestimmung der Stickstoffloeslichkeit in fluessigem Molybdän (Determination of the solubility of nitrogen in liquid molybdenum). Z Metallkd 65(9):615–617 (in German)
148. Jehn H, Ettmayer P (1978) The molybdenum-nitrogen phase diagram. J Less-Common Met 58(1):85–98
149. Samsonov GV, Vereikin LL (1961) Fosfidy (Phosphides). UkrSSR Academy of Sciences, Kyiv (in Russian)
150. Kandler H, Reiss B (1966) Zur Kristallstruktur der intermetallischen Phasen MoAs und Mo_3As (The crystal structure of the intermetallic phases MoAs and Mo_3As). Z Naturforsch A 21:549–554 (in German)

151. Guerin R, Sergent M, Prigent J (1975) Etude des chaines metal-metal dans la structure type MnP: Les arseniure et phosphure "MoAs" et WP et leurs solutions solides avec les composes MX (M = element de transition 3*d*; X = As, P) (Study of metal-metal chains in the structure type MnP: The arsenide and phosphide "MoAs" and WP and their solid solutions with the compounds MX (M = 3*d* transition element, X = As, P)). Mater Res Bull 10(9):957–966 (in French)
152. Phillips B, Chang LLY (1965) Condensed-phase relations in the system Mo-O. Trans AIME 233(7):1433–1436
153. Chang LLY, Phillips B (1969) Phase relations in refractory metal – oxygen systems. J Am Ceram Soc 52(10):527–533
154. Zador S, Alcock CB (1970) Thermodynamic study of $MoO_{2\pm x}$ with small deviations from stoichiometry. J Chem Thermodyn 2(1):9–16
155. Srivastava SC, Seigle LL (1974) Solubility and thermodynamic properties of oxygen in solid molybdenum. Metall Trans 5(1):49–52
156. Ekstrom T, Tilley RJD (1976) Ternary tungsten oxides with the Mo_5O_{14} structure. J Solid State Chem 19(2):125–133
157. Bygden J, Sichen D, Seetharaman S (1994) A thermodynamic study of the molybdenum-oxygen system. Metall Mater Trans B 25(6):885–891
158. Cannon P (1959) Melting point and sublimation of molybdenum disulphide. Nature 183:1612–1613
159. Anderson E (1964) The equilibrium diagram of the system molybdenum-palladium. J Less-Common Met 6(1):81–84
160. Stäfer SC, Larson AH, Schlechten AW (1964) Sulfur pressure variation of molybdenum disulfide at 1100 °C. Trans AIME 230:594–595
161. De Jonge R, Popma TJA, Wiegers GA, Jellinek F (1970) Structure and phase transitions of molybdenum (III) sulfide and some related phases. J Solid State Chem 2(2):188–192
162. Chevrel R, Sergent M, Prigent J (1974) Un nouveau sulfure de molybdene: Mo_3S_4 preparation, proprietes et structure cristalline (A new molybdenum sulfide: Mo_3S_4 preparation, properties and crystal structure). Mater Res Bull 9(11):1487–1489 (in French)
163. Poulard G, Perrot P (1975) Enthalpies libres de formation et domaine de stabilité des sulfures de molybdéne Mo_2S_3 et MoS_2 (Free energies of formation and stability region of molybdenum sulfides Mo_2S_3 and MoS_2). Compt Rend Acad Sci C 281:143–146 (in French)
164. Johnson WB, Hong WS, Readey DW (1983) A molybdenum sulphur binary phase diagram. Scr Metall 17(7):919–922
165. Frey GL, Elani S, Homyonfer M, Feldman Y, Tenne R (1998) Optical-absorption spectra of inorganic fullerenelike MS_2 (M = Mo, W). Phys Rev B 57(11):6666–6671
166. Remskar M, Mrzel A, Skraba Z, Jesih A, Ceh M, Demsÿar J, Stadelmann P, Levy F, Mihailovic D (2001) Self-assembly of subnanometer-diameter single-wall MoS_2 nanotubes. Science 292:479–481
167. Suemitsu M, Toshimi A (2010) Synthesis and applications of molybdenum oxide nanotubes. In: Kijima T (ed) Inorganic and metallic nanotubular materials, pp. 83–96. Springer, Berlin, Heidelberg
168. Towle LC, Oberbeck V, Brown BE, Stajdohar RE (1966) Molybdenum diselenide: rhombohedral high pressure – high temperature polymorph. Science 154:895–896
169. Spiesser M, Rouxel J, Kerriou M, Goureaux MG (1969) Caractérisation et étude physico-chimique de séléniures et tellures non stœchiométriques de molybdène (Physico-chemical characterization and study of non-stoichiometric selenides and tellurides of molybdenum). Bull Soc Chim France (5):1427–1431 (in French)
170. Al-Hilli AA, Evans BL (1972) The preparation and properties of transition metal dichalcogenide single crystals. J Cryst Growth 15(2):93–101
171. Bars O, Guillevic J, Grandjean D (1973) Étude structurale de combinaisons sulfurées et séléniées du molybdène: I. Structure cristalline de Mo_3Se_4 (Structural study of sulfur and selenium compounds of molybdenum: I. Crystal structure of Mo_3Se_4). J Solid State Chem 6:48–57 (in French)

172. Glazunov MP, Mikhailov ES, Piskarev NV, Chupakhin MS (1976) A mass-spectrometric investigation of the evaporation of molybdenum and tantalum diselenides. Powder Metall Met Ceram 15(11):866–868
173. Hershfinkel M, Gheber LA, Volterra V, Hutchison JL, Margulis L, Tenne R (1994) Nested polyhedra of MX_2 (M = W, Mo; X = S, Se) probed by high-resolution electron microscopy and scanning tunneling microscopy. J Am Chem Soc 116(5):1914–1917
174. Revolinsky E, Beerntsen DJ (1966) Electrical properties of α- and β-$MoTe_2$ as affected by stoichiometry and preparation temperature. J Phys Chem Solids 27(3):523–526
175. Vellinga MB, De Jonge R, Haas CU (1970) Semiconductor to metal transition in $MoTe_2$. J Solid State Chem 2(2):299–302
176. Opalovskii AA, Fedorov VE, Lobkov EU, Tsikanovskii BI (1971) Issledovanie telluridov molibdena i volframa tenzimetricheskim metodom (A study of molybdenum and tungsten tellurides by tensometric method). Zh Fiz Khim 45(7):1864 (in Russian)
177. Yanaki AA, Obolonchik VA (1974) Termicheskaya ustoichivost telluridov perekhodnykh metallov V-VI grupp periodicheskoi sistemy elementov (The thermal resistance of tellurides of transition metals V-VI groups of the periodic table). Zh Prikl Khim 47(7):1454–1458 (in Russian)
178. Zelikman AN (1970) Molibden (Molybdenum). Metallurgiya, Moscow (in Russian)
179. Mercer M (1967) Molybdenum hexachloride. Chem Commun (3):119–121
180. Kepert DL, Mandyczewsky R (1968) α-Molybdenum tetrachloride. A structural isomer containing molybdenum- molybdenum interactions. Inorg Chem 7(10):2091–2093
181. Nirsha VM, Korshunov VG (1969) Sintez oksitrikhlorida i oksitetrakhlorida molibdena (Synthesis of molybdenum oxytrichloride and oxytetrachloride). Zh Neorg Khim 14(6):1693–1694 (in Russian)
182. Drobot DV, Sapranova EA (1974) Sintez trikhlorida molibdena i issledovanie fazovykh ravnovesii v sisteme $MoCl_3$ – $MoCl_5$ (Synthesis of molybdenum trichloride and study of phase relations in the $MoCl_3$ – $MoCl_5$ system). Zh Neorg Khim 19(1):228–231 (in Russian)
183. Oppermann H, Stöver G (1972) Beiträge zur Chemie der Oxidhalogenide von Molybdän und Wolfram. VI. Thermische Zersetzung von $MoCl_3$ und $MoOCl_2$ (Contributions to the chemistry of molybdenum and tungsten oxyhalides. VI. Thermal decomposition of $MoCl_3$ and $MoOCl_2$). Z Anorg Allgem Chem 387(2):218–229 (in German)
184. Schaefer H, Schering HGV, Tillack J, Kuhnen F, Wöhrle H, Baumann H (1967) Neue Untersuchungen über die Chloride des Molybdäns (New research on the chlorides of molybdenum). Z Anorg Allgem Chem 353(5–6):281–310 (in German)
185. Babel D (1972) Die Verfeinerung der $MoBr_3$-Struktur (The refinement of the structure $MoBr_3$). J Solid State Chem 4(3):410–416 (in German)
186. Oppermann H (1975) Gleichgewichtsmessungen im System Molybdän-Brom (Equilibrium measurements in the system molybdenum-bromine). Z Anorg Allgem Chem 395(2–3):249–261 (in German)
187. Hashimoto K, Hanamura T (1999) Phase stability and mechanical properties of Nb-rich Nb-Mo-Al ternary system at elevated temperatures. Mater Trans JIM 40(2):152–158
188. Kovalchenko MS, Samsonov GV, Yasinskaya GA (1960) Splavy boridov perekhodnykh metallov s drugimi metallami (Alloys of transition metals borides with other metals). Izv AN SSSR OTN Metallurgiya Toplivo (2):115–119 (in Russian)
189. Kuzma YuB, Telegus VS, Kovalyk DA (1969) X-ray diffraction investigation of the ternary systems V-Cr-B, Nb-Cr-B and Mo-Cr-B. Powder Metall Met Ceram 8(5):403–410
190. Kolomytsev PT, Moskaleva NV, Snetkov AYa (1969) Phase composition and some properties of molybdenum-chromium-boron alloys. Powder Metall Met Ceram 8(10):836–839
191. Zakharov AM, Yudkovskij SI, Popova YuS (1982) Molibdenovyi ugol troinoi sistemy Mo-Cr-B (The molybdenum-rich angle in the Mo-Cr-B ternary system). Izv AN SSSR Neorg Mater 18(10):1714–1716 (in Russian)
192. Tojo M, Tokunaga T, Ohtani H, Hasebe M (2010) Thermodynamic analysis of phase equilibria in the Cr-Mo-B ternary system. Calphad 34:263–270

193. Kuzma YuB (1971) An x-ray structural investigation of the systems niobium-titanium-boron and niobium-molybdenum-boron. Powder Metall Met Ceram 10(4):298–300
194. Yamada K, Ohtani H, Hasebe M (2009) Thermodynamic analysis of the Mo-Nb-B ternary phase diagram. Nippon Kinzoku Gakkaishi 73(3):180–188 (in Japanese)
195. Katrych S, Grytsiv A, Bondar A, Rogl P, Velikanova T, Bohn M (2002) Structural materials metal-silicon-boron. On the melting behavior of Mo-Si-B alloys. J Alloys Compd 347(1–2):94–100
196. Yang Y, Chang YA (2005) Thermodynamic modeling of the Mo-Si-B system. Intermetallics 13(2):121–128
197. Yoshimi K, Ha S-H, Maruyama K, Tu R, Goto T (2011) Microstructural evolution of Mo-Si-B ternary alloys through heat treatment at 1800 °C. Adv Mater Res 278:527–532
198. Jéhanno P, Heilmaier M, Saage H, Böning M, Kestler H, Freudenberger J, Drawin S (2007) Assessment of the high temperature deformation behavior of molybdenum silicide alloys. Mater Sci Eng A 463(1-2):216–223
199. Yoshida M, Takasugi T (1997) Phase relation and microstructure of Nb-Cr-V and Nb-Cr-Mo alloy systems. Mater Sci Eng A 224:69–76
200. Savitskii EM, Baron VV, Bychkova MI, Bakakuta SA, Gladyshevskii EI (1965) Diagramma sostoyaniya I nekotorye svoistva splavov sistemy Nb-Mo-Si (The constitution diagram and some properties of alloys of the Nb-Mo-Si system). Izv AN SSSR Metally (2):159–166 (in Russian)
201. Ma CL, Tan Y, Tanaka H, Kasama A, Tanaka R, Miura S, Mishima Y, Hanada S (2000) Phase equilibria in Nb-Mo-rich zone of the Nb-Si-Mo ternary system. Mater Trans JIM 41(10):1329–1336
202. Kim W-Y, Tanaka H, Kasama A, Tanaka R, Hanada S (2001) Microstructure and room temperature deformation of Nb_{ss}/Nb_5Si_3 in situ composites alloyed with Mo. Intermetallics 9:521–527
203. Huang Q, Ma CL, Zhao X, Xu H (2008) Phase equilibria in Nb-Si-Mo ternary alloys at 1273 K and 2073 K. Chin J Aeronaut 21(5):448–454
204. Geng T, Li C, Zhao X, Xu H, Du Z, Guo C (2010) Thermodynamic assessment of the Nb-Si-Mo system. Calphad 34:363–376
205. Geng T, Li C, Zhao X, Xu H, Guo C, Du Z (2010) Experimental study on the as-cast solidification of the Si-rich alloys of the Nb-Si-Mo ternary system. Intermetallics 18(5):1007–1015
206. Liu Y, Shao G, Tsakiropoulos P (2000) Thermodynamic reassessment of the Mo-Si and Al-Mo-Si systems. Intermetallics 8(8):953–962
207. Gokhale AB, Abbaschian GJ (1991) The Mo-Si (molybdenum-silicon) system. J Phase Equilibria 12(4):493–498
208. Ordanyan SS, Serbezova RYa, Lebedeva TA (1972) Vzaimodeistvie diborida tsirkoniya s molibdenom (The interaction of zirconium diboride with molybdenum). Izv AN SSSR Neorg Mater 8(11):2037–2038 (in Russian)
209. Ordanyan SS, Maksimova NM, Smirnov VV (1979) Reactions in the HfB_2-Mo system. Powder Metall Met Ceram 18(10):719–721
210. Kolomytsev PT, Moskaleva NV (1966) Phase composition and some properties of alloys of the system molybdenum – nickel – boron. Powder Metall Met Ceram 5(8):665–670.
211. Ilnitskaya ON, Kuzma YuB (1982) Diagrammy fazovykh ravnovesii v sistemakh (Cr, Mo) – (Si, B) – P (Diagrams of phase equilubria in the (Cr, Mo) – (Si, B) – P systems. In: Tezisy dokladov 4-oi Vsesoyuznoi konferentsii po diagrammam sostoyaniya metallicheskikh sistem (Summaries of papers to the 4th All-Union conference on the constitution diagrams of metallic systems), pp. 122–123. Nauka, Moscow (in Russian)
212. Kuzma YuB, Chaban NF (1990) Dvoinye i troinye sistemy soderzhashchie bor (Binary and ternary systems containing boron). Metallurgiya, Moscow (in Russian)
213. Chaban NF, Mikhalenko SI, Kuzma YuB (1998) New compounds with a Y_2ReB_6 type structure. Powder Metall Met Ceram 37(11–12):635–637

214. Chaban NF, Kuzma YuB (1999) Phase diagrams for the Lu – Cr – B and Lu – Mo – B systems. Powder Metall Met Ceram 38(9–10):458–461
215. Huebsch JJ, Kramer MJ, Zhao HL, Akinc M (2000) Solubility of boron in $Mo_{5+y}Si_{3-y}$. Intermetallics 8:143–150
216. Chaban NF, Mikhalenko SI, Kuzma YuB (2000) Component interactions in (Y,Gd,Tm) – Mo – B ternary systems at 1270 K. Powder Metall Met Ceram 39(1–2):48–54
217. Pokropivnyi VV (2001) Non-carbon nanotubes (review). II. Types and structures. Powder Metall Met Ceram 40(11–12):582–594
218. Kubliy VZ, Bondar AA, Utkin SV, Petyukh VM, Lysenko SI, Velikanova TYa (2008) Phase equilibria in the nickel corner of the Mo – Ni – B system at temperatures close to melting. Powder Metall Met Ceram 47(3–4):211–222
219. Volkov NA, Gusei LS, Chunikhina LL, Khayurov SS (1984) Issledovanie sistemy Ni-Mo-B v oblasti bogatoi nikelem (Investigation of Ni-Mo-B system in nickel-rich region). Moscow Univ Chem Bull 25(3):317–319 (in Russian)
220. Morishita M, Koyama K, Yagi S, Zhang C (2001) Calculated phase diagram of the Ni-Mo-B ternary system. J Alloys Compd 314(1–2):212–218
221. Kuzma YuB, Chepiga MV (1969) An x-ray diffraction investigation of the systems Ti-Ni-B, Mo-Ni-B and W-Ni-B. Powder Metall Met Ceram 8(10):832–835
222. Omori S, Koyama K, Hashimoto Ya, Yamashita M (1984) Phase relations in Ni-Mo-B and Ni-W-B systems at 1223 K. J Japan Inst Metals 48(7):682–687
223. Egorov FF, Kislyi PS (1978) Reactions of zirconium nitride with alumina and molybdenum. Powder Metall Met Ceram 17(6):446–449
224. Barabash OM, Shurin AK (1978) Fazovye ravnovesiya v splavakh Mo-Ti-N i Mo-Hf-N (Phase equilibria in Mo-Ti-N and Mo-Hf-N alloys). Izv AN SSSR Metally (4):243–246 (in Russian)
225. Barabash OM, Shurin AK (1974) Rastvorimost nitridov Ti, Zr i Hf v vanadii (The solubility of Ti, Zr and Hf nitrides in vanadium). Izv AN SSSR Metally (4):194–197 (in Russian)
226. Ordanyan SS (1975) Reactions of rhenium and other refractory metals with some metal-like compounds. Powder Metall Met Ceram 14(2):125–129
227. Mikhalenko SI, Kuzma YuB (1976) Reactions of molybdenum and tungsten with rare-earth metals and boron. Powder Metall Met Ceram 15(2):128–130
228. Kuzma YuB, Svarichevskaya SI, Sobolev AS (1973) Sistemy ittrii-molibden-bor i ittrii-volfram-bor (The yttrium-molybdenum-boron and yttrium-tungsten-boron systems). Izv AN SSSR Neorg Mater 9(10):1697–1702 (in Russian)
229. Chaban NF (1982) Ternary systems Cr(Mo,W) – Gd – B. Powder Metall Met Ceram 21(1):53–54
230. Kuzma YuB, Zakharchuk NP, Maksimova LT (1988) Isothermal sections of diagrams of phase equilibria of the (terbium, dysprosium, holmium) – molybdenum – boron systems at 1273 K. Powder Metall Met Ceram 27(9):738–741
231. Klesnar H, Aselage TL, Morosin B, Kwei GH, Lawson AC (1996) The diboride compounds of molybdenum: MoB_{2-x} and Mo_2B_{5-y}. J Alloys Compd 241(1–2):180–186
232. Kornilov II, Polyakov RS (1958) Fazovaya diagramma troinoi sistemy titan-niobii-molibden (Phase diagram of the ternary system titanium-niobium-molybdenum). Zh Neorg Khim 3(4):62–74 (in Russian)
233. Rogl P, Nowotny H, Benesovsky F (1971) Complex Boride in den Systemen Hf-Mo-B und Hf-W-B (Complex borides in the systems Hf-Mo-B and Hf-W-B). Monatsh Chem 102(4):971–984 (in German)
234. Dion C, Noel A (1981) Etude et interprétation de la ligne UO_2MoO_4-Na_2MoO_4 dans le carde du systeme UO_3-MoO_3-Na_2O (Study and interpretation of the line UO_2MoO_4-Na_2MoO_4 – part of the system UO_3-MoO_3-Na_2O). Bull Soc Chim Fr (9–10):1371–1376 (in French)
235. Fournier JP, Fournier J, Kohlmuller R (1970) Etude des systemes La_2O_3-MoO_3, Y_2O_3-MoO_3 et des phases Ln_6MoO_{12} (Study of the La_2O_3-MoO_3, Y_2O_3-MoO_3 systems and phases Ln_6MoO_{12}). Bull Soc Chim Fr (12):4277–4283 (in French)

236. Yanushkevich TM, Zhukovskii VM (1973) Fazovaya diagramma sistemy MoO_3 – CaO (Phase diagram of the MoO_3 – CaO system). Zh Neorg Khim 18(8):2234–2237 (in Russian)
237. Antonova SS, Shakhno IV, Plyushchev VE (1971) Izuchenie vzaimodeistviya okislov samariya, ittriya i erbiya s trekhokisyu molibdena (A study of the interaction of samarium, yttrium and erbium oxides with molybdenum trioxide). Izv Vyssh Uchebn Zaved Khim Khim Tekhnol 14(1): 17–20 (in Russian)
238. Tsuzuki A, Kani K, Watari K, Torii Y (1992) Phase relations in the MoO_3-$MgMoO_4$ system. J Mater Sci Lett 11(6):334–335
239. Rosen E, Saitton B (1994) Studies of phase equilibria in the system MgO-Mo-O in the temperature range 1100–1400 K. Acta Chem Scand 48(9):720–723
240. Lindblom B (1989) Studies of phase relations and equilibria in the system CaO-Mo-O in the temperature range 1000–1500 K. Scand J Metall 18(2):61–66
241. Yanushkevich TM, Shevchenko NN, Zhukovskii VM, Ustyantsev VM, Lykova LN (1973) Ob usloviyakh obrazovaniya i fiziko-khimicheskikh svoistvakh trekhkaltsievogo molibdata Ca_3MoO_6 (On the formation conditions and physico-chemical properties of tricalcium molybdate Ca_3MoO_6). Zh Neorg Khim 18(11):2931–2935 (in Russian)
242. Andruszkiewicz R (1992) On the Mo-CaO system. J Alloys Compd 186(2):369–378
243. Kunev DK, Belyaevskaya LV, Zelikman AN (1966) Sistemy MoO_3 – $CaMoO_4$, MoO_3 – $PbMoO_4$, MoO_3 – $ZnMoO_4$ (The MoO_3 – $CaMoO_4$, MoO_3 – $PbMoO_4$, MoO_3 – $ZnMoO_4$ systems). Zh Neorg Khim 11(8):1989–1991 (in Russian)
244. Bart JCJ, Giordano N (1976) Phase relationships in the cerium-molybdenum oxide system. J Less-Common Met 46(1):17–24
245. Ran Q, Rokhlin L, Dobatkina T, Semenova E, Kolchugina N (2009) Aluminium – boron – molybdenum system. In: Effenberg G, Ilyenko S (eds) Ternary alloy systems, Subvol. E, Part 1, pp. 24–32. Springer, Berlin, Heidelberg
246. Rieger W, Nowotny H, Benesovsky F (1965) Complex Boride der Übergangsmetalle (Mo, W, Fe, Co, Ni) (Complex borides of the transition metals (Mo, W, Fe, Co, Ni)). Monatsh Chem 96(3):844–851 (in German)
247. Jeitschko W (1966) Die Kristallstruktur von MoAlB (The crystal structure of MoAlB). Monatsh Chem 97:1472–1476 (in German)
248. Higashi I, Takahashi Y, Atoda T (1976) Crystal growth of borides and carbides of transition metals from Al solutions. J Cryst Growth 33:207–211
249. Kornienko K, Bondar A (2009) Boron – iron – molybdenum system. In: Effenberg G, Ilyenko S (eds) Ternary alloy systems, Subvol. E, Part 1, pp. 500–513. Springer, Berlin, Heidelberg
250. Gladyshevskii EI, Fedorov TF, Kuzma YuB, Skolozdra RV (1966) Isothermal section of the molybdenum – iron – boron system. Powder Metall Met Ceram 5(4):305–309
251. Rogl P (2009) Boron – hafnium – molybdenum system. In: Effenberg G, Ilyenko S (eds) Ternary alloy systems, Subvol. E, Part 1, pp. 514–522. Springer, Berlin, Heidelberg
252. Zakharov AM, Golubev MY (1980) The polythermal cross section Mo-HfB_2 of the Mo-Hf-B system. Inorg Mater 16:579–581
253. Kuznetsov V (2007) Molybdenum – oxygen – uranium system. In: Effenberg G, Ilyenko S (eds) Ternary alloy systems, Subvol. C, Part 4, pp. 328–336. Springer, Berlin, Heidelberg
254. Gebhardt E, Ondracek G (1964) Verfassung der UO_2-Mo-System (Constitution of the UO_2-Mo system). J Nucl Mater 13:220–228 (in German)
255. Kovba LM, Trunov VK (1965) Rentgenostrukturnoe issledovanie dvoinykh okislov v sisteme UO_2-MoO_2-MoO_3 (X-ray investigation of double oxides in the system UO_2-MoO_2-MoO_3). Radiokhimiya 7:316–319 (in Russian)
256. Chattopadhyay G, Tripathi SN, Kerkar AS (1984) Thermodynamic investigations in the system U-Mo-O. J Am Ceram Soc 67:610–614
257. Sundberg M, Tabachenko V (1990) HREM studies of complex uranium oxides containing molybdenum and tungsten. Microscopy Microanalysis Microstructures 1:373–385
258. Sundberg M, Marinder B-O (1994) New complex uranium-molybdenum oxides with intergrowth structures: an HREM study. Eur J Solid State Inorg Chem 31:855–866

259. Tabachenko VV, Dyachenko OG, Sundberg M (1995) The crystal structures of UMo_5O_{16} and $U_{0.75}Mo_5O_{16}$ studies by X-ray diffraction and high-resolution electron microscopy. Eur J Solid State Inorg Chem 32:1137–1149
260. Dyachenko OG, Tabachenko VV, Tali R, Kovba LM, Marinder B-O, Sundberg M (1996) Structure of $UMoO_5$ studied by single-crystal X-ray diffraction and high-resolution transmission electron microscopy. Acta Crystallogr B 52:961–965
261. Politis C, Thümmler F, Wedemeyer H (1969) Untersuchungen über die Verträglichkeit von Uranmononitrid mit Molybdän, Wolfram und Thoriumoxid bei hohen Temperaturen (Studies on the compatibility of uranium mononitride with molybdenum, tungsten and thoria at high temperatures). J Nucl Mater 32(2):181–192 (in German)
262. Nowotny H, Rogl P (1977) Ternary metal borides. In: Matkovich VI (ed) Boron and refractory borides, pp. 413–438. Springer, Berlin, Heidelberg, New York
263. Rogl P, Nowotny H (1973) Neue κ- (kappa-) Phasen (New κ- (kappa-) phases). Monatsh Chem 104(6):1497–1504 (in German)
264. Jeitschko W (1968) The crystal structure of MoCoB and related compounds. Acta Crystallogr B 24:930–934
265. Rieger W, Nowotny H, Benesovsky F (1966) Die Kristallstruktur von W_2CoB_2 und isotypen Phasen (The crystal structure of W_2CoB_2 and isotypic phases). Monatsh Chem 97(2):378–382 (in German)
266. Rieger W, Nowotny H, Benesovsky F (1964) Die Kristallstruktur von Mo_2FeB_2 (The crystal structure of Mo_2FeB_2). Monatsh Chem 95(6):1502–1503 (in German)
267. Telegus VS, Kuzma YuB (1971) Phase equilibrium in the systems vanadium-manganese-boron, molybdenum-manganese-boron and tungsten-manganese-boron. Powder Metall Met Ceram 10(1):52–56
268. Rogl P, Benesovsky F, Nowotny H (1972) Über einige Komplexboride mit Platinmetallen (About complex boride with some platinum metals). Monatsh Chem 103(4):965–989 (in German)
269. Rogl P, Nowotny H (1974) Ternäre Komplexboride mit $ThMoB_4$-Typ (Ternary complex borides with $ThMoB_4$-type structure). Monatsh Chem 105(5):1082–1098 (in German)
270. Rogl P, Nowotny H (1975) Uran-haltige Komplexboride (Complex borides with uranium). Monatsh Chem 106(2):381–387 (in German)
271. Argon AS (1996) Mechanical properties of single-phase crystalline media: deformation at low temperatures. In: Cahn RW, Haasen P (eds) Physical metallurgy, 4th ed., Vol. 3, pp. 1877–1955. Elsevier Science BV, Amsterdam
272. Briggs JZ, Linteau J (1990) Molybdenum. In: Metals handbook, Vol. 2 – Properties and selection: nonferrous alloys and special-purpose materials, pp. 3102–3113. ASM International, Metals Park, Ohio
273. Somenkov VA, Glazkov VP, Irodova AV, Shilshtein SS (1987) Crystal structure and volume effects in the hydrides of *d*-metals. J Less-Common Met 129:171–180
274. Okamoto H (1991) The Cs-Mo (cesium-molybdenum) system. J Phase Equilib 12:701–702
275. Moffat WG (1978) The handbook of binary phase diagrams. General Electric Company, Schenectady, New York
276. English JJ (1961) Binary and ternary phase diagrams of columbium, molybdenum, tantalum and tungsten. Report DMIC-152, Contract AF-33(616)-7747, pp. 1–226. Defence Metals Information Center, Battelle Memorial Institute, Columbus, Ohio
277. Palenzona A, Cirafici S (1996) The Ce-Mo (cerium-molybdenum) system. J Phase Equilib 17(1):57–59
278. Zinkevich MV, Mattern N, Seifert HJ (2001) Thermodynamic assessment of Gd-Zr and Gd-Mo systems. J Phase Equilib 22:43–50
279. De Boer FR, Dijkman WH, Mattens WCM, Miedema AR (1979) On the valence state of Yb and Ce in transition metal intermetallic compounds. J Less-Common Met 64(2):241–253
280. Chiotti P, Akhachinskij VV, Ansara I, Rand MH (1982) The Mo-Th (molybdenum-thorium) system. Bull Alloy Phase Diagrams 3:100–101

281. Mardon PG, Evans JP, Hodkin DJ, North JM, Pearce JH (1961) The constitution and fabrication of uranium-molybdenum-plutonium fuels. In: Plutonium 1960. Proceedings of 2nd International Conference on plutonium, pp. 329–352. Institute of Metals, London
282. Schonfeld FW, Cramer EM, Miner WN, Ellinger FH, Coffinberry AS (1959) Plutonium constitutional diagrams. Prog Nucl Energy Ser 5 2:579–599
283. Guminski C (1994) The Hg-Mo (mercury-molybdenum) system. J Phase Equilibria 15(1):108–110
284. Dieva EN (1974) Rastvorimost tugoplavkikh metallov v zhidkom indii (The solubility of refractory metals in liquid indium). In: Bamburov VG (ed) Fiziko-khimicheskie issledovaniya zhidkikh metallov i splavov (Physico-chemical studies of liquid metals and alloys), p. 105–106. Uralskii Nauchnyi Tsentr AN SSSR, Sverdlovsk (in Russian)
285. Ettmayer P, Kieffer R.: (1970) Nitrid- und Karbonitridsysteme bei hohem Stickstoffdruck (Nitride and carbonitride systems at high nitrogen pressure). Radex Rundsch 191–198 (in German)
286. Tsuya K, Aritomi N (1968) On the effects of vacuum annealing and carburizing on the ductility of coarse-grained molybdenum. J Less-Common Met 15:245–257
287. Frisk K (1991) A thermodynamic evaluation of the Cr-N, Fe-N, Mo-N and Cr-Mo-N systems. Calphad 15(1):79–106
288. Hörz G, Steinheil E (1971) Gleichgewichtsuntersuchungen im System Niob-Molybdän-Stickstoff. III. Zum Phasendiagram (Studies of equilibrium in the system niobium-molybdenum-nitrogen. III. Phase diagram). Z Metallkd 62:893–896 (in German)
289. Popov AP, Tsvetnikov AK, Goncharuk VK (1978) Equilibrium diagram of the MoF_5-MoF_6 system. Russ J Inorg Chem 23:132–133
290. Khaldoyanidi KA, Yakovlev II, Ikorskii VN (1981) Phase equilibria in the fluorine-molybdenum system. Russ J Inorg Chem 26:1639–1640
291. Hunt CR Jr, Raman A (1968) Alloy chemistry of $\sigma(\beta U)$-related phases. I. Extension of μ- and occurrence of μ'-phases in the ternary systems Nb(Ta)-X-Al (X = Fe, Co, Ni, Cu, Cr, Mo). Z Metallkd 59:701–707
292. Guzei LS (1993) The Al-Mo-Nb (aluminium-molybdenum-niobium) system. Ternary Alloys VCH 7:196–198
293. Gubbels GHM, Wolff LR, Metselaar R (1990) A thermionic energy converter with a molybdenum-alumina cermet emitter. J Appl Phys 68:5856–5865
294. Nickel KG (1993) The Al-Mo-O (aluminium-molybdenum-oxygen) system. Ternary Alloys, VCH 7:219–220
295. Harrison WTA (1995) Crystal structures of paraelastic aluminum molybdate and ferric molybdate β-$Al_2(MoO_4)_3$ and β-$Fe_2(MoO_4)_3$. Mater Res Bull 30:1325–1331
296. Kuzma YuB, Nych OV, Skolozdra RV (1966) Molybdenum-cobalt-boron system. Inorg Mater 2:1709–1712
297. Stadelmaier HH, Davis HH (1966) Die Kobaltecke im Dreistoffsystem Kobalt-Molybdän-Bor (The cobalt corner in the ternary system cobalt-molybdenum-boron). Monatsh Chem 97:1489–1493 (in German)
298. Kuzma YuB, Mikhalenko SI, Chaban NF (1983) Vzaimodeistvie Mo, W i Re s redkozemelnymi metallami i borom (Interaction of Mo, W and Re with rare-earth metals and boron). In: Savitskii EM (ed) Issledovaniya i primenenie splavov tugoplavkikh metallov (Studies and application of refractory metal alloys), pp. 5–11. Nauka, Moscow (in Russian)
299. Ilnitskaya ON, Kuzma YuB (1985) Diagram of phase equilibria in the Mo-P-B system in the range 0–0.67 at. fraction of P. Powder Metall Met Ceram 24(3):226–228
300. Dheeradhada VS, Johnson DR, Dayananda MA (2006) Diffusional analysis of a multiphase oxide scale formed on a Mo-Mo_3Si-Mo_5SiB_2 alloy. J Phase Equilib Diffus 27:582–589
301. Nowotny H, Kieffer R, Benesovsky F (1957) Silicoboride der Übergangsmetalle Vanadin, Niob, Tantal, Molybdän und Wolfram (Silicoborides of the transition metals vanadium, niobium, tantalum, molybdenum and tungsten). Planseeber Pulvermetall 5:86–93 (in German)

302. Zakharov AM, Polkin VS (1972) Molibdenovyi ugol sistem Mo-Ti-B i Mo-Zr-B (The molybdenum corner of the systems Mo-Ti-B and Mo-Zr-B) Izv Vyssh Uchebn Zaved Tsvetn Metall 15(4):109–113 (in Russian)
303. Valovka IP, Kuzma YuB (1986) Isothermal section of the diagram of the systems U-Mo-B and U-Re-B. Powder Metall Met Ceram 25(12):986–988
304. Konrad T, Jeitschko W (1996) $U_5Mo_{10}B_{24}$, a boride containing three different kinds of boron polyanions. J Alloys Compd 233:L3-L7
305. Kuzma YuB, Marko MA, Petrovskaya MV (1972) Rentgenograficheskoe issledovanie troinykh sistem V-(Nb,Ta)-B, Nb-Ta-B i V-(Mo,W)-B (X-ray investigation of the ternary systems V-(Nb,Ta)-B, Nb-Ta-B and V-(Mo,W)-B). Visn Lviv Derzh Univ Ser Khim 13:3–8 (in Russian)
306. Zakharov AM, Novikov II, Polkin VS, Gimelfarb FA (1973) The molybdenum corner of the Mo-Zr-B phase diagram. Russ Metall (4):165–168
307. Rogl P, Nowotny H, Benesovsky F (1973) Neue K-Boride und verwandte Phasen (Re_3B-Typ, aufgefüllt) (New K-borides and related phases (Re_3B type, packed)). Monatsh Chem 104:182–193 (in German)
308. Voroshilov YV, Kuzma YuB (1969) Reaction of zirconium with the transition metals and boron. Sov Powder Metall Met Ceram 8:941–944
309. Prior TJ, Battle PD (2003) Facile synthesis of interstitial metal nitrides with the filled β-manganese structure. J Solid State Chem 172:138–147
310. Raghavan V (1987) Phase diagrams of ternary iron alloys, Part 1. The Indian Institute of metals, Calcutta
311. Allen S, Ward RJ, Hampson MR, Gover RKB, Evans JSO (2004) Structures and phase transitions of trigonal $ZrMo_2O_8$ and $HfMo_2O_8$. Acta Crystallogr B 60:32–40
312. Stümke M, Petzow G (1975) Kristallstrukturen und Gitterabmessungen von Übergangsmetall-Diberylliden und -Diboriden in ternären Mischkristallbereichen (Crystal structures and lattice dimensions of the transition metal diborides and diberyllides in ternary mixed crystal regions). Z Metallkd 66:292–297 (in German)
313. Allibert CH, Wicker A, Driole J, Bonnier E (1970) Determination de diagrammes de phases a haute temperature dans les systemes de metaux refractaires (Determination of phase diagrams at high temperature in the systems of refractory metals) Rev Int Hautes Temp Refract 7:45–50 (in French)
314. Svechnikov VN, Shurin AK, Alfintseva RA (1970) Issledovanie fazovykh ravnovesii v sisteme molibden-niobii-gafnii (Investigation of the phase equilibria in alloys of the system molybdenum-niobium-hafnium). Metallofizika (Akad Nauk Ukr SSR Inst Metallofiz) 32:25–27 (in Russian)
315. Lomnytska YF (1992) Isothermal section of the equilibrium diagram of the Nb-Mo-P system at 1070 K. Powder Metall Met Ceram 31:343–345
316. Ivanov OS, Terekhov GI (1963) Izotermicheskie razrezy pri 500 i 560 °C fazovoi diagrammy troinoi sistemy uran-niobii-molibden (Isothermal cross sections for 500 and 560 °C of the phase diagram of the triple system uranium-niobium-molybdenum). In: Ivanov OS (ed) Struktura splavov nekotorykh sistem soderzhashchikh uran i torii (Structure of alloys of certain systems containing uranium and thorium), pp. 200–212. Nauka, Moscow (in Russian)
317. Ivanov OS, Terekhov GI (1963) Izotermicheskie razrezy pri 575–1200 °C fazovoi diagrammy troinoi sistemy uran-niobii-molibden (Isothermal cross sections at 575–1200 °C of the phase diagram of the uranium-niobium-molybdenum system) In: Ivanov OS (ed) Struktura splavov nekotorykh sistem soderzhashchikh uran i torii (Structure of alloys of certain systems containing uranium and thorium), pp. 213–231. Nauka, Moscow (in Russian)
318. Tate EF, Nicholson S (1963) The $(\beta+\gamma)/\gamma$ phase boundaries at 675°, 700° and 720 °C in the uranium-rich corner of the U-Mo-Nb diagram. J Nucl Mater 9:365–366
319. Bannister GH, Murray DJR (1960) Some observations on uranium-molybdenum-niobium alloys. J Less-Common Met 2:372–382

320. Lukas HL (2010) Molybdenum – niobium – zirconium system. In: Effenberg G, Ilyenko S (eds) Ternary alloy systems, Subvol. E, Part 3, pp. 366–376. Springer, Berlin, Heidelberg
321. Okamoto H (2010) The Al-Mo (aluminium-molybdenum) system. J Phase Equilib Diffus 31(5):492–493
322. Okamoto H (2012) The Mo-U (molybdenum-uranium) system. J Phase Equilib Diffus 33(6):497
323. Okamoto H (2011) The Mo-Si (molybdenum-silicon) system. J Phase Equilib Diffus 32(2):176
324. Nunes CA, Coelho GC, Ramos AS (2001) On the invariant reactions in the Mo-rich portion of the Mo-Si system. J Phase Equilib 22(5):556–559
325. Ewh A, Perez E, Keiser DD Jr, Sohn YH (2010) Microstructural characterization of U-Nb-Zr, U-Mo-Nb and U-Mo-Ti alloys via electron microscopy. J Phase Equilib Diffus 31(3):216–222
326. Okamoto H (2000) The Mo-Ru (molybdenum-ruthenium) system. J Phase Equilib 21(6):572
327. Ghosh G, Olson GB (2000) Thermodynamic modeling of the Cr-Pd and Mo-Pd systems. J Phase Equilib 21(1):32–39
328. Zheng F, Argent BB, Smith JF (1999) Thermodynamic computation of the Mo-V binary phase diagram. J Phase Equilib 20(4):370–372
329. Davydov A, Kattner UR (1999) Thermodynamic assessment of the Co-Mo system. J Phase Equilib 20(1):5–16
330. Okamoto H (1994) Comment on Mo-Pd (molybdenum-palladium) system. J Phase Equilib 15(4):452–453
331. Okamoto H (1993) The Mo-Pd (molybdenum-palladium) system. J Phase Equilib 14(3):400
332. Okamoto H (1992) The Mo-Pd (molybdenum-palladium) system. J Phase Equilib 13(3):332–334
333. Okamoto H (1994) Comment on Mo-Rh (molybdenum-rhodium) system. J Phase Equilib 15(3):368
334. Smith JF (1992) The Mo-V (molybdenum-vanadium) system. J Phase Equilib 13(1):50–53
335. Okamoto H (1991) The Mo-Ni (molybdenum-nickel) system. J Phase Equilib 12(6):703
336. Okamoto H (1991) The Mo-Nb (molybdenum-niobium) system. J Phase Equilib 12(5):616–617
337. Ordanyan SS, Vikhman SV, Nagaeva YuS (2011) Reaction of $MoSi_2$ with niobium and tantalum diborides. Refract Indust Ceram 52(4):282–285
338. Ordanyan SS, Kosterova NV, Avgustinik AI (1977) Phase equilibria in the system Ti-B-Mo at 1400 °C. Inorg Mater 13:691–693

Chapter 8
Niobium

8.1 Structures

Niobium (or columbium) is the element No. 41 of the periodic table (period—5, similar to tantalum group—5 (or VB), relates to transition metals) with the ground state level $^6D_{½}$ and electron configuration $1s^2 2s^2 2p^6 3s^2 3p^6 3d^{10} 4s^2 4p^6 4d^4 5s^1$. The general oxidation states (numbers) of niobium in various chemical compounds are (–1), (+1), (+2), (+3), (+4) and (+5); the oxidation state (+3) and (+5) are the most common; the radii of niobium are:

atomic (metallic, CN = 8)—0.143 nm,
atomic (metallic, CN = 12)—0.147 nm,
atomic (covalent)—0.134 nm,
ionic (+3)—0.072 nm (CN = 6),
ionic (+3)—0.079 nm (CN = 8),
ionic (+4)—0.068 nm (CN = 6),
ionic (+5)—0.048 nm (CN = 4),
ionic (+5)—0.064 nm (CN = 6),
ionic (+5)—0.074 nm (CN = 8);

its electronegativity is 1.6 in Pauling scale, or 1.47 in Allred–Rochow scale [1–3, 6–8, 11]. Elemental niobium has body-centred cubic (bcc) metal crystal structure (space group—*Im(−3)m*, W type) with lattice parameter $a = 0.33007$ nm (Z = 2) at room temperature (minimum interatomic distance—0.28585 nm, CN = 8), slip plane (110) and slip direction <111> [64–66].

At room temperature, the XRD density of niobium is 8.578 g cm^{-3} and recommended value for the bulk density of common metal parts—8.55–8.60 g cm^{-3} [4, 6, 11].

I. L. Shabalin, *Ultra-High Temperature Materials I*,
DOI: 10.1007/978-94-007-7587-9_8, © Springer Science+Business Media Dordrecht 2014

8.2 Thermal Properties

The melting point of niobium is one of the highest among the elements of the periodic table; it is exceeded only by tungsten, rhenium, osmium, tantalum and molybdenum for metals, and carbon. The general thermodynamic properties of niobium are summarized in Table 8.1. For the molar heat capacity $c_p = f(T, \text{K})$, J mol^{-1} K^{-1}, the following relationship is recommended in the range of temperatures from 298 to 2500 K [5]:

Table 8.1 General thermodynamic properties of niobium

Characteristics	Symbol	Unit	Value	References
Standard molar entropy (at 298.15 K and 100 kPa)	$S°_{298}$	J mol^{-1} K^{-1}	37.7 ± 0.4	[4]
			36.4	[6–7]
			36.27	[8–11]
Enthalpy difference	$H_{298} - H_0$	kJ mol^{-1}	5.220	[8]
Standard molar heat capacity (at 298.15 K and 100 kPa)	$c°_{p,298}$	J mol^{-1} K^{-1}	24.60	[4, 7]
			24.69	[8]
			24.67	[6]
Specific heat capacity (at 298.15 K)	c	J kg^{-1} K^{-1}	265	[4, 6–7]
			265.75	[11]
			260	[35]
Molar enthalpy (heat) of melting (at the melting point)	ΔH_m	kJ mol^{-1}	30.0	[6–8]
			29.3	[11]
			27.53	[9]
			26.8	[4]
Specific enthalpy (heat) of melting (at the melting point)		kJ kg^{-1}	315	[11]
			290	[35–36]
			288	[4]
Molar enthalpy (heat) of vaporization (at the boiling point)	ΔH_v	kJ mol^{-1}	690	[6, 11]
			683	[8]
			680	[4]
Specific enthalpy (heat) of vaporization (at the boiling point)		kJ kg^{-1}	7320	[4]
			7490	[35]
			7456	[36]
			7426	[11]
Melting point	T_m	K (°C)	2740 (2470)	[4, 6]
			2750 (2477)	[7–8]
			2742 (2469)	[9]
			2741 (2468)	[11, 35–36]

(continued)

Table 8.1 (continued)

Characteristics	Symbol	Unit	Value	References
Boiling point	T_b	K (°C)	5020 (4745)	[7–8]
			5200 (4925)	[35–36]
			5115 (4840)	[9]
			5015 (4740)	[11]

$$c_p = 23.70 + \left(4.019 \times 10^{-3}\right)T, \tag{8.1}$$

For the specific heat capacity $c_p = f(T, \text{K})$, J kg^{-1} K^{-1}, the variation with temperature in the range from 0 to 2500 °C is shown in Fig. 8.1 [10, 66]. The equilibrium vapour pressure of niobium P, Pa, at temperatures 298−2500 K obeys the rule [7]:

$$\lg P = -37818/T - 0.2575 \lg T + 13.888, \tag{8.2}$$

where T is temperature, K. In high vacuum, the rate of niobium vaporization at the temperatures of 1750, 1960 and 2230 °C approximately amounts to 10^{-10}, 10^{-8} and 10^{-6} kg m^{-2} s^{-1}, respectively [4]. The values of standard molar entropy $S°_{298}$, molar c_p and specific c heat capacities, enthalpies (heats) of melting and vaporization, molar and specific mass enthalpy differences $H_T - H_{298}$, vapour pressures

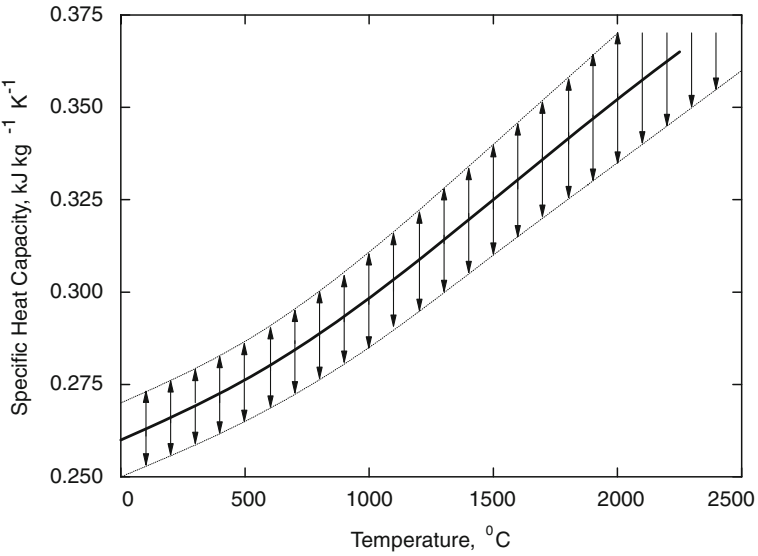

Fig. 8.1 The generalized variation of the specific heat capacity of pure niobium with temperature (*curve*—recommended values, *arrows*—data spread available in the literature) [10, 66]

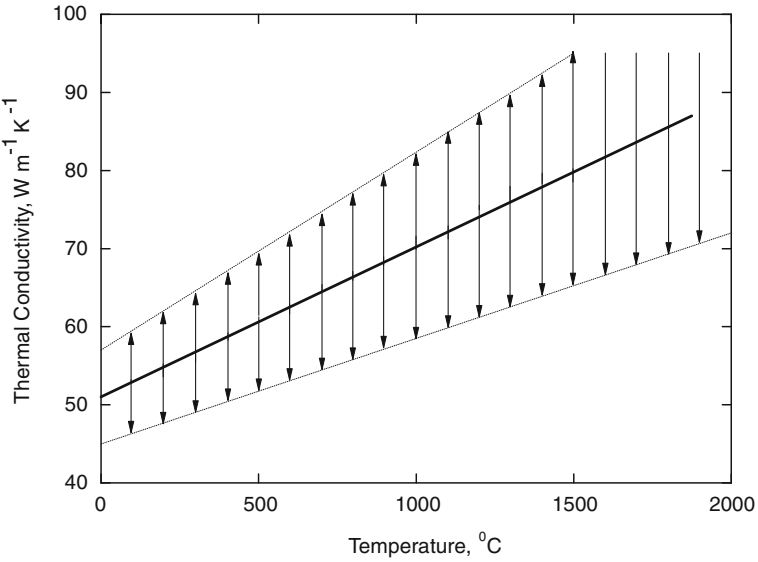

Fig. 8.2 Variation of the thermal conductivity of unalloyed niobium with temperature (*curve*—recommended values), taking into account data spread (*arrows*) available in the literature [4, 10, 42, 66]

and mass/linear vaporization rates for niobium are given in Addendum in comparison with carbon (graphite) and other ultra-high temperature materials (refractory metals) in the wide ranges of temperatures. At ambient temperatures, the thermal conductivity of unalloyed niobium $\lambda = 45{-}59$ W m^{-1} K^{-1} [4, 8–11, 35, 66]; the general character of its variation with temperature [4, 10, 42, 66] is shown in Fig. 8.2.

At room temperature, the coefficient of linear thermal expansion of pure niobium $\alpha = (7.1 \div 7.4) \times 10^{-6}$ K^{-1} [8–11, 42, 66], while for the interval from 20 to 1700 °C the recommended value is 8.9×10^{-6} K^{-1} [4]. In the range of temperatures from 300 to 1000 °C, the variation of the relative thermal expansion $\Delta l/l_0$ with temperature is expressed by the equation as follows [66]:

$$\Delta l/l_0 = 6.892 \times 10^{-6} T + 8.17 \times 10^{-10} T^2 \tag{8.3}$$

where T denotes the value of temperature, K; for the wider range of temperatures the variation of the coefficient of linear thermal expansion is presented in Fig. 8.3 [4, 10, 42]. The surface tension of liquid niobium (density 7.83 g cm^{-3}) is 2.0 N m^{-1} (its temperature coefficient is -0.24×10^{-3} N m^{-1} K^{-1}) [8].

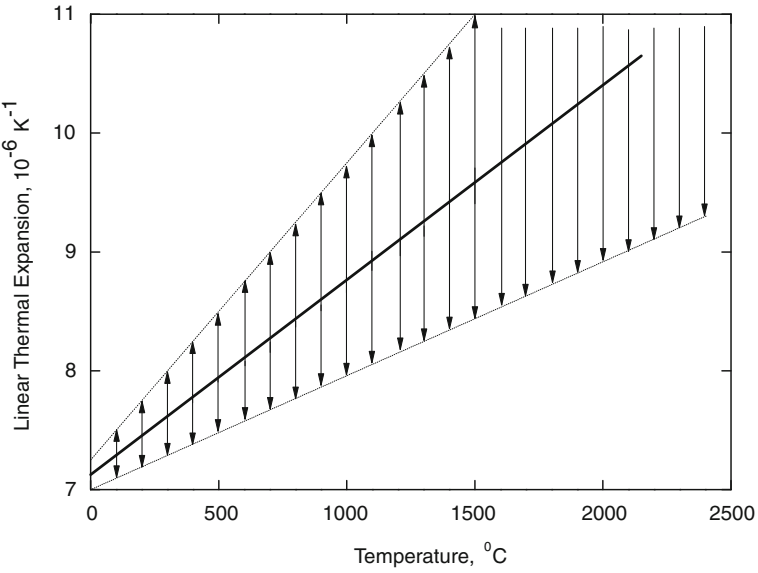

Fig. 8.3 Variation of the linear thermal expansion of pure niobium with temperature (*curve*—recommended values, *arrows*—data spread available in the literature) [4, 10, 42]

In comparison with other ultra-high temperature materials (graphite and refractory metals), the values of thermal conductivity and thermal expansion of niobium in the wide range of temperatures are summarized in Addendum.

8.3 Electro-Magnetic and Optical Properties

At room temperature, the specific electrical resistance (resistivity) of pure niobium $\rho = 146-170$ nΩ m; in the range of temperatures from 13 to 300 K, it varies approximately from 5 to 150 nΩ m, and at elevated and ultra-high temperatures, the resistivity almost obeys the classic metal model (with small deviation from linearity) and slightly exceeds 0.75 μΩ m at 2000 °C (Fig. 8.4). In the range of temperatures from 1500 to 2500 K, the resistivity ρ, μΩ m, is described by the following equation:

$$\lg\rho = 0.7354\lg T - 2.586 \tag{8.4}$$

where T denotes the value of temperature, K [4]. In the interval 0–100 °C, the thermal coefficient of resistivity equals 2.63×10^{-3} K^{-1}, and in the interval 20–1730 °C it is 1.94×10^{-3} K^{-1} (the pressure coefficient is -1.37×10^{-5} MPa^{-1})

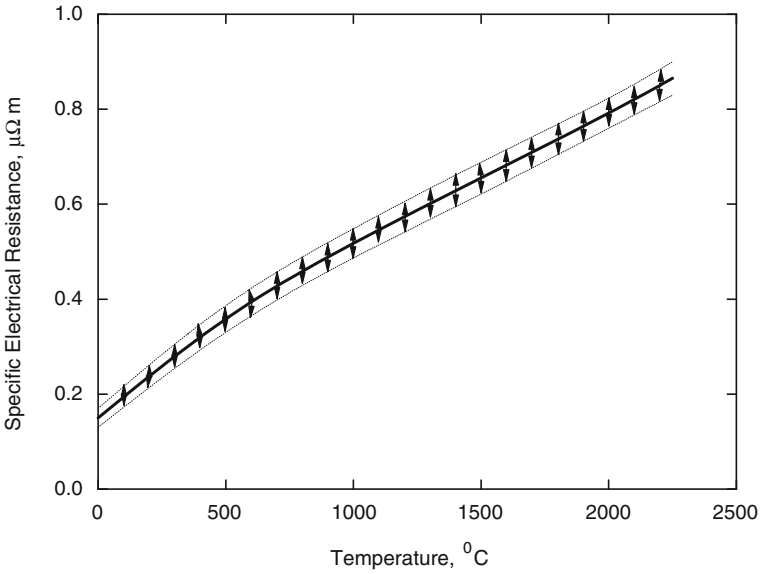

Fig. 8.4 Variation of specific electrical resistance of unalloyed niobium with temperature (*curve*—recommended values, *arrows*—data spread available in the literature) [4, 8, 10]

[4, 8–11, 66]. Together with the temperature growth, relatively minute amounts of oxygen also increase the resistivity of niobium from 162.5 to 306 nΩ m with oxygen content increasing from 0.03 to 0.565 mas.% [10]. At 0 °C, the Hall coefficient of niobium equals $R = 0.88 \times 10^{-10}$ m^3 A^{-1} s^{-1} ($B = 0.5$–2.9 T). Niobium is a paramagnetic metal with molar magnetic susceptibility χ_m (SI) $= 2.614 \times 10^{-3}$ cm^3 mol^{-1} at 22 °C [8].

The magnitudes of main optical properties of niobium and their variations with wavelength λ are following [9, 11]:

index of refraction (polycrystalline materials)—2.27 (electrolytic polishing, $\lambda = 0.60$ μm) and varies from 1.39 ($\lambda = 1.5$ μm) to 22.4 ($\lambda = 10.0$ μm);
index of absorptance (polycrystalline materials)—3.25 ($\lambda = 0.60$ μm), varies from 2.99 ($\lambda = 0.4$ μm) to 44.3 ($\lambda = 10.0$ μm);
reflective index under normal incidence (polycrystalline materials)—0.505 ($\lambda = 0.65$ μm) and varies from 0.75 ($\lambda = 1.0$ μm) to 0.97 ($\lambda = 15.0$ μm).

In the range of temperatures from 700 to 2300 °C the monochromatic emittance (spectral emissivity) ε_λ ($\lambda = 0.65$ μm) of non-oxidized niobium varies from 0.38–0.44 to 0.32–0.36 decreasing with temperature growth, while the integral emittance ε_T increases linearly with temperature growth from 0.05 at 100 °C to 0.23–0.28 at 2200–2300 °C [4, 9–10]. The influence of surface smoothness on the integral emittance ε_T is shown in Table 8.2 [4]. For the surface of oxidized niobium, ε_λ varies from 0.79 at 100 °C to 0.52–0.54 at 700–900 °C [10].

Table 8.2 The integral emittance of niobium with various surface conditions [34]

Temperature, °C	Integral emittance for the surfaces with various smoothness (height of roughnesses, μm)				
	0.1–0.125	2–2.5	2.5–3.2	4–5	5–6.3
930	0.140	0.150	0.154	0.160	0.163
1230	0.171	0.180	0.185	0.193	0.196
1530	0.196	0.206	0.210	0.218	0.221
1730	0.209	0.220	0.224	0.232	0.236

The averaged magnitude of electron work function of pure niobium is ~4.0 eV [4, 9]; for the faces of single crystal with various (*hkl*)-indices the magnitudes are: (100)—4.00 eV, (110)—4.80 eV, (111)—3.88 eV, (112)—4.47 eV, (116)—3.94 eV and (335)—4.52 eV [9]. The approximate Richardson constant (thermo-electronic emission constant) of niobium is 57 A m^{-2} K^{-2} [4]. The recommended values of electrical resistivity, magnetic susceptibility, integral and spectral emittances and thermoionic emission characteristics (electron work function and Richardson constant) for niobium are given in comparison with other ultra-high temperature elements (carbon and refractory metals) in Addendum.

8.4 Physico-Mechanical Properties

The physico-mechanical characteristics of niobium are extremely sensitive to the microstructure features, which are highly dependent on metal working (treatment) as well as metal purity, particularly the content of interstitial elements, such as oxygen, nitrogen, carbon and hydrogen. Wrought niobium is twice higher in hardness than the annealed metal [66]. The oxygen content increases the hardness of niobium from 0.85 GPa (HV) for pure niobium to 1.94 GPa (HV) for niobium containing about 0.9 at.% oxygen, or 3.90 GPa (HV) for niobium with 3.3 at.% oxygen [4, 10]. The temperature behaviour of hardness for niobium is very complicated because of the presence of minimum and maximum points on the hardness-temperature curve, which are connected with changing the principal mechanisms of deformation affected by the microstructure modifications [4].

Similar to tantalum, highly purified niobium is deformed easily and characterized by a high ductility at room temperature. The ultimate tensile strength of unalloyed niobium at room temperature in the main microstructure states comes to the following values [4, 10–11, 42, 44, 66]:

as-cast metal—0.54–0.59 GPa (yield strength—0.49 GPa, elongation—10–13 %, reduction in area—20–30 %);
wrought (hardened) metal—0.585 GPa (elongation—5 %);

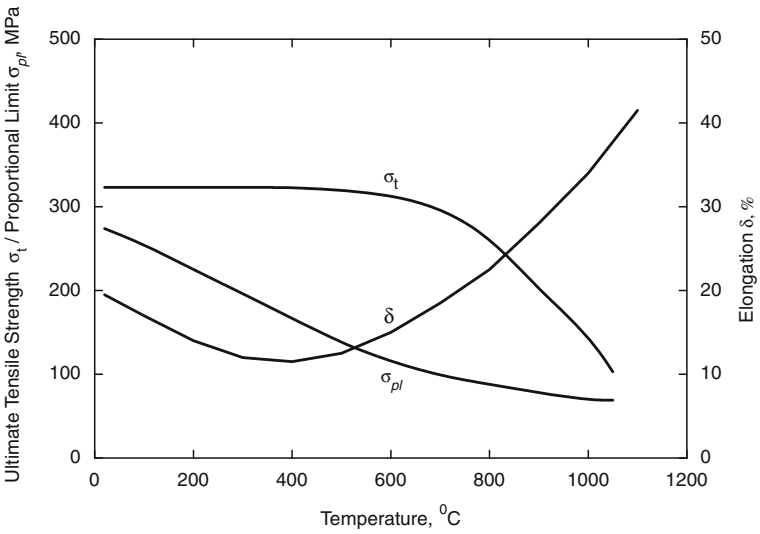

Fig. 8.5 Variations of the ultimate tensile strength (σ_t), proportional limit (σ_{pl}) and fracture elongation (δ) for specimen length—31.8 mm of pure annealed niobium with temperature [44]

hot-worked metal—0.59–0.69 GPa (yield strength—0.59 GPa, elongation—20–25 %, reduction in area—25–35 %);
hot-worked and annealed (at 1300 °C in vacuum 0.013 Pa) metal—0.54–0.59 MPa (elongation—25–30 %);
hot-worked and annealed (at 1600 °C in vacuum 0.013 Pa) metal—0.49–0.54 MPa (yield strength—0.44–0.49 GPa, elongation—25–30 %, reduction in area—35–40 %);
annealed (recrystallized) metal—0.195–0.275 GPa (yield strength—0.21 GPa, elongation—20–50 %, reduction in area—80 %).

The variations of ultimate tensile strength, proportional limit and fracture elongation of pure niobium with temperature are presented in Fig. 8.5 [44].

In the wide range of temperatures from cryogenics to ambient conditions, the fracture toughness of recrystallized niobium varies slightly and amounts to 37–40 MPa $m^{1/2}$ [42, 59]. At room temperature, the apparent work of fracture (impact testing) of hot-worked niobium is about 3.63 MJ m^{-2}, but this characteristic decreases considerably at cryogenic temperatures—up to 0.98–1.27 MJ m^{-2} at −70 °C and 0.20–0.30 MJ m^{-2} at −196 °C [44]. For highly purified niobium, the ductile-to-brittle transition temperature is lower than −126 °C, but it increases sharply with lower purity [66].

The examples of the creep behaviour of wrought niobium are given in Table 8.3 [66]. The fatigue-related properties of niobium are considered in [42].

At room temperature, the main elastic properties of pure polycrystalline niobium have the following numerical values [8, 10–11, 66]:

Table 8.3 Creep and creep-rupture behaviour[a] of wrought niobium at various temperatures [66]

Temperature, °C	1 h stress, MPa	10 h stress, MPa	100 h stress, MPa	1000 h stress, MPa
400	– / – / – / –	160 / 276 / 360 / –	83 / 140 / 200 / –	45 / 66 / 107 / –
500	– / – / – / –	186 / 214 / 230 / –	121 / 140 / 160 / –	80 / 93 / 110 / –
700	– / – / – / –	– / – / – / –	– / 20 / 25 / –	– / 17 / 12 / –
870	– / – / – / 62	– / – / – / 55	– / – / – / 48	– / – / – / –
980	– / – / – / 48	– / – / – / 45	– / – / – / 42	– / – / – / –
1200	– / – / – / 35.8	– / – / – / 32	– / – / – / 28	– / – / – / –

[a] The data are given in the following form: for 0.05 % creep / for 0.1 % creep / for 0.2 % creep / rupture

Young's modulus E, GPa		104–110
Coulomb's (shear) modulus G, GPa		37.5–59.5
Poisson's ratio ν		0.35–0.40
Bulk (compression) modulus K, GPa		170–180
Volume compressibility κ, MPa^{-1}		0.56×10^{-5}
Longitudinal velocity of sound V_S, m s^{-1}		3480–4900
Transversal velocity of sound V_T, m s^{-1}		2090–2100
Elastic compliance	s_{11}, TPa^{-1}	6.56
	s_{44}, TPa^{-1}	35.2
	s_{12}, TPa^{-1}	–2.29
Elastic stiffness	c_{11}, GPa	245
	c_{44}, GPa	28.4
	c_{12}, GPa	132

The influence of metal working (treatment) on the Young's modulus of highly purified niobium is negligible, but the presence of interstitial impurities affects the values of elastic characteristics considerably [4].

The magnitudes of physico-mechanical (strength, elasticity) properties of unalloyed niobium in the wide range of temperatures are summarized in Addendum in comparison with other ultra-high temperature materials (graphite and refractory metals).

8.5 Nuclear Physical Properties

The isotopes of niobium (standard atomic mass—92.90638 u) from ^{81}Nb to ^{113}Nb, including metastable states ($^{84m-89m}$Nb, $^{90m1-5}$Nb, $^{91m1-2}$Nb, $^{92m1-3}$Nb, $^{93m-95m}$Nb, $^{97m-100m}$Nb, ^{102m}Nb and ^{104m}Nb), and their general characteristics are summarized in Table 8.4; the naturally occurring isotopes are listed in order of decreasing abundance, and unstable artificial (radioactive) isotopes—in order of decreasing half-life period of decay.

Table 8.4 General characteristics of the isotopes of niobium [7, 9, 37–39]

Isotope	Mass, u	Abundance, %	Half-life period	Decay mode, excitation (radiation) energy, MeV
^{93}Nb[a]	92.906378	100.00	–	–
^{92}Nb[b]	91.907194	–	3.47×10^7 y	β^+ (99.95 %), β^- (0.05 %)
^{94}Nb	93.907284	–	2.03×10^4 y	β^-, 0.6; γ, 0.726, 0.903, 1.65
^{91}Nb	90.906996	–	680 y	*K*-capture (99.98 %), β^+ (0.013 %); γ, 1.22, 0.105
^{93m}Nb	–	–	16.13 y	Isomer, γ, 0.031
^{91m1}Nb	–	–	60,86 d	Isomer, γ, 0.105 (93 %), K-capture (7 %), β^+ (0.0028 %)
^{95}Nb	94.906836	–	34,99 d	β^-, 0.160; γ, 0.745
^{92m1}Nb	–	–	10,15 d	Isomer, β^+, 0.135
^{95m}Nb	–	–	3.61 d	Isomer, γ (94.4 %), 0.235; β^- (5.6 %)
^{96}Nb	95.908101	–	23,35 h	β^-, 0.750 (92 %), 0.37 (8 %); γ from 0.22 to 1.19
^{90}Nb	89.911265	–	14,60 h	β^+, 0.55, 0.87, 1.50; γ, 1.75
^{89}Nb	88.913418	–	2,03 h	β^+; γ, 2.9
^{89m}Nb	–	–	1.10 h	Isomer, β^+
^{97}Nb	96.908099	–	72,1 min	β^-, 1.267; γ, 0.665
^{98m}Nb	–	–	51.3 min	Isomer, γ, 0.084 (0.1 %); β^- (99.9 %)
^{88}Nb	87.91833	–	14,55 min	β^+
^{88m}Nb	–	–	7.8 min	Isomer, β^-
^{87}Nb	86.92036	–	3,75 min	β^+
^{94m}Nb	–	–	6.26 min	Isomer, γ, 0.041 (99.5 %); β^- (0.5 %)
^{99m}Nb	–	–	2.6 min	Isomer, γ, 0.365 (3.8 %); β^- (96.2 %)
^{87m}Nb	–	–	2.6 min	Isomer, γ, 0.0038; β^+
^{86}Nb	85.92504	–	88 s	β^+
^{86m}Nb	–	–	56 s	Isomer, γ, 0.250; β^+
^{97m}Nb	–	–	52.7 s	Isomer, γ, 0.743
^{85}Nb	84.92791	–	20.9 s	β^+
^{90m2}Nb	–	–	18,8 s	Isomer, γ, 0.125
^{99}Nb	98.911618	–	15.0 s	β^-, 3.2
^{85m}Nb	–	–	12 s	Isomer, γ, 0.759
^{84}Nb	83.93357 (?)	–	9.8 s	β^+ (>99.9 %); β^+, p (<0.1 %)
^{101}Nb	100.915252	–	7.1 s	β^-
^{104}Nb	103.92246	–	4.9 s	β^- (99.94 %); β^-, n (0.06 %)
^{102m}Nb	–	–	4.3 s	Isomer, γ, 0.130; β^-
^{83}Nb	82.93671	–	4.1 s	β^+
^{100m}Nb	–	–	2.99 s	Isomer, γ, 0.470; β^-
^{105}Nb	104.92394	–	2.95 s	β^- (98.3 %); β^-, n (1.7 %)
^{98}Nb	97.910328	–	2.86 s	β^-
^{100}Nb	99.914182	–	1.5 s	β^-
^{103}Nb	102.91914	–	1.5 s	β^-
^{102}Nb	101.91804	–	1.3 s	β^-
^{104m}Nb	–	–	0.94 s	Isomer, γ, 0.220; β^- (99.95 %); β^-, n (0.05 %)

(continued)

Table 8.4 (continued)

Isotope	Mass, u	Abundance, %	Half-life period	Decay mode,excitation (radiation) energy, MeV
^{106}Nb	105.92797 (?)	–	0.92 s	β^- (95.5 %); β^-, n (4.5 %)
^{107}Nb	106.93031 (?)	–	0.30 s	β^- (94 %); β^-, n (6 %)
^{108}Nb	107.93484 (?)	–	0.19 s	β^- (93.8 %); β^-, n (6.2 %)
^{109}Nb	108.93763 (?)	–	0.19 s	β^- (69 %); β^-, n (31 %)
^{110}Nb	109.94244 (?)	–	0.17 s	β^- (60 %); β^-, n (40 %)
^{111}Nb	110.94565 (?)	–	80 ms (?)	–
^{112}Nb	111.95083 (?)	–	60 ms (?)	–
^{82}Nb	81.94313 (?)	–	51 ms	β^+
^{113}Nb	112.95470 (?)	–	30 ms (?)	–
^{90m4}Nb	–	–	6,2 ms	Isomer, γ, 0.382
^{90m1}Nb	–	–	63 μs	Isomer, γ, 0.122
^{92m2}Nb	–	–	5.9 μs	Isomer, γ, 0.226
^{91m2}Nb	–	–	3.76 μs	Isomer, γ, 2.034
^{90m3}Nb	–	–	<1 μs	Isomer, γ, 0.171
^{90m5}Nb	–	–	0.47 μs	Isomer, γ, 1.880
^{92m3}Nb	–	–	0.17 μs	Isomer, γ, 2.203
^{84m}Nb	–	–	0.103 μs	Isomer, γ, 0.338
^{81}Nb	8094903 (?)	–	<44 ns	β^+, p; p; β^+

[a] Theoretically capable of spontaneous fission, lightest nuclide so capable
[b] Longest half-life of all non-primordial radionuclides

Nuclear physical properties of niobium (isotopic mass range, total number of isotopes, thermal neutron macroscopic cross sections, moderating ability and capture resonance integral), compared with other ultra-high temperature elements (carbon and refractory metals), are given in Addendum.

8.6 Chemical Properties

The comprehensive information on the chemical properties and interaction of niobium with all the elements of the periodic table is given in Table 8.5. The niobium containing systems and corresponding binary compounds are described and considered there in accordance to the groups of elements from 1 to 17.

Table 8.5 Chemical interaction of niobium with elements of the periodic table (binary systems in accordance to the groups of elements)[a]

System	Type of phase diagram (constituent phases, temperatures and compositions of transformations)	Character of interaction	References
Group 1			
Nb–H	H, δ-NbH_{2-x} (<at least 250 °C, ~48–49 at.% Nb, ?), β-NbH_{1-x} (<~150 °C, homog. range—~50–60 at.% Nb), γ-NbH_{1-x} (<~−150 °C, homog. range—~54–55 at.% Nb), ξ-NbH_{1-x} (<~–110 °C, homog. range—~55.4–56.0 at.% Nb), ν-NbH_{1-x} (<~–70 °C, homog. range—~56.2–56.3 at.% Nb), μ-NbH_{1-x} (< –56 °C, homog. range—~56.5–56.6 at.% Nb), δ-NbH_{1-x} (or O-phase, <~–120 °C, homog. range—~56.8–56.9 at.% Nb), λ-NbH_{1-x}(orL-NbH_{1-x}, <~–50 °C, invariable compos., ~58 at.% Nb), ε-NbH_{1-x} (< –48 °C, invariable compos., ~59 at.% Nb), θ-NbH_{1-x} (<~–(80÷90) °C, homog. range—~62–80 at.% Nb), η-NbH_{1-x} (< –65 °C, homog. range—~63–88 at.% Nb), Nb Extended solid solution based on Nb (up to ~45–46 at.% H at 140–250 °C) with miscibility gap (critical point—~170 °C, ~77–80 at.% Nb; from ~66–68 to ~89–90 at.% Nb at ~80–85 °C) Data on the system available in literature are controversial.	The interaction between Nb and H is exothermic and initiates at ~250–400 °C. The solubility of H in Nb (pressure 0.1 MPa) is 28, 7.4 and 3.2 at.% at 500, 700 and 900 °C, respectively. The intensive absorption of H by Nb is observed at 330 °C and 630–830 °C (two maximum points). Nb is considerably affected by brittleness in H_2 atmosphere. For diffusion rate in the system at various temp. see Addendum.	[4, 10, 12–13, 16, 46, 62, 67–72, 304–305, 360–361]

(continued)

Table 8.5 (continued)

System	Type of phase diagram (constituent phases, temperatures and compositions of transformations)	Character of interaction	References
Nb–D (^{2}H)	Plotted partially Extended solid solution based on Nb with miscibility gap (critical point—177 °C, ~75 at.% Nb; ~67–88 at.% Nb at 135 °C)	–	[13, 73–74, 378]
Nb–T (^{3}H)	Plotted partially Extended solid solution based on Nb with miscibility gap (critical point—~170 °C, ~77 at.% Nb; ~66–90 at.% Nb at ~100 °C)	–	[67]
Nb–Li	α-Li, β-Li, γ-Li, no binary compounds, Nb	No chemical interaction, practically no miscibility in the solid and liquid states. At 500–1000 °C the solubility of Nb in liquid Li is $\sim 10^{-3}$–10^{-5} at.%. Nb is resistant to corrosion in liquid Li and compatible for long-term applications at 1000 °C.	[4, 14, 75–76]
Nb–Na	α-Na, β-Na, no binary compounds, Nb	No chemical interaction, practically no miscibility in the solid and liquid states. No wettability of Nb by Na at temp. ≤150 °C. At 800–1400 °C the solubility of Nb in liquid Na is $\sim(1 \div 2) \times 10^{-3}$ at.%; the solubility is considerably dependent on the O contamination of liquid Na, contaminated Na dissolves more Nb than highly purified melt. Nb is resistant to corrosion in liquid Na at 600–1000 °C; at 600 °C the corrosion rate is ≤0.025 mm per year.	[4, 14, 16, 77–78]

(continued)

Table 8.5 (continued)

System	Type of phase diagram (constituent phases, temperatures and compositions of transformations)	Character of interaction	References
Nb–K	K, no binary compounds, Nb	No chemical interaction, practically no miscibility in the solid and liquid states. At temp. <1200 °C the solubility of Nb in liquid K < 0.001 at.%; the solubility increases noticeably in the case of O contamination. An increase in O contents in K from 10^{-4} to 1.9 at.% corresponds to increase in Nb solubility in K from 0.005 to 1.3 at.%. Nb is resistant to corrosion in liquid K at 600–1000 °C; at 600 °C the corrosion rate is <0.025 mm per year.	[4, 14, 16, 43, 79, 306]
Nb–Rb	Rb, no binary compounds, Nb	No chemical interaction, practically no miscibility in the solid and liquid states.	[14, 16, 76, 80]
Nb–Cs	Cs, no binary compounds, Nb	No chemical interaction, practically no miscibility in the solid and liquid states. Nb is highly resistant to Cs melt and vapour (with low O contamination), good performance during 6000–8000 h at 1150–1265 °C; the presence of O (>0.3 at.%) leads to intercrystalline (intergranular) corrosion with depth—up to 0.1 mm.	[4, 16, 76]
Nb–Fr	No data	–	–

(continued)

Table 8.5 (continued)

System	Type of phase diagram (constituent phases, temperatures and compositions of transformations)	Character of interaction	References
Group 2			
Nb–Be	α-Be, *β*-Be, $NbBe_{12}$ (<1665–1675 °C, incongruent melt. point, invariable compos.), Nb_2Be_{17} (from 1415 °C (?) to 1750–1850 °C, congruent melt. point, invariable compos.), $NbBe_5$ (<1485 °C, invariable compos., ?), $NbBe_3$ (<~1600–1920 °C, congruent melt. point, invariable compos.), $NbBe_2$ (<1520–1660 °C, incongruent melt. point, invariable compos.), Nb_3Be_2 (<~1590–1700 °C, melt. point (?), invariable compos.), Nb Eutectic (degenerated) $NbBe_{12}$–*β*- or α-Be (~1210–1289 °C, ~0.25 at.% Nb, ?) Eutectic Nb_2Be_{17}–$NbBe_3$ (~1590–1650 °C, ~15 at.% Nb) Eutectic Nb_3Be_2–$NbBe_2$ (~1440–1600 °C, ~43–50 at.% Nb) Eutectic Nb_3Be_2–Nb (~1570–1630 °C, ~65–70 at.% Nb, ?) Data on the system available in the literature are controversial	At 850–1150 °C, the solubility of Nb in Be is ~0.015–0.100 at.%. The max. solid solubility of Be in Nb is ~16 at.% at 1590 °C; it declines with temperature decreasing—up to 9 at.% at 700 °C. The direct interaction between Nb and Be leads to the formation of $NbBe_2$ and $NbBe_{12}$. For diffusion rate in the system at various temp. see Addendum.	[4, 12, 15–16, 81–85, 396]
Nb–Mg	Mg, no binary compounds, Nb Data on the system available in the literature are controversial	The presence of Mg decreases Nb melt. point—up to 2380 °C (?). The solubility of Mg in Nb is 0.20 at.% at 2380 °C and 0.16 at.% at room temp., and that of Nb in Mg is negligible.	[4, 14, 16]

(continued)

Table 8.5 (continued)

System	Type of phase diagram (constituent phases, temperatures and compositions of transformations)	Character of interaction	References
Nb–Ca	α-Ca, β-Ca, no binary compounds, Nb No diagram plot	No interaction at least at temp. ≤870 °C.	[15]
Nb–Sr	No data	–	–
Nb–Ba	No data	–	–
Nb–Ra	No data	–	–
Group 3			
Nb–Sc	α-Sc, β-Sc, no binary compounds, Nb Eutectic β-Sc–Nb (~1500 °C, 3 at.% Nb) Some data on the system available in the literature are controversial	The max. solid solubility of Nb in Sc is ≤0.4 at.% and that of Sc in Nb is ≤0.1 at.%; data on mutual solubilities in the system available in literature are controversial. For diffusion rate in the system at various temp. see Addendum.	[14, 16, 307–308]
Nb–Y	α-Y, β-Y, no binary compounds, Nb Eutectic α-Y–Nb (1470 °C, ~5.8–6.0 at.% Nb) Miscibility gap in the liquid state (from 46.0–46.1 to 99.5 at.% Nb at ~2400 °C)	At 1470 °C, the solid solubility of Nb in α-Y is <0.1 at.%. For diffusion rate in the system at various temp. see Addendum.	[14, 16 , 32, 86, 309]
Lanthanides			
Nb–La	α-La, β-La, γ-La, no binary compounds, Nb Peritectic γ-La (~925 °C, ~1 at.% Nb, ?) Miscibility gap in the liquid state (from ~10–15 to ~97.0–99.8 at.% Nb at 2400 °C)	The presence of Nb increases La melt. point, but it does not have an influence upon the temp. of β-La–γ-La transformation. At room temp. the solid solubility of La in Nb is 0.3 at.%.	[14, 16, 55, 87, 310]
Nb–Ce	α-Ce, β-Ce, γ-Ce, δ-Ce, no binary compounds, Nb Peritectic δ-Ce (~805–820 °C, ~2 at.% Nb, ?) Miscibility gap in the liquid state (from ~25–26 to ~98–99 at.% Nb at ~2350–2420 °C)	The presence of Nb increases Ce melt. point —up to ~805–820 °C and decreases the temp. of γ-Ce–δ-Ce transformation —up to 700–705 °C. The solubility of Ce in Nb is ~1 at.% at 2350–2390 °C and <0.05 at.% at room temp.	[15–16, 87, 307, 311]

(continued)

Table 8.5 (continued)

System	Type of phase diagram (constituent phases, temperatures and compositions of transformations)	Character of interaction	References
Nb–Pr	α-Pr, β-Pr, no binary compounds, Nb No diagram plot	The components are mainly immiscible in the liquid state.	[14]
Nb–Nd	α-Nd, β-Nd, no binary compounds, Nb No diagram plot	At the melt. point of Nd, the solubility of Nb in it is negligible.	[14, 55]
Nb–Pm	No data	–	–
Nb–Sm	α-Sm, β-Sm, γ-Sm, no binary compounds, Nb Peritectic γ-Sm (∼1135–1145 °C, ∼2 at.% Nb, ?)	The presence of Nb increases Sm melt. point—up to ∼1135–1145 °C and the temp. of β-Sm–γ-Sm transformation—up to ∼925–927 °C. The solubility of Sm in Nb is <0.09 at.% at ∼2460 °C and <0.05 at.% at ∼500–750 °C. The solubility of Nb in α-Sm is <0.01 at.%. In general, data on mutual solubilities in the system available in literature are controversial.	[14, 312]
Nb–Eu	Eu, no binary compounds, Nb	The components are mainly immiscible in the liquid and solid states.	[13, 16]
Nb–Gd	α-Gd, β-Gd, no binary compounds, Nb Miscibility gap in the liquid state (?) No diagram plot	The components are mainly immiscible in the liquid state.	[13]
Nb–Tb	α′-Tb, α-Tb, β-Tb, no binary compounds, Nb No diagram plot	The components are mainly immiscible in the liquid state.	[14]
Nb–Dy	α′-Dy, α-Dy, β-Dy, no binary compounds, Nb No diagram plot	The components are mainly immiscible in the liquid state.	[13]
Nb–Ho	α-Ho, β-Ho, no binary compounds, Nb No diagram plot	The components are mainly immiscible in the liquid state.	[13]

(continued)

Table 8.5 (continued)

System	Type of phase diagram (constituent phases, temperatures and compositions of transformations)	Character of interaction	References
Nb–Er	α-Er, β-Er, no binary compounds, Nb Eutectic β-Er–Nb (~1425–1525 °C, ~9 at.% Nb, ?) Miscibility gap in the liquid state (from ~21–22 to ~98–99 at.% Nb at 2460–2470 °C, ?)	The components are mainly immiscible in the liquid state.	[13, 307]
Nb–Tm	α-Tm, β-Tm, no binary compounds, Nb No diagram plot	The components are mainly immiscible in the liquid state.	[14]
Nb–Yb	α-Yb, β-Yb, γ-Yb, no binary compounds, Nb Miscibility gap in the liquid state (from ~1–2 to ~98–99 at.% Nb at ~2450 °C)	The mutual solid solubilities of the components are negligible. In the liquid state, the components are mainly immiscible.	[14, 16]
Nb–Lu	α-Lu, β-Lu, no binary compounds, Nb Eutectic β-Lu–Nb (1620 °C, ~2.0–7.5 at.% Nb, ?)	The max. solid solubility of Nb in β-Lu is ~0.3–4.0 at.%. In general, data on mutual solubilities in the system available in the literature are controversial.	[307, 313]
Actinides			
Nb–Ac	No data	–	–
Nb–Th	α-Th, β-Th, no binary compounds, Nb Eutectic β-Th–Nb (1435 °C, ~16–18 at.% Nb)	The presence of Nb decreases the temp. of α-Th–β-Th transformation—up to 1355 °C. The solid solubility of Nb in α-Th is <0.25 at.% and in β-Th—<2 at.%. The solubility of Th in Nb is negligible. In general, some data on mutual solubilities in the system available in the literature are controversial. For diffusion rate in the system at various temp. see Addendum.	[4, 14, 16, 314]
Nb–Pa	No data	–	–

(continued)

Table 8.5 (continued)

System	Type of phase diagram (constituent phases, temperatures and compositions of transformations)	Character of interaction	References
Nb–U	α-U, β-U, γ-U, no binary compounds, Nb Continuous solid solution γ-U–Nb (up to melt. points; miscibility gap: critical point—~955–990 °C, ~50–52 at.% Nb; from ~14.5–30.0 to ~72–86 at.% Nb at ~645–650 °C)	The max. solid solubility of Nb in α-U is 0.08 at.% at 550 °C, 0.16 at.% at 600 °C, 0.24 at.% at 630 °C, ~0.5–1.9 at.% at 640–665 °C. The max. solid solubility of Nb in β-U is 3.8 at.% at 650 °C, >1.27 at.% at 660–665 °C and 1.9 at.% at 720 °C. In general, solid U is compatible with Nb. Molten U impregnates Nb porous preforms perfectly. For diffusion rate in the system at various temp. see Addendum.	[4, 14, 16, 88–92, 362, 388]
Nb–Np	No data	–	–
Nb–Pu	α-Pu, β-Pu, γ-Pu, δ-Pu, δ′-Pu, ε-Pu, no binary compounds, Nb Eutectic (degenerated) ε-Pu–Nb (~625–630 °C, ~0.5–1.0 at.% Nb, ?)	The solid solubility of Pu in Nb is <0.4 at.%.	[14, 16, 315–316]
Nb–Am	No data	–	–
Group 4			
Nb–Ti	α-Ti, β-Ti, metastable α′-, α″- and ω-phases, no binary compounds, Nb Continuous solid solution β-Ti–Nb (up to melt. points)	Nb stabilizes β-Ti phase; in the presence of Nb the melt. point of Ti increases, and temp. of α-Ti–β-Ti polymorphic transformation decreases considerably. The max. solubility of Nb in α-Ti is ~2.5 at.% at 600 °C. At lower temp., the solubility declines noticeably—up to 1 at.% at 400 °C, 0.25 at.% at 200 °C and <0.01 at.% at room temp. For diffusion rate in the system at various temp. see Addendum.	[4, 14, 16, 93–100]

(continued)

Table 8.5 (continued)

System	Type of phase diagram (constituent phases, temperatures and compositions of transformations)	Character of interaction	References
Nb–Zr	α-Zr, β-Zr, no binary compounds, Nb Continuous solid solution β-Zr–Nb (up to melt. points, min. melt. point 1740 °C corresp. to 21.7 at.% Nb; miscibility gap: critical point—988 °C, 60.6–61.0 at.% Nb; from 17.5–18.8 to 91.0–92.1 at.% Nb at 610–630 °C)	Nb stabilizes β-Zr phase; in the presence of Nb the temp. of α-Zr–β-Zr polymorphic transformation decreases. The solid solubility of Nb in α-Zr is 0.6–6.5 at.% at 560–690 °C, and that of Zr in Nb in the same temp. range is ~7.9–9.0 at.%; at lower temp. the mutual solid solubilities decrease considerably. For diffusion rate in the system at various temp. see Addendum.	[4, 14, 16, 56, 89, 101–104, 397]
Nb–Hf	α-Hf, β-Hf, metastable ω-phase, no binary compounds, Nb Continuous solid solution β-Hf–Nb (up to melt. points, min. melt. point ~2065–2140 °C corresp. to ~ 25–55 at.% Nb, ?) Data on the system available in the literature are controversial.	Nb stabilizes β-Hf phase; in the presence of Nb the temp. of α-Hf–β-Hf polymorphic transformation decreases. The max. solubility of Nb in α-Hf is ~2–4 at.% at 1000 °C; at lower temp. the mutual solid solubilities decline considerably. Two phase area in the system is very sensitive to the contamination by interstitial atoms.	[13, 16, 96, 105–108]
Group 5			
Nb–V	V, no binary compounds, Nb Continuous solid solution V–Nb (min. melt. point ~1720–1870 °C corresp. to ~22–27 at.% Nb)	For diffusion rate in the system at various temp. see Addendum.	[4, 14, 16, 57, 109–111]
Nb–Ta	See Ta–Nb in Table 6.3.		

(continued)

Table 8.5 (continued)

System	Type of phase diagram (constituent phases, temperatures and compositions of transformations)	Character of interaction	References
Group 6			
Nb–Cr	Cr, λ_2-$NbCr_{2\pm x}$ (or λ_2-Nb_2Cr_{3+x}, <1585–1625 °C, homog. range—~31–38 at.% Nb, Laves phase), λ_1–$NbCr_{2\pm x}$ (or λ_1–Nb_2Cr_{3+x}, from 1585–1625 °C to ~1675–1820 °C, congruent melt. point, homog. range—~30–39 at.% Nb, Laves phase), Nb Eutectic λ_1-$NbCr_{2\pm x}$–Cr (~1600–1660 °C, ~12–22 at.% Nb) Eutectic λ_1-$NbCr_{2\pm x}$–Nb (~1600–1715 °C, ~39–53 at.% Nb)	The max. solid solubility of Nb in Cr is ~6 at.% at ~1600–1660 °C, and that of Cr in Nb is ~15 at.% at 1600–1715 °C. At lower temp., the solubility of Nb decreases up to ~1 at.% at 1000 °C, and that of Cr at the same temp. decreases up to ~2–3 at.%. The direct interaction between Nb and Cr leads usually to the formation of λ_2-$NbCr_{2\pm x}$. For diffusion rate in the system at various temp. see Addendum.	[4, 13, 16, 58, 61, 112–114, 395]
Nb–Mo	See Mo–Nb in Table 7.4.		
Nb–W	See W–Nb in Table 3.5.		
Group 7			
Nb–Mn	α-Mn, β-Mn, γ-Mn, δ-Mn, $Mn_{2\pm x}Nb$ (<1500 °C, congruent melt. point, homog. range—~28–40 at.% Nb, Laves phase), Nb Eutectic $Mn_{2\pm x}Nb$–δ-Mn (~1200–1225 °C, ~3.5–3.6 at.% Nb) Eutectic $Mn_{2\pm x}Nb$–Nb (1400 °C, ?)	In the presence of Nb, the temp. of α-Mn–β-Mn polymorphic transformation increases—up to 800 °C. The max. solid solubility of Nb in β- and δ-Mn is ~2.1–2.4 at.% at 1150–1200 °C.	[4, 14, 16, 32, 115–116, 317]
Nb–Tc	Tc, $Tc_{3\pm x}Nb$ (wide homog. range, ?), Nb No diagram plot	–	[14, 40]
Nb–Re	See Re–Nb in Table 4.5.		

(continued)

Table 8.5 (continued)

System	Type of phase diagram (constituent phases, temperatures and compositions of transformations)	Character of interaction	References
Group 8			
Nb–Fe	α-Fe, γ-Fe, δ-Fe, ε-$Fe_{2\pm x}Nb$ (<~1625–1665 °C, congruent melt. point, homog. range—~26–38 at.% Nb at 600–1200 °C, Laves phase), μ-Fe_7Nb_{6+x} (or μ-$FeNb_{1\pm x}$, or $Fe_{21}Nb_{19\pm x}$, <~1600–1700 °C, congruent melt. point, homog. range—~47–52 at.% Nb (?) at 600–1200 °C), Nb Eutectic ε-$Fe_{2\pm x}Nb$–μ-Fe_7Nb_{6+x} (1535 °C, ~42–43 at.% Nb) Eutectic ε-$Fe_{2\pm x}Nb$–δ-Fe (~1370–1375 °C, 12 at.% Nb) Eutectic μ-Fe_7Nb_{6+x}–Nb (~1400 °C, ~64 at.% Nb, ?)	The max. solubilities of Nb in Fe modifications are: in δ-Fe–3.2 at.% at 1370–1375 °C, in γ-Fe—0.9–1.0 at.% at 1210 °C and in α-Fe—0.7 at % at 960 °C; at lower temp. the solubility of Nb decreases up to 0.33 at.% at 900 °C, 0.185 at.% at 800 °C, 0.115 at.% at 700 °C and 0.095 at.% at 600 °C. The max. solubility of Fe in Nb is ~7.5 at.% at 1400 °C; at lower temp. the solubility of Fe decreases up to ~4–7 at.% at 1300 °C. For diffusion rate in the system at various temp. see Addendum.	[4, 13, 16, 117–118, 391–392]
Nb–Ru	Ru, $Ru_{3\pm x}Nb$ (<1540 °C, homog. range—~24–27 at.% Nb at 1000–1400 °C), Nb Extended solid solution based on Ru (up to 29 at.% Nb at 1775 °C) Extended solid solution based on Nb (up to ~58–60 at.% Ru at 1540–1775 °C; liquidus-solidus extreme points: min. melt. point 1870 °C corresp. to 61 at.% Nb and max. melt. point ~1940 °C corresp. to 50 at.% Nb) Eutectic Nb–Ru (~1775 °C, 65 at.% Nb)	The solid solubility of Nb in Ru is 29 at.% at ~1775 °C and 15 at.% at 1540 °C; at lower temp. the solubility of Nb declines considerably. For diffusion rate in the system at various temp. see Addendum.	[4, 14, 119–120]
Nb–Os	See Os–Nb in Table 5.3.		

(continued)

Table 8.5 (continued)

System	Type of phase diagram (constituent phases, temperatures and compositions of transformations)	Character of interaction	References
Group 9			
Nb–Co	ε-Co, α-Co, χ-$Co_7Nb_{2\pm x}$ (<1050 °C, homog. range—21–23 at.% Nb), λ_3-Co_3Nb (~1000–1245 °C, incongruent melt. point, homog. range width <1 at.%), $\lambda_2(\alpha)$-$Co_{2\pm x}Nb$ (?), λ_2-$Co_{2\pm x}Nb$ (or $\lambda_2(\beta)$-$Co_{2\pm x}Nb$, <1480–1520 °C, congruent melt. point, homog. range—27–34 at.% Nb at 400–1000 °C), λ_1-Co_5Nb_{3-x} (1200–1420 °C, incongruent melt. point, homog. range—~34.0–37.5 at.% Nb), μ-$Co_7Nb_{6\pm x}$ (or μ-$CoNb_{1\pm x}$, <~1400–1480 °C, congruent melt. point, homog. range—from ~49–56 at.% Nb at 400–1200 °C), Nb Eutectic λ_1-Co_5Nb_{3-x} (or λ_2-$Co_{2\pm x}Nb$, ?)–μ-$Co_7Nb_{6\pm x}$ (~1370–1380 °C, ~43–47 at.% Nb) Eutectic λ_3-Co_3Nb–α-Co (~1210–1245 °C, ~14 at.% Nb) Eutectic μ-$Co_7Nb_{6\pm x}$–Nb (~1370–1375 °C, ~61–62 at.% Nb)	The max. solid solubility of Nb in α-Co—5.5 at.% at 1210–1245 °C; at lower temp. it declines noticeably—up to 4 at.% at 1000 °C and 1 at.% at 800 °C. The max. solubility of Co in Nb is ~4–5 at.% at 1370–1375 °C; at lower temp. the solubility of Co declines slightly. For diffusion rate in the system at various temp. see Addendum.	[4, 13, 16, 121–122, 376, 385]

(continued)

Table 8.5 (continued)

System	Type of phase diagram (constituent phases, temperatures and compositions of transformations)	Character of interaction	References
Nb–Rh	Rh, $Rh_{3\pm x}Nb$ (<1950 °C, congruent melt. point corresp. to ~$Rh_{2.6}Nb$, homog. range—~21–27 at.% Nb at ~1300–1800 °C), η-$Rh_{2\pm x}Nb$ (<~1900 °C, incongruent melt. point, homog. range—~30–34 at.% Nb), ζ-$Rh_{3\pm x}Nb_2$ (<~1625 °C, incongruent melt. point, homog. range—~36–41 at.% Nb), ε-$RhNb_{1-x}$ (from ~1335–1420 °C to ~1580–1600 °C, incongruent melt. point, homog. range—~38–45 at.% Nb), δ-$RhNb_{1-x}$ (<~1420 °C, homog. range—~44–46 at.% Nb), γ-$RhNb_{1-x}$ (<~ 1350 °C, homog. range—~47–49 at.% Nb), β-$RhNb_{1\pm x}$ (from ~1335–1420 to ~1550–1580 °C, incongruent melt. point, homog. range—~43–54 at.% Nb), σ-$RhNb_{2\pm x}$ (<1660 °C, incongruent melt. point, homog. range—~60–72 at.% Nb), $RhNb_{3\pm x}$ (<1220 °C, homog. range width <1 at.%), Nb Extended solid solution based on Rh (up to 16.5 at.% Nb at ~1990 °C) Extended solid solution based on Nb (up to 20.5 at.% Rh at 1660 °C) Eutectic β-$RhNb_{1\pm x}$–σ-$RhNb_{2\pm x}$ (1550 °C, 55 at.% Nb) Eutectic $Rh_{3\pm x}Nb$–Rh (~1900 °C, ~17 at.% Nb)	The presence of Nb results in decrease in the melt. temp. of Rh. At lower temp. the solid solubility of Rh in Nb declines—up to 14 at.% at ~1200 °C. The solubility of Nb in Rh is affected by temp. slightly. The direct interaction between Nb and Rh leads usually to the formation of $RhNb_{3\pm x}$.	[4, 14, 123]

(continued)

Table 8.5 (continued)

System	Type of phase diagram (constituent phases, temperatures and compositions of transformations)	Character of interaction	References
Nb–Ir	Ir, $Ir_{3\pm x}Nb$ (<2435–2440 °C, congruent melt. point corresp. to ~$Ir_{3.1}Nb$, homog. range—~16–28 at.% Nb at 2400 °C, ~23–36.5 at.% Nb at 1985 °C and ~24–32 at.% Nb at 1400 °C), α_2-$IrNb_{1-x}$ (<~1985 °C, incongruent melt. point, homog. range —~39.5–45.5 at.% Nb at 1900 °C and 40.5–45.5 at.% Nb at 1400 °C), α_1-$IrNb_{1-x}$ (<~1900 °C, incongruent melt. point, homog. range—~47–48 at.% Nb at 1400–1840 °C), σ-$IrNb_{2-x}$ (<~2060 °C, incongruent melt. point, homog. range—58.5–67.0 at.% Nb at 1840 °C and ~59.5–67.0 at.% Nb at 1400 °C), $IrNb_{3\pm x}$ (<2125–2130 °C, congruent melt. point corresp. to ~$IrNb_3$, homog. range—~71–78 at.% Nb at 2060–2110 °C and ~72–79 at.% Nb at 1400 °C), Nb Extended solid solution based on Ir (up to 16 at.% Nb at 2400 °C) Extended solid solution based on Nb (up to 12 at.% Ir at 2110 °C) Eutectic α_1-$IrNb_{1-x}$–σ-$IrNb_{2-x}$ (1840 °C, 55 at.% Nb) Eutectic $Ir_{3\pm x}Nb$–Ir (2400 °C, ~16.5 at.% Nb) Eutectic $IrNb_{3\pm x}$–Nb (2110 °C, 80 at.% Nb)	The presence of Nb results in decrease in the melt. temp. of Ir. The solubility of Nb in Ir declines with temp. decreasing—up to ~11 at.% at 1400 °C. At lower temp., the solubility of Ir also declines noticeably—up to ~7 at.% at 1400 °C. The direct interaction between Nb and Ir leads usually to the formation of $IrNb_{3\pm x}$.	[4, 14, 16, 124, 364]

(continued)

Table 8.5 (continued)

System	Type of phase diagram (constituent phases, temperatures and compositions of transformations)	Character of interaction	References
Group 10			
Nb–Ni	Ni, Ni_8Nb (<535 °C, invariable compos.), $Ni_{3\pm x}Nb$ (<~1400 °C, congruent melt. point corresp. to ~Ni_3Nb, homog. range—~23.5–26.5 at.% Nb), μ-Ni_6Nb_{7-x} (or μ-$NiNb_{1+x}$, <1290 °C, incongruent melt. point, homog. range—~50–54 at.% Nb at 400–1175 °C), Nb Extended solid solution based on Ni (up to ~12.5 at.% Nb at 1280 °C) Eutectic μ-Ni_6Nb_{7-x}–$Ni_{3\pm x}Nb$ (1175–1180 °C, 40.5 at.% Nb) Eutectic $Ni_{3\pm x}Nb$–Ni (1282 °C, ~16 at.% Nb)	The solid solubilities of the components decline with temp. decrease considerably: the solubility of Nb in Ni—from ~12.5 at.% at 1280 °C to ~3.5 at.% at 400–600 °C, and that of Ni in Nb—from ~4.5–8.0 at.% (?) at 1400–1570 °C to ~1–2 at.% at 400–800 °C. Data on the mutual solubilities available in the literature are controversial. The direct interaction between Nb and Ni results in the formation of $Ni_{3\pm x}Nb$ and μ-Ni_6Nb_{7-x}. For diffusion rate in the system at various temp. see Addendum.	[4, 14, 16, 124–128, 389, 393, 398]
Nb–Pd	Pd, β-$Pd_{3\pm x}Nb$ (<~1610 °C, homog. range—~23–27 at.% Nb at 700–1300 °C), α-$Pd_{3\pm x}Nb$ (?), $Pd_{2\pm x}Nb$ (<~1610 °C, incongruent melt. point, homog. range —~32.5–34.0 at.% Nb at 700–1560 °C), α-$Pd_{1\pm x}Nb$ (1255–1565 °C, homog. range—~40–51 at.% Nb), δ-Pd_2Nb_3 (metastable, ?), Nb Extended solid solution based on Pd (up to ~31 at.% Nb at ~1610 °C with max. melt. point ~1625–1665 °C corresp. to ~25–26 at.% Nb) Extended solid solution based on Nb (up to ~35–36 at.% Pd at 1255–1520 °C) Eutectic α-$Pd_{1\pm x}Nb$–Nb (1510–1530 °C, ~53 at.% Nb)	At 700–1300 °C the solubility of Nb in Pd is ~18.5 at.%. The solubility of Pd in Nb declines with temp. decrease at temp. <1255 °C—from ~35 at.% to ~20 at.% at 700 °C. For diffusion rate in the system at various temp. see Addendum.	[4, 14, 16, 129–130]

(continued)

Table 8.5 (continued)

System	Type of phase diagram (constituent phases, temperatures and compositions of transformations)	Character of interaction	References
Nb–Pt	Pt, α-$Pt_{3\pm x}Nb$ (<2040 °C, congruent melt. point corresp. to ~$Pt_{3.2}Nb$, homog. range—~24–26 at.% Nb), β-$Pt_{3\pm x}Nb$ (?), $Pt_{2\pm x}Nb$ (<1990 °C, incongruent melt. point, homog. range—~32–34.5 at.% Nb), α′-$PtNb_{1-x}$ (or α′-Pt, 1670–1780 °C, incongruent melt. point, homog. range—~43–44 at.% Nb), $Pt_{1+x}Nb_{1-x}$ (<1750 °C, incongruent melt. point, homog. range —~47–49 at.% Nb), σ-$PtNb_{2\pm x}$ (<1800 °C, incongruent melt. point, homog. range—62–69 at.% Nb at 1700 °C and ~64–67 at.% Nb at 1000 °C), $PtNb_{3\pm x}$ (<2040 °C, incongruent melt. point, homog. range—~72–81 at.% Nb), Nb Extended solid solution based on Pt (up to ~20 at.% Nb at ~2000 °C) Extended solid solution based on Nb (up to ~12 at.% Pt at 2040 °C) Peritectic Pt (~2000 °C, ~20 at.% Nb) Eutectic σ-$PtNb_{2\pm x}$–$Pt_{1+x}Nb_{1-x}$ (1690–1710 °C, ~57 at.% Nb)	The presence of Nb results in increase in the melt. temp. of Pt. The max. melt. point (~2000 °C) and max. solid solubility of Nb in Pt (~20 at.%) are correspond. to the peritectic alloy. The solubility of Nb in Pt is slightly affected by temp.; the solubility of Pt in Nb declines with temp. decrease considerably—up to ~5 at.% at 1150 °C.	[4, 14, 131, 390]

(continued)

Table 8.5 (continued)

System	Type of phase diagram (constituent phases, temperatures and compositions of transformations)	Character of interaction	References
Group 11			
Nb–Cu	Cu, no binary compounds, Nb Peritectic Cu (~1090–1095 °C, ~0.3–1.7 at.% Nb, ?) Eutectic (degenerated) Cu–Nb (~1080 °C, ~0.3 at.% Nb, ?) Miscibility gap in the liquid state (critical point—~1620–1780 °C, ~20–25 at.% Nb; from ~3–19 to ~33–44 at.% Nb at ~1550–1680 °C, ?) Data on the system available in the literature are controversial.	The solubility of Nb in Cu is ~0.3–1.7 at.% (?) at ~1100 °C, ~0.20–0.45 at.% at 1000 °C and 0.14–0.15 at.% at 20–800 °C. At 1200 °C, the solubility of Cu in Nb is ~0.9 at.% at 1670–1680 °C and ~0.6–0.7 at.% at 800–1000 °C. Data on mutual solubilities in the system available in literature are controversial. For diffusion rate in the system at various temp. see Addendum.	[4, 13, 16, 52, 132–135, 318–320, 371, 386]
Nb–Ag	Ag, no binary compounds, Nb No diagram plot	Practically, no mutual solubility between Nb and Ag in the liquid and solid states. At 1400–1700 °C the solubility of Nb in liquid Ag is negligible and that of Ag in solid Nb is extremely low.	[15, 321]
Nb–Au	Au, Au_2Nb (<1035 °C, invariable compos.), Au_2Nb_3 (<~1220 °C, invariable compos.), $AuNb_{3\pm x}$ (<1560 °C, homog. range—~73–83 at.% Nb), Nb Extended solid solution based on Au (up to ~57 at.% Nb at 1570 °C) Extended solid solution based on Nb (up to ~36 at.% Au at 1570 °C) Peritectic Au (~1570 °C, ~57 at.% Nb)	At temp. <1035 °C the solubility of Nb in Au declines considerably with temp. decrease; it falls to ~9 at.% at 500 °C. The solubility of Au in Nb is also strongly affected by temp. decrease (at temp. <1560 °C); it declines considerably up to ~10 at.% at 500 °C.	[15–16, 136–138]

(continued)

Table 8.5 (continued)

System	Type of phase diagram (constituent phases, temperatures and compositions of transformations)	Character of interaction	References
Group 12			
Nb–Zn	Zn, $NbZn_{15}$ (<429 °C, incongruent melt. point, invariable compos.), $NbZn_7$ (<478 °C, incongruent melt. point, invariable compos.), $NbZn_{3\pm x}$ (<~1035 °C, incongruent melt. point, homog. range width ≤1 at.%), $NbZn_2$ (<~1055 °C, incongruent melt. point, Laves phase), Nb_2Zn_{3-x} (<~1115 °C, incongruent melt. point), $NbZn_{1+x}$ (or Nb_6Zn_7, <1120 °C, incongruent melt. point, homog. range width ≤1 at.%), Nb Eutectic (degenerated) $NbZn_{15}$–Zn (~418 °C, ~0.01 at.% Nb, ?)	No data on mutual solubilities are available in literature. At 500 °C, Nb is resistant to corrosion in molten Zn.	[4, 14, 16, 139, 152]
Nb–Cd	Cd, $NbCd_3$ (?), Nb No diagram plot	–	[322]
Nb–Hg	Hg, no binary compounds, Nb	No interaction. The solubility of Nb in liquid Hg is $\sim 10^{-9}$ at.% Nb at room temp. and $\sim 6\times 10^{-6}$ at.% Nb at 500–750 °C. At 300–600 °C Nb is highly resistant to corrosion and erosion in Hg.	[4, 16, 323]

(continued)

Table 8.5 (continued)

System	Type of phase diagram (constituent phases, temperatures and compositions of transformations)	Character of interaction	References
Group 13			
Nb–B	β-B, $NbB_{2\pm x}$ (<3000 °C, congruent melt. point corresp. to ~$NbB_{2.1}$, homog. range—~28–36 at.% Nb at 2700 °C, ~25–36 at.% Nb at 2000 °C and ~24–36 at.% Nb at 1400 °C), Nb_2B_3 (?), Nb_3B_4 (<2700 °C, incongruent melt. point, invariable com-pos.), Nb_5B_6 (<at least 2200 °C, invariable compos., ?), $NbB_{1\pm x}$ (<~2270–2325 °C, congruent melt. point corresp. to ~$NbB_{1.0}$, homog. range—49–51 at.% Nb), Nb_3B_2 (<~1800–2230 °C, incongruent melt. point, invariable compos.), Nb Eutectic Nb_3B_4–$NbB_{1\pm x}$ (~2250–2295 °C, ~47–48 at.% Nb) Eutectic Nb_3B_2–Nb (~1600–2170 °C (?), ~85–88 at.% Nb) Eutectic $NbB_{2\pm x}$–β-B (~1850–2000 °C, ~1.5–8.5 at.% Nb, ?)	The max. solid solubility of B in Nb is 2.9 at.% at ~2170 °C; it declines with temp. decrease—up to 2.2 at.% at 1950 °C, 1.3 at.% at 1600 °C and 0.4 at.% at 1200 °C. Nb borides are formed by the direct interaction between the elements at 1500–1600 °C in vacuum. The contact interaction between compact metal Nb and $NbB_{2\pm x}$ initiates from 1600–1800 °C and leads to the formation of $NbB_{2\pm x}$. For diffusion rate in the system at various temp., see Addendum.	[4, 12, 15, 16, 18–19, 30, 45, 53, 140, 232, 237, 288, 374–375, 383]

(continued)

Table 8.5 (continued)

System	Type of phase diagram (constituent phases, temperatures and compositions of transformations)	Character of interaction	References
Nb–Al	Al, $NbAl_{3-x}$ (<1605–1680 °C (?), congruent melt. point corresp. to $NbAl_{3.0}$, homog. range—~25–26.5 at.% Nb at 1000–1590 °C and ~25.5–26.5 at.% Nb at 600 °C, ?), Nb_5Al_3 (?), σ-$Nb_{2\pm x}Al$ (<~1860–1940 °C, incongruent melt. point, homog. range—~58–70 at.% Nb at 1590 °C, ~65–71 at.% Nb at 1000 °C and ~66.5–70 at.% Nb at 600 °C), $Nb_{3+x}Al$ (<~1950–2060 °C, incongruent melt. point, homog. range—~75–79 at.% Nb at 1860–1940 °C, ~79–83 at.% Nb at 1000 °C and ~79.5–83.5 at.% Nb at 600 °C), Nb_5Al (?), Nb Extended solid solution based on Nb (up to ~21.5–23.0 at.% Al at 1950–2060 °C) Peritectic Al (661.4 °C, <0.1–0.3 at.% Nb, ?) Eutectic σ-$Nb_{2\pm x}Al$–$NbAl_{3-x}$ (~1500–1550 °C, ~42–45 at.% Nb) Eutectic (degenerated) $NbAl_{3-x}$–Al (?) Data on the system available in the literature are controversial.	The max. solid solubility of Nb in Al is <0.1–0.3 at.%; it declines with temp. decrease—up to ~0.05 at.% at 500 °C and ~0.03 at.% at 20–300 °C. The max. solubility of Al in Nb is ~21.5–23.0 at.% at ~1950–2060 °C. At higher and lower temp., the solid solubility of Al in Nb declines considerably. The reaction between Nb and Al with the formation of aluminides initiates from 850 °C. For diffusion rate in the system at various temp. see Addendum.	[4, 12, 15–16, 52, 141–144]

(continued)

Table 8.5 (continued)

System	Type of phase diagram (constituent phases, temperatures and compositions of transformations)	Character of interaction	References
Nb–Ga	Ga, $NbGa_3$ (<1235 °C, incongruent melt. point, homog. range width ≤1 at.%), Nb_5Ga_{13} (?), Nb_4Ga_5 (<1300 °C, incongruent melt. point, invariable compos.), Nb_5Ga_4 (<1540 °C, incongruent melt. point, invariable compos.), Nb_5Ga_3 (<1950 °C, congruent melt. point, homog. range width ≤1 at.%), $Nb_{3+x}Ga$ (<1860 °C, incongruent melt. point, homog. range—~75–80 at.% Nb at 1740 °C, ~77–80 at.% Nb at 1000 °C and ~77.5–80 at.% Nb at 20 °C), Nb Extended solid solution based on Nb (up to 19.0 at.% Ga at 1850–1860 °C) Eutectic $Nb_{3+x}Ga$–Nb_5Ga_3 (1740 °C, ~31.5 at.% Nb) Eutectic (degenerated) $NbGa_3$–Ga (~28 °C, ?)	The solubility of Nb in Ga is negligible and that of Ga in Nb has max. value of 19.0 at.% at 1850–1860 °C; it declines at lower temp. to 15.8 at.% at 1800 °C, 12.0 at.% at 1700 °C, 11.3 at.% at 1600 °C, 7.7 at.% at 1500 °C, 2.5 at.% at 1200 °C and 1.3 at.% at 700 °C. At 300–450 °C Nb is resistant to corrosion in liquid Ga; at temp. ≥600 °C the resistance is poor.	[4, 13, 145–148]
Nb–In	In, $InNb_{3+x}$ (<475 °C, incongruent melt. point, homog. range—~76–88 at.% Nb at 390 °C and ~75–87 at.% Nb at 140 °C), ε-$InNb_{9\pm x}$ (or ε-$InNb_y$, $y \approx 5.5 \div 24.0$, 280–1005 °C, incongruent melt. point, homog. range—~83–96 at.% Nb), Nb Eutectic (degenerated) $InNb_{3+x}$–In (~140 °C, ~0.5 at.% Nb, ?)	The mutual solid solubilities Nb and In are negligible.	[14, 16, 47]
Nb–Tl	α-Tl, β-Tl, $TlNb_3$ (metastable, Frank-Kasper phase, ?), Nb Data on the system available in the literature are controversial.	No interaction (?), no mutual solubilities in the solid and liquid states.	[14, 16, 47, 324]

(continued)

Table 8.5 (continued)[a]

System	Type of phase diagram (constituent phases, temperatures and compositions of transformations)	Character of interaction	References
Group 14			
Nb–C	See C–Nb in Table 2.13.		
Nb–Si	Si, $NbSi_2$ (<~1920–1960 °C, congruent melt. point, invariable compos.), α-Nb_5Si_{3+x} (<~1635–1960 °C, homog. range width ≤1 at.%), β-Nb_5Si_{3+x} (from ~1635–1960 °C to ~2490–2545 °C, congruent melt. point corresp. to $NbSi_{0.6}$, homog. range—~59.5–62.5 at.% Nb), Nb_3Si (~1655–2000 °C, incongruent melt. point, invariable compos.), Nb Eutectic β-Nb_5Si_{3+x}–$NbSi_2$ (~1880–1920 °C, ~39–43 at.% Nb) Eutectic $NbSi_2$–Si (1390–1410 °C, ~2–4 at.% Nb) Eutectic Nb_3Si–Nb (~1870–1940 °C, ~81–85 at.% Nb) Data on the system available in the literature are controversial.	The max. solid solubility of Si in Nb amounts to ~1.2–3.5 at.% at 1870–1940 °C; at higher or lower temp. the solubility of Si declines considerably. Practically, there is no solubility of Nb in Si. Nb silicides are synthesized directly from the elements at 1000–1500 °C. In vacuum, at 1150–1370 °C the contact interaction between bulk Nb and $NbSi_2$ results in the formation of α-Nb_5Si_{3+x}. For diffusion rate in the system at various temp. see Addendum.	[4, 12, 14, 16, 19, 149–151, 209, 303, 380–381, 394]
Nb–Ge	Ge, $NbGe_{2\pm x}$ (<1680–1715 °C, congruent melt. point, homog. range—~32.5–34.5 at.% Nb), α-$Nb_{10}Ge_7$ (?), β-$Nb_{10}Ge_7$ (?), Nb_3Ge_2 (metastable, ?), α-$Nb_5Ge_{3\pm x}$ (?), β-$Nb_5Ge_{3\pm x}$ (or $Nb_3Ge_{2\pm x}$, <~2060–2190 °C, congruent melt. point, homog. range—~57.5–63 at.% Nb at 1865 °C, ~56–63 at.% Nb at 1580 °C and ~60–62 at.% Nb at 600 °C), Nb_2Ge (?), α-Nb_3Ge (?), β-$Nb_{3+x}Ge$ (<1900–1960 °C, incongruent melt. point, Frank-Kasper phase,	The max. solid solubility of Ge in Nb is ~10.5–12.5 at.% at 1900 °C; it declines with temp. decrease noticeably—up to ~3–5 at.% at 1000 °C. The direct interaction between Nb and Ge leads to the formation of Nb germanides.	[4, 12–13, 16, 153–155, 325–326, 334, 372]

(continued)

Table 8.5 (continued)

System	Type of phase diagram (constituent phases, temperatures and compositions of transformations)	Character of interaction	References
	homog. range—from 76–78 to 81.5–82.5 at.% Nb at 1865 °C, 79–84 at.% Nb at 1650 °C, from 78–80 to 82–85 at.% Nb at 1600 °C, at temp. ≤1000 °C homog. range width ≤1 at.%), Nb Extended solid solution based on Nb (up to ~10.5–12.5 at.% Ge at 1900 °C) Peritectic Ge (~950 °C, ?) Eutectic β-$Nb_{3+x}Ge$–β-$Nb_5Ge_{3\pm x}$ (~1865–1920 °C, 73 at.% Nb) Eutectic $NbGe_{2\pm x}$–β-$Nb_5Ge_{3\pm x}$ (~1580–1590 °C, 41–42 at.% Nb) Eutectic (degenerated) $NbGe_{2\pm x}$–Ge (~930–938 °C, ?) Data on the system available in the literature are controversial.		
Nb–Sn	α-Sn, β-Sn, $NbSn_{2-x}$ (<~815–870 °C, incongruent melt. point, homog. range—33.3–40.0 at.% Nb at 20–500 °C, ?), Nb_6Sn_{5-x} (or Nb_3Sn_{2+x}, <~895–940 °C or from ~750–820 °C to ~895–940 °C (?), incongruent melt. point, homog. range—54.5–56.5 at.% Nb, ?), $Nb_{3\pm x}Sn$ (<~2115–2145 °C or from ~750–775 °C to ~2115–2145 °C (?), incongruent melt. point, homog. range—~74–84 at.% Nb at 1800 °C, ~74–77 at.% Nb at 1500 °C, ~70–85 at.% Nb at 1400 °C, ~69–86 at.% Nb at 1000 °C and ~73–87 at.% Nb at 700 °C, ?), Nb Miscibility gap in the liquid state (critical point–?, near 3 at.% Nb at 960 °C, metastable, ?)	The max. solid solubility of Sn in Nb is ~9–10 at.% at 2115–2145 °C; it declines with temp. decrease noticeably—up to 3 at.% at 1800 °C and ~1–2 at.% at 500–1500 °C. The solubility of Nb in liquid Sn is low and amounts to ~0.15 at.% at 1000 °C and ~0.025 at.% at 580 °C. The direct interaction between Nb and Sn leads to the formation of $Nb_{3\pm x}Sn$. For diffusion rate in the system at various temp. see Addendum.	[4, 14, 16, 156–159, 384, 387]

(continued)

Table 8.5 (continued)

System	Type of phase diagram (constituent phases, temperatures and compositions of transformations)	Character of interaction	References
	Peritectic β-Sn ($\sim$232 °C, ?) Eutectic (degenerated) $NbSn_{2-x}$–β-Sn ($\sim$219–231 °C, 0.04 at.% Nb, ?) Data on the system available in the literature are controversial.		
Nb–Pb	Pb, no binary compounds at normal pressures (?), Nb No diagram plot	No interaction (?); no miscibility in each other. Metastable Nb_3Pb (Frank–Kasper phase) is synthesized at higher pressures (20 MPa) and elevated temp. (1100–1500 °C). At 850–1000 °C Nb parts are fit for long-term applications in liquid Pb.	[4, 14, 324]
Group 15			
Nb–N	N, Nb_4N_5 (?), Nb_5N_6 (?), ε-$NbN_{1\pm x}$ ($<\sim$1310–1360 °C, homog. range—from $\sim$49.4 to $\sim$50.5–52.0 at.% Nb, ?), δ-NbN_{1-x} (from $\sim$1250–1360 °C to $\sim$2050–2300 °C (?), homog. range—$\sim$50.5–54 at.% Nb), δ'-NbN_{1-x} (homog. range—$\sim$50.5–51.2 at.% Nb, metastable, ?), γ-Nb_4N_{3+x} (ordered phase (?), <1500–2200 °C (?), homog. range—$\sim$55.5–57.5 at.% Nb, ?), β-$Nb_{2\pm x}N$ ($<\sim$2300–2430 °C, melt. point, homog. range—from $\sim$65.6–66.7 at.% Nb to $\sim$71.4–71.5 at.% Nb, ?), $Nb_{32}N_3$ (?), Nb Extended solid solution based on Nb (up to $\sim$12–17 at.% N at 2350 °C) Eutectic β-$Nb_{2\pm x}N$–Nb ($\sim$2350 °C, $\sim$86.5 at.% Nb, ?) Data on the system available in the literature are controversial.	The solubility of N in solid Nb (x, at.%) is obeyed the rules: $\lg x = 0.06 - 875/T$ (for 450–800 °C), $\lg x = 0.5\lg p - 3.1 + 9300/T$ (for 1500–2220 °C), where p is pressure N_2, MPa, and T is temp., K. The interaction between Nb and N_2 initiates from $\sim$300 °C. For 2 h exposure the mass gains of Nb samples at 400 and 800 °C in N_2 atmosphere are 31 and 740 mg m^{-2}, respectively. The main products of the interaction between Nb and N_2 are β-$Nb_{2\pm x}N$, γ-Nb_4N_{3+x} and ε-$NbN_{1\pm x}$. For diffusion rate in the system at various temp. see Addendum.	[4, 12, 14, 16, 19–20, 27, 30, 41, 48, 160–165]

(continued)

Table 8.5 (continued)

System	Type of phase diagram (constituent phases, temperatures and compositions of transformations)	Character of interaction	References
Nb–P	P, Nb_2P_5 (metastable, ?), NbP_2 (<~1730 °C, incongruent melt. point, ?), Nb_4P_7 (metastable, ?), NbP (?, congruent melt. point), Nb_8P_5 (?), Nb_5P_3 (?), Nb_7P_4 (?), Nb_2P (?), Nb_3P (?), Nb Eutectic NbP–Nb (?, ~84 at.% Nb, ?) No diagram plot	Nb phosphides are synthesized directly from the elements in vacuum at higher temp. For diffusion rate in the system at various temp. see Addendum.	[4, 12, 14, 327]
Nb–As	As, $NbAs_2$, NbAs (narrow homog. range), Nb_4As_3, Nb_5As_3, Nb_7As_4, Nb_3As, Nb No diagram plot	$NbAs_2$ and NbAs are synthesized directly from the elements.	[12, 15, 49, 166–168]
Nb–Sb	Sb, $NbSb_2$ (<1080 °C, incongruent melt. point, invariable compos., ?), Nb_5Sb_4 (or NbSb, Nb_4Sb_5, <750–1320 °C, incongruent melt. point, homog. range width ≤1 at.%, ?), Nb_3Sb_2 (< 1120–1160 °C, incongruent melt. point, invariable compos., ?), $Nb_{3\pm x}Sb$ (< 1730–1770 °C, incongruent melt. point, homog. range width ≤2–3 at.%), Nb Extended solid solution based on Nb (up to ~20 at.% Sb (?) at 1730–1770 °C) Eutectic $NbSb_2$–Sb (~600–620 °C, ~1 at.% Nb, ?) Data on the system available in the literature are controversial.	At 800 °C the solubility of Sb in Nb is ~4 at.%; it increases at higher temp.—up to max. value at 1730–1770 °C. The solubility of Nb in Sb is negligible.	[14, 166, 169–170, 328, 377]

(continued)

Table 8.5 (continued)

System	Type of phase diagram (constituent phases, temperatures and compositions of transformations)	Character of interaction	References
Nb–Bi	Bi, no binary compounds at normal conditions, Nb Eutectic (degenerated) Bi–Nb (~271 °C, <0.001 at.% Nb, ?)	The solubility of Nb in molten Bi is 0.16 at.% at 1200 °C, ~0.10 at.% at 1100 °C, ~0.08 at.% at 1000 °C, ~0.04 at.% at 750 °C, 0.006–0.015 at.% at 500–525 °C and ~0.003 at.% at 440 °C. Metastable Nb_3Bi is synthesized at ultra-high pressures (3.2–4.0 GPa) and elevated temp. (1000–1500 °C). At 600–900 °C Nb is resistant to corrosion in Bi; at 750 °C Nb parts are fit for long-term applications in liquid Bi.	[4, 15–16, 32]
Group 16			
Nb–O	O, β-Nb_2O_{5-x} (<1495–1510 °C, incongruent melt. point), α'-Nb_2O_{5-x} (?), α-Nb_2O_5 (<~800–850 °C, metastable (?), invariable compos.), γ-Nb_2O_5 (~1285–1510 °C, metastable (?), invariable compos.), $Nb_{53}O_{132}$ (or $NbO_{2.49}$, at least at ~1240–1400 °C, ?), $Nb_{25}O_{62}$ (or $NbO_{2.47\div2.48}$, at least from ~970–1245 °C to 1400 °C, ?), $Nb_{47}O_{116}$ (or $NbO_{2.46\div2.47}$, at least from ~1020–1035 °C to 1400 °C, ?), $Nb_{22}O_{54}$ (or $NbO_{2.45}$, at least from ~1120–1245 °C to 1400 °C, ?), $Nb_{12}O_{29}$ (or $NbO_{2.417\div2.42}$, at least from ~950 to 1100–1400 °C, ?), α-$NbO_{2\pm x}$ (<~820 °C, invariable compos. at temp. <700 °C, ?), β-$NbO_{2\pm x}$ (from ~820 °C to ~900 °C, ?), γ-$NbO_{2\pm x}$ (from ~900 °C to ~1910–1920 °C, congruent melt. point,	The max. solid solubility of O in Nb is ~8–9 at.% at 1915 °C; at higher and lower temp. it declines considerably and amounts to ~3.5 at.% at 1200 °C and ~1.5 at.% at 850 °C; at 800–1500 °C the solubility of O (x, at.%) is obeyed the rule: $\lg x = -0.33 - 1680/T$, where T is temp., K. In terms of rate equations the oxidation of Nb varies considerably with temp. growth: logarithmic at ~300–400 °C (with NbO and $NbO_{2\pm x}$ as products), linear at ~400–650 °C (with $NbO_{2\pm x}$ and Nb_2O_5 modifications as products), parabolic at ~650–800 °C (with $NbO_{2\pm x}$ and Nb_2O_5 modifications as products) and accelerated (up to oxidation failure) at the temp. >800 °C. The	[4, 10, 12, 14, 16, 21–22, 26, 41, 171–184, 266]

(continued)

Table 8.5 (continued)

System	Type of phase diagram (constituent phases, temperatures and compositions of transformations)	Character of interaction	References
	homog. range—~32.8–33.5 at.% Nb), Nb_2O_3 (?), Nb_4O_5 (?), NbO (<1945 °C, congruent melt. point, invariable compos.), NbO_x (or $Nb_{5\div6}O$ suboxides, ?), Nb Eutectic NbO–NbO_2 (~1810–1820 °C, 39.3 at.% Nb) Eutectic NbO–Nb (1915 °C, 59.5 at.% Nb)	mechanism of Nb oxidation is very complicated. In air at atmospheric pressure the intensive oxidation of Nb and formation of noticeable oxide scales begins from 250–500 °C. For diffusion rate in the system at various temp. see Addendum.	
Nb–S	α–S, β-S, NbS_3 (<630 °C, incongruent melt. point, invariable compos.), α-$NbS_{2\pm x}$ (<~800–850 °C, ?), β-$NbS_{2\pm x}$ (~850–1050 °C, ?), α-NbS_{2-x} (or α-$Nb_{1+y}S_2$, $0.12 \le y \le 0.25\div0.5$, at least at ~800–1100 °C, ?), β-NbS_{2-x} (or β-$Nb_{1+y}S_2$, $0.30 \le y \le 0.43$, at least at temp. ≥~1000°C, ?), Nb_3S_4 (?), α-NbS_{1+x}, (or α-$Nb_{2-y}S_2$, $0 \le y \le 0.3$, < 780–850 °C, ?), β-NbS_{1+x}, (or β-$Nb_{2-y}S_2$, $0 \le y \le 0.3$, >780–850 °C, ?), α-NbS (at least at temp. ~770–850 °C, ?), β-NbS (<~770–1000 °C, ?), NbS_{1-x} (or $Nb_{10}S_9$, ?), Nb Eutectic (degenerated) NbS_3–S (~110–115 °C, ?) Data on the system available in the literature are controversial.	Nb sulphides are synthesized by the direct interaction between the elements in sealed vacuum ampules. For diffusion rate in the system at various temp. see Addendum.	[4, 12, 14, 16, 185]

(continued)

Table 8.5 (continued)

System	Type of phase diagram (constituent phases, temperatures and compositions of transformations)	Character of interaction	References
Nb–Se	Se, α-Nb_2Se_9 (<690 °C, incongruent melt. point, invariable compos., ?), β-Nb_2Se_9 (?), γ-Nb_2Se_9 (?), α-$NbSe_4$ (?), β-$NbSe_4$ (?), $NbSe_3$ (<780 °C, incongruent melt. point, invariable compos.), $NbSe_2$ (≤at least 800 °C, invariable compos., some polytypes, ?), Nb_2Se_3 (or $NbSe_{1.5}$, some polytypes, ?), Nb_3Se_4 (or $NbSe_{1.33}$), Nb_5Se_4 (or $NbSe_{0.8}$), Nb_2Se (or $NbSe_{0.5}$), Nb Eutectic (degenerated) α-Nb_2Se_9–Se (~220 °C, ?)	Nb selenides are synthesized by the direct interaction between the elements.	[12, 14, 16, 50, 185–189]
Nb–Te	Te, α-$NbTe_4$ (?), β-$NbTe_{4\pm x}$ (<~465–470 °C, homog. range—~19–24 at.% Nb), α-$NbTe_3$ (invariable compos., ?), β-$NbTe_{3-x}$ (at least from ~430 °C to ~550 °C, homog. range—~26–28 at.% Nb), α-Nb_3Te_8 (<425 °C, invariable compos., ?), β-Nb_3Te_{8+x} (invariable compos., ?), α-Nb_3Te_7 (<450 °C, invariable compos., ?), β-Nb_3Te_{7+x} (invariable compos.), α-$NbTe_2$ (?), β-$NbTe_2$ (?), γ-$NbTe_{2+x}$ (at least from ~450 °C to ~650 °C, homog. range—~29–30 at.% Nb), Nb_3Te_4, α-NbTe (?), β-NbTe (?), $NbTe_{1-x}$ (or $NbTe_{0.82}$, $x \approx 0.18$, ?), Nb_5Te_4, Nb	Nb tellurides are synthesized by the direct interaction between the elements.	[12, 14, 16, 32, 50, 185–186, 190]
Nb–Po	No data	–	–
Group 17			
Nb–F	F, NbF_5 (<79–80 °C, melt. point, invariable compos.), NbF_4 (invariable compos.), NbF_3 (invariable compos.), Nb_6F_{15} (or Nb_2F_5, $NbF_{2.5}$), Nb No diagram plot	The direct interaction between Nb and F_2 initiates at room temp. At temp. ≥250 °C, the intensive interaction results in the formation of NbF_5.	[2–3, 12, 51, 191]

(continued)

Table 8.5 (continued)

System	Type of phase diagram (constituent phases, temperatures and compositions of transformations)	Character of interaction	References
Nb–Cl	Cl, $NbCl_5$ (<205–210 °C, melt. point, invariable compos.), $NbCl_4$ (invariable compos.), $NbCl_{3\pm x}$ (or $NbCl_{2.67\div3.13}$, variable compos.), Nb_3Cl_8 (?), Nb_6Cl_{14} (or Nb_3Cl_7, $NbCl_{2.33}$, invariable compos.), Nb No diagram plot	The interaction between Nb and Cl_2 at 350 °C results in the formation of $NbCl_5$; $NbCl_3$ is formed from the elements at 450 °C. $NbCl_4$ and Nb_2Cl_{14} are synthesized by special chemical reaction pathways.	[2–3, 12, 51]
Nb–Br	Br, $NbBr_5$ (<267–268 °C, melt. point, invariable compos.), $NbBr_4$ (invariable compos.), $NbBr_{3-x}$ (or $NbBr_{2.67\div3.0}$, variable compos.), Nb_3Br_8 (?), $NbBr_2$, Nb No diagram plot	At 250–300 °C, the interaction between the elements is noticeable; it is intensive at temp. >500 °C and results in the formation of $NbBr_5$. Other Nb bromides are synthesized by special chemical reaction pathways.	[2–3, 12, 51]
Nb–I	I, α-NbI_5 (?), β-NbI_5 (<~320–400 °C, melt. point, invariable compos.), α-NbI_4 (<~350 °C, invariable compos.), β-NbI_4 (~350–415 °C, invariable compos.), γ-NbI_4 (~415–505 °C, incongruent melt. point, invariable compos.), NbI_{3-x} (or $NbI_{2.67\div3.0}$, variable compos.), Nb_3I_8 (?), NbI_2 (?), Nb_6I_{11}, Nb	At 290–300 °C, the interaction between the elements results in the formation of NbI_5. Nb iodides with lower valencies are synthesized by special chemical reaction pathways.	[2–3, 12, 51, 329]
Nb–At	No data	–	–

[a] The intervals of temperatures and compositions for the melting and invariant equilibria points, homogeneity ranges and thermal stability regions of constituent phases are given taking into account the minimal and maximal values (data spread) available in literature

The data on the selected ternary, quaternary, quasi-binary and quasi-ternary niobium containing systems, which are the most important for the design, manufacture and application of ultra-high temperature materials, are summarized in Table 8.6. The composition and temperature stability regions for the main binary and ternary niobium containing high-temperature phases are given in Tables 8.5–8.6 taking into account the spread of numerical magnitudes available in the literature currently.

Table 8.6 Chemical interaction of niobium with elements and compounds at high temperatures (selected ternary, quaternary, quasi-binary and quasi-ternary systems in alphabetical order)[a]

System	Type of phase diagram (temperature and composition sections, constituent phases or phase fields) and/or character of interphase interaction and materials compatibility	References
Nb–Al–B	Plotted at 900 and 1200 °C: $Nb_{10}Al_9B$, Nb_6Al_3B, $NbB_{2\pm x}$(Al) (extended solid solution based on $NbB_{2\pm x}$—up to ~12 at.% Al), Al_2B_3 (≤~955 °C, ?), AlB_2 (≤~955–980 °C), AlB_{10} (1660–1850 °C), α-AlB_{12} (≤~1450–1550 °C), β-AlB_{12} (~1450–2150 °C, ?), γ-AlB_{12} (~1550–2150 °C, ?), $NbAl_{3-x}$, σ-$Nb_{2\pm x}Al$, $Nb_{3+x}Al$, $NbB_{2\pm x}$, Nb_3B_4, Nb_5B_6, $NbB_{1\pm x}$, Nb_3B_2, β-B, Al, Nb No solid solutions based on binary and ternary compounds apart from $NbB_{2\pm x}$ In vacuum (~10^{-2} Pa), the interaction between $NbB_{2\pm x}$ and Al initiates from 1250 °C; at temp. <1600 °C it results in the formation of solid solutions.	[19, 330–331]
Nb–Al–B–N	No diagram plot In vacuum (~10^{-1}–10^{-3} Pa), the interaction between Nb and near equimolar composition of AlN–BN initiates from 1300 °C for mixture of powders and from 1400 °C for dense specimens, and results in the formation of Nb_3B_4 and $NbB_{2\pm x}$.	[25]
Nb–Al–C	See C–Al–Nb in Table 2.14.	
Nb–Al–C–Ti	See C–Al–Nb–Ti in Table 2.14.	
Nb–Al–C–V	See C–Al–Nb–V in Table 2.14.	
Nb–Al–C–Zr	See C–Al–Nb–Zr in Table 2.14.	
Nb–Al–Ir	Plotted at 1100 °C: ~$Ir_{2+x}Nb_5Al_{8-x}$ (or $Nb_{0.33}Al_{0.54-0.05y}Ir_{0.13+0.05y}$, $0 \le y \le 1$, or $Nb(Al_{1-z}Ir_z)_2$, $0.190 \le z \le 0.265$, Laves phase), ~$Ir_{4+x}Nb_{7+z}Al_{11-x-z}$ (or $Nb_{0.33+0.045x}Al_{0.49-0.11x}Ir_{0.18+0.065x}$, $0 \le x \le 1$), ~$Ir_4Nb_{15}Al_{12}$ (or $Nb_{0.48}Al_{0.39}Ir_{0.13}$, metastable, ?), ~$Ir_5Nb_8Al_4$ (or $Nb_{0.48}Al_{0.225}Ir_{0.295}$), ~$Ir_8Nb_7Al_6$ (or $Nb_{0.33}Al_{0.28}Ir_{0.38}$), ~$Ir_{11+x}Nb_{7+z}Al_{5-x-z}$ (or $Nb_{0.310+0.030x}Al_{0.225-0.075x}$ $Ir_{0.465+0.045x}$, $0 \le x \le 1$, or $(Nb_{0.4}Ir_{0.6})_{0.775+0.075x}$ $Al_{0.225-0.075x}$), σ-$Nb_{2\pm x}$(Al,Ir) (σ-$Nb_{2\pm x}Al$–σ-$IrNb_{2\pm x}$ continuous solid solution, <~1860–2060 °C), α1-(Ir,Al)Nb_{1-x} (solid solution based on α1-$IrNb_{1-x}$—up to ~6 at.% Al), α2-(Ir,Al)Nb_{1-x} (extended solid solution based on α2-$IrNb_{1-x}$—up to ~8 at.% Al), Nb_{3+x}(Al,Ir) (solid solution based on $Nb_{3+x}Al$—up to ~2.5 at.% Ir), (Ir,Al)$Nb_{3\pm x}$ (solid solution based on $IrNb_{3+x}$—up to ~2.2 at.% Al), $IrAl_{1\pm x}$ (<2120 °C), Ir_2Al_{5+x} (<~1615 °C), $IrAl_3$ (<1450 °C), Ir_4Al_{13} (<1015 °C), Ir_2Al_9 (<900 °C), $Ir_{3\pm x}Nb$, $NbAl_{3-x}$, Al, Ir, Nb	[14, 16, 54, 193, 201–203, 363]
Nb–Al–Ir–Ni	Plotted partially: phase relations are considered	[222, 382]
Nb–Al–Ir–Pt	Plotted partially at 1500 °C: $Ir_{3\pm x}Nb$–$Pt_{3\pm x}Al$ continuous solid solution, (Ir,Pt), Al, Nb	[223]
Nb–Al–Mo	See Mo–Al–Nb in Table 7.5.	

(continued)

Table 8.6 (continued)

System	Type of phase diagram (temperature and composition sections, constituent phases or phase fields) and/or character of interphase interaction and materials compatibility	References
Nb–Al–N	Plotted at 1000 and 1500 °C: Nb_3Al_2N (or $Nb_{0.5}Al_{0.33}N_{0.17}$), AlN (<2400–2450 °C), $NbAl_{3-x}$, σ-$Nb_{2\pm x}Al$, $Nb_{3+x}Al$, ε-$NbN_{1\pm x}$, δ-NbN_{1-x}, γ-Nb_4N_{3+x}, β-$Nb_{2\pm x}N$, N, Al, Nb No solid solutions based on binary and ternary compounds. In vacuum, at 900 °C δ-NbN_{1-x} is resistant to Al melts. The interaction between bulk metal Nb and AlN initiates at 1300 °C and results in the formation of δ-NbN_{1-x}, β-$Nb_{2\pm x}N$ and $NbAl_{3-x}$; at temp. >1500 °C δ-NbN_{1-x} is not formed.	[19, 332–333]
Nb–Al–Si	Plotted at 500–1840 °C: $Nb_5(Si_{1-x}Al_x)_3$ ($0.45 \le x \le 0.60$, or $Nb_{10}Si_3Al_3$), $Nb(Si_{1-x}Al_x)_2$ ($0.3 \le x \le 0.375$, or $Nb_3Si_5Al_2$), α-$Nb_5(Si,Al)_{3+x}$ (extended solid solution based on α-Nb_5Si_{3+x}—up to ~15 at.% Al, ?), β-$Nb_5(Si,Al)_{3+x}$ (solid solution based on β-Nb_5Si_{3+x}—up to ~20 at.% Al, ?), $Nb(Si,Al)_2$ (extended solid solution based on $NbSi_2$—up to ~10 at.% Al), $Nb_{3+x}(Al,Si)$ (extended solid solution based on $Nb_{3+x}Al$—up to compos. $Nb_{3+x}Al_{0.3}Si_{0.7}$), σ-$Nb_{2\pm x}(Al,Si)$ (solid solution based on σ-$Nb_{2\pm x}Al$), $Nb(Al,Si)_{3-x}$ (solid solution based on $NbAl_{3-x}$), Nb_3Si, Al, Si, Nb	[212–213, 215, 216, 280–283]
Nb–Al–Si–Ti	Plotted partially: phase relations are considered	[229]
Nb–Al–Ta	See Ta–Al–Nb in Table 6.4.	
Nb–As–C	See C–As–Nb in Table 2.14.	
Nb–B–Bi	No diagram plot In Ar atmosphere, no interaction between $NbB_{2\pm x}$ and Bi at temp. <320 °C.	[19]
Nb–B–C	See C–B–Nb in Table 2.14.	
Nb–B–C–N	See C–B–N–Nb in Table 2.14.	
Nb–B–C–Si	See C–B–Nb–Si in Table 2.14.	
Nb–B–Fe	Plotted at 600–1800 °C: NbFeB (≤at least 1200 °C), $Nb_3Fe_3B_4$ (≤at least 600 °C), $(Nb_{1-x}Fe_x)_3B_2$ (extended solid solution based on Nb_3B_2, $0 < x < 0.33$), $(Nb,Fe)B_{2\pm x}$ (extended solid solution based on $NbB_{2\pm x}$—up to 20 at.% Fe at 800 °C, ?), Fe_2B (<1407 °C), FeB (<1588 °C), ε-$Fe_{2\pm x}Nb$, μ-$FeNb_{1\pm x}$, $NbB_{1\pm x}$, Nb_5B_6, Nb_3B_4, Nb_2B_3, β-B, α-Fe, γ-Fe, δ-Fe, Nb	[19, 235–236, 284]
Nb–B–Ga	No diagram plot In vacuum ($\sim 10^{-2}$ Pa), no interaction between $NbB_{2\pm x}$ and Ga at temp. <800 °C.	[19]
Nb–B–Gd	Plotted at 1000 °C: ~Gd_2NbB_6 (or $Gd_{0.7}Nb_{0.3}B_2$, solid solution based on GdB_2, ?), GdB_{66} (<2150 °C), $GdB_{6\pm x}$ (<2510 °C), GdB_4 (<~2650 °C), Gd_2B_5 (<2100 °C), GdB_2 (<~2050 °C), Nb_3B_2, $NbB_{1\pm x}$, Nb_5B_6, Nb_3B_4, $NbB_{2\pm x}$, β-B, α-Gd, β-Gd, Nb	[196]

(continued)

Table 8.6 (continued)

System	Type of phase diagram (temperature and composition sections, constituent phases or phase fields) and/or character of interphase interaction and materials compatibility	References
Nb–B–Ge	Plotted at 900 °C: $Nb_5Ge_3B_{1-x}$, Nb_5Ge_2B, $NbGe_{2\pm x}$, α-$Nb_{10}Ge_7$ (?), β-$Nb_{10}Ge_7$ (?), α-$Nb_5Ge_{3\pm x}$ (?), β-$Nb_5Ge_{3\pm x}$, α-Nb_3Ge (?), β-$Nb_{3+x}Ge$, $NbB_{2\pm x}$, Nb_3B_4, Nb_5B_6, $NbB_{1\pm x}$, Nb_3B_2, β-B, Ge, Nb No solid solutions based on binary and ternary compounds.	[16, 63, 334]
Nb–B–Hf	Plotted at 1200–1950 °C: $(Nb,Hf)B_{2\pm x}$ ($NbB_{2\pm x}$–$HfB_{2\pm x}$ continuous solid solution at least at 1400 °C), $(Nb,Hf)B_{1\pm x}$ (extended solid solution based on $NbB_{1\pm x}$—up to $\sim(Nb_{0.6}Hf_{0.4})B_{1\pm x}$ compos. at 1400 °C), $(Nb,Hf)_3B_4$ (extended solid solution based on Nb_3B_4—up to $\sim(Nb_{0.85}Hf_{0.15})_3B_4$ compos. at 1400 °C), $HfB_{1\pm x}$ (<2100 °C), Nb_5B_6, Nb_3B_2, β-B, α-Hf, (β-Hf,Nb)	[19, 285, 335–336]
Nb–B–In	No diagram plot In Ar atmosphere, no interaction between $NbB_{2\pm x}$ and In at temp. <500 °C.	[19]
Nb–B–Mo	See Mo–B–Nb in Table 7.5.	
Nb–B–Mo–Si	See Mo–B–Nb–Si in Table 7.5.	
Nb–B–N	Plotted at 1200 and 1400 °C: Nb_2BN_{1-x} (at least at 1200 °C), $Nb_xB_yN_z$ ($x \approx 5 \div 7$, $y \approx 5.5 \div 7.5$, $z \approx 3 \div 5.5$, at least at 1200 °C, ?), α-BN (or h-BN, graphene/graphite like, <2400 °C), ε-$NbN_{1\pm x}$, δ-NbN_{1-x} γ-Nb_4N_{3+x}, β-$Nb_{2\pm x}N$, Nb_3B_2, $NbB_{1\pm x}$, Nb_5B_6, Nb_3B_4, Nb_2B_3, $NbB_{2\pm x}$, β-B, N, Nb Mutual solid solubilities in the system are rather small, i.e. practically no B dissolves in the Nb nitrides and no N—in the Nb borides. In vacuum ($\sim 10^{-1}$–10^{-3} Pa), the interaction between Nb and BN initiates from 1400 °C for equimolar mixture of powders and from 1700 °C for dense specimens, and results in the formation of $NbB_{1\pm x}$, $NbB_{2\pm x}$, Nb_3B_4, β-$Nb_{2\pm x}N$ and δ-NbN_{1-x}; at temp. ≥1900 °C $NbB_{1\pm x}$, $NbB_{2\pm x}$, Nb_3B_4 and β-$Nb_{2\pm x}N$ are formed and at temp. ≥2000 °C—only $NbB_{1\pm x}$ and $NbB_{2\pm x}$. At all temp., the reactions take place also through vapour phase.	[19, 25, 245]
Nb–B–N–O	No diagram plot In inert atmosphere, at 1750 °C the interaction between Nb oxides and α-BN results in the formation of Nb_3B_4.	[26]
Nb–B–Ni	Plotted at 800 and 950 °C: $NbNiB_2$, NbNiB (or $Nb_5Ni_{11}B_4$, ?), $Nb_3Ni_{20}B_6$ (or $Nb_2Ni_{21}B_6$, $Nb_{2.5}Ni_{20.5}B_6$), $Nb_{12}Ni_6B$ (or $Nb_2NiB_{0.16}$), Ni_3B (<~1155 °C), Ni_2B (<1125 °C), Ni_4B_{3-x} (or o-Ni_4B_3, $x \approx 0.2$, <1025 °C), Ni_4B_{3+x} (or m-Ni_4B_3, $x \approx 0.1$, <~1030 °C), NiB (<1035 °C), $NbB_{2\pm x}$, Nb_3B_4, Nb_5B_6, $NbB_{1\pm x}$, Nb_3B_2, Ni_8Nb, $Ni_{3\pm x}Nb$, μ-Ni_6Nb_{7-x} (or μ-$NiNb_{1+x}$), β-B, Ni, Nb Eutectic $Nb_3Ni_{20}B_6$–Ni (~1085 °C, ~78 at.% Ni, ~6.5 at.% Nb). No solid solutions based on binary and ternary compounds. In vacuum ($\sim 10^{-2}$ Pa), the interaction between $NbB_{2\pm x}$ and Ni at 1450 °C results in the formation of $NbNiB_2$.	[19, 63, 337–339]

(continued)

Table 8.6 (continued)

System	Type of phase diagram (temperature and composition sections, constituent phases or phase fields) and/or character of interphase interaction and materials compatibility	References
Nb–B–Ni–Ta	See Ta–B–Nb–Ni in Table 6.4.	
Nb–B–O	No diagram plot $NbBO_4$ In Ar atmosphere, the interaction between $NbB_{2\pm x}$ and Nb_2O_5 results in the formation of NbO_2—at 1000–1100 °C; NbO_2 and $NbB_{1\pm x}$—at 1200–1700 °C; Nb, Nb_3B_2 and $NbB_{1\pm x}$—at 1800–1900 °C.	[19, 340]
Nb–B–Pb	No diagram plot In Ar atmosphere, no interaction between $NbB_{2\pm x}$ and Pb at temp. <350 °C.	[19]
Nb–B–Re	See Re–B–Nb in Table 4.6.	
Nb–B–Ru–Ta	See Ta–B–Nb–Ru in Table 6.4.	
Nb–B–Sc	No diagram plot $(Nb,Sc)B_{2\pm x}$ (solid solution based on $NbB_{2\pm x}$, at least—up to $\sim(Nb_{0.9}Sc_{0.1})B_{2\pm x}$ compos.)	[63]
Nb–B–Si	Plotted at 1600, 1700 and 1800 °C: $Nb_5Si_{3-x}B_x$ ($0 \le x \le 2$, α-Nb_5Si_{3+x}–Nb_5SiB_2 extended solid solution (?), $<\sim$2245 °C, incongruent melt. point), $Nb_5Si_{3+x}B_y$, $NbSi_2$, Nb_3Si, $NbB_{2\pm x}$, Nb_3B_4, Nb_5B_6, $NbB_{1\pm x}$, Nb_3B_2, SiB_n ($n \approx 23$, <2040 °C), SiB_6 (<1850 °C), $SiB_{3\pm x}$ (<1270 °C), β-B, Si, Nb Eutectic $Nb_5Si_{3+x}B_y$–$NbSi_2$–$NbB_{2\pm x}$ ($\sim$1795 °C) Eutectic $Nb_5Si_{3+x}B_y$–α-Nb_5Si_{3+x}–$NbSi_2$ ($\sim$1865 °C) Eutectic $NbSi_2$–SiB_6–Si (1375 °C) Eutectic $Nb_5Si_{3-x}B_x$ ($x \approx 1$)–Nb ($\sim$1880 °C) $NbB_{2\pm x}$–$NbSi_2$ is plotted: eutectic—1860–1900 °C, $\sim$12.5 mol.% $NbB_{2\pm x}$; the max. solid solubility of $NbB_{2\pm x}$ in $NbSi_2$ is $\sim$6–9 mol.% (at eutectic temp.) and that of $NbSi_2$ in $NbB_{2\pm x}$ is negligible.	[32, 195, 226, 243–244, 286–289, 373]
Nb–B–Si–W	See W–B–Nb–Si in Table 3.6.	
Nb–B–Sn	No diagram plot In Ar atmosphere, no interaction between $NbB_{2\pm x}$ and Sn at temp. <600 °C.	[19]
Nb–B–Ta	See Ta–B–Nb in Table 6.4.	

(continued)

Table 8.6 (continued)

System	Type of phase diagram (temperature and composition sections, constituent phases or phase fields) and/or character of interphase interaction and materials compatibility	References
Nb–B–Ti	Plotted at 1200, 1400 and 1950 °C: $(Nb,Ti)B_{2\pm x}$ ($NbB_{2\pm x}$–$TiB_{2\pm x}$ continuous solid solution, <~3000–3250 °C), $(Nb,Ti)B_{1\pm x}$ (extended solid solution based on $NbB_{1\pm x}$—up to ~15–30 at.% Ti), $(Ti,Nb)B_{1-x}$ (extended solid solution based on TiB_{1-x}—up to ~20–30 at.% Nb, <~2180–2200 °C), $(Nb,Ti)_3B_2$ (extended solid solution based on Nb_3B_2—up to ~5–10 at.% Ti), $(Nb,Ti)_3B_4$ (extended solid solution based on Nb_3B_4—up to ~5–10 at.% Ti), $(Nb,Ti)_5B_6$ (extended solid solution based on Nb_5B_6—up to ~5–10 at.% Ti), $(Ti,Nb)_3B_4$ (solid solution based on Ti_3B_4—up to 2 at.% Nb, <~2200 °C), Nb_2B_3, β-B, α-Ti, (β-Ti,Nb) $TiB_{2\pm x}$–Nb is plotted: $TiNbB_2$ (<~2840 °C, congruent melt. point, invariable compos., ?); $TiB_{2\pm x}$–$TiNbB_2$ eutectic—~2690 °C, ~5 mol.% Nb; $TiNbB_2$–Nb eutectic—~2130 °C, ~90 mol.% Nb; the solubility of $TiB_{2\pm x}$ in Nb and that of Nb in $TiB_{2\pm x}$ are ≤~1 mol.%. Data on the system available in the literature are controversial. The interaction between compact metal Nb and $TiB_{2\pm x}$ initiates from 1200 °C and results in the formation of Nb_3B_2 and $NbB_{1\pm x}$ at 1300–1400 °C, and Nb_3B_2, $NbB_{1\pm x}$ and TiB_{1-x} at 1500–1700 °C.	[4, 10, 19, 28, 60, 232–234, 237–238, 290]
Nb–B–U	No diagram plot Metal Nb is compatible with UB_4 in powdered blend at temp. ≤1000 °C.	[4]
Nb–B–W	See W–B–Nb in Table 3.6.	
Nb–B–Zr	Plotted at 1500 °C: $(Nb,Zr)B_{1\pm x}$ (extended solid solution based on $NbB_{1\pm x}$—up to compos. ~$(Nb_{0.4}Zr_{0.6})B_{1\pm x}$), $(Nb,Zr)_3B_2$ (extended solid solution based on Nb_3B_2—up to compos. ~$(Nb_{0.9}Zr_{0.1})_3B_2$), $ZrB_{2\pm x}$ (<3225–3265 °C), ZrB_{12} (~1695–2290 °C), Nb_3B_4, Nb_5B_6, Nb_2B_3, $NbB_{2\pm x}$, β-B, (β-Zr,Nb) The binary compounds in the system, with the exception of $NbB_{1\pm x}$ and Nb_3B_2, dissolve only slight amounts of the third component. At ultra-high temp. it is very probable that $NbB_{2\pm x}$–$ZrB_{2\pm x}$ continuous solid solution exists. Zr-enriched β-Zr–Nb continuous solid solution is in equilibrium with (Nb,Zr)B, $(Nb,Zr)_3B_2$ and $ZrB_{2\pm x}$. In vacuum, the interaction between compact metal Nb and $ZrB_{2\pm x}$ initiates from 1100–1200 °C and results in the formation of Nb borides.	[10, 14–17, 19, 27, 29, 192, 291–294]
Nb–Be–Mo	See Mo–Be–Nb in Table 7.5.	

(continued)

Table 8.6 (continued)

System	Type of phase diagram (temperature and composition sections, constituent phases or phase fields) and/or character of interphase interaction and materials compatibility	References
Nb–Be–O	No diagram plot In vacuum, the interaction between metal Nb and α-BeO initiates at temp. >1600–1700 °C (0.5–1 h exposure); at 1800–1900 °C the contact interaction leads to the formation of new phases, Nb beryllides mainly, and materials corrosion and damage. In inert atmosphere, at 1800 °C the interaction is observed along the grain boundaries, and Nb oxides are formed.	[4, 10, 26]
Nb–C–Co	See C–Co–Nb in Table 2.14.	
Nb–C–Co–Hf	See C–Co–Hf–Nb in Table 2.14.	
Nb–C–Co–Ta	See C–Co–Nb–Ta in Table 2.14.	
Nb–C–Co–Ti	See C–Co–Nb–Ti in Table 2.14.	
Nb–C–Co–V	See C–Co–Nb–V in Table 2.14.	
Nb–C–Co–Zr	See C–Co–Nb–Zr in Table 2.14.	
Nb–C–Cr	See C–Cr–Nb in Table 2.14.	
Nb–C–Fe	See C–Fe–Nb in Table 2.14.	
Nb–C–Fe–N	See C–Fe–N–Nb in Table 2.14.	
Nb–C–Fe–N–Ti	See C–Fe–N–Nb–Ti in Table 2.14.	
Nb–C–Fe–N–Ti–V	See C–Fe–N–Nb–Ti–V in Table 2.14.	
Nb–C–Fe–V	See C–Fe–Nb–V in Table 2.14.	
Nb–C–Ga	See C–Ga–Nb in Table 2.14.	
Nb–C–H	See C–H–Nb in Table 2.14.	
Nb–C–Hf	See C–Hf–Nb in Table 2.14.	
Nb–C–Hf–U	See C–Hf–Nb–U in Table 2.14.	
Nb–C–Hf–V	See C–Hf–Nb–V in Table 2.14.	
Nb–C–In	See C–In–Nb in Table 2.14.	
Nb–C–Ir	See C–Ir–Nb in Table 2.14.	
Nb–C–Mg–O	See C–Mg–Nb–O in Table 2.14.	
Nb–C–Mn	See C–Mn–Nb in Table 2.14.	
Nb–C–Mo	See C–Mo–Nb in Table 2.14.	
Nb–C–Mo–Ta	See C–Mo–Nb–Ta in Table 2.14.	
Nb–C–Mo–U	See C–Mo–Nb–U in Table 2.14.	
Nb–C–Mo–Zr	See C–Mo–Nb–Zr in Table 2.14.	
Nb–C–N	See C–N–Nb in Table 2.14.	
Nb–C–N–W	See C–N–Nb–W in Table 2.14.	
Nb–C–Ni	See C–Nb–Ni in Table 2.14.	
Nb–C–Ni–Ta	See C–Nb–Ni–Ta in Table 2.14.	
Nb–C–Ni–V	See C–Nb–Ni–V in Table 2.14.	
Nb–C–Ni–Zr	See C–Nb–Ni–Zr in Table 2.14.	
Nb–C–O	See C–Nb–O in Table 2.14.	
Nb–C–O–Si	See C–Nb–O–Si in Table 2.14.	
Nb–C–O–W	See C–Nb–O–W in Table 2.14.	
Nb–C–O–Zr	See C–Nb–O–Zr in Table 2.14.	
Nb–C–Os	See C–Nb–Os in Table 2.14.	

(continued)

Table 8.6 (continued)

System	Type of phase diagram (temperature and composition sections, constituent phases or phase fields) and/or character of interphase interaction and materials compatibility	References
Nb–C–P	See C–Nb–P in Table 2.14.	
Nb–C–Pd	See C–Nb–Pd in Table 2.14.	
Nb–C–Pt	See C–Nb–Pt in Table 2.14.	
Nb–C–Pu	See C–Nb–Pu in Table 2.14.	
Nb–C–Re	See C–Nb–Re in Table 2.14.	
Nb–C–Rh	See C–Nb–Rh in Table 2.14.	
Nb–C–Ru	See C–Nb–Ru in Table 2.14.	
Nb–C–S	See C–Nb–S in Table 2.14.	
Nb–C–Si	See C–Nb–Si in Table 2.14.	
Nb–C–Sn	See C–Nb–Sn in Table 2.14.	
Nb–C–Ta	See C–Nb–Ta in Table 2.14.	
Nb–C–Ta–Ti	See C–Nb–Ta–Ti in Table 2.14.	
Nb–C–Ta–W	See C–Nb–Ta–W in Table 2.14.	
Nb–C–Tc	See C–Nb–Tc in Table 2.14.	
Nb–C–Th	See C–Nb–Th in Table 2.14.	
Nb–C–Ti	See C–Nb–Ti in Table 2.14.	
Nb–C–Ti–U	See C–Nb–Ti–U in Table 2.14.	
Nb–C–Ti–V	See C–Nb–Ti–V in Table 2.14.	
Nb–C–Ti–W	See C–Nb–Ti–W in Table 2.14.	
Nb–C–U	See C–Nb–U in Table 2.14.	
Nb–C–U–V	See C–Nb–U–V in Table 2.14.	
Nb–C–U–Zr	See C–Nb–U–Zr in Table 2.14.	
Nb–C–V	See C–Nb–V in Table 2.14.	
Nb–C–W	See C–Nb–W in Table 2.14.	
Nb–C–Zr	See C–Nb–Zr in Table 2.14.	
Nb–Ca–O	Nb_2O_5–CaO is plotted: CaO (<2565–2585 °C), $11CaO{\cdot}2Nb_2O_5$ (or $Ca_{11}Nb_4O_{21}$, <2105 °C), $5CaO{\cdot}Nb_2O_5$ (or $Ca_5Nb_2O_{10}$, <2065 °C), solid solution based on α-$4CaO{\cdot}Nb_2O_5$ (or α-$Ca_4Nb_2O_9$, ~18–22.5 mol.% Nb_2O_5, <~1375–1425 °C), solid solution based on β–$4CaO{\cdot}Nb_2O_5$ (or β-$Ca_4Nb_2O_9$, ~18–22.5 mol.% Nb_2O_5, from ~1375–1425 to 1560 °C, ?), solid solution based on γ-$4CaO{\cdot}Nb_2O_5$ (or γ-$Ca_4Nb_2O_9$, ~18–21.5 mol.% Nb_2O_5, ~1560–1990 °C, ?), $3CaO{\cdot}Nb_2O_5$ (or $Ca_3Nb_2O_8$, <~1475–1560 °C, ?), $2CaO{\cdot}Nb_2O_5$ ($Ca_2Nb_2O_7$, <~1570 °C), $CaO{\cdot}Nb_2O_5$ ($CaNb_2O_6$, <1550 °C), β-Nb_2O_5, α-Nb_2O_5; CaO–$Ca_{11}Nb_4O_{21}$ eutectic—2035 °C, 13.7 mol.% Nb_2O_5; solid solution based on β-$Ca_4Nb_2O_9$ (or $Ca_3Nb_2O_8$, ?)–$Ca_2Nb_2O_7$ (or $CaNb_2O_6$, ?) eutectic—~1535–1540 °C, ~29–29.5 mol.% Nb_2O_5; $CaNb_2O_6$–$Ca_2Nb_2O_7$ eutectic—~1490 °C, ~41–42 mol.% Nb_2O_5; $CaNb_2O_6$–β-Nb_2O_5 eutectic—~1360–1370 °C, ~77–78 mol.% Nb_2O_5 Data on the system available in the literature are controversial.	[267–275]

(continued)

Table 8.6 (continued)

System	Type of phase diagram (temperature and composition sections, constituent phases or phase fields) and/or character of interphase interaction and materials compatibility	References
Nb–Ce–O	α-$Ce_2O_3{\cdot}Nb_2O_5$ (or α-$CeNbO_4$), β-$Ce_2O_3{\cdot}Nb_2O_5$ (or β-$CeNbO_4$), $Ce_2O_3{\cdot}3Nb_2O_5$ (or $CeNb_3O_9$, $Ce_{0.67}Nb_2O_6$, ?), $Ce_2O_3{\cdot}5Nb_2O_5$ (or $CeNb_5O_{14}$), $Ce_2O_3{\cdot}7Nb_2O_5$ (or $CeNb_7O_{19}$), $Ce_2O_3{\cdot}2CeO_2{\cdot}2Nb_2O_5$ (or $CeNbO_{4.25}$, $Ce_4Nb_4O_{17}$), $Ce_2O_3{\cdot}4CeO_2{\cdot}3Nb_2O_5$ (or $CeNbO_{4.33}$, $Ce_3Nb_3O_{13}$)	[276–277, 342]
Nb–Co–Mo	See Mo–Co–Nb in Table 7.5.	
Nb–Co–N	Plotted at 1200 °C: η-$Nb_4Co_2N_{1-x}$ (homog. range—~44–57 at.% Nb, ~30–42 at.% Co, ~14 at.% N), $Co_{3\pm x}N$ (or $Co_{2+x}N$, <~1595 °C), Co_4N (<~1065 °C), χ-$Co_7Nb_{2\pm x}$, λ_3-Co_3Nb, $\lambda_2(\alpha)$-$Co_{2\pm x}Nb$ (?), λ_2-$Co_{2\pm x}Nb$ (or $\lambda_2(\beta)$-$Co_{2\pm x}Nb$), λ_1-Co_5Nb_{3-x}, μ-$CoNb_{1\pm x}$, ε-$NbN_{1\pm x}$, δ-NbN_{1-x}, γ-Nb_4N_{3+x}, β-$Nb_{2\pm x}N$, N, α-Co, ε-Co, Nb No solid solutions based on binary and ternary compounds. At 1600 °C, δ-NbN_{1-x} interacts with Co melts intensively	[19, 23, 341]
Nb–Co–Ta	See Ta–Co–Nb in Table 6.4.	
Nb–Co–W	See W–Co–Nb in Table 3.6.	
Nb–Cr–Fe–Si	Plotted at 1200 and 1300 °C: $Nb_{7-x}Fe_{1+x}Cr_4Si_8$ ($0 \le x \le 0.4$), $Nb_3Fe_3CrSi_6$, $(Nb_{0.5}Fe_{0.5-x}Cr_x)_2Si$ ($0 \le x \le 0.09$), $(Nb_{0.5}Fe_xCr_{0.5-x})_2Si$ ($0 \le x \le 0.36$), $(Fe_{1-x-y}Cr_yNb_x)_5Si_{3\pm x}$ (homog. range limits: $(Fe_{0.85}Cr_{0.15})_5Si_{3\pm x}$, $(Fe_{0.45}Cr_{0.55})_5Si_{3\pm x}$ and $(Nb_{0.15}Fe_{0.2}Cr_{0.65})_5Si_{3\pm x}$), $Nb_{2+x}Cr_{4-x}Si_5$, $(Nb,Cr,Fe)_{11}Si_8$ (extended solid solution based on $(Nb,Cr)_{11}Si_8$ (or $Nb_{3+x}Cr_{8-x}Si_8$)—up to compos. $(Nb_{1.3}Cr_{2.2}Fe_{7.5})Si_8$), $(Nb,Cr,Fe)_6Si_5$ (extended solid solution based on $(Nb,Cr)_6Si_5$—up to compos. $(Nb_2Cr_2Fe_2)Si_5$), $Nb_2Cr_3Si_3$, Nb_4CrSi_3 (narrow homog. range), $Nb(Fe_{1-x}Si_x)_2$, NbFeSi, $Nb_4Fe_3Si_5$, $Nb_4Fe_4Si_7$, $Nb_4Fe_3Si_5$, Nb_2FeSi_2, $CrSi_2$ (<~1470–1590 °C), CrSi (<~1410–1485 °C), β-$Cr_5Si_{3\pm x}$ (from ~1505–1510 to ~1635–1730 °C), α-$(Cr,Nb,Fe)_5Si_{3\pm x}$ (extended solid solution based on α-$Cr_5Si_{3\pm x}$ <1505–1510 °C, triangular homog. range, at 1200 °C the solubility of Nb and Fe is limited to 4 and 28 at.%, respectively), $Cr_{3\pm x}Si$ (<~1725–1780 °C), α_1-Fe_3Si (<1155 °C), α_2-Fe_3Si (<~1300 °C), Fe_5Si_2 (965–1250 °C), β-Fe_2Si (1040–1210 °C), η-Fe_5Si_3 (~825–1100 °C), ε-FeSi (<1410 °C), ζ_1-$FeSi_2$ (~935–1220 °C), ζ_2-$FeSi_2$ (<980 °C), $FeSi_{2+x}$ ($x \approx 0.3$, 935–1220 °C), σ-$FeCr_{1-x}$ (from 440–520 °C to 815–830 °C), $NbSi_2$, β-Nb_5Si_{3+x}, α-Nb_5Si_{3+x} (the solubility of Cr and Fe is low), Nb_3Si, λ_2-$NbCr_{2\pm x}$, λ_1-$NbCr_{2\pm x}$, ε-$Fe_{2\pm x}Nb$, μ-$FeNb_{1\pm x}$ Si, α-Fe, γ-Fe, δ-Fe, Cr, Nb	[13–14, 16, 200]
Nb–Cr–Mo	See Mo–Cr–Nb in Table 7.5.	

(continued)

Table 8.6 (continued)

System	Type of phase diagram (temperature and composition sections, constituent phases or phase fields) and/or character of interphase interaction and materials compatibility	References
Nb–Cr–N–Ni	No diagram plot At 1600 °C, δ-NbN_{1-x} interacts with 80 %Ni–20 %Cr melts intensively.	[19]
Nb–Cr–Re	See Re–Cr–Nb in Table 4.6.	
Nb–Cr–Si	Plotted at 1000–1500 °C: Nb_4CrSi_3, NbCrSi (or $Nb_5Cr_7Si_7$, or $Nb_2Cr_3Si_3$, ?), $(Nb,Cr)_{11}Si_8$ (or $Nb_4Cr_7Si_8$, ?), $(Nb,Cr)_6Si_5$ (or $Nb_2Cr_4Si_5$, or $Nb_2Cr_3Si_6$, ?), $NbCr_4Si$, α-$(Nb,Cr)_5Si_{3+x}$ (extended solid solution based on α-Nb_5Si_{3+x}—up to ~10 at.% Cr), β-$(Nb,Cr)_5Si_{3+x}$ (solid solution based on β-Nb_5Si_{3+x}, ?), α-$(Cr,Nb)_5Si_{3\pm x}$ (solid solution based on α-$Cr_5Si_{3\pm x}$—up to ~5–10 at.% Nb, <1505–1510 °C), β-$(Cr,Nb)_5Si_{3\pm x}$ (solid solution based on β-$Cr_5Si_{3\pm x}$, ?), $(Cr,Nb)_{3\pm x}Si$ (solid solution based on $Cr_{3\pm x}Si$, <~1725–1780 °C), $CrSi_2$ (solubility of Nb is negligible, <~1470–1590 °C), CrSi (<~1410–1485 °C), β-$Cr_5Si_{3\pm x}$ (from ~1505–1510 to ~1635–1730 °C), $NbSi_2$ (solubility of Cr is negligible), Nb_3Si, λ_2-$NbCr_{2\pm x}$, λ_1-$NbCr_{2\pm x}$, Si, Cr, Nb At 1000 °C, the mutual solubilities of $NbSi_2$ and $CrSi_2$ are negligible. The formation of Nb_5Si_{3+x} phases in the ternary system is suppressed.	[13–14, 16, 19, 31, 33, 198, 200, 212–213, 215, 228, 230, 240, 295]
Nb–Cr–Ta	See Ta–Cr–Nb in Table 6.4.	
Nb–Cr–Ta–Ti	See Ta–Cr–Nb–Ti in Table 6.4.	
Nb–Cr–W	See W–Cr–Nb in Table 3.6.	
Nb–Cu–Mo	See Mo–Cu–Nb in Table 7.5.	
Nb–Cu–N	No diagram plot In vacuum, at 1200 °C Nb nitrides are resistant to Cu melts.	[19]
Nb–Cu–Ta	See Ta–Cu–Nb in Table 6.4.	
Nb–Fe–Mo	See Mo–Fe–Nb in Table 7.5.	
Nb–Fe–N	Plotted at 1200 °C (pressure N_2–1 kPa): η-$Nb_{4-x}Fe_{2+x}N$ (homog. range—~42–58 at.% Nb, ~27–43 at.% Fe, ~14–15 at.% N), ξ-$Fe_{2\pm x}N$ (<500 °C), ε-(Fe,N), γ'-$Fe_{4+x}N$ (<680 °C), ε-$Fe_{2\pm x}Nb$, μ-$FeNb_{1\pm x}$ (or μ-Fe_7Nb_{6+x}), ε-$NbN_{1\pm x}$, δ-NbN_{1-x}, γ-Nb_4N_{3+x}, β-$Nb_{2\pm x}N$, N, α-Fe, γ-Fe, δ-Fe, Nb No solid solutions based on binary and ternary compounds. At 1600 °C, δ-NbN_{1-x} interacts with Fe melts intensively.	[19, 23, 341, 343]

(continued)

Table 8.6 (continued)

System	Type of phase diagram (temperature and composition sections, constituent phases or phase fields) and/or character of interphase interaction and materials compatibility	References
Nb–Fe–Si	Plotted at 1000–1300 °C: NbFeSi (at least at ~1150 °C), $NbFeSi_2$ (at least at ~1150 °C), Nb_2FeSi_2 (at least at ~1150 °C), $Nb_4Fe_4Si_7$ (at least at ~1150 °C), α-$Nb_4Fe_3Si_5$ (<~1120–1140 °C), β-$Nb_4Fe_3Si_5$ (from 1120–1140 °C to ?), Nb_4FeSi (at least at 1100 °C), $Nb_6Fe_{16}Si_7$ (metastable, ?), ε-$(Fe,Si)_{2\pm x}Nb$ (or λ-$Nb_z(Fe_{1-y}Si_y)_2$, $0 \le y \le 0.375$, $\sim 0.79 \le z \le \sim 1.06$, extended solid solution based on ε-$Fe_{2\pm x}Nb$), μ-$(Fe,Si)Nb_{1\pm x}$ (extended solid solution based on μ-$FeNb_{1\pm x}$—up to ~10–15 at.% Si), α_1-Fe_3Si (<~1155–1235 °C), α_2-Fe_3Si (<~1300 °C), Fe_5Si_2 (965–1250 °C), β-Fe_2Si (1040–1210 °C), η-Fe_5Si_3 (~825–1100 °C), ε-FeSi (<1410 °C), ζ_1-$FeSi_2$ (~935–1220 °C), ζ_2-$FeSi_2$ (<980 °C), $FeSi_{2+x}$ ($x \approx 0.3$, 935–1220 °C), $NbSi_2$, α-Nb_5Si_{3+x}, β-Nb_5Si_{3+x}, Nb_3Si, Si, α-Fe, γ-Fe, δ-Fe, Nb	[32, 296–298]
Nb–Fe–Ta	See Ta–Fe–Nb in Table 6.4.	
Nb–Fe–W	See W–Fe–Nb in Table 3.6.	
Nb–Ga–Ir	Plotted partially at 1000 °C: ~Ga_4IrNb_3 (or $Nb_{37}Ga_{50}Ir_{13}$), ~Ga_2IrNb_2 (or $Nb_{43}Ga_{40}Ir_{17}$), ~$Ga_{2+x}Ir_{3-x}Nb_5$ ($0 \le x \le 0.5$, or $Nb_{48}Ga_{22\div27}Ir_{25\div30}$), ~$Ga_7Ir_7Nb_6$ (or $Nb_{30}Ga_{35}Ir_{35}$), ~Ga_2IrNb (or $Nb_{25}Ga_{52}Ir_{23}$), ~$Ga_3Ir_{12}Nb_5$ (or $Nb_{25}Ga_{15}Ir_{60}$), $(Ir,Ga)Nb_{3\pm x}$ ($IrNb_{3\pm x}$–$GaNb_{3+x}$ continuous solid solution, <1860–2130 °C), σ-$(Ir,Ga)Nb_{2\pm x}$ (extended solid solution based on σ-$IrNb_{2\pm x}$—up to ~15–18 at.% Ga), α_2-$Ir(Nb,Ga)_{1-x}$ (extended solid solution based on α_2-$IrNb_{1-x}$—up to ~15 at.% Ga), α_1-$Ir(Nb,Ga)_{1-x}$ (extended solid solution based on α_1-$IrNb_{1-x}$—up to ~10 at.% Ga), $(Ir,Ga)_{3\pm x}(Nb,Ga)$ (extended solid solution based on $Ir_{3\pm x}Nb$—up to ~12 at.% Ga), $(Ga,Ir)_3Nb_5$ (solid solution based on Ga_3Nb_5—up to ~3 at.% Ir), $(Ga,Ir)_5Nb_4$ (solid solution based on Ga_5Nb_4—up to ~2 at.% Ir), $(Ga,Ir)_3Nb$ (solid solution based on Ga_3Nb—up to ~1 at.% Ir), Ga_4Nb_5, $Ga_{13}Nb_5$ (?), Ga_9Ir_2, Ga_3Ir, Ga_5Ir_3, GaIr, Ga, Ir, Nb	[13–14, 16, 194, 204]
Nb–H–Ir	No diagram plot Nb_3IrH_x ($x = 4.3$, Frank-Kasper phase)	[353]
Nb–H–N–Ti	No diagram plot $(Nb_{0.2}Ti_{0.8})(N_{0.3}H_{1.3})$, $(Nb_{0.4}Ti_{0.6})(N_{0.4}H_{1.1})$ and $(Nb_{0.6}Ti_{0.4})(N_{0.45}H_{0.67})$ single-phase complex hydronitrides were synthesized by two-stage SHS from Nb and Ti powders at gas pressures $N_2 > 7$ MPa and $H_2 = 1$ MPa	[211]

(continued)

Table 8.6 (continued)

System	Type of phase diagram (temperature and composition sections, constituent phases or phase fields) and/or character of interphase interaction and materials compatibility	References
Nb–H–N–Zr	No diagram plot $(Nb_{0.1}Zr_{0.9})(N_{0.3}H_{1.3})$, $(Nb_{0.3}Zr_{0.7})(N_{0.33}H_{1.15})$, $(Nb_{0.4}Zr_{0.6})(N_{0.35}H_{1.1})$ and $(Nb_{0.5}Zr_{0.5})(N_{0.35}H_{1.05})$ single-phase complex hydronitrides were synthesized by two-stage SHS from Nb and Zr powders at gas pressures $N_2 > 7$ MPa and $H_2 = 1$ MPa	[211]
Nb–H–Ta	See Ta–H–Nb in Table 6.4.	
Nb–Hf–Ir	Plotted partially at 2000 °C: (Nb,Hf)$Ir_{3\pm x}$ ($HfIr_{3+x}$–$NbIr_{3\pm x}$ continuous solid solution)	[366–369]
Nb–Hf–Mo	See Mo–Hf–Nb in Table 7.5.	
Nb–Hf–N	Plotted at 1200, 1500 and 2200 °C: (Nb,Hf)$N_{1\pm x}$ (δ-NbN_{1-x}–$HfN_{1\pm x}$ continuous solid solution at least at 1200 °C, or extended solid solutions based on δ-NbN_{1-x} and $HfN_{1\pm x}$, <~2050–3390 °C), Hf_4N_3 (~1200–2300 °C), Hf_3N_2 (<1970 °C), ε-$NbN_{1\pm x}$, γ-Nb_4N_{3+x}, β-$Nb_{2\pm x}N$, N, (α-Hf,Nb), (β-Hf,Nb) $HfN_{1\pm x}$ ($x = 0$)–Nb is plotted: eutectic—2460 °C, ~70 mol.% $HfN_{1\pm x}$ (~17 at.% Nb); the max. solid solubility of $HfN_{1\pm x}$ in Nb is ~6 mol.% and that of Nb in $HfN_{1\pm x}$ is ~18–20 mol.% (at the eutectic temp.) Hf-rich (Nb,Hf)$N_{1\pm x}$ is in equilibrium with Nb alloy.	[13–14, 16, 23, 344–345]
Nb–Hf–O	Plotted partially at 1000 and 1500 °C: α-HfO_{2-x} (<1670 °C), β-HfO_{2-x} (1670–2200 °C), γ-HfO_{2-x} (2200–2900 °C), α-Nb_2O_5, β-Nb_2O_5, γ-Nb_2O_5, α-$NbO_{2\pm x}$, β-$NbO_{2\pm x}$, γ-$NbO_{2\pm x}$, NbO, O, α-Hf, (β-Hf,Nb) Nb_2O_5–HfO_2 is plotted: solid solutions based on HfO_2 (α-HfO_{2-x}, β-HfO_{2-x}, γ-HfO_{2-x}), solid solution based on $6HfO_2{\cdot}Nb_2O_5$ (or $Hf_6Nb_2O_{17}$), $HfO_2{\cdot}12Nb_2O_5$ (or $HfNb_{24}O_{62}$, ?), solid solutions based on Nb_2O_5 (α-Nb_2O_5, β-Nb_2O_5, γ-Nb_2O_5)	[257, 266]
Nb–Hf–Si	Plotted at 1500 °C: (Nb,Hf)Si_2 (extended solid solution based on $NbSi_2$—up to ~10 at.% Hf), α-$(Nb,Hf)_5Si_{3+x}$ (extended solid solution based on α-Nb_5Si_{3+x}—up to ~15 at.% Hf), β-$(Nb,Hf)_5Si_{3+x}$ (extended solid solution based on β-Nb_5Si_{3+x}, ?), (Hf,Nb)Si (extended solid solution based on HfSi—up to ~5 at.% Nb, <~2125–2155 °C), $(Hf,Nb)_5Si_4$ (extended solid solution based on Hf_5Si_4—up to ~25 at.% Nb, <~2305–2335 °C), $(Hf,Nb)_3Si_2$ (extended solid solution based on Hf_3Si_2—up to ~12.5 at.% Nb, <~2460–2500 °C), $(Hf,Nb)_5Si_3$ (extended solid solution based on Hf_5Si_3, ~7.5–37.5 at.% Nb, from ~1500–1600 to ~2400 °C, ?), $(Hf,Nb)_2Si$ (extended solid solution based on Hf_2Si—up to ~50 at.% Nb, <~2070–2095 °C), $(Nb,Hf)_3Si$ (solid solution based on Nb_3Si, ?), $(Hf,Nb)Si_2$ (solid solution based on $HfSi_2$, <~1535–1550 °C, ?), Si, (α-Hf,Nb), (β-Hf,Nb)	[13–14, 16, 208, 214–215]

(continued)

Table 8.6 (continued)

System	Type of phase diagram (temperature and composition sections, constituent phases or phase fields) and/or character of interphase interaction and materials compatibility	References
Nb–Hf–Si–Ti	General consideration of the system.	[379]
Nb–Ir–Ni	Plotted at 1300 °C: $(Ni,Ir)_{3\pm x}Nb$ (extended solid solution based on $Ni_{3\pm x}Nb$—up to ~$(Ni_{0.7}Ir_{0.3})_{3\pm x}Nb$ compos.), $(Ir,Ni)_{3\pm x}Nb$ (solid solution based on $Ir_{3\pm x}Nb$—up to ~5 at.% Ni), α_2-$(Ir,Ni)Nb_{1-x}$ (solid solution based on α_2-$IrNb_{1-x}$—up to ~5 at.% Ni), α_1-$IrNb_{1-x}$, σ-$IrNb_{2-x}$, $IrNb_{3\pm x}$, Ni_8Nb, μ-Ni_6Nb_{7-x}, (Ir,Ni), Nb	[370]
Nb–Ir–O	Plotted partially at 900 °C: ~$Nb_{20}Ir_{12}O_7$ (or ~$Nb_5Ir_3O_{1.75}$, or $Nb_{0.52}Ir_{0.30}O_{0.185}$, <at least 1700 °C, Nowotny phase), $Nb_{11}Ir_9O$ (or $Nb_{55}Ir_{45}O_5$, ?), $Ir_{3\pm x}Nb$, α_2-$IrNb_{1-x}$, α_1-$IrNb_{1-x}$, σ-$IrNb_{2\pm x}$, $IrNb_{3\pm x}$, β-Nb_2O_5, α-Nb_2O_5, α-$NbO_{2\pm x}$, β-$NbO_{2\pm x}$, γ-$NbO_{2\pm x}$, NbO, IrO_2 (<~700–900 °C), O, Ir, Nb	[14, 16, 205–207]
Nb–Ir–Rh	No diagram plot $(Ir,Rh)Nb_{3\pm x}$ ($IrNb_{3\pm x}$–$RhNb_{3\pm x}$ continuous solid solution)	[354]
Nb–Ir–S	β-NbS_2–IrS_2 is plotted at 700–1000 °C: β-NbS_2, $(Nb,Ir)S_2$, IrS_2	[355]
Nb–Ir–Si	Plotted partially (60–100 at.% Nb) at 1200 °C: NbIrSi (?), σ-$IrNb_{2-x}(Si)$ (extended solid solution based on σ-$IrNb_{2-x}$—up to ~25 at.% Si), $(Ir,Si)Nb_{3\pm x}$ (extended solid solution based on $IrNb_{3\pm x}$—up to ~15 at.% Si), $IrSi_3$ (at least at ~1400–1500 °C), $IrSi_2$ (at least at ~1400–1500 °C), Ir_2Si_3 (at least at ~1250–1400 °C), Ir_3Si_4 (?), Ir_4Si_5 (?), IrSi (<at least ~1500 °C), Ir_3Si_2 (at least from ~500–700 to ~1500 °C), Ir_2Si (<at least ~1500 °C,), Ir_3Si (<at least ~1500 °C), $Ir_{3\pm x}Nb$, α_2-$IrNb_{1-x}$, α_1-$IrNb_{1-x}$, $NbSi_2$, α-Nb_5Si_{3+x}, β-Nb_5Si_{3+x}, Nb_3Si, Si, Ir, Nb	[356–358, 365]
Nb–Ir–Ta	See Ta–Ir–Nb in Table 6.4.	
Nb–Ir–Te	No diagram plot $NbIrTe_4$	[359]
Nb–Ir–Ti	Plotted partially at 2000 °C: $(Nb,Ti)Ir_{3\pm x}$ ($TiIr_{3\pm x}$–$NbIr_{3\pm x}$ continuous solid solution)	[367, 369]
Nb–Ir–Zr	Plotted partially at 1500, 1800 and 2100 °C: $Ir_{3\pm x}(Nb,Zr)$ ($Ir_{3\pm x}Nb$–$Ir_{3\pm x}Zr$ continuous solid solution)	[224–225]

(continued)

Table 8.6 (continued)

System	Type of phase diagram (temperature and composition sections, constituent phases or phase fields) and/or character of interphase interaction and materials compatibility	References
Nb–Mg–O	Nb_2O_5–NbO–MgO is plotted: (Nb,Mg)O (NbO–MgO continuous solid solution), $(Nb,Mg)O_{2\pm x}$ (extended solid solution based on γ-$NbO_{2\pm x}$), $3MgO{\cdot}4NbO{\cdot}2NbO_2$ (or $Mg_3Nb_6O_{11}$), $4MgO{\cdot}(1–x)Nb_2O_5$ (or $Mg_4Nb_2O_{9–x}$, <1715–1745 °C, incongruent melt. point), $5MgO{\cdot}2Nb_2O_5$ (or $Mg_5Nb_4O_{15}$, from 1195–1205 to 1565–1595 °C), $(5–x)MgO{\cdot}(2 + x/2)Nb_2O_5$ (or $Mg_{5–x}Nb_{4+x}O_{15–\delta}$, $1.14 \le x \le 1.60$, at least at 1150 °C), $MgO{\cdot}(1 – x)Nb_2O_5$ (or $MgNb_2O_{6–x}$, <1555–1585 °C, congruent melt. point corresp. to $MgNb_2O_6$), $2MgO{\cdot}17Nb_2O_5$ (or $Mg_2Nb_{34}O_{87}$, from 1240–1250 °C to 1435–1455 °C), $(Nb,Mg)_2O_{5–x}$ (solid solution based on Nb_2O_5—up to 1.5 mol. % MgO at 1435–1455 °C); $Mg_2Nb_{34}O_{87}$–$MgNb_2O_{6–x}$ eutectic—~1420–1440 °C, 73 mol.% Nb_2O_5; $Mg_2Nb_{34}O_{87}$–$Mg_5Nb_4O_{15}$ eutectic—~1515–1545 °C, 37 mol.% Nb_2O_5 In vacuum, the interaction between metal Nb and MgO initiates at 1800–1900 °C (5 h exposure); in inert atmosphere, at 1800 °C the interaction is observed along the grain boundaries, and Nb oxides are formed.	[4, 10, 26, 246–249]
Nb–Mo–N	See Mo–N–Nb in Table 7.5.	
Nb–Mo–Ni	See Mo–Nb–Ni in Table 7.5.	
Nb–Mo–O	See Mo–Nb–O in Table 7.5.	
Nb–Mo–P	See Mo–Nb–P in Table 7.5.	
Nb–Mo–Re	See Re–Mo–Nb in Table 4.6.	
Nb–Mo–Si	See Mo–Nb–Si in Table 7.5.	
Nb–Mo–Si–W	See W–Mo–Nb–Si in Table 3.6.	
Nb–Mo–Ta	See Ta–Mo–Nb in Table 6.4.	
Nb–Mo–Ti	See Mo–Nb–Ti in Table 7.5.	
Nb–Mo–U	See Mo–Nb–U in Table 7.5.	
Nb–Mo–V	See Mo–Nb–V in Table 7.5.	
Nb–Mo–W	See W–Mo–Nb in Table 3.6.	
Nb–Mo–W–Zr	See W–Mo–Nb–Zr in Table 3.6.	
Nb–Mo–Zr	See Mo–Nb–Zr in Table 7.5.	
Nb–N–Ni	Plotted at 1200 °C (pressure N_2 – 1 MPa): η-Nb_4Ni_2N, Ni_3N (<480 °C), Ni_8Nb, $Ni_{3\pm x}Nb$, μ-$Ni_6Nb_{7–x}$ (or μ-$NiNb_{1+x}$), ε-$NbN_{1\pm x}$, δ-$NbN_{1–x}$, γ-Nb_4N_{3+x}, β-$Nb_{2\pm x}N$, N, Ni, Nb No solid solutions based on binary and ternary compounds. At 1600 °C δ-$NbN_{1–x}$ interacts with Ni melts intensively.	[19, 23, 341]

(continued)

Table 8.6 (continued)

System	Type of phase diagram (temperature and composition sections, constituent phases or phase fields) and/or character of interphase interaction and materials compatibility	References
Nb–N–Si	Plotted at 1000, 1500 and 1600 °C: $Nb_5Si_3N_7$ (?), β-$Nb_5Si_{3+x}N_y$ (or β-$Nb_5Si_3N_{1-x}$, extended solid solution based on β-Nb_5Si_{3+x}, ?), α-Nb_5Si_{3+x}, $NbSi_2$, ε-$NbN_{1\pm x}$, δ-NbN_{1-x} γ-Nb_4N_{3+x}, β-$Nb_{2\pm x}N$, β-Si_3N_4, Si, N, Nb Addition of N stabilizes β-Nb_5Si_{3+x} at lower temp. At 1600–1850 °C, the interaction between Nb and β-Si_3N_4 leads to the formation of $NbSi_2$, α-Nb_5Si_{3+x}, β-Nb_5Si_{3+x}, δ-NbN_{1-x} and β-$Nb_{2\pm x}N$.	[19, 24, 27, 216]
Nb–N–Ta	See Ta–N–Nb in Table 6.4.	
Nb–N–Ti	Plotted at 1200, 1250 and 1300 °C: δ-$(Nb,Ti)N_{1\pm x}$ (δ-NbN_{1-x}–δ-$TiN_{1\pm x}$ continuous solid solution, $<\sim$2020–2980 °C), β-$(Nb,Ti)_{2\pm x}N$ (extended solid solution based on β-$Nb_{2\pm x}N$—up to $\sim(Nb_{0.7}Ti_{0.3})_{2\pm x}N$ compos. at 1300 °C, ?), ε-$(Ti,Nb)_{2\pm x}N$ (solid solution based on ε-$Ti_{2\pm x}N$—up to $\sim(Ti_{0.9}Nb_{0.1})_{2\pm x}N$ compos. at 1300 °C, ?), ε-$NbN_{1\pm x}$, N, (α-Ti,Nb), (β-Ti,Nb) δ-$TiN_{1\pm x}$ ($x = 0$)–Nb is plotted: eutectic—2350 °C, $\sim$12 mol.% δ-$TiN_{1\pm x}$ ($\sim$77–78 at.% Nb); the max. solid solubility of δ-$TiN_{1\pm x}$ in Nb is $\sim$10 mol.% and that of Nb in δ-$TiN_{1\pm x}$ is $\sim$20 mol.% (at the eutectic temp.) δ-NbN_{1-x}–δ-$TiN_{1\pm x}$ is plotted: continuous solid solution—up to the melt. points $\sim$2020–2980 °C Ti–rich δ-$(Nb,Ti)N_{1\pm x}$ is in equilibrium with Nb alloy. The interaction between compact metal Nb and δ-$TiN_{1\pm x}$ initiates from 1800 °C; at 2100 °C (2–5 h exposure) it is intensive, and leads to the formation of solid solutions.	[4, 10, 14, 16, 23, 27, 344, 346–347]
Nb–N–U	Plotted at 1000 (pressure N_2 – 100 kPa) and 2000 °C (pressure N_2 – 40 kPa): $UNbN_2$ ($<\sim$1700 °C), $(U,Nb)N_{1-x}$ (extended solid solution based on UN_{1-x}—up to $\sim U_{0.5}Nb_{0.5}N_{1-x}$ compos. at 2000 °C (?), <2810–2885 °C), δ-$(Nb,U)N_{1-x}$ (extended solid solution based on δ-NbN_{1-x}—up to $\sim Nb_{0.80\div0.85}U_{0.15\div0.20}N_{1-x}$ compos. at 2000 °C), α-U_2N_{3+x} (<1132 °C), β-U_2N_{3-x} (from 940–1100 °C to 1352 °C), ε-$NbN_{1\pm x}$, β-$Nb_{2\pm x}N$, N, α-U, β-U, (γ-U,Nb) No solid solutions based on binary and ternary compounds at temp. $\leq$1000 °C. At 1000 °C, the interaction between metal Nb and UN_{1-x} is weak (for 500 h penetration is 5 μm).	[4, 14, 16, 19, 23]
Nb–N –W	See W–N–Nb in Table 3.6.	

(continued)

Table 8.6 (continued)

System	Type of phase diagram (temperature and composition sections, constituent phases or phase fields) and/or character of interphase interaction and materials compatibility	References
Nb–N–Zr	Plotted at 1200, 1700 and 1740 °C (partially): (Nb,Zr)$N_{1\pm x}$ (δ-NbN_{1-x}–$ZrN_{1\pm x}$ continuous solid solution, $<\sim$2020–2915 °C), ε-$NbN_{1\pm x}$, γ-Nb_4N_{3+x}, β-$Nb_{2\pm x}N$, α-Zr, (β-Zr,Nb) $ZrN_{1\pm x}$ ($x = 0$)–Nb is plotted: eutectic—$\sim$2430–2435 °C, $\sim$10–12 mol. % $ZrN_{1\pm x}$ ($\sim$78–80 at.% Nb); the max. solid solubility of $ZrN_{1\pm x}$ in Nb is $\sim$6 mol.% and that of Nb in $ZrN_{1\pm x}$ is $\sim$13–14 mol.% (at the eutectic temp.) The interaction between compact metal Nb and $ZrN_{1\pm x}$ initiates from 1900–2000 °C (5 h exposure) and leads to the formation of solid solutions.	[10, 19, 23, 27, 302, 344, 348]
Nb–Ni–Re	See Re–Nb–Ni in Table 4.6.	
Nb–Ni–Ta	See Ta–Nb–Ni in Table 6.4.	
Nb–Ni–W	See W–Nb–Ni in Table 3.6.	
Nb–O–Ta	See Ta–Nb–O in Table 6.4.	
Nb–O–Th	Nb_2O_5–ThO_{2-x} is plotted: ThO_{2-x} ($<\sim$3270–3400 °C), α-$2ThO_2{\cdot}Nb_2O_5$ (or α-$Th_2Nb_2O_9$, <1310 °C), β-$2ThO_2{\cdot}Nb_2O_5$ (or β-$Th_2Nb_2O_9$, $\sim$1310–1360 °C), $ThO_2{\cdot}2Nb_2O_5$ (or $ThNb_4O_{12}$, $<\sim$1390 °C), β-Nb_2O_5, α-Nb_2O_5, γ-Nb_2O_5; β-$Th_2Nb_2O_9$–ThO_{2-x} eutectic—$\sim$1335 °C, 27 mol.% Nb_2O_5 (?); $ThNb_4O_{12}$–β-$Th_2Nb_2O_9$ eutectic—$\sim$1320–1350 °C, $\sim$37–50 mol.% Nb_2O_5, $ThNb_4O_{12}$–β-Nb_2O_5 eutectic–$\sim$1375 °C, 74 mol.% Nb_2O_5 Data on the system available in the literature are controversial. At 1800 °C the interaction between metal Nb and ThO_{2-x} leads to the oxide materials corrosion and damage. In vacuum, at 2100 °C Nb is compatible with ThO_{2-x} (?).	[4, 26, 278–279]
Nb–O–U	Plotted partially at 800–1100 °C: $UO_2{\cdot}Nb_2O_5$(or UNb_2O_7), $U_3O_8{\cdot}NbO_2{\cdot}4Nb_2O_5$(or UNb_3O_{10}), $U_3O_8{\cdot}2NbO_2{\cdot}4Nb_2O_5$(or UNb_4O_{12}), $3U_3O_8{\cdot}7UO_3{\cdot}12Nb_2O_5$(or $U_{16}Nb_{24}O_{105}$), $7U_3O_8{\cdot}U_4O_9{\cdot}8\,1/3{\cdot}NbO_2$ (or $U_3NbO_{9.68}$), U_2O_2, α-UO_3, β-UO_3, α-U_3O_8, β-U_3O_8, γ-U_3O_8, U_4O_9 (<1135 °C), UO_{2+x}($<2780-2840°C$), β-Nb_2O_5, α-Nb_2O_5, γ-Nb_2O_5, α-$NbO_{2\pm x}$, β-$NbO_{2\pm x}$, γ-$NbO_{2\pm x}$, NbO, O, α-U, β-U, (γ-U,Nb) Data on the compatibility of metal Nb with UO_{2+x} are very controversial; more likely, it depends on O contents in the oxide. The reaction between Nb and α-U_3O_8 leads to the formation of UO_{2+x} and initiates from 500 °C.	[4, 14, 16, 26, 197, 250–251]
Nb–O–W	See W–Nb–O in Table 3.6.	

(continued)

Table 8.6 (continued)

System	Type of phase diagram (temperature and composition sections, constituent phases or phase fields) and/or character of interphase interaction and materials compatibility	References
Nb–O–Y	Plotted at 1100 °C: $Y_2O_3{\cdot}Nb_2O_5$ (or $YNbO_4$, ?), $Y_2O_3{\cdot}Nb_2O_5{\cdot}2NbO_2$ (or YNb_2O_6, ?), $3Y_2O_3{\cdot}Nb_2O_5$ (or Y_3NbO_7, ?), α-Y_2O_{3-x} (<2325–2350 °C), β-Y_2O_{3-x} (from ~2310–2325 °C to ~2410–2460 °C), α-Nb_2O_5, β-Nb_2O_5, γ-Nb_2O_5, α-$NbO_{2\pm x}$, β-$NbO_{2\pm x}$, γ-$NbO_{2\pm x}$, NbO, O, α-Y, β-Y, Nb Nb_2O_5–Y_2O_3 is plotted: β-$(Y,Nb)_2O_{3-x}$ (extended solid solution based on β-Y_2O_{3-x}—up to ~2.5–15 mol.% Nb_2O_5, ?), extended solid solution based on $3Y_2O_3{\cdot}Nb_2O_5$ (or Y_3NbO_7, from ~20–23 to ~30–31.5 mol.% Nb_2O_5, <2145–2160 °C, ?), extended solid solution based on β-$Y_2O_3{\cdot}Nb_2O_5$ (or β-$YNbO_4$, from ~44–46 to ~50–51 mol.% Nb_2O_5, from 900 to 1970–2030 °C, ?), extended solid solution based on α-$Y_2O_3{\cdot}Nb_2O_5$ (or α-$YNbO_4$, from ~44–46 to ~50–51 mol.% Nb_2O_5, <900 °C, ?), β-Nb_2O_5; β-$(Y,Nb)_2O_{3-x}$–solid solution based on Y_3NbO_7 eutectic—~2100–2120 °C, ~15–20 mol.% Nb_2O_5; solid solution based on $YNbO_4$—solid solution based on Y_3NbO_7 eutectic—~1940–1950 °C, ~35–37 mol.% Nb_2O_5; solid solution based on $YNbO_4$–β-Nb_2O_5 eutectic—~1410–1485 °C, 75 mol.% Nb_2O_5 Data on the system available in the literature are controversial. The interaction between Nb and α-Y_2O_{3-x} initiates from ~1100 °C.	[26, 260–265]
Nb–O–Zr	Plotted at 1000–1600 °C: α-ZrO_2 (<~1205 °C), β-ZrO_2 (~970–2380 °C), γ-ZrO_{2-x} (~1525–2710 °C), α-Nb_2O_5, β-Nb_2O_5, γ-Nb_2O_5, α-$NbO_{2\pm x}$, β-$NbO_{2\pm x}$, γ-$NbO_{2\pm x}$, NbO, O, α-Zr, (β-Zr,Nb) Nb_2O_5–ZrO_2 is plotted: solid solutions based on ZrO_2 (α-ZrO_2, β-ZrO_2, γ-ZrO_{2-x}), $8ZrO_2{\cdot}Nb_2O_5$ (or $Zr_8Nb_2O_{21}$, <1640 °C), $15ZrO_2{\cdot}2Nb_2O_5$ (or $Zr_{15}Nb_4O_{40}$, <~1600 °C), $7ZrO_2{\cdot}Nb_2O_5$ (or $Zr_7Nb_2O_{19}$, <~1560 °C), $13ZrO_2{\cdot}2Nb_2O_5$ (or $Zr_{13}Nb_4O_{36}$, <~1525 °C), solid solution based on $6ZrO_2{\cdot}Nb_2O_5$ (or $Zr_6Nb_2O_{17}$, <~1450–1670 °C, ?), $11ZrO_2{\cdot}2Nb_2O_5$ (or $Zr_{11}Nb_4O_{32}$, <~1465 °C), $5ZrO_2{\cdot}Nb_2O_5$ (or $Zr_5Nb_2O_{15}$, <1435 °C), $ZrO_2{\cdot}Nb_2O_5$ (or $ZrNb_2O_7$) $ZrO_2{\cdot}(5\div7)Nb_2O_5$ (or $ZrNb_{10\div14}O_{27\div37}$, ?), $ZrO_2{\cdot}12Nb_2O_5$ (or $ZrNb_{24}O_{62}$, <1400–1450 °C, ?), $ZrO_2{\cdot}16Nb_2O_5$ (or $ZrNb_{32}O_{82}$, ?), solid solutions based on Nb_2O_5 (α-Nb_2O_5, β-Nb_2O_5, γ-Nb_2O_5); solid solution based on Nb_2O_5 (or $ZrNb_{24}O_{62}$, ?)–solid solution based on $Zr_6Nb_2O_{17}$ (or $Zr_5Nb_2O_{15}$, ?) eutectic—1435 °C, 75 mol.% Nb_2O_5 Data on the system available in literature are controversial. In vacuum, the interaction between metal Nb and γ-ZrO_{2-x} initiates from 1800–2000 °C; in inert atmosphere, at 1800 °C the interaction is observed along the grain boundaries.	[4, 10, 26, 217–218, 231, 252–259]

(continued)

Table 8.6 (continued)

System	Type of phase diagram (temperature and composition sections, constituent phases or phase fields) and/or character of interphase interaction and materials compatibility	References
Nb–Os–Rh	See Os–Nb–Rh in Table 5.4.	
Nb–Os–Ta	See Os–Nb–Ta in Table 5.4.	
Nb–Os–W	See W–Nb–Os in Table 3.6.	
Nb–Re–Ta	See Re–Nb–Ta in Table 4.6.	
Nb–Re–V	See Re–Nb–V in Table 4.6.	
Nb–Re–W	See W–Nb–Re in Table 3.6.	
Nb–Si–Ta	See Ta–Nb–Si in Table 6.4.	
Nb–Si–Ti	Plotted at 500–1800 °C: $(Nb,Ti)_3Si$ (Nb_3Si–Ti_3Si continuous solid solution, homog. range—strongly dependent on temp., $<\sim$1170–1980 °C), α-$(Nb,Ti)_5Si_{3+x}$ (extended solid solution based on α-Nb_5Si_{3+x}–up to ~10–25 at.% Ti), β-$(Nb,Ti)_5Si_{3+x}$ (extended solid solution based on β-Nb_5Si_{3+x}, ?), $(Ti,Nb)_5Si_{3\pm x}$ (extended solid solution based on $Ti_5Si_{3\pm x}$—up to ~10–20 at.% Nb, <2130 °C), $(Ti,Nb)_5Si_4$ (extended solid solution based on Ti_5Si_4—up to ~50 at.% Nb at 1200 °C, $<\sim$1900–1920 °C), $(Nb,Ti)Si_2$ (extended solid solution based on $NbSi_2$—up to compos. ~$(Nb_{0.55}Ti_{0.45})Si_2$), $(Ti,Nb)Si_2$ (solid solution based on $TiSi_2$, $<\sim$1480–1500 °C; the solubility of $NbSi_2$ is ≤3 mol.%, ?), (Ti,Nb)Si (solid solution based on TiSi, $<\sim$1540–1570 °C), Si, α-Ti, (β-Ti,Nb) Addition of Ti stabilizes Nb_3Si at lower temp.	[4, 14, 16, 31, 33, 199, 209–210, 215, 219–221, 227, 239, 241–242, 299]
Nb–Si–U	Plotted at 850 and 1000 °C: $U_2Nb_3Si_4$, $U_{2-x}Nb_{3+x}Si_4$, USi_3 (<1510 °C), USi_2 (<450 °C), α-USi_{2-x}, β-USi_{2-x} ($x = 0.12$, <1710 °C), α-U_3Si_5, β-U_3Si_5, γ-U_3Si_5 (<1770 °C), USi (<1580 °C), U_3Si_2 (<1665 °C), U_3Si (<930 °C), $NbSi_2$, α-Nb_5Si_{3+x}, β-Nb_5Si_{3+x}, Nb_3Si, Si, α-U, β-U, (γ-U,Nb)	[300–301]
Nb–Si–V	Plotted at 800 °C: NbVSi (?), $(Nb,V)Si_2$ ($NbSi_2$–VSi_2 continuous solid solution, at least at 800–1550 °C, $<\sim$1675–1940 °C), $(V,Nb)_5Si_3$ (extended solid solution based on V_5Si_3—up to compos. ~$(V_{0.3}Nb_{0.7})_5Si_3$, <2010 °C, ?), $(V,Nb)_{3+x}Si$ (extended solid solution based on $V_{3+x}Si$—up to compos. ~$(V_{0.75}Nb_{0.25})_{3+x}Si$, <1925 °C), α-$(Nb,V)_5Si_{3+x}$ (solid solution based on α-Nb_5Si_{3+x}—up to compos. ~$(Nb_{0.9}V_{0.1})_5Si_{3+x}$), V_6Si_5 (forms solid solution, 1160–1670 °C), β-Nb_5Si_{3+x}, Nb_3Si, Si, (V,Nb)	[19, 33, 349–351]
Nb–Si–W	See W–Nb–Si in Table 3.6.	

(continued)

Table 8.6 (continued)

System	Type of phase diagram (temperature and composition sections, constituent phases or phase fields) and/or character of interphase interaction and materials compatibility	References
Nb–Si–Zr	Plotted at 900 °C: ZrNbSi (?), (Nb,Zr)Si_2 (extended solid solution based on $NbSi_2$—up to compos. $\sim(Nb_{0.7\div0.8}Zr_{0.2\div0.3})Si_2$ at 900–1300 °C), (Zr,Nb)Si_2 (extended solid solution based on $ZrSi_2$—up to compos. $\sim(Zr_{0.75}Nb_{0.25})Si_2$ at 900 °C; at temp. >1300 °C the solubility of $NbSi_2$ is ~6 mol.%, ?), β-$(Zr,Nb)_5Si_3$ (extended solid solution based on β-Zr_5Si_3—up to compos. $\sim(Zr_{0.4}Nb_{0.6})_5Si_3$ at 900 °C, ?), α-$(Nb,Zr)_5Si_{3+x}$ (extended solid solution based on α-Nb_5Si_{3+x}—up to compos. $\sim(Nb_{0.7}Zr_{0.3})_5Si_{3+x}$ at 900 °C), α-$(Zr,Nb)_5Si_4$ (extended solid solution based on α-Zr_5Si_4—up to compos. $\sim(Zr_{0.6}Nb_{0.4})_5Si_4$ at 900 °C, <1860 °C), $(Zr,Nb)_3Si_2$ (solid solution based on Zr_3Si_2—up to compos. $\sim(Zr_{0.9}Nb_{0.1})_3Si_2$ at 900 °C, <2215–2220 °C), $(Zr,Nb)_2Si$ (solid solution based on Zr_2Si—up to compos. $\sim(Zr_{0.9}Nb_{0.1})_2Si$ at 900 °C, <1925 °C), Zr_3Si (<1650 °C), β-Zr_5Si_4 (1860–2250 °C), α-Zr_5Si_3 (?), α-ZrSi (solubility of Nb is low, <1460 °C), β-ZrSi (1460–2210 °C), β-Nb_5Si_{3+x}, Nb_3Si, α-Zr, (β-Zr,Nb)	[31, 33, 350, 352]
Nb–Ta–Ti	See Ta–Nb–Ti in Table 6.4.	
Nb–Ta–V	See Ta–Nb–V in Table 6.4.	
Nb–Ta–W	See W–Nb–Ta in Table 3.6.	
Nb–Ta–Zr	See Ta–Nb–Zr in Table 6.4.	
Nb–Ti–W	See W–Nb–Ti in Table 3.6.	
Nb–V–W	See W–Nb–V in Table 3.6.	
Nb–W–Zr	See W–Nb–Zr in Table 3.6.	

[a] See notes to Table 8.5

The character of chemical interaction and general reactions of niobium with common chemicals (solids, liquids and aqueous solutions) and complex gases are summarized in Table 8.7.

Table 8.7 The interaction of niobium with some chemicals and complex gases [4, 10, 12, 36][a]

Reagent, formula	Character of chemical interaction, examples of general reactions
Air, $N_2 + O_2$	In air the oxidation of Nb initiates from 250–300 °C and leads to the formation of α-Nb_2O_5 at temp. <800 °C, or β-Nb_2O_5 at 800–1285 °C (γ-Nb_2O_5 is formed at higher temp.): $4Nb + 5O_2 \rightarrow 2Nb_2O_5$. At temp. >850–900 °C the oxidation process is very intensive.
Water, H_2O	No interaction at the moderate conditions.

(continued)

Table 8.7 (continued)

Reagent, formula	Character of chemical interaction, examples of general reactions
Hydrogen peroxide, H_2O_2	No interaction.
Carbon monoxide, CO	The interaction leads to the formation of carbide NbC_{1-x} or oxycarbide NbC_xO_y.
Carbon dioxide, CO_2	The interaction with dry CO_2 leads to the formation of Nb oxides.
Hydrocarbons, CH_n	The interaction between Nb and hydrocarbons leads to the formation of Nb carbides.
Ammonia (aqueous solution), NH_4OH	No interaction.
Sodium hydroxide, NaOH	The interaction with molten NaOH results in the formation of Na niobates; the interaction with aqueous solutions NaOH is negligible.
Potassium hydroxide, KOH	The interaction with molten KOH results in the formation of K niobates; the interaction with aqueous solutions KOH is negligible.
Nitric acid, HNO_3	Practically, no interaction.
Sulphuric acid, H_2SO_4	The interaction is negligible.
Hydrochloric acid, HCl	No interaction.
Hydrofluoric acid, HF	Nb dissolves in HF.
Hydrochloric acid with nitric acid (aqua regia), $HCl + HNO_3$	While heating the interaction is negligible.
Nitric acid with hydrofluoric acid, $HNO_3 + HF$	The interaction leads to the solution of Nb: $3Nb + 5HNO_3 + 21HF \rightarrow 3H_2[NbF_7] + 5NO + 10H_2O$.

[a] Etching agents for niobium: 48 % HF aqueous solution + H_2SO_4 concentrated aqueous solution + H_2O mixture (ratio 1:1:1) with addition of H_2O_2 (for grain boundaries and sub-boundaries), 175 ml 40 % HF aqueous solution + 175 ml 70 % HNO_3 aqueous solution + 650 ml H_2O (electrochemical polishing, platinum cathode, 50 °C, 12–20 V, 0.2–0.3 A cm^{-2}), 50 ml 40 % HF aqueous solution + 170 ml 70 % HNO_3 aqueous solution + 5 ml citric acid + 510 ml methanol (electrochemical polishing, 4.95–6.05 A cm^{-2})

The self-diffusion characteristics of niobium atoms, diffusion characteristics in niobium—element and niobium—chemical compound systems in the wide range of temperatures and summarized data on the physico-chemical interaction of niobium with elements of the periodic table are given in Addendum.

References

1. Steurer W (1996) Crystal structure of the metallic elements. In: Cahn RW, Haasen P (eds) Physical metallurgy, 4th ed., Vol. 1, pp. 1–46. Elsevier Science BV, Amsterdam
2. Cotton FA, Wilkinson G (1965) Advanced inorganic chemistry. Wiley, New York, London
3. Akhmetov NS (2001) Obschaya i neorganicheskaya khimiya (General and inorganic chemistry), 4th ed. Vysshaya Shkola, Moscow (in Russian)
4. Kotelnikov RB, Bashlykov SN, Galiakbarov ZG, Kashtanov AI (1968) Osobo tugoplavkie elementy i soedineniya (Extra refractory elements and compounds). Metallurgiya, Moscow (in Russian)
5. Zefirov AP (ed), Veryatin UD, Mashirev VP, Ryabtsev NG, Tarasov VI, Rogozkin BD, Korobov IV (1965) Termodinamicheskie svoistva neorganicheskikh veschestv (Thermodynamic properties of inorganic substances). Atomizdat, Moscow (in Russian)
6. Speight JG, ed (2005) Lange's handbook of chemistry, 16th ed. McGraw-Hill, New York
7. Lide DR, ed (2010) CRC handbook of chemistry and physics, 90th ed. CRC Press, Boca Raton, New York
8. Martienssen W (2005) The elements. In: Martienssen W, Warlimont H (eds) Springer handbook of condensed matter and materials data, pp. 45–158. Springer, Berlin, Heidelberg
9. Samsonov GV, ed (1976) Svoistva elementov (Properties of elements), 2nd ed., Vol. 1. Metallurgiya, Moscow (in Russian)
10. Marmer ÉN, Gurvich OS, Maltseva LF (1967) Vysokotemperaturnye materialy (High-temperature materials). Metallurgiya, Moscow (in Russian)
11. Cardarelli F (2008) Materials handbook, 2nd ed. Springer, London
12. Samsonov GV, ed (1976) Svoistva elementov (Properties of elements), 2nd ed., Vol. 2. Metallurgiya, Moscow (in Russian)
13. Lyakishev NP, ed (1997) Diagrammy sostoyaniya dvoinykh metallicheskikh sistem (Phase diagrams of binary metal systems), Vol. 2. Mashinostroenie, Moscow (in Russian)
14. Lyakishev NP, ed (2001) Diagrammy sostoyaniya dvoinykh metallicheskikh sistem (Phase diagrams of binary metal systems), Vol. 3, Part 1. Mashinostroenie, Moscow (in Russian)
15. Lyakishev NP, ed (1996) Diagrammy sostoyaniya dvoinykh metallicheskikh sistem (Phase diagrams of binary metal systems), Vol. 1. Mashinostroenie, Moscow (in Russian)
16. Massalski TB, Subramanian PR, Okamoto H, Kacprzak L, eds (1990) Binary alloy phase diagrams, 2nd ed. ASM International, Metals Park, Ohio
17. Rudy E (1969) Compendium of phase diagram data. In: Ternary phase equilibria in transition metal-boron-carbon-silicon systems. Report AFML-TR-65–2, Contracts USAF 33(615)-1249 and USAF 33(615)-67-C-1513, Part 5, pp. 1–689. Air Force Materials Laboratory, Wright-Patterson Air Force Base, Ohio
18. Rudy E, Benesovski F, Toth L (1963) Untersuchungen der Dreistoffsysteme der Va- und VIa-Metalle mit Bor und Kohlenstoff (Studies of the ternary systems of the group Va and VIa metals with boron and carbon). Z Metallkd 54(6):345–353 (in German)
19. Kosolapova TYa, ed (1990) Handbook of high-temperature compounds: properties, production and applications. Hemisphere, New York
20. Toth LE (1971) Transition metal carbides and nitrides. Academic Press, New York, London
21. Kofstad P (1966) High-temperature oxidation of metals. Wiley, New York, London
22. Kofstad P (1988) High-temperature corrosion. Elsevier Applied Science, London, New York
23. Holleck H (1984) Binäre und ternäre Carbid- und Nitridsysteme der Ubergangsmetalle (Binary and ternary carbide and nitride systems of the transition metals). Gebrüder Borntträeger, Berlin, Stuttgart (in German)
24. Rogl P, Schuster JC (1992) Phase diagrams of ternary boron nitride and silicon nitride systems. ASM International, Materials Park, Ohio
25. Borisova AL, Martsenyuk IS (1975) Reactions of boron and aluminum nitrides and materials based on them with refractory metals. Powder Metall Met Ceram 14(10):822–826

26. Samsonov GV, ed (1978) Fiziko-khimicheskie svoistva okislov (Physico-chemical properties of oxides), 2nd ed., Metallurgiya, Moscow (in Russian)
27. Samsonov GV, Vinitskii IM (1980) Handbook on refractory compounds. IFI/Plenum, New York
28. Yasinskaya GA, Groisberg MS (1963) Interaction of titanium boride with niobium and tungsten. Powder Metall Met Ceram 2(6):457–458
29. Voroshilov YuV, Kuzma YuB (1969) Reaction of zirconium with the transition metals and boron. Powder Metall Met Ceram 8(11):941–944
30. Andrievskii RA, Spivak II (1989) Prochnost tugoplavkikh soedinenii i materialov na ikh osnove (Strength of refractory compounds and materials based on them). Metallurgiya, Chelyabinsk (in Russian)
31. Setton M, Van Der Spiegel J (1991) A review of some aspects of ternary metal-metal-Si and metal-B-Si systems. J Appl Phys 69(2):994–999
32. English JJ (1961) Binary and ternary phase diagrams of columbium, molybdenum and tungsten. Report AD-TR-257–739, Contract AF 33(616)-7747, pp. 1–241. Defence Metals Information Center, Battelle Memorial Institute, Columbus, Ohio
33. Gladyshevskii EI, Lakh VI, Skolozdra RV, Stadnik BI (1964) The mutual solubility of disilicides of the transition metals from group IV, V and VI. Powder Metall Met Ceram 3(4):278–282
34. Gordon AR, Muchnik GF (1964) Opredelenie integralnoi stepeni chernoty metallov v zavisimosti ot stepeni sherokhovatosti poverkhnosti (The determination of the integral emittance of metals affected on surface roughness grade). Teplofiz Vys Temp 2(2):292–294 (in Russian)
35. Habashi F (1997) Handbook of extractive metallurgy. Wiley-VCH, Weinheim, New York
36. Savitskii EM, Burkhanov GS (1971) Metallovedenie splavov tugoplavkikh i redkih metallov (Metallography of refractory and less-common metal alloys), 2nd ed. Nauka, Moscow (in Russian)
37. Audi G, Wapstra AH, Thibault C, Blachot J, Bersillon O (2003) The NUBASE evaluation of nuclear and decay properties. Nucl Phys A 729:3–128
38. De Laeter JR, Bohlke JK, De Bievre P, Hidaka H, Peiser HS, Rosman KJR, Taylor PDP (2003) Atomic weights of the elements. Review 2000 (IUPAC Technical report). Pure Appl Chem 75(6):683–800
39. Wieser ME (2006) Atomic weights of the elements 2005. (IUPAC Technical report). Pure Appl Chem 78(11):2051–2066
40. Darby JB, Jr, Lam DJ, Norton LJ, Downey JW (1962) Intermediate phases in binary systems of technetium-99 with several transition elements. J Less-Common Met 4(6):558–563
41. Fromm E, Gebhardt, E (1976) Gase und Kohlenstoff in Metallen (Gases and carbon in metals). Springer, Berlin (in German)
42. Goodwin F, Guruswamy S, Kainer KU, Kammer C, Knabl W, Koethe A, Leichtfried G, Schlamp G, Stickler R, Warlimont H (2005) Metals. In: Martienssen W, Warlimont H (eds) Springer handbook of condensed matter and materials data, pp. 161–430. Springer, Berlin, Heidelberg
43. Klueh RL (1969) Effect of oxygen on the compatibility of niobium with potassium. Corrosion 25(10):416–422
44. Kolchin OP, Kurganov GV, Zhorova LP (1964) Niobii (Niobium). In: Tumanov AT (ed) Konstruktsionnye materialy (Structural materials). Vol. 2, pp. 317–319. Sovetskaya Entsiklopediya, Moscow (in Russian)
45. Nowotny H, Benesovsky F, Kieffer R (1959) Beitrag zum Aufbau der Syteme Niob-Bor und Tantal-Bor (Contribution to building the systems niobium-boron and tantalum-boron). Z Metallkd 50(7):417–423 (in German)
46. Andrievskii RA (1986) Materialovedenie gidridov (Materials science of hydrides). Metallurgiya, Moscow (in Russian)
47. Villars P, Girgis K (1982) Die Zustandbilder Nb-In, Nb-Tl, Ta-In und Ta-Tl (Phase diagrams of Nb-In, Nb-Tl, Ta-In and Ta-Tl alloys). Z Metallkd 73(3):169–171 (in German)

48. Samsonov GV (1969) Nitridy (Nitrides). Naukova Dumka, Kyiv (in Russian)
49. Saini GS, Calvert LD, Taylor JB (1964) Preparation and characterization of crystals of MX- and MX_2-type arsenides of niobium and tantalum. Canad J Chem 42(3):630–634
50. Revolinsky E, Brown BE, Beerntsen DJ, Armitage CH (1965) The selenide and telluride systems of niobium and tantalum. J Less-Common Met 8(1):63–75
51. Nekrasov BV (1973) Osnovy obschei khimii (Foundations of general chemistry), 3rd ed., Vol. 1. Khimiya, Moscow (in Russian)
52. Kaufman L (1991) Calculation of multicomponent tantalum based phase diagrams. Calphad 15(3):261–282
53. Zakharov AM, Novikov II, Pshokin VP (1971) Niobievyi ugol troinoi sistemy Nb-Ti-B (The niobium-rich angle of the Nb-Ti-B ternary system). Izv Vyssh Uchebn Zaved Tsvet Metall (4):111–114 (in Russian)
54. Miura S, Ohkubo K, Terada Y, Kimura Y, Mishima Y, Yamabe-Mitarai Y, Harada H, Mohri T (2005) Phase equilibria in Ir-rich portion of Ir-Al-X (X: V, Nb and Ta) ternary systems. J Alloys Compd 395(1–2):263–271
55. Gschneidner KA (1961) Rare earth alloys: a critical review of. Van Nostrand Reinhold, New York
56. Kubaschewski O, Von Goldbeck O (1976) Phase diagrams. In: Zirconium. Physico-chemical properties of its compounds and alloys. Atomic Energy Review, Special Issue N 6, pp. 67–140. International Atomic Energy Agency, Vienna
57. Kocherzhinskii YuA, Vasilenko VI (1985) Diagrammy plavkosti sistem Mo-Nb(V,Cr), V-Nb(Cr) i Mo-V-Nb(Cr) (The meltability diagram of the Mo-Nb(V,Cr), V-Nb(Cr) and Mo-V-Nb(Cr) systems). Izv AN SSSR Metally (2):188–190 (in Russian)
58. Goldschmidt HJ, Brand JA (1961) The constitution of the chromium-niobium-molybdenum system. J Less-Common Met 3(1):44–61
59. Padhi D III, Lewandowski JJ (2003) Effects of test temperature and grain size on the charpy impact toughness and dynamic toughness (K_{ID}) of polycrystalline niobium. Metall Mater Trans A 34(4):967–978
60. Kuzma YuB (1971) An x-ray structural investigation of the systems niobium-titanium-boron and niobium-molybdenum-boron. Powder Metall Met Ceram 10(4):298–300
61. Balykova YuV, Knyazev AV, Kerimov EYu, Kalmykov KB, Slyusarenko EM (2009) New Laves phase in the Nb-Cr-Re ternary system. Metal Sci Heat Treatment 51(9–10):411–414
62. Köbler U, Welter J-M (1982) Low temperature susceptibility and phase diagrams of the Nb-H and Ta-H systems. J Less-Common Met 84:225–235
63. Nowotny H, Rogl P (1977) Ternary metal borides. In: Matkovich VI (ed) Boron and refractory borides, pp. 413–438. Springer, Berlin, Heidelberg, New York
64. Smirnov YuM, Finkel VA (1975) Crystal structure of tantalum, niobium and vanadium at 110–400 K. Soviet Physics JETP 22:750–753
65. Argon AS (1996) Mechanical properties of single-phase crystalline media: deformation at low temperatures. In: Cahn RW, Haasen P (eds) Physical metallurgy, 4th ed., Vol. 3, pp. 1877–1955. Elsevier Science BV, Amsterdam
66. Bartlett ES, Droegkamp RE (1990) Niobium. In: Metals handbook, Vol. 2 – Properties and selection: nonferrous alloys and special-purpose materials, pp. 3114–3121. ASM International, Metals Park, Ohio
67. Lässer R, Bickmann K (1985) Phase diagram of the Nb-T system. J Nucl Mater 132(3):244–248
68. Pesch W, Schober T, Wenzl H (1978) A TEM investigation of anisotropic lattice distortions in ordered NbH and NbD alloys. Scr Metall 12(9):815–820
69. Makenas BJ, Birnbaum HK (1982) Phase changes in the niobium-hydrogen system II. Low temperature hydride phase transitions. Acta Metall 30(2):469–481
70. Schober T, Linke U (1976) A metallographic study of the niobium-hydrogen system. Part II. γ-, δ-, ζ- and ε-phase precipitation. J Less-Common Met 44:77–86

71. Hwang YS, Torgeson DR, Barnes RG (1978) Nuclear magnetic resonance evidence for the occurrence of a low-temperature pseudo-cubic phase in the Nb-H system near $NbH_{0.75}$. Scr Metall 12(6):507–510
72. Schober T, Wenzl H (1976) β-phase melting and solidification phenomena in the niobium-hydrogen system. Phys Status Solidi A 33(2):673–681
73. Westlake DG, Ocker ST (1975) The isotope effect and the influence of interstitial impurities on the hydrogen solubility limit in niobium and vanadium. Metall Trans A 6(2):399–402
74. Fujita K, Huang YC, Tada M (1979) The studies on the equilibria of Ta-D, Nb-D and V-D systems. J Japan Inst Metals 43(7):611–617
75. Smith JF, Lee KJ (1988) The Li-Nb (lithium-niobium) and Li-V (lithium-vanadium) systems. Bull Alloy Phase Diagrams 9(4):474–478
76. Niessen AK, De Boer FR, Boom R, De Châtel PF, Mattens WCM, Miedema AR (1983) Model predictions for the enthalpy of formation of transition metal alloys. II. Calphad 7(1):51–70
77. Barker MG (1979) Reactions of the liquid alkali metals with the metals Zr, Nb, Ta, Mo and W and their oxides. Rev Int Haut Temp Refract 16(3):237–243
78. Smith JF, Lee KJ (1988) The Na-V (sodium-vanadium) and Na-Nb (sodium-niobium) systems. Bull Alloy Phase Diagrams 9(4):479–483
79. Distefano JR, Litman AP (1964) Effect of impurities in some refractory metal – alkali metal systems. Corrosion 20(12):392–399
80. Chase MW (1983) Heats of transition of the elements. Bull Alloy Phase Diagrams 4(1):123–124
81. Arzhanyi PM, Volkova RM, Prokoshkin DA (1963) Issledovanie sistemy niobii-berillii (An investigation of the niobium-beryllium system). Doklady AN SSSR 150(1):96–98 (in Russian)
82. Raevskii II, Grigorev AT (1968) Phase diagram of the Nb-Be system. Russ Metall (5):134–136
83. Ananin VM, Gladkov VP, Svetlov AV, Skorov DM, Tenishev VI (1976) Koeffitsienty diffuzii i rastvorimost vanadiya, niobiya i tseriya v berillii (Diffusion coefficients and solubility of vanadium, niobium and cerium in beryllium). Atom Energiya 40(3):304–305 (in Russian)
84. Stuemke M, Petzow G (1975) Kristallstrukturen und Gitterabmessungen von Uebergangsmetall-Diberylliden und -Diboriden in ternaeren Mischkristallbereichen (Crystal structure and lattice constants of transition metal diberyllides and diborides in ternary solid solutions). Z Metallkd 66(5):292–295 (in German)
85. Miller GL, Cox FG (1960) Development of oxidation resistance of some refractory metals. J Less-Common Met 2(2–4):207–222
86. Palenzona A, Cirafici S (1991) The Nb-Y (niobium-yttrium) system. J Phase Equilibria 12(2):204–207
87. Savitskii EM, Terekhova VF, Burov IV (1959) Alloys formed by niobium with lanthanum and cerium. Russ J Inorg Chem 4(6):658
88. Gomozov LI, Ivanov OS (1963) Povedenie splavov sistemy uran-tsirkonii-niobii pri zakalke s otpuskom (The behavior of alloys of the uranium-zirconium-niobium system during quenching and tempering). In: Ivanov OS (ed) Struktura splavov nekotorykh sistem soderzhashchikh uran i torii (Structure of alloys of certain systems containing uranium and thorium), pp. 118–130. Nauka, Moscow (in Russian)
89. Badaeva TA, Kuznetsova RI (1971) Investigation of the solidus and liquidus temperatures in the U-Zr-Nb system. Russ Metall (2):126–128
90. Williams RO (1979) Stability of the body-centered cubic gamma phase in the uranium-zirconium-niobium system. J Nucl Mater 82(1):184–192
91. Kutaitsev VI (1962) Splavy toriya, urana i plutoniya (Thorium, uranium and plutonium alloys). Gosatomizdat, Moscow (in Russian)
92. Terekhov GI (1982) Features of the structure of the U-Nb phase diagram. Russ Metall (4):170–171

93. Ivanov OS, Raevskii II, Stepanov NV (1971) Sverkhprovodyashchie splavy sistemy niobii-titan-tsirkonii-gafnii (Superconducting alloys in the niobium-titanium-zirconium-hafnium system). Nauka, Moscow (in Russian)
94. Kornilov II (1975) Titan (Titanium). Nauka, Moscow (in Russian)
95. Murray JL (1981) The Nb-Ti (niobium-titanium) system. Bull Alloy Phase Diagrams 2(1): 55–61
96. Eremenko VN, Tretyachenko LA (1987) Troinye sistemy titana s perekhodnymi metallami IV-VI grup (Ternary systems of titanium with IV-VI groups transition metals). Naukova Dumka, Kyiv (in Russian)
97. Guseva LN, Dolinskaya LK (1982) Metastabilnye fazy v zakalennykh titanovykh splavakh s perekhodnymi metallami (Metastable phases in quenched titanium alloys with transition elements). Doklady AN SSSR 266(3):634–637 (in Russian)
98. Koul MK, Breedis JF (1970) Phase transformations in beta isomorphous titanium alloys. Acta Metall 18(6):579–588
99. Chernov DB, Shinyaev AYa (1975) Calculation of the interaction parameters of titanium with vanadium, niobium and molybdenum. Russ Metall (5):167–172
100. Rogl P (1983) Phase diagrams. In: Titanium. Physico-chemical properties of its compounds and alloys. Atomic Energy Review, Special Issue N 9, pp. 201–369. International Atomic Energy Agency, Vienna
101. Ivanov OS, Adamova AS, Tararaeva EM, Tregubov IA (1971) Struktura splavov tsirkoniya (Structure of zirconium alloys). Nauka, Moscow (in Russian)
102. Abriata JP, Bolcich JC (1982) The Nb-Zr (niobium-zirconium) system. Bull Alloy Phase Diagrams 3(1):34–44
103. Fernandez-Guillermet A (1991) Thermodynamic analysis of the stable phases in the Zr-Nb system and calculation of the phase diagram. Z Metallkd 82(6):478–487
104. Nakai K, Kinoshita C, Kitajima S (1981) Effects of oxygen and/or nitrogen on phase transformations above the monotectoid temperature in Nb-Zr alloys. J Nucl Mater 98(1–2):131–143
105. Okamoto H (1991) The Hf-Nb (hafnium-niobium) system. J Phase Equilibria 12(2):211–214
106. Taylor A, Doyle NJ (1964) The constitution diagram of the niobium-hafnium system. J Less-Common Met 7(1):37–53
107. Jackson WA, Perkins AJ, Hehemann RF (1970) Omega transformation in Hf-Nb alloys. Metall Trans 1(7):2014–2016
108. Carpenter RW, Liu CT, Mardon RG (1971) Phase relations in concentrated Ta-Hf and Nb-Hf alloys. Metall Trans 2(1):125–131
109. Geiss RC, Hartley CS, Steedly JE (1965) Interdiffusion in niobium-vanadium alloys. J Less-Common Met 9(5):309–320
110. Smith JF, Carlson ON (1983) The Nb-V (niobium-vanadium) system. Bull Alloy Phase Diagrams 4(1):46–49
111. Molokanov VV, Chernov DB, Budberg PB (1977) Calculations of the phase diagrams for the vanadium-chromium, vanadium-niobium and chromium-niobium systems in terms of the regular solution approximation. Russ J Phys Chem 51(8):1181–1183
112. Pan VM (1961) Polymorphous transformation in the metalloid $NbCr_2$. Phys Met Metallogr 12(3):139–141
113. Kornilov II, Alisova SP, Budberg PB (1965) Equilibrium phase diagram for the $NbCr_2$-$ZrCr_2$ metallic compound system. Inorg Mater 1:1993–1995
114. Venkatraman M, Neumann JP (1986) The Cr-Nb (chromium-niobium) system. Bull Alloy Phase Diagrams 7(5):462–466
115. Hellawell A (1959) The constitution of manganese base alloys with metals of the second transition series. J Less-Common Met 1(5):343–347
116. Savitskii EM, Kopetskii ChV (1960) Physico-chemical behaviour of manganese with niobium. Russ J Inorg Chem 5(3):363–364

117. Paul E, Swartzendruber LI (1986) The Fe-Nb (iron-niobium) system. Bull Alloy Phase Diagrams 7(3):248–254
118. Lü FX, Jack KH (1985) The occurrence of high-speed steel carbide-type η phases in the Fe-Nb system. J Less-Common Met 114(1):123–127
119. Hurley GF, Brophy JH (1964) A constitution diagram for the niobium-ruthenium system above 1100 °C. J Less-Common Met 7(4):267–277
120. Das BK, Schmerling MA, Lieberman DS (1970) Some aspects of phase transformations in near-equiatomic niobium-ruthenium alloys. Mater Sci Eng 6(4):248–254
121. Raman A (1966) X-ray investigation in the niobium (columbium) – cobalt system. Trans AIME 236(4):561–565
122. Kuzma YuB, Shuryn AK, Dmitrieva GI, Gladyshevskii EI (1964) Kristallicheskaya struktura β-fazy v sisteme Nb-Co i rastvorimost kremniya v nei (Crystal structure of the β-phase of the system Nb-Co and solubility of silicon in it). Dopov Akad Nauk Ukr RSR Ser A Fiz Mat Tekh Nauki 26(5):600–603 (in Russian)
123. Ritter DL, Giessen BC, Grant NJ (1964) The niobium (columbium) – rhodium binary system. Part I: The constitution diagram. Part II: Crystal structure relationships. Trans AIME 230:1250–1267
124. Giessen BC, Koch R, Grant NJ (1964) The niobium (columbium) – iridium constitution diagram. Trans AIME 230:1268–1273
125. Duerden IJ, Hume-Rothery W (1966) The equilibrium diagram of the system niobium-nickel. J Less-Common Met 11(6):381–387
126. Kornilov II, Pylaeva EN (1966) The niobium-nickel system. Russ Metall (5):69–70
127. Quist WE, Van Der Wekken CJ, Taggart R, Polonis DH (1969) Intermediate compound Ni_8Nb(Cb) in nickel-rich nickel – niobium (columbium) alloys. Trans AIME 245(2):345–349
128. Nash P, Nash A (1986) The Nb-Ni (niobium-nickel) system. Bull Alloy Phase Diagrams 7(2):124–130
129. Giessen BC, Grant NJ (1965) The crystal structures of VNi_2, VPd_2, VPt_2 and related AB_2 phases. J Less-Common Met 8(2):114–119
130. Giessen BC, Grant NJ, Parker DP, Manuszewski RC, Waterstrat RM (1980) The niobium (columbium) – palladium constitution diagram. Metall Trans A 11(5):709–715
131. Waterstrat RM, Giessen BC (1985) The niobium (columbium) – platinum constitution diagram. Metall Trans A 16(11):1943–1949
132. Popov IA, Shiryaeva NV (1961) Equilibrium diagram of the copper- niobium system. Russ J Inorg Chem 6(10):1184–1187
133. Kaufman L (1978) Coupled phase diagrams and thermochemical data for transition metal binary systems – III. Calphad 2(2):117–146
134. Chakrabarti DJ, Laughlin DE (1982) The Cu-Nb (copper-niobium) system. Bull Alloy Phase Diagrams 2(4):455–460
135. Terekhov GI, Aleksandrova LN (1984) The copper-niobium phase diagram. Russ Metall (4):218–221
136. Röschel E, Loebich O, Jr, Raub CJ (1973) Das Zustandsdiagramm Niob-Gold (Phase diagram niobium-gold). Z Metallkd 64(5):359–361 (in German)
137. Wire MS, Webb GW (1981) Superconductivity and the b.c.c. to A-15 transformation in Nb-Au alloys. J Phys Chem Solids 42(3):233–238
138. Okamoto H, Massalski TB (1985) The Au-Nb (gold-niobium) system. Bull Alloy Phase Diagrams 6(2):134–136
139. Meussner RA, Goode RJ (1965) The niobium (columbium) – zinc constitution diagram. Trans AIME 233(4):661–671
140. Samsonov GV, Serebryakova TI, Neronov VA (1975) Boridy (Borides). Atomizdat, Moscow (in Russian)
141. Elliott RP, Shunk FA (1981) The Al-Nb (aluminum-niobium) system. Bull Alloy Phase Diagrams 2:75–81

142. Baron VV, Savitskii EM (1961) Structure and properties of niobium-aluminium alloys. Russ J Inorg Chem 6(1):90–92
143. Lundin CE, Yamamoto AS (1966) The equilibrium phase diagram niobium (columbium) – aluminium. Trans AIME 236(6):863–872
144. Jorda JL, Flükiger R, Müller J (1980) A new metallurgical investigation of the niobium-aluminium system. J Less-Common Met 75(2):227–239
145. Oden LL, Siemens RF (1968) Phase relations in the niobium-gallium system. J Less-Common Met 14(1):33–40
146. Feschotte P, Spitz EL (1974) Le systeme binaire niobium-gallium (The niobium-gallium binary system). J Less-Common Met 37(2):233–246 (in French)
147. Ashby DA, Rawlings RD (1976) The Nb-rich part of the Nb – Ga phase diagram. J Less-Common Met 50(1):111–124
148. Jorda JL, Flükiger R, Müller J (1977) On the formation and stability of the A15 phase in the niobium-gallium system. J Less-Common Met 55(2):249–264
149. Leger J-M, Hall HT (1973) Pressure and temperature formation of A_3B compounds. I. Nb_3Si and V_3Al. J Less-Common Met 32(2):181–187
150. Kaufman L (1979) Coupled phase diagrams and thermochemical data for transition metal binary systems – VI. Calphad 3(1):45–76
151. Kocherzhinskii YuA, Yupko LM, Shishkin EA (1980) Diagramma ravnovesiya sistemy Nb-Si (Equilibrium diagram of the Nb-Si system). Izv AN SSSR Metally (1):206–211 (in Russian)
152. Moser Z (1992) The Nb-Zn (niobium-zinc) system. J Phase Equilibria 13(4):425–429
153. Kloska M, Haase EL (1984) On the existence of the hexagonal Nb_3Ge_2 phase. J Less-Common Met 99(2):241–248
154. Jorda JL, Flükiger R, Müller J (1978) The phase diagram of the niobium-germanium system. J Less-Common Met 62:25–37
155. Carpenter JH (1963) The composition range, decomposition pressure and thermodynamic stability of Nb_3Ge. J Phys Chem 67(10):2141–2144
156. Ellis TG, Wilhelm HA (1964) Phase equilibria and crystallography for the niobium-tin system. J Less-Common Met 7(1):67–83
157. Charlesworth JP, MacPhail J, Madsen PE (1970) Experimental work on the niobium-tin constitution diagram and related studies. J Mater Sci 5(7):580–603
158. Kogan VS, Krivko AI, Lazarev BG, Lazareva LS, Matsako AA, Ovcharenko ON (1963) Constitution diagram of the system Nb-Sn. Phys Met Metallogr 15(1):132–134
159. Leger J-M, Hall HT (1974) Pressure and temperature formation of A_3B compounds. II. Nb_3Ge, Nb_3Sn, Nb_3Pb, V-In and V-Pb. J Less-Common Met 34(1):17–24
160. Gebhardt E, Dürrschnabel W, Hörz G (1966) Untersuchungen im System Niob-Stickstoff: I. Eigenschaftsänderungen von Niob durch gelösten Stickstoff (Investigations in the niobium-nitrogen system: I. Changes in the properties of niobium by dissolved nitrogen). J Nucl Mater 18(2):119–133 (in German)
161. Taylor A, Doyle NJ (1967) The solid solubility of nitrogen in Nb and Nb-rich Nb-Hf, Nb-Mo and Nb-W alloys: Part I: The binary system Nb-N. J Less-Common Met 13(4):399–412
162. Terao N (1971) New phases of niobium nitride. J Less-Common Met 23(2):159–169
163. Gusev AI, Ivanov NA, Shveikin GP, Geld PV (1976) Some properties of solutions of the systems $ZrC_{0.97}$-$NbN_{0.93}$ and $Zr_{0.5}Nb_{0.5}C_xN_{0.98-x}$. Inorg Mater 12:1149–1153
164. Gebhardt E, Fromm E, Jakob D (1964) Gleichgewichtsuntersuchungen im System Niob-Stickstoff (Equilibrium studies in the system niobium-nitrogen). Z Metallkd 55:423–431 (in German)
165. Levinskii YuV (1975) Diagrammy sostoyaniya metallov s gazami (The constitution diagrams of metals with gases). Metallurgiya, Moscow (in Russian)
166. Furuseth S, Kjekshus A (1964) On the preparation of niobium arsenides and antimonides. J Less-Common Met 7(3):227–230

167. Carlsson B, Rundqvist S (1971) The crystal structure of Nb_4As_3. Acta Chem Scand 25(5):1742–1752
168. Laohavanich S, Thanomkul S, Pramatus S (1981) Structure refinement of niobium arsenide Nb_5As_3. Acta Crystallogr B 37(1):227–228
169. Furuseth S, Kjekshus A (1964) On the arsenides and antimonides of niobium. Acta Chem Scand 18:1180–1195
170. Myzenkova LF, Baron VV, Savitskii EM (1966) Constitution diagram of the niobium-antimony system. Russ Metall (2):89–91
171. Cava RJ, Batlogg B, Krajewski JJ, Poulsen HF, Gammel P, Peck WF, Jr, Rupp LW, Jr (1991) Electrical and magnetic properties of $Nb_2O_{5-\delta}$ crystallographic shear structures. Phys Rev B 44(13):6973–6981
172. Moiseev GK, Vatolin NA (1978) Sostav faz, obrazuyushchikhsya pri ravnovesnom nagrevanii okislov niobiya (Composition of the phases forming during equilibrium heating of niobium oxides). Izv AN SSSR Neorg Mater 14(8):1462–1467 (in Russian)
173. Inaba H, Mima T, Naito K (1984) Measurement of enthalpies of formation of niobium oxides at 920 K in a Tian-Calvet-type calorimeter. J Chem Thermodyn 16(5):411–418
174. Matsui T, Naito K (1981) Vaporization study on nonstoichiometric $NbO_{2\pm x}$ by mass-spectrometric method. J Nucl Mater 102(3):227–234
175. Marucco JF, Tetot R, Gerdanian P, Picard (1976) Etude thermodynamique du dioxide de Niobium à haute temperature (Thermodynamic study of niobium dioxide at high temperature). J Solid State Chem 18(2):97–110 (in French)
176. Janninck RF, Whitmore DH (1966) Electrical conductivity and thermoelectric power of niobium dioxide. J Phys Chem Solids 27(6–7):1183–1187
177. Klechkovskaya VV (1970) Oxidation of thin niobium films at low temperatures. Phys Crystallogr 15:299–301
178. Gebhardt E, Rothenbacher R (1963) Untersuchungen im System Niob-Sauerstoff. II. Lösung von Sauerstoff in Niob und Ausscheidungen von Oxiden aus übersättigten Mischkristallen (Investigations in the system niobium-oxygen. II. Solution of oxygen in oxides of niobium and excretions from supersaturated solid solutions). Z Metallkd 54:623–630 (in German)
179. Naito K, Kamegashira N, Sasaki N (1980) Phase equilibria in the system between NbO_2 and Nb_2O_5 at high temperatures. J Solid State Chem 35(3):305–311
180. Kimura S (1973) Phase equilibria in the system NbO_2-Nb_2O_5: Phase relations at 1300 and 1400 °C and related thermodynamic treatment. J Solid State Chem 6(3):438–449
181. Marucco JF (1974) Thermodynamic study of the system NbO_2-Nb_2O_5 at high temperatures. J Solid State Chem 10(3):211–218
182. Altstetter CJ (1984) Metal-oxygen systems. Bull Alloy Phase Diagrams 5(6):543–553
183. Yamaguchi O, Tomihisa DO, Shirai M, Shimizu K (1988) Formation and transformation of solid solutions in the system Nb_2O_5-Ta_2O_5. J Am Ceram Soc 71:C260-C262
184. Zakharova GV, Popov IA, Zhorova LP, Fedin BV (1961) Niobii i ego splavy (Niobium and its alloys). Metallurgizdat, Moscow (in Russian)
185. Mishchenko AV, Yushina IV, Fedorov VE (1988) Phase equilibria in niobium-sulphur and niobium-tellurium systems. Russ J Inorg Chem 33:244–247
186. Selte K, Bjerkelund E, Kjekshus A (1966) Intermediate phases in the systems niobium-selenium, niobium-tellurium, tantalum-selenium and tantalum-tellurium. J Less-Common Met 11(1):14–30
187. Meerschant A, Rouxel J (1975) Le seleniure $NbSe_3$: Obtention et structure (Selenide $NbSe_3$: Obtaining and structure). J Less-Common Met 39(2):197–204 (in French)
188. Meerschaut A, Guemas L, Berger R, Rouxel J (1979) The crystal structure of niobium selenide Nb_2Se_9 from twin-crystal data. Acta Crystallogr B 35(8):1747–1750
189. Fedorov VE, Mishchenko AV, Ustimenko YuB (1984) Interaction in the Nb-Se system. Inorg Mater 20(7):935–939
190. Smith DI, Mochel AR, Banewicz JJ, Maguire JA (1972) A phase study of the niobium-tellurium system in the composition range from Nb_3Te_7 to Te. J Less-Common Met 26(1):139–144

191. Fairbrother F (1967) The chemistry of niobium and tantalum. Elsevier, New York
192. Voroshilov YuV, Kuzma YuB (1967) Phase equilibria in the ternary systems zirconium-vanadium-boron, zirconium-niobium-boron and zirconium-manganese-boron. Powder Metall Met Ceram 6(6):466–469
193. Horyn R (1976) The niobium-aluminium-iridium ternary system. Part I. Phase equilibria at 1100 °C and superconductivity of alloys. J Less-Common Met 44:221–227
194. Drys M (1977) The niobium-gallium-iridium ternary system. I. Phase equilibria at 1000 °C and superconductivity in the niobium-rich part of the system. J Less-Common Met 52:81–85
195. Stepanenko EK, Dogadaeva IM, Ordanyan SS (1982) Reactions in the NbC-$NbSi_2$ and NbB_2-$NbSi_2$ systems. Powder Metall Met Ceram 21(7):568–570
196. Chaban (1984) Ternary systems Gd – (V, Nb) – B. Powder Metall Met Ceram 23(10):796–797
197. Yamanaka S, Shimizu J, Miyake M (1993) Thermodynamic study of the compatibility of oxide fuel with metals. J Nucl Mater 201:27–34
198. Pitman SH, Tsakiropoulos P (1995) Study of the microstructure and oxidation of $NbSi_2$ base alloys. Proc Mater Res Soc Symp 364(2):1321–1326
199. Bewlay BP, Jackson MR, Lipsitt HA (1997) The Nb-Ti-Si ternary phase diagram: evaluation of liquid-solid phase equilibria in Nb- and Ti-rich alloys. J Phase Equilib 18(3):264–278
200. Vilasi M, Francois M, Brequel H, Podor R, Venturini G, Steinmetz J (1998) Phase equilibria in the Nb-Fe-Cr-Si system. J Alloys Compd 269(1–2):187–192
201. Horyn R (1976) The niobium-aluminium-iridium ternary system. Part II. X-ray study of the intermediate phases and phase equilibria at 1100 °C. J Less-Common Met 45:315–321
202. Horyn R (1976) The crystal structure of the "A(NbAlIr)" phase. J Less-Common Met 50:7–14
203. Horyn R (1977) Crystal structure of the A′(NbAlIr) phase. J Less-Common Met 56:103–111
204. Drys M (1978) The niobium-gallium-iridium ternary system. II. Phase equilibria at 1000 °C and crystallographic data for ternary intermediate phases. J Less-Common Met 58:173–177
205. Horyn R, Folcik-Kokot L, Iliev N (1978) On superconductivity of in the Nb-Ir-O system. J Less-Common Met 57:P69-P74
206. Horyn R, Folcik-Kokot L (1978) Crystal structure of the H(NbIrO) phase. J Less-Common Met 57:P75-P78
207. Johnson WL, Poon SJ (1975) Superconductivity of new metastable phases of niobium-iridium, tantalum-iridium and tantalum-rhodium. J Less-Common Met 42(3):355–358
208. Bewlay BP, Bishop RR, Jackson MR (1999) Nb-Hf-Si ternary phase diagram: liquid-solid phase equilibria in Nb- and Hf-rich alloys. Z Metallkd 90(6):413–422
209. Liang H, Chang YA (1999) Thermodynamic modelling of the Nb-Si-Ti ternary system. Intermetallics 7:561–570
210. Subramanian PR, Mendiratta MG, Dimiduk DM (1994) High temperature silicides and refractory alloys. Proc Mater Res Soc Symp 322:491–502
211. Agadzhanyan NN, Akopyan AG, Beibutyan VM, Ter-Galstyan OP, Dolukhanyan SK, Shekhtman VSh (1999) Complex hydrides and hydronitrides of transition metals prepared by SHS II. Systems involving group V metals and nitrogen (Ti – V – N – H, Ti – Nb – N – H, Zr – Nb – N – H). Powder Metall Met Ceram 38(3–4):176–178
212. Villars P, Prince A, Okamoto H, eds (1995) Handbook of ternary alloy phase diagrams,. Vol. 7. ASM International, Metals Park, Ohio
213. Murakami T, Sasaki S, Ichikawa K, Kitahara A (2001) Oxidation resistance of powder compacts of the Nb-Si-Cr system and $Nb_3Si_5Al_2$ matrix compacts prepared by spark plasma sintering. Intermetallics 9:629–635
214. Zhao J-C, Bewlay BP, Jackson MR (2001) Determination of Nb-Hf-Si phase equilibria. Intermetallics 9:681–689
215. Zhao J-C, Bewlay BP, Jackson MR, Peluso LA (2001) Alloying and phase stability in niobium silicide in-situ composites. In: Hemker KJ, Dimiduk DM, Clemens H, Darolia R

(eds) Proc. Int. symp. on structural intermetallics, pp. 483–491. TMS, Jackson Hole, Wyoming
216. Murakami T, Sasaki S, Ichikawa K, Kitahara A (2001) Microstructure, mechanical properties and oxidation behavior of Nb-Si-Al and Nb-Si-N powder compacts prepared by spark plasma sintering. Intermetallics 9:621–627
217. Mestres L, Martinez-Sarrion ML, Castano O, Fernandez-Urban J (2001) Phase diagram at low temperature of the system ZrO_2/Nb_2O_5. Z Anorg Allgem Chem 627:294–298
218. Allpress JG, Roth RS (1970) Structural studies by electron microscopy: polymorphism of $ZrO_2{\cdot}12Nb_2O_5$. J Solid State Chem 2(3):366–376
219. Wang R-C, Liu C-L, Jin Z-P (2002) Transformations and phase relations in Nb-Ti-Si ternary system at 1373–1473 K. Trans Nonferrous Metal Soc China 12(3):383–387
220. Bewlay BP, Jackson MR, Lipsitt HA (1997) The Nb-Ti-Si ternary phase diagram: evaluation of liquid-solid phase equilibria in Nb- and Ti-rich alloys. J Phase Equilib 18(3):264–278
221. Bewlay BP, Jackson MR, Bishop RR (1998) The Nb-Ti-Si ternary phase diagram: determination of solid-state phase equilibria in Nb- and Ti-rich alloys. J Phase Equilib 19(6):577–586
222. Yu X, Yamabe-Mitarai Y, Ro Y, Harada H (2000) New developed quaternary refractory superalloys. Intermetallics 8:619–622
223. Huang C, Yamabe-Mitarai Y, Nishida K, Harada H (2003) Phase constituents of Ir-Nb-Pt-Al quaternary alloys. Intermetallics 11:917–926
224. Yamabe-Mitarai Y, Harada H (2003) Face centered cubic and $L1_2$ two-phase structure of Ir-Nb-Zr alloys. J Alloys Compd 361(1–2):169–179
225. Yamabe-Mitarai Y, Yamamoto Y., Nishida K, Harada H (2004) Analysis of Ir-base alloys. J Mater Sci 39:299–301
226. Katrych S, Grytsiv A, Bondar A, Rogl P, Velikanova T, Bohn M (2004) Structural materials: metal-silicon-boron. The Nb-rich corner of the Nb-Si-B system. J Solid State Chem 177:493–497
227. Zhao J-C, Jackson MR, Peluso LA (2004) Mapping of the Nb-Ti-Si phase diagram using diffusion multiples. Mater Sci Eng A 372:21–27
228. Shao G (2005) Thermodynamic modelling of the Cr-Nb-Si system. Intermetallics 13:69–78
229. Semenova OL, Meleshevich KA, Petyukh VM, Saltikov SA, Samelyuk AV, Firstov SO (2005) Phase equilibria in the titanium corner of hypoeutectic alloys in the Ti-Nb-Si-Al system. Powder Metall Met Ceram 44(11–12):557–566
230. Geng J, Shao G, Tsakiropoulos P (2006) Study of three-phase equilibrium in the Nb-rich corner of Nb-Si-Cr system. Intermetallics 14:832–837
231. Perez RJ, Massih AR (2007) Thermodynamic evaluation of the Nb-O-Zr system. J Nucl Mater 360:242–254
232. Borisov DB, Artyukh LV, Bondar AA, Martsenyuk PS, Samelyuk AV, Tsiganenko NI, Fomichev OS, Velikanova TYa Titanium-boride eutectic materials. Structure of the Ti-Nb-B alloys and phase equilibria. Powder Metall Met Ceram 46(1–2):58–71
233. Ma X, Li C, Du Z, Zhang W (2004) Thermodynamic assessment of the Ti-B system. J Alloys Compd 370(1–2):149–158
234. Nakama Y, Ohtani H, Hasebe M (2009) Thermodynamic analysis of the Nb-Ti-B ternary phase diagram. Mater Trans 50(5):984–993
235. Kuzma YuB, Tsolkovskii TI, Baburova OP (1968) The systems Nb-Fe-B and Nb-Co-B. Inorg Mater 4(7):950–953
236. Yoshitomi K, Nakama Y, Ohtani H, Hasebe M (2008) Thermodynamic analysis of the Fe-Nb-B ternary system. ISIJ Int 48(6):835–844
237. Witusiewicz VT, Bondar AA, Hecht U, Rex S, Velikanova TYa (2008) The Al-B-Nb-Ti system. I. Re-assessment of the constituent binary systems B-Nb and B-Ti on the basis of new experimental data. J Alloys Compd 448(1–2):185–194

238. Witusiewicz VT, Bondar AA, Hecht U, Rex S, Velikanova TYa (2008) The Al-B-Nb-Ti system. II. Thermodynamic description of the constituent ternary system B-Nb-Ti. J Alloys Compd 456(1–2):143–150
239. Bao J, Huang Q, Tang L, Geng T, Zhao X, Ma C (2008) Liquid-solid phase equilibria of Nb-Si-Ti ternary alloys. Chin J Aeronautics 21:275–280
240. Bewlay BP, Yang Y, Casey RL, Jackson MR, Chang YA (2009) Experimental study of the liquid-solid phase equilibria at the metal-rich region of the Nb-Cr-Si system. Intermetallics 17:120–127
241. Geng T, Li C, Bao J, Zhao X, Du Z, Guo C (2009) Thermodynamic assessment of the Nb-Si-Ti system. Intermetallics 17:343–357
242. Zhan Y, Sun Z, Jiang J, Ma J, Zhang X, Zhuang Y (2009) The 773 isothermal section of the ternary phase diagram of the Nb-Ti-Si system. J Alloys Compd 468(1–2):150–153
243. Nowotny H, Benesovsky F, Rudy E, Wittman A (1960) Aufbau und Zunderverhalten von Niob-Bor-Silicium Legierungen (Constitution and oxidation resistance of the niobium-boron-silicon alloys). Monatsh Chem 91(5):975–990 (in German)
244. Sun Z, Yang Y, Guo X, Zhang C, Chang YA (2011) Thermodynamic modelling of the Nb-rich corner in the Nb-Si-B system. Intermetallics 19:26–34
245. Rogl P, Klesnar HP, Fischer P, Chevalier B, Buffat B, Demazeau G, Etourneau J (1988) Structural chemistry and phase equilibria in the ternary system niobium-boron-nitrogen. J Mater Sci Lett 7(11):1229–1230
246. Gruehn R, Schäfer H (1966) Oxidische Nb- und Ta-Verbindungen mit O/Me = 2.33 – 2.50 (Nb and Ta oxide compounds with O/Me = 2.33 – 2.50). J Less-Common Met 10(2): 152–154 (in German)
247. Abbattista FA, Rolando P, Grassi GB (1970) On system MgO-Nb_2O_5. Ann Chim (Rome) 60(6):426–435
248. Abbattista FA, Rolando P (1972) A study of the Nb2O5-NbO-MgO system at 1100–1250 °C. Ceramica (Florence) 25(5–6):38–44
249. Pagola S, Carbonio RE, Alonso JA, Fernandez-Diaz MT (1997) Crystal structure refinement of $MgNb_2O_6$ columbite from neutron powder diffraction data and study of the ternary system MgO – Nb_2O_5 – NbO with evidence of formation of new reduced pseudobrookite $Mg_{5-x}Nb_{4+x}O_{15-\delta}$ ($1.14 \leq x \leq 1.60$) phases. J Solid State Chem 134(1):76–84
250. Labeau M, Grey IE, Joubert JC, Chenavas J, Collomb A, Guitel JC (1985) The structure of the A-cation-deficient perovskite UNb_4O_{12}. Acta Crystallogr B 41:33–41
251. Kovba LM, Sirotinkin S, Trunov VK (1965) Investigation of some double oxides of uranium. Russ J Inorg Chem 10:188–189
252. Thompson JG, Withers RL, Sellar J, Barlow PJ, Hyde BG (1990) Incommensurate composite modulated $Nb_2Zr_{x-2}O_{2x+1}$: x = 7.1–10.3. J Solid State Chem 88:465–475
253. Roth RS, Waring JL, Brower WS, Parker HS (1972) Superstructure of the orthorhombic Nb_2O_5•$6ZrO_2$ type phases in the Nb_2O_5 – ZrO_2 and Ta_2O_5 – ZrO_2 systems. In: Roth RS, Schneider SJ (eds) Proc. 5th materials research symp. on solid state chemistry, National Bureau of Standards, Gaithersburg, Maryland, October 18–21, 1971, pp. 183–195. US Department of Commerce, Washington, DC
254. Galy J, Roth RS (1973) The crystal structure of $Nb_2Zr_6O_{17}$. J Solid State Chem 7(3):277–285
255. Marcotte VC, Larsen WL (1966) Phase studies of high-niobium-content Nb-Zr-O alloys. J Less-Common Met 10(4):229–300
256. Hunt CEL, Niessen P (1970) The effect of oxygen on the equilibrium $\beta/\alpha+\beta$ transformation temperature of zirconium-niobium alloys. J Nucl Mater 35(10:134–136
257. Magunov RL, Sotulo VS, Magunov IR (1993) Fazovye sootnosheniya v sistemakh ZrO_2 (HfO_2) – Nb_2O_5 (The phase relations in the ZrO_2 (HfO_2) – Nb_2O_5 systems). Zh Neorg Khim 38(2):363–365 (in Russian)
258. Gopalakrishnan R, Viswanathan B, Ramakrishnan V, Kuriacose JC (1987) Photoelectrochemical properties of $Zr_xTi_{1-x}Nb_2O_7$ mixed oxides. Mater Chem Phys 10(1–2):171–179

259. Trunov VK, Vladimirova ZA, Kovba LM, Komissarova LN (1965) X-ray of the double oxides of zirconium and niobium. Inorg Mater 1:1760–1762
260. Klimenko AN, Lonov VM, Tomilin NA, Sergeev VS, Sirotinkin VP, Prozorovskii AE, Rybakov VB, Zhukov SG (1990) Phase transitions in the lanthanide niobates R_3NbO_7 at high temperatures. Russ J Inorg Chem 35:338–341
261. Bazuev GV, Shveikin GP (1973) Interaction in the yttrium-niobium-oxygen system. Russ J Inorg Chem 18:1021–1024
262. Lee JH, Yashima M, Kakihana M, Yoshimura M (1998) Phase diagram and oxygen-ion conductivity in the Y_2O_3-Nb_2O_5 system. J Am Ceram Soc 81(4):894–900
263. Zhang MX, Chang YA (1994) Phase diagrams of Ti-Al-C, Ti-Y-O, Nb-Y-O and Nb-Al-O at 1100 °C. J Phase Equilibria 15(5):470–472
264. Allpress JG, Rossell HJ (1979) Fluorite-related phases Ln_3MO_7, Ln = rare earth, Y, or Sc, M = Nb, Sb, or Ta. I. Crystal chemistry. J Solid State Chem 27(1):105–114
265. Barker WW (1984) The systems Y_2O_3-Nb_2O_5 and Ho_2O_3-Nb_2O_5: the cubic solid-solution region. J Mater Sci Lett 3(6):492–494
266. Taylor A, Doyle NJ (1967) The solid solubility of oxygen in Nb and Nb-rich Nb-Hf, Nb-Mo and Nb-W alloys: Part I: The Nb-O system. J Less-Common Met 13(3):313–330
267. Ibrahim M, Bright NFH, Rowland JF (1962) The binary system CaO-Nb_2O_5. J Am Ceram Soc 45(7):329–334
268. Jongejan A (1969) Phase relationships in the high-lime part of the system CaO-Nb_2O_5. J Less-Common Met 19(3):185–191
269. Dneprova VG, Rezukhina TN, Gerasimov YaI (1968) Termodinamicheskie svoistva nekotorykh niobatov kaltsiya (The thermodynamic properties of certain calcium niobates). Doklady AN SSSR 178(1):135–137 (in Russian)
270. Brixner LH, Babcock K (1968) Inorganic single crystals from reactions in fused salts. Mater Res Bull 3(10):817–824
271. Vanderah TA, Febo W, Chan JY, Roth RS, Loezos JM, Rotter LD, Geyer RG, Minor DB (2000) Phase equilibria and dielectric behaviour in the CaO:Al_2O_3:Nb_2O_5 system. J Solid State Chem 155(1):78–85
272. Levin I, Bendersky LA, Cline JP, Roth RS, Vanderah TA (2000) Octahedral tilting and cation ordering in perovskite-like $Ca_4Nb_2O_9$ = 3·$Ca(Ca_{1/3}Nb_{2/3})O_3$ polymorphs. J Solid State Chem 150(1):43–61
273. Levin I, Chan JY, Geyer RG, Maslar JE, Vanderah TA (2001) Cation ordering types and dielectric properties in the complex perovskite $Ca(Ca_{1/3}Nb_{2/3})O_3$. J Solid State Chem 156(1):122–134
274. Bendersky LA, Levin I, Roth RS, Shapiro AJ (2001) $Ca_4Nb_2O_9$ – $CaTiO_3$: phase equilibria and microstructures. J Solid State Chem 160(1):257–271
275. Hervieu M, Studer F, Raveau B (1977) Oxydes de type perovskite du systeme Ca – Nb – O (Perovskite-type oxides of the system Ca – Nb – O). J Solid State Chem 22(3):273–289 (in French)
276. Negas T, Roth RS, McDaniel CL, Parker HS, Olson CD (1977) Oxidation-reduction reactions of $CeMO_{4+x}$ (M = Ta or Nb) phases. Mater Res Bull 12(12):1161–1171
277. Roth RS, Negas T, Parker HS, Minor DB, Jones C (1977) Crystal chemistry of cerium titanates, tantalates and niobates. Mater Res Bull 12(12):1173–1182
278. Keller C (1965) Die Reaktion der Dioxide der Elemente Thorium bis Americium mit Niob- und Tantalpentoxid (The reaction of the dioxides of the elements thorium to americium with niobium and tantalum pentoxide). J Inorg Nucl Chem 27(6):1233–1246 (in German)
279. Cava RJ, Roth RS, Minor DB (1981) Revised ThO_2 – Nb_2O_5 phase diagram. J Am Ceram Soc 64(4):C64-C65
280. Mueller A (1971) Supraleitung in der A15-Phase in der Nb-Al-Si System (Superconductivity in the A15 phase in the Nb-Al-Si system). Z Naturforsch A 26:1035–1039 (in German)
281. Allibert C, Wicker A, Driole J, Bonnier E (1973) Étude du systeme niobium-aluminium-silicium. I. Sections isothermes partielles à 1500 et 1300 °C et comportement de la phase

$Nb(Si,Al)_2$ (Study of the system niobium-aluminium-silicon. I. Partial isothermal sections at 1500 and 1300 °C and behaviour of the phase $Nb(Si,Al)_2$). J Less-Common Met 31(2):221–228 (in French)
282. Pan VM, Latysheva VI, Kulik OG, Popov AG, Litvinenko EN (1983) Fazovaya diagramma Nb-$NbAl_3$-Nb_5Si_3 (The Nb-$NbAl_3$-Nb_5Si_3 phase diagram). Izv AN SSSR Metally (4):225–226 (in Russian)
283. Baetzner C, Beuers J, Hoch M, Kornienko K (2009) Aluminium – niobium – silicon system. In: Effenberg G, Ilyenko S (eds) Ternary alloy systems, Subvol. E, Part 1, pp. 193–208. Springer, Berlin, Heidelberg
284. Rogl P (2008) Boron – iron – niobium system. In: Effenberg G, Ilyenko S (eds) Ternary alloy systems, Subvol. D, Part 1, pp. 379–387, Springer, Berlin, Heidelberg
285. Eckert TE (1966) Ti-Zr-B system. Investigation of pseudo-binary systems ZrB_2-NbB_2, ZrB_2-TaB_2 and HfB_2-NbB_2. In: Ternary phase equilibria in transition metal-boron-carbon-silicon systems. Report AFML-TR-65–2, Contract USAF 33(615)-1249, Part 2, Vol. 12, pp. 1–47. Air Force Materials Laboratory, Wright-Patterson Air Force Base, Ohio
286. Nowotny H (1963) Alloy chemistry of transition element borides, carbides, nitrides, aluminides and silicides. In: Beck PA (ed) Electronic structure and alloy chemistry of the transition elements, pp. 179–220, Interscience, New York
287. Candioto KCG, Nunes CA, Coelho GC, Suzuki PA (2001) Microstructural characterization of Nb-B-Si alloys with composition in the Nb-Nb_5Si_2B (T_2-phase) vertical section. Mater Charact 47:241–245
288. Nunes CA, Kaczorowski D, Rogl P, Baldissera MR, Suzuki PA, Coelho GC, Grystiv A, Andre G, Bouree F, Okada S (2005) The NbB_2-phase revisited: homogeneity range, defect structure, superconductivity. Acta Mater 53:3679–3687
289. Kornienko K, Rogl P, Velikanova T (2010) Boron – niobium – silicon system. In: Effenberg G, Ilyenko S (eds) Ternary alloy systems, Subvol. E, Part 2, pp. 91–108, Springer, Berlin, Heidelberg
290. Bondar A (2010) Boron – niobium – titanium system. In: Effenberg G, Ilyenko S (eds) Ternary alloy systems, Subvol. E, Part 2, pp. 109–126, Springer, Berlin, Heidelberg
291. Borisova AL, Kuzma YuB, Petrova EM, Sleptsov VM, Chaban NF (1979) Reaction of niobium with zirconium diboride. Powder Metall Met Ceram 18(8):555–559
292. Bovkun GA, Petrova EM, Sleptsov VM, Tkachenko YuG (1980) Wear resistance of sintered alloys of niobium and zirconium diboride. Powder Metall Met Ceram 19(2):138–141
293. Verkhoturov AD, Bovkun GA, Petrova EM, Kirilenko SN, Sleptsov VM (1980) Electric-spark alloying of steel with alloys of the Nb-Zr-B system. Powder Metall Met Ceram 19(3):173–176
294. Serbruyns A, Lebrun N, Perrot P, Tedenac J-C (2010) Boron – niobium – zirconium system. In: Effenberg G, Ilyenko S (eds) Ternary alloy systems, Subvol. E, Part 2, pp. 127–132, Springer, Berlin, Heidelberg
295. Cornish L, Cupid DM, Grobner J, Malfliet A (2010) Chromium – niobium – silicon system. In: Effenberg G, Ilyenko S (eds) Ternary alloy systems, Subvol. E, Part 3, pp. 210–221, Springer, Berlin, Heidelberg
296. Singh BN, Gupta KP (1972) Laves and μ phases in the Nb-Fe-Si and Nb-Co-Si systems. Metall Trans 3:1427–1431
297. Malaman B, Steinmetz J, Venturini G, Roques B (1982) Structure crystalline de la phase $Nb_4Fe_{\sim 3}Si_{\sim 5}$-$\beta$ et diagramme d'equilibre du systeme Nb-Fe-Si (Crystal structure of the phase $Nb_4Fe_{\sim 3}Si_{\sim 5}$-$\beta$ and a diagram of the Nb-Fe-Si system). J Less-Common Met 87(1):31–43 (in French)
298. Tretyachenko L (2009) Iron – niobium – silicon system. In: Effenberg G, Ilyenko S (eds) Ternary alloy systems, Subvol. D, Part 5, pp. 55–68, Springer, Berlin, Heidelberg
299. Bulanova M, Fartushna I (2010) Niobium – silicon – titanium system. In: Effenberg G, Ilyenko S (eds) Ternary alloy systems, Subvol. E, Part 3, pp. 505–522, Springer, Berlin, Heidelberg

300. Le Bihan T, Rogl P, Noel H (2000) The niobium – silicon – uranium system. J Nucl Mater 277:82–90
301. Rogl P, Noel H (2007) Niobium – silicon – uranium system. In: Effenberg G, Ilyenko S (eds) Ternary alloy systems, Subvol. C, Part 4, pp. 374–379, Springer, Berlin, Heidelberg
302. Barabash OM, Kozyrskii GYa, Sulzhenko VP, Shurin AK (1976) Structure and strength of Nb-Zr-N alloys. Rus Metall (3):166–169
303. Schlesinger ME, Okamoto H, Gokhale AB, Abbaschian R (1993) The Nb-Si (niobium-silicon) system. J Phase Equilibria 14(4):502–509
304. Smith JF (1983) The H-Nb (hydrogen-niobium) and D-Nb (deuterium-niobium) systems. Bull Alloy Phase Diagrams 4:39–46
305. Kuji T, Oates WA (1984) Thermodynamic properties of Nb-H alloys. III: Calculation of part of the phase diagram. J Less-Common Met 102:273–279
306. Smith JF, Lee KJ (1988) The K-V (potassium-vanadium) and K-Nb (potassium-niobium) systems. Bull Alloy Phase Diagrams 9(4):469–474
307. Savitskii EM. Efimov YV, Kozlova ND, Zvolinskii OI (1973) Vliyanie redkozemelnykh metallov na sverkhprovodimost vanadiya, niobiya i tantala (The influence of rare-earth metals on superconductivity of vanadium, niobium and tantalum). Dokl Akad Nauk SSSR 213:826–829 (in Russian)
308. Savitskii EM, Terekhova VF, Torchinova RS, Markova IA, Naumkin OP, Kolesnichenko VE, Stroganova VF (1970) Etudes des proprietes physiques et chimiques d'alliages de terres rares (Studies of physical and chemical properties of rare earth alloys). Colloq Int CNRS 180(1):47–60 (in French)
309. Markova IA, Terekhova VF, Savitskii EM (1964) Ittrii i perspektivy ego primeneniya (Yttrium and perspectives of its application). In: Savitskii EM (ed) Voprosy teorii i primeneniya redkozemelnykh metallov. Materialy Vsesoyuznogo soveshchaniya. (The items of theory and application of rare-earth metals. Proc. All-Union meeting), pp 124–128. Nauka, Moscow (in Russian)
310. Okamoto H (1994) The La-Nb (lanthanum-niobium) system. J Phase Equilib 15:202–203
311. Savitskii EM (1960) Redkie metally v zharoprochnykh splavakh (Rare metals in refractory alloys). Izv Akad Nauk SSSR Otd Tekh Nauk Metall Topl (5):52–69 (in Russian)
312. Okamoto H (1992) The Nb-Sm (niobium-samarium) system. J Phase Equilib 13:334–335
313. Okamoto H (1999) The Lu-Nb (lutetium-niobium) system. J Phase Equilib 20:94
314. Kassner ME (1994) The Nb-Th (niobium-thorium) system. J Phase Equilib 15(5):561–563
315. Kassner ME, Adamson MG (1994) The Nb-Pu (niobium-plutonium) system. J Phase Equilib 15(5):558–560
316. Schonfeld FW, Cramer EM, Miner WN, Ellinger FH, Coffinberry AS (1959) Plutonium constitutional diagrams. Prog Nucl Energy Ser 5 2:579–599
317. Svechnikov VN, Petkov VV (1976) Obrazovanie faz Lavesa v splavakh margantsa s perekhodnymi metallami IVA-VA grupp (Formation of laves phases in alloys of manganese with transition metals of the groups IVA-VA). Metallofizika (Akad Nauk Ukr SSR Inst Metallofiz) 64:24–27 (in Russian)
318. Okamoto H (1991) The Cu-Nb (copper-niobium) system. J Phase Equilib 12:614–615
319. Hämäläinen M, Jääskeläinen K, Luoma R, Nuotio M, Taskinen P, Teppo O (1990) A thermodynamic analysis of the binary alloy systems Cu-Cr, Cu-Nb and Cu-V. Calphad 14:125–137
320. Allibert CH, Wicker A, Driole J, Bonnier E (1970) Determination de diagrammes de phases a haute temperature dans les systemesde metaux refractaires (Determination of phase diagrams at high temperature in the systems of refractory metals). Rev Int Hautes Temp Refract 7:45–50 (in French)
321. Baren MR (1989) The Ag-Nb (silver-niobium) system. Bull Alloy Phase Diagrams 10(6):640
322. Holleck H (1966) Die Phase $NbCd_3$ (Phase $NbCd_3$). Acta Crystallogr 21(3):451 (in German)
323. Guminski C (1993) The Hg-Nb (mercury-niobium) system. J Phase Equilibria 14(3):388–390

324. Kammerdiner L, Luo HL (1974) Preparation of new β-W phases by film-deposition techniques. J Appl Phys 45:4590–4593
325. Feschotte P, Polikar A, Burri G (1979) Equilibres de phases dans les systèmes binaires Nb-Ge et Nb-Sn (Phase equilibria in binary systems Nb-Ge and Nb-Sn). C R Seances Acad Sci Ser C 288:125–128 (in French)
326. Kistaiah P (1991) Thermal expansion of Nb_xGe (x = 3,4,5) intermetallics. Phys Status Solidi A 127:K5–K8
327. Lomnytska YF, Koval LS (1996) Interaction of niobium (tantalum) with silicon and phosphorus. Russ J Inorg Chem 41:1828–1830
328. Melnyk GA, Rogl P, Skolozdra RV, Maccio D, Saccone A, Ferro R (1999) The antimony-niobium (Sb-Nb) system. J Phase Equilib 20(5):475–478
329. Seabaugh PW, Corbett JD (1965) The niobium iodides. Characterization of niobium(IV) iodide, niobium(III) iodide and triniobium octaiodide. Inorg Chem 4:176–181
330. Rieger W, Nowotny H, Benesovsky F (1965) Über einige Komplexboride von Übergangsmetallen (Some complex borides of transition metals). Monatsh Chem 96:844–851 (in German)
331. Ran Q, Bätzner C (1990) The Al-B-Nb (aluminium-boron-niobium) system. Ternary Alloys VCH 3:194–197
332. Schuster JC, Nowotny H (1985) Phase equilibria in the ternary systems Nb-Al-N and Ta-Al-N. Z Metallkd 76:728–729
333. Kuznetsov V (1993) The Al-N-Nb (aluminium-nitrogen-niobium). Ternary Alloys VCH 7:275–278
334. Marko MA, Kuzma YuB, Gladyshevskii EI (1976) Rentgenograficheskoe issledovanie sistem Nb-Ge-B i Ta-Ge-B (The x-ray study of Nb-Ge-B and Ta-Ge-B systems). Dopov Akad Nauk Ukr RSR Ser A Fiz Mat Tekh Nauki 38:555–558 (in Russian)
335. Kuzma YuB, Telegus VS, Marko MA (1972) Phase equilibria in the systems hafnium-niobium-boron and tantalum-chromium-boron. Powder Metall Met Ceram 11:308–312
336. Zakharov AM, Pshokin VP (1985) Phase equilibria in the niobium corner of the Nb-Hf-B system. Russ Metall (6):195–198
337. Sobolev AS, Kuzma YB, Fedorov TF (1967) System niobium-nickel-boron. Inorg Mater 3:561–565
338. Schöbel JD, Stadelmaier HH (1964) Ein ternäres Borid mit Chromkarbid-($Cr_{23}C_6$)-Struktur und die Lage der Gleichgewichte in der Nickelecke des Dreistoffsystems Nickel-Niob-Bor (The boride with a ternary chromium carbide ($Cr_{23}C_6$) structure and the position of equilibrium in the field of the ternary system nickel-boron-niobium). Metall 18:1285–1287 (in German)
339. Lugscheider E, Reimann H, Pankert R (1982) Mit 4a- und 5a-Metallen stabilisierte tau-Boride des Nickel (Tau borides of nickel stabilized with 4a and 5a group metals). Metall 36:247–251 (in German)
340. Range KJ, Wildenauer M, Heyns AM (1988) Extrem kurze nichtbindende Sauerstoff-Sauerstoff-Abstände: Die Kristallstrukturen von $NbBO_4$, $NaNb_3O_8$ und $NaTa_3O_8$ (Extremely short non-bonded oxygen-oxygen distances: the crystal structures of $NbBO_4$, $NaNb_3O_8$ and $NaTa_3O_8$). Angew Chem 100:973–975 (in German)
341. Holleck H, Thümmler F (1967) Ternäre Komplex-carbide, -nitride und -oxide mit teilweise aufgefüllter Ti_2Ni-Struktur (Ternary complex carbides, nitrides and oxides with partially filled Ti_2Ni structure). Monatsh Chem 98:133–134 (in German)
342. Orgaz E, Huanosta A (1992) Electric transport properties of the β-$LnNb_3O_9$ phases (Ln = La, Ce, Pr, and Nd). J Solid State Chem 97:65–73
343. Lü FX, Jack KH (1985) The occurrence of high-speed steel carbide-type η phases in the Fe-Nb system. J Less-Common Met 114:123–127
344. Barabash OM, Shurin AK (1978) Fazovye ravnovesiya v splavakh na osnove niobiya s nitridami titana, tsirkoniya i gafniya (Phase equilibria in alloys based on niobium with nitrides of titanium, zirconium and hafnium). Metallofizika (Akad Nauk Ukr SSR Inst Metallofiz) 71:83–87 (in Russian)

345. Taylor A, Doyle NJ (1967) The solid solubility of nitrogen in Nb and Nb-rich Nb-Hf, Nb-Mo and Nb-W alloys. Part II: The ternary systems Nb-Hf-N, Nb-Mo-N and Nb-W-N. J Less-Common Met 13:413–430
346. Frisk K, Dumitrescu L, Ekroth M, Jansson B, Kruse O, Sundman B (2001) Development of a database for cemented carbides: thermodynamic modeling and experiments. J Phase Equilib 22:645–655
347. Andrievskii RA, Anisimova IA (1991) Calculated phase diagrams of pseudo-binary nitrides based on TiN. Inorg Mater 27:1220–1223
348. Bankovskii OI, Maiseev VF, Pechkovskii EP, Trefilov VI (1974) Fazovyi sostav litykh splavov Nb-Zr-N pri temperature solidusa (Phase composition of as-cast alloys Nb-Zr-N at the temperature of solidus). Metallofizika (Akad Nauk Ukr SSR Inst Metallofiz) 53:103–109 (in Russian)
349. Baron VV, Efimov YV, Savitskii EM, Gladyshevskii EI (1964) The niobium-silicon-vanadium system. Russ J Inorg Chem 9:895–899
350. Mittal RC, Si SK, Gupta KP (1978) Si-stabilised C14 Laves phases in the transition metal systems. J Less-Common Met 60:75–82
351. Steinmetz J, Roques B (1977) Une famille de siliciures ternaires isotypes de V_6Si_5: $(T,T')_6Si_5$ ou T = V, Cr, Mn et T' = Ti, Nb, Ta (A family of ternary silicides V_6Si_5 isotypes: $(T,T')_6Si_5$ or T = V, Cr, Mn and T' = Ti, Nb, Ta) J Less-Common Met 52:247–258 (in French)
352. Seropegin YD, Bodak OI, Guseva IA, Panteleimonov LA (1980) Fazovye ravnovesiya v sisteme Nb-Zr-Si pri 900 °C (Phase equilibria in the Nb-Zr-Si system at 900 °C). Moscow Univ Chem Bull 35(2):85–86 (in Russian)
353. Baier M, Wordel R, Wagner FE, Antonova TE, Antonov VE (1991) Mössbauer study of the hydrides of Nb_3Me with A15 structure. J Less-Common Met 172–174:358–365
354. Zegler ST (1965) Superconductivity in Cr_3Si-type ternary phases with niobium and group VIII metals. Phys Rev 137:A1438–A1440
355. Shimakawa M, Kawachi K, Nishikawa S, Hayashi K (1997) Structural stability of the 1T structure on transition-metal dichalcogenides. 1. Compounds in the NbS_2-IrS_2 system. J Solid State Chem 129:242–249
356. Waterstrat RM (1975) Observations on Nb_3Si and the relative stability of A15 versus Ti_3P-type structures. J Less-Common Met 43:105–115
357. Waterstrat RM, Haenssler F, Muller J (1979) Nb-Si A15 compounds produced by liquid quenching. J Appl Phys 50:4763–4766
358. Mishra R, Pöttgen R, Kotzyba G (2001) New metal-rich compounds NbIrSi, NbIrGe and TaIrSi – synthesis, structure, and magnetic properties. Z Naturforsch B 56:463–468
359. Mar A, Ibers JA (1992) Synthesis and physical properties of the new layered ternary tellurides $MIrTe_4$ (M = Nb, Ta) and the structure of $NbIrTe_4$. J Solid State Chem 97:366–376
360. Wang J, Zhao X, Huang Q, Wang L, Shen J (2011) Thermodynamic assessment of the H-Nb system. J Nucl Mater 412:268–273
361. Okamoto H (2013) The H-Nb (hydrogen-niobium) system. J Phase Equilib Diffus 34(2):163–164
362. Okamoto H (2009) The Nb-U (niobium-uranium) system. J Phase Equilib Diffus 30(4):411
363. Raghavan V (2008) The Al-Ir-Nb (aluminum-iridium-niobium) system. J Phase Equilib Diffus 29(4):369
364. Okamoto H (1994) The Ir-Nb (iridium-niobium) system. J Phase Equilib 15(1):52–54
365. Sha JB, Yamabe-Mitarai Y (2007) Ir-Nb-Si ternary refractory superalloys with a three-phase fcc/$L1_2$/silicide structure for high-temperature applications. Intermetallics 15:1638–1649
366. Sha JB, Yamabe-Mitarai Y (2013) Ultra-high strength of Ir-Hf-Nb ternary alloys with an fcc/$L1_2$ microstructure at 1950 °C. Intermetallics 32:145–150
367. Huang C, Yamabe-Mitarai Y, Harada H (2007) Morphology evolution of Ir-Nb-X (X = Hf, Ta, or Ti) ternary alloys. J Alloys Compd 428:220–229

368. Sha JB, Yamabe-Mitarai Y (2006) Saturated solid-solution hardening behaviour of Ir-Hf-Nb refractory superalloys for ultra-high temperature applications. Scr Mater 54(1):115–119
369. Huang C, Yamabe-Mitarai Y, Nakazawa S, Nishida K, Harada H (2005) Investigation on phase relationships and creep properties of Ir-Nb-X (X = Hf, Ta, or Ti) ternary alloys. Mater Sci Eng A 412(1–2):191–197
370. Gu Y, Yamabe-Mitarai Y, Ro Y, Yokokawa T, Harada H (1998) Microstructure and compressive properties of Ir-15Nb refractory superalloy containing nickel. Scr Mater 39(6):723–728
371. Okamoto H (2012) The Cu-Nb (copper-niobium) system. J Phase Equilib Diffus 33(4):344
372. Okamoto H (2012) The Ge-Nb (germanium-niobium) system. J Phase Equilib Diffus 33(3):250–251
373. Nunes CA, Junior DMP, Coelho GC, Suzuki PA, Da Silva AAAP, Tomasiello RB (2011) Isothermal section of the Nb-Si-B system at 1700 °C in the Nb-$NbSi_2$-NbB_2 region. J Phase Equilib Diffus 32(2):92–96
374. Okamoto H (2010) The B-Nb (boron-niobium) system. J Phase Equilib Diffus 31(2):208–209
375. Okamoto H (2008) The B-Nb (boron-niobium) system. J Phase Equilib Diffus 29(2):201
376. Okamoto H (2010) The Co-Nb (cobalt-niobium) system. J Phase Equilib Diffus 31(1):94–95
377. Okamoto H (2007) The Nb-Sb (niobium-antimony) system. J Phase Equilib Diffus 28(6):589–590
378. Bulak J, Jimenez G, Millette N, Rebeiz K, Craft A (2007) Stress-induced changes to the triple-point phase boundary of the niobium-deuterium system. J Phase Equilib Diffus 28(5):422–426
379. Yang Y, Bewlay BP, Chang YA (2007) Liquid-solid phase equilibria in metal-rich Nb-Ti-Hf-Si alloys. J Phase Equilib Diffus 28(1):107–114
380. Amancherla S, Kar S, Bewlay B, Ying Y, Chang A (2007) Thermodynamic and microstructural modelling of Nb-Si based alloys. J Phase Equilib Diffus 28(1):2–8
381. Okamoto H (2005) The Nb-Si (niobium-silicon) system. J Phase Equilib Diffus 26(6):649
382. Raghavan V (2006) The Al-Ir-Nb-Ni (aluminium-iridium-niobium-nickel) system. J Phase Equilib Diffus 27(5):511
383. Borges LA Jr, Coelho GC, Nunes CA, Suzuki PA (2003) New data on phase equilibria in the Nb-rich region of the Nb-B system. J Phase Equilib 24(2):140–146
384. Toffolon C, Servant C, Gachon JC, Sundman B (2002) Reassessment of the Nb-Sn (niobium-tin) system. J Phase Equilib 23(2):134–139
385. Okamoto H (2000) The Co-Nb (cobalt-niobium) system. J Phase Equilib 21(5):495
386. Li D, Robinson MB, Rathz TJ (2000) Measurements of liquidus temperatures in the Cu-Nb and Cu-Cr systems. J Phase Equilib 21(2):136–140
387. Toffolon C, Servant C, Sundman B (1998) Thermodynamic assessment of the Nb-Sn (niobium-tin) system. J Phase Equilib 19(5):479–485
388. Koike J, Kassner ME, Tate RE, Rosen RS (1998) The Nb-U (niobium-uranium) system. J Phase Equilib 19(3):253–260
389. Bolcavage A, Kattner UR (1996) A reassessment of the calculated Ni-Nb (nickel-niobium) phase diagram. J Phase Equilib 17(2):92–100
390. Tripathi SN, Bharadwaj SR, Dharwadkar SR (1995) The Nb-Pt (niobium-platinum) system. J Phase Equilib 16(5):465–470
391. Okamoto H (1995) Comment on Fe-Nb (iron-niobium) system. J Phase Equilib 16(4):369–370
392. Okamoto H (1993) The Fe-Nb (iron-niobium) system. J Phase Equilib 14(5):650–652
393. Okamoto H (1994) Comment on Nb-Ni (niobium-nickel) system. J Phase Equilib 15(2):229
394. Schlesinger ME, Okamoto H, Gokhale AB, Abbaschian R (1993) Errata: the Nb-Si (niobium-silicon) system. J Phase Equilibria 14(5):541

395. Okamoto H (1993) The Cr-Nb (chromium-niobium) system. J Phase Equilib 14(4):534
396. Okamoto H (1993) The Be-Nb (beryllium-niobium) system. J Phase Equilib 14(4):532–534
397. Okamoto H (1992) The Nb-Zr (niobium-zirconium) system. J Phase Equilib 13(5):577
398. Okamoto H (1992) The Nb-Ni (niobium-nickel) system. J Phase Equilib 13(4):444–445

Chapter 9
Iridium

9.1 Structures

Iridium is the element No. 77 of the periodic table (period—6, group—9 (or VIIIb), relates to transition metals) with the ground state level $^4F_{9/2}$ and electron configuration $1s^2 2s^2 2p^6 3s^2 3p^6 3d^{10} 4s^2 4p^6 4d^{10} 4f^{14} 5s^2 5p^6 5d^7 6s^2$. The general oxidation states (numbers) of iridium in various chemical compounds are (–3), (–2), (–1), 0, (+1), (+2), (+3), (+4), (+5) and (+6); the oxidation states (+6), (+4), (+3) and (+2) are the most common; the radii of iridium are:

atomic (metallic, CN = 12)—0.136 nm,
atomic (covalent)—0.127 nm,
ionic (+3)—0.068 nm (CN = 6),
ionic (+4)—0.063 nm (CN = 6),
ionic (+5)—0.057 nm (CN = 6);

its electronegativity is 2.2 in Pauling scale, or 1.44 in Allred–Rochow scale [1–3, 7–8]. Elemental iridium has cubic face-centered (fcc) metal crystal structure (space group—*Fm(–3)m*, Cu type) with lattice parameters: $a = 0.38390$ nm, (Z = 4), minimum interatomic distance—0.27146 nm (CN = 12), slip plane (111) and slip direction <110> [53, 54]. At room temperature, the XRD density of iridium is 22.56 g cm^{-3} and recommended value for the bulk density of common metal parts—22.4–22.5 g cm^{-3} [4, 8].

9.2 Thermal Properties

Iridium is a refractory noble metal; it belongs to the platinum family. The general thermodynamic properties of iridium are summarized in Table 9.1. For the molar heat capacity $c_p = f(T, \text{K})$, J mol^{-1} K^{-1}, the following relationship is recommended for the range of temperatures from 298 to 2500 K [5]

I. L. Shabalin, *Ultra-High Temperature Materials I*,
DOI: 10.1007/978-94-007-7587-9_9,

Table 9.1 General thermodynamic properties of iridium

Characteristics	Symbol	Unit	Value	References
Standard molar entropy (at 298.15 K and 100 kPa)	$S°_{298}$	J mol^{-1} K^{-1}	35.505	[8]
			35.48	[6]
			36.4	[5, 9]
Enthalpy difference	$H_{298} - H_0$	kJ mol^{-1}	5.268	[8]
Standard molar heat capacity (at 298.15 K and 100 kPa)	$c°_{p,298}$	J mol^{-1} K^{-1}	25.05	[5]
			24.98	[8]
			25.06	[6]
			25.10	[7, 9]
Specific heat capacity (at 298.15 K)	c	J kg^{-1} K^{-1}	130	[55]
			131	[7]
Molar enthalpy (heat) of melting (at the melting point)	ΔH_m	kJ mol^{-1}	41.12	[6–8]
			26	[56]
Specific enthalpy (heat) of melting (at the melting point)		kJ kg^{-1}	214	[7]
			135	[56]
Molar enthalpy (heat) of vaporization (at the boiling point)	ΔH_v	kJ mol^{-1}	604	[8]
			560	[56]
Specific enthalpy (heat) of vaporization (at the boiling point)		MJ kg^{-1}	3.14	[8]
Melting point	T_m	K (°C)	2720 (2445)	[6–9, 55]
			2740 (2465)	[139]
			2700 ± 20 (2430 ± 20)	[4]
			2685 (2410)	[10]
Boiling point	T_b	K (°C)	4700 (4430)	[7–8, 139]
			4850 (4580)	[9]
			4800 (4530)	[57]
			4770 (4500)	[55]
			4405 (4130)	[10]

$$c_p = 23.28 + \left(5.95 \times 10^{-3}\right)T. \tag{9.1}$$

The equilibrium vapor pressure of iridium P, Pa, at temperatures 298–2500 K is obeyed the rule [7]:

$$\lg P = -35099/T - 0.7500\lg T + 15.512, \tag{9.2}$$

where T is temperature, K. The values of standard molar entropy $S°_{298}$, molar c_p and specific c heat capacities, enthalpies (heats) of melting and vaporization, molar

and specific mass enthalpy differences $H_T - H_{298}$, vapor pressures for iridium are given in Addendum in comparison with other ultra-high temperature materials. At room temperature, the thermal conductivity of iridium is 147–150 W m^{-1} K^{-1} [8, 10, 55, 139]. The linear thermal expansion of iridium in the range of temperatures from 30 to 2220 °C is expressed by the equation as follows [58]:

$$(L_t - L_0)/L_0 = 6.167 \times 10^{-6}t + 1.519 \times 10^{-9}t^2 - 0.2816 \times 10^{-12}t^3 + 0.1463 \times 10^{-15}t^4 \quad (9.3)$$

where L_0 and L_t are linear dimensions at 30 °C and higher temperature, respectively; t denotes the value of temperature, °C. For the ambient temperature, the recommended value is $\alpha = 6.8 \times 10^{-6}$ K^{-1} [8, 10, 55]. The surface tension of liquid iridium (density 20.0 g cm^{-3}) is 2.25 N m^{-1} (its temperature coefficient is —0.31 $\times$ 10^{-3} N m^{-1} K^{-1}) [8]. In comparison with other ultra-high temperature materials (graphite and refractory metals), the values of thermal conductivity and thermal expansion of iridium in the wide range of temperatures are summarized in Addendum.

9.3 Electro-Magnetic and Optical Properties

At room temperature, the specific electrical resistance (resistivity) of unalloyed iridium is 47–53 nΩ m, at 630, 1230, and 1530 °C it amounts to 0.18, 0.34, and 0.46 μΩ m, respectively; in the range of temperatures from 0 to 100 °C the thermal coefficient of resistivity is (4.1 ÷ 4.3) $\times$ 10^{-3} K^{-1} [8–10, 28, 55]. At 20 °C, the Hall coefficient of iridium equals $R = 31.8 \times 10^{-10}$ m^3 A^{-1} s^{-1} (B = 4.5–5.0 T), Seebeck coefficient (absolute thermoelectric power) is 1.2 μV K^{-1} [8, 10]. Iridium is a paramagnetic metal with the magnitude of molar magnetic susceptibility χ_m (SI) = 314 $\times$ 10^{-6} cm^3 mol^{-1} (22 °C) increasing almost linearly with temperature growth [8, 28]; the relative magnetic susceptibility $\chi(T)/\chi(293\ K)$ amounts to ~1.3 at 400 °C [29]. The variations of reflective index (polished materials) of iridium with wavelength λ amount from 0.78 (λ = 1.0 μm) to 0.96 (λ = 12.0 μm). In the range of temperatures 1030–2230 °C, the monochromatic emittance (spectral emissivity) ε_λ (λ = 0.65 μm) of non-oxidized iridium varies from 0.27–0.30 to 0.215, and the integral emittance ε_T—from 0.129 to 0.211 [9–10]. The electron work function of iridium is ~4.7–5.7 eV; for the various (*hkl*)-index of oriented iridium single crystal it is 5.50 eV (100), 4.85 eV (110) and 5.74 eV (111) [9]. The recommended values of electrical resistivity, magnetic susceptibility, integral, and spectral emittances and thermoionic emission characteristics (electron work function and Richardson constant) for iridium are given in comparison with other ultra-high temperature elements (carbon and refractory metals) in Addendum.

9.4 Physico-Mechanical Properties

Unalloyed metallic iridium is extremely hard and can only be deformed above 600 °C with repeated annealing steps at temperatures higher than 1200 °C [44], its physico-mechanical properties are highly anisotropic. At room temperature, the hardness (HV) of annealed iridium is 200–330 kgf mm^{-2} (2.0–3.2 GPa), although for hardened metal it could be reached up to 1000–1760 kgf mm^{-2} (9.8–17.2 GPa) HV [10, 28, 129]. Approximately, the changes of hardness (HV) with degree cold forming are [28]:

for 10 %—425 kgf mm^{-2} (4.15 GPa);
for 20 %—485 kgf mm^{-2} (4.75 GPa);
for 60 %—590 kgf mm^{-2} (5.8 GPa).

At higher temperatures, the hardness (HV) of iridium averages [28]:

at 500 °C—138 kgf mm^{-2} (1.35 GPa);
at 800 °C—112 kgf mm^{-2} (1.10 GPa);
at 1000 °C—97 kgf mm^{-2} (0.95 GPa).

The value of ultimate tensile strength of hardened pure iridium at room temperature amounts to 0.55–1.1 GPa (yield strength—0.23 GPa, tensile elongation—6.8 %), it decreases with temperature growth to 0.53 (9 %), 0.45 (18 %) and 0.33 GPa at 500, 800, and 1000 °C, respectively (the corresponding values of elongation are given in brackets) [8, 10, 44]. The variations of tensile strength, yield strength and tensile elongation in the range of temperatures 1600–2300 °C are given in Fig. 9.1 [128]. Pure iridium loses its long-term rupture strength considerably with increasing temperature; some creep properties, in particular average stationary creep rate $(d\varepsilon/dt)_m$ as a function of the applied initial stress, of deformed and subsequently recrystallized without significant grain growth iridium sheet tested at 1650–2300 °C are presented in Fig. 9.2 [128].

Iridium possesses very high magnitudes of elastic properties at room temperature [8, 10, 28, 59]:

Young's modulus E, GPa		525–540
Coulomb's (shear) modulus G, GPa		210–220
Poisson's ratio ν		0.20–0.26
Volume compressibility κ, MPa^{-1}		0.26×10^{-5}
Longitudinal velocity of sound V_S, m s^{-1}		5380
Transversal velocity of sound V_T, m s^{-1}		3050
Elastic compliance	s_{11}, TPa^{-1}	2.28
	s_{44}, TPa^{-1}	3.90
	s_{12}, TPa^{-1}	−0.67
Elastic stiffness	c_{11}, GPa	580
	c_{44}, GPa	256
	c_{12}, GPa	242

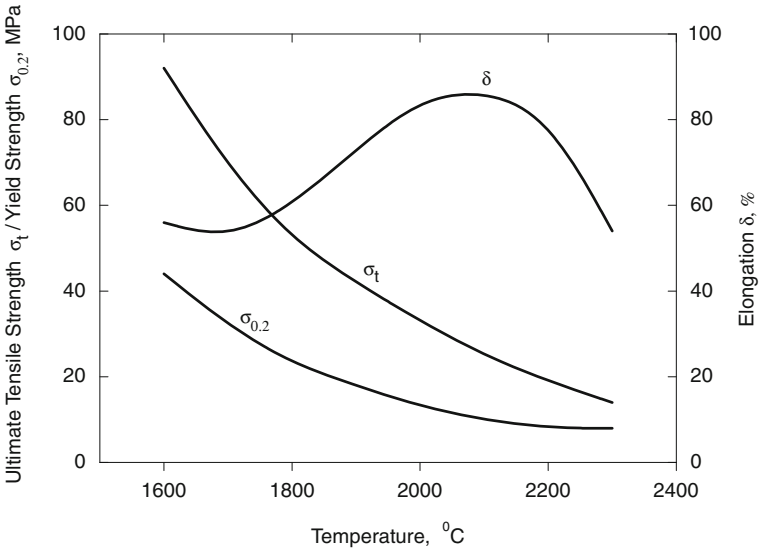

Fig. 9.1 Variations of the ultimate tensile strength (σ_t), yield strength ($\sigma_{0.2}$) and tensile elongation (δ) of pure deformed and subsequently recrystallized iridium sheet with temperature [128]

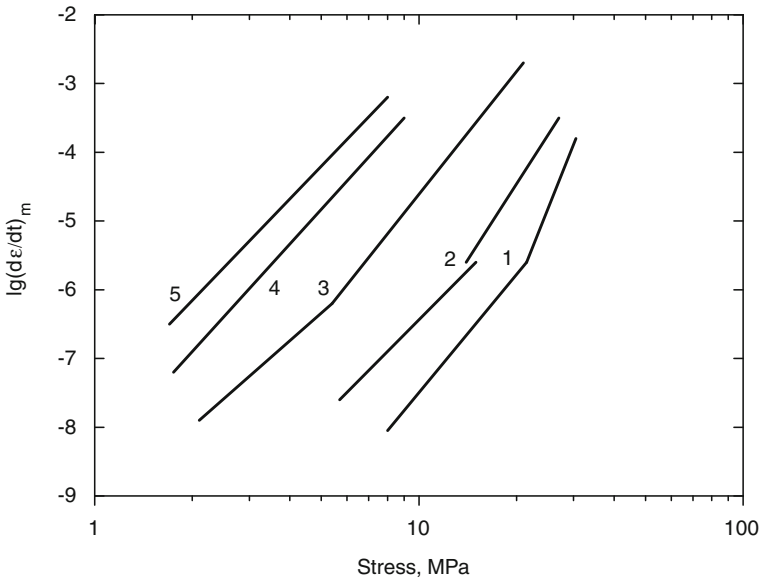

Fig. 9.2 Average stationary creep rate $(d\varepsilon/dt)_m$ of pure deformed and subsequently recrystallized iridium sheet as a function of the applied initial stress at the temperatures: *1*—1650 °C, *2*—1800 °C, *3*—2000 °C, *4*—2200 °C, and *5*—2300 °C [128]

With temperature increase, the values of Young's and Coulomb's (shear) moduli fall linearly to about 420 and 170 GPa (at 1000 °C), respectively [28, 59]. The magnitudes of physico-mechanical (strength, elasticity) properties of unalloyed iridium in the wide range of temperatures are summarized in Addendum in comparison with other ultra-high temperature materials (graphite and refractory metals).

9.5 Nuclear Physical Properties

The isotopes of iridium (standard atomic mass—192.217 u) from ^{164}Ir to ^{199}Ir, including metastable states ($^{164m-174m}$Ir, $^{184m1-184m2}$Ir, ^{186m}Ir, $^{187m1-187m2}$Ir, ^{188m}Ir, $^{189m1-189m2}$Ir, $^{190m1-190m3}$Ir, $^{191m1-191m2}$Ir, $^{192m1-192m2}$Ir, ^{193m}Ir, $^{194m1-194m2}$Ir, $^{195m-197m}$Ir), and their general characteristics are summarized in Table 9.2; the naturally occurring isotopes are listed in order of decreasing abundance, and unstable artificial (radioactive) isotopes—in order of decreasing half-life period of decay.

Table 9.2 General characteristics of the isotopes of iridium[a] [7, 9, 22–24]

Isotope	Mass, u	Abundance, %	Half-life period	Decay mode, excitation (radiation) energy, MeV
^{193}Ir[b]	192.962926	62.7	–	–
^{191}Ir[b]	190.960594	37.3	–	–
^{192m2}Ir	–	–	241 y	Isomer; γ, 0.168
^{194m2}Ir	–	–	171 d	Isomer; γ, 0.370
^{192}Ir	191.962605	–	73.83 d	β^- (95.24 %); *K*-capture (4.76 %); γ (7 principal energy packets—from ~0.2 to ~0.6)
^{189}Ir	188.958719	–	13.2 d	*K*-capture; γ, 0.135, 0.245
^{190}Ir	189.960546	–	11.78 d	β^+; γ, 0.19, 0.35, 0.51
^{193m}Ir	–	–	10.53 d	Isomer; γ, 0.080
^{188}Ir	187.958853	–	41.5 h	β^+; γ, 0.15, 0.475, 0.625
^{194}Ir	193.965078	–	19.28 h	β^-; γ (from ~0.29 to ~2.04)
^{186}Ir	185.957946	–	16.64 h	β^+
^{185}Ir	184.95670	–	14.4 h	β^+
^{187}Ir	186.957363	–	10.5 h	β^+; γ, 0.135, 0.3, 0.435
^{195m}Ir	–	–	3.8 h	Isomer; β^- (95 %); *K*-capture (5 %); γ, 0.100
^{184}Ir	183.95748	–	3.09 h	β^+
^{190m3}Ir	–	–	3.087 h	Isomer; γ, 0.376
^{195}Ir	194.965980	–	2.5 h	β^-; γ, 0.42, 0.66, 0.88
^{186m}Ir	–	–	1.92 h	Isomer (rare); β^+; γ, 0.0008
^{196m}Ir	–	–	1.40 h	Isomer; β^- (99.7 %); γ, 0.210
^{190m1}Ir	–	–	1.12 h	Isomer; γ, 0.026
^{183}Ir	182.956846	–	57 min	β^+ (99.95 %); α (0.05 %)
^{182}Ir	181.958076	–	15 min	β^+

(continued)

Table 9.2 (continued)

Isotope	Mass, u	Abundance, %	Half-life period	Decay mode, excitation (radiation) energy, MeV
^{197m}Ir	–	–	8.9 min	Isomer (0.25 %); β^- (99.75 %); γ, 0.115
^{197}Ir	196.969653	–	5.8 min	β^-
^{181}Ir	180.957625	–	4.90 min	β^+
^{180}Ir	179.959229	–	1.5 min	β^+
^{192m1}Ir	–	–	1.45 min	Isomer; γ, 0.057
^{179}Ir	178.959122	–	79 s	β^+
^{196}Ir	195.96840	–	52 s	β^-; γ, 0.58, 0.76
^{177}Ir	176.961302	–	30 s	β^+ (99.94 %); α (0.06 %)
^{199}Ir	198.97380	–	20 s (?)	β^-
^{178}Ir	177.961082	–	12 s	β^+
^{173}Ir	172.967502	–	9.0 s	β^+ (93 %); α (7 %)
^{175}Ir	174.964113	–	9 s	β^+ (99.15 %); α (0.85 %)
^{176}Ir	175.963649	–	8.3 s	β^+ (97.9 %); α (2.1 %)
^{198}Ir	197.97228 (?)	–	8 s	β^-; γ, 0.78
^{174}Ir	173.966861	–	7.9 s	β^+ (99.5 %); α (0.5 %)
^{191m2}Ir	–	–	5.5 s	Isomer; γ, 2.120
^{191m1}Ir	–	–	4.94 s	Isomer; γ, 0.171
^{174m}Ir	–	–	4.9 s	Isomer; β^+ (99.53 %); α (0.47 %); γ, 0.193
^{172}Ir	171.97046 (?)	–	4.4 s	β^+ (98 %); α (2 %)
^{171}Ir	170.97163	–	3.6 s	α (58 %); β^+ (42 %)
^{173m}Ir	–	–	2.2 s	Isomer; β^+ (88 %); α (12 %); γ, 0.253
^{172m}Ir	–	–	2.0 s	Isomer; β^+ (77 %); α (23 %); γ, 0.280 (?)
^{171m}Ir	–	–	1.4 s	Isomer; γ, 0.180 (?)
^{170}Ir	169.97497 (?)	–	0.91 s	β^+ (64 %); α (36 %)
^{169}Ir	168.976295	–	0.78 s	α; β^+ (rare)
^{170m}Ir	–	–	0.44 s	Isomer; γ, 0.270 (?)
^{169m}Ir	–	–	0.308 s	Isomer; α (72 %); β^+ (28 %); γ, 0.154
^{168}Ir	167.97988	–	0.161 s	α; β^+ (rare)
^{168m}Ir	–	–	0.125 s	Isomer; α; γ, 0.050 (?)
^{167}Ir	166.981665	–	35.2 ms	α (48 %); p (32 %); β^+ (20 %)
^{194m1}Ir	–	–	31.85 ms	Isomer; γ, 0.147
^{187m1}Ir	–	–	30.3 ms	Isomer; γ, 0.186
^{167m}Ir	–	–	30.0 ms	Isomer; α ($\sim$80 %); β^+ ($\sim$20 %); p (0.4 %); γ, 0.175
^{166m}Ir	–	–	15.1 ms	Isomer; α (98.2 %); p (1.8 %); γ, 0.172
^{189m1}Ir	–	–	13.3 ms	Isomer; γ, 0.372
^{166}Ir	165.98582 (?)	–	10.5 ms	α (93 %); p (7 %)
^{188m}Ir	–	–	4.2 ms	Isomer; β^+ (rare); γ, 0.970
^{189m2}Ir	–	–	3.7 ms	Isomer; γ, 2.333
^{164}Ir	163.99220 (?)	–	1 ms	
^{184m1}Ir	–	–	0.47 ms	Isomer; γ, 0.226

(continued)

Table 9.2 (continued)

Isotope	Mass, u	Abundance, %	Half-life period	Decay mode, excitation (radiation) energy, MeV
^{165m}Ir	–	–	0.30 ms	Isomer; p (87 %); α (13 %); γ, 0.180, (?)
^{164m}Ir	–	–	94 μs	Isomer; γ, 0.270, (?)
^{190m2}Ir	–	–	>2 μs	Isomer; γ, 0.036
^{165}Ir	164.98752 (?)		<1 μs	p; α (rare)
^{184m2}Ir	–	–	0.35 μs	Isomer; γ, 0.328
^{187m2}Ir	–	–	0.15 μs	Isomer; γ, 0.433

[a] Naturally occurring iridium includes two nearly stable (see below note *b*) isotopes (^{191}Ir and ^{193}Ir) with half-life periods longer than the age of universe (?)
[b] Believed to undergo α decay (?)

Nuclear physical properties of iridium (isotopic mass range, total number of isotopes, thermal neutron macroscopic cross sections and capture resonance integral), compared with other ultra-high temperature elements (carbon and refractory metals), are given in Addendum.

9.6 Chemical Properties

The comprehensive information on the chemical properties and interaction of iridium with all the elements of the periodic table is given in Table 9.3. The iridium containing systems and corresponding binary compounds are described and considered there in accordance to the groups of elements from 1 to 17.

Table 9.3 Chemical interaction of iridium with elements of the periodic table (binary systems in accordance to the groups of elements)[a]

System	Type of phase diagram (constituent phases, temperatures, and compositions of transformations)	Character of interaction	References
Group 1			
Ir–H	H, no binary compounds, Ir No diagram plot	At 1400–1600 °C the solubility of H (x, at.%) is obeyed the following rule: $\lg x = 0.5\lg p - 2.02 - 3847/T$, where p is pressure H_2, Pa, and T is temp., K. At pressure H_2 0.1 MPa, its solubility increases from 1.3×10^{-5} at.% at 1390 °C to 2.2×10^{-5} at.% at 1580 °C.	[11–12, 30, 40, 60]

(continued)

Table 9.3 (continued)

System	Type of phase diagram (constituent phases, temperatures, and compositions of transformations)	Character of interaction	References
Ir–Li	α-Li, β-Li, γ-Li, $IrLi_{1\pm x}$ (<2080–2120 °C, congruent melt. point, ?), $Ir_{3\pm x}Li$ (<at least 1500 °C, ?), Ir Eutectic (degenerated) $IrLi_{1\pm x}$–γ-Li (~180 °C, ?) Eutectic $IrLi_{1\pm x}$–Ir (1800 °C, ~73 at.% Ir, ?)	–	[13, 15, 61, 140–141]
Ir–Na	α-Na, β-Na, $IrNa_3$ (?), $IrNa_2$ (?), IrNa (?), Ir_2Na (?), Ir_3Na (?), Ir No diagram plot	At 150–300 °C Ir is resistant to liquid Na (6 h exposure).	[13, 48–51]
Ir–K	K, no binary compounds (?), Ir No diagram plot	At 110–260 °C Ir is resistant to liquid K (6 h exposure).	[13]
Ir–Rb	Rb, $IrRb_3$ (?), $IrRb_2$ (Laves phase, ?), IrRb (?), Ir_2Rb (Laves phase, ?), Ir_3Rb (?), Ir No diagram plot	No experimental data.	[13, 15]
Ir–Cs	Cs, no binary compounds (?), Ir No diagram plot	The mutual solubilities of the components are negligibly small (?).	[142–143]
Ir–Fr	No data	–	–
Group 2			
Ir–Be	α-Be, β-Be, Ir_2Be_{17} (or $IrBe_{6.6}$, ?), Ir_5Be_{22}, $IrBe_2$, IrBe, Ir No diagram plot	–	[14, 18, 31–32, 62–63]
Ir–Mg	Mg, ζ-$IrMg_{6\div8}$ (or $Mg_{44}Ir_{7-x}$, $Mg_{29}Ir_{4\pm x}$, <925 °C, incongruent melt. point, homog. range—~11–14 at.% Ir at 615 °C, ?), $IrMg_4$ (or Ir_3Mg_{13}, <1025 °C, incongruent melt. point, invariable compos., ?), δ-$IrMg_3$ (or $IrMg_{2.8}$, <1150 °C, incongruent melt. point, invariable compos., ?), Ir_3Mg_7 (?), IrMg (?), $Ir_{3-x}Mg_{2+x}$ ($x = 0.30$, ?), Ir_2Mg (Laves phase, ?), Ir Eutectic Mg–ζ-$IrMg_{6\div8}$ (~615 °C, 3.2 at.% Ir)	The max. solubility of Ir in solid Mg is <0.18 at.%.	[13, 15, 64, 144–150]
Ir–Ca	α-Ca, β-Ca, Ca_5Ir (?), $CaIr_2$ (Laves phase), Ir No diagram plot	–	[14, 151]
Ir–Sr	α-Sr, β-Sr, $SrIr_2$ (Laves phase), $SrIr_3$, Sr_2Ir_7 (?), $SrIr_5$ (?), Ir No diagram plot	–	[13, 65–66]
Ir–Ba	No data	–	–

(continued)

Table 9.3 (continued)

System	Type of phase diagram (constituent phases, temperatures, and compositions of transformations)	Character of interaction	References
Ir–Ra	Ra, $IrRa_5$ (Laves phase, ?), $IrRa_3$ (?), $IrRa_2$ (?), IrRa (?), Ir_2Ra (Laves phase, ?), Ir_3Ra (?), Ir_5Ra (Laves phase, ?), Ir No diagram plot	No experimental data.	[13]
Group 3			
Ir–Sc	α-Sc, β-Sc, $Sc_{44}Ir_{7\pm x}$ (<1420 °C, incongruent melt. point, homog. range—~11–14 at.% Ir at 1240 °C and ~13–14 at.% Ir at 1290 °C), $Sc_{57}Ir_{13\pm x}$ (<1480 °C, congruent melt. point, homog. range—~17–19 at.% Ir at 1420 °C and ~17–20 at.% Ir at 1290 °C, invariable compos. at temp. <1000 °C), $Sc_{11}Ir_4$ (<1410 °C, congruent melt. point, invariable compos.), $Sc_{2+x}Ir$ (<1420 °C, incongruent melt. point, homog. range—~30–34 at.% Ir at 1370 °C), $ScIr_{1\pm x}$ (<2100 °C, congruent melt. point, homog. range—~46–52 at.% Ir at 2020 °C, ~45–50 at.% Ir at 1420 °C and ~47–50 at.% Ir at 800 °C), $ScIr_{2\pm x}$ (<2150 °C, congruent melt. point, homog. range—~65–70 at.% Ir at 1980–2020 °C, invariable compos. at temp. <1200–1600 °C, Laves phase), $ScIr_{3+x}$ (<1980 °C, incongruent melt. point, homog. range—~77–86 at.% Ir at 700–1950 °C), Ir Eutectic $Sc_{44}Ir_7$–β-Sc (1240 °C, ~6 at.% Ir) Eutectic $Sc_{57}Ir_{13\pm x}$–$Sc_{11}Ir_4$ (1290 °C, ~24 at.% Ir) Eutectic $Sc_{2+x}Ir$–$Sc_{11}Ir_4$ (1370 °C, ~29 at.% Ir) Eutectic $ScIr_{1\pm x}$–$ScIr_{2\pm x}$ (2020 °C, ~54 at.% Ir) Eutectic $ScIr_{3+x}$–Ir (1950 °C, ~88 at.% Ir)	The max. solid solubilities of Ir in Sc modifications are ~1 at.% in α-Sc (1180 °C) and ~4 at.% in β-Sc (1240 °C). The max. solid solubility of Sc in Ir is ~10 at.% at 1950 °C; the solubility of Sc declines noticeably with temp. decrease—up to ~4 at.% at 700 °C.	[13, 67–68, 152–155]

(continued)

Table 9.3 (continued)

System	Type of phase diagram (constituent phases, temperatures, and compositions of transformations)	Character of interaction	References
Ir–Y	α-Y, β-Y, Y_3Ir (<1425 °C, incongruent melt. point, invariable compos.), Y_5Ir_2 (<1525 °C, incongruent melt. point, invariable compos.), $Y_{64}Ir_{37}$ (?), α'-$Y_5Ir_{3\pm x}$ (?), α-$Y_5Ir_{3\pm x}$ (?), β-$Y_5Ir_{3\pm x}$ (<1600 °C, incongruent melt. point, width homog. range $\leq$1 at.%), Y_3Ir_2 (<1725 °C, incongruent melt. point, invariable compos.), YIr (<2150 °C, congruent melt. point, invariable compos.), $YIr_{2\pm x}$ (<2400 °C, congruent melt. point, homog. range—~65–68 at.% Ir at 0–2000 °C, Laves phase), YIr_3 (<2100 °C, incongruent melt. point, invariable compos.), Ir Eutectic Y_3Ir–β-Y (1325 °C, ~10 at.% Ir) Eutectic YIr–$YIr_{2\pm x}$ (1900 °C, ~57 at.% Ir) Eutectic YIr_3–Ir (1850 °C, ~85 at.% Ir)	–	[13, 15, 21, 67, 69, 156–157]
Lanthanides			
Ir–La	α-La, β-La, γ-La, La_4Ir (<820 °C, incongruent melt. point, invariable compos.), La_3Ir (<1080 °C, incongruent melt. point, invariable compos.), La_7Ir_3 (or La_5Ir_2, <1140 °C, congruent melt. point, invariable compos.), La_5Ir_3 (or La_3Ir_2, <1165 °C, congruent melt. point, invariable compos.), LaIr (<1180 °C, incongruent melt. point, invariable compos.), $LaIr_2$ (<~2520 °C, congruent melt. point, invariable compos., Laves phase, ?), $LaIr_3$ (<2420 °C, invariable compos.), La_2Ir_7 (<2400 °C, invariable compos.), $LaIr_5$ (<2450 °C, invariable compos.), La_2Ir_{17} (<~2500 °C, congruent melt. point, invariable compos., ?), Ir Eutectic La_4Ir–β-La (730 °C, ~5–9 at.% Ir) Eutectic La_7Ir_3–La_5Ir_3 (?) Eutectic LaIr–La_5Ir_3 (?)	–	[13, 15, 21, 67, 69–70, 208]

(continued)

Table 9.3 (continued)

System	Type of phase diagram (constituent phases, temperatures, and compositions of transformations)	Character of interaction	References
Ir–Ce	α-Ce, β-Ce, γ-Ce, δ-Ce, Ce_4Ir (<710 °C, incongruent melt. point, invariable compos.), Ce_3Ir (<~880–950 °C, incongruent melt. point, invariable compos.), Ce_7Ir_3 (<950 °C, incongruent melt. point, invariable compos., ?), Ce_3Ir_2 (?), Ce_5Ir_3 (or Ce_2Ir, <1100 °C, incongruent melt. point, invariable compos., ?), Ce_5Ir_4 (or $Ce_{15}Ir_{13}$ (?), <1180 °C, incongruent melt. point, invariable compos.), $CeIr_{2\pm x}$ (<2250 °C, congruent melt. point, homog. range—~63–70 at.% Ir, Laves phase), $CeIr_3$ (<~2000–2120 °C, incongruent melt. point, invariable compos.), Ce_2Ir_7 (<~2000 °C, incongruent melt. point, invariable compos.), $CeIr_5$ (<1955–1960 °C, congruent melt. point, invariable compos.), Ir Eutectic Ce_2Ir_7–$CeIr_5$ (~1900–1925 °C, 82 at.% Ir) Eutectic Ce_4Ir–γ-Ce (650 °C, 8 at.% Ir) Eutectic $CeIr_5$–Ir (1880 °C, 85 at.% Ir)	No data on solubility.	[14–15, 19, 67, 69, 71, 164–165, 210]
Ir–Pr	α-Pr, β-Pr, Pr_3Ir (?), Pr_5Ir_2 (incongruent melt. point, invariable compos.), Pr_7Ir_3 (?), Pr_5Ir_3 (incongruent melt. point, invariable compos.), $PrIr_{2\pm x}$ (congruent melt. point, homog. range—~65–68 at.% Ir, Laves phase), $PrIr_3$(incongruent melt. point, invariable compos.), Pr_2Ir_7 (incongruent melt. point, invariable compos.), $PrIr_5$ (congruent melt. point, invariable compos.), Ir Eutectic Pr_5Ir_2–α-Pr (~720–730 °C, 12 at.% Ir) Eutectic Pr_2Ir_7–$PrIr_5$ (?) Eutectic $PrIr_5$–Ir (?)	The presence of Ir diminishes the melt. point of Pr and temp. of α-Pr–β-Pr polymorphic transformation. The max. solid solubility of Ir in β-Pr is 0.35 at.%.	[13, 15, 20, 67, 69, 71, 143, 162]

(continued)

Table 9.3 (continued)

System	Type of phase diagram (constituent phases, temperatures, and compositions of transformations)	Character of interaction	References
Ir–Nd	α-Nd, β-Nd, Nd_4Ir (incongruent melt. point, invariable compos.), Nd_3Ir (incongruent melt. point, invariable compos.), Nd_5Ir_2 (incongruent melt. point, invariable compos.), Nd_7Ir_3 (?), Nd_5Ir_3 (incongruent melt. point, invariable compos.), $NdIr_{2\pm x}$ (congruent melt. point, homog. range—~65–68 at.% Ir, Laves phase), $NdIr_3$ (incongruent melt. point, invariable compos.), Nd_2Ir_7 (incongruent melt. point, invariable compos.), $NdIr_5$ (?, invariable compos.), Ir Eutectic Nd_4Ir–β-Nd (?) Eutectic $NdIr_5$–Ir (?)	The mutual solubilities of the components are low.	[13, 15, 21, 67, 69, 71, 76, 143, 162]
Ir–Pm	α-Pm, β-Pm, Pm_5Ir (?), Pm_3Ir (incongruent melt. point, invariable compos.), Pm_5Ir_2 (incongruent melt. point, invariable compos.), Pm_2Ir (Laves phase, ?), Pm_5Ir_3 (incongruent melt. point, invariable compos.), PmIr (?), $PmIr_{2\pm x}$ (congruent melt. point, homog. range—~65–68 at.% Ir, Laves phase), $PmIr_3$ (incongruent melt. point, invariable compos.), $PmIr_5$ (?), Ir Eutectic Pm_3Ir–β-Pm (?) Eutectic $PmIr_3$–Ir (?)	No experimental data.	[13, 15, 143, 162]
Ir–Sm	α-Sm, β-Sm, γ-Sm, Sm_3Ir (incongruent melt. point, invariable compos.), Sm_5Ir_2 (incongruent melt. point, invariable compos.), Sm_5Ir_3 (incongruent melt. point, invariable compos.), $SmIr_{2\pm x}$ (congruent melt. point, homog. range—~65–68 at.% Ir, Laves phase), $SmIr_3$ (incongruent melt. point, invariable compos.), Ir Eutectic Sm_3Ir–γ-Sm (?) Eutectic $SmIr_3$–Ir (?)	–	[13, 15, 21, 69, 72–74, 143, 162]
Ir–Eu	Eu, Eu_4Ir (?), $EuIr_2$ (Laves phase), Ir No diagram plot	–	[12, 158]

(continued)

Table 9.3 (continued)

System	Type of phase diagram (constituent phases, temperatures, and compositions of transformations)	Character of interaction	References
Ir–Gd	α-Gd, β-Gd, Gd_3Ir (incongruent melt. point, invariable compos.), Gd_5Ir_2 (incongruent melt. point, invariable compos.), α-$Gd_5Ir_{3\pm x}$ (?), β-$Gd_5Ir_{3\pm x}$ (incongruent melt. point, homog. range width—≤1.5 at.% Ir), Gd_3Ir_2 (incongruent melt. point, invariable compos.), $GdIr_{2\pm x}$ (congruent melt. point, homog. range—~65–68 at.% Ir, Laves phase), α-$GdIr_3$ (?), β-$GdIr_3$ (incongruent melt. point, invariable compos.), Ir Eutectic Gd_3Ir–β-Gd (?) Eutectic β-$GdIr_3$–Ir (?)	–	[12, 15, 19, 69, 74–76, 143, 159, 162–163]
Ir–Tb	α′-Tb, α-Tb, β-Tb, Tb_3Ir (incongruent melt. point, invariable compos.), Tb_5Ir_2 (incongruent melt. point, invariable compos.), $Tb_{64}Ir_{37}$ (?), α-Tb_5Ir_3 (?), β-Tb_5Ir_3 (incongruent melt. point, invariable compos.), Tb_3Ir_2 (incongruent melt. point, invariable compos.), $TbIr_{2\pm x}$ (congruent melt. point, homog. range—~65–68 at.% Ir, Laves phase), Ir Eutectic Tb_3Ir–β-Tb (?) Eutectic $TbIr_{2\pm x}$–Ir (?)	–	[13, 15, 19, 21, 69, 143, 162–163]
Ir–Dy	α′-Dy, α-Dy, β-Dy, Dy_3Ir (incongruent melt. point, invariable compos.), Dy_5Ir_2 (incongruent melt. point, invariable compos.), α-Dy_5Ir_3 (?), β-Dy_5Ir_3 (incongruent melt. point, invariable compos.), Dy_3Ir_2 (incongruent melt. point, invariable compos.), $DyIr_{2\pm x}$ (congruent melt. point, homog. range—~65–68 at.% Ir, Laves phase), $DyIr_3$ (?), Ir Eutectic Dy_3Ir–β-Dy (?) Eutectic $DyIr_{2\pm x}$–Ir (?)	–	[12, 15, 69, 75, 143, 163, 205]

(continued)

Table 9.3 (continued)

System	Type of phase diagram (constituent phases, temperatures, and compositions of transformations)	Character of interaction	References
Ir–Ho	α-Ho, β-Ho, Ho_3Ir (incongruent melt. point, invariable compos.), Ho_5Ir_2 (incongruent melt. point, invariable compos.), α-Ho_5Ir_3 (?), β-Ho_5Ir_3 (incongruent melt. point, invariable compos.), Ho_3Ir_2 (incongruent melt. point, invariable compos.), HoIr (congruent melt. point, invariable compos.), $HoIr_{2\pm x}$ (congruent melt. point, homog. range—~65–68 at.% Ir, Laves phase), Ir Eutectic Ho_3Ir–β-Ho (?) Eutectic $HoIr_{2\pm x}$–HoIr (?) Eutectic $HoIr_{2\pm x}$–Ir (?)	–	[12, 15, 69, 143, 163]
Ir–Er	α-Er, β-Er, Er_3Ir (incongruent melt. point, invariable compos.), Er_5Ir_2 (incongruent melt. point, invariable compos.), α-$Er_5Ir_{3\pm x}$ (?), β-$Er_5Ir_{3\pm x}$ (incongruent melt. point, homog. range width—≤1.5 at.% Ir), Er_3Ir_2 (incongruent melt. point, invariable compos.), ErIr (congruent melt. point, invariable compos.), $ErIr_{2\pm x}$ (congruent melt. point, homog. range—~65–68 at.% Ir, Laves phase), Ir Eutectic Er_3Ir–β-Er (?) Eutectic $ErIr_{2\pm x}$–ErIr (?) Eutectic $ErIr_{2\pm x}$–Ir (?)	–	[15, 69, 143, 162, 204]
Ir–Tm	α-Tm, β-Tm, Tm_3Ir (incongruent melt. point, invariable compos.), Tm_5Ir_2 (incongruent melt. point, invariable compos.), α-Tm_5Ir_3 (?), β-Tm_5Ir_3 (incongruent melt. point), Tm_3Ir_2 (incongruent melt. point, invariable compos.), TmIr (congruent melt. point, invariable compos.), $TmIr_{2\pm x}$ (congruent melt. point, homog. range—~65–68 at.% Ir, Laves phase), Ir Eutectic Tm_3Ir–β-Tm (?) Eutectic $TmIr_{2\pm x}$–TmIr (?) Eutectic $TmIr_{2\pm x}$–Ir (?)	–	[13, 15, 21, 69, 143]

(continued)

Table 9.3 (continued)

System	Type of phase diagram (constituent phases, temperatures, and compositions of transformations)	Character of interaction	References
Ir–Yb	α-Yb, β-Yb, γ-Yb, α-Yb_5Ir_3 (<at least 900 °C, invariable compos., ?), β-Yb_5Ir_3 (at least at ~950–1410 °C, congruent melt. point, invariable compos., ?), Yb_3Ir_2 (<at least 1500 °C, invariable compos., ?), YbIr (<at least 1500 °C, ?), $YbIr_{2\pm x}$ (<at least 1500 °C, homog. range—from ~66 to ? at.% Ir, Laves phase, ?), Ir Eutectic (degenerated) α-Yb_5Ir_3–γ-Yb (~819 °C, ?) Miscibility gap in the liquid state (critical point—?; from ~65 to 95 at.% Ir at ~1410 °C)	–	[13, 15, 21, 160–161, 203]
Ir–Lu	α-Lu, β-Lu, Lu_3Ir (incongruent melt. point, invariable compos.), Lu_5Ir_2 (incongruent melt. point, invariable compos.), α-Lu_5Ir_3 (?), β-Lu_5Ir_3 (incongruent melt. point), Lu_3Ir_2 (incongruent melt. point, invariable compos.), LuIr (congruent melt. point, invariable compos.), $LuIr_{2\pm x}$ (congruent melt. point, homog. range—~66–68 at.% Ir, Laves phase), Ir Eutectic Lu_3Ir–β-Lu (?) Eutectic $LuIr_{2\pm x}$–LuIr (?) Eutectic $LuIr_{2\pm x}$–Ir (?)	–	[13, 15, 21, 69, 143, 162]
Actinides			
Ir–Ac	No data	–	–
Ir–Th	α-Th, β-Th, Th_7Ir_3 (<~1600 °C, congruent melt. point, invariable compos.), $ThIr_{1-x}$ ($x \approx 0.33$–0.45, ~1460–1600 °C, incongruent melt. point, invariable compos., ?), ThIr (<1900 °C, congruent melt. point, invariable compos.), $ThIr_{2\pm x}$ (<at least ~2000 °C, congruent melt. point, variable compos., Laves phase, ?), $ThIr_3$ (<2280 °C, congruent melt. point, invariable compos., ?), $ThIr_5$ (<2260 °C, congruent melt. point, invariable compos.), Ir	The solubility of Ir in Th is negligible.	[13, 15, 21, 77, 207]

(continued)

Table 9.3 (continued)

System	Type of phase diagram (constituent phases, temperatures, and compositions of transformations)	Character of interaction	References
	Eutectic Th_7Ir_3–α-Th (~1325–1350 °C, ~15 at.% Ir) Eutectic Th_7Ir_3–$ThIr_{1-x}$ (~1450–1475 °C, 35 at.% Ir) Eutectic $ThIr_{2\pm x}$–ThIr (~1500–1800 °C, ~57 at.% Ir) Eutectic $ThIr_5$–$ThIr_3$ (2150 °C, 80 at.% Ir) Eutectic $ThIr_5$–Ir (2080 °C, ~87–90 at.% Ir, ?)		
Ir–Pa	α-Pa, β-Pa, Pa_3Ir (?), PaIr (?), $PaIr_2$ (Laves phase, ?), $PaIr_3$ (?), $PaIr_5$ (?), Ir No diagram plot	No experimental data.	[13, 167]
Ir–U	α-U, β-U, γ-U, U_3Ir (~750–945 °C, incongruent melt. point, invariable compos.), U_2Ir (<775 °C), α-U_3Ir_2 (<~900 °C, invariable compos.), β-U_3Ir_2 (~900–1120 °C, incongruent melt. point, invariable compos.), UIr (<1470 °C, congruent melt. point, invariable compos.), UIr_2 (<~1850–1875 °C, incongruent melt. point, invariable compos., Laves phase), UIr_3 (<~2000–2005 °C, congruent melt. point, invariable compos.), Ir Eutectic U_3Ir–γ-U (~915 °C, 15 at.% Ir) Eutectic UIr–UIr_2 (1450 °C, ~51 at.% Ir) Eutectic UIr_3–Ir (1950 °C, ~80–85 at.% Ir)	The solubility of U in Ir is ~3.0–6.5 at.% at 1950 °C. The max. solid solubilities of Ir in U modifications are following: in α-U—< 0.3 at.%, in β-U—~0.4–2.0 at.% and in γ-U—~5.5–6.5 at.%.	[13, 15, 21, 201]
Ir–Np	α-Np, β-Np, γ-Np, $NpIr_2$ (Laves phase, ?), Ir No diagram plot	–	[166–167]
Ir–Pu	α-Pu, β-Pu, γ-Pu, δ-Pu, δ′-Pu, ε-Pu, Pu_3Ir (?), Pu_5Ir_3 (?), Pu_5Ir_4 (?), $PuIr_2$ (Laves phase, ?), $PuIr_3$ (?), Ir No diagram plot	–	[13, 78–79]

(continued)

Table 9.3 (continued)

System	Type of phase diagram (constituent phases, temperatures, and compositions of transformations)	Character of interaction	References
Ir–Am	α-Am, β-Am, γ-Am, Am_xIr (?), $AmIr_2$ (Laves phase, ?), Ir No diagram plot	–	[167]
Ir–Cm	α-Cm, β-Cm, $CmIr_2$ (Laves phase, ?), Ir No diagram plot	–	[167]
Ir–Bk	α-Bk, β-Bk, $BkIr_2$ (Laves phase, ?), Ir No diagram plot	–	[168]
Ir–Cf	No data	–	–
Group 4			
Ir–Ti	α-Ti, β-Ti, $Ti_{3-x}Ir$ (<1515 °C, incongruent melt. point, homog. range—~25–27 at.% Ir), α-$TiIr_{1\pm x}$ (<~1745 °C, homog. range—from ~39–40 to ~55–57.5 at.% Ir), β-$TiIr_{1\pm x}$ (<~2130 °C, congruent melt. point, homog. range—from ~35–41 to ~45–57.5 at.% Ir), $TiIr_{3\pm x}$ (<~2115–2125 °C, incongruent melt. point, homog. range—from ~73–74 to ~76–77 at.% Ir), Ir Extended solid solution based on β-Ti (up to ~15 at.% Ir at ~1470 °C) Extended solid solution based on Ir (up to ~11 at.% Ti at ~2115–2125 °C) Eutectic $Ti_{3-x}Ir$–β-Ti (~1470 °C, ~17 at.% Ir) Eutectic β-$TiIr_{1\pm x}$–$TiIr_{3\pm x}$ (2000 °C, ~60.5 at.% Ir)	The presence of Ir diminishes the melt. point of Ti and temp. of α-Ti–β-Ti polymorphic transformation. The max. solid solubility of Ir in β-Ti is ~15 at.% at ~1470 °C. The max. solubility of Ir in α-Ti is ~1 at.% at 720 °C, and that of Ti in Ir is ~11 at.% at ~2115–2125 °C.	[13, 15, 80, 202]
Ir–Zr	α-Zr, β-Zr, Zr_3Ir (<1305 °C, incongruent melt. point, invariable compos.), Zr_2Ir (<1340 °C, incongruent melt. point, invariable compos.), Zr_5Ir_3 (<1730 °C, incongruent melt. point, invariable compos.), α-$ZrIr_{1-x}$ (<900–950 °C, homog. range—~49–50 at.% Ir), β-$ZrIr_{1\pm x}$ (from 900–950 °C to 2050 °C, congruent melt. point, homog. range—~47–52 at.% Ir at 1870 °C), $ZrIr_2$ (<2085 °C, incongruent melt. point,	The presence of Ir diminishes the melt. point of Zr and temp. of α-Zr–β-Zr polymorphic transformation; it stabilizes β-Zr. The solid solubility of Ir in β-Zr is 5 at.% at 1240 °C; it is affected by temp. decrease very slightly. The max. solubility of Ir in α-Zr is ≤1 at.%. The solubility of Zr in Ir is ~7 at.% at 2120 °C; at lower temp. it decreases considerably.	[13, 15, 33, 81, 192, 199]

(continued)

Table 9.3 (continued)

System	Type of phase diagram (constituent phases, temperatures, and compositions of transformations)	Character of interaction	References
	invariable compos., Laves phase), $ZrIr_{3\pm x}$ (<2280 °C, congruent melt. point, homog. range—~70–81 at.% Ir at ~2085–2120 °C, ~73.5–79 at.% Ir at 1700 °C and ~74.5–78 at.% Ir at 500–700 °C), Ir Eutectic Zr_3Ir–β-Zr (1240 °C, 18 at.% Ir) Eutectic $ZrIr_2$–β-$ZrIr_{1\pm x}$ (1870 °C, ~58 at.% Ir) Eutectic $ZrIr_{3\pm x}$–Ir (2120 °C, ~87 at.% Ir)		
Ir–Hf	α-Hf, β-Hf, $Hf_{2+x}Ir$ (<~1720–1775 °C, incongruent melt. point, homog. range—~28.5–33.3 at.% Ir at 1425 °C), Hf_5Ir_3 (or Hf_3Ir_2, <~1930–1970 °C, incongruent melt. point, invariable compos.), $HfIr_{1+x}$ (or $Hf_{47}Ir_{53}$, <~2410–2440 °C, congruent melt. point corresp. to compos. $HfIr_{1.0}$, homog. range—~50–57 at.% Ir at 2085 °C and ~50–53 at.% Ir at 1200 °C), $HfIr_{3+x}$ (<~2460–2470 °C, congruent melt. point corresp. to compos. $HfIr_{3.0}$, homog. range—~75–81 at.% Ir at 2250 °C and ~75–76 at.% Ir at 1600 °C), Ir Eutectic $Hf_{2+x}Ir$–β-Hf (~1425–1470 °C, ~16–18 at.% Ir) Eutectic $HfIr_{1+x}$–$HfIr_{3+x}$ (~2085–2130 °C, ~61–63 at.% Ir) Eutectic $HfIr_{3+x}$–Ir (~2250–2290 °C, ~86–88 at.% Ir)	The presence of Ir diminishes the melt. point of Hf and temp. of α-Hf–β-Hf polymorphic transformation and stabilizes β-Hf. The max. solid solubility of Ir in β-Hf is ~10 at.% at 1425 °C, and in α-Hf it is ~1 at.% at 1375–1380 °C. The max. solid solubility of Hf in Ir is ~9 at.% at 2250 °C; at lower temp. the solubility decreases considerably.	[12, 15, 47, 82, 198]

(continued)

Table 9.3 (continued)

System	Type of phase diagram (constituent phases, temperatures, and compositions of transformations)	Character of interaction	References
Group 5			
Ir–V	V, $V_{3\pm x}Ir$ (<~1900–1960 °C, congruent melt. point, homog. range—24.5–39 at.% Ir at 1400–1800 °C), VIr_{1+x} (≤at least 1880 °C, incongruent melt. point, homog. range—50–51.5 at.% Ir), $V_{1-x}Ir_{1+x}$ (or $(V_{1-x}Ir_x)Ir$, $0.04 < x < 0.19$, ≤at least 1900 °C, incongruent melt. point, homog. range—52–59.5 at.% Ir), $VIr_{3\pm x}$ (≤at least 2000 °C, incongruent melt. point, homog. range—~61–77.5 at.% Ir at ~1900 °C and 63–77.5 at.% Ir at ~1000 °C), Ir Extended solid solution based on V (≤at least 1900 °C, up to ~20.5–22.5 at.% Ir at 1850–1950 °C) Extended solid solution based on Ir (up to 19 at.% V at 2100 °C) Eutectic $V_{3\pm x}Ir$–(V,Ir) extended solid solution (~1870–1930 °C, 23 at.% Ir) Eutectic $V_{3\pm x}Ir$–VIr_{1+x} (~1820–1880 °C, 45 at.% Ir)	The presence of Ir (<~15 at.%) increases the melt. point of V slightly. The max. solid solubility of Ir in V is ~20.5–22.5 at.% at 1850–1950 °C, and that of V in Ir is 19 at.% at 2100 °C. At lower temp. the mutual solubilities decrease.	[13, 15, 83]
Ir–Nb	See Nb–Ir in Table 8.5.		
Ir–Ta	See Ta–Ir in Table 6.3.		
Group 6			
Ir–Cr	Cr, β-$Cr_{3\pm x}Ir$ (<1740–1760 °C, incongruent melt. point, homog. range—~17–26 at.% Ir at 1680 °C and ~18–28 at.% Ir at 1000 °C), ε-$CrIr_{1\pm x}$ (<2150–2250 °C, incongruent melt. point, homog. range—from ~32–42 to ~70 at.% Ir at higher temp. and ~40–68 at.% Ir at 1000–1100 °C), Ir Extended solid solution based on Cr (up to 12–13 at.% Ir at 1680 °C) Extended solid solution based on Ir (up to 27 at.% Cr at 2150–2250 °C) Eutectic (Cr,Ir) extended solid solution—β-$Cr_{3\pm x}Ir$ (~1670–1690 °C, ~15 at.% Ir)	The solubility of Ir in Cr is 12–13 at.% at 1680 °C, ~6 at.% at 1100 °C and 2.5 at.% at 900 °C. The solubility of Cr in Ir is 27 at.% at 2150–2250 °C; it is slightly affected by temp.	[12, 15, 84–85]

(continued)

Table 9.3 (continued)

System	Type of phase diagram (constituent phases, temperatures, and compositions of transformations)	Character of interaction	References
Ir–Mo	See Mo–Ir in Table 7.4.		
Ir–W	See W–Ir in Table 3.5.		
Group 7			
Ir–Mn	α-Mn, β-Mn, γ-Mn, δ-Mn, $Mn_{3\pm x}Ir$ (or γ′-Mn, ordered phase, <~850–950 °C, homog. range—~15–35 at.% Ir, ?), α-$MnIr_{1\pm x}$ (≤at least ~940–1300 °C, homog. range—~36–56 at.% Ir, ?), β-$MnIr_{1\pm x}$ (at least at ~940–1300 °C, homog. range—~36–56 at.% Ir, ?), Ir Extended solid solution based on γ-Mn (up to ~35 at.% Ir at 500–1000 °C) Extended solid solution based on Ir (up to ~48 at.% Mn at 1350 °C)	The max. solid solubilities of Ir in Mn modifications are: δ-Mn—~1.5 at.%, γ-Mn—~35 at.% (500–1000 °C), in β-Mn—~2.5 at.% and in α-Mn—~4.5 at.%. The max. solid solubility of Mn in Ir is ~48 at.% at 1350 °C; it declines to 40 at.% at 500 °C.	[13, 15, 169, 195]
Ir–Tc	Tc, no binary compounds, Ir Extended solid solution based on Tc (up to ~70 at.% Ir) Extended solid solution based on Ir (≤25 at.% Tc) Peritectic Tc (~2200–2300 °C, ~70 at.% Ir, ?)	At 1050 °C the solubility of Ir in Tc is ~70 at.%, and that of Tc in Ir is ≤25 at.% at ~2200–2300 °C. Alloy containing 25 at.% Tc is two-phase structured.	[13, 15, 86]
Ir–Re	See Re–Ir in Table 4.5.		
Group 8			
Ir–Fe	α-Fe, γ-Fe, δ-Fe, ε-$Fe_3Ir_{2\pm x}$ (<~625 °C, homog. range—~19–50 at.% Ir at 440 °C and ~21–61 at.% Ir at 200 °C), Ir Continuous solid solution γ-Fe–Ir Peritectic δ-Fe (~1540–1545 °C, ~2.5–2.8 at.% Ir)	The presence of Ir raises the melt. temp. of Fe and temp. of δ-Fe–γ-Fe polymorphic transformation. The max. solubility of Ir in α-Fe is ~8 at.% at ~440 °C and that in δ-Fe is 2.5–2.8 at.% at ~1545 °C.	[12, 15, 34–35, 87–88]
Ir–Ru	Ru, no binary compounds, Ir Extended solid solution based on Ru (up to 49 at.% Ir at ~2350–2395 °C) Extended solid solution based on Ir (up to 45 at.% Ru at ~2350–2395 °C) Peritectic Ru (~2350–2395 °C, 49 at.% Ir)	The solubility of Ir in Ru is 49 at.% at ~2350–2395 °C and ~42–48 at.% at 2000 °C, and that of Ru in Ir is 45 at.% at ~2350–2395 °C and ~42.5 at.% at 2000 °C.	[13, 15, 21, 89–90, 200]
Ir–Os	See Os–Ir in Table 5.3.		

(continued)

Table 9.3 (continued)

System	Type of phase diagram (constituent phases, temperatures, and compositions of transformations)	Character of interaction	References
Group 9			
Ir–Co	ε-Co, α-Co, $Co_{3\pm x}Ir$ (ordered phase, <∼900 °C, homog. range—20–30 at.% Ir at 500–700 °C), $CoIr_{3\pm x}$ (ordered phase, <∼1300 °C, homog. range—70–80 at.% Ir at 500–1100 °C), Ir Continuous solid solution α-Co–Ir Extended solid solution based on ε-Co (up to ∼70 at.% Ir at 0 °C)	The presence of Ir diminishes the melt. point of Co. For diffusion rate in the system at various temp. see Addendum.	[12, 15]
Ir–Rh	Rh, no binary compounds, Ir Continuous solid solution Rh–Ir (up to melt. points, miscibility gap: critical point—∼850 °C, ∼50 at.% Ir; from ∼9 to 90 at.% Ir at 400 °C)	–	[13, 15, 21, 52, 209]
Group 10			
Ir–Ni	Ni, $Ni_{3\pm x}Ir$ (ordered phase, <∼1150 °C, homog. range—∼20–30 at.% Ir at ∼1000 °C), $NiIr_{1\pm x}$ (ordered phase, <∼1300 °C, homog. range—∼45–55 at.% Ir at ∼1100 °C), $NiIr_{3\pm x}$ (ordered phase, <∼1450 °C, homog. range—70–80 at.% Ir at ∼1300 °C), Ir Continuous solid solution Ni–Ir	–	[13, 15, 91–92]
Ir–Pd	Pd, no binary compounds, Ir Continuous solid solution Pd–Ir (up to melt. points, miscibility gap: critical point—∼1470–1480 °C, ∼49–50.5 at.% Ir; from ∼3 to ∼85–98 at.% Ir at 700 °C, ?) Extended solid solution based on Ir (up to ∼25 at.% Pd at ∼1735–1785 °C, ?) Extended solid solution based on Pd (up to 27 at.% Ir at ∼1735–1785 °C, ?) Peritectic Pd (∼1735–1785 °C, ∼27 at.% Ir, ?) Data on the system available in literature are controversial.	The data on the mutual solubilities of the components available in literature are controversial.	[13, 15–16, 21, 45, 93–94, 206]

(continued)

Table 9.3 (continued)

System	Type of phase diagram (constituent phases, temperatures, and compositions of transformations)	Character of interaction	References
Ir–Pt	Pt, no binary compounds, Ir Continuous solid solution Pt–Ir (up to melt. points, miscibility gap: critical point—~960–1300 °C (?), 50 at.% Ir; 7–99 at.% Ir at 700 °C)	–	[13, 15, 95–96, 196]
Group 11			
Ir–Cu	Cu, no binary compounds, Ir Peritectic Cu (~1135–1145 °C, ~8 at.% Ir)	The solid solubility of Ir in Cu is ~8 at.% at peritectic temp., 6.5 at.% at 1020 °C, 5.5 at.% at 860 °C and 3.1 at.% at 700 °C. The solid solubility of Cu in Ir is 6.3 at.% at 1850 °C, 5.1 at.% at 1400 °C, 3.2 at.% at 1200 °C, 3.0 at.% at 1090 °C and 1.4 at.% at 800 °C. At peritectic temp. the max. solubility of Ir in liquid Cu is ~4 at.%. For diffusion rate in the system at various temp. see Addendum.	[12, 15, 97–99, 171]
Ir–Ag	Ag, no binary compounds, Ir Eutectic (degenerated) Ag–Ir (~961 °C, ~0.1 at.% Ir, ?) Miscibility gap in the liquid state: critical point—~3200 °C, ~51 at.% Ir; ~12–90 at.% Ir at ~2320 °C	The solid solubility of Ir in Ag is ≤0.3 at.%. Near the melt. point liquid Ag dissolves ~0.1 at.% Ir. The solid solubility of Ag in Ir is ≤1.8 at.%.	[14–15, 100–101]
Ir–Au	Au, no binary compounds, Ir Peritectic Au (~1065 °C, ~1.5 at.% Ir, ?) Miscibility gap in the liquid state: ~7.5–91 at.% Ir at ~2370 °C (?)	The solid solubility of Ir in Au is ≤0.1 at.% (?), and that of Au in Ir is ≤2 at.%. For diffusion rate in the system at various temp. see Addendum.	[14, 102–103]
Group 12			
Ir–Zn	Zn, $Zn_{11}Ir_2$ (?), ZnIr (?), Ir No diagram plot	At 470–620 °C Ir is not resistant to corrosion in liquid Zn (6 h exposure); Zn penetrates along the grain boundaries and dissolves Ir.	[13, 170]

(continued)

Table 9.3 (continued)

System	Type of phase diagram (constituent phases, temperatures, and compositions of transformations)	Character of interaction	References
Ir–Cd	No data	–	–
Ir–Hg	Hg, no binary compounds, Ir	No interaction. The solubility of Ir in Hg is extremely low; at 25 °C the estimated value is $\sim 10^{-9}$–10^{-25} at.% Ir.	[12, 104, 143, 172]
Group 13			
Ir–B	β-B, IrB_{50} (?), IrB_2 (?), $Ir_2B_{3\pm x}$ (or $IrB_{1.50}$, <1300–1330 °C, congruent melt. point, homog. range—$\sim$38–41 at.% Ir at 1230–1250 °C), Ir_3B_{4+x} ($x = 0.02$, or $IrB_{1.35}$, $<\sim$1600 °C, congruent melt. point, invariable compos., ?), Ir_4B_5 (or $Ir_2B_{2.5}$, ?), α-IrB_{1+x} ($x = 0.1$, or α-IrB_{2-y}, invariable compos., ?), β-IrB_{1+x} ($x = 0.1$, or β-IrB_{2-y}, congruent melt. point, invariable compos., ?), α-IrB_{1-x} ($x \approx 0.10$–0.11, $\leq$1100 °C, ?), β-IrB_{1-x} ($x \approx 0.10$–0.11, $\sim$1100–1340 °C, homog. range—$\sim$51–54 at.% Ir at 1240–1260 °C, ?), $Ir_3B_{2\pm x}$ (<1260–1300 °C, homog. range—$\sim$59–62 at.% Ir at 1245–1255 °C, ?), Ir Eutectic β-IrB_{1+x}–Ir_3B_{4+x} ($\sim$900–1000 °C, $\sim$44–45 at.% Ir, ?) Eutectic β-IrB_{1-x}–$Ir_2B_{3\pm x}$ ($\sim$1240–1260 °C, $\sim$48–50 at.% Ir) Eutectic β-IrB_{1-x}–$Ir_3B_{2\pm x}$ ($\sim$1230–1245 °C, $\sim$55–59 at.% Ir) Eutectic Ir_3B_{4+x}–β-B ($\sim$1000–1100 °C, $\sim$35–36 at.% Ir, ?) Eutectic $Ir_2B_{3\pm x}$–β-B ($\sim$1230–1250 °C, $\sim$34 at.% Ir, ?) Eutectic β-IrB_{1+x}–Ir ($<\sim$1000–1100 °C, $\sim$53–55 at.% Ir, ?) Eutectic $Ir_3B_{2\pm x}$–Ir ($<\sim$1245–1255 °C, $\sim$63–5 at.% Ir, ?) Data on the system available in literature are controversial.	The solid solubility of B in Ir is $\leq$1 at.%.	[11, 14, 43, 46, 105–107, 114, 130, 136–137]

(continued)

Table 9.3 (continued)

System	Type of phase diagram (constituent phases, temperatures, and compositions of transformations)	Character of interaction	References
Ir–Al	Al, Ir_2Al_9 (<900 °C, incongruent melt. point, invariable compos.), Ir_4Al_{13} (<1015 °C, incongruent melt. point, invariable compos.), $IrAl_3$ (<1450 °C, incongruent melt. point, invariable compos.), Ir_2Al_{5-x} (<~1615 °C, incongruent melt. point, homog. range—~26.5–28.0 at.% Ir), $IrAl_{1\pm x}$ (2120 °C, congruent melt. point, homog. range—~48–52 at.% Ir), Ir Eutectic (degenerated) Ir_2Al_9–Al (~650 °C, ?) Eutectic $IrAl_{1\pm x}$–Ir (~2020 °C, ~69 at.% Ir)	The max. solid solubility of Al in Ir is 18 at.% at ~2020 °C.	[14–15, 36, 190, 193]
Ir–Ga	Ga, $IrGa_6$, Ir_2Ga_9, α-$IrGa_3$, β-$IrGa_3$, $IrGa_2$, Ir_3Ga_5, IrGa, Ir No diagram plot	–	[12, 108–112, 173, 194]
Ir–In	In, α-$IrIn_{3+x}$ (<~350–360 °C, homog. range—~24–25 at.% Ir at 160–340 °C), β-$IrIn_{3+x}$ (<~980–985 °C, incongruent melt. point, homog. range—~23.5–25.0 at.% Ir at 360 °C), $IrIn_{2\pm x}$ (<~1185–1195 °C, incongruent melt. point, homog. range width—~30.8–38.4 at.% Ir), Ir_2In_3 (?), $IrIn_{1+x}$ (metastable, ?), Ir_3In (?), Ir Peritectic In (156.8 °C, ?)	The max. solid solubility of In in Ir is 3.8 at.% at ~1190 °C.	[13, 143, 174–176, 186–189]
Ir–Tl	α-Tl, β-Tl, $IrTl_3$ (?), $IrTl_2$ (?), IrTl (?), Ir_2Tl (Laves phase, ?), Ir_3Tl (?), Ir No diagram plot	No experimental data.	[13, 17]

(continued)

Table 9.3 (continued)

System	Type of phase diagram (constituent phases, temperatures, and compositions of transformations)	Character of interaction	References
Group 14			
Ir–C	See C–Ir in Table 2.13.		
Ir–Si	Si, α-$IrSi_{3-x}$ (?), β-$IrSi_{3-x}$ ($x \approx 0.4$, <975 °C, invariable compos., ?), γ-$IrSi_{3-x}$ ($x \approx 0.4$, 975–1260 °C, incongruent melt. point, invariable compos.), $IrSi_2$ (invariable compos., ?), Ir_3Si_5 (<~1400 °C, incongruent melt. point, invariable compos.), Ir_2Si_3 (or $IrSi_{\sim 1.5}$, invariable compos., ?), Ir_3Si_4 (<~1410 °C, incongruent melt. point, invariable compos.), Ir_4Si_5 (<1315 °C, incongruent melt. point, invariable compos.), IrSi (<~1710 °C, congruent melt. point, invariable compos.), Ir_3Si_2 (or $Ir_{1.5}Si$, <~1450 °C, congruent melt. point, invariable compos.), Ir_2Si (~1265–1450 °C, incongruent melt. point, invariable compos.), Ir_3Si (<1545 °C, incongruent melt. point, invariable compos.), Ir Eutectic Ir_3Si_2–Ir_2Si (~1415 °C, ~38 at.% Ir) Eutectic Ir_3Si_2–IrSi (1425 °C, 40.5 at.% Ir) Eutectic γ-$IrSi_3$–Si (~1220 °C, 80.5 at.% Ir) Eutectic Ir_3Si–Ir (1470 °C, ~90.5 at.% Ir, ?) Data on the system available in literature are controversial.	The max. solid solubility of Si in Ir is ~2 at.% at 1545 °C. Ir silicides are formed directly from the elements in vacuum or inert gas atmosphere at 1000–1200 °C.	[11, 13, 25, 37–39, 43, 113–114, 177–179, 191]
Ir–Ge	Ge, $IrGe_4$, Ir_3Ge_7, Ir_3Ge_4, Ir_4Ge_5, IrGe, Ir No diagram plot	Ir germanides are formed directly from the elements.	[11–12, 25–26, 115]
Ir–Sn	α-Sn, β-Sn, α-$IrSn_4$, β-$IrSn_4$, $IrSn_3$, Ir_3Sn_7 (?), $IrSn_2$, Ir_5Sn_7, IrSn (?), Ir No diagram plot	Ir does not dissolve in liquid Sn (?).	[13, 21, 116, 180–181]
Ir–Pb	Pb, $IrPb_3$ (?), $IrPb_2$ (Laves phase, ?), IrPb (incongruent melt., ?), Ir_2Pb (Laves phase, ?), Ir_3Pb (?), Ir No diagram plot	–	[13]

(continued)

Table 9.3 (continued)

System	Type of phase diagram (constituent phases, temperatures, and compositions of transformations)	Character of interaction	References
Group 15			
Ir–N	N, IrN_3 (?), IrN_2 (?), Ir No diagram plot	No interaction between Ir and N_2 at least at 900–2150 °C. Ir nitrides are superhard hypothetical structures.	[13, 182–183]
Ir–P	P, IrP_3 (at least at 500–1200 °C, invariable compos.), IrP_2 (<1230 °C, sublimation point, invariable compos.), Ir_2P (<1310–1360 °C, congruent melt. point, invariable compos.), Ir Eutectic Ir_2P–Ir (∼1260 °C, ∼76 at.% Ir)	Ir phosphides are formed directly from the elements in sealed ampules at 1100 °C.	[11, 13, 15, 43, 114, 117–118]
Ir–As	As, $IrAs_3$ (<∼1000–1200 °C, decompos. point), $IrAs_{3-x}$ (or $IrAs_{2+x}$, ?), $IrAs_2$, IrAs (?), Ir No diagram plot	Ir arsenides are formed directly from the elements in sealed ampules.	[11, 14, 119–120, 123–124]
Ir–Sb	Sb, $IrSb_3$ (<∼900–1140 °C, incongruent melt. point, invariable compos.), $IrSb_2$ (<1445–1505 °C, incongruent melt. point, invariable compos.), IrSb (<1620–1670 °C, incongruent melt. point, invariable compos.), Ir Eutectic (degenerated) $IrSb_3$–Sb (∼615–625 °C, ?)	Ir antimonides are formed directly from the elements in sealed ampules in Ar atmosphere.	[13, 15, 121–124, 184, 197]
Ir–Bi	Bi, $IrBi_3$ (<∼400–700 °C, incongruent melt. point, invariable compos., ?), $IrBi_2$ (<∼700–900 °C, incongruent melt. point, invariable compos., ?), IrBi (<∼1420 °C, congruent melt. point, invariable compos., ?), Ir_2Bi (<∼1440 °C, incongruent melt. point, invariable compos.), Ir Eutectic IrBi–Ir_2Bi (1410 °C, ∼52–55 at.% Ir) Eutectic (degenerated) $IrBi_3$–Bi (∼265 °C, ∼0.7 at.% Ir)	The solid solubility of Ir in Bi is ∼0.25 at.%.	[14, 125]

(continued)

Table 9.3 (continued)

System	Type of phase diagram (constituent phases, temperatures, and compositions of transformations)	Character of interaction	References
Group 16			
Ir–O	O, IrO_3 (gaseous), IrO_{3-x} ($x \approx 0.3$, ?), IrO_2 (<~750–1220 °C, decompos. point), Ir_2O_3 (<~400 °C, decompos. point), Ir No diagram plot	In O_2 the oxidation of Ir initiates from ~300 °C and leads to the direct formation of IrO_2. Ir_2O_3 and IrO_3 are formed by indirect reaction pathways.	[2, 11, 13, 21, 44, 126, 131]
Ir–S	α-S, β-S, IrS_3 (<~700 °C, decomposes), Ir_3S_8 (?), IrS_2 (<~700 °C, decomposes), IrS_{2-x} ($x \approx 0.1$, ?), Ir_2S_3 (?), IrS (<~750 °C, decomposes), Ir No diagram plot	Ir_3S_8, IrS_2 and Ir_2S_3 are formed by the direct interaction between Ir and S.	[11, 13, 21, 27, 185]
Ir–Se	Se, α-$IrSe_{3-x}$ (?), β-$IrSe_{3-x}$ (?), $IrSe_{2-x}$ ($x \approx 0.09 \div 0.1$), Ir_2Se_3, Ir No diagram plot	Needle-shape $IrSe_{2-x}$ microrods with max. thickness—6 μm, max. width—17 μm and 20 mm in length were synthesized.	[11, 13, 41, 135]
Ir–Te	Te, Ir_3Te_8 (<at least 600 °C, invariable compos., ?), $IrTe_{2+x}$ (?), $IrTe_2$ (<at least 600 °C, invariable compos., in equilibrium with Ir, ?), IrTe (at least at 400–600 °C, invariable compos.), Ir Peritectic Te (~450 °C, ?)	–	[11, 13, 15, 42, 127, 143]
Ir–Po	No data	–	–
Group 17			
Ir–F	F, α-IrF_6 (?), β-IrF_6 (<44 °C, melt. point), IrF_5 (or Ir_4F_{20}, $(IrF_5)_4$, <104 °C, melt. point), IrF_4, IrF_3, Ir No diagram plot	The direct interaction between Ir and F_2 at ~360 °C results in the formation of IrF_5; at lower temp. IrF_6 and IrF_3 are formed. IrF_4 is synthesized by indirect reaction pathways.	[2–3, 11, 43]
Ir–Cl	Cl, $IrCl_4$, α-$IrCl_3$ (or α-Ir_2Cl_6, <~650 °C), β-$IrCl_3$ (~650–765 °C, ?), $IrCl_2$, IrCl (~775–800 °C, decomposes), Ir No diagram plot	The direct interaction between Ir and Cl_2 results in the formation of $IrCl_3$ at ~600 °C, $IrCl_4$ at 600–700 °C, $IrCl_2$ at ~765–775 °C and IrCl at ~770–775 °C.	[2–3, 11, 43]
Ir–Br	Br, $IrBr_4$, $IrBr_3$, $IrBr_2$, Ir No diagram plot	The direct interaction between Ir and Br_2 results in the formation of $IrBr_2$.	[2–3, 11, 43]

(continued)

Table 9.3 (continued)

System	Type of phase diagram (constituent phases, temperatures, and compositions of transformations)	Character of interaction	References
Ir–I	I, IrI_4 (<~100 °C, decomposes), IrI_3 (<427 °C, decompos. point), $IrI_{2\pm x}$ (variable compos.), IrI, Ir No diagram plot	The direct interaction between Ir and I_2 results in the formation of IrI_3.	[2–3, 11]
Ir–At	No data	–	–

[a] The intervals of temperatures and compositions for the melting and invariant equilibria points, homogeneity ranges, and thermal stability regions of constituent phases are given taking into account the minimal and maximal values (data spread) available in literature

The data on the selected ternary, quaternary and quasi-binary iridium containing systems, which are the most important for the design, manufacture, and application of ultra-high temperature materials, are summarized in Table 9.4. The composition and temperature stability regions for the main binary and ternary iridium containing high-temperature phases are given in Tables 9.3 and 9.4 taking into account the spread of numerical magnitudes available in the literature currently.

Table 9.4 Chemical interaction of iridium with elements and compounds at high temperatures (selected ternary, quaternary and quasi-binary systems in alphabetical order)[a]

System	Type of phase diagram (temperature and composition sections, constituent phases or phase fields) and/or character of interphase interaction and materials compatibility	References
Ir–Al–B	Plotted partially at 1000 °C: Ir_3AlB_{1+x} (~25 at.% B), Ir_3B_{4+x}, α-IrB_{1+x}, β-IrB_{1+x}, α-IrB_{1-x}, β-IrB_{1-x}, Ir_3B_2, Ir_2Al_9, Ir_4Al_{13}, $IrAl_3$, Ir_2Al_{5-x}, $IrAl_{1\pm x}$, β-B, Al, Ir	[130]
Ir–Al–C	See C–Al–Ir in Table 2.14	
Ir–Al–Nb	See Nb–Al–Ir in Table 8.6	
Ir–Al–Nb–Ni	See Nb–Al–Ir–Ni in Table 8.6	
Ir–Al–Nb–Pt	See Nb–Al–Ir–Pt in Table 8.6	
Ir–Al–Ta	See Ta–Al–Ir in Table 6.4	
Ir–B–C–Th	See C–B–Ir–Th in Table 2.14	
Ir–B–Hf	Plotted partially at 1100 °C: $HfIr_3B_4$, $HfIr_{\sim 3}B_{\sim 2}$, $HfIr_{\sim 5}B_{\sim 4}$, $Hf_3Ir_5B_2$, $HfIr_{30}B_{19}$ (?), $HfIr_{3+x}(B_y)$ (extended solid solution based on $HfIr_{3+x}$—up to 8 at.% B), $HfB_{2\pm x}$ (<3250–3410 °C), $HfB_{1\pm x}$ (<2100 °C), $Hf_{2+x}Ir$, Hf_5Ir_3, $HfIr_{1+x}$, Ir_3B_{4+x}, α-IrB_{1+x}, β-IrB_{1+x}, α-IrB_{1-x}, β-IrB_{1-x}, Ir_3B_2, β-B, α-Hf, β-Hf, Ir The mutual solid solubilities of all the binary phases are low, with the exception of $HfIr_{3+x}$. $HfB_{2\pm x}$ cannot coexist with metal Ir.	[136–137]
Ir–B–Mo	See Mo–B–Ir in Table 7.5	

(continued)

Table 9.4 (continued)

System	Type of phase diagram (temperature and composition sections, constituent phases or phase fields) and/or character of interphase interaction and materials compatibility	References
Ir–B–Sc	No diagram plot $ScIr_3B_{1-x}$, $ScIr_3B_4$	[136, 138]
Ir–B–W	See W–B–Ir in Table 3.6	
Ir–B–Zr	Plotted partially at 1100 °C: $ZrIr_3B_{4-x}$ ($0 \le x \le 0.26$), $ZrIr_{\sim 3}B_{\sim 2}$, $ZrIr_{\sim 5}B_{\sim 4}$, $ZrIr_{3\pm x}(B_y)$ (extended solid solution based on $ZrIr_{3\pm x}$—up to 8–9 at.% B), $ZrB_{2\pm x}$ (<3225–3265 °C), ZrB_{12} (~1695–2290 °C), Zr_3Ir, Zr_2Ir, Zr_5Ir_3, α-$ZrIr_{1-x}$, β-$ZrIr_{1\pm x}$, $ZrIr_2$, Ir_3B_{4+x}, α-IrB_{1+x}, β-IrB_{1+x}, α-IrB_{1-x}, β-IrB_{1-x}, Ir_3B_2, β-B, α-Zr, β-Zr, Ir The mutual solid solubilities of all the binary phases are low, with the exception of $ZrIr_{3\pm x}$. $ZrB_{2\pm x}$ cannot coexist with metal Ir.	[136]
Ir–C–Ce	See C–Ce–Ir in Table 2.14	
Ir–C–Cr	See C–Cr–Ir in Table 2.14	
Ir–C–Er	See C–Er–Ir in Table 2.14	
Ir–C–Hf	See C–Hf–Ir in Table 2.14	
Ir–C–Mo	See C–Ir– Mo in Table 2.14	
Ir–C–Nb	See C–Ir–Nb in Table 2.14	
Ir–C–Rh	See C–Ir–Rh in Table 2.14	
Ir–C–Sc	See C–Ir–Sc in Table 2.14	
Ir–C–Si	See C–Ir–Si in Table 2.14	
Ir–C–Ta	See C–Ir–Ta in Table 2.14	
Ir–C–Th	See C–Ir–Th in Table 2.14	
Ir–C–Ti	See C–Ir–Ti in Table 2.14	
Ir–C–U	See C–Ir–U in Table 2.14	
Ir–C–V	See C–Ir–V in Table 2.14	
Ir–C–W	See C–Ir–W in Table 2.14	
Ir–C–Y	See C–Ir–Y in Table 2.14	
Ir–C–Zr	See C–Ir–Zr in Table 2.14	
Ir–Ca–O	IrO_2–CaO is plotted: $CaIrO_3$ (or $CaO{\cdot}IrO_2$, <1135 °C), Ca_2IrO_4 (or $2CaO{\cdot}IrO_2$, <1170 °C), Ca_4IrO_6 (or $4CaO{\cdot}IrO_2$, <1240 °C) Ir–IrO_2–CaO (in air) is plotted at 1020–1240 °C: $CaIrO_3$, Ca_2IrO_4, Ca_4IrO_6	[131–134]
Ir–Co–Ta	See Ta–Co–Ir in Table 6.4	
Ir–Fe–Os	See Os–Fe–Ir in Table 5.4	
Ir–Ga–Nb	See Nb–Ga–Ir in Table 8.6	
Ir–H–Nb	See Nb–H–Ir in Table 8.6	
Ir–H–Ta	See Ta–H–Ir in Table 6.4	
Ir–Hf–Nb	See Nb–Hf–Ir in Table 8.6	
Ir–Hf–Os	See Os–Hf–Ir in Table 5.4	
Ir–Hf–Zr	Plotted schematically and partially at 1800 and 2000 °C: $(Hf,Zr)Ir_{3\pm x}$ ($HfIr_{3+x}$–$ZrIr_{3\pm x}$ continuous solid solution), $(Hf,Zr)Ir_{1\pm x}$ ($HfIr_{1+x}$–β-$ZrIr_{1\pm x}$ continuous solid solution, ?) The solubility of Hf + Zr in metal Ir is ~6 at.%. $(Hf,Zr)Ir_{3\pm x}$ contains >25 at.% Hf + Zr. A dual-phase (Ir,Hf,Zr)–$(Hf,Zr)Ir_{3\pm x}$ field exists with ~6–25 at.% Hf + Zr.	[129, 211]

(continued)

Table 9.4 (continued)

System	Type of phase diagram (temperature and composition sections, constituent phases or phase fields) and/or character of interphase interaction and materials compatibility	References
Ir–Nb–Ni	See Nb–Ir–Ni in Table 8.6	
Ir–Nb–O	See Nb–Ir–O in Table 8.6	
Ir–Nb–Rh	See Nb–Ir–Rh in Table 8.6	
Ir–Nb–S	See Nb–Ir–S in Table 8.6	
Ir–Nb–Si	See Nb–Ir–Si in Table 8.6	
Ir–Nb–Ta	See Ta–Ir–Nb in Table 6.4	
Ir–Nb–Te	See Nb–Ir–Te in Table 8.6	
Ir–Nb–Ti	See Nb–Ir–Ti in Table 8.6	
Ir–Nb–Zr	See Nb–Ir–Zr in Table 8.6	
Ir–Ni–Ta	See Ta–Ir–Ni in Table 6.4	
Ir–Os–Th	See Os–Ir–Th in Table 5.4	
Ir–Os–Ti	See Os–Ir–Ti in Table 5.4	
Ir–Os–Zr	See Os–Ir–Zr in Table 5.4	
Ir–Pt–Ta	See Ta–Ir–Pt in Table 6.4	
Ir–Si–Ta	See Ta–Ir–Si in Table 6.4	
Ir–Ta–Te	See Ta–Ir–Te in Table 6.4	

[a] See notes to Table 9.3

The character of chemical interaction and general reactions of iridium with common chemicals (solids, liquids, aqueous solutions) and complex gases are summarized in Table 9.5.

Table 9.5 The interaction of iridium with some chemicals and complex gases [11, 44]

Reagent, formula	Character of chemical interaction, examples of general reactions
Air, $N_2 + O_2$	No interaction at room temp. At atmospheric pressure the oxidation of Ir initiates at ~600–700 °C: $Ir + O_2 \rightarrow IrO_2$. The weight gain of Ir sheet at 1000 °C during 50 h exposure in air amounts to 70 mg cm^{-2}. At temp. >1000 °C Ir forms volatile oxides, but it can be heated up to 2300 °C without danger of catastrophic oxidation.
Water, H_2O	No interaction at room temp., at higher temp. water vapour interacts with Ir: $Ir + 2H_2O \rightarrow IrO_2 + 2H_2$.
Sodium hydroxide, NaOH	No interaction with NaOH in aqueous solution; weak interaction with molten NaOH.
Potassium hydroxide, KOH	No interaction with KOH in aqueous solution; weak interaction with molten KOH.
Potassium nitrate with potassium hydroxide (melt), $KNO_3 + KOH$	The interaction results in the formation of iridates: $Ir + 3KNO_3 + 2(n + 1)KOH \rightarrow K_{2(n+1)}IrO_{n+4} + 3KNO_2 + (n + 1)H_2O$.

(continued)

Table 9.5 (continued)

Reagent, formula	Character of chemical interaction, examples of general reactions
Potassium chlorate with potassium hydroxide (melt), $KClO_3 + KOH$	The interaction results in the formation of iridates: $Ir + KClO_3 + 2(n + 1)KOH \rightarrow K_{2(n+1)}IrO_{n+4} + KCl + (n + 1)H_2O$.
Sodium peroxide with sodium hydroxide (melt), $Na_2O_2 + NaOH$	The interaction results in the formation of iridates: $Ir + 3Na_2O_2 + 2nNaOH \rightarrow Na_{2(n+3)}IrO_{n+6} + nH_2O$.
Potassium pyrosulfate (melt), $K_2S_2O_7$	The interaction results in the formation of potassium iridate: $Ir + 2K_2S_2O_7 \rightarrow K_2IrO_4 + K_2SO_4 + 3SO_2$.
Potassium chloride in the presence of chlorine $KCl + Cl_2$	The interaction results in the formation of dipotassium hexachloroiridate: $Ir + 2KCl + 2Cl_2 \rightarrow K_2[IrCl_6]$.
Nitric acid,	No interaction.
Sulphuric acid, H_2SO_4	No interaction.
Hydrochloric acid, HCl	No interaction.
Hydrochloric acid with nitric acid (aqua regia), $HCl + HNO_3$	No interaction.
Hydrochloric acid with nitroso-sulfonic acid, $HCl + NOHSO_3$	Intensive interaction.
Phosphoric acid, H_3PO_4	Weak interaction in the presence of O_2.

The self-diffusion characteristics of iridium atoms, diffusion characteristics in iridium containing systems in the wide range of temperatures, and summarized data on the physico-chemical interaction of iridium with elements of the periodic table are given in Addendum.

References

1. Steurer W (1996) Crystal structure of the metallic elements. In: Cahn RW, Haasen P (eds) Physical metallurgy, 4th ed., Vol. 1, pp. 1–46. Elsevier Science BV, Amsterdam
2. Cotton FA, Wilkinson G (1965) Advanced inorganic chemistry. Wiley, New York, London
3. Akhmetov NS (2001) Obschaya i neorganicheskaya khimiya (General and inorganic chemistry), 4th ed. Vysshaya Shkola, Moscow (in Russian)
4. Kotelnikov RB, Bashlykov SN, Galiakbarov ZG, Kashtanov AI (1968) Osobo tugoplavkie elementy i soedineniya (Extra refractory elements and compounds). Metallurgiya, Moscow (in Russian)
5. Zefirov AP (ed), Veryatin UD, Mashirev VP, Ryabtsev NG, Tarasov VI, Rogozkin BD, Korobov IV (1965) Termodinamicheskie svoistva neorganicheskikh veschestv (Thermodynamic properties of inorganic substances). Atomizdat, Moscow (in Russian)
6. Speight JG, ed (2005) Lange's handbook of chemistry, 16th ed. McGraw-Hill, New York
7. Lide DR, ed (2010) CRC handbook of chemistry and physics, 90th ed. CRC Press, Boca Raton, New York
8. Martienssen W (2005) The elements. In: Martienssen W, Warlimont H (eds) Springer handbook of condensed matter and materials data, pp. 45–158. Springer, Berlin, Heidelberg

9. Samsonov GV, ed (1976) Svoistva elementov (Properties of elements), 2nd ed., Vol. 1. Metallurgiya, Moscow (in Russian)
10. Cardarelli F (2008) Materials handbook, 2nd ed. Springer, London
11. Samsonov GV, ed (1976) Svoistva elementov (Properties of elements), 2nd ed., Vol. 2. Metallurgiya, Moscow (in Russian)
12. Lyakishev NP, ed (1997) Diagrammy sostoyaniya dvoinykh metallicheskikh sistem (Phase diagrams of binary metal systems), Vol. 2. Mashinostroenie, Moscow (in Russian)
13. Lyakishev NP, ed (2001) Diagrammy sostoyaniya dvoinykh metallicheskikh sistem (Phase diagrams of binary metal systems), Vol. 3, Part 1. Mashinostroenie, Moscow (in Russian)
14. Lyakishev NP, ed (1996) Diagrammy sostoyaniya dvoinykh metallicheskikh sistem (Phase diagrams of binary metal systems), Vol. 1. Mashinostroenie, Moscow (in Russian)
15. Massalski TB, Subramanian PR, Okamoto H, Kacprzak L, eds (1990) Binary alloy phase diagrams, 2nd ed. ASM International, Metals Park, Ohio
16. Savitskii EM, Polyakova VP, Gorina NB, Roshan NR (1975) Metallovedenie platinovykh metallov (Metallography of platinum metals). Metallurgiya, Moscow (in Russian)
17. Savitskii EM, Gribulya VB (1977) Prognozirovanie neorganicheskikh soedinenii s pomoschyu EVM (The prediction of inorganic compounds by means of computing). Nauka, Moscow (in Russian)
18. Papirov II (1981) Struktura i svoistva splavov berilliya (Structure and properties of beryllium alloys). Energoizdat, Moscow (in Russian)
19. Gladyshevskii EI, Bodak OI (1982) Kristallokhimiya intermetallicheskikh soedinenii redkozemelnykh metallov (The crystal chemistry of intermetallic compounds of rare earth metals). Vyshcha Shkola, Lviv (in Russian)
20. Griffin RB, Gschneidner KA, Jr (1971) Effect of the sixth period elements on the melting and transformation temperatures of praseodymium: Part I. Experimental. Metal Trans 2(9):2517–2524
21. Savitskii EM, ed (1984) Blagorodnye metally (Noble metals). Metallurgiya, Moscow (in Russian)
22. Audi G, Wapstra AH, Thibault C, Blachot J, Bersillon O (2003) The NUBASE evaluation of nuclear and decay properties. Nucl Phys A 729:3–128
23. De Laeter JR, Bohlke JK, De Bievre P, Hidaka H, Peiser HS, Rosman KJR, Taylor PDP (2003) Atomic weights of the elements. Review 2000 (IUPAC Technical report). Pure Appl Chem 75(6):683–800
24. Wieser ME (2006) Atomic weights of the elements 2005. (IUPAC Technical report). Pure Appl Chem 78(11):2051–2066
25. Gladyshevskii EI (1971) Kristallokhimiya silitsidov i germanidov (The crystal chemistry of silicides and germanides). Metallurgiya, Moscow (in Russian)
26. Samsonov GV, Bondarev VN (1968) Germanidy (Germanides). Metallurgiya, Moscow (in Russian)
27. Samsonov GV, Drozdova SV (1972) Sulfidy (Sulfides). Metallurgiya, Moscow (in Russian)
28. Degussa AG (1995) Edelmetal – Taschenbuch (Precious metal – paperback), 2nd ed. Hüthig, Heidelberg (in German)
29. Benner LS, Suzuki T, Meguro K, Tanaka S, eds (1991) Precious metals, science, technology. International Precious Metals Institute, Allentown
30. Antonov VE, Belash IT, Malyshev VYu, Ponyatovsky EG (1984) Solubility of hydrogen in the platinum metals under high pressure. Platinum Met Rev 28(4):158–163
31. Obrowski W (1963) Alloys of ruthenium with boron, beryllium and aluminium. Metall 17(2):108–112
32. Verkhorobin LF, Kovtun GP, Kruglykh AA, Matyushenko NN, Pugachev AS, Tikhinskii GF (1971) Berillidy ruteniya, osmiya, rodiya i iridiya sostava M_2Be_{17} (Ruthenium, osmium, rhodium and iridium beryllides with M_2Be_{17} composition). Izv AN SSSR Metally (6):168–171 (in Russian)

33. Eremenko VN, Semenova EA, Shtepa TD (1978) Vliyanie rodiya, iridiya i osmiya na polimorfnoe ($\alpha \leftrightarrow \beta$)-prevrashchenie tsirkoniya (The effects of rhodium, iridium and osmium on the ($\alpha \leftrightarrow \beta$)-transformation of zirconium). Izv AN SSSR Metally (2):200–203 (in Russian)
34. Kubaschewski O (1982) Iron binary phase diagrams. Springer, Berlin
35. Bannykh OA, Budberg SP, Alisova SP (1986) Diagrammy sostoyaniya dvoinykh i mnogokomponentnykh system na osnove zheleza (The constitution diagrams of binary and multi-component systems based on iron). Metallurgiya, Moscow (in Russian)
36. Esslinger P, Schubert K (1957) Zur Systematik der Strukturfamilie des NiAs. I. Verbeitung der Strukturen der NiAs-Familie (The systematics of the family structure of NiAs. I. Distribution of the structures of NiAs family). Z Metallkd 48(3):126–134 (in German)
37. Berezhnoy AS (1958) Kremnii i ego binarnye sistemy (Silicon and its binary systems). UkrSSR Academy of Sciences, Kyiv (in Russian)
38. Finnie LN (1962) Structures and compositions of the silicides of ruthenium, osmium, rhodium and iridium. J Less-Common Met 4(1):24–34
39. Samsonov GV, Dvorina LA, Rud BM (1979) Silitsidy (Silicides). Metallurgiya, Moscow (in Russian)
40. Fromm E, Gebhardt, E (1976) Gase und Kohlenstoff in Metallen (Gases and carbon in metals). Springer, Berlin (in German)
41. Obolonchik VA (1972) Selenidy (Selenides). Metallurgiya, Moscow (in Russian)
42. Chizhikov DM, Schastlivyi VP (1966) Tellur i telluridy (Tellurium and tellurides). Nauka, Moscow (in Russian)
43. Nekrasov BV (1973) Osnovy obschei khimii (Foundations of general chemistry), 3rd ed., Vol. 2. Khimiya, Moscow (in Russian)
44. Goodwin F, Guruswamy S, Kainer KU, Kammer C, Knabl W, Koethe A, Leichtfried G, Schlamp G, Stickler R, Warlimont H (2005) Metals. In: Martienssen W, Warlimont H (eds) Springer handbook of condensed matter and materials data, pp. 161–430. Springer, Berlin, Heidelberg
45. Savitskii EM, Polyakova VP, Tylkina MA (1967) Splavy palladiya (Palladium alloys). Nauka, Moscow (in Russian)
46. Crespo AJ, Tergenius L-E, Lundström T (1981) The solid solution of 4*d*, 5*d* and some *p* elements in β rhombohedral boron. J Less-Common Met 77(1):147–150
47. Khoruzhaya VG (1996) Interaction of transition metals of group IV with high-melting platinum metals in binary and ternary systems. Powder Metall Met Ceram 35(7–8):433–440
48. Savitskii EM, Devingtal YuV, Gribulya VB (1968) Prognoz metallicheskikh soedinenii tipa A_3B s pomoshchyu elektronno-vychislitelnoi mashiny (Prognosis of A_3B type metallic compounds by means of computing). Doklady AN SSSR 183(5):1110–1112 (in Russian)
49. Savitskii EM, Devingtal YuV, Gribulya VB (1969) Raspoznavanie tipa reaktsii obrazovaniya i otsenka intervala gomogennosti metallicheskikh faz pri pomoshchi EVM (Identification of formation reaction type and evaluation of homogeneity range of metallic phases by means of computing). Doklady AN SSSR 185(3):561–563 (in Russian)
50. Savitskii EM, Gribulya VB (1970) Opyt prognozirovaniya sostava i svoistv soedinenii s pomoshchyu EVM (Prognosis experience in compound compositions and properties by means of computing). Doklady AN SSSR 190(5):1147–1150 (in Russian)
51. Savitskii EM, Gribulya VB (1972) Prognoz faz Lavesa pri pomoshchi EVM (Prognosis of Laves phases by means of computing). Doklady AN SSSR 206(4):848–851 (in Russian)
52. Raub E (1959) Metals and alloys of the platinum group. J Less-Common Met 1(1):3–18
53. Argon AS (1996) Mechanical properties of single-phase crystalline media: deformation at low temperatures. In: Cahn RW, Haasen P (eds) Physical metallurgy, 4th ed., Vol. 3, pp. 1877–1955. Elsevier Science BV, Amsterdam
54. Singh HP (1968) Determination of thermal expansion of germanium, rhodium and iridium by x-rays. Acta Crystallogr A 24(4):469–471
55. Bozza L, Toth L (1990) Iridium. In: Metals handbook, Vol. 2 – Properties and selection: nonferrous alloys and special-purpose materials, pp. 3015–3016. ASM International, Metals Park, Ohio

56. Winter M (2012) WebElements: the periodic table on the WWW. Iridium: enthalpies and thermodynamic properties. http://www.webelements.com/iridium/thermochemistry.html Accessed 18 April 2012.
57. Panish MB, Reif L (1961) Vaporization of iridium and rhodium. J Chem Phys 34(6):1915–1918
58. Halvorson JJ, Wimber RT (1972) Thermal expansion of iridium at high temperatures. J Appl Phys 43(6):2519–2522
59. Merker J, Lupton D, Töpfer M, Knake H (2001) High temperature mechanical properties of the platinum group metals: elastic properties of platinum, rhodium and iridium and their alloys at high temperatures. Platinum Met Rev 45(2):74–82
60. McLellan RB, Oates WA (1973) The solubility of hydrogen in rhodium, ruthenium, iridium and nickel. Acta Metall 21(3):181–185
61. Donkersloot HC, Van Vucht JHN (1976) The crystal structure of IrLi, Ir_3Li and $LiRh_3$. J Less-Common Met 50(2):279–282
62. Matyushenko NN (1969) Kristallicheskie struktury dvoinykh soedinenii (The crystal structure of binary compounds). Metallurgiya, Moscow (in Russian)
63. Johnson O, Smith GS, Krikorian OH, Sands DE (1970) The crystal structure of $RhBe_{6.6}$. Acta Crystallogr B 26:109–113
64. Ferro R, Rambaldini G, Capelli R (1962) Research on the alloys of noble metals with the more electropositive elements. V. Micrographic and x-ray examination of some magnesium-iridium alloys. J Less-Common Met 4(1):16–23
65. Wood EA, Compton VB (1958) Laves-phase compounds of alkaline earths and noble metals. Acta Crystallogr 11:429–433
66. Bruzzone G, Merlo F (1982) Crystal chemical remarks on the alloying behaviour of calcium, strontium and barium. J Less-Common Met 85:285–306
67. Compton VB, Matthias BT (1959) Laves phase compounds of rare earths and hafnium with noble metals. Acta Crystallogr 12:651–654
68. Chabot B, Cenzual K, Parthe E (1980) $Sc_{11}Ir_4$, $Sc_{11}Os_4$, $Sc_{11}Ru_4$, $Zr_{11}Os_4$ with a new cubic structure type described by means of a cluster concept. Acta Crystallogr B 36:7–11
69. Le Roy J, Paccard D, Moreau J-M (1980) R_5Ir_2 compounds (R ≡ Pr, Nd, Sm, Gd, Tb, Dy, Ho, Er, Tm, Lu, Y) with the monoclinic Mn_5C_2 structure. J Less-Common Met 72(1):P11-P15
70. Vorobev VD, Melnikova VA (1974) Rentgenograficheskie issledovaniya sistem iridii-lantan i iridii-tserii (X-ray studies of the iridium-lanthanum and iridium-cerium systems). Kristallografiya 19(3):642–643 (in Russian)
71. Olcese GL (1973) Crystal structure and magnetic properties of some 7:3 binary phases between lanthanides and metals of the 8th group. J Less-Common Met 33(1):71–81
72. Teslyuk YuM (1969) Metallicheskie soedineniya so strukturami faz Lavesa (Metallic compounds with Laves phase structures). Nauka, Moscow (in Russian)
73. Lewy RM (1970) Indirect exchange in the rare-earth intermetallics. J Appl Phys 41(3):902–904
74. Le Roy J, Moreau J-M, Paccard D, Parthe E (1979) Rare earth (and yttrium) – iridium and – platinum compounds with the Fe_3C structure type. Acta Crystallogr B 35:1437–1439
75. Le Roy J, Moreau J-M, Paccard D, Parthe E (1980) Rare earth – iridium compounds with Pu_5Rh_3 and Y_3Rh_2 structure types: members of a new structural series with formula $R_{5n+6}T_{3n+5}$. J Less-Common Met 76(1–2):131–135
76. Paccard D, Le Roy J, Moreau J-M (1979) Nd_5Ir_3: a new tetragonal phase with Ir-centred square antiprisms of Nd atoms. Acta Crystallogr B 35:1315–1318
77. Thompson JR (1964) Alloys of thorium with certain transition metals. II. The systems thorium-osmium, thorium-iridium and thorium-platinum. J Less-Common Met 6(1):3–10
78. Kutaitsev VI, Chebotarev NT, Andrianov MA, Konev VN, Lebedev IG, Bagrova VI, Beznosikova AV, Kruglov AA, Petrov PN, Smotritskaya ES (1967) Phase diagrams of plutonium with metals of groups IIA, IVA, VIII and IB. Sov Atom Energy 23(6):1279–1287
79. Cromer DT (1974) Plutonium-iridium Pu_5Ir_3. Acta Crystallogr B 33:1996–1997

80. Eremenko VN, Shtepa TD (1970) Diagramma sostoyaniya sistemy Ti-Ir (The constitution diagram of the Ti-Ir system). Izv AN SSSR Metally (6):198–203 (in Russian)
81. Eremenko VN, Semenova EA, Shtepa TD (1980) Diagramma sostoyaniya sistemy Zr-Ir (The constitution diagram of the Zr-Ir system). Izv AN SSSR Metally (5):237–241 (in Russian)
82. Kubaschewski O, Von Goldbeck O (1976) Phase diagrams. In: Hafnium. Physico-chemical properties of its compounds and alloys. Atomic Energy Review, Special Issue N 8, pp. 57–118. International Atomic Energy Agency, Vienna
83. Giessen BC, Dangel PN, Grant NJ (1967) New phases in the vanadium-iridium system and tentative constitution diagram. J Less-Common Met 13(1):62–70
84. Waterstrat RM, Manuszewski RC (1973) The chromium-iridium constitution diagram. J Less-Common Met 32(1):79–89
85. Venkatraman M, Neumann JP (1990) The Cr-Ir (chromium-iridium) system. Bull Alloy Phase Diagrams 11(1):5–8
86. Darby JB, Norton LJ, Downey JW (1963) A survey of the binary systems of technetium with group VIII transition elements. J Less-Common Met 5(5):397–402
87. Swartzendruber LJ (1984) The Fe-Ir (iron-iridium) system. Bull Alloy Phase Diagrams 5(1):48–52
88. Swartzendruber LJ (1984) The Fe-Ir (iron-iridium) system. Bull Alloy Phase Diagrams 5(2):134
89. Eremenko VN, Khoruzhaya VG, Shtepa TD (1988) Temperatury nonvariantnykh ravnovesii v sistemakh Zr-Ru i Ru-Ir (The temperatures of non-variant equilibria in the Zr-Ru and Ru-Ir systems). Izv AN SSSR Metally (1):197–202 (in Russian)
90. FactSage (2010) Data from SGnobl metal alloy database. Collection of phase diagrams. http://www.crct.polymtl.ca/fact/phase_diagram.php?file=Ir-Ru.jpg&dir=SGnobl Accessed 7 May 2012
91. Bucher E, Brinkman WF, Maita JP, Cooper AS (1970) Properties of the Ni-Ir alloy system. Phys Rev B 1:274–277
92. Raub E, Röschel E (1970) Alloys of nickel with iridium and rhodium. Z Metallkd 61(2):113–115
93. FactSage (2010) Data from FSnobl noble metal databases. Collection of phase diagrams. http://www.crct.polymtl.ca/fact/phase_diagram.php?file=Ir-Pd.jpg&dir=FSnobl Accessed 7 May 2012
94. Tylkina MA, Polyakova VP, Savitskii EM (1962) Diagramma sostoyaniya sistemy palladii-iridii (The phase diagram of the palladiumiridium system). Zh Neorg Khim 7(6):1471–1473 (in Russian)
95. FactSage (2010) Data from SGnobl-SGTE noble metal alloy database. Collection of phase diagrams. http://www.crct.polymtl.ca/fact/phase_diagram.php?file=Ir-Pt.jpg&dir=SGnobl Accessed 7 May 2012
96. Tripathi SN, Chandrasekharaiah MS (1983) Thermodynamic properties of binary alloys of platinum metals II: Ir-Pt system. J Less-Common Met 91(2):251–260
97. FactSage (2010) Data from SGnobl-SGTE noble metal alloy database. Collection of phase diagrams. http://www.crct.polymtl.ca/fact/phase_diagram.php?file=Cu-Ir.jpg&dir=SGnobl Accessed 7 May 2012
98. Raub E, Röschel E (1969) Copper iridium alloys. Z Metallkd 60(2):142–144
99. Chakrabarti DJ, Laughlin DE (1987) The Cu-Ir (copper-iridium) system. J Phase Equilibria 8(2):132–136
100. Karakaya I, Thompson WT (1986) The Ag-Ir (silver-iridium) system. Bull Alloy Phase Diagrams 7(4):359–360
101. FactSage (2010) Data from SGnobl-SGTE noble metal alloy database. Collection of phase diagrams. http://www.crct.polymtl.ca/fact/phase_diagram.php?file=Ag-Ir.jpg&dir=SGnobl Accessed 7 May 2012
102. Okamoto H, Massalski TB (1984) The Au-Ir (gold-iridium) system. Bull Alloy Phase Diagrams 5(4):381

103. FactSage (2010) Data from SGnobl-SGTE noble metal alloy database. Collection of phase diagrams. http://www.crct.polymtl.ca/fact/phase_diagram.php?file=Au-Ir.jpg&dir=SGnobl Accessed 7 May 2012
104. Jangg G, Dörtbudak T (1973) Untersuchungen an den Systemen der Platinmetalle und des Rheniums mit Quecksilber (Investigations of the platinum metal mercury and rhenium mercury systems). Z Metallkd 64(10):715–719 (in German)
105. Aronsson B (1963) The crystal structure of RuB_2, OsB_2 and $IrB_{1.35}$ and some general comments on the crystal chemistry of borides in the composition range MeB-MeB_3. Acta Chem Scand 17(7):2036–2050
106. Rogl P, Nowotny H, Benesovsky F (1971) Ein Beitrag zur Strukturchemie der Iridiumboride (A contribution to the structural chemistry of iridium boride). Monatsh Chem 102(3):678–686 (in German)
107. Lundström T, Tergenius L-E (1973) Refinement of the crystal structure of the non-stoichiometric boride $IrB_{\sim 1.35}$. Acta Chem Scand 27(12):3705–3711
108. Holleck H, Nowotny H, Benesovsky F (1963) Die Verbindungen Ta_3Ga_2 and IrGa (The connections of Ta_3Ga_2 and IrGa). Monatsh Chem 94(5):841–843 (in German)
109. Völlenkle H, Wittmann A, Nowotny H (1966) Abkömmlinge der $TiSi_2$-Struktur – ein neues Bauprinzip (Descendants of the $TiSi_2$-structure – a new design principle). Monatsh Chem 97(2):506–516 (in German)
110. Edshammar L-E (1970) The crystal structure of Rh_5Ga_9 and Ir_2Ga_9. Acta Chem Scand 24(4):1457–1458
111. Schulz KJ, Musbah OA, Chang YA (1990) An investigation of the Ir-Ga-As system. Bull Alloy Phase Diagrams 11(3):211–215
112. Anres P, Gaune-Escard M, Bros JP (1997) First thermodynamic approach of the (Ir+Ga) system. J Alloys Compd 259(1–2):225–233
113. Korst WL, Finnie LN, Searcy AW (1957) The crystal structure of the monosilicides of osmium, iridium and ruthenium. J Phys Chem 61(11):1541–1543
114. Reinacher G (1965) Hot-stage microscope determination of the solidus temperatures of iridium alloys with about 1 wt.% boron, phosphoros or silicon. Metall 19(7):707–711
115. Bhan S, Schubert K (1960) Constitution of the systems cobalt-germanium, rhodium-germanium and some related alloys. Z Metallkd 51:327–339
116. Hamilton DC, Raub ChJ, Matthias BT, Corenzwit E, Hull GW, Jr (1965) Some new superconducting compounds. J Phys Chem Solids 26(3):665–667
117. Okamoto H (1990) The Ir-P (iridium-phosphorus) system. Bull Alloy Phase Diagrams 11(4):413–415
118. Kjekshus A (1971) On the properties of binary compounds with the $CoSb_2$ type crystal structure. Acta Chem Scand 25(2):411–422
119. Quesnel JC, Heyding RD (1962) Transition metal arsenides: a note on the rhodium/arsenic system and the monoclinic diarsenides of the cobalt family. Canad J Chem 40(4):814–818
120. Hulliger F (1963) Semiconductivity in $CoSb_2$-type compounds. Phys Lett 4(5):282–283
121. Zhuravlev NN, Zhdanov GS, Kuzmin RN (1960) Atomnoe stroenie nekotorykh soedinenii vismuta i surmy (The atomic structure of certain compounds of bismuth and antimony). Kristallografiya 5(4):553–562 (in Russian)
122. Caillat T, Borshchevsky A, Fleurial J-P (1993) Phase diagram of the Ir-Sb system on the antimony-rich part. J Alloys Compd 199(1–2):207–210
123. Kjekshus A (1961) High temperature x-ray study of the thermal expansion of $IrAs_3$ and $IrSb_3$. Acta Chem Scand 15:678–681
124. Kjekshus A, Pedersen G (1961) The crystal structures of $IrAs_3$ and $IrSb_3$. Acta Crystallogr 14:1065–1070
125. Zhuravlev NN, Smirnova EM (1965) Ustanovlenie dvukh novykh soedinenii $IrBi_3$ i $IrBi_2$ v sisteme vismut-iridii (The ascertainment of two new compounds $IrBi_3$ and $IrBi_2$ in the bismuth-iridium system). Kristallografiya 10(6):828–832 (in Russian)

126. Schäfer H, Heitland H-J (1960) Gleichgewichtsmessungen im System Iridium – Sauerstoff Gasförmiges – Iridiumtrioxyd (Equilibrium measurements in the system iridium – gaseous oxygen – iridium trioxide). Z Anorg Allgem Chem 304(5–6):249–265 (in German)
127. Hockings EF, White JG (1960) The system iridium-tellurium. J Phys Chem 64(8):1042–1045
128. Weiland R, Lupton DF, Fischer B, Merker J, Scheckenbach C, Witte J (2006) High-temperature mechanical properties of the platinum group metals. Properties of pure iridium at high temperature. Platinum Met Rev 50(4):158–170
129. Sha JB, Yamabe-Mitarai Y, Harada H (2006) Microstructural evaluation and mechanical properties of Ir-Hf-Zr ternary alloys at room and high temperatures. Intermetallics 14(10–11):1364–1369
130. Kimura Y, Iida K, Wei F-G, Mishima Y (2006) Phase equilibria in the T-Al-C (T: Co, Ni, Rh, Ir) and T-Al-B (T: Rh, Ir) systems for the design of $E2_1$-Co_3AlC based heat resistant alloys. Intermetallics14(5):508–514
131. McDaniel CL, Schneider SJ (1972) Phase relations in the CaO-IrO_2-Ir system in air. J Solid State Chem 4(2):275–280
132. Sarkozy RF, Moeller CW, Chamberland BL (1974) The characterization of calcium iridium oxides. J Solid State Chem 9(3):242–246
133. Jacob KT, Okabe TH, Uda T, Waseda Y (1999) Solid-state cells with buffer electrodes for the measurement of thermodynamic properties of IrO_2, $CaIrO_3$, Ca_2IrO_4 and Ca_4IrO_6. J Electrochem Soc 146(5):1854–1861
134. Keawprak N, Tu R, Goto T (2009) Thermoelectric properties of Ca-Ir-O compounds prepared by spark plasma sintering. Mater Trans 50(4):853–858
135. Liang CH, Chan YH, Tiong KK, Huang YS, Dumcenco DO, Liao (2009) Synthesis and characterization of needle-like $IrSe_2$ microrods. J Alloys Compd 480(1):70–72
136. Rogl P, Nowotny H (1979) Studies of the (Sc, Zr, Hf) – (Rh, Ir) – B systems. J Less-Common Met 67(1):41–50
137. Brukl CE, Rudy E (1967) The hafnium-iridium-boron system. In: Ternary phase equilibria in transition metal-boron-carbon-silicon systems. Report AFML-TR-65–2, Contracts USAF 33(615)-1249, Part 2, Vol. 14, pp. 1–54. Air Force Materials Laboratory, Wright-Patterson Air Force Base, Ohio
138. Holleck H (1977) Carbon- and boron-stabilized ordered phases of scandium. J Less-Common Met 52(1):167–172
139. Winter M (2012) WebElements: the periodic table on the WWW. Iridium: physical properties. http://www.webelements.com/iridium/physics.html Accessed 18 April 2012.
140. Sangster J, Pelton AD (1992) The Ir-Li (iridium-lithium) system. J Phase Equilib 13(1):59–62
141. Varma SK, Chang FC, Magee CB (1978) Compounds and phase relationships in the lithium-iridium-hydrogen system. J Less-Common Met 60(2):P47-P63
142. Loebich O Jr, Raub ChJ (1981) Reactions beween some alkali metals and platinum group metals. Platinum Met Rev 25(3):113–120
143. Moffatt WG (1986) Binary phase diagrams handbook. General Electric Co., Schenectady, New York
144. Hlukhyy V, Pöttgen R (2004) The hexagonal Laves phase $MgIr_2$. Z Naturforsch B 59:943–946
145. Hlukhyy V, Rodewald UC, Hoffmann RD, Pöttgen R (2004) Synthesis and structure of $RhMg_3$ and Ir_3Mg_{13}. Z Naturforsch B 59:251–255
146. Bonhomme F, Yvon K (1995) Cubic $Mg_{29}Ir_4$ crystallizing with an ordered variant of the Mg_6Pd-type structure. J Alloys Compd 227:L1–L3
147. Range KJ, Hafner P (1993) Structure refinement of $AuMg_3$, $IrMg_3$ and $IrMg_{2.8}$. J Alloys Compd 191:L5-L7
148. Hlukhyy V, Pöttgen R (2004) $Mg_{2+x}Ir_{3-x}$ (x = 0.30) − a binary variant of the monoclinic $V_2(Co_{0.57}Si_{0.43})_3$ type. Solid State Sci 6:1175–1180

149. Schlüter M, Häussermann U, Heying B, Pöttgen R (2003) Tin-magnesium substitution in Ir_3Sn_7-structure and chemical bonding in $Mg_xIr_3Sn_{7-x}$ (x = 0–1.67). J Solid State Chem 173:418–424
150. Cerny R, Renaudin G, Tokaychuk YO, Favre-Nicolin V (2006) Complex intermetallic compounds in the Mg-Ir system solved by powder diffraction. Z Kristallogr S23:411–416
151. Pani M, Palenzona A (2007) Ca_5Rh and Ca_5Ir: isotypic compounds with a new structure type. J Alloys Compd 436:91–94
152. Okamoto H (1995) The Ir-Sc (iridium-scandium) system. J Phase Equilib 16(3):285–286
153. Tripathi SN, Bharadwaj SR (1996) The Ir-Sc (iridium-scandium) system. J Phase Equilib 17(5):445–450
154. Okamoto H (1997) The Ir-Sc (iridium-scandium) system. J Phase Equilib 18:224–225
155. Eremenko VN, Khorujaya VG, Martsenyuk PS (1994) The scandium-iridium phase diagram. J Alloys Compd 204:83–87
156. Le Roy J, Moreau JM, Parthé E (1978) The crystal structures of $R_{64}Ir_{37}$ (R = Gd, Tb, Dy, Ho, Er, Y) and $R_{64}Rh_{37}$. Acta Crystallogr A 34 S180c
157. Okamoto H (1992) The Ir-Y (iridium-yttrium) system. J Phase Equilib 13:651–653
158. Palenzona A (1989) The crystal structure of Eu_4Ir. J Less-Common Met 154(1):227–228
159. Ning Y-T, Zhou X-M, Zhen Y, Chen N-Y, Xu H, Zhu J-Z (1989) The prediction and synthesis of some new intermetallic compounds between transition metals and rare earth metals. J Less-Common Met 147(2):167–173
160. Iandelli A, Palenzona A (1976) Das Verhalten des Ytterbiums mit den Metallen der achten Gruppe des periodischen Systems (The reaction of the ytterbium to the metals of the eighth group of the periodic table). Rev Chim Miner 13(1):55–61 (in German)
161. Iandelli A, Palenzona A (1982) On the crystal structures of Yb_5Ir_3. J Less-Common Met 83(1):L1-L5
162. Blazina Z, Mohanty RC, Raman A (1989) Intermediate phases in some rare earth metal – iridium systems. Z Metallkd 80(3):192–196
163. Le Roy J, Moreau JM, Paccard D (1982) R_5T_3 compounds (R ≡ rare earth; T ≡ Rh, Ir) with an Mn_5Si_3-type structure. J Less-Common Met 86:63–67
164. Krikorian NH (1971) The reaction of selected lanthanide carbides with platinum and iridium. J Less-Common Met 23(3):271–279
165. Raman A (1976) Crystal structure of Ce_5Rh_4 and analogous phases. J Less-Common Met 48(1):111–117
166. Lam DJ, Mitchell AW (1972) Laves phases of actinide elements. J Nucl Mater 44(3):279–284
167. Erdmann B, Keller C (1973) Actinide (lanthanide) – noble metal alloy phases, preparation and properties. J Solid State Chem 7(1):40–48
168. Radchenko VM, Seleznev AG, Shushakov VD, Droznik RR, Ryabinin MA, Lebedeva LS, Vasilyev VY (1990) Intermetallics and alloys of transplutonium elements with metals of the platinum group. J Radioanal Nucl Chem 143(1):261–267
169. Raub E, Mahler W (1955) Die Legierungen des Mangans mit Platins, Iridium, Rhodium und Ruthenium (Alloys of manganese with platinum, iridium, rhodium and ruthenium). Z Metallkd 46(4):282–290 (in German)
170. Arnberg L, Westman S (1972) Note on the structure of the gamma brass like phase Ir_4Zn_{22}. Acta Chem Scand 26:513–517
171. Chakrabarti DJ, Laughlin DE (1987) The Cu-Ir (copper-iridium) system. Bull Alloy Phase Diagrams 8(2):132–136
172. Guminski C (2003) The Hg-Ir (mercury-iridium) system. J Phase Equilib 24(4):373–374
173. Boström M, Prots Y, Grin Y (2004) Synthesis, crystal structure and chemical bonding of the novel compound $IrGa_2$. Solid State Sci 6(5):499–503
174. Anres P, Fossati P, Richter K, Gambino M, Gaune-Escard M, Bros J-P (2000) Thermodynamics of the Ir-In system. J Alloys Compd 296(1–2):119–127

175. Flandorfer H, Richter KW, Hayer E, Ipser H, Borzone G, Bros J-P (2002) The binary system In-Ir: a new investigation of phase relationships, crystal structures and enthalpies of mixing. J Alloys Compd 345(1–2):130–139
176. Flandorfer H (2004) The crystal structure of a new low temperature modification of In_3Ir. J Alloys Compd 368(1–2):256–259
177. Allevato CE, Vining CB (1993) Phase diagram and electrical behavior of silicon-rich iridium silicide compounds. J Alloys Compd 200(1–2):99–105
178. Okamoto H (1995) Comment on Ir-Si (iridium-silicon) system. J Phase Equilib 16(5):473a-474
179. Sha JB, Yamabe-Mitarai Y (2006) Phase and microstructural evolution of Ir-Si binary alloys with fcc/silicide structure. Intermetallics 14:672–684
180. Nordmark E-L, Wallner O, Häussermann U (2002) Polymorphism of $IrSn_4$. J Solid State Chem 168(1):34–40
181. Künnen B, Niepmann D, Jeitschko W (2000) Structure refinements and some properties of the transition metal stannides Os_3Sn_7, Ir_5Sn_7, $Ni_{0.402(4)}Pd_{0.598}Sn_4$, α-$PdSn_2$ and $PtSn_4$. J Alloys Compd 309(1–2):1–9
182. Yu R, Zhan Q, De Jonghe LC (2007) Crystal structures of and displacive transitions in OsN_2, IrN_2, RuN_2 and RhN_2. Angew Chem Int Ed 46(7):1136–1140
183. Wu Z-J, Zhao E-J, Xiang H-P, Hao X-F, Liu X-J, Meng J (2007) Crystal structures and elastic properties of superhard IrN_2 and IrN_3 from first principles. Phys Rev B 76(5):054115
184. Okamoto H (1994) Comment on Ir-Sb (iridium-antimony) system. J Phase Equilib 15(5):567–568
185. Munson RA (1968) The synthesis of iridium disulfide and nickel diarsenide having the pyrite structure. Inorg Chem 7:389–390
186. Okamoto H (2000) The In-Ir (indium-iridium) system. J Phase Equilib 21(4):412
187. Okamoto H (2004) The In-Ir (indium-iridium) system. J Phase Equilib 25(1):103
188. Servant C, Idbenali M (2011) Thermodynamic assessment of the In-Ir system in the In rich part. Thermochim Acta 517:1–8
189. Okamoto H (2012) The In-Ir (indium-iridium) system. J Phase Equilib Diffus 33(2):158
190. Okamoto H (2009) The Al-Ir (aluminum-iridium) system. J Phase Equilib Diffus 30(2):206–207
191. Okamoto H (2007) The Ir-Si (iridium-silicon) system. J Phase Equilib Diffus 28(5):495
192. Okamoto H (2007) The Ir-Zr (iridium-zirconium) system. J Phase Equilib Diffus 28(5):496
193. Okamoto H (2000) The Al-Ir (aluminum-iridium) system. J Phase Equilib Diffus 21(4):409
194. Anres P, Gaune-Escard M, Bros J-P (1997) Comment on gallium-iridium (Ga-Ir) system. J Phase Equilib 18(5):415–416
195. Okamoto H (1996) The Ir-Mn (iridium-manganese) system. J Phase Equilib 17(1):60–62
196. Bharadwaj SR, Tripathi SN, Chandrasekharaiah MS (1995) The Ir-Pt (iridium-platinum) system. J Phase Equilib 16(5):460–464
197. Okamoto H (1994) The Ir-Sb (iridium-antimony) system. J Phase Equilib 15(6):640–642
198. Okamoto H (1994) Comment on Hf-Ir (hafnium-iridium) system. J Phase Equilib 15(3):365
199. Okamoto H (1992) The Ir-Zr (iridium-zirconium) system. J Phase Equilib 13(6):653–656
200. Okamoto H (1992) The Ir-Ru (iridium-ruthenium) system. J Phase Equilib 13(5):565–567
201. Okamoto H (1992) The Ir-U (iridium-uranium) system. J Phase Equilib 13(5):567–570
202. Okamoto H (1992) The Ir-Ti (iridium-titanium) system. J Phase Equilib 13(3):329–331
203. Okamoto H (1992) The Ir-Yb (iridium-ytterbium) system. J Phase Equilib 13(2):193–194
204. Okamoto H (1992) The Er-Ir (erbium-iridium) system. J Phase Equilib 13(2):179–181
205. Okamoto H (1992) The Dy-Ir (dysprosium-iridium) system. J Phase Equilib 13(2):177–179
206. Tripathi SN, Bharadwaj SR, Chandrasekharaiah MS (1991) The Ir-Pd (iridium-palladium) system. J Phase Equilib 12(5):603–605
207. Okamoto H (1991) The Ir-Th (iridium-thorium) system. J Phase Equilib 12(5):568–570

208. Okamoto H (1991) The Ir-La (iridium-lanthanum) system. J Phase Equilib 12(5):565–567
209. Tripathi SN, Bharadwaj SR, Chandrasekharaiah MS (1991) The Ir-Rh (iridium-rhodium) system. J Phase Equilib 12(5):606–608
210. Okamoto H (1991) The Ce-Ir (cerium-iridium) system. J Phase Equilib 12(5):563–565
211. Sha JB, Yamabe-Mitarai Y (2013) Ir-Hf-Zr ternary refractory superalloys for ultra-high temperatures – phase and microstructural constitution. Intermetallics 41:1–9

Addendum

A.1 Structures

Summarized general data on the structural properties (atomic weights, crystal space groups, systems and types, lattice parameters and densities) of all the most high-melting elements of the periodic table: carbon (graphene/graphite) and refractory metals (in alphabetical order), which were considered above separately and comprehensively in the main chapters of this volume, are given in Table A.1 [1–12].

A.2 Thermal Properties

The most important thermodynamic properties (standard molar entropy, molar and specific heat capacities, molar and specific enthalpies (heats) of melting (fusion) and vaporization, molar and specific enthalpy differences) of carbon (graphite) and refractory metals are summarized in Tables A.2, A.3 [1–2, 9–14, 19]. For the general comparison, some other thermal properties (melting and boiling points, coefficients of linear thermal expansion, relative thermal expansion, thermal conductivity, vapour pressure and vaporization rate) of the elemental substances (graphite and refractory metals in alphabetical order) are given in Tables A.4, A.5 [4, 9–12, 15, 16]. The values of the heat capacities, enthalpy differences, thermal expansion and thermal conductivity properties and vaporizations parameters of the elemental materials are presented there in the wide range from room (or moderate) to ultra-high temperatures.

A.3 Electro-Magnetic and Optical Properties

For the general comparison, the main electro-magnetic and optical properties (specific electrical resistance, temperature coefficient of electroresistance, integral and monochromatic emittances, thermoionic emission characteristics and molar magnetic susceptibility) of carbon (graphite) and refractory metals are given in

I. L. Shabalin, *Ultra-High Temperature Materials I*,
DOI: 10.1007/978-94-007-7587-9,

Table A.6 [4, 9–12, 17, 18]. The values of the electrical resistance and integral and monochromatic emittances of the elemental materials are presented in the wide range from room (or moderate) to ultra-high temperatures.

A.4 Physico-Mechanical Properties

The relative comparison of some physico-mechanical properties (hardness, tensile and compressive strengths and Young's modulus) of ultra-high temperature elemental materials (graphite and refractory metals), which were considered above separately and comprehensively in the main chapters of this volume, can be carried out on the basis of the data presented in Table A.7 [4, 9–12, 20]. The values of the hardness, strength and elasticity of the materials are given there for the wide range from room to ultra-high temperatures.

A.5 Nuclear Physical Properties

Nuclear physical properties (isotopic mass range, total number of isotopes, thermal neutron macroscopic cross sections, moderating ability and capture resonance integral) of the elements (carbon and refractory metals) are given in Table A.8 [9, 21–25].

A.6 Chemical Properties

For the ultra-high temperature elemental materials considered in detail in the main chapters of the volume, the diffusion rates in species pairs (in alphabetical order) are presented in the various ranges of temperatures in Table A.9 [9, 26–32, 39]. The following tables of the Addendum contain the summarized general information on the chemical interaction of ultra-high temperature elemental materials with other elements of the periodic table (binary systems):

carbon—Tables A.10, A.11, A.12,
tungsten—Tables A.13, A.14, A.15,
rhenium—Tables A.16, A.17, A.18,
osmium—Tables A.19, A.20, A.21,
tantalum—Tables A.22, A.23, A.24,
molybdenum—Tables A.25, A.26, A.27,
niobium—Tables A.28, A.29, A.30,
iridium—Tables A.31, A.32, A.33.

The contents of these tables are stylized in the form of the periodic table and based on the corresponding sections of the main chapters and some universal sources [3, 9, 11, 33–38, 40–54].

Table A.1 Structural properties (atomic weight, crystal structure and densities)

Material formula	Atomic weight	Crystal structure						Z[a]	Density, g cm^{-3}	
		System	Type	Space group	Lattice parameters, nm				Calculated (XRD)	Experimental (pycnometric)
					a	*c*	*c*/*a*			
C (graphite)[b]	12.0107	Hexagonal	Graphite	*P6$_3$/mmc*	0.2464	0.6711	2.7236	4	2.267	2.26
Ir	192.217	Cubic (fcc)	Cu	*Fm(–3)m*	0.3839	–	–	4	22.56	22.45
Mo	95.94	Cubic (bcc)	W	*Im(–3)m*	0.3147	–	–	2	10.22	10.24
Nb	92.90638	Cubic (bcc)	W	*Im(–3)m*	0.3301	–	–	2	8.578	8.59
Os	190.23	Hexagonal (hcp)	Mg	*P6$_3$/mmc*	0.2734	0.4320	1.580	2	22.60	22.48
Re	186.207	Hexagonal (hcp)	Mg	*P6$_3$/mmc*	0.2762	0.4457	1.614	2	21.01	21.00
Ta	180.9479	Cubic (bcc)	W	*Im(–3)m*	0.3303	–	–	2	16.68	16.60
W	183.84	Cubic (bcc)	W	*Im(–3)m*	0.3165	–	–	2	19.25	19.20

[a] Number of formula units per lattice
[b] 2H-Graphite (α-carbon, α-graphite)

Table A.2 Thermodynamic properties (standard molar entropy, molar and specific heat capacities)

Material formula	Standard molar entropy $S°_{298}$, J mol^{-1} K^{-1}	Molar heat capacity c_p, J mol^{-1} K^{-1}, at temp., K (°C)					Specific heat capacity c, J kg^{-1} K^{-1}, at temp., K (°C)				
		298 (25)	1000 (730)	2000 (1730)	3000 (2730)	4000 (3730)	298 (25)	1000 (730)	2000 (1730)	3000 (2730)	4000 (3730)
C (graphite)	5.74	8.5	21.0	25.0	26.5	–	700	1750	2100	2200	–
Ir	35.5	25.0	29.2	35.2	–	–	130	153	191	–	–
Mo	28.6	24.0	28.7	36.9	41.8	–	250	300	385	435	–
Nb	36.5	24.7	27.7	31.8	33.5	–	265	300	340	360	–
Os	32.6	24.9	27.5	31.2	34.9	37.7	130	145	164	183	198
Re	36.5	25.5	29.0	34.9	42.3	46.0	138	156	188	227	247
Ta	41.5	25.4	27.9	31.0	44.1	–	140	154	171	244	–
W	32.8	24.3	27.6	32.3	37.2	41.8	132	150	176	202	227

Table A.3 Thermodynamic properties (molar and specific enthalpies (heats) of melting/vaporization, molar and specific enthalpy differences)

Material formula	Enthalpy (heat) of melting[a]		Enthalpy (heat) of vaporization[b]		Molar enthalpy differences $H_T - H_{298}$, kJ mol^{-1}, at temp., K (°C)						Specific enthalpy differences $H_T - H_{298}$, kJ kg^{-1}, at temp., K (°C)					
	molar, kJ mol^{-1}	specific, MJ kg^{-1}	molar, MJ mol^{-1}	specific, MJ kg^{-1}	1000 (730)	2000 (1730)	3000 (2730)	4000 (3730)	5000 (4730)	6000 (5730)	1000 (730)	2000 (1730)	3000 (2730)	4000 (3730)	5000 (4730)	6000 (5730)
C (graphite)	146	10	0.71	59	12.8	36.6	62.8	–	–	–	1067	3050	5230	–	–	–
Ir	41.1	0.214	0.60	3.14	18.9	52.0	118.2	160.1	–	–	98.3	271	615	833	–	–
Mo	37.5	0.290	0.60	6.16	18.5	51.0	123.6	165.4	799	856	192.2	531	1288	1723	8324	8920
Nb	30.0	0.315	0.69	7.32	18.5	48.2	108.2	141.7	175	892	198.5	518	1164	1525	1884	9598
Os	57.9	0.304	0.73	3.84	18.4	47.7	80.7	149.4	187	962	96.6	251	424	786	983	5058
Re	34.1	0.178	0.70	3.74	19.2	51.0	89.5	167.9	214	–	103	274	481	902	1149	–
Ta	36.6	0.200	0.75	4.15	19.0	48.2	83.6	150.6	186	–	104.9	266	462	832	1029	–
W	52.3	0.220	0.80	4.33	18.3	48.1	83.8	158.6	200	–	99.3	262	456	867	1090	–

[a] For refractory metals molar and specific enthalpies (heats) of melting are given at the melting points

[b] For refractory metals molar and specific enthalpies (heats) of vaporization are given at the boiling points

Table A.4 Thermal properties (melting and boiling points, coefficients of linear thermal expansion, relative thermal expansion and thermal conductivity)

Material formula	Melting point, K (°C)	Boiling point, K (°C)	Average coefficient of linear thermal expansion, 10^{-6} K^{-1}		Relative thermal expansion, %, affected by heating from room temp. to *T*, K (°C)					Thermal conductivity, W m^{-1} K^{-1}, at temp., K (°C)					
			at room temp.	20-1700 °C	1000 (730)	1500 (1230)	2000 (1730)	2500 (2230)	3000 (2730)	290 (20)	1000 (730)	1500 (1230)	2000 (1730)	2500 (2230)	3000 (2730)
C (graphite[a])	4200 (3930)[b]	4200 (3930)[b]	2.5-3.5	5.1-5.8	0.25-0.30	0.50-0.58	0.80-0.92	1.13-1.28	1.47-1.70	100-200	60-70	45-60	35-50	35-45	35-45
C (graphite[c])	4200 (3930)[b]	4200 (3930)[b]	0-20	1.5-25	0.08-1.30	0.19-2.40	0.32-3.60	0.49-4.90	–	3-1000	1.5-200	1-150	0.7-100	0.5-70	–
Ir	2720 (2450)	4700 (4430)	6.8	9.2	0.52	0.98	1.55	2.18[d]	–	145	130	115[e]	110	100[d]	–
Mo	2890 (2620)	5100 (4830)	5.4	6.7	0.38	0.74	1.15	1.66	–	135	115	95	80	70	–
Nb	2740 (2470)	5020 (4750)	7.1	8.9	0.56	1.02	1.52	2.00	–	50	60	70	80	90	–
Os	3320 (3050)	5300 (5030)	6.1	~9	0.32 (?)	–	–	–	–	88[f]	85[f]	84[f]	85[f]	~80	–
Re	3450 (3180)	5870 (5600)	6.6	7.0	0.47	0.85	–	–	–	70	56[g]	50	45	42	–
Ta	3270 (3000)	5700 (5430)	6.5	7.7	0.50	0.88	1.32	1.82	2.40	60	70	76	80	84	–
W	3680 (3410)	6000 (5730)	4.3	5.0	0.32	0.52	0.88	1.20	1.60	160	120	105	100	95	92

[a] Industrial polycrystalline (quasi-isotropic) graphite

[b] Total gas pressure over the solid/liquid surface – 10 MPa

[c] Highly oriented pyrolitic graphite

[d] Extrapolated values

[e] Interpolated value

[f] Average values; in different directions the minimal and maximal values are 76 and 111 W m^{-1} K^{-1} at 1000 (730) K (°C), 75 and 110 W m^{-1} K^{-1} at 1500 (1230) K (°C), 77 and 107 W m^{-1} K^{-1} at 2000 (1730) K (°C)

[g] Average value; in different directions the minimal and maximal values are 54 and 60 W m^{-1} K^{-1}

Table A.5 Thermal properties (vapour pressure and vaporization rate)

Material formula	Temperature, K (°C), corresponding to vapour pressure over materials surface, Pa							Temperature, K (°C), corresponding to surface vaporization rate, kg m^{-2} s^{-1}					Temperature, K (°C), corresponding to surface vaporization rate, m s^{-1}				
	10^{-7}	10^{-5}	10^{-3}	0.1	10	10^{3}	10^{5}	10^{-10}	10^{-8}	10^{-6}	10^{-4}	10^{-2}	10^{-14}	10^{-12}	10^{-10}	10^{-8}	10^{-6}
C (graphite)	1790 (1520)	1950 (1680)	2160 (1890)	2410 (2140)	2740 (2470)	3170 (2900)	3790 (3520)	2000 (1730)	2200 (1930)	2450 (2180)	2800 (2530)	3300 (3030)	1950 (1680)	2130 (1860)	2360 (2090)	2700 (2430)	3100 (2830)
Ir	1750 (1480)	1940 (1670)	2190 (1920)	2510 (2240)	–	–	–	–	–	–	–	–	–	–	–	–	–
Mo	1750 (1480)	1960 (1690)	2210 (1940)	2550 (2280)	3010 (2740)	3770 (3500)	~5100 (~4830)	1750 (1480)	1960 (1690)	2230 (1960)	2560 (2290)	3020 (2750)	1750 (1480)	1960 (1690)	2220 (1950)	2560 (2290)	3030 (2760)
Nb	1930 (1660)	2120 (1850)	2380 (2110)	2720 (2450)	3220 (2950)	3940 (3670)	~4530 (~4260)	1930 (1660)	2130 (1860)	2400 (2130)	2750 (2480)	3250 (2980)	1930 (1660)	2130 (1860)	2390 (2120)	2740 (2470)	3230 (2960)
Os	~1880 (~1610)	~2090 (~1820)	~2370 (~2100)	~2700 (~2430)	~3160 (~2890)	~3850 (~3580)	~4880 (~4610)	~1870 (~1600)	~2080 (~1810)	~2350 (~2080)	~2700 (~2430)	>3150 (>2880)	~1910 (~1640)	~2120 (~1850)	~2410 (~2140)	~2780 (~2510)	~3270 (~3000)
Re	2070 (1800)	2320 (2050)	2630 (2360)	3040 (2770)	3610 (3340)	4460 (4190)	~5920 (~5650)	2060 (1790)	2300 (2030)	2620 (2350)	3040 (2770)	–	2100 (1830)	2350 (2080)	2680 (2410)	3120 (2850)	–
Ta	2110 (1840)	2350 (2080)	2650 (2380)	3050 (2780)	3590 (3320)	4350 (4080)	~5700 (~5430)	2100 (1830)	2340 (2070)	2650 (2380)	3020 (2750)	–	2130 (1860)	2360 (2090)	2670 (2400)	3070 (2800)	–
W	2250 (1980)	2500 (2230)	2820 (2550)	3220 (2950)	3760 (3490)	4520 (4250)	5800 (5530)	2230 (1960)	2480 (2210)	2810 (2540)	3220 (2950)	–	2270 (2000)	2520 (2250)	2860 (2590)	3290 (3020)	–

Table A.6 Electro-magnetic and optical properties (specific electrical resistance, temperature coefficient of electroresistance, integral and monochromatic emittances, thermoionic emission characteristics and molar magnetic susceptibility)

Material formula	Specific electrical resistance (resistivity), nΩ m, at temp., K (°C)						Thermal coef. of electro-resistance at 20-1700 °C, 10^{-3} K^{-1}	Integral emittance ε_T[a] at temp., K (°C)				Monochromatic emittance (spectral emissivity) ε_λ (λ= 0.665 μm)[a] at temp., K (°C)				Thermoionic emission characteristics		Molar magnetic susceptibility χ_{mol}(SI)[b], 10^{-6} cm^3 mol^{-1}
	290 (20)	1000 (730)	1500 (1230)	2000 (1730)	2500 (2230)	3000 (2730)		1000 (730)	2000 (1730)	2500 (2230)	3000 (2730)	1000 (730)	2000 (1730)	2500 (2230)	3000 (2730)	electron work function, eV	Richardson constant, 10^4 A m^{-2} K^{-1}	
C (graphite[c])	10^4	8.5×10^3	9.5×10^3	1.1×10^4	1.2×10^4	1.3×10^4	–	0.59-0.78	0.72-0.84	–	–	0.78-0.94	0.75-0.89	0.74-0.88	–	4.0-5.0	~ 15-60	–
C (graphite[d])	500-10^7	2.5×10^3-3.5×10^6	-2.5×10^3-2×10^6	-3.5×10^3-1.3×10^6	-4×10^3-0.7×10^6	–	–	0.60-0.75	0.73-0.86	–	–	0.77-0.92	0.77-0.92	–	–	–	–	(–3200) -(–75)
Ir	50	200	340	480	>600	–	5.1	–	~0.18[e]	0.21	–	–	~0.25[e]	0.215	–	4.7-5.7	100-120	+314
Mo	55	220	360	450	550	–	3.6	0.06	0.21	0.26	–	0.39	0.35	0.34	–	4.0-5.0	55-115	+905
Nb	150	430	550	700	830	–	1.9	~0.10	0.22	0.25	–	0.38	0.37	0.36	–	3.9-4.9	~ 35-70	+2614
Os	90	380[f]	550	–	–	–	~4.2	–	–	–	–	–	~0.4	~0.4	–	4.7-5.9	~10^5 (?)	+138
Re	180	640	840	10^3	1.1×10^3	–	2.4	~0.15	~0.25	0.29	0.33	0.43	0.40	0.38	0.36	4.7-5.3	~50-700	+842
Ta	135	440	620	790	950	1.1×10^3	2.8	~0.10	0.23	0.28	0.33	0.46	0.42	0.40	0.38	3.9-4.8	~40-120	+1935
W	55	245	400	570	750	925	5.5	0.11	0.26	0.30	0.33	0.45	0.43	0.42	0.41	4.2-5.8	60-200	+666

[a] Measured on non-oxidized surfaces
[b] Measured at room temp.
[c] Industrial p-cr. (quasi-isotropic) graphite
[d] Highly oriented pyrolitic graphite
[e] Interpolated data
[f] Average value; in different directions the minimal and maximal values are 270 and 430 nΩ m, respectively

Table A.7 Physico-mechanical properties (hardness, tensile and compressive strengths and Young's modulus)

Material formula	Hardness[a] *HV*, GPa, at temp., K (°C)					Ultimate tensile strength[b], MPa, at temp., K (°C)						Ultimate compressive strength, MPa, at temp., K (°C)					Young's modulus, GPa, at temp., K (°C)				
	290 (20)	1000 (730)	1500 (1230)	2000 (1730)	2500 (2230)	290 (20)	1000 (730)	1500 (1230)	2000 (1730)	2500 (2230)	3000 (2730)	290 (20)	1000 (730)	1500 (1230)	2000 (1730)	2500 (2230)	290 (20)	1000 (730)	1500 (1230)	2000 (1730)	2500 (2230)
C (graphite[c])	0.3-1.0	0.3-1.0	0.3-1.0	0.4-1.0	0.4-1.0	6.4-10.0	7.8-15.0	8.8-18.0	10-21	~22	–	68	70	70	75	95	2.6-8.0	3.3-8.5	4.0-9.5	5.1-10.2	6-11.5
C (graphite[d])	1.4-3.7	–	–	–	–	5-170	~140[e]	~160[e]	120-170[e]	150-190[e]	~350[e]	120-470	150-470	170-470	~200	–	~3-40	10-28[e]	~26[e]	23-24[e]	18-21[e]
Ir	2.0-17.2	~1	–	–	–	500-1100	–	–	~75	~20	–	–	–	–	–	–	525-540	–	<420	–	–
Mo	1.6-4.0	~0.7	~0.45	~0.14	~0.045	250-800	120-500	60-200	25-80	~7	–	–	–	–	–	–	320-330	280-300	~250	~200	–
Nb	0.7-2.5	~0.7	~0.12	~0.04	~0.006	200-700	160-300	~60	~20	–	–	–	–	–	–	–	104-110	~105	~105	–	–
Os	3.0-10.0[f]	~1.9-4.0[f]	~1.3-4.0[f]	–	–	2000-7200[f]	–	–	–	–	–	1000-3600	–	–	–	–	~560	~500	–	–	–
Re	1.3-8.0	~2.0[g]	~1.25	–	–	500-2300	500-1200	400-700	300-400	50-100	~20	–	–	–	–	–	460-520	~390	~330	–	–
Ta	0.4-3.0	~0.5[g]	~0.2	–	–	200-1000	~190	~85	~35	~15	<6	–	–	–	–	–	~185	–	–	–	–
W	1.4-6.0	0.9-1.6	0.6-1.2	0.3-0.5	~0.1	300-1900	180-800	100-350	60-140	35-45	~15	–	–	–	–	–	400-415	370	350	330	250

[a] For refractory metals the minimal values of hardness range are given for annealed specimens and maximal – for hardened (cold-worked) specimens

[b] For refractory metals the minimal values of ultimate tensile strength range are given for annealed specimens and maximal – for hardened (cold-worked) specimens

[c] Polycrystalline (quasi-isotropic) graphite

[d] Highly oriented pyrolitic graphite

[e] In parallel direction to deposition plane

[f] Hardness and ultimate tensile strength of Os varies in magnitude also depending on crystal orientation

[g] For hardened (cold-worked) specimens

Table A.8 Nuclear physical properties (isotopic mass range, total number of isotopes, thermal neutron macroscopic cross sections, moderating ability and capture resonance integral)

Material formula	Isotopic mass range (minimal and maximal mass numbers)	Total number of isotopes (stable or nearly stable / radioactive / metastable isomers)	Macroscopic (microscopic) thermal neutron cross sections[a], cm^{-1} (b)		Neutron moderating ability (macroscopic slowing down power)[b] $\xi\Sigma_s$, 10^{-3}	Resonance integral for neutron capture I_γ, b
			capture (absorption) Σ_a (σ_a)	scattering[c] Σ_s(σ_s)		
C	8-22	15 (2/13/0)	~0.32×10^{-3} (3.50×10^{-3})	~0.43 (~4.75)	~70	1.57×10^{-3}
Ir	164-199	68 (2/34/32)	29.9 (425.3)	0.984 (14.0)	–	2150
Mo[d]	83-115	41 (7/26/7)	0.163 (2.51-2.55)	0.368 (5.71)	9.27	24
Nb (^{93}Nb)	81-113	58 (1/32/25)	0.0640 (1.15)	0.348 (6.255)	5.82	8.5
Os	162-197	45 (7/28/10)	1.14 (16.0)	1.05 (14.7)	8.2	180
Re[e]	160-194	56 (2/33/21)	6.09 (89.7)	0.781 (11.5)	14.2	831
Ta (^{181}Ta)	155-190	73 (1/35/37)	1.14 (20.6)	0.333 (6.01)	3.04	660
W[f]	158-192	46 (5/30/11)	1.16 (18.4)	0.292 (4.60)	3.35	352

[a] For 2200 m s^{-1} neutrons

[b] ξ – the average logarithmic decrement (or the average change in the logarithm of neutron energy per collision)

[c] Total bound scattering cross sections

[d] For ^{98}Mo: $\sigma_a = 0.127$ b and $\sigma_s = 5.44$ b, for ^{96}Mo: $\sigma_a = 0.5$ b and $\sigma_s = 4.83$ b, for ^{95}Mo: $\sigma_a = 13.1$ b and $\sigma_s = 6.5$ b, for ^{92}Mo: $\sigma_a = 0.019$ b and $\sigma_s = 6$ b

[e] For ^{187}Re $\sigma_a = 76.4$ b and $\sigma_s = 11.9$ b, for ^{185}Re $\sigma_a = 112$ b and $\sigma_s = 10.7$ b

[f] For ^{184}W: $\sigma_a = 1.7$ b and $\sigma_s = 7.03$ b, for ^{186}W: $\sigma_a = 37.9$ b and $\sigma_s = 0.065$ b, for ^{182}W: $\sigma_a = 20.7$ b and $\sigma_s = 6.1$ b, for ^{183}W: $\sigma_a = 10.1$ b and $\sigma_s = 5.7$ b, for ^{180}W: $\sigma_a = 30$ b and $\sigma_s = 3$ b

Table A.9 Physico-chemical properties (diffusion rate in species pairs at various temperatures)

Species pair	Temperature dependence of the diffusion coefficient (diffusivity) $D = D_0\exp[(E_A/R)/T]$, $cm^2\ s^{-1}$	Temp. range, K (°C)	Remarks on materials characteristics and measurement method
C → C	$D_{perp} = 2.5\times10^{-14}$, $D_{paral} = (2.7\div3.0)\times10^{-13}$	2470 (2200)	Natural graphite s-cr. in parallel and perpendicular directions to the basal plane, ^{14}CO exchange method
	$(0.4\div14.4)\exp[(-82000\pm6000)/T]$	2265-2620 (1995-2350)	Natural graphite s-cr. in parallel direction to the basal plane, ^{14}CO exchange method
	$0.91\exp(-79000/T)$	2665-3175 (2395-2905)	In the growth direction of columnar pyrocarbon, residual activity method using radioactive diffusant
	$0.4\exp(-23000/T)$	2270-2970 (2000-2700)	P-cr. synthetic graphite (bulk), ^{14}C-isotope tracer technique
	$(0.012\div10560)\times10^{-6}\times$ $\times\exp[-(40500\div74700)/T]$	2470 (2200)	Various synthetic isotropic graphites, ^{14}CO exchange method
C ← B	$3.02\exp(-28625/T)$	2210-2670 (1940-2400)	Formation of solid solution
C → Be	$3.2\times10^{-5}\exp(-19080/T)$	-	P-cr. Be, thin layer method with measurement of $c \sim x$ curves by sectioning and counting using ^{14}C radioactive diffusant
C → Ca	$2.7\times10^{-3}\exp(-11700/T)$	770-1070 (500-800)	99.95 % purified p-cr. Ca, residual activity method using ^{14}C radioactive diffusant
C → Co	$8.72\times10^{-2}\exp(-18000/T)$	720-1070 (450-800)	Thin layer method with measurement of $c \sim x$ curves by sectioning and counting (for paramagnetic Co)
	$0.31\exp(-18500/T)$	1070-1670 (800-1400)	Thin layer method with measurement of $c \sim x$ curves by sectioning and counting (for ferromagnetic and paramagnetic Co)
C → Cr	$8.74\times10^{-3}\exp(-13340/T)$	420-1870 (150-1600)	Indirect method by internal friction (for lower temp.) and in-diffusion method, calculated from $c \sim x$ curves (for higher temp.)
C → Er	$1.14\times10^{-2}\exp(-14100/T)$	950-1470 (680-1200)	P-cr. Er, residual activity method using ^{14}C radioactive diffusant
C → α-Fe	$\lg D = -0.9064 - 0.5199(10^4/T) +$ $+ 1.61\times10^{-3}(10^4/T)^2$	-	From various sources
C → γ-Fe	$0.234\exp(-17780/T)$	-	Diffusion couple method with determination of $c \sim x$ curves

(continued)

Table A.9 (continued)

Species pair	Temperature dependence of the diffusion coefficient (diffusivity) $D = D_0\exp[(-E_A/R)/T]$, $cm^2\ s^{-1}$	Temp. range, K (°C)	Remarks on materials characteristics and measurement method
C → α-Hf	$74\exp(-37560/T)$	1390-2030 (1120-1760)	P-cr. Hf (1.5 wt.% Zr), residual activity method using ^{14}C radioactive diffusant
C → β-Hf	$0.8\exp(-25430/T)$	2070-2370 (1800-2100)	P-cr. Hf (3 wt.% Zr), diffusion couple method with determination of $c \sim x$ curves by calculation from an analytical solution
C → HfC_{1-x}	$63\exp[(-65600\pm6560)/T]$	2470-3070 (2200-2800)	P-cr. HfC_{1-x} (x = 0.008, 20-30 μm grain size, 5-6 % porosity, O+N ≤ 0.05 %), ^{14}C radiotracer
	$4.7\times10^{-4}\exp[(-64460\pm3270)/T]$	1860-2270 (1590-2000)	P-cr. HfC_{1-x} (x = 0.19, 5 % porosity, C_f^a − 0.9 %), ^{14}C radiotracer
C → Ho	$2.8\times10^{-2}\exp(-15100/T)$	870-1430 (600-1160)	P-cr. Ho, residual activity method using ^{14}C radioactive diffusant
C → β-La	$4.1\times10^{-3}\exp(-10100/T)$	720-1125 (450-855)	P-cr. La, residual activity method using ^{14}C radioactive diffusant
C → Mg	$2.1\times10^{-7}\exp(-6290/T)$	770-870 (500-600)	P-cr. Mg, residual activity method using ^{14}C radioactive diffusant
C → Mo	$2.0\times10^{-3}\exp(-13930/T)$	490-540 (220-270)	Calculation based on C precipitation rate
	$1.04\times10^{-2}\exp(-16700/T)$	1530-2280 (1260-2010)	P-cr. Mo, in-diffusion method
	$7.80\exp[(-41500\pm4300)/T]$	–	Calculation based on the thickness of $Mo_{2\pm x}C$ layer
	$4.14\times10^{-5}\exp(-14500/T)$, ?	1470-2270 (1200-2000)	–
	$2.04\times10^{-2}\exp(-20500/T)$	1470-1670 (1200-1400)	Sectioning technique
C → β-$Mo_{2\pm x}C$	$(80\pm20)\exp[(-46100\pm2260)/T]$	1740-2000 (1470-1730)	P-cr. (cast) β-$Mo_{2\pm x}C$ (C – 6.1 mas.%), ^{14}C radiotracer
	$(300\pm60)\exp[(-47830\pm2510)/T]$	1720-2270 (1450-2000)	β-$Mo_{2\pm x}C$ prepared by carbidization of s-cr. Mo, ^{14}C radiotracer
C → Nb	$1\times10^{-2}\exp(-17070/T)$	400-2610 (130-2340)	Combined data from several sources
	$1.94\times10^{-6}\exp(-8250/T)$, ?	1270-2270 (1200-2000)	Calculation based on the thickness of NbC_{1-x} layer
	$1.09\times10^{-5}\exp(-16000/T)$	–	^{95}Nb radiometric method, sectioning technique

(continued)

Table A.9 (continued)

Species pair	Temperature dependence of the diffusion coefficient (diffusivity) $D = D_0\exp[(-E_A/R)/T]$, $cm^2\ s^{-1}$	Temp. range, K (°C)	Remarks on materials characteristics and measurement method
	$4.5\times10^{-3}\exp[(-13645\pm40)/T]$	–	–
	$9.32\times10^{-3}\exp(-17500/T)$	1470-1670 (1200-1400)	Sectioning technique
C → NbC_{1-x}	$0.86\exp(-44060/T)$	2070-2470 (1800-2200)	NbC_{1-x} ($x \approx 0$), ^{14}C radiotracer
	$(0.11^{+0.003}_{-0.1})\times$ $\times\exp[(-47340\pm910)/T]$	2670-3070 (2400-2800)	P-cr. NbC_{1-x} ($x = 0.03$, 1-3 % porosity), ^{14}C radiotracer
	$(0.21^{+0.18}_{-0.1})\times$ $\times\exp[(-48600\pm1820)/T]$	2670-3070 (2400-2800)	P-cr. NbC_{1-x} ($x = 0.085$, 1-3 % porosity), ^{14}C radiotracer
	$(1.47^{+0.52}_{-0.38})\times$ $\times\exp[(-50360\pm850)/T]$	2670-3070 (2400-2800)	P-cr. NbC_{1-x} ($x = 0.22$, 1-3 % porosity), ^{14}C radiotracer
	$0.5\exp[(-51370\pm5140)/T]$	2570-3070 (2300-2800)	P-cr. NbC_{1-x} ($x = 0.08$, 250-270 μm grain size, 2-3 % porosity, O+N ≤ 0.7 %), ^{14}C radiotracer
	$1.49\times10^{-2}\exp(-38570/T)$	1900-3100 (1630-2830)	P-cr. NbC_{1-x} ($x \approx 0$, porosity ≤ 5 %, O+N ≤ 0.32 %), ^{14}C radiotracer
	$(2.59^{+1.82}_{-1.07})\times$ $\times\exp[(-50570\pm1110)/T]$	1900-2315 (1630-2045)	NbC_{1-x} ($x \approx 0.13$), plane (110), ^{14}C radiotracer
	$(7.44^{+9.36}_{-4.14})\times$ $\times\exp[(-52870\pm1660)/T]$	1900-2315 (1630-2045)	NbC_{1-x} ($x \approx 0.17$), plane (100), ^{14}C radiotracer
	$(2.22^{+1.98}_{-1.04})\times10^{-2}\times$ $\times\exp[(-38280\pm1360)/T]$	1900-2315 (1630-2045)	NbC_{1-x} ($x \approx 0.23$), plane (110), ^{14}C radiotracer
C → $Nb_yZr_zC_{1-x}$	$(2.28^{+0.47}_{-0.3})\times$ $\times\exp[(-48500\pm1260)/T]$	2770-3470 (2500-3200)	P-cr. $Nb_yZr_zC_{1-x}$ ($x = 0.03$, $y = 0.52$, $z = 0.48$), ^{14}C radiotracer
	$(0.84^{+0.47}_{-0.3})\times$ $\times\exp[(-50600\pm1730)/T]$	2770-3470 (2500-3200)	P-cr. $Nb_yZr_zC_{1-x}$ ($x = 0.18$, $y = 0.52$, $z = 0.48$), ^{14}C radiotracer
C → Ni	$0.12\exp(-16500/T)$	870-1670 (600-1400)	P-cr. Ni (0.1 wt.% C), diffusion couple method with determination of $c \sim x$ curves by calculation from an analytical solution, ^{14}C radiotracer
C → α-Sc	$4.5\exp(-24700/T)$	1270-1570 (1000-1300)	P-cr. Sc, residual activity method using ^{14}C radioactive diffusant
C → Si	$0.33\exp(-33900/T)$	1340-1670 (1070-1400)	Radiotracer ^{14}C with mechanical sectioning
	$33\exp(-34100/T)$	1220-1370 (950-1100)	Sectioning technique
	$6.5\exp(-34800/T)$	1425-1635 (1155-1365)	Radiotracer ^{14}C with mechanical sectioning
	$0.95\exp(-35300/T)$	1170-1655 (900-1385)	Radiotracer ^{14}C with mechanical sectioning

(continued)

Table A.9 (continued)

Species pair	Temperature dependence of the diffusion coefficient (diffusivity) $D = D_0\exp[(-E_A/R)/T]$, $cm^2\ s^{-1}$	Temp. range, K (°C)	Remarks on materials characteristics and measurement method
C → α-SiC	$(8.62\pm2.01)\times10^5\times$ $\times\exp[(-86050\pm580)/T]$	2120-2450 (1850-2180)	Radiotracer ^{14}C diffusion in intrinsic s-cr. SiC
	$(3.32\pm1.43)\times10^7\times$ $\times\exp[(-95220\pm930)/T]$	2120-2450 (1850-2180)	Radiotracer ^{14}C diffusion in N-doped n-type s-cr. SiC
	$3\times10^2\exp(-71850/T)$	2125-2335 (1855-2065)	Radiotracer ^{14}C diffusion in Al-doped p-type 6H-SiC
	$2\times10^{17}\exp(-151800/T)$	2250-2360 (1980-2090)	Radiotracer diffusion in N-doped n-type 6H-SiC
C → β-SiC	$(2.62\pm1.83)\times10^8\times$ $\times\exp[(-101260\pm1620)/T]$	2130-2370 (1860-2100)	Radiotracer ^{14}C diffusion in p-cr. SiC
C → α-Sm	$3.6\exp(-17600/T)$	–	P-cr. Sm, residual activity method using ^{14}C radioactive diffusant
C → Ta	$6.7\times10^{-3}\exp(-19400/T)$	460-2950 (190-2680)	Combined data, several sources
	$4\times10^{-3}\exp[(-16500\pm90)/T]$	–	–
	$3.43\times10^{-6}\exp(-10500/T)$	1270-2070 (1200-1800)	Calculation based on the thickness of $Ta_{2+x}C$ layer
	$2.57\times10^{-2}\exp(-21500/T)$	1470-1870 (1200-1600)	–
C → TaC_{1-x}	$3.9\exp[(-59800\pm5940)/T]$	2630-3230 (2360-2960)	P-cr. TaC_{1-x} (x = 0.08, 15-20 μm grain size, 7-8 % porosity, O+N ≤ 0.6 %), ^{14}C radiotracer
C → β-Th	$2.2\times10^{-2}\exp(-13600/T)$	1710-1910 (1440-1640)	P-cr. Th, diffusion couple method with determination of $c \sim x$ curves by calculation from an analytical solution
C → α-Ti	$7.9\times10^{-4}\exp(-15360/T)$	870-1070 (600-800)	P-cr. Ti, residual activity method using ^{14}C radioactive diffusant
C → β-Ti	$3.2\times10^{-3}\exp(-9500/T)$	1220-1920 (950-1650)	P-cr. Ti, residual activity method using ^{14}C radioactive diffusant
	$3.02\times10^{-3}\exp(-10000/T)$	1370-1670 (1100-1400)	Sectioning technique
C → TiC_{1-x}	$(6.98\pm1.24)\exp[(-48000\pm350)/T]$	1720-2550 (1450-2280)	P-cr. (arc-cast)TiC_{1-x} (x = 0.03), ^{14}C radiotracer
	$(45.44\pm5.12)\exp[(-53800\pm200)/T]$	1720-2550 (1450-2280)	P-cr. (arc-cast) TiC_{1-x} (x = 0.11), ^{14}C radiotracer
	$(114\pm66)\exp[(-55300\pm1000)/T]$	2020-2350 (1750-2080)	P-cr. (arc-cast) TiC_{1-x} (x = 0.33), ^{14}C radiotracer
	$(2.85\pm0.2)\times10^{-3}\times$ $\times\exp[(-25000\pm150)/T]$	2350-2990 (2080-2720)	P-cr. (arc-cast) TiC_{1-x} (x = 0.33), ^{14}C radiotracer

(continued)

Table A.9 (continued)

Species pair	Temperature dependence of the diffusion coefficient (diffusivity) $D = D_0\exp[(-E_A/R)/T]$, $cm^2\ s^{-1}$	Temp. range, K (°C)	Remarks on materials characteristics and measurement method
C → γ-U	$0.218\exp(-14800/T)$	1130-1270 (860-1000)	P-cr. U, diffusion couple method with determination of $c \sim x$ curves by calculation from an analytical solution, ^{14}C radiotracer
C → $UC_{1\pm x}$	$32.3\exp[(-42810\pm3020)/T]$	1720-2070 (1450-1800)	P-cr. (arc-cast) $UC_{1\pm x}$ (C − 4.7 %, O+N ≤ 0.025 %), ^{14}C radiotracer
	$1.75\exp[(-31730\pm510)/T]$	1520-1970 (1250-1700)	P-cr. (arc-cast) $UC_{1\pm x}$ (C − 4.8 %, O+N ≤ 0.025 %), ^{14}C radiotracer
	$3.21\times10^{-2}\exp[(-27700\pm4030)/T]$	1470-1920 (1200-1650)	P-cr. (arc-cast) $UC_{1\pm x}$ (C − 5.0 %, O+N ≤ 0.025 %), ^{14}C radiotracer
	$2.95\times10^{-2}\exp[(-27200\pm7550)/T]$	1470-1870 (1200-1600)	P-cr. (arc-cast) $UC_{1\pm x}$ (C − 5.1 %, O+N ≤ 0.025 %), ^{14}C radiotracer
	$2.76\times10^{-3}\exp[(-22660\pm3020)/T]$	1470-1900 (1200-1630)	P-cr. (arc-cast) $UC_{1\pm x}$ (C − 5.6 %, O+N ≤ 0.025 %), ^{14}C radiotracer
C → β-UC_{2-x}	$7.6\times10^{-3}\exp(-41000/T)$	1920-2620 (1650-2350)	Sectioning chemical analysis
	$51\exp(-42700/T)$	2100-2620 (1830-2350)	β-UC_{2-x} ($x \approx 0.2$), ^{14}C radiotracer
	$9.5\exp(-38850/T)$	2100-2620 (1830-2350)	β-UC_{2-x} ($x \approx 0.1$), ^{14}C radiotracer
C → UC_xN_z	$16\exp(-42200/T)$	1770-2070 (1500-1800)	P-cr. UC_xN_z ($x = 0.67$, $z = 0.33$, 14.6 % porosity, O − 0.04 mas.%), ^{14}C radiotracer
	$D = 7.5\times10^{-11}$	1880 (1610)	P-cr. UC_xN_z ($x = 0.26$, $z = 0.74$) under pressure N_2 − 0.07-1.33 MPa, ^{14}C radiotracer
	$D = 1.5\times10^{-10}$	1920 (1650)	
	$D = 4.5\times10^{-10}$	1980 (1710)	
	$D = 2.3\times10^{-9}$	2050 (1780)	
	$D = 1.4\times10^{-11}$	1880 (1610)	P-cr. UC_xN_z ($x = 0.18$, $z = 0.82$, 9 % porosity, O − 0.02 mas.%), under pressure N_2 − 0.07-1.33 MPa, ^{14}C radiotracer
	$D = 2.1\times10^{-10}$	1980 (1710)	
	$D = 5.6\times10^{-10}$	2050 (1780)	
C → V	$8.8\times10^{-3}\exp(-14000/T)$	330-2095 (60-1825)	Combined data – several sources
C → VC_{1-x}	$0.13\exp(-36100/T)$	1270-2270 (1000-2000)	P-cr. VC_{1-x} ($x \approx 0.1$, 10-30 μm grain size, 2.0-4.5 % porosity), ^{14}C radiotracer
	$(5\pm1)\times10^{-2}\times$ $\times\exp[(-33740\pm1770)/T]$	1770-2170 (1500-1900)	P-cr. (arc-cast)VC_{1-x} ($x = 0.13$), ^{14}C radiotracer
C → W	$9.22\times10^{-3}\exp(-20340/T)$	2070-3070 (1800-2800)	P-cr. W, diffusion couple method with determination of $c \sim x$ curves by calculation from an analytical solution, ^{14}C radiotracer
	$3.15\times10^{-3}\exp(-20700/T)$	370-670 (100-400)	P-cr. W, indirect method by internal friction

(continued)

Table A.9 (continued)

Species pair	Temperature dependence of the diffusion coefficient (diffusivity) $D = D_0\exp[(-E_A/R)/T]$, $cm^2\ s^{-1}$	Temp. range, K (°C)	Remarks on materials characteristics and measurement method
C → α-$W_{2+x}C$	$18.3\exp(-46100/T)$	1470-2270 (1200-2000)	α-$W_{2+x}C$ (C_{total} – 3.25 mas.%), ^{14}C radiotracer
C → δ-$WC_{1\pm x}$	$1.9\times10^{-6}\exp(-44300/T)$	2240-2640 (1970-2370)	P-cr. δ-$WC_{1\pm x}$ (O ≤ 0.03 mas.%), ^{14}C radiotracer
C → Y	$1.7\times10^{-4}\exp(-32700/T)$, ?	1270-1730 (1000-1460)	P-cr. Y, combined recalculated data
C → Zn	$1.0\times10^{-5}\exp(-6040/T)$	440-655 (170-385)	P-cr. Zn, residual activity method using ^{14}C radioactive diffusant
C → α-Zr	$2.0\times10^{-3}\exp(-18200/T)$	870-1120 (600-850)	P-cr. Zr, residual activity method using ^{14}C radioactive diffusant
C → β-Zr	$8.9\times10^{-2}\exp(-16000/T)$	1140-1520 (870-1250)	Residual activity method using ^{14}C radioactive diffusant
	$4.8\times10^{-3}\exp(-13400/T)$	1170-1520 (900-1250)	P-cr. Zr, diffusion couple method with determination of $c \sim x$ curves by calculation from an analytical solution
C → ZrC_{1-x}	$1.32\times10^{2}\exp(-56900/T)$	1620-2420 (1350-2150)	S-cr. ZrC_{1-x} ($x = 0.035$), ^{14}C radiotracer
	$(3.30\pm0.6)\times10^{2}\times$ $\times\exp[(-57400\pm3020)/T]$	1870-2370 (1600-2100)	P-cr. ZrC_{1-x} ($x = 0.04$, 5 % porosity), ^{14}C radiotracer
	$0.564\times10^{2}\exp[(-62400\pm6240)/T]$	2520-3010 (2250-2740)	P-cr. ZrC_{1-x} ($x = 0.19$, 110-130 μm grain size, 3 % porosity, O+N ≤ 0.6 %), ^{14}C radiotracer
	$(14.1^{+13.5}_{-12.7})\times$ $\times\exp[(-54800\pm3060)/T]$	2670-3070 (2400-2800)	P-cr. ZrC_{1-x} ($x = 0.03$, 1-3 % porosity, O+N ≤ 1.5÷2 %), ^{14}C radiotracer
	$(19.5^{+40.5}_{-13})\times$ $\times\exp[(-60200\pm3130)/T]$	2670-3070 (2400-2800)	P-cr. ZrC_{1-x} ($x = 0.075$, 1-3 % porosity, O+N ≤ 1.5÷2 %), ^{14}C radiotracer
	$(61.2^{+45.2}_{-54})\times$ $\times\exp[(-64200\pm6040)/T]$	2670-3070 (2400-2800)	P-cr. ZrC_{1-x} ($x = 0.12$, 1-3 % porosity, O+N ≤ 1.5÷2 %), ^{14}C radiotracer
	$(2.64^{+4.26}_{-1.63})\times10^{2}\times$ $\times\exp[(-67000\pm4200)/T]$	2670-3070 (2400-2800)	P-cr. ZrC_{1-x} ($x = 0.15$, 1-3 % porosity, O+N ≤ 1.5÷2 %), ^{14}C radiotracer
	$(3.16^{+8.80}_{-2.32})\times10^{2}\times$ $\times\exp[(-69240\pm3820)/T]$	2670-3070 (2400-2800)	P-cr. ZrC_{1-x} ($x = 0.16$, 1-3 % porosity, O+N ≤ 1.5÷2 %), ^{14}C radiotracer
	$(2.8^{+5.0}_{-2.0})\times10^{4}\times$ $\times\exp[(-82600\pm2600)/T]$	2770-3270 (2500-3000)	P-cr. ZrC_{1-x} ($x = 0.30$, 1-3 % porosity, O+N ≤ 1.5÷2 %), ^{14}C radiotracer
Ir → Ir	$0.36\exp(-52800/T)$	2090-2660 (1820-2390)	99.9 % purified s-cr. Ir, ^{192}Ir radiometric method, sectioning technique

(continued)

Table A.9 (continued)

Species pair	Temperature dependence of the diffusion coefficient (diffusivity) $D = D_0\exp[(-E_A/R)/T]$, $cm^2\ s^{-1}$	Temp. range, K (°C)	Remarks on materials characteristics and measurement method
Ir ← Au	$0.49\exp(-52000/T)$	1370-1900 (1100-1630)	99.99 % purified s-cr. Ir, in-diffusion method, secondary ion mass spectrometry
Ir ← Co	$0.11\exp(-47200/T)$	1545-1780 (1275-1510)	99.99 % purified s-cr. Ir, in-diffusion method, secondary ion mass spectrometry
Ir → Cu	$10.6\exp(-33250/T)$	1180-1300 (910-1030)	99.99 % purified s-cr. Cu, thin layer method with measurement of $c \sim x$ curves by sectioning and counting using ^{192}Ir radioactive diffusant
Ir → W	$0.32\exp(-60900/T)$	2010-2960 (1740-2690)	S-cr. W, thin layer method with measurement of $c \sim x$ curves by sectioning and counting using ^{192}Ir radioactive diffusant
Mo → Mo	$0.13\exp(-52610/T)+$ $+1.39\times10^{2}\exp(-66080/T)$	1360-2770 (1090-2500)	99.99 % purified s-cr. Mo, ^{99}Mo radiometric method, sectioning technique
	$(4.0\div5.7)\exp[(-57500\div57900)/T]$	2070-2445 (1800-2175)	99.3 % purified p-cr. Mo (0.7% W), residual activity method using ^{99}Mo radioactive diffusant
	$2.77\exp(-55900/T)$	1970-2190 (1700-1920)	~99.9 % purified p-cr. Mo (1-2 mm grain size), serial sectioning with ^{99}Mo radioactive diffusant
	$8\exp(-58700/T)$	1360-2770 (1090-2500)	99.99 % purified s-cr. Mo, ^{99}Mo radioactive diffusant
	$1.8\exp(-55000/T)$	2430-2830 (2160-2560)	99.98 % purified metal, ^{99}Mo radiometric method
	$0.280\exp(-36600/T)$	1470-1870 (1200-1600)	–
	$(0.2\div1.2)\exp[(-43450\pm2200)/T]$	2120-2620 (1850-2350)	^{99}Mo radiometric method, sectioning technique
	$4.52\exp[(-56650\pm100)/T]$	–	–
Mo ← B	$6.96\times10^{-2}\exp[(-22500\pm2900)/T]$	–	Calculation based on the thickness of $Mo_{2\pm x}B$ layer
	$2.53\times10^{-6}\exp(-12000/T)$	1370-2070 (1100-1800)	–
Mo ← Co	$3.0\exp(-50360/T)$	2210-2600 (1940-2330)	99.97 % purified p-cr. Mo (1-2 mm grain size), autoradiography using ^{60}Co radioactive diffusant
	$18\exp(-53740/T)$	2120-2600 (1850-2330)	99.99 % purified s-cr. and 99.97 % purified p-cr. Mo, thin layer method with measurement of $c \sim x$ curves by serial sectioning and counting using ^{60}Co radioactive diffusant

(continued)

Table A.9 (continued)

Species pair	Temperature dependence of the diffusion coefficient (diffusivity) $D = D_0\exp[(-E_A/R)/T]$, $cm^2\ s^{-1}$	Temp. range, K (°C)	Remarks on materials characteristics and measurement method
	$6\exp(-39030/T)$	1270-1770 (1000-1500)	P-cr. Mo, residual activity method using ^{60}Co radioactive diffusant
	$2.82\times10^{-6}\exp(-17400/T)$	1170-1970 (900-1700)	Metallography and sectioning chemical analysis
Mo ← Cr	$1.88\exp[(-40800\div41200)/T]$	1270-1420 (1000-1150)	~99.7 % purified s-cr. Mo, residual activity method using ^{51}Cr radioactive diffusant
	$2.5\times10^{-4}\exp(-27200/T)$	1270-1770 (1000-1500)	P-cr. Mo, residual activity method using ^{51}Cr radioactive diffusant
Mo → Cr	$2.7\times10^{-3}\exp(-29200/T)$	1370-1690 (1100-1420)	P-cr. Cr, residual activity method using ^{99}Mo radioactive diffusant
Mo ← Fe	$0.15\exp(-41650/T)$	1270-1620 (1000-1350)	99.96 % purified p-cr. Mo, residual activity method using ^{59}Fe radioactive diffusant
	$3.7\times10^{-3}\exp(-35100/T)$	1200-1475 (930-1205)	P-cr. Mo, residual activity method using ^{59}Fe radioactive diffusant
Mo → α-Fe	$1.48\times10^{-2}\exp(-34000/T)$	830-1160 (560-890)	99.995 % purified p-cr. Fe (3-5 mm grain size), ^{99}Mo radioactive diffusant
	$45.9\exp(-34240/T)$	980-1030 (710-760)	99.97 % purified p-cr. Fe (ferromagnetic), residual activity method using ^{99}Mo radioactive diffusant
	$30.6\exp(-32840/T)$	1050-1170 (780-900)	99.97 % purified p-cr. Fe (paramagnetic), residual activity method using ^{99}Mo radioactive diffusant
Mo → γ-Fe	$25.1\exp(-38930/T)$	1220-1570 (950-1300)	99.97 % purified p-cr. Fe, residual activity method using ^{99}Mo radioactive diffusant
Mo ← H	$5.9\times10^{-2}\exp(-7350/T)$	800-1250 (530-980)	–
	$7.6\times10^{-5}\exp(-4200/T)$	–	–
Mo ← K	$2.86\times10^{-10}\exp(-7300/T)$	1070-1370 (800-1100)	P-cr. Mo, isotope method
	$9.34\times10^{-9}\exp(-13250/T)$	1070-1370 (800-1100)	S-cr. Mo
Mo ← Li	$1\times10^{-2}\exp(-56600/T)$	1840-2240 (1570-1970)	S-cr. Mo with natural Li, in-diffusion method, calculated from $c \sim x$ curves
Mo ← Nb	$1.0\times10^{3}\exp(-70000/T)$	2070-2435 (1800-2165)	P-cr. Mo, electron microprobe analysis

(continued)

Table A.9 (continued)

Species pair	Temperature dependence of the diffusion coefficient (diffusivity) $D = D_0\exp[(-E_A/R)/T]$, $cm^2\ s^{-1}$	Temp. range, K (°C)	Remarks on materials characteristics and measurement method
	$14\exp(-54440/T)$	2120-2620 (1850-2350)	99.98 % purified p-cr. Mo, thin layer method with measurement of $c \sim x$ curves by sectioning and counting using ^{95}Nb radioactive diffusant
	$(2.9\div4.5)\exp[(-57800\div68500)/T)]$	2095-2450 (1825-2180)	99.9 % purified p-cr. Mo, diffusion couple method with determination of $c \sim x$ curves by electron microprobe analysis
	$1.7\times10^{-2}\exp(-45620/T)$	1970-2270 (1700-2000)	P-cr. Mo, residual activity method using ^{95}Nb radioactive diffusant
	$0.7\exp(-41500/T)$	1370 (1100)	Electron-beam probe technique
Mo → Nb	$92\exp(-61500/T)$	1995-2455 (1725-2185)	99.7 % purified p-cr. Nb, diffusion couple method with determination of $c \sim x$ curves by electron microprobe analysis
	$1.3\times10^{-2}\exp(-42150/T)$	1970-2295 (1700-2025)	P-cr. Nb, residual activity method using ^{99}Mo radioactive diffusant
Mo ← Ni	$D = (2.4\div3.2)\times10^{-12}$	1620 (1350)	S-cr. Mo, residual activity method using ^{63}Ni radioactive diffusant
Mo ← P	$0.19\exp(-40500/T)$	2270-2490 (2000-2220)	99.97 % purified s-cr. Mo, residual activity method using ^{32}P radioactive diffusant
Mo ← Re	$9.7\times10^{-2}\exp(-47690/T)$	1970-2370 (1700-2100)	P-cr. Mo, thin layer method with measurement of $c \sim x$ curves by serial sectioning using ^{186}Re radioactive diffusant
	$9.68\times10^{-3}\exp[(-47350\pm750)/T]$	–	–
Mo ← S	$(0.32\div3.80)\times10^{3}\times$ $\times\exp[(-51000\div63000)/T]$	2490-2740 (2220-2470)	99.97 % purified s-cr. Mo, using ^{35}S radioactive diffusant
	$3.4\times10^{-2}\exp(-35760/T)$	1235-1440 (965-1170)	P-cr. Mo, residual activity method using ^{35}S radioactive diffusant
Mo ← Si	$56.1\exp(-18420/T)$	1170-1370 (900-1100)	Calculation based on the thickness of $MoSi_2$ layer
Mo ← Ta	$3.5\times10^{-4}\exp(-41800/T)$	1190-1420 (920-1150)	P-cr. Mo, residual activity method using ^{182}Ta radioactive diffusant
	$1.9\exp(-56900/T)$	2095-2445 (1825-2175)	99.9 % purified p-cr. Mo, diffusion couple method with determination of $c \sim x$ curves, electron microprobe analysis
	$7.7\times10^{-11}\exp(-106000/T)+$ $+2.8\times10^{-4}\exp(-35400/T)$	1770-2490 (1500-2220)	Electron microprobe analysis
Mo → Ta	$8.38\times10^{-10}\exp(-12000/T)+$ $+2.56\times10^{-4}\exp(-35700/T)$	1770-2490 (1500-2220)	Electron microprobe analysis

(continued)

Table A.9 (continued)

Species pair	Temperature dependence of the diffusion coefficient (diffusivity) $D = D_0\exp[(-E_A/R)/T]$, $cm^2\ s^{-1}$	Temp. range, K (°C)	Remarks on materials characteristics and measurement method
	$1.8\times10^{-3}\exp(-40790/T)$	2020-2500 (1750-2230)	P-cr. Ta, residual activity method using ^{99}Mo radioactive diffusant
	$0.28\exp(-52900/T)$	2195-2445 (1925-2175)	99.7 % purified p-cr. Ta, electron microprobe analysis
Mo ← Th	$D = 3.6\times10^{-10}$	1890 (1620)	Thermoionic-emission method
	$D = 1.0\times10^{-6}$	2270 (2000)	Thermoionic-emission method
Mo ← Ti	$0.8\exp(-50750/T)$	1670-1910 (1400-1640)	Metallography method
Mo → β-Ti	$20\exp(-36760/T)+$ $+8.0\times10^{-3}\exp(-21650/T)$	1170-1920 (900-1650)	99.7-99.9 % purified p-cr. Ti, thin layer method with measurement of $c \sim x$ curves by sectioning and counting using ^{99}Mo radioactive diffusant
	$2.82\times10^{-4}\exp[(-16600\div16700)/T]$	1170-1370 (900-1100)	99.94 % purified p-cr. Ti, ^{99}Mo radiometric method, sectioning technique
	$0.24\exp[(-25650\div25840)/T]$	1370-1830 (1100-1560)	99.94 % purified p-cr. Ti, ^{99}Mo radiometric method, sectioning technique
Mo ← U	$7.6\times10^{-3}\exp(-38500/T)$	1770-2270 (1500-2000)	99.98 % purified p-cr. Mo, residual activity method using ^{235}U diffusant
	$1.3\times10^{-6}\exp(-38100/T)$	2070-2370 (1800-2100)	P-cr. Mo, thin layer method using ^{235}U diffusant
	$8.9\times10^{-2}\exp(-38400/T)$	1770-2270 (1500-2000)	Sectioning technique
Mo ← V	$2.9\exp(-57000/T)$	1995-2445 (1725-2175)	99.9 % purified p-cr. Mo, diffusion couple method with determination of $c \sim x$ curves, electron microprobe analysis
Mo ← W	$1.7\exp(-55400/T)$	1970-2530 (1700-2260)	P-cr. Mo, thin layer method with measurement of $c \sim x$ curves by sectioning and counting using ^{185}W radioactive diffusant
	$3.6\exp(-62000/T)$	2170-2540 (1900-2270)	S-cr. Mo, electron microprobe analysis
	$4.5\times10^{-4}\exp(-39030/T)$	1970-2420 (1700-2150)	P-cr. Mo, residual activity method using ^{185}W radioactive diffusant
	$(1.4\div1.5)\times10^{2}\exp(-68500/T)$	2090-2450 (1820-2180)	99.9 % purified p-cr. Mo, diffusion couple method with determination of $c \sim x$ curves, electron microprobe analysis
	$5\times10^{-4}\exp(-39000/T)$	1970-2240 (1700-1970)	Sectioning technique

(continued)

Table A.9 (continued)

Species pair	Temperature dependence of the diffusion coefficient (diffusivity) $D = D_0\exp[(-E_A/R)/T]$, $cm^2\ s^{-1}$	Temp. range, K (°C)	Remarks on materials characteristics and measurement method
Mo → W	$5\times10^{-2}\exp(-60930/T)$	2270-2670 (2000-2400)	P-cr. W, ^{99}Mo radiometric method
	$0.3\exp(-50900/T)$	1970-2370 (1700-2100)	P-cr. W, residual activity method using ^{99}Mo radioactive diffusant
	$1.4\exp[(-68100\div68200)/T]$	1910-2655 (1640-2385)	~99.999 % purified s-cr. W, measurement of concentration distribution, secondary ion mass spectrometry
	$1.45\exp(-68200/T)$	2080-2530 (1810-2260)	S-cr. W, secondary ion mass spectrometry
	$6.3\times10^{-4}\exp(-40250/T)$	1810-2530 (1540-2260)	S-cr. W, sectioning chemical analysis
	$5.3\times10^{-3}\exp(-40250/T)$	1810-2530 (1540-2260)	P-cr. W, sectioning chemical analysis
Mo ← Y	$1.8\times10^{-4}\exp(-25840/T)$	1470-1870 (1200-1600)	99.8-99.9 % purified s-cr. Mo, residual activity method using ^{91}Y radioactive diffusant
Mo ← Zr	$(1.9\div2.1)\times10^{-3}\exp(-44070/T)$	2070-2370 (1800-2100)	P-cr. Mo, residual activity method using ^{95}Zr radioactive diffusant
Mo → α-Zr	$6.22\times10^{-8}\exp(-12500/T)$	870-1120 (600-850)	P-cr. Zr, residual activity method using ^{99}Mo radioactive diffusant
Mo → β-Zr	$3.63\times10^{-2}\exp[-(22200\div22360)/T]$	1170-1470 (900-1200)	99.7 % purified p-cr. Zr, residual activity method using ^{99}Mo radioactive diffusant
	$1.29\exp[-(29100\div29300)/T]$	1625-1830 (1355-1560)	99.7 % purified p-cr. Zr, residual activity method using ^{99}Mo radioactive diffusant
	$1.99\times10^{-4}\exp(-17700/T)+$ $+2.63\exp(-34400/T)$	1170-1870 (900-1600)	P-cr. Zr, residual activity method using ^{99}Mo radioactive diffusant
Nb → Nb	$0.115\exp(-45060/T)+$ $+65\exp(-60500/T)$	1150-2695 (880-2425)	Combined and recalculated data from several sources
	$8\times10^{-3}\exp(-42050/T)+$ $+3.7\exp(-52730/T)$	1350-2695 (1080-2425)	99.98 % purified s-cr. Nb, ^{95}Nb radiometric method, sectioning technique
	$1.5\times10^{-2}\exp(-42600/T)+$ $+4.6\exp(-53300/T)$	1925-2670 (1655-2400)	S-cr. Nb, ^{95}Nb and ^{92}Nb radiometric methods
	$1.1\exp(-48350/T)$	1150-2665 (880-2395)	99.75 % purified s-cr. and p-cr. Nb, ^{95}Nb radiometric method
	$0.61\exp(-47800/T)$	1420-2510 (1150-2240)	99.9 % purified s-cr. Nb, residual activity method using ^{95}Nb radioactive diffusant
	$(12.4\pm0.8)\exp[(-52500\pm1500)/T]$	1810-2390 (1540-2120)	^{95}Nb radiometric method, sectioning technique

(continued)

Table A.9 (continued)

Species pair	Temperature dependence of the diffusion coefficient (diffusivity) $D = D_0\exp[(-E_A/R)/T]$, $cm^2\ s^{-1}$	Temp. range, K (°C)	Remarks on materials characteristics and measurement method
	$49\exp(-57500/T)$	–	S-cr. Nb, radiometric method, sectioning technique
	$17\exp(-55000/T)$	–	Cast Nb, radiometric method, sectioning technique
	$5\times10^{2}\exp(-42000/T)$	–	Powder metallurgy produced Nb, radiometric method, sectioning technique
Nb → NbC_{1-x}	$5.5\times10^{-6}\exp(-22500/T)$	1970-2370 (1700-2100)	Radiotracer diffusion
Nb ← Al	$4.5\times10^{2}\exp(-51730/T)$	1700-2000 (1430-1730)	Out-diffusion method
	$(0.055\div0.11)\exp(-40400/T)$	1620-1820 (1350-1550)	99.99 % purified p-cr. Nb, electron microprobe analysis
Nb ← B	$1.26\times10^{-7}\exp[(-29500\pm4250)/T]$	–	Calculation based on the thickness of $NbB_{2\pm x}$ layer
	$1.76\times10^{-7}\exp(-7500/T)$, ?	1670-2270 (1400-2000)	Calculation based on the thickness of $NbB_{2\pm x}$ layer
Nb → Be	$2\times10^{4}\exp(-43250/T)$	1315-1510 (1045-1240)	99.7 % purified p-cr. Be, residual activity method using ^{95}Nb radioactive diffusant
Nb ← Co	$4.18\times10^{-2}\exp(-30940/T)$	1345-2170 (1075-1900)	S-cr. Nb, thin layer method with measurement of $c \sim x$ curves by sectioning and counting using ^{60}Co radioactive diffusant
	$0.11\exp(-33040/T)$	1580-1920 (1310-1650)	99.99 % purified p-cr. Nb, thin layer method with measurement of $c \sim x$ curves by sectioning and counting using ^{60}Co radioactive diffusant
	$0.74\exp(-35500/T)$	1830-2320 (1560-2050)	99.74 % purified p-cr. Nb, thin layer method with measurement of $c \sim x$ curves by autoradiography using ^{60}Co radioactive diffusant
Nb ← Cr	$0.3\exp(-42050/T)$	1225-1705 (955-1435)	> 99.98 % purified s-cr. Nb, thin layer method with measurement of $c \sim x$ curves by sectioning and counting using ^{51}Cr radioactive diffusant
	$0.13\exp(-40600/T)$	1220-1765 (950-1495)	99.96 % purified p-cr. Nb, thin layer method with measurement of $c \sim x$ curves by sectioning and counting using ^{51}Cr radioactive diffusant
Nb ← Cu	$D = 3.71\times10^{-10}$ $D = 1.02\times10^{-9}$	1830 (1560) 1910 (1640)	99.9 % purified p-cr. Nb, thin layer method with measurement of $c \sim x$ curves by sectioning and counting using ^{64}Cu radioactive diffusant

(continued)

Table A.9 (continued)

Species pair	Temperature dependence of the diffusion coefficient (diffusivity) $D = D_0\exp[(-E_A/R)/T]$, $cm^2\ s^{-1}$	Temp. range, K (°C)	Remarks on materials characteristics and measurement method
Nb → Cu	$2.04\exp(-30250/T)$	1080-1180 (810-910)	99.999 % purified p-cr. Cu, residual activity method using ^{95}Nb radioactive diffusant
Nb ← Fe	$1.5\exp(-39130/T)$	1660-2370 (1390-2100)	99.74 % purified p-cr. Nb, thin layer method with measurement of $c \sim x$ curves by autoradiography using ^{55}Fe radioactive diffusant
	$0.14\exp(-35400/T)$	1660-2165 (1390-1895)	99.9 % purified p-cr. Nb, thin layer method with measurement of $c \sim x$ curves by sectioning and counting using ^{59}Fe radioactive diffusant
Nb → α-Fe	$D = 1.0\times10^{-12}$ $D = 5.4\times10^{-12}$	990 (720) 1025 (755)	99.98 % purified p-cr. Fe (ferromagnetic), thin layer method with measurement of $c \sim x$ curves by sectioning and counting using radioactive diffusant
	$0.502\times10^{2}\exp(-30300/T)$	1060-1160 (790-890)	99.98 % purified p-cr. Fe (paramagnetic), thin layer method with measurement of $c \sim x$ curves by sectioning and counting using radioactive diffusant
	$1.40\times10^{3}\exp(-36050/T)$	820-1160 (550-890)	99.995 % purified p-cr. Fe, ^{95}Nb radioactive diffusant
Nb → γ-Fe	$0.83\exp(-32050/T)$	1210-1600 (940-1330)	99.98 % purified p-cr. Fe, thin layer method with measurement of $c \sim x$ curves by sectioning and counting using radioactive diffusant
	$(0.69\div0.75)\exp(-31750/T)$	1220-1470 (950-1200)	99.99 % purified p-cr. Fe, ^{94}Nb and ^{95}Nb radioactive diffusants
Nb ← H	$2.10\times10^{-2}\exp[(-9685\pm300)/T]$	870-970 (600-700)	–
Nb ← N	$8.05\times10^{-4}\exp(-3630/T)$	770-870 (500-600)	Formation of solid solution
	$6.16\times10^{-4}\exp(-3080/T)$	870-1170 (600-900)	Calculation based on the thickness of β-$Nb_{2\pm x}N$ layer
	$4.5\times10^{-3}\exp(-5000/T)$	1170-1470 (900-1200)	Calculation based on the thickness of δ-NbN_{1-x} layer
	$9.8\times10^{-2}\exp(-19300/T)$	630-930 (360-660)	–
	$8.7\times10^{-3}\exp[(-17460\pm45)/T]$	420-565 (150-295)	–
Nb ← Ni	$9.3\exp(-40500/T)$	1260-1520 (990-1250)	99.82 % purified p-cr. Nb, residual activity method using ^{63}Ni radioactive diffusant

(continued)

Table A.9 (continued)

Species pair	Temperature dependence of the diffusion coefficient (diffusivity) $D = D_0\exp[(-E_A/R)/T]$, $cm^2\ s^{-1}$	Temp. range, K (°C)	Remarks on materials characteristics and measurement method
	$7.7\times10^{-2}\exp(-31780/T)$	1430-2165 (1160-1895)	99.9 % purified p-cr. Nb, thin layer method with measurement of $c \sim x$ curves by autoradiography using ^{63}Ni radioactive diffusant
Nb ← O	$1.47\times10^{-2}\exp(-13800/T)$	420-620 (150-350)	–
	$2.2\times10^{-2}\exp[(-13455\pm125)/T]$	310-420 (40-150)	–
	$D = 7.9\times10^{-10}$ $D = 6.5\times10^{-9}$	870 (600) 1085 (815)	Calculation based on oxygen loss from metal
Nb ← P	$5.1\times10^{-2}\exp(-25930/T)$	1570-2070 (1300-1800)	99.9 % purified s-cr. Nb, residual activity method using ^{32}P radioactive diffusant
Nb ← Pd	$2.4\exp(-48000/T)$	1965-2340 (1695-2070)	P-cr. Nb, electron microprobe analysis
Nb ← Ru	$29\exp(-55000/T)$	2025-2340 (1755-2070)	P-cr. Nb, steady-state method with average gradient calculated from c_1 and c_2 as deduced from equilibrium data, ^{103}Ru as a radiotracer
Nb ← S	$2.6\times10^{3}\exp(-36810/T)$	1370-1770 (1100-1500)	99.6 % purified s-cr. and p-cr. Nb, thin layer method with measurement of $c \sim x$ curves by sectioning and counting using ^{35}S radioactive diffusant
Nb ← Sc	$0.11\exp(-6500/T)$, ?	1270-1470 (1000-1200)	Radiotracer diffusion
Nb ← Si	$56.1\exp(-18420/T)$	1170-1370 (900-1100)	–
Nb ← Sn	$0.14\exp(-39730/T)$	2120-2660 (1850-2390)	99.85 % purified p-cr. Nb, thin layer method with measurement of $c \sim x$ curves by sectioning and counting using ^{113}Sn radioactive diffusant
Nb ← Ta	$1.0\exp(-50000/T)$	1375-2345 (1105-2075)	99.76 % purified s-cr. Nb, thin layer method with measurement of $c \sim x$ curves by sectioning and counting using ^{182}Ta radioactive diffusant
Nb → Ta	$2.05\times10^{-2}\exp(-46000/T)+$ $+13.6\exp(-61550/T)$	1190-2755 (920-2485)	Combined and recalculated data from several sources

(continued)

Table A.9 (continued)

Species pair	Temperature dependence of the diffusion coefficient (diffusivity) $D = D_0\exp[(-E_A/R)/T]$, $cm^2\ s^{-1}$	Temp. range, K (°C)	Remarks on materials characteristics and measurement method
	$0.32\exp(-50900/T)$	2375-2755 (2105-2485)	99.7 % purified s-cr. and p-cr. Ta, thin layer method with measurement of $c \sim x$ curves by sectioning and counting using ^{95}Nb radioactive diffusant
	$6.8\times10^{-2}\exp(-48000/T)$	1190-2275 (920-2005)	99.7 % purified s-cr. and p-cr. Ta, thin layer method with measurement of $c \sim x$ curves by sectioning and counting using ^{95}Nb radioactive diffusant
	$0.23\exp(-49700/T)$[b]	1190-2770 (920-2500)	99.7 % purified s-cr. and p-cr. Ta, thin layer method with measurement of $c \sim x$ curves by sectioning and counting using ^{95}Nb radioactive diffusant
	$0.76\exp(-44500/T)$	1370 (1100)	Electron-beam probe technique
Nb → β-Th	$0.5\exp(-24270/T)$	1640-1930 (1370-1660)	99.95 % purified p-cr. Th, diffusion couple method with determination of $c \sim x$ curves by calculation from an analytical solution
Nb ← Ti	$0.4\exp(-44560/T)$	1895-2345 (1625-2075)	99.7 % purified p-cr. Nb, diffusion couple method with determination of $c \sim x$ curves, electron microprobe analysis
	$9.9\times10^{-2}\exp(-43800/T)$	1265-1765 (995-1495)	99.98 % purified s-cr. Nb, thin layer method with measurement of $c \sim x$ curves by sectioning and counting using ^{44}Ti radioactive diffusant
Nb → β-Ti	$20\exp(-36760/T)+$ $+5.0\times10^{-3}\exp(-19800/T)$	1270-1920 (1000-1650)	99.7 % purified p-cr. Ti, thin layer method with measurement of $c \sim x$ curves by autoradiography using ^{95}Nb radioactive diffusant
Nb → TiC_{1-x}	$2.4\exp(-42000/T)$	2200-2450 (1930-2180)	Radiotracer diffusion
Nb ← U	$8.9\times10^{-2}\exp(-38680/T)$	1770-2270 (1500-2000)	99.55 % purified p-cr. Nb, residual activity method using ^{235}U diffusant
	$5\times10^{-6}\exp(-38620/T)$	1970-2270 (1700-2000)	P-cr. Nb, serial sectioning with ^{235}U radiotracer
Nb → γ-U	$4.87\times10^{-2}\exp(-20000/T)$	1060-1375 (790-1105)	99.99 % purified p-cr. U, thin layer method with measurement of $c \sim x$ curves by sectioning and counting using ^{95}Nb radioactive diffusant
Nb ← V	$0.47\exp(-45300/T)$	1895-2345 (1625-2075)	99.9 % purified p-cr. Nb, diffusion couple method with determination of $c \sim x$ curves, electron microprobe analysis

(continued)

Table A.9 (continued)

Species pair	Temperature dependence of the diffusion coefficient (diffusivity) $D = D_0\exp[(-E_A/R)/T]$, $cm^2\ s^{-1}$	Temp. range, K (°C)	Remarks on materials characteristics and measurement method
	$2.21\exp(-42810/T)$	1270-1670 (1000-1400)	99.98 % purified s-cr. Nb, residual activity method using ^{48}V radioactive diffusant
Nb ← W	$5\times10^{4}\exp(-77400/T)$	2070-2470 (1800-2200)	99.9 % purified p-cr. Nb, residual activity method using ^{185}W radioactive diffusant
	$7\times10^{4}\exp(-78600/T)$	2175-2440 (1905-2240)	99.7 % purified p-cr. Nb, diffusion couple method with determination of $c \sim x$ curves, electron microprobe analysis
Nb → W	$3.01\exp(-69300/T)$	1580-2640 (1310-2370)	S-cr. W, thin layer method with measurement of $c \sim x$ curves by sectioning and counting using ^{95}Nb radioactive diffusant
Nb ← Y	$1.5\times10^{-3}\exp(-28000/T)$	1470-1870 (1200-1600)	99.8-99.9 % purified s-cr. Nb, residual activity method using ^{91}Y radioactive diffusant
Nb ← Zr	$0.47\exp(-43800/T)$	1855-2355 (1585-2085)	99.9 % purified p-cr. Nb, diffusion couple method with determination of $c \sim x$ curves, electron microprobe analysis
	$0.85\exp(-45630/T)$	1920-2520 (1650-2250)	S-cr. Nb, thin layer method with measurement of $c \sim x$ curves by sectioning and counting using ^{95}Zr radioactive diffusant
	$0.28\exp(-43000/T)$	1855-2520 (1585-2250)	–
Nb → α-Zr	$6.6\times10^{-6}\exp(-15900/T)$	1010-1130 (740-860)	99.99 % purified p-cr. Zr, residual activity method using ^{95}Nb radioactive diffusant
Nb → β-Zr	$9\times10^{-6}\times(T/1136)^{18.1}\times$ $\times\exp\{-[12640+17630\times(T-1136)]/T\}$	1155-2030 (885-1760)	99.94 % purified p-cr. Zr, thin layer method with measurement of $c \sim x$ curves by sectioning and counting using ^{95}Nb radioactive diffusant
	$7.8\times10^{-4}\exp(-18400/T)$	1500-1905 (1230-1635)	P-cr. Zr, residual activity method using ^{95}Nb radioactive diffusant
	$1.23\times10^{-4}\exp(-15900/T)$	1165-1430 (895-1160)	99.77 % purified p-cr. Zr, thin layer method with measurement of $c \sim x$ curves by sectioning and counting using ^{95}Nb radioactive diffusant
Os[c] ← O	$D = 3.2\times10^{-13}$	1200 (930)	S-cr. Os, ^{18}O nuclear microanalysis
Os → W	$0.64\exp(-64800/T)$	2105-2925 (1835-2655)	S-cr. W, thin layer method with measurement of $c \sim x$ curves by sectioning and counting using ^{191}Os radioactive diffusant

(continued)

Table A.9 (continued)

Species pair	Temperature dependence of the diffusion coefficient (diffusivity) $D = D_0\exp[(-E_A/R)/T]$, $cm^2\ s^{-1}$	Temp. range, K (°C)	Remarks on materials characteristics and measurement method
Re → Re	$D = D_0\exp(-61500/T)$	> 1520 (1250)	Field electron microscopy
Re → W	$2.75\times10^{2}\exp(-82000/T)$	2940-3500 (2670-3230)	99.99 % purified s-cr. W, thin layer method with measurement of $c \sim x$ curves by sectioning and counting using $^{183\text{-}184}$Re radioactive diffusant
	$4\exp(-71800/T)$	2110-2900 (1840-2630)	~99.99 % purified s-cr. W, thin layer method with measurement of $c \sim x$ curves by sectioning and counting using ^{186}Re radioactive diffusant
Ta → Ta	$1.3\times10^{-3}\exp(-44130/T)+$ $+1.0\exp(-55050/T)$	1260-2990 (990-2720)	Combined data from several sources
	$1.89\times10^{-3}\exp(-44600/T)+$ $+1.16\exp(-55500/T)$	1260-2990 (990-2720)	Combined data from several sources
	$(0.090\div0.124)\exp(-49700/T)$	1520-2575 (1250-2305)	99.7 % purified s-cr. and p-cr. Ta, ^{182}Ta radiometric method, sectioning technique
	$0.21\exp(-51000/T)$	1260-2990 (990-2720)	99.95 % purified s-cr. Ta, ^{182}Ta radiometric method, sectioning technique
	$2\exp(-55000/T)$	2070-2770 (1800-2500)	–
	$0.1\exp(-49350/T)$	1190-2770 (920-2500)	Radiotracer diffusion
Ta ← Al	$1.5\exp(-36830/T)$	1780-2000 (1510-1730)	P-cr. Ta, out-diffusion method, atomic absorption
Ta ← B	$6.12\times10^{-6}\exp(-9350/T)$, ?	1470-2270 (1200-2000)	Calculation based on the thickness of $TaB_{2\pm x}$ layer
	$9.44\times10^{-4}\exp[(-23500\pm3000)/T]$	–	–
Ta ← Co	$D = 1.4\times10^{-9}$ $D = 8.0\times10^{-9}$	2125 (1855) 2330 (2060)	P-cr. Ta, thin layer method with measurement of $c \sim x$ curves by sectioning and counting using ^{60}Co radioactive diffusant
Ta ← Fe	$5.9\times10^{-2}\exp(-39680/T)$	2050-2330 (1780-2060)	P-cr. Ta, thin layer method with measurement of $c \sim x$ curves by sectioning and counting using ^{59}Fe radioactive diffusant
	$0.505\exp[(-35950\div36700)/T]$	1200-1510 (930-1240)	P-cr. Ta, radiotracer diffusion
Ta → α-Fe	$2.75\times10^{4}\exp(-39000/T)$	1100-1170 (830-900)	~99.9 % purified p-cr. Fe (paramagnetic), electron microprobe analysis

(continued)

Table A.9 (continued)

Species pair	Temperature dependence of the diffusion coefficient (diffusivity) $D = D_0\exp[(-E_A/R)/T]$, $cm^2\ s^{-1}$	Temp. range, K (°C)	Remarks on materials characteristics and measurement method
Ta → γ-Fe	$67.2\exp(-38400/T)$	1420-1620 (1150-1350)	~99.9 % purified p-cr. Fe, electron microprobe analysis
Ta ← H	$3.79\times10^{3}\exp[(-15730\pm500)/T]$	570-970 (300-700)	–
	$3.05\times10^{2}\exp[(-14730\pm720)/T]$	570-970 (300-700)	–
Ta ← N	$1.23\times10^{-2}\exp(-19900/T)$	630-930 (360-660)	Relaxation time study
Ta ← Ni	$D = 1.1\times10^{-9}$ $D = 1.14\times10^{-9}$	2050 (1780) 2830 (2560)	P-cr. Ta, thin layer method with measurement of $c \sim x$ curves by sectioning and counting using radioactive diffusant
Ta ← O	$1.9\times10^{-2}\exp(-13650/T)$	420-620 (150-350)	Relaxation time study
	$4.4\times10^{-3}\exp[(-12720\pm65)/T]$	320-520 (50-250)	–
	$1.5\times10^{-2}\exp(-13350/T)$	970-1670 (700-1400)	–
Ta ← S	$10^{2}\exp(-35250/T)$	1970-2110 (1700-1840)	99 % purified p-cr. Ta, residual activity method using ^{35}S radioactive diffusant
Ta ← Si	$3.62\times10^{-2}\exp[(-10760\pm840)/T]$	1170-1470 (900-1200)	Calculation based on the thickness of $TaSi_2$ layer
Ta → β-Ti	$13\exp(-37260/T)+$ $+3.0\times10^{-4}\exp(-16900/T)$	1185-1870 (915-1600)	Purified ("iodide") p-cr. Ti, thin layer method with measurement of $c \sim x$ curves by sectioning and counting using ^{182}Ta radioactive diffusant
Ta ← U	$7.6\times10^{-5}\exp(-42500/T)$	1865-2400 (1595-2130)	P-cr. Ta, residual activity method using ^{235}U diffusant
	$1.03\times10^{-6}\exp(-14100/T)$	2185-2530 (1915-2260)	99.9997 % purified p-cr. Ta, thin layer method with measurement of $c \sim x$ curves by radiography using fission fragment of natural U
Ta → V	$0.244\exp(-36250/T)$	1370-2070 (1100-1800)	P-cr. V, thin layer method with measurement of $c \sim x$ curves by sectioning and counting using ^{182}Ta radioactive diffusant
Ta → W	$3.05\exp(-70500/T)$	1575-2645 (1305-2375)	S-cr. and p-cr. W, thin layer method with measurement of $c \sim x$ curves by sectioning and counting using ^{182}Ta radioactive diffusant
	$6.2\exp(-72400/T)$	2100-2900 (1830-2630)	S-cr. W, ^{182}Ta radiometric method

(continued)

Table A.9 (continued)

Species pair	Temperature dependence of the diffusion coefficient (diffusivity) $D = D_0\exp[(-E_A/R)/T]$, $cm^2\ s^{-1}$	Temp. range, K (°C)	Remarks on materials characteristics and measurement method
Ta ← Y	$0.12\exp(-36360/T)$	1470-1770 (1200-1500)	99.8-99.9 % purified s-cr. Ta, residual activity method using ^{91}Y radioactive diffusant
Ta → α-Zr	$1.0\times10^{2}\exp(-35250/T)$	970-1070 (700-800)	99.6 % purified p-cr. Zr, residual activity method using ^{182}Ta radioactive diffusant
Ta → β-Zr	$5.0\times10^{-5}\exp(-13600/T)$	1170-1470 (900-1200)	99.6 % purified p-cr. Zr, residual activity method using ^{182}Ta radioactive diffusant
W → W	$0.13\exp(-65300/T)+$ $+2\times10^{2}\exp(-85120/T)$	1700-3410 (1430-3140)	Combined data from several sources
	$4\times10^{-2}\exp(-63300/T)+$ $+46\exp(-80130/T)$	1700-3410 (1430-3140)	99.999 % purified s-cr. W, ^{187}W radiometric method, sectioning technique
	$1.88\exp(-70650/T)$	2070-2670 (1800-2400)	S-cr. W, ^{188}W radiometric method
	$15.3\exp(-75340/T)$	2040-2815 (1770-2545)	~99.999 % purified s-cr. W, ^{187}W radiometric method
	$42.8\exp(-77000/T)$	–	S-cr. W
	$(0.54\pm0.32)\exp[(-60250\pm2400)/T]$	2270-2970 (2000-2700)	–
	$11.5\exp(-71000/T)$	–	–
W → δ-$WC_{1\pm x}$	$7.33\exp[(-69500\pm9560)/T]$	2240-2640 (1970-2370)	P-cr. δ-$WC_{1\pm x}$ ($O \le 0.03$ mas.%), ^{185}W radiotracer
W ← B	$1.48\exp[(-32000\pm3150)/T]$	–	Calculation based on the thickness of $W_{2\pm x}B$ layer
	$2.62\times10^{-5}\exp(-15300/T)$	1270-2170 (1000-1900)	Calculation based on the thickness of $W_{2\pm x}B$ layer
W ← Ce	$1.15\exp(-41500/T)$	2000 (1730)	Thermoionic-emission method
W ← Co	$0.16\exp(-59800/T)$	1680-2260 (1410-1990)	99.999 % purified s-cr. W, ^{57}Co radiotracer diffusion
	$0.71\exp(-62800/T)$	1770-2260 (1500-1990)	–
W ← Cr	$0.89\exp(-65840/T)$	2080-2655 (1810-2385)	S-cr. W, secondary ion mass spectrometry
W → Cu	$1.69\exp(-27150/T)$	1160-1305 (890-1035)	P-cr. Cu, thin layer method with measurement of $c \sim x$ curves by sectioning and counting
W ← Fe	$1.4\times10^{-2}\exp[(-33000\div33200)/T]$	1210-1510 (940-1240)	P-cr. W, ^{59}Fe radiotracer diffusion

(continued)

Table A.9 (continued)

Species pair	Temperature dependence of the diffusion coefficient (diffusivity) $D = D_0\exp[(-E_A/R)/T]$, $cm^2\ s^{-1}$	Temp. range, K (°C)	Remarks on materials characteristics and measurement method
	$11.5\exp(-70000/T)$	2200-2800 (1930-2530)	–
	$D = 7.2\times10^{-13}$ [d]	2300 (2030)	~99.999 % purified s-cr. W, secondary ion mass spectrometry
W →α-Fe	$1.5\times10^{2}\exp(-34500/T)$	830-1170 (560-900)	99.99 % purified p-cr. Fe (3-4 mm grain size), ^{181}W radiotracer diffusion
	$1.1\exp(-28730/T)$	1090-1170 (820-900)	~99.97 % purified p-cr. Fe (paramagnetic), electron microprobe analysis
	$0.29\exp(-27750/T)$	1050-1150 (780-880)	~99.5 % purified p-cr. Fe (paramagnetic), residual activity method using ^{185}W radioactive diffusant
W → γ-Fe	$0.13\exp(-32160/T)$	1380-1640 (1110-1370)	~99.9 % purified p-cr. Fe (0.4 mm grain size), electron microprobe analysis
	$0.509\exp(-32700/T)$	1260-1580 (990-1310)	~99.97 % purified p-cr. Fe, residual activity method using ^{185}W radioactive diffusant
W ← Hf	$(2.2\div3.6)\exp[(-67100\div68300)/T]$	2015-2570 (1745-2300)	~99.999 % purified s-cr. W, secondary ion mass spectrometry
W ← Mn	$D = 5.9\times10^{-13}$ [d]	2300 (2030)	~99.999 % purified s-cr. W, secondary ion mass spectrometry
W ← Ni	$D = 6\times10^{-11}$	1910 (1640)	P-cr. W, diffusion couple method with determination of $c \sim x$ curves, electron microprobe analysis
	$D = 1.03\times10^{-12}$ [d]	2300 (2030)	~99.999 % purified s-cr. W, secondary ion mass spectrometry
W → Ni	$2.0\exp(-36000/T)$	1370-1565 (1100-1295)	99.95 % purified p-cr. Ni, thin layer method with measurement of $c \sim x$ curves by sectioning and counting using ^{185}W radioactive diffusant
	$2.87\exp(-37060/T)$	1345-1665 (1075-1395)	99.98 % purified s-cr. Ni, thin layer method with measurement of $c \sim x$ curves by sectioning and counting using ^{181}W radioactive diffusant
W ← O	$D = (3\div5)\times10^{-8}$	1970 (1700)	P-cr. W
	$D \approx 10^{-7}$	1970 (1700)	P-cr. W
	$D = (5\div7)\times10^{-8}$	1970 (1700)	S-cr. W

(continued)

Table A.9 (continued)

Species pair	Temperature dependence of the diffusion coefficient (diffusivity) $D = D_0\exp[(-E_A/R)/T]$, $cm^2\ s^{-1}$	Temp. range, K (°C)	Remarks on materials characteristics and measurement method
W ← P	$26.8\exp(-61300/T)$	2150-2450 (1880-2180)	99.99 % purified s-cr. W, in-diffusion method by serial sectioning and calculating from $c \sim x$ curves, ^{32}P radiotracer
W ← S	$2.17\times10^{-5}\exp(-35150/T)$	2150-2450 (1880-2180)	S-cr. W, residual activity method using ^{35}S radioactive diffusant
W ← Sc	$2.96\exp(-67400/T)$	1970-2465 (1700-2195)	~99.999 % purified s-cr. W, secondary ion mass spectrometry
W ← Si	$4.4\times10^{-6}\exp(-31500/T)$, ?	1170-1370 (900-1100)	Calculation based on the thickness of WSi_2 layer
W ← Th	$1.13\exp(-47000/T)$	2060-2300 (1790-2030)	P-cr. W, thermoionic-emission method
	$4.1\exp(-47200/T)$	2060-2300 (1790-2030)	P-cr. W with coarse grain structure
	$0.75\exp(-47200/T)$	2060-2300 (1790-2030)	P-cr. W with fine grain structure
	$1.0\exp(-60000/T)$	2060-2300 (1790-2030)	Bulk diffusion
W ← Ti	$D = 1.18\times10^{-14}$	2085 (1815)	~99.999 % purified s-cr. W, secondary ion mass spectrometry
W → β-Ti	$3.6\times10^{-3}\exp[(-21950\div22110)/T]$	1170-1520 (900-1250)	98.94 % purified p-cr. Ti, surface decrease method using ^{185}W radioactive diffusant and sectioning technique
W ← U	$2\times10^{-3}\exp(-52100/T)$	1970-2470 (1700-2200)	P-cr. W, thin layer method with measurement of $c \sim x$ curves using serial sectioning and ^{235}U diffusant
	$1.8\times10^{-2}\exp(-46840/T)$	2030-3000 (1760-2730)	99.99 % purified p-cr. W, out-diffusion method from U-doped W filaments, mass spectrometry
	$1.14\exp(-50000/T)$	2000 (1730)	Thermoionic-emission method
W ← V	$D = 1.03\times10^{-14}$	2090 (1820)	~99.999 % purified s-cr. W, secondary ion mass spectrometry
	$D = 1.99\times10^{-13}$	2290 (2020)	

(continued)

Table A.9 (continued)

Species pair	Temperature dependence of the diffusion coefficient (diffusivity) $D = D_0\exp[(-E_A/R)/T]$, $cm^2\ s^{-1}$	Temp. range, K (°C)	Remarks on materials characteristics and measurement method
W ← Y	$6.7\times10^{-3}\exp(-34300/T)$	1470-1870 (1200-1600)	99.8-99.9 % purified s-cr. W, residual activity method using ^{91}Y radioactive diffusant
	$0.11\exp(-31000/T)$	2000 (1730)	Thermoionic-emission method
W ← Zr	$1.1\exp(-39000/T)$	2000 (1730)	Thermoionic-emission method
W → β-Zr	$0.41\exp[-(27900\div28100)/T]$	1170-1520 (900-1250)	99.7 % purified p-cr. Zr, surface decrease method using ^{185}W radioactive diffusant and sectioning technique

[a] Non-combined carbon contents
[b] Average values – Arrhenius plot very slightly curved
[c] For osmium no data on self-diffusion are available in literature
[d] Simultaneous diffusion of Fe, Mn, Ni
[e] Abbreviations used: p-cr. – polycrystalline, s-cr. – single crystal

Table A.10 Chemical properties of carbon (interaction with 1–9 groups elements: binary compounds, interaction temp. range, solubilities and eutectic temp.)

Group 1 (IA)	*Group 2 (IIA)*	*Group 3 (IIIB)*	*Group 4 (IVB)*	*Group 5 (VB)*	*Group 6 (VIB)*	*Group 7 (VIIB)*	*Group 8 (VIII)*	*Group 9 (VIII)*
H Variety of hydrocarbon compounds (e.g. CH_4, C_2H_2 etc) DI[a]: >1700 °C, or with catalysts								
Li α, β, γ, δ-Li_2C_2, layered compounds DI: > 800 °C CSM[b]: ~0.4 at.%. at 735 °C β-Li – α-Li_2C_2: 175 °C[c]	**Be** Be_2C, BeC_2 DI: at higher temp. CSS[d]: < 0.1 at.% (?)							
Na α, β-Na_2C_2, layered and intercalated fullerene compounds CSM: ~0.04 at.%. at 700 °C	**Mg** MgC (?), Mg_2C_3, MgC_2							

(continued)

Table A.10 (continued)

Group 1 (IA)	*Group 2 (IIA)*	*Group 3 (IIIB)*	*Group 4 (IVB)*	*Group 5 (VB)*	*Group 6 (VIB)*	*Group 7 (VIIB)*	*Group 8 (VIII)*	*Group 9 (VIII)*
K	**Ca**	**Sc**	**Ti**	**V**	**Cr**	**Mn**	**Fe**	**Co**
K_2C_2, layered ($KC_{8\pm x}$, $KC_{16\pm x}$, $KC_{24\pm x}$, $KC_{36\pm x}$, $KC_{48\pm x}$, $KC_{60\pm x}$, $KC_{72\pm x}$) and intercalated fullerene (α, β, γ, δ-$K(C_{60})$, $K_3(C_{60})$, α, β-$K_4(C_{60})$, $K_6(C_{60})$, $K(C_{70})$, $K_4(C_{70})$, $K_9(C_{70})$, $K(C_{72})$) compounds DI: > 300-400 °C	α, β, γ, δ-CaC_2, layered (CaC_{6+x}) and intercalated fullerene ($Ca_{3+x}(C_{60})$, $Ca_5(C_{60})$, $Ca_7(C_{60})$) compounds DI: at higher temp.	ScC_{1-x}, Sc_3C (?), Sc_2C (?), α-Sc_4C_3, β-Sc_4C_{3+x}, Sc_3C_{4-x}, intercalated fullerenes $Sc_2(C_{84})$ CSS: ~4.5 at.% (α-Sc) at 1540-1545 °C and ~2.5 at.% (β-Sc) at 1575-1580 °C Sc_3C_{4-x} – C: 1720 °C[c]	$Ti_{2\pm x}C$ (?), $Ti_3C_{2\pm x}$ (?), $Ti_6C_{5\pm x}$ (?), TiC_{1-x} DI: > 1700-2100 °C CSS: 2 at.% (α-Ti) at 920 °C and 0.50-0.55 at.% (β-Ti) at 920-1640 °C β-Ti – TiC_{1-x}: 1650 °C[c] TiC_{1-x} – C: 2780 °C[c]	$V_{64}C$ (?), V_5C (?), α-$V_{2+x}C$, β, β′-$V_{2\pm x}C$, ζ-V_4C_{3-x}, $V_6C_{5\pm x}$, $V_8C_{7\pm x}$, VC_{1-x} DI: > 1100-1200 °C CSS: ~ 4.3-5.5 at.% at 1650 °C V – β-$V_{2\pm x}C$: 1650 °C[c] VC_{1-x} – C: 2650 °C[c]	$Cr_{23}C_{6\pm x}$, Cr_3C (?), $Cr_7C_{3\pm x}$, Cr_2C (?), Cr_3C_{2-x}, CrC (?) DI: > 1400-1800 °C CSS: ~ 0.3-1.9 at.% at 1530-1580 °C Cr – $Cr_{23}C_{6\pm x}$: 1560 °C[c] $Cr_7C_{3\pm x}$–Cr_3C_{2-x}: 1730 °C[c]	ε-$Mn_{4\pm x}C$, $Mn_{23}C_6$, $Mn_{15}C_4$, Mn_3C, Mn_5C_2, Mn_7C_3 DI: > 1200-1300 °C CSS: ~7 at.% (α-Mn) at 770-900 °C, 2.5 at.% (β-Mn) at 820-900 °C, ~ 13-16 at.% (γ-Mn) at 990-1240 °C and 1-2 at.% (δ-Mn) at 1220-1240 °C	Metastable carbides θ-Fe_3C, Fe_4C, χ-Fe_5C_2, α, β-Fe_7C_3, η, ε, α-Fe_2C) CSS: 0.090-0.096 at.% (α-Fe) at 727-740 °C, ~ 8.9-9.1 at.% (γ-Fe) at 1147-1153 °C and ~ 0.4-0.5 at.% (δ-Fe) at 1493-1499 °C γ-Fe – C: 1153 °C[c]	Metastable carbides Co_3C and Co_2C CSS: ~0.5 at.% (ε-Co) and ~ 4.1-4.3 at.% (α-Co) at 1310-1320 °C CSM: ~12 at.% at 1320 °C α-Co – C: 1320 °C[c]

(continued)

Table A.10 (continued)

Group 1 (IA)	*Group 2 (IIA)*	*Group 3 (IIIB)*	*Group 4 (IVB)*	*Group 5 (VB)*	*Group 6 (VIB)*	*Group 7 (VIIB)*	*Group 8 (VIII)*	*Group 9 (VIII)*
Rb Rb_2C_2 (?), layered ($RbC_{8\pm x}$, $RbC_{16\pm x}$, α, β-$RbC_{24\pm x}$, $RbC_{36\pm x}$, $RbC_{48\pm x}$, $RbC_{60\pm x}$) and intercalated fullerene (α, β, γ-$Rb(C_{60})$, $Rb_3(C_{60})$, $Rb_4(C_{60})$, $Rb_6(C_{60})$, $Rb_{8.8}(C_{84})$) compounds DI: > 300-450 °C	**Sr** α, β, γ-SrC_2, layered ($SrC_{6\pm x}$, $SrC_{12\pm x}$, $SrC_{18\pm x}$, $SrC_{24\pm x}$ $SrC_{30\pm x}$, $SrC_{36\pm x}$) intercalated fullerene compounds ($Sr_{2.08}(C_{60})$, $Sr_3(C_{60})$, $Sr_6(C_{60})$) DI: at higher temp. γ-SrC_2 – C: ?[c]	**Y** Y_3C (?), $Y_{2\pm x}C$, $YC_{1\pm x}$, α, β-Y_3C_{4-x}, α, β-Y_2C_{3-x}, α-YC_2, β-$YC_{2\pm x}$, intercalated fullerenes $Y(C_{82})$ CSS: ~8.8 at.% (α-Y) at 1520 °C and ~7.0 at.% (β-Y) at 1560 °C β-$YC_{2\pm x}$ – C: 2290 °C[c]	**Zr** $Zr_{2\pm x}C$ (?), $Zr_3C_{2\pm x}$ (?), $Zr_6C_{5\pm x}$ (?), ZrC_{1-x} DI: > 1800-2200 °C CSS: ~3 at.% (α-Zr) at 870-885 °C and ~1 at.% (β-Zr) at 1805-1835 °C β-Zr – ZrC_{1-x}: 1820 °C[c] ZrC_{1-x} – C: 2900 °C[c]	**Nb** α-Nb_2C, β-$Nb_{2+x}C$, γ-$Nb_{2\pm x}C$, ζ-Nb_4C_{3-x}, $Nb_6C_{5\pm x}$, NbC_{1-x} DI: > 1300-1400 °C CSS: ~ 5.5-7.2 at.% at 2230-2350 °C Nb – β-$Nb_{2+x}C$: 2350 °C[c] NbC_{1-x} – C: 3280 °C[c]	**Mo** α, α′-$Mo_{2+x}C$, β-$Mo_{2\pm x}C$, η, α-MoC_{1-x}, γ-MoC DI: > 1200-1400 °C CSS: ~ 1.1-1.3 at.% at 2200-2205 °C Mo – β-$Mo_{2\pm x}C$: 2200 °C[c] β-$Mo_{2\pm x}C$ – η-MoC_{1-x}: 2510 °C[c] α-MoC_{1-x} – C: 2585 °C[c]	**Tc** TcC_{1-x} CSS: ~1 at.% at 910 °C TcC_{1-x} – C: ~1770 °C[c]	**Ru** Metastable carbides (?) CSS: ~3 at.% at 1940-1965 °C CSM: ~30 at.% at 4150 °C Ru – C: 1950 °C[c]	**Rh** Metastable carbides (?) CSS: ~ 3.75-4.0 at.% at 1670-1700 °C CSM: ~16 at.% at 3700 °C Rh – C: 1680 °C[c]

(continued)

Table A.10 (continued)

Group 1 (IA)	*Group 2 (IIA)*	*Group 3 (IIIB)*	*Group 4 (IVB)*	*Group 5 (VB)*	*Group 6 (VIB)*	*Group 7 (VIIB)*	*Group 8 (VIII)*	*Group 9 (VIII)*
Cs Cs_2C_2 (?), layered ($CsC_{8\pm x}$, $CsC_{16\pm x}$, α, β-$CsC_{24\pm x}$, $CsC_{36\pm x}$, $CsC_{48\pm x}$, $CsC_{60\pm x}$, $CsC_{84\pm x}$) and intercalated fullerene (α, β-Cs(C_{60}), $Cs_3(C_{60})$, α, β-$Cs_4(C_{60})$, $Cs_6(C_{60})$) compounds	**Ba** α, β-BaC_2, layered ($BaC_{6\pm x}$, $BaC_{8\pm x}$, $BaC_{12\pm x}$, $BaC_{18\pm x}$, $BaC_{24\pm x}$, $BaC_{30\pm x}$, $BaC_{36\pm x}$) and intercalated fullerene ($Ba_6(C_{60})$, $Ba_3(C_{70})$) compounds DI: > 575-700 °C Ba – β-BaC_2: ?[c]	**La**[e] La_2C_{3-x}, α-LaC_2, β-$LaC_{2\pm x}$, ε-LaC_2 (?), intercalated fullerenes La(C_{82}) CSS: ~ 3.4-4.3 at.% (β-La) at 800-875 °C β-La – La_2C_{3-x}: 800 °C[c] β-$LaC_{2\pm x}$ – C: 2250 °C[c]	**Hf** $Hf_3C_{2\pm x}$ (?), $Hf_6C_{5\pm x}$ (?), HfC_{1-x} DI: > 1900-2300 °C CSS: ~ 14-15 at.% (α-Hf) at 2240-2360 °C and ~ 0.6-1.0 at.% (β-Hf) at 2180-2220 °C α-(Hf,C) – β-(Hf,C): 2200 °C[c] HfC_{1-x} – C: 3170 °C[c]	**Ta** $Ta_{64}C$ (?), α-$Ta_{2+x}C$, β-$Ta_{2\pm x}C$, ε-$Ta_3C_{2\pm x}$, ζ-Ta_4C_{3-x}, $Ta_6C_{5\pm x}$, TaC_{1-x} DI: > 1300-1500 °C CSS: ~ 7.0-7.5 at.% at 2800-2860 °C Ta – β-$Ta_{2\pm x}C$: 2830 °C[c], TaC_{1-x} – C: 3420 °C[c]	**W** α, β-$W_{2+x}C$, γ-$W_{2\pm x}C$, γ-WC_{1-x}, δ-$WC_{1\pm x}$ DI: > 1400-1600 °C CSS: < 1 at.% at 2710-2715 °C W – γ-$W_{2\pm x}C$: 2715 °C[c] γ-$W_{2\pm x}C$ – γ-WC_{1-x}: 2750 °C[c] γ-WC_{1-x} – δ-$WC_{1\pm x}$: 2740 °C[c]	**Re** Metastable carbides (?) CSS: ~ 11-17 at.% at 2480-2505 °C Re – C: 2490 °C[c]	**Os** Metastable carbides (?) CSS: negligible CSM: 39.1-39.7 at.% at 5010 °C Os – C: 2730 °C[c]	**Ir** Metastable carbides (?) CSS: 3.1 at.% at 2280-2310 °C CSM: ~31.5 at.% at 4400 °C Ir – C: 2300 °C[c]
Fr N/A	**Ra** N/A	**Ac**[f] N/A						

[a] DI – temp. range of direct interaction with C (graphite)
[b] CSM – solubility of C in molten matter (metal or semi-metal)
[c] Eutectic temp.
[d] CSS – solubility of C in solid matter (metal or semi-metal)
[e] For lanthanides see Table A.12
[f] For actinides see Table A.12

Table A.11 Chemical properties of carbon (interaction with 10–18 groups elements: binary compounds, interaction temp. range, solubilities and eutectic temp.)[a]

Group 10 (VIII)	*Group 11 (IB)*	*Group 12 (IIB)*	*Group 13 (IIIA)*	*Group 14 (IVA)*	*Group 15 (VA)*	*Group 16 (VIA)*	*Group 17 (VIIA)*	*Group 18 (VIIIA)*
								He –
			B $B_{51}C$, $B_{56}C_2$ (?), $B_{50}C_2$, $B_{49}C_3$ (?), $B_{24}C$ (?), B_8C (?), $B_{13}C_{2\pm x}$, $B_{13}C_{3-x}$ (?), $B_{4\pm x}C$, $B_{11}C_4$ (?), ~BC_2 (?), ~BC_3 (?) DI: at elevated temp. CSS: negligible β-B – $B_{4\pm x}C$: 2080 °C[c] $B_{4\pm x}C$ – C: 2350 °C[c]	**C**	**N** Variety of compounds (e.g. C_2N_2, some polymorphs of C_3N_4, azafullerenes $(C_{59}N)_2$, $C_{58}N_2$, $C_{57}N_3$, $C_{48}N_{11}$, cyanofullerenes $(C_{60}(CN)_{2n}$, n = 1÷9), percyanoalkynes, perazidoalkynes etc) DI: > 2500-3000 °C, or with some special activation (e.g. microwave radiation)	**O** CO_2, CO, metastable C_3O_2 (?), fullerene containing compounds (e.g. $(O_3)_x(C_{60})$, $(O_3)_x(C_{70})$) DI: > 450-500 °C (in air, in normal conditions)	**F** Variety of compounds, including fullerene containing (e.g. CF_4, C_2F_6, $(C_{60})F_{18}$ etc) DI: > 450 °C	**Ne** –

(continued)

Table A.11 (continued)

Group 10 (VIII)	*Group 11 (IB)*	*Group 12 (IIB)*	*Group 13 (IIIA)*	*Group 14 (IVA)*	*Group 15 (VA)*	*Group 16 (VIA)*	*Group 17 (VIIA)*	*Group 18 (VIIIA)*
			Al Al_3C_2 (?), Al_4C_3 DI: at temp. > 1200-1300 °C CSS: negligible CSM: 0.7 at.% at 1200 °C	**Si** Si_5C_3 (?), α-SiC (variety of polytypes), β-SiC, SiC_2 (?) DI: > 1200-1300 °C CSS: ~0.001 at.% at 1400 °C Si – SiC: 1400 °C[c]	**P** Some unstable compounds (e.g. C_6P_6), intercalated fullerenes ($P_8(C_{60})$) DI: No	**S** CS_2, CS, C_3S_2, fullerene containing compounds ($S_8CS_2(C_{60})$, $(S_8)_2(C_{60})$, $S_{48}(C_{70})$, $S_{48}(C_{76})$) DI: at elevated temp.	**Cl** Variety of compounds, including fullerene containing (e.g. CCl_4, C_2Cl_6, $(C_{60})Cl_5$ etc) DI: > 2300 °C	**Ar** –
Ni Metastable carbide Ni_3C CSS: ~ 2.5-2.7 at.% at 1317-1327 °C CSM: 10.9 at.% at 1450 °C Ni – C: 1320 °C[c]	**Cu** Unstable carbides Cu_2C_2 and CuC_2 DI: No CSS: ~ 0.03 at.% at 1085 °C CSM: 0.016 at.% at 1700 °C	**Zn** Unstable carbide ZnC_2 DI: No CSS, CSM: negligible	**Ga** No binary compounds No interaction CSS, CSM: negligible	**Ge** No binary compounds No interaction CSS: negligible CSM: 0.23 at.% at 940 °C Ge – C: 938 °C[c]	**As** AsC_3 (?) CSS: negligible	**Se** CSe_2 DI: No	**Br** CBr_4, layered (C_8Br) and fullerene containing $((C_{60})Br$, $\alpha\beta$-$(C_{60})Br_{24}{\cdot}Br_2$, $(C_{70})Br_{14})$ compounds	**Kr** –

(continued)

Table A.11 (continued)

Group 10 (VIII)	*Group 11 (IB)*	*Group 12 (IIB)*	*Group 13 (IIIA)*	*Group 14 (IVA)*	*Group 15 (VA)*	*Group 16 (VIA)*	*Group 17 (VIIA)*	*Group 18 (VIIIA)*
Pd No binary compounds DI: No CSS: ~ 7-9 at.% at 1505-1515 °C CSM: ~ 16-18 at.% at 2965 °C Pd – C: 1510 °C[c]	**Ag** Unstable carbide Ag_2C_2 DI: No CSS: > 0.035 at.% at 962 °C CSM: 0.02 at.% at 1940 °C	**Cd** Unstable carbide CdC_2 DI: No CSS, CSM: negligible	**In** No binary compounds No interaction CSS, CSM: negligible	**Sn** No binary compounds No interaction CSS: negligible	**Sb** No binary compounds No interaction CSS: negligible	**Te** No binary compounds No interaction	**I** CI_4	**Xe** –
Pt Metastable carbides Pt_7C (?) and Pt_2C CSS: ~ 2.5-4.0 at.% at 1705-1740 °C CSM: ~19 at.% at 3800 °C Pt – C: 1730 °C[c]	**Au** Metastable carbide Au_2C_2 CSS: ~ 0.080-0.082 at.% at 1040-1050 °C CSM: ~4.9 at.% at 2860 °C Au – C: 1040 °C[c] (?)	**Hg** Metastable carbides (Hg_2C_2, HgC_2) and layered compounds (HgC_{16}) DI: No CSS, CSM: negligible	**Tl** Metastable carbide TlC_x (?) CSS, CSM: negligible	**Pb** Metastable carbide PbC_2 (?) CSS: negligible CSM: 1.6 at.% at 1555 °C	**Bi** No binary compounds No interaction CSS, CSM: negligible	**Po** No binary compounds No interaction	**At** N/A	**Rn** –

[a] See the notes for Table A.10

Table A.12 Chemical properties of carbon (interaction with lanthanides and actinides: binary compounds, interaction temp. range, solubilities and eutectic temp.)[a]

Ce	Pr	Nd	Pm	Sm	Eu	Gd	Tb	Dy	Ho	Er	Tm	Yb	Lu
Ce_2C (?), CeC (?), Ce_2C_3, α-CeC_2, β-$CeC_{2\pm x}$, CeC_3 (?), intercalated fullerenes $Ce(C_{82})$ DI: > 800-900 °C CSS: ~10 at.% (γ-Ce) at 650-700 °C δ-Ce – Ce_2C_3: 680 °C[c] β-$CeC_{2\pm x}$ – C: 2240 °C[c]	Pr_2C_{3-x}, α-PrC_2, β-$PrC_{2\pm x}$ DI: > 900-1000 °C CSS: ~5 at.% (α-Pr) and ~8 at.% (β-Pr) β-Pr – Pr_2C_{3-x}: 800 °C[c] β-$PrC_{2\pm x}$ – C: 2250 °C[c]	Nd_2C_{3-x}, α, β-NdC_2 DI: > 1000-1100 °C CSS: low β-NdC_2 – C: 2275 °C[c]	N/A	$Sm_{3-x}C$, Sm_2C_{3-x}, α, β-SmC_2, layered compounds ($SmC_{6\pm x}$, $SmC_{12\pm x}$, $SmC_{18\pm x}$, $SmC_{24\pm x}$, $SmC_{30\pm x}$, $SmC_{36\pm x}$), intercalated fullerenes ($Sm_3(C_{60})$, $Sm_6(C_{60})$, $Sm_3(C_{70})$) DI: > 1075-1150 °C β-SmC_2 – C: 2240 °C[c]	$Eu_{3-x}C$, Eu_2C_3, α, β-EuC_2, layered compounds ($EuC_{6\pm x}$, $EuC_{12\pm x}$, $EuC_{18\pm x}$, $EuC_{24\pm x}$, $EuC_{30\pm x}$, $EuC_{36\pm x}$), intercalated fullerenes ($Eu_{2.82}(C_{60})$, $Eu_6(C_{60})$, $Eu_3(C_{70})$, $Eu_9(C_{70})$) DI: > 800-900 °C	β-$Gd_{3-x}C$, α-Gd_2C, Gd_4C_5 (?), Gd_2C_{3-x}, α, β-GdC_2, layered compound $GdC_{6\pm x}$ (?) DI: > 1300-1400 °C β-GdC_2 – C: 2320 °C[c]	$Tb_{3-x}C$, α,β-Tb_2C?, Tb_4C_5 (?), $Tb_{15}C_{19}$(?), Tb_2C_{3-x}, α, β-TbC_2 DI: > 1350-1400 °C β-TbC_2 – C: 2275 °C[c]	$Dy_{3-x}C$, α,β-Dy_2C?, Dy_4C_5 (?), $Dy_{15}C_{19}$(?), Dy_2C_{3-x}, α, β-DyC_2, α′-DyC_2? DI: > 1400-1500 °C β-DyC_2 – C: 2290 °C[c]	$Ho_{3-x}C$, α,β-Ho_2C?, Ho_4C_5 (?), $Ho_{15}C_{19}$(?), Ho_3C_4 (?), Ho_4C_7 (?), Ho_2C_{3-x}, α,β-HoC_2, α′-HoC_2? DI: > 1480-1550 °C CSS: negligible at 1300 °C β-HoC_2 – C: 2270 °C[c]	$Er_{3-x}C$, $Er_{15}C_{19}$, Er_3C_4 (?), Er_4C_7 (?), Er_2C_3 (?), α,β -ErC_2, α′-ErC_2? DI: > 1500-1600 °C β-ErC_2 – C: 2250 °C[c]	$Tm_{3-x}C$, $Tm_{15}C_{19}$, Tm_2C_3?, Tm_3C_4?, Tm_4C_7?, α,β-TmC_2, α′-TmC_2?, TmC_3, intercalated fullerenes ($Tm(C_{82})$) DI: > 1550-1600 °C β-TmC_2 – C: 2250 °C[c]	$Yb_{3-x}C$, α-YbC_{1-x}, $YbC_{1.25+y}$, $Yb_{15}C_{19}$, $Yb_3C_{4\pm x}$ Yb_2C_3 (?), α,β-YbC_2, layered compounds ($YbC_{6\pm x}$, $YbC_{12\pm x}$), intercalated fullerenes $Yb_{2.75}(C_{60})$ DI: > 800-900 °C β-YbC_2 – C: 2220 °C[c]	$Lu_{3-x}C$, $Lu_{15}C_{19}$, Lu_3C_4 (?), Lu_4C_7 (?), Lu_2C_3 (?), α, β-LuC_2 DI: > 1650-1750 °C β-LuC_2 – C: 2230 °C[c]

(continued)

Table A.12 (continued)

Th	Pa	U	Np	Pu	Am	Cm	Bk	Cf	Es	Fm	Md	No	Lr
$ThC_{1\pm x}$, Th_2C_3 (?), α, β, γ-ThC_{2-x} DI: > 1700-1900 °C CSS: ~66.0 at.% (α-Th) at 1500-2400 °C and ~9.2 at.% (β-Th) at 1710 °C γ-ThC_{2-x} – C: 2475 °C[c]	PaC, PaC_2	$UC_{1\pm x}$, ζ-U_2C_3, α,β-UC_{2-x} DI: > 1700-1900 °C CSS: < 0.006 at.% (α-U) at 660 °C, 0.02 at.% (β-U) at 770 °C and 0.22-0.37 (γ-U) at 1115-1120 °C CSM: ~5.4 at.%. at 1600 °C γ-U – $UC_{1\pm x}$: 1120 °C[c] β-UC_{2-x} – C: 2480 °C[c]	NpC_{1-x}, Np_2C_3, NpC_2	Pu_3C_2, PuC_{1-x}, Pu_2C_{3-x}, α-PuC_2 (?), β-PuC_2 DI: > 1500-1700 °C CSM: ~2.3 at.%. at 800 °C ε-Pu – PuC_{1-x}: 634 °C[c]	Am_2C_3, AmC_2	N/A	N/A	N/A	N/A	N/A	N/A	N/A	N/A

[a] See the notes for Table A.10

Table A.13 Chemical properties of tungsten (interaction with 1–9 groups elements: binary compounds, interaction temp. range, solubilities and eutectic temp.)

Group 1 (IA)	*Group 2 (IIA)*	*Group 3 (IIIB)*	*Group 4 (IVB)*	*Group 5 (VB)*	*Group 6 (VIB)*	*Group 7 (VIIB)*	*Group 8 (VIII)*	*Group 9 (VIII)*
H No binary compounds under standard pressure No interaction up to melt. point SiW[a]: low								
Li No binary compounds WSM[b]: ~4×10^{-3} at.% at 715 °C SiW: negligible	**Be** WBe_{22}, WBe_{12}, $WBe_{2\pm x}$, WBe ? DI[b]: > 750-880 °C WSS[b]: 0.05 at.% (β-Be) SiW: ~5 at.% at 2100 °C $WBe_{2\pm x}$ – W: 2100 °C[c]							
Na No binary compounds WSM: ~10^{-11} at.%	**Mg** No binary compounds WSS, WSM: negligible							

(continued)

Table A.13 (continued)

Group 1 (IA)	*Group 2 (IIA)*	*Group 3 (IIIB)*	*Group 4 (IVB)*	*Group 5 (VB)*	*Group 6 (VIB)*	*Group 7 (VIIB)*	*Group 8 (VIII)*	*Group 9 (VIII)*
K No binary compounds WSM: negligible	**Ca** No binary compounds WSM: negligible	**Sc** No binary compounds WSM: 7.9 at.% at 2045 °C SiW: ≤ 0.0165 at.% at 1625 °C β-Sc – W: 1510 °C[c]	**Ti** No binary compounds CSS[d]: β-Ti – W (> 1250 °C) WSS: ≤ 0.2 at.% (α-Ti) at 740 °C SiW: ~25 at.% at 740 °C	**V** No binary compounds CSS: V – W	**Cr** CrW_3 (?) CSS: Cr – W (> 1677 °C)	**Mn** No binary compounds WSS: very high (α-Mn) at 800 °C (?) WSM: negligible (?)	**Fe** λ-Fe_2W (metastable), μ-Fe_7W_{6-x}, δ-$FeW_{1\pm x}$ WSS: 14.3 at.% (α/δ-Fe) at 1548 °C and 1.46 at.% (γ-Fe) at 1140 °C SiW: 2.6 at.% at 1635 °C	**Co** κ-$Co_{3\pm x}W$, μ-$Co_7W_{6\pm x}$, Co_2W_3 (?) WSS: ~1 at.% (ε-Co) at 350 °C and ~17.5 at.% (α-Co) at 1470 °C SiW: 0.9 at.% at 1690 °C α-Co – μ-$Co_7W_{6\pm x}$: 1470 °C[c]
Rb No binary compounds WSM: negligible	**Sr** No binary compounds WSM: negligible	**Y** No binary compounds WSM: 0.5 at.% at 2100 °C SiW: < 1 at.% at 1625 °C β-Y – W: 1520 °C[c]	**Zr** ZrW_2 WSS: 0.5 at.% (α-Zr) at 863 °C and ~4 at.% (β-Zr) at 1735-1795 °C SiW: ~3.5-10.0 at.% at 2160-2210 °C β-Zr – ZrW_2: 1770 °C[c]	**Nb** No binary compounds CSS: Nb – W	**Mo** No binary compounds CSS: Mo – W	**Tc** σ-$TcW_{3\pm x}$ WSS: ~14 at.% at 1900 °C SiW: ~55 at.% at 1800 °C σ-$TcW_{3\pm x}$ – W: 1800 °C[c]	**Ru** σ-$Ru_2W_{3\pm x}$ WSS: ~48 at.% at ~2200 °C SiW: ~23 at.% at 2300 °C Ru – σ-$Ru_2W_{3\pm x}$: 2205 °C[c]	**Rh** Rh_3W (?), ε-$Rh_{2\pm x}W$ WSS: ~19 at.% at ~2100 °C SiW: ~6 at.% at 2240 °C ε-$Rh_{2\pm x}W$ – W: 2240 °C[c]

(continued)

Table A.13 (continued)

Group 1 (IA)	*Group 2 (IIA)*	*Group 3 (IIIB)*	*Group 4 (IVB)*	*Group 5 (VB)*	*Group 6 (VIB)*	*Group 7 (VIIB)*	*Group 8 (VIII)*	*Group 9 (VIII)*
Cs No binary compounds WSM: negligible	**Ba** No binary compounds WSM: negligible	**La**[e] No binary compounds WSM: 0.025 at.% at 1940 °C γ-La – W: 920 °C[c]	**Hf** $HfW_{2\pm x}$ WSS: 0.7-0.9 at.% (α-Hf) at 1480 °C and ~13.5 at.% (β-Hf) at 1950 °C SiW: ~9 at.% at 2510 °C β-Hf – $HfW_{2\pm x}$: 1950 °C[c]	**Ta** No binary compounds CSS: Ta – W	**W**	**Re** σ-$W_2Re_{3\pm x}$, χ-WRe_{3-x} WSS: ~ 15-20 at.% at 2820 °C SiW: ~ 37-45 at.% at 3000 °C Re – σ-$W_2Re_{3\pm x}$: 2820 °C[c]	**Os** σ-$OsW_{3\pm x}$ WSS: ~55 at.% at 2725 °C SiW: ~18.5 at.% at 2945 °C Os – σ-$OsW_{3\pm x}$: 2725 °C[c]	**Ir** δ-$Ir_{3-x}W$ (?), β-$Ir_3W_{2\pm x}$, ε-$IrW_{1\pm x}$ (?), σ-$IrW_{3\pm x}$ WSS: ~19 at.% at ~2310 °C SiW: ~10 at.% at 2545 °C Ir – β-$Ir_3W_{2\pm x}$: 2310 °C[c] β-$Ir_3W_{2\pm x}$ – σ-$IrW_{3\pm x}$: 2470 °C[c]
Fr N/A	**Ra** No binary compounds No interaction	**Ac**[f] N/A						

[a] SiW – solubility in W

[b] DI – temp. range of direct interaction with W, WSM – solubility of W in molten matter (metal or semi-metal), WSS - solubility of W in solid matter (metal or semi-metal)

[c] Eutectic temp.

[d] CSS – continuous solid solution

[e] For lanthanides see Table A.15

[f] For actinides see Table A.15

Table A.14 Chemical properties of tungsten (interaction with 10–18 groups elements: binary compounds, interaction temp. range, solubilities and eutectic temp.)[a]

Group 10 (VIII)	*Group 11 (IB)*	*Group 12 (IIB)*	*Group 13 (IIIA)*	*Group 14 (IVA)*	*Group 15 (VA)*	*Group 16 (VIA)*	*Group 17 (VIIA)*	*Group 18 (VIIIA)*
								He –
			B $WB_{\sim 12}$ (?), WB_{4+x}, α-W_2B_{5-x} (?), β-W_2B_{5-x}, α, β-$WB_{1\pm x}$, $W_{2\pm x}B$ DI: > 500 °C WSS: ≤ ~1 at.% SiW: ~ 0.1-0.2 at.% at 2600 °C β-B – WB_{4+x}: 1950 °C[c] β-$WB_{1\pm x}$ – β-W_2B_{5-x}: 2340 °C[c] $W_{2\pm x}B$ – β-$WB_{1\pm x}$: 2580 °C[c] $W_{2\pm x}B$ – W: 2620 °C[c]	**C** δ-$WC_{1\pm x}$, γ-WC_{1-x}, γ-$W_{2\pm x}C$, α, β-$W_{2+x}C$, DI: > 1400-1600 °C SiW: < 1 at.% at 2710-2715 °C γ-WC_{1-x} – δ-$WC_{1\pm x}$: 2740 °C[c] γ-$W_{2\pm x}C$ – γ-WC_{1-x}: 2750 °C[c] γ-$W_{2\pm x}C$ – W: 2715 °C[c]	**N** δ-WN_2, δ-WN_{1-x}, β-W_2N_{1+x} and some metastable (e.g. δ-WN_{1+x}, W_2N_3, γ′-WN_{1+x}, γ-WN, δ-W_2N) DI: > 2000 °C SiW: 0.001-0.01 at.% at 2400-3050 °C	**O** α, β, γ, δ, ε-WO_{3-x}, ζ, η, θ, κ, λ, μ-WO_3, $W_{25}O_{74}$, W_nO_{3n-2} (Magneli's phases, e.g. $W_{25}O_{73}$, $W_{24}O_{70}$, $W_{20}O_{58}$), $W_{24}O_{68}$, $W_{18}O_{49}$, $WO_{2\pm x}$, W_3O (?) DI: > ~400 °C SiW: negligible α-WO_{3-x} – W_nO_{3n-2}: 1460 °C[c] $W_{18}O_{49}$ – W_nO_{3n-2}: 1590 °C[c]	**F** α, β-WF_6, WF_5 (?), WF_4 DI: > room temp.	**Ne** –

(continued)

Table A.14 (continued)

Group 10 (VIII)	*Group 11 (IB)*	*Group 12 (IIB)*	*Group 13 (IIIA)*	*Group 14 (IVA)*	*Group 15 (VA)*	*Group 16 (VIA)*	*Group 17 (VIIA)*	*Group 18 (VIIIA)*
			Al γ-WAl_{12}, β, β′-WAl_{12} (?), δ-WAl_{5-x}, ε-$WAl_{4\pm x}$, ζ-$WAl_{3\pm x}$, η-$W_3Al_{7\pm x}$, θ-WAl_{2+x} DI: > 650-680 °C WSS: ~ 0.02-0.25 at.% at 550-650 °C WSM: high SiW: ~15 at.% at 1100-1400 °C (?)	**Si** WSi_2, W_2Si_3 (?), W_5Si_{3+x}, W_5Si_2 (?), W_5Si (?) DI: > 1100 °C WSS: negligible SiW: ~5.5 at.% at 2085-2210 °C WSi_2 – Si: 1400 °C[c] WSi_2 – W_5Si_{3+x}: 1970 °C[c] W_5Si_{3+x} – W: 2150 °C[c]	**P** α, β-WP_2, WP, W_2P (?), W_3P (?) DI: > 700-950 °C	**S** WS_3, α-WS_2 (?), β-WS_{2-x}, $W_{21}S_8$ (?), $W_{14}S_5$ (?) DI: > ~400 °C WSS, WSM, SiW: negligible β-WS_{2-x} – W: 1900 °C (or 1480 °C at the low pressure of S vapour)[c]	**Cl** α, β-WCl_6, WCl_5, WCl_4, WCl_3 (?), WCl_2 DI: > 250-300 °C	**Ar** –
Ni Ni_6W (?), β-$Ni_{4+x}W$, δ-NiW_{1-x}, γ-NiW_2 WSS: ~17.5 at.% at 1500 °C SiW: 0.6 at.% at 1925 °C Ni – W: 1500 °C[c]	**Cu** No binary compounds WSS, WSM, SiW: negligible Cu – W: 1084 °C (?)[c]	**Zn** No binary compounds WSS, WSM, SiW: negligible	**Ga** No binary compounds at normal pressures WSS: negligible WSM: (0.4÷3.0) $\times 10^{-3}$ at.% at 815 °C SiW: negligible Ga – W: 29 °C (?)[c]	**Ge** WGe_2 (?), W_2Ge_3, W_5Ge_3 (?) WSS: negligible WSM: ~ 3-6 at.% at 1700 °C (?) SiW: ~3 at.% at 935 °C Ge – W: 935 °C[c]	**As** WAs_2, W_2As_3, W_4As_5, W_2As (?) DI: > 600-620 °C SiW: negligible	**Se** WSe_3, WSe_{2-x}, WSe DI: > 300-400 °C WSS, WSM, SiW: negligible	**Br** WBr_6, WBr_5, WBr_4, WBr_3, W_3Br_8 (?), W_3Br_7 (?), WBr_2 DI: > 450-500 °C	**Kr** –

(continued)

Table A.14 (continued)

Group 10 (VIII)	*Group 11 (IB)*	*Group 12 (IIB)*	*Group 13 (IIIA)*	*Group 14 (IVA)*	*Group 15 (VA)*	*Group 16 (VIA)*	*Group 17 (VIIA)*	*Group 18 (VIIIA)*
Pd No binary compounds WSS: ~ 20-22 at.% at 1815 °C SiW: ~ 3.6-5.0 at.% at 1820 °C	**Ag** No binary compounds WSS, WSM, SiW: negligible	**Cd** No binary compounds No interaction	**In** No binary compounds No interaction WSS, WSM: negligible	**Sn** No binary compounds No interaction WSS, WSM: negligible	**Sb** WSb (?)	**Te** WTe_2 DI: > 600-700 °C WSS, WSM, SiW: negligible	**I** WI_4, WI_3, WI_2, WI (?) DI: > 550-700 °C	**Xe** –
Pt γ-Pt_2W (?), ε-PtW (?) WSS: ~ 60-64 at.% at 2465 °C SiW: ≤ ~ 3.5-5.0 at.% at 2465 °C	**Au** No binary compounds WSS, WSM, SiW: negligible Au – W: 1063 °C (?)[c]	**Hg** No binary compounds WSS, WSM, SiW: negligible	**Tl** No binary compounds No interaction WSS, WSM: negligible	**Pb** No binary compounds No interaction WSS, WSM: negligible Pb – W: 328 °C (?)[c]	**Bi** No binary compounds No interaction WSS, WSM: negligible	**Po** No binary compounds No interaction WSS, WSM, SiW: negligible Po – W: 255 °C (?)[c]	**At** N/A	**Rn** –

[a] See the notes for Table A.13

Table A.15 Chemical properties of tungsten (interaction with lanthanides and actinides: binary compounds, solubilities and eutectic temp.)[a]

Ce	Pr	Nd	Pm	Sm	Eu	Gd	Tb	Dy	Ho	Er	Tm	Yb	Lu
CeW ?, CeW_2 ? WSM: 0.09 at.% at 1940 °C δ-Ce-W: 795 °C[c]	No binary compounds WSM: 0.09 at.% at 2035 °C β-Pr – W: 935 °C[c]	No binary compounds WSM: 0.25 at.% at 2140 °C β-Nd – W: 1010 °C[c]	N/A	No binary compounds WSM: 0.015 at.% at 1765 °C γ-Sm – W: 1070 °C[c]	No binary compounds WSM: ~10^{-3} at.% at 1820 °C Eu – W: 820 °C[c]	No binary compounds WSM: 0.225 at.% at 2020 °C β-Gd – W: 1310 °C[c]	No binary compounds WSM: 0.47 at.% at 2020 °C β-Tb – W: 1355 °C[c]	No binary compounds WSM: 0.71 at.% at 2075 °C β-Dy – W: 1410 °C[c]	No binary compounds WSM: 2.22 at.% at 2070 °C β-Ho – W: 1470 °C[c]	No binary compounds WSM: 1.1 at.% at 2030 °C β-Er – W: 1520 °C[c]	No binary compounds WSM: 1.78 at.% at 2095 °C β-Tm – W: 1545 °C[c]	No binary compounds WSM: ~10^{-3} at.% at 1710 °C γ-Yb – W: 820 °C[c]	No binary compounds WSM: 2.24 at.% at 2100 °C β-Lu – W: 1650 °C[c]
Th	**Pa**	**U**	**Np**	**Pu**	**Am**	**Cm**	**Bk**	**Cf**	**Es**	**Fm**	**Md**	**No**	**Lr**
No binary compounds SiW: 0.24 at.% at 2000 °C	N/A	No binary compounds WSS: negligible (α, β-U) and 0.2-	N/A	No binary compounds WSS, SiW: negligible	N/A	N/A	N/A	N/A	N/A	N/A	N/A	N/A	N/A

(continued)

Table A.15 (continued)

β-Th – W: 1550 °C[c], ?		0.9 at.% (γ-U) at 1000 °C WSM: 33.2 at.% at 2660 °C SiW: ~0.1 at.%. at 1000 °C γ-U – W: 1135 °C[c], ?		WSM: 0.038 at.%. at 950 °C ε-Pu – W: 640 °C[c], ?									

[a] See the notes for Table A.13

Table A.16 Chemical properties of rhenium (interaction with 1–9 groups elements: binary compounds, interaction temp. range, solubilities and eutectic temp.)

Group 1 (IA)	*Group 2 (IIA)*	*Group 3 (IIIB)*	*Group 4 (IVB)*	*Group 5 (VB)*	*Group 6 (VIB)*	*Group 7 (VIIB)*	*Group 8 (VIII)*	*Group 9 (VIII)*
H No binary compounds No interaction – up to melt. point SiR[a]: negligible								
Li Li_3Re (?), Li_2Re (?), LiRe, $LiRe_2$ (?) RSM[b]: $(2\div6)\times10^{-6}$ at.% at 1200-1600 °C	**Be** $ReBe_{22}$, $ReBe_{16+x}$, $ReBe_6$, $ReBe_{2\pm x}$ DI[b]: > 1200 °C RSS[b]: 0.5-1 at.% SiR: ~10 at.% $ReBe_{22}$ – Be: ?[c]							
Na N/A	**Mg** No binary compounds (?) RSM: ~0.05 at.% at 650 °C							

(continued)

Table A.16 (continued)

Group 1 (IA)	*Group 2 (IIA)*	*Group 3 (IIIB)*	*Group 4 (IVB)*	*Group 5 (VB)*	*Group 6 (VIB)*	*Group 7 (VIIB)*	*Group 8 (VIII)*	*Group 9 (VIII)*
K K_2Re, KRe (?), KRe_2 (?)	**Ca** N/A	**Sc** $ScRe_2$, Sc_5Re_{24} RSS: < 1 at.% (β-Sc) at 1360 °C SiR: ~5 at.% at 2570 °C $ScRe_2$ – β-Sc: 1360 °C[c]	**Ti** χ-Ti_5Re_{24} RSS: ~8 at.% (α-Ti) at 600 °C and ~50 at.% (β-Ti) at 2025 °C SiR: 2.3 at.% at 2750 °C	**V** δ-$V_3Re_{7\pm x}$, σ-VRe_{3+x} RSS: 66 at.% at 2400 °C SiR: 10-14 at.% at 2460 °C σ-VRe_{3+x} – V: 2380 °C[c]	**Cr** σ-$Cr_2Re_{3\pm x}$ RSS: 43-50 at.% at 2135-2285 °C) SiR: 17-25 at.% at 2320-2355 °C	**Mn** σ-$MnRe_{1+x}$ RSS: 5.5 at.% (α-Mn) and lower (β, γ, δ-Mn)	**Fe** η-$Fe_{3\pm x}Re$, Fe_2Re, σ-Fe_3Re_2, Fe_2Re_3 RSS: 18-19 at.% (α-Fe) at 895 °C, 16.0-16.5 at.% (γ-Fe) at 1205 °C and 8 at.% (δ-Fe) at 1375 °C	**Co** No binary compounds RSS: 15 at.% (α-Co) at 1550 °C CSS[d]: (ε-Co) – Re
Rb N/A	**Sr** N/A	**Y** YRe_2 RSS: < 1 at.% (β-Y) SiR: ≤ 1 at.% YRe_2 – α-Y: 1450 °C[c], ?	**Zr** σ-Zr_2Re, λ-$ZrRe_{2-x}$, χ-Zr_5Re_{24+x} RSS: ~1.5 at.% (α-Zr) at 400-500 °C and 8 at.% (β-Zr) at 1600 °C SiR: ~0.2 at.% at 2500 °C σ-Zr_2Re – β-Zr: 1600 °C[c] χ-Zr_5Re_{24+x} – Re: 2430 °C[c]	**Nb** σ-Nb_2Re_{3-x}, χ-$NbRe_{3\pm x}$ RSS: 45.5-46.5 at.% at 2400 °C SiR: 3.5-4.5 at.% at 2520-2715 °C σ-Nb_2Re_{3-x} – Nb: 1600 °C[c] χ-$NbRe_{3\pm x}$ – Re: 2715 °C[c]	**Mo** σ-$Mo_2Re_{3\pm x}$, χ-$MoRe_{3+x}$ RSS: 42-43 at.% at 2480 °C SiR: ~21 at.% at 2645 °C σ-$Mo_2Re_{3\pm x}$ – Mo: 2480 °C[c]	**Tc** No binary compounds CSS: Tc – Re	**Ru** No binary compounds CSS: Ru – Re	**Rh** No binary compounds RSS: 25-26 at.% at 2595-2645 °C SiR: ~24 at.% at 2595-2645 °C

(continued)

Table A.16 (continued)

Group 1 (IA)	*Group 2 (IIA)*	*Group 3 (IIIB)*	*Group 4 (IVB)*	*Group 5 (VB)*	*Group 6 (VIB)*	*Group 7 (VIIB)*	*Group 8 (VIII)*	*Group 9 (VIII)*
Cs N/A	**Ba** N/A	**La**[e] No binary compounds No interaction	**Hf** $HfRe_{1\pm x}$, λ-$HfRe_{2\pm x}$, χ-$Hf_5Re_{24\pm x}$ RSS: ~ 0.8-3.0 at.% (α-Hf) at 1250-1300 °C and 12.5 at.% (β-Hf) at 1840-2100 °C SiR: ~ 0.2-3.5 at.% at 2915-2975 °C $HfRe_{1\pm x}$ – β-Hf: 1950 °C[c] χ-$Hf_5Re_{24\pm x}$ – Re: 2930 °C[c]	**Ta** σ-Ta_2Re_{3-x} χ-$TaRe_{3\pm x}$ RSS: 47 at.% at 2460 °C SiR: ~ 3-5 at.% at 2755-2830 °C σ-Ta_2Re_{3-x} – Ta: 2550 °C[c] χ-$TaRe_{3\pm x}$ – Re: 2760 °C[c]	**W** σ-$W_2Re_{3\pm x}$, χ-WRe_{3-x} RSS: ~ 37-45 at.% at 3000 °C SiR: ~ 15-20 at.% at 2820 °C σ-$W_2Re_{3\pm x}$ – Re: 2820 °C[c]	**Re**	**Os** No binary compounds CSS: Os – Re	**Ir** No binary compounds RSS: ~ 36-40 at.% at 2800 °C SiR: ~44 at.% at 2800 °C
Fr N/A	**Ra** N/A	**Ac**[f] N/A						

[a] SiR – solubility in Re

[b] DI – temp. range of direct interaction with Re, RSM – solubility of Re in molten matter (metal or semi-metal), RSS - solubility of Re in solid matter (metal or semi-metal)

[c] Eutectic temp.

[d] CSS – continuous solid solution

[e] For lanthanides see Table A.18

[f] For actinides see Table A.18

Table A.17 Chemical properties of rhenium (interaction with 10–18 groups elements: binary compounds, interaction temp. range, solubilities and eutectic temp.)[a]

Group 10 (VIII)	*Group 11 (IB)*	*Group 12 (IIB)*	*Group 13 (IIIA)*	*Group 14 (IVA)*	*Group 15 (VA)*	*Group 16 (VIA)*	*Group 17 (VIIA)*	*Group 18 (VIIIA)*
								He –
			B $ReB_{2\pm x}$, Re_7B_{3+x}, $Re_{3\pm x}B$ DI: > 1400 °C RSS: < 1 at.% at 2030-2050 °C SiR: < 2.5 at.% at 2150 °C $ReB_{2\pm x}$ – β-B: 2040 °C[c] $ReB_{2\pm x}$ – Re_7B_{3+x}: 1830 °C[c]	**C** Metastable carbides (?) SiR: ~ 11-17 at.% at 2480-2505 °C Re – C: 2490 °C[c]	**N** $Re_{2+x}N$ and unstable $ReN_{2\pm x}$ and $Re_{3\pm x}N$ DI: > 900 °C SiR: $(0.6\div1.5)\times10^{-3}$ at.% at 2000-2750 °C	**O** Re_2O_7, Re_3O_{10}, ReO_3, $Re_2O_{5\pm x}$, Re_7O_{18}, α, β-ReO_{2+x}, Re_2O_3 (?) DI: > 150 °C SiR: ~0.2 at.% Re_2O_7 – ReO_3: 300 °C[c]	**F** ReF_7, α, β-ReF_6, ReF_5, ReF_4	**Ne** –

(continued)

Table A.17 (continued)

Group 10 (VIII)	*Group 11 (IB)*	*Group 12 (IIB)*	*Group 13 (IIIA)*	*Group 14 (IVA)*	*Group 15 (VA)*	*Group 16 (VIA)*	*Group 17 (VIIA)*	*Group 18 (VIIIA)*
			Al $ReAl_{12}$, $ReAl_6$, $ReAl_4$, $ReAl_2$, ReAl (?), Re_3Al_2 DI: > 800 °C RSS: ~0.25 at.% at 600 °C RSM: low SiR: ~2.8 at.% at 1900-2000 °C	**Si** $ReSi_2$, ReSi, Re_5Si_3, Re_2Si, Re_3Si (?) DI: > 1400 °C RSS: low $ReSi_2$ – Si: 1250 °C[c] Re_2Si – ReSi: ~1800 °C[c] Re_2Si – Re: ~1800 °C[c]	**P** ReP_4, ReP_3, Re_2P_5, ReP_2, Re_3P_4, ReP, Re_2P DI: > 800 °C	**S** Re_2S_7 (?), ReS_3, Re_2S_5, ReS_2, Re_2S_3, ReS DI: > ~700 °C	**Cl** $ReCl_6$, $ReCl_5$, α, β-$ReCl_4$, $ReCl_3$, $ReCl_2$ (?) DI: > 200 °C	**Ar** –
Ni No binary compounds RSS: ~17 at.% at 1620 °C SiR: ~ 14-18 at.% at 1620 °C	**Cu** No binary compounds RSS, RSM, SiR: negligible Cu – Re: 1083 °C (?)[c]	**Zn** No binary compounds RSS, RSM, SiR: negligible	**Ga** No binary compounds at normal pressures RSS, RSM, SiR: negligible	**Ge** $ReGe_2$ (?), Re_3Ge_7 RSS: ~3 at.% at 930 °C Re_3Ge_7 ($ReGe_2$, ?) – Ge: 930 °C[c]	**As** Re_3As_7 DI: at elevated temp.	**Se** Re_2Se_7, $ReSe_2$ DI: > 600 °C	**Br** $ReBr_5$, $ReBr_4$, $ReBr_3$ DI: > 400 °C	**Kr** –

(continued)

Table A.17 (continued)

Group 10 (VIII)	*Group 11 (IB)*	*Group 12 (IIB)*	*Group 13 (IIIA)*	*Group 14 (IVA)*	*Group 15 (VA)*	*Group 16 (VIA)*	*Group 17 (VIIA)*	*Group 18 (VIIIA)*
Pd No binary compounds RSS: ~16 at.% at 1650 °C SiR: > 5 at.% at 1650 °C	**Ag** No binary compounds RSS, RSM, SiR: negligible Ag – Re: 961 °C (?)[c]	**Cd** N/A	**In** No binary compounds RSM: low	**Sn** No binary compounds RSM: negligible Sn – Re: 230 °C (?)[c]	**Sb** No binary compounds No interaction	**Te** Re_2Te_7, $Re_2Te_{5\pm x}$, β-$ReTe_{2+x}$, α-$ReTe_{1-x}$, Re_2Te β-$ReTe_{2+x}$ (Re_2Te_7, ?) – Te: 440 °C[c] β-$ReTe_{2+x}$ – α-$ReTe_{1-x}$: ~850 °C[c] Re_2Te – α-$ReTe_{1-x}$: ~850 °C[c]	**I** ReI_4, ReI_3, ReI_2, ReI	**Xe** –
Pt No binary compounds (ordered phases, ?) RSS: ~ 40-42 at.% at 2450 °C SiR: ~ 40-44 at.% at 2450 °C	**Au** No binary compounds RSS: ~0.1 at.% at 1000 °C RSM, SiR: negligible	**Hg** No binary compounds No interaction RSS, RSM, SiR: negligible	**Tl** N/A	**Pb** N/A	**Bi** No binary compounds No interaction RSM: negligible	**Po** N/A	**At** N/A	**Rn** –

[a] See the notes for Table A.16

Table A.18 Chemical properties of rhenium (interaction with lanthanides and actinides: binary compounds, solubilities and eutectic temp.)[a]

Ce	Pr	Nd	Pm	Sm	Eu	Gd	Tb	Dy	Ho	Er	Tm	Yb	Lu
No binary compounds (?)	α, β-$PrRe_2$ (?) RSM: 4.5 at.% at 1765 °C β-Pr – Re ($PrRe_2$, ?): 930 °C[c] (?)	$NdRe_2$ (?) SiR: negligible	N/A	$SmRe_2$ SiR: negligible	$EuRe_2$	$GdRe_2$ RSS: < 1 at.% (β-Gd) SiR: ~0.4 at.% $GdRe_2$ – β-Gd: 1290 °C[c]	$TbRe_2$ SiR: ~0.2 at.% $TbRe_2$ – β-Tb: 1310 °C[c]	$DyRe_2$ SiR: < 1 at.%	$HoRe_2$ SiR: < 1 at.%	$ErRe_2$ RSS: ≤ 1 at.% SiR: < 0.3 at.% $ErRe_2$ – β-Er: 1440 °C[c]	$TmRe_2$	$YbRe_2$ (?)	$LuRe_2$
Th	**Pa**	**U**	**Np**	**Pu**	**Am**	**Cm**	**Bk**	**Cf**	**Es**	**Fm**	**Md**	**No**	**Lr**
$ThRe_2$ RSS: ~1.5 at.% (β-Th, ?) SiR: negligible $ThRe_2$ – β-Th: ~1400 °C[c]	N/A	U_2Re, α, β-URe_2 RSS: 0.5 at.% (α-U) at 643 °C, 2.4 at.% (β-U) at 680 °C and 8.8	$NpRe_2$	$PuRe_2$ $PuRe_2$ – ε-Pu: 625 °C[c], ?	N/A	N/A	N/A	N/A	N/A	N/A	N/A	N/A	N/A

(continued)

Table A.18 (continued)

$ThRe_2$ – Re: 2315 °C[c]		at.% (γ-U) at 1105 °C SiR: ~4 at.%. at 2105 °C β-URe_2 – γ-U: 1110 °C[c] β-URe_2 – Re: 2130 °C[c]											

[a] See the notes for Table A.16

Table A.19 Chemical properties of osmium (interaction with 1–9 groups elements: binary compounds, interaction temp. range, solubilities and eutectic temp.)

Group 1 (IA)	*Group 2 (IIA)*	*Group 3 (IIIB)*	*Group 4 (IVB)*	*Group 5 (VB)*	*Group 6 (VIB)*	*Group 7 (VIIB)*	*Group 8 (VIII)*	*Group 9 (VIII)*
H No binary compounds SiO[a]: very low								
Li No binary compounds No interaction	**Be** $OsBe_{12}$, Os_2Be_{17}, $OsBe_2$, OsBe (?) DI[b]: > 1150 °C							
Na No binary compounds No interaction	**Mg** No binary compounds (?) OSS[b]: ~0.06 at.% at 649 °C Mg – Os: 649 °C[c] (?)							

(continued)

Table A.19 (continued)

Group 1 (IA)	*Group 2 (IIA)*	*Group 3 (IIIB)*	*Group 4 (IVB)*	*Group 5 (VB)*	*Group 6 (VIB)*	*Group 7 (VIIB)*	*Group 8 (VIII)*	*Group 9 (VIII)*
K KOs (?), KOs_2 (?)	**Ca** Ca_2Os_3 (?), $CaOs_2$ (?), $CaOs_5$ (?)	**Sc** $Sc_{44}Os_7$, $Sc_{11}Os_4$, $ScOs_2$	**Ti** δ-$TiOs_{1\pm x}$ OSS: ~1 at.% (α-Ti) at 600 °C and ~ 20-23 at.% (β-Ti) at 1710 °C SiO: ~21 at.% at 2100 °C δ-$TiOs_{1\pm x}$ – Os: 2100 °C[c]	**V** $V_3Os_{2\pm x}$, VOs_{1-x} OSS: ~ 30-46 at.% at 1570-2010 °C SiO: 46-48 at.% at 1910-2240 °C $V_3Os_{2\pm x}$ – Os: 1910 °C[c] (?) V – Os: 2240 °C[c] (?)	**Cr** $Cr_{3\pm x}Os$, σ-$Cr_{2\pm x}Os$ OSS: ~28 at.% at 1845 °C SiO: ~62 at.% at 1845 °C Cr – Os: 1845 °C[c]	**Mn** No binary compounds (?) OSS: ~17 at.% (α-Mn) at 400-600 °C and > 40 at.% (β-Mn) at 400-600 °C	**Fe** No binary compounds OSS: ~5 at.% (α-Fe) at 620 °C, ~25 at.% (γ-Fe) at 1720 °C and 1.5-3.0 at.% (δ-Fe) at 1535-1565 °C SiO: 75-78 at.% at 400-600 °C	**Co** No binary compounds CSS[d]: (ε-Co) – Os OSS: 20-22 at.% (α-Co) at 1600 °C
Rb No binary compounds OSM[b], OSS, SiO: very low	**Sr** N/A	**Y** Y_3Os, YOs_2 OSM[b], OSS, SiO: very low Y_3Os – α-Y: 1150 °C[c] YOs_2 – Os: 2100 °C[c]	**Zr** $Zr_{11}Os_4$, ZrOs, λ_1-$ZrOs_{2\pm x}$ OSS: < 1 at.% (α-Zr) and ~14 at.% (β-Zr) at 1260-1280 °C SiO: ~8 at.% at 2420-2460 °C $Zr_{11}Os_4$ – β-Zr: 1270 °C[c] λ_1-$ZrOs_{2\pm x}$ – Os: 2440 °C[c]	**Nb** β-$Nb_{3-x}Os$, σ-$Nb_3Os_{2\pm x}$, χ-$Nb_2Os_{3\pm x}$ OSS: ~19 at.% at 2175 °C SiO: 27 at.% at 2270 °C σ-$Nb_3Os_{2\pm x}$ – Nb: 2175 °C[c] σ-$Nb_3Os_{2\pm x}$ – χ-$Nb_2Os_{3\pm x}$: 2120 °C[c]	**Mo** β-$Mo_{3\pm x}Os$, σ-$Mo_{2\pm x}Os$ OSS: 19.5 at.% at 2370-2390 °C SiO: 52 at.% at 2420-2440 °C σ-$Mo_{2\pm x}Os$ – Mo: 2380 °C[c]	**Tc** No binary compounds CSS: Tc – Os (?)	**Ru** No binary compounds CSS: Ru – Os	**Rh** No binary compounds OSS: ~55 at.% at 2575-2625 °C SiO: ~30 at.% at 2575-2625 °C

(continued)

Table A.19 (continued)

Group 1 (IA)	*Group 2 (IIA)*	*Group 3 (IIIB)*	*Group 4 (IVB)*	*Group 5 (VB)*	*Group 6 (VIB)*	*Group 7 (VIIB)*	*Group 8 (VIII)*	*Group 9 (VIII)*
Cs No binary compounds OSM[b], OSS, SiO: very low	**Ba** N/A	**La**[e] La_3Os, α, β-$LaOs_2$	**Hf** θ-$Hf_{3+x}Os$, ε-$Hf_{2+x}Os$, η-$Hf_{2\pm x}Os$, δ-$HfOs_{1\pm x}$, λ-$HfOs_{2\pm x}$ OSS: < 2 at.% (α-Hf) at 1200-1250 °C and ~12 at.% (β-Hf) at 1580 °C SiO: > 10 at.% at 2600 °C θ-$Hf_{3+x}Os$ – β-Hf: 1580 °C[c] λ-$HfOs_{2\pm x}$ – Os: 2600 °C[c]	**Ta** σ-$Ta_3Os_{2\pm x}$ γ-$Ta_2Os_{3\pm x}$ OSS: ~22 at.% at 2500 °C SiO: ~25 at.% at 1600 °C σ-$Ta_3Os_{2\pm x}$ – γ-$Ta_2Os_{3\pm x}$: 2380 °C[c]	**W** σ-$OsW_{3\pm x}$ OSS: ~18.5 at.% at 2945 °C SiO: ~55 at.% at 2725 °C Os – σ-$OsW_{3\pm x}$: 2725 °C[c]	**Re** No binary compounds CSS: Os – Re	**Os**	**Ir** No binary compounds OSS: 44.5 at.% at 2625-2695 °C SiO: 38 at.% at 2625-2695 °C
Fr N/A	**Ra** N/A	**Ac**[f] N/A						

[a] SiO – solubility in Os

[b] DI – temp. range of direct interaction with Os, OSM – solubility of Os in molten matter (metal or semi-metal), OSS - solubility of Os in solid matter (metal or semi-metal)

[c] Eutectic temp.

[d] CSS – continuous solid solution

[e] For lanthanides see Table A.21

[f] For actinides see Table A.21

Table A.20 Chemical properties of osmium (interaction with 10–18 groups elements: binary compounds, interaction temp. range, solubilities and eutectic temp.)[a]

Group 10 (VIII)	*Group 11 (IB)*	*Group 12 (IIB)*	*Group 13 (IIIA)*	*Group 14 (IVA)*	*Group 15 (VA)*	*Group 16 (VIA)*	*Group 17 (VIIA)*	*Group 18 (VIIIA)*
								He –
			B OsB_2, Os_2B_3, OsB_{1+x} DI: > 800 °C OsB_2 – β-B: 2000 °C[c] Os_2B_3 – OsB_{1+x}: 1500 °C[c] OsB_{1+x} – Os: 1480 °C[c]	**C** Metastable carbides (?) SiO: negligible (solid) and 39.1-39.7 at.% (liquid) at 5010 °C Os – C: 2730 °C[c]	**N** Metastable nitride Os_2N (?) No interaction at normal pressures	**O** OsO_4, OsO_3 (?), OsO_2, Os_2O_3 (?) DI: > room temp.	**F** OsF_8 (?), OsF_7 (?), OsF_6, OsF_5, OsF_4 DI: > 250 °C	**Ne** –
			Al $OsAl_5$ (?), $OsAl_3$, $OsAl_2$, Os_2Al_3, OsAl	**Si** $OsSi_3$ (?), $OsSi_2$, Os_2Si_3, $OsSi_{1\pm x}$ DI: > 1000 °C $OsSi_2$ – Si: 1360 °C[c] $OsSi_{1\pm x}$ – Os: 1720 °C[c]	**P** α, β-OsP_4, OsP_2 DI: > 500 °C	**S** OsS_2 DI: > 900 °C OsS_2 – Os: 2000 °C[c]	**Cl** $OsCl_4$, $OsCl_3$, $OsCl_2$ DI: > 300 °C (?)	**Ar** –

(continued)

Table A.20 (continued)

Group 10 (VIII)	*Group 11 (IB)*	*Group 12 (IIB)*	*Group 13 (IIIA)*	*Group 14 (IVA)*	*Group 15 (VA)*	*Group 16 (VIA)*	*Group 17 (VIIA)*	*Group 18 (VIIIA)*
Ni No binary compounds OSS: 12.0-13.3 at.% at 1465-1500 °C SiO: ~ 12-64 at.% (?) at 1465-1500 °C	**Cu** No binary compounds OSS: negligible small at 900 °C Cu – Os: 1081 °C (?)[c]	**Zn** No binary compounds No interaction	**Ga** $OsGa_3$, $OsGa_2$, ?	**Ge** $OsGe_2$, Os_2Ge_3	**As** $OsAs_{2\pm x}$	**Se** $OsSe_2$	**Br** $OsBr_4$, $OsBr_3$ DI: > 500 °C	**Kr** –
Pd No binary compounds OSS: ~ 1-3 at.% at 1615-1665 °C SiO: 5.2 at.% at 1615-1665 °C	**Ag** No binary compounds OSS, OSM, SiO: negligible Ag – Os: 961 °C (?)[c]	**Cd** N/A	**In** In_3Os (?), In_2Os (?), InOs (?), $InOs_2$ (?) OSM: low	**Sn** No binary compounds at normal pressures OSM: very low	**Sb** $OsSb_2$	**Te** α-$OsTe_2$ (?), β-$OsTe_2$	**I** OsI_4, OsI_3, OsI_2, OsI	**Xe** –

(continued)

Table A.20 (continued)

Group 10 (VIII)	*Group 11 (IB)*	*Group 12 (IIB)*	*Group 13 (IIIA)*	*Group 14 (IVA)*	*Group 15 (VA)*	*Group 16 (VIA)*	*Group 17 (VIIA)*	*Group 18 (VIIIA)*
Pt	**Au**	**Hg**	**Tl**	**Pb**	**Bi**	**Po**	**At**	**Rn**
No binary compounds OSS: ~25 at.% at 1940-1970 °C SiO: ≤ 9.3 at.%	No binary compounds OSS: absolutely negligible at 900-950 °C	No binary compounds OSS, OSM: extremely low SiO: < 1 at.%	N/A	N/A	No binary compounds No interaction OSM: negligible	N/A	N/A	–

[a] See the notes for Table A.19

Table A.21 Chemical properties of osmium (interaction with lanthanides and actinides: binary compounds, solubilities and eutectic temp.)[a]

Ce	**Pr**	**Nd**	**Pm**	**Sm**	**Eu**	**Gd**	**Tb**	**Dy**	**Ho**	**Er**	**Tm**	**Yb**	**Lu**
Ce_3Os, α-$CeOs_2$?, β-$CeOs_2$	Pr_3Os, α-$PrOs_2$?, β-$PrOs_2$ β-$PrOs_2$ – α-Pr: 670 °C[c] (?)	Nd_3Os, $NdOs_2$	N/A	Sm_3Os, $SmOs_2$	N/A	Gd_3Os, $GdOs_2$	Tb_3Os, $TbOs_2$	Dy_3Os, $DyOs_2$	Ho_3Os, $HoOs_2$	Er_3Os, $ErOs_2$	Tm_3Os, $TmOs_2$	$YbOs_2$ (?)	Lu_3Os, $LuOs_2$
Th	**Pa**	**U**	**Np**	**Pu**	**Am**	**Cm**	**Bk**	**Cf**	**Es**	**Fm**	**Md**	**No**	**Lr**
Th_7Os_3, $ThOs_{1-x}$, $ThOs_2$ Th_7Os_3 – β-Th: 1285 °C[c] Th_7Os_3 – $ThOs_{1-x}$: 1480 °C[c]	N/A	U_3Os, U_2Os, U_5Os_4, $UOs_{2\pm x}$ OSS: <0.5 at.% (α-U) at 620 °C, 4 at.% (β-U) at 685 °C	?, $NpOs_2$	η$Pu_{19\pm x}Os$, α-$Pu_{3\pm x}Os$, β-$Pu_{3+x}Os$, Pu_5Os_3, $PuOs_2$ OSS: <0.3 at.% (α,β,γ-Pu), 0.4 at.% (δ-Pu) at	?, $AmOs_2$	N/A	N/A	N/A	N/A	N/A	N/A	N/A	N/A

(continued)

Table A.21 (continued)

$ThOs_2$ – Os: 2200 °C[c] (?)		and 18 at.% (γ-U) at 970 °C SiO: <1 at.% U_3Os – γ-U: 970 °C[c] U_2Os – U_5Os_4: 900 °C[c] $UOs_{2\pm x}$ – Os: 2170 °C[c]		418 °C and 6.8 at.% (ε-Pu) at 495 °C $\alpha\text{-}Pu_{3\pm x}Os$ – ε-Pu: 495 °C[c]									

[a] See the notes for Table A.19

Table A.22 Chemical properties of tantalum (interaction with 1–9 groups elements: binary compounds, interaction temp. range, solubilities and eutectic temp.)

Group 1 (IA)	*Group 2 (IIA)*	*Group 3 (IIIB)*	*Group 4 (IVB)*	*Group 5 (VB)*	*Group 6 (VIB)*	*Group 7 (VIIB)*	*Group 8 (VIII)*	*Group 9 (VIII)*
H δ-TaH_{1-x}, γ-$Ta_{4\div5}H_{3\div4}$, ζ-Ta_3H_{2+x}, η-Ta_3H_{2-x}, θ-$Ta_{2-x}H$, β-TaH_x, ε-$Ta_{2\pm x}H$ DI[a]: > ~300 °C SiT[b]: 42-44 at.% at 20-70 °C								
Li No binary compounds TSM[b]: ~7×10^{-3} at.% at 1005 °C	**Be** $TaBe_{12}$, Ta_2Be_{17}, $TaBe_3$, $TaBe_2$, Ta_3Be_2, Ta_2Be							
Na No binary compounds TSM: ~3×10^{-4} at.% at 525 °C	**Mg** No binary compounds TSS[b]: ~0.2 at.% at 652 °C TSM: ~0.1 at.% at 652 °C							

(continued)

Table A.22 (continued)

Group 1 (IA)	*Group 2 (IIA)*	*Group 3 (IIIB)*	*Group 4 (IVB)*	*Group 5 (VB)*	*Group 6 (VIB)*	*Group 7 (VIIB)*	*Group 8 (VIII)*	*Group 9 (VIII)*
K No binary compounds TSM: 1.4×10^{-4}-3×10^{-3} at.% at 400-1330 °C	**Ca** N/A	**Sc** No binary compounds TSM: low β-Sc – Ta: 1519 °C[c]	**Ti** No binary compounds CSS[d]: β-Ti – Ta TSS: ~3 at.% (α-Ti) at 600 °C	**V** $V_{2\pm x}Ta$ CSS: V – Ta (> 1310-1420 °C)	**Cr** $TaCr_3$, λ_1, λ_2-$TaCr_{2\pm x}$ TSS: 3.5-4.0 at.% at 1700-1775 °C SiT: 27.0-27.5 at.% at 1945-1985 °C λ_1-$TaCr_{2\pm x}$ – Cr: 1760 °C[c] λ_1-$TaCr_{2\pm x}$ – Ta: 1965 °C[c]	**Mn** Mn_2Ta, MnTa TSS: ~1 at.% (α-Mn) at 750 °C, ~0.7 at.% (β-Mn) at 1060-1070 °C, ~1.5 at.% (γ-Mn) at 1150-1175 °C and ~0.5 at.% (δ-Mn) at 1190-1200 °C SiT: 3-4 at.% at 1700 °C Mn_2Ta – MnTa: 1600 °C[c] Mn_2Ta – γ-Mn: 1160 °C[c]	**Fe** ε-$Fe_{2\pm x}Ta$, μ-Fe_7Ta_{6+x} TSS: 0.7 at.% (α-Fe) at 965 °C, 0.85-0.90 at.% (γ-Fe) at 1215 °C and 2.8 at.% (δ-Fe) at 1442 °C SiT: ~7 at.% at 1670 °C ε-$Fe_{2\pm x}Ta$ – δ-Fe: 1442 °C[c] μ-Fe_7Ta_{6+x} – Ta: 1670 °C[c]	**Co** κ-Co_7Ta_2, Co_3Ta (?), λ_3-$Co_{3-x}Ta$, λ_2-$Co_{2\pm x}Ta$, λ_1-Co_3Ta_{2-x}, μ-$Co_7Ta_{6\pm x}$, $CoTa_2$ TSS: 4.6-4.7 at.% (ε-Co) at 1008 °C and 4.2-4.4 at.% (α-Co) at 1200-1270 °C SiT: ~20 at.% at 1800 °C λ_3-$Co_{3-x}Ta$ (λ_2-$Co_{2\pm x}Ta$, ?) – α-Co: 1275 °C[c] λ_2-$Co_{2\pm x}Ta$ – μ-$Co_7Ta_{6\pm x}$: 1560 °C[c] $CoTa_2$ – μ-$Co_7Ta_{6\pm x}$: 1670 °C[c]

(continued)

Table A.22 (continued)

Group 1 (IA)	*Group 2 (IIA)*	*Group 3 (IIIB)*	*Group 4 (IVB)*	*Group 5 (VB)*	*Group 6 (VIB)*	*Group 7 (VIIB)*	*Group 8 (VIII)*	*Group 9 (VIII)*
Rb No binary compounds No interaction	**Sr** N/A	**Y** No binary compounds TSM: 1.35 at.% at 2085 °C SiT: $\leq 2\times10^{-4}$ at.% at 1585 °C β-Y – Ta: 1510 °C[c]	**Zr** No binary compounds CSS: β-Zr – Ta (> 1780 °C) TSS: 1.0-2.5 at.% (α-Zr) at 775-800 °C SiT: ~ 6.5-9.5 at.% at 775-800 °C	**Nb** No binary compounds CSS: Nb – Ta	**Mo** No binary compounds CSS: Mo – Ta	**Tc** Tc_5Ta (?), TcTa (?)	**Ru** γ-Ru_3Ta_{2-x}, μ, μ′, μ″-$RuTa_{1\pm x}$ TSS: 24-28 at.% at 1665 °C SiT: ~50 at.% at 2080 °C μ-$RuTa_{1\pm x}$ – Ru: 1970 °C[c]	**Rh** $Rh_{3\pm x}Ta$, α_2-$Rh_{2\pm x}Ta$, α_1-$Rh_{3\pm x}Ta_2$, α_3-$RhTa_{1-x}$, σ-$RhTa_{2\pm x}$ TSS: 17.5 at.% at 1995-2035 °C SiT: ~16 at.% at 2080-2140 °C α_3-$RhTa_{1-x}$ – σ-$RhTa_{2\pm x}$: 1740 °C[c]
Cs No binary compounds No interaction	**Ba** N/A	**La**[e] No binary compounds TSM: 0.05 at.% at 2015 °C	**Hf** No binary compounds CSS: β-Hf – Ta (> 1140, or 1670 °C, ?)	**Ta**	**W** No binary compounds CSS: W – Ta	**Re** σ-Ta_2Re_{3-x} χ-$TaRe_{3\pm x}$ TSS: ~ 3-5 at.% at 2755-2830 °C	**Os** σ-$Ta_3Os_{2\pm x}$ γ-$Ta_2Os_{3\pm x}$ TSS: ~25 at.% at 1600 °C	**Ir** β-$Ir_{3\pm x}Ta$, γ-Ir_3Ta_{2+x}, δ-$IrTa_{1-x}$, σ-$IrTa_{3\pm x}$ TSS: 15.5 at.%

(continued)

Table A.22 (continued)

Group 1 (IA)	*Group 2 (IIA)*	*Group 3 (IIIB)*	*Group 4 (IVB)*	*Group 5 (VB)*	*Group 6 (VIB)*	*Group 7 (VIIB)*	*Group 8 (VIII)*	*Group 9 (VIII)*
		β-La – Ta: 850 °C[c]	TSS: ~7 at.% (α-Hf) at 1020-1085 °C			SiT: 47 at.% at 2460 °C σ-Ta_2Re_{3-x} – Ta: 2550 °C[c]	SiT: ~22 at.% at 2500 °C σ-$Ta_3Os_{2\pm x}$ – γ-$Ta_2Os_{3\pm x}$: 2380 °C[c]	at 2380-2385 °C SiT: 7.2-7.3 at.% at 2475-2580 °C δ-$IrTa_{1-x}$ – σ-$IrTa_{3\pm x}$: 1950 °C[c] β-$Ir_{3\pm x}Ta$ – Ir: 2385 °C[c] (?)
Fr N/A	**Ra** N/A	**Ac**[f] N/A						

[a] DI – temp. range of direct interaction with Ta

[b] SiT – solubility in Ta, TSM – solubility of Ta in molten matter (metal or semi-metal), TSS - solubility of Ta in solid matter (metal or semi-metal)

[c] Eutectic temp.

[d] CSS – continuous solid solution

[e] For lanthanides see Table A.24

[f] For actinides see Table A.24

Table A.23 Chemical properties of tantalum (interaction with 10–18 groups elements: binary compounds, interaction temp. range, solubilities and eutectic temp.)[a]

Group 10 (VIII)	*Group 11 (IB)*	*Group 12 (IIB)*	*Group 13 (IIIA)*	*Group 14 (IVA)*	*Group 15 (VA)*	*Group 16 (VIA)*	*Group 17 (VIIA)*	*Group 18 (VIIIA)*
								He –
			B $TaB_{2\pm x}$, $Ta_3B_{4\pm x}$, λ-$TaB_{1\pm x}$, $Ta_3B_{2\pm x}$, $Ta_{2+x}B$ DI: > 1500 °C TSS, SiT: ~2 at.% $TaB_{2\pm x}$ – $Ta_3B_{4\pm x}$: ~2700 °C[c] $TaB_{2\pm x}$ – β-B: 2060 °C[c] $Ta_{2+x}B$ – Ta: 2375 °C[c]	**C** $Ta_{64}C$ (?), α-$Ta_{2+x}C$, β-$Ta_{2\pm x}C$, ε-$Ta_3C_{2\pm x}$, ζ-Ta_4C_{3-x}, $Ta_6C_{5\pm x}$, TaC_{1-x} DI: > 1300-1500 °C SiT: 7.0-7.5 at.% at 2800-2860 °C β-$Ta_{2\pm x}C$ – Ta: 2830 °C[c], TaC_{1-x} – C: 3420 °C[c]	**N** TaN_2 (?), Ta_3N_5, Ta_4N_5 (?), ε-TaN_{1-x}, δ-TaN_{1-x}, γ-$Ta_{2\pm x}N$, Ta_3N (?), Ta_9N_2, β-TaN_x, $Ta_{27\pm x}N$ (?) DI: > 300 °C SiT: ~ 10-14 at.% at 2900 °C γ-$Ta_{2\pm x}N$ – δ-TaN_{1-x}: ~2900 °C[c], γ-$Ta_{2\pm x}N$ – Ta: ~2600 °C[c]	**O** α, β-Ta_2O_5, TaO_2 (?), TaO (?), Ta_2O (?), Ta_4O (?) DI: > ~250 °C SiT: ~ 4-6 at.% at 1500-1900 °C α-Ta_2O_5– Ta: 1550 °C[c]	**F** TaF_5, TaF_3 DI: > room temp.	**Ne** –

(continued)

Table A.23 (continued)

Group 10 (VIII)	*Group 11 (IB)*	*Group 12 (IIB)*	*Group 13 (IIIA)*	*Group 14 (IVA)*	*Group 15 (VA)*	*Group 16 (VIA)*	*Group 17 (VIIA)*	*Group 18 (VIIIA)*
			Al $TaAl_3$, $TaAl_2$, α, β-Ta_2Al_3, TaAl, δ-$Ta_{2\pm x}Al$, Ta_3Al (?) TSS: ≤ 0.25 at.% TSM: high SiT: ~ 4-12 at.% at 2000-2100 °C (?) β-Ta_2Al_3 – δ-$Ta_{2\pm x}Al$: 1550 °C[c]	**Si** $TaSi_2$, α, β-Ta_5Si_3, Ta_2Si, $Ta_{3+x}Si$ DI: > 1000-1500 °C TSS: negligible SiT: 1.3-6.0 at.% at 2260-2300 °C α(or β)-Ta_5Si_3 – $TaSi_2$: 2030 °C[c] Ta_2Si – $Ta_{3+x}Si$: ~2400 °C[c] $TaSi_2$ – Si: 1390 °C[c] $Ta_{3+x}Si$ – Ta: 2280 °C[c]	**P** TaP_5, TaP_2, α, β-TaP (?), Ta_5P_4, Ta_5P_3, Ta_2P (?), Ta_3P (?)	**S** α, β-TaS_3, α, β, γ, δ, ε-TaS_2, α, β, γ-TaS_{2-x}, TaS, Ta_3S_2, Ta_2S, Ta_6S DI: > 450 °C	**Cl** $TaCl_5$, $TaCl_4$, $TaCl_3$, Ta_2Cl_5 DI: > 150-250 °C	**Ar** –
Ni ζ-$Ni_{8\pm x}Ta$, κ-$Ni_{3\pm x}Ta$, $Ni_{2\pm x}Ta$, μ-Ni_7Ta_{6+x}, $NiTa_{2+x}$	**Cu** No binary compounds TSS, SiT: extremely low TSM: 0.009 at.% at 1200 °C	**Zn** $TaZn_2$ (?), Ta_6Zn_7 (?)	**Ga** $TaGa_3$, $TaGa_2$ (?), Ta_4Ga_5, Ta_3Ga_2, α, β-Ta_5Ga_3, Ta_2Ga	**Ge** $TaGe_2$, α, β-Ta_5Ge_3, α, β, γ, δ-Ta_2Ge, α, β-Ta_3Ge TSS: 0.045 at.% at 910 °C	**As** $TaAs_2$, TaAs, Ta_5As_4, Ta_2As, α, β-Ta_3As (?) DI: > 800 °C	**Se** η-$TaSe_3$, ε, ζ-$TaSe_{2-x}$, α, β, γ, δ-$TaSe_{1+x}$ DI: > 800 °C	**Br** $TaBr_5$, $TaBr_4$, $TaBr_3$, Ta_2Br_5, Ta_3Br_7, $TaBr_2$ (?) DI: > 450-500 °C	**Kr** –

(continued)

Table A.23 (continued)

Group 10 (VIII)	*Group 11 (IB)*	*Group 12 (IIB)*	*Group 13 (IIIA)*	*Group 14 (IVA)*	*Group 15 (VA)*	*Group 16 (VIA)*	*Group 17 (VIIA)*	*Group 18 (VIIIA)*
TSS: 14-15 at.% at 1360 °C SiT: ~20 at.% at 1790 °C $Ni_{2\pm x}Ta$ – μ-Ni_7Ta_{6+x}: 1350 °C[c] κ-$Ni_{3\pm x}Ta$ – Ni: 1360 °C[c]	Cu – Ta: 1083 °C (?)[c]						$TaBr_5$ – $TaBr_4$: 265 °C[c]	
Pd $Pd_{3\pm x}Ta$, $Pd_{2\pm x}Ta$, PdTa (?), α, β-$Pd_{1\pm x}Ta$, σ-$PdTa_{3\pm x}$ TSS: ~ 18-22 at.% at 1730-1860 °C SiT: ~ 20-25 at.% at 2350-2550 °C $Pd_{3\pm x}Ta$ – $Pd_{2\pm x}Ta$: 1725 °C[c] PdTa (β-$Pd_{1\pm x}Ta$, ?) – σ-$PdTa_{3\pm x}$: 1720 °C[c] (?)	**Ag** No binary compounds TSS, SiT: negligible	**Cd** N/A	**In** No binary compounds No interaction TSS, TSM, SiT: negligible	**Sn** Ta_2Sn_3, Ta_3Sn	**Sb** $TaSb_2$, Ta_5Sb_4, Ta_3Sb	**Te** $TaTe_4$, α′, α″, β-$TaTe_{2-x}$, $TaTe_{1-x}$ DI: > 600 °C	**I** TaI_5, TaI_4, TaI_3, Ta_3I_7 DI: > 150-250 °C	**Xe** –

(continued)

Table A.23 (continued)

Group 10 (VIII)	*Group 11 (IB)*	*Group 12 (IIB)*	*Group 13 (IIIA)*	*Group 14 (IVA)*	*Group 15 (VA)*	*Group 16 (VIA)*	*Group 17 (VIIA)*	*Group 18 (VIIIA)*
Pt	**Au**	**Hg**	**Tl**	**Pb**	**Bi**	**Po**	**At**	**Rn**
Pt_4Ta (?), $Pt_{3\pm x}Ta$, $Pt_{2\pm x}Ta$, $Pt_{1\pm x}Ta$, σ-$PtTa_{2+x}$, $PtTa_{3+x}$ TSS: 19 at.% at 1970 °C SiT: ≤ 8 at.% at 2470 °C $Pt_{3\pm x}Ta$ – $Pt_{2\pm x}Ta$: 2050 °C[c] $Pt_{1\pm x}Ta$ – σ-$PtTa_{2+x}$: 1760 °C[c]	Au_2Ta, AuTa (?), α, β-Au_2Ta_3, $AuTa_3$ (?), σ-$AuTa_{3\pm x}$, $AuTa_{5\pm x}$ TSS: ~ 10-30 at.% at 1200-1300 °C (?) SiT: ~20 at.% at 1600 °C (?) α-Au_2Ta_3– Au: ~1000 °C (?)[c]	No binary compounds No interaction TSS, TSM, SiT: negligible	No binary compounds No interaction TSS, TSM, SiT: negligible	No binary compounds No interaction TSS, TSM, SiT: negligible	No binary compounds No interaction TSS, TSM, SiT: negligible	No binary compounds No interaction	N/A	–

[a] See the notes for Table A.22

Table A.24 Chemical properties of tantalum (interaction with lanthanides and actinides: binary compounds, solubilities and eutectic temp.)[a]

Ce	Pr	Nd	Pm	Sm	Eu	Gd	Tb	Dy	Ho	Er	Tm	Yb	Lu
No binary compounds TSM: < 0.04 at.% at ~800 °C δ-Ce-Ta: ?[c]	No binary compounds TSM: 0.17 at.% at 2000 °C β-Pr – Ta: ~930 °C[c] (?)	No binary compounds TSS, TSM, SiT: very low β-Nd – Ta: ~1020 °C[c] (?)	N/A	No binary compounds TSS, SiT: very low γ-Sm – Ta: ~1000 °C[c] (?)	No binary compounds TSM: 0.05 at.% at 1870 °C Eu – Ta: 822 °C[c] (?)	No binary compounds TSM: ≤ 0.4 at.% at 1770 °C β-Gd – Ta: ~1310 °C[c] (?)	No binary compounds TSS, SiT: very low TSM: ~0.6 at.% at 1745 °C β-Tb – Ta: 1355 °C[c] (?)	No binary compounds TSS, SiT: very low TSM: ~0.4 at.% at 1730 °C β-Dy – Ta: ~1410 °C[c] (?)	No binary compounds TSS, SiT: very low β-Ho – Ta: ~1470 °C[c] (?)	No binary compounds TSS, SiT: very low TSM: 1.24 at.% at 1775 °C β-Er – Ta: ~1500 °C[c] (?)	No binary compounds TSS, SiT: very low TSM: ~1.6 at.% at 1800 °C β-Tm – Ta: ~1540 °C[c] (?)	No binary compounds TSS, SiT: very low TSM: 0.028 at.% at 1750 °C γ-Yb – Ta: ~820 °C[c] (?)	No binary compounds TSS, SiT: very low TSM: ~1.7 at.% at 1730 °C β-Lu – Ta: ~1650 °C[c] (?)
Th	**Pa**	**U**	**Np**	**Pu**	**Am**	**Cm**	**Bk**	**Cf**	**Es**	**Fm**	**Md**	**No**	**Lr**
$ThTa_2$ TSS: 0.5 at.% at ~1600 °C SiT: 0.25 at.% at ~1600 °C β-Th – Ta: ~1600 °C[c]	N/A	No binary compounds TSS: negligible (α, β-U) and ~3 at.% (γ-U) at 1160 °C SiT: ~2.5 at.% at 1160 °C	N/A	No binary compounds TSS: 0.8-1.5 at.% (ε-Pu) at 660-680 °C (?) SiT: ? ε-Pu – Ta: ~640 °C[c] (?)	N/A	N/A	N/A	N/A	N/A	N/A	N/A	N/A	N/A

[a] See the notes for Table A.22

Table A.25 Chemical properties of molybdenum (interaction with 1–9 groups elements: binary compounds, interaction temp. range, solubilities and eutectic temp.)

Group 1 (IA)	*Group 2 (IIA)*	*Group 3 (IIIB)*	*Group 4 (IVB)*	*Group 5 (VB)*	*Group 6 (VIB)*	*Group 7 (VIIB)*	*Group 8 (VIII)*	*Group 9 (VIII)*
H MoH_x (?) No interaction at high and ultra-high temp. SiM[a]: ≤ 0.01 at.% at 1600 °C								
Li No binary compounds MSM[b]: 1.1×10^{-4} at.% at 925 °C (?) SiM: very low	**Be** $MoBe_{22}$, $MoBe_{12}$, $MoBe_2$, Mo_3Be DI[b]: > 800 °C MSS[b]: negligible SiM: 0.53 at.% at 1830 °C $MoBe_2$ – $MoBe_{12}$: 1690 °C[c] $MoBe_{22}$ – Be: 1289 °C[c] $MoBe_2$ – Mo: 1825 °C[c]							

(continued)

Table A.25 (continued)

Group 1 (IA)	*Group 2 (IIA)*	*Group 3 (IIIB)*	*Group 4 (IVB)*	*Group 5 (VB)*	*Group 6 (VIB)*	*Group 7 (VIIB)*	*Group 8 (VIII)*	*Group 9 (VIII)*
Na No binary compounds MSM: < 6×10^{-4} at.% at 700-1000 °C	**Mg** No binary compounds MSS, MSM (< 1000 °C), SiM: negligible							
K No binary compounds MSM: < 8×10^{-6} at.% at 1200 °C (?) SiM: negligible	**Ca** No binary compounds No interaction MSM: 3.5×10^{-2} at.% at 1480 °C	**Sc** No binary compounds SiM: 7×10^{-3} at.% at 2125 °C (?) β-Sc – Mo: 1380 °C[c]	**Ti** No binary compounds CSS[d]: β-Ti – Mo (> 800-850 °C) MSS: ≤ 0.4 at.% (α-Ti) at 650-700 °C	**V** No binary compounds CSS: V – Mo	**Cr** No binary compounds CSS: Cr – Mo (> 880 °C)	**Mn** σ-Mn_5Mo_{3-x}, μ-$Mn_5Mo_{4\pm x}$ MSS: 14-20 at.% (α-Mn) at 1050-1150 °C, 2.6 at.% (β-Mn) at 1100-1120 °C, ≤ 0.6 at.% (γ-Mn) at 1100-1120 °C and ~20 at.% (δ-Mn) at 1225-1425 °C SiM: ~36 at.% at 1500 °C	**Fe** λ-Fe_2Mo, ρ-Fe_3Mo_{2-x}, μ-Fe_7Mo_{6-x}, σ-$FeMo_{1\pm x}$ MSS: 21-25 at.% (α/δ-Fe) at 1450 °C and 1.6-1.7 at.% (γ-Fe) at 1140 °C SiM: 22-31 at.% at 1540-1610 °C	**Co** θ-Co_9Mo_{2+x}, κ-$Co_{3\pm x}Mo$, μ-$Co_7Mo_{6\pm x}$, σ-Co_2Mo_{3+x} MSS: ≤ 9 at.% (ε-Co) at 550-850 °C and 19.5 at.% (α-Co) at 1300 °C SiM: 7.0-11.5 at.% at 1620 °C μ-$Co_7Mo_{6\pm x}$ – α-Co: 1335 °C[c]

(continued)

Table A.25 (continued)

Group 1 (IA)	*Group 2 (IIA)*	*Group 3 (IIIB)*	*Group 4 (IVB)*	*Group 5 (VB)*	*Group 6 (VIB)*	*Group 7 (VIIB)*	*Group 8 (VIII)*	*Group 9 (VIII)*
Rb No binary compounds No interaction	**Sr** No binary compounds No interaction	**Y** No binary compounds MSS: 0.1 at.% (α-Y) at 1475 °C and ~0.02 at.% (β-Y) at 1500 °C SiM: 0.2 at.% at 2130 °C α-Y – Mo: 1430 °C[c]	**Zr** σ-$ZrMo_{2\pm x}$ MSS: < 0.01 at.% (α-Zr) at < 400 °C and ~ 31-41 at.% (β-Zr) at 1500-1600 °C SiM: ~ 10-20 at.% at 1880-2000 °C σ-$ZrMo_{2\pm x}$ – β-Zr: 1525 °C[c]	**Nb** No binary compounds CSS: Nb – Mo	**Mo**	**Tc** σ-$Tc_{3-x}Mo$, β-$TcMo_{1-x}$ MSS: ~ 27-30 at.% at 2090 °C SiM: ~ 50-52 at.% at 1925-2125 °C σ-$Tc_{3-x}Mo$ – Mo: 2025 °C[c] (?)	**Ru** σ-$Ru_3Mo_{5\pm x}$ MSS: 51 at.% at 1950 °C SiM: 30.5-32.0 at.% at 1950 °C Ru – Mo: 1950 °C[c]	**Rh** $Rh_{3\pm x}Mo$, ε-$Rh_{2\pm x}Mo$, ε′-$RhMo_{1\pm x}$ MSS: ~15 at.% at 2000 °C SiM: ~20 at.% at 1940 °C ε-$Rh_{2\pm x}Mo$ – Mo: 1940 °C[c]
Cs No binary compounds MSM, SiM: negligible (?)	**Ba** No binary compounds MSM: 6×10^{-3} at.% at 1680 °C	**La**[e] No binary compounds MSS: < 0.01 at.% SiM: ~0.2 at.% at 2545 °C γ-La – Mo: 918 °C[c] (?)	**Hf** α, β, β′-$HfMo_{2\pm x}$ MSS: 1 at.% (α-Hf) at 1165-1235 °C and 42-46 at.% (β-Hf) at 1890-1910 °C SiM: ~ 26-28	**Ta** No binary compounds CSS: Ta – Mo	**W** No binary compounds CSS: W – Mo	**Re** σ-$Mo_2Re_{3\pm x}$, χ-$MoRe_{3+x}$ MSS: ~ 15-21 at.% at 2645 °C SiM: 42-43 at.% at 2480 °C	**Os** β-$Mo_{3\pm x}Os$, σ-$Mo_{2\pm x}Os$ MSS: 52 at.% at 2420-2440 °C SiM: 19.5 at.% at 2370-2390 °C	**Ir** $Ir_{3-x}Mo$, ε-$IrMo_{1\pm x}$, $IrMo_{1\pm x}$, σ-Ir_3Mo_{7+x}, $IrMo_{3+x}$ MSS: 22-23 at.% at 2300 °C

(continued)

Table A.25 (continued)

Group 1 (IA)	*Group 2 (IIA)*	*Group 3 (IIIB)*	*Group 4 (IVB)*	*Group 5 (VB)*	*Group 6 (VIB)*	*Group 7 (VIIB)*	*Group 8 (VIII)*	*Group 9 (VIII)*
			at.% at 2130-2210 °C β-$HfMo_{2\pm x}$ – β-Hf: 1900 °C[c] (?)			σ-$Mo_2Re_{3\pm x}$ – Mo: 2480 °C[c]	σ-$Mo_{2\pm x}Os$ – Mo: 2380 °C[c]	SiM: 16.0-16.5 at.% at 2100-2120 °C ε-$IrMo_{1\pm x}$ – σ-Ir_3Mo_{7+x}: 2080 °C[c]
Fr No binary compounds No interaction	**Ra** No binary compounds No interaction	**Ac**[f] No binary compounds MSS: ~10^{-4} at.% at 925-1050 °C SiM: ? Ac – Mo: 1025 °C[c] (?)						

[a] SiM – solubility in Mo

[b] DI – temp. range of direct interaction with Mo, MSM – solubility of Mo in molten matter (metal or semi-metal), MSS – solubility of Mo in solid matter (metal or semi-metal)

[c] Eutectic temp.

[d] CSS – continuous solid solution

[e] For lanthanides see Table A.27

[f] For actinides see Table A.27

Table A.26 Chemical properties of molybdenum (interaction with 10–18 groups elements: binary compounds, interaction temp. range, solubilities and eutectic temp.)[a]

Group 10 (VIII)	*Group 11 (IB)*	*Group 12 (IIB)*	*Group 13 (IIIA)*	*Group 14 (IVA)*	*Group 15 (VA)*	*Group 16 (VIA)*	*Group 17 (VIIA)*	*Group 18 (VIIIA)*
								He –
			B $MoB_{\sim 12}$ (?), MoB_{4-x}, Mo_2B_{5-x}, MoB_{2-x}, α, β-$MoB_{1\pm x}$, Mo_3B_2, $Mo_{2\pm x}B$ DI: > 800 °C MSS: ~1 at.% at 1895-1945 °C SiM: ~ 1.0-1.75 at.% at 2000-2200 °C $MoB_{\sim 12}$ – β-B: 2030 °C[c] (?) Mo_2B_{5-x} – β-B: 1920 °C[c] $Mo_{2\pm x}B$ – Mo: 2190 °C[c]	**C** α, α′-$Mo_{2+x}C$, β-$Mo_{2\pm x}C$, η, α-MoC_{1-x}, γ-MoC DI: > 1200-1400 °C SiM: ~ 1.1-1.3 at.% at 2200-2205 °C Mo – β-$Mo_{2\pm x}C$: 2200 °C[c] β-$Mo_{2\pm x}C$ – η-MoC_{1-x}: 2510 °C[c] α-MoC_{1-x} – C: 2585 °C[c]	**N** MoN_3 (?), $Mo_{1-x}N$, δ-MoN, Mo_3N_2, γ-$Mo_{2\pm x}N$, β-$Mo_{2\pm x}N$, $Mo_{16}N_7$ DI: > 1000 °C SiM: ~2 at.% at 1800-1920 °C γ-$Mo_{2\pm x}N$ – Mo: 1860 °C[c]	**O** MoO_3, ξ, β-Mo_9O_{26}, Mo_5O_{14} (?), $Mo_{17}O_{47}$ (?), $Mo_{18}O_{52}$ (?), Mo_8O_{23}, η, γ-Mo_4O_{11}, Mo_2O_5 (?), Mo_nO_{3n-m}, α, β-$MoO_{2\pm x}$, Mo_3O (?) DI: > 300-400 °C SiM: low MoO_3 – β-Mo_9O_{26}: 770 °C[c] β-$MoO_{2\pm x}$ – Mo: 2150 °C[c]	**F** α′, α-MoF_6, Mo_4F_{23}, Mo_2F_{11}, α′, α-MoF_5, Mo_2F_9 (?), MoF_4, α, β-MoF_3 DI: > room temp. α′-MoF_5 – Mo_2F_{11}: 8 °C[c] Mo_4F_{23} – Mo_2F_{11}: 1 °C[c] Mo_4F_{23} – α-MoF_6: 8 °C[c]	**Ne** –

(continued)

Table A.26 (continued)

Group 10 (VIII)	*Group 11 (IB)*	*Group 12 (IIB)*	*Group 13 (IIIA)*	*Group 14 (IVA)*	*Group 15 (VA)*	*Group 16 (VIA)*	*Group 17 (VIIA)*	*Group 18 (VIIIA)*
			Al	**Si**	**P**	**S**	**Cl**	**Ar**
			$MoAl_{12}$, $MoAl_{6\pm x}$, $MoAl_5$, Mo_5Al_{22}, Mo_4Al_{17}, $MoAl_4$, $MoAl_{3-x}$, $MoAl_{2-x}$, Mo_2Al_3, $MoAl_{1\pm x}$, $Mo_{3\pm x}Al$ DI: > 650 °C MSS: 0.07 at.% at 660 °C SiM: ≤ 19.5 at.% at 2050-2250 °C $MoAl_{3-x}$ – $MoAl_{2-x}$: 1530 °C[c] $MoAl_{1\pm x}$ – $Mo_{3\pm x}Al$: 1720 °C[c] (?) $MoAl_{2-x}$ – $Mo_{3\pm x}Al$: 1760 °C[c] (?)	α, β-$MoSi_2$, $Mo_5Si_{3\pm x}$, Mo_3Si DI: > 1100 °C MSS: extremely low SiM: ~ 3.5-9.0 at.% (?) at 2025-2070 °C α-$MoSi_2$ – Si: 1400 °C[c] β- (or α-) $MoSi_2$ – $Mo_5Si_{3\pm x}$: 1900 °C[c] $Mo_5Si_{3\pm x}$ – Mo_3Si: 2050 °C[c]	MoP_2, MoP, Mo_4P_3, Mo_8P_5, $Mo_{2-x}P$, Mo_3P SiM: ~ 14-16 at.% (?) Mo_3P (or $Mo_{2-x}P$) – Mo_8P_5: 1650 °C[c] (?) MoP – P: ~1300 °C[c] (?)	MoS_3 (?), Mo_2S_5 (?), MoS_{2+x}, Mo_2S_{3-x}, Mo_3S_4 (?) DI: > ~600 °C SiM: 3.5 at.% at 1450-1650 °C Mo_2S_{3-x} – MoS_{2+x}: 1630 °C[c] Mo_2S_{3-x} – Mo: 1550 °C[c]	$MoCl_6$, α, β-$MoCl_5$, α, β-$MoCl_4$, β-$MoCl_{3+x}$, α-$MoCl_{3-x}$, $MoCl_2$ DI: > ~250 °C β-$MoCl_5$ – α- (or β-) $MoCl_4$: 180 °C[c] (?)	–

(continued)

Table A.26 (continued)

Group 10 (VIII)	*Group 11 (IB)*	*Group 12 (IIB)*	*Group 13 (IIIA)*	*Group 14 (IVA)*	*Group 15 (VA)*	*Group 16 (VIA)*	*Group 17 (VIIA)*	*Group 18 (VIIIA)*
Ni β-$Ni_{4+x}Mo$, γ-$Ni_{3+x}Mo$, $Ni_{17}Mo_5$ (?), μ-$NiMo_{1\pm x}$ MSS: 28.5 at.% at 1315-1320 °C SiM: 1.8 at.% at 1360-1365 °C μ-$NiMo_{1\pm x}$ – Ni: 1320 °C[c]	**Cu** No binary compounds MSS: 0.061 at.% at 1083 °C (?) MSM: 11.8-13.0 at.% at 2415-2615 °C SiM: 1.6-2.0 at.% at 2415-2615 °C (?) Cu – Mo: 1084 °C[c]	**Zn** $MoZn_{22\pm x}$, $MoZn_{7\pm x}$ MSS, SiM: extremely low MSM: 1.5×10^{-2} at.% at 550-750 °C	**Ga** Mo_8Ga_{41}, Mo_6Ga_{31}, $MoGa_2$, MoGa, $Mo_{3\pm x}Ga$ SiM: ~15 at.% at 1800-1840 °C	**Ge** α-$MoGe_2$, β-$MoGe_2$ (?), $Mo_{13}Ge_{23\pm x}$, Mo_3Ge_2 (?), Mo_5Ge_3, Mo_3Ge MSS: negligible SiM: ~ 5.0-5.5 at.% at 1800 °C α-$MoGe_2$– Ge: 935 °C[c]	**As** $MoAs_5$, $MoAs_2$, Mo_2As_3, Mo_3As_4 (?), Mo_4As_5 (?), $MoAs_{1+x}$, MoAs (?), Mo_5As_4 DI: > 500-600 °C	**Se** $MoSe_3$ (?), Mo_2Se_5 (?), $MoSe_{2-x}$, $Mo_3Se_{4\pm x}$ SiM: < 1-2 at.% at higher temp.	**Br** $MoBr_4$, $MoBr_3$, $MoBr_2$ DI: > 450-500 °C	**Kr** –
Pd $Pd_{2+x}Mo$, ε-$PdMo_{1-x}$ MSS: 32.0-47.5 at.% (?) at 1200-1700 °C SiM: 5-25 at.% (?) at 1400-1765 °C ε-$PdMo_{1-x}$ – Pd: ~1700 °C[c]	**Ag** No binary compounds MSS: 0.15 at.% at 959 °C MSM: 5.6 at.% at 1600 °C SiM: 0.006 at.% at 959 °C Ag – Mo: 959 °C[c]	**Cd** No binary compounds Cd – Mo: 321 °C[c] (?)	**In** No binary compounds MSM: 14.0 at.% at ~2100 °C	**Sn** $MoSn_2$, $MoSn_{1\pm x}$, Mo_3Sn MSM: 5×10^{-3} at.% at 1450 °C	**Sb** Mo_3Sb_7 SiM: ? Mo_3Sb_7 – Sb: 630 °C[c]	**Te** α, β-$MoTe_{2-x}$, α-$Mo_3Te_{4\pm x}$ (?), β-$Mo_3Te_{4\pm x}$, DI: > 600 °C MSS, MSM: negligible SiM: 0.5-2.0 at.% at 1230-1370 °C β-$MoTe_{2-x}$ – β-$Mo_3Te_{4\pm x}$: ?[c] β-$Mo_3Te_{4\pm x}$ – Mo: ?[c]	**I** MoI_4, MoI_3, MoI_2 DI: > 300 °C	**Xe** –

(continued)

Table A.26 (continued)

Group 10 (VIII)	*Group 11 (IB)*	*Group 12 (IIB)*	*Group 13 (IIIA)*	*Group 14 (IVA)*	*Group 15 (VA)*	*Group 16 (VIA)*	*Group 17 (VIIA)*	*Group 18 (VIIIA)*
Pt	**Au**	**Hg**	**Tl**	**Pb**	**Bi**	**Po**	**At**	**Rn**
η-$Pt_{2\pm x}Mo$, δ-$PtMo_{1\pm x}$, ε′, ε-$PtMo_{3-x}$, β-$PtMo_{6-x}$ MSS: ~ 54-58 at.% at 1570-1630 °C SiM: ~ 14-16 at.% at 2060-2100 °C ε-$PtMo_{3-x}$ – Mo: 2080 °C[c]	No binary compounds MSS: 1.25 at.% at 1054 °C SiM: 0.4 at.% at 1260 °C Au – Mo: 1054 °C[c]	No binary compounds at normal pressures MSM: ~10^{-5} at.% at room temp.	No binary compounds No interaction	No binary compounds MSM: ~ 10^{-2}-10^{-3} at.% at 1200-1750 °C Pb – Mo: 328 °C (?)[c]	No binary compounds MSM: ~ 0.005-0.030 at.% (?) at 1010-1030 °C	No binary compounds No interaction	$MoAt_2$ (?)	–

[a] See the notes for Table A.25

Table A.27 Chemical properties of molybdenum (interaction with lanthanides and actinides: binary compounds, solubilities and eutectic temp.)[a]

Ce	Pr	Nd	Pm	Sm	Eu	Gd	Tb	Dy	Ho	Er	Tm	Yb	Lu
No binary compounds MSM: < 0.3 at.% at 1300 °C SiM: 0.10-0.15 at.% δ-Ce – Mo: 795 °C[c] (?)	No binary compounds SiM: 0.02-0.30 at.% β-Pr – Mo: 931 °C[c] (?)	No binary compounds SiM: ~0.3 at.% at 2570 °C β-Nd – Mo: 1010 °C[c] (?)	No binary compounds SiM: ~0.3 at.% at 2560-2570 °C β-Pm – Mo: 1042 °C[c] (?)	No binary compounds γ-Sm – Mo: 1068 °C[c] (?)	No binary compounds Eu – Mo: 822 °C[c] (?)	No binary compounds SiM: 0.05 at.% at 2570 °C β-Gd – Mo: ~1300 °C[c] (?)	No binary compounds β-Tb – Mo: ~1330 °C[c] (?)	No binary compounds MSS, SiM: ? at 825-1115 °C β-Dy – Mo: 1375 °C[c] (?)	No binary compounds MSS: 0.6 at.% at 1430 °C SiM: ~0.6 at.% at 2515 °C β-Ho – Mo: ~1430 °C[c] (?)	No binary compounds MSS, SiM: < 0.1 at.% at 725-1115 °C β-Er – Mo: ~1480 °C[c] (?)	No binary compounds β-Tm – Mo: ~1480 °C[c] (?)	Yb_3Mo ?, Yb_2Mo ?, YbMo ?, $YbMo_2$?, $YbMo_3$?, $YbMo_5$? MSS, SiM: negligible γ-Yb – Mo: 824 °C[c] (?)	No binary compounds MSS: ~3.5 at.% at 1545 °C SiM: ~1.5 at.% at 1900-2100 °C β-Lu – Mo: 1545 °C[c] (?)

(continued)

Table A.27 (continued)

Th	Pa	U	Np	Pu	Am	Cm	Bk	Cf	Es	Fm	Md	No	Lr
No binary compounds MSS: 0.12 at.% (α-Th) at 1335 °C and 0.8-2.0 at.% (β-Th) at 1370-1390 °C SiM: ~1.5 at.% at 1370-1390 °C β-Th – Mo: 1380 °C[c]	$MoPa_2$ (?) MSS: ~20 at.% (β-Pa) at 1415-1515 °C SiM: ~ 3-4 at.% at 1700-2100 °C β-Pa – Mo: ~1470 °C[c]	$MoU_{2\pm x}$ MSS: 0.2-0.7 at.% (α-U) at 570 °C, 1.2-3.0 at.% (β-U) at 635-650 °C and 40-43 at.% (γ-U) at 1280-1285 °C SiM: 3.5 at.%. at 1500-1900 °C	$MoNp_2$ MSS: low SiM: ≤ 0.01 at.% at 505 °C γ-Np – Mo: ~500 °C[c]	No binary compounds MSS: ~0.2 at.% (ε-Pu) at ~610 °C SiM: ~2 at.% at 2100 °C ε-Pu – Mo: ~610 °C[c] (?)	No binary compounds MSS: ~0.4 at.% (γ-Am) at ~1175 °C SiM: ~1.25 at.% at 1900 °C γ-Am – Mo: ~1175 °C[c] (?)	No binary compounds MSS: ~0.4 at.% (β-Cm) at ~1345 °C SiM: ~2 at.% at 2000 °C β-Cm – Mo: ~1345 °C[c] (?)	No binary compounds No interaction MSS, SiM: negligible β-Bk – Mo: ~1050 °C[c] (?)	No binary compounds No interaction MSS: $\sim 10^{-2}$ at.% at 830 °C β-Cf – Mo: ~1075 °C[c] (?)	No binary compounds No interaction MSS, SiM: negligible β-Es – Mo: ~925 °C[c] (?)	No binary compounds No interaction MSS, SiM: negligible	No binary compounds No interaction MSS, SiM: negligible	No binary compounds No interaction MSS, SiM: negligible	No binary compounds MSS: ~5 at.% at ~1385 °C SiM: ~5 at.% at 2000-2200 °C Lr – Mo: ~1385 °C[c] (?)

[a] See the notes for Table A.25

Table A.28 Chemical properties of niobium (interaction with 1–9 groups elements: binary compounds, interaction temp. range, solubilities and eutectic temp.)

Group 1 (IA)	*Group 2 (IIA)*	*Group 3 (IIIB)*	*Group 4 (IVB)*	*Group 5 (VB)*	*Group 6 (VIB)*	*Group 7 (VIIB)*	*Group 8 (VIII)*	*Group 9 (VIII)*
H δ-NbH_{2-x}, β, γ, ξ, ν, μ, ο, λ, ε, θ, η-NbH_{1-x} DI[a]: > ~ 250-400 °C SiN[b]: 45-46 at.% at 140-250 °C								
Li No binary compounds NSM[b]: ~ 10^{-3}-10^{-5} at.% at 500-1000 °C	**Be** $NbBe_{12}$, Nb_2Be_{17}, $NbBe_5$, $NbBe_3$, $NbBe_2$, Nb_3Be_2 NSS[b]: ~ 0.015-0.100 at.% at 850-1150 °C SiN: ~16 at.% at 1590 °C $NbBe_{12}$ – β- (or α-) Be: ~1250 °C[c] Nb_2Be_{17} – $NbBe_3$: 1620 °C[c] $NbBe_2$ – Nb_3Be_2: 1520 °C[c] Nb_3Be_2 – Nb: 1600 °C[c]							

(continued)

Table A.28 (continued)

Group 1 (IA)	*Group 2 (IIA)*	*Group 3 (IIIB)*	*Group 4 (IVB)*	*Group 5 (VB)*	*Group 6 (VIB)*	*Group 7 (VIIB)*	*Group 8 (VIII)*	*Group 9 (VIII)*
Na No binary compounds NSM: ~(1÷2)×10^{-3} at.% at 800-1400 °C	**Mg** No binary compounds NSS: negligible SiN: 0.20 at.% at 2380 °C							
K No binary compounds NSM: < ~10^{-3} at.% at < 1200 °C	**Ca** No binary compounds No interaction (≤ 870 °C)	**Sc** No binary compounds NSS: ≤ 0.4 at.% (?) SiN: ≤ 0.1 at.% (?) β-Sc – Nb: ~1500 °C[c]	**Ti** No binary compounds CSS[d]: β-Ti – Nb NSS: ~2.5 at.% (α-Ti) at 600 °C	**V** No binary compounds CSS: V – Nb	**Cr** λ_1, λ_2-$NbCr_{2\pm x}$ NSS: ~6 at.% at 1600-1660 °C SiN: ~15 at.% at 1600-1715 °C λ_1-$NbCr_{2\pm x}$ – Cr: 1630 °C[c] λ_1-$NbCr_{2\pm x}$ – Nb: ~1660 °C[c]	**Mn** $Mn_{2\pm x}Nb$ NSS: ~ 2.1-2.4 at.% (β- and δ-Mn) at 1150-1200 °C $Mn_{2\pm x}Nb$ – δ-Mn: 1210 °C[c] $Mn_{2\pm x}Nb$ – Nb: ~1400 °C[c] (?)	**Fe** ε-$Fe_{2\pm x}Nb$, μ-Fe_7Nb_{6+x} NSS: 0.7 at.% (α-Fe) at 960 °C, 0.9-1.0 at.% (γ-Fe) at 1210 °C and 3.2 at.% (δ-Fe) at 1370-1375 °C SiN: ~7.5 at.% at 1400 °C ε-$Fe_{2\pm x}Nb$ – μ-Fe_7Nb_{6+x}: 1535 °C[c] ε-$Fe_{2\pm x}Nb$ – δ-Fe: 1370 °C[c] μ-Fe_7Nb_{6+x} – Nb: ~1400 °C[c]	**Co** χ-$Co_7Nb_{2\pm x}$, , λ_3-Co_3Nb, $\lambda_2(\alpha,\beta)$-$Co_{2\pm x}Nb$, λ_1-Co_5Nb_{3-x}, μ-$Co_7Nb_{6\pm x}$ NSS: 5.5 at.% (α-Co) at 1210-1245 °C SiN: ~ 4-5 at.% at 1370-1375 °C λ_1-Co_5Nb_{3-x} (λ_2-$Co_{2\pm x}Nb$, ?) – μ-$Co_7Nb_{6\pm x}$: 1375 °C[c] λ_3-Co_3Nb – α-Co: 1220 °C[c] μ-$Co_7Nb_{6\pm x}$ – Nb: 1370 °C[c]

(continued)

Table A.28 (continued)

Group 1 (IA)	*Group 2 (IIA)*	*Group 3 (IIIB)*	*Group 4 (IVB)*	*Group 5 (VB)*	*Group 6 (VIB)*	*Group 7 (VIIB)*	*Group 8 (VIII)*	*Group 9 (VIII)*
Rb No binary compounds No interaction	**Sr** N/A	**Y** No binary compounds NSS: < 0.1 at.% (α-Y) at 1470 °C α-Y – Nb: 1470 °C[c]	**Zr** No binary compounds CSS: β-Zr – Nb (> 1780 °C) NSS: 0.6-6.5 at.% (α-Zr) at 560-690 °C SiN: ~ 7.9-9.0 at.% at 560-690 °C	**Nb**	**Mo** No binary compounds CSS: Mo – Nb	**Tc** $Tc_{3\pm x}Nb$ (?)	**Ru** $Ru_{3\pm x}Nb$ NSS: 29 at.% at 1775 °C SiN: ~ 58-60 at.% at 1540-1775 °C Ru – Nb: 1775 °C[c]	**Rh** $Rh_{3\pm x}Nb$, η-$Rh_{2\pm x}Nb$, ζ-$Rh_{3\pm x}Nb_2$, ε, δ, γ-$RhNb_{1-x}$, β-$RhNb_{1\pm x}$, σ-$RhNb_{2\pm x}$, $RhNb_{3\pm x}$ NSS: 16.5 at.% at ~1990 °C SiN: 20.5 at.% at 1660 °C β-$RhNb_{1\pm x}$ – σ-$RhNb_{2\pm x}$: 1550 °C[c] $RhNb_{3\pm x}$ – Nb: ~1900 °C[c]

(continued)

Table A.28 (continued)

Group 1 (IA)	*Group 2 (IIA)*	*Group 3 (IIIB)*	*Group 4 (IVB)*	*Group 5 (VB)*	*Group 6 (VIB)*	*Group 7 (VIIB)*	*Group 8 (VIII)*	*Group 9 (VIII)*
Cs No binary compounds No interaction	**Ba** N/A	**La**[e] No binary compounds NSS: ~1 at.% (γ-La) at ~925 °C (?) SiN: 0.3 at.% at room temp.	**Hf** No binary compounds CSS: β-Hf – Nb NSS: ~ 2-4 at.% (α-Hf) at 1000 °C	**Ta** No binary compounds CSS: Ta – Nb	**W** No binary compounds CSS: W – Nb	**Re** σ-Nb_2Re_{3-x}, χ-$NbRe_{3\pm x}$ NSS: 3.5-4.5 at.% at 2520-2715 °C SiN: 45.5-46.5 at.% at 2400 °C σ-Nb_2Re_{3-x} – Nb: 1600 °C[c] χ-$NbRe_{3\pm x}$ – Re: 2715 °C[c]	**Os** β-$Nb_{3-x}Os$, σ-$Nb_3Os_{2\pm x}$, χ-$Nb_2Os_{3\pm x}$ NSS: 27 at.% at 2270 °C SiN: ~19 at.% at 2175 °C σ-$Nb_3Os_{2\pm x}$ – Nb: 2175 °C[c] σ-$Nb_3Os_{2\pm x}$ – χ-$Nb_2Os_{3\pm x}$: 2120 °C[c]	**Ir** $Ir_{3\pm x}Nb$, α_1, α_2-$IrNb_{1-x}$, σ-$IrNb_{2-x}$, $IrNb_{3\pm x}$ NSS: 16 at.% at 2400 °C SiN: 12 at.% at 2110 °C α_1-$IrNb_{1-x}$ – σ-$IrNb_{2-x}$: 1840 °C[c] $Ir_{3\pm x}Nb$ – Ir: 2400 °C[c] $IrNb_{3\pm x}$ – Nb: 2110 °C[c]
Fr N/A	**Ra** N/A	**Ac**[f] N/A						

[a] DI – temp. range of direct interaction with Nb

[b] SiN – solubility in Nb, NSM – solubility of Nb in molten matter (metal or semi-metal), NSS - solubility of Nb in solid matter (metal or semi-metal)

[c] Eutectic temp.

[d] CSS – continuous solid solution

[e] For lanthanides see Table A.30

[f] For actinides see Table A.30

Table A.29 Chemical properties of niobium (interaction with 10–18 groups elements: binary compounds, interaction temp. range, solubilities and eutectic temp.)[a]

Group 10 (VIII)	*Group 11 (IB)*	*Group 12 (IIB)*	*Group 13 (IIIA)*	*Group 14 (IVA)*	*Group 15 (VA)*	*Group 16 (VIA)*	*Group 17 (VIIA)*	*Group 18 (VIIIA)*
								He –
			B $NbB_{2\pm x}$, Nb_2B_3 (?), Nb_3B_4, Nb_5B_6, $NbB_{1\pm x}$, Nb_3B_2 DI: > 1500 °C SiN: 2.9 at.% at ~2170 °C $NbB_{1\pm x}$ – Nb_3B_4: 2270 °C[c] $NbB_{2\pm x}$ – β-B: 1920 °C[c] Nb_3B_2 – Nb: ~2000 °C[c] (?)	**C** α-Nb_2C, β-$Nb_{2+x}C$, γ-$Nb_{2\pm x}C$, ζ-Nb_4C_{3-x}, $Nb_6C_{5\pm x}$, NbC_{1-x} DI: > 1300-1400 °C SiN: ~ 5.5-7.2 at.% at 2230-2350 °C Nb – β-$Nb_{2+x}C$: 2350 °C[c] NbC_{1-x} – C: 3280 °C[c]	**N** Nb_4N_5 (?), Nb_5N_6 (?), ε-$NbN_{1\pm x}$, δ, δ′-NbN_{1-x}, γ-Nb_4N_{3+x}, β-$Nb_{2\pm x}N$, $Nb_{32}N_3$ (?) DI: > ~300 °C SiN: ~ 12-17 at.% at 2350 °C γ-$Nb_{2\pm x}N$ – Nb: ~2350 °C[c]	**O** α, α′, β, γ-Nb_2O_5, $Nb_{53}O_{132}$ (?), $Nb_{25}O_{62}$ (?), $Nb_{47}O_{116}$ (?), $Nb_{22}O_{54}$ (?), $Nb_{12}O_{29}$ (?), α-, β-, γ-$NbO_{2\pm x}$, Nb_2O_3 (?), Nb_4O_5 (?), NbO DI: > ~250 °C SiN: ~ 8-9 at.% at 1915 °C NbO_2– NbO: 1820 °C[c] NbO – Nb: 1915 °C[c]	**F** NbF_5, NbF_4, NbF_3, Nb_6F_{15} DI: > room temp.	**Ne** –

(continued)

Table A.29 (continued)

Group 10 (VIII)	*Group 11 (IB)*	*Group 12 (IIB)*	*Group 13 (IIIA)*	*Group 14 (IVA)*	*Group 15 (VA)*	*Group 16 (VIA)*	*Group 17 (VIIA)*	*Group 18 (VIIIA)*
			Al $NbAl_{3-x}$, Nb_5Al_3 (?), σ-$Nb_{2\pm x}Al$, $Nb_{3+x}Al$, Nb_5Al (?) DI: > 850 °C NSS: < 0.1-0.3 at.% at 661 °C, ? SiN: ~ 21.5-23.0 at.% at 1950-2060 °C σ-$Nb_{2\pm x}Al$ – $NbAl_{3-x}$: 1520 °C[c]	**Si** $NbSi_2$, α, β-Nb_5Si_{3+x}, Nb_3Si DI: > 1000 °C NSS: negligible SiN: ~ 1.2-3.5 at.% at 1870-1940 °C β-Nb_5Si_{3+x} – $NbSi_2$: 1900 °C[c] $NbSi_2$ – Si: 1400 °C[c] Nb_3Si – Nb: 1900 °C[c]	**P** Nb_2P_5 (?), NbP_2, Nb_4P_7 (?), NbP, Nb_8P_5 (?), Nb_5P_3 (?), Nb_7P_4 (?), Nb_2P (?), Nb_3P (?) DI: at higher temp.	**S** NbS_3, α, β-$NbS_{2\pm x}$, α, β-NbS_{2-x}, Nb_3S_4 (?), α, β-NbS_{1+x}, α, β-NbS, NbS_{1-x} NbS_3 – S: 110 °C[c]	**Cl** $NbCl_5$, $NbCl_4$, $NbCl_{3\pm x}$, Nb_3Cl_8 (?), Nb_6Cl_{14} DI: > 300 °C	**Ar** –
Ni Ni_8Nb, $Ni_{3\pm x}Nb$, μ-Ni_6Nb_{7-x} NSS: ~12.5 at.% at 1280 °C SiN: ~ 4.5-8.0 at.% at 1400-1570 °C (?)	**Cu** No binary compounds NSS: ~ 0.3-1.7 at.% (?) at ~1100 °C SiN: ~0.9 at.% at 1670-1680 °C	**Zn** $NbZn_{15}$, $NbZn_7$, $NbZn_{3\pm x}$, $NbZn_2$, Nb_2Zn_{3-x}, $NbZn_{1+x}$ $NbZn_{15}$ – Zn: ~418 °C[c] (?)	**Ga** $NbGa_3$, Nb_5Ga_{13} (?), Nb_4Ga_5, Nb_5Ga_4, Nb_5Ga_3, $Nb_{3+x}Ga$ NSS: negligible SiN: 19.0 at.% at 1850-1860 °C	**Ge** $NbGe_{2\pm x}$, α, β-$Nb_{10}Ge_7$ (?), Nb_3Ge_2 (?), α, β-$Nb_5Ge_{3\pm x}$, Nb_2Ge (?), α-Nb_3Ge (?), β-$Nb_{3+x}Ge$ SiN: ~ 10.5-12.5	**As** $NbAs_2$, NbAs, Nb_4As_3, $NbAs_3$, Nb_7As_4, Nb_3As	**Se** α, β, γ-Nb_2Se_9, α, β-$NbSe_4$ (?), $NbSe_3$, $NbSe_2$ (some poly-types), Nb_2Se_3, Nb_3Se_4, Nb_5Se_4, Nb_2Se α-Nb_2Se_9 – Se:	**Br** $NbBr_5$, $NbBr_4$, $NbBr_{3-x}$, Nb_3Br_8 (?), $NbBr_2$ DI: > 250-300 °C	**Kr** –

(continued)

Table A.29 (continued)

Group 10 (VIII)	*Group 11 (IB)*	*Group 12 (IIB)*	*Group 13 (IIIA)*	*Group 14 (IVA)*	*Group 15 (VA)*	*Group 16 (VIA)*	*Group 17 (VIIA)*	*Group 18 (VIIIA)*
$Ni_{3\pm x}Nb$ – μ-Ni_6Nb_{7-x}: 1180 °C[c] $Ni_{3\pm x}Nb$ – Ni: 1282 °C[c]	TSM: 0.009 at.% at 1200 °C Cu – Nb: ~1080 °C (?)[c]		Nb_5Ga_3 – $Nb_{3+x}Ga$: 1740 °C[c] $NbGa_3$ – Ga: ~28 °C[c] (?)	at.% at 1900 °C β-$Nb_5Ge_{3\pm x}$ – β-$Nb_{3+x}Ge$: 1900 °C[c] $NbGe_{2\pm x}$ – β-$Nb_5Ge_{3\pm x}$: 1580 °C[c] $NbGe_{2\pm x}$ – Ge: ~935 °C[c] (?)		~220 °C[c] (?)		
Pd	**Ag**	**Cd**	**In**	**Sn**	**Sb**	**Te**	**I**	**Xe**
α, β-$Pd_{3\pm x}Nb$, $Pd_{2\pm x}Nb$, α-$Pd_{1\pm x}Nb$, δ-Pd_2Nb_3 (?) NSS: ~31 at.% at ~1610 °C SiN: ~ 35-36 at.% at 1255-1520 °C α-$Pd_{1\pm x}Nb$ – Nb: 1520 °C[c]	No binary compounds NSS, NSM (1400-1700 °C), SiN: negligible	$NbCd_3$ (?)	$InNb_{3+x}$, ε-$InNb_{9\pm x}$ NSS, SiN: negligible	$NbSn_{2-x}$, Nb_6Sn_{5-x}, $Nb_{3\pm x}Sn$ NSM: ~0.15 at.% at 1000 °C SiN: ~ 9-10 at.% at 2115-2145 °C $NbSn_{2-x}$ – Sn: ~230 °C[c] (?)	$NbSb_2$, Nb_5Sb_4, Nb_3Sb_2, $Nb_{3\pm x}Sb$ NSS, NSM: negligible SiN: ~20 at.% (?) at 1730-1770 °C $NbSb_2$ – Sb: ~610 °C[c] (?)	α-$NbTe_4$ (?), β-$NbTe_{4\pm x}$, α-$NbTe_3$, β-$NbTe_{3-x}$, α-Nb_3Te_8, β-Nb_3Te_{8+x}, α-Nb_3Te_7, β-Nb_3Te_{7+x}, α, β-$NbTe_2$ (?), γ-$NbTe_{2+x}$, Nb_3Te_4, α, β-NbTe (?), $NbTe_{1-x}$, Nb_5Te_4	α-NbI_5 (?), β-NbI_5, α, β, γ-NbI_4, NbI_{3-x}, Nb_3I_8 (?), NbI_2 (?), Nb_6I_{11} DI: > 250 °C	–

(continued)

Table A.29 (continued)

Group 10 (VIII)	*Group 11 (IB)*	*Group 12 (IIB)*	*Group 13 (IIIA)*	*Group 14 (IVA)*	*Group 15 (VA)*	*Group 16 (VIA)*	*Group 17 (VIIA)*	*Group 18 (VIIIA)*
Pt	**Au**	**Hg**	**Tl**	**Pb**	**Bi**	**Po**	**At**	**Rn**
α-$Pt_{3\pm x}Nb$, β-$Pt_{3\pm x}Nb$ (?), $Pt_{2\pm x}Nb$, α′-$PtNb_{1-x}$, $Pt_{1+x}Nb_{1-x}$, σ-$PtNb_{2\pm x}$, $PtNb_{3\pm x}$ NSS: ~20 at.% at ~2000 °C SiN: ~12 at.% at 2040 °C $Pt_{1+x}Nb_{1-x}$ – σ-$PtNb_{2\pm x}$: 1700 °C[c]	Au_2Nb, Au_2Nb_3, $AuNb_{3\pm x}$ NSS: ~57 at.% at 1570 °C SiN: ~36 at.% at 1570 °C	No binary compounds No interaction NSM: ~6×10^{-6} at.% at 500-750 °C	$TlNb_3$ (?) NSS, NSM, SiN: negligible	No binary compounds at normal pressures No interaction NSS, NSM, SiN: negligible	No binary compounds at normal pressures NSM: 0.16 at.% at 1200 °C Bi – Nb: ~271 °C[c] (?)	N/A	N/A	–

[a] See the notes for Table A.28

Table A.30 Chemical properties of niobium (interaction with lanthanides and actinides: binary compounds, solubilities and eutectic temp.)[a]

Ce	Pr	Nd	Pm	Sm	Eu	Gd	Tb	Dy	Ho	Er	Tm	Yb	Lu
No binary compounds NSS: ~2 at.% at ~810 °C SiN: ~1 at.% at 2350-2390 °C	No binary compounds NSM: negligible	No binary compounds NSM: negligible at ~1010 °C	N/A	No binary compounds NSS: < 0.01 at.% (α-Sm) and ~2 at.% (γ-Sm) at ~1130 °C SiN: < 0.09 at.% at ~2460 °C	No binary compounds NSS, NSM: negligible	No binary compounds NSM: negligible	No binary compounds NSM: negligible	No binary compounds NSM: negligible	No binary compounds NSM: negligible	No binary compounds NSM: negligible β-Er – Nb: ~1475 °C[c] (?)	No binary compounds NSM: negligible	No binary compounds NSS, NSM, SiN: negligible	No binary compounds NSS: ~ 0.3-4.0 at.% (β-Lu) β-Lu – Nb: 1620 °C[c] (?)

Th	Pa	U	Np	Pu	Am	Cm	Bk	Cf	Es	Fm	Md	No	Lr
No binary compounds NSS: < 0.25 at.% (α-Th) and < 2 at.% (β-Th) SiN: negligible β-Th – Nb: 1435 °C[c]	N/A	No binary compounds CSS: γ-U – Nb (> 955-990 °C NSS: ~ 0.5-1.9 (?) at.% (α-U) at 640-665 °C and 3.8 at.% (β-U) at 650 °C	N/A	No binary compounds SiN: < 0.4 at.% ε-Pu – Nb: ~630 °C[c] (?)	N/A	N/A	N/A	N/A	N/A	N/A	N/A	N/A	N/A

[a] See the notes for Table A.28

Table A.31 Chemical properties of iridium (interaction with 1–9 groups elements: binary compounds, interaction temp. range, solubilities and eutectic temp.)

Group 1 (IA)	*Group 2 (IIA)*	*Group 3 (IIIB)*	*Group 4 (IVB)*	*Group 5 (VB)*	*Group 6 (VIB)*	*Group 7 (VIIB)*	*Group 8 (VIII)*	*Group 9 (VIII)*
H No binary compounds SiI[a]: 2.2×10^{-5} at.% at 1580 °C (0.1 MPa H_2)								
Li $IrLi_{1\pm x}$, $Ir_{3\pm x}Li$ $IrLi_{1\pm x}$ – γ-Li: ~180 °C[c] (?) $IrLi_{1\pm x}$ – Ir: 1800 °C[c] (?)	**Be** Ir_2Be_{17}, Ir_5Be_{22}, $IrBe_2$, IrBe							
Na $IrNa_3$ (?), $IrNa_2$ (?), IrNa (?), Ir_2Na (?), Ir_3Na (?)	**Mg** ζ-$IrMg_{6\div8}$, $IrMg_4$, δ-$IrMg_3$, Ir_3Mg_7 (?), IrMg (?), $Ir_{3-x}Mg_{2+x}$, Ir_2Mg ISS[b]: < 0.18 at.% ζ-$IrMg_{6\div8}$ – Mg: ~615 °C[c]							

(continued)

Table A.31 (continued)

Group 1 (IA)	*Group 2 (IIA)*	*Group 3 (IIIB)*	*Group 4 (IVB)*	*Group 5 (VB)*	*Group 6 (VIB)*	*Group 7 (VIIB)*	*Group 8 (VIII)*	*Group 9 (VIII)*
K	**Ca**	**Sc**	**Ti**	**V**	**Cr**	**Mn**	**Fe**	**Co**
No binary compounds (?)	Ca_5Ir (?), $CaIr_2$	$Sc_{44}Ir_{7\pm x}$, $Sc_{57}Ir_{13\pm x}$, $Sc_{11}Ir_4$, $Sc_{2+x}Ir$, $ScIr_{1\pm x}$, $ScIr_{2\pm x}$, $ScIr_{3+x}$ ISS: ~1 at.% (α-Sc) at 1180 °C and ~4 at.% (β-Sc) at 1240 °C SiI: ~10 at.% at 1950 °C $Sc_{44}Ir_7$ – β-Sc: 1240 °C[c] $Sc_{57}Ir_{13\pm x}$ – $Sc_{11}Ir_4$: 1290 °C[c] $Sc_{2+x}Ir$ – $Sc_{11}Ir_4$: 1370 °C[c] $ScIr_{1\pm x}$ – $ScIr_{2\pm x}$: 2020 °C[c] $ScIr_{3+x}$ –Ir: 1950 °C[c]	$Ti_{3-x}Ir$, α, β-$TiIr_{1\pm x}$, $TiIr_{3\pm x}$ ISS: ~1 at.% (α-Ti) at 720 °C and ~15 at.% (β-Ti) at 1470 °C SiI: ~11 at.% at 2115-2125 °C β-$TiIr_{1\pm x}$ – $TiIr_{3\pm x}$: 2000 °C[c] $Ti_{3-x}Ir$ – β-Ti: ~1470 °C[c]	$V_{3\pm x}Ir$, VIr_{1+x}, $V_{1-x}Ir_{1+x}$, $VIr_{3\pm x}$ ISS: ~ 20.5-22.5 at.% at 1850-1950 °C SiI: !9 at.% at 2100 °C $V_{3\pm x}Ir$ – VIr_{1+x}: 1850 °C[c] $V_{3\pm x}Ir$ – V: 1900 °C[c]	β-$Cr_{3\pm x}Ir$, ε-$CrIr_{1\pm x}$ ISS: 12-13 at.% at 1680 °C SiI: 27 at.% at 2150-2250 °C β-$Cr_{3\pm x}Ir$ – Cr: 1680 °C[c]	$Mn_{3\pm x}Ir$, α, β-$MnIr_{1\pm x}$ ISS: ~4.5 at.% (α-Mn), ~2.5 at.% (β-Mn), ~35 at.% (γ-Mn) at 500-1000 °C and ~1.5 at.% (δ-Mn) SiI: ~48 at.% at 1350 °C	ε-$Fe_3Ir_{2\pm x}$ CSS[d]: (γ-Fe) – Ir ISS: ~8 at.% (α-Fe) at ~440 °C and 2.5-2.8 at.% (δ-Fe) at ~1545 °C	$Co_{3\pm x}Ir$, $CoIr_{3\pm x}$ (ordered phases) CSS: (α-Co) – Ir ISS: ~70 at.% (ε-Co) at 0 °C

(continued)

Table A.31 (continued)

Group 1 (IA)	*Group 2 (IIA)*	*Group 3 (IIIB)*	*Group 4 (IVB)*	*Group 5 (VB)*	*Group 6 (VIB)*	*Group 7 (VIIB)*	*Group 8 (VIII)*	*Group 9 (VIII)*
Rb	**Sr**	**Y**	**Zr**	**Nb**	**Mo**	**Tc**	**Ru**	**Rh**
$IrRb_3$ (?), $IrRb_2$ (?), IrRb (?), Ir_2Rb (?), Ir_3Rb (?)	$SrIr_2$, $SrIr_3$, Sr_2Ir_7 (?), $SrIr_5$ (?)	Y_3Ir, Y_5Ir_2, Y_5Ir_2, $Y_{64}Ir_{37}$ (?), α′, α-$Y_5Ir_{3\pm x}$ (?), β-$Y_5Ir_{3\pm x}$, Y_3Ir_2, YIr, $YIr_{2\pm x}$, YIr_3 YIr – $YIr_{2\pm x}$: 1900 °C[c] Y_3Ir – β-Y: 1325 °C[c] YIr_3 – Ir: 1850 °C[c]	Zr_3Ir, Zr_2Ir, Zr_5Ir_3, α-$ZrIr_{1-x}$, β-$ZrIr_{1\pm x}$, $ZrIr_2$, $ZrIr_{3\pm x}$ ISS: ≤ 1 at.% (α-Zr) and 5 at.% (β-Zr) at 1240 °C SiI: ~7 at.% at 2120 °C $ZrIr_2$ – β-$ZrIr_{1\pm x}$: 1870 °C[c] Zr_3Ir – β-Zr: 1240 °C[c] $ZrIr_{3\pm x}$ – Ir: 2120 °C[c]	$Ir_{3\pm x}Nb$, α_1, α_2-$IrNb_{1-x}$, σ-$IrNb_{2-x}$, $IrNb_{3\pm x}$ ISS: 12 at.% at 2110 °C SiI: 16 at.% at 2400 °C α_1-$IrNb_{1-x}$ – σ-$IrNb_{2-x}$: 1840 °C[c] $Ir_{3\pm x}Nb$ – Ir: 2400 °C[c] $IrNb_{3\pm x}$ – Nb: 2110 °C[c]	$Ir_{3-x}Mo$, ε-$IrMo_{1\pm x}$, $IrMo_{1\pm x}$, σ-Ir_3Mo_{7+x}, $IrMo_{3+x}$ ISS: 16.0-16.5 at.% at 2100-2120 °C SiI: 22-23 at.% at 2300 °C ε-$IrMo_{1\pm x}$ – σ-Ir_3Mo_{7+x}: 2080 °C[c]	No binary compounds ISS: ~70 at.% at 1050-2300 °C SiI: ≤ 25 at.% at ~ 2200-2300 °C	No binary compounds ISS: 49 at.% at ~ 2350-2395 °C SiI: 45 at.% at ~ 2350-2395 °C	No binary compounds CSS: Rh – Ir (> ~850 °C)

(continued)

Table A.31 (continued)

Group 1 (IA)	*Group 2 (IIA)*	*Group 3 (IIIB)*	*Group 4 (IVB)*	*Group 5 (VB)*	*Group 6 (VIB)*	*Group 7 (VIIB)*	*Group 8 (VIII)*	*Group 9 (VIII)*
Cs No binary compounds ISM[b], ISS, SiI: very low	**Ba** N/A	**La**[e] La_4Ir, La_3Ir, La_7Ir_3, La_5Ir_3, LaIr, $LaIr_2$, $LaIr_3$, La_2Ir_7, $LaIr_5$, La_2Ir_{17} La_7Ir_3 – La_5Ir_3: (?)[c] LaIr – La_5Ir_3: (?)[c] La_4Ir – β-La: 730 °C[c]	**Hf** $Hf_{2+x}Ir$, Hf_5Ir_3, $HfIr_{1+x}$, $HfIr_{3+x}$ ISS: ~1 at.% (α-Hf) at 1375-1380 °C and ~10 at.% (β-Hf) at 1425 °C SiI: ~9 at.% at 2250 °C $HfIr_{1+x}$ – $HfIr_{3+x}$: ~2100 °C[c] $Hf_{2+x}Ir$ – β-Hf: ~1450 °C[c] $HfIr_{3+x}$ – Ir: 2270 °C	**Ta** $\beta\text{-}Ir_{3\pm x}Ta$, $\gamma\text{-}Ir_3Ta_{2+x}$, $\delta\text{-}IrTa_{1-x}$, $\sigma\text{-}IrTa_{3\pm x}$ ISS: 7.2-7.3 at.% at 2475-2580 °C SiI: 15.5 at.% at 2380-2385 °C $\delta\text{-}IrTa_{1-x}$ – $\sigma\text{-}IrTa_{3\pm x}$: 1950 °C[c] $\beta\text{-}Ir_{3\pm x}Ta$ – Ir: 2385 °C[c] (?)	**W** $\delta\text{-}Ir_{3-x}W$, $\beta\text{-}Ir_3W_{2\pm x}$, $\varepsilon\text{-}IrW_{1\pm x}$, $\sigma\text{-}IrW_{3\pm x}$ ISS: ~10 at.% at 2545 °C SiI: ~19 at.% at ~2310 °C Ir – $\beta\text{-}Ir_3W_{2\pm x}$: 2310 °C[c] $\beta\text{-}Ir_3W_{2\pm x}$ – $\sigma\text{-}IrW_{3\pm x}$: 2470 °C[c]	**Re** No binary compounds ISS: ~44 at.% at 2800 °C SiI: ~ 36-40 at.% at 2800 °C	**Os** No binary compounds ISS: 38 at.% at 2625-2695 °C SiI: 44.5 at.% at 2625-2695 °C	**Ir**
Fr N/A	**Ra** N/A	**Ac**[f] N/A						

[a] SiI – solubility in Ir

[b] DI – temp. range of direct interaction with Ir, ISM – solubility of Ir in molten matter (metal or semi-metal), ISS - solubility of Ir in solid matter (metal or semi-metal)

[c] Eutectic temp.

[d] CSS – continuous solid solution

[e] For lanthanides see Table A.33

[f] For actinides see Table A.33

Table A.32 Chemical properties of iridium (interaction with 10–18 groups elements: binary compounds, interaction temp. range, solubilities and eutectic temp.)[a]

Group 10 (VIII)	*Group 11 (IB)*	*Group 12 (IIB)*	*Group 13 (IIIA)*	*Group 14 (IVA)*	*Group 15 (VA)*	*Group 16 (VIA)*	*Group 17 (VIIA)*	*Group 18 (VIIIA)*
								He –
			B IrB_{50} (?), IrB_2 (?), $Ir_2B_{3\pm x}$, Ir_3B_{4+x}, Ir_4B_5 (?), α, β-IrB_{1+x}, α, β-IrB_{1-x}, $Ir_3B_{2\pm x}$ SiI: ≤ 1 at.% β-IrB_{1+x} – Ir_3B_{4+x}: ~950 °C (?)[c] β-IrB_{1-x} – $Ir_2B_{3\pm x}$: 1250 °C[c] β-IrB_{1-x} – $Ir_3B_{2\pm x}$: 1240 °C[c] Ir_3B_{4+x} – β-B: ~1000 °C[c] (?) $Ir_2B_{3\pm x}$ – β-B: ~1240 °C[c] (?) β-IrB_{1+x} – Ir: < ~1000 °C[c] (?) $Ir_3B_{2\pm x}$ – Ir: < ~1250 °C[c] (?)	**C** Metastable carbides (?) SiI: 3.1 at.% (solid) at 2280-2310 °C and ~31.5 at.% (liquid) at 4400 °C Ir – C: 2300 °C[c]	**N** IrN_3, IrN_2 (superhard hypothetical structures, ?) No interaction at least at 900-2150 °C	**O** IrO_3 (gaseous), IrO_{3-x} (?), IrO_2, Ir_2O_3 DI: > ~300 °C	**F** α-IrF_6 (?), β-IrF_6, IrF_5, IrF_4, IrF_3 DI: > 200 °C	**Ne** –

(continued)

Table A.32 (continued)

Group 10 (VIII)	*Group 11 (IB)*	*Group 12 (IIB)*	*Group 13 (IIIA)*	*Group 14 (IVA)*	*Group 15 (VA)*	*Group 16 (VIA)*	*Group 17 (VIIA)*	*Group 18 (VIIIA)*
			Al Ir_2Al_9, Ir_4Al_{13}, $IrAl_3$, Ir_2Al_{5-x}, $IrAl_{1\pm x}$ SiI: 18 at.% at ~2020 °C Ir_2Al_9 – Al: ~650 °C[c] $IrAl_{1\pm x}$ – Ir: ~2020 °C[c]	**Si** α-$IrSi_3$ (?), β, γ- $IrSi_3$, $IrSi_2$, Ir_3Si_5, Ir_2Si_3, Ir_3Si_4, Ir_4Si_5, IrSi, Ir_3Si_2, Ir_2Si, Ir_3Si DI: > 1000 °C SiI: ~2 at.% at 1545 °C Ir_3Si_2 – Ir_2Si: ~1415 °C[c] Ir_3Si_2 – IrSi: 1425 °C[c] γ-$IrSi_3$ – Si: ~1220 °C[c] Ir_3Si – Ir: 1470 °C[c] (?)	**P** IrP_3, IrP_2, Ir_2P DI: > 1000 °C (?) Ir_2P – Ir: ~1260 °C[c]	**S** IrS_3, Ir_3S_8 (?), IrS_2, IrS_{2-x}, Ir_2S_3 (?), IrS	**Cl** $IrCl_4$, α, β-$IrCl_3$, $IrCl_2$, IrCl DI: > 500 °C (?)	**Ar** –
Ni $Ni_{3\pm x}Ir$, $NiIr_{1\pm x}$, $NiIr_{3\pm x}$ (ordered phases) CSS: Ni – Ir	**Cu** No binary compounds ISS: ~8 at.% at ~1140 °C ISM: ~4 at.% at ~1140 °C SiI: 6.3 at.% at 1850 °C	**Zn** $Zn_{11}Ir_2$ (?), ZnIr (?)	**Ga** $IrGa_6$, Ir_2Ga_9, α, β-$IrGa_3$, $IrGa_2$, Ir_3Ga_5, IrGa	**Ge** $IrGe_4$, Ir_3Ge_7, Ir_3Ge_4, Ir_4Ge_5, IrGe	**As** $IrAs_3$, $IrAs_{3-x}$ (?), $IrAs_2$, IrAs (?)	**Se** α, β-$IrSe_{3-x}$ (?), $IrSe_{2-x}$, Ir_2Se_3	**Br** $IrBr_4$, $IrBr_3$, $IrBr_2$	**Kr** –

(continued)

Table A.32 (continued)

Group 10 (VIII)	*Group 11 (IB)*	*Group 12 (IIB)*	*Group 13 (IIIA)*	*Group 14 (IVA)*	*Group 15 (VA)*	*Group 16 (VIA)*	*Group 17 (VIIA)*	*Group 18 (VIIIA)*
Pd No binary compounds CSS: Pd – Ir (> ~ 1470-1480 °C (?) ISS: 27 at.% at ~ 1735-1785 °C (?) SiI: ~25 at.% at ~ 1735-1785 °C (?)	**Ag** No binary compounds ISS: ≤ 0.3 at.% ISM: ~0.1 at.% at ~962 °C SiI: ≤ 1.8 at.% Ag – Ir: ~961 °C (?)[c]	**Cd** N/A	**In** α, β-$IrIn_{3+x}$, $IrIn_{2\pm x}$, Ir_2In_3 (?), $IrIn_{1+x}$ (?), Ir_3In (?) SiI: 3.8 at.% at ~1190 °C	**Sn** α, β-$IrSn_4$, $IrSn_3$, Ir_3Sn_7 (?), $IrSn_2$, Ir_5Sn_7, IrSn (?), ISM: very low (?)	**Sb** $IrSb_3$, $IrSb_2$, IrSb $IrSb_3$ – Sb: ~620 °C[c]	**Te** Ir_3Te_8, $IrTe_{2+x}$ (?), $IrTe_2$, IrTe	**I** IrI_4, IrI_3, $IrI_{2\pm x}$, IrI	**Xe** –
Pt No binary compounds CSS: Pt – Ir (> ~ 960-1300 °C, ?)	**Au** No binary compounds ISS: ~ 0.1-1.5 at.% (?) SiI: ≤ 2 at.%	**Hg** No binary compounds No interaction ISM: extremely low	**Tl** $IrTl_3$ (?), $IrTl_2$ (?), IrTl (?), Ir_2Tl (?), Ir_3Tl (?)	**Pb** $IrPb_3$ (?), $IrPb_2$ (?), IrPb (?), Ir_2Pb (?), Ir_3Pb (?)	**Bi** $IrBi_3$, $IrBi_2$, IrBi, Ir_2Bi ISS: ~0.25 at.% IrBi – Ir_2Bi: 1410 °C[c] $IrBi_3$ – Bi: ~265 °C[c]	**Po** N/A	**At** N/A	**Rn** –

[a] See the notes for Table A.31

Table A.33 Chemical properties of iridium (interaction with lanthanides and actinides: binary compounds, solubilities and eutectic temp.)[a]

Ce	Pr	Nd	Pm	Sm	Eu	Gd	Tb	Dy	Ho	Er	Tm	Yb	Lu
Ce_4Ir, Ce_3Ir, Ce_7Ir_3, Ce_3Ir_2 (?), Ce_5Ir_3, Ce_5Ir_4, $CeIr_{2\pm x}$, $CeIr_3$, Ce_2Ir_7, $CeIr_5$	Pr_3Ir (?), Pr_5Ir_2, Pr_7Ir_3 (?), Pr_5Ir_3, $PrIr_{2\pm x}$, $PrIr_3$, Pr_2Ir_7, $PrIr_5$	Nd_4Ir, Nd_3Ir, Nd_5Ir_2, Nd_7Ir_3, Nd_5Ir_3, $NdIr_{2\pm x}$, $NdIr_3$, Nd_2Ir_7, $NdIr_5$	Pm_5Ir (?), Pm_3Ir, Pm_5Ir_2, Pm_2Ir (?), Pm_5Ir_3, PmIr (?), $PmIr_{2\pm x}$, $PmIr_3$, $PmIr_5$ (?)	Sm_3Ir, Sm_5Ir_2, Sm_5Ir_3, $SmIr_{2\pm x}$, $SmIr_3$	Eu_4Ir (?), $EuIr_2$	Gd_3Ir, Gd_5Ir_2, α-$Gd_5Ir_{3\pm x}$ (?), β-$Gd_5Ir_{3\pm x}$, Gd_3Ir_2, $GdIr_{2\pm x}$, α-$GdIr_3$ (?), β-$GdIr_3$	Tb_3Ir, Tb_5Ir_2, $Tb_{64}Ir_{37}$ (?), α-Tb_5Ir_3 (?), β-Tb_5Ir_3, Tb_3Ir_2, $TbIr_{2\pm x}$	Dy_3Ir, Dy_5Ir_2, α-Dy_5Ir_3 (?), β-Dy_5Ir_3, Dy_3Ir_2, $DyIr_{2\pm x}$, $DyIr_3$ (?)	Ho_3Ir, Ho_5Ir_2, α-Ho_5Ir_3 (?), β-Ho_5Ir_3, Ho_3Ir_2, HoIr, $HoIr_{2\pm x}$	Er_3Ir, Er_5Ir_2, α-$Er_5Ir_{3\pm x}$ (?), β-$Er_5Ir_{3\pm x}$, Er_3Ir_2, ErIr, $ErIr_{2\pm x}$	Tm_3Ir, Tm_5Ir_2, α-Tm_5Ir_3 (?), β-Tm_5Ir_3, Tm_3Ir_2, TmIr, $TmIr_{2\pm x}$	α-Yb_5Ir_3, β-Yb_5Ir_3, Yb_3Ir_2, YbIr, $YbIr_{2\pm x}$	Lu_3Ir, Lu_5Ir_2, α-$Lu_5Ir_{3\pm x}$ (?), β-$Lu_5Ir_{3\pm x}$, Lu_3Ir_2, LuIr, $LuIr_{2\pm x}$
Ce_2Ir_7 – $CeIr_5$: ~1910 °C[c]	ISS: 0.35 at.% (β-Pr)	ISS, SiI: low	Pm_3Ir – β-Pm: (?)[c]	Sm_3Ir – γ-Sm: (?)[c]		Gd_3Ir – β-Gd: (?)[c]	Tb_3Ir – β-Tb: (?)[c]	Dy_3Ir – β-Dy: (?)[c]	Ho_3Ir – β-Ho: (?)[c]	Er_3Ir – β-Er (?)[c]	Tm_3Ir – β-Tm: (?)[c]	α-Yb_5Ir_3 – γ-Yb: ~819 °C[c]	Lu_3Ir – β-Lu: (?)[c]
Ce_4Ir – γ-Ce: 650 °C[c]	Pr_5Ir_2 – α-Pr: ~725 °C[c]	Nd_4Ir – β-Nd: (?)[c]	$PmIr_3$ – Ir: (?)[c]	$SmIr_3$ – Ir: (?)[c]			$TbIr_{2\pm x}$ – Ir: (?)[c]	$DyIr_{2\pm x}$ – Ir: (?)[c]	$HoIr_{2\pm x}$ – HoIr: (?)[c]	$ErIr_{2\pm x}$ – ErIr: (?)[c]	$TmIr_{2\pm x}$ – TmIr: (?)[c]		$LuIr_{2\pm x}$ – LuIr: (?)[c]
$CeIr_5$ – Ir: 1880 °C[c]	Pr_2Ir_7 – $PrIr_5$: (?)[c]	$NdIr_5$ – Ir: (?)[c]							$HoIr_{2\pm x}$ – Ir: (?)[c]	$ErIr_{2\pm x}$ – Ir (?)[c]	$TmIr_{2\pm x}$ – Ir: (?)[c]		$LuIr_{2\pm x}$ – Ir: (?)[c]
	$PrIr_5$ – Ir: (?)[c]												

(continued)

Table A.33 (continued)

Th	Pa	U	Np	Pu	Am	Cm	Bk	Cf	Es	Fm	Md	No	Lr
Th_7Ir_3, $ThIr_{1-x}$, ThIr, $ThIr_{2\pm x}$, $ThIr_3$, $ThIr_5$ ISS: negligible Th_7Ir_3 – $ThIr_{1-x}$: ~1460 °C[c] $ThIr_{2\pm x}$ – ThIr: ~1650 °C[c] $ThIr_5$ – $ThIr_3$: 2150 °C[c] Th_7Ir_3 – α-Th: ~1340 °C[c] $ThIr_5$ – Ir: 2080 °C[c]	Pa_3Ir (?), PaIr (?), $PaIr_2$ (?), $PaIr_3$ (?), $PaIr_5$ (?)	U_3Ir, U_2Ir, α, β-U_3Ir_2, UIr, UIr_2, UIr_3 ISS: <0.3 at.% (α-U), ~ 0.4-2.0 at.% (β-U) and ~ 5.5-6.5 at.% (γ-U) SiI: ~ 3.0-6.5 at.% at 1950 °C UIr – UIr_2: 1450 °C[c] U_3Ir – γ-U: ~915 °C[c] UIr_3 – Ir: 1950 °C[c]	$NpIr_2$ (?)	Pu_3Ir (?), Pu_5Ir_3 (?), Pu_5Ir_4 (?), $PuIr_2$ (?), $PuIr_3$ (?)	Am_xIr (?), $AmIr_2$ (?)	$CmIr_2$ (?)	$BkIr_2$ (?)	N/A	N/A	N/A	N/A	N/A	N/A

[a] See the notes for Table A.31

References

1. Lide DR (ed) (2010) CRC handbook of chemistry and physics, 90th edn. CRC Press, Boca Raton
2. Speight JG (ed) (2005) Lange's handbook of chemistry, 16th edn. McGraw-Hill, New York
3. Nekrasov BV (1973) Osnovy obschei khimii (Foundations of general chemistry), vol 1, 3rd edn. Khimiya, Moscow (in Russian)
4. Samsonov GV (ed) (1976) Svoistva elementov (Properties of elements), vol 1, 2nd edn. Metallurgiya, Moscow (in Russian)
5. Bushuev YuG, Persin MI, Sokolov VA (1994) Uglerod-uglerodnye kompozitsionnye materialy (Carbon-carbon composite materials). Metallurgiya, Moscow (in Russian)
6. Steurer W (1996) Crystal structure of the metallic elements. In: Cahn RW, Haasen P (eds) Physical metallurgy, vol 1, 4th edn. Elsevier Science BV, Amsterdam, pp 1–46
7. Cotton FA, Wilkinson G (1965) Advanced inorganic chemistry. Wiley, New York
8. Waseda Y, Hirata K, Ohtani M (1975) High-temperature thermal expansion of platinum, tantalum, molybdenum and tungsten measured by X-ray diffraction. High Temp High Press 7:221–226
9. Kotelnikov RB, Bashlykov SN, Galiakbarov ZG, Kashtanov AI (1968) Osobo tugoplavkie elementy i soedineniya (Extra refractory elements and compounds). Metallurgiya, Moscow (in Russian)
10. Martienssen W (2005) The elements. In: Martienssen W, Warlimont H (eds) Springer handbook of condensed matter and materials data. Springer, Berlin, pp 45–158
11. Marmer ÉN, Gurvich OS, Maltseva LF (1967) Vysokotemperaturnye materialy (High-temperature materials). Metallurgiya, Moscow (in Russian)
12. Cardarelli F (2008) Materials handbook, 2nd edn. Springer, London
13. Zefirov AP (ed), Veryatin UD, Mashirev VP, Ryabtsev NG, Tarasov VI, Rogozkin BD, Korobov IV (1965) Termodinamicheskie svoistva neorganicheskikh veschestv (Thermodynamic properties of inorganic substances). Atomizdat, Moscow (in Russian)
14. Leider HR, Krikorian OH, Young DA (1973) Thermodynamic properties of carbon up to the critical point. Carbon 11:555–563
15. Savvatimskii AI, Knyazkov AM (2011) Plavlenie izotropnogo grafita pri impulsnom nagreve (Melting isotropic graphite by impulse heating). Kratk Soobshch Fiz FIAN (1):41–44 (in Russian)
16. Panish MB, Reif L (1961) Vaporization of iridium and rhodium. J Chem Phys 34:1915–1918
17. Fomenko VS, Podchernyaeva IA (1975) Emissionnye i adsorbtsionnye svoistva veshchestv i materialov (The thermoionic emission and absorptance properties of substances and materials). Atomizdat, Moscow (in Russian)
18. Fomenko VS (1981) Emissionnye svoistva materialov (The thermoionic emission properties of materials). Naukova Dumka, Kyiv (in Russian)
19. Barin I (1995) Thermochemical data of pure substances, 3rd edn. VCH, Weinheim
20. Tumanov AT (ed) (1964) Konstruktsionnye materialy (Structural materials). Sovetskaya Entsiklopediya, Moscow (in Russian)
21. Mattes M, Keinert J (2005) Status of thermal neutron scattering data for graphite. IAEA Nuclear Data Section, Vienna
22. Mughabghab SF (2003) Thermal neutron capture cross sections resonance integral and G-factors. IAEA Nuclear Data Section, Vienna
23. Gordeev NV, Kardashev DA, Malyshev AV (1963) Yaderno-fizicheskie konstanty (Nuclear physics constants). Gosatomizdat, Moscow (in Russian)
24. Emsley J (1991) The elements, 2nd edn. Clarendon Press, Oxford
25. DoE Fundamentals Handbook (1993) Nuclear physics and reactor theory. US Department of Energy, Washington
26. Feates FS (1968) The diffusion of carbon in single crystal graphite. J Nucl Mater 27:325–330
27. Golovina ES, Chaplygina VS, Kotova LL (1970) Self-diffusion and temperature field in carbon particle reacting with gases. Carbon 8:125–129
28. Sach RS, Williams WJ (1974) The diffusion of ^{14}C in nuclear graphites. Carbon 12:425–432

29. Guillemot F, Boliveau M, Bohn M, Debuigne J, Ansel D (2001) On the diffusion in the Mo-Ta refractory system. Int J Refract Met Hard Mater 19:183–189
30. Neumann G, Tuijn C (2009) Self-diffusion and impurity diffusion in pure metals: handbook of experimental data. Pergamon Elsevier, Oxford
31. Mehrer H (2007) Diffusion in solids. Springer, Berlin
32. Gale WF, Totemeir TC (eds) (2004) Smithells metals reference book, 8th edn. Elsevier Butterworth Heinemann, ASM International Materials Information Society, Boston
33. Massalski TB, Subramanian PR, Okamoto H, Kacprzak L (eds) (1990) Binary alloy phase diagrams, 2nd edn. ASM International, Metals Park
34. Lyakishev NP (ed) (1996) Diagrammy sostoyaniya dvoinykh metallicheskikh sistem (Phase diagrams of binary metal systems), vol 1. Mashinostroenie, Moscow (in Russian)
35. Lyakishev NP (ed) (1997) Diagrammy sostoyaniya dvoinykh metallicheskikh sistem (Phase diagrams of binary metal systems), vol 2. Mashinostroenie, Moscow (in Russian)
36. Lyakishev NP (ed) (2001) Diagrammy sostoyaniya dvoinykh metallicheskikh sistem (Phase diagrams of binary metal systems), vol 3, Part 1. Mashinostroenie, Moscow (in Russian)
37. Lyakishev NP (ed) (2000) Diagrammy sostoyaniya dvoinykh metallicheskikh sistem (Phase diagrams of binary metal systems), vol 3, Part 2. Mashinostroenie, Moscow (in Russian)
38. Samsonov GV (ed) (1976) Svoistva elementov (Properties of elements), vol 2, 2nd edn. Metallurgiya, Moscow (in Russian)
39. Andrievskii RA, Spivak II (1989) Prochnost tugoplavkikh soedinenii i materialov na ikh osnove (Strength of refractory compounds and materials based on them). Metallurgiya, Chelyabinsk (in Russian)
40. Kosolapova TYa (1968) Karbidy (Carbides). Metallurgiya, Moscow (in Russian)
41. Kosolapova TYa, Andreeva TV, Bartnitskaya TB, Gnesin GG, Makarenko GN, Osipova II, Prilutskii ÉV (1985) Nemetallicheskie tugoplavkie soedineniya (Non-metallic refractory compounds). Metallurgiya, Moscow (in Russian)
42. Kosolapova TYa (ed) (1990) Handbook of high-temperature compounds: properties, production and applications. Hemisphere, New York
43. English JJ (1961) Binary and ternary phase diagrams of columbium, molybdenum, tantalum and tungsten. Report DMIC-152, Contract AF-33(616)-7747, pp 1–226. Defence Metals Information Center, Battelle Memorial Institute, Columbus
44. Samsonov GV, Serebryakova TI, Neronov VA (1975) Boridy (Borides). Atomizdat, Moscow (in Russian)
45. Samsonov GV (ed) (1978) Fiziko-khimicheskie svoistva okislov (Physico-chemical properties of oxides), 2nd edn. Metallurgiya, Moscow (in Russian)
46. Samsonov GV, Upadkhaya GS, Neshpor VS (1974) Fizicheskoe materialovedenie karbidov (Physical materials science of carbides). Naukova Dumka, Kyiv (in Russian)
47. Samsonov GV, Portnoy KI (1961) Splavy na osnove tugoplavkikh soedineniy (Alloys based on refractory compounds). Oborongiz, Moscow (in Russian)
48. Samsonov GV (1966) Berillidy (Beryllides). Naukova Dumka, Kyiv (in Russian)
49. Savitskii EM, Burkhanov GS (1971) Metallovedenie splavov tugoplavkikh i redkih metallov (Metallography of refractory and less-common metal alloys), 2nd edn. Nauka, Moscow (in Russian)
50. Savitskii EM, Tylkina MA, Povarova KB (1970) Rhenium alloys. IPST Press, Jerusalem
51. Goodwin F, Guruswamy S, Kainer KU, Kammer C, Knabl W, Koethe A, Leichtfried G, Schlamp G, Stickler R, Warlimont H (2005) Metals. In: Martienssen W, Warlimont H (eds) Springer handbook of condensed matter and materials data. Springer, Berlin, pp 161–430
52. Savitskii EM, Polyakova VP, Gorina NB, Roshan NR (1975) Metallovedenie platinovykh metallov (Metallography of platinum metals). Metallurgiya, Moscow (in Russian)
53. Savitskii EM (ed) (1984) Blagorodnye metally (Noble metals). Metallurgiya, Moscow (in Russian)
54. Gschneidner KA (1961) Rare earth alloys: a critical review of the alloy systems of the rare earth, scandium, and yttrium metals. Van Nostrand Reinhold, New York

Index (Physical Properties)

I. L. Shabalin, *Ultra-High Temperature Materials I*,
DOI: 10.1007/978-94-007-7587-9, © Springer Science+Business Media Dordrecht 2014

N

R

S

T

Index (Chemical Systems)

I. L. Shabalin, *Ultra-High Temperature Materials I*,
DOI: 10.1007/978-94-007-7587-9,

B

C

D

E

F

G

H

I

N

O

P

R